

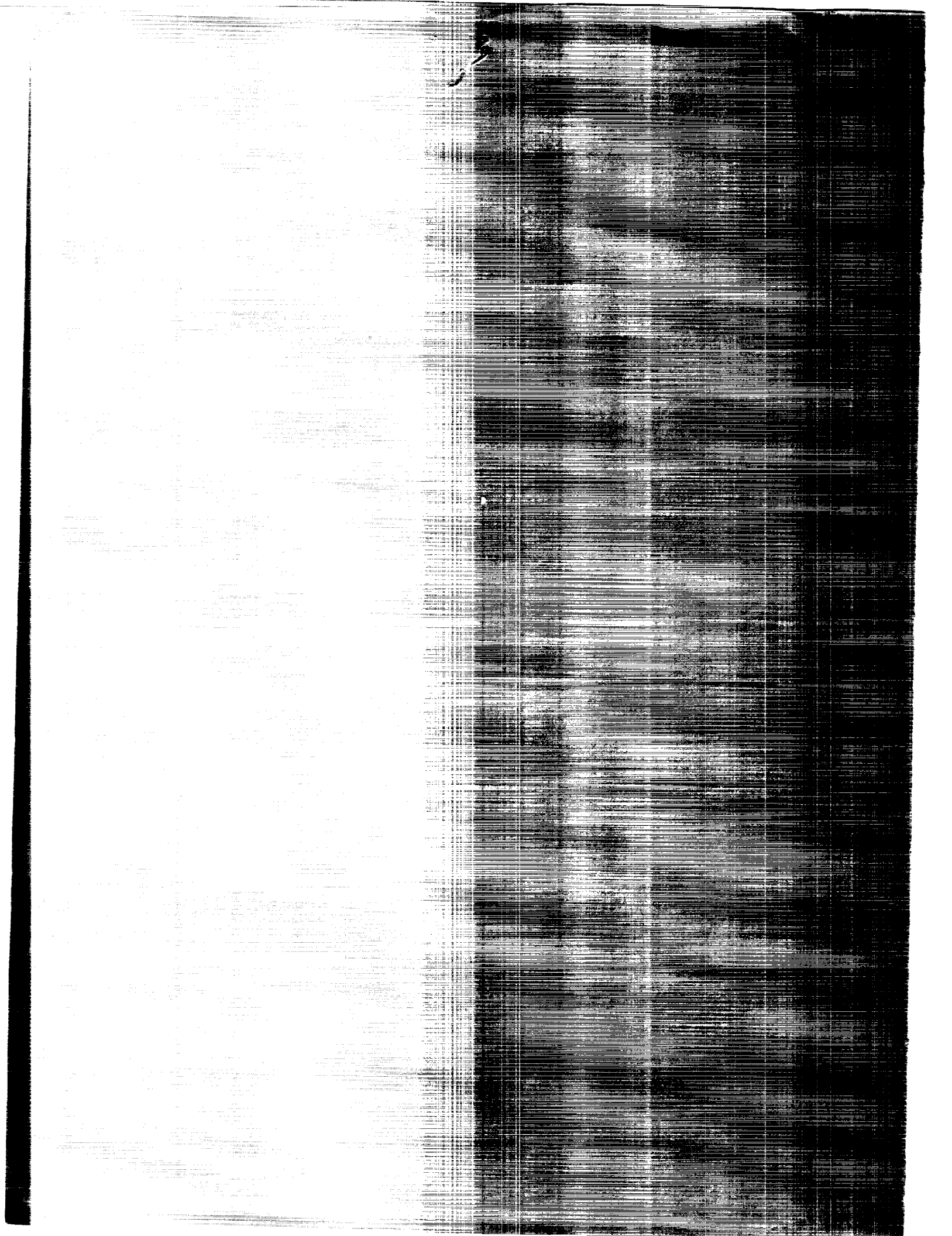
Primary Geology  
Program 288

(NASA-TM-4130) REPORTS OF PLANETARY GEOLOGY  
AND GEOPHYSICS PROGRAM, 1969 (NASA) 528 p  
CSCL 032

NASA-11

Unclas

11/71 0246022





NASA Technical Memorandum 4130

# Reports of Planetary Geology and Geophysics Program—1988

*NASA Office of Space Science and Applications  
Washington, D.C.*



National Aeronautics and  
Space Administration  
Office of Management  
Scientific and Technical  
Information Division

1989



## **Foreword**

This is a compilation of abstracts of reports from Principal Investigators of NASA's Office of Space Science and Applications, Solar System Exploration Division, Planetary Geology and Geophysics Program.

The purpose of this publication is to document in summary form research work conducted in this program over the past year (1988). Each report reflects significant accomplishments within the area of the author's funded grant or contract.

No attempt has been made to introduce editorial or stylistic uniformity; on the contrary, the style of each report is that of the Principal Investigator and may best portray his research.

Joseph Boyce  
Discipline Scientist  
Planetary Geoscience Programs

# CONTENTS

Foreword.....	iii
CHAPTER 1 - VENUS	
Basic Assemblages of Geologic Units in the Venus Northern Hemisphere..... J.W. Head	3
Morphologies of Ten Venusian Shields Between Lat 30° and 90° N..... G.G. Schaber and R.C. Kozak	6
Characteristics and Geologic/Terrain Associations of Small Dome-Like Hills on Venus..... J.C. Aubele	9
Geology of Southern Guinevere Planitia, Venus, Based on Analyses of Goldstone Radar Data..... R.E. Arvidson, J.J. Plaut, R.F. Jurgens, R.S. Saunders, and M.A. Slade	12
Clotho Tessera, Venus: A Fragment of Fortuna Tessera?..... R.C. Kozak and G.G. Schaber	13
Models of Venus Tectonics: Evaluation and Application to Tessera Terrain..... D.L. Bindschadler and J.W. Head	15
Venus Tessera as Analogs to Earth Oceanic Crust Formed at Spreading Centers..... J.W. Head	18
Eastern Aphrodite Terra, Venus: Evidence for Additional Divergent Plate Boundary Characteristics and Crustal Spreading from Diana Chasma to Atla Regio..... L.S. Crumpler and J.W. Head	21
Lakshmi Planum Volcanism: Style, Origin, and Relation to Other Volcanic Deposits on Venus..... K.M. Roberts and J.W. Head	24
Western Eistla Regio, Venus: Geology and Origin of an Equatorial Highland..... D.A. Senske and J.W. Head	26
Synthesis of Venus Equatorial Geology: Variations in Styles of Tectonism and Volcanism and Comparison with the Northern High Latitudes..... D.A. Senske and J.W. Head	28
Lakshmi Planum: A Distinctive Highland Volcanic Province..... K.P. Magee and J.W. Head	30
Multi-Stage Tectonic Evolution of Eastern Ishtar Terra, Venus..... R.W. Vorder Bruegge and J.W. Head	33
Spacing of Ridge Belts in the Plains-Ridge Belt Assemblage: Venus..... S.L. Frank and J.W. Head	36
Influence of Volatile Loss on the Mantle Temperature of Venus..... P.J. McGovern and S.C. Solomon	39

Tectonic Response to Mantle Dynamics in Venus.....	41
R.J. Phillips	
Lithospheric Flexure Beneath the Freyja Montes Foredeep, Venus: Constraints on Lithospheric Thermal Gradient and Heat Flow.....	43
S.C. Solomon and J.W. Head	
Implications of Gravity Modeling for a Thermal Isostasy Hypothesis for Bell Regio, Venus.....	46
S. Smrekar and R.J. Phillips	
Implications for Interpretation of Venera 15/16 and Magellan Data of Volcanic Terrains on Venus.....	48
L. Gaddis	

## CHAPTER 2 - OUTER PLANET SATELLITES AND RINGS

Dynamic Geophysics of Io.....	53
A.S. McEwen, J.I. Lunine, and M.H. Carr	
Icy Satellite Tectonics: Ariel, Tethys, and Ganymede.....	54
W.B. McKinnon, L.A.M. Benner, and P.M. Schenk	
Origin and Evolution of Pluto and Triton.....	57
W.B. McKinnon, A.C. Leith, and S. Mueller	
Volatile Processes in the Outer Solar System.....	60
J.I. Lunine	
Formation of Antipodal Terrains on Icy Satellites.....	63
A. Watts, R. Greeley, and H.J. Melosh	
Ridge and Trough Terrain in Elsinore Corona, Miranda.....	66
R. Pappalardo and R. Greeley	
Rheologies of Planetary Ices.....	69
W.B. Durham and S.H. Kirby	
Coupled Geophysical and Dynamical Processes on Icy Satellites.....	72
R. Greenberg	
The Tectonic and Igneous Evolution of Enceladus.....	75
S. Pozio and J.S. Kargel	
Icy Greenhouse on Europa.....	77
F.P. Fanale, and J.R. Salvail	
Laboratory Reflectance Spectra of Irradiated Ices: Applications to Europa.....	79
J.W. Boring	
Speculative Histories of the Uranian Satellite System.....	81
S.J. Peale	
Vacuum Weathering: A Newly Recognized Planetary Surface Process.....	82
D.B. Nash	

Charged-Particle Induced Alterations of Surfaces in the Outer Solar System.....	85
R.E. Johnson	
Color Changes in Elemental Sulfur Following X-Ray Exposure: Implications for Jupiter's Satellite Io.....	88
R.M. Nelson and W.D. Smythe	
Dynamics and Structure of Planetary Rings.....	91
R.G. French	
Planetary Ring Studies.....	92
J.N. Cuzzi, R.H. Durisen, and M.R. Showalter	
Numerical Simulations of Narrow Planetary Rings.....	95
R.A. Kolvoord and J.A. Burns	
Orbital Evolution of Circumplanetary Dust by Resonant Charge Variations.....	96
J.A. Burns and L.E. Schaffer	
Uranian Dust Ring: Have We Learned Anything from Models of Other Ethereal Rings?.....	97
J.A. Burns, J.N. Cuzzi, and L.E. Schaffer	
 CHAPTER 3 - COMETS AND ASTEROIDS	
Rotation of Halley's Comet.....	101
S.J. Peale and J. Lissauer	
On the Mass Density of Halley's Comet.....	102
S.J. Peale	
Solid State Problems in the Solar System.....	103
R. Smoluchowski	
Asteroid and Comet Flux in the Neighborhood of the Earth.....	105
E.M. Shoemaker, C.S. Shoemaker, and R.F. Wolfe	
Temporal and Spatial Distribution of Meteoroid Impacts Detected by the Lunar Seismic Network: A Summary Report.....	108
J. Oberst and Y. Nakamura	
Accumulation and Fragmentation Model of the Asteroid Belt.....	109
G.W. Wetherill	
Are Asteroids the Source of the Period of Late Heavy Bombardment in the Inner Solar System?.....	110
R.G. Strom	
Asteroid Collisional Evolution: The Holistic Approach.....	112
P. Paolicchi, A. Cellino, D. Davis, P. Farinella, and V. Zappalá	
An Integrated Model for Collisional Evolution of Asteroid Sizes and Spins.....	115
D.R. Davis, P. Farinella, and P. Paolicchi	
Collisional Disruption Experiments: Impact Strength Analysis and Velocity Distributions.....	116
E.V. Ryan and D.R. Davis	

The Water Regime of Asteroid (1) Ceres.....	119
F.P. Fanale and J.R. Salvail	
Loss of Water from Phobos.....	121
F.P. Fanale and J.R. Salvail	
Meteorite Spectroscopy and Characterization of Asteroid Surface Materials.....	123
M.J. Gaffey	
The CV/CO Chondrites: Discovery of Asteroidal Analogs.....	126
J.F. Bell	
The H-G Asteroid Magnitude System: Mean Slope Parameters.....	127
A.W. Harris	
Application of Photometric Models to Asteroids.....	129
E. Bowell, B. Hapke, K. Lumme, A. Harris, D. Domingue, and J. Peltoniemi	
Fitting Theoretical Photometric Functions to Asteroid Phase Curves.....	130
D. Domingue and B. Hapke	
Asteroid Lightcurve Inversion.....	131
S.J. Ostro	

#### CHAPTER 4 - COSMOGONY AND DYNAMICS

The Role of Interstellar Inheritance in Solar System Chemistry .....	137
D.J. Stevenson	
Accumulation of the Earth from Runaway Embryos.....	139
G.W. Wetherill	
Planetesimal Accretion.....	141
D. Spaute	
Planetary Accretion by Runaway Growth: Formation of the Earth.....	142
C. Patterson and D. Spaute	
Numerical N-Body Simulation of the Accretion Process of the Terrestrial Planets.....	143
N. Namiki and T. Matsui	
Planetesimal Accretion Studies: Effects of Numerical Parameters.....	146
D. Spaute, D.R. Davis, and S.J. Weidenschilling	
Constraints on the Magnitude and Time Dependence of the Intense Early Bombardment.....	149
D.H. Grinspoon and W.K. Hartmann	
Planetesimal Effects on Planet Orbits, Spin, and Heating.....	150
W.M. Kaula	
Three-Dimensional Cartesian Code for Protosolar Collapse.....	153
E. Myhill	
3D Solar Nebula Models: Implications for Earth Origin.....	156
A.P. Boss	



Particle-Gas Dynamics in the Protoplanetary Nebula.....	158
J.N. Cuzzi, J.M. Champney, T.J. Coakley, and A.R. Dobrovolskis	
Atomic and Plasma Processes Affecting Angular Momentum Transfer in the Early Solar System.....	161
W.I. Newman	
Computer Search for Stable Orbits Between Jupiter and Saturn.....	162
W. M. Weibel, W.M. Kaula, and W.I. Newman	
Angular Momentum Transport by Gravitational Torques in the Early Solar Nebula.....	164
A.P. Boss	
Rotational Dynamics of Mercury and the State of Its Core.....	167
S.J. Peale	
Rapid Jupiter Formation and the Early Solar Nebula.....	168
A.P. Boss	
The Dynamical Evolution of the Protosolar Nebula.....	169
S.P. Ruden and J.B. Pollack	
Some Unsolved Problems in Evolutionary Dynamics in the Solar System.....	170
S.J. Peale	
Viscosity and Mass Transport in Non-Uniform Keplerian Disks.....	171
G.W. Ojakangas and R. Greenberg	
Fractal Aggregates and Planetesimal Formation.....	173
S.J. Weidenschilling	
Accretion of the Earth.....	174
S.J. Weidenschilling	
Thermal and Dynamical Processes in the Evolution of Planets and Satellites.....	177
G. Schubert	
Solar System Dynamics.....	180
J. Wisdom	

## CHAPTER 5 - PLANETARY INTERIORS, PETROLOGY, AND GEOCHEMISTRY

Composition and Dynamics of the Earth's Mantle.....	185
R. Jeanloz	
Ultrahigh P-T Experiments, the Core-Mantle Boundary, and Geomagnetic Variations: A New Electromagnetism of the Earth.....	186
R. Jeanloz, X. Li, E. Knittle, and Q. Williams	
Giant Impact Theory of the Moon's Origin: Implications for the Thermal State of the Early Earth.....	187
H.J. Melosh and M.E. Kipp	
A Well Stirred Magma Ocean: Implications for Crystal Settling and Chemical Evolution.....	190
W.B. Tonks and H.J. Melosh	

Solubility of Noble Gases and Nitrogen in Silicate Melts to 5000 Bars.....	193
E. Stolper and M.R. Carroll	
Primary Martian Magmas.....	196
J.R. Holloway	
The Melting of $\text{MgSiO}_3$ and $(\text{Mg,Fe})\text{SiO}_3$ by Laser Heating in the Diamond Anvil Cell at Pressures Between 300 kbar and 600 kbar.....	197
W.A. Bassett and M.S. Weathers	
High Pressure Cosmochemistry of Major Planetary Interiors: Laboratory Studies of the Water-Rich Region of the System Ammonia-Water.....	198
M. Nicol, S. Boone, H. Cynn, and A. Koumvakalis	
Mantle Convection on Venus and Mars.....	200
W.S. Kiefer and B.H. Hager	
Estimating Lithospheric Thermal Gradient on Mars from Elastic Lithosphere Thickness: New Constraints on Heat Flow and Mantle Dynamics.....	203
S.C. Solomon and J.W. Head	
Research on Structure and Evolution of Planetary Interiors.....	206
G. Schubert	
Mercury: A Key to Understanding the Formation and Evolution of the Terrestrial Planets.....	207
R.G. Strom	
Implications of Convection in the Moon and the Terrestrial Planets.....	209
D.L. Turcotte	
Olivine Alteration Phases in Shergottite ALHA 77005: Information from 4.2°K Mossbauer Spectra.....	211
R.G. Burns	
Oxidized Olivines on Mars: Spectroscopic Investigations of Heat-Induced Aerial Oxidation Products.....	213
K.S. Bartels and R.G. Burns	
Sulfide Mineralization Related to Early Crustal Evolution of Mars.....	215
R.G. Burns and D.S. Fisher	
Weathering of Sulfides on Mars.....	217
R.G. Burns and D.S. Fisher	
Acid Weathering on Mars: Spectroscopic Investigations of Sulfuric Acid-Degraded Olivines and Sulfides.....	220
D.S. Fisher and R.G. Burns	
Chemical Weathering Under Sub-Freezing Conditions: Special Effects of Ice Nucleation.....	222
J.L. Gooding	
Depth to Unoxidized Material in the Martian Regolith.....	224
C.F. Chyba, S.W. Squyres, and C. Sagan	

## CHAPTER 6 - SPECTROSCOPY AND REMOTE SENSING

Geology Remote Sensing Field Experiment (GRSFE)..... R.E. Arvidson and E.A. Guinness	229
Photometry and Surface Properties of the Galilean Satellites..... B.J. Buratti	230
Albedo and Color Maps of Mimas, Enceladus, Tethys, Rhea, and Dione..... B.J. Buratti, J.A. Mosher, and T.V. Johnson	231
Backscattering Frost in the Outer Solar System..... A. Verbiscer, P. Helfenstein, and J. Veverka	233
The Absorption Coefficient of Liquid and Frozen CH <sub>4</sub> from 0.5 to 1.0 Microns..... U. Fink and W. Grundy	236
Analysis of Planetary Photometry with Hapke's Model: A Working Analytical Strategy..... P. Helfenstein and J. Veverka	237
Mars' Global Color and Albedo..... A.S. McEwen, L.A. Soderblom, J.D. Swann, and T.L. Becker	240
Regional Albedo and Photometric Studies of Mars: Viking IRTM Observations..... S.W. Lee and R.T. Clancy	242
Multispectral Study of Valles Marineris..... P.E. Geissler, R.B. Singer, and B.K. Lucchitta	245
Valles Marineris: Compositional Constraints from Viking Multispectral Images..... P.E. Geissler, R.B. Singer, and B.K. Lucchitta	246
Isolation of Compositional Variance from Viking Lander Multispectral Images..... M.O. Smith and J.B. Adams	247
Viking Optical and Thermal Evidence for Widespread Duricrust Substrate on Mars..... E.A. Guinness and R.E. Arvidson	250
An Independent Test of Reflection Theories for Intimate Mixtures through Monte Carlo Computer Simulations..... J.W. Boardman and B.M. Jakosky	252
Seeing Through the Dust and Alteration Products of Mars..... C.M. Pieters	253
Determination of Regional Surficial Geology for Aeolian Terrains Utilizing a Linear Mixing Algorithm for Remote Sensing Data..... G. Blount, R. Greeley, P. R. Christensen, N. Lancaster, J. B. Adams, and M. O. Smith	255
Thermal Conductivity and Near-Surface Temperature Gradients in Thermal-Infrared Spectroscopy of Planetary Surfaces..... B.M. Jakosky	257
A Search for Subsurface Ice on Mars Using Viking Thermal Mapper Observations..... D.A. Paige	258

CO <sub>3</sub> <sup>2-</sup> - and SO <sub>4</sub> <sup>2-</sup> - Bearing Anionic Complexes Detected in Martian Atmospheric Dust.....	261
T. Roush, J. Pollack, C. Stoker, F. Witteborn, J. Bregman, D. Wooden, and D. Rank	
Scapolite on Mars.....	264
R.N. Clark, G.A. Swayze, R.B. Singer, and J. Pollack	
Mid-Infrared (2.1-25.0 $\mu$ m) Spectroscopic Studies.....	267
J.W. Salisbury	
Systematics of the 1.0 $\mu$ m Absorption Band in Reflectance Spectra of Actinolite .....	270
J.F. Mustard, C.M. Pieters, and S.F. Pratt	
Mathematical Deconvolution of Mineral Absorption Bands.....	272
J.M. Sunshine, C.M. Pieters, and S.F. Pratt	
The Fe-Al Relation of Lunar Soils and Orbital Chemical Data: Implications for Al Abundances Estimated from Apollo Orbital Gamma-Ray Data.....	274
P.D. Spudis, P.A. Davis, and B. Pattanaborwornsak	
Compositional Stratigraphy of the Lunar Highland Crust.....	276
C.M. Pieters	
Results of a Remote Sensing Analysis of the Alphonsus Crater Region.....	278
C.R. Coombs, B.R. Hawke, P.G. Lucey, and J.W. Head	
A Remote Sensing Analysis of Crüger Crater and Vicinity on the Moon.....	281
B.R. Hawke, C.R. Coombs, and P.G. Lucey	

## CHAPTER 7 - RADAR APPLICATIONS

New Arecibo High-Resolution Radar Images of Venus: Preliminary Interpretation.....	287
D.B. Campbell, A.A. Hine, J.K. Harmon, D.A. Senske, R.W. Vorder Bruegge, P. C. Fisher, S. Frank, and J.W. Head	
Martian Quasi-Specular Echoes: Preliminary 1986 Results.....	290
T.W. Thompson and H.J. Moore	
Analysis of 1971 and 1973 Mars Goldstone Data.....	293
A.P. Zent, F.P. Fanale, and L.E. Roth	
Developments in the Buried-Crater Model for Radar Echoes from Icy Moons.....	295
E.M. Gurrola and V.R. Eshleman	
Numerical Modeling of Radiowave Scattering.....	296
R.A. Simpson and G.L. Tyler	
Radar Scattering from Desert Terrains, Pisgah/Lavic Region, California.....	299
J.J. Plaut, J.J. vanZyl, and R.E. Arvidson	
Comparison of TIMS and Airborne Imaging Radar Data over the Pisgah Volcanic Flow and Adjacent Lavic Lake Playa.....	301
S.J.B. Petroy, R.E. Arvidson, and A.B. Kahle	

## CHAPTER 8 - FLUVIAL, PERIGLACIAL, AEOLIAN, AND MASSWASTING PROCESSES

Distinguishing the Morphology of Sapping- and Runoff-Dominated Valleys on Earth and Mars.....	307
R.C. Kochel and S.M. Orbock Miller	
Geothermal Hot Springs as an Alternative Hypothesis for Small Valley Origins.....	310
G.R. Brakenridge	
Morphometry of Planimetric Landforms.....	313
A.D. Howard	
Fluvial Processes: Toward a Martian Paradigm.....	316
V.R. Baker and V.C. Gulick	
Simulation Models of Scarp and Valley Development.....	319
A.D. Howard	
An Unusual Martian Channel.....	322
D.H. Scott and M.G. Chapman	
Release of Martian Catastrophic Floods by Fracture Discharge from Volcanotectonic Regions.....	323
K.L. Tanaka and D.J. MacKinnon	
Lower Maja Vallis.....	325
J.W. Rice, S.M. Archibald, and R.A. De Hon	
Hydrology of a Flow Event in Kasei Valles, Mars.....	326
M.S. Robinson and K.L. Tanaka	
Kasei Valles, Mars: Formed by Flood or Ice?.....	328
B.K. Lucchitta	
Water of the Elysium Basin, Mars: Volumetric Analysis and Sources.....	331
D.H. Scott, K.L. Tanaka, and M.G. Chapman	
Valley Terminal Deposits: The Martian Sedimentary Record.....	332
R.A. De Hon	
Ephemeral Martian Lakes: Temporary Ponding and Local Sedimentation.....	334
R.A. De Hon	
Water Wave Dynamics in Martian Gravity.....	336
T.J. Parker	
A Kinematic Wave Model for Catastrophic Flooding on Mars .....	339
S. Baloga and T. Parker	
Mechanisms of Resurfacing in the Amenthes and Tyrrhena Cratered Highlands of Mars.....	342
T.A. Maxwell and R.A. Craddock	
Martian Sublimation Rates.....	344
G.D. Clow and R.M. Haberle	
Laboratory Studies of Sublimation of Ice/Silicate Mixtures.....	346
J. Moore	

Ground Ice Along the Northern Highland Scarp, Mars.....	349
B.K. Lucchitta and M.G. Chapman	
Size-Mobility Relations in Valles Marineris Landslides, Mars.....	351
A.S. McEwen	
Miniature Analog of Spur-and-Gully Landforms in Valles Marineris Scarps.....	355
A.D. Howard	
Preliminary Estimates of Sediment Volume in the North Polar Sand Seas of Mars.....	358
N. Lancaster and R. Greeley	
Comparison of Martian Aeolian Features and Results from the Global Circulation Model.....	361
R. Greeley, A. Skyeck, and J. B. Pollack	
Rock Populations as Indicators of Geologic Processes.....	363
M.C. Malin	
Applications of Grain-Pivoting and Sliding Analyses to Selective Entrainment of Gravel and to Flow-Competence Evaluations.....	366
P.D. Komar and Z. Li	
Grain-Size Variations During Transport and the Equal Mobility of Gravels in Oak Creek, Oregon.....	367
P.D. Komar and S. Shih	
Flow-Competence Evaluations and the Non-Equal Mobility of Gravels in Oak Creek, Oregon.....	368
P.D. Komar	

## CHAPTER 9 - VOLCANIC PROCESSES AND LANDFORMS

Rheological Extremes of Cryogenic Liquids on Icy Satellites .....	371
J.S. Kargel and S.K. Croft	
Can We Radiometrically Date Cryovolcanic Flows on Icy Satellites?.....	373
J.S. Kargel	
Characterization of Small Scale Properties of Basaltic Lava Plains: Application to Mars Rover Sample Return Missions.....	375
J.C. Aubele and L.S. Crumpler	
Erosional and Depositional Processes in the Martian Heavily-Cratered Terrain.....	377
J. Moore	
Mars: Volcanism in the Valles Marineris Overlooked?.....	380
B.K. Lucchitta	
Late Epochs of Widespread Gradation on Mars.....	382
J.A. Grant and P.H. Schultz	
Origin of the Martian Highland Paterae: Consideration of Eruptive Activity at Hadriaca Patera and Tyrrhena Patera.....	384
D.A. Crown and R. Greeley	
Martian and Terrestrial Lava Flows .....	387
H.J. Moore and J.A. Ackerman	

Methods for Estimating Eruption Rates of Planetary Lava Flows.....	390
J. Crisp and S. Baloga	
Eruptive Conditions and Volcano Morphology.....	393
S.B. Posin and R. Greeley	
Lunar Pyroclastic Deposits: Their Resource Potential.....	396
B.R. Hawke, C.R. Coombs, and B. Clark	
A Search for Intact Lava Tubes on the Moon.....	399
C.R. Coombs and B.R. Hawke	
Terrestrial Analogs to Lunar Sinuous Rilles: Kauhako Conduit System, Kalaupapa, Molokai, and Other Hawaiian Lava Channels.....	402
C.R. Coombs and B.R. Hawke	
A Geologic Study of Picacho Butte and Vicinity, Arizona.....	405
A.P. Kisiel and J.S. King	
Volcanism and Tectonism of the Colorado Plateau-Basin and Range Transition Zone of West-Central Arizona: Implications for the Martian Tharsis Uplift.....	408
A.M. Simmons and J.S. King	
The Changbaishan Volcanoes of Eastern China.....	411
M. Feny, J. Li, and J.L. Whitford-Stark	
Laboratory Simulations of Lava Flows with Solid Crusts.....	414
J. Fink and R. Griffiths	
Composition and Textural Variations in Glass Mountain, Calif. Lava: Evidence from Thermal Spectroscopy.....	416
J. Ondrusek, P. Christensen, and J. Fink	

## CHAPTER 10 - CRATERING PROCESSES AND CHRONOLOGIES

Giant Impact Theory of the Moon's Origin: First 3-D Hydrocode Results.....	419
H.J. Melosh and M.E. Kipp	
Earth Rocks on Mars: Must Planetary Quarantine Be Rethought?.....	421
H.J. Melosh	
Atmospheric Erosion by High Speed Impact Ejecta.....	424
H.J. Melosh and A.M. Vickery	
Atmospheric Erosion by Impacts: An Analytic Investigation.....	425
A.M. Vickery and H.J. Melosh	
Was the Early Atmosphere of Mars Sustained by Impact-Induced Release of CO <sub>2</sub> ?.....	427
M.H. Carr	
Climatic Effects of Episodic Release of SO <sub>2</sub> on Mars.....	429
S.E. Postawko and F.P. Fanale	



Impact Induced Devolatilization of Water in Serpentine and Meteorites and D/H Ratio in Evolving Planetary Atmospheres.....	431
J.A. Tyburczy, R.V. Krishnamurthy, S. Epstein, and T.J. Ahrens	
Impact Erosion of Mars' Atmosphere: An Analytic Model.....	434
H.J. Melosh and A.M. Vickery	
The Martian Impact Cratering Record.....	437
R.G. Strom, N.G. Barlow, and S.K. Croft	
Crater Saturation Equilibrium in the Solar System: New Evidence .....	439
W.K. Hartmann	
Factors Controlling Impact Ejecta Emplacement on Mars.....	442
P.H. Schultz	
Crater Scaling, Calculations with Variable Gravity, and Crustal Strength .....	444
J.D. O'Keefe and T.J. Ahrens	
Multi-Ring Basins on Mars: Geology, Structure, and Statistics.....	447
R.A. Schultz and H.V. Frey	
Overlapping Large Impacts and the Origin of the Northern Lowlands of Mars.....	449
H. Frey and R. Schultz	
The Cratering Record of Ganymede and Callisto: Evidence for the Character of the Crater-Forming Impactor Populations.....	451
S.L. Murchie, J.W. Head, and J.B. Plescia	
Ganymede: "Moat" Craters Compared with Palimpsests and Basins.....	454
B.K. Lucchitta and H.M. Ferguson	
Stratigraphy and Cratering History of the Moon: Our Understanding 20 Years After Apollo 11.....	457
P.D. Spudis	
The Lunar Crisium Basin: Geology, Rings, and Deposits.....	459
P.D. Spudis, B.R. Hawke, and P.G. Lucey	
A New Estimate of the Meteoroid Impact Flux on the Moon.....	461
J. Oberst and Y. Nakamura	
Phobos: Comparison of Small Craters on Phobos and the Moon.....	463
W.K. Hartmann	
Non-Random Cratering Flux in Recent Time.....	466
P.H. Schultz and S. Posin	
Sources of Clasts in Impact Melts.....	468
K. McCormick, G.J. Taylor, K. Keil, P.D. Spudis, R.A.F. Grieve, and G. Ryder	
Jetting and the Origin of Tektites.....	470
A.M. Vickery	
Jetting: A Semi-Analytic Approach.....	472
A.M. Vickery	

Intense Early Bombardment and Its Effects on Primordial Earth .....	473
D.H. Grinspoon and W.K. Hartmann	
Effect of Early Impact Cratering on Growth of the Earth's Crust.....	474
W.K. Hartmann	
Protracted Global Catastrophes from Oblique Impacts.....	475
P.H. Schultz and D.E. Gault	
Catastrophic Impacts in Planetary Evolution.....	477
C.R. Chapman	
Loss of Large Craters in the Terrestrial Impact Record.....	478
R.W. Wichman and P.H. Schultz	
An Impact Interpretation of the Proterozoic Bushveld-Vredefort Complexes, South Africa.....	480
W.E. Elston and D. Twist	
The Erosional State and Style of Meteor Crater, Arizona.....	483
J.A. Grant and P.H. Schultz	
Effects on Ambient Magnetic Fields and Plasma of the Expanding Vapor Cloud Produced in Lunar Basin-Forming Impacts.....	485
L.L. Hood and Z. Huang	
Magnetic Probing of Early-Time Impact Phenomena.....	487
D.A. Crawford, P.H. Schultz, and L.J. Srnka	
 CHAPTER 11 - STRUCTURE AND TECTONICS	
Discontinuities in the Shallow Martian Crust.....	491
P.A. Davis and M.P. Golombek	
The Shallow Structure of the Martian Lithosphere in the Vicinity of the Ridged Plains.....	493
M.T. Zuber and L.L. Aist	
A Reevaluation of Long-Wavelength Stress Models for Mars.....	495
W.B. Banerdt and M.P. Golombek	
Involvement of the Lithosphere in the Formation of Wrinkle Ridges on Mars.....	498
M. Golombek, J. Suppe, W. Narr, J. Plescia, and B. Banerdt	
Chronology and Global Distribution of Fault and Ridge Systems on Mars.....	501
D.H. Scott and J.M. Dohm	
Strike-Slip Faulting in the Ridged Plains of Mars.....	503
R.A. Schultz	
Striked-Slip Faulting Associated with the Folded Columbia River Basalts: Implications for the Deformed Ridged Plains of Mars .....	506
T.R. Watters and M.J. Tuttle	
Periodically Spaced Wrinkle Ridges on the Tharsis Plateau of Mars.....	509
T.R. Watters	

Resurfacing in Coprates and Thickness of the Ridged Plains.....	511
H. Frey and T.D. Grant	
Crosscutting Periodically Spaced First-Order Ridges in the Ridged Plains of Hesperia Planum: Another Case for a Buckling Model.....	514
T.R. Watters and D.J. Chadwick	
The Olympus Mons Scarp and Aureole: A Structural and Rheological Model for Their Formation.....	517
A. Borgia	
Geometry of Stresses Around Tharsis on Mars.....	520
M.P. Golombek	
Faulting and Its Relation to Volcanism: Mars Western Equatorial Region.....	523
D.H. Scott and J. Dohm	
Fault and Ridge Systems: Historical Development in Western Region of Mars.....	526
D.H. Scott and J. Dohm	
An Ancient Valles Marineris?.....	530
R.W. Wichman and P.H. Schultz	
Structural Mapping and Interpretation of Valles Marineris, Mars.....	532
R.A. Schultz	
Quantitative Volumetric Analyses of Valles Marineris of Mars.....	534
S.S.C. Wu, P.A. Garcia, and A. Howington-Kraus	
Canyon Structure in the Hebes-Juventae-Gangis Area, Mars.....	537
S.K. Croft	
Do Pit-Crater Chains Grow Up to be Valles Marineris Canyons? .....	539
R.A. Schultz	
Origin of the Martian Crustal Dichotomy: A Review.....	541
G.E. McGill	
Structural Modification Along the Cratered Terrain Boundary, Eastern Hemisphere, Mars.....	543
T.A. Maxwell	
Geologic Evolution of the Highland/Lowland Transition Zone in the Ismenius Lacus Quadrangle, Mars.....	545
A. M. Dimitriou	
Timing of Resurfacing Events in the Amenthes and Tyrrhena Cratered Highlands of Mars.....	547
R.A. Craddock and T.A. Maxwell	
Geologic Evidence Supporting an Endogenic Origin for the Martian Crustal Dichotomy.....	549
G.E. McGill	
Terrestrial Analogues for Planetary Extensional Structures.....	551
G.E. McGill	
Planetary Response of Thick Lithospheres to Loading.....	554
D.M. Janes and H.J. Melosh	

Early Tectonic Processes Around Martian Multi-Ring Basins .....	556
R.W. Wichman and P.H. Schultz	
Tectonic Response of One-Plate Planets to Loads: Variability Due to Load Width, Lithospheric Thickness, and Planetary Composition.....	558
D.M. Janes and H.J. Melosh	
The Importance of an Elastic Lithosphere for Crater Retention on Icy Bodies.....	559
V.J. Hillgren and H.J. Melosh	
Geology and Deposits of the Lunar Nectaris Basin.....	561
P.D. Spudis, B.R. Hawke, and P.G. Lucey	
Shallow Moonquakes—Extraterrestrial Analog of Intraplate Earthquakes.....	563
Y. Nakamura and J. Oberst	

## CHAPTER 12 - GEOLOGIC MAPPING, CARTOGRAPHY, AND GEODESY

New Geologic Maps of the Uranian Satellites Titania, Oberon, Umbriel, and Miranda.....	567
S.K. Croft	
The Volcanic and Tectonic Evolution of Dark Terrain on Ganymede.....	568
S.L. Murchie, J.W. Head, and J.B. Plescia	
Polar Deposits of Mars: North-South Comparisons.....	571
P.C. Thomas	
North Kasei Valles—Geology and Hydrology.....	573
M.G. Chapman and D.H. Scott	
Stratigraphy of the Kasei Valles Region, Mars.....	575
M.S. Robinson and K.L. Tanaka	
Geologic Mapping of Southern Mangala Valles, Mars.....	578
J.R. Zimbelman	
Preliminary Geologic Mapping in the Western Utopia Planitia Region of Mars.....	580
S.H. Williams and J.R. Zimbelman	
Volcanotectonic Patterns on the Southeast Flank of Alba Patera.....	583
C.D. Condit	
Geology of the Connolly Basin Impact Structure, Western Australia.....	586
E.M. Shoemaker and C.S. Shoemaker	
Gravity Investigation of the Connolly Basin Impact Structure, Western Australia.....	588
E.M. Shoemaker, C.S. Shoemaker, and J.B. Plescia	
Topographic and Shaded Relief Maps of Part of the Northern Hemisphere of Venus.....	590
R.M. Batson, P.M. Bridges, R. Jordan, and H.F. Morgan	
Atlas of the Solar System.....	591
R.M. Batson and H.R. Morgan	

Mapping Irregular Satellites.....	592
R.M. Batson, K. Edwards, and T.C. Duxbury	
Publication of Mars Control Network.....	599
S.S.C. Wu, F.J. Schafer, A. Howington-Kraus, and J. Billideau	
Distortions in Lunar Orbiter Photographs.....	600
S.S.C. Wu, Y. Kim, P.A. Garcia, and A. Howington-Kraus	
Photogrammetric Mapping of Ariel Using Voyager 2 Images.....	601
S.S.C. Wu and F.J. Schafer	
A Unified Lunar Control Network.....	602
M.E. Davies, T.R. Colvin, and D.L. Meyer	
The Control Network of Mars: February 1989.....	605
M.E. Davies	
The Control Networks of the Satellites of Jupiter and Saturn.....	607
M.E. Davies	

#### CHAPTER 13 - SPECIAL PROGRAMS

Image Retrieval and Processing System (IRPS) for the Regional Planetary Image Facilities.....	611
S. Slavney, E.A. Guinness, B. Weiss, M. Dale-Bannister, and R.E. Arvidson	
Viking Orbiter Image CDROM Production.....	613
A. Guinness, S. Slavney, and R.E. Arvidson	
Mars Sample Return: A General Philosophy for Site Selection.....	615
D.H. Scott	
The Galilean Satellite Geological Mapping Program, 1988.....	617
B.K. Lucchitta	
Planetary Geology and Geophysics Program: A Summary, FY 88.....	618
J.R. Underwood, Jr.	

#### CHAPTER 14 - LATE ABSTRACTS

Author Index.....	635
-------------------	-----



## CHAPTER 1

### VENUS





The Venera 15/16 missions provided altimetry and high resolution images of the northern 20% of the surface of Venus and this complemented moderate resolution altimetry coverage and permitted the detailed geologic mapping and analysis<sup>1</sup> of a portion of Venus previously viewed at lower resolution by Pioneer Venus. The detailed geologic map<sup>1</sup>(Fig. 1) outlines the distribution of geologic units, tectonic structure, and the distribution of craters of impact origin, permitting an estimate of the average age of the mapped area of about one billion years<sup>1</sup>. Approximately 70 percent of the mapped area is dominated by plains of apparent volcanic origin, while units of tectonic origin make up less than 30 percent. Examination of the distribution of geologic units shows that they do not occur randomly. On the basis of the areal distribution of geologic units, six basic assemblages can be defined (Fig. 1), where an assemblage is a region of the planet characterized by the dominance of single types of units (for example, different plains units), or the association of several units (for example, plains and corona), in a manner different than adjacent terrain.

The six assemblages are characterized by distinctive and differing geological and tectonic styles as follows: Plains Assemblage- dominated by lowland smooth plains and lowland rolling plains interpreted to be of volcanic origin; Plains-Corona Assemblage- dominated by lowland smooth plains and lowland rolling plains interpreted to be of volcanic origin, at least ten coronae structures concentrated in the northern half of the region, and at least five large volcanoes, generally concentrated in the southern and western half of the region; Plains-Ridge Belt Assemblage- dominated by lowland smooth plains and lesser amounts of lowland rolling plains, major occurrences of ridge belts, and very minor and patchy occurrences of tessera; Plains-Corona-Tessera Assemblage- dominated by approximately equal amounts of lowland smooth plains and lowland rolling plains, at least five coronae concentrated in the northern part of the region, a small number of volcanoes, also in the northern part of the region, and numerous small patches of tessera scattered throughout the region; Tessera-Ridge Belt Assemblage- dominated by a few large patches (Fortuna, Laima, Tellus) and several smaller patches (Dekla, Meni) of tessera, ridge belts generally arrayed in an angular and often orthogonal pattern different than the fan-shaped pattern of the Plains-Ridge Belt Assemblage, lowland rolling plains and lesser amounts of lowland smooth plains, and an upland rise (Bell Regio); Tessera-Mountain Belt Assemblage- centered on the two volcanoes Colette and Sacajawea in Lakshmi Planum, and characterized by surrounding terrain types of mountain belt/tessera pairs, with the tessera on the outboard side: Danu (S), Akna (W), Freyja (N), and Maxwell Montes (E).

These assemblages show that the dominant surface geological processes differ markedly from region to region on Venus and that the assemblages can be characterized in a tectonic sense as having been formed by either predominantly horizontally directed deformational forces (Plains-Ridge Belt; Tessera-Mountain Belt) or predominantly vertically directed deformational forces (coronae and domal uplifts in the Plains-Corona and Plains-Corona-Tessera assemblages). These characteristics and relationships indicate that the tectonic style of Venus<sup>2</sup> is not dominated by one style of activity, movement, or deformation, but contains elements of several styles. These include: 1) thermal uplift and vertical motion possibly related to hot spots or mantle plumes at several different scales<sup>3</sup> as seen in the domal uplifts, coronae, and volcanoes; 2) regional lateral motion including extension and compression at a range of scales<sup>4</sup> as seen in the ridge belts, rifts, mountain belts, and in the more highly deformed tessera, and 3) gravitational relaxation<sup>5</sup> as seen in local areas around coronae and possibly in the tessera.

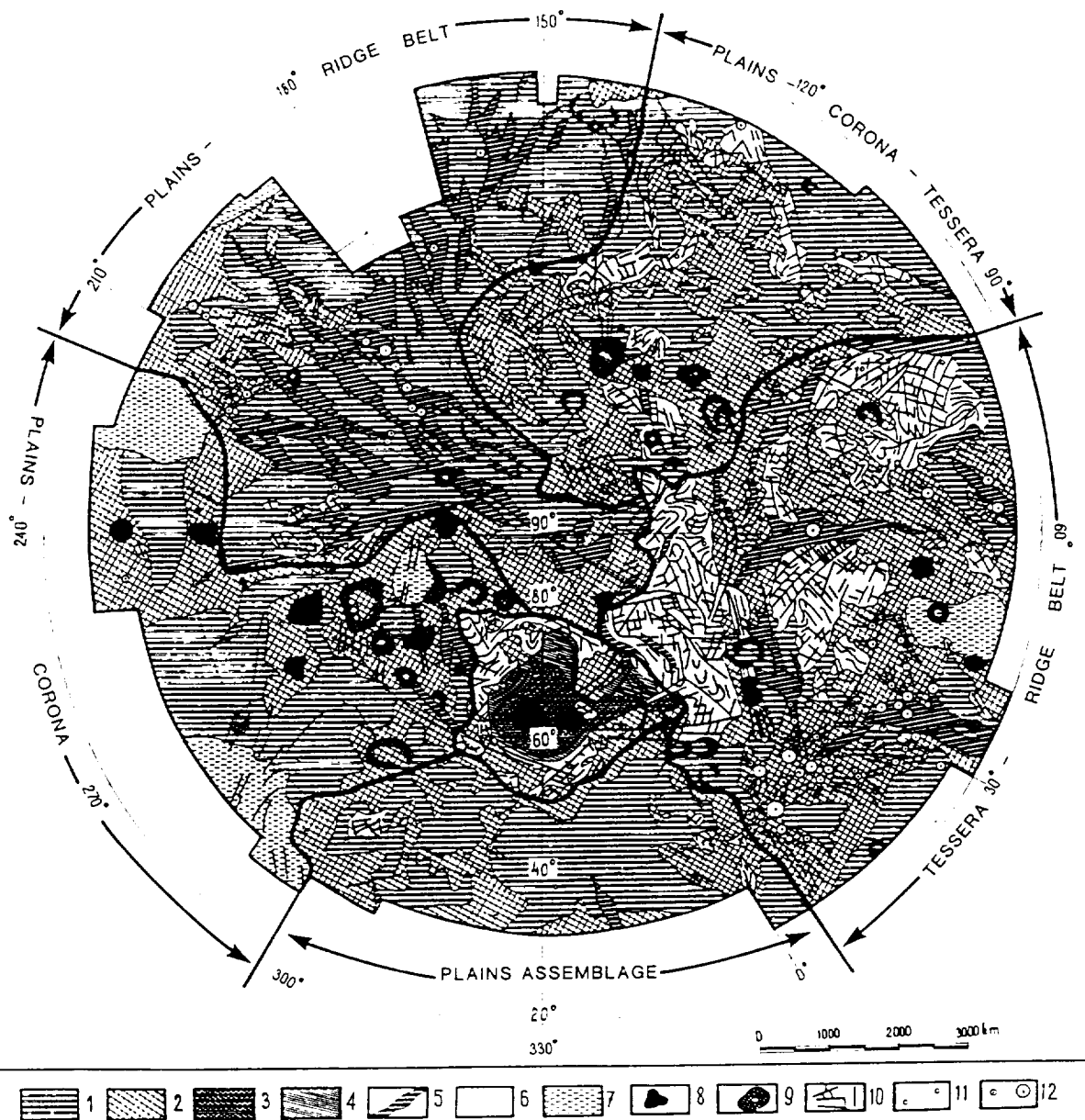
The Tessera-Mountain Belt Assemblage has the highest crater density, and the Plains-Ridge Belt Assemblage the lowest. Some assemblages may be related to each other in terms of tectonic

PRECEDING PAGE BLANK NOT FILMED

style and deformation. The detailed origin and relationships of the assemblages is unclear, however, primarily because there is at present no consensus on the origin of several of the major geologic units (e.g., ridge belts, tessera). Additional insight into the significance and lateral extent of these assemblages will come from linking analyses of the equatorial region<sup>6</sup> to the characteristics of the northern mid-to-high latitudes and from the high resolution global coverage of the Magellan mission.

References: 1) V. Barsukov et al. (1986) JGR, 91, D378; A. Basilevsky et al. (1986), JGR, 91, D399; B. Ivanov et al. (1986) JGR, 91, D413; V. Barsukov and A. Basilevsky (1986) Priroda, 24. 2) S. Solomon and J. Head (1982) JGR, 87, 9236. 3) P. Morgan and R. Phillips (1983) JGR, 88, 8305. 4) L. Crumpler et al. (1986) Geology, 14, 1031. 5) D. Bindschadler and E. Parmentier (1987) LPSC XVIII, 75. 6) D. Senske (1988) MSc Thesis, Brown Univ.

Figure 1. Geologic/morphologic map of the Venera 15/16 region<sup>1</sup> with Assemblage boundaries marked by superposed heavy black lines. 1 (lowland smooth plains); 2 (lowland rolling plains); 3 (highland plains); 4 (mountain belts); 5 (ridge belts); 6 (tesserae); 7 (dome uplifts); 8 (volcanoes); 9 (coronae); 10 (faults); 11 (impact craters); 12 (arachnoids).



ORIGINAL PAGE IS  
OF POOR QUALITY

MORPHOLOGIES OF TEN VENUSIAN SHIELDS BETWEEN LAT 30° AND 90° N.  
G.G. Schaber and R.C. Kozak, U.S. Geological Survey, Flagstaff, AZ 86001.

The gross morphologies of ten Venusian shields greater than 250 km in basal diameter between lat 30° and 90° N. have been determined from Venera 15/16 data (Fig. 1, Table 1). Nine of these shields have been previously identified and formally named [1]. "Bachue" (informal name), located on the south rim of Bachue Coronae in Metis Regio, was identified from a synthetic stereopair [2] produced from Venera datafiles (Fig. 2). As shown in Fig. 1 and Table 1, nine of the shields have extremely low heights (0.7 to 2.3 km) despite large basal diameters (253 to 782 km). Tepev Mons in western Bell Regio is the notable exception; its slopes are 1.4 to 3.8 times steeper than those on Renpet and Sekmet Montes and 6.4 to 22.5 times steeper than those on the seven remaining shields. It was suggested by Janle et al. [3] that the Bell Regio upland may be only a few hundred million years old, and they hypothesized the presence of a supportive elastic lithosphere 30 to 100 km thick on the basis of their analysis of bending flexure associated with the ring moat (depression) surrounding Tepev Mons. The low aspect ratios of the other nine shields are likely due to lithosphere that is locally more thermally weakened and thinner than found at Bell Regio.

Six of the Venusian shields equal or surpass the total volume of the Hawaiian shield, however, none approach the volumes of Olympus, Arsia, Pavonis, Ascraeus, and Elysium Montes (Table 1). "Bachue" is 34.5 times more voluminous than the Hawaiian shield but 9 times less voluminous than Olympus Mons. The volume of Tepev is approximately the same as that of the Hawaiian shield; however, its aspect ratio indicates an edifice that is about twice as flat in profile as Hawaii and Olympus, Ascraeus, and Elysium Montes. The Venusian shields (with the exception of Tepev Mons) have aspect ratios similar to Syrtis Major and Tyrrhena, Hadrica, and Alba Paterae on Mars. The initial style of volcanism at several of these Martian highland volcanic centers has been attributed to volatile-rich magmatic (and/or hydromagmatic) eruptions, which resulted in extensive pyroclastic ash plains surrounding a slightly younger low lava shield [4,5]. However, the congruency in aspect ratio between the highland paterae on Mars and the major Venusian shields is certainly not sufficient evidence to infer similar volcanic histories.

The presence of large depressions (paterae) near the summits of Sacajawea and Colette on Lakshmi Planum may suggest the possibility of regional explosive volcanic activity (despite the high surface pressure) and subsequent caldera collapse. Such activity could be associated with rapid exsolution of anomalously high levels of volatiles (>2-3 percent; [6]); alternatively, caldera collapse may have following an extended period of quiet lava eruptions. The paterae in Sacajawea and Colette extend, respectively, 0.7 and 1.4 km below the planum surface, and they may indicate the depth to the tops of high level magma chambers into which the calderas collapsed.

**Acknowledgements:** Support to the U.S. Geological Survey was provided by the NASA Planetary Geology/Geophysics Program under Contract W-15,814.

**References:** [1] Masursky, Harold and nine others (1986) Annual Gazetteer of Planetary Nomenclature, U.S. Geol. Surv. Open-file Rept. 84-692; [2] Kozak, R.C. and Schaber, G.G. (1988) Lunar and Planet. Sci. XIX, 643-644; [3] Janle, P., Janssen, D., and Basilevsky, A.T. (1988) Earth, Moon, and Planets, 41, 127-139; [4] Mouginus-Mark, P.J., Wilson, L., and Zimbelman, J.R., (1989) Bull. Volcanology, 50, 6, 361-379; [5] Greeley, Ronald, and Spudis, P.D. (1981) Rev. Geophys. and Space Phys., 19, 1, 13-41; [6] Head, J.W. and Wilson, Lionel (1986) J. Geophys. Res., 91, B9, 9407-9446; [7] Wu, S.S.C. and four

others (1984) *Nature*, 309, 5967, 432-435; [8] Wu, S.S.C. and three others (1988) *Lunar and Planet. Sci.* XIX, 1298-1299; [9] Bargar, K.E., and Jackson, E.D. (1974) *J. Res., U.S. Geol. Survey*, 2, 5, 545-550; [10] Decker, R.W., Wright, T.L., and Stauffer, Eds. (1987) *U.S. Geol. Surv. Prof. Paper* 1350, 1-189.

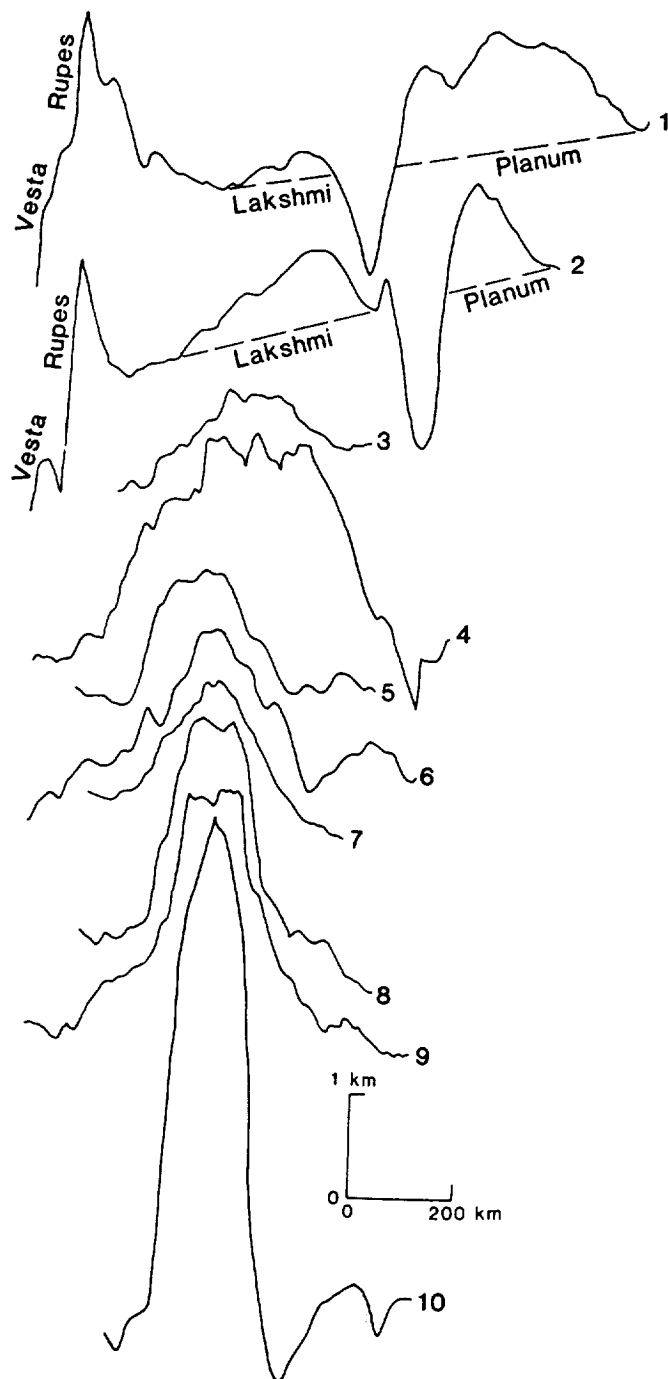


FIG. 1

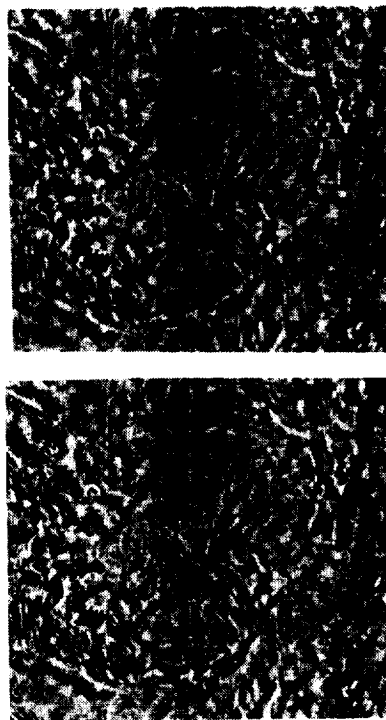


Fig. 2

**Figure 1** Venera 15/16 profiles across ten Venusian shields (Table 1); name/orbit: (1) Sacajawea/191, (2) Colette/181, (3) Atira/437, (4) "Bachue"/99, (5) Melia/310, (6) Venilia/410, (7) Api/259, (8) Sekmet/412, (9) Renpet/416, (10) Tepev/250. All Venera 16 orbits except (3); vert. exagg. 200X. **Figure 2** Synthetic stereopair of "Bachue" produced from Venera datatapes [2]; relief greatly exaggerated; image is 1000 km.

ORIGINAL PAGE IS  
OF POOR QUALITY

TABLE 1 - MORPHOLOGIC ELEMENTS ON SELECTED SHIELDS ON VENUS, MARS, AND EARTH

Feature (lat/long)	Edifice height (h) (km)	Avg. basal diameter (d) (km)	Avg. flank slopes (s) (degrees)	Calculated volume of shield (v) (km <sup>3</sup> )	Aspect ratio (h:d)
<b>VENUS (LAT 30° - 90° N)</b>					
"Bachue shield" (71.5° N, 255°)	2.0 <sup>1</sup> / <sub>1</sub>	632	N=0.7, S=0.4	4.4x10 <sup>5</sup>	1:316
Sacajawea (64.5° N, 336°)	1.2	772	0.2	2.8x10 <sup>5</sup>	1:643
Colette (66.8° N, 324°)	1.0	7 <sup>1</sup>	N=0.3, S=0.2	2.2x10 <sup>5</sup>	1:782
Venilia Mons (32.2° N, 238.5)	1.6	475	0.5	1.4x10 <sup>5</sup>	1:297
Tepev Mons (29.7° N, 45.7°)	5.2	253	avg.=2.7, max.=4.5	1.2x10 <sup>5</sup>	1:49
Renpet Mons (76° N, 237°)	2.3	248, 458 <sup>2</sup> / <sub>1</sub>	3.2, 0.6 <sup>2</sup> / <sub>1</sub>	1.0x10 <sup>5</sup>	1:108, 1:199 <sup>2</sup> / <sub>1</sub>
Api Mons (38.8° N, 54.8°)	1.3	400	0.5	8.2x10 <sup>4</sup>	1:308
Sekmet Mons (43.7° N, 241.2°)	2.2	317, 414 <sup>2</sup> / <sub>1</sub>	1.2, 0.3 <sup>2</sup> / <sub>1</sub>	7.0x10 <sup>4</sup>	1:144, 1:188 <sup>2</sup> / <sub>1</sub>
Atira Mons (52.5° N, 267.5°)	0.7	400	0.2	4.4x10 <sup>4</sup>	1:571
Melia Mons (62.5° N, 120°)	1.2	299	0.6	4.2x10 <sup>4</sup>	1:249
<b>MARS</b>					
Olympus Mons	24.4 [7]	600	see <sup>3</sup> / <sub>1</sub>	3.8x10 <sup>6</sup> [7]	1:25
Arsia Mons	10	400	3	9.4x10 <sup>5</sup> [8]	1:40
Ascraeus Mons	16	400	5	7.7x10 <sup>5</sup> [8]	1:25
Pavonis Mons	8	450	2	5.9x10 <sup>5</sup> [8]	1:56
Elysium Mons	12	350	4	5.8x10 <sup>5</sup>	1:29
Tyrrhena Patera [4]	0.8	250	0.3	2.0x10 <sup>5</sup>	1:333
Hadrlica Patera	1.5	450	0.4	1.2x10 <sup>5</sup>	1:300
Syrtis Major	<1	800	0.2	2.4x10 <sup>4</sup>	1:800
Alba Patera (central shield)	1.0	250	0.5	1.8x10 <sup>4</sup>	1:250
<b>EARTH</b>					
Hawaiian shield (Big Island)					
Ocean floor to summit	8.6	200	see <sup>4</sup> / <sub>1</sub>	1.1x10 <sup>5</sup> [9]	1:23
Subaerial shield only	4.2	150	see <sup>4</sup> / <sub>1</sub>	1.2x10 <sup>4</sup> [9]	1:36

<sup>1</sup>/From recalculated Venus 15/16 altimetry dataset (L. Soderblom, pers. commun., 1988)

<sup>2</sup>/1st number, higher, steeper flanks; 2nd number, lower, flatter base

<sup>3</sup>/From [7]: 2-7 km elevation, 2°-3°; 7-16 km, 8°-24°; 13-24 km, 2.5°-6.5°; volume above 2-km contour

<sup>4</sup>/From [10]: unmodified subaerial slopes, 3°-10°; submarine slopes, 10°-20°



# CHARACTERISTICS AND GEOLOGIC/TERRAIN ASSOCIATIONS OF SMALL DOME-LIKE HILLS ON VENUS

J. C. Aubele, Dept. of Geological Sciences, Brown University, Providence, R.I. 02912

*Introduction.* Approximately 22,000 small dome-like hills have been recognized on the northern 20% of the surface of Venus imaged by Venera 15/16. These features have been described [1] as generally circular in planimetric outline, with a range in basal diameter from the effective resolution of the Venera images (1-2km) up to 20 km.

*General Characteristics.* The small hills have been called domes [1,2] following the lunar nomenclature, because of their broad apparent form. The nomenclature used here, "small dome-like hills", is preferred because of the strict volcanological definition of a dome and terrestrial lithologic connotations. Based on constraints on the appearance of features imaged by this radar system, individual slopes are less than  $10^\circ$ . Assuming these slopes, simple geometric models imply maximum height of approximately 1 km, and average height less than 1 km. Recent radar-clinometric data confirms these estimates [3]. Most of the small dome-like hills show no individually associated features; however, a small number exhibit summit pits, bright aureoles, low basal platforms extending beyond the basal diameter of the dome, and radial or lobe-like bright features interpreted to be volcanic flows. Summit pits are occasionally observed in dome-like hills larger in basal diameter than 8 km, and more frequently in ones larger than 15 km. Bright circular aureoles, without apparent topographic relief, appear to be associated with small dome-like hills northeast of Atalanta Planitia. Low basal platforms and bright features interpreted to be volcanic flows are rare but do occur in a few cases.

*Dome Distribution.* Slyuta, et al [2,4] have produced dome density contour maps and find that most dome-like hills occur in groups of several tens within areas of  $10^3$  km<sup>2</sup>. Adjacent groups form clusters consisting of 10-20 groups within areas of  $10^5$  km<sup>2</sup>. The greatest concentration of clusters of dome-like hills occurs in the general area of  $60^\circ\text{N}, 120^\circ\text{E}$ . The outline of this region of cluster concentration generally corresponds to the Plains-Corona-Tessera Assemblage described by Head [10]. Major concentrations of clusters [2] are located in Tethus Regio ( $65^\circ\text{N}, 110^\circ\text{E}$ ), Atalanta Planitia ( $60^\circ\text{N}, 155^\circ\text{E}$ ), Ananke Tessera ( $55^\circ\text{N}, 138^\circ\text{E}$ ), and Akkruva Colles (from Niobe Planitia,  $35^\circ\text{N}, 130^\circ\text{E}$ , to Allat Dorsa,  $65^\circ\text{N}, 70^\circ\text{E}$ ).

*Topographic Association.* The cluster concentrations in Tethus, Ananke and Akkruva are associated with broad regional topographic highs. However, many small groups or clusters of groups occur on low plains or inside circular depressions and the cluster concentration in Atalanta occurs in the general area of the topographically lowest region of Venus.

*Terrain Unit Association.* Almost all of the areas of cluster concentration occur on mottled plains units designated as "rolling plains" interpreted to be of volcanic origin [5, 10]. Major clusters frequently occur on such plains units at the margins of areas of tessera, while very small groups occasionally occur in intra-tessera plains near the margins of large tessera units. Smaller cluster concentrations occur in regions of predominant arachnoids, in the area between Sedna Planitia and Bell Regio and in the area south of the ridge belt province at  $40^\circ\text{N}, 215^\circ\text{E}$ ; and also occur at the northern end of Beta Regio (the only portion of this area imaged by Venera). No major concentrations of dome-like hills occur in areas of predominant ridge-belts or in the Mnemosyne area of predominant coronae, although very small groups and isolated dome-like hills occur associated with both of these types of geologic features.

*Regional and Global Structure Association.* As stated previously, major cluster concentrations of small dome-like hills are associated with the margins of tessera. A small number of dome-like hills occasionally occur at the ends of linear ridge belts. Individual groups of dome-like hills exhibit occasional minor alignments but, in most cases, there is no dominant trend direction. The general area of cluster concentration in Akkruva Colles, northeast of Niobe Planitia exhibits an overall NW-SE alignment. This zone, an area of topographic relief, is also the area of a linear positive gravity anomaly [4]. Although domes occur on the plains to the north and south of Ishtar Terra, Lakshmi Planum and the horizontal compressional fold belts [6] of Akna and Freyja Montes exhibit one of the lowest densities of small dome-like hills on Venus.

*Geologic Feature Association.* Small groups of dome-like hills always appear to be associated with the following specific geologic features: coronae, arachnoids, intermediate (20-50 km) sized hills interpreted to be volcanic constructs, large volcanic centers and calderas, and large circular features of uncertain origin.

*Coronae.* Groups of dome-like hills (10-15 km diameter) occur predominantly inside the annular concentric ridges of coronae, while smaller groups occur on the surrounding plains. Flow-like features and domes in the interior of corona structures have been previously interpreted as evidence of volcanic activity occurring at various times throughout the evolution of the coronae [7].

*Arachnoids.* Arachnoids occur in clusters in lowland regions; and have been described as characterized by "central domes" ( $\leq 10$  to over 30 km in diameter, commonly with central pits) surrounded by rings and linear features interpreted to be tectonic in origin [8]. The central domes have been interpreted to be volcanic in origin [8]. Groups of small dome-like hills occur on the plains surrounding and between adjacent arachnoids.

*Intermediate and Large Volcanic Centers.* A few intermediate sized hills, commonly exhibiting summit pits and associated radial or lobate flow features, and interpreted to be small volcanic constructs, are generally found to be spatially associated with groups of small dome-like hills. These intermediate sized features are fewer in absolute number than the small dome-like hills and generally occur as isolated features scattered on plains units near groups or clusters of small dome-like hills. Groups and clusters of groups of small dome-like hills occur predominantly on the lower flanks, or beyond the distal edges, of the bright radial markings associated with large volcanic centers. This may imply that the spatially associated small dome-like hills pre-date final volcanic eruptions at these centers, or they may be difficult to identify in radar images on the, presumably, rough volcanic flows. Very few isolated domes occur on Lakshmi Planum, with small groups occurring on the rims and periphery of the calderas, Collette and Sacajawea [9].

*Circular Features.* Small groups of dome-like hills generally occur within large circular features of uncertain origin, particularly where the interior is lower in topographic elevation than is the surrounding plain.

*Summary and Interpretation.* The major cluster concentrations of small dome-like hills on Venus occur on rolling plains units interpreted to be volcanic, primarily around the margins of tessera terrain. Minor cluster concentrations occur in areas of predominant arachnoids. Small groups of dome-like hills always occur in association with the following individual geologic features: coronae, arachnoids, intermediate (20-50 km) sized hills interpreted to be volcanic constructs, large volcanic centers and calderas, and large circular features of uncertain origin. There appears to be a dominant association of small dome-like hills with geologic features generally interpreted to be volcanic in origin. An exception to this association is in the Lakshmi Planum (volcanic plains) area, where there are a small number of dome-like hills. Altitude and crustal thickness are two potential distinguishing characteristics of this area. The existence of small dome-like hills ( $\leq 20$  km), intermediate sized volcanic constructs (20-50 km), and large volcanic centers implies a continuum of volcanic edifices grading from less than 2 km to more than 100 km in diameter. The intermediate volcanic constructs may simply represent gradational diameters between the small dome-like hills and the large volcanic centers, and need not represent differences in eruptive style. There is a distinct distribution of number versus size range such that the number of edifices increases as the size decreases. This type of distribution is similar to that observed for volcanic edifices on Earth, both continental and oceanic. Detailed terrain,

geologic and structural associations for the four major areas of cluster concentration are currently in progress.

#### REFERENCES

- [1] Barsukov, V.L. et al, 1986, Proc. LPSC XVI, JGR, 91, B4, D378; [2] Slyuta, E.N., et al, 1988, LPSC XIX (Abst), 1097; Aubele, J.C., et al, 1988, LPSC XIX (Abst), 21; [3] Slyuta, E.N., et al, 1989, LPSC XX (Abst); [4] Slyuta, E.N., et al, 1988, Aston. Vestnik, 22, #4, 287 (in Russian); [5] Barsukov, V.L and Basilevsky, A., 1986, Piroda, 24; [6] Crumpler, L.S., et al, 1986, Geology, 14, 1031; [7] Stofan, E.R. and Head, J.W., 1989, Submitted to Icarus; [8] Stofan, E.R. and Head, J.W., 1988, LPSC XIX (Abst), 1127; [9] Magee, K.P. and Head, J.W., 1988, LPSC XIX (abst), 711; Magee, K.P. and Head, J.W., 1988, LPSC XIX (abst), 713; [10] Head, J.W., 1989, LPSC XX (Abst).

## **GEOLOGY OF SOUTHERN GUINEVERE PLANITIA, VENUS, BASED ON ANALYSES OF GOLDSTONE RADAR DATA**

R. E. Arvidson, J. J. Plaut, McDonnell Center for the Space Sciences, Department of Earth and Planetary Sciences, Washington University, St. Louis, Missouri 63130, R. F. Jurgens, R. S. Saunders, M. A. Slade, Jet Propulsion Laboratory, Pasadena, California 91103

The ensemble of forty-one backscatter images of Venus acquired by the S Band (12.6 cm) Goldstone radar system covers approximately 35 million square kilometers and includes the equatorial portion of Guinevere Planitia, Navka Planitia, Heng-O Chasma, and Tinatin Planitia, and parts of Devana Chasma and Phoebe Regio. The images and associated altimetry data combine relatively high spatial resolution (1 to 10 km) with small incidence angles (less than 10 degrees) for regions not covered by either Venera Orbiter or Arecibo radar data. Systematic analyses of the Goldstone data show that: (a) Volcanic plains dominate, including groups of small volcanic constructs, radar bright flows on a NW-SE arm of Phoebe Regio and on Ushas Mons and circular volcano-tectonic depressions. The radar bright, flow-like features have length scales similar to those seen in Venera Orbiter and Arecibo data covering Sedna Planitia. The relative abundance of volcanic features is similar to that found in Venera radar images in northern Guinevere Planitia and in Sedna Planitia; (b) Some of the regions imaged by Goldstone have high radar cross sections, including the flows on Ushas Mons and the NW-SE arm of Phoebe Regio, and several other unnamed hills, ridged terrains, and plains areas. While some of the high returns are probably associated with surfaces tilted toward the radar nadir, other regions with high cross sections are not associated with obvious topography and retain high values over a range of incidence angles. These areas expose materials with high dielectric constants. The global trend observed in Pioneer-Venus data, where higher elevations are found to preferentially expose such materials, may be because higher elevations are simply sites of vigorous volcanism and thus maximum exposure of these materials; (c) A 1000 km diameter multiringed structure is observed and appears to have a morphology not observed in Venera data. The northern section corresponds to Heng-O Chasma; (d) A 150 km wide, 2 km deep, 1400 km long rift valley with upturned flanks is located on the western flank of Phoebe Regio and extends into Devana Chasma. The floor has low backscatter values. At the low incidence angles for Goldstone observations, backscatter is controlled by quasi-specular reflections and low returns correspond to surfaces that are rough at length scales many times the radar wavelength. Thus, rifting processes, associated volcanism, and perhaps mass wasting seem to be ongoing processes that continue to generate rough topography; (e) Ridge belts can be discerned in the Goldstone data, mainly trending NW-SE and NE-SW, directions similar to those discerned in Pioneer-Venus topography throughout the equatorial region. The ridge belt and topographic orientations suggest deformation due to a large-scale stress system. For example, with an appropriately thin lithosphere, equatorial to mid latitude strike-slip faulting may have occurred as the planet's equatorial bulge relaxed as the spin rate slowed to its present value; and (f) The abundance of circular and impact features is similar to the plains global average defined from Venera and Arecibo data, implying that the terrain imaged by Goldstone has typical crater retention ages, measured in hundreds of millions of years. The rate of resurfacing is  $\leq 4$  km/Ga.

### **Clotho Tessera, Venus: A fragment of Fortuna Tessera?;**

Richard C. Kozak and G.G. Schaber, U.S. Geological Survey, Flagstaff, AZ 86001

Clotho Tessera, adjacent to southeast Lakshmi Planum, may provide additional evidence for lateral crustal motions, and a model for the origin of small tessera fragments.

Clotho Tessera and Lakshmi Planum are so noticeably different, and in such close proximity, it is difficult to derive a reasonable model of their formation in situ. Squeezing of material out from beneath Lakshmi has been suggested as an origin for Moira Tessera [1], which is also adjacent to Lakshmi and 1400 km west of Clotho. However, a logical model of juxtaposition of the two different terrains, originally from points once distant, can be made for Clotho and Lakshmi (and perhaps other small tesserae as well).

The 4.5-km-high Danu Montes between Clotho and Lakshmi clearly indicate convergence. Parallel to the WSW trend of the Danu mountain belt is a distinct lineament, across which the character of the terrain changes (in some places radically), and the tessera ridges appear deflected. The deflection of ridges along a 50-km segment of this Danu lineament suggests drag caused by right-lateral offset. At the northeast extent of both Danu Montes and Clotho Tessera is a 120-km-wide diffuse lineament zone (DLZ) trending southeast. These lineaments are traceable for 700 km before they disappear, apparently buried for almost 500 km by flows from the northeast that are related to a large volcano-tectonic depression whose southeast rim is roughly defined by Valkyrie Fossae. Beyond Valkyrie Fossae, a similar lineament zone continues an additional 800 km southeastward before abruptly terminating 150 km short of Sigrun Fossae. (The abrupt termination follows a line subparallel to Sigrun Fossae -- itself nearly perpendicular to the lineament zone -- and is probably one of the faults which form the Sigrun rift valley). This eastern segment of the DLZ is 100 km wide near Valkyrie and fans out eastward to as much as 400 km or more wide near Sigrun.

I suggest that Clotho Tessera was once part of Fortuna Tessera, but was cut off by a transcurrent fault zone (the DLZ) striking perpendicular to the Sigrun "rift" [1,2] and carried westward where it collided with Lakshmi Planum (forming Danu Montes). A gravity anomaly along the southern border of Lakshmi, in the area of Danu Montes, has been interpreted as indicating subduction there [3], providing additional supporting evidence for the collision hypothesis. The Danu Montes right-lateral fault(?) is explained by the obliquity of the collision of Clotho with Lakshmi (the path of least resistance for the migrating terrain being toward the southwest).

Diffusion of the DLZ with proximity to Sigrun Fossae may be due to either higher ductility near the postulated Sigrun "rift", or to burial by flows away from the rift nearer to Valkyrie Fossae. (The latter hypothesis is reinforced by inselbergs of the sheared-type terrain near Valkyrie). If this is indeed the case, it indicates that the visibility of transcurrent structures resulting from crustal movements may be difficult to see in the plains, due to much higher ductility there and/or to burial by the plains-forming flows.

Other possible examples of migrating tesserae occur elsewhere: small pieces of Ananke Tessera can be fit back together as though they had rifted apart, and the spreading apart of Ananke and Virilis Tesserae has been suggested because of their symmetric locations about the axis of an inferred spreading zone [4]. Other tessera fragments appear to have been isolated by rifting, with little, if any, significant lateral motion (e.g., Meni and Tellus Tesserae, and Tethus and Fortuna Tesserae). The migrating terrain model for Clotho Tessera supports Sukhanov's [5] interpretation of tesseral fragments as rafts of lighter crustal material.

# References

- [1] Pronin, A.A., et al., 1986, A geologic and morphological description of Lakshmi Planum, Astron. Vestnik, 20, 83-98.
- [2] Kozak, R.C., and Schaber, G.G., 1987, A spreading center on Venus?, Lunar Plan. Sci., XVIII, 513-514.
- [3] Janle, P., and Jannsen, D., 1984, Tectonics of the southern escarpment of Ishtar Terra on Venus from observations of morphology and gravity, Earth, Moon, and Planets, 31, 141-155.
- [4] Sukhanov, A.L., 1986, Parquet: areas of regional plastic deformation, Geotektonika, 1986, no. 4, 60-76.
- [5] Sukhanov, A.L., et al., 1986, Geologic-morphological description of Laima Tessera area and Bereghiniya Planitia, Astron. Vestnik, 20, 272-286.

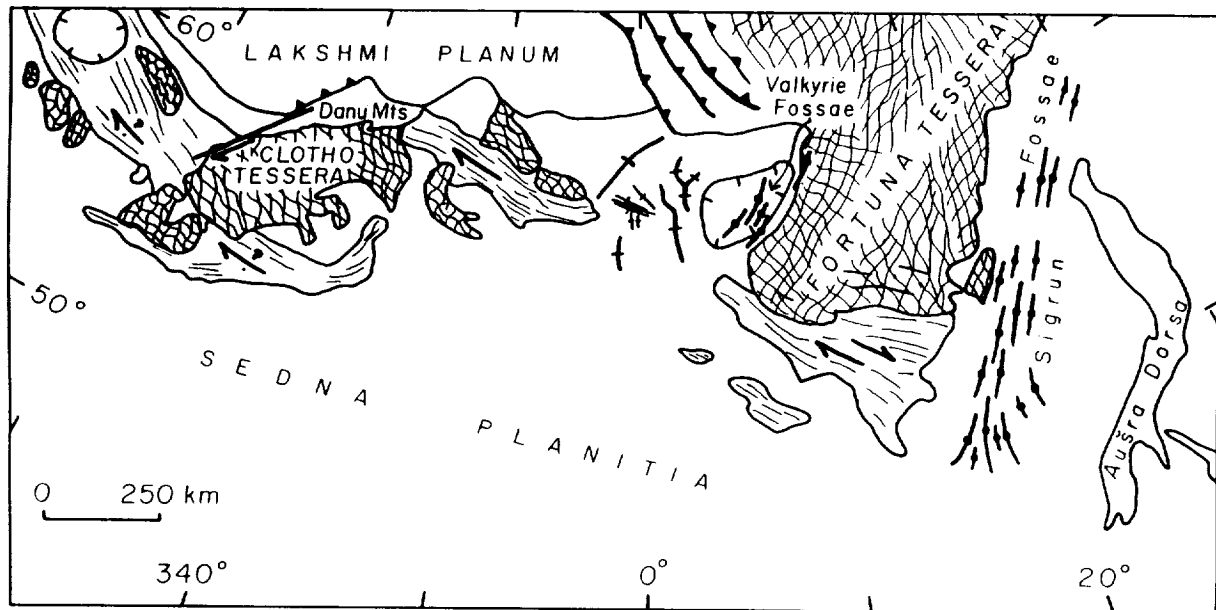
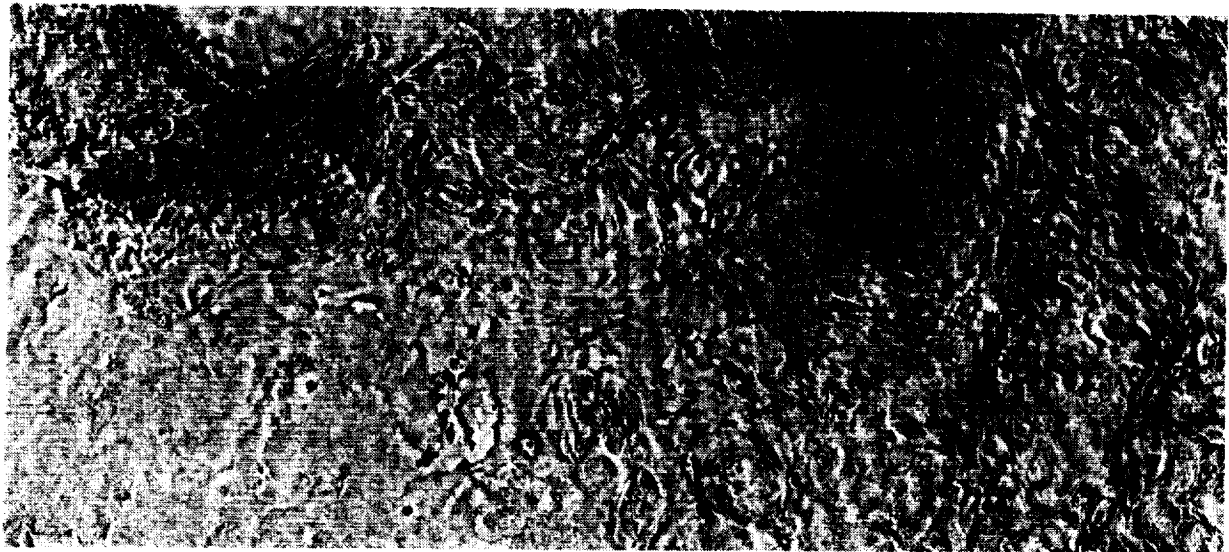


Figure 1. (top) Venera 15/16 mosaic of the suggested "Clotho-Sigrun shear zone" area. (bottom) Interpretive sketch map of the area.

## Models of Venus Tectonics: Evaluation and Application to Tessera Terrain.

D.L. Bindshadler, and J.W. Head, Brown University Dept. of Geological Sciences,  
Providence, RI, 02912 (SPAN BRNPSG::BINDSCH)

**Models:** A number of models have been suggested for the formation of the complexly deformed tessera terrain of Venus [1-4]. We have used these and other models to set forth working hypotheses for the formation of tessera [5], which can be broadly divided into three formational models (those which produce the observed high-standing topography of the tessera) and two modificational models (those which are a direct result of high topography). The complexity of the tessera, including at least three distinctive subtypes [6], raises the possibility that this terrain may have more than a single mode of formation. Here we describe each model, note its basic predictions, and compare those predictions to observational constraints such as topography, LOS (line of sight) gravity anomaly data [7], morphologic and structural information derived from Venera image data.

**Horizontal convergence and crustal thickening** may be driven by in-plane lithospheric stresses (as on Earth) or by flow within the mantle of Venus [8,9]. In general, convergent motion is expected to result in high topography, steep topographic slopes, and fold-and-thrust deformation at the surface. Crustal compensation of topography should result in a relatively small LOS anomaly over regions of tessera, given predicted crustal thicknesses for Venus of  $\leq 30$  km [10,11]. In addition, both strike-slip and extensional deformation are observed in terrestrial orogens such as the India-Asia collision and the Andean orogen, and might also be expected to occur on Venus.

**Mantle upwelling** may be manifested as the upwelling limb of a convection cell, a long-lived hotspot, or a diapir-like body. Such an upwelling will result in the formation of a dome-shaped region of high topography, characterized by extensional deformation, and possibly by volcanism [12]. Relatively large LOS gravity anomalies are anticipated, unless the characteristic depth of the source is quite shallow. Numerous workers have identified Beta, Bell, and Atla Regiones as likely surface manifestations of mantle upwelling. Such regions are thus likely to represent some part of the evolution of any tessera formed due to upwelling.

**Seafloor spreading** or an analogous process is suggested to occur within Aphrodite Terra [13]. On Earth, seafloor spreading results in the formation of an approximately orthogonal structural fabric consisting of transform faults and fracture zones in one direction, and abyssal hill topography in the other. Tessera formed near Aphrodite and transported north is predicted to be old compared to the undeformed plains that surround it. High topography is explained as being due to a relatively thick crust, suggesting that topography at plains-tessera contacts should be gently sloping. Steep topography is expected to occur at transforms due to juxtaposition of lithosphere of different ages and to thermal stress-supported bending of plate segments [14]. Finally, a common feature of the terrestrial ocean floor are volcanic seamounts, which may be observable as small domes on the surfaces produced by a spreading process.

**Gravity sliding** is defined here as a thin-skinned, predominantly brittle process involving the downslope movement and deformation of a wedge of material above a

decollement. This process is expected to produce extensional features (e.g. a detachment fault) at or near local topographic highs, with structures becoming increasingly compressional toward local topographic lows. If topographic slopes are approximately radial about the highest topography, radial graben would also be expected to form, as observed in the aureole surrounding Olympus Mons on Mars [15].

**Gravitational relaxation** of compensated topography is distinguished from gravity sliding as a predominantly ductile process driven by gradients in vertical normal stress due to surface and/or crust-mantle boundary topography. In the case of crustally compensated topography, calculations predict extension of high topography and increasingly compressional deformation toward the edges of a topographic high [16]. Highest rates of extension occur at the highest elevations, but extension may occur even in relative lows if they lie above the level of the surrounding plains. If the high topography of the tessera is due to uplift rather than crustal thickness variations, a somewhat different scenario is predicted, see [5].

**Evaluations.** Of the three formational models, characteristics of the tessera are in least agreement with the predictions of the mantle upwelling model. LOS gravity data suggest relatively shallow compensation of Tellus Regio [7,6], in contrast to the great depths of Airy compensation calculated for Beta and Bell Regiones [17,18]. Regions of tessera are typically characterized by steep slopes near the plains-tessera boundary and lower relief interiors, a plateau-like shape. Regions such as Bell and Beta are characterized by more gradually sloping, dome-shaped topography. In contradiction of the prediction of increasing surface deformation with time, we observe embayed regions of tessera on the flanks of Bell, which appear to predate the smooth, undeformed plains that dominate the surfaces of domal uplifts. It therefore seems unlikely that regions of tessera represent more-evolved Bell or Beta-like regions. We also suggest that gravity sliding may be ruled out as a significant contributor to formation of tessera. Examination of Venera images reveals a lack of features that could be considered analogous to detachment faults. Moreover, the simple structural fabric of upslope extensional features and downslope compressional features is not generally observed, with one notable exception. A small region of tessera southwest of Lakshmi Planum (~58°N, 310°E) exhibits structures predicted for gravity sliding [19]. This deformational pattern has not been observed elsewhere in the tessera.

A number of predictions of the seafloor spreading model are consistent with characteristics of the tessera in eastern Laima Tessera (~50°N, 50°E). The region is characterized by an approximately orthogonal fabric (*trough and ridge tessera* [6]) consisting of features suggested to be analogous to fracture zones and abyssal hills [20]. Other major regions of tessera are characterized by different morphologic subtypes [6]. Topography and age relationships along the boundaries of Laima are consistent with model predictions, and available LOS gravity data are consistent with crustal isostatic support of topography. However, domes analogous to terrestrial seamounts are not observed, and no topographic stepdowns are observed across troughs. The approximately orthogonal fabric of eastern Laima merges gradually into a non-orthogonal fabric in western and southern Laima, and the two longest and most distinct troughs in Laima (Baba-jaga and Mezas-mate Chasmata) are non-parallel. Such disturbances of the structural fabric could be associated



with minor deformation, and we are currently quantifying observations as to the parallel/orthogonal nature of features in order to more objectively assess the model.

Predictions of a model in which crustal convergence is followed by gravitational relaxation are consistent with most of the overall characteristics of *sub-parallel ridged terrain* (Tsr) and *disrupted terrain* (Tds), the remaining tessera subtypes [6]. These include LOS gravity data, the presence of both Type II boundaries (which suggest deformation to plains to form tessera) [6], the presence of Tsr near the edges of regions of tessera [6], and the association of tessera with the mountains of western Ishtar Terra. Within the Tds, extensional features commonly crosscut other structures, indicating the late-stage extension predicted for gravitational relaxation.

We are currently attempting to assess the seafloor spreading, convergence, and relaxation models in terms of the various tessera subtypes. One goal of this study is to link particular modes of origin with the morphologic classification scheme. Of particular importance would be the identification of transitional subtypes suggesting that at least some tessera have been reworked by distinct processes. Finally we plan to consider the implications of the models for the driving mechanisms of Venus tectonics.

### References:

- 1) Basilevsky, A. T. (1986) *Geotektonika*, 20, 282-288.
- 2) Kozak, R.C. and G.G. Schaber (1986) *Lunar Planet Sci. XVII*, 444-445.
- 3) Sukhanov, A. L. (1986) *Geotectonics* 20, 294-305.
- 4) Smrekar, S., and R.J. Phillips (1988) *GRL* 15, 693-696.
- 5) Bindschadler, D.L. and J.W. Head (1988) *Lunar Planet. Sci. XIX*, 78-79.
- 6) Bindschadler, D.L. and J.W. Head (1988) *Lunar Planet. Sci. XIX*, 76-77.
- 7) Sjogren, W. L., et al. (1983) *JGR* 88, 1119-1128
- 8) Phillips, R.J. (1986) *GRL* 13, 1141-1144.
- 9) Bindschadler, D.L. and E.M. Parmentier (1988) *EOS Trans. AGU*, 69, 1450.
- 10) Zuber, M. T. (1987) *Proc. Lunar Planet. Sci. Conf. XVII*, Part 2, *JGR* 92, E541-E551.
- 11) Grimm, R.E. and S.C. Solomon (1988) *JGR* 93, 11911-11929.
- 12) Bindschadler, D.L. and E.M. Parmentier (1989) *Lunar Planet. Sci. XX*, 78-79.
- 13) Head, J. W. and L. S. Crumpler (1987) *Science* 238, 1380-1385.
- 14) Haxby, W.F., and E.M. Parmentier (1988) *JGR* 93, 6419-6429.
- 15) Francis, P.W. and G. Wadge (1983) *JGR* 88, 8333-8344.
- 16) Bindschadler, D.L. et al. (1989) Tectonic effects of gravitational relaxation of topography on Earth and Venus, submitted to *Icarus*.
- 17) Esposito, P.B., et al. (1982) *Icarus* 51, 448-459.
- 18) Janle, P. et al. (1987) *Earth Moon Planets* 39, 251-273.
- 19) Pronin, A.A. (1986) *Geotektonika* 20, 271-281.
- 20) Head, J.W. (1989) *Lunar Planet. Sci. XX*, 394-395.

Tessera is an upland terrain type shown by Venera 15/16 radar images to have a very distinctive morphology and texture dominated by densely packed systems of grooves and ridges intersecting each other in a variety of patterns. The morphology of tessera has been interpreted to be related to deformation which has acted with primarily horizontal components over broad areas<sup>1</sup>, but the origin of the deformation is still controversial. A range of models for tessera origin<sup>2</sup> includes: horizontal compression and crustal thickening due to asthenospheric currents; vertical uplift due to shallow mantle processes; gravity driven deformation manifested as gravity sliding or gravitational relaxation; and analogy to the terrestrial sea floor where structural patterns are related to rise-crest and spreading processes. A three-part classification scheme, outlined in order of increasing complexity of structural patterns has been proposed for the tessera<sup>3</sup>: 1) trough and ridged terrain; 2) sub-parallel ridged terrain; and 3) disrupted terrain. In this analysis, the characteristics of the type example of the trough and ridged terrain (Eastern Laima Tessera), the least complex type of tessera terrain is investigated (Fig. 1), and compared to the texture of the terrestrial ocean floor.

Laima Tessera covers approximately  $14 \times 10^6$  km<sup>2</sup> and is centered at about 50°, 50°N (Fig. 1). The major fabric associated with Laima Tessera is a generally orthogonal structural fabric composed of WNW to NW trending long and throughgoing faults and large troughs up to 30 km in width, and a NNE to NE trending set of much shorter linear elements of alternating ridges and valleys spaced 6 to 12 km apart and oriented locally orthogonally to the larger structures. The troughs/fractures (Fig. 1, 2) are characterized by their linearity and extreme length, and their often-changing nature along strike. Several troughs completely cross the width of Laima Tessera, with one extending for a distance of about 1400 km. The individual features themselves are most often trough-shaped in cross-section, with inward dipping walls and a flat floor which usually appears to be covered by plains units of probable volcanic origin. Troughs range in width from about 8-30 km with most in the range of 10-12 km. In some cases the flat-floored trough narrows and the walls merge into a single linear fracture zone, generally less than 8 km in width. The major troughs are generally parallel (Fig. 1) with the distance between any two being similar, but they are not evenly spaced across strike relative to each other. A NNE-oriented transect across eastern Laima Tessera shows that the spacing ranges from 20 to 100 km with an average spacing for 13 troughs of about 50 km.

The striped terrain between the troughs/fractures is characterized by parallel ridges and valleys oriented generally perpendicular to the troughs/fractures. The edges of the ridges and valleys are often sharp and linear and appear to be fault bounded (Fig. 1, 2). In eastern Laima Tessera, the linear elements of the striped terrain are commonly continuous between the orthogonal trough/fractures, and do not show a consistent relationship in terms of crossing or terminating against the trough/fracture zones. In many cases, particularly where the edge of the striped terrain is defined by a trough, individual linear elements do not appear to cross into the adjacent striped segment. In some cases, particularly where the edge of the striped terrain is defined by a fracture, many linear segments can be traced across the fracture, while others terminate against it. Few striped elements carry further than across one trough/fracture zone (see map patterns in Fig. 1). The lengths of the valleys and ridges in the striped terrain are thus generally comparable to the separation distances between the orthogonally oriented trough/fractures, commonly in the range 20 to 100 km, and much shorter than the orthogonal fabric of the troughs/fractures. The separation distances of the hills are about 6-12 km, averaging about 8-10 km.

The fundamental fabric of the terrestrial sea floor is the combination of the linear rise crest and median valley of the spreading center, and the orthogonally oriented pattern of transforms and fracture zones<sup>4-6</sup>. In addition, the linear ridges and troughs that are formed parallel to the rise crest (abyssal hills) produce a closely spaced pattern of linear ridges and valleys extending away from the rise crest, oriented normal to the transforms/fracture zones<sup>4-7</sup>. Fracture zones are pervasive in the ocean basins, occur in a variety of sizes and scales, and are defined by a central trough 5-20 km in width that has regional inward-dipping convex-downward slopes down to the trough floor, with subsidiary basins and ridges along the valley floor. Fracture zones are linear, arcuate, and slightly sinuous, depending on a number of factors including changes in spreading rate, poles of rotation, and deformation. Fracture zones over several thousands of kilometers in length are known. The spacing between FZ's is relatively constant between any pair of FZ's, but is variable in a cross-strike direction across a series of FZ's. The spacing is about 30 km along slow-spreading ridges and 70 km along fast-spreading ridges<sup>8</sup>. Average spacing in the North Atlantic is 55 km<sup>4</sup>. A distinctive linear fabric of abyssal hills occurs parallel to the rise crest and normal to the fracture zones. Recent work<sup>7</sup> has shown that the spacing of abyssal hills is inversely related to spreading rate, with slow spreading ridges having an average spacing of 10 km, and fast spreading ridges being less widely spaced (average spacing of 4.2 km). The linear extent of these ridges is 10 km to 40-50 km.

There are many similarities between the components of the tessera terrain and terrestrial sea-floor fabric and structure. Oceanic fracture zones and tessera troughs/fractures are similar in their linearity, parallelism, length, width, spacing, and general morphology (Figs. 1-2). Oceanic abyssal hills are similar to the ridges and valleys of the striped terrain in their orthogonal orientation to, and different scale from, the fracture zones/troughs. They are also similar in their parallelism, their consistent occurrence and relatively constant widths over large areas, the relatively sharp fault-like boundaries of the valleys and ridges, their spacing, their heights, and in their relation to the fracture zones.

On the basis of these similarities it is concluded that the trough and ridged tessera type<sup>3</sup> covering  $14 \times 10^6$  km<sup>2</sup> in Laima Tessera originated through processes analogous to those responsible for the ocean floor fabric on Earth. Specifically, it is interpreted that the tessera originated at a rise crest analogous to divergent boundaries and spreading centers on the Earth's sea floor and evolved to its present morphology and configuration through processes of crustal spreading. This process may be related to the patterns of topography, morphology, and structure comparable to terrestrial spreading centers observed in the Western Aphrodite Terra region to the south of Laima Tessera<sup>9</sup>. The more complex tessera patterns could be due to deformation of the basic trough and ridge tessera pattern or to complex tectonic patterns from other sources of deformation. Recognition of these key basic patterns (long troughs/fractures and short orthogonal striped terrain) should provide a 'marker' structural type and help in deciphering the origin of the more complex tessera occurrences.

**References:** 1) A. Basilevsky et al. (1986) *JGR*, 91, D399. 2) D. Bindschadler and J. Head (1988) *LPSC XIX*, 78, and references therein. 3) *ibid*, 76. 4) K. McDonald (1986) *Geology of N. Amer.*, *GSA*, 51. 5) P. Fox and D. Gallo (1986) *ibid*, 157. 6) K. Kastens (1987) *JGR*, 25, 1554. 7) P. Fox et al. (1989) *EOS*, 69, 1421. 8) D. Abbott (1986) *GRL*, 13, 157. 9) J. Head and L. Crumpler (1987) *Science*, 238, 1380.

Fig. 1. Structure of the tessera in Laima Tessera<sup>1</sup>. 1) lavas, 2) ridges of linear belts, 3) lineaments in tessera, 4) circular blocks, 5) volcanoes, 6) impact craters, 7) main faults.

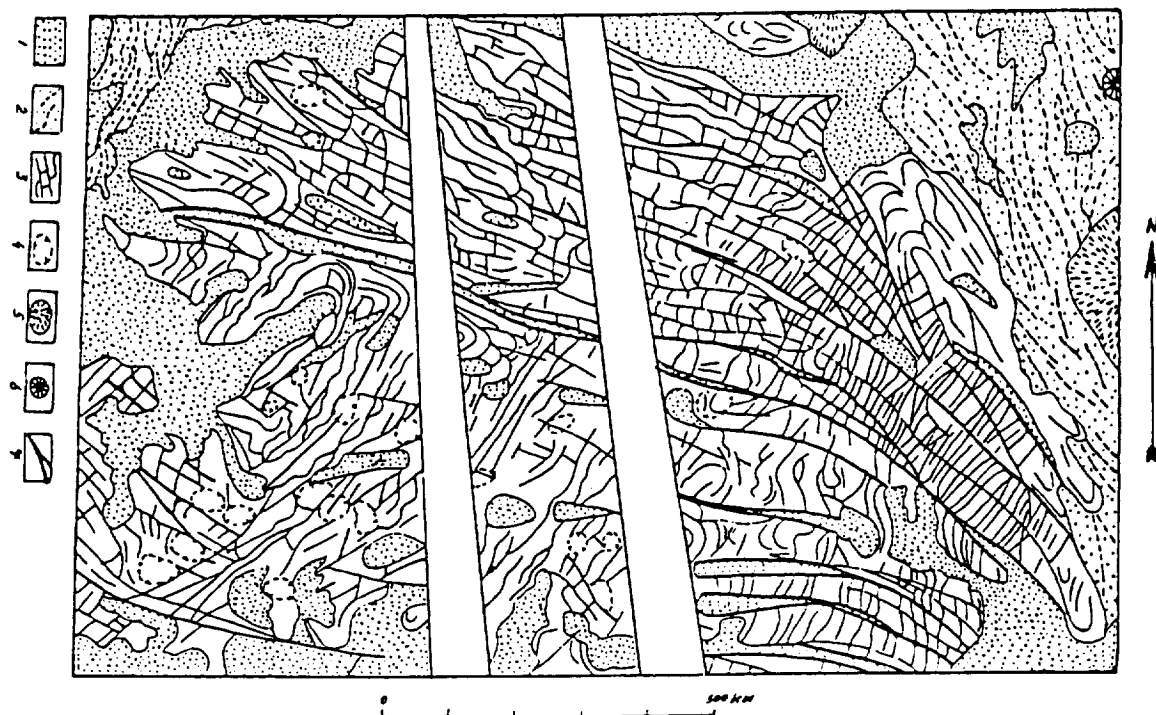
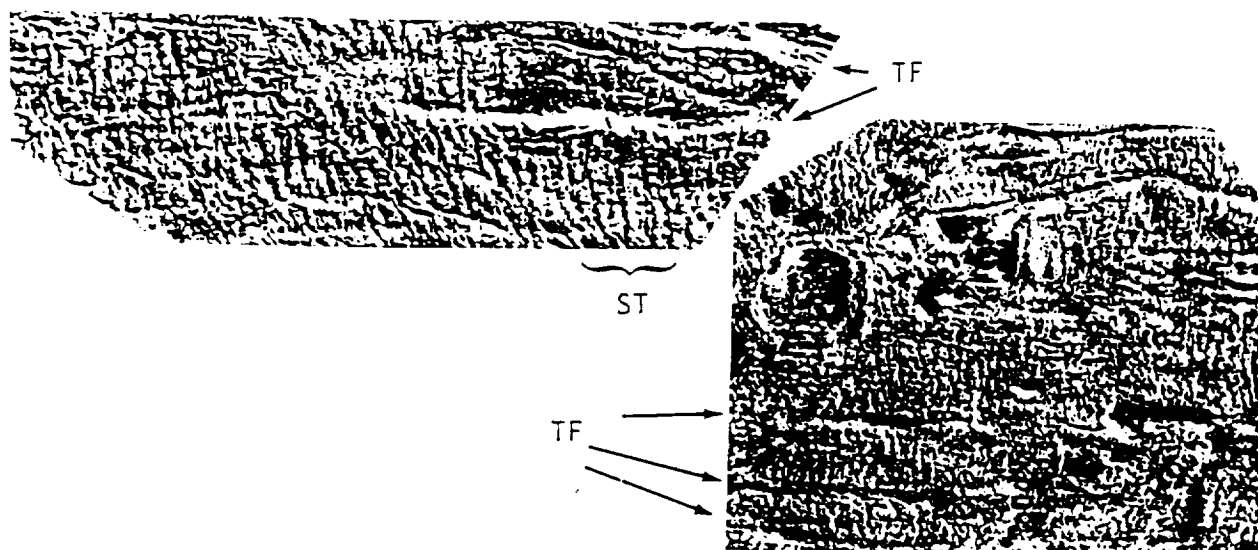


Fig. 2. Venera 15/16 images and sketch maps of troughs/fractures (TF), and the striped terrain (ST) in Laima Tessera. Spacing of stripes averages about 8-10 km.



ORIGINAL PAGE IS  
OF POOR QUALITY

**EASTERN APHRODITE TERRA, VENUS: EVIDENCE FOR ADDITIONAL DIVERGENT  
PLATE BOUNDARY CHARACTERISTICS AND CRUSTAL SPREADING FROM DIANA  
CHASMA TO ATLA REGIO**

L.S. Crumpler and J. W. Head, *Department of Geological Sciences, Brown University, Providence, R.I. 02912*

**Introduction.** The combination of linear discontinuities, regional and local symmetry, offset of symmetry axes, and predictable regional altimetric form in *Western Aphrodite*, have been interpreted recently as analogous to many of the characteristics occurring at terrestrial spreading centers [1, 2]. The continuity between the *Western* and *Eastern Aphrodite* raises the question of whether or not the two segments of the equatorial highlands share a similar structure and origin. There are numerous morphologic similarities between *Eastern Aphrodite* and *Western Aphrodite*, as well as some fundamental morphologic differences. In the following we examine the known characteristics of *Eastern Aphrodite* using techniques previously applied in *Western Aphrodite* in order to address this question.

**General Characteristics and Analysis.** *Eastern Aphrodite*, naturally divided from *Western Aphrodite* along CSD 8 at the eastern margin of *Thetis Regio*, is relatively ridge-like, and rises 1 to 2 km above the surrounding lowlands. Linear chasma, 1 to 3 km deep such as *Diana* and *Dali*, previously interpreted as possible extensional rift zones [3,4], strike approximately N70-90°E along the rise crest, and each is typically accompanied by flanking ridges. Distinctive domical mountains 2 to 3 km high that occur distributed about the flanks of the chasma are responsible for much of the local relief throughout *Eastern Aphrodite*, their isolation and association with the central rift-like chasma suggests that they may be large volcanoes.

**Linear discontinuities.** Several characteristics of the central rise crest in *Eastern Aphrodite* are segmented along the strike including (i) central chasma, (ii) rise crest axis, and (iii) margins of the highland, and offsets in each of these features results in an overall segmented appearance. The detailed characteristics of the rise crests flanks, such as the abundance and distribution of the domical mountains and the paired ridges and troughs parallel with chasma, differ in directions at right angles to each chasma segment, accentuating the overall segmented appearance of the highland. These changes in the flanks and central chasma are relatively abrupt, occur across linear zones of regional altimetric rise or fall according to high-resolution *Arecibo* altimetric profiles [5] crossing their projected lowlands locations, and are oriented at right angles to the strike of the highland. When plotted on the altimetric contour map (Fig. 1), these zones define a series of nearly-parallel, linear discontinuities crossing the overall east-west strike of the highland at approximately right angles to the strike of the central chasma and with orientations similar to the CSD's previously identified in *Western Aphrodite*.

**Bilateral Symmetry.** Altimetric profiles across *Eastern Aphrodite* parallel to the discontinuities are regionally symmetric with one or more deep central troughs along the altimetric crest [5], and with sloping flanks that tend to be convex in the west and more concave toward the east. Alternating ridges and troughs are frequently symmetrically distributed about the central rise crest, which together with the central troughs, are equidistant from the 6052 km altimetric contour marking the morphological margin of the highland. In addition to the offset of chasma and other features, altimetric profiles show that the central axis of symmetry in adjacent profiles parallel to the discontinuities is offset across each of the identified discontinuities in a manner similar to those in *Western Aphrodite*.

**Interpretation of Similarities between Eastern and Western Aphrodite.** In *Western Aphrodite*, linear discontinuities striking across the highland are similar to fracture zones and transform faults in terms of their length, width, altimetric form, nature of their influence on the highlands, and the way in which the regional altimetry steps up or down across them [1,2,6]. *Western Aphrodite* contains a symmetry similar to that derived from thermal boundary layer-related topography on the seafloor [6], and a bilateral symmetry of small scale features like that formed by the splitting, separating, and drifting apart of individual altimetric features initially formed on a rise crest [7].

The linear discontinuities, regional symmetry characteristic, altitude of the slopes, slope coefficients, and slope lengths in *Eastern Aphrodite* are similar to that in *Western Aphrodite*. The altitude varies as the square root of distance from the central rise crest symmetry axis in both highland areas, and because of this, the regional slopes can be accurately predicted in directions at right angles to the symmetry axes. Wherever there is

an offset in the symmetry axis, regional altimetric steps and discontinuities such as those that are observed in the highland are a predicted consequence. In addition, the slopes are similar in both broad behavior and overall magnitude to that predicted from simple thermal boundary layer theory in general [8,9], and similar in particular to that predicted for a thermal boundary layer topography on Venus in association with divergence at rates of 0.5 to 2 cm/yr.

**Interpretation of Differences between Eastern and Western Aphrodite.** Western and Eastern Aphrodite highland show a range of fundamental morphological and structural similarities, but Western Aphrodite is dominated by central plateaus, whereas Eastern Aphrodite is characterized by a relatively simple ridge-like form similar to "normal" rise crests on Earth (Fig. 2). Plateaus, similar to Western Aphrodite, are known to form along rise crests on Earth in which the characteristic thermal boundary layer topography occurs in the lowlands and the plateau (13). Oceanic rise-crest plateaus are currently restricted in occurrence on Earth where anomalous volcanism has resulted in a greater than average crustal thickness. Rise crest plateaus may have been more common at times in the past, particularly during the Cretaceous [10], as the abundance of oceanic plateaus in the Western Pacific suggests.

The origin of the difference between normal rise crests (normal crustal thickness) and rise crest plateaus (larger than average crustal thickness) can be related to any of the processes that result in anomalous mantle melting, including chemical, thermal, and convective inhomogeneities in the mantle characteristics, or the interaction of a "plume" with a normal divergent boundary as proposed for Iceland [11]. Recently, Reid and Jackson [12] have discussed how relatively small differences in mantle temperature on Earth will result in excess melting, volcanism, and crustal thickness along a divergent boundary in which the resulting crustal thicknesses will be characteristic of oceanic plateaus. If Aphrodite Terra represents a divergent plate boundary, the plateau-like form of Western Aphrodite can result from an increase in the crustal thickness [1] associated with modest local increases in mantle temperature [13].

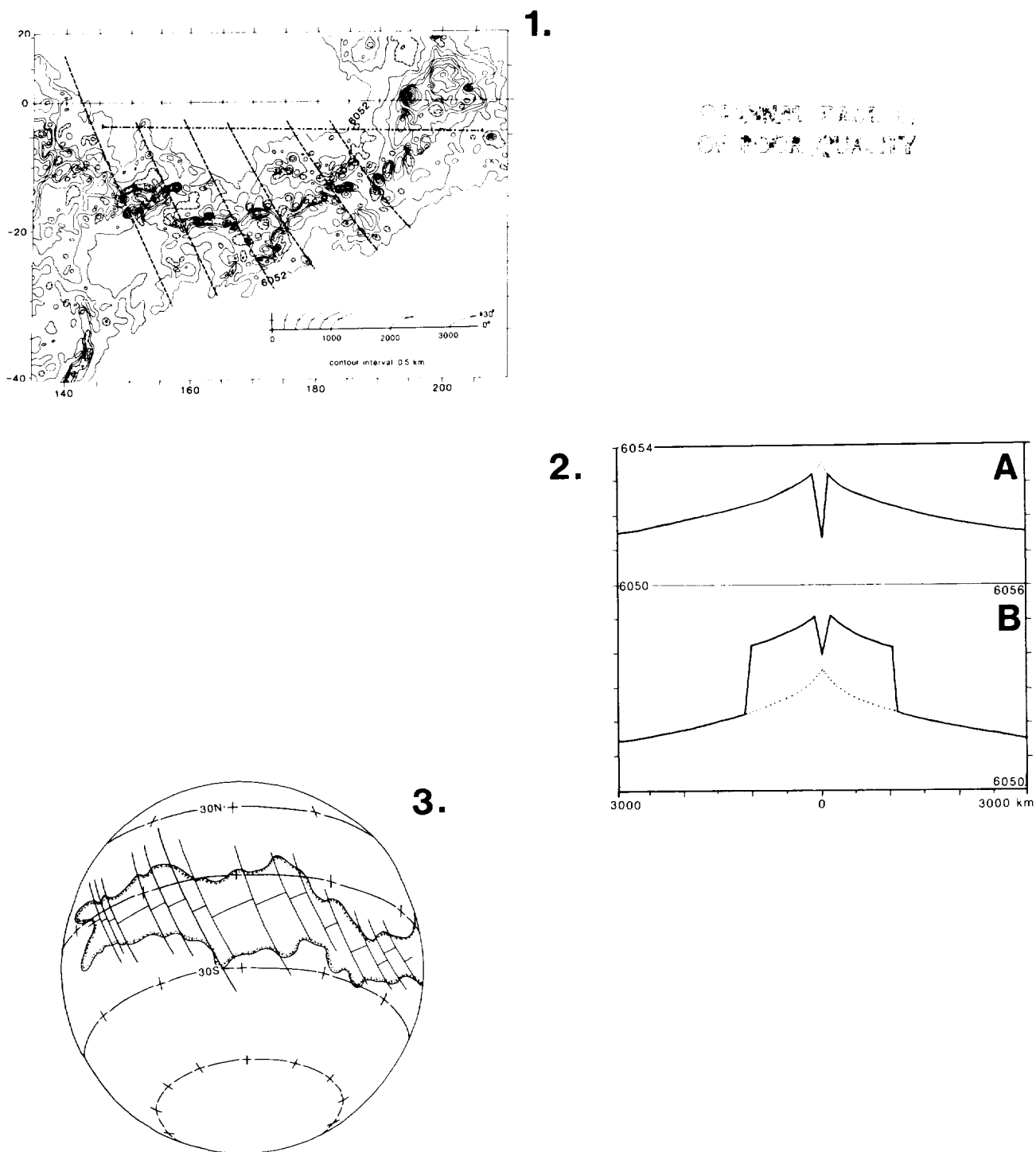
**Conclusions.** Eastern and Western Aphrodite Terra are similar in a variety of characteristics, including linear discontinuities, axial symmetry, and predictable surface altitude characteristics with respect to distance from the symmetry axes. These characteristics in association with the length, width, parallelism, offset of symmetry axes, and influence on the highlands of discontinuities, as well as the evidence for extensional rifting, large volcanoes, and axial plateaus are comparable to the known characteristics of spreading centers on Earth. The differences between Western Aphrodite (central symmetric plateaus) and Eastern Aphrodite (symmetric ridge) can occur along spreading centers where the underlying mantle supplying melts to the rise crest is characterized by variable temperatures. For regions of higher temperature, no volcanism and crustal thicknesses result, and a broad plateau replaces a normal rise crest. The total length of Eastern and Western Aphrodite is 14,000 km, or more than one-third of the global circumference, implying that spreading center characteristics may exert an influence on the tectonic style of a significant proportion of the surface of Venus (Fig.3).

**References.** [1] Head, J.W., and L.S. Crumpler, 1987, *Science* **238**, 1380-1385. [2] Crumpler, L.S., and J.W. Head, 1988, *Jour. Geophys. Res.* **93**, 301-312. [3] McGill, G.E., and others, 1982, *Venus, (U.of A. Press)*, 69-130. [4] Schaber, G.G., 1982, *Geophys. Res. Letts.* **9**, 499-502. [5] Crumpler, L.S., and J.W. Head, 1989, Eastern Aphrodite, in prep. [6] Crumpler, L.S., and J.W. Head, 1989, Western Aphrodite, in prep. [7] Crumpler, L.S., and J.W. Head, 1988, *LPSC XIX*, 235-236, and in prep. [8] Davis, E.E., and C. R.B. Lister, 1974, *Earth Planet. Sci. Letts.* **21**, 405-413. [9] Parsons, B. and J.G. Sclater, 1977, *Jour. Geophys. Res.* **82**, 803-827. [10] Ben-Avraham, Z., and others, 1981, *Science* **213**, 47-54. [11] Vink, G.E., 1984, *Jour. Geophys. Res.* **89**, 9949-9959. [12] Reid, I., and H.R. Jackson, 1981, *Marine Geophys. Res.* **5**, 165-172. [13] Sotin, C., and others, 1989, submitted to *Earth Planet. Sci. Letts.*

Figure 1. Location and distribution of linear discontinuities within the highland part of Eastern Aphrodite.

Figure 2. Difference between "normal" rise crest like that in Eastern Aphrodite(A), and rise crest with anomalous crustal thickness similar to that in Western Aphrodite (B).

Figure 3. Global perspective on the distribution of known linear discontinuities and symmetry axes in Aphrodite Terra



## LAKSHMI PLANUM VOLCANISM: STYLE, ORIGIN, AND RELATION TO OTHER VOLCANIC DEPOSITS ON VENUS

Kari Magee Roberts, James W. Head, Dept. of Geological Sciences, Brown University, Providence, R.I. 02912

Lakshmi Planum, located in western Ishtar Terra, has been interpreted as a highland plain of volcanic origin.<sup>1-6</sup> Lakshmi rises 3-5 km above the datum and is surrounded on all sides by bands of mountains interpreted to be of compressional tectonic origin.<sup>3,11,12</sup> Lakshmi is distinctive and unique on the surface of Venus as an expansive ( $1.5-2.0 \times 10^6 \text{ km}^2$ ), relatively smooth, flat plateau containing two large shield volcanoes in the midst of a region of extreme relief. As a result of our detailed mapping, we have compiled a province map which illustrates some of the basic characteristics and large-scale distribution of surface units on Lakshmi Planum. The map and its units have been described elsewhere;<sup>6</sup> this abstract will focus on the styles and possible origin of the volcanism observed on Lakshmi and how it compares to other volcanic regions on Venus.

We have recognized three styles of volcanism that dominate the surface of Lakshmi. Centralized effusive volcanism is primarily associated with the two major caldera structures (Colette and Sacajawea) and their circumferential low-shield-forming deposits which dominate the plateau. Colette is 130 x 180 km in dimension, elongated in a N-S direction, 1-2 km deep,<sup>2,3,5</sup> and is surrounded by an extensive radiating system of flows having an average width of 15 km and lengths of 100-300 km. The shield structure surrounding Colette is about 500 x 700 km in dimension and descends about 1 km from the rim to the surrounding plains. Sacajawea is a 200 x 120 km oval-shaped depression elongated in a SW-NE direction and approximately 1.5-2 km deep. Sacajawea lacks the distinctive radial lobate flow patterns of Colette,<sup>2,3,5</sup> although mottled deposits surrounding Sacajawea, and distinct from the undivided plains, have been mapped extending about 300 km from the center of the caldera. Adjoining Sacajawea to the SE is a system of linear features interpreted by Pronin<sup>3</sup> to be fault scarps with characteristics similar to graben, at least one of which contains a volcanic dome. The concurrence of these two features suggests the presence of a flanking rift zone similar to those occurring in Hawaii. However, these graben lack the distinctive patterns of lobate flows (emanating at high angles to strike) that characterize eruptions along the rift zones of Mauna Loa and Kilauea. Rift zones which form as a result of listric faulting may be unable to develop on Lakshmi due to the low elevation of the shields there. Perhaps rift zones are only able to form in response to regional stresses, such as those associated with the surrounding orogenic belts. This origin is suspected for the rift zone which adjoins Sacajawea to the SE. On the basis of the relative crispness and distinctiveness of the flows and structures comprising the Colette shield it is interpreted to be younger than Sacajawea.<sup>2,3,5</sup>

Distributed effusive volcanism is associated with domes and cones 1-50 km in diameter and smooth plains for which no specific sources can be found. The abundance and extent of smooth volcanic plains which appear to predate the deposits of Colette and Sacajawea suggest that an episode of volcanic flooding occurred earlier in the history of Lakshmi. It is unclear why there was such a dramatic shift from volcanic flooding to extremely centralized, caldera-forming volcanism.

A third style of volcanism on Lakshmi is pyroclastic activity which may be associated with a 50 km diameter feature to the SE of Colette. This feature is surrounded by an elongated halo of deposits that is apparently superimposed on the more distinctive flow deposits of Colette. The diffuse character, the lack of distinctive lobate patterns, the elongation and the superposition of the deposits suggest that they may be of pyroclastic origin. If the classification of this feature is confirmed, and eruption is determined to have occurred under present conditions, then the presence of volatile-rich magmas on Venus is directly implied.<sup>8</sup>

Three primary characteristics distinguish Lakshmi from other volcanic regions known on the planet.<sup>5-7</sup> These are: 1) its high altitude and plateau-like nature, 2) the presence of two very large, low shield volcanoes with very large distinctive central calderas, Colette and Sacajawea, and 3) its compressional tectonic environment. Lakshmi Planum was originally mapped in its entirety as a smooth highland volcanic plain<sup>2</sup> on the basis of its elevation and smooth contrast to the extreme relief of the surrounding mountain belts. However, our mapping<sup>6</sup> has shown Lakshmi to be more complex and varied, containing additional elements of



many of the plains types defined by Barsukov *et al.* (1986). Beta and Bell Regions are volcanic provinces which, like Lakshmi, are characterized by high altitudes. However, unlike Lakshmi, they lack a plateau-like configuration and are not in compressional tectonic environments. The volcanic plains of Sedna, Guinevere, and Niobe Planitiae are similar to Lakshmi in that they are typified by numerous volcanic constructs, lava flows and sheets, and smooth or gently rolling topography. Unlike Lakshmi, they are at very low elevations and lack sharp, well-defined mountainous boundaries and large volcanic shields. In fact, in the areas imaged by Veneras 15 and 16, there is no other region similar in general characteristics to Lakshmi Planum. While particular aspects of the planum may be observed elsewhere (volcanic regions at high elevations, plains containing numerous volcanic constructs and flows) the combination of features that define Lakshmi is apparently unique on the surface of Venus.

The distinctiveness of Lakshmi Planum is enhanced by the presence of the volcanic shields Colette and Sacajawea, which are themselves quite distinctive structures. Colette and Sacajawea are distinguished by large basal diameters, large, elongate, complex central calderas, and low elevations relative to the surrounding plain. There are numerous large volcanic constructs located outside of Lakshmi Planum but few are the size of Colette and Sacajawea. Theia Mons in Beta Regio is ~350 km in diameter and has an elevation of 1.5-2.0 km<sup>15</sup> above the surrounding topography, making it steeper sloped than Colette. Like Colette, Theia has a large (60-90 km across) summit caldera, although it does not appear to have as complex a system of concentric fault scarps. The smaller basal diameter, steeper slopes, and, perhaps most importantly, the presence of Devana Chasma make Theia Mons notably dissimilar to Colette. Renpet Mons (76°N, 238°) and Tepev Mons (on the SW flank of Bell Regio) also have significant basal diameters (~300 km each) but are still smaller than Colette and Sacajawea. They are typified by higher elevations (up to 5.5 km above the surrounding plains) and steeper slopes than Colette and Sacajawea. Both have weakly defined summit depressions and are surrounded by radar-bright flows, although the lobate character of individual flows is not as distinct as that of flows about Colette. Api Mons (NE of Bell Regio), Atira Mons (52°N, 268°), and Melia Mons (SE of Tethus Tessera) are all characterized by radar-bright flows radiating ~200-250 km from complex summit regions. These structures may represent more highly developed calderas than those present at Theia, Renpet, and Tepev Montes. In particular, Melia Mons has an elongate, almost heart-shaped, caldera-like structure 170 km across. Interior to the structure are numerous domes, craters, and linear features suggestive of a caldera that has undergone several episodes of collapse and rejuvenation. In terms of caldera complexity, Melia Mons is most similar to Colette, although in general morphology they are quite distinct.

Our interpretation of the origin of Lakshmi Planum is based on several key observations. The relative synchronism of volcanism on Lakshmi and tectonism in the surrounding orogenic belts is indicated by the following: 1) the calderas of Colette and Sacajawea are not circular, but elongate, and their walls are oriented parallel to major structural trends within the planum and surrounding mountain belts, 2) smooth volcanic plains have been deformed into ridged plains which follow the borders of the plateau and strike parallel to the adjacent orogenic belts, and 3) the plains become increasingly more elevated as they approach some of the surrounding mountain belts. These observations, in conjunction with the topographic elevation of the plateau itself and the evidence for compressional deformation<sup>11,12</sup> and crustal thickening in excess of several tens of km in Akna, Freyja, and Maxwell Montes<sup>9-14</sup> lead us to conclude that volcanism on Lakshmi Planum is linked to melting associated with the processes of convergence and crustal thickening. We are currently investigating the sequence of tectonic deformation, crustal thickening processes, and the implications for crustal melting and differentiation in relation to the evolution of volcanic deposits on Lakshmi Planum.

**REFERENCES:** 1) H. Masursky *et al.* (1980) *JGR*, **85**, 8232; 2) V. Barsukov *et al.* (1986) *JGR*, **91**, D378; 3) A. Pronin (1986) *Geotectonica*, **4**, 26 (in Russian); 4) A. Basilevsky *et al.* (1986) *JGR*, **91**, D399; 5) E. R. Stofan *et al.* (1987) *Earth, Moon, and Planets*, **38**, 183; 6) Magee and Head (1988) *Lunar Planet. Sci.*, **XIX**, 713; 7) Philips and Malin (1983) from *Venus*, Hunten, *et al.*, eds., p. 150; 8) Head and Wilson (1986) *JGR*, **91**, 9407; 9) Head (1986) *Lunar Planet. Sci.*, **XVII**, 323; 10) Head (1988) *Lunar Planet. Sci.*, **XIX**, 467; 11) Crumpler *et al.* (1986) *Geology*, **14**, 1031; 12) Campbell *et al.* (1983) *Science*, **221**, 644; 13) Vorder Bruegge and Head (1988) *Lunar Planet. Sci.*, **XIX**, 1221; 14) Vorder Bruegge and Head (1988) *Lunar Planet. Sci.*, **XIX**, 1218; 15) Campbell *et al.* (1984) *Science*, **226**, 167.

**Introduction** Venera 15/16 imaging of the northern high latitudes of Venus, north of 30° N, shows that the northern highlands of Ishtar Terra is characterized by broad zones of compression (1,2,3). In contrast, highlands in the equatorial region of the planet (e.g. Beta Regio, Aphrodite Terra) appear to be associated with zones of extension (4,5). In order to compare the processes forming highlands in the equatorial region with those in the northern high latitudes the geology, morphology, and geophysical characteristics of a number of highland features in the Venus equatorial region have been studied (6). In this study, we examine in detail the geologic and geophysical characteristics of the equatorial highland of Western Eisila Regio. We first describe the morphology and general structure of this highland using Pioneer Venus (PV) altimetry data. The local geologic history along with patterns of tectonic deformation are then examined from a radar unit map produced from the PV radar image and structural mapping from Venera 15/16 imaging. In addition, analysis of line-of-sight (LOS) gravity data is carried out in order to estimate an apparent depth of compensation. Finally we use the geologic and geophysical information to assess formational models for this region and compare them with a formational model for the highland of Ishtar Terra.

**Structure and Morphology** Western Eisila Regio is the western most of a chain of equatorial Upland Rises characterized by broad radar-dark domal topographic rises, individual peaks, and extensive volcanism (7). This highland centered at 20° N, 355° between Sedna Planitia and Guenevere Planitia is characterized by 1) an elongated topographic rise approximately 2400 km wide striking N 60° W and 2) two peaks, Sif Mons and Gula Mons located on the crest of the topographic rise which rise 2.2 km and 4.0 km above a datum of 6051.0 km respectively (Figure 1).

**PV Radar Unit Map** Using the PV radar image, seven radar units have been defined on the basis of radar brightness and texture and have been used to map Western Eisila Regio. This map shows the broad topographic rise of Western Eisila Regio to be characterized by units ranging from Very dark in the east, showing characteristics similar to the surrounding plains, to Mottled bright in the west. Mottled bright units are associated with the summit and flanks of Sif Mons. The flanking mottled bright deposits extend radially (averaging 315 km) in all directions from the summit, are lobate, and suggest the presence of a complex system of lava flows superimposed on the broad high (7).

The radar units mapped on Gula Mons, located 740 km to the east of Sif Mons, show properties different from those mapped on Sif Mons. The summit is characterized by a Very bright unit with flanking Dark and Very dark Units confined to areas of lower topography which form a pattern radial from a region just below the summit of Gula Mons (18° N, 358°). These deposits form a cross-cutting relation with adjacent mottled bright and mottled dark units associated with Sif Mons, suggesting that the Very dark units in this area are relatively young and are associated with a system of flows originating from flank eruptions. Gula Mons is therefore interpreted to be younger than Sif Mons.

**Venera 15/16 Imaging** Venera 15/16 radar imaging (1) overlaps the far north and northeast corner of our study area (Figure 1). A number of sub-parallel ridges are located in the overlap region between latitudes of 25° N and 40° N and longitudes 2° E and 10° E. These ridges are located near the flanks of the broad topographic rise in low lying plains. The ridges show a relatively uniform spacing of 20 km and parallel the NNW trend of high topography along the eastern edge of Western Eisila Regio suggesting they are structurally controlled. Between latitudes of 35° N and 40° N and longitudes of 5° E and 10° E, the ridge pattern becomes chaotic. This area corresponds closely to the point where the general trend of high topography changes from a NNW direction to EW. The ridges closest to the flanks of the topographic rise do not have radar shadows, suggesting that they are scarps, possibly associated with normal faulting. Further to the east, radar shadows are present and may be associated with ridge formation due to the rotation of blocks along low angle normal faults.

**LOS Gravity** Examination of line-of-sight (LOS) gravity data shows Western Eisila Regio to be characterized by a maximum positive anomaly of +35 mgal at a spacecraft altitude of 150 km. An analysis of gravity due to topography at spacecraft altitude (8) predicts an anomaly of +40 mgal. Using this information, assuming that the gravity can be modeled by a single wavelength ( $\lambda = 3200$  km), and incorporating the method of Esposito *et al.*, (1982), we calculate an apparent depth of compensation for Western Eisila Regio of approximately 1000 km.

**Formational models** On the basis of our observations we propose two models to explain the formation of Western Eisila Regio: 1) construction and crustal thickening due to volcanic loading in the absence of a thermal anomaly and 2) doming due to a thermal anomaly with secondary volcanism forming Sif Mons and

Gula Mons. The presence of Sif Mons and Gula Mons on the crest of a topographic rise suggests a formational mechanism by construction and crustal thickening. The flows radiating from Sif Mons, however, are of limited extent and appear superimposed on the domal rise suggesting that they represent a thin veneer of material and that constructional volcanism is localized, arguing against a thick crust built up of volcanic deposits. Mapping shows that the broad topographic rise exhibits properties similar to material forming the surrounding plains. This suggests a formational mechanism by uplifting of plains rather than construction. The ridges in the lowlands along the eastern flanks interpreted to be associated with normal faulting form a pattern consistent with models of updoming under regional extension as proposed by Withjack and Scheiner, 1982. The estimated apparent depth of compensation can be interpreted in terms of representing a crustal root or dynamic support of topography. The interpretation of the ridges forming in association with normal faulting related to doming, the presence of plains material similar to adjacent regions on the domal rise, and the interpretation of volcanic deposits as being a thin veneer, along with the deep apparent compensation argue for a model of formation related to doming due to a thermal uplift. Similar models have been proposed for Beta Regio (9,4), Bell Regio (11), and Atla Regio (6). In a global context, the equatorial region of Venus appears to be the site of mantle upwelling and extension forming domal rises along with being the site of possible crustal accretion (5). The highland of Ishtar Terra in the north polar region, on the other hand is characterized by large scale compression, forming high topography through thrust faulting and crustal thickening (2,3).

#### References:

- (1) Barsukov, V. L. *et al.*, *JGR.*, 91, D378, 1986. (2) Crumpler, L. *et al.*, *Geology*, 14, 1031, 1986. (3) Vorder Bruegge, R. MS Thesis, 1987. (4) Stofan, E. R. *et al.*, *GSA Bull.* in press 1988. (5) Head, J. and L. Crumpler, *Science*, 238, 1280, 1987. (6) Senske, D. A. and J. W. Head, *LPSC XIX*, 1061, 1988. (7) Senske, D. A. and J. W. Head, *LPSC XIX*, 1063, 1988. (8) Sjogren, W. L. *et al.*, *JGR.*, 88 1119, 1983. (9) Esposito, P. B., *et al.*, *Icarus*, 51, 448, 1982. (10) Withjack, M. D. and C. Scheiner, *AAPG Bull.*, 66, 302, 1982. (11) Basilevsky, A. T., and P. Janle, *Astron. Vestnik.*, 21, 109, 1987.

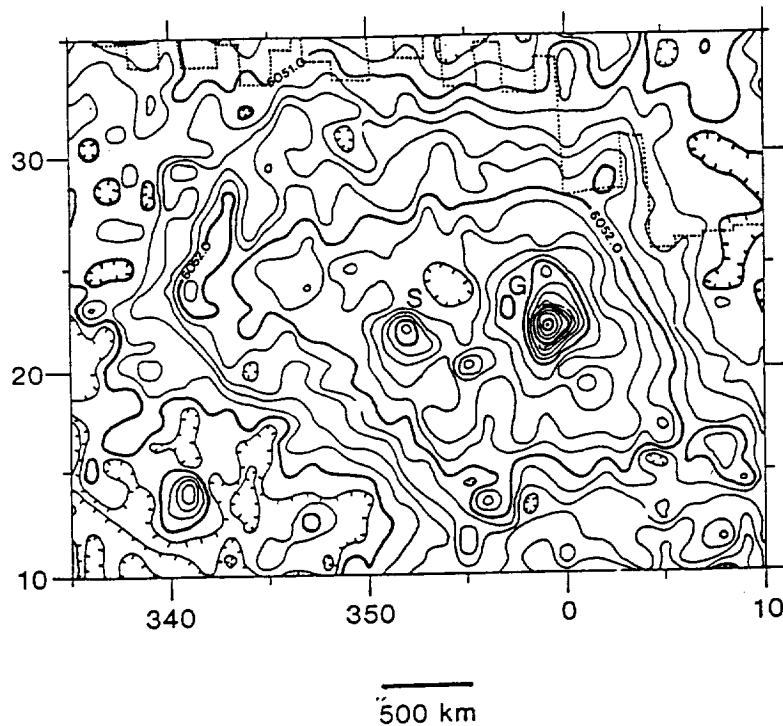


Figure 1. Pioneer Venus topography of Western Eistla Regio. Data is contoured at 200 m intervals. Two peaks, Sif Mons (S) and Gula Mons (G), interpreted to be volcanoes are located on the crest of a broad topographic rise. The dotted line marks the southern extent of Venera 15/16 image coverage.

**Synthesis of Venus Equatorial Geology: Variations in Styles of Tectonism and Volcanism and Comparison with the Northern High Latitudes** D. A. Senske and J. W. Head,  
Department of Geological Sciences, Brown University, Providence, RI 02912.

**Introduction.** Geologic mapping from Pioneer Venus (PV) radar image data shows that the equatorial region of Venus ( $15^{\circ}$  S to  $45^{\circ}$  N) is characterized by seven distinct physiographic units along with four classes of tectonic and volcanic features (1,2). The northern  $15^{\circ}$  of the PV-imaged region overlaps Venera 15/16 radar image data (3) allowing correlations to be made between units mapped in both data sets. This correlation facilitates the extrapolation of Venera units into the equatorial region. In this paper an analysis is made of the region of overlap between the two radar images, examining the correspondence between units mapped in the northern high latitudes with those in the equatorial region. We also examine the spatial distributions and geologic relationships of the different equatorial units.

**Analysis of the Region of Venera 15/16 and PV image Overlap.** Six of the units mapped in the equatorial region are found in the region of overlap with Venera data: plains (undivided), upland rises, tectonic junctions, inter-highland tectonic zones, upland plateaus, and coronae. Plains units (undivided) are radar-dark to mottled dark regions of low topography corresponding to Venera units mapped as smooth plains and rolling plains (3,4). This is the most pervasive geologic unit on the planet, covering approximately 70% of both the equatorial region and the northern high latitudes (4). The PV units defined as upland rises and the tectonic junction of Beta Regio correspond to the general Venera unit of large dome-like uplands. On the basis of stratigraphic relations between radar units and analysis of LOS gravity data, both of these units are interpreted to be associated with doming and thermal uplift (1,5,6). An additional large dome-like upland corresponds to the northern extension of an inter-highland tectonic zone located at northern Ulfrun Regio, and is characterized by a central graben structure and volcanic peaks. Two distinct regions of upland plateaus are found in the equatorial region: the first is located in the vicinity of Aphrodite Terra, and the second on the east and west flanks of Beta Regio. The large upland plateau of Tellus Regio, located to the north of Aphrodite Terra, has been mapped as tessera from Venera imaging (3). In addition to Tellus, correlations with the upland plateau unit have been made between two smaller areas of tessera, Shimti Tessera and Kutue Tessera, which are located to the east of Tellus. On the basis of these correlations and the distinctive characteristics of tessera (elevated topographic plateau, high roughness, low reflectivity, highly diffuse scattering) (1,2), the southward continuation of mapping into the equatorial region suggests the presence of a tessera-like upland plateau along the northern flank of Thetis Regio (1). The upland plateau on the eastern flanks of Beta Regio has recently been studied from high resolution Arecibo images (1,7), and has been shown to possess a complex system of ridges and valleys interpreted to be tessera-like (1). Two coronae, the first located in Bell Regio and the second to the north of Sappho, are identified in both the Venera and PV image data. Within the PV data these structures are characterized by locally elevated topography, narrow radar-bright discontinuous rims, and radar-dark interiors (2). Similar characteristics are observed for coronae mapped in Mnemosyne Regio from both Arecibo and Venera radar images (8). On the basis of this characterization, two large circular features interpreted as coronae are identified in the area imaged exclusively by PV. The first, Pavlova, is located in Eastern Eisila Regio, possesses an elliptical shape with dimensions of 525 km x 370 km, and is characterized by a 50-km wide discontinuous rim which exhibits 600 m of relief. The discontinuous part of the rim correlates with flanking topographic depressions mapped as very dark, that possess similarities to units mapped elsewhere as volcanic plains. The second (840 km diameter) corona is located to the south of Western Eisila Regio ( $2.0^{\circ}$  N,  $355.0^{\circ}$ ). Like Pavlova, this structure is characterized by a discontinuous rim which is radar-bright and elevated to the south while the northern rim possesses no topographic relief and is radar-dark (1). Stratigraphic relations between the rim and radar-dark interior deposits suggests lava flooding, forming plains, has occurred in the interior of this structure.

**Distribution of Equatorial Highlands** On the basis of variations in structure and morphology, the physiographic units are divided into three distinct longitudinal zones: upland rises ( $330^{\circ}$  to  $55^{\circ}$ ), tectonically segmented linear highlands-upland plateaus ( $55^{\circ}$  to  $145^{\circ}$ ), and inter-highland tectonic zones-tectonic junctions ( $145^{\circ}$  to  $315^{\circ}$ ). The zone of upland rises contains two highland structures, Bell Regio and Eisila Regio whose volcanic nature has been previously established (4,9,10). Eisila Regio is characterized by three distinct regions, Western Eisila with its volcanic peaks Sif Mons and Gula Mons, Central Eisila with the volcanic peak Sappho (11,12), and Eastern Eisila Regio with its corona structure, Pavlova. Detailed analysis of Western Eisila Regio suggests that the volcanoes and their deposits represent a thin veneer of material superimposed on a broad topographic high. In addition, ridges in the lowlands along the eastern flanks of Western Eisila Regio are interpreted to be normal faults (13) whose relation to high topography is consistent with a model of uplift under extension (14). This arrangement of structures and association with volcanism in Western Eisila suggests

formation by doming associated with thermal uplift. A similar model has been previously proposed for Bell Regio (9,10). The volcanic nature of both Central Eüsila and Eastern Eüsila and their similarities to Bell and Western Eüsila suggests that these features may also have formed by doming and thermal uplift. The region of tectonically segmented linear highlands and upland plateaus is made up of the highlands of Western Aphrodite (Ovda Regio and Thetis Regio) and Tellus Regio. Previous studies of the tectonically segmented linear highland of Western Aphrodite show it to be characterized by bilaterally symmetric topography and an en echelon central trough offset in a right lateral sense along cross-strike structural and topographic discontinuities (CSD's) (15,16). The structure of Western Aphrodite is similar to that of terrestrial mid-ocean ridges, and has on this basis been interpreted to be a site of possible spreading (15,16). The upland plateaus of Tellus Regio and the units flanking northern Aphrodite form a second distinctive set of highland features in the equatorial region (2). The location of an upland plateau adjacent to Thetis Regio, a region interpreted to be the site of crustal spreading (15,16), suggests two possible models for upland plateau formation: 1) the upland plateau is a preexisting old crustal block; doming and rifting analogous to that of old terrestrial continental crust, followed by spreading as suggested by Head and Crumpler (1987) (15), have split the block and formed the intervening high topography associated with Thetis; 2) the upland plateau originated by crustal spreading. In this second model, developed by Sotin *et al.*, (1988) (17), an increase in mantle temperature and associated production of thicker crust created the high topography in central Thetis Regio. The region of inter-highland tectonic zones and tectonic junctions has previously been described as zones of extension (18). Unlike the upland rises and tectonically segmented linear highlands, which are predominantly linear features striking east-west, the inter-highland tectonic zones have a variety of orientations forming an interconnecting radial pattern between tectonic junctions (2). The presence of a bilaterally symmetric topographic rise with a central trough offset along CSD's suggests that the inter-highland tectonic zone of Eastern Aphrodite is a site of rifting and crustal spreading (19). This and other inter-highland tectonic zones converge at tectonic junctions. Two of these junctions, Beta Regio and Atla Regio, have been interpreted to be associated with deep mantle thermal anomalies (1,5,6).

**Conclusions.** Examination of the 15° overlap region between the Venera and PV imaging data has allowed a one-to-one correlation between large-scale features in the two data sets to be made. On the basis of this correlation and the characteristic radar properties of these features, it is possible to extrapolate units mapped in the northern high latitudes into the equatorial region. We make four major conclusions based on this mapping: 1) Upland Plateaus, which are interpreted to be tessera-like tectonic units, cover approximately 6% of the region imaged by PV, which is slightly less than the percentage of unit area mapped as tessera in the northern high latitudes. 2) Tectonic junctions, tectonically segmented linear highlands, and inter-highland tectonic zones are unique to the equatorial region. 3) The equatorial region is interpreted to be characterized by regions of high topography associated with thermal uplift (e.g. hot spots), and long linear zones of extension and possible crustal spreading. 4) In contrast to the equatorial region, the northern high latitudes are characterized by several broad zones of compression forming highlands and orogenic belts (20,21).

**References:** (1) Senske, D. A., M. S. Thesis in preparation, 1989. (2) Senske, D. A. and J. W. Head, *LPSC XX*, this volume. (3) Barsukov, V. L. *et al.*, *JGR*, D378, 1986. (4) Senske, D. A. and J. W. Head, *LPSC XIX*, 1061, 1988. (5) Esposito P. B. *et al.*, *Icarus*, 51, 448, 1982. (6) Stofan E. R., *et al.*, *GSA Bulletin*, in press 1989. (7) Campbell D. B., *et al.*, *LPSC XX*, this volume. (8) Stofan E. R. and J. W. Head, submitted to *Icarus*, 1989. (9) Basilevsky, A. T. and P. Janle, *Astron Vestnik*, 21,109, 1987. (10) Janle, P. *et al.*, *Earth Moon, and Planets*, 39, 251, 1987. (11) Burns, B. and D. B. Campbell, *JGR*, 90, 3037, 1985. (12) Stofan, E. R., M. S. Thesis, 1-64, 1985. (13) Senske D. A. and J. W. Head, submitted to *IGC*, 1988. (14) Withjack M. D. and C. Scheiner, *AAPG Bull.*, 66,302, 1982. (15) Head, J. W. and L. S. Crumpler, *Science*, 238, 1380, 1987. (16) Crumpler L. S., and J. W. Head, *JGR*, 93, 301, 1988. (17) Sotin *et al.*, submitted to *EPSL*, 1988. (18) Schaber, G. *GRL*, 9, 499, 1982. (19) Crumpler L. S. and J. W. Head, *LPSC XIX*, 223, 1988. (20) Crumpler L. S. *et al.*, *Geology*, 14, 1031, 1986. (21) Vorder Bruegge, R. M. S. Thesis, 1987.

## LAKSHMI PLANUM: A DISTINCTIVE HIGHLAND VOLCANIC PROVINCE

Kari P. Magee, James W. Head, Dept. of Geological Sciences, Brown University, Providence, R. I. 02912

**Introduction-** Lakshmi Planum, a broad smooth plain located in western Ishtar Terra and containing two large oval depressions (Colette and Sacajawea), has been interpreted as a highland plain of volcanic origin.<sup>1-5</sup> Lakshmi is situated about 3 km above the mean planetary radius and is surrounded on all sides by bands of mountains interpreted to be of compressional tectonic origin (Fig. 1).<sup>5-7</sup> Four primary characteristics distinguish Lakshmi from other volcanic regions known on the planet, such as Beta Regio: 1) high altitude, 2) plateau-like nature, 3) the presence of very large, low volcanic constructs with distinctive central calderas (Colette and Sacajawea), and 4) its compressional tectonic surroundings. Building on the previous work of Pronin,<sup>5</sup> the purpose of this study is to establish the detailed nature of the volcanic deposits on Lakshmi, interpret eruption styles and conditions, sketch out an eruption history, and determine the relationship between volcanism and the tectonic environment of the region.

**Observations and Interpretations-** On the basis of our detailed mapping we have compiled a province map (Fig 1.) that illustrates some of the basic characteristics and relationships in Lakshmi Planum. **Major shields/calderas:** Two major caldera structures (Colette, C; Sacajawea, S) and their circumferential low-shield-forming flow deposits dominate the region. Colette is 130 x 180 km, elongated in a N-S direction, is approximately 2 km deep<sup>4,5</sup> and is surrounded by an extensive radiating system of flows having an average width of 15 km, and lengths of 100-300 km. The shield structure surrounding Colette is about 500 x 700 km in dimension and descends about 1 km from the rim to the surrounding plains. Sacajawea is a 200 x 120 km oval-shaped depression elongated in a SW-NE direction, approximately 1.5 km deep, and lacks the distinct radial lobate flow patterns of Colette, although mottled deposits surrounding Sacajawea, and distinct from the undivided plains, have been mapped extending about 300 km from the center of Sacajawea. The Sacajawea shield structure (defined by the caldera and the surrounding deposits) is very low (less than 1 km from the rim to the surrounding plains). On the basis of the relative crispness and distinctiveness of the flows and structures comprising the Colette shield, it is interpreted to be younger than Sacajawea.<sup>4,5</sup> Elsewhere, we describe the characteristics and relationships of Colette and Sacajawea calderas.<sup>8</sup>

A wide range of additional structures interpreted to be volcanic source vents have been mapped including: 1) domes and cones, which range from 1-50 km in diameter and include small cones (<10 km diameter) scattered throughout the region; small domes (10-15 km in diameter) sometimes containing summit depressions and apparently preferentially located in association with structural features (e.g., inside Colette, along a rift associated with Sacajawea, and within the Ridged Terrain); and low shields, up to 75 km across, almost indiscernable topographically, and containing a summit pit; 2) Diffuse halo (Fig. 1, [1]); SE from Colette is a large, dark semicircular feature about 50 km in diameter surrounded by an elongated halo of diffuse radar-bright deposits that are apparently superimposed on the more distinct flow deposits of Colette. The diffuse character, the lack of distinctive lobate patterns, the elongation and the superposition of the deposits suggest that they may be of pyroclastic origin; 3) Vent Complex (Fig. 1, [2]); flanking Sacajawea to the S-SW is a very broad (~200 km diameter) radar-bright feature of seemingly negligible height that appears to be a localized center of volcanism characterized by very mottled lobate flow deposits which become more continuous towards a central region which contains at least four 15 km wide depressions.

**Plains units** dominate the surface of Lakshmi and are interpreted to be volcanic on the basis of their embayment relationships, their flatness and uniform albedo, and their association with volcanic source vents. **Undivided Plains units** (PU) are characterized as smooth low-albedo plains in which individual flow features are not seen in either Venera 15/16 or Arecibo data. They cover a large part of Lakshmi, and may be derived from the major shields, from the numerous domes and cones, or from presently buried sources. **Grooved Plains** (PG) occur in a single patch about 150 km to the north of Sacajawea and are typified by very finely spaced furrows or grooves arranged in sweeping curvilinear sets trending generally N-S but frequently curving to the NE or NW. This system of faults<sup>5</sup> appears to be extensional in origin, and is embayed by Sacajawea deposits and undivided plains. **Ridged Plains** (PR) are defined by faint bright lineaments on plains material arranged in subparallel sets that follow the borders of the planum or trend S-SE across it. On the basis of the ridge-like nature of some of these bands, and their association with the compressional deformation in the surrounding orogenic belts, we have interpreted them to be of compressional origin. The parallelism of many of these ridged units with the adjacent orogenic belts, and the general tilting of the ridged plains away from the mountains, strongly suggest that the plains have been involved in at least the latter phases of deformation producing the orogenic belts.

**Structural features and units** occur within the plains, as well as dominating the surrounding mountains. **Ridged Terrain** (RT) is characterized by a very rough-textured system of ridges and grooves and is concentrated in east central Lakshmi where, in at least one occurrence, the ridges and grooves are arranged in rhomboidal sets with the small angle subtending about 35° and the bisectrix oriented about N35°W. Virtually all other units are superposed on or embay RT, and we thus concur with Pronin<sup>5</sup> that this unit is representative of an episode of deformation early in the history of

Lakshmi. Adjoining Sacajawea to the SE is a system of linear features interpreted by Pronin<sup>5</sup> to be fault scarps with characteristics similar to graben, at least one of which contains a volcanic dome. This may be a flanking rift zone similar to those occurring on Hawaii. In addition, a series of domes and cones appear to be arrayed in a preferred orientation, trending E-SE along a line connecting Colette and Sacajawea.

#### Conclusions-

1) Volcanic style: The range of deposits and structures mapped in Lakshmi Planum indicates that the region is dominated by at least three styles of volcanism: a) centralized effusive, very large low shield structures (>500 km) with numerous long flows and extremely large calderas<sup>8</sup> (100-200 km); b) distributed effusive, with a wide range of source vents most typically forming cones and domes in the 1-50 km diameter size range; although dispersed throughout Lakshmi, many are localized along structural trends; on the basis of their radar characteristics, most mapped effusive deposits appear to be relatively smooth at scales of decimeters to meters; c) possible pyroclastic, represented by the Diffuse Halo; if further mapping confirms a pyroclastic origin, this would imply the presence of volatile-rich magmas on Venus.<sup>9</sup>

2) Sequence and Geologic History: Formation of the Ridged Terrain was followed by emplacement of plains which were subsequently deformed to produce the Grooved Plains N of Sacajawea. Sacajawea was formed and its related deposits embayed the Grooved Plains and Ridged Plains. The Vent Complex postdated Sacajawea and some PU, but its age is not known relative to younger deposits. Colette and its associated flows were formed subsequent to Sacajawea, and it is not known if activity in the two structures overlaps in time. The Diffuse Halo appears to postdate Colette. Ridged Plains appear to have formed throughout the history of Lakshmi, apparently deforming in response to compressional deformation and regional tilting in the adjacent mountain ranges. Ivanov et al<sup>10</sup> have argued that the radar brightness (decimeter to meter scale roughness) associated with fresh impact crater haloes is lost by a smoothing process after about 120-250 my. If this is true, and bright units on Lakshmi have a similar roughness, then this may imply that at least some of the volcanism occurred relatively recently.

3) Relation to Tectonic Deformation: There is abundant evidence for the synchronicity of volcanism and tectonism (elongation of calderas, rift zones adjacent to calderas, association of domes and cones with preexisting structure, Grooved Plains, Ridged Plains of various ages and orientations, etc.). Further analysis is required to determine the sequence of deformation in the adjacent orogenic belts and its link to Lakshmi volcanic history, but it tentatively appears that the center of volcanism has migrated from east to west during the history of Lakshmi. 4)

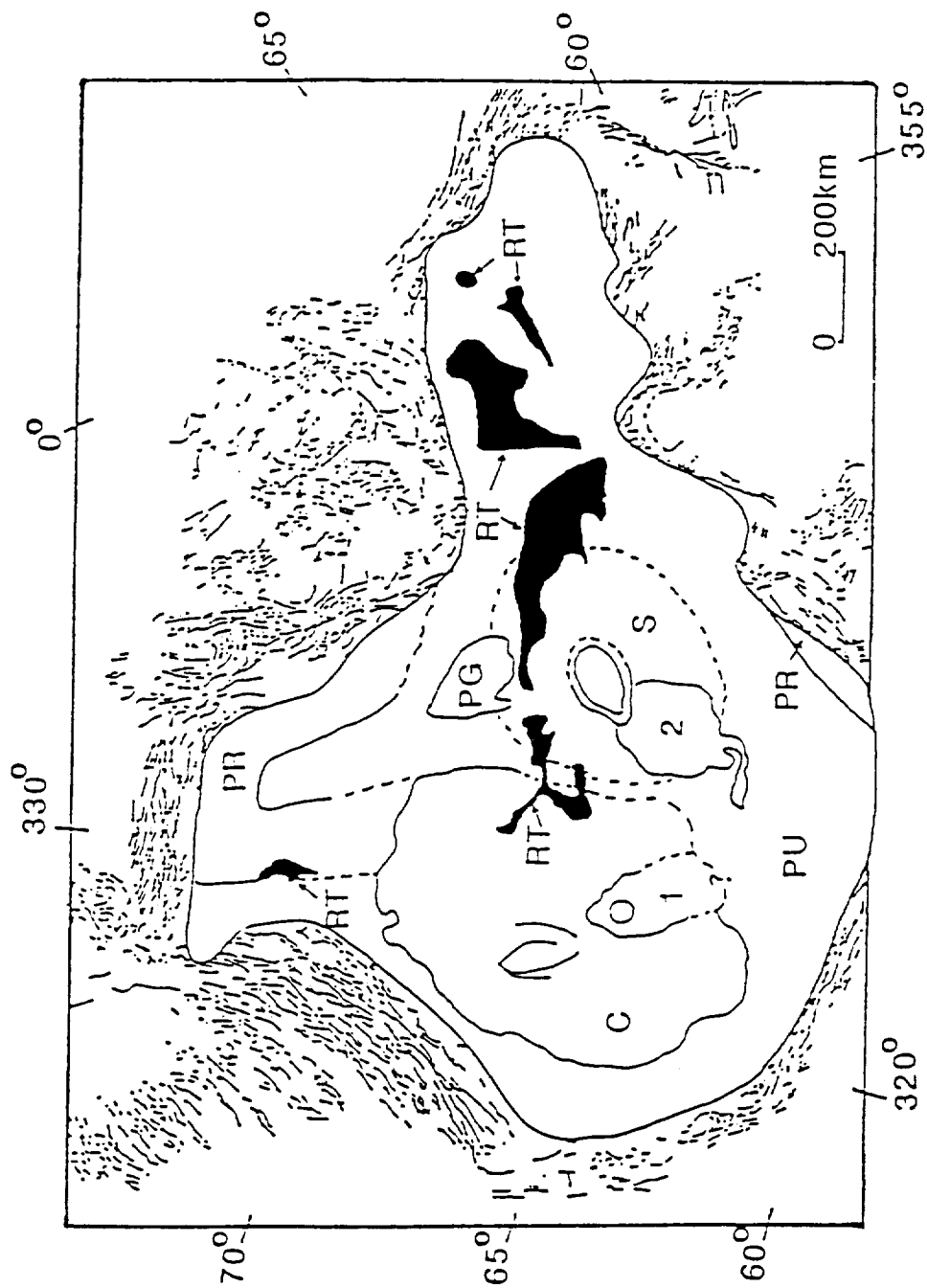
Distinctiveness of Lakshmi Planum: Our studies further emphasize the unique nature of Lakshmi Planum in terms of its compressional tectonic environment, altitude, and presence of large low shields with extremely large calderas. No other such volcanic province has yet been identified on Venus.

5) Origin of Lakshmi Planum: On the basis of the presence of distributed regional compressional deformation surrounding Lakshmi Planum,<sup>6-7,11-12</sup> the sense of tectonic transport in toward Lakshmi from the north<sup>11</sup> and the east,<sup>12</sup> the evidence for crustal thickening in Freyja and Maxwell Montes in excess of several tens of kilometers,<sup>11-12</sup> and the topographic elevation of the plateau itself, we interpret Lakshmi Planum to be the locus of convergence and crustal thickening, and the volcanic activity there to be linked to melting associated with processes of convergence and crustal thickening. This model is in contrast to that of Pronin,<sup>5</sup> who attributes the volcanism to a large hot spot upwelling below Lakshmi, and spreading laterally to cause the surrounding deformation.

**References:** (1) H. Masursky, *et al.* (1980) *JGR*, **85**, 8232; (2) V. Barsukov, *et al.* (1986) *JGR*, **91**, D378; (3) A. Basilevsky, *et al.* (1986) *JGR*, **91**, D399; (4) E. Stofan *et al.* (1987) *Earth, Moon*, **38**, 183; (5) A. Pronin (1986) *Geotectonica*, **4**, 26 (in Russian); (6) Campbell *et al.* (1983) *Science*, **221**, 644; (7) Crumpler *et al.* (1986) *Geology*, **14**, 1031; (8) Magee and Head (1988) *Lunar Planet. Sci.*, **XIX**, 711; (9) Head and Wilson (1986) *JGR*, **91**, 9407; (10) B. Ivanov, *et al.*, (1986) *JGR*, **91**, D413; (11) Head (1988) *Lunar Planet. Sci.*, **XIX**, 467; (12) Vorder Bruegge and Head (1988) *Lunar Planet. Sci.*, **XIX**, 1220.

**Figure 1.** Province map of Lakshmi Planum. See text for explanation. Lines outside of Lakshmi Planum indicate structural trends in adjacent deformed terrain.

# PROVINCE MAP OF LAKSHMI PLANUM



P = PLAINS (PU = UNDIVIDED, PR = RIDGED, PG = GROOVED)

RT = RIDGED TERRAIN

C = COLETTE

S = SACAJAWEA

Figure 1



**MULTI-STAGE TECTONIC EVOLUTION OF EASTERN ISHTAR TERRA, VENUS.**  
**R.W.Vorder Bruegge and J.W. Head, Dept. of Geo. Sci., Brown Univ., Providence, RI 02912.**

**Introduction:** Previous analyses have established the compressional nature of the Maxwell Montes mountain range [1-6] and the adjacent high plateau of western Fortuna Tessera [6-10] on Venus. This compression has been interpreted as resulting from WSW-directed convergence of crustal materials accompanied by crustal thickening, and involving small-scale folding and buckling [5-10]. In order to integrate these findings with the surrounding areas, this study has been extended to include all of Fortuna Tessera. From this analysis a scenario has been constructed describing the tectonic evolution of the entire eastern half of the Ishtar Terra highland region.

**Observations:** Ridge/valley pairs, individual troughs, and large-scale scarps have been mapped in Eastern Ishtar Terra (Figure 1). Three distinctive regions have been identified from analysis of these features: 1) Maxwell Montes and western Fortuna Tessera, which is dominated by NNW-trending ridge/valley pairs; 2) Central and Northern Fortuna Tessera, which is dominated by both large, WNW-trending scarps and WNW-trending ridge/valley pairs, which gradually change to NNW-trends in easternmost Fortuna; and 3) Southeastern Fortuna Tessera, which is characterized by a complex pattern of intersecting ridges, valleys, and troughs. The topography of these regions is shown in Figure 1d. In both Maxwell/western Fortuna and northern Fortuna, the ridge/valley pairs approximately parallel the topographic contours along gradual slopes to the east and north, respectively. Northern Fortuna, however, is also characterized by steep, NNE-facing topographic scarps with up to 2 km of relief. Finally, the topography of southeastern Fortuna is a broad, NW-trending arch. Unlike the other two regions, ridges here do not parallel the topographic contours, but NW-trending troughs parallel the crest of the topographic arch.

**Interpretations:** We examine the relationship between morphology and topography in these regions as an aid in interpreting their tectonic evolution. A correlation between large-scale topography and the tectonic fabric of ridges is observed in western Fortuna Tessera and is interpreted to be due to WSW-directed compressional deformation, accompanied by crustal convergence and thickening, resulting in the formation of Maxwell Montes and the high plateau to its immediate east [7,8]. The predominance of WNW-oriented ridges and large scarps in northern Fortuna Tessera and their correspondence to steep topography falling off to the NNE is similar to features and topography observed north of Freyja Montes, which has been interpreted as a region of large-scale compression, including flexure, buckling, and crustal imbrication [11]. Note that the pattern of WNW-oriented ridges and scarps, along with the steep topographic drop off to the NNE, occurs along the entire northern flank of Eastern Ishtar Terra. This suggests that the entire northern flank of Eastern Ishtar Terra is undergoing SSW-directed crustal convergence involving large-scale crustal buckling and imbrication, with the plains areas to the north underthrusting northern Fortuna Tessera, as suggested for Western Ishtar Terra, north of Freyja Montes [11].

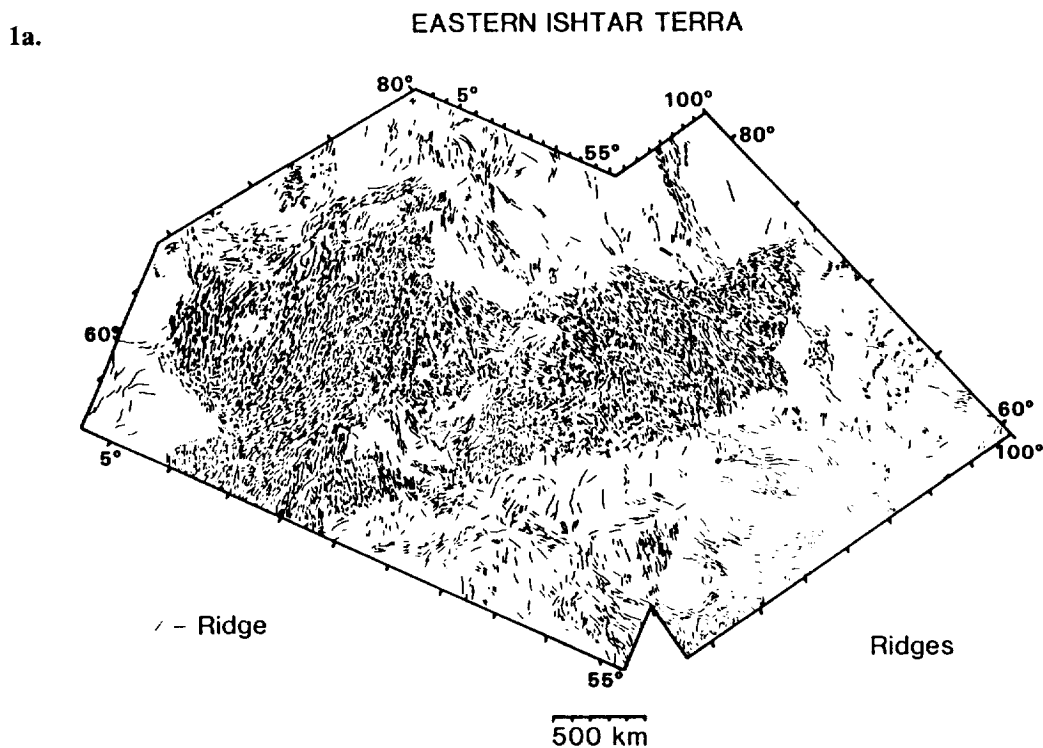
The final region, southeastern Fortuna Tessera, represents a more complex picture with its range of typical tessera morphology of intersecting ridges and troughs [3,4,12]. Bindschadler and Head [12] identified three subtypes of tessera and all three of these can be recognized in southeastern Fortuna Tessera: Sub-parallel Ridged Terrain near 60°E/70°N; Trough and Ridge Terrain near 65°E/69°N and 51°E/69°N; and Disrupted Terrain in the region 40-50°E/65-70°N. The relationship between these subtypes is uncertain, however, we note that transitions from one subtype to another in this region occur gradually, as does the transition from the disrupted (tessera) terrain in southeastern Fortuna to the sub-parallel ridges in northern Fortuna. A similar gradual transition of morphology is observed from central Fortuna to Maxwell Montes [7,8,10]. In this case, the WSW-compression appears to be taking place at the expense of the basic tessera pattern in central Fortuna with Disrupted Terrain being modified into Sub-parallel Ridged Terrain [10]. The gradual south-to-north transition from the basic tessera pattern of southeastern Fortuna to the sub-parallel ridges in northern Fortuna Tessera is interpreted to be due to a similar process in which SSW-compression in northern Fortuna occurs from the north, so that the basic disrupted tessera terrain is interpreted as the original fabric of these areas. The origin of this basic

tessera terrain, however, is uncertain [13].

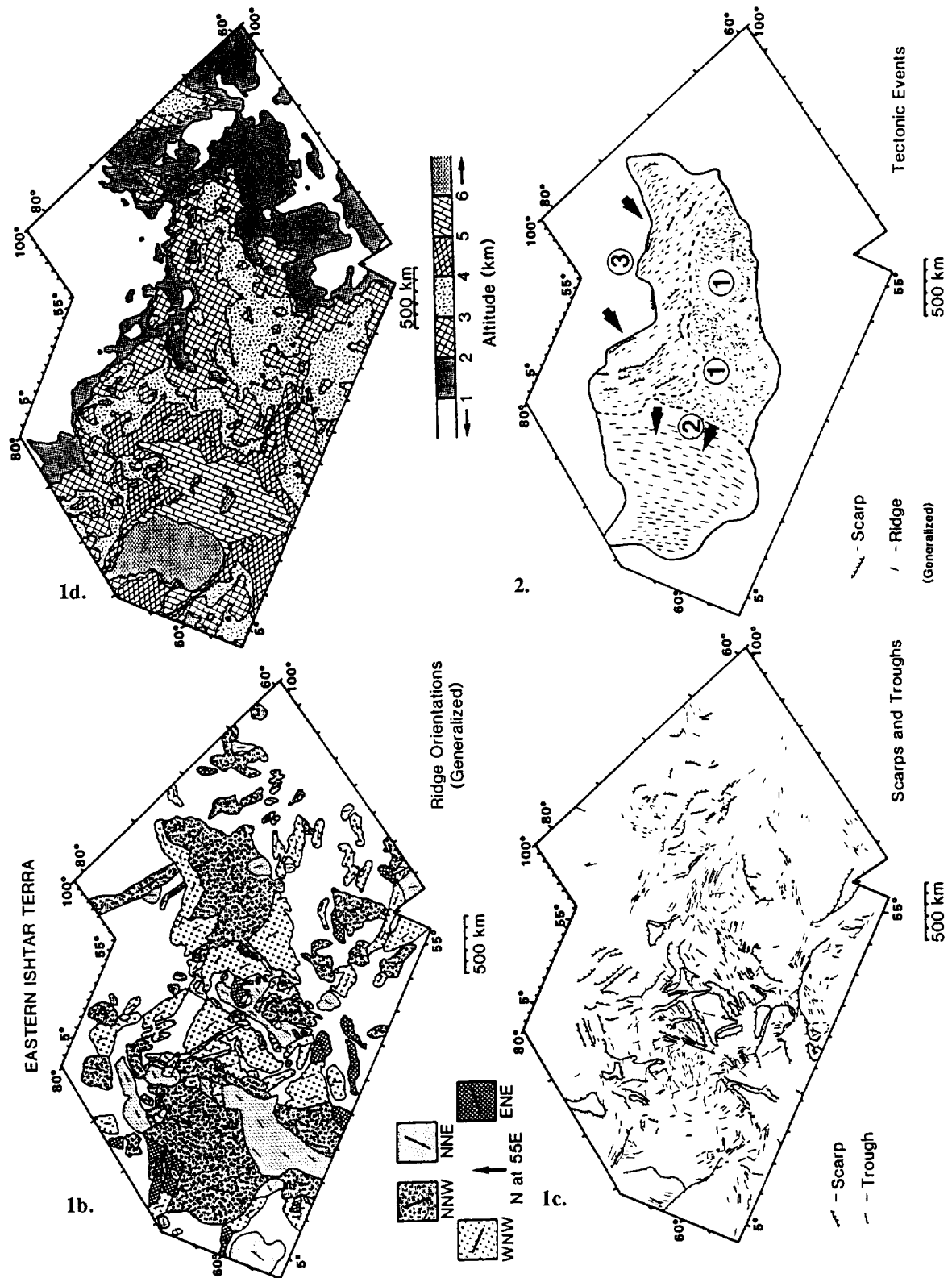
**Sequence:** Since both the WSW- and SSW-directed compressional events appear to have taken place at the expense of the basic, disrupted tessera terrain, then the formation of tessera areas is interpreted to be the first event. Some large WNW-trending arches and swales appear to disrupt NNW-trending ridges in northwestern Fortuna, indicating that the WSW-compression in western Fortuna preceded the SSW compression in northern Fortuna. This sequence of deformation is depicted in Figure 2. The first event was tessera formation (1), followed by WSW-convergence involving small-scale folding and buckling, along with crustal thickening resulting in Maxwell Montes and western Fortuna Tessera (2). The third event was the SSE-convergence with large-scale buckling and crustal imbrication in Northern Fortuna Tessera (3). Thus, multiple stages and directions of deformation can be distinguished, but the degree to which they may overlap in time is yet to be determined.

**References:** 1) D.B. Campbell *et al.*, (1983) *Science*, **221**, 644. 2) S.C. Solomon & J.W. Head (1984) *J.G.R.*, **89**, 6885. 3) V.L. Barsukov *et al.*, (1986) *J.G.R.*, **91**, 378. 4) A.T. Basilevsky *et al.*, (1986) *J.G.R.*, **91**, 401. 5) R.W. Vorder Bruegge *et al.*, (1988) Orogeny and large-scale strike-slip faulting: Tectonic evolution of Maxwell Montes, Venus, submitted to *J.G.R.* 6) L.B. Ronca and A.T. Basilevsky (1986) *Earth, Moon, and Planet.*, **36**, 23. 7) R.W. Vorder Bruegge & J.W. Head (1988) *LPSC XIX* (abs.), 1218. 8) R.W. Vorder Bruegge & J.W. Head (1988) *LPSC XIX* (abs.), 1220. 9) R.W. Vorder Bruegge & J.W. Head (1988) *EOS* (abs.), 1295. 10) R.W. Vorder Bruegge & J.W. Head (1989) Fortuna Tessera, Venus: Evidence of horizontal convergence and crustal thickening, in preparation. 11) J.W. Head (1988) *LPSC XIX* (abs.) 467. 12) D.L. Bindschadler and J.W. Head (1988) *LPSC XIX* (abs.) 76. 13) D.L. Bindschadler and J.W. Head (1988) *LPSC XIX* (abs.) 78.

**Figure 1.** a. Sketch map of individual ridge segments in Eastern Ishtar Terra. b. Map of ridge groupings with similar orientations. c. Sketch map showing troughs and scarps. d. Topographic map of Eastern Ishtar Terra from Venera 15/16. **Figure 2.** Sequence of deformation in Eastern Fortuna Tessera. Arrows indicate convergence or extension, numbers indicate sequence of events with 1 first, 2 second, etc., where possible.



EASTERN ISHTAR TERRA



**SPACING OF RIDGE BELTS IN THE PLAINS-RIDGE BELT ASSEMBLAGE: VENUS.**  
Sharon L. Frank and James W. Head, Department of Geological Sciences, Brown University,  
Providence RI, 02912.

**Introduction:** Ridge belts, first identified in the Venera 15/16 images (1,2) are a common tectonic feature in northern Venus. Between 0°E and 90°E in the Tessera-Ridge Belt assemblage (3), the ridge belts form an orthogonal pattern surrounding large blocks of tesserae, while in the Plains-Ridge Belt assemblage, between 150°E and 250°E, the belts trend predominantly N-S, occasionally coalescing and dividing to form a fan pattern (Fig. 1) (3,4). The origin of these ridge belts is a matter of controversy, with both compressional origins (2,5) and extensional origins (6,7,8) proposed. We have measured the spacing of the ridge belts in the fan region and present the data here, with some preliminary applications to the mode of formation of these belts.

**Approach:** We first outlined the extent of the ridge belts in the fan area, and defined the center crest of each belt. In places where two belts merge to form a wider belt and then separate again, we defined the crest of each through-going belt separately to retain the continuity of the belts. Where two belts merge into one and form a belt about the same width as the widest of the two belts, each belt was considered to be separate until the two belts coalesce, at which point only the crest of the most prominent belt was considered. The distance between crests was then measured along lines of latitude at 2.5° intervals. The average spacings were determined as a function of latitude and longitude, and compared with the width of the fan and the number of belts with latitude.

**Results:** The data are summarized in Figs. 2-4. Fig. 2 shows that the spacing of belts is clustered between 300 and 450 km, and the spacings are skewed towards the longer wavelengths. The average value of these 60 measurements is 393 km, with a standard deviation of 138 km. This value is higher than the 300 km obtained earlier (9), using only the western-most belts. The number of belts and the width of the fan both decrease from 50°N to 80°N (Fig. 3), as one would expect from the fan pattern. However, the fan shape is probably not strictly due to more ridge belts, as the spacing between belts also appears to increase towards lower latitudes (Fig. 4a) with a correlation coefficient for the best-fit line of -0.63. The major deviant from this trend is the southernmost point. This point is also anomalous because, as shown in Fig. 3, south of 50°N the fan pattern no longer increases in width or number of ridge belts, and belts become less well defined as one moves south from 50°N. Therefore, when we eliminate this anomalous data, the trend is much clearer, and has a correlation coefficient of -0.89. Fig. 4b shows a possible increase in spacing to the east in the fan, with a correlation coefficient of 0.70.

**Discussion and Conclusions:** These data add constraints to the origin of the fan of belts; any model which relates to the formation of the ridge belts must explain the apparent increase in spacing to the south and east in this assemblage. The regular spacing of the belts observed by Zuber (9) is confirmed, but the spacing is larger than she observed, and several belts have a much larger spacing. This regularity of spacing has been explained by unstable compression or extension of the venusian lithosphere (9), and by elastic buckling (10). The variation in spacing observed here could be due to inhomogeneities in the crustal thickness, as Zuber (11) has shown that the crustal thickness, and thus the isostatic elevation, could affect the wavelength of the ridge belts under either extension or compression. However, while some topographic variation exists locally within this assemblage (~2 km overall), there is no distinct trend in topography. Higher resolution topography may show a trend which could explain the observations above. The other proposed origin which can be addressed using these data is the spreading model (6,7,8). Sukhanov & Pronin argue that all of the ridges belts in the Plains-Ridge Belt assemblage

were formed by extension, and cite three possible models by which this may have occurred (8). Of these, the one that can be addressed with the data presented here is that in which spreading has occurred down the middle of the region, splitting Metis and Atalanta apart (6,8). If this is the case, the above data show that the spreading was more rapid in the south, resulting in larger spacing, and perhaps has been active for longer there to produce more belts. Furthermore, if the increase in spacing to the east is a true trend, the spreading would have to be asymmetric over a long period of time. We are presently studying the morphology and structure of these belts in order to test these hypotheses further.

**References:** (1) Barsukov, *et al* (1986) *JGR* 91, D378-D398. (2) Basilevsky, *et al* (1986) *JGR* 91, D399-D411. (3) Head (1989) *LPSC XX*, 392-393. (4) Frank & Head (1988) *LPSC XIX*, 348-349. (5) Frank & Head (1988) *LPSC XIX*, 350-351. (6) Sukhanov (1987) *LPSC XVIII*, 974-975. (7) Sukhanov & Pronin (1988) *LPSC XIX*, 1143-1144. (8) Sukhanov & Pronin (1989) *Proc. LPSC XIX* (in press). (9) Zuber (1987) *Proc. LPSC XVII*, E541-E551. (10) Banerdt & Golombek (1988) *JGR* 93, 4759-4772. (11) Zuber (1987) *LPSC XVIII*, 1140-1141.

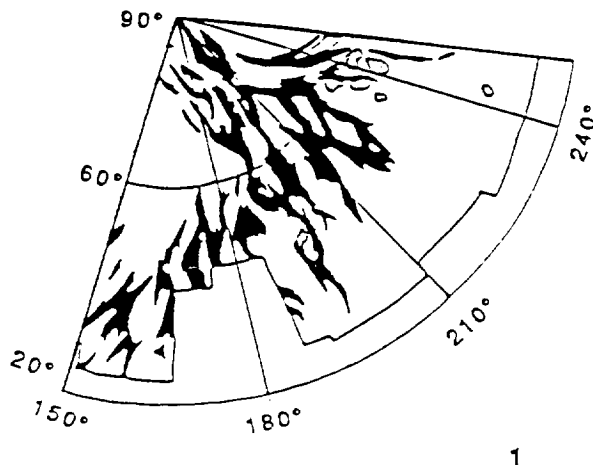


Fig. 1: Ridge belts in Plains-Ridge Belt assemblage.

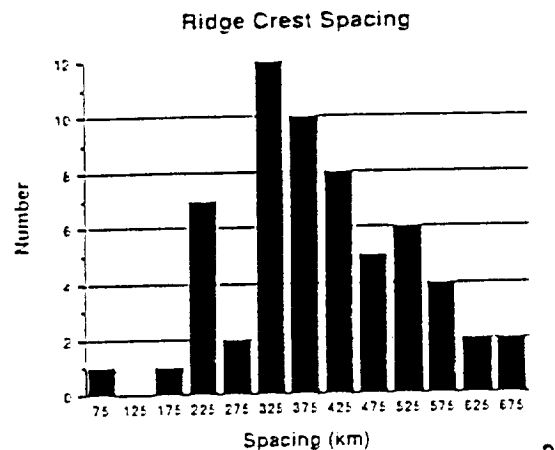
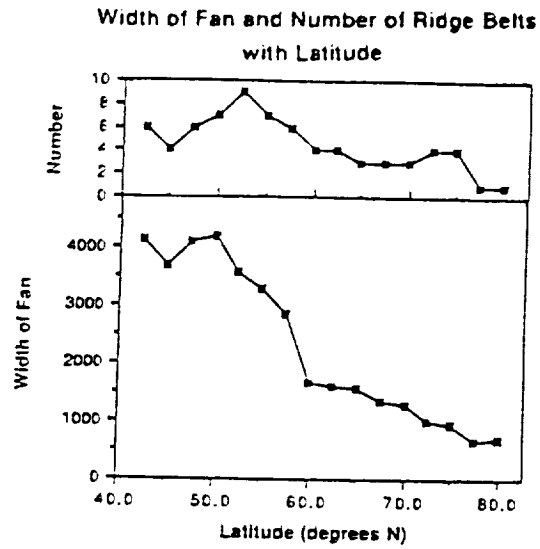


Fig. 2: Histogram of ridge crest spacing in Plains-Ridge Belt assemblage.



3

Fig. 3: Width of fan and number of ridge belts as a function of latitude. (South of 50°N there are large gaps in the data. The width measurements include the width of this gap, but the number of ridge belts is that only in the regions for which there is coverage.)

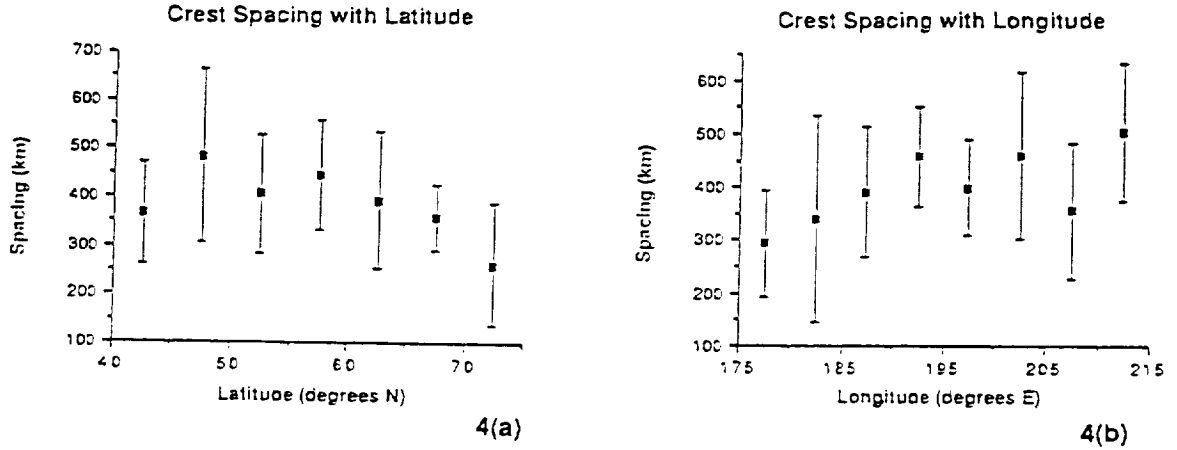


Fig. 4: (a) Crest spacing as a function of latitude. (b) Crest spacing as a function longitude. Error bars represent  $\pm 1$  standard deviation

## INFLUENCE OF VOLATILE LOSS ON THE MANTLE TEMPERATURE OF VENUS.

Patrick J. McGovern and Sean C. Solomon, Department of Earth, Atmospheric, and Planetary Sciences, Massachusetts Institute of Technology, Cambridge, MA 02139.

*Introduction.* Determination of the characteristic mantle temperature of Venus relative to that of Earth is a problem with many important implications for the divergent evolution of these two planets. Parameterized mantle convection models [1] have been utilized to predict a warmer mantle temperature on Venus, while scenarios based on plume-dominated convection [2] have been invoked to predict a colder Venus mantle. An important difference between Earth and Venus is the disposition of volatiles (especially water) in their atmospheres and interiors. In this paper a parameterized convection model which includes the effect of volatile exchange between planetary atmosphere and interior [3] is used to examine the effects that possible differences in volatile evolution may have had on the thermal histories of the two planets.

*Model.* In the spirit of conducting exploratory calculations of the principal effects of volatile evolution, the thermal history model is kept very simple. We consider whole mantle convection with internal heating from the decay of radiogenic elements and no heat flow from the core [4]. Dissolved volatiles have been demonstrated to reduce the activation energy (or equivalently the activation temperature [4]) for solid-state creep in mantle rocks [5,6]. A "wet" mantle thus has a lower viscosity than a "dry" one. A linear fit to laboratory data [6] has been used to parameterize activation temperature as a function of mantle volatile content [3]. Mantle degassing and regassing rates are parameterized as functions of the heat flow  $q$  from the mantle. We then solve for both volatile content and mean mantle temperature as functions of time.

*Results.* We reference our results to a nominal Earth case [3] in which about 1.5 ocean masses (o.m.) of volatiles are degassed over 4.6 Gyr. The evolution of mean mantle temperature with time in this model is shown in Figure 1, curve a. The effect of changing only the surface temperature  $T_s$  from 273 K to a Venus value of 740 K is to increase the present day mantle temperature by about 100 K (Figure 1, curve b). However, the atmospheric  $^{40}\text{Ar}$  abundance [7] may be taken to suggest that Venus has degassed only 1/4 to 1/3 as much as Earth. Volatile-dependent thermal history calculations for the Earth [3] have indicated that the mantle tends to balance volatile content and temperature so as to maintain an "optimum" value of viscosity and thus of convective vigor. Degassing stiffens the mantle, which compensates by a rise in temperature. Regassing (or lessened degassing) weakens the mantle, which adjusts by lowering temperature. A model with a value for  $T_s$  appropriate to Venus and about 0.5 o.m. total degassing is only slightly hotter than the nominal case (Figure 1, curve c). The reduction in temperature from the lessened degassing effectively compensates for the higher value of  $T_s$ .

The initial volatile content of Venus (or of the Earth), of course, is a poorly constrained parameter. A model in which the initial mantle volatile abundance is three times the nominal amount, but the final degassed mass is one-third of nominal (for about a factor of 10 reduction in the fractional amount of degassing) has also been examined. This volatile-rich mantle model has a significantly reduced viscosity, which enhances convective vigor and heat flow from the mantle. This results in a reduction of the present mantle temperature by almost

600 K (Figure 1, curve d). Models for Venus with higher volatile contents and lower amounts of degassing than the Earth can thus yield a colder Venus mantle despite the higher surface temperature. Such a low mantle temperature may result in a low rate of magma genesis and crustal formation, consistent with some current estimates obtained on geological grounds [8].

**Conclusions.** Thermal history models for Venus incorporating the effects of volatiles on mantle rheology allow for a range of thermal states for the Venus mantle. The higher surface temperature causes an increase in mantle temperature relative to that of Earth. If Venus has degassed less than the Earth, however, then this effect is compensated to some degree by the enhancement of heat flow from a more volatile-rich mantle. If the difference in present mantle volatile content is sufficiently great, the mantle temperature of Venus could be less than that of the Earth.

**References.** [1] D. J. Stevenson, T. Spohn, and G. Schubert, *Icarus*, 54, 466, 1983; [2] N. H. Sleep, M. A. Richards, and B. H. Hager, *JGR*, 93, 7672, 1988; [3] P. J. McGovern and G. Schubert, in preparation, 1989; [4] G. Schubert, D. Stevenson, and P. Cassen, *JGR*, 85, 2531, 1980; [5] P. N. Chopra and M. S. Paterson, *Tectonophysics*, 78, 453, 1981; [6] P. N. Chopra and M. S. Paterson, *JGR*, 89, 7861, 1984; [7] J. H. Hoffman, V. I. Oyama, and U. von Zahn, *JGR*, 85, 7871, 1980; [8] R. E. Grimm and S. C. Solomon, *JGR*, 93, 11911, 1988.

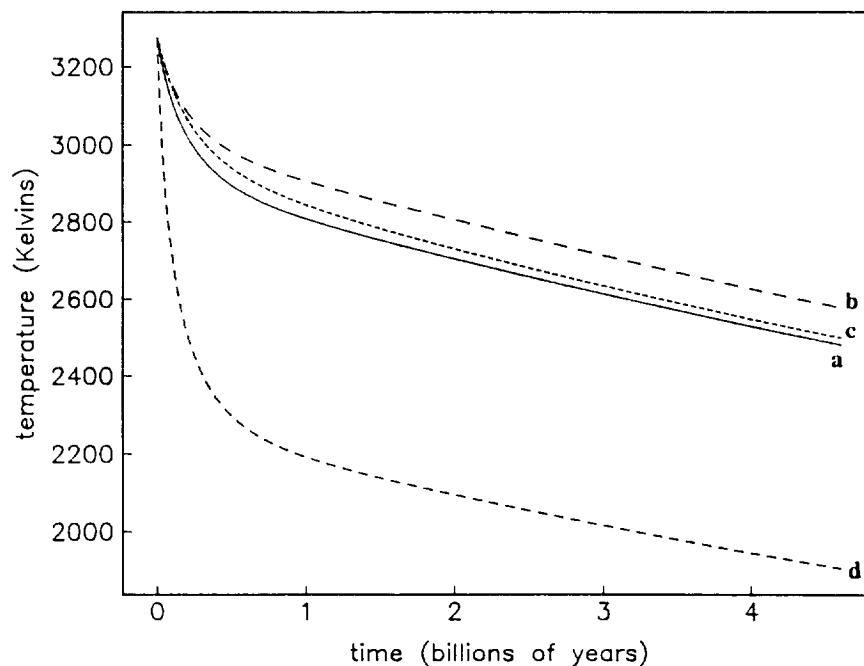


Figure 1. Volatile-dependent thermal history models for Earth and Venus. Shown are curves of average mantle temperature versus time for four thermal evolution models discussed in the text.



# TECTONIC RESPONSE TO MANTLE DYNAMICS IN VENUS

R. J. Phillips, Dept. of Geological Sciences, Southern Methodist University, Dallas, TX 75275

**Introduction.** Large apparent depths of isostatic compensation on Venus (ADCs), interpreted in conjunction with Earth-scaled temperature gradients [1], lead to the hypothesis that some of the topography of Venus must be dynamically supported by flow in the mantle [2,3]. Here we examine the consequences of such flow for tectonic stresses in the lithosphere and, in particular, whether such stresses could lead to large-scale tectonic disruption both locally and at large distances.

**Stresses Magnitudes.** In elementary terms, we view the interaction between mantle convective flow and an overlying lithosphere in terms of shear stresses ( $\sigma_{xz}$ ) and normal stresses ( $\sigma_{zz}$ ) imparted by the flow to the base of the lithosphere. Normal stresses are largely responsible for uplift of the topography, but may also give rise to modest deviatoric horizontal normal stresses ( $^z\sigma_{xx}$ ) in the lithosphere. Shear stresses can impart large horizontal normal stresses ( $^x\sigma_{xx}$ ). Estimates for  $\sigma_{xz}$  and  $\sigma_{zz}$  can be obtained from the topography and the free-air gravity field, respectively, provided that the dominant wavelengths of these fields are large compared to the depth of the convective flow.

For compensated topography, regardless of the mechanism of compensation,  $^z\sigma_{xx} \equiv \rho_t g_0 h_t / 2$ , where  $\rho_t$  is topographic density,  $g_0$  is planetary gravity, and  $h_t$  is topographic height. On Venus, this yields about 13 MPa of stress for each kilometer of elevation. For a diabase rheology [4] and a temperature gradient of 15 K/km, 13 MPa of stress will cause significant creep strain in crusts of thickness 10 km or more.

If the base of the lithosphere is subject to shear tractions from mantle flow, then a stretching mode [5] of lithospheric deformation,  $^x\sigma_{xx}$ , may be important. Under the long wavelength constraint stated above, the shear stress  $\sigma_{xz}$  is directly proportional to the depth-density "dipole" [6] of the mantle flow field, as is the free-air gravity anomaly. The horizontal stress in the lithosphere is directly related to  $\sigma_{xz}$  through the equilibrium equation. This leads to an estimate [7] of a lower bound of the magnitude of the lithospheric in-plane force,  $F_b(k) = [g_0 / (2\pi k G)] g(k)$ , where  $k$  is wavenumber,  $G$  is the universal gravitational constant, and  $g(k)$  is the free-air gravity anomaly. An identical result is obtained when the dipole is the isostatic structure of the cooling oceanic boundary layer on Earth [8,9]. This result remains a lower bound as long as there is no low viscosity channel (LVC) beneath the lithosphere. Large ADC values imply that there is no LVC in Venus [7].

Fast Fourier Transform techniques have been used to generate the spatial distribution of  $F_b(x,y)$  in the Tellus Regio/Bell Regio/Leda Planitia region by performing an inverse transform on  $F_b(k)$  as calculated from the free-air gravity anomaly for that region [10]. No directional information was retained in this calculation and  $\sigma_{xy}$  is assumed to be negligible. The gravity field was downward continued to the surface and resolution considerations dictated that wavelengths shorter than 700 km be excluded. The results of this calculation are shown in Figure 1. A strict interpretation of these results, which we do not promote, would be that all of the topography in this region of Venus is dynamically supported and that regions of positive topography (e.g., Bell Regio, 50° E, 30° N) are associated with mantle up-welling, while negative topography (e.g., Leda Planitia, 60° E, 45° N) is associated with down-welling. There certainly may be other mechanisms of topographic compensation, notably crustal thickness variations [11] and thermal compensation in the lithosphere [10,12]. The main point here is that dynamic support of topography should be accompanied by stretching forces in the overlying lithosphere and that free-air anomalies on Venus imply that their magnitude might be at least a few times  $10^{12}$  N/m.

**Comparisons to Earth.** The basal shear stresses associated with the  $F_b$  solution in Figure 1 are typically a few MPa. This falls within the range, although at the upper end, of various estimates of the basal shear stress acting on the terrestrial oceanic lithosphere [13,14,15,16]. These stresses are generally considered to be tectonically unimportant. On Earth, the existence of a low viscosity zone that would lead to low values of basal stress and uncouple the oceanic plates from the underlying convecting mantle is uncertain. On Venus, the postulated thinner, hotter lithosphere leads to more tectonic disruption for the same level of stress. This is il-

illustrated in Figure 2, where we show the deformation associated with a 1 km dynamic uplift of a lithosphere composed of a 10 km diabase crust overlying a websterite mantle ( $dT/dz = 15$  K/km,  $d\epsilon/dt = 10^{-14}/s$ ). Failure zones are associated with stresses that exceed the yield stress in a strength envelope diagram.

**Transmittal of Stress Over Large Distances.** The in-plane forces,  $F_b$ , determined here are comparable in magnitude to ridge push forces,  $F_r$ , estimated for the Earth. We next ask, are the tectonic forces on Venus discussed above capable of being transmitted over large distances and initiating faulting far from their source of origin? At long wavelengths, where flexural effects are unimportant, simple compensated uplift of a lithospheric layer will lead to tensional stresses in the "uplands". But there will be no stress in the "plains", unless the lithosphere starts to creep. This is because the local potential energy anomaly associated with topography is supported by local stresses. Out in the plains there is no potential energy anomaly (or defect). Creep effects cannot be expected to affect the plains more than a distance of approximately the horizontal dimension of the uplift.

A cooling, moving, thermal boundary layer, such as the oceanic lithosphere, carries a potential energy defect out into the plains: it is the cool over-dense lithosphere (negatively buoyant) that must be balanced by local internal stresses [8,9]. A key element in this model is that the isostasy is carried entirely in the lithosphere, and that the sub-lithosphere is of constant density. In this configuration, the internal pressure of the lithosphere, which is a maximum in the plains, can be directly equated, because of the isostatic assumption, with the maximum ridge height, confounding what is a local phenomenon with the concept of a ridge push. Presumably, this local stress could, in places, lead to compressional failure, enabling underthrusting or even subduction. In order to apply the concept of long-distance stress transmittal to Venus, we have to postulate that the region between the area of dynamic topography and the area of tectonic disruption is itself tectonized, for example, part of a thermal boundary layer of convection.

**Conclusions.** Topography caused by dynamic processes in Venus could be associated with extensive deformation, but the stresses may not be transmitted great distances away from regional disturbances. Testing of these hypotheses is currently underway.

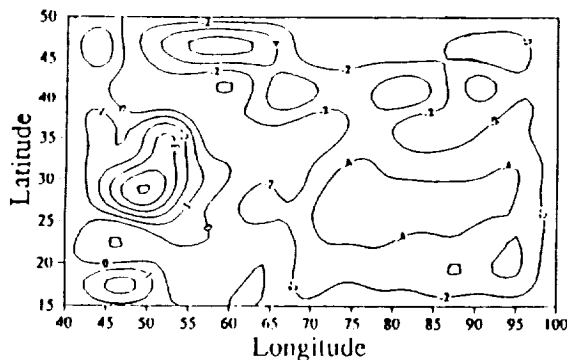


Figure 1. Map of in-plane stress,  $F_b$ . Contour units are  $10^{12}$  N/m.

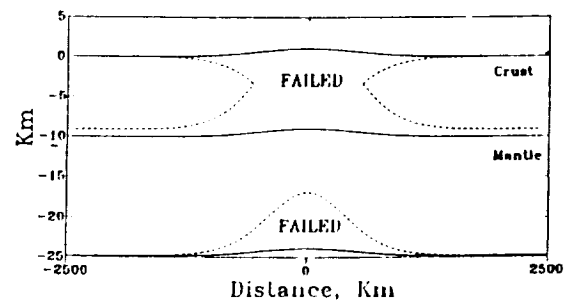


Figure 2. Lithospheric failure zones for 1 km of dynamic uplift.

- References.** [1] Solomon, S.C., and J.W. Head, *J. Geophys. Res.*, 87, 9236-9246, 1982; [2] Phillips, R.J., and M.C. Malin, in *Venus*, D.M. Hunten et al., eds., 159-214, Univ. of Arizona Press, Tucson, 1983; [3] Phillips, R.J., and M.C. Malin, in *Ann. Rev. Earth. Planet. Sci.*, 12, 411-443, 1984; [4] Caristan, Y., in *J. Geophys. Res.*, 87, 6781-6790, 1982; [5] Fung, Y.C., *Foundations of Solid Mechanics*, Prentice Hall, Englewood Cliffs, NJ, 525 pp., 1965; [6] Haxby, W.F., and D.L. Turcotte, *J. Geophys. Res.*, 83, 5473-5478, 1978; [7] Phillips, R.J., in revision for *J. Geophys. Res.*, 94, 1989; [8] Parsons, B., and F.M. Richter, *Earth Planet. Sci. Lett.*, 51, 445-450, 1980; [9] Dahlen, F.A., *J. Geophys. Res.*, 86, 7801-7807, 1981; [10] Smrekar, S., and R.J. Phillips, *LPSC XX*, this volume, 1989; [11] Janle, P.J. et al., *Earth, Moon, and Planets*, 39, 251-273, 1987; [12] Morgan, P., and R.J. Phillips, *J. Geophys. Res.*, 88, 8305-8317, 1983; [13] Weins, D.A., and S. Stein, *Tectonophysics*, 116, 143-162, 1985; [14] Davies, G.F., *Geophys. Res. Lett.*, 5, 161-164, 1978; [15] Melosh, J., *Pure and Appl. Geophys.*, 115, 429-439, 1977; [16] Chapple W.M., and T.E. Tullis, *J. Geophys. Res.*, 82, 1967-1984, 1977.

# **LITHOSPHERIC FLEXURE BENEATH THE FREYJA MONTES FOREDEEP, VENUS: CONSTRAINTS ON LITHOSPHERIC THERMAL GRADIENT AND HEAT FLOW.**

Sean C. Solomon, Department of Earth, Atmospheric, and Planetary Sciences, Massachusetts Institute of Technology, Cambridge, MA 02139, and James W. Head, Department of Geological Sciences, Brown University, Providence, RI 02912.

*Introduction.* The heat budget of Venus is poorly known. On the basis of the  $^{40}\text{Ar}$  abundance in the atmosphere [1] and the U, Th, and K concentrations in surface soils [2], heat production within Venus has been commonly scaled from estimates for the Earth. Under the assumption that Venus presently loses heat at the same rate per mass as the Earth, the heat flux is  $74 \text{ W/m}^2$  and the average vertical thermal gradient in the lithosphere is 20-25 K/km if conduction is the dominant heat transport mechanism in the outer layer of the planet [3]. It is important to seek tests of the premise that heat flux on Venus may be scaled from the Earth. One means to do so is to determine the thickness of the elastic lithosphere on Venus from the flexural response to surface loads, since the lithospheric thickness is limited by the temperature-dependent depth at which ductile behavior dominates brittle behavior at flexural strain rates [4]. Janle et al. [5] inferred an elastic lithosphere 30-100 km thick beneath the volcano Tepev Mons in Bell Regio from the radial position of a circumferential depression interpreted to be of flexural origin. As described below, even the lower limit of this range places a strong constraint on the lithospheric thermal gradient in this region.

An additional opportunity to estimate elastic lithosphere thickness is afforded by the Freyja Montes region of Ishtar Terra. Analysis of Venera 15 and 16 radar images and topographic data suggest that this mountain belt formed as a result of a sequence of southward underthrusts of the lithosphere of the North Polar Plains beneath Ishtar Terra [6]. To the north of a steep boundary scarp 1-3 km in height is a closed depression several hundred meters in relief. In cross section the topographic profile of the depression [6] is remarkably similar to that of a foreland deep formed by the flexure of the underthrusting plate beneath a terrestrial mountain range [e.g., 7,8]. While terrestrial foredeeps are typically filled with sediments, the much lower rates of erosion and sedimentation on Venus and limited infilling by young volcanic deposits [6] have apparently left the flexural signature of the topography at least partially intact. In this paper we employ that flexural signature to constrain the elastic lithosphere thickness and thermal gradient beneath the North Polar Plains.

*Elastic Lithosphere Thickness.* We have estimated the thickness  $T_e$  of the effective elastic lithosphere and the depth  $T_m$  to the base of the mechanical lithosphere [9] from Venera 15 and 16 topographic profiles of the unloaded portion of the underthrusting lithosphere of the North Polar Plains. Estimates of  $T_e$  are obtained by fitting individual topographic profiles to deflection curves for broken elastic plates [10]; free parameters in the fit are the flexural parameter  $\alpha$ , the magnitude of the vertical load applied to the end of the plate, and the horizontal position. The principal source of uncertainty in estimating  $\alpha$  arises from errors in the zero datum for deflection remaining after correcting for the long-wavelength topography of the North Polar Plains. For all of the Venera 15/16 orbits yielding topographic data for this region (orbits 85-91), there is a pronounced linear slope to the topographic profile between the Freyja Montes foredeep and the high-latitude culmination point of the orbit; the opposite-side data display a long-wavelength linear slope of opposite sign, with the break in slopes approximately coinciding with the culmination point. Since all of these data

correspond to locations northward of Pioneer Venus altimetry coverage, we do not presently know if these long-wavelength linear slopes are real or are artifacts of the data reduction. In the absence of better information, we have removed from the topographic profiles a linear trend obtained by least squares from the portion of each profile between the orbit culmination point and a position 250 km northward of the Freyja Montes foredeep. One such profile is shown in Figure 1.

The flexure models fit the topographic profiles, corrected for long-wavelength slope, to within an rms misfit of about 50 m, comparable to the stated error in relative along-track elevations at short wavelength in the Venera data [11]. The best-fitting values for the flexural parameter  $\alpha$  for the three profiles (orbits 89-91) with the best-developed signature of the foredeep are in the range 37-52 km, corresponding to flexural rigidity  $D$  in the range  $(1-5) \times 10^{22}$  N m. Flexural rigidity may be converted to  $T_e$  for assumed effective values of Poisson's ratio  $\nu$  and Young's modulus  $E$ . We take  $\nu = 0.25$  and  $E$  in the range 10 - 100 GPa; the extreme values for  $E$  correspond to  $T_e$  in the ranges 25-37 km and 12-17 km, respectively. We favor higher values of  $E$ , and thus lower values of  $T_e$ , within these ranges.

*Thermal Gradient.* These values of  $T_e$  may be converted to the mean lithospheric thermal gradient  $dT/dz$ , given a representative strain rate and a flow law for ductile deformation of material in the lower lithosphere. This conversion is accomplished by constructing models of bending stress consistent with the strength envelope and finding for each model the equivalent elastic plate model having the same bending moment and curvature  $K$  [9]. We take  $10^{-16} \text{ s}^{-1}$  as the representative strain rate, and we assume that ductile flow is limited by the creep strength of olivine [12], consistent with the inference from the depths of impact craters and the characteristic spacing of tectonic features that the crust beneath plains units on Venus is no more than 10-20 km thick [13,14]. The conversion from  $T_e$  to  $T_m$  and  $dT/dz$  as functions of  $K$  is illustrated in Figure 2. The curvature  $K$  at the zero crossings of the flexural profiles for the uniform elastic plate model (e.g., Figure 1) is  $(1-1.5) \times 10^{-7} \text{ m}^{-1}$ . From Figure 2, the values of  $T_e$  for  $E = 10$  and 100 GPa correspond to mean lithospheric thermal gradients of 7-12 K/km and 16-25 K/km, respectively.

*Implications.* For a lithospheric Young's modulus at the upper end of the range considered here, the flexural topographic profile of the Freyja Montes foredeep is consistent with a lithospheric thermal gradient similar to that expected for the global mean gradient on the basis of scaling from Earth [3]. This is a reasonable result in that the elevation of the North Polar Plains to the immediate north of the foredeep and associated outer rise [6] is similar to the mean elevation of the planet [15]. In contrast, the thermal gradients if  $E$  is at the lower end of the range considered, and that implied (see Figure 2) by the least value of  $T_e$  inferred by Janle et al. [5], are no more than half that expected from scaling arguments. We suggest that an internally consistent description of the current internal structure and tectonics of Venus includes a strong ( $E \approx 100$  GPa) but thin ( $T_m \approx 15-20$  km) mechanical lithosphere, a thin (10-20 km) crust, and a thermal gradient appropriate to scaling global heat loss from the Earth (20-25 K/km) beneath typical plains regions of the planet.

*References.* [1] J.H. Hoffman et al., *JGR*, 85, 7882, 1980; [2] Yu.A. Surkov, *PLSC* 8th, 2665, 1977; [3] S.C. Solomon and J.W. Head, *JGR*, 9236, 1982; [4] C. Goetze and B. Evans, *GJRS*, 59, 463, 1979; [5] P. Janle et al., *Earth Moon Planets*, 41, 127, 1988; [6] J.W. Head, *LPS*, 19, 467, 1988; [7] G.D. Kerner and A.B. Watts, *JGR*, 88, 10449, 1983; [8] L. Royden, *JGR*, 93, 7747, 1988; [9] M.K. McNutt, *JGR*, 89, 11180, 1984; [10] D.L. Turcotte and G. Schubert, *Geodynamics*, p. 127, Wiley, 1982; [11] Yu.N. Alexandrov et al.,

*Science*, 231, 1271, 1986; [12] C. Goetze, *Phil. Trans. Roy. Soc. Lond.*, A288, 99, 1978; [13] R.E. Grimm and S.C. Solomon, *JGR*, 93, 11911, 1988; [14] M.T. Zuber, *JGR*, 92, E541, 1987; [15] P. Ford, *Pioneer Venus Hypsometry*, MIT CSR rept., 1986.

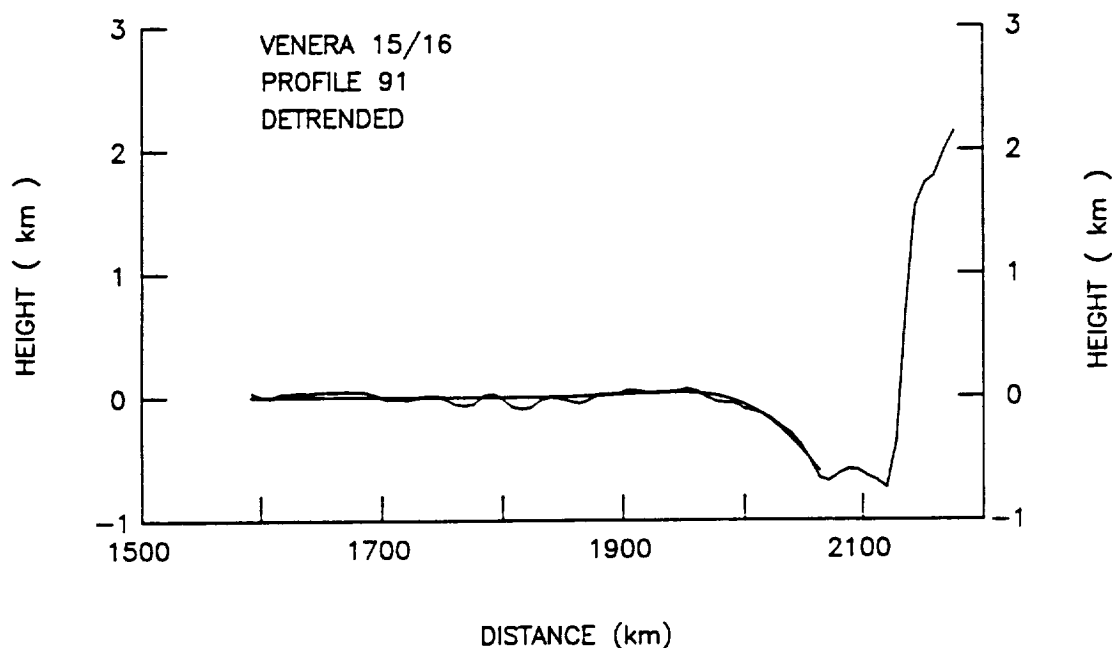


Figure 1. Topographic profile across Freyja Montes (Venera orbit 91), after correcting for long-wavelength slope. Also shown is a model profile for flexure of a uniform plate subjected to an end vertical load.

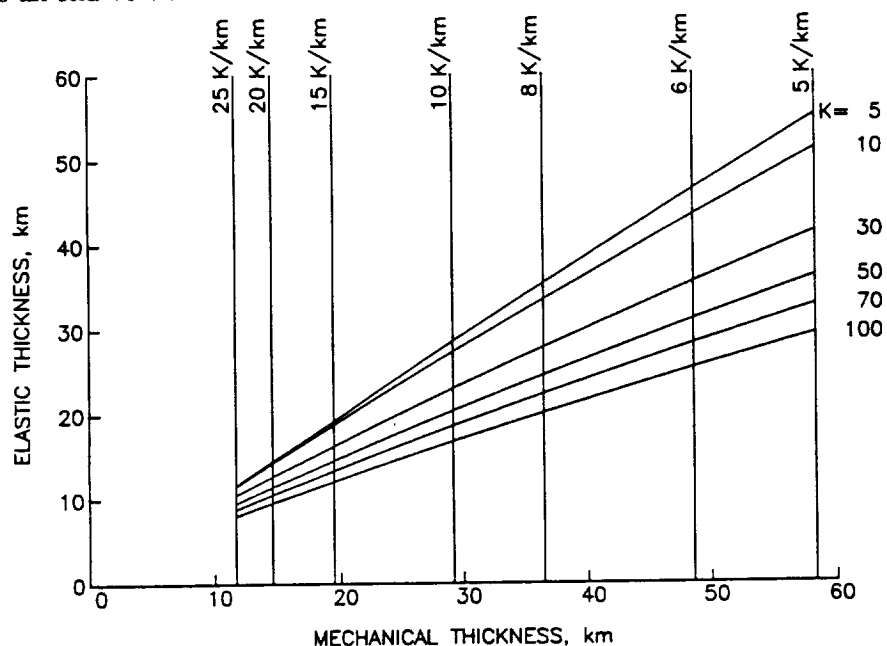


Figure 2. Conversion of  $T_e$  to  $T_m$  and  $dT/dz$  as functions of curvature  $K$  (in units of  $10^{-8} \text{ m}^{-1}$ ), after [9]. Mean thermal gradients shown correspond to a strain rate of  $10^{-16} \text{ s}^{-1}$ .

# IMPLICATIONS OF GRAVITY MODELING FOR A THERMAL ISOSTASY HYPOTHESIS FOR BELL REGIO, VENUS

S. Smrekar and R.J. Phillips, Dept. of Geological Sciences, SMU, Dallas, TX 75275

**Introduction.** We have tested the hypothesis that the topography of Bell Regio, Venus is supported by thermal isostasy in the lithosphere (e.g., 1). In this type of model, excess heat flux leads to increased temperature gradients, replacement of normal lithosphere with hot, low density material, and an increase in elevation to maintain isostatic balance. The model is tested using Pioneer Venus topography and gravity data to constrain the thinning of the lithosphere for a given reference thickness and temperature.

**Gravity Data.** In order to put line-of-sight (LOS) gravity data into a convenient format for interior modeling, we have inverted the LOS data in a region bounded by 40-100° E longitude and 15-50° N latitude for a point mass model. The solution was obtained by Singular Value Decomposition and the required partial derivatives were obtained using the ORBSIM program (2) within the Geophysical Data Facility at the Lunar and Planetary Institute. The 308 estimated point mass values were used to generate the vertical gravity component at 350 km altitude.

**Modeling.** If the topography is supported entirely by thermal isostasy, then a model for the lower boundary of the lithosphere ( $z$  is positive downward) is given by:  $h_L(x,y) = L_o - h_T(x,y)\rho_L/\Delta\rho$ , where  $L_o$  is the thickness of a reference lithosphere,  $h_T(x,y)$  is surface topography,  $\rho_L$  is lithospheric density, and  $\Delta\rho$  is the density contrast of lithosphere and sub-lithosphere ( $=\rho_L - \rho_A$ ). Here  $\rho_L = \rho_A(1 + \alpha\Delta T/2)$ , where  $\alpha$  is the coefficient of thermal expansion, and  $\Delta T$  is the temperature change across the lithosphere ( $=T_A - T_O$ ). The gravity signal  $g_p(x,y)$  from this model is the sum of contributions from  $h_L$  and  $h_T$ . In principle,  $g_p(x,y)$  depends on both  $L_o$  and  $\Delta T$ . We calculated the gravity signal from  $h_L$  and  $h_T$  using a power series representation of the Green's function (3). However, the resolution of the gravity data is not sufficient to distinguish between the three dimensional surface of  $h_L$  and a surface density product,  $\Delta\rho h_L$ , at a depth  $L_o$ . In effect, a low density region of high heat flow which extends upward, thinning the lithosphere, cannot be distinguished from a low density crustal root (Airy compensation). Thus the resulting apparent depth of compensation (ADC) can be interpreted in a variety of ways, and cannot be uniquely attributed to thermal isostasy.

**Results.** The standard deviation of the isostatic anomaly for Bell Regio (defined as 22-39° N latitude and 40-61° E longitude) was used to select the best ADC (Figure 1.). The best fit for the entire region was for a depth of 120 km; 160 km gives a better fit for the southern "swell" (26-33° N latitude by 44-55° E longitude). As Figure 1 shows, the best depth of compensation varies considerably over the region. The depth shallows to the north, and increases to the south. The best fitting model, which has a standard deviation of ~5 mgal, can account for only about 80% of the gravity signal, which has a maximum of ~22 mgal. Most of the region appears over-compensated (areas with a positive isostatic anomaly), implying that an additional compensation mechanism is also operating. Flexural support may not be very important, as the wavelengths of features that can be supported by Venus' mechanical lithosphere may be too small to contribute much to the observed gravity signal. Dynamic support will be considered below.

**Interpretation.** If we interpret the ADC as Airy compensation, the low density crustal root extends down below a reference thickness of 160 km. Pratt compensation, in the long wavelength approximation requires double this thickness. Even if we use the ADC of the entire region, 120 km, rather than that for just the southern swell, this may be an improbably large thickness for Venus, even in comparison to liberal estimates of crustal thickness (4).

If we interpret the ADC in terms of thermal isostasy, then the compensation is produced by a hot region which replaces the lower portion of the lithosphere. This implies a thermal lithosphere thicker than 160 km in the southern portion, or 120 km for the whole region. For thermal isostasy to produce the highest topography observed at Bell Regio, the relief on the sub-lithospheric boundary (the amount of thermal thinning) has to be over 100 km, for a  $\Delta T$  of

1000° K.

Either of these interpretations of the ADC require a thermal gradient of 6-8° K/km in the reference lithosphere, outside of the root or the thermal thinning. These low values led us to consider the possibility of thermal isostasy in combination with dynamic support. These two effects are both likely to accompany a hot mantle "plume". The ADC can then be interpreted as the mean depth,  $L_c$ , of a hot, low density blob, ( $\rho_A$ ), overlain by a thermally-thinned lithosphere (see Figure 2). The reference lithosphere,  $L_o$ , which results from thermal boundary layer modeling is approximately 100 km thick, with a  $\Delta T$  between the surface and the bottom of the lithosphere of around 1000° K (5). This fixes the reference  $dT/dz$  at 10° K/km. The  $\Delta T$  from the thermal boundary layer model can be combined with an assumed density in the normal mantle (3.25 g/cm<sup>3</sup>) to fix the density of the lithosphere. A plausible average temperature contrast between the plume and the surrounding mantle is 300° K (6). This  $\Delta T$  determines the density of the normal mantle. In the thermally-thinned region, the temperature we use to calculate density is the average of that at the base of the lithosphere and the temperature in the hot region. These density contrasts are used to determine the dimensions of a low density region, relative to the ADC, which compensates the maximum topography of Bell Regio. The 'plume' which supports the topography extends down 100 km below the ADC, and 90 km above it. A reference lithosphere 100 km thick is thus thinned by 30 km (the ADC is 60 km below the bottom of the reference lithosphere).

**Conclusions.** Gravity modeling of Bell Regio cannot distinguish variations in crustal thickness (Airy compensation) from thermal thinning of the lithosphere. The fit of the isostatic anomaly further implies an additional compensation mechanism, and variable depths of compensation. The crustal thickness variation interpretation requires an average crustal thickness of 120-160 km. The thermal thinning model requires a thermal lithosphere of 120-160 km which is locally thinned by up to 100 km. Both of these models require a reference thermal gradient of 6-8° K/km. A combination of thermal thinning and dynamic support requires less drastic thermal thinning, has a somewhat higher regional thermal gradient, and may be the most plausible interpretation of the gravity data.

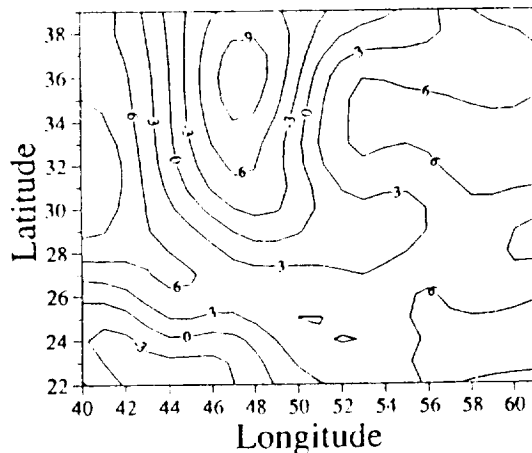


Figure 1. Isostatic anomaly (mgal) for an ADC of 120 km.

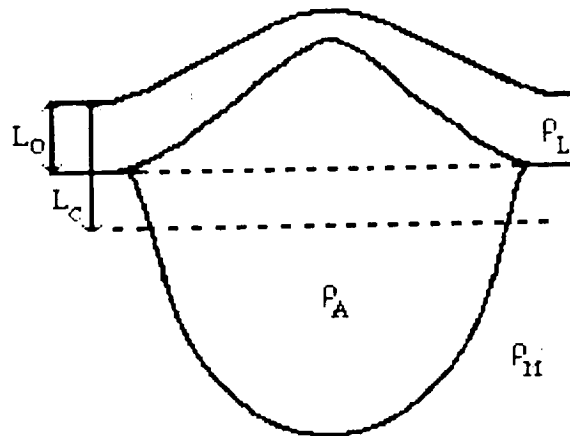


Figure 2. Schematic view of a hotspot region isostatically supported by thermal thinning of the lithosphere and a low density plume.

- (1) Morgan, P., and R. J. Phillips, *J. Geophys. Res.*, 88, 8305-8317, 1983. (2) Phillips, R. J., et al., *J. Geophys. Res.*, 83, 5455-5464, 1978. (3) Parker, R. L., *Geophys. J. R. Astro. Soc.*, 31, 447-455, 1972. (4) Kaula, W. M., *EOS*, 69, 1294, 1988. (5) Kaula, W. M., and R. J. Phillips, *Geophys. Res. Lett.*, 8, 1187-1190, 1981. (6) Richards, M. A. et al., *J. Geophys. Res.*, 93, 7690-7708, 1988.

# IMPLICATIONS FOR INTERPRETATION OF VENERA 15/16 AND MAGELLAN DATA OF VOLCANIC TERRAINS ON VENUS

*Lisa Gaddis, Department of Geology, Arizona State University, Tempe, AZ 85287*

Geologic analyses of imaging radar data of volcanic terrains on Earth have illustrated a need for understanding how such data can be used to interpret eruptive styles and to characterize the geologic history of volcanic centers. This report summarizes results of a geologic analysis of Shuttle Imaging Radar (SIR-B) data of Kilauea Volcano<sup>1</sup> and discusses implications for interpretation of Venera 15/16 and Magellan radar data for volcanic centers on Venus. SIR-B obtained two radar images (25 m resolution, 23 cm wavelength, 28° and 48° incidence angles) over southeastern Hawaii in October, 1984; the target area of these data takes was the summit and Southwest Rift Zone of Kilauea Volcano<sup>2</sup>. Geologic analyses of these data indicated that while large-scale landforms (e.g., the summit caldera, pit craters, and fault scarps) and deposits with smooth (e.g., the 1790 tephra deposit) or rough (e.g., aa lava flows) surfaces are readily distinguished on the SIR-B data, many additional landforms (e.g., pahoehoe lava flows, cinder cones, and small fissures) are difficult to detect, particularly if the adjacent or underlying substrate has comparable radar signatures.

To understand the use of SAR data for geologic analysis of a volcanic terrain, the eruptive history of the summit and Southwest Rift Zone of Kilauea as it is currently understood and as it can be interpreted on the basis of the SIR-B data alone were compared<sup>1</sup>. From the SIR-B data, Kilauea is accurately interpreted to be a volcanic shield, with a well-developed summit caldera indicating multiple episodes of collapse; evidence of radial and concentric rifting is observed in the form of faults, fissure traces, and flows from small-scale eruptive centers. The extensive low-return unit observed near Kilauea Caldera correctly suggests that explosive volcanism has played a major role in the development of the summit caldera. Effusive volcanism, observed in the form of radar-bright lava flows, is inferred to have played a more important role away from the summit along the radial rift zone of the Southwest Rift. Variable backscatter intensity from these rough-surfaced lava flows suggests that eruptive centers with associated bright (young?) lava flows evolved from earlier, more randomly distributed volcanism along the rifts.

Although this interpretation of volcanism is generally correct, misinterpretation of aspects of the volcanic history of Kilauea result from reliance upon the SIR-B data alone. Pyroclastic volcanism, as evidenced by the extensive low-return units near the summit (inferred to be ash deposits) and the apparent absence of pahoehoe lava flows, appears to be the dominant style of volcanism at the Kilauea summit. In reality, pyroclastic eruptions comprise only a small percentage of Kilauea eruptions; explosive volcanism has occurred primarily at the summit, covering less than 2% of the present subaerial surface of Kilauea<sup>3</sup>. The apparent lack of pahoehoe lava flows on the SIR-B data erroneously suggests that effusive eruption of these very fluid lavas was not common at Kilauea. In addition, since pahoehoe lavas often comprise the near-vent portions of longer flows, both the number of flows and the dimension, especially the lengths, of many lava flows would be greatly underestimated. The apparent prevalence of aa lavas along the rift zones also suggests that Kilauea lavas had higher average viscosities than they do, and that the average eruption rates of Kilauea lavas were higher than they are. Finally, the inability to distinguish cinder cones, low-relief lava shields, and small fissure systems falsely indicates that effusive or strombolian activity was a less important style of volcanism than large-scale pyroclastic eruptions.

These complexities in the use of SIR-B data for characterization of volcanic landforms and interpretation of the eruptive history of Kilauea result from the combined influence of system, data acquisition, and terrain parameters. The directional nature of the SIR-B radar beam (NW to SE) enhanced large-scale topographic features such as the summit caldera and a radial system of normal faults oriented approximately perpendicular to the radar antenna. The sensitivity of the 23 cm wavelength of SIR-B to the roughness of the surface at a comparable scale permitted mapping of the location and distribution of rough-surfaced aa lava flows along the Southwest



Rift Zone of Kilauea. Limitations of the SIR-B data for geologic analyses of Kilauea included an inability to resolve small-scale topographic features such as cinder cones and fissures, and insensitivity to variations in small-scale roughness, resulting in an inability to distinguish pahoehoe lava flows from other low-return volcanic units.

The similarity in expected flow morphologies and eruptive styles on Venus and Earth<sup>4</sup> suggests that the results of this radargeologic analysis of Kilauea can be extended to the interpretation of eruptive styles of volcanic centers on the basis of Venera 15/16 (resolution from 1 to 3 km, 8 cm wavelength, 10° incidence angle) and future Magellan (resolution about 300 m, 12.6 cm wavelength, about 15° to 50° incidence angles) SAR images of Venus. In particular, these results permit an estimate of the influence of radar imaging parameters (such as resolution, wavelength, and incidence angle) on the geologic characterization of volcanic units on Venus. For example, at the 1 to 3 km resolution of the Venera 15/16 images, only large-scale volcanic landforms such as calderas, rift systems, lava shields or domes, lava flows, and possible pyroclastic deposits should be identifiable. Smaller-scale features such as cinder cones, pit craters, fissures, vents, lava channels, levees, and flow lobes would generally remain undetected, inhibiting the recognition of smaller volcanic centers on the Venera 15/16 data. In addition, at the 8 cm effective surface roughness defined by the wavelength of the Venera 15/16 system, many volcanic landforms might be expected to be radar-rough and thus to have bright returns. Certainly most lava flows should appear as bright units on the Venera 15/16 data, and the distinction between flow types such as aa and pahoehoe should not be possible. Because pyroclastic deposits may vary greatly in average surface roughness, such deposits on Venus could have either bright (e.g., radar-rough) or dark (radar-smooth) returns. Due to the steepness of the slope of the curve describing the radar scattering law for Venus<sup>5</sup> (where specular reflections from facets oriented perpendicular to the radar antenna dominate radar return), smooth (less than a few cm in average roughness) units (e.g., ash deposits, sand sheets) may have higher radar returns than rough units (e.g., lava flows) at the Venera 15/16 wavelength. For geologic interpretation of volcanic centers with the Magellan data, the significant improvement in resolution (about 300 m) may result in identification of smaller-scale (<100 m) volcanic landforms such as cones, domes, small eruptive centers, vents, and pit craters. Details of flow morphologies and vent structures are likely to remain unresolved with the Magellan data. At the 12.6 cm Magellan wavelength, lava flows should still exhibit bright returns, and distinction between aa and pahoehoe should not be observable. Due to the 15° to 50° range of incidence angles of the Magellan data, units of comparable surface morphology in areas imaged at different incidence angles should have variable return intensities.

#### References Cited:

- (1) Gaddis, L.R., P.J. Mouginis-Mark, R.B. Singer, and V. Kaupp, *Geol. Soc. Am. Bull.*, in press, 1988; (2) Cimino, J., C. Elachi, and M. Settle, 1986, *IEEE Trans. Geosci. Rem. Sens.*, v. GE-24, pp. 445-452; (3) Holcomb, R.T., 1987, *U.S.G.S. Prof. Paper #1350*, pp. 261-350; (4) Head, J.W., and L. Wilson, 1986, *J. Geophys. Res.*, v. 91, pp. 9407-9446; (5) Campbell, D.B. and B.A. Burns, 1980, *J. Geophys. Res.*, v. 85, pp. 8271-8281.



CHAPTER 2

OUTER PLANET SATELLITES AND RINGS

PRECEDING PAGE BLANK NOT FILMED

PAGE 50 INTENTIONALLY BLANK



# DYNAMIC GEOPHYSICS OF IO

A. S. McEwen (U. S. Geological Survey, 2255 N. Gemini Dr., Flagstaff, AZ 86001), J. I. Lunine (Lunar and Planetary Lab., Tucson, AZ), and M. H. Carr (U. S. Geological Survey, Menlo Park, CA)

Numerous volcanic eruptions and hot spots show that Io is the most geologically active solid body known in the Solar System. The resurfacing rate is remarkably high; as much as  $10 \text{ cm yr}^{-1}$  is the global average. Surface landforms include calderas, mountains, shield volcanoes, plateaus, flows, grabens, and eroded scarps. The bulk density and topographic relief suggest a dominantly silicate composition, but spectral observations indicate that the surface is covered by  $\text{SO}_2$  and other sulfurous materials. The lithosphere is probably more than 30 km thick under regions showing substantial relief. Io's volcanism is most likely powered by tidal heating mechanisms that also differentiated the satellite and drove volatiles to the surface. All recent models place the tidal heating below the lithosphere; disagreement exists, however, as to whether the heating is episodic over geologic time. Active volcanic plumes are of two types. The Prometheus type, concentrated within 30 degrees of the equator, is relatively small ( $\sim 100 \text{ km}$  high) and of long duration (months to years), producing bright halo deposits 200-600 km in diameter. The Pele type, concentrated in the region from longitude  $240^\circ$  to  $360^\circ$ , is large ( $\sim 300 \text{ km}$  high) and of short duration (days to months), depositing relatively dark and reddish materials over areas of 1000-1500 km diameter. The Prometheus-type plumes are probably driven by  $\text{SO}_2$  vapor from reservoirs near 400 K, whereas the Pele-type plumes may be driven by sulfur vapor from reservoirs near 1000 K. The hot spots on Io correspond to low-albedo areas, usually on the floors of calderas. Hot-spot temperatures generally range from 200 to 400 K, and the radiation may be due to convecting sulfur lakes with rapid evaporative outflow or to cooling silicate lavas. The global energy flow from the hot spots, by conduction through the lithosphere, and by the kinetic energy of the plumes is from 1 to  $3 \text{ W m}^{-2}$ . A global asymmetry in the structure or composition of Io is suggested by the longitudinal variation of the orbital lightcurve,  $\text{SO}_2$  abundance, Pele-type plumes, steady-state heat flow, short-lived enhancements at  $5 \mu\text{m}$ , and topographic relief.

PRECEDING PAGE BLANK NOT FILMED

## ICY SATELLITE TECTONICS: ARIEL, TETHYS, AND GANYMEDE

William B. McKinnon and L.A.M. Benner, Department of Earth and Planetary Sciences and McDonnell Center for the Space Sciences, Washington University, Saint Louis, MO 63130; and Paul M. Schenk, MS 183-501, Jet Propulsion Laboratory, Caltech, Pasadena 91109.

### *Viscous relaxation and the composition of Ariel's crust*

Among topics in icy satellite tectonics, the long term evolution of craters is of particular interest, because it can be used to constrain important satellite properties such as surface viscosity, composition, lithospheric thickness, or heat flow. As an example, an apparently volcanic plains unit on Ariel has buried older cratered terrain to ~1–2 km depth. Several craters in the 8–15 km diameter range are 50 to 70% shallower than comparably sized fresh craters on Ariel (Schenk 1989). As these craters do not appear degraded (and are on a young unit), they are interpreted as *viscously relaxed* (Schenk and McKinnon 1988). Assuming an age of 4 Gyr and Newtonian rheology, an effective viscosity can be calculated along lines used previously for Ganymede and Enceladus (Passey 1982, 1983). The plains unit overlaps a larger crater that is not viscously relaxed. This leads to two hypotheses. The first is that the plains unit is a region of anomalously high heat flow, but otherwise has the same composition as nearby regions that do not show evidence for viscous relaxation. Treating the surface as a uniform half-space with a heat flow varying from zero to very great, surface viscosities in the range  $10^{24} \pm 1$  Pa s are required to explain the degree of flattening of the craters above. This range of viscosities overlaps that estimated for the surface of Enceladus,  $10^{23-24}$  Pa s (Passey 1983), but is less than or equal to that estimated for the surface of Ganymede,  $1.0 (\pm 0.5) \times 10^{25}$  Pa s (Passey 1982). New depth measurements for fresh Ganymede craters by Schenk are less than that assumed by Passey, though, so the estimate for Ganymede's effective surface viscosity may eventually be raised. If so, the difference between the Ariel and Ganymede estimates can be used to argue that Ariel's surface has a different composition than that of Ganymede, perhaps ammonia–water ice. Passey (1983) used the difference between his Ganymede and Enceladus estimates to argue for a different composition for the surface of Enceladus (also ammonia–water ice).

The second hypothesis for the plains is even more intriguing. Here the plains unit is interpreted as having a different composition from the surface below. The overlapped crater and other nearby landforms not covered by plains material survive not because of lower heat flow but because of a different (and stiffer) composition. In this case the viscosity in the plains unit required to account for the crater flattening, assuming the ice below is much more rigid, is  $10^{22} \pm 1$  Pa s. This low number almost demands a softer rheology such as that of  $\text{NH}_3\text{--H}_2\text{O}$  (W.B. Durham, personal communication, 1989). It is also consistent with other geologic evidence for ammonia–water ice volcanism on Ariel (Jankowski and Squyres 1988).

### *Origin of Ithaca Chasma: Importance of the lithosphere*

A second tectonic problem, Ithaca Chasma, also received attention. This nearly globe-girdling canyon system on Tethys is apparently unique in the solar system. It forms a great

circle nearly  $90^\circ$  from the large basin Odysseus, which suggests the two are related. It has been hypothesized that viscous rebound of Odysseus caused the observed fracturing by inducing viscous drag at the base of the Tethyan lithosphere (McKinnon 1985), essentially a slow, steady-state version of multiringed basin mechanics (Melosh and McKinnon 1978, Melosh 1982). Another principal difference would be that the crater driving the flow is large compared to the satellite radius. Recently, Thomas and Squyres (1988) modeled the viscous flow induced in whole satellites by large craters. They found that the flow can switch to a unidirectional "whole-satellite" mode for crater-diameter-to-body-radius ratios similar to that of Odysseus (the largest ratio known). They postulate that this is the reason Ithaca Chasma formed and that other similar structures have not. Tangential (colatitudinal) stresses,  $\sigma_{\theta\theta}$ , were shown to remain extensional out to  $\sim 90^\circ$  only in the case of unidirectional flow. These were viscous flow stresses evaluated at the deforming free surface, however. McKinnon and Benner (1989) have more carefully evaluated the influence of the elastic lithosphere.

The lithosphere is modeled as a thin shell subject to basal drag toward or away from the crater and the stresses determined by numerical integration. The colatitudinal membrane stress,  $\sigma_{\theta\theta}$ , is set to zero at the crater rim, reflecting the thinness or weakness of the lithosphere there or simply the role of the rim as a stress boundary during uplift (of the basin floor). For small craters, and for plausible functional forms of the basal shear, results are similar to the planar case, meaning that  $\sigma_{\theta\theta}$  goes through a tensional maximum and the hoop stress  $\sigma_{\phi\phi}$  is compressive near the crater. For larger craters, the tensional maximum is suppressed, and it is interesting to note that the relative crater size where the tensional maximum disappears is similar to that where unidirectional flow first appears in the results of Thomas and Squyres (1988). Also, depending on the basal shear, significant tension is generated in the hemisphere opposite the crater; the lithosphere acts as a stress guide, and such antipodal extension may have contributed to the significant plains volcanism opposite Odysseus, with or without "unidirectional" flow. These results also have implications for "smaller" ringed basins such as Orientale on the Moon. Effects of the spherical shell are important even in this case, and can lead to a suppression of the compressive hoop stress near the crater, making generation of the primary ring fault near the position of the  $\sigma_{\theta\theta}$  tensional maximum more likely. Further work needs to be done, such as explicitly incorporating the effect of uplift close to the crater and determining (rather than assuming) the basal drag induced by the viscous rebound flow. The present results will be incorporated in Moore and McKinnon (1989), which discusses the geological effects of large impacts on icy satellites (tectonics, volcanism, resetting the cratering record, etc.).

#### *A geological map of the Jg-15 quadrangle of Ganymede*

Lastly, as part of the USGS Galilean Satellite Mapping Program, Andrew Leith, Rene De Hon, and I have produced a map of the Hathor Quadrangle of Ganymede (Jg-15). To assist in the mapping, a photomosaic of the better resolved half of the region, all of which is south of  $65^\circ$  S, was constructed from 16 Voyager 2 images. The map and photomosaic were presented as a poster at the 20th LPSC, and the map has been submitted to Survey review (De Hon *et al.* 1989).

In terms of geologic history, the inferred sequence of events is now familiar, except that

the exceptional resolution in this region makes relationships clearer. The small polygons of the oldest terrains are characterized by small craters that probably do not represent the initial high impactor flux. The surface has been extensively modified by endogenous processes. Dominant were crustal extensional tectonics and accompanying water-ice volcanism. The older dark terrains were extensively fractured by normal faulting, and as blocks off the old terrain were down-dropped as graben, they were nearly completely filled by brighter (clean) material from beneath. Within the quadrangle, there is a very dominant extensional stress direction oriented along the 190° meridian. Later bright lane units near the crater Isis have a variety of orientations, suggesting a more uniform extensional stress field. Groove formation must have taken place over an extensive period of time as the crater density on the various grooved terrains shows considerable range. Impacts on the surface were not generally preserved until after the major period of groove formation. Early-formed craters and basins were lost by extensive resurfacing and by topographic relaxation. The penepalimpsest Hathor formed during the period of groove formation, but the Gilgamesh multiringed basin formed later, after the major period of groove formation was over. As the complex grooved terrain is not extensively cratered, groove formation took place near the end of the heaviest influx but early in the satellite's history. Late-stage eruptions of resurfacing material formed smooth terrains and partially flooded other units, but without attendant groove-forming tectonism.

### References

- De Hon, R.A., A.C. Leith, and W.B. McKinnon (1989). Geologic map of the Hathor Quadrangle of Ganymede. U.S. Geol. Surv. Misc. Inv. Map., submitted.
- Jankowski, D.G., and S.W. Squyres 1988. Solid-state ice volcanism on the satellites of Uranus. *Science* **241**, 1322–1325.
- McKinnon, W.B. 1985. Origin of Ithaca Chasma, Tethys. *Bull. Am. Astron. Soc.* **17**, 922.
- McKinnon, W.B., and L.A.M. Benner 1989. Origin of Ithaca Chasma, Tethys, II: The importance of the lithosphere. *Lunar Planet Sci. XX*, 679–680.
- Melosh, H.J. 1982. A simple mechanical model of Valhalla basin, Callisto. *J. Geophys. Res.* **87**, 1880–1890.
- Melosh, H.J., and W.B. McKinnon 1978. The mechanics of ringed basin formation. *Geophys. Res. Lett.* **5**, 985–988.
- Moore, J.M., and W.B. McKinnon (1989). Large impact features on middle-sized icy satellites. *Icarus*, in preparation.
- Passey, Q.R. 1982. *Viscosity structure of the lithospheres of Ganymede, Callisto, Enceladus, and of the Earth's mantle*. Ph.D Thesis, Caltech.
- Passey, Q.R., 1983. Viscosity of the lithosphere of Enceladus. *Icarus* **53**, 105–120.
- Schenk, P.M. 1989. Crater formation and modification on the icy satellites of Uranus and Saturn: Depth/diameter and central peak occurrence. *J. Geophys. Res.* **94**, 3815–3832.
- Schenk, P.M., and W.B. McKinnon 1988. Viscous relaxation of craters on Ariel: Implications for crustal composition. *Bull. Am. Astron. Soc.* **20**, 881.
- Thomas, P.J., and S.W. Squyres 1988. Relaxation of impact basins on icy satellites. *J. Geophys. Res.* **93**, 14,919–14,932.



## ORIGIN AND EVOLUTION OF PLUTO AND TRITON

William B. McKinnon and Andrew C. Leith, Department of Earth and Planetary Sciences and McDonnell Center for the Space Sciences, Washington University, Saint Louis, MO 63130; and Steve Mueller, Department of Geological Sciences, Southern Methodist University, Dallas, MO 75275.

### *A prediction for the density of Triton*

Pluto is a very rock-rich body, and its high rock/ice ratio is consistent with theoretical predictions for the composition of objects formed directly in the solar nebula (McKinnon and Mueller 1988). In contrast, satellites form in nebulae around giant planets, and are predicted to be and are much icier. This is strong evidence for Pluto's origin in the solar nebula as opposed to being an escaped satellite (a dynamically dubious proposition that nonetheless has great popular appeal). We also offer a prediction for Triton's density, based on the *assumptions* that it was captured from solar orbit by Neptune, and thus has a rock/ice ratio similar to that of the Pluto–Charon system (McKinnon and Mueller 1989). The best estimates for Triton's radius as of this writing are 1000–2000 km, and if our origin hypothesis is correct, its density should be greater than  $2.0 \text{ g cm}^{-3}$ , increasing slowly with radius. On the other hand, if Triton is an original regular satellite whose orbit has been perturbed, its density should be lower and more consistent with the derived rock fractions of other icy satellites.

### *Origin of the Pluto–Charon binary*

Having looked at the density of Pluto–Charon system, it is natural to examine the angular momentum budget and implications for Pluto's formation (McKinnon 1989). The normalized angular momentum density  $J$  of Pluto–Charon, assuming equal densities for both components and that Pluto's mutual occultation radius is close to correct, is 0.45. This exceeds the critical  $J$ , 0.39, above which no stably rotating single object exists. A collisional origin for the binary is strongly implied.  $J$  exceeds 0.39 for Charon densities  $\rho_C$  above  $1.77 \text{ g cm}^{-3}$ , and is significantly greater than that of the Earth–Moon system for any plausible  $\rho_C$ . Moreover, for  $\rho_C \geq 2.3 \text{ g cm}^{-3}$ , a tidally evolved Charon starting at the appropriate Roche limit implies a Pluto with  $J > 0.39$  alone. This is not a possible initial configuration, so  $2.3 \text{ g cm}^{-3}$  is the dynamical upper limit to Charon's density. The dynamical lower limit is too low to be meaningful, so a plausible cosmochemical lower limit of  $1.0 \text{ g cm}^{-3}$  is assumed. These density limits hint at but do not prove that Charon is less dense than Pluto; a lower density Charon would be consistent with a collisional origin if one or both proto-objects were differentiated. A density upper limit closer to the system mean is possible if the rapidly rotating Pluto, as a Jacobi ellipsoid, is not allowed to contact Charon at the Roche limit. Viscosity may constrain Pluto to a more biaxial figure, however. The angular momentum of the system requires that the proto-objects be comparably (if not equally) sized, if off-center impact velocities vary between escape ( $\sim 1.3 \text{ km s}^{-1}$ ) and somewhat greater values ( $\sim 2.5 \text{ km s}^{-1}$ ) appropriate to Pluto's eccentric and inclined solar orbit. The average temperature

increase, post-Charon-formation, could be as great as 100 K (for a 3/1 rock/ice mass ratio), triggering differentiation. This formation scenario differs (potentially) from that of the Moon in that the comparable mass ratios of the impactors allow non-Keplerian gravitation and viscous coupling to move Charon's mass to Roche altitude. The impact velocities are too low for vaporization of water ice except during jetting. Loss of material during the jetting phase may be substantial, though, affecting the final system ice/rock ratio in the case of differentiated proto-objects. If the new solar abundances of Anders and Grevesse (1989) for C and O are correct, then some fractionation of ice from rock is necessary to explain Pluto's high density. This work was presented at the Spring 1988 AGU Special Session on Pluto.

### *Gas drag and the evolution of a captured Triton*

The physics of Triton's possible capture by gas drag have also been reexamined (McKinnon and Leith 1989). This was done to compare the role of gas drag in orbital evolution with tides and to evaluate the general likelihood of capture by this mechanism. Pure tidal evolution of a captured Triton causes massive heating in the satellite. Gas drag causes the inclination to become more prograde, and Triton's nearly retrograde status potentially places an upper limit on the orbital energy lost due to gas drag and hence a lower limit on the amount of tidal heating. A putative Neptune nebula was modeled after a minimum mass Uranus nebula and is assumed to be isothermal and cool ("nominal"). Triton's initial apocenter was set at the radius of the sphere of influence, consistent with numerical studies of retrograde temporary captures, and its initial pericenter is within the nebula. Despite strong evolution of both semimajor axis and eccentricity, Triton's inclination changed by only a small amount ( $< 6^\circ$  overall and usually smaller). Results are not sensitive to variations in the surface density or temperature, or to the radius and density of Triton. Thus Triton could have evolved to its present retrograde circular orbit by gas drag alone, and massive tidal heating is not an inevitable consequence of capture. Non-trivial tidal heating is still likely, though, because Triton's post gas drag orbit would probably be significantly eccentric.

Despite Triton's large mass, single-pass capture is found to be energetically favorable for the nominal nebula. Capture is also possible for nebulae that are less massive by an order of magnitude or for the solar gas flowing into Neptune's accretion sphere at an earlier stage of formation. Survival of Triton against gas drag in the latter case is unlikely, but the former may be appropriate for the compact H and He depleted nebulae that form around planets such as Uranus and Neptune in a variety of formation scenarios. Once captured, evolution is rapid (as in most gas drag calculations), with the orbital angular momentum reduced to Triton's present value in  $\sim 10^2$  to several  $10^3$  yr. Nevertheless Triton may survive, for it is massive and nebular evolution may be rapid; after all, capture into a circum-Neptunian nebula implies that the solar nebula has dissipated or is in the process of dissipating. The mass and angular momentum of Triton and that of a low-mass (H and He depleted) nebula are comparable, so orbital evolution for such a capture may "self-terminate." In particular, Triton may clear an annular region in the nebula after multiple passes through it, and for sufficiently low nebular kinematic viscosities (but still much greater than molecular values), greatly extend its lifetime. The possibility of "self-termination," by whatever mechanism, is particularly exciting.

## *Coupled orbital and thermal evolution of a captured Triton*

Analysis of purely tidally evolving Triton has also been pursued (McKinnon 1988). Only ~4% of the orbital energy available post-capture is needed to completely melt (and differentiate) the satellite. As such, orbital collapse and circularization depend on Triton's internal configuration (its effective  $Q$  and Love number  $k$ ). Dissipation in a mostly molten Triton is likely to be restricted to thin solid shells, water ice at the surface and silicate at the core mantle boundary. Subsolidus ice and rock in these shells have Maxwell times smaller than the orbital period. Conductive heat flow through the shells will be in steady-state balance with tidal input. The effective  $Q$ s of the shells are of order 10 for Maxwell rheologies. In this case, heat flows are lower than in a constant  $Q/k$  model with  $Q = 100$  and a  $k$  appropriate to a uniform ice sphere (and with plausible values for Triton's mass and radius). Even so, the ice shell is under 1 km thick and the silicate shell (provided it is a floating differentiate) is under a few km. Variation of heat flow with orbital evolution is muted (by the  $1/2$  power) compared to constant  $Q/k$  models. In fact, Triton's heat flow varies by less than a factor of two over an ~500 Myr period. With the lifetime of a molten Triton so extended, any early cratering record will not be retained. During this time, tidal energy dominates insolation at the surface, and Triton's effective temperature is ~65–70 K. An extended  $N_2$  (or CO) atmosphere is possible, but not one of  $CH_4$ . All  $CH_4$  will be driven to the surface, though, and may be liquid. A radius of 1750 km and a density of  $2.0 \text{ g/cm}^3$  (similar to that of Pluto) is assumed. Thus, even with an elevated effective temperature, Triton is a high enough gravity body that atmospheric losses, modeled after Hunten and Watson (1982), are small, <500 m of surface  $CH_4$  or condensed  $N_2$  over 500 Myr. Losses may be increased through interaction with a Neptunian magnetosphere. Heat flow may be lowered and orbital evolution further stretched out if the core silicate shell is negatively buoyant, overturning before it reaches its equilibrium thickness. Dissipation within the liquid regions has the opposite effect. A fundamental caveat is that the amount of orbital evolution due to gas drag, described above, is poorly constrained. The amount of tidal heating that Triton could have experienced may be much smaller.

## *References*

- Anders, E., and N. Grevesse 1989. Abundances of the elements: Meteoritic and solar. *Geochim. Cosmochim. Acta* **53**, 197–214.
- Hunten, D.M., and A.J. Watson 1982. Stability of Pluto's atmosphere. *Icarus* **51**, 665–667.
- McKinnon, W.B. 1988. Coupled thermal and orbital evolution of a captured Triton. *EOS Trans. AGU* **69**, 1297.
- McKinnon, W.B. 1989. Origin of the Pluto–Charon binary. *Ap. J. (Lett.)*, submitted.
- McKinnon, W.B., and A.C. Leith 1989. Gas drag and the evolution of a captured Triton. *Icarus*, submitted.
- McKinnon, W.B., and S. Mueller (1988). Pluto's structure and composition suggest origin in the solar, not a planetary, nebula. *Nature* **335**, 240–243.
- McKinnon, W.B., and S. Mueller (1989). The density of Triton: A prediction. *Geophys. Res. Lett.* **16**, in press.

## VOLATILE PROCESSES IN THE OUTER SOLAR SYSTEM

Jonathan I. Lunine, Lunar and Planetary Laboratory, University of Arizona, Tucson, AZ 85721

### Thermal Evolution of Titan's Atmosphere (with Bashar Rizk)

A semi-analytic model is constructed of the evolution of Titan's atmosphere and surface. The model assumes the presence of a massive (kilometer-deep) ethane-methane ocean at the surface, which serves as a reservoir for atmospheric gases important in determining the thermal balance of the troposphere. As stratospheric photolysis irreversibly converts methane to higher hydrocarbons with time, the ocean becomes progressively enriched in ethane and depleted in methane. The resulting change in the abundance of gases drives the evolution of the atmospheric thermal structure. The solubility in the ocean of nitrogen, argon and hydrogen is quantified as a function of methane content, which permits the atmospheric composition to be calculated as a function of ocean composition. The surface temperature as a function of atmospheric composition and surface pressure is calculated using a grey atmosphere, two-stream approximation with infrared opacities supplied by collisions among nitrogen, methane and hydrogen molecules.

A suite of evolution models corresponds to different present-day ocean compositions, various atmospheric hydrogen abundances, and different schemes for frequency-averaging the gas opacity for use in the grey atmosphere formalism. Over a plausible range of parameters characterizing present-day ocean and atmospheric compositions, slow evolution over several billion years is obtained (Lunine and Rizk, 1989). This result is consistent with the original motivation for postulating an ethane-methane ocean, namely, that it provide a means for maintaining the atmosphere observed by Voyager over a reasonable fraction of geologic time (figure 1). Models of atmospheric evolution in the absence of an ocean are driven by stochastic resupply of methane to the atmosphere by volcanism or impacts. Variation of solar radiation at the surface due to changes in haze column abundance, tropospheric clouds and the increasing solar luminosity with time are not considered in the present effort. The results show that methane photolysis connects the properties and time history of Titan's atmosphere and possible ocean, not only by the production of ethane from methane, but equally importantly through the formation of molecular hydrogen.

### Comet Halley: the Role of Primitive Bodies in Understanding the Physics and Chemistry of the Outer Solar System

The most recent results on abundances of molecules in Halley's comet are examined in the context of various models for the environment in which comets formed. These environments include molecular clouds associated with star-forming regions, the solar nebula, gaseous disks around proto-planets, and combinations of these. Of all constituents in a cometary nucleus, the highly volatile molecules such as methane, ammonia, molecular nitrogen and carbon monoxide are most sensitive to the final episode of cometary grain formation and incorporation in the comet's nucleus; hence they likely reflect at least some chemical processing in the solar nebula. Proper interpretation requires modeling of a number of physical processes including gas phase chemistry, chemistry on grain surfaces, and fractionation effects

resulting from preferential incorporation of certain gases in proto-cometary grains. The abundance of methane in Halley's comet could be a key indicator of where that comet formed, provided the methane abundance on grains in star-forming regions can be observationally constrained.

A model was constructed of the nebular gas from which Halley formed based on the assumption that the most volatile gases in Halley (except ammonia) were trapped in clathrate hydrates (Lunine, 1989a). The results can be summarized as follows (1) the nebular CO/CH<sub>4</sub> ratio was of order 10<sup>2</sup>; (2) the ammonia abundance in the nebula was in the range 10<sup>-3</sup> - 10<sup>-2</sup> relative to water; (3) molecular nitrogen may well have been the most abundant nitrogen species in the nebula, but was not efficiently incorporated in the icy comet grains; (4) carbon dioxide is present in Halley as both dry-ice and trapped gas in water ice. Implications for nebular physical and chemical processes (figure 2) is work in progress with S. Engel and J.S. Lewis.

#### Cosmochemical inferences concerning the identity of the heavier gas in Pluto's atmospheres (with R.V. Yelle and W.B. Hubbard)

Recent analysis of the thermal structure of Pluto's atmosphere yields a mean molecular weight of 22 to 28 a.m.u. (Yelle and Lunine, 1989), well above that of methane, the only spectroscopically identified gas in Pluto's atmosphere. The derived thermal structure reproduces certain features of the stellar occultation data (Hubbard, Yelle and Lunine, 1989), so the presence of a gas heavier than methane appears to be a robust conclusion. Candidate gases which are plausible from the standpoint of solar nebula models are carbon monoxide, molecular nitrogen and argon. Cosmochemical models predict argon to be at least two orders of magnitude less abundant than the carbon-bearing species, and roughly an order of magnitude less abundant than nitrogen. Molecular nitrogen is a potentially attractive candidate as the heavier gas, insofar as it dominates the atmosphere of Titan and may be present on Triton. However, its presence on Titan is most readily explained as the product of photolysis and shock chemistry of ammonia early in that satellite's history. If Pluto formed in a gaseous nebula dominated by water, methane and ammonia (as predicted for Titan), it would have a bulk density of 1.5 to 1.6 g/cm<sup>3</sup>, well below the system value of roughly 2.0 g/cm<sup>3</sup>. The most likely heavy gas for Pluto is carbon monoxide, predicted to have been an abundant carbon-bearing gas in the outer solar nebula. The bulk density of Pluto is consistent with a solar nebula dominated by carbon monoxide as the major carbon-bearing molecule. Small amounts of methane in the nebula would have been preferentially trapped in water ice which accreted to form Pluto, consistent with a mixed methane-carbon monoxide atmosphere at present (and consistent with the methane and carbon monoxide abundances in Comet Halley). Lesser amounts of nitrogen and argon in Pluto's atmosphere are predicted by this model.

#### References

- Hubbard, W.B., Yelle, R.V. and Lunine, J.I. 1989. Icarus, submitted.  
Lunine, J.I. 1989a. In Origin and Evolution of Planetary Systems, eds. H.A. Weaver, L. Danly and F. Paresce. Cambridge Univ. Press, in press.  
Lunine, J.I. 1989b. Icarus, submitted.  
Lunine and Rizk, 1989. Icarus, in press.  
Yelle, R.V. and Lunine, J.I. 1989. Nature, in press.

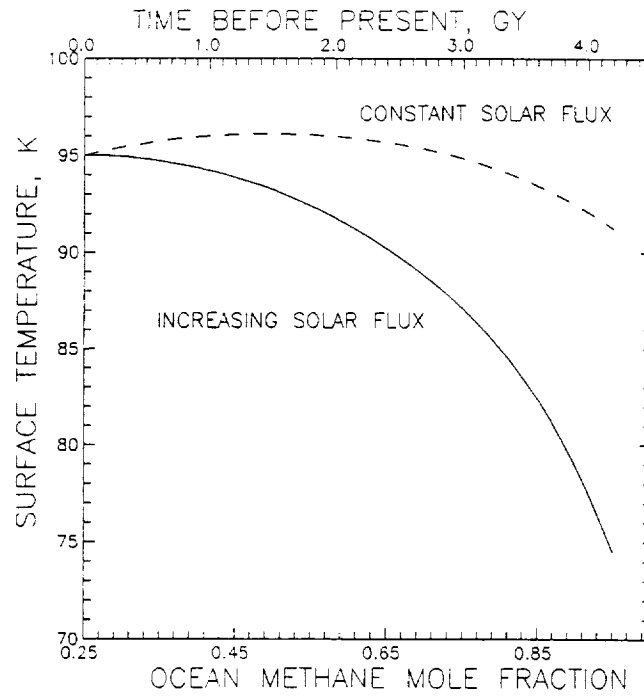


Figure 1: Evolution of Titan's surface temperature with time, both with and without a changing solar flux. From Lunine and Rizk (1989).

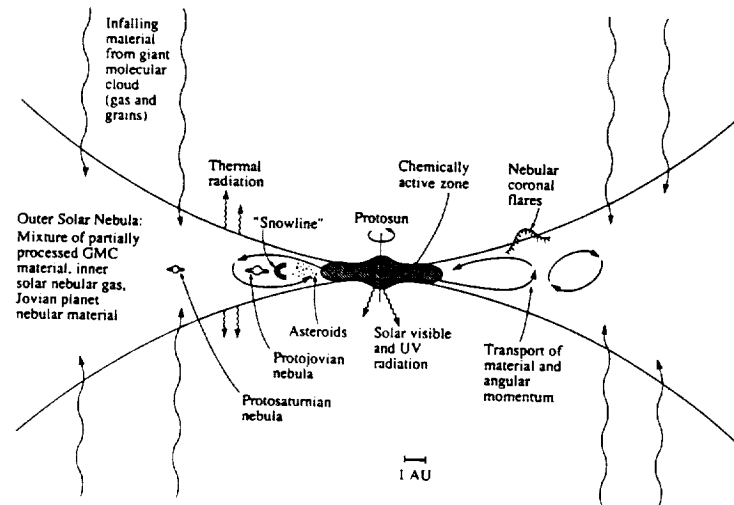


Figure 2: Physical and chemical processes in the solar nebula. From Lunine (1989b).

## FORMATION OF ANTIPODAL TERRAINS ON ICY SATELLITES

*A. Watts, R. Greeley, Arizona State University, Tempe, Arizona, 85287 and  
H. J. Melosh, University of Arizona, Tucson, Arizona, 85721*

It has been proposed (Schultz and Gault, 1975) that seismic energy from a major impact could cause extensive crustal fracturing and surface disruption on the portion of the planet directly opposite the impact. Disrupted terrains of this type have been identified on Mercury antipodal to the Caloris impact, and on the Moon antipodal to Imbrium. Although some analyses have assessed the focusing of seismic energy at the planetary antipodes (Schultz and Gault, 1975; Hughes et al., 1977; Rial and Cormier, 1985), an in-depth analysis of the problem has not been performed for icy satellites or for a layered body of any composition. Schultz and Gault (1975) calculated the seismic effects from a major basin formation on a homogeneous silicate Moon. This study did not include the effects of either attenuation or layering, but showed clearly that some degree of seismic focusing of both body waves and surface waves should occur at the antipode. In 1977 Hughes, App and McGetchin re-evaluated the problem using a finite difference computer code.

The study in progress extends the work of Hughes et al. (1977) to include the effects of layering (especially in the form of a high density core), and composition (both icy and silicate). It also includes an analytical treatment of spallation, an effect which is not discussed in detail in either of the previous papers. Calculations are performed on a two dimensional half circle grid; three dimensional interactions and deviations from a homogeneous concentric shell model are beyond the scope of the current phase of this study. The calculated disruptions will then be compared to those observed areas on icy satellites which occur antipodal to major impacts. The presence or absence of an observed "antipodal terrain" in an area where models predict disruption may make it possible to constrain models of satellite interiors at the time of impact. In the first section of this study theoretical calculations are being used to predict antipodal disruption under a variety of conditions. In the second section a set of calculations specifically designed to simulate particular satellites will be run. The surfaces of these satellites antipodal to major impacts will be compared to the calculated disruption for an impact of that size on that planet/satellite.

*Part 1; analytical models.* The initial impact energy distribution models are produced using a modified SALE (Simplified Arbitrary Lagrangian Eulerian) computational code written by A.A. Amsden et al. in 1980. This code will be used to calculate the development of a material flow. The code is initialized as a computational grid with the desired pressures, material characteristics, and initial velocities defined for each grid element. It then calculates the response of the material over time, both from internal forces and external forces.

A series of calculations have been performed for planets with a range of compositions and core sizes. It has been found that in a planet with a high density core surrounded by a lighter mantle material (ice over a silicate core, or silicate over iron), the incident pressure wave splits when it strikes the core. The part which passes through the core moves more rapidly and is refracted away from the antipode. It strikes the surface at some distance from the antipode and may overlap with the second part of the wave, which, missing the core, has traveled directly through the mantle. Refraction of the wavefront through the core may, therefore, decrease the pressure generated at the antipode and redistribute some of the pressure front to the surface adjacent to, but not at, the antipode. Antipodal and near antipodal calculated pressures have been plotted as a function of core size (Fig. 1). It can be seen that the redistribution is minimal for the smallest and largest core sizes, and largest for a core with a radius of about 1/3 the planetary radius.

*Part 2; Calculations and comparison.* When studying antipodal terrains on satellite surfaces two factors must be considered: the conditions of the body at the time of impact, and modifying effects which may have subsequently altered the surface. If initial conditions were such that a impact would be expected to produce an antipodal terrain, but no antipodal features are observed, resurfacing effects must be considered. Resurfacing could effectively erase features, and although viscous relaxation would not be expected to erase short wavelength features such as the hummocky terrain found on the Earth's moon and Mercury, it could produce degradation of longer wavelength features (Parmentier and Head, 1981).

If antipodal features are retained on the surface they could occur in several forms. Hummocky terrain, mass wasting, and furrowed crater walls have been recognized antipodal to major impacts on the Earth's moon and Mercury (Schultz and Gault, 1975). Radial lineaments and concentric ring features have also been noted antipodal to the Caloris impact on Mercury (Schultz and Gault, 1975). Features which may have formed in response to an antipodal impact have been identified on several icy satellites. Thomas and Veverka (1979) have suggested that the large number of fissures and grooves on Mimas are related to impact. The abundant lineaments on Tethys (Moore and Ahern, 1983) and the wispy terrain on Dione (Plescia, 1983) may also be impact related features. Blount et al. (1987) identified one or more possibly impact induced antipodal features on eight icy satellites.

Fig. 2 lists the highest antipodal pressures generated for the models run to date. The initial energy listed is the total impact energy required to form the observed crater. This energy has been calculated with the Holsapple-Schmidt crater scaling law. The compressive strength of ice is approximately  $5 \times 10^7$  Pa, slightly greater than the pressure generated at the Tethys/Odysseus antipode. The tensile strength ( $4.0 \times 10^6$  Pa) is exceeded by the pressure generated by all impacts run to date except the Tirawa impact on Rhea. Spallation will occur on surfaces where the tensile strength has been exceeded, and the surface material undergoes acceleration.

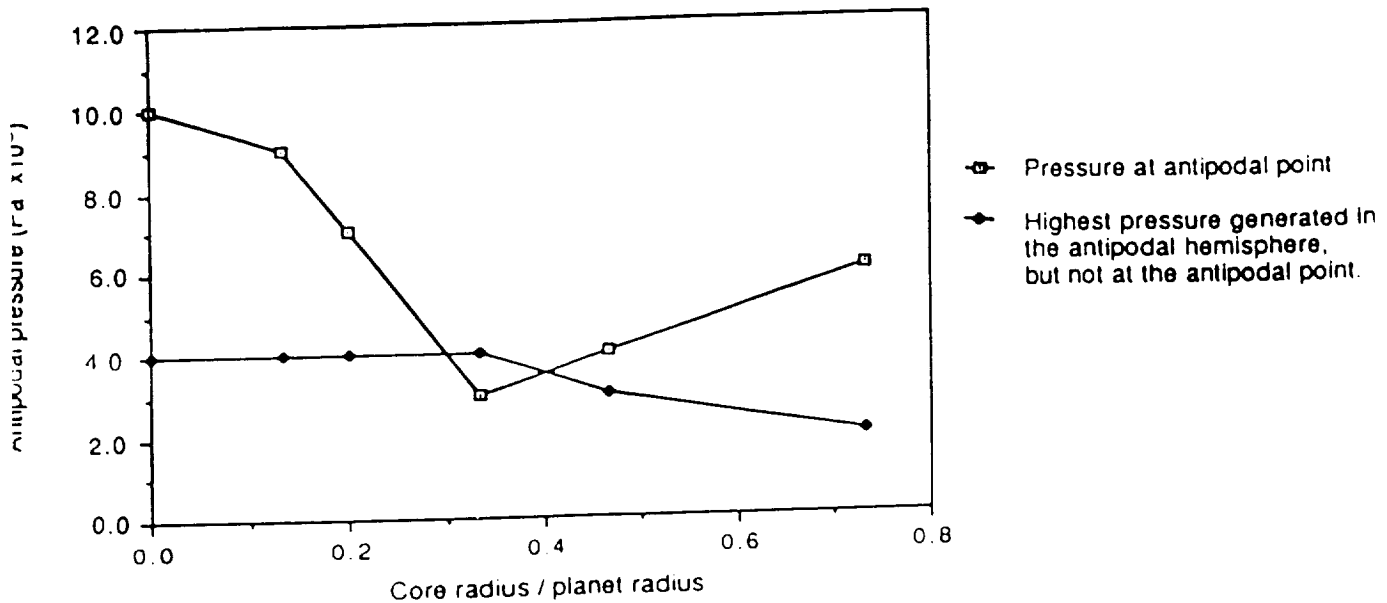
This project has produced a versatile code which can be used to calculate antipodal disruptions for a variety of planetary models and impact types. We have found that while antipodal focusing should occur on icy satellites the presence of a core may inhibit the antipodal focusing effect and may even redirect the focusing to an area away from the antipode.

## REFERENCES

- A.A. Amsden, H.M. Ruppel and C.W. Hirt, 1980, Los Alamos Scientific Laboratory Report, LA-8095.
- Blount, G.B., P.Barbera. R. Pappalardo, S. Posin, and A. Watts, 1987, *Lunar and Planetary Science Conference*, XVII, pp 93-94.
- Holsapple, K.A., and R.M. Schmidt, 1982, *Journal of Geophysical Research*, v 87 pp. 1849-1870.
- Hughes, H.G., F.N. App, and T.R. McGetchin, 1977, *Physics of Earth and Planetary Interiors*, 15, pp 251-263.
- Moore, J.M. *Icarus* 59, 1984, pp 205-220.
- Moore, J.M. and J.L. Ahern, 1983, *Proc. of the Lunar and Planetary Science Conference* 13, 577-584.
- Parmentier, E.M. and J.W. Head, 1983, *Icarus* 47, pp 100-111.
- Plescia, J.B, 1983, *Icarus* 56, pp 255-277.
- Rial, J.A. and V.F. Cormier, 1980, *Journal of Geophysical Research*, vol 85, pp 2661-2668.
- Schultz, P.H. and D.E. Gault, 1975, *The Moon* 12, pp 159-177.
- Thomas, P. and J. Veverka, 1979, *Icarus* 40, pp 394-405.



### Core Size vs Antipodal Pressure



- g. 1 Core radius vs antipodal pressure. When the core is either very small or large the wave is passing primarily through one composition and the focusing effects are very similar to those in a single composition. But as the core approaches one third the planetary diameter the wave is split such that the portion which passes through the core is refracted away from the antipode and may overlap with, and reinforce, the portion which has traveled through the mantle.

### SALE Generated Antipodal Pressures.

PLANET	CRATER (Km Diam)	E <sub>TOT</sub> (J)	PRESSURE(Pa)
Moon	Imbrium (600)	6.1E27	1.9E9
Moon w/core			1.9E9
Tethys	Odysseus (400)	3.2E24	7.1E7
Tethys w/core			4.5E7
Rhea	Tirawa (350)	5.4E23	4.0E6
Rhea w/core			3.1E6
Mimas	Herschel (130)	3.0E21	
Callisto	Vallhala (400)	1.0E25	9.0E6

- g. 2. Table showing antipodal pressures computed for several impacts.

## RIDGE AND TROUGH TERRAIN IN ELSINORE CORONA, MIRANDA

*Robert Pappalardo and Ronald Greeley, Department of Geology, Arizona State University, Tempe AZ 85287*

The Voyager encounters have revealed both diversity and similarity in the appearance of outer planet satellites. A geologic terrain common to four icy satellites of Jupiter, Saturn, and Uranus is "ridge and trough terrain," whose characteristic geomorphic form is a series of alternating ridges and troughs. Such terrain includes the "grooved terrain" of Ganymede [1], the "ridged plains" of Enceladus [2], the coronae of Miranda, and several areas on Ariel. The morphology of this terrain differs among the four icy satellites on which it occurs and different ridge and trough morphologies can be identified on a single icy body. This morphological variation implies that either a) all ridge and trough terrain is the product of a fundamental process which varies in its expression as a result of differences in satellite-specific parameters, or b) different processes have produced terrains of comparable ridge and trough morphology on icy satellites. An understanding of the process(es) which creates ridge and trough terrain is critical to interpretation of the surface and interior histories of all icy satellites.

The objective of our study is to constrain the origin and evolution of ridge and trough terrain on icy satellites and assess the similarities and differences in the process(es) which have shaped this terrain. This involves a reassessment of models established for Ganymede and Enceladus [1-7], and critical evaluation of newer models [e.g. 8-11] in light of the uranian satellite data. Processes which are capable of producing subparallel ridges and troughs are: tension fracturing, normal faulting, thrust faulting, folding, wrench tectonics, laccolithic intrusion, fissure extrusion of low or high viscosity material, and surface folding of extruded material during emplacement. A variety of possible terrestrial analogues are being examined to assess specific predictions as to plan, cross-section, and geological associations expected to result from these processes.

A non-genetic classification scheme (Table 1) has been developed to categorize the observed morphologies in order to facilitate testing of the models. This classification is based primarily on planimetric form as determined from Voyager images and takes into consideration factors such as scale, spacing, sinuosity, termination behavior, and geologic associations. Topographic analysis of ridges and troughs as determined from photoclinometry is being used to refine and improve this classification and to test formation models. These geomorphological observations along with quantitative analyses are being used to test and rank the likelihood of the formation models for each terrain type and to evaluate the possible effects of satellite parameters on morphology.

Summarized here is a preliminary analysis of subparallel ridges and troughs in the outer bands of Elsinore Corona, located in the western hemisphere of Miranda (the "ridged ovoid" of [8]). The origin of Miranda's coronae and the ridges and troughs contained within has been the subject of much debate. Ridges in the outer bands of Elsinore Corona have been suggested to be compressional features [9], horsts [9,10], or linear volcanic constructs [10,11] (perhaps analogous to those observed at terrestrial fast-spreading oceanic ridges [12]).

A sketch map of the types of ridges and troughs observed in Elsinore Corona (Figure 1) shows that two landforms, here called Elsinore Ridges (M2 of Table 1) and Straight Troughs (M1), dominate the corona's outer bands, giving the "ridged" (and/or "grooved") appearance. Elsinore Ridges are observed to occur only in the east-west trending band of the corona (hereafter the "Ridged" band), subparallel to the corona's boundaries. Straight Troughs of various scales, some with broad floors and some bounding Elsinore Ridges, also occur throughout the Ridged band. Some close-packed ridges and troughs (M3) can be recognized near the limit of image resolution.

In the adjacent north-south trending band, a set of Straight Troughs disappears into the terminator. Elsinore Ridges do not appear in this north-south band. Neither Elsinore Ridges nor Straight Troughs can be unambiguously traced across the juncture of the two bands; instead, some Straight Troughs of the north-south band terminate against a mottled unit (Figure 1). Straight Troughs are typically separated from each other by broad and relatively flat regions. Their wide spacing and the topography of the intervening terrain argues that they are true negative relief features. Of the possible formation processes listed above, extensional-tectonic processes (tension

fracturing and normal faulting) can produce this morphology. Local extension might occur in a compressional stress regime (along fold crests), but the lack of candidate compressional features in the north-south band means that there is no clear evidence for compression there, only extension.

Sinker and riser models [9] predict identical stress states in the north-south and the Ridged bands. Thus, the evidence for extension and the lack of evidence for compression in the north-south band calls the compressional model into question. Additional arguments can be made for the outer bands of Elsinore Corona having formed in an environment of extensional stress. 1) Straight Troughs, which are probably tension fractures or graben (as discussed above), also occur in the Ridged band. 2) It has been argued that Elsinore Corona is at least partially volcanically resurfaced [8], suggestive of an extensional regime. 3) Limb profiles [13] and images demonstrate that troughs bound Elsinore Corona on its three visible sides. Prominent bounding troughs are predicted to occur at the margins of rift zones [14], and the presence of similar structures has been used to argue an extensional origin for Ganymede's ridge and trough terrain [e.g. 4]. 4) Beyond the bounding trough, Elsinore Corona is bordered by a rise of ~1 km [13] that can be interpreted as an isostatic response to adjacent normal faulting [15]. 5) Within its southern boundary, the Ridged band contains troughs that appear to be arranged *en echelon* (Figure 1), indicative of oblique extension. This evidence indicates that the outer bands of Elsinore Corona are likely to have been sites of extension.

An extensional environment implies that Elsinore Ridges may be horsts, linear extrusions of high or low viscosity material, or anticlinal laccoliths lifted by large-scale linear intrusions. Some Elsinore Ridges are morphologically similar to Ganymede ridges (type G2) as examined by [16] in that they can be sharp-crested and terraced in profile; moreover, they are of essentially the same scale. The major morphological differences are that Elsinore Ridges pinch and swell, can be discontinuous along their length, and blend into the level of surrounding terrain where one or both of their bounding troughs terminate. Topographic lows adjacent to Elsinore Ridges do not appear flooded, arguing against formation of these ridges by extrusion of low-viscosity material. The ridges do not exhibit smooth parabolic profiles and lobate termini, as would be expected of viscous extrusions. No evidence exists for associated laccoliths of circular plan, arguing against formation of ridges by laccolithic intrusion. The observations are consistent with the formation of these ridges as horsts, separated by graben of various widths. Research continues, however, into other possible mechanisms. The presence of Elsinore Ridges in the Ridged band and their absence in the north-south band may be due to differences in lithospheric thickness at the times of band formation, in amount or rate of extension, or in degree or timing of volcanic resurfacing.

The influence of extensional-tectonics appears to be pervasive on all four icy satellites on which ridge and trough terrain is observed. Such has been previously argued for Ganymede and Enceladus [3-7], and the morphologic characteristics of certain ridge and trough types on Miranda and Ariel point to an extensional-tectonic origin. However, while it is tempting to attribute the variety of observed morphologies to similar processes, not all ridge and trough terrains on icy satellites display those fundamental characteristics (such as bounding troughs, negative relief, or widely spaced troughs) which have been used to argue an extensional origin for Ganymede's prototypical "grooved" terrain. Extrusive/intrusive processes may be locally important in creating ridges and troughs on all four satellites, and research into this possibility is continuing.

#### References:

- [1] Smith *et al.*, *Science* **204**, 945 (1979).
- [2] Smith *et al.*, *Science* **215**, 504 (1982).
- [3] Squyres, *Icarus* **52**, 545 (1982).
- [4] Shoemaker *et al.*, in *Satellites of Jupiter*, 435 (1982).
- [5] Squyres *et al.*, *Icarus* **53**, 319 (1983).
- [6] Fink and Fletcher, *NASA TM-84211*, p.51 (1981).
- [7] Allison and Clifford, *JGR* **92**, 7865 (1987).
- [8] Smith *et al.*, *Science* **233**, 43 (1986).
- [9] Janes and Melosh, *JGR* **93**, 3127 (1988).
- [10] McKinnon, *Nature* **333**, 701 (1988).
- [11] Croft *et al.*, *in preparation*.
- [12] Lonsdale, *Tectonophys.* **116**, 255 (1985).
- [13] Thomas, *Icarus* **73**, 427 (1988).
- [14] Gibbs, *J. Geol. Soc. London* **141**, 609 (1984).
- [15] Jackson and McKenzie, *J. Struct. Geol.* **5**, 471 (1983).
- [16] Squyres, *Icarus* **46**, 156 (1981).
- [17] Plescia, *Nature* **327**, 201 (1987).
- [18] Murchie *et al.*, *JGR* **91**, E222 (1986).

Ridge/Trough Type*	Distinguishing characteristics	Occurrences
<b>Miranda</b>		
M1: Straight Troughs	Linear to curvilinear, narrow (~1-3 km), may be widely spaced in sets.	E, I
M2: Elsinore Ridges	Small ridge-width/trough-width, ~2-6 km wide, discontinuous along strike, may pinch and swell, bounding troughs, terraced, flat to sharp-crested profile.	E
M3: Close-Packed†	Linear to curvilinear, narrow (~1 km), close-packed.	I
M4: Asymmetrical	Topographically low, asymmetrical in profile.	A, I
<b>Ariel</b>		
A1: Medial Troughs	Sinuuous to curvilinear, raised rims, occur singly or in sets.	M
A2: Curvilinear Ridges	Flat to convex, widths ~10 km, trough-bounded, indistinct sets.	RT
A3: Curvilinear Troughs	May have broad flat intervening ridges, widths ~10 km, indistinct sets.	RT
A4: Close-Packed†	Linear to curvilinear, narrow width (~5 km).	RT, CT
<b>Enceladus</b>		
E1: Curvilinear Troughs	Widely spaced, may bound Type E2 ridges, may display raised flanks.	RP
E2: Large Ridges	Curvilinear, small length/width ratio, bounding troughs, convex.	RP
E3: Sinuous Ridges	Sinuuous, narrow (~4 km), associated with largest Type E2 ridge.	RP
<b>Ganymede</b>		
G1: Broad Ridges	Flat to rounded, intervening narrow troughs.	GL
G2: Close-Packed†	Linear to curvilinear, may intersect or merge along strike, close-packed, secondary spacing distances, terraced, sharp-crested, U-shaped troughs [4,16].	GL, GP
G3: Braided	Ridges display fine 'braided' pattern, bounding troughs.	GL

\*Designation of a type as consisting of "Ridges," "Troughs," or "Ridges and Troughs" is descriptive and is not intended to imply process. Where unspecified in a type's name, "Ridges and Troughs" is implied.  
†"Close-packed" indicates a series of adjacent ridges and troughs of similar width, as is common on Ganymede.  
§E=Elsinore Corona, I=Inverness Corona, A=Arden Corona, RT=Ridged Terrain of [17], CT=Cratered Terrain of [17], M=Medial to smooth-floored graben, RP=Ridged Plains of [2], GL=Groove Lanes of [18], GP=Grooved Polygons of [18].

Table 1. Classification of ridge and trough morphologies.

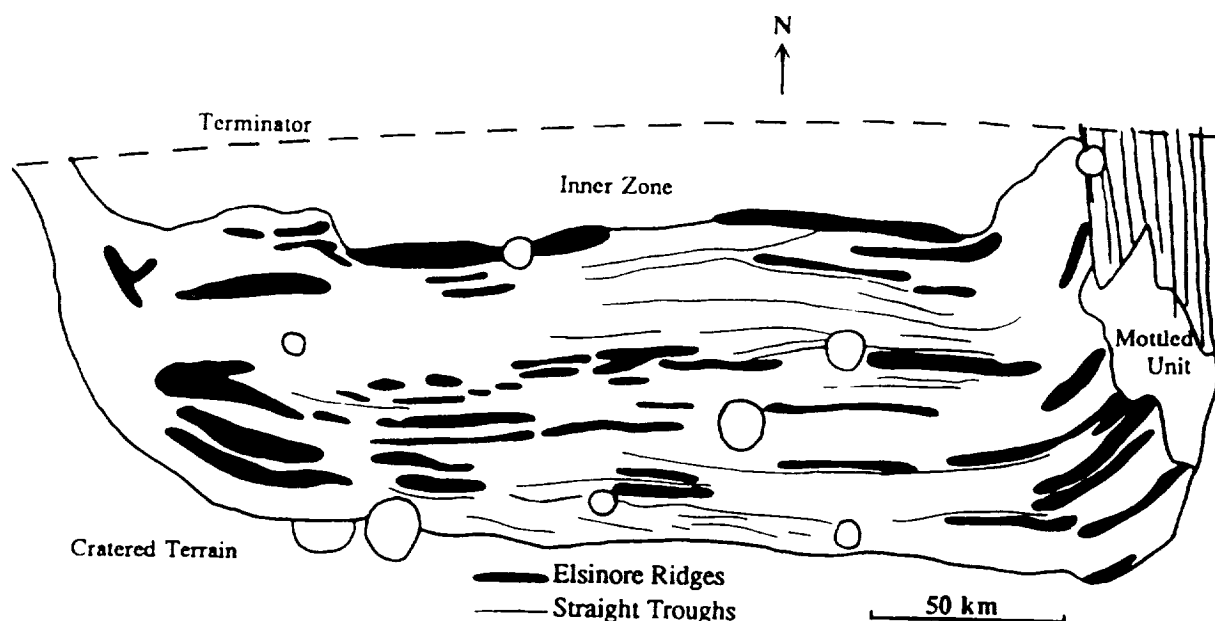


Figure 1. Sketch map of major ridges and troughs in the outer bands of Elsinore Corona, Miranda, drawn from a Lambertian equal-area projection centered about -30° latitude, 255° longitude.

## RHEOLOGIES OF PLANETARY ICES

W. B. Durham, UCLLNL, Livermore, CA 94550; and S. H. Kirby, USGS, Menlo Park, CA 94025;

As part of an ongoing experimental study of the mechanical behavior of ices under extraterrestrial conditions, we have been measuring the strength of various kinds of ices that are likely to be present on the surfaces and in the interiors of icy moons in the outer solar system. We report here recent progress on two phases of our work, mixtures of rock + water ice (which has application to the icy Galilean giants Ganymede and Callisto), and ices in the  $\text{NH}_3\text{-H}_2\text{O}$  system (which has application to the satellites of Saturn and beyond).

**Flow and Fracture of Ice/Rock Mixtures.** We have studied the effects of sized particulates of SiC, calcite, and quartz, in volume concentrations  $\phi$  from 0.001 to 0.56, of grain sizes 1 to 150  $\mu\text{m}$ , at temperatures from 77 to 223 K, at confining pressures to 100 MPa, and at strain rates from  $3.5 \times 10^{-4}$  to  $3.5 \times 10^{-6} \text{ s}^{-1}$ , in an ice matrix of grain size 0.8 to 1.5 mm. To summarize our findings, below  $\phi = 0.10$  none of the particulates has a measurable effect (resolution is about  $\pm 5\%$ ) on the steady-state strength of ice in the so-called ductile field, where plastic flow occurs. At  $\phi > 0.10$ , the ductile strength of ice increases with increasing particulate concentration. Coarse particulates also toughen ice, that is, they extend its range of ductility and make it less prone to catastrophic brittle failure.

Some of the more important results are shown in Figs. 1 and 2. In Fig. 1 we compare the stress vs strain behavior of pure ice, ice mixed with calcite ( $\phi = 0.20$ ), and ice mixed with quartz sand ( $\phi = 0.10$  and 0.56) at conditions of fixed temperature and strain rate. These results are typical for the temperature range 160 to 223 K. One sees subtle differences in the transient portion of the curves (where differential stress changes with shortening). In the steady-state portion, where the curves flatten out, the pure ice samples and SiC-doped samples (not shown in Fig. 1) converge to nearly the same strength. The  $\phi = 0.20$  calcite samples are about 10% stronger than the pure ice. For silicate particulates in the ductile field (Figs. 1 and 2), the strength for  $\phi = 0.10$  is barely distinguishable from that of pure ice; for  $\phi = 0.56$ , strength is a factor of 3 higher than for pure ice. The one  $\phi = 0.30$  sample tested was stronger than pure ice by a factor of less than 1.5. These strength contrasts are about one-half to one-third those predicted for Newtonian-viscous matrix material (1). Ice is non-Newtonian at the conditions of our experiments (strain rate depends on stress raised to the power  $n$ , where  $n = 4$  to 5), and the lower strength contrasts are to be expected.

The data are sparse in the brittle field. Two samples of  $\phi = 0.30$  (quartz) failed catastrophically at 77 K and a differential load of 189 and 152 MPa, respectively, vs approximately 170 MPa for pure ice. Four samples of  $\phi = 0.30$  and 0.56 at 77 K apparently had jacket leaks, but rather than failing at the 50-MPa level typical of pure ice in the unconfined condition, they failed at 62 to 119 MPa.

The presence of quartz particles (and perhaps SiC and calcite, although it was not investigated) toughens as well as strengthens ice. For example, although the  $\phi = 0.10$  ice/quartz mixture has about the same ductile strength as pure ice, the brittle-to-ductile transition occurs at much lower temperatures than for pure ice. Thus, at 143 K and a strain rate of  $3.5 \times 10^{-6}$ , where pure ice fails in a brittle

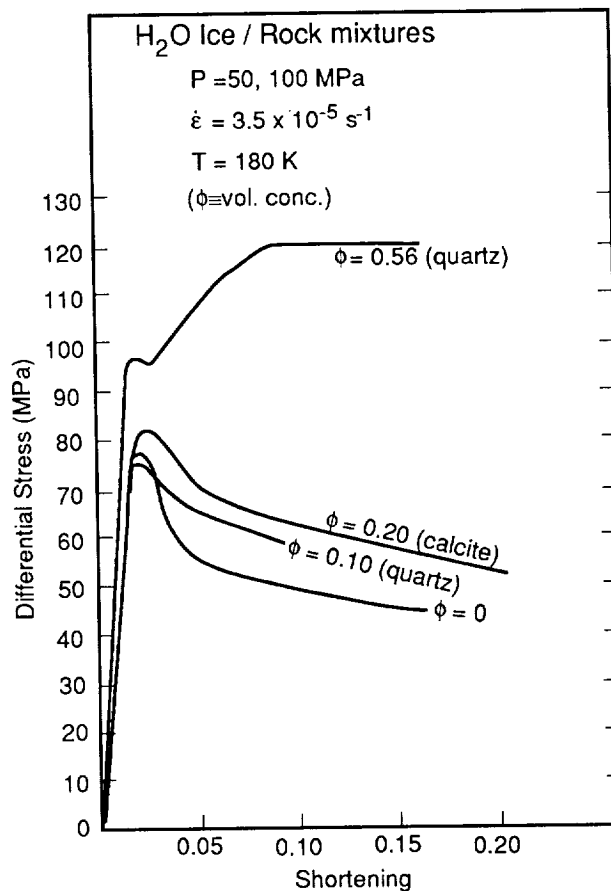


Figure 1. Experimental stress-strain curves for various ice/rock mixtures. Stresses have been corrected for cross-section changes during deformation. Shortening is defined as displacement divided by original sample length.

manner, the  $\phi = 0.10$  mix flows plastically at 141 MPa. Even at 77 K, the ice/rock samples showed signs of toughening. The higher-than-normal unconfined strengths cited above is one example. The failure that occurred at 77 K was also not as sudden as with pure ice, but was drawn out over a period of 1 or 2 s, or was preceded by behavior reminiscent of yielding. We suggest that the silicate particles toughen the ice by limiting the flaw (i.e., microcrack) size, either to the size of the particles or to the interparticle spacing.

No evidence for dispersion hardening (dislocation and grain boundary pinning) was observed using SiC and calcite particulates in ice samples, even for grain sizes near 1  $\mu\text{m}$ .

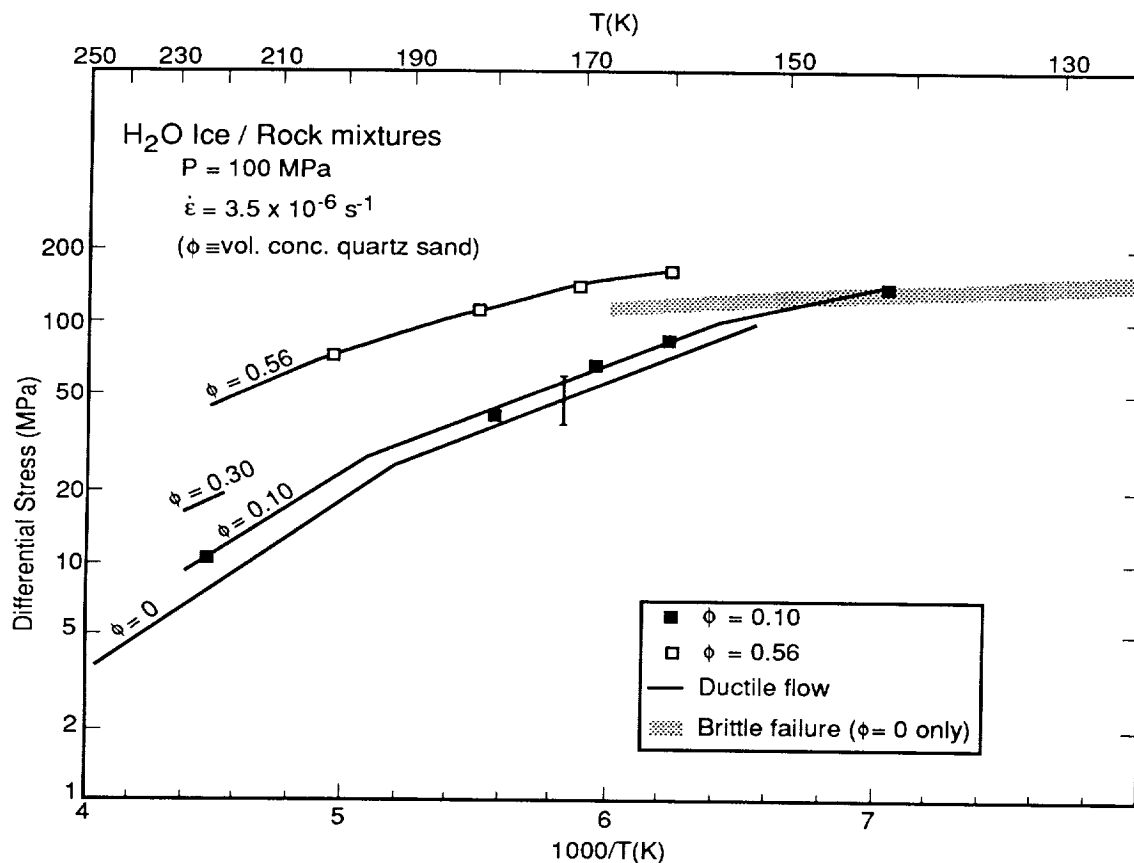


Figure 2. Steady-state flow strengths compared for volume concentrations of quartz sand from  $\phi = 0$  to 0.56. The  $\phi = 0$  line was taken from earlier work (2) and the error bar encompasses the scatter of experimental data. Solid and open squares represent results from the present study. The curve for  $\phi = 0.30$  is derived from measurements (not shown) at higher strain rates.

**Rheology of  $\text{NH}_3\text{-H}_2\text{O}$  Ices.** We have measured the mechanical strength of ammonia-water mixtures with bulk compositions of 1, 5, 15, and 29 wt%  $\text{NH}_3$  at temperatures between 130 and 179 K. The phase diagram for  $\text{NH}_3\text{-H}_2\text{O}$  predicts that these samples should all be mixtures of water ice plus ammonia dihydrate ( $\text{NH}_3\cdot 2\text{H}_2\text{O}$ ). X-ray diffraction analyses performed on 7 of our undeformed samples verified that our starting samples of 1, 5, and 15 wt%  $\text{NH}_3$  are almost entirely composed of the expected amounts of  $\text{H}_2\text{O}$  ice and dihydrate, with only minor quantities (<1%) of the metastable monohydrate phase.

Most of our latest results are shown in Fig. 3. The qualitative indication of the results is that the water and dihydrate phases do not interact physically or chemically in a way that affects rheology at these temperatures. Peritectic melting has a dramatic effect on strength at 15 and 29%  $\text{NH}_3$ , but not at 5%. The effect of increasing confining pressure up to 100 MPa appears to be only the familiar weakening effect that occurs in ice I (2).

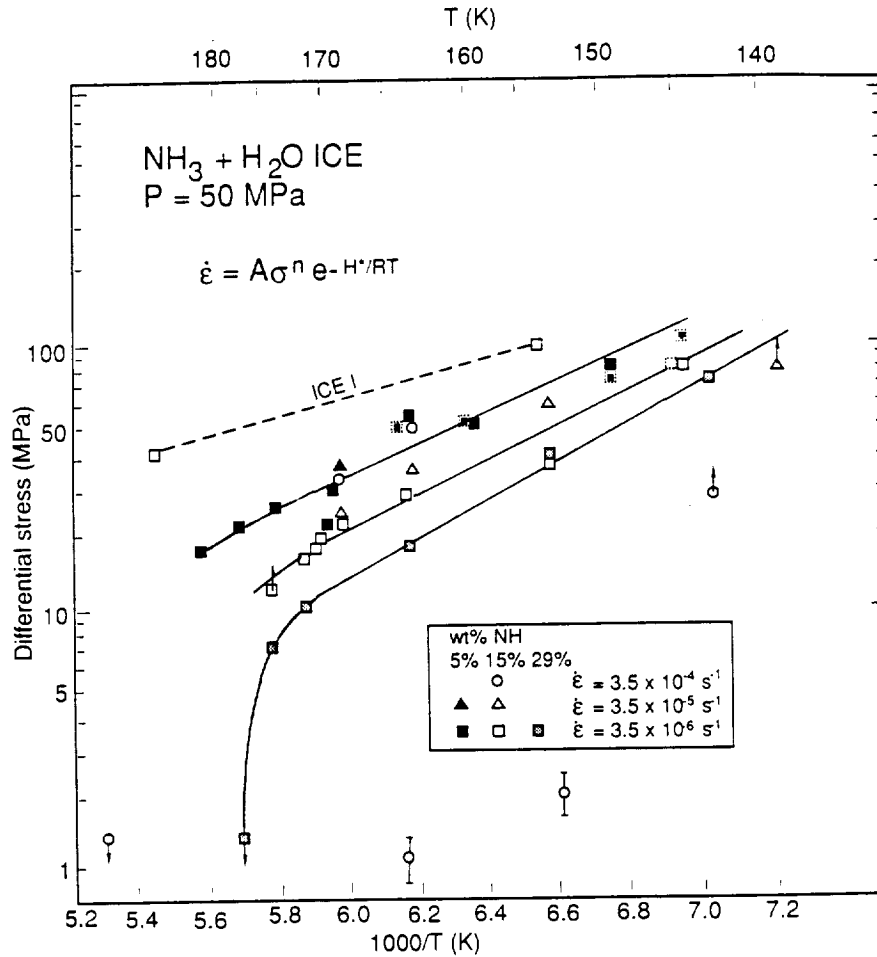


Figure 3. Experimental data on the flow and fracture of ices in the  $\text{NH}_3\text{-H}_2\text{O}$  system. Symbols have shapes and fillings to indicate strain rate ( $\dot{\epsilon}$ ) and  $\text{NH}_3$  content. The ghost figures represent data measured at  $P = 80$  to  $100$  MPa (vs.  $50$  MPa for most of the data) and indicate a neutral to slight weakening effect of increasing pressure. The flow law for ice I is taken from reference (2). Down- and up-pointing arrows indicate that data are upper and lower limits, respectively. Low-strength data along the bottom of the figure are from a  $15\%\text{-NH}_3$  sample that was inadvertently warmed to  $189$  K before deformation. X-ray analysis showed considerable development of monohydrate in the refrozen sample. The three solid curves are visual aids to the behavior at  $\dot{\epsilon} = 3.5 \times 10^{-6} \text{ s}^{-1}$  at the three different  $\text{NH}_3$  concentrations. Note that the total loss of strength that occurs at the peritectic temperature  $T = 176$  K for the  $29\%\text{-NH}_3$  sample is delayed to higher temperatures for the  $15\%$  sample, and not yet seen (to  $T = 180$  K) in the  $5\%$  sample. Not shown is one point measured on a  $29\%\text{-NH}_3$  sample at  $T = 130$  K and  $\dot{\epsilon} = 3.5 \times 10^{-6} \text{ s}^{-1}$ . That sample failed in brittle fashion at a differential stress of  $97$  MPa.

## References

- (1) Friedson, A. J. and D. J. Stevenson (1983) *Icarus*, **56**, 1-14.
- (2) Kirby, S. H., W. B. Durham, M. L. Beeman, H. C. Heard, and M. A. Daley (1987) *J. Physique*, **48**, supplement (VIIth Symposium on the Physics and Chemistry of Ice), 227-232.

Coupled Geophysical and Dynamical Processes on Icy Satellites  
Richard Greenberg, University of Arizona

1. Miranda

Miranda is the innermost and smallest of the major Uranian satellites. Before the Voyager encounter, Miranda was expected to be a cold, cratered snowball similar to Mimas, virtually devoid of endogenically derived surface features. The only known anomaly was Miranda's inclined orbit. However, the actual encounter revealed a unique and startling assemblage of geologic structures: a rolling, heavily cratered terrain, probably the oldest surface in the Uranian system; three enigmatic coronae, the youngest surfaces in the system, exhibiting variations on a basic concentric pattern; and a network of canyons, both bounding and cutting the other terrains. Understanding Miranda's unique and complex structure requires an interdisciplinary approach. Drawing on the observed geology, photometry and geophysical data, with a consortium of researchers we have examined various processes and properties that may have contributed to Miranda's evolution.

The global network of extensional graben indicates a planetary volume expansion of a few percent. The temperature rise necessary for such an expansion could not be the result of accretional or solar heating. Radiogenic heating would be sufficient if clathrates provided insulation. Tidal dissipation, which would be accompanied by orbital changes, could also provide significant amounts of heat. Flow features on the surface additionally require some admixture of a viscosity-lowering material. Sufficient quantities of such exotic materials are cosmochemically plausible and are not ruled out by spectroscopy.

Two distinct populations of impact craters are seen: young, fresh ones and old, worn ones. Their statistics and comparisons with other satellites suggest that the impactor source population evolved through time. Temporal demarcation between the two crater populations is most likely an impact in the area of Arden Corona which mantled the entire imaged portion of the moon with ejecta. The coronae themselves are unique to Miranda, certainly in scale and perhaps in morphology as well. Proposed methods of formation include relaxation of topographic highs, lithospheric stress driven by density anomalies in the asthenosphere, and diapirs, which either breach the surface or feed large scale volcanic flooding through pre-existing crack structure. The competing scenarios have specific requirements and implications, but current data are insufficient to choose between them, or even to determine whether all the coronae were formed the same way. Despite being the object of Voyager's closest examination, Miranda remains tantalizingly enigmatic. However, comparison with other icy moons of similar size helps define the possible variety of physical and chemical processes involved in satellite formation and evolution.



## 2. Tidal Heating of a Blocky Satellite (with G. Ojakangas)

If Miranda is composed of a weakly consolidated aggregation of large, discrete blocks, as suggested in some scenarios, cyclical tidal strains as well as strains due to chaotic rotation may be largely confined to regions near the boundaries of the constituent blocks. The total rate of tidal dissipation in such a body is roughly

$$dE/dt = GM^2(n/a)(r/a)^5 e^2 [(\eta/\rho g r)(s/\delta)/(1+C(\eta/\rho g r)^2(s/\delta)^2)]$$

(Ojakangas 1989, in preparation) where  $\eta$  is the viscosity of the material near the boundaries of the blocks (where the strain occurs),  $s$  and  $\delta$  are the characteristic linear dimension of the blocks and the characteristic separation between them, respectively,  $\rho$  is the satellite density, and  $C$  is a constant of order unity. For non-synchronous (e.g. chaotic) rotation, the rate is increased by removing the factor  $e^2$  from the equation.

The factor in square brackets balances the relative effects of viscous stresses and self-gravity. It is equivalent to  $3k_2/Q$  in the usual tidal dissipation equation. The equation above was derived assuming that the gaps between blocks are considerably narrower than the block size ( $s/\delta \gg 1$ ); within this range of validity, as gap width increases ( $s/\delta$  decreases), the equation approaches the expression for a homogeneous viscous body. The derivation also assumes that there is no dissipation within the blocks. Thus, for vanishingly small interstices ( $\delta = 0$ ), the equation gives zero dissipation. In fact in this limit the satellite is a monolith and dissipation within the solid material dominates.

If Miranda comprises blocks that came together by collisional accretion, they probably do not fit together very closely:  $s/\delta$  would probably be no larger than  $\sim 10^2$ . On the other hand, if Miranda has been cracked (e.g. by geophysical or impact effects) into large blocks that were originally seamlessly connected,  $s/\delta$  could be larger. For example, if the blocks are 10 - 100 km in size, separated by shear zones of 10 - 100 m in thickness,  $s/\delta$  could be as large as  $10^4$ .

The dissipation rate given above is a maximum for viscous stresses comparable to self-gravity:  $\eta \sim 10^{13}/(s/\delta)$  P. For example, if  $s/\delta \sim 100$  the maximum dissipation is achieved with a viscosity of  $10^{11}$  P. The equivalent value of  $k_2/Q$  would be  $\sim 1$ , a very dissipative body. Significant enhancement of dissipation over simple elastic dissipation would be possible for a wide range of values of  $s/\delta$  and viscosity. Viscosities of the required order at block boundaries are quite plausible for the materials possible in Miranda. Major enhancements in tidal heating rates are thus possible with blocky structure.

It should be noted that although dissipation is concentrated along block interfaces in this model, the heat produced cannot remain confined to the regions between blocks unless a heating event occurs on a timescale shorter than the thermal diffusion time across a distance  $\delta$ ,  $\Delta t \sim \delta^2/\kappa \sim (\delta/100 \text{ m})^2 50 \text{ yr}$  for thermal diffusivity  $\kappa \sim 0.1 \text{ cm}^2/\text{sec}$ . Thus,

if volcanism or other geophysical processes occurred as a result of heating along block boundaries, the temperature of most of the interior of the body must be raised to the temperature at which inter-block material is mobilized (unless thermal runaways at block boundaries can occur on extremely short timescales). These considerations argue against the speculation that non-uniformity of heat deposition played an important role.

While we have shown here that blocky structure may have greatly increased the tidal heating rate compared to the standard lossy-elastic model, it is important to emphasize that the total amount of available energy is still limited. The faster dissipation means that the eccentricity of Miranda's orbit and/or any non-synchronous rotation would tend to damp proportionately quickly, shutting off the tidal heating process.

### 3. Cycloidal Ridges on Europa (with M. C. Nolan)

The curved shape of island arcs on Earth is generally attributed to bending subducting crustal plates under the constraints of spherical geometry. Quantitatively, this explanation does not fit parameters measured on Earth, presumably due to geological complications. However, we find it fits the cycloidal ridges on Europa well. In our model, horizontal compressive stress is relieved with minimal energy expenditure by bending one part of the crust under the other, as thrust faulting if not as true subduction. Spherical geometry requires that bending occur along an arcuate path. If the joint continues along an arc more than a few tens of degrees, it changes direction significantly; so at intervals there must be discontinuities (cusps) to keep the joint oriented correctly. On the other hand, the minimum energy constraint tends to minimize the number of cusps, each of which requires local crushing to relieve stress. This determines the configuration of long chains of arcuate ridges on Europa. Our quantitative analysis shows that compressive distance has been  $\sim 0.5$  km per ridge if effective lithospheric thickness is  $\sim 10$  km. Surface contraction might have thus been a few km on a global scale.

## THE TECTONIC AND IGNEOUS EVOLUTION OF ENCELADUS

S. Pozio<sup>1</sup> and J.S. Kargel<sup>2</sup>; <sup>1</sup> Reparto di Planetologia, Viale dell'Università 11, 00185 Roma, Italy; <sup>2</sup> Lunar and Planetary Lab, University of Arizona, Tucson, AZ 85721.

Voyager 2 provided high-resolution images of the small, icy Saturnian satellite, Enceladus. These images show evidence of a complex history, during which the satellite was subjected to widespread tectonic activity and several episodes of partial re-surfacing. Squyres *et al.* described extensional tectonic features; they recognized only one ridge, and as it is bounded on either side by troughs, they ascribed to it an extensional origin as well (1). Smith *et al.*, on the other hand, observed both extensional and compressional tectonic features (2).

This work supports that of Smith *et al.*, as we also observe a highly complex tectonic style. Figure 1 is a tectonic map of Enceladus. This map is non-interpretive, as features are mapped only according to their topographic expression. Included are features of likely compressional origin (ridges), others of probable extensional nature (troughs, scarps, and crater chains), and features of uncertain character.

Near the sub-Saturn point is a system of troughs oriented perpendicular to and truncated by a west-dipping fault scarp which previously was interpreted as a strike-slip fault by Kargel (3). South of these troughs are several other sub-parallel lineaments, at least two of which also are troughs. This whole area is a lightly cratered plains unit exhibiting only extensional and possibly trans-tensional tectonic styles. North of this area, extending to the North Pole, the crater density is substantially higher, although again, compressional tectonics are absent. At high latitudes and near the terminator in the highest resolution images, many craters appear to be highly relaxed, as if this region at some time experienced a regionally elevated thermal gradient (4).

Centered on the trailing hemisphere is an area of 'ridged plains' bounded by a 750-km-long system of curvilinear ridges. We observed only two small craters on this entire area (109,000 km<sup>2</sup>); several more could be present under high solar incidence, but we are confident the crater density actually is extremely low, since many craters are visible in other areas under similar illumination and lower resolution; of course, this requires that the ridged plains are the youngest region observed on Enceladus. The marginal ridges characteristically are bounded by troughs. These ridges have either a compressional or an igneous constructional origin. Photometric profiles have indicated local relief of about 1.5 km (4); however, local relief as great as 4 km can be observed in limb profile (e.g. PICNO 1320S2). The whole system looks remarkably like the Himalayan Orogen or the complex series of island arcs in the western Pacific Ocean. We have considered two models for the possible origin of the curvilinear ridges: 1) folding; and, 2) plate flexure under volcanic line loads. Either case requires a mechanically layered lithosphere, with layer thicknesses on the order of 10-100 cm in case 1, or 100-1000 m in case 2. The inferred layering, in either case, suggests a volcanic origin for the lithosphere; therefore, the mechanical lithosphere of Enceladus also appears to be a chemically differentiated crust.

In the middle of the ridged plains, nearly symmetrically disposed relative to the marginal ridges, is a system of lineaments which truncate each other in a rectilinear pattern. Since this system is situated near the sub-solar point in the best images it is not possible, taking into account the lack of shadows, to say if many of them are ridges or troughs. However, at least one ridge in this region was observed in limb profile (PICNO 1505S2); and, it appears that at least one other feature here also is probably a ridge. The tectonic relationship of this rectilinear grid to the marginal curvilinear ridges, and to the ridged plains in general, is uncertain, but is likely to be significant.

North of the ridged plains, between 210 and 320° longitude, is a photometrically banded terrain, where diffuse-appearing bands may be the fronts of either en echelon overthrusts, or of thick (100's of m)

volcanic flows. This area has about the same crater density as the younger areas of cratered plains.

Other extensional features include two morphologically similar rifts. The most prominent one is located between 30-80° N. lat., 310-335° long. Crater densities indicate that the floor of this rift was resurfaced, but not very recently. Following or concurrent with resurfacing the floor of this rift was again extensionally disrupted. The other rift is centered near 25° N. lat, 180° long. and is bounded by two scarps. It is poorly resolved, but may also have been resurfaced.

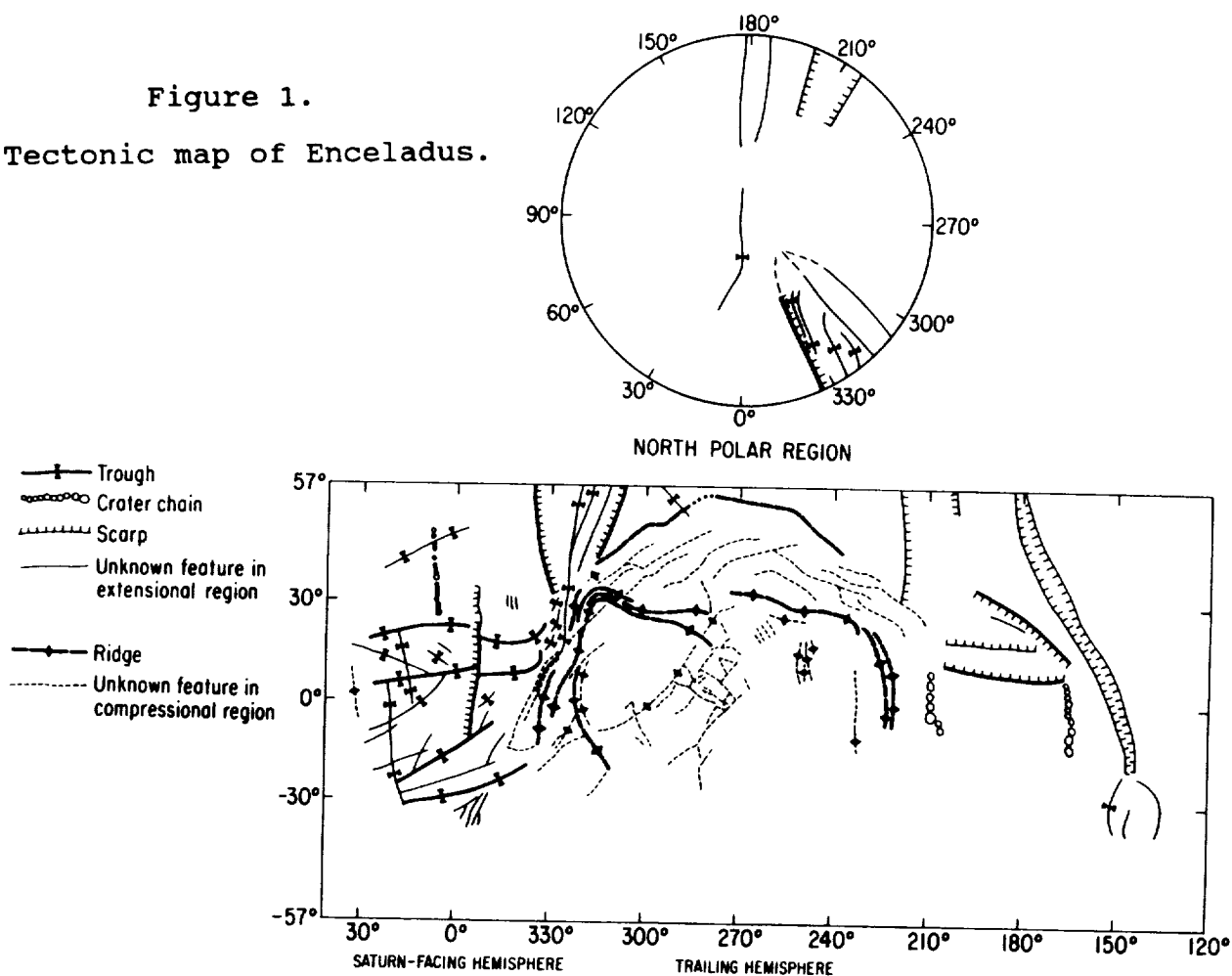
The global tectonic pattern is quite interesting. Extensional tectonics dominate the North Polar region, the Saturn-facing region, and the anti-Saturn region; apparently compressional tectonics dominate the region near the trailing point. It appears that the internal convective patterns in Enceladus either are governed by or control the orientation of the tidal/rotational axes of Enceladus.

We have constructed models of the thermal steady-state evolution of Enceladus and find that for reasonable circumstances radiogenic heating alone was sufficient to permit melting near the ammonia-water peritectic early in Enceladus' history; with the enhanced tidal deformation of a differentiated body, tidal heating then may have allowed Enceladus to remain magmatically and tectonically active until the present day.

#### REFERENCES

1. Squyres, S., *et al.*, 1983, *Icarus*, **53**, 319-331.
2. Smith, B., *et al.*, 1982, *Science*, **215**, 504-537.
3. Kargel, J.S., 1983, abstract, *Lun. Plan. Sci. XIV*, 363-364.
4. Passey, Q.R., 1983, *Icarus*, **53**, 105-120.

Figure 1.  
Tectonic map of Enceladus.



## ICY GREENHOUSE ON EUROPA

F.P. Fanale and J.R. Salvail. Planetary Geosciences Div., Univ. of Hawaii, Honolulu, HI 96822.

This work is an expansion of the "ice greenhouse" hypothesis of Matson and Brown (1988). All previous thermal models of volatile materials or materials containing volatiles have operated on the assumption that sublimation occurs only at the boundary of ice containing materials. However, for any porous material containing ices, it is clear that both sublimation and condensation can occur at any gas-solid interface within the medium. Just as the latent heat of sublimation can significantly affect the surface temperature of an icy body, sublimation and condensation throughout the interior of a porous icy body should be able to significantly change the temperatures throughout the volume. Convection can also affect the temperatures, although this effect is typically small compared to those caused by phase changes.

We have derived equations for an icy crust that include the effects of sublimation and condensation as well as convection throughout the volume. The insolation absorption term given by Matson and Brown has also been included. The icy crust was modeled as a porous medium in which tortuous capillaries extend in three dimensions. The pores of the ice contain water vapor, which when at equilibrium with the ice, are maintained at the equilibrium vapor pressure governed by the local temperature as given by the integrated Clausius-Clapeyron equation. A temperature variation with depth results in a predictable vapor pressure variation with depth. The resulting pressure gradient induces a flow which momentarily perturbs the gas pressure in the pores away from the equilibrium vapor pressure. When this occurs, ice is sublimed or vapor is condensed, depending on the direction of the pressure perturbation, at a rate such that the local equilibrium vapor pressure is reestablished. Separate differential equations have been derived for the cases of flow in the free molecular regime and in the continuum regime. Each equation satisfies the conservation of mass and conservation of energy principles at each point in the volume. Volume sublimation and condensation can also cause at least temporary changes in certain physical properties of an icy porous medium. Changes in density and porosity have been explicitly accounted for in the derivation of the equations, and equations to calculate density and porosity as a function of depth and time are also given. Thermal conductivity was considered as a free parameter for the purposes of this investigation. This was done for reasons of practicality, since temperature dependent expressions for the thermal conductivity of a porous medium are extremely complex and would have greatly increased the complexity of the equations and the computation time. However, we have examined a reasonable range of possible thermal conductivities.

Water ice is one of those materials which readily admits visual and UV radiation but cannot reradiate in the infrared from the subsurface. Therefore, radiation initially deposited below the surface can escape only by conduction. If the thermal conductivity is sufficiently low, the heat input will exceed the heat loss, and the temperatures and temperature gradient near the surface will increase until the heat loss due to conduction is equal

to the heat input from insolation. Matson and Brown have shown that insolation absorption by water ice can cause ice temperatures to be hundreds of degrees higher than was previously thought, depending on the thermal conductivity and the sunlight extinction coefficient of the ice.

Our model was applied to Europa, since there has been considerable speculation concerning the existence of liquid water below the icy crust, and also to compare our results with the earlier results of Matson and Brown. For a thermal conductivity of 100 ergs/cm-s-K and a sunlight extinction coefficient of 0.2/cm, we found that maximum temperatures were reduced by about 180K to a value near 260K. Temperatures near 440K were obtained for a model with sunlight extinction alone. When the thermal conductivity was increased to 1000 ergs/cm-s-K, the sunlight absorption effect was insignificant. When the extinction coefficient was increased to 0.1/cm, the sunlight absorption effect became significant, with the maximum temperature increasing by about 30K over that which would be expected without sunlight absorption below the surface. We concluded that the "ice greenhouse" effect is important for porous water ice having a low thermal conductivity and/or very translucent ice that allows significant sunlight penetration below the surface. However, this effect is greatly mitigated by volume sublimation, compared with previously published temperature estimates. If the ice is sufficiently translucent, temperatures close to the melting point of water ice can be achieved a few centimeters below the surface. A paper based on this work has been submitted to *Icarus*.

#### References:

- Matson, D.L. and R.H. Brown (1988). Solid state greenhouses and their implications for icy satellites. *Icarus*, in press.

LABORATORY REFLECTANCE SPECTRA OF IRRADIATED ICES:  
APPLICATIONS TO EUROPA

J.W. Boring  
University of Virginia

Much of the information we have about planets and their satellites is a result of observing the reflectance of sunlight from their surfaces. It is clear in many cases that the surfaces have become altered as a result of incident radiation, either photons or charged particles. A major need in being able to interpret the reflectance spectra from these objects in terms of the chemical species present and the topography of the surface region is laboratory data that details the changes in reflectance for a known irradiation of the surface. The purpose of the present investigation is the study of the effects of ion bombardment on the reflectance spectra of several ices, principally  $\text{H}_2\text{O}$ ,  $\text{SO}_2$ ,  $\text{NH}_3$  and mixtures of these. This will provide information about changes in the surfaces of the satellites and rings of several of the outer planets, but we focus our attention on the Jovian moon Europa that is bombarded by ions trapped in the magnetosphere of Jupiter.

The specific concern of these studies is the changes in the reflectance spectra of visible and UV light reflected from ices upon bombardment by keV ions. A major question in these measurements is whether any observed change is a result of implantation of the incident ion to incorporate it into new chemical species, or whether the important changes are a result of bond breaking and atomic rearrangement within the original ice. Since the latter is an important possibility it is important to study the effects as a function of ice temperature since this affects the mobility of species within the solid and their ability to recombine into new molecules. Another important matter in these studies is the topography of the surface of the ice, since the amount of surface area presented to the bombarding ions and the light to be reflected can easily affect the reflectance spectra.

In our first set of measurements we studied  $\text{H}_2\text{O}$  ice grown at 25K and at 120K. The 25K ice was very frosty looking with a lot of surface area and was probably amorphous. The 120K ice was smooth and clear and was most likely crystalline. For the 120K ice there was little evidence of changes in the reflectance spectra in the wavelength range 0.22-0.54  $\mu\text{m}$ , whether the bombardment by  $\text{SO}_2^+$  and  $\text{Ar}^+$  ions took place at 25K or at 120K. For the 25K ice bombarded at 25K we see two absorption features for  $\text{SO}_2^+$ ,  $\text{Ar}^+$  and  $\text{He}^+$  ions. The stronger feature extends from 0.32  $\mu\text{m}$  down to the lowest wavelength that we can study, namely 0.22  $\mu\text{m}$ . The weaker feature extends from 0.47  $\mu\text{m}$  down to 0.32  $\mu\text{m}$ . The main point here is that the rare gas ions give the same result as for  $\text{SO}_2^+$ , indicating that sulfur implantation and subsequent formation of SO bonds is not the principal cause of this UV absorption. The fact that this absorption feature is not seen at the higher temperature seems to indicate that it is caused by radicals and stable species formed from the  $\text{H}_2\text{O}$  molecules and that the

lower temperature is required to keep these products from recombining or escaping from the solid. The fact that ice grown at 120K and bombarded at 25K shows only weak evidence of this absorption feature is a puzzle, but may indicate that the larger surface area for the ice grown at 25K is a necessary condition for the strong absorption.

Our present studies in this program are aimed at investigating in greater detail the dependence of the results on temperature, both the growing temperature and that at which bombardment takes place. We will then study other ices, starting with  $\text{SO}_2$  and mixtures of  $\text{H}_2\text{O}$  and  $\text{SO}_2$ . We also intend to study the effect of putting thin layers of ice on top of a bombarded sample to simulate the redistribution of material, through sputtering, that occurs on a satellite such as Europa.



## Speculative Histories of the Uranian Satellite System

S. J. Peale, Physics, University of California at Santa Barbara

A long term occupancy of Ariel and Umbriel in a 2/1 orbital resonance could lead to sufficient tidal dissipation in Ariel to account for the observed series of resurfacing events. The dissipation in Umbriel is always negligibly small in this history, which is consistent with its primordial cratered surface. The eventual disruption of this resonance might have been effected by the growing perturbations by Titania. We consider several possible histories of the satellite system which are very sensitive on the assumed masses of the satellites within the errors of their determinations and on the  $Q$  of Uranus. The resonances which could have been encountered in these histories and constraints on the orbital eccentricities for certain capture are determined. If Miranda's mass were the upper extreme value, it, too, could have been locked in a long term 2/1 orbital resonance with Ariel forming a Laplace-like 3 body resonance including Umbriel. However, the tidal dissipation in Miranda is probably too small even in this history to have softened the interior, and much more violent events seem necessary to account for its exotic surface. Titania could have been a member only of rather high order orbital resonances with the inner satellites, so tidal heating during resonance occupancy cannot be invoked for its resurfacing.

## VACUUM WEATHERING: A NEWLY RECOGNIZED PLANETARY SURFACE PROCESS

Douglas B. Nash  
Jet Propulsion Laboratory, Pasadena, Ca 91101  
San Juan Institute, San Juan Capistrano, Ca 92675

A serendipitous discovery in the laboratory during studies of the effects of irradiation on sulfur has led to a new way of thinking about the effects of a vacuum environment on the surface properties of small solar-system bodies such as icy satellites and comets. The experiments were initially undertaken to study the surface properties of Jupiter's satellite Io, which was shown to exhibit active sulfur volcanism during the Voyager flybys. During the experiments it was discovered that the surface of freshly frozen sulfur is drastically modified by the effects of vacuum evaporation (Nash 1987; Nash and Moses 1988). These "vacuum weathering" effects are caused by differential sublimation of two different molecular phases that make up the solid material and that have very different sublimation rates. In the case of sulfur, which is composed of ring and chain molecules that by exsolution form a distinct grain intergrowth structure, the ring sulfur has a much higher sublimation rate than the chain sulfur. As a result, under continuous vacuum pumping the surface of sulfur gradually becomes depleted in ring sulfur, enriching the surface with a residual layer of chain (polymeric) sulfur. The chain sulfur forms a highly porous, extremely fine-grained fluffy material that reaches a thickness of about 1 mm at vacuum maturity.

This process produces major changes in the visible and ultraviolet reflectivity of the surface of sulfur: in the visible wavelengths the surface brightens and the color changes from an original yellow, tan, or brown (depending on the maximum temperature and thermal history of the sulfur during its pre-freeze molten state) to white -- the color it takes on when the weathering process has gone to a "vacuum mature" stage. The corresponding spectral reflectance changes are shown in Figure 1: the shoulder of the spectral absorption edge (that causes normal sulfur to appear yellow) shifts in wavelength from 0.52  $\mu\text{m}$  to 0.46  $\mu\text{m}$ ; at the same time the UV absorption trough shifts from near 0.45  $\mu\text{m}$  to 0.39  $\mu\text{m}$ , and the overall UV reflectivity near 0.35  $\mu\text{m}$  decreases from about 12% to 3% or less.

The rate of this vacuum weathering process is highly dependent on the temperature of the surface; this is due to the steep temperature-dependence of the vapor pressure curve of volatile substances such as sulfur. For temperatures around 300 K (typical of volcanic hot spots on Io's surface) the

sublimation rate is on the order of  $10^{14}$  sulfur atoms per square centimeter, which is equivalent to an erosion rate of about 1 mm per year. The sublimation rate increases by an order of magnitude with a temperature increase of about 20 degrees K.

At these rates the changes in appearance of sulfur on Io's surface will be large on time-scales of only tens to hundreds of hours. Since the corresponding spectral and textural changes that are possible in freshly emplaced sulfur lava deposits on Io are large, their detection by telescopic observation is possible and would signal that active volcanic resurfacing of Io may be occurring (Nash and Moses, 1988).

A thorough understanding of this newly recognized vacuum weathering process -- as summarized in Figure 2 for sulfur and Io's surface -- may have application to deciphering the observed properties of other condensed-volatile surfaces of planetary bodies. Examples are the Galilean satellites Europa and Ganymede, that exhibit contaminated water-ice rich surfaces (Clark et al 1983), Neptune's satellite Triton that may have a surface containing a solid mixture of methane and nitrogen (Lunine and Stevenson 1985), and comets that contain sulfur-laden ices (Moore et al 1988). Continued laboratory experimentation and theoretical modeling of the vacuum weathering process may lead to further insight into the nature and mode of origin of the surface properties of condensed solar system objects.

#### References

- Clark, R. N., F.P. Fanale, and A.P. Zent (1983). Frost grain size metamorphism: implications for remote sensing of planetary surfaces. ICARUS, vol. 56, pp 233-245.
- Lunine, J.E. and D.J. Stevenson (1985). Physical state of volatiles on the surface of Triton. NATURE, vol. 317, pp. 238-240.
- Moore, M.H., B. Donn, And R.L. Hudson (1988). Vaporization of Ices containing  $S_2$  -- implications for comets. ICARUS, vol. 74, pp. 399-412.
- Nash, D.B. (1987). Sulfur in Vacuum: sublimation effects on frozen melts, and applications to Io's surface and torus. ICARUS, vol. 72, pp. 1-34.
- Nash, D.B. and J.I. Moses (1988). Vacuum weathering of sulfur: temperature effects and applications to Io. GEOPHYS. RES. LTRS., (in press).

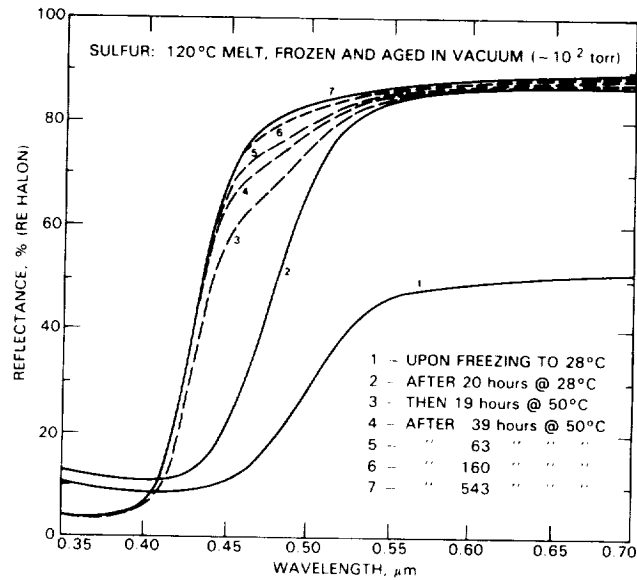


Figure 1. UV-visible reflectance spectra showing how the surface spectrum of solid sulfur varies progressively with time after freezing and during continuous vacuum pumping.

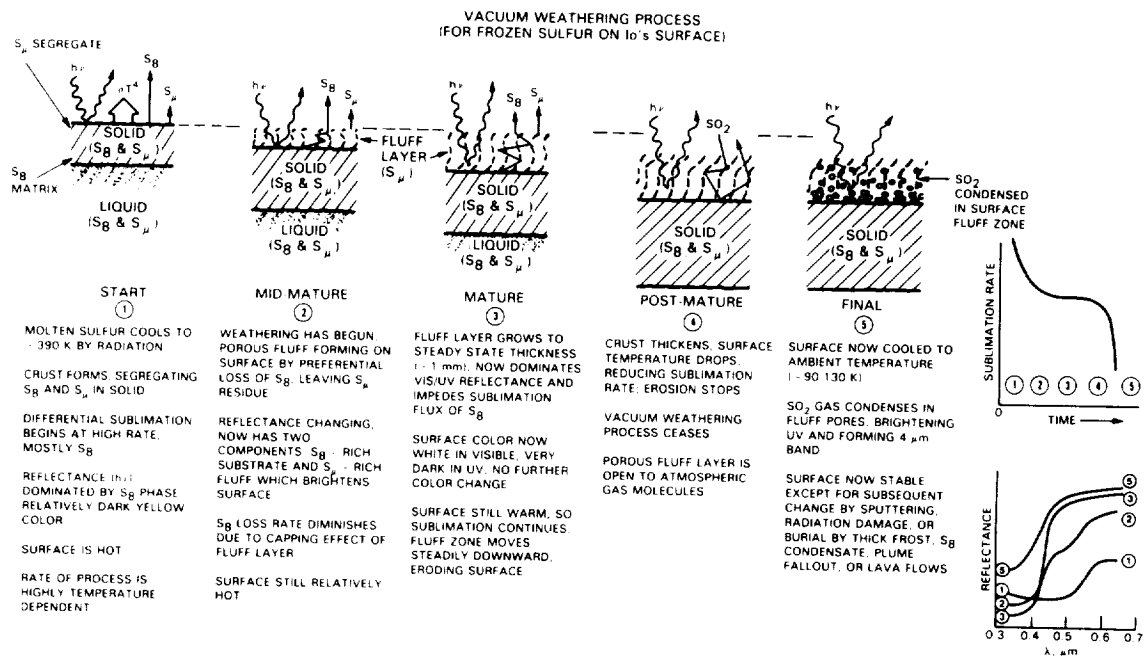


Figure 2. Schematic representation of the postulated vacuum weathering process on the surface of frozen sulfur on Io. Starting condition is on left; time progresses toward right from step 1 to step 5.

## Charged-Particle Induced Alterations of Surfaces in the Outer Solar System

R.E. Johnson  
University of Virginia

Solar system surfaces unprotected by an atmosphere can be modified by plasma bombardment. This knowledge can be used to establish the age of the surface layer. The list of possible irradiation effects is long and, indeed, the list is likely to increase as the data on Uranus, Halley, and Pluto are further analyzed, the Neptune data is received, and Galileo gets going. In this work we make accurate assessments of problems for which laboratory information on irradiation effects is available or can be successfully extrapolated. Until sample return missions are possible, the limitations of observations to the outer layers of solid objects requires careful evaluation of those surface modifications which can affect interpretations of remote sensing data. Sputtering and other irradiation effects have been used to account for many initially uncertain observations, and often these initial guesses have been wrong. This occurred because the scale of the effects were unknown. Our models for our laboratory data, therefore, provide important constraints and we have shown that plasma interactions are important for interpreting solar system observation in a number of cases.

Laboratory data on  $\text{Na}_2\text{S}$  and sulfur were analyzed in order to ascertain the likelihood of the sputter generation of the Na atmosphere at Io. It was concluded that an average surface atomic concentration of more than 1% of Na was required. Further, the Na in the atmosphere will predominantly occur in a molecular form (e.g.  $\text{NaS}$ ) so the recent observations of atomic Na in Io's atmosphere only give lower limits to atmospheric Na. Also we showed that Na must be ejected from a surface containing  $\text{Na}_2\text{S}_x$  with  $x \gg 1$ .

Plasma bombardment profiles of satellites were calculated by tracing plasma ions to the surface of a satellite Figure 1. At Dione we showed that the dominant sputter component bombarded nearly isotopically. This is at variance with the observations of Clark et al. that larger grain sizes on the trailing hemisphere were due to plasma erosion. At Europa the calculated plasma profile was shown to agree well with the relative UV absorption coefficient (Figure 1a) which we extracted from the Voyager data as corrected by Nelson et al. and McEwen. This confirms that plasma bombardment is responsible for a part of the UV absorption at Europa. These plasma profiles also made clear that pitch angle distribution is as important as gyroradius for determining whether the leading hemisphere is bombarded. These spatial maps (e.g. Figure 1b) can now be compared to satellite surface analysis.

Data on sulfur implanted into an ice matrix was analyzed and shows that  $\text{S}_2$ ,  $\text{S}_3$ , etc formed rapidly in ice. This data is being used to re-examine scenarios for plasma production of absorption features on the Galilean satellites. Finally, an assessment of the application of laboratory data to a regolith was made. Much smaller reductions in the effective yields were found than suggested by Hapke. The appropriate reductions are consistent with those made by us earlier. The four publications associated with this are in the list following.

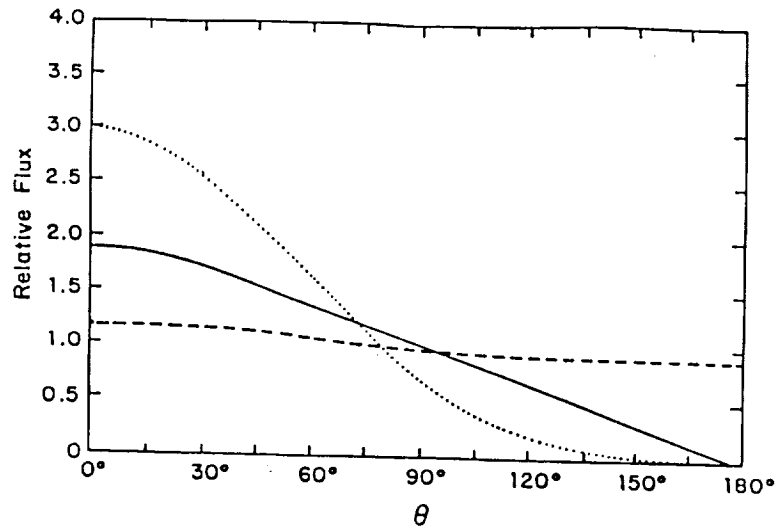
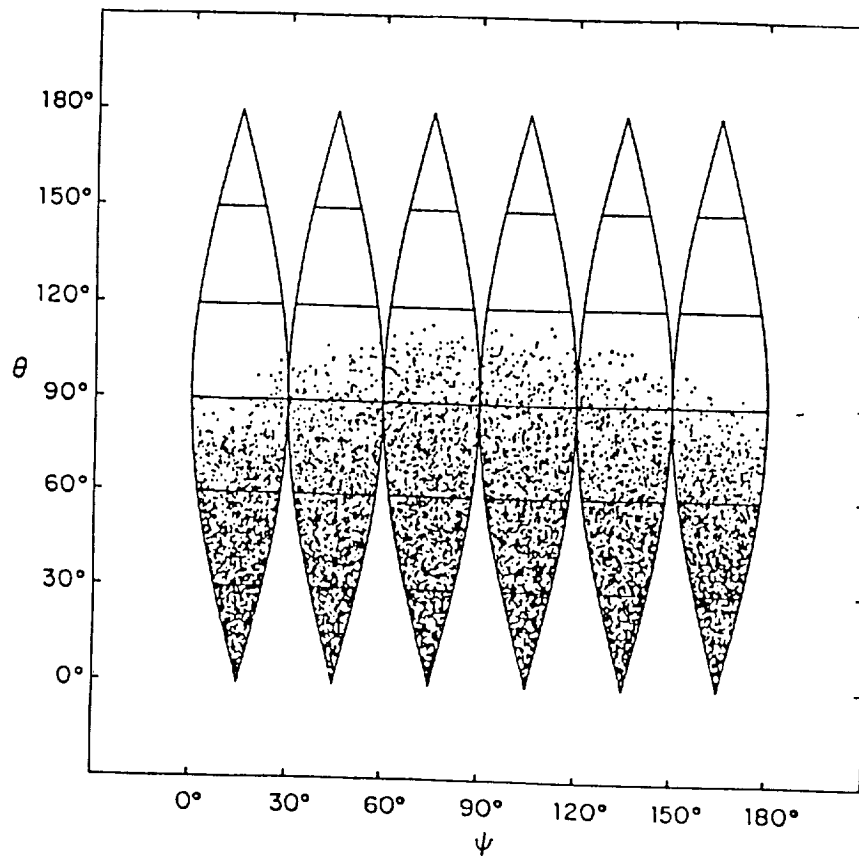


Figure 1(a) Because of the complication of gyromotion and pitch angle we traced plasma particles onto the surfaces of the satellites.  $\theta$  is longitude from the trailing hemisphere. Dotted line, cold plasma at Dione, solid hot plasma at Europa, dashed hot plasma at Dione. Clear leading trailing differences are seen. These results can now be applied (submitted to Icarus).



1(b) As in 1(a), view of northern hemisphere: cold plasma at Dione,  $\psi$  is the angle from the inner hemisphere to outer hemisphere (submitted to Icarus).

Some Papers

Ejection of Sodium from Sodium Sulfide by the Sputtering of the Surface of Io.  
Icarus 74 (1988)

Analysis of Voyager Images of Europa: Plasma Bombardment Profiles Icarus 75  
(1988)

Magnetospheric Ion Bombardment Profiles of the Icy Satellites: Europa and  
Dione 76 (1988)

Application of Laboratory Data to the Sputtering of a Regolith Icarus 77 1989

Neutral Cloud and Heavy Ion Inner Torus at Saturn Icarus 77 (1989)

COLOR CHANGES IN ELEMENTAL SULFUR FOLLOWING X-RAY EXPOSURE  
IMPLICATIONS FOR JUPITER'S SATELLITE IO

by

Robert M. Nelson and William D. Smythe  
Jet Propulsion Laboratory

Jupiter's satellite Io has been known for many years to have unusual surface reflection properties. Broadband filter photometric studies done nearly three decades ago (Harris, 1961) reported that Io's spectrum was strongly absorbing at blue and ultraviolet wavelengths (see also subsequent work by Johnson and McCord, 1970; Johnson, 1971). These data implied that a ultraviolet absorbing material comprised a significant fraction of Io's surface.

Reflection spectra of elemental sulfur taken in the laboratory are known to be strongly absorbing at blue and ultraviolet wavelengths (Sill, 1973) and thus a surface with elemental sulfur in widespread abundance was suggested in order to explain Io's spectral properties (Wamsteker, 1973; Kuiper, 1973). The presence of other materials such as certain ices (as might be found in Saturn ring material) or salts (as might be expected from evaporite deposits), in addition to elemental sulfur, was shown to improve the spectral agreement (Wamsteker, et al., 1973; Fanale, et al., 1974; Nash and Fanale, 1977).

Nelson and Hapke (1978) noted that elemental sulfur occurs in many allotropic forms other than cyclooctal S<sub>8</sub>, the most common allotrope. They suggested that mixtures of several sulfur allotropes might produce a better agreement between laboratory spectra and Io's spectral geometric albedo. These allotropes might also explain several features in Io's spectrum which cannot be explained by cyclooctal sulfur alone thereby minimizing the number of mineralogical species which must be invoked in order to explain the absorption features in Io's spectral geometric albedo. They noted that these allotropes can be produced on Io by an environment in which sulfur can be either vapor deposited, melted and then rapidly quenched (suggesting volcanic activity), or exposed to electromagnetic and particle radiation while at low temperature.

Following the 1978 Voyager spacecraft encounter with the jovian system there was much discussion of the role of sulfur as an agent of coloration of Io's surface, and in its connection with the newly discovered Ionian volcanic activity (Smith et al., 1979; Soderblom et al., 1980; Sagan, 1979; Gradie and Moses, 1982; Gradie and Veverka, 1984).

While most authors agree that sulfur is present as a significant chemical specie on Io's surface, the presence of free elemental sulfur in widespread abundance has been questioned. Young (1984), in calling attention to the misleading representation of Io's color in the data released by the Voyager imaging team (Smith et al., 1980) also challenged the suggestions by previous workers that the reflection spectrum of elemental sulfur, as modified by the Io environment, is consistent with Io's spectral geometric albedo. Young, in summarizing the chemistry literature, specifically states that, "A particular weakness of any attempt to explain the colors of the inner jovian satellites with unstable sulfur allotropes is their instability to both light and x-rays, which are produced in abundance in the jovian radiation belts. This is a basic property of all colored sulfur compounds (polysulfides as well as sulfur itself), because it is a basic property of the disulfide bond." Young's statement is inconsistent with the results of a very brief series of laboratory studies done in 1977 by Nelson and Hapke



which were consistent with their 1978 report that exposure to radiation is a means for producing colors (and presumably non-cyclooctal allotropes) in cyclooctal sulfur and possibly in other allotropes as well.

In an effort to clarify the confusion regarding the effect of x-rays on elemental sulfur we have measured the spectral reflectance of allotropic forms of elemental sulfur powders that have been produced by exposing the cyclooctal allotrope of sulfur to x-rays. When the sulfur is at temperatures near 77°K, the effect of the x-ray exposure on the reflection spectrum of the sulfur sample is to produce absorption features at 0.42 and 0.52 microns. These features are not present in cyclooctal sulfur at the same temperature that had not been exposed to x-rays. These features are stable at low temperatures, however they fade when the sample is warmed (see figures 1 and 2). This result is not consistent with the argument that x-rays in the jovian environment would destroy non-cyclooctal sulfur allotropes on Io's surface (Young, 1984). The spectral reflectance of the sulfur allotropes created by x-rays while at low temperature differs from the spectral reflectance of sulfur allotropes made by melting sulfur and subsequently quenching the melts. The reflection spectra of these types of allotropes have been reported by Gradie and Veverka (1984). The spectra reported from the heating and quenching studies do not exhibit either the band at 0.42 or the band at 0.52 microns.

We believe that the allotropic form of sulfur that we have produced from x-ray exposure is different from the allotropes that have been investigated by other efforts directed at understanding Io's spectral geometric albedo. This is primarily because we have shown that exposure of sulfur while at low temperature to x-rays can produce an absorption feature at 0.52 microns. This has not been observed in studies of sulfur allotropes involving heating and quenching and those involving exposure to ultraviolet light.

Allotropes of sulfur created by radiation exposure, if present on Io's surface, would explain much of Io's spectral geometric albedo in the ultraviolet to visible spectral range. The results of these experiments have been presented at meetings (Nelson et al 1987, 1988) and a manuscript has been submitted for publication.

#### REFERENCES

- Fanale, F. P., T. V. Johnson, D. L. Matson (1974). Io: A surface evaporite deposit? *Science*, 186, 922-924.
- Gradie, J. and J. Moses (1983). Spectral Reflectance of unquenched Sulfur. *Proc. Lun. Plan. Sci. Conf. XIV*, 255-256.
- Gradie, J and J. Veverka (1984). Photometric properties of powdered sulfur. *Icarus*, 58, 227-245.
- Harris, D. L. (1961). "Photometry and colorimetry of planets and satellites," in The Solar System vol III Planets and Satellite, (G. P. Kuiper and B. W. Middlehurst eds., University of Chicago Press, 272-342.
- Johnson, T. V. (1971). Galilean satellites: Narrowband photometry, 0.30-1.1 microns. *Icarus*, 14, 94-111.
- Johnson, T. V. and T. B. McCord (1971). Galilean satellites: The spectral reflectivity 0.30-1.1 micron. *Icarus*, 13, 37-42.
- Kuiper, G. P. (1973). Comments on the Galilean satellites. *Comm. Lunar Planet. Lab #187*, 10, 28-34.
- Nash, D. B. and F. P. Fanale (1977). Io's surface composition based on reflectance spectra of Sulfur/salt mixtures and proton irradiation

experiments. *Icarus*, 31, 40-80.

Nelson, R. M. and B. W. Hapke (1978). Spectral reflectivities of the Galilean satellites and Titan, 0.32-0.86 micrometers. *Icarus*, 36, 304-329.

Nelson, R. M., W. D. Smythe, B. W. Hapke, A. J. Cohen (1987). Color of Sulfur after x-irradiation at low temperature. *Bull. Am. Ast. Soc.*, 19, 855.

Nelson, R. M. and A. L. Lane (1987). "Planetary Satellites", Chapter 4 of the volume, *Exploring the Universe with the IUE Satellite*. (Y. Kondo, ed.) D. Reidel, Dordrecht, pp 67-99.

Sagan, C. (1979). Sulfur flows on Io. *Nature*, 280, 750-753.

Sill, G. T. (1973). Reflection spectra of some solids of planetary interest. *Comm. Lunar and Planetary Lab #184*, 10, 1-8.

Soderblom, L. A., T. V. Johnson, D. Morrison, G. E. Danielson, B. Smith, J. Veverka, A. Cook, C. Sagan, P. Kupferman, D. Pieri, J. Mosher, C. Avis, J. Gradie, T. Clancy, (1980). Spectrophotometry of Io: Preliminary Voyager I results. *Geophys. Res. Lett.*, 7, 963-966.

Smith, B. A., L. A. Soderblom, T. V. Johnson, A. P. Ingersoll, S. A. Collins, E. M. Shoemaker, G. E. Hunt, H. Masursky, M. H. Carr, M. E. Davies, A. F. Cook II, J. Boyce, G. E. Danielson, T. Owen, C. Sagan, R. F. Beebe, J. Veverka, R. G. Strom, J. F. McCauley, D. Morrison, G. A. Briggs, V. E. Suomi (1979). The Jupiter system through the eyes of voyager 1. *Science*, 204, 13-31.

Wamsteker, W. (1973). Narrowband photometry of the Galilean satellites. *Communications of the Lunar and Planetary Lab.*, #167, 9, 171-177.

Wamsteker, W., R. L. Kroes, and J. A. Fountain (1974). On the surface composition of Io. *Icarus*, 10, 1-7.

Young, A. T. (1984). No sulfur flows on Io. *Icarus*, 58, 197-276.

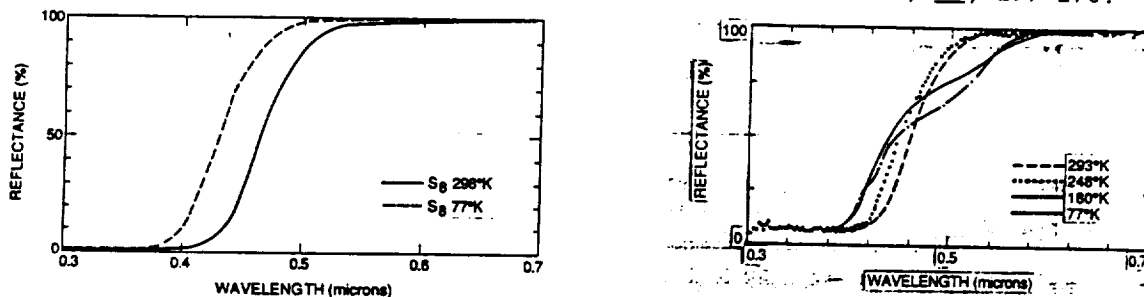


Figure 1. Bi-directional spectral reflectance relative to HALON of ultrapure elemental sulfur at 298°K and 77°K. The spectral change in the absorption edge is  $0.000145 \pm 0.000013$  microns/°K which is consistent with results by other workers (Gradie and Veverka, 1984).

Figure 2. Spectral reflectance of sulfur allotropes formed by exposing the cyclooctal sulfur allotrope (while at low temperature) to x-rays. The effect of the x-ray exposure is to form an allotrope (or an ensemble of allotropes) that has spectral absorption features at 0.42 and 0.52 microns.

The line and dot show the spectral reflectance of these allotropes at 77 °K. The solid line shows the effect of warming the sample to 180°K which is to cause the 0.42 micron feature to bleach and the 0.52 micron feature to fade. The dotted line shows the effect of increasing the temperature to 248°K. The dashed line shows the spectral reflectance when the temperature is increased to 293°K. The spectrum is identical to that of cyclooctal sulfur, which indicates that increasing the temperature cause the allotropes to revert to cyclooctal sulfur.

## Dynamics and Structure of Planetary Rings

Richard G. French

Department of Astronomy, Wellesley College

Department of Earth, Atmospheric, and Planetary Sciences, MIT

The P.I. has been investigating several independent studies pertaining primarily to the Uranian system. Recent results are summarized briefly below:

### **A) Uranus Ring Edge Wave Search**

We have completed a comprehensive search for edge waves that might be associated with the two small satellites, Cordelia and Ophelia, on either side of the  $\epsilon$  ring. If these waves could be detected, precise measurement of their pattern speeds could be used to determine the geometry of the ring system and the mean motions of the shepherd satellites quite precisely, as well as to provide further information about the shepherding mechanism. We have found no evidence of edge waves with amplitudes of a few hundred meters or larger. We conclude that either the expected high wavenumber patterns are very weak, or that they are significantly damped downstream of the perturbing satellites. If the latter is the case, it may still be possible to find evidence of edge waves by restricting the search to those occultation cuts that sampled ring longitudes in the near downstream vicinity of each shepherd satellite, before damping has become significant.

### **B) Recent Uranus Occultation Observations**

The stellar occultations by the Uranian rings of U34 on 26 February 1987 and of u1052 on 12 May 1988 have been analyzed using standard methods, and the event times for the individual ring profiles have been incorporated in the latest in-house ring orbit model. The atmospheric occultation profiles of the U34 event have been reduced to determine the temperature structure of the upper atmosphere at the sub-occultation points.

### **C) Width-Radius Relation of the Narrow Uranian Rings**

We have undertaken a comprehensive search for width-longitude and width-radius relations of all of the Uranian rings by simultaneously solving for low wavenumber ( $m=0$  through  $m=6$ ) width variations with ring longitude. We have found that the  $\delta$  ring does follow a linear width-radius relation, and that its wavenumber and pattern speed match the  $m=2$  normal mode of the ring itself. In contrast, none of the other narrow rings ( $\epsilon$ ,  $\gamma$ ) show any hint of a linear width-radius relation, or of the presence of any low wavenumber modes in their width variations.

### **D) Oblateness of Uranus**

Previous studies of Uranus' oblateness from stellar occultation data have been limited by small data sets and by significant uncertainties in the occultation geometry. Recent spacecraft and occultation data and groundbased observations have been incorporated into a new ring orbit model that has provided much improved positional accuracy, and new data have become available for inclusion in the oblateness solution. We have used these results to determine the figure of Uranus at approximately the  $1 \mu\text{bar}$  level. A least-squares fit to the limb profile yielded an equatorial radius of  $R_e = 26071 \pm 3 \text{ km}$  and an oblateness of  $\epsilon = (1 - R_p/R_e)$  of  $0.0197 \pm 0.0010$ . The inferred rotation period is  $17.7 \pm 0.6 \text{ hr}$  for the latitude range  $(-30^\circ < \theta < 30^\circ)$  sampled by the observations.

## Planetary Ring Studies

Jeffrey N. Cuzzi (Ames Research Center), Richard H. Durisen (Indiana University), and Mark R. Showalter (Stanford)

**Meteoroid bombardment and ballistic transport in ring systems:** Several years ago, we noted that the longitude distribution of the rate of the most energetic impacts on the rings which results from the combination of ring orbital and planetary orbital aberration effects shows an intriguing similarity to the longitudinal distribution of "spoke" creation frequency (Grün et al 1984), providing support for spoke creation hypotheses that rely initially on meteoroid impact (Goertz and Morfill 1983). This year, we finalized our results and submitted our bombardment formalism (Cuzzi and Durisen 1989) to *Icarus*. As shown in figure 1, the preponderance of spokes *seen* in and around the dawn quadrant implies a preponderance of *creation* at longitudes around midnight, in quite good agreement with impact rates which are thresholded or weighted by impact velocity in reasonable ways. We believe this effect may explain the orbit longitude asymmetry of spokes; clearly, other (electromagnetic) dependencies remain unexplained.

Our bombardment formalism (Cuzzi and Durisen 1989) also allows us to quantify for the first time the net deposition rate of angular momentum in the ring system for "Oort cloud" projectiles, including *both* the orbital asymmetry effect (noted qualitatively by Ip 1984) *and* the mass loading effect (noted qualitatively by Lissauer 1984). The results are shown in figure 2. The timescales we obtain are extremely short. For instance, for the meteoroid flux of Ip (1984) and Grün et al (1985), the entire C ring of Saturn and the  $\alpha$  and  $\beta$  rings of Uranus fall into their parent planet in something like  $10^8$  years. Thus, the drift due to mass loading dominates all other mechanisms for radial evolution of optically thin planetary rings of centimeter-to-meter sized particles, given the mass fluxes we have adopted.

**Model evolutions of ring structure due to ballistic transport:** Going beyond our first numerical evolutions of ring structure under ballistic transport and viscosity (Durisen et al 1989), we have begun modeling the behavior of a realistic ring boundary where regions of low and moderate optical depth adjoin each other. Prior, more simplified calculations (by us) indicated that initially smooth inner edges may be "sharpened" by this process. Our evolutions now include realistic angular and velocity distributions of the ejecta produced by bombardment (Cuzzi and Durisen 1989). Our new calculations show the effects to be more complex, but interesting structure is produced reminiscent of that observed near Saturn's A and B ring inner edges. Once again, viscosity is seen to play an important role.

**A and B ring structure and particle properties:** The currently accepted (but uncertain) level of meteoroid bombardment, if it consists of primordial, Carbon-rich material such as Halley dust, could easily darken the ring particles to much lower albedos than Dones (Thesis, 1987) and Doyle (Thesis, 1987) have found, even if the particles started out as pure water ice. Using a radiative transfer "deep atmosphere" model of the ring particle regoliths, Doyle et al (1989) estimate an upper limit of some  $10^8$  years on the "exposure age" of the ring particles. This paper also obtains important new results on the size distribution and surface properties of the macroscopic particles and the "dust" in spoke regions. In other work on the A and B rings, we have studied the fine structure of the inner edges of these rings (Cuzzi et al. 1988) and have begun to study the regional variation of the spatial scale of the irregular structure using maximum entropy techniques.

**Faint features in the rings of Saturn and Uranus:** We have interpreted all of the available E Ring data based on a three-dimensional ring model, which was designed to be

consistent with Earthbased observations by Baum and Kreidl. This single model made it possible to intercompare observations made from a broad variety of viewing geometries. We have found that the ring is composed almost exclusively of micron-sized particles with a peak normal optical depth of  $1 \times 10^{-5}$ . Less than  $\sim 25\%$  of the ring's backscattering intensity can be accounted for by larger bodies, despite the fact that such bodies would be emphasized in this viewing geometry. Further, we find that the particle size distribution is rather narrowly peaked; no broad, power-law distribution is compatible with the available observations. These results are consistent with the prior conclusions of Pang and collaborators.

Only two Voyager images captured the G Ring, and we have now examined both in great detail. A third places a significant upper limit on the G Ring's intensity in backscatter. Based on our determination of the smear, we can state with confidence that the ring is clearly several thousand kilometers wide, with boundaries at radial limits of 166,000 and 174,000 km, with a density peak near 168,000 km. Although we are unable to severely constrain its particle size distribution, the ring has an optical depth roughly comparable to that of Ring E (Showalter and Cuzzi 1988).

#### Bibliography for FY 1989

Cuzzi, J. N., and R. H. Durisen (1989); Bombardment of planetary rings by meteoroids: General formulation and effects of Oort cloud projectiles; submitted to *Icarus*.

Cuzzi, J. N., M. E. Ockert, and L. Dones (1988) Photometric and Occultation studies of the inner edges of Saturn's A and B rings; *B. A. A. S.* 20, 854

Dones, L., and J. N. Cuzzi (1988) Interparticle Shadowing in Saturn's Rings, *B.A.A.S.* 20, 640 (1988) (AAS, Austin, 1988)

Dones, L., M.R. Showalter, and J. N. Cuzzi (1988). Interparticle shadowing in planetary rings. *BAAS* 20, 858 (DPS, Austin, 1988).

Doyle, L.R., Dones, H., and Cuzzi, J.N., 1988, Photometric Constraints On the Age of Saturn's Rings, A.S.P. 100th Meeting, Victoria, Canada, June 29 - July 3, (P.A.S.P., in press)

Doyle, L. R., L. Dones, and J. N. Cuzzi (1989) Radiative transfer modeling of Saturn's outer B ring; *Icarus*, in press

Durisen, R. H., N. L. Cramer, B. W. Murphy, J. N. Cuzzi, T. L. Mullikin, and S. E. Cederbloom (1989) Ballistic Transport in planetary ring systems due to particle erosion mechanisms. I: Theory, numerical methods, and illustrative examples; *Icarus*, in press

Flynn, B.C., and J. N. Cuzzi (1989); Structure in the Cassini Division of Saturn; *Icarus*, in press

Showalter, M.R., and J.N. Cuzzi (1988). Morphology and particle properties of Saturn's faint outer rings. *BAAS* 20, 855 (DPS, Austin, 1988).

#### Additional references

Goertz, C., and G. Morfill (1983) A model for the formation of spokes in Saturn's ring, *Icarus*, 53, 219-229

Grün, E., G. W. Garneau, R. J. Terrile, T. V. Johnson, and G. E. Morfill (1984) Kinematics of Saturn's spokes; *Adv. Sp. Res.*, 4, 143-148

Ip, W.-H. (1984) Ring torque of Saturn from interplanetary meteoroid impact; *Icarus*, 60, 547 - 552

Lissauer, J. J. (1984) Ballistic Transport in Saturn's rings: an analytic theory; *Icarus*, 57, 63-71

Figure 1: The longitudinal distribution of the most energetic impacts of "Oort cloud" type projectiles in Saturn's rings, obtained by counting only those impacts occurring at velocities larger than  $30 \text{ km sec}^{-1}$ , and weighting the impact rate by different powers of impact velocity (curves). The triangles represent the observed distribution of spoke creation rate, as obtained by shifting the histograms of integrated spoke activity Grün et al (1984) by one-half of a spoke lifetime. The agreement is intriguing, to say the least (figure from Cuzzi and Durisen 1989).

Figure 2: Radial (inward) drift of ring material as a function of normal optical depth, for a particle size distribution typical of Saturn's rings ( $\sigma/\tau \sim 100 \text{ g cm}^{-2}$ ), including calculated gravitational focussing. Long dashed curve: mass loading for the interplanetary flux of Ip (1984) and Grün et al. (1985); Solid curve: radial drift due to mass loading alone; short dashed curve: radial drift due to longitudinal asymmetry in angular momentum deposition (figure from Cuzzi and Durisen 1989).

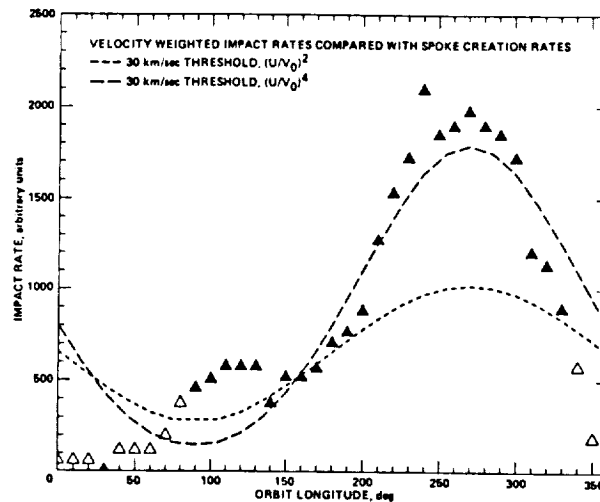


FIG. 1

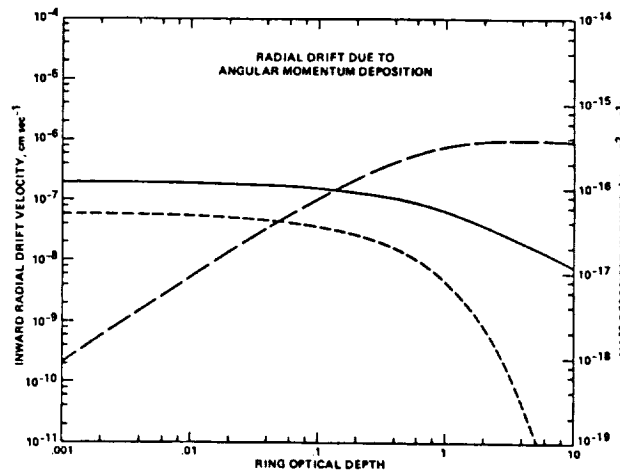


FIG. 2

## Numerical Simulations of Narrow Planetary Rings

R. A. Kolvoord and J. A. Burns (Cornell University)

Narrow rings are much more ubiquitous than was thought only a decade ago. These narrow structures show a startling variety of time varying features, such as the kinks, clumps and braids of Saturn's F ring and the incomplete ring arcs of Neptune. In our continuing attempt to understand this odd collection of effects, we have numerically modelled a system consisting of 2400 independent particles, comprising three concentric narrow rings, gravitationally interacting with two nearby moonlets. Both the satellites and the ring particles are allowed to be on eccentric, and/or inclined, but noncolliding orbits. The self-gravity of the ring particles is also ignored. We use the planetary equations of Lagrange to solve for the relevant perturbations (cf. Showalter and Burns *Icarus* **52**, 526-544 and Kolvoord *BAAS* **18**, 671).

Interpreting the results of the three dimensional calculations poses a much more difficult challenge than our earlier planar work. It is necessary to both choose an appropriate viewing geometry and simultaneously remember that the resulting structures change depending upon the vantage point, i.e. as the particles orbit the planet, their radial positions depend upon the exact position of their pericenters. Consequently, a group of particles that appear clumped at one longitude do not appear to be so associated on the other side of the planet. The presence of clumps and wave-like features with wavelength,  $\lambda = 3\pi\Delta a$ , as shown by Showalter and Burns, appears to carry over to the three dimensional calculations. Our results continue to show azimuthal and temporal variability akin to that seen in Saturn's F ring. They are also strongly dependent on the relative positions of the moonlets and the initial configuration of the system. Animation techniques are also helpful in this milieu, but the choice of reference geometry is somewhat arbitrary. As we continue our work on the Voyager images of the F ring, we hope to cast our graphical results in a geometry that allows direct comparison of our model with actual images.

## Orbital Evolution of Circumplanetary Dust by Resonant Charge Variations

J. A. Burns (Cornell U.) and L. E. Schaffer (Queen Mary College, London)

Jupiter, Saturn, and Uranus are encircled by broad tenuous rings composed of orbiting dust grains roughly  $1 \mu\text{m}$  in radius. Such grains develop electric charges  $q$  that are determined by the grain's velocity  $\mathbf{v}$  through magnetospheric ions and electrons; this plasma corotates with the planet (spin rate  $\Omega$ ) and its magnetic field  $\mathbf{B}$ .  $q$  will vary systematically with the orbit period because  $\mathbf{v}$  and/or the plasma conditions change periodically as the grain on its elliptical path moves closer to - and then further from - the planet. Electromagnetic perturbations  $(q/m)(\mathbf{E} + \mathbf{v}/c \times \mathbf{B})$  - where  $m$  is the grain's mass,  $c$  is the speed of light, and  $\mathbf{E}$  is the corotational electric field - on circumplanetary dust are significant, and have a resonant character, since the periodicity of  $q$  matches the orbital period  $2\pi/n$ . As in other celestial mechanics problems, orbital evolution is expected, except that this resonance occurs everywhere rather than at discrete orbital radii.

We follow the resultant orbital evolution numerically and analytically. Our numerical code integrates the equations of motion and simultaneously tracks the varying charge state of the grain  $q(t)$ . We find large excursions in semimajor axis  $a$  and eccentricity  $e$ . Our analytic solution comes from computing systematic changes in the grain's orbital energy  $E$  and angular momentum  $\mathbf{L}$  over a Kepler orbit, and then relating these variations to  $\dot{a}$ ,  $\dot{e}$ . We calculate  $q(t)$  by linearizing the charging equation or by measuring from our numerical solutions. If we consider a homogeneous plasma then  $\dot{a}$ , which depends on the charge history, is found to be

$$\frac{\dot{a}}{a} = \frac{\Omega B_0 (R/a)^3}{nmc(1-e^2)} e Q_1 \sin \theta_1,$$

where  $q$  as a function of true anomaly  $\theta$  is  $\sum_k Q_k \cos k(\theta - \theta_k)$  and  $\theta_k$  are phase lags due to the grain's finite charging time. The  $Q_k$  and  $\theta_k$  depend on  $a$  and  $e$  as well as the plasma density, composition and temperature.  $B_0$  is the strength of the axisymmetric, dipolar component of the magnetic field at the planet's surface (radius  $R$ ).

In many cases of interest the initial orbital evolution is more rapid than by any other process. Orbits however stabilize after evolving to some given  $a_f$  and  $e_f$ ;  $e_f$  is either zero or relatively large ( $\sim .25$ ), depending on  $\dot{a}_0$ ,  $\dot{e}_0$ . We show that for the planar problem, this is understandable in terms of the Jacobi integral  $E - \Omega \cdot \mathbf{L} = \text{constant}$ .



## Uranian Dust Ring: Have We Learned Anything From Models of Other Ethereal Rings?

J. A. Burns (Cornell U.), J. N. Cuzzi (NASA-Ames), and L. E. Schaffer (Queen Mary College, London)

The highest phase angle image ( $172.5^\circ$ ) of the Uranian rings shows an expanse of dust punctuated by a series of ringlets, among which the classically known rings are unexceptional members. We compare the fractional areas of dust and parent bodies in the classical rings to upper bounds of similar quantities for the dust ringlets; the small percentage of dust (2% for all classical rings) is in sharp contrast to the situation for the F ring and Encke ringlet, but not in disagreement with the main Saturnian rings (2%). Grains may be liberated off moonlets that jostle one another during collisions and by impacts of micrometeoroids onto unseen moonlets as well as onto the large bodies in the classical rings. In either case, dust concentrations may be low in and near optically thick regions because of the likelihood of immediate reabsorption, but relatively high in rarified regions where re-collision times are longer. Reabsorption of dust onto embedded moonlets may provide an effective sink for material, and thus create gaps or edges in the ringlets. There are a number of quite narrowly confined features with sharp radial gradients in density. The abruptness of these edges argues against any overall orbital evolution by plasma/neutral drag or diffusion driven by Kepler shear. We assess the possibility of confining tenuous ringlets by shepherds and resonances with more distant satellites. Orbital evolution by plasma drag is not likely to be effective because any thermal plasma tied to highly distorted magnetic field lines will be depleted through absorption onto the classical (optically thick) rings. However, drag due to neutral exospheric particles which are on ballistic trajectories originating in the atmosphere imposes firm lifetimes on crisp structures. Grain charges will be proportional to the temperature  $T$  of the ambient plasma; both  $T$  and density  $n$  will be determined by the ability of the plasma to diffuse through the rings from exterior sources. Charges on grains would tend to smear out narrow features because of radial excursions induced by Lorentz forces. This is especially true of the  $\epsilon$  ring which lies near the inner  $m = 2$  Lorentz resonance; grains generated there may only escape by leapfrogging the band.



CHAPTER 3

COMETS AND ASTEROIDS

PRECEDING PAGE BLANK NOT FILMED

PAGE 98 INTENTIONALLY BLANK

Page 99 IS ENTIRELY BLANK

## Rotation of Halley's Comet

S. J. Peale and Jack Lissauer, Physics, University of California at Santa Barbara

The two distinct periodicities of 2.2 days and 7.4 days inferred from the coma structure and light curves of Halley's comet together with the irregular shape of its nucleus suggest that the nucleus is not in a state of principal axis rotation. We model this situation using numerical simulations supported by analytic calculations. It is easy to numerically generate light curves from modulated jets of material which exhibit both periodicities if we choose initial conditions for a representative nucleus such that the shorter period is the rotation period and the longer period is that of precession of the spin vector in the body frame of reference. The dominant spectral power in such curves most often corresponds to the 7.4 day period unless the amplitude of precession is very small. Although curves similar to those observed over short time intervals are obtained for precession about either of the axes with extreme moments of inertia, the observed marked seasonal changes in the light curve are only produced for precession about the axis of maximum moment of inertia. The generation and stability of a wobble-type rotation state is investigated by numerically solving Euler's equations for the reaction torque from a jet of ejected material. A nonprincipal axis rotation is easy to excite from an initial rotation about the axis of maximum moment of inertia (minimum energy) only if the nucleus is nearly axisymmetric. Except for almost perfect axial symmetry, excitation of a precession about the axis of minimum moment of inertia is always frustrated by an initial precession about the axis of maximum moment of inertia. In the more probable case of significant triaxiality, even a precession of the spin about the axis of maximum moment of inertia is difficult to excite from an initial minimum energy state, and it can change only slowly from the jet-induced torques. However, this slow change could suffice to generate a substantial amplitude wobble from the cumulative effects of many apparitions. The damping time for the wobble is  $O(10^6 \text{ to } 10^8)$  years, which rules out a primordial origin of a wobble but allows a gradual excitation. Significant changes in the spin angular momentum can occur in a single apparition, but the stability of the amplitude of precession about the axis of maximum moment of inertia means that a rotation state which is relatively stable over many apparitions is not unreasonable. The improbability of exciting a spin precession about the axis of minimum moment of inertia, the relative instability of this state to the jet-induced torques and the smaller probability of observing significant seasonal changes in the light curve in this state all favor the model in which Halley's nucleus precesses about the axis of maximum moment of inertia.

PRECEDING PAGE BLANK NOT FILMED

## On the Mass Density of Halley's Comet

S. J. Peale, Physics, University of California at Santa Barbara

The four day increase in the orbital period of Halley's comet for each apparition which is not accounted for by gravitational perturbations has long been attributed to the reaction of the nucleus to the jets of gas and dust coming from the surface (Marsden *et al.*, 1973). Estimates of the mass flux from the surface and the ejection velocities obtained during the 1986 apparition lead to estimates of the reaction force and thereby of the mass and density of the nucleus, (Rickman, 1987; Sagdeev *et al.*, 1988), where the nucleus volume is known from spacecraft images (Keller *et al.*, 1987). In the present calculation of the density, the rate of mass ejection at the time of the spacecraft flybys is used as a basis for estimating the mass flux at other parts of the orbit from the light curve of Green and Morris (1987). The light scattered from ejected material is assumed to be proportional to the total mass of such material within the telescope aperture at any instant. The latter is connected to the mass flux through a weighted integral of the flux over a specified time interval. A reaction force from a jet of material is averaged over a rotation period, and the resultant is assumed to lie in the plane of the orbit at a small angle  $\alpha$  from the Sun-comet line. The density  $\rho$  of the nucleus is obtained as a function of the time interval over which the flux is assumed to contribute to the instantaneously visible material, the variation of that interval with heliocentric distance, where this variation is constrained by the energy available to evaporate water ice, the estimate of the reaction force at the time of spacecraft flyby and the heliocentric visual magnitude at the time of flyby. If the reaction force is entirely radial, a nominal value of the density of about  $2 \text{ gm/cm}^3$  is obtained. But the uncertainties in the assumptions and observations yield  $0.7 \lesssim \rho \lesssim 5 \text{ gm/cm}^3$ . This result is compared with the  $0.2 \text{ gm/cm}^3$  obtained by Rickman (1987) and  $0.2 \lesssim \rho \lesssim 1.5 \text{ gm/cm}^3$  obtained by Sagdeev *et al.* (1988). It is noteworthy that the larger mass ejection rate after perihelion passage compared with that before leads to reasonable densities even if the reaction force is entirely radial, and a tangential component of the force may not be necessary for the non gravitational perturbation of the orbital period. But Halley's density is otherwise not sufficiently constrained to be very informative.

## SOLID STATE PROBLEMS IN THE SOLAR SYSTEM

R. Smoluchowski, University of Texas, Astronomy Department

1. Cometary nuclei. The observed behavior of a comet is dominated by the heat transport in the nucleus which can be understood in terms of the large scale structure, such as shape and inhomogeneity, and the thermal properties of the fine structure, porous, icy materials that compose the nucleus. Results focus on the role of the small scale structure, such as pore shape and size, in the evaluation of effective thermal conductivities for comet material. Three dimensional finite element models have been developed to calculate the effective thermal conductivity of crystalline and amorphous water ice as a function of: porosity pore shape, pore size, pore vapor composition, pore orientation with respect to heat flow, pore size distribution, pore packing geometry, and grain-grain interface size. The modeling has included heat transport due to solid and vapor conduction, viscous and Knudsen flow, and radiation across the pore space. As well as serving as the input for calculations of the large scale heat transport, the fine scale results offer insight into the influence of pores on the transport of heat in comet material. Arguments, based on laboratory measurements of condensation products and the mechanics and evolution of porous icy materials, agree with larger estimates for comet density. In particular, calculations indicate that the thermal stress within a comet near perihelion would exceed the fracture strength of a highly porous, low density comet matrix material. The fact that relatively few comets are observed to fracture catastrophically lends support to the hypothesis favoring a higher density comet material such as that recently proposed by S. Peale. Given this evidence in support of a higher density, lower porosity material, the calculations focus on determining the effective thermal conductivity of a higher density, lower porosity icy comet matrix.

The thermal conductivity of non-porous water ice is a strong function of temperature. Calculations of the effective thermal conductivity of water ice include the contribution of the pore space to the conductivity of the material. At low temperatures, the pore space impedes the flow of heat in the material, thus lowering the effective conductivity. At temperatures above  $\sim 200$  K, water vapor in the pore space can greatly enhance the effective thermal conductivity. For example, in non-porous water ice at 80 K and 24 K, the thermal conductivities are  $7.1 \text{ Wm}^{-2}\text{K}^{-1}$  and  $2.4 \text{ Wm}^{-2}\text{K}^{-1}$ . At 25% porosity, with spherical  $1\text{mm}$  pores, the corresponding thermal conductivities are  $4.7 \text{ Wm}^{-2}\text{K}^{-1}$  and  $3.6 \text{ Wm}^{-2}\text{K}^{-1}$ , not including the contribution from the radiative heat transport. At low temperatures, the thermal conductivity is decreased by 33% due to the influence of the virtually empty pore space. The empty pores space is ineffective at conducting heat through the material. However, at high temperatures, the pore space vapor causes the effective thermal conductivity to increase by 53% again apart from radiative heat flow. In another part of this study, the influence of pores shapes on the effective thermal conductivity was investigated. As an example of the potentially great influence of pore shape, for a 25% porous water ice material with ellipsoidal, cigar shaped  $1\text{mm}$  pores, the effective thermal conductivities were calculated to be  $5.2 \text{ Wm}^{-2}\text{K}^{-1}$  and  $4.4 \text{ Wm}^{-2}\text{K}^{-1}$  at 80 K and 240 K. Similarly, for a thin, pancake shaped pore of the same volume, the effective thermal conductivities were  $1.7 \text{ Wm}^{-2}\text{K}^{-1}$  and  $3.5 \text{ Wm}^{-2}\text{K}^{-1}$  at the corresponding temperatures. The material possessing the long, cigar shaped pores is extremely effective at transporting heat at the high temperatures. The thermal conductivity is increased by 21% over that of the material containing spherical pores. This is in contrast to the conductivity of the material containing spherical pores. This is in contrast to the conductivity of the material containing the pancake shaped pores in which the conductivity was only 2% above the value for the material possessing the spherical pores. Due to their orientation with respect to the flow of heat, the flat pancake shaped pores do not act as efficient channels for heat flow as do the long, cigar shaped pores. Similar

comparisons can be made for low temperatures, in which we see that the pancake shaped pores cause a greater reduction in the effective thermal conductivity than do the cigar shaped pores, a 63% reduction versus a 9% reduction. The pancake shaped pores greatly impede the flow of heat through the material. These are just two examples out of the many cases that have been calculated in this study. As stated above, the effect of porosity, pore shape, pores size, pore orientation, pore size distribution, pore vapor composition, solid ice composition, grain/pore packing, grain-grain interface relative dimension and transport mechanism are included in this research.

2. Interstellar diffuse absorption lines. We have been successful in accounting for the order of magnitude of the width of the interstellar diffuse absorption lines produced by atoms entrapped in thin graphitic shells  $C_{60}$  in terms of the change of the volume available to the excited electron. Also, the existence of a number of pairs of absorption lines can be understood if free vibrations of the thin shells are taken into account. A study has been made of the possible mechanisms and sites in space where the carbon shells  $C_{60}$  could be formed. The most efficient sites appear to be the SNI supernovae. It is hoped that it will be possible to explain the intensity and the total number of the interstellar diffuse absorption lines in terms of known atomic spectra.



## Asteroid and Comet Flux in the Neighborhood of the Earth

Eugene M. Shoemaker, Carolyn S. Shoemaker, and Ruth F. Wolfe  
U.S. Geological Survey, Flagstaff, Arizona 86001

Significant advances in our knowledge and understanding of the flux of large solid objects in the neighborhood of Earth have occurred since the last Snowbird Conference. We present here our best estimates of the collision rates with Earth of asteroids and comets and the corresponding production of impact craters.

Approximately 80 Earth-crossing asteroids have been discovered through May 1988. The rate of discovery increased to 8 per year in 1986 and 1987, more than double the previous 10-year average. As shown by this high rate, the discovery of Earth crossers is far from complete. Among 42 new Earth-crossing asteroids found in the last decade, two-thirds were discovered from observations at Palomar Observatory and 15 were discovered or independently detected in dedicated surveys with the Palomar 46-cm Schmidt. On the basis of these latter observations and 6 discoveries made in a prior survey using the 46-cm Schmidt [1], we estimate that the population of Earth crossers brighter than absolute V magnitude (H) of 17.7 is about 1100. The estimated populations of each orbital type, based on the proportions of known objects brighter than mag 17.7, is as follows (numbers enclosed in parentheses indicate assumed values):

	Number Discovered	Percent Discovered	Estimated Population
Atens	4	(5)	$80 \pm 50$
Apollos	36	5.1	$700 \pm 300$
Earth-crossing Amors	<u>15</u>	<u>(5)</u>	<u><math>300 \pm 150</math></u>
Total Earth crossers	55	5	$1080 \pm 500$

Probabilities of collision with Earth have been calculated for about two-thirds of the known Earth-crossing asteroids by the method of Shoemaker et al. [2]; the mean of the calculated collision probabilities is  $0.49 \times 10^{-8} \text{ yr}^{-1}$ . When multiplied by the estimated population of Earth crossers, this yields an estimated present rate of collision of  $(5.2 \pm 2.5) \times 10^6 \text{ yr}^{-1}$  to H-17.7. This estimate is about 65% higher than that reported in [2], owing chiefly to the discovery in the last 10 years of several asteroids with unusually high probabilities of collision. When improved data on the proportion of S- and C-type asteroids, the distribution of impact speeds, and the theoretical distribution of zenith angles of impact are taken into account, we estimate from the above collision rate that the production of asteroid impact craters larger than 10 km in diameter is  $(1.6 \times/ - 2) \times 10^{14} \text{ km}^2 \text{ yr}^{-1}$ , somewhat lower than that given in [2] and [3].

Present evidence indicates that the discovery of Earth-crossing asteroids is essentially complete at H=13, close to the magnitude of the brightest known objects. Because the completeness of discovery declines for fainter objects, the magnitude-frequency distribution of the population can only be inferred from indirect evidence. For Earth crossers fainter than mag 15, the slope of the magnitude-frequency distribution is assumed to be similar to that of main belt asteroids (cumulative frequency approximately proportional to  $e^{0.9H}$ ). If so, the frequency evidently drops precipitously for objects brighter than mag 15 (cumulative frequency roughly proportional to  $e^{2H}$ ). In this model, the collision rate of Earth crossers to  $H \leq 15$  (roughly equivalent to S-type asteroids with diameters greater than 3 km) is about  $3 \times 10^7 \text{ yr}^{-1}$ ; the collision rate to  $H \leq 13$  (asteroids roughly 8 km in diameter and larger) is about  $5 \times 10^9 \text{ yr}^{-1}$ .

Spectrophotometric data obtained chiefly in the last decade show that the large majority of observed Earth crossers are similar to asteroids found in the inner part of the main belt. The combination of asteroid-asteroid collisions in the main belt, resonant perturbations of the orbits of collision fragments, and further perturbation of asteroid fragments by encounters with Mars appears adequate to replace losses of Earth-crossing asteroids due to collisions

with planets as well as ejection from the solar system. The population of Earth crossers to  $H=17.7$  probably has remained steady within about  $\pm 5\%$  through most of the last 3 billion years. However, surges of about 25% above the mean level in the population, which were due to breakup of main belt asteroids on the order of 100 km in diameter, probably occurred at average intervals of about half a billion years [4]. Durations of these surges above half maximum are estimated to be about  $3 \times 10^7$  years. The number of Earth crossers brighter than mag 13 may have increased by an order of magnitude at the peak of these

surges. In addition to these stochastic fluctuations of the population, periodic modulation of the near-Earth asteroid flux has occurred at a frequency of  $10^5 \text{ yr}^{-1}$  as a result of secular variation of the eccentricity of the Earth's orbit. The amplitude of this modulation is estimated to be about  $\pm 10\%$  from the mean flux.

The number of discovered Earth-crossing comets is more than 4 times greater than the number of known Earth-crossing asteroids, but reliable data on the sizes of comet nuclei are sparse. Photographic observations of comets, obtained when they were relatively far from the Sun, and the record of comet discoveries have been used to estimate the magnitude-frequency distribution and flux of the nuclei [5]. The near-Earth flux is found to be dominated by long period comets. After correction for contamination of the observations by unresolved coma, the estimated present rate of collision with the Earth of comet nuclei brighter than absolute B magnitude 18 is about  $10^{-7} \text{ yr}^{-1}$ .

Several lines of evidence suggest that the albedos of comet nuclei generally are very low; this inference has been confirmed from spacecraft images of the nucleus in the case of P/Halley [6]. Adopting a geometric albedo of 0.03 in the B band [5], we calculate the diameter of comet nuclei to be 2.5 km at absolute B magnitude 18 and 10 km at mag 15. At the rms speed of  $57.7 \text{ km sec}^{-1}$ , found for long period comets, and a modal zenith angle of impact of  $45^\circ$ , comet nuclei of B magnitude 18 are estimated to produce craters 40 to 50 km in diameter, if their densities are in the range of 0.5 to  $1.2 \text{ gm cm}^{-3}$ . Craters of this size are comparable with those produced by S-type asteroids of absolute V magnitude 14.2 to 14.8 (diameters of 3.3 to 4.5 km) impacting at the rms speed of  $17.5 \text{ km sec}^{-1}$  found for Earth-crossing asteroids.

At the present comet flux, the estimated rate of collision with Earth of comet nuclei  $\geq 10 \text{ km}$  diameter is  $10^{-8} \text{ yr}^{-1}$ , and the corresponding mean rate at which these objects pass the Earth at a distance of  $4.67 \times 10^6 \text{ km}$  (0.0312 AU), the miss distance of comet IRAS-Araki-Alcock (1983 VIII), is about once per 200 years. The geometric mean diameter of the elongate nucleus of IRAS-Araki-Alcock, determined from radar and infrared observations, is 9.3 km [7]. We conclude that the close approach of this large comet, during the  $\sim 20$ -year period in which the radar observations of its nucleus could have been made, either was a stroke of luck (probability  $\sim 0.1$ ) or our estimate of the present flux of comets about 10 km in diameter is conservative.

The flux of comets almost certainly has been highly variable over late geologic time, owing to the random perturbation of the Oort comet cloud by stars in the solar neighborhood. Monte Carlo studies [8] suggest that surges in the near-Earth flux from 3 to more than 30 times the mean background occurred at typical intervals of a few tens of millions of years. The majority of comet impacts probably occurred during these surges or comet showers. Even the background flux probably has varied by factors of about 2 over time intervals of  $10^7$  years, and it is not known from direct observations of comets whether the present flux lies close to the mean background or whether it might represent a shower or possibly a comet "drought."

The record of terrestrial impact craters and impact glass suggests that a mild comet shower may have occurred at  $\sim 35 \text{ Ma}$ , and a weak shower may have peaked at  $\sim 1 \text{ Ma}$  [9]. On the basis of bounds on the total crater production set by the Copernican crater record of the Moon [10], we suggest that the present comet flux is about twice the mean background for the last billion years; comet impacts probably account for no more than half the Phanerozoic impact craters larger than 20 km in diameter. During the late Phanerozoic, the mean rate of

collision with the Earth of 10-km-diameter and larger objects capable of producing craters larger than ~150 km in diameter may have been about  $1 \text{ to } 2 \times 10^8 \text{ yr}^{-1}$ . Production of these giant craters probably was dominated by comet impact.

Our best estimate of the production of terrestrial impact craters over the last 100 million years is as follows:

	Crater Diameters						
	$\geq 10 \text{ km}$	$\geq 20 \text{ km}$	$\geq 30 \text{ km}$	$\geq 50 \text{ km}$	$\geq 60 \text{ km}$	$\geq 100 \text{ km}$	$\geq 150 \text{ km}$
Asteroid impacts	820	180	73	10	4.5	0.3	0
Comet impacts	(270)	60	24	8	5.3	1.7	1
Total crater production	(1090)	240	97	18	10	2	1

The uncertainty to be attached to each of the above figures is at least a factor of 2. Production by comet impact of craters smaller than 20 km in diameter may have been suppressed by atmospheric breakup of comet nuclei [11]. To obtain the approximate number of craters expected to have formed on the continents, the

figures given above should be divided by 3. The estimated total cratering rate to 20-km crater diameter is  $(4.7 \times \pm 2) \times 10^{15} \text{ km}^2 \text{ yr}^{-1}$ , which is very close to the rate of  $(5.4 \pm 2.7) \times 10^{15} \text{ km}^2 \text{ yr}^{-1}$  estimated by Grieve [12] from the geologic record of impact for the last 120 million years. On the other hand, the corresponding number of craters larger than 30 km in diameter expected to have been produced on the Moon from the beginning of the Eratosthenian period (the last 3.3 billion years) is about twice the number of Copernican and Eratosthenian craters mapped by Wilhelms [10]. We repeat the observation [2,12] that the mean cratering rate may have increased in late geologic time. An increase by as much as a factor of 2 could be most readily explained by an increase in the mean comet flux, but only if more than half the production of craters  $\geq 20 \text{ km}$  diameter during the last 100 million years is due to impact of comets (including extinct comets, which would be recognized at the telescope as asteroids).

## References

- [1] Helin, E.F. and Shoemaker, E.M. 1979, *Icarus*, v. 40, pp. 321-328.
- [2] Shoemaker, E.M.; Williams, J.G.; Helin, E.F.; and Wolfe, R.F. 1979, in Gehreis, T., ed., *Asteroids*, Univ. Arizona Press, pp. 253-282.
- [3] Shoemaker, E.M. 1983, *Ann. Rev. of Earth and Planet. Sci.*, v. 11, pp. 461-499.
- [4] Shoemaker, E.M. 1984, in Holland, H.D. and Trendall, A.F., eds., *Patterns of Change in Earth Evolution*, Dahlem Konferenzen, Springer-Verlag, pp. 15-40.
- [5] Shoemaker, E.M. and Wolfe, R.F. 1982, in Morrison, D., ed., *The Satellites of Jupiter*, Univ. of Arizona Press, pp. 277-339.
- [6] Sagdeev, R.Z., et al. 1986, *Nature*, v. 321, pp. 262-266; Keller, H.U., et al. 1986, *Nature*, v. 321, pp. 320-326.
- [7] Sekanina, Z. 1988, *Astron. Jour.*, v. 95, pp. 1876-1894.
- [8] Heisler, J.; Tremaine, S.; and Alcock, C. 1987, *Icarus*, v. 70, pp. 264-288.
- [9] Shoemaker, E.M. and Wolfe, R.F. 1986, in Smoluchowski, R.; Bahcall, J.N.; and Matthews, M.; eds., *The Galaxy and the Solar System*, Univ. Arizona Press, pp. 338-386.
- [10] Wilhelms, D.E. 1987, U.S. Geol. Survey Prof. Paper 1348, 302 pp.
- [11] Melosh, H.J. 1981, in Shultz, P.H. and Merrill, R.B., eds., *Proc. Lunar and Planet. Sci.*, 12A, pp. 29-35.
- [12] Grieve, R.A.F. 1984, *Proc. Lunar and Planet. Sci. Conf., Jour. Geophys. Res.*, v. 89, pp. B403-B408.

## TEMPORAL AND SPATIAL DISTRIBUTION OF METEOROID IMPACTS DETECTED BY THE LUNAR SEISMIC NETWORK — A SUMMARY REPORT

Jürgen Oberst and Yosio Nakamura, Department of Geological Sciences and Institute for Geophysics; The University of Texas; Austin, Texas 78713; USA.

The meteoroid impacts detected by the lunar seismic station network from 1969 to 1977 are examined in terms of a) the distribution of impact locations and energies, b) the diurnal variation of impact rate, and c) temporal clustering. Small meteoroids (mass < 1 kg) show strong clustering. Several known cometary showers are identified; the Perseids, Leonids, and Aquarids being the most prominent. Since the majority of these objects appears to approach from orbits of high inclination, their sources are suggested to be mostly long-period comets. Large meteoroids (mass > 1 kg), in contrast, predominantly travel in orbits of low inclination. Short-period comets and near-Earth asteroids are suggested sources. The average impact flux on the lunar surface based on the 10 largest impacts detected is estimated to be  $\log_{10} N = -0.99 \log_{10} E + 11.4$  for the energy range of  $2 \times 10^{11}$  J to  $2 \times 10^{12}$  J, where N is the cumulative number of meteoroids having impact energies greater than E (in Joule) impacting the entire lunar surface per year. Seismic efficiency, i.e., the portion of the preimpact kinetic energy transformed into seismic energy, appears to be nearly constant over a wide range of masses, velocities, and densities of impactors.

Recent advances in understanding the physical principles of planetesimal accumulation provide the opportunity of developing self-consistent quantitative models of asteroid formation that can be compared with observational data on asteroidal meteorites, and telescopic and spacecraft observations of asteroids themselves. By iteration of theory and observation one can thereby make more complete use of the unique record of early solar system history preserved in meteorites.

It is plausible to assume that the solar nebula filled the asteroid belt in a continuous manner. A straightforward application to the asteroid belt of the planetesimal accumulation model proposed for the terrestrial planets (1) then leads to a reductio ad absurdum because runaway accumulation predicts formation of  $\sim 1/3$  Earth-mass planet-size bodies in  $\sim 3 \times 10^5$  years. Merger of these bodies will then lead to at least one "terrestrial" planet in the asteroid belt.

An alternative is quenching the asteroidal runaway by perturbations by an early-formed Jupiter, possible models for which have been obtained (2,3). These same models still permit runaway growth at 1 A.U. and formation of the terrestrial planets in the manner described earlier (1,4,5). If modest external perturbations lead to eccentricities  $\sim 10^{-3}$  to  $10^{-2}$ , asteroidal growth will be satisfactorily limited to formation of  $\sim 10^{24}$  g bodies in  $\sim 10^6$  years. During the growth of these larger asteroids, the smaller members of the planetesimal swarm will be destroyed by mutual collisions, leading to loss of material by fragmentation with an initial characteristic time scale of  $\sim 2$  m.y. The largest bodies will be nearly invulnerable to destruction. During this period of growth, much of the material in the larger bodies will consist of breccias, formed by low velocity impact, as well as by reaccumulation of fragments of smaller bodies, derived from limited regions of the asteroid belt,  $\sim 0.03$  A.U. in width.

Further gradual increase in eccentricity to present asteroidal values on a  $\sim 10^7$  year time scale, (presumably externally driven) is then found to cause collisional destruction of  $>99.9\%$  of the asteroidal material within 150 m.y., after which time asteroidal evolution resembles that observed today. This model is amenable to future comparison with observational evidence obtainable from petrography of meteorites, evidence for a "late veneer" on the terrestrial planets, their cratering history, and asteroidal observation.

#### References:

- (1) Wetherill, G.W. and Stewart, G.R. (1988) Accumulation of a swarm of small planetesimals, submitted to Icarus.
- (2) Lissauer, J.J. (1987) Time scales for planetary accretion and the structure of the protoplanetary disk. Icarus 69, 249-265.
- (3) Wetherill, G.W. (1988) Origin of the asteroid belt. Submitted to Asteroids II, R.P. Binzel, ed., University of Arizona Press, Tucson.
- (4) Wetherill, G.W. (1986) Accumulation of the terrestrial planets and implications concerning lunar origin. In Origin of the Moon, ed. Hartmann, W.K. et al, pp. 519-550, Lunar Planet. Inst., Houston.
- (5) Wetherill, G.W. (1988) Accumulation of Mercury from planetesimals. In Press, Mercury, C. Chapman and F. Vilas, ed. Univ. of Arizona Press, Tucson.

**Are Asteroids the Source of the Period of Late Heavy Bombardment in the Inner Solar System?; R.G. Strom, Department of Planetary Sciences, University of Arizona, Tucson, Arizona 85721**

In the inner Solar System, the heavily cratered terrain on the Moon, Mercury, and Mars all have similar size/frequency distributions representing the period of late heavy bombardment. On Mercury and Mars, there is a paucity of craters less than about 40 km diameter relative to the Moon. This paucity of craters is probably the result of crater obliteration by intercrater plains formation on Mercury and both intercrater plains and atmospheric erosion and deposition on Mars.

A comparison of the cratering curves for the Moon, Mercury, and Mars shows that they are laterally displaced with respect to each other at diameters between about 40 km and 150 km, where the curves are probably unaffected by erosion and deposition and where the statistics are relatively good. They are displaced in such a manner that higher impact velocities are required at planets with smaller heliocentric distances, i.e., larger craters at Mercury and smaller craters on Mars compared to a given size crater on the Moon. This is consistent with a single family of objects in heliocentric orbits. The Martian curve is laterally displaced to smaller diameters by about one  $\sqrt{2}$  diameter bin compared to the lunar curve, while the Mercurian curve appears to be displaced to larger diameters by about a half a  $\sqrt{2}$  diameter bin compared to the Moon.

In order to determine the orbital elements of the objects responsible for the period of late heavy bombardment, Monte Carlo computer simulations were devised to attempt to reproduce the observed displacements of the crater curves from impact velocities appropriate for objects with various semimajor axes and eccentricities. In these early simulations, a projectile size/frequency distribution was recovered from the lunar highlands cratering curve using a modified Holsapple-Schmidt crater scaling law and randomly selected impact velocities derived from objects with semimajor axes from 0.5 to 2.5 AU and eccentricities from 0.5 to 0.9. This projectile population was then used in another Monte Carlo simulation to generate crater size/frequency distributions on the Moon, Mercury, and Mars using randomly selected impact velocities derived from objects with various orbital elements.

These early initial simulations indicated that only objects confined to the inner Solar System and with large eccentricities ( $> 0.5$ ) could produce the observed lateral shift in the crater curves. However, these simulations did not take into account the impact probability of the objects. Some orbital elements have collisional lifetimes that are greater than the age of the Solar System, while others are very short. In order to account for the impact probabilities of objects, new Monte Carlo computer simulations were devised to take into account the lifetimes of the objects and therefore the impact frequency. In these simulations, the number of times an impact velocity was used in a simulation was derived from its lifetime by normalizing it to the age of the Solar System so that the shorter the lifetime, the more frequently the impact velocity was used. Impact velocities for objects with lifetimes greater than the age of the Solar System were rejected. These new simulations more accurately portray the impact velocity distributions for various orbital elements.

Currently four models are being tested. One model assumes that the population of impacting objects is collisionally evolved so that relatively large orbital inclinations are associated with large eccentricities, or  $i \sim e/2$  where  $e$  is in radians. A second model

is the opposite case where the population is not collisionally evolved and relatively large orbital inclinations are associated with small eccentricities, i.e., evolution along surfaces of constant Tisserand invariant in  $a, e, i$  space. The third model will consider an intermediate case of partial collisional evolution, while the fourth model derives impact velocities from the orbital elements of present day terrestrial planet-crossing asteroids and short-period comets.

To date only two models have been tested. The first model where objects are collisionally evolved with semimajor axes from 0.5 to 1.5 AU and eccentricities from 0.1 to 0.9 does not generate the impact velocity differences between the Moon, Mercury, and Mars required to produce the observed lateral displacement in the cratering curves. However, present-day terrestrial planet-crossing asteroids produce the observed shift in the crater curves when their impact probabilities are taken into account. Although the other cases have yet to be tested, it appears possible that objects on orbits similar to present-day terrestrial planet-crossing asteroids could have been responsible for the period of late heavy bombardment in the inner Solar System. Perhaps such objects could have originated from a now depleted innermost part of the asteroid belts by Mars' perturbations early in Solar System history as suggested by Wetherill (personal communication).

ASTEROID COLLISIONAL EVOLUTION: THE HOLISTIC APPROACH  
P. Paolicchi (U. of Pisa), A. Cellino (Obs. Astro. of  
Torino), D. Davis (Planetary Sci. Inst.), P. Farinella (U.  
of Pisa), and V. Zappalá (Obs. Astro. of Torino)

The current distribution of asteroid sizes and spin rates is the product of collisional modification of the "initial" or "primordial" size and spin distribution. Understanding how collisions have changed these two observable characteristics of the asteroid population will enable us to establish their "starting" values, which were presumably the result of the accretionary phase of asteroids. In this fashion, the study of asteroids allows insights into the process of planetary accretion and the asteroid belt is the only place in the solar system where it is possible to infer information about properties of the early planetesimal population.

We have developed and applied a new numerical simulation for studying the simultaneous effects on asteroid sizes and spins of their mutual collisions. This program was created by adding a model for changes in the spin rates of asteroids due to mutual impacts to a previous simulation that treated asteroid size evolution alone (1). Spin changes due to the physical processes of collisional spinup and drag, angular momentum drain and catastrophic disruption are included in this model. For cratering impacts, defined to be those that shatter less than half of the target body, effects of collisional spinup and drag were modeled using the theory of Harris (3) while the angular momentum drain was incorporated using the results of Dobrovolskis and Burns (2). However, the dominant type of collision that changes asteroid sizes and spin is that of collisional disruption, defined to be a collision that shatters and disperses the fragments against their mutual gravitational binding such that the largest post impact body contains less than half the mass of the original target. The outcome of such a collision consists dominantly of discrete fragments, but the largest body may be a "rubble pile", formed when some of the fragments gravitationally reaccumulate.

Our model for the spin rates of fragments and rubble piles resulting from collisional disruption is based on laboratory impact experiments and on a numerical



simulation of the collisional fragmentation of a discrete body (4). Earlier work using this model is described in the forthcoming Asteroids III Volume (R. Binzel, ed.) and treated the "rubble pile" as if they were large solid fragments. This algorithm always produced spin up of the reaccumulated core, yet physical arguments suggest that spin down should occur when there is significant angular momentum drain, analogous to that for cratering impacts. We have developed an improved model for the post impact spins of these reaccumulated cores based on extensive computer simulations using the model described in Paolicchi et al. (4). Figure 1 presents the first results of this analysis. We have incorporated this angular momentum "splash" effect into our simulation of asteroid collisional evolution by computing the spin of the reaccumulated core as a fraction ( $M_c/M_i$ ) times the post impact target spin rate, provided  $M_c/M_i > 0.2$ , i.e.  $\omega_c/\omega_i = M_c/M_i$ , where  $\omega_c$ ,  $M_c$ ,  $\omega_i$  and  $M_i$  are the angular velocity and mass of the core and initial target body, respectively. Otherwise, the core is treated as a fragment as before. With this addition to our spin rate algorithm, we now have a comprehensive model for the changes to asteroid spin rates due to their mutual collisions. Applications of this new tool to study asteroid collisional history are now in progress.

- (1) Davis, D.R., Chapman, C.R., Weidenschilling, S.J. and Greenberg, R. (1985). Icarus 62, 30-53.
- (2) Dobrovolskis and Burns, J. (1984). Icarus 57, 464-476.
- (3) Harris, A.W. (1979). Icarus 40, 145-153.
- (4) Paolicchi, P., Cellino, A., Farinella, P. and Zappalá, V. (1989). Icarus, in press.

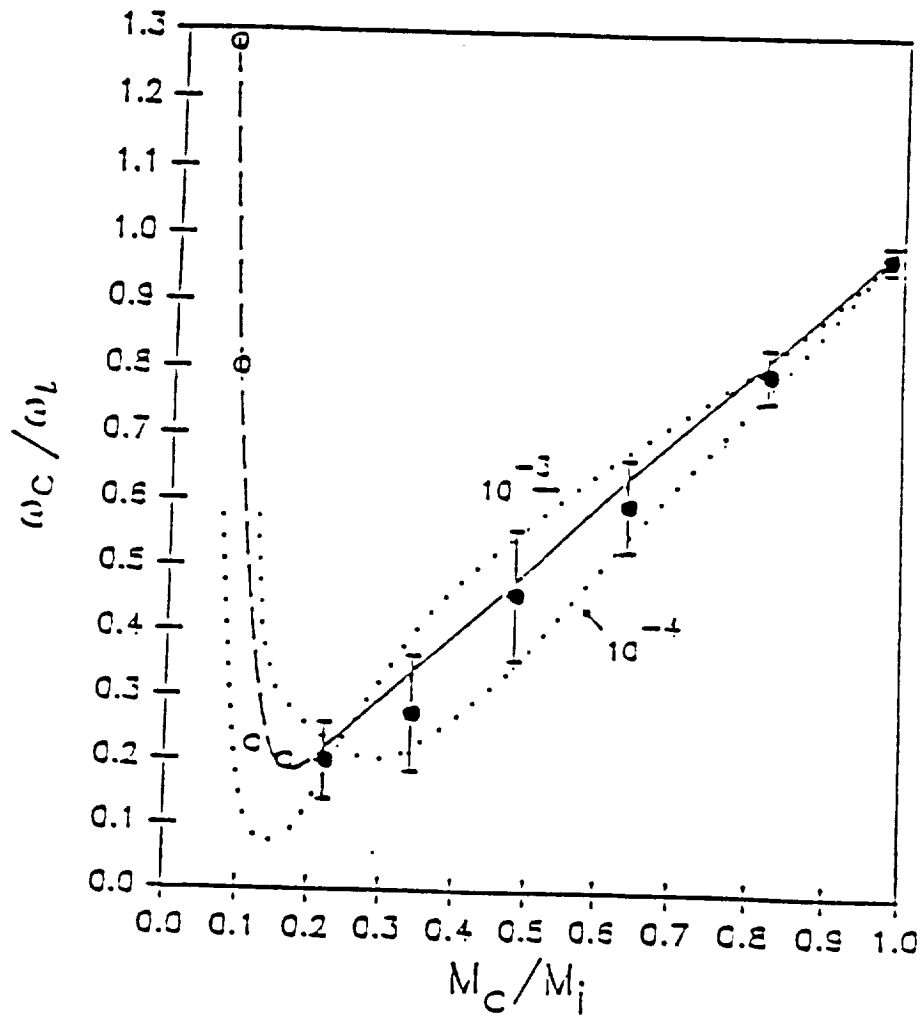


Figure 1: Spin rate of a reaccumulated core (normalized to the post impact spin rate of the target,  $\omega_c/\omega_i$ ) as a function of the core mass (normalized to the initial target mass). The dotted lines indicate the envelope of solutions obtained when the initial spin velocity varies from  $10^{-3}\text{sec}^{-1}$  to  $10^{-4}\text{ (sec}^{-1})$  (period = 1.7 hrs to 17 hrs) and different random points are selected for the computations.

AN INTEGRATED MODEL FOR COLLISIONAL EVOLUTION OF ASTEROID  
SIZES AND SPINS

Donald R. Davis (Planetary Science Institute), Paolo  
Farinella, Paolo Paolicchi (U. of Pisa)

Sizes and rotation rates are two fundamental properties of the asteroids that have been altered by collisions over solar system history. We present results from a new numerical simulation which models the simultaneous changes in the sizes and spin of asteroids due to their mutual collisions. The collisional model described by Davis et al. (1985) was augmented by a calculation of rotational changes due to collisional spinup and drag, angular momentum drain, and catastrophic disruption. Large asteroids ( $\geq$  (100-200) km diameter) are dominantly survivors from the primordial population whose spin periods have changed only modestly over solar system history. We illustrate effects of different choices of material parameters on the evolution of the asteroidal population and describe our best estimate of the asteroid size distribution of the time that asteroid collision speeds were pumped up to their current value of  $\sim 5$  km/s.

Davis, D.R., Chapman, C.R., Weidenschilling, S.J. (1985). Collisional History of Asteroids: Evidence from Vesta and the Hirayama Families, Icarus 62, 30-53.

COLLISIONAL DISRUPTION EXPERIMENTS: IMPACT STRENGTH  
ANALYSIS AND VELOCITY DISTRIBUTIONS  
E.V. Ryan and D.R. Davis (Planetary Science Inst.)

Collisions in the solar system involve a wide variety of material types for both target and projectile ranging from strong metallic to weak icy bodies. To avoid the difficulties of a multi-material experimental program, but still study how target strength differences might affect collisional outcomes, we chose to use a single material, cement mortar, where we could vary the strength over an order of magnitude. We have used weak ( $3.5 \times 10^7$  dynes/cm<sup>2</sup>) and strong ( $3.5 \times 10^8$  dynes/cm<sup>2</sup>) homogeneous targets, as well as differentiated (strong core, weak mantle) mortar targets. Impact velocities ranged from 50 to 6000 m/s. Projectiles included pyrex, aluminum, steel, weak and strong cement mortar, and ice. By using the variety of parameters described above, we studied which factors influenced collisional outcomes, i.e., fragment size and velocity distributions, energy partitioning, etc.

A fundamental quantity used to model collisional outcomes is the impact strength, defined as the collisional energy density partitioned into the body necessary to produce barely catastrophic shattering. By combining our data with other published results (1-11), we showed that impact strength could be correlated with quasi-static material strengths for most materials ranging from basalt to ice. Two materials which did not follow the trend are weak mortar and clay targets. Both materials had unusually high impact strengths, and contrary to what we would expect from their static compressive strengths, the impact strengths of strong and weak mortar targets were found to be nearly identical.

It has been confirmed (12) that material strength is a function of the rate at which energy is delivered to the body, i.e., the strain rate  $\dot{\epsilon}$  (where  $\dot{\epsilon} = V/D$  in which  $V$  is the impact velocity and  $D$  is the projectile diameter (13)). Thus, strength has a static as well as a "dynamic" rate-dependent component. The static component is what is usually laboratory-measured as the "compressive" strength, while the impact strength determined from collisional experiments includes the strain-rate dependent component. Previously, it has been assumed that, given a particular material, collisional outcome was solely dependent on the specific energy. Strain-rate scaling introduces additional dependence on both momentum ( $V$ ) and projectile size ( $D$ ). The dynamic strength ( $\sigma$ ) is related to the strain rate ( $\dot{\epsilon}$ )

as:  $\sigma \propto \dot{\epsilon}^\gamma$ . The exponent  $\gamma$  has been found to vary from  $1/4$  -  $1/3$  for most silicates and ices. The anomalously high impact strength of the weak mortar and clay targets could be explained if the impact stress wave is highly attenuated near the impact site due to the granular nature of these "lossy" materials. It has been noted (14) that for porous materials, also highly dissipative media,  $\sigma$  varies with a much higher power of the strain rate, i.e.,  $\gamma \approx 0.65$ , than for silicates and ices. If we assume that this strong dependence is valid for weak mortar and clay, and use the relatively weak dependence that is reported for the other materials, we may calculate a new strain rate-dependent impact strength. The result (figure 1b) is a greatly improved correlation between impact strength and material compressive strength.

The mass-velocity distribution for fragments following catastrophic impact is a vital factor for understanding asteroid collisions. For large bodies (those having significant gravity) how the ejecta velocity compares to the escape velocity governs whether the object is disrupted and the fragments dispersed, or if the ejecta gravitationally reaccumulate to form a "rubble pile" structure. Since fragment velocities depend on the incident reflected stress pulse, which in turn is a function of projectile/target type and impact velocity, we have explored how variation of these parameters affect the resultant velocity distributions. In addition, we have obtained estimates for the fraction of impact energy partitioned into ejecta kinetic energy ( $f_{KE}$ ) under a variety of impact conditions. Previously (4)  $f_{KE}$  had been found to be on the order of 1%. Thus far, we find two regimes:  $f_{KE} \leq 0.04$  or  $f_{KE} \sim 0.11-0.17$ . Further data reduction is necessary to more definitely isolate connections to target/ projectile types.

Preliminary analysis shows that for the same projectile type, mean fragment speeds are lower for weak differentiated targets than they are for strong homogeneous targets. It has also been possible to fit the mass velocity distributions with a power law; the slopes determined from these fits are much shallower than the -2.25 slope inferred from high speed cratering impacts (15, 16). Additional analysis will help to better clarify the above general trends.

- (1) Cintala, M.J. et al. (1984). LPSC XV, p. 158. (2) Cintala, M.J. et al. (1985). LPSC XVI, p. 129. (3) Fujiwara, A. et al. (1977). Icarus 31, 277. (4) Fujiwara, A. et al. (1980). Icarus 44, 142. (5) Fujiwara, A. and N.

Asada (1983). Icarus 56, 590. (6) Kawakami, S. et al. (1983). JGR 88, 5806. (7) Lange, A. and T.J. Ahrens (1981). Proc. LPSC 12th, 1667. (8) Matsui, T., et al. (1982). JGR 87, 10968. (9) Matsui, T., et al. (1984). JGR 89, suppl., p. B700. (10) Takagi, Y. et al. (1984). Icarus 59, 462. (11) Smrekar et al. (1985). LPSC 16th, 795. (12) Grady, D.E. and M.E. Kipp (1980). Int. J. rock Mech. Min. Sci. and Geomech. Abstr. 17, 147. (13) Davis, D. and Ryan, E. (1988). Submitted to Icarus. (14) Holsapple, K. and Housen, K. (1986). Mem.S.A.It. 57, 65. (15) Gault et al. (1963). NASA Tech. Note D-1767. (16) Stöffler et al. (1975). JGR 80, 4062.

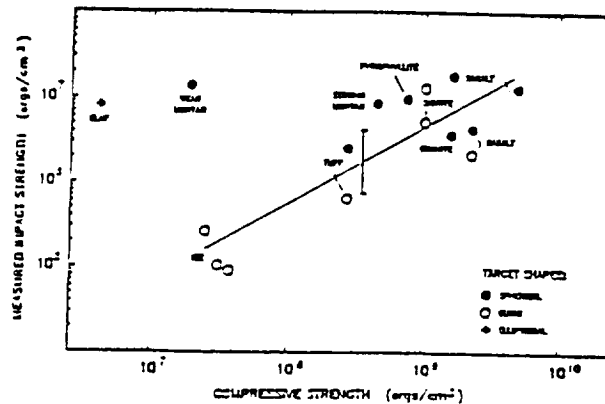


Fig. 1(a). Experimentally determined impact strength as a function of measured compressive strength. The solid line is the linear fit to all the data except clay (5) and weak mortar.

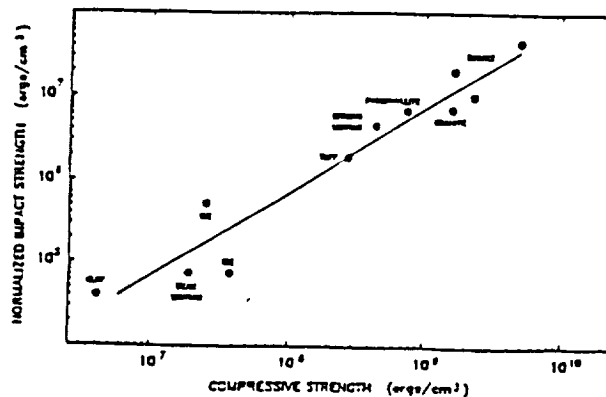


Fig. 1(b). A strain rate dependence is included, and a normalized (to basalt (3), (4)) impact strength is now shown. The clay and weak mortar points have undergone a large shift due to their stronger dependence on strain rate ( $\sim 0.65$  power) than the other materials shown ( $1/3$ - $1/4$  power).

## THE WATER REGIME OF ASTEROID (1) CERES

F.P. Fanale and J.R. Salvail. Planetary Geosciences Div., Univ. of Hawaii, Honolulu, HI 96822.

This work was motivated by observations (Lebofsky et al. 1981) which indicated that there may be a small but significant amount of water ice on the surface of Ceres. They estimated that this film of frost would be about 0.01 microns thick if planet-wide and could not exceed 0.3 microns. They concluded that it would not be saturated and would not be stable against sublimation, even near the poles. The two possible explanations for the frost feature given were that (1) water frost is stable in the interlayer position in clay minerals and that the water frost observed was "bound" ice, or (2) that water frost is replenished from regolith material by migration of the adsorbed water in clay minerals. Jones et al. (1988) have also reported indications of a thin layer of water ice on Ceres.

We have developed a theoretical model based on a variation of the second postulate given above. Subsurface water ice, derived from adsorbed water, sublimates and is transported through a porous crust to the surface where a fraction of the water is lost by thermal and nonthermal escape processes, and the remainder is redistributed over the surface as frost or into the atmosphere. Our analytical model consists of two parts. The first part presents equations for computing surface and subsurface temperatures, water fluxes and ice depths for various latitudes over the geologic history of Ceres. Current water fluxes were integrated over the surface of Ceres to provide a global subsurface water supply rate. The second part presents equations for computing latitude dependent thermal escape fractions and atmospheric flight times for molecules in ballistic orbits. The nonthermal escape processes, photodissociation and sputtering, were also considered quantitatively. Using the global water supply rate and globally averaged molecular ballistic flight times and thermal escape fractions, an approximate expression for the pseudo-steady-state mass of atmospheric water plus surface frost was derived.

Our results predicted that the current water supply rate from the subsurface ice reservoir is between 34 and 240 g/s, assuming pore radii and porosities of 1  $\mu\text{m}$  and 0.1, and 10  $\mu\text{m}$  and 0.5, respectively. For these same sets of assumed values, the current depth of subsurface ice at the equator is between 7 and 50 meters. Thermal escape is shown to be crucial in preventing the buildup of a kinetic atmosphere. The global average thermal escape fraction is near 0.37. This escape fraction, operating on residual water molecules each time they reimpact the surface and rethermalize, insure that the atmosphere remains ballistic, despite a continuous supply of water from the regolith. The mass loss rate due to sputtering is about 30 g/s, and the mass loss rate due to photodissociation is between 1 and 7 g/s. The pseudo-steady-state mass of atmospheric water plus "free" surface frost was calculated to be between  $5 \times 10^5$  and  $3 \times 10^6$  g. It was also desired to determine whether and, if so, where stable water ice could exist on the surface. Comparing the minimum global water thermal escape rates where surface ice is present down to a given latitude to the global water supply rate, we concluded that water ice at the average albedo of Ceres (0.09) could not exist at latitudes less than about

80°. If the albedo of the ice were as high as 0.6, which is very doubtful, water ice could not exist below about 60° latitude. Our conclusions are shown to be virtually unaffected by regolith stirring by meteorite impacts. This paper is pending publication in *Icarus*.

References:

- Jones, T.D., L.A. Lebofsky and J.S. Lewis (1988). The 3 micron hydrated silicate signature on C class asteroids: Implications for origins of outer belt objects. Proc. Asteroids II Conf., Tucson, AZ.
- Lebofsky, L.A., M.A. Feierberg, A.T. Tokunaga, H.P. Larson and J.R. Johnson (1981). The 1.7 to 4.2 micron spectrum of Asteroid 1 Ceres: Evidence for structural water in clay minerals. *Icarus*, **48**, 453-459.



## LOSS OF WATER FROM PHOBOS

F.P. Fanale and J.R. Salvail. Planetary Geosciences Div., Univ. of Hawaii, Honolulu, HI 96822.

This work focuses on the question of whether Phobos currently contains water ice in its interior. Knowledge of the water regime of Phobos is important from the point of view of space resources, as well as being reflective of the conditions of accretion and subsequent evolution of solar system objects. There are several reasons for believing that Phobos once contained a substantial amount of water ice in its interior. Phobos appears to be similar to C-class asteroids and carbonaceous chondritic meteorites (Veverka and Burns 1980, and Veverka and Thomas 1979). The link between C-class asteroids and CI and CM carbonaceous chondritic meteorites has been firmly established (Johnson and Fanale 1973). It is known that the CI meteorites were subjected to intensive alteration by liquids resulting in such textural features as veins of epsomite, and that many of the phyllosilicates were secondary and produced by such a process (Du Fresne and Anders 1962). However, the canonical view has been that some phyllosilicates were primary and produced by solid-gas interaction in the pre-planetary nebula. In this scenario, water would have been released from primary hydrous silicates by the warming of the interior of Ceres or larger sized objects. It would have migrated to the near surface where it would have caused hydrothermal alteration beneath a permafrost cover. Recently, observational and theoretical studies have pointed to a somewhat different scenario. Jones et al. (1988) have now measured the strength of the fundamental O-H stretch band in the optical surface materials of many C-class asteroids. They found relatively weak correlation between band depth and heliocentric distance. At the same time, geochemical studies of matrix materials have suggested that all the phyllosilicates may be of secondary origin (McSween 1987). These and other observations suggest an alternative scenario in which asteroids accreted as a mixture of relatively anhydrous materials, organics and a component of water ice (Jones et al. 1988). Thus, there are two possible scenarios for the existence of free water within Phobos. Whether or not Phobos is a captured fragment of a much larger protoasteroid, the weak correlation between band depth and size and the stronger correlation which may have occurred with inverse heliocentric distance suggests that a major electromagnetic induction heating event was capable of mobilizing significant amounts of water on a time scale of  $10^4$  to  $10^5$  years, even in an object as small as Phobos (Herbert 1988, Herbert and Sonnet 1979). Images of Phobos show that it has sets of craters with raised rims aligned along grooves, which may suggest volatile venting associated with impact events (Thomas 1979). In our model the irregular Phobos was modeled as an 18 km sphere. Temperatures were calculated throughout Phobos as a prerequisite for obtaining water fluxes. In doing this it was assumed that temperatures reached a steady state before the ice began to recede. It was also necessary to take into account interior heat transport across latitudes, since the ice could have receded a significant fraction of Phobos' radius. We also assumed for simplicity that the obliquity of Phobos is zero. The numerical solution of the two dimensional steady state problem required that we first obtain the solution in cartesian coordinates; fit the results to a suitable

function, and convert to spherical coordinates. This made it possible to calculate the temperature of the receding ice interface. Knowing the temperatures of the ice interface, water fluxes and the depths of the ice were calculated over the geologic history of Phobos. Computations were performed using two sets of values for pore radius and porosity, 1  $\mu\text{m}$  and 0.1, and 10  $\mu\text{m}$  and 0.5. Our results showed that current water fluxes at the equator are between  $6.5 \times 10^{-15}$  and  $5.0 \times 10^{-14}$   $\text{g cm}^{-2} \text{s}^{-1}$  for the low and high porosity cases, respectively. The current ice depths at the equator are between 20 and 150 m. These results were based on the assumption that the pores are filled to capacity with ice. If the larger depth were assumed to exist planet-wide, this would represent a mass loss of only about 0.3% of Phobos' mass over geologic time.

We conclude that negative results for water on Phobos would have to be attributed to an initial paucity of water within Phobos rather than any inherent inability of an object with Phobos characteristics to retain water ice. This paper has recently been published in *Geophysical Research Letters*.

#### References:

- Du Fresne, E.R. and E. Anders (1962). On the chemical evolution of the carbonaceous chondrites. *Geochim et Cosmochim Acta*, **26**, 1085-1114.
- Herbert, F. and C.P. Sonnett (1979). Electromagnetic heating of minor planets in the solar system. *Icarus*, **40**, 484-493.
- Herbert F. (1988). T-Tauri solar wind induction heating of planetesimals and asteroids. Proc. Asteroids II Conf., Tucson, AZ.
- Johnson, T.V. and F.P. Fanale (1973). Optical properties of carbonaceous chondrites: Relationship to asteroids. *J. Geophys. Res.*, **78**, 8507-8518.
- Jones, T.D., L.A. Lebofsky and J.S. Lewis (1988). The 3 micron hydrated silicate signature on C class asteroids: Implications for origins of outer belt objects. Proc. Asteroids II Conf., Tucson, AZ.
- McSween, H.Y. Jr. (1987). Matrix compositions in antarctic and non-antarctic CM carbonaceous chondrites. [Abstract] *LPSC XVIII*, Houston, TX, p. 631-632.
- Thomas, P. (1979). Surface features of Phobos and Deimos. *Icarus*, **40**, 223-243.
- Veverka, J. and P. Thomas (1979). Phobos and Deimos: A preview of what asteroids are like, in 'Asteroids' (T. Gehrels, ed.), 628-651.
- Veverka, J. and J.A. Burns (1980). The moons of Mars. *Ann. Rev. Earth Planet Sci.*, **8**, 527-558.

**METEORITE SPECTROSCOPY AND CHARACTERIZATION OF ASTEROID SURFACE MATERIALS**  
Michael J. Gaffey, Geology Department, Rensselaer Polytechnic Institute,  
Troy, New York 12181.

The minor planets are the surviving primordial remnants for the inner solar system, just as the cometary objects are for the outer solar system. The asteroids and comets by virtue of their small size have limited potential for internally driven thermal evolution. These minor bodies are composed either of primitive materials which are essentially unaltered samples accreted from the solar nebula, or of materials altered primarily during the very earliest epoch of solar system history, a period dominated by processes quite different than those seen in the present solar system. The asteroids - and their natural samples, the meteorites - preserve our best record of the conditions and of the process present in the inner solar system during and just subsequent to the accretionary epoch.

The purpose of this research program is an improved understanding of the nature and history of these minor planets, of their relationships to the meteorites, and of the early post-accretionary history of the inner solar system. This is accomplished by means of sophisticated mineralogical and petrological characterizations of asteroid surface materials. It is axiomatic in the geosciences that the history of a rock is written in its mineralogy. This facies concept, in its various versions, is the guiding principle which permits the detailed mineralogy, mineral chemistry, and petrology of a sample or suite of samples - whether terrestrial, lunar, martian, or meteoritic - to be translated into an understanding of the conditions and processes which produced that specimen. These basic principles are employed to unravel the history of asteroids from characterizations of surface mineralogy.

These surface material characterizations are derived from analysis of high precision visible and near infrared (VNIR) reflectance spectra of selected asteroids observed with earth-based telescopes in order to provide the data base to investigate the nature and evolutionary history of individual objects. Such data on individual members of the population provides the basis for investigating the broader inter-relations between the asteroids and meteorites (to establish a spatial context for the more detailed meteorite data) and between asteroids at different heliocentric distances (to establish the nature of nebular compositional gradients and the distribution of post-accretionary thermal events). The sophistication of the asteroidal and inner solar system models developed from this surface materials data base is directly related to the quality and appropriateness of those characterizations.

It seems unlikely that any significant portion of the diverse asteroid population will be targets of spacecraft missions within the professional lifetimes of most current investigators. Therefore, asteroidal mineralogic characterizations from earth-based spectral studies will continue to be a primary source of information on the natures and histories of the minor planets for at least the next few decades.

The recent results of two aspects of the present research program are outlined in the subsequent sections.

**THERMAL HISTORY OF INNER BELT PLANETESIMALS** - Consideration of the properties and evolutionary histories of the S-type asteroids has led to a significant constraint on planetesimal evolution in the inner asteroid belt and on planetary accretion in the inner solar system. If asteroids are sorted into those which have igneous histories (ie. exhibit surface assemblages requiring at least partial melting;  $T > 1000^{\circ}\text{C}$ ) and those which do not, the relative proportion of igneous bodies decreases linearly from 100% at about 1.8AU to 0% at 3.5AU (figure 1). There are several major

implications for asteroid and inner solar system history, including:

1) This pattern implies a strongly heliocentric thermal event similar to that modeled for inductance heating during the T-Tauri stage of solar evolution. The consequences of these asteroidal results on models of early solar evolution are explored in a manuscript submitted to the "Sun in Time" conference volume (Herbert, Sonett, and Gaffey, 1989).

2) It implies that only minimal mixing took place across the belt, consistent with the conclusions of several other recent investigations.

3) It implies that the compositional structure of the belt (ie. the variation in the relative abundance of asteroid types with semimajor axis) is not a simply a fossil of the nebular compositional gradient, but that the inner regions of the asteroid belt have been strongly modified by post-accretionary heating.

4) It implies that all the planetesimals formed inward of the asteroid belt should have undergone similar early, intense heating. Unless other evidence relaxes these requirements, models of terrestrial planet accretion which take more than a few million years to assemble these planets should assume that the accreting planetesimal population is predominantly composed of hot, igneously evolved bodies. These results have been outlined in a manuscript submitted to the proceedings volume for the "Origin of the Earth" conference (Gaffey, 1989).

ANALYSIS OF CCD SPECTRA OF LOW ALBEDO OUTER BELT AND TROJAN ASTEROIDS - A joint analysis of the CCD spectra of low albedo asteroids (types C, F, P, D, and T) and those at greater heliocentric distances has begun using the observational data of Dr. F. Vilas (NASA-JSC). In their raw form, most of these spectra exhibit a range of slopes but otherwise appear to be featureless. Careful examination of these spectra, however, suggested the presence of subtle features which were largely obscured by the channel to channel scatter in these high resolution spectra.

These spectra were transferred to RPI for additional processing. Initial analysis steps included smoothing the data to suppress channel-to-channel noise and the removal of the net slope by dividing out a linear continuum. In the continuum-removed spectra (figure 2), these nominally featureless asteroid types exhibit a wide variety of weak but well-defined absorption features, with a significant range in both intensity and wavelength position. We have eliminated the standard stars and atmospheric extinction as potential sources of these features and have strong confidence in their reality in the asteroidal spectra themselves.

Some of these features are interpretable in terms of known meteorite types and/or minerals. Figure 3 shows the close match between the smoothed, continuum-removed spectrum of asteroid 1467 Mashona [a GC-type in the Cybele group located at 3.4AU just outside the main belt] and similar (300A smooth, continuum-removed) spectra of Meghei and Nogoya, CM2 meteorites which underwent significant aqueous alteration within their parent bodies (e.g. McSween, 1987, Geochim. Cosmochim. Acta 51, 2469-2477). Considering the range of spectral variation in the dark asteroids and in the CI-CM meteorites, it is probable that the surface material of 1467 Mashona was altered in a similar fashion, to a material with an Fe-bearing serpentine such as antigorite as a major phase.

Some asteroid types (e.g. type T) and dynamical groups (e.g. the Trojan objects) generally appear to be genuinely featureless at our level of detection (approximately 1% intensity). The overall pattern of features is consistent with the recent suggestion by Jones, Lebofsky, Lewis and Marley (1989, Icarus, submitted) that the Trojan asteroids have not undergone aqueous alteration and contain anhydrous silicates and that heating was insufficient to melt water ice in these bodies. These results are included in a manuscript submitted to Science (Vilas and Gaffey, 1989).

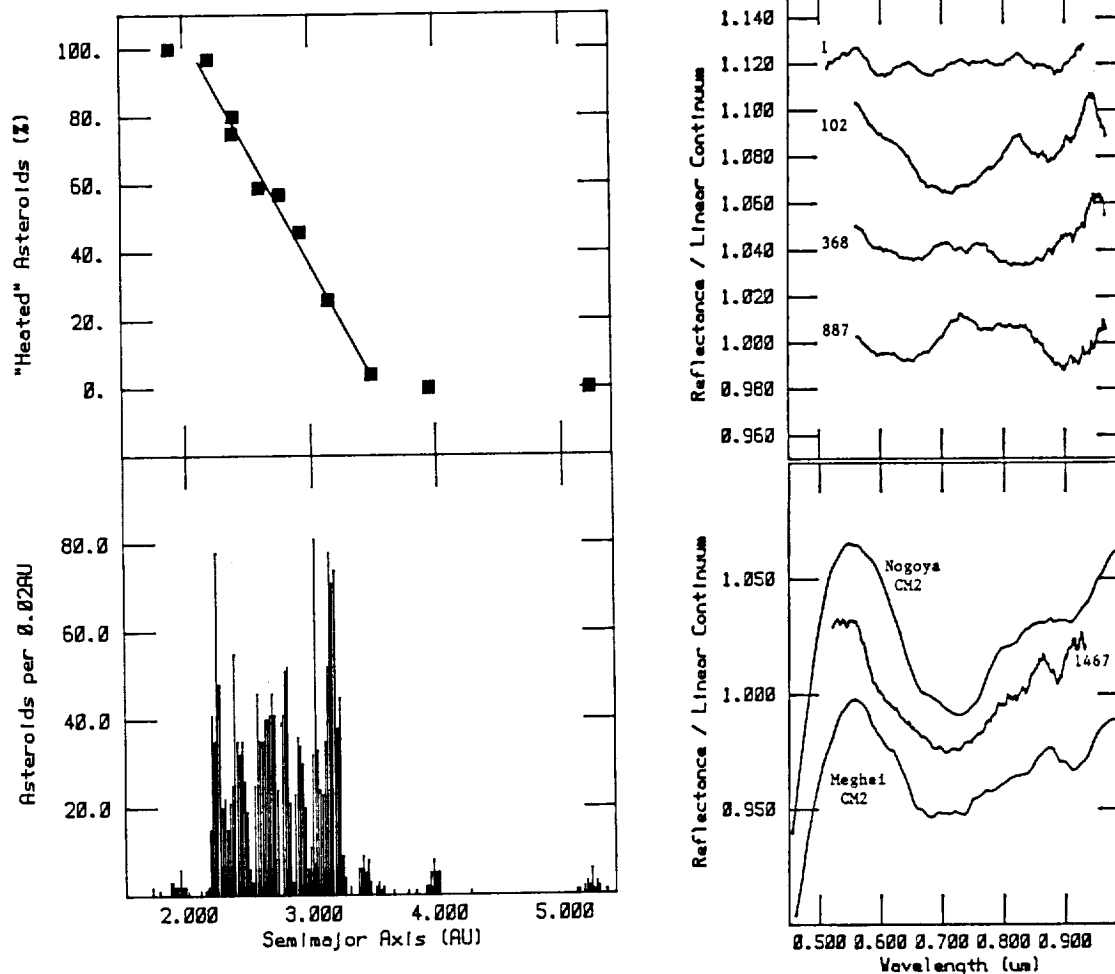


Figure 1 (left): A) The relative proportions of igneous bodies (types A,E, M,S,R,V) among 423 classified asteroids as a function of semimajor axis in eleven dynamical zones. B) Histogram of asteroid density versus semimajor axis for asteroid #'s 1-2016 in 0.02AU bins.

Figure 2 (top, right): The continuum-removed, 300A smoothed spectra of four low albedo asteroid with different spectral features. Asteroids 570 and 1467 are in the Cybele-group, 368 is in the outer main belt, and 877 is in the inner main belt. [Spectra offset 0.04 for clarity.]

Figure 3 (bottom, right): Smoothed, continuum-removed spectrum of asteroid 1467 Mashona compared to that of the CM2-meteorites, Meghe1 and Nogoya [offset  $\pm 0.03$ , respectively].

#### REFERENCES

- Gaffey, M.J. (1989) Thermal history of the asteroid belt: Implications for accretion of the terrestrial planets. "Origin of the Earth" proceedings volume, submitted.
- Herbert, F., C.P. Sonett, and M.J. Gaffey (1989) Protoplanetary thermal metamorphism: The protosolar wind electromagnetic induction hypothesis. "Sun in Time" proceedings volume, submitted.
- Vilas, F., and M.J. Gaffey (1989) Identification of phyllosilicate absorption features in main-belt and outer-belt asteroid reflectance spectra. Science, submitted.

## THE CV/CO CHONDRITES: DISCOVERY OF ASTEROIDAL ANALOGS.

Jeffrey F. Bell (Hawaii Institute of Geophysics, 2525 Correa Road, Honolulu HI 96822)

"Carbonaceous chondrites" as a class have been traditionally associated with the Class C asteroids. In fact this association only applies to the CI and CM chondrites. The asteroidal affiliations of the anhydrous CV and CO chondrites have been much more mysterious. They have moderate albedos and shallow olivine/pyroxene bands, inconsistent with the low albedos and flat IR spectra of the traditional C-type asteroids. Some workers have associated CV/CO mineralogies with atypical C-type objects, while others have selected certain S-type asteroids as the most likely candidates (e. g. Gaffey and McCord, *Space Sci. Rev.* **21**, 555.) on the basis on visible-wavelength telescopic spectra

This long-standing mystery has been unexpectedly clarified by results from a spectral survey of asteroid families being conducted at the NASA Infrared Telescope Facility at Mauna Kea. "Families" are groups of asteroids on similar orbits which are presumed to be fragments of a common parent body disrupted by a collision in geologically recent time. The Eos family has traditionally posed a difficult problem for asteroid classification schemes. Gradie and Zellner (*Science* **197**, 254-255) found that the UVB colors of the Eos family asteroids clustered tightly on the boundary between the S and C fields, and that their radiometric albedos were also intermediate to these two classes. This led to the apparently contradictory situation in which the Eos family was thought to be homogenous in composition, while the individual objects were classed as C, S, or U based on very small variations in color and albedo. The classification scheme of Tholen (Ph.D. thesis, 1984) eliminated this discrepancy by putting almost all Eos family objects into an enlarged S class.

The new IR spectral observations have revealed that Eos family asteroids 221 Eos, 653 Berenike, and 661 Cloelia exhibit flat IR reflectance curves with very shallow silicate absorption bands. These spectra are totally atypical of other S-type asteroids, and more closely resemble classical C-type spectra. The visual and IR data as a whole suggest that the Eos family parent body was not a true member of either the C or S class. (The picture is complicated somewhat by 639 Latona, which has a spectrum and albedo very close to the average for "normal" S asteroids, and consequently does not match the rest of the family. This object appears to be an "interloper" or "background object" which existed before the Eos parent body was disrupted.)

Comparison of the spectral and albedo data for "normal" Eos family asteroids with the available meteorite spectra reveals a close similarity with CV and CO chondrites. Other meteorites with similar intermediate albedos such as ureilites and "black chondrites" (highly shocked ordinary chondrites) appear much less likely candidates from both spectral and petrologic grounds. It seems probable that either CVs or COs (but not both) are actually derived from the Eos family. (This family is believed to be the source of the dust responsible for the bright bands in the thermal component of the zodiacal light which were detected by the IRAS satellite.) If we accept both this compositional interpretation and the Tholen classifications, a new paradox exists: the most common classes of carbonaceous chondrites are derived from Class S asteroids, instead of the Class C asteroids usually associated with dark meteorites. To simplify terminology and properly recognise the unique properties of the Eos family asteroids, a new asteroid class "K" is proposed to incorporate them. This nomenclature phonetically suggests their apparent identity with carbonaceous chondrites, while reminding us that their telescopically observed parameters are intermediate to the classical C and S classes (since K is halfway between C and S in the alphabet). This class is provisionally defined as objects with albedos near 0.09, S-like spectral curvature at visual wavelengths, weak 1-micron absorption bands, and flat reflectance from 1.1 to 2.5 microns. Although the known asteroids of this class to date are Eos family members, the existence of both CV and CO chondrites indicates that some other asteroids currently classed as S-types on the basis of visible spectra will turn out to be K-types as near-IR observations are extended to fainter objects.

THE H-G ASTEROID MAGNITUDE SYSTEM: MEAN SLOPE PARAMETERS  
A. W. Harris, Jet Propulsion Laboratory, Caltech

The H-G magnitude system (1) was developed for the purpose of predicting the magnitude of an asteroid as a function of solar phase angle, but can also be used for physical studies, by providing a basis for interpolating or extrapolating brightnesses from the phase angles observed at one apparition to the phase angles observed at another apparition, thus allowing one to identify the intrinsic difference in brightness from one apparition to another. This is usually necessary for studies of asteroid shapes and pole positions. In order to do this, it is necessary that the phase relation model accurately represents the behaviour of real asteroids, and to be able to make the best possible a priori estimate of the slope parameter,  $G$ , for an asteroid where the available data is insufficient to determine it well from observations. The first of these issues has been addressed in several of our recent publications (2,3,4); we find that the quality of the fit is generally satisfactory, except for the highest and lowest albedo objects. Here we address the second matter, establishing nominal values of the slope parameter for various taxonomic classes of asteroids.

We have performed least squares fits of the H-G function, in the manner described in (1) to magnitude data for 84 asteroids. We have used only data spanning a substantial phase angle range, from a single apparition, and corrected for lightcurve variation, so that the derived values of  $G$  are reliable to less than 0.1, and typically much less. Table I summarizes the data set of 84 asteroids, listing asteroid number, taxonomic class (5), IRAS albedo (6), the solution values of  $G$  and the formal uncertainty in  $G$ , and finally the reference(s) to the data on which the solution was based. We identify the references by the numbers used in the Asteroids II lightcurve database (7). References not included there are given as A, B, etc., and are given in the references at the end of this paper. An asterisk following the asteroid number indicates that the phase curve is referenced to maximum light; otherwise the fit is to the mean light level. The differences are generally small and insignificant for our purposes. Table II summarizes the results of the determination of mean values of  $G$  for groups of taxonomic classes of low, medium, and high albedo asteroids. We list the mean albedo and mean  $G$  value for each group, along with the bias corrected dispersion of the values within each group (the RMS deviation from the mean). The error bars are just the bias corrected dispersions divided by  $N^{1/2}$ . The mean values of  $G$  are, for each of the four classes, not far from the values recommended by IAU Commission 20 for predicting magnitudes of objects when  $G$  is not measured: 0.15, 0.25, 0.25, and 0.40, respectively. Our values are systematically larger than those found in a similar study using Carlsberg Meridian transit observations (8,9); we have no explanation for the discrepancy.

Another point which should be noted is that the dispersions in both albedo and  $G$  are much greater than the measurement errors. Thus the variation among members of the respective classes is real. We have done a linear regression of  $G$  vs albedo, to see if albedo is a better predictor of  $G$  than simply taxonomic class. The dispersion of  $G$  values from the linear fit with albedo is 0.096; for a linear fit to  $\log(\text{albedo})$ , it is 0.097. Thus, albedo is, if anything, a slightly poorer predictor of  $G$  value. The failure of  $G$  to be an accurate predictor of albedo and vice versa is not a failing of the photometric system; other surface properties, such as roughness, also

influence the slope of the phase curve, so the dispersion of G values simply indicates that not all asteroid surfaces of a given albedo are alike.

This work is supported at JPL, Caltech, under contract with NASA, under the Planetary Astronomy and Planetary Geology/Geophysics programs.

REFERENCES: (1) Bowell, E., et al. (1989). Icarus, in preparation. (2) Harris, A.W., Young, J.W. (1988). Lunar and Planetary Science XIX, 447. (3=B) Harris, A.W., Young, J.W. (1989). Icarus, in press. (4=C) Harris, A.W., et al. (1989). Icarus, submitted. (5) Tholen, D.J. (1988). Asteroids II database, diskette version, dated 12/88. (6) Tedesco (1988). Asteroids II database, diskette version, dated 12/88. (7) Lagerkvist, et al. (1988). Asteroids II database, diskette version, dated 12/88. (8) Lagerkvist, C.-I., Williams, I.P. (1987). Astron. Astrophys. Supl. 68, 295. (9) Lagerkvist, C.-I., et al. (1988). Astron. Astrophys. Supl. 73, 395. (A) Harris, A.W., et al. (1989) Icarus 77, in press. (D) Harris, unpublished results. (E) Taylor, et al. (1988). Icarus 73, 314.

Table I. Well determined slope parameters for 84 Asteroids.

1	G	0.10	0.102	0.009	249	75	M	0.12	0.23	0.02	B	230	S	0.14	0.275	0.003	B
2	B	0.14	0.098	0.010	220	77	MJ	0.13	0.16	0.01	B	233M	T	0.073	0.14	0.04	93
3	S	0.22	0.32	0.03	221,A	78	C	0.064	0.080	0.009	B	236	S	0.10	-0.020	0.014	B
4	V	0.38	0.349	0.003	76	79	S	0.27	0.027	0.014	178	258	S	0.15	0.23	0.02	B
6M	S	0.25	0.28	0.01	79	82M	S	0.17	0.29	0.02	95	261	B	0.10	0.19	0.03	A
8	S	0.22	0.33	0.02	264	93M	CJ	0.085	0.09	0.02	0	284	CX	0.055	0.12	0.11	B
12	S	0.16	0.22	0.02	252	101	S	0.15	0.32	0.01	B	287M	S	0.16	0.24	0.08	93
15	S	0.19	0.15	0.04	176	103M	S	0.17	0.19	0.03	93	304M	C	0.047	0.08	0.02	92
16M	M	0.10	0.261	0.009	130,250	109	GC	0.060	0.035	0.008	B	308M	T	0.043	0.21	0.03	93
20	S	0.19	0.25	0.02	74	110	M	0.17	0.196	0.009	235	324M	CP	0.057	0.09	0.02	186
22M	M	0.12	0.22	0.01	182	113M	S	0.27	0.35	0.01	93	345	C	0.056	0.21	0.10	B
24	C	-	0.18	0.02	A	115M	S	0.25	0.12	0.03	187	349	R	0.34	0.38	0.02	274
29	S	0.16	0.20	0.01	131,248	124M	S	0.15	0.20	0.01	93	354	S	0.19	0.35	0.04	274
33	S	-	0.34	0.02	B	129	M	0.17	0.32	0.06	180	386	C	0.063	0.10	0.02	B
37	S	0.17	0.273	0.007	B	133	SR	0.21	0.13	0.02	96,B	388	C	0.053	0.07	0.10	B
41	C	0.073	-0.12	0.04	180	134	C	0.041	0.28	0.02	B	410M	C	0.054	0.01	0.03	93
43	S	0.28	-0.01	0.03	24	144	C	0.059	0.17	0.04	B	419	F	0.044	0.01	0.06	B
44	E	0.49	0.51	0.01	93,C	146	C	0.052	0.19	0.03	B	433M	S	0.23	0.34	0.02	66,178,
45M	FC	0.048	0.04	0.03	E	156	C	0.040	-0.12	0.08	B	444M	C	0.044	0.11	0.02	95,244
46M	P	0.046	0.06	0.03	187	161	M	0.12	0.13	0.02	B	451M	CJ	0.073	0.05	0.03	93
51M	CJ	0.086	0.150	0.009	D	163	C	0.047	-0.04	0.01	B	497M	M	0.085	0.18	0.01	93
52M	CF	0.057	0.18	0.04	279	192	S	0.21	0.219	0.009	178	505M	FC	-	-0.034	0.025	272
60	S	0.15	0.259	0.006	A	201	M	0.14	0.17	0.02	B	511M	C	0.053	0.03	0.02	284
63	S	0.17	0.23	0.02	181	211	C	0.059	0.12	0.04	B	593	C	0.053	0.06	0.02	B
64	E	-	0.51	0.01	C	214M	E	0.40	0.45	0.02	93	704	F	0.064	-0.02	0.01	253
69M	M	0.12	0.21	0.02	171	216	M	0.088	0.28	0.03	B	712	C	0.046	0.03	0.01	B
70	C	0.070	0.13	0.10	B	218	S	0.15	0.319	0.008	B	804M	PC	0.049	0.10	0.02	93
71	S	0.28	0.40	0.14	B	221M	S	0.12	0.15	0.03	93	980	SJ	0.17	0.063	0.003	B

Table III. Mean slope parameters for various taxonomic classes.

Asteroid Classes	Number in Sample	Mean Albedo	Bias-corrected Dispersion	Mean G	Bias-corrected Dispersion
C, G, B, F, P, T, D	37	0.058 $\pm$ 0.004	0.024	0.086 $\pm$ 0.015	0.088
M	11	0.124 $\pm$ 0.009	0.028	0.214 $\pm$ 0.017	0.057
S, Q	31	0.184 $\pm$ 0.011	0.059	0.227 $\pm$ 0.020	0.109
E, V, R	5	0.403 $\pm$ 0.032	0.064	0.440 $\pm$ 0.033	0.074



Application of Photometric Models to Asteroids  
E. Bowell (Lowell Obs.), B. Hapke (U. Pittsburgh), K. Lumme  
(U. Helsinki), A. Harris (JPL), D. Domingue (U. Pittsburgh)  
and J. Peltoniemi (U. Helsinki)

The way an asteroid or other atmosphereless solar system body varies in brightness in response to changing illumination and viewing geometry depends in a very complicated way on the physical and optical properties of its surface and on its overall shape. We summarize the formulation and application of recent photometric models by Hapke and by Lumme and Bowell. In both models, the brightness of a rough and porous surface is parameterized in terms of the optical properties of individual particles, by shadowing between particles, and by the way in which light is scattered among collections of particles. Both models succeed in their goal of fitting the observed photometric behavior of a wide variety of bodies, but neither has led to a very complete understanding of the properties of asteroid regoliths, primarily because in most cases the parameters in the present models cannot be adequately constrained by observations of integral brightness alone over a restricted range of phase angles.

## Fitting Theoretical Photometric Functions to Asteroid Phase Curves

D. Domingue and B. Hapke, University of Pittsburgh

The theoretical photometric function developed by Hapke can successfully fit photometric phase data of asteroids. However, a question of major importance is the uniqueness of the fits. This discussion explores how variations in the parameters of this function affect the shape of the theoretical curve. The observational data for main belt asteroids are often limited to angles less than  $25^\circ$ , and measurements close to zero phase can be difficult to obtain. The fit of theoretical curves to data within these limits is not unique. Unless there are observations at less than about  $2^\circ$ , it is nearly impossible to establish the extent of the opposition effect. Between the phase angles of  $2^\circ$  and  $25^\circ$ , the opposition effect parameters, the roughness parameter and the single-particle phase function parameter have similar effects on the shape of the photometric curve and are difficult to separate using only disk-integrated data. Absolute photometric data can somewhat constrain the single-scattering albedo. At present, the uniqueness of physical properties of asteroid surfaces deduced from phase curve observations over a limited range of phase angles is questionable.

## ASTEROID LIGHTCURVE INVERSION

Steven J. Ostro, Jet Propulsion Laboratory  
California Institute of Technology, Pasadena, CA 91109

This research focuses on a new approach, called "convex-profile inversion," or CPI, to the interpretation of asteroid lightcurves. Originally developed by Ostro and Connelly (1984), this approach constitutes a promising solution to problems, first posed by Russell (1906), encountered in extracting information about an asteroid's shape from its optical lightcurve. This endeavor is important because (i) shape is a fundamental attribute of any planetary object, (ii) asteroid shapes, which range from nearly spherical to grossly irregular, can be diagnostic of the object's history of exogenic and endogenic modification; and (iii) except for the relative handful of objects observable with radar, speckle interferometry, or during stellar occultations, lightcurves provide the only clues to an asteroid's shape. Unfortunately, the form of a lightcurve is determined by the viewing/illumination geometry and by the surface's light-scattering properties as well as by body shape. As Russell proved, it is impossible to separate the effects of albedo variation from effects of surface curvature, so neither the light-scattering properties nor the shape can be modelled uniquely. Even if we had lightcurves for an asteroid for all possible Sun-Earth-asteroid configurations, it would still be impossible to determine the three-dimensional shape from those disk-integrated measurements. The best we can hope to do is to obtain useful constraints on shape that exploit all the available information.

Ostro and Connelly (1984) showed that any lightcurve can be inverted to yield a convex profile, and that under certain ideal conditions that profile represents an average of the asteroid's shape. The ideal conditions, which include equatorial viewing/illumination geometry and geometric scattering, rarely are satisfied for actual lightcurves, so the derived averages generally contain systematic error. Hence, one goal of this research during the past few years (Ostro et al. 1988) has been to calibrate the sensitivity of CPI to departures from ideal conditions; another has been to apply the inversion technique to real asteroid lightcurves.

The power of CPI lies not just in the calculation of profiles from lightcurves, but also in the precise definition of what shape information is available from a lightcurve and of the circumstances that let us access that information in an optimal manner. Shape constraints derived from a lightcurve are intrinsically less informative than, say, a stellar-occultation profile, which is a two-dimensional projection of the three-dimensional shape. Given a lightcurve, the best constraint we can obtain is a two-dimensional average of the three-dimensional shape. That average is called the mean cross section,  $\bar{C}$ , and is defined as the convex set equal to the average of the convex envelopes on all surface contours parallel to the asteroid's equatorial plane.

A convex profile can be represented by a radius-of-curvature function or by that function's Fourier series. Deletion of a profile's odd harmonics "symmetrizes" the profile. For example, an asteroid's symmetrized mean cross section  $\bar{C}_s$  has the same even harmonics as  $\bar{C}$  but no odd harmonics.

The following ideal conditions pertain to estimation of  $\mathcal{Q}$  from a lightcurve:

Condition GEO: The scattering is uniform and geometric.

Condition EVIG: The viewing/illumination geometry is equatorial, i.e., the Sun and the Earth are in the asteroid's equatorial plane.

Condition CONVEX: All surface contours parallel to the equatorial plane are convex.

Condition PHASE: The solar phase angle  $\phi$  does not equal  $0^\circ$  or  $180^\circ$ .

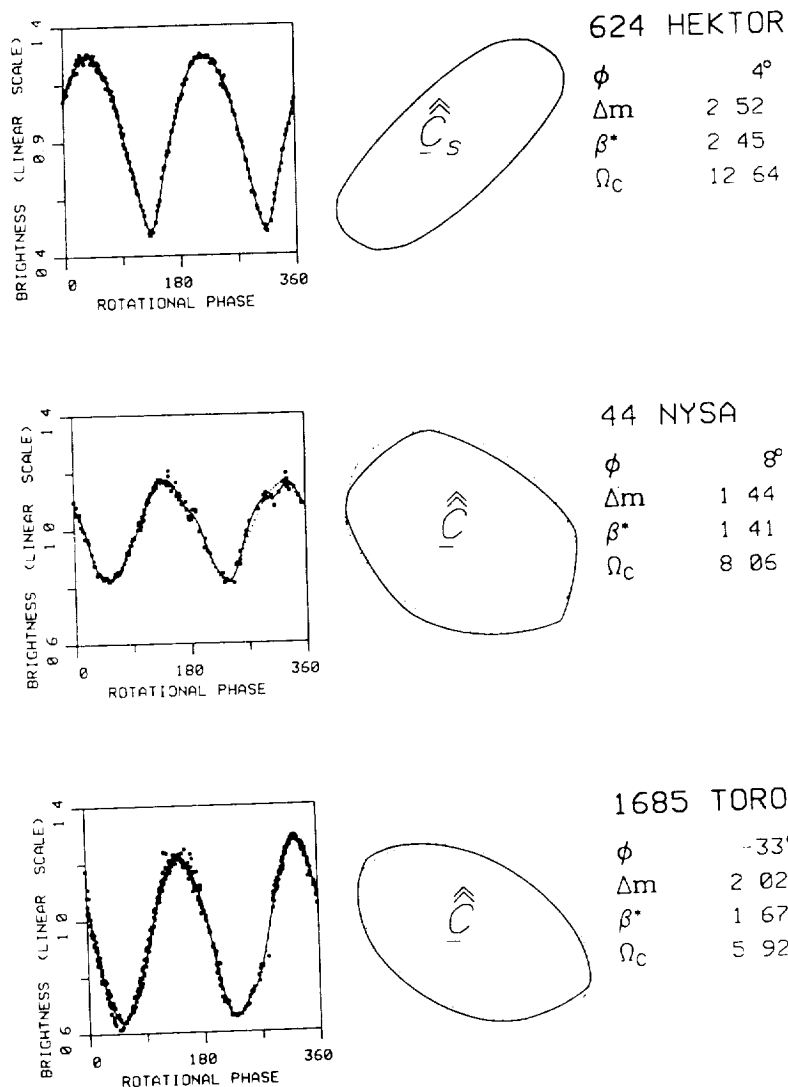
Although we cannot estimate  $\mathcal{Q}$  from an opposition lightcurve, we can estimate  $\mathcal{Q}$ 's even harmonics and hence its symmetrization,  $\mathcal{Q}_s$ . Estimation of  $\mathcal{Q}_s$  from opposition lightcurves is less "burdened" by ideal conditions than is estimation of  $\mathcal{Q}$  from non-opposition lightcurves, for three reasons. First, for estimation of  $\mathcal{Q}$ , Condition CONVEX ensures the absence of visible shadows between the limb and the terminator, which might distort determination of  $\mathcal{Q}$ . However, at opposition, there are no visible shadows, so Condition CONVEX is irrelevant and  $\mathcal{Q}_s$  can be estimated reliably as long as Conditions GEO and EVIG are satisfied. Second, Conditions GEO and EVIG are "satisfied more easily" for opposition lightcurves than for non-opposition lightcurves. The geometric scattering approximation is more valid at opposition than at large solar phase angles. Condition EVIG can be satisfied at large phase angles only if the pole lies nearly normal to the Earth-asteroid-Sun plane, but is satisfied at any opposition occurring when the asteroid is at an equinox, i.e., with the pole normal to the Earth-asteroid line. Hence, geometry dictates that opportunities to estimate  $\mathcal{Q}_s$  far outnumber opportunities to estimate  $\mathcal{Q}$ . Third, to assess how close the viewing/illumination geometry is to equatorial for a given non-opposition lightcurve, one must know the asteroid's pole direction; for an opposition lightcurve it is sufficient to know just the location of the asteroid's line of equinoxes.

In describing or comparing any two profiles  $P_1$  and  $P_2$ , it is useful to define a measure of the distance between them as

$$\Omega = 10 \min_{\theta} | \mathbf{d}_1/d_{10} - \Theta \mathbf{d}_2/d_{20} |$$

where  $\mathbf{d}_j$  is the vector of complex Fourier coefficients in the expansion of  $P_j$ 's radius-of-curvature function;  $\mathbf{d}_{j0}$  is the constant term in that expansion; and the diagonal matrix  $\Theta$  rotates  $\mathbf{d}_{2n}$  by  $e^{in\theta}$ . This distance measure is rotation-invariant and scale-invariant. A profile's noncircularity  $\Omega_c$  is defined as its distance from a circle. It is also useful to define the breadth ratio,  $\beta^*$ , of the maximum and minimum values of the profile's breadth function  $\beta(\theta)$ , where  $\theta$  is rotational phase.  $\mathcal{Q}$  and  $\mathcal{Q}_s$  have identical breadth functions. At opposition, under Conditions EVIG and GEO, (i) the lightcurve is equal to  $\mathcal{Q}$ 's breadth function, and (ii)  $\beta^* = 100.4\Delta m$ , where  $\Delta m$  is the lightcurve peak-to valley amplitude in magnitudes; this is the only situation where  $\Delta m$  has a unique physical interpretation.

The figure shows results of using CPI to estimate  $C_s$  for 624 Hektor, and both  $C$  (solid curve) and  $C_s$  (dotted curve) for 44 Nysa and 1685 Toro. In the lightcurve plots, the large symbols are the data and the dotted lightcurve corresponds to the mean-cross-section estimate. The sources of the lightcurves are: Hektor (Dunlap et al. 1969), Nysa (di Martino et al. 1987), and Toro (Dunlap et al. 1973).



#### REFERENCES

- Di Martino, M., V. Zappalà, G. de Sanctis, and C. Cacciatori 1987. *Icarus* **69**, 338-353.
- Dunlap, J. R., and T. Gehrels 1969. Minor planets. III. *Astron. J.* **74**, 797-803.
- Dunlap, J. L., T. Gehrels, and M. L. Howes 1973. *Astron. J.* **78**, 491-501.
- Ostro, S. J., and R. Connelly 1984. *Icarus* **57**, 443-463.
- Ostro, S. J., R. Connelly, and M. Dorogi (1988). *Icarus* **75**, 30-63.
- Russell, H. N. 1906, *Astroph. J.* **24**, 1-18.



CHAPTER 4

COSMOGONY AND DYNAMICS

PRECEDING PAGE BLANK NOT FILMED

PAGE 134 INTENTIONALLY BLANK





# THE ROLE OF INTERSTELLAR INHERITANCE IN SOLAR SYSTEM CHEMISTRY

David J. Stevenson, Caltech, Pasadena, CA 91125.

The atoms and molecules in our solar system came from the interstellar medium and suffered an uncertain amount of chemical processing before reaching their eventual resting place in the Sun, the planets, and smaller bodies. It is of fundamental importance to understand the extent to which the chemical speciation and form of this material was determined prior to arrival in the solar nebula. How much of the solid material in meteorites or comets has survived largely unaltered from the interstellar dust? Is the gas phase speciation of important atoms (oxygen, carbon, and nitrogen especially) determined prior to arrival in the solar nebula or is it determined by local processing? The answers to these questions affect how we develop our concepts of solar system and planetary origin.

## Chemical Heterogeneity and Imperfect Mixing in the Solar Nebula

I have shown that for the "standard" accretion disk model of the solar nebula, the efficiency of mixing the products of thermochemical processing from small to large disk radii depends only on the ratio of  $D/\nu \equiv k$  ( $D$  = eddy diffusivity,  $\nu \equiv$  eddy viscosity). This quantity is at most of order unity. In the steady-state limit, where mixing is most efficient, the fractional contamination at radius  $R$  due to the thermochemical processing at radius  $R_p < R$  is found to be  $\sim (R_p/R)^\gamma$  where  $\gamma \equiv 3/2k \sim 1$ . Since most of the mass resides at large radii  $R \gg R_p$ , I conclude that most of the solar nebula was not contaminated by the consequences of thermochemical equilibria that were established at "small" radii (e.g., of order 1 AU). Interstellar dominance is implied for most solar nebula speciation and is predicted for cometary speciation except possibly for a small contamination due to catalyzed hydrogenation of CO to CH<sub>4</sub> and other hydrocarbons. If primordial giant planets possessed accretion disks then the chemical speciation of the disk may have been primarily that of the solar nebula. However, greater mixing and gas processing (including conversion of CO to CH<sub>4</sub> and N<sub>2</sub> to NH<sub>3</sub>) might have occurred in these circumstances. The formalism developed here may have applicability to the interpretation of compositional gradients in the nebulae of Young Stellar Objects, and may be relevant to the survivability of interstellar dust grains.

There are a few ways in which this "standard" model could be violated. One is to have a low angular momentum cloud which collapses to a small initial radius before expanding by viscous effects. All the material could then be processed at the initial collapse. However, this requires an unusually low angular momentum. Another possibility, suggested by Prinn, is that the effective viscosity  $\nu$  of the disk is lower than commonly estimated. This is possible, in principle, since the origin of this "viscosity" is poorly understood. However, it cannot be too low otherwise the disk fragments and evolves in a way that is different from our solar system. If the "viscosity" is derived from waves, then the mixing is probably very inefficient (i.e.,  $D \ll \nu$ ), actually strengthening my results. The "standard" model might be irrelevant, however, if accretion shock processing is important.

PRECEDING PAGE BLANK NOT FILMED

## The Nature of the Accretion Shock

As gas flows in from interstellar space, an accretion shock forms high above the disk midplane. It is conventional (e.g., Cassen *et al.*, 1985) to treat the shock energy boundary condition by balancing incoming kinetic energy flux with outgoing radiative flux:

$$\frac{1}{2} \rho u^3 \simeq \sigma T_e^4$$

( $\rho$  = infall gas density,  $u$  = infall velocity,  $T_e$  = postshock temperature), at least for the simple case of no "viscous" dissipation. In fact, the temperature just below the shock front is very high, of order  $u^2/2C_p$  ( $C_p \equiv$  specific heat, including effects of dissociation and ionization). This is several thousand degrees, even at 10 AU (orbit of Saturn). Implicitly, it has been assumed in the past that this hot layer is so thin that it does not matter (i.e., gas and dust pass through too fast). In fact, this is an invalid assumption, because the *dust* is the main opacity source, yet it is not very hot. (If it is water ice, it does not heat significantly above  $\sim 200$  K.) The very low emissivity of the gas prevents rapid cooling. It can take days or months in the comoving frame for gas to cool down to  $\sim T_e$  from its peak temperature. During this period, cold dust particles are bathed in a hot radiation bath and subjected to collisions by hot atoms. This may have chemical consequences, e.g., by low energy sputtering.

### Drag Heating of Dust Passing through the Accretion Shock

Past estimates of the temperature reached by dust as it passes through the accretion shock (Wood, 1984) have omitted the fact that small particles have very low emissivity (because radius  $\ll$  IR wavelength). As a result, these particles can be much hotter than previously suspected. This work, carried out by graduate student Joel Schwartz, indicates (as an example) that dust radiation temperatures  $\sim 500$  K are possible for submicron particles at 10 AU (orbit of Saturn). This may destroy the more fragile molecules and molecular aggregates that developed within interstellar grains prior to accretion.

### References

- Cassen, P., Shu, F.H., and Terebey, S. (1985). In *Protostars and Planets II*, Univ. Arizona Press, p. 448.  
Wood, J.A. (1984). *Earth Planet. Sci. Lett.* **70**, 11.

ORIGINAL PAGE IS  
OF POOR QUALITY

ACCUMULATION OF THE EARTH FROM RUNAWAY EMBRYOS; G. W. Wetherill,  
Dept. of Terrestrial Magnetism, Carnegie Institution of Washington,  
Washington, D.C. 20015.

Most earlier 3D simulations of the final stages of accumulation of the terrestrial planets assumed initial states based on the theories of embryo formation of Safronov (1) and Nakagawa et al (2). These are characterized by a "marching front" of a large number of sublunar-size bodies of nearly equal mass, followed by a power law tail of smaller bodies (3,4,5). It now seems more likely that terrestrial planet embryo formation involved runaway growth to form a smaller number of larger embryos (6). The principal cause of the runaway is energy equipartition that lowers the velocities of the largest bodies relative to those of the average mass bodies of the swarm (7,8).

Only a few simulations using runaway initial planetesimals have been reported (5). In the present work 42 new simulations of the growth of planets from 151 runaway embryos have been calculated for comparison with 38 "orderly growth" simulations reported earlier. An initial surface density of 20 g/cm<sup>2</sup> between 0.7 and 1.1 A.U. is assumed. This decreases uniformly inside and outside this range as described previously (5). Runaways were assumed to be limited to a spacing of 4 Hill sphere radii. The principal mass of the initial swarm consisted of 29 bodies ranging in mass from  $6.4 \times 10^{26}$  g at 1.1 A.U. to  $1.7 \times 10^{26}$  g at 0.7 A.U. The smallest bodies were closely spaced ( $\sim 10^{-3}$  A.U.)  $7 \times 10^{23}$  g objects at 0.45 A.U. This distribution was not arbitrary, being constrained by the mass, energy, and angular momentum of the present terrestrial planets and the limits to runaway growth. The calculations were grouped into sets corresponding to different assumptions regarding the fractionation of impact energy into heating and fragmentation, and rate of completion of embryo growth as a function of semi-major axis.

In general the results are similar to those found for orderly non-runaway growth. In 60% of the calculations 2 final planets  $> 1.5 \times 10^{27}$  g were formed, and 3 final planets of this size were formed in 36% of the cases. The total number of final planets larger than one lunar mass ranged from 2 to 6 and averaged 3.6. The time scale for growth was the same as found before. Some differences in final mass distributions were found for variations in the initial conditions, but these were confined to the formation of the smaller planets.

In all cases the growth of the largest planets was punctuated by giant impacts. For those 25 cases where the number of large final planets was 2, the body with the greater heliocentric distance (usually  $\sim 1.0$ ) was designated "Earth". For that body the number of "catastrophic" events are tabulated below:

<u>Event</u>	<u>Average No./Simulation</u>
Mercury < impact mass < Mars	3.0
Mars < impact mass < 2 X Mars	1.2
2 X Mars < impact mass	0.8
Impact energy > 1/2 gravitational binding	0.2
Impact energy > gravitational binding	0
Rotational instability	0.04
Within 50% of rotational instability	2.1

Typically, "Earth" was totally melted by the time it grew to  $\sim 60\%$  of its final radius, requiring a time  $< 10^7$  years.

## References:

- (1) Safronov, V. S., Evolution of the protoplanetary cloud and formation of the earth and planets, Moscow: Nauka, 1969. Translated for NASA and NSF by Israel Program for Scientific Translations, 1972. NASA TT F-677.
- (2) Nakagawa, Y., Hayashi, C., and Nakazawa, K., 1983. Accumulation of planetesimals in the solar nebula, Icarus 54, 361-376.
- (3) Wetherill, G. W., 1985. Giant impacts during the growth of the terrestrial planets, Science 228, 877-879.
- (4) Wetherill, G. W., 1989. Accumulation of Mercury from planetesimals. In press, Mercury (C. Chapman and F. Vilas, eds.) Univ. of Arizona Press, Tucson.
- (5) Wetherill, G. W., Accumulation of the terrestrial planets and implications concerning lunar origin, 1986. Origin of the Moon, (W. K. Hartmann, R. J. Philips, and G. J. Taylor, eds.) pp. 519-550.
- (6) Wetherill, G. W., and Stewart, G. R., 1988. Accumulation of a swarm of small planetesimals. In press, Icarus.
- (7) Stewart, G. R., and Kaula, W. M., 1980. Gravitational kinetic theory for planetesimals, Icarus 44, 154-171.
- (8) Stewart, G. R., and Wetherill, G. W., 1988. Evolution of planetesimal velocities, Icarus 74, 552-553.

## PLANETESIMAL ACCRETION

Dominique Spaute, Planetary Science Institute

We developed a numerical simulation based on a Monte-Carlo statistical method permitting the study of the dynamical and collisional evolution of a  $10^{10}$  particle swarm assuming a low mass density of  $.1 M_{\odot}$  in the primitive solar nebula. More details of this model can be found in Spaute et al. (1988, COSPAR). This simulation allows us to follow the distribution of the particles as a function of their size and their heliocentric distance to the primary. The velocity distribution can be studied on a less accurate but nonetheless valuable level.

Wetherill and Stewart (1988, *Icarus*, in press), using a different numerical model, presented results concerning the runaway growth of large embryos in the terrestrial zone. We have taken their initial conditions and tried to match the physical phenomena they used as closely as possible (e.g., effects of gravitational stirring, gas drag and cross-section enhancement factor). Using our code, we have reproduced the same shape for the velocity and mass distributions as Wetherill and Stewart. The timescales are marginally different; nevertheless, such a good correspondence between results obtained using two different approaches reinforces the validity of both the codes and their physical meaning.

We are now: a) studying in more detail the effects of distant encounters and dynamical isolation of the large embryos using a "discrete body algorithm" allowing us to follow each large particle as a single entity with its own corresponding size and elliptic elements; and b) using the capability of our code to handle a heliocentric distance distribution to study the radial migration of the swarm particles under gas drag, resonances, and gravitational interactions effects. This phenomena is of interest for it might affect the growth of the large embryos in either way.

PLANETARY ACCRETION BY RUNAWAY GROWTH: FORMATION OF THE EARTH  
Chris Patterson, Los Alamos National Laboratory  
Dominique Spaute, Planetary Science Institute

The outcome of runaway growth is examined in the Earth's accretion zone. It is found that runaway growth of a few planetary embryos quickly leads to high relative velocities ( $>10$  m/sec) of the 1- to 10-km diameter swarm planetesimals due to gravitational stirring. Such velocities cause the swarm planetesimals to fragment by mutual collisions. This fragmentation of swarm planetesimals during runaway growth leads to a size distribution with most of the mass in fragments less than 10-m diameter independent of the initial planetesimal size.

In the presence of solar nebula gas, these fragments will have reduced relative velocities and enhanced accretion cross sections with the embryos, thereby aiding in their rapid runaway growth. Orbital decay due to gas drag enables fragments to be continuously fed to the embryos and greatly expands their feeding zones. It seems likely that much of the Earth accreted from fragments originally at much farther distance from the Sun, possibly including fragments originally in the asteroid belt.

## NUMERICAL N-BODY SIMULATION OF THE ACCRETION PROCESS OF THE TERRESTRIAL PLANETS.

Noriyuki Namiki<sup>1,2</sup> and Takafumi Matsui<sup>2</sup>. <sup>1</sup>Dept. of Earth, Atmospheric, and Planetary Sciences, MIT, Cambridge, MA 02139, U.S.A.; <sup>2</sup>Geophysical Institute, Faculty of Science, Univ. of Tokyo, Bunkyo-ku, Tokyo 113, Japan.

*Introduction.* It is widely believed that planets are formed by an accretion of planetesimals [1]. Although this basic framework has been now accepted by many scientists, there still remain many unresolved issues, such as the planetary formation time, whether or not there is runaway growth, the degree of mixing of planetesimals at different orbital distances, and so on. These issues are fundamental for understanding planetary compositions, the differentiation of planetary interiors, thermal histories, and the origin of atmospheres and oceans [2]. We have developed a numerical code for a three-dimensional N-body simulation of the planetary formation process by modifying Cox and Lewis' two dimensional model [3]. The planetary formation time so obtained is much longer than that expected from previous work [4].

*Numerical Method.* Planetesimals basically follow Keplerian motion because most of the mass is contained in the sun. Their orbits change only in response to mutual gravitational interactions when planetesimals experience close encounters. Because of this, the motion of two planetesimals can be separated into two regions according to the radius  $R_s$  of the "sphere of influence." If the distance between an encountering pair is larger than  $R_s$ , each planetesimal is assumed to follow Keplerian motion independently. When two planetesimals approach within  $R_s$ , their mutual gravitational attraction becomes sufficiently large that their motions depart from Keplerian orbits.

Once a pair of planetesimals encounter each other, coagulation or gravitational scattering changes their orbits. The initial condition when two planetesimals enter the "sphere of influence" determines whether coagulation or scattering occurs. When two planetesimals coagulate upon collision, a new planetesimal with mass equal to the sum of the two planetesimals is formed. The orbit of the new planetesimal is given by conservation of momentum. When two planetesimals are scattered, the outcomes may be divided into two cases depending on their relative velocity. If the relative velocity is higher than  $0.07V_{\text{escape}}$  [5], the relative motion of the planetesimals is assumed to be given only by their mutual gravitational force, and their center of mass is assumed to follow Keplerian motion around the sun (the two-body approximation). When the relative velocity is lower than  $0.07V_{\text{escape}}$ , the perturbation is chaotic and its behavior is not well understood [6]. In the latter case we use the Monte Carlo method to perturb the two orbits assuming isotropic scattering. Energy conservation and angular momentum conservation must be satisfied during encounter. A summary of the numerical procedure is shown in Figure 1.

*Numerical Results.* We have conducted numerical simulations for three sets of cases. In *case 1*, the motion of planetesimals is restricted to lie in a plane (two-dimensional assumption) and no gravitational scattering occurs upon encounter (Figure 2a). Curves with the same initial number of planetesimals evolve into three clusters of curves corresponding to the initial distributions of orbital eccentricity  $e$  from 0 to 0.1, 0.3 and 0.5, respectively. The planetary formation time is dependent on  $e$ . That is, large  $e$  increases the number of encountering pairs. As a result encounters occur more frequently and planetary accretion proceeds more rapidly. The planetary formation time is shown to be of the order of the  $10^{5-6}$

yr in this case. In *case 2*, the two-dimensional assumption is retained but gravitational scattering upon encounter is assumed to occur (Figure 2b). The planetary formation time ( $\approx 10^4$  yr) is shorter than that of case 1 because  $e$  in case 2 is larger than in case 1 when the same number of planetesimals remain. The planetary formation time does not depend on the initial number of planetesimals, but rather on initial  $e$ . In *case 3*, the motions of planetesimals are three dimensional (Figure 2c). The simulations are stopped at  $t \approx 10^6$  yr because of computational time constraints. The planetary formation time is much longer than those of the two dimensional cases and is in excess of  $10^6$  yr.

For all cases, a large value of  $e$  shortens planetary formation time. However, a large value of orbital inclination  $i$  causes the number density of planetesimals to decrease, which then decreases the frequency of encounters and thus lengthens the planetary formation time. In general, accretion in three dimensions takes longer than in two.

*References.* [1] V.S. Safronov (1972) *NASA Tech. Transl.*, TTF-677, 206 pp. [2] T. Matsui and Y. Abe (1986) *Nature*, 319; 303. [3] L.P. Cox and J.S. Lewis (1980) *Icarus*, 44; 706. [4] G.W. Wetherill (1985) *Science*, 228; 877. [5] G.W. Wetherill and L.P. Cox (1984) *Icarus*, 60; 40. [6] S. Nishida (1983) *Prog. Theor. Phys.*, 70; 93.

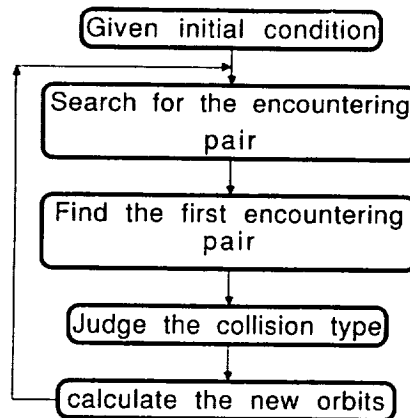


Figure 1. Flow chart of the algorithm.



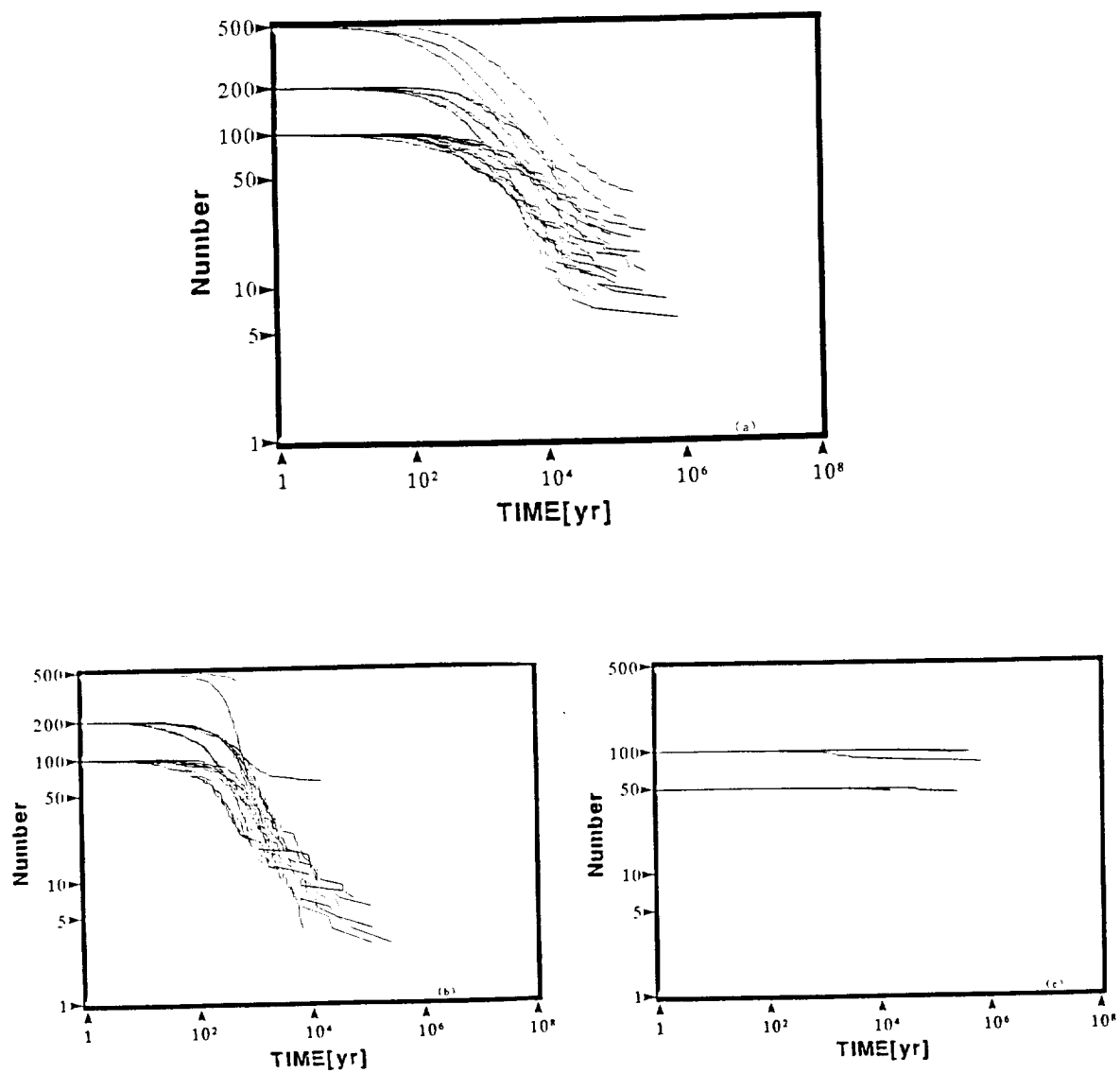


Figure 2. Temporal variations in the total number of planetesimals for (a) Case 1, (b) Case 2, (c) Case 3.

# PLANETESIMAL ACCRETION STUDIES: EFFECTS OF NUMERICAL PARAMETERS

D. Spaute, D.R. Davis, and S.J. Weidenschilling  
(Planetary Science Institute)

Planet formation in low mass models of the solar nebula invokes accretionary growth of planetesimals in at least some phase of planet evolution. Numerical simulations of this process have proliferated recently in attempts to understand the many interrelated phenomena involved. Two general classes of problems need to be addressed to develop realistic simulations of planetary accretion: (a) understanding and modeling the complex physical processes that are involved; and (b) developing numerical algorithms that combine these physical processes into a realistic simulation of accretionary growth. Recent progress has been made in understanding and modeling mutual gravitational stirring by an interacting swarm of particles (1,2), collisional cross-section of orbiting bodies (3), and gas drag and resonances (4). Additional work has recently focused on (b), namely on numerical binning algorithms used to model the size distribution during accretionary growth. Patterson and Spaute (5) found that the algorithm used by Greenberg et al. (6) led to unrealistically short growth times for planetary embryos, while Ohtsuki et al. (7) found that their numerical code produced erroneously short growth times if their bin widths exceeded a critical value. Here we present results from numerical tests on the growth algorithm that we have incorporated into a new simulation of planetesimal accretion (8).

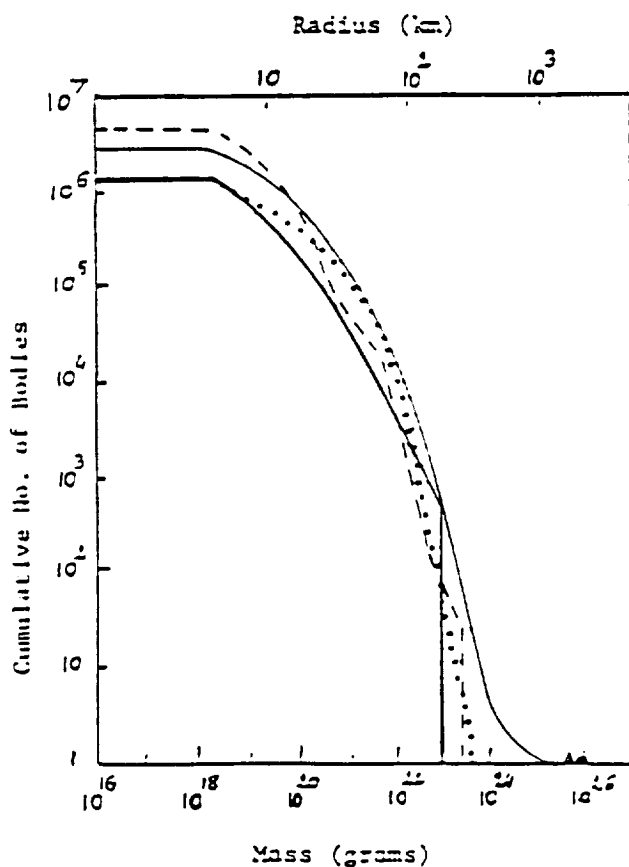
This new multi-zone code incorporates an algorithm for growth of the largest bodies, developed originally for studying growth of grains in the solar nebula (9), which incorporates a variable width bin at the large mass end of the distribution. As growth occurs the largest body at some point becomes larger than the upper limit to the then existing largest bin. A new largest bin is then opened which is initially narrower than the smaller bins. As further growth takes place, the width of this largest bin expands until it exceeds that of the other bins. The rate of expansion is determined by a parameter  $a$ , defined as the ratio of the change in mass of a particle at the upper end of the bin to that of the mean mass of particles in this bin. The  $a$  parameter has a significant effect on the growth rate of particles in the largest bin

as will be shown in the described experiments. Other concerns are the effect of the width of the mass bins on the evolution of the mass distribution as well as a parameter for the effect of the scale height of the swarm on gravitational stirring (G. Wetherill, private communication). We have run a series of numerical experiments to test size distributions and growth rates for different choices of the model parameters; Figure 1 summarizes these results. We compare our results with the same case run by Wetherill and Stewart (10) using the same initial conditions but with a different numerical technique. The initial conditions are a 0.1 Earth mass swarm of  $\sim 10$  km sized particles at 1 AU over a range of .02 AU, with relative velocity  $\sim 10$  m/sec. The physics involved are accretional collisions, gravitational perturbations, gas drag and dynamical friction. Results obtained by Wetherill and Stewart (10) are shown with the dotted line: after  $\sim 2.6 \times 10^5$  years, one embryo of  $\sim 10^{26}$  g has formed by runaway growth processes and is detached from the continuous distribution. Our first experiment uses the parameters:  $\alpha=1$  (which tends to suppress runaway), the mass ratio of 8 between bins, and the scale height parameter used in Stewart's stirring equations has a lower limit given by the Hill sphere radius of the particle. This experiment is represented by the dashed line and the small triangle showing the growth of an embryo to  $\sim 10^{26}$  g after  $\sim 2.6 \times 10^5$  years. This result is similar to Wetherill and Stewart's (10).

In our next experiment, we decreased the mass ratio between bins to  $\sqrt{2}$  as in (10), keeping the same other parameters. The heavy line shows that in this case the accretion is limited to the growth of  $\sim 10^3$  particles of  $\sim 10^{23}$  g. The choice of the bin mass ratio is consequently of huge importance. The next experiment (light line) shows evolution of the swarm with a bin mass ratio of  $\sqrt{2}$  and parameter  $\alpha$  computed to be  $>1$ . This case leads to the formation of a  $\sim 2 \times 10^{25}$  g body after  $\sim 2.6 \times 10^5$  years, but by that time no runaway had occurred.

Communications with G. Wetherill, suggested that the differences in our results might be due to our choices of the scale height for Stewart's gravitational stirring formulas. We ran an experiment using no lower boundary for this scale height of the particles as did Wetherill. In that case, our results show a decrease in stirring, resulting in very fast runaway growth with evolution

similar to Wetherill's results (dotted line) except that the embryo reaches  $\sim 10^{26}$  g in 6000 years. Consequently, we show that all the parameters included in the growth of the largest bin, the initial choice of the mass ratio and the choice of scale height in Stewart's formulas strongly affect the size distribution and the growth rate of the particles. Comparisons are also made with analytic solutions, but only for cases involving much simpler physics than is included in the simulations shown in Figure 1.



- (1) Stewart, G. and Wetherill, G. (1988). Icarus 74, 542.
- (2) Weidenschilling, S. (1989). Icarus, in press.
- (3) Lissauer, J. and Greenzweig, Y. (1989). In preparation.
- (4) Weidenschilling, S., and Davis, D. (1985). Icarus 62, 16.
- (5) Patterson, C. and Spaute, D. (1989). Icarus, submitted.
- (6) Greenberg, R., Wacker, J., Hartmann, W., and Chapman, C. Icarus 35, 1.
- (7) Ohtsuki, Nakagawa, Y., and Nakazawa, K. (1989). Icarus, submitted.
- (8) Spaute, D., Davis, D. and Weidenschilling, S. (1989). Adv. Space Res., in press.
- (9) Weidenschilling, S. (1984). Icarus 60, 553.
- (10) Wetherill, G. and Stewart, G. (1989). Icarus, in press.

# CONSTRAINTS ON THE MAGNITUDE AND TIME DEPENDENCE OF THE INTENSE EARLY BOMBARDMENT

David H. Grinspoon (Department of Planetary Sciences, University of Arizona, Tucson, AZ 85721) and William K. Hartmann (Planetary Science Institute, Tucson, AZ 85719)

Many recent studies have increased awareness of the dominance of impact processes in early crustal evolution, origin and early evolution of the atmosphere and hydrosphere, and early climatic evolution (Grinspoon and Sagan (1987), BAAS 19, 872). However, the magnitude and time-dependence of the intense early bombardment of the Earth are poorly known quantities. We are attempting to refine knowledge of this important function through the application of dynamical models and whatever observational constraints exist. The formation interval as determined through isotopic studies constrains the formation of the Earth to a few tens of My. This allows the derivation of a peak flux which was necessary to accrete the Earth on this timescale. This accretionary flux is estimated to be  $2 \times 10^9$  times the current terrestrial mass influx, at time  $t = -4.5$  Gy (Hartmann (1980) Proc. Conf. Lunar Highlands Crust 155). Crater counts of dated surfaces on the Moon reveal a flux at  $t = -4.0$  Gy of approximately  $10^3$  times the current influx. The transition between these regimes is being modeled as the consequence of a combination of accretional remnant planetesimals with a range of dynamical lifetimes and collision probabilities. A successful model for this function must also be able to reproduce the observed age distribution of lunar highlands rocks. New methods of predicting the age distribution for a given time-dependent flux are being developed.

PLANETESIMAL EFFECTS ON PLANET ORBITS, SPIN, AND HEATING.  
W. M. Kaula, Department of Earth & Space Sciences, University of California, Los Angeles.

A major problem of the origin of the Earth is why it became so different in secondary properties from Venus, the body by far the most nearly similar in primary properties: the two planets differ less than 20 percent in mass, mean density, and equilibrium black-body temperature. Several of the secondary differences-- the surface temperature, the absences of water, magnetic field, and plate tectonics in Venus-- are explicable as consequences of evolution. But there are two great differences that must depend on formation: the states of spin + satellite, the Earth being prograde with a satellite, and Venus being retrograde; and the retention of heavy primordial inert gases, especially  $^{36+38}\text{Ar}$ , of which Venus has about 80 times as much as the Earth. Dissipative processes must evolve and maintain Venus's very slow spin (1), but primordially Venus must start retrograde (2): the more so, the lower the  $1/Q$  required to slow down (3). Regarding the argon difference, attempts to explain it by nebula or solar wind effects (4,5) have remained unpersuasive. The obvious hypothesis for the two differences is the late stage impact history, as suggested by Cameron (6): the Earth got hit by a big body, degassing it and knocking off the protolunar matter, while Venus was not hit by anything nearly as large.

Hence the question is what was the population of bodies --masses and orbits-- characterizing the penultimate stage of terrestrial planet formation: what constraints can be placed on it by these differences in secondary properties of Venus and Earth (as well as the primary properties of all four planets)? Wetherill (7,8) showed that, given a suitable confinement in semi-major axis of a starting swarm of 500 planetesimals, about four planets will be obtained, with the final stages entailing impacts of bodies of about  $0.3 M_0$  at velocities of about 9 km/sec. Hence his Monte Carlo models support Cameron's (6) conjecture, but he did not calculate the spins resulting from collisions in the model, and did not explore in any detail the implications of the observed outcomes in spin and volatile retention for the planetesimal population.

Earlier discussions of the implications of planet spin rates and obliquities (9,10) concluded that they limited the size of the forming planetesimals. Indeed, Safronov's (9) main observational argument for the runaway growth of the largest body in a zone was the obliquities. This problem has been reexamined by Hartmann & Vail (11) with a model defined by distributions in mass and approach velocity & offset of impactors with the conclusion that impactors could have had masses 20% of the planet's.

We have adapted an Opik algorithm, developed for another purpose, to this problem. The main difference of the algorithm from Wetherill's is that a priori four bodies are designated as "planets"; the remainder, as "planetesimals"; and only planet: planetesimal interactions are taken into account. The application discussed here is essentially a combination of the later stages of the modelling by Wetherill (8) with the impact: spin modelling of Hartmann & Vail (11). In addition to spin orientation and magnitude, energy dissipation upon collision is calculated, since variation therein would pertain to the hypothesis of an impact-generated volatile difference (6).

The starting conditions for the runs already made approximate those of the 31 My, or 81% accreted, stage of Wetherill [p. 537 of (8)]: four planets, 81% as massive as the final, plus fifty planetesimals of masses  $m$  randomly selected from a distribution  $n(m) = k m^{-1.5}$ , with a maximum not more than 200 times the minimum, and a total mass 23.5% of the total mass of the planets. Random selections were also made of the action elements from distributions of similar form, with negative correlations of -0.3 of the eccentricities and inclinations with masses. The starting spins were all prograde, with magnitudes in accord with the empirical rule that the angular momentum densities were proportionate to  $M^{5/6}$  (3): i.e., LOD's of 19 hours for proto-Earth and proto-Venus, 27 hours for proto-Mars, and 30 hours for proto-Mercury. In the thirty runs made to date, there were no significant differences in the averages of the outcomes for Venus and Earth, but appreciable variations about these averages in individual cases for these two planets: 1. retrograde spins for 15% of cases; 2. slow downs of spins for 15%; 3. speed ups of spins to angular momenta of the Earth + Moon (i.e., LOD of less than six hours) for 10%; 5. summed energy dissipations/unit mass ranging from  $3 \times 10^6$  to  $2 \times 10^7$  J/kg (equivalent to 3,000 to 20,000° C temperature rise); and 6. orbit eccentricities ranging from 0.001 to 0.039. These effects may be too low because the  $m^{-1.5}$  formula for masses gave maxima too low: .02 to .05  $M_0$ , less than suggested by Wetherill's (8) figure. The results for Mercury were fragmentation in 90% of cases: i.e., spin ups to instability ( $\text{LOD} < 2.6\text{h}$ ), with energy dissipations of  $10^7$  to  $2 \times 10^8$  J/kg. Mars was fragmented in 50% of cases, and had dissipations of  $2 \times 10^6$  to  $4 \times 10^7$  J/kg.

The modellings are thus consistent with the hypotheses that the spin + satellite states of Venus and Earth; a greater outgassing of the Earth; the stunted growths of Mars and Mercury; and the predominantly iron composition of Mercury are all results of the late stages of their growths being impacts by planetesimals with masses ranging up to well above the Moon's. However, an appreciably greater range of

parameters needs to be explored, and better physical models of impact effects on fragmentation, satellite formation, and outgassing need to be developed.

References: (1) Dobrovolskis A. R. & Ingersoll A. P. (1980) *Icarus* 41 1-35. (2) Goldreich P. & Peale S. (1970) *Astron. J.* 75 273-284. (3) Goldreich P. & Soter S. (1966) *Icarus* 5 375-389. (4) Pollack J. B. & Black D. C. (1982) *Icarus* 51 169-198. (5) Wetherill G. W. (1981) *Icarus* 46 70-80. (6) Cameron A. G. W. (1983) *Icarus* 56 195-201. (7) Wetherill G. W. (1985) *Science* 228 877-879 (8) Wetherill G. W. (1986) Origin of the Moon, Hartmann W. K., Phillips R. J. & Taylor G. J. eds., LPI Houston, 519-550. (9) Safronov V. S. & Zvjagina E. V. (1969) *Icarus* 10 109-115. (10) Harris A. W. (1977) *Icarus* 31 168-174. (11) Hartmann W. K. & Vail S. M. (1986) Origin of the Moon, Hartmann W. K., Phillips R. J. & Taylor G. J. eds., LPI Houston, 551-566.



THREE-DIMENSIONAL CARTESIAN CODE FOR PROTOSOLAR COLLAPSE.  
Elizabeth Myhill, Department of Earth & Space Sciences, University of California, Los Angeles.

Cartesian coordinates are advantageous to study the evolution of secondary concentrations.

A numerical model to treat isothermal collapse has been completed. The code is being modified to include the equations of radiative transfer and to handle shocks that arise in the nonisothermal regime. The computational scheme is more accurate than the one developed by Boss (1) because it involves a second-order difference scheme rather than a first-order, donor cell method. This results in much less numerical viscosity acting to dampen density perturbations. The continuity and momentum equations are the principal equations governing the collapse, while Poisson's equation and the equation of state relate the gravitational potential and the pressure to the density distribution. These equations are expressed in a conservative, nondimensional form. The source terms are evaluated with a second-order centered difference method, and the advection terms are calculated with the Van Leer upwind interpolation scheme (2). The source and advection terms are evaluated separately with an update of momentum in between because this has been found to suppress numerical noise and improve energy conservation (3). A Fourier method developed by Hockney (4) for finding the potential of an isolated source distribution is used to solve Poisson's equation. The code has been vectorized to take full advantage of the CRAY-XMP supercomputer.

The Poisson solver was tested by calculating the potentials for an isolated point source and a uniform density parallelepiped. These results agreed with analytic solutions (5). The full isothermal code has been run successfully for a number of test cases. Figures 1 and 2 illustrate the collapse of a rapidly rotating cloud whose initial density is approximately 4.7 times the critical Jeans density. To follow the collapse, a surface of constant density equal to the initial cloud density was drawn after 50 and 150 iterations (Figure 1). 50 and 150 iterations correspond to 1.0 and 3.0 times the initial free fall time respectively. Figure 2 shows a density cross section cut vertically through the axis of rotation after 100 iterations.

References: (1) Boss, A. P. 1980. Astrophys. J. 236, 619. (2) Van Leer, B. 1977. J. Comp. Phys. 23, 263-275. (3) Norman, M. L. & K. H. Winkler 1986. Astrophysical Radiation Hydrodynamics, D. Reidel, Dordrecht. (4) Hockney, R. W. 1970. Meth. Comp. Phys. 9, 135-211. (5) Macmillan, W. D. 1930: The Theory of Potential. McGraw-Hill, New York.

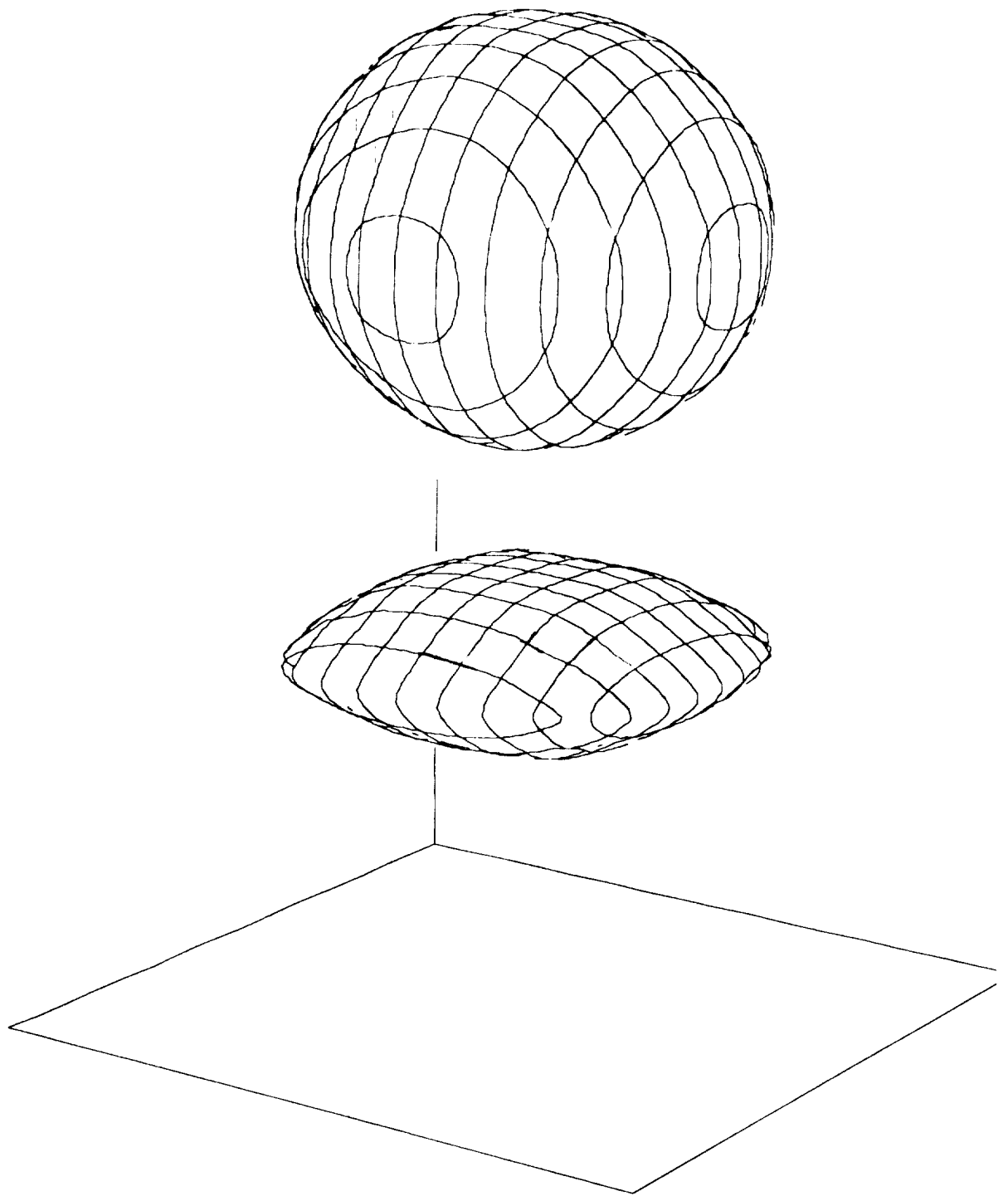


Figure 1. Surfaces of constant density of a collapsing cloud after 50 (upper) and 150 (lower) iterations, the latter of which corresponds to 3.0 free-fall times.

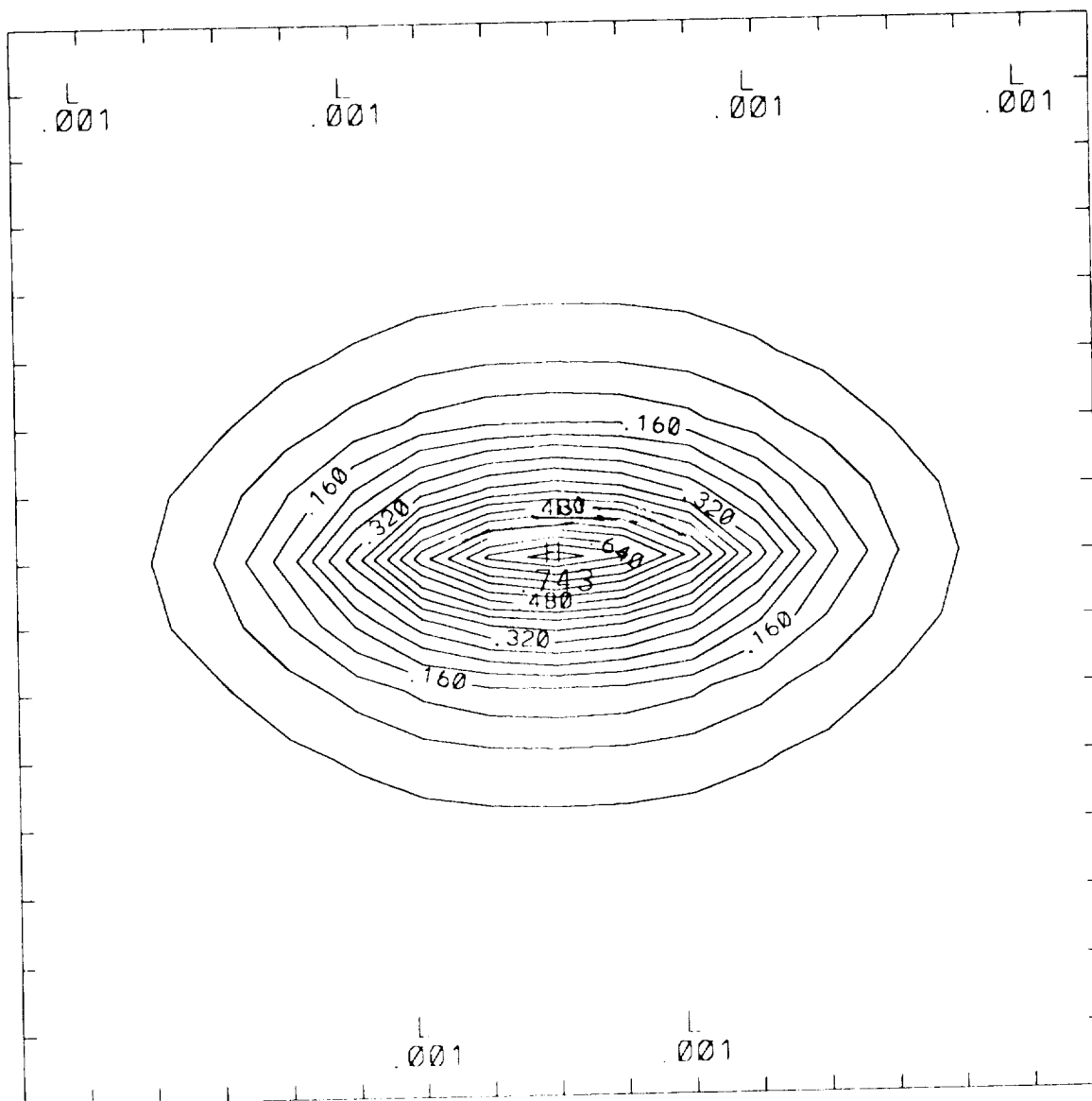


Figure 2. Density cross section of a collapsing cloud after 100 iterations. This figure is computed using  $17 \times 17 \times 17$  cells. At least twice as many cells will be used in the final computations.

# 3D SOLAR NEBULA MODELS: IMPLICATIONS FOR EARTH ORIGIN

Alan P. Boss, DTM, Carnegie Institution of Washington

Formation of the solar nebula through the collapse of a dense interstellar cloud has been studied through a set of 16 three dimensional (3D) numerical models [1]. This abstract summarizes the implications of these models for the dynamics and thermodynamics of terrestrial planet formation.

The solar nebula models are produced by calculating the collapse of initially uniform density and rotation, spherical clouds, onto protosuns of variable mass. The calculations involve solutions of the three dimensional equations of hydrodynamics, gravitation, and radiative transfer in the diffusion approximation. Improvements over previous calculations [2] include updated opacities, enhanced spatial resolution for thin disks, a central sink cell to simulate the growing protosun, and initial densities sufficiently high to reach phases where the protosun has formed and is surrounded by a growing solar nebula. The detailed thermodynamical treatment means that the temperature of the nebula is self-consistently determined. Forming the nebula from a collapsing cloud means that *ad hoc* initial conditions for the nebula (e.g., strongly unstable disks) are avoided.

Three parameters have been varied in the 16 models: the initial mass of the protosun (0.0 to  $1.0 M_{\odot}$ ), the initial mass of the nebula (0.10 to  $1.0 M_{\odot}$ ), and the initial specific angular momentum of the nebula ( $2.0 \times 10^{18}$  to  $6.2 \times 10^{19} \text{ cm}^2 \text{ s}^{-1}$ ). The final models have protosun masses ranging from 0.001 to  $1.8 M_{\odot}$  and nebula masses ranging from 0.002 to  $1.02 M_{\odot}$ . Hence the models represent a wide range of possible solar nebula models (from minimum mass to massive nebula models) as well as a considerable range of evolutionary phases (both through the time evolution of each model as well as through the different total masses in each model).

## DYNAMICAL IMPLICATIONS:

(1) The solar nebula may have been significantly nonaxisymmetric, i.e., bar-like, and gravitational torques within a nonaxisymmetric nebula may have been responsible for nebula evolution and partial clearing on time scales of  $10^6$  to  $10^7$  years. If so, this would obviate the need for ascribing nebula evolution to viscous torques.

(2) Surface densities in the inner solar nebula are high enough in essentially all the models to account for terrestrial planet formation through the gravitational instability of a dust sub-disk [3,4]. However, in the outer solar nebula densities are insufficient for a similar rapid formation of rocky cores [5], unless the nebula is quite massive ( $\approx 1 M_{\odot}$ ).

## THERMODYNAMICAL IMPLICATIONS:

(1) Compressional energy produced by the collapse of the presolar cloud was trapped within the nebula for time scales on the order of  $10^5$  years. Midplane temperatures at 1 AU could well have reached 1500 K or more during this phase [6]. In addition, if the nebula was strongly nonaxisymmetric, temperatures at 1 AU could have varied substantially in azimuth, opening up the possibility of periodic thermal cycling of solids moving on Keplerian orbits.

(2) High temperatures in the inner solar nebula imply that sequential condensation of solids as the nebula cooled may well have occurred [7]. However, maximum temperatures may have been regulated to  $\sim 1500$  K by the thermostatic effect of the opacity. Because the nebula opacity at high temperatures is primarily provided by iron grains, which vaporize around 1420 K [8], the opacity drops precipitously when temperatures reach  $\sim 1500$  K, leading to enhanced radiative cooling. When temperatures drop below  $\sim 1500$  K, the iron grains reform, the opacity rises, and radiative losses drop, effectively regulating the temperature. This means that equilibrium condensation sequences may

have to be recalculated in order to take into account finite initial temperatures and hence survival of the most refractory interstellar grains.

(3) While cooling from high temperatures implies equilibrium condensation sequences were operative, condensation need not have led to a strong compositional gradient in the terrestrial planet region, because of the thermostatic effect previously noted. That is, if the thermal gradient is nearly zero because of the thermostat effect, condensation sequences may have been similar throughout the inner solar nebula. Furthermore, stochastic orbital evolution of large planetesimals (leading to large scale radial mixing) tends to erase the effects of any primordial compositional gradients [9].

(4) High temperatures in the inner solar nebula may have been directly responsible for the depletion of volatile species (C, N, H<sub>2</sub>O) in the terrestrial planets by factors of order 10<sup>4</sup> or more compared to solar abundances [10]. The volatiles may have been removed from the terrestrial planet region along with the rest of the gaseous portion of the nebula through dynamical evolution of the nebula itself or through the enhanced early solar wind.

(5) While temperatures around 1500K imply that equilibrium chemistry is likely to have occurred in the inner solar nebula and that thermochemistry was the dominant energy source [10], vaporization of iron grains at the midplane may have limited the effectiveness of the Fe catalysis (Fischer-Tropsch-type reactions) suggested as a means of converting CO to CH<sub>4</sub> [10] and of forming other organic compounds found in carbonaceous chondrites, at least during these hot early phases. The question then becomes, how much cooling occurred prior to inner solar nebula removal?

#### REFERENCES:

- [1] Boss, A. P. (1989), *Astrophys. J.*, submitted.
- [2] Boss, A. P. (1985), *Icarus*, **61**, 3.
- [3] Safronov, V. S. (1969), *Evolution of the protoplanetary cloud and formation of the Earth and planets* (Moscow: Nauka), 206 pp.
- [4] Goldreich, P. and Ward, W. R. (1973), *Astrophys. J.*, **183**, 1051.
- [5] Lissauer, J. J. (1987), *Icarus*, **69**, 249.
- [6] Boss, A. P. (1988), *Science*, **241**, 565.
- [7] Grossman, L. (1972), *Geochim. Cosmochim. Acta*, **36**, 597.
- [8] Pollack, J. B., McKay, C. P., and Christofferson, B. M. (1985), *Icarus*, **64**, 471.
- [9] Wetherill, G. W. (1986), in *Origin of the Moon*, eds. W. K. Hartmann, R. J. Phillips, and G. J. Taylor (Houston: Lunar and Planetary Institute), p. 519.
- [10] Prinn, R. G. and Fegley, B., Jr. (1988), in *Origin and Evolution of Planetary and Satellite Atmospheres*, eds. S. K. Atreya, J. B. Pollack, and M. S. Matthews (Tucson: University of Arizona), in press.
- [11] Larson, R. B. (1969), *M.N.R.A.S.*, **145**, 271.
- [12] Wood, J. A. and Morfill, G. E. (1988), in *Meteorites and the Early Solar System*, eds. J. F. Kerridge and M. S. Matthews (Tucson: University of Arizona), in press.

## Particle-gas dynamics in the protoplanetary nebula

Jeffrey N. Cuzzi (Ames Research Center), Joelle M. Champney (ATM, inc.), Thomas J. Coakley (Ames Research Center), and Anthony R. Dobrovolskis (U. C. Santa Cruz)

We have developed a fully viscous, two-phase numerical model of the protoplanetary nebula which treats the situation in which a layer of macroscopic particles, settling toward the nebula midplane, generates vertical wind shear and turbulence in the surrounding gas which prevents further settling. Our model uses a “perturbation” approach to the problem in which the full state (density and 3-D mean velocity vector of both gas and particles) is broken down into a zero order solution and a smaller, first order perturbation solution. The numerical model itself is only used to solve for the small first-order perturbed quantities. Our investigations into the properties of shear-driven turbulence, and those of others, have demonstrated that a variety of parametrizations provide satisfactory representations of turbulence in real shear flows of many sorts by relating the turbulent velocity fluctuations to the mean *local* properties of the flow such as its shear. We have explored two of these models this year; a so-called “zero-equation” or Prandtl model and a so-called “two-equation” or  $k - \epsilon$  model. Finally, we have developed a simple new model relating particle diffusion to gas phase turbulence using a size-dependent “Schmidt number”.

**Parametrization of turbulent viscosity** The simplest possible estimate for the turbulent viscosity  $\nu_T$  due to shear comes from a mixing length model:

$$\nu_T = \frac{\Delta V \delta}{Re^*} \simeq \frac{2\pi\eta^2 r^2 \Omega}{(Re^*)^2}$$

where  $Re^*$  is the critical Reynolds number,  $\delta = (\nu_T P)^{1/2}$  is the boundary layer thickness in a system rotating with period  $P = 2\pi/\Omega$ , and  $\Delta V$  is the velocity difference across the boundary layer which, in our case, depends on the nebula pressure gradient parameter  $\eta$  (Nakagawa et al. 1986). Using the value of  $\eta = 1.8 \times 10^{-3}$  and  $Re^* = 500$ , we get  $\nu_T \sim 3 \times 10^9 \text{cm}^2 \text{sec}^{-1}$ . This viscosity will act on the small local scales appropriate to structure and evolution of the particle layer, and independently of the more uncertain presence or absence of buoyancy-driven convective turbulence. The corresponding depth of the shear layer  $\delta \sim \Delta V P / Re^*$  only amounts to  $10^{-4} - 10^{-5}$  of the radius of the nebula, compared to a typical gas scale height of  $10^{-1}$  of the nebula radius.

This year, we successfully coded two new parametrizations for a spatially variable turbulent viscosity  $\nu_T$ , both being more sophisticated than this simple constant  $\nu_T$  mixing layer approach. Thus, our model of the particle density evolution is now fully self consistent. The zero-equation or Prandtl model has the form

$$\nu_T(x) = c_0 \delta^2 \frac{\partial w}{\partial x}.$$

This model allows the viscosity to be largest where the turbulence is largest; i.e. in the region of largest velocity shear. The two-equation model is considerably more complex. Basically, it solves the transport equations for the turbulence itself. Turbulence propagates away from the local region of its generation (the region of maximum wind shear) to the extent permitted by the rate at which it dissipates. The model is characterized by two more partial differential equations. They determine the distribution of the turbulent kinetic energy  $k$  and the turbulent dissipation  $\epsilon$ ; hence the appellation  $k - \epsilon$  model. The advantage of the  $k - \epsilon$  model is that it can provide the most realistic spatial distribution of the turbulence. For example, in the nebula, the vertical velocity shear at the midplane is zero by symmetry; consequently, the Prandtl model above would predict

$\nu_T = 0$  at the midplane. However, the turbulence and therefore the turbulent viscosity is probably not zero there, since turbulence can propagate away from its source in the region of large shear.

**Schmidt number:** Having a good parametrization for the turbulent viscosity in the nebula, we may now use our particle mass conservation equation to determine the extent to which gravitational settling is impeded by the turbulence generated by the layer itself. The diffusion coefficient in the particle mass conservation equation is just the gas viscosity  $\nu_T$  divided by the Schmidt number,  $Sc$ . We have come up with a simple and physically reasonable parametrization for  $Sc$ , by extending a line of argument presented by Safronov (1972), which is of the form

$$Sc = (1 + r^2/R_0^2)^2$$

for the Stokes regime, and obtain a similar form with slightly different scale constant for the Epstein regime. This expression makes it clear that the importance of diffusion will decrease with particle size.

**Results of the viscous model** Last year, we presented comparisons with the analytical (inviscid) solutions of Nakagawa et al. (1986) for a realistic range of nebula parameters, obtained by setting our nebula viscosity equal to zero to make our results consistent with their formulation. The agreement was quite good, as shown in Cuzzi et al. (1989).

Of course, without viscosity, shear stresses are negligible in the Nakagawa et al. model (they do not formulate the viscous terms at all). In these inviscid models, the gas entrained within the particle layer is driven to more rapid orbital velocity *only* by *local* drag with the particles. As the particles settle and the "headwind" experienced by solitary particles (those, for example, at higher altitudes) decreases, particles in the layer cease their inward radial drift. Since the orbital velocity difference has not reached zero, even the gas within the layer drifts slowly outward relative to the surrounding gas. In the absence of turbulence, the particle layer merely continues to settle.

We have determined the turbulent viscosity in our models self-consistently using both the Prandtl and the  $k - \epsilon$  models, although we have had insufficient time to explore these results over a wide range of model parameter space. The presence of shear stresses due to this turbulent viscosity produces a very different behavior for the mean flow than seen in the Nakagawa et al. solutions. Figure 1 shows the vertical profile of the radial velocity for the gas in a case when the particle density at the midplane starts out at ten times the gas density. The shear stress exerted at the boundary layer, not allowed for in the inviscid model, exerts itself as a torque on the particle layer which causes it to drift radially inward. Simultaneously, an Ekman-like flow is seen within and just above the particle layer, where the reverse torque is applied to the gas sending it streaming radially outward at a higher velocity than predicted by the inviscid model.

As shown in figure 2, the particles partake of the outward drift as well as of the inward drift. That is, in the Ekman layer just above the particle layer, particles are being advected outwards by the streaming gas. Those particles that make it into the central dense layer drift inwards as a group. As in the inviscid model, there does seem to be a residual outward drift of the gas relative to the particles within the particle layer.

Finally, the time history of the particle density profile is seen in the dashed curves. Even for a Schmidt number as small as 5 - 10, the particle layer is "puffed up" by turbulence and is not able to settle into a sufficiently dense state to allow the onset of gravitational instability (Weidenschilling 1980).

## Bibliography

Champney, J. M., J. N. Cuzzi, and T. J. Coakley (1989) A turbulent two-phase flow model for nebula flows; in preparation.

Cuzzi, J. N., J. M. Champney, T. R. Coakley, and A. R. Dobrovolskis (1989) Particle-gas dynamics in the protoplanetary nebula; L. P. S. C. Abstracts XX, Part 1, pgs. 216-217

**Additional references:** Nakagawa, Y., M. Sekiya, and C. Hayashi (1986) Settling and growth of particles in a laminar phase of a low-mass solar nebula; *Icarus*, 67, 375-390

Safronov, V. S. (1972), Evolution of the protoplanetary cloud and the formation of the Earth and planets; NASA TTF-677

Weidenschilling, S. J. (1980) Dust to planetesimals: settling and coagulation in the solar nebula; *Icarus*, 44, 172-189

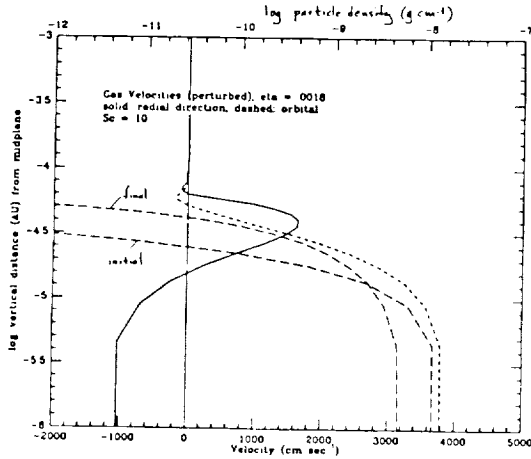


FIG. 1

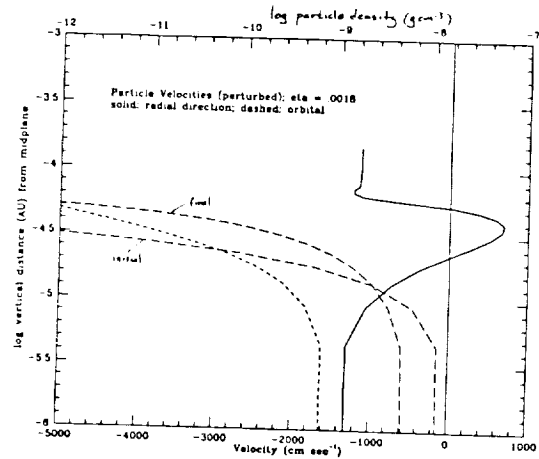


FIG. 2

Figure 1: Gas velocities ( $\text{cm sec}^{-1}$ ), and relative to pressure supported motion, obtained from our code. Solid line: radial velocity; short dash: azimuthal velocity. The long dashed curves are particle density profile at the beginning and at the end of a 6-year evolution (upper scale:  $\log \rho_p$ , in  $\text{g cm}^{-3}$ ). In these runs, the Schmidt number was 10.

Figure 2: Particle velocities, relative to circular Keplerian motion. Solid line: radial velocity; short dashed line: azimuthal velocity. Long dash: particle density profile at the beginning and at the end of a 6-year evolution (upper scale:  $\log \rho_p$ , in  $\text{g cm}^{-3}$ ). In these runs, the Schmidt number was 10.



ATOMIC AND PLASMA PROCESSES AFFECTING ANGULAR MOMENTUM  
TRANSFER IN THE EARLY SOLAR SYSTEM.

W. I. Newman, Department of Earth & Space Sciences,  
University of California, Los Angeles.

The discovery of kilogauss magnetic fields associated with forming stars (1) inspires a reexamination of hydro-magnetic mechanisms for angular momentum transfer.

An early sun with a kilogauss magnetic field can be shown to create a magnetosphere that could extend to many 10's or even 100's of AU, depending on the details of the model. In this extended magnetosphere, which mimics that of Jupiter or of pulsars (2), charged particles would be obliged to corotate with the sun with velocity exceeding 1000's of km/sec. The dynamics of a solar nebula with such strong fields becomes unrecognizably altered by atomic processes such as charge exchange and collisional ionization which would ionize a substantial part of the disk's core, and provide an important mechanism for energizing and ejecting particles from the solar system. Charged particles leaving the solar system would do so with angular momenta consistent with corotation velocities that one would obtain at great distances from the sun, not the velocities appropriate to the outer envelope of the sun's atmosphere. Consequently, the angular momentum withdrawn by a given ion from the solar system could be  $10^8$  greater than the angular momentum it had when it left the sun's atmosphere. Concomitant with this picture, the transfer of angular momentum via the magnetic field to material at a great distance from the early sun would substantially reduce that field and remove the magnetic barrier to accretion of disk material. It is important to note that this mechanism may be intermittent and relatively short-lived, but could nevertheless be an important ingredient combined with other mechanisms (alpha viscosity mechanism, gravitational torquing, solar-sector spin-up mechanism, etc.) for momentum transport.

References: (1) Hartmann, L.W. & R. W. Noyes 1987. Ann. Rev. Astron. Astrophys., 25, 271-301. (2) Hill, T.W. 1979. J. Geophys. Res., 84, 6554-6558.

COMPUTER SEARCH FOR STABLE ORBITS BETWEEN JUPITER AND SATURN.  
W. M. Weibel, W. M. Kaula, W. I. Newman, Department of Earth  
& Space Sciences, University of California, Los Angeles.

A fourth-order predictor-corrector integrator, based on the direct N-body code of Aarseth (1), was applied to 125 test particles placed in orbits at uniform intervals from 5.7 to 8.8 AU, with starting eccentricities randomly distributed between 0.00 and 0.02, and inclinations between 0.000 and 0.063 radians. The orbits were integrated under the influence of Jupiter and Saturn. The results are summarized in figure 1. Particles in three zones nearly all became planet crossers or were ejected within 20,000 years:

- o 5.7-6.4 AU, within the 3:4 Jupiter commensurability;
- o 7.25-7.4 AU, around the 3:2 Saturn and 3:5 Jupiter commensurabilities; and
- o 7.8-8.8 AU, beyond the 4:3 Saturn commensurability.

After 100,000 years only three particles remained, at 7.12, 7.22, and 7.45 AU, and after 300,000 years only one particle persisted at 7.22 AU to the end of the integration at 567,000 years: almost 100 times as long as the previous most comparable study by Lecar & Franklin (2).

The orbits going unstable within 20,000 years all had oscillations in the semi-major axis from the start. Those lasting longer had slight variability in semi-major axis to start, but were eventually nudged into resonances by the secular variations. Normally, the initial changes in semi-major axis were positive; with the concomitant increase in eccentricity, the planet orbit first crossed is Saturn's 80 percent of the time. Apparently Jupiter is usually the main perturber, with outward transfer of energy disproportionate to angular momentum at resonances, reminiscent of Lindblad resonances (3).

References: (1) Aarseth, S. J. 1972. Gravitational N-Body Problem (M. Lecar, Ed.) pp. 29-43. D. Reidel Pub. Co., Dordrecht. (2) Lecar, M., & F. Franklin 1973. Icarus 73, 422-436. (3) Goldreich, P. & S. Tremaine 1980. Astrophys. J. 241, 425-441.

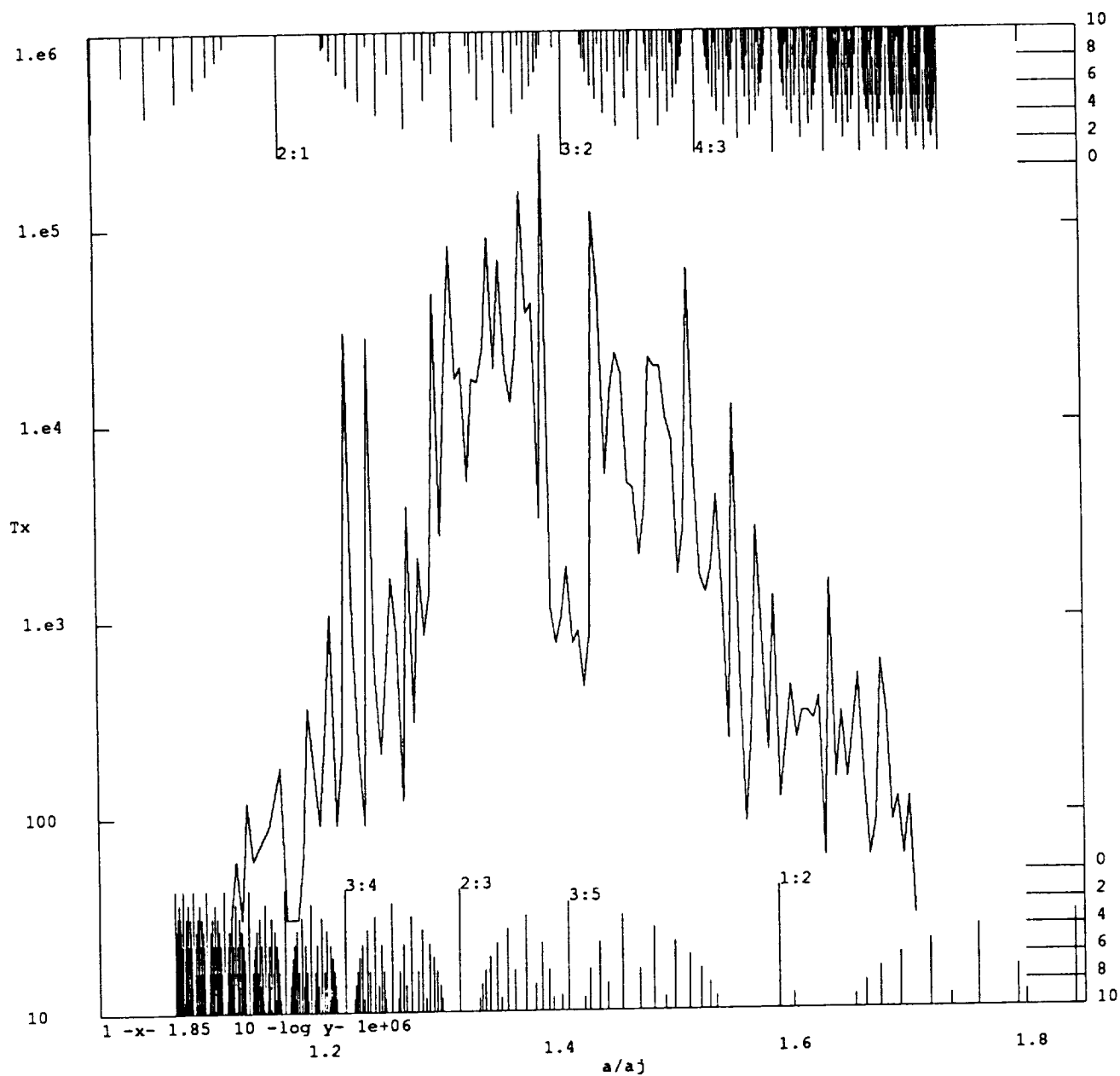


FIG. 1. Times to crossing of planet orbit in JTU (1.89 yr) at intervals of 0.025 AU from 5.7 AU to 8.8 AU. Commensurabilities up to 9th order are marked across the top for Saturn and across the bottom for Jupiter.

# ANGULAR MOMENTUM TRANSPORT BY GRAVITATIONAL TORQUES IN THE EARLY SOLAR NEBULA

Alan P. Boss, DTM, Carnegie Institution of Washington

The solar nebula probably formed from the collapse of a slowly rotating, dense interstellar cloud [1,2]. Even a slowly rotating cloud, however, may have large enough specific angular momentum ( $J/M \approx 10^{19} - 10^{20} \text{ cm}^2 \text{ s}^{-1}$ ) to ensure that much of the cloud collapses onto a disk, rather than directly onto a central protosun [3]. In this case, substantial solar nebula evolution is necessary in order to transport mass inward onto the protosun, as well as angular momentum outward. Several physical processes have been suggested for causing this early evolution: turbulent viscosity [4], magnetic stresses [5], and gravitational torques [6,7]. Additionally, these processes might have had a role in later phases in removing the last vestiges of the nebula. Convective instability [8] has been the most promising means of driving turbulence, but now appears to be defective [9]. Processes such as ambipolar diffusion control the importance of magnetic fields, and there is evidence that magnetic fields become dynamically unimportant prior to formation of protostellar disks [10]. On the other hand, angular momentum transport by gravitational torques requires only the presence of a mass distribution which is asymmetric about the nebula rotation axis (i.e., nonaxisymmetry such as spiral arms). Because of differential rotation, the secular effect of gravitational torques should be to transport angular momentum outward, and hence mass inward. The primary uncertainty about angular momentum transport by gravitational torques is the amount of nonaxisymmetry likely to have been present in the early solar nebula, and hence the magnitude of the torques. The present study attempts to quantitatively resolve this uncertainty.

Nearly all detailed solar nebula models have assumed axisymmetry and hence neglected the possible importance of gravitational torques. The two exceptions found that significant nonaxisymmetry could result from the gravitational instability of massive, cold protostellar disks [11], and from the three dimensional collapse of slowly rotating, dense clouds [2]. The former work studied the dependence of the stability of infinitely thin disks with  $\rho \propto r^{-1}$  density profiles on the mass of the central object and on the isothermal disk temperature. The latter work, while taking a rigorously correct approach to presolar nebula formation, nevertheless was prevented by inherent numerical difficulties from giving much more than an indication of the possible extent of non-axisymmetry in the early solar nebula. The present study abandons the approach of starting the evolution from interstellar cloud densities and sizes [2], and instead assumes that some aspects of the collapse phase can be approximated by an evolution starting from a much higher density, smaller size configuration. This approach allows the new numerical models to have a spatial resolution of 1 AU, perhaps large compared to many processes of interest in the nebula, but small enough to give a reasonable representation of the global stability of the nebula.

The intention is thus to study the growth of nonaxisymmetry in solar nebula models produced by the collapse of initially uniform density and rotation, spherical clouds, onto protosuns of variable mass. The calculations involve solutions of the three dimensional equations of hydrodynamics, gravitation, and radiative transfer (see [3] and [12] for details). Several improvements have been made over the previous calculations [2], including updated opacities, enhanced spatial resolution for thin disks, a central sink cell, and diffusion approximation radiative transfer. Constant volume boundary conditions are applied at a sphere of radius 40 AU. With the assumptions of equatorial

symmetry and symmetry through the rotation axis, the spatial resolution is equivalent to  $N_r = 41$ ,  $N_\theta = 23$ , and  $N_\phi = 32$ .

The models start from a uniform temperature of 10 K, and often undergo compressional heating to central temperatures of 2000 K or more. The detailed description of thermodynamics means that the temperature of the nebula is no longer a free parameter: the temperature is self-consistently determined. This aspect, coupled with the fully three dimensional and true fluid nature of the calculations, is a substantial improvement over the calculations of [11]. In addition, the fact that the present calculations include the buildup of the nebula from a collapsing cloud means that *ad hoc* initial conditions for the nebula (e.g., a strongly unstable disk) are avoided. Hence the present calculations should give the most physically accurate representation of the three dimensional structure of the solar nebula to date, subject only to the uncertainty of the initial conditions for collapse.

Three parameters have been varied in the models: the initial mass of the protosun (0.0 to  $1.0 M_\odot$ ), the initial mass of the nebula (0.10 to  $1.0 M_\odot$ ), and the initial specific angular momentum of the nebula ( $2.0 \times 10^{18}$  to  $6.2 \times 10^{19} \text{ cm}^2 \text{ s}^{-1}$ ). Nebula mass and angular momentum are allowed to flow onto the central protosun (sink cell) and are thereafter removed from the calculation of the nebula structure, except through their addition to the protosun's mass.

The amount of nonaxisymmetry can be quantified by the coefficients in a Fourier expansion of the density with respect to the  $\phi$  coordinate, in the equatorial plane of a solar nebula model. We concentrate on the amplitude of the lowest order ( $m = 2$ ) mode present in these calculations,  $a_{m=2}$ , because low order modes tend to grow the fastest and hence are the most important for global stability, because the  $m = 2$  mode quantifies the presence of bars and two-armed spiral density waves, and because the numerical resolution is best for the lowest order modes. Odd modes, e.g.,  $m = 1$ , are prevented by the assumed symmetry about the rotation axis.

All models are given an initial density perturbation with  $a_{m=2} = 0.01$ , which is roughly equal to the maximum level of steady state numerical noise associated with this computer code. Hence only values of  $a_{m=2} > 0.01$  imply physically significant growth of nonaxisymmetry. In all models calculated so far, significant growth of the  $m = 2$  mode occurs, nearly always to  $a_{m=2} \approx 0.1 - 1.0$  in the central regions; however, in the outer regions of some models,  $a_{m=2}$  decays below 0.01. Some models appear chaotic, with jagged  $a_{m=2}$  profiles, while in others  $a_{m=2}$  is relatively smooth. The phase of the  $m = 2$  mode is also of importance for angular momentum transport: a trailing spiral pattern leads to outward transport. The models also indicate when the Schwarzschild criterion for convective instability is satisfied, implying the presence of small scale turbulence in some regions of the nebula.

For a model with an initial protosun mass of  $0.1 M_\odot$ , initial nebula mass of  $1.0 M_\odot$ , and initial nebula specific angular momentum of  $6.2 \times 10^{19} \text{ cm}^2 \text{ s}^{-1}$ , at a time ( $1.024 t_{ff}$ ) when the protosun has grown to  $0.17 M_\odot$ , a trailing spiral arm phase appears, with  $a_{m=2} \approx 0.1$ , and leads to an angular momentum transport rate  $dJ/dt \approx 10^{40} \text{ g cm}^2 \text{ s}^{-2}$ , a rate high enough to transport all the angular momentum in this model in  $10^5 - 10^6$  years.

CONCLUSIONS: The calculations show that even mildly nonaxisymmetric solar nebula models may have rates of angular momentum transport through gravitational torques sufficiently large to produce global transport times small enough to satisfy astronomical evidence for nebula clearing on time scales of  $10^6$  to  $10^7$  years. Rates this high would obviate significant nebula evolution through the action of turbulent viscosity, even though the models show that turbulence is likely to be present at some level. Because a nebula evolving primarily through gravitational torques should basically maintain the radial ordering of fluid elements, little large scale mixing need occur, so that presolar elemental and isotopic heterogeneity may be preserved during the solar nebula phase.

REFERENCES: [1] V. S. Safronov and T. V. Ruzmaikina, in *Protostars and Planets*, ed. T. Gehrels (Tucson: University of Arizona Press), p. 545 (1978). [2] A. P. Boss, *Icarus*, **61**, 3 (1985). [3] A. P. Boss, *Ap. J.*, **277**, 768 (1984). [4] A. G. W. Cameron, *Moon Planets*, **18**, 5 (1978). [5] T. V. Ruzmaikina, *Adv. Space Res.*, **1**, 49 (1981). [6] R. B. Larson, *M.N.R.A.S.*, **206**, 197 (1984). [7] A. P. Boss, *M.N.R.A.S.*, **209**, 543 (1984). [8] D. N. C. Lin and J. Papaloizou, *M.N.R.A.S.*, **191**, 37 (1980). [9] W. Cabot, V. M. Canuto, O. Hubickyj, and J. B. Pollack, *Icarus*, **69**, 423 (1987). [10] M. H. Heyer, *Ap. J.*, **324**, 311 (1988). [11] P. M. Cassen, B. F. Smith, R. H. Miller, and R. T. Reynolds, *Icarus*, **48**, 377 (1981). [12] A. P. Boss, *Ap. J.*, **236**, 619 (1980).

## Rotational Dynamics of Mercury and the State of Its Core

S. J. Peale, Physics, University of California at Santa Barbara

The dynamical evolution of Mercury's spin angular momentum controlled by the dissipative processes of tidal friction and relative motion between a solid mantle and liquid core is shown to lead naturally to the current state of rotation. This is a very ordered state where Mercury's spin angular velocity is exactly 1.5 times its mean orbital angular velocity (a "spin-orbit resonance") and with the spin vector fixed in a frame precessing with the orbit and locked in a direction which deviates a small but significant amount from the direction of the normal to the orbit plane (a "Cassini state"). If Mercury had a large molten core over much of its history, the initial spin rate may be constrained to a value less than twice the mean orbital angular velocity and the initial angular separation of the spin and orbital angular momenta (obliquity) to less than  $90^\circ$ . Theoretical arguments are not conclusive about the current existence of a molten core in spite of the detection of an intrinsic magnetic field. The need for a more precise knowledge of Mercury's interior to constrain theories of planetary magnetic field generation and thermal history and to possibly constrain the initial rotation state creates a strong motivation for a direct observational determination of the core properties. A technically feasible experiment is described which uses precise measurements of the amplitude of the physical libration about the resonance spin rate, the obliquity and the lowest degree gravitational harmonic coefficients to determine the existence and extent of a Mercurian molten core.

## Rapid Jupiter Formation and the Early Solar Nebula

A. P. Boss (DTM - Carnegie Institution of Washington)

Observational evidence for nebula removal around solar-type pre-main-sequence stars implies that Jupiter formation must have been completed within  $\sim 10^5 - 10^7$  years after nebula formation. The most promising means for forming Jupiter rapidly involves runaway accumulation of planetesimals to the  $\sim 15M_{\oplus}$  size thought to characterize the solid cores of the giant planets. Rapid growth requires relatively high dust surface densities at 5 AU, on the order of  $\sigma_{cr} \approx 20 \text{ g cm}^{-2}$ .

This paper investigates the likelihood of achieving  $\sigma > \sigma_{cr}$  at 5 AU through examination of 16 models of the formation of the early solar nebula from the collapse of uniform density and uniform rotation gas clouds onto central protosuns of variable mass. Three parameters are varied in the 16 models: the initial mass of the protosun ( $0.0$  to  $1.0 M_{\odot}$ ), the initial mass of the nebula ( $0.10$  to  $1.0 M_{\odot}$ ), and the initial specific angular momentum of the nebula ( $2.0 \times 10^{18}$  to  $6.2 \times 10^{19} \text{ cm}^2 \text{ s}^{-1}$ ). The models involve solutions of the three dimensional equations of hydrodynamics, gravitation, and radiative transfer in the diffusion approximation; the protosun is represented by a point source of gravity.

Surface densities in these models exceed  $\sigma_{cr}$  at 5 AU only for massive ( $\sim 1M_{\odot}$ ) nebulae, and survival of proto-Jupiter during the subsequent evolution of a massive nebula is doubtful. Low mass nebulae ( $\sim 0.1M_{\odot}$ ) have  $\sigma \sim 0.1\sigma_{cr}$  at 5 AU. Coupled with the lack of strong evidence for direct formation of giant planets through gas disk gravitational instability, these models suggest that rapid Jupiter formation is still a major problem. Possible solutions include: (1) Alternative choices for the initial angular momentum distribution may increase  $\sigma$  at 5 AU in low mass nebulae. (2) Diffusive redistribution of water vapor and preferential condensation of ice at 5 AU could enhance  $\sigma$  provided that  $T(5 \text{ AU}) \approx 160 \text{ K}$  and that at least localized turbulence exists. The 16 models suggest that it is feasible to satisfy both of these requirements. (3) Subsequent nebula evolution through the action of gravitational torques may enhance surface densities in the outer nebula in a fashion similar to nebulae subject to viscous evolution.



## THE DYNAMICAL EVOLUTION OF THE PROTOSOLAR NEBULA

STEVEN P. RUDEN

Department of Astronomy, University of California, Berkeley

JAMES B. POLLACK

Space Science Division, NASA-Ames Research Center

We calculate the global evolution of protostellar nebulae for a variety of initial disk masses and angular momenta. Although we approximate the viscous stress by an alpha model, we calibrate the constant alpha in terms of the properties of turbulent thermal convection. As the evolution proceeds, the nebula viscously spreads and is partially accreted by the proto-star. The consequent decrease of the surface density renders portions of the disk optically thin in the vertical direction. When the optical depth decreases below a critical value, we assume the disk is unable locally to sustain thermal convection and the turbulent viscosity and energy dissipation cease. We further assume that once convection subsides no other sources of turbulent stress take its place. We calculate the resulting disk profiles under these assumptions and make comparisons to the solar system. We find that 1) moderately viscous disks with  $\alpha \sim 10^{-2}$  evolve to optically thin conditions in  $\sim 10^5$  years, 2) the resulting disk radii are primarily sensitive to the initial amount of nebular angular momentum and insensitive to the initial disk mass, 3) significant amounts of optically thin mass can remain in the disk if the convective efficiency is low (alpha less than  $10^{-3}$ ), 4) the heating of the disk surface by the protosun is unable to alter the convective evolution, 5) the optically thin remnant gas disk can be dispersed by a typical T Tauri wind, 6) constraints on giant planet formation require greater than or equal to  $10^{-2}$  and may require a non-convective mechanism for viscous stress in optically thin regions.

## **Some Unsolved Problems in Evolutionary Dynamics in the Solar System**

S. J. Peale, Physics, University of California at Santa Barbara

Several unsolved problems in the evolutionary histories leading to current dynamical configurations of the planets and their systems of satellites are discussed. These include the possibilities of rather tight constraints on the primordial rotation states of Mercury and Venus and the stabilizing mechanism for the latter's retrograde spin, a brief mention of the problem of origin of the moons of Earth and Mars, the excessive heat flow from Jupiter's satellite Io which is not compatible with an otherwise self-consistent model of origin of the Laplace three-body libration, the mechanism for the long history of resurfacing of Saturn's satellite Enceladus and the possibly short lifetime of the A ring and the mechanisms for resurfacing the satellites of Uranus, especially Ariel, if the high stability of the mean motion orbital resonances at the 2/1 commensurability involving Ariel and Umbriel precludes a long term occupancy of the resonance. Finally, excessive times of accumulation of the outer planets in current models may possibly be reducible from the effects of nebular gas drag.

VISCOSITY AND MASS TRANSPORT IN NON-UNIFORM KEPLERIAN DISKS  
By G.W. Ojakangas and R. Greenberg

Theories describing the dynamics of Keplerian disks of many colliding bodies (e.g. the rings of Saturn or the planetesimal swarm from which the planets accreted) have involved statistical mechanics or fluid dynamical approaches (cf. Safronov 1972, NASA TT F-677; Goldreich and Tremaine 1978, *Icarus* 34, 227, called GT here) with complicated mathematics that can obscure the underlying physics governing the evolution of such disks. Heuristic treatments of collisional disk evolution, intended to clarify the issues, can nevertheless sometimes be misleading. For example, the physical description of viscosity in planetary rings by GT gave the same qualitative result as their detailed mathematical development, yet it lacks some of the critical physics that determines angular momentum transport (Greenberg 1988, *Icarus* 75, 527).

Extension of GT's heuristic development leads to an apparent paradox: Random motions, superimposed on the Keplerian shear, cause particles from a given locality to experience collisions with particles from localities at greater orbital radii (and vice-versa), during the course of their epicyclic motion. In the classical description of viscous transport, these particles carry momentum across the shear surface: particles from the fast lane bring momentum with them when they collide in the slower, outer lane. However, when a particle approaches its apocenter in Keplerian motion, it is moving slower than the mean flow in the region it encounters, suggesting that collisions transfer momentum inward, rather than outward. Thus the sign of the viscosity would appear to be negative, with the apparent consequence that planetary rings should contract rather than expand with time. Such a result would violate angular momentum and energy constraints.

Greenberg (1988) showed that this apparent paradox is resolved by, in effect, keeping an account of where in a particle's epicyclic motion sequential pairs of collisions take place, as well as the average momentum transferred during collisions. With such an approach, Greenberg was able to describe the process in physical terms and obtain the correct form for the viscosity,  $\nu$ , in a planetary ring as a function of its optical depth,  $\tau$ , in the limits of large and small  $\tau$ .

We are now applying the same general approach to particle disks with a radial gradient in surface density. The complexity of statistical mechanical or fluid dynamical treatments has made them less amenable to this more difficult problem, but we find that Greenberg's (1988) physical approach can serve as the basis for a useful analysis of it. We find that our method, in the case of a uniform disk, gives relationships between  $\nu$  and  $\tau$  and between the coefficient of restitution  $\epsilon$  and  $\tau$  that are similar to those of GT at all values of  $\tau$ . The analysis uses a different set of assumptions than those used in previous studies of the same subject. Thus the confirmation of previous results helps strengthen their credibility. In extending our method to the problem of a disk with a radial density gradient, we are modelling planetary rings, but the results may be applicable to other astrophysical disks as well, including the planetesimal swarm from which the planets probably accreted.

In our analysis, we represent the population of a Keplerian particulate disk by the number of particles  $N$  in a phase space described by the coordinates  $(V_t, V_r/2, r)$ , where  $V_t$  and  $V_r$  are the tangential and radial velocities relative to a local circular orbit of radius  $r$ . Particle budget considerations yield a very simple form for the Boltzmann equation in this space. As in the modified Krook approach used by Shu and Stewart (1985, *Icarus* 62, 360), we assume that the collisional source function  $S$  is an isotropic Gaussian, with a variance reduced by inelastic collisions. We divide  $S$  into a part  $S_c$  that has circular symmetry in  $(V_t, V_r/2)$ , and a remainder  $S^*$  which we approximate by four delta functions. With this approximation, we solve the Boltzmann equation for  $N$ :  $S_c$  gives rise to a part of  $N$  that has circular symmetry, and  $S^*$  gives rise to four circular "streams" that decay exponentially with azimuth about the  $r$ -axis. Our development thus does not make the standard assumption that the velocity distribution is a Gaussian; rather, it employs a different assumption that, while also approximate, contains explicitly the systematic nature of Keplerian epicyclic motion. With comparatively simple mathematics, our development predicts relationships between viscosity  $\nu$  and optical depth  $\tau$ , and between the coefficient of restitution  $\epsilon$  and  $\tau$ , that agree quite well with the results of GT and Shu and Stewart (1985). The method is extended to a radially nonuniform disk, with allowance for nonzero mean values of  $V_t$  and  $V_r$ , as well as radial gradients of  $\tau$  and random velocity. The radial particle flux is obtained directly from the solution of the Boltzmann equation. The result predicts diffusion down or up the density gradient depending on the value of  $\tau$ , when functional relations between  $\epsilon$  and impact velocity are used that approximate the data of Bridges et al. (1984, *Nature* 309, 333).

Fractal Aggregates and Planetesimal Formation  
S.J. Weidenschilling (Planetary Science Institute)

Formation of planetesimals required concentration of solid matter to the central plane of the solar nebula. Small (sub- $\mu\text{m}$ ) grains had to coagulate into larger aggregates in order to settle. Analytic and numerical models of this process have yielded settling timescales of a few thousand years at  $r=1$  AU in a laminar nebula, with growth dominated by differential settling, i.e., larger particles sweeping up smaller ones. Those studies assumed spherical particles of uniform density, regardless of size, implying that coagulation of two particles produced a spherical body with the same total volume. That assumption is valid for coalescence of liquid drops, but not for solid grains; their aggregation typically produces fluffy structures with irregular shapes. These have fractal properties, with density varying roughly inversely with size. I have modeled growth and settling of such aggregates, using aerodynamic properties determined by Meakin and Donn (Ap. J. 329, L39, 1988), and assuming fractal properties only for aggregates  $< \text{mm}$  in size. Even if fractal structure exists only in this size range, timescales for "rainout" to the central plane are increased by an order of magnitude, to a few times  $10^4\text{y}$ . The reason for this lengthened timescale is not simply the lower settling rate due to lower particle density. The larger cross-section for particles of a given mass makes thermal motions more effective for causing collisions. Thermal coagulation produces a narrow size distribution, preventing growth by differential settling. The large area/mass ratio of fluffy aggregates also renders coagulation much less effective for lowering opacity than for the assumption of compact spherical particles. Thus, the solar nebula was probably relatively opaque for an extended period.

## ACCRETION OF THE EARTH

S.J. Weidenschilling, Planetary Science Institute,  
Tucson, Arizona

Earth's origin must be considered in the context of the formation of (at least) the terrestrial planets and the Moon. The present paradigm is accretion of  $\sim 10^{12}$  initial km-sized planetesimals into a few planets. Current debate concerns mechanisms and details of the accretion process. Some necessary conditions to be satisfied include:

(a) Accretion must proceed to production of  $\approx 4$  planets, although a larger number of smaller planets in more closely spaced orbits seems stable. The accreting bodies "communicate" over distances  $\gtrsim 0.1$  AU by acquiring large orbital eccentricities and/or evolution of semimajor axes by diffusion or systematic drift, e.g. by drag.

(b) Rotational obliquities require a large stochastic component of spin angular momentum presumably due to large impacts. A systematic prograde component does not appear to be necessary.

(c) Planetary compositions vary. Noble gas content decreases monotonically (systematically?) from Venus to Mars. Other variations (Fe) do not appear systematic.

(d) If SNC meteorites are from Mars, the oxygen isotope reservoir in the terrestrial planet zone was nonuniform, and preserved some variation, but Earth and Moon have identical O isotopic compositions.

Accretion scenarios divide on two major issues and their consequences: Was nebular gas present or absent during accretion of the terrestrial planets? Was the size distribution of accreted bodies dominated by large or small objects (relative to identifiable planetary embryos)? Four end-member permutations are possible:

I. Gas-free, Small Bodies. Sweeping up of small planetesimals by a dominant embryo was implicitly assumed by some early analytic models (1), and mentioned as a possible (but not inevitable) continuation of "runaway growth" of a small number of embryos (2). More elaborate numerical models (3) still require a single "designated embryo" in a "feeding zone"; (a) and (c) are assumptions rather than results. In the absence of gas, there seems to be no way for embryos to clear small bodies completely from the spaces between their orbits. Small impacts would not produce significant variation in obliquities. The lack of mixing between zones would satisfy (d), but lunar origin is difficult (4). Accretion timescales are  $\sim 10^7$ – $10^8$  y.

II. Gas-free, Large Bodies. Safronov's (5) analytic model derived a power-law size distribution dominated by the

largest bodies. Emergence of dominant embryos was constrained by (b), with second largest bodies  $\sim 10^{-3}$ - $10^{-2}$  times the final planetary masses. Wetherill's (6-8) numerical simulations of a few hundred bodies on crossing orbits result in growth of many large bodies, with no clearly dominant embryos until very late in accretion. The last impacts involve very large mass ratios  $\gtrsim 0.1$ . Conservation of orbital angular momentum and energy imply an initially narrow swarm in the Earth-Venus region, with spreading yielding Mercury and Mars as "edge effects." There are no distinct feeding zones and much radial mixing; planetary compositions are correlated with location, but with large stochastic variations. This model can satisfy conditions (a,b), and (c) with possible exception of noble gases. It is consistent with origin of the Moon by giant impact, but seems to require coincidence to explain (d); the impactor and target must have the same O isotopic composition. Accretion timescales are  $\sim 10^7$ - $10^8$  y.

III. Gas-rich, Large Bodies. This scenario corresponds to the "Kyoto" model (9), which assumes presence of the solar nebular during accretion. The Kyoto scenario neglects collisional fragmentation. Gas drag induces radial migration, but it is slow, due to the large sizes of planetesimals. Accretion timescales are  $\gtrsim 10^7$  y, which exceeds current astrophysical estimates of the nebular lifetime. Conditions (a,b) are not explicitly treated but may be satisfied. Earth and Venus would capture massive, temporary H-He atmospheres during accretion, causing extensive heating and melting of their outer layers. Their noble gas systematics may require complex fractionation processes (10). The Kyoto group assumes a capture origin for the Moon, but the impact model is not excluded.

IV. Gas-rich, Small Bodies. This scenario depends on gas drag to bring small ( $\ll$  km-sized) fragments of planetesimals to a growing embryo. Radial migration times can be very short, allowing rapid growth, in  $< 10^6$  y. Patterson and Spaute (11) assume very weak planetesimals fragmented at low impact velocities due to gravitational stirring by a few early-formed embryos. Resonances can produce higher velocities over distances comparable to planetary spacings (12), possibly satisfying (a). In pure form, this model yields only small impacts, violating (b), but growth of  $> 4$  embryos with some large late-stage impacts is not ruled out (13). Other conditions, including lunar origin, have not been addressed yet. This model depends on unknown mechanical properties of planetesimals.

Conclusions. Of the four basic scenarios, (II) appears to be the most self-consistent and successful at meeting the

constraints. Scenario (IV) is relatively new and needs more development. The lifetime of the solar nebula is poorly constrained, so "hybrid" models, in which gas is present only at some early stage of accretion, are possible. Further work is needed to determine interactions of relatively rare large bodies with smaller bodies in the swarm, when "continuum" models for gravitational stirring (14) break down, and distant perturbations and resonances may become important. There is little justification for the canonical km-sized initial planetesimals (15); the effects of other starting conditions should be examined to determine effects on "runaway growth" of planetary embryos. Accretion probably involved large impacts or thermal blanketing by a massive captured atmosphere, or both. Thus, it is highly probable that the Earth formed hot (7).

#### References

1. S. Weidenschilling, Icarus 22, 426 (1974).
2. R. Greenberg, J. Wacker, W.K. Hartmann, C.R. Chapman, Icarus 35, 1 (1978).
3. G.P. Horedt, Icarus 64, 448 (1985).
4. S. Weidenschilling et al., in Origin of the Moon, W. Hartmann, R. Phillips, G. Taylor, Eds., LPI, 731 (1986).
5. V.S. Safronov, NASA TTF-677 (1969).
6. G. Wetherill, in Protostars and Planets, T. Gehrels, Ed., U. of Ariz., 565 (1978).
7. G. Wetherill, Ann. Rev. Astron. Astrophys. 18, 77 (1980).
8. G. Wetherill, in Mercury, F. Vilas, C.R. Chapman and M. Matthews, Eds., U. of Ariz., in press (1988).
9. C. Hayashi, K. Nakazawa, Y. Nakagawa, in Protostars and Planets II, D. Black and M. Matthews, Eds., U. of Ariz., 1100 (1985).
10. R. Pepin, this meeting.
11. C. Patterson, D. Spaute, this meeting.
12. S. Weidenschilling, D. Davis, Icarus 62, 16 (1985).
13. S. Weidenschilling, Gerlands Beitr. zur Geophys. 96, 21 (1987).
14. G. Stewart, G. Wetherill, Icarus 74, 542 (1988).
15. S. Weidenschilling, B. Donn, P. Meakin, in Formation and Evolution of Planetary Systems, Space Telescope Inst., in press (1989).



## Thermal and Dynamical Processes in the Evolution of Planets and Satellites

G. Schubert, Department of Earth and Space Sciences, University of California, Los Angeles, L. A., CA 90024

We wrote a review paper, "Mercury's Thermal History and the Generation of its Magnetic Field," by G. Schubert, M. N. Ross, D. J. Stevenson and T. Spohn, for the University of Arizona Press. We advocated a Mercury model with a hot start and early core formation. Mercury's large iron core cools and partially freezes, but complete solidification of the core is prevented by the depression of the core-freezing temperature by sulfur in the core. It is possible to maintain convection in Mercury's outer liquid core to the present, perhaps accounting for the dynamo generation of Mercury's magnetic field. Tidal heating in the inner solid core may have been a significant source of energy for the core.

We have used Goldstone 13-cm radar observations of Mars during the 1971-1982 oppositions to study the morphology of Martian craters as revealed in their topographic profiles (Roth et al., 1989). Degraded Martian craters are shallow and have very low rim heights. Structures without a discernable rim have retained a basin shape. Low exterior relief rather than overall low relief distinguishes the large degraded craters in the Goldstone sample.

We modelled the coupled thermal-dynamical evolution of the Earth-Moon system including solid planet tidal dissipation and dissipation by the Earth's oceans (Ross and Schubert, 1989a). Solid Earth tidal friction has been the main energy sink in the Earth-Moon system; oceanic dissipation has a relatively small effect over geologic time, even though it is important at present. About 90% of the angular momentum transferred from the Earth to the Moon is a consequence of solid-body tidal friction.

We have written a review paper for a forthcoming University of Arizona Press book ("Evolution of the Atmospheres-Interiors of Planets and Satellites" by G. Schubert, D. L. Turcotte, S. C. Solomon, and N. Sleep) that discusses how the atmospheres and interiors of terrestrial planets evolve in a coupled manner. The physical mechanisms that couple the atmospheres and interiors of planets are analyzed in detail. The major coupling mechanisms involve the dependences of subsolidus mantle viscosity and degree of partial melting on volatile content.

We have investigated tidal heating of Enceladus using multilayered viscoelastic models of the satellite (Ross and Schubert, 1989b). Dissipation on Enceladus can be as large as about 900 GW at the current eccentricity, nearly a factor of 2000 greater than previously thought. Among the suite of interior structures capable of large amounts of tidal heating is one that includes a sublithospheric internal ocean of accumulated  $\text{NH}_3\text{-H}_2\text{O}$  eutectic melt. The models suggest that Enceladus' thermal and dynamical evolution may have been relatively simple, involving only Dione in a 2:1 resonance.

We have constructed interior models of Mimas that are consistent with its observed density and triaxial ellipsoidal shape (Ross and Schubert, 1988). A variety of internal structures are consistent with the observed shape and density. Mimas could be in hydrostatic equilibrium with an ice outer layer surrounding a rock core, or it could have a low density, porous outer ice layer surrounding a homogeneous ice-rock interior. Mimas need

not be in hydrostatic equilibrium, however. It could be a homogeneous body with an elastic lithosphere about 20 km thick having an effective shear modulus of 10 MPa.

We have studied the implications of the atmospheric inventories of the radiogenic noble gases  $^4\text{He}$  and  $^{40}\text{Ar}$  for the tectonic processes in planetary interiors (Turcotte and Schubert, 1988). All the  $^{40}\text{Ar}$  and  $^4\text{He}$  in the Earth's atmosphere can be obtained by only a partial outgassing of the mantle. An even lesser amount of mantle outgassing suffices to account for the  $^{40}\text{Ar}$  in Venus' atmosphere. The small amount of  $^{40}\text{Ar}$  in the atmosphere of Mars could be obtained by only a negligible degree of mantle outgassing. Since the large volcanoes on Mars imply substantial degassing of the interior, the small  $^{40}\text{Ar}$  content of the atmosphere supports the suggestion of past atmospheric erosion by collisions with planetesimals and large meteorites.

Viscous relaxation of craters on the icy satellite Ganymede has been modelled by a finite element numerical approach that takes into account the nonlinear stress dependence and the temperature dependence of ice rheology (Thomas and Schubert, 1988). Recent laboratory determinations of ice rheological parameters under temperature conditions appropriate to Ganymede are incorporated in the modelling. Computed relaxation times of craters with diameter < 100 km are shorter than the population of these craters on Ganymede would suggest. This indicates that either the laboratory data are not applicable to Ganymede or that other effects, such as silicate suspensions or dispersion hardening, stiffen the ice on Ganymede.

We have calculated spatial distributions of tidal heating in layered viscoelastic models of Io (Segatz et al., 1988). Tidal heating is concentrated at the equator if dissipation occurs mainly in an asthenosphere; heating is concentrated at the poles if dissipation occurs throughout Io. Equatorial hotspots and the concentration of Prometheus-type plumes near the equator favor asthenosphere heating. Io's observed figure supports the existence of an Fe-FeS core with a radius of about 1,000 km.

In a more recent study, we calculated global topography for multilayer Io models with dissipation occurring in a viscous asthenosphere and a solid mantle (Ross et al., 1989). The derived topography was compared with observed topographic variations which feature alternating basins and swells along the equator and moderately elevated or depressed regions at the poles. Theoretical models match observations if about 2/3 of the tidal heating occurs in a partially molten asthenosphere and 1/3 occurs in the underlying solid mantle. In addition, the modelling suggests that Io's lithosphere is compositionally distinct from the asthenosphere.

#### REFERENCES

- Ross, M. N. and Schubert, G. (1989a). Evolution of the lunar orbit with temperature- and frequency-dependent dissipation. *J. Geophys. Res.*, in press.
- Ross, M. N. and Schubert, G. (1989b). Viscoelastic models of tidal heating in Enceladus. *Icarus*, 78, 90-101.
- Ross, M. N. and Schubert, G. (1988). Internal structure and shape of Mimas. *Icarus*, 75, 479-484.

- Ross, M. N., Schubert, G., Spohn, T., and Gaskell, R. W. (1989). Internal structure of Io and the global distribution of its topography. *Icarus*, submitted.
- Roth, L. E., Saunders, R. S., Downs, G. S., and Schubert, G. (1989). Radar altimetry of large Martian craters. *Icarus*, in press.
- Schubert, G., Ross, M. N., Stevenson, D. J. and Spohn, T. (1988). Mercury's thermal history and the generation of its magnetic field. In *Mercury*, eds., F. Vilas, C. R. Chapman and M. S. Matthews, University of Arizona Press, Tucson, AZ, pp. 429-460.
- Schubert, G., Turcotte, D. L., Solomon, S. C. and Sleep, N. (1989). Coupled evolution of the atmospheres and interiors of planets and satellites. In Origin and Evolution of Planetary and Satellite Atmospheres, eds. S. K. Atreya, J. B. Pollack and M. S. Matthews, University of Arizona Press, Tucson, AZ. In press.
- Segatz, M., Spohn, T., Ross, M. N. and Schubert, G. (1988). Tidal dissipation, surface heat flow and figure of viscoelastic models of Io. *Icarus*, 75, 187-206.
- Thomas, P. J. and Schubert, G. (1988). Power-law rheology of ice and the relaxation style and retention of craters on Ganymede. *J. Geophys. Res.*, 93, 13,755-12,762.
- Turcotte, D. L., and Schubert, G. (1988). Tectonic implications of radiogenic noble gases in planetary atmospheres. *Icarus*, 74, 36-46.

## SOLAR SYSTEM DYNAMICS

Jack Wisdom, Department of Earth, Atmospheric and Planetary Sciences, Massachusetts Institute of Technology, Cambridge, Massachusetts 02139

### I. Chaotic Evolution of the Orbit of Pluto

One of the most outstanding questions in dynamical astronomy is the nature of the long-term evolution of the solar system. Obviously, the great age of the solar system suggests a high level of stability, but instabilities may still be present. We have previously shown that asteroids near mean-motion commensurabilities with Jupiter may appear to be stable for many millions of years and then suddenly the orbits become irregular, developing large planet-crossing eccentricities. Thus, the stability of the solar system must not be taken for granted. In fact one would not at all be surprised to find instabilities with timescales of order the age of the solar system since such instabilities would not have had time to damage the system. We have carried out a near *billion* year integration of the outer planets with the Digital Orrery (Applegate, et al., 1985) to address this question of the stability of the solar system. Our numerical integration indicates that in fact the motion of the planet Pluto is chaotic. Furthermore, the timescale for exponential divergence of nearby trajectories is only 20 million years, which is remarkably short compared to the age of the solar system.

Our new integration is significantly longer and more accurate than all previously reported long-term integrations of the outer planets. Those integrations include the classic  $\pm 500,000$  year integration of Cohen, Hubbard, and Oesterwinter (1973), the 6 million year integration of Kinoshita and Nakai (1984), the  $\pm 50$  million year integration of project LONGSTOP (Nobili, 1987), and our  $\pm 100$  million year integration (Applegate, et al. 1986). The rate of growth of errors in these integrations are all comparable. They lead to an estimated error in the longitude of Jupiter of about 50 degrees after 100 million years. A clever trick has allowed us to improve the conservation of energy by a factor of about 600. We have verified that the improved conservation of energy is accompanied by correspondingly smaller position and velocity errors. In our new integration the estimated error in the longitude of Jupiter after 100 million years is now only 4 minutes of arc, and after the full 845 million years of our new integration the error in the longitude of Jupiter is estimated to be only 5 degrees. The estimated error in the longitude of Pluto after 845 million years is only 10 minutes of arc.

Exponential divergence of nearby trajectories is the hallmark of chaotic behavior. For Pluto, we have measured the rate of divergence of nearby trajectories by two independent methods. The results of the two methods are in excellent agreement. Both methods indicate that nearby trajectories diverge exponentially. Thus our calculation indicates that the motion of the planet Pluto is chaotic. The timescale for exponential divergence is only 20 million years. Again, this is a remarkably short divergence time considering the age of the solar system.

Usually the demonstration of exponential divergence of trajectories only confirms what is already visible to the eye: chaotic trajectories look irregular. In this case the plot of the orbital elements of Pluto do not look particularly irregular. The irregularity of the motion can however be seen in the power spectra. The fourier transforms of the orbital elements of Neptune appear consistent with the line spectrum expected of a quasiperiodic trajectory. On the other hand, the fourier transforms of Pluto's orbital elements has a broad band component which is characteristic of chaotic motion. The lack of obvious irregularity in the orbital element plots simply means that the region of the chaotic zone in which Pluto is currently moving is rather small.

As yet we know nothing about the shape of the chaotic zone. It may open up to a larger region of the chaotic zone, in which case Pluto could relatively suddenly begin

to behave more irregularly, as actually occurs in numerical simulations of the motion of asteroids on chaotic trajectories.

This work was carried out in collaboration with Gerald J. Sussman (MIT). An account of the highlights of this work has been published in *Science*, **241**, 433.

## II. Tidal Evolution of the Uranian Satellites

We have carried out a thorough, systematic investigation of the tidal evolution of the orbits of the Uranian satellites. This study was motivated by several mysteries presented by the satellites: the curious lack of participation by the Uranian satellites in mean-motion commensurabilities, the anomalously large inclination of Miranda, the anomalously large free eccentricities of Miranda and Ariel, and the spectacular geologic histories of Miranda and Ariel as indicated by Voyager images. All of these mysteries are potentially accounted for by the past tidal evolution of the satellite system through mean-motion commensurabilities. For the Uranian satellites, motion near the mean-motion commensurabilities is quite complicated. We must achieve a clear understanding of that dynamics before we can hope to draw scientifically secure conclusions concerning the origin of the mysteries the satellites present.

As a general rule, the strength of a resonance decreases as the order increases. We have therefore concentrated our efforts on studying the dynamics of the first and second order resonances. The most recently encountered of the first and second order resonances is the 5:3 resonance between Ariel and Umbriel. This resonance would have been encountered if the  $Q$  of Uranus is less than about 100,000. We found that there is a significant chaotic zone associated with this resonance, even in the planar approximation. As the resonance is encountered there are chaotic variations in the eccentricities of both Ariel and Umbriel. As tidal evolution proceeds, the peak eccentricities tend to gradually increase as long as the trajectory remains chaotic. The presence of the chaotic zone makes the standard single resonance model of passage through resonance inapplicable. In our numerical studies the largest eccentricity obtained by Ariel during passage through resonance was 0.023, which is probably insufficient to have a significant effect on the thermal history of Ariel. Inclusion of secular perturbations from Titania, and relaxation of the restriction of the motion to the equatorial plane naturally leads to more complicated dynamics. Nevertheless, our study of these more realistic models indicates that the dynamics of resonance passage is still qualitatively the same as in the planar model.

The 3:1 Miranda-Umbriel commensurability has been encountered if the  $Q$  of Uranus is less than about 39,000. Passage through this commensurability is particularly interesting. As the commensurability is approached the second order inclination resonances are encountered first. We began our study with the circular inclined approximation in order to understand the structure of the phase space with surfaces of sections. We found that the passage through the suite of inclination resonances is controlled by a new dynamical mechanism. The system is initially captured with high probability by the inclination resonances; in this case the probabilities can all be estimated analytically. Subsequent evolution carries the inclination to large values comparable to the currently observed  $4.2^\circ$ . As the inclination increases, the strengths of the resonances increases; the surfaces of section reveal that the separatrices of the inclination resonances grow in size. The measured width of these chaotic separatrices agrees well with analytic estimates. Ultimately, the primary resonances are so strong that, in perturbation theory, the regions of libration overlap, and large scale chaotic behavior ensues. However, the existence of large chaotic zones in the phase space need not affect the motion, since small amplitude libration in stable quasiperiodic resonance is also generally possible. Next, a very interesting thing happens. As the evolution carries the inclination to higher values the frequency of the libration in the resonance changes. The system encounters secondary resonances between the frequency of libration and the frequency which splits the primary inclination resonances. The periodic orbit at the center

of the libration zone undergoes bifurcation, and new stable islands are shed. If the system is captured into one of these secondary islands, the system is dragged out of the libration region with these islands. Thus we have identified a specific dynamical mechanism which allows the system to escape from a stable libration into the chaotic zone. From the chaotic zone the system may be recaptured into the libration region and then again be ejected by another shedding of secondary resonances. Escape occurs when the trajectory is captured from the chaotic zone into the quasiperiodic circulation region. Miranda often emerges from the resonance passage with an inclination near that observed. We have also studied the passage with the orbital eccentricities included. We found that the passage through the suite of inclination resonances was relatively unaffected by the eccentricity resonances. However, there is a large chaotic zone associated with the eccentricity resonances which is encountered after passage through the inclination resonances. The eccentricity of Miranda can evolve to relatively large values before escaping from the chaotic zone. Tidal heating which results from the induced eccentricity could have had some effect on the thermal history, though probably did not result in any large scale melting. The current anomalous eccentricity of Miranda can plausibly be understood as a tidal remnant of a large eccentricity obtained during passage through the 3:1 resonance, if resonance passage occurred within the last billion years. Inclinations comparable to the anomalous  $4.2^\circ$  inclination of Miranda still arise naturally upon passage of Miranda through the 3:1 resonance with Umbriel. This gives compelling evidence that this resonance has indeed been encountered, which in turn constrains the  $Q$  of Uranus to be less than about 39,000.

Another important constraint on the rate of internal dissipation in Uranus comes from the examination of the 2:1 Ariel-Umbriel commensurability. This resonance provides a potential barrier to further evolution. Our simulations have indeed confirmed that with plausible initial eccentricities passage through this resonance is very unlikely. We have studied both the effects of secular interactions and inclinations. Though there are secondary bifurcations as we found for the 3:1 Miranda-Umbriel commensurability, in this case they do not lead to escape from the resonance. The 2:1 Ariel-Umbriel resonance thus appears to be an absolute barrier to tidal evolution. In order for it to have never been encountered the  $Q$  of Uranus must be greater than about 11,000.

In summary, we have carried out an extensive investigation of the tidal evolution of the Uranian satellites through the most important mean-motion commensurabilities. Our principal results are: (1) Mean-motion commensurabilities among the Uranian satellites are all associated with significant chaotic zones. The existence of these chaotic zones dramatically changes the dynamics of resonance passage and the probabilities of various outcomes. (2) Passage through the 3:1 Miranda-Umbriel commensurability naturally accounts for the anomalous  $4^\circ$  inclination of Miranda. (3) Miranda acquires a moderately large eccentricity upon passage through the 3:1 commensurability, which could have affected its thermal history. (4) Passage through the 2:1 Ariel-Umbriel commensurability is very unlikely. The  $Q$  of Uranus must be in the range  $11,000 < Q < 39,000$  to avoid the 2:1 resonance but allow passage through the 3:1 Miranda-Umbriel resonance.

This work has been carried out in a continuing collaboration with my graduate student William Tittmore, who is now Assistant Professor of Planetary Science at the University of Arizona. The first two papers on this research have been published: *Icarus*, **74**, 172-230, and *Icarus*, **78**, 63-89. A third has been submitted to *Icarus*.

CHAPTER 5

PLANETARY INTERIORS, PETROLOGY, AND  
GEOCHEMISTRY





## Composition and Dynamics of the Earth's Mantle

Raymond JEANLOZ

Dept. Geology and Geophysics, Univ. California, Berkeley, CA 94720

Ultrahigh pressure-temperature experiments with the laser-heated diamond cell document that the major phases comprising the Earth's lower mantle are  $(\text{Mg,Fe})\text{SiO}_3$  and  $\text{CaSiO}_3$  perovskites coexisting with  $(\text{Mg,Fe})\text{O}$  magnesiowüstite. Thermal equations of state (pressure-volume-temperature relations) are derived for assemblages of these phases based on experimental measurements of compressibilities, thermal expansions and related properties, all of which are fitted to a physically-based formulation for the temperature-dependent compressibility: the anharmonic Eulerian finite-strain equation of state. A comparison with seismological profiles of density and compressibility vs. depth (implicitly pressure) within the Earth demonstrates that the lower mantle is approximately 5 ( $\pm 2$ ) percent denser than assemblages of upper mantle composition that are characterized by a ratio of Mg to Fe components  $\text{Mg}/(\text{Mg}+\text{Fe}) \geq 0.88$ . A satisfactory fit to lower-mantle properties is obtained with  $\text{Mg}/(\text{Mg}+\text{Fe}) \approx 0.80$  ( $\pm 0.02$ ), more iron-rich and possibly more Si rich than the upper mantle, but this is not a unique interpretation. Therefore, the mantle is *stratified* in that it consists of two regions of fundamentally different rock type or bulk composition: the upper mantle which is readily sampled, and the lower mantle that comprises over 60 (atomic) percent of the Earth but is not easily sampled.

The intrinsic density difference inferred to exist between the upper and lower mantle is sufficient to keep these regions dynamically separated. That is, although some leakage is possible between the convecting upper and lower mantle, intermixing of these regions must be small over geological time in order that these regions remain distinct. Consequently, transfer of heat out of the Earth's deep interior is inhibited by the (inferred) stratification of the mantle, and temperatures in the lower mantle are likely to be high: above about 2500 K, or near the melting point of the perovskite.

A mechanism by which the mantle could have become stratified is that melting and differentiation processes are intrinsically different in the uppermost mantle and in the lower mantle. Specifically, experiments demonstrate that whereas melts near the surface are buoyant and escape to the surface on a short geological time scale, melts at depth are essentially neutrally buoyant. Therefore, melt extraction and differentiation are inefficient at lower-mantle conditions. It is for this reason that the upper mantle may have been effectively differentiated through the formation of continents and through plate-tectonic processes, while the lower mantle has remained relatively unprocessed throughout geological history.

Current thinking is that the Moon was likely formed by a major impact on Earth early in geological history. If correct, this suggests that the bulk lunar composition is closely related to the composition of the Earth's lower mantle (the role of the Earth's core is uncertain in such scenarios of lunar origin). Indeed, the best existing estimates of lunar composition are

compatible with the observed properties of the lower mantle. Prior thinking that has emphasized the difference between the composition of the Moon's mantle and the Earth's mantle has been based on, hence biased by, estimates of upper mantle composition. Though highly speculative, it is possible that the composition of the Moon is more representative of the Earth's bulk silicate composition (excluding the most volatile constituents) than is the composition of the upper mantle.

**Ultrahigh P-T Experiments, the Core-Mantle Boundary and Geomagnetic Variations: A New Electromagnetism of the Earth**

**Raymond Jeanloz** and X. Li, Dept. Geology and Geophysics, University of California, Berkeley, CA 94720; E. Knittle and Q. Williams, U. California, Santa Cruz, CA 95064

Results of ultrahigh pressure-temperature experiments with the laser-heated diamond cell show that: *i*) the lower mantle consists predominantly of the silicate perovskite high-pressure phase coexisting with (Mg,Fe)O, *ii*) this assemblage is electrically insulating at conditions throughout the deep mantle, *iii*) the temperature at the base of the mantle is 5000 ( $\pm$  1000) K, significantly higher than previously thought, and *iv*) liquid Fe-rich alloys react aggressively with the high-pressure silicate assemblage to form mixtures of metallic alloys and insulating oxides at the conditions of the core-mantle boundary. Assuming that no secondary phases are present, we infer from our measurements that the entire mantle above D'' is insulating (electrical conductivity  $\sigma \leq 10^{-2}$  S/m); hence it is a completely transparent window for the geomagnetic field, contrary to previous thinking. Our experiments suggest that the Earth's core and mantle must react vigorously over geological time, forming a heterogeneous layer at the base of the mantle with  $\sigma$  varying laterally by over 8 orders of magnitude (*viz.* D''). Therefore, temporal fluctuations of the internal geomagnetic field are not directly related to the flow field in the core, as has been assumed in most analyses of the field to date. Instead, we expect that effects of induction and magnetic diffusion are significant if not overriding at the bottom of the mantle. If correct, this also implies that paleomagnetic observations of field reversals show a severely distorted picture of the geodynamo; they may primarily be revealing the paleostructure of the core-mantle boundary.

## GIANT IMPACT THEORY OF THE MOON'S ORIGIN: IMPLICATIONS FOR THE THERMAL STATE OF THE EARLY EARTH

H. J. Melosh, Lunar and Planetary Laboratory, University of Arizona, Tucson, AZ 85721, and M. E. Kipp, Sandia National Laboratory, Albuquerque, NM 87185.

Ideas on the early thermal structure of the earth have evolved rapidly over the last few decades. Most of this evolution is ultimately traceable to the size of the planetesimals from which the earth is believed to have formed. Less than twenty years ago most authors (eg. 1,2) supposed that the earth accreted from myriads of small planetesimals that, upon impacting the surface of the growing proto-earth, proceeded to radiate most of their heat to space. Under such conditions the earth would have had to accrete over the remarkably short interval of 0.5 Myr (1) if melting temperatures were to be reached anywhere within its interior. Less than ten years ago, Kaula (3) realized that if most of the planetesimals are in the 30-100 km diameter range, then a large fraction  $h$  (where  $h \approx 0.5$ ) of their original kinetic and gravitational energy would be buried below the earth's surface at depths too large for conduction or radiation to easily dissipate it to space. Kaula's model predicts that the temperature distribution in a growing planet is a parabolic function of radius  $R$  in the planet, increasing from the inside of the planet toward the surface as  $R^2$  until the solidus is reached, at which point liquid convection holds the temperature between the liquidus and solidus. This initial temperature inversion would have been wiped out by core formation as density-driven convection mixed the initially cool interior with the hotter external regions (as well as released more gravitational energy). This model permits the earth to grow over the much longer interval of ca. 50 Myr, which is more in consonance with the predicted dynamical growth timescales.

Most recently it has been suggested that the moon formed as a result of a collision between the proto-earth and a Mars-size planetesimal (4). Computations by Wetherill (5) show that large impacts of this kind are plausible events near the end of planetary accretion, about 100 Myr after accretion began. The chemistry of the moon, particularly its low abundance of metallic iron, suggests that the earth's core had already formed at the time the putative giant impact event took place. The initial state of the earth's mantle is unknown, although the  $10^{31}$  J released by core formation (if the earth was initially homogeneous) would have been enough to raise the mean temperature of the earth 1,500 °K. Thus, the earth's early mantle was probably already molten at the time of the impact. Even if it was not, we will show below that an impact energetic enough to have ejected the moon would certainly have left the entire mantle molten (and some of it vaporized!) afterwards.

The idea of a Mars-size impactor was first suggested by the anomalously large angular momentum of the earth-moon system. It is easy to show the present angular momentum could have been imparted only by the impact of a body with a mass in the vicinity of that of Mars, although other factors such as impact velocity and impact parameter (a measure of the obliquity of the impact) also play a role. The *total* energy that such an impact would add to the earth is the sum of the projectile's gravitational potential energy, ca.  $6.7 \times 10^6$  J/kilogram of the earth, and the projectile's kinetic energy,  $0.054 v^2$  per kilogram of the earth, where  $v$  is the encounter velocity between the projectile and the proto-earth. Taking a typical silicate heat capacity of 700 J/kg°K and a latent heat of melting of  $4.2 \times 10^5$  J/kg, this implies that even if the entire earth's mantle started out cold, the distributed energy of the impact would raise the earth's mean temperature nearly 9,000 °K for  $v=0$ . For  $v=10$  km/sec the mean temperature would rise by more than 16,000 °K. Given a mantle liquidus in the neighborhood of 3000 °K (6), it is clear that melting, even vaporization, must be widespread in such a collision.

Although the total energy available from the collision of a Mars-size projectile with the proto-earth is impressive, the *distribution* of the energy within the earth is equally important.

If, as has been suggested by Stevenson (7), this energy is mainly expended in vaporizing the projectile, the earth may acquire a transient silicate vapor atmosphere without strongly heating the deeper mantle. Some simple considerations of the physics of impact cratering makes this situation unlikely, however. When two bodies collide at high speed, strong shock waves propagate from the point of the impact into the adjacent target and projectile. These shock waves weaken as they spread, with the maximum pressure falling off approximately as  $P_0(r/r_p)^{2-3}$ , where  $P_0$  is the pressure at the contact between projectile and target,  $r_p$  is the projectile radius and  $r$  is the distance from the impact site. Although the complex geometry in a planet-sized collision makes this relation difficult to apply exactly, it suggests that if  $r_p$  is roughly half the earth's radius, the shock pressure at the earth's center is at most a factor 5 less than  $P_0$ . But even in the lowest velocity impact, when the projectile strikes at the earth's escape velocity, 11.2 km/sec,  $P_0$  is on the order of 240 GPa, so that the shock pressure perturbation deep in the earth generally exceeds about 50 GPa. This is close to the shock pressure needed to cause melting in initially cold rocks.

To address the temperature rise in the earth more exactly, we have performed a series of 2-dimensional numerical hydrocode computations designed to simulate the impact between the proto-earth and a Mars-size protoplanet. We used the code CSQ II, implemented on the Cray II supercomputers of the Sandia National Laboratory. This computation uses realistic equations of state for dunite in the mantles and iron in the cores of the two colliding planets. The earth has a central gravitational field, and is initially adjusted so that it has a temperature profile similar to that of the present-day earth. These models thus start out relatively cold, with the mantle temperatures initially below the solidus of dunite. We have performed computations at a variety of initial velocities and impact parameters, including pairs that give the earth-moon system its present angular momentum.

At the lowest velocity ( $v=0$ ), for impact parameters of 0.5, 0.88, 1.0, and 1.25 times the earth's radius, the strongest heating upon impact is initially confined to the hemisphere on which the projectile strikes. Temperatures rise typically 3,000 to 4,000 °K between the site of the impact and the earth's core. Unfortunately, our computations do not extend to long enough times for the entire projectile to merge with the earth in the high impact parameter runs. In these cases we had to stop the computation while some of the projectile was still falling on portions of the earth more distant from the impact site. In these cases we believe that more than half the mantle will be strongly heated, so the quoted results must be seen as a lower limit.

The results for the higher impact velocity  $v = 7.8$  km/sec are more spectacular. For all the impact parameters studied (0.5, 0.59, 1.0, and 1.25 earth radii) the mantle was heated nearly uniformly by 3,000 to 4,000 °K. The projectile's core was almost entirely vaporized, being heated to more than 8,000 °K after release from high pressure. A fast, much hotter vapor plume also carries several lunar masses of material out along trajectories that eventually take up elliptical orbits about the earth.

These computations, in conjunction with the more general considerations described above, indicate that a moon-forming impact would have had a profound effect on the earth's thermal state. The shock produced by the impact would have heated the earth to great depths, raising at least the hemisphere adjacent to the impact above the melting temperature. There seems to be no way to avoid the conclusion that a large moon-forming impact is inevitably accompanied by widespread melting of most or all of the earth's mantle. This scenario raises implications for the geochemistry of the earth that will be dealt with in an accompanying abstract (8).

REFERENCES: (1) T. C. Hanks and D. L. Anderson, *Phys. Earth Planet. Int.* **2**, 19-29 (1969). (2) H. Mizutani, T. Matsui and H. Takeuchi, *Moon*, **4**, 476-489 (1972). (3) W. M. Kaula, *J. Geophys. Res.* **84**, 999-1008 (1979); W. M. Kaula, *Geol. Assoc. Canada Sp. Pap.* **20**, 25-34 (1980). (4) See, eg, the introductory discussion in H. J. Melosh and C. P. Sonett in *Origin of the Moon*, LPI (1986) pp. 621-642. (5) G. W. Wetherill, *Science* **228**, 877-879 (1985). (6) E. Takahashi, *J. Geophys. Res.* **91**, 9367-9382 (1986). (7) D. J. Stevenson, *Ann. Rev. Earth Planet. Sci.* **15**, 271-315 (1987). (8) W. B. Tonks and H. J. Melosh, this volume (1988).

## A WELL STIRRED MAGMA OCEAN: IMPLICATIONS FOR CRYSTAL SETTLING AND CHEMICAL EVOLUTION

W. B. Tonks and H. J. Melosh, Lunar and Planetary Laboratory, University of Arizona, Tucson, AZ 85721.

The cooling of a magma ocean is the generally accepted explanation of the observed dichotomy between the Europium-enriched anorthositic crust and the Europium-depleted basaltic source regions of the moon (i.e. Wood, 1970). Since the Earth does not have this distinctive signature, it has been argued by a number of workers (i.e. Kato et. al. (1988) and Drake et. al. (1988)) that it never had a magma ocean. However, the accretion models of Kaula (1979), together with the energetics of core formation strongly suggest that if the moon had a magma ocean the Earth should have had one also. This is especially true if the moon was formed by the giant impact of a Mars-sized body as noted in the works of Melosh and Kipp (1988) and Cameron and Benz (1988).

The cooling of a magma ocean was studied in detail by Hofmeister (1983). She assumed that crystals are removed from the magma when formed and modeled the chemical evolution as a batch fractionation process resulting in a layered structure very different than the present Earth. It seems, however, that the effect of convection in keeping the magma ocean well stirred has not been taken into account in the past. This work is a preliminary analysis of this effect. It is presumed (McBirney and Murase, 1984) that the magma behaves as an ordinary liquid until the concentration of crystals in the crystal-magma mush exceeds about 50%, at which point the mush locks up, the crystals and liquid are then unable to separate, and any further heat transfer must take place by subsolidus convection. The magma will thus solidify into the same chemical composition as the starting material since the liquid fraction and solid fraction remain intimately mixed. Note that in this study we explicitly exclude consideration of liquid-mush separation. We are well aware that this effect may be important, but limit our work to the question of crystal settling for reasons of practicality.

We investigated the suspension of crystals in a convecting magma ocean using the following relatively simple model, shown in figure 1.

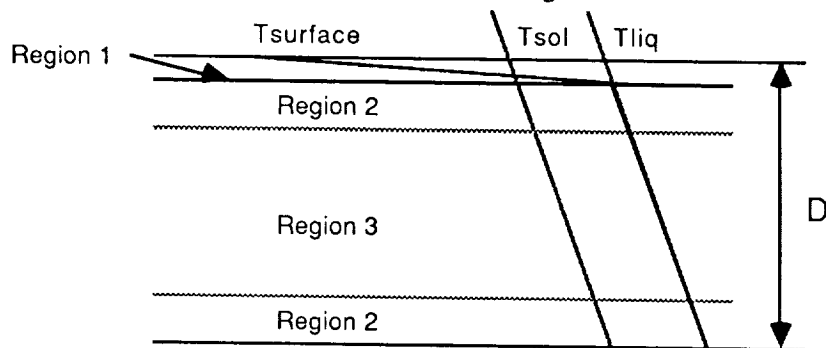


Figure 1. Basic model showing 3 distinct regions of behavior at the beginning of the computation.

It is assumed that the liquidus and solidus temperature profiles of the planet follow the adiabat. This is only strictly valid for a very small planet although recent experiments on the melting curves of peridotite at very high pressures (Takahashi, 1986) indicate that this simplification may not be too unrealistic. The planet is melted uniformly to depth D, and is originally at the liquidus. The temperature difference between the surface and the magma sets

up free convection. The model considers only the effect of the cooling magma. After a time  $\Delta t$ , the ocean has lost an amount of energy equal to  $h\Delta t$ , where  $h$  is the heat flux. The heat flux  $h$  is derived from the Nusselt number  $Nu$  ( $h=h_c Nu$ , where  $h_c$  is the heat that would be conducted through a slab of thickness  $D$ ), which itself is related to the Rayleigh number of the convection through the following relationship:

$$Nu = 0.89 Ra^n$$

The magma ocean on both the earth and moon is initially convecting vigorously with an initial Rayleigh number ( $Ra$ ) on the order of  $10^{27}$ , in a regime described by Kraichnan (1962). The flow is broken into 3 regions if the following condition is met:

$$3.5 Ra^{1/3} > \sqrt{Pr}$$

where  $Pr$  is the Prandtl number.

Region 1 is a thin region where heat is transported by conduction, region 2 is a turbulent boundary layer where heat is transferred primarily by convection but in which viscosity dominates. Region 3 consists of highly turbulent fluid in which large eddies of spatial scale on the order of the depth of the ocean dominate. These eddies give rise to upward directed forces which have potential to keep the crystals in suspension (Bagnold, 1965). In particular, if the effective frictional velocity arising from region 3 is about the same as the terminal velocity of settling crystals, the crystals should stay in suspension. Thus the ratio ( $S$ ) of the frictional velocity to the terminal velocity was calculated, using Kraichnan's equations and a routine that calculated the Stoke's fall velocity if the local Reynold's number of the crystals was  $<1$  (which it was in all cases calculated thus far) and invoked the drag coefficient if the local Reynold's number was  $>1$ . Thus if  $S>1$ , the magma ocean remains well stirred with a significant fraction of its crystals remaining in suspension. It is of interest to discover what factors, if any, cause  $S>1$ . It should be noted that the only parameters that changed between the Earth and Moon models were the bulk compositions and the acceleration of gravity. The liquidus and solidus temperatures, among other parameters were purposely kept constant in these calculations.

The terminal velocity falls off as  $1/v$  but the frictional velocity falls off as  $1/v^{n/3}$  where  $v$  is the kinematic viscosity and  $n$  is the power in the Rayleigh-Nusselt number relationship. Thus  $S$  increases as the viscosity increases as crystallization proceeds as shown above. This also implies that  $S$  increases as the  $SiO_2$  content of the magma increases. The above models indicate that millimeter sized crystals are likely to be suspended in both lunar and terrestrial magma oceans, but crystals of size 1-10 cm will probably not stay suspended. Increasing the depth of the ocean enhances the likelihood that the crystals will be suspended, but the decrease of the acceleration of gravity between the Earth and Moon seems to have only a small effect. A potentially large effect not yet modeled is that of an increase in the liquidus and solidus temperatures with pressure. This may markedly enhance the terrestrial ocean's ability to keep crystals in suspension. Another aspect for study is the point at which region 3 disappears. If there is no region 3, the magma ocean's ability to keep crystals in suspension drops greatly. None of the models run thus far have had region 3 disappear even at 50% crystallization.

In spite of these uncertainties, it seems likely that crystals in a lunar magma ocean are more likely to sink (or float) than crystals in a deeper, more vigorously stirred terrestrial magma ocean. Although our initial runs show this effect to be smaller than we initially expected, we feel that a thorough discussion of the physics of crystal suspension in a convecting magma ocean may clarify some of the geochemical differences between the earth and the moon.

REFERENCES: Bagnold, R. A. (1965) U. S. G. S. Prof. Pap **422 I**; Cameron, A. G. W. and W. Benz (1988), this volume; Drake, M. J., Malvin, D. J., and Capobianco, C. J. (1988), this volume; Hofmeister, A. M. (1983) J. Geophys. Res. **88**, B6. 4963-4982; Kato, T., Ringwood A. E., and Irifune T. (1988) Earth Planet. Sci Let. **89**, 123-145; Kaula, W. M. (1979) J. Geophys. Res. **84**, 999-1008; Kraichnan, R. H. (1962) Phys. Fluids **5**, 1374-1389; Melosh, H. J. and Kipp, M. E. (1988), this volume; Takahashi, E. (1986), J. Geophys. Res. **91**, 9367-9382; Wood, J. A. (1970) J. Geophys. Res. **32**, 6497-6513.



## Solubility of noble gases and nitrogen in silicate melts to 5000 bars

Edward Stolper<sup>1</sup> and Michael R. Carroll<sup>2</sup>, <sup>1</sup>Division of Geological and Planetary Sciences, California Institute of Technology, Pasadena, California, 91125, and <sup>2</sup>Bayerisches Geoinstitut, Universität Bayreuth, Bayreuth, Federal Republic of Germany

A principal source of the atmospheres of the terrestrial planets is volcanism. Volatile constituents dissolve in magmas when they form by partial melting deep in planetary interiors. As the magmas rise toward the surface and the pressure on them decreases, dissolved gases exsolve into bubbles and may ultimately escape into the atmosphere. Although major changes in atmospheric chemistry occur subsequent to degassing by processes such as weathering, interaction with sediments, interaction with ice and water, and loss to space, it is generally accepted that understanding of atmospheric evolution must begin with the volcanic input.

The goals of this project are (1) to measure the pressure and temperature dependence of the solubility of rare gases and nitrogen in a range of silicate melt compositions relevant to planetary volcanism; (2) to study the influence of the major volatile species, water and carbon dioxide, and other rare gases on the solubility of individual rare gases; (3) to measure the diffusivities of rare gases and nitrogen as functions of pressure and temperature in silicate melts; and (4) to develop an understanding of the thermodynamics and, if possible, the solubility mechanisms of these volatile species in silicate melts so as to generalize our results to a wider range of compositions and conditions. The results will be applied to understanding the behavior of volatile components during igneous processes on Mars and their possible influence on the composition of the martian atmosphere.

**a. Effects of silicate chemistry on the diffusion and solubility of argon in silicate melts and glasses:** The solubility of Ar in silicate glasses and melts is a strong function of silicate chemistry. This is illustrated in Figure 1, which summarizes results at pressures up to 4000 bars on silica glass, albitic glass, and rhyolitic glass at 700°C, and on basaltic melt at 1200°C. Figure 2 shows the temperature dependence of Ar solubility in silica, albitic, and rhyolitic glasses/melts at a constant pressure of 1190 bars. The curves shown in Figures 1 and 2 are thermodynamic fits to our data. Note that the rhyolitic and basaltic compositions we have studied span the range of common igneous rock compositions found on earth and anticipated on the other terrestrial planets.

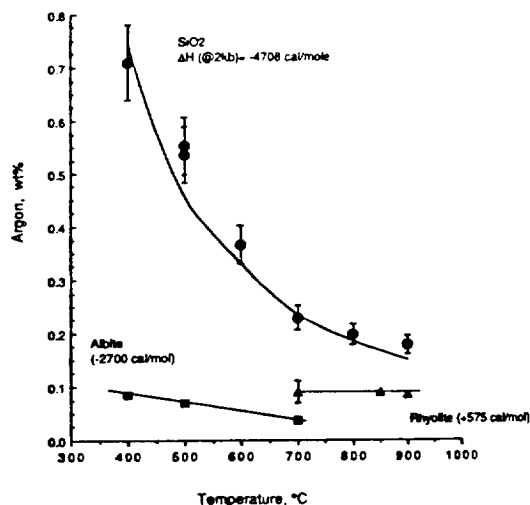


Fig. 1. Ar solubility, ~1190 bars

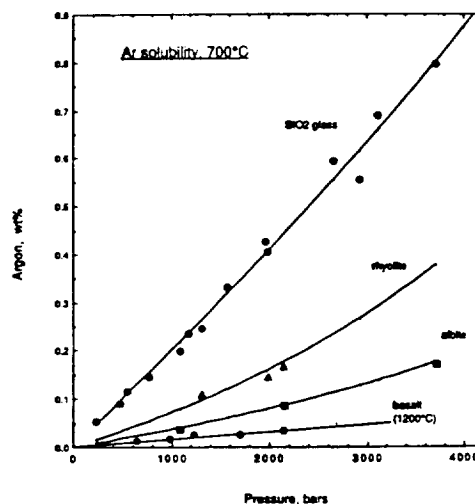


Fig. 2. Ar solubility, 700°C

Figure 3 summarizes our results on the temperature dependence of the diffusion coefficient for argon in silica, albite, and rhyolitic glasses/ melts at pressures between 1.1 and 1.5 kbar. These results were obtained by allowing Ar to diffuse into glass or melt at elevated temperature and pressure and, after quenching, analyzing the concentration profile in Ar at the sample edge and fitting it to a curve with the form of the error function complement.

The temperature dependence of the diffusion coefficient for Ar is clearly approximately Arrhenian for each composition. It is interesting that there is no apparent "kink" in the rhyolite data at the glass transition temperature ( $10^4/T(K) \sim 9-10$ ). We do not at this time understand the significant difference in the activation energies for diffusion between silica and albitic glass (23-27 kcal/mole) on the one hand and rhyolitic glass/melt (45 kcal/mole) on the other hand. Curiously, crystalline potassium feldspars have activation energies for diffusion similar to that of rhyolitic melt, but a factor of two higher than of albitic melt. It is not obvious how to rationalize these large differences in the activation energy for diffusion (or in the enthalpy of vaporization; see figure 2) of Ar; all of these glasses/melts are thought to have similar arrangements of essentially fully polymerized aluminosilicate tetrahedra with or without charge-balancing cations (e.g., Na, K, Ca) in interstitial positions. Clearly, the charge-balancing cations must play a major role in both the diffusivity of Ar and the energetics of its solubility. We suspect that the answer lies in the likelihood that the Ar and the charge-balancing cations occupy related structural positions in the melt or glass structure.

b. Solubility and diffusion of nitrogen in silicate melts and glasses: Experiments to determine nitrogen solubility were begun during the current grant period. Silica glass was equilibrated with  $N_2$  gas at 700°C at pressures between 200 and 2000 bars. Initial efforts to analyze these samples using Raman spectroscopy were unsuccessful. However, Dr. S. Sutton of Brookhaven National Laboratory analyzed them for nitrogen using the nuclear reaction  $^{14}N(d,\alpha)^{12}C$ . This technique appears to be ideal for our work with excellent spatial resolution (beam diameter  $\sim 20$  microns) and precision (detection limit on the order of 1 ppm; precision on the order of a few percent is achievable at higher concentrations). Figure 4 shows our preliminary results on the solubility of nitrogen in silica glass at 700°C as a function of pressure and Figure 5 shows an example of a concentration profile in one of the experiments, illustrating the kinds of data from which diffusion coefficients can be determined.

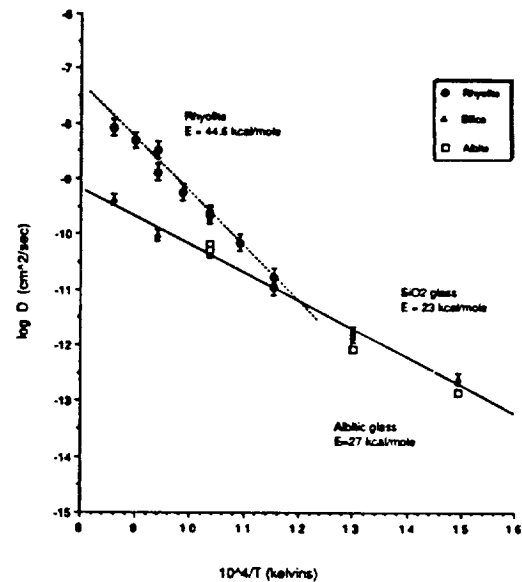


Fig. 3. Ar diffusion,  $P = 1.1$  to 1.5 kbar

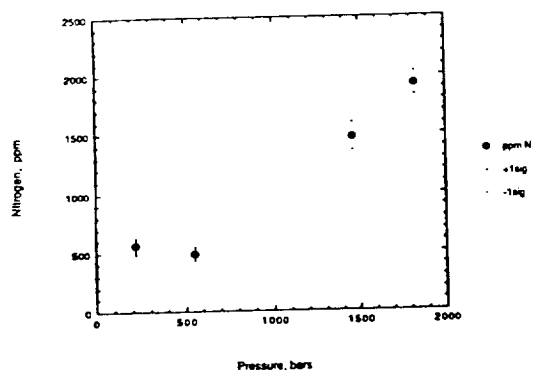


Fig. 4 Nitrogen-SiO<sub>2</sub> glass, 700°C

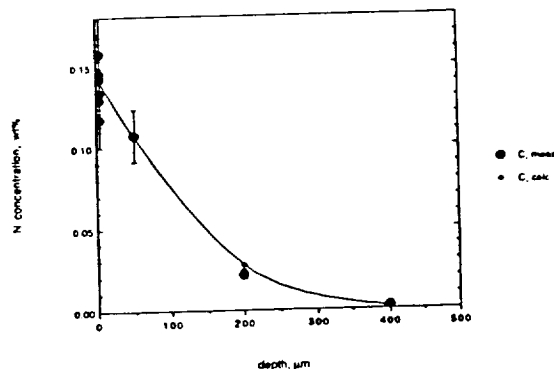


Fig. 5. AX-10, 700°C, 1450 bar, 32 day  
Log D =  $-10.37 \pm .13$ ; Co = .145 wt%  
error bars  $\pm 15\%$

c. Diffusivity of carbon dioxide and water in silicate glasses and melts: Carbon dioxide is likely in most cases to be the major gaseous species evolved during the degassing of basaltic magmas. Likewise, water is expected to be the major species in bubbles exsolved from more silicic magmas. It is important to establish the influence of the presence of water and carbon dioxide on the solubilities of the minor gaseous species that are our focus. In addition, evaluation of the possibility of kinetic fractionations during bubble growth can only be undertaken if the relative diffusivities of carbon dioxide, water, the rare gases, and nitrogen are known, as well as the influence of the major components on the diffusion of the minor components. That this could be an important effect is illustrated by our results on the diffusivity of Ar in silica glass, which suggest that the presence of even small amounts of water can result in a substantial decrease in the diffusivity of Ar.

We have begun to study the diffusivity of water in a series of silicate glasses and melts (e.g., rhyolite, albite, orthoclase, diopside, silica). Figure 6 illustrates a typical concentration profile for a rhyolitic sample dehydrated at 540°C for one and one-half weeks. Note that we are able to distinguish between different dissolved hydrous species (i.e., water molecules and hydroxyl groups). This has the potential to allow us to model more realistically the diffusion mechanism of water in glasses and melts.

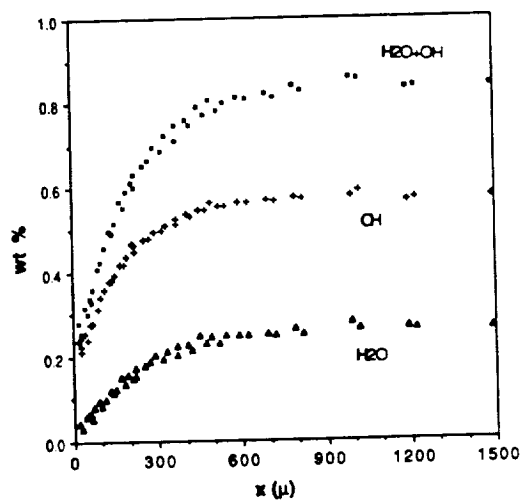


Fig. 6. Concentration profile of hydrous species developed by dehydration of rhyolitic glass at 540°C, 11.4 days.

## PRIMARY MARTIAN MAGMAS

John R. Holloway, Departments of Chemistry and Geology, Arizona State University, Tempe AZ 85287

The overall goal of this research is to experimentally determine the composition of magmas generated in the Martian mantle, and to evaluate the effect of volatiles ( $\text{H}_2\text{O}$ ,  $\text{CO}_2$ ,  $\text{H}_2$ ,  $\text{CH}_4$ ) on those compositions. In addition, the rheologically important melt density and viscosity will be determined as a function of pressure. These data will then be used to predict the composition and rheology of Martian volcanic rocks and of volcanic gases emitted during eruption. This research will provide a link between volcanic lavas, mantle mineralogy, and the source composition of Martian atmospheres.

Density and viscosity measurements have been completed on the anhydrous primary melt composition at 23 kbar (Bertka & Holloway, 1989). These experiments have been complicated by the fact that the viscosity of the volatile-free primary Martian magma at 23 kbar is the lowest yet measured for a probable naturally occurring melt, with a range of 0.1 - 5 poise. The melt density measured, 3.03 g/cm<sup>3</sup>, is lower than anticipated by our earlier experiments and is consistent with a density cross-over between olivine and melt at about 70-90 kbar.

We have nearly completed a set of experiments at 10 kilobars to determine the solidus temperature, minimum melt composition, and melting range equilibria for a volatile-free Martian mantle.

Our on-going experiments and their implications for the interior of Mars were summarized in two presentations in the last year (Holloway & Bertka, 1988; Holloway, 1989).

Experiments on the composition, stability and melting relations of carbonate minerals in the Martian mantle were initiated during the last year. Prior experiments on carbonate minerals under mantle conditions had always been in iron-free simple systems and the Martian mantle is believed to be rather iron-rich. So the first step in this project had to be the determination of Fe/Mg/Ca partitioning between silicate minerals and the stable carbonate phase. A set of preliminary experiments delineating that stability were presented at the Twentieth LPSC (Odezynskyj & Holloway, 1989).

## REFERENCES

- Bertka, C. M. and Holloway, J. R. (1988) Martian mantle primary melts: An experimental study of iron-rich garnet lherzolite minimum melt composition. *Proc. 18th Lunar Planet. Sci. Conf.*, 723-739.
- Bertka, C.M. and Holloway, J. R. (1989) Martian mantle primary melts: An experimental study of melt density and viscosity at 23 kb. *Lunar Planet. Sci. XX abstract*, 69-70.

The Melting of  $\text{MgSiO}_3$  and  $(\text{Mg}_{.9}\text{Fe}_{.1})\text{SiO}_3$  by laser heating in the diamond anvil cell at pressures between 300 kbar and 600 kbar  
 William A. Bassett and Maura S. Weathers  
 Department of Geological Sciences, Snee Hall, Cornell  
 University, Ithaca, New York 14853

We have measured the effect of pressure on the melting temperature of  $(\text{Mg}_{.9}\text{Fe}_{.1})\text{SiO}_3$  in the perovskite structure from 300 to 600 kbar using laser heating and measuring the temperature by fitting spectra of the incandescent sample to black body curves. Over this portion of the melt curve the melting temperature is 2800 (+/- 200) K and is independent of pressure (Figure 1). We have also made some measurements on pure end-member  $\text{MgSiO}_3$  and found the temperature of melting to be 2800 (+/- 200) K and independent of pressure as in the iron-bearing sample. The experiments on the end-member sample require the addition of an opaque powder to absorb the radiation. We have used platinum and and are now using tantalum carbide which is absorbing, inert, and refractory.

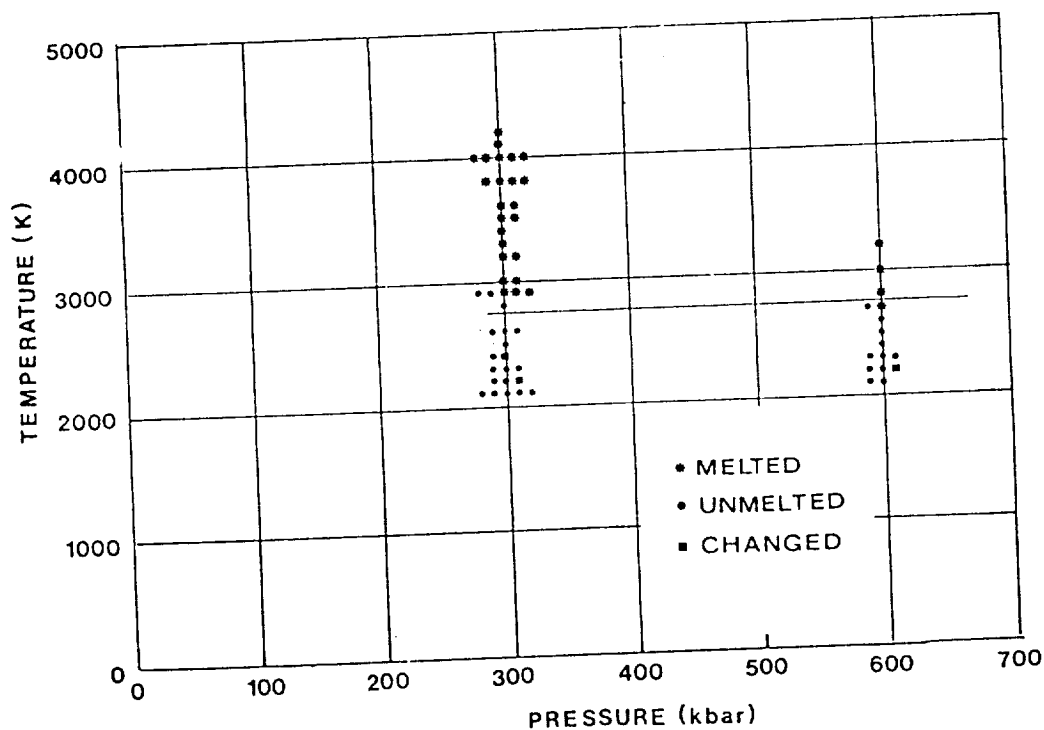


Figure 1. A plot of the melting temperature of  $(\text{Mg}_{.9}\text{Fe}_{.1})\text{SiO}_3$  between the pressures of 300 and 600 kbar.

HIGH PRESSURE COSMOCHEMISTRY OF MAJOR PLANETARY INTERIORS: LABORATORY  
STUDIES OF THE WATER-RICH REGION OF THE SYSTEM AMMONIA-WATER  
Malcolm Nicol, Steven Boone, Hyunchee Cynn, and Andrea Koumvakalis  
Department of Chemistry and Biochemistry  
University of California, Los Angeles, CA 90024-1569

Models of the major planets and their satellites make simple, rather arbitrary assumptions concerning deep interiors. "Rock" cores or "ice" (water-ammonia-methane) layers are often invoked without considering thermodynamic consistency. Properties of "gas-ice" mixtures at very high pressures are poorly understood, even under laboratory conditions. When this project began, few measurements existed on binary or multicomponent gas-ice systems at 1 GPa and higher pressures. We set out, therefore, to determine the pressure-temperature-composition (P-T-X) diagram of ammonia ( $\text{NH}_3$ ) and water ( $\text{H}_2\text{O}$ ) and to extend to the water-methane ( $\text{CH}_4$ ) system.

After much work, we have shown that a reactive multi-phase binary system can be characterized at high pressures with reasonable precision. We started to work with ammonia-water because their mixtures are easy to prepare and had to learn to overcome the reactivity of this system with components of the high pressure cells. These problems have been solved. Dr. Koumvakalis's doctoral research [1988] determined phase boundaries for equimolar ammonia-water, where ammonia monohydrate is the solid phase to 8 GPa; showed that this hydrate has only one solid phase below 13.5 GPa from 120 to 450 K; and identified Raman spectra of perproto- and perdeutero- monohydrate that distinguish this from other solid hydrates.

Mr. Boone completed isoplethic phase diagrams of  $\text{NH}_3\text{-H}_2\text{O}$  mixtures at up to 50 mol percent ammonia, with emphasis on ammonia dihydrate. His results and their implications for icy satellites were outlined in a paper in the proceedings of Lunar and Planetary Science XIX [Cynn et al., 1988] and are described in detail in his doctoral dissertation, which will be filed in June 1989. With Mr. Cynn, Mr. Boone examined the  $X = 0.33$  isopleth to more than 5 GPa between 100 and 400 K both visually and by Raman spectroscopy. They detected four phases by visual methods and identified three of these phases by Raman spectra as: fluid, Ice VII, and ammonia monohydrate. The fourth phase, which melts incongruently to ammonia monohydrate and Ice VII at high pressures, can be crystallized from the liquid at pressures less than 1.8 GPa and temperatures below 240 K. This phase has been identified as ammonia dihydrate. Mr. Boone also showed that large crystals of this dihydrate could be grown between 0.5 and 2 GPa and recovered at atmospheric pressure and 77 K. However, he could not obtain good single-crystal x-ray diffraction patterns; the measured intensities were very low, as if the recovered crystals were too strained to diffract well.

Mr. Cynn has attempted to collect single-crystal x-ray diffraction patterns of ammonia monohydrate at high pressure in order to determine its compressability and define conditions under which single-crystal work on the structure of ammonia dihydrate kept at low temperatures and high pressures might be possible. He has shown that conventional x-ray sources are too weak for this work and plans to try a new diffractometer with an intense rotating-anode source at Los Alamos during Summer 1989.

Mr. Boone also succeeded in loading samples of methane clathrate, grown at ambient temperature, in a diamond-anvil cell by working at cryogenic temperatures; and he used Raman spectroscopy to identify its decomposition pressure at ambient temperature. Mr. Cynn will continue this work to obtain the P-T phase diagram at the clathrate composition to determine decomposition pressures, spectra of the clathrate and separate phases, and kinetics for regrowing clathrate in the high pressure cell. He will then extend the study to other compositions which may be loaded by mixing crystals of chathrate, water ice, solid ammonia, and ammonia hydrates.

#### References

1. Koumvakalis, A. High Pressure Studies of Ammonia Monohydrate. (University of California, Los Angeles, 1988).
2. Cynn, H.-C., Boone, S., Koumvakalis, A., Nicol, M., and Stevenson, D.J. Ammonia-Water Mixtures at High Pressures: Applications to Icy Satellites. Lunar and Planetary Science XIX (1988) 856-857.

## MANTLE CONVECTION ON VENUS AND MARS

Walter S. Kiefer and Bradford H. Hager (Division of Geological and Planetary Sciences, California Institute of Technology, Pasadena CA, 91125)

Our research focuses on the dynamics of mantle convection on Venus and Mars and the relationship between convection and geoid anomalies, highland topography, and tectonic structures. We have concentrated our modeling efforts on several distinctive geologic provinces: the Equatorial Highlands of Venus, the Ishtar Terra region of Venus, and the Tharsis and Elysium provinces of Mars.

### The Venus Equatorial Highlands

The Equatorial Highlands of Venus consists of several quasi-circular regions of high topography (up to 5 km above mean planetary radius (m.p.r.)), large geoid anomalies (up to 100 m), and extensional tectonism (1-3). Isostatic processes can not plausibly account for the observed geoid and topography (4), suggesting that mantle processes, particularly hot, upwelling plumes, may play a dominant role in the formation of these features.

We have modeled mantle plumes using a cylindrical axisymmetric finite element code. We find that the plume model can explain the observed geoid and topography of the Equatorial Highlands if Venus's asthenosphere is significantly more viscous than Earth's asthenosphere (5). A high viscosity asthenosphere is also consistent with models of Venus's long-wavelength admittance spectrum (4). Experiments have shown that the presence of even a small amount of water can substantially weaken the rheology of olivine (6,7). We hypothesize that the lack of an asthenosphere on Venus is due to Venus's mantle being much drier than Earth's mantle.

### Ishtar Terra

Like the Equatorial Highlands, Ishtar Terra is region of high topography and a positive geoid anomaly on Venus (1,2). Eastern Ishtar (east of Maxwell Montes) consists primarily of tessera terrain and is 1 to 3 km above m.p.r. Western Ishtar is centered on Lakshmi Planum, a 1500 km wide oblong to irregularly shaped plateau which is 3 to 4 km above m.p.r. and shows little evidence of tectonic deformation. Lakshmi is surrounded on three sides by the mountain belts Akna, Freyja, and Maxwell Montes, which rise 7 to 11 km above m.p.r. These mountain belts show a pronounced banded structure which approximately parallels the contact between the mountains and Lakshmi and which is typically interpreted as having a compressive origin (8-11).

Although a mantle plume model for western Ishtar has been proposed (12,13), the strong contrast in tectonic styles between Ishtar and the Equatorial Highlands makes a plume model for Ishtar implausible. A second thermal mechanism for supporting topography, lithospheric delamination, can account for only 1.5 km of topography at Ishtar Terra (14). Because thermal mechanisms for supporting the topography of western Ishtar appear to be inadequate, the high topography in this region is most likely due to crust which is thicker than normal (14,15). We propose that the crust in this region has been thickened as a result of crustal convergence over a region of mantle downwelling (15). This model can also explain the observed compressive deformation in the mountain belts.



The high topography of Ishtar causes a large pressure gradient directed away from the center of Ishtar. If Ishtar formed as a result of crustal convergence, then the inward force due to shear stresses applied by the mantle at the base of the crust must have overcome the outward force due to Ishtar's high topography. The required shear stress level depends both on the horizontal length scale of the convection cell and on the crustal thickness in the plains surrounding Ishtar. Assuming that convection extends throughout the entire mantle of Venus, a horizontal length scale of about 3000 km is probably an upper bound on the horizontal scale over which tractions can be applied, and hence sets a lower bound on the magnitude of the required shear stresses. If the crust in Venus's plains regions is 10 to 20 km thick (16-18), then the required shear stress is about 8 to 11 bars. On the other hand, if the crustal thickness in the plains is 100 to 170 km (19), then the required shear stress is 40 to 60 bars. These are minimum estimates of the required shear stress because they consider only the shear stress needed to support the topography of Lakshmi Planum. In order to support the topography of Akna, Freyja, and Maxwell Montes, the mantle shear stress in at least some areas around Ishtar will need to be substantially higher than the above estimates. Estimates of the shear stress at the base of the lithosphere on Earth are typically only a few bars (20-22). Because of Venus's high surface temperature and consequent low crustal viscosities, shear stresses at the crust-mantle interface are likely to be low, a result which favors a thin crust. Because of the time-dependent nature of mantle convection, the shear stresses which are supporting Ishtar's high topography may decrease in magnitude at some time, leading to relaxation of the high topography. Gravitational relaxation of high topography has sometimes been suggested as a mechanism for producing tessera terrain (23-25). We suggest that gravitational relaxation of Maxwell Montes may be at least partially responsible for producing or modifying Fortuna Tessera in eastern Ishtar. For net convergence rates of a few cm/yr and crustal thicknesses of a few tens of kilometers in the plains, our model predicts that Ishtar can form in a few hundred million years, consistent with the observed cratering of its surface.

## Tharsis and Elysium

The Tharsis and Elysium regions of Mars are regions of broad-scale topographic uplift and contain numerous volcanic structures. These observations suggest that mantle convection has been an important process in the origin and evolution of these regions. Existing quantitative models of the geoid and topography of Tharsis have focused on isostatic and flexural processes in the Martian lithosphere (26-30). In these models, the contribution of convection to the geoid and topography of Tharsis was neglected on the grounds that convective support could not be maintained over the age of the solar system. However, Mars is a sufficiently large planet that mantle heat transport must still be dominated by convection, and in the absence of plate tectonics, Tharsis and Elysium could stay over mantle upwellings for an indefinite length of time. Moreover, cratering statistics show that volcanic activity at two shield volcanoes in the Tharsis province, Olympus Mons and Ascraeus Mons, may have been active in the last 100 million years (31). Some geologically recent volcanism may also have occurred in the Elysium region (e.g., 32). We interpret this as indicating that convective upwelling in these regions has continued until recent times and is probably important today.

We have used a cylindrically axisymmetric finite element code to assess the possible contribution of mantle convection to the geoid and topography of Tharsis and Elysium. The neglect of spherical geometry is probably not a significant problem for models of Elysium, but will be more important for models of Tharsis and will need to be addressed in future work. Our results are sensitive to a variety of poorly known parameters, including the Rayleigh

number, the variation of viscosity with depth, and the thickness of the elastic lithosphere. We find that for some plausible choices of parameters that convection can contribute significantly to the observed long-wavelength topography and geoid of Tharsis and Elysium (33). We also find that increasing the horizontal scale of convective upwelling leads to larger amplitude topographic uplift and geoid anomalies. This suggests that the large observed differences in the topography and geoid of Tharsis and Elysium may be largely due to differences in the horizontal scales of the underlying convection cells. Our models predict that any extensional features which form should be oriented radially to the center of the uplift, in agreement with observations of extensional features in Tharsis (34). Although isostatic and flexural processes must play some role in supporting the current long-wavelength geoid and topography in Tharsis and Elysium, our results show that convective processes played an important role both in the formation of Tharsis and Elysium and in maintaining the current geoid and topography.

## References

- (1) USGS Map I-1562, 1984.
- (2) Bills, Kiefer, and Jones, JGR 92, 10,335-10,351, 1987.
- (3) Schaber, GRL 9, 499-502, 1982.
- (4) Kiefer et al., GRL 13, 14-17, 1986.
- (5) Kiefer and Hager, LPSC 19, 601-602, 1988.
- (6) Chopra and Paterson, JGR 89, 7861-7876, 1984.
- (7) Karato et al., JGR 91, 8151-8176, 1986.
- (8) Campbell et al., Science 221, 644-647, 1983.
- (9) Solomon and Head, JGR 89, 6885-6897, 1984.
- (10) Basilevsky et al., JGR 91, D399-D411 (Proc. LPSC 16), 1986.
- (11) Crumpler et al., Geology 14, 1031-1034, 1986.
- (12) Basilevsky, Geotectonics 20, 282-288, 1986.
- (13) Pronin, Geotectonics 20, 271-281, 1986.
- (14) Morgan and Phillips, JGR 88, 8305-8317, 1983.
- (15) Kiefer and Hager, LPSC 20, 520-521, 1989.
- (16) Zuber, JGR 92, E541-E551, (Proc. LPSC 17), 1987.
- (17) Banerdt and Golombek, JGR 93, 4759-4772, 1988.
- (18) Grimm and Solomon, JGR 93, 11,911-11,929, 1988.
- (19) Anderson, GRL 7, 101-102, 1980.
- (20) Melosh, Pure Appl. Geophys. 115, 429-439, 1977.
- (21) Chapple and Tullis, JGR 82, 1967-1984, 1977.
- (22) Davies, GRL 5, 161-164, 1978.
- (23) Sukhanov, Geotectonics 20, 294-305, 1986.
- (24) Bindshadler and Head, LPSC 19, 78-79, 1988.
- (25) Smrekar and Phillips, GRL 15, 693-696, 1988.
- (26) Banerdt et al., JGR 87, 9723-9233, 1982.
- (27) Willemann and Turcotte, JGR 87, 9793-9801, 1982.
- (28) Solomon and Head, JGR 87, 9755-9774, 1982.
- (29) Sleep and Phillips, JGR 90, 4469-4489, 1985.
- (30) Finnerty et al., JGR 93, 10,225-10,235, 1988.
- (31) Plescia and Saunders, Proc. LPSC 10, 2841-2859, 1979.
- (32) Tanaka and Scott, LPSC 18, 998-999, 1987.
- (33) Kiefer and Hager, MEVTV-LPI Workshop: Early Tectonic and Volcanic Evolution of Mars, LPI Technical Report, in press, 1988.
- (34) Carr, JGR 79, 3943-3949, 1974.

# ESTIMATING LITHOSPHERIC THERMAL GRADIENT ON MARS FROM ELASTIC LITHOSPHERE THICKNESS: NEW CONSTRAINTS ON HEAT FLOW AND MANTLE DYNAMICS.

Sean C. Solomon, Department of Earth, Atmospheric, and Planetary Sciences, Massachusetts Institute of Technology, Cambridge, MA 02139, and James W. Head, Department of Geological Sciences, Brown University, Providence, RI 02912.

*Introduction.* The thickness of the elastic lithosphere on a planet is essentially a measure of the reciprocal of the vertical thermal gradient in the lithosphere, i.e., the depth to a temperature at which ductile behavior replaces brittle behavior at typical geological strain rates. Under flexure there is an elastic "core" of the lithosphere occupying the depth interval over which the bending stress is less than an envelope of "strength" versus depth defined by a frictional failure curve at shallow depths and a ductile flow law at greater depth [1,2]. The depth of the lower limit to "elastic" behavior is governed primarily by temperature and also by strain rate, composition, and load magnitude. Estimates of elastic lithosphere thickness derived from simple models of flexure have been quantitatively related to the average vertical thermal gradient of the lithosphere on the Earth [e.g., 3] and Moon [4], and similar concepts have been used to constrain the thickness of the elastic lithosphere on Venus [e.g., 5]. In this paper we apply these concepts to Mars.

*Elastic Lithosphere Thickness.* The thickness  $T_e$  of the elastic lithosphere of Mars has been estimated from the tectonic response to individual loads [6-8] and from the global response to the long-wavelength load of the Tharsis rise [9,10]. A summary of these results is given in Table 1. The values for  $T_e$  derived for individual loads are not consistent with a simple progressive increase with time in the thickness of the elastic lithosphere of Mars. The largest estimates of  $T_e$ , for instance, are for perhaps the oldest (Isidis mascon) and youngest (Olympus Mons) features considered [11]. Spatial variations in elastic lithosphere thickness must have been at least as important as temporal variations [7]. In particular, there appears to have been a dichotomy in lithosphere thickness that spanned a significant interval of time, with comparatively thin elastic lithosphere ( $T_e = 20$  to  $50$  km) beneath the central regions of major volcanic provinces and substantially thicker elastic lithosphere ( $T_e$  in excess of  $100$  km) beneath regions more distant from volcanic province centers and appropriate for the planet as a whole.

*Thermal Gradients.* The values of  $T_e$  may be converted to the mean lithospheric thermal gradient, given a representative strain rate and a flow law for ductile deformation of material in the lower lithosphere. Formally, this is done by converting  $T_e$  to  $T_m$ , the depth to the rheological boundary marking the base of the mechanical lithosphere. This conversion is accomplished by constructing models of bending stress consistent with the strength envelope and finding for each model the equivalent elastic plate model having the same bending moment and curvature [3]. We take the representative strain rate for the flexural response to each local load to be the quotient of the maximum horizontal strain given by the elastic model and the growth time of the load, taken to be  $10^{8\pm1}$  yr. A large uncertainty arises from the poorly known value for the thickness of the martian crust and the distinct flow laws for crustal and mantle material. The mean crustal thickness consistent with global topography and gravity must be at least  $30$  km [12], which corresponds to zero thickness beneath the Hellas basin. Viking line-of-sight (LOS) residuals over the Hellas basin and the  $370$ -km-diameter crater Antoniadi are best fit if the topographic depressions are compensated at  $120$ - $130$  km depth [13,14]. LOS data over Elysium Planitia and Olympus Mons can

be fit with varying degrees of Airy isostatic compensation and crustal thicknesses of 30-150 km [8,15].

We assume that the large values of elastic lithosphere thickness determined from the local response to the Isidis mascon and Olympus Mons and from the global response to the Tharsis rise exceed the thickness of the martian crust. Because flexurally-induced curvature is modest for these loads, the depth  $T_m$  to the base of the mechanical lithosphere is approximately equal to  $T_e$  [3] and is determined by the ductile strength of the mantle, assumed to be limited by the creep strength of olivine [16]. The minimum values of  $T_e$  for the Isidis mascon and Olympus Mons correspond, by this line of reasoning, to mean lithospheric thermal gradients of no greater than 5-6 K/km.

The values of  $T_e$  derived from the Tharsis Montes and Alba Patera are less than or comparable to the thickness of the crust. The mechanical lithosphere thickness  $T_m$ , which exceeds  $T_e$  for these loads [3], is likely governed by the strength of crustal material, taken to be limited by the creep strength of anorthosite [17]. The mean thermal gradients consistent with the values of  $T_m$  for these loads under this assumption are in the range 11-18 K/km (Table 1). The thermal gradient corresponding to the value  $T_e = 54$  km determined for Elysium Mons [7] depends strongly on the thickness of the martian crust but generally falls between those for Olympus Mons and Isidis and those for the Tharsis Montes and Alba Patera.

*Implications.* While the heat flow and thermal structure of Mars are not known, we may compare these gradients with values derived from scaling arguments. If Mars loses heat at the same rate per mass as the Earth [18], then the mean heat flux would be about 30 mW/m<sup>2</sup>-K. For a representative value of lithospheric thermal conductivity of 2-3 W/m-K, the mean lithospheric thermal gradient would be 10-15 K/km. The gradient implied by the global response to the Tharsis rise falls below this range by at least 30-50%. Two possible explanations are that the fractional heat loss contributed by secular global cooling is much lower on Mars than on Earth or that a higher fraction of radioactive heat sources on Mars are concentrated in the crust. The low <sup>40</sup>Ar abundance in the Martian atmosphere [19] provides an argument against the second possibility.

As noted above, the differences in lithospheric thermal gradients implied by the different values of  $T_e$  must be at least in part due to lateral variations in temperature within and beneath the lithosphere. These variations can be due to lithospheric reheating beneath the centers of major volcanic provinces, thermal differences remaining from major pre-volcanic events such as large impacts [20], or some combination of these two effects [21]. Essentially contemporaneous temperature differences of at least 400 K at 30 km depth at a late stage in the development of the Tharsis province are implied by the variation in gradients in Table 1. Such differences are too large to be solely the effect of large impacts of order 10<sup>9</sup> yr earlier [22]. They are, however, similar to the temperature variations associated with lithospheric reheating beneath hot spot volcanic centers on Earth [23]. The areas of anomalously high temperature gradients on Mars must be similarly affected by mantle dynamic processes, including convective upwelling and associated magmatism. These results thus provide new constraints on the spatial pattern of heat delivered by mantle upwelling beneath major volcanic provinces on Mars.

*References.* [1] C. Goetze and B. Evans, *GJRS*, 59, 463, 1979; [2] W.F. Brace and D.L. Kohlstedt, *JGR*, 85, 6248, 1980; [3] M.K. McNutt, *JGR*, 89, 11180, 1984; [4] S.C.

Solomon, *LPS*, 16, 799, 1985; [5] S.C. Solomon and J.W. Head, *JGR*, 89, 6885, 1984; [6] C.H. Thurber and M.N. Toksoz, *GRL*, 5, 977, 1978; [7] R.P. Comer, S.C. Solomon and J.W. Head, *Rev. Geophys.*, 23, 61, 1985; [8] P. Janle and D. Jannsen, *Annal. Geophys.*, 4, B 537, 1986; [9] R.J. Willemann and D.L. Turcotte, *JGR*, 87, 9793, 1982; [10] W.B. Banderdt et al., *JGR*, 87, 9723, 1982; [11] K.L. Tanaka et al., *PLPSC 18th*, 665, 1988; [12] B.G. Bills and A.J. Ferrari, *JGR*, 83, 3497, 1978; [13] W.L. Sjogren and R.N. Wimberly, *Icarus*, 45, 331, 1981; [14] W.L. Sjogren and S.J. Ritke, *GRL*, 9 739, 1982; [15] P. Janle and J. Ropers, *PEPI*, 32, 132, 1983; [16] C. Goetze, *Phil. Trans. Roy. Soc. Lond.*, A288, 99, 1978; [17] G. Shelton and J. Tullis, *Eos*, 62, J96, 1981; [18] J.G. Sclater et al., *RGSP*, 18, 269, 1980; [19] V.B. Pollack and D.C. Black, *Science*, 205, 56, 1979; [20] P.H. Schultz and H. Glicken, *JGR*, 84, 8033, 1979; [21] S.C. Solomon and J.W. Head, *JGR*, 87, 9755, 1982; [22] S.R. Bratt, S.C. Solomon and J.W. Head, *JGR*, 90, 12415, 1985; [23] M. McNutt, in *Seamounts, Islands, and Atolls*, AGU, 123, 1987.

Table 1. Estimates of elastic lithosphere thickness and lithospheric thermal gradient on Mars

Feature	Age of deformation	D, 10 <sup>30</sup> dyn cm	T <sub>e</sub> , km	dT/dz, K/km
Arsia Mons	UA	0.5	18	18
Ascraeus Mons	UA	1.0	22	14
Pavonis Mons	UA	1.6	26	13
Alba Patera	LA	3.2	33	11
Elysium Mons	LA	14	54	7-13
Olympus Mons	UA	50 - 240	140 - 230	< 5
Isidis mascon	UN	>150	>120	< 6
Tharsis rise	MN - UA	>100	>100	< 7

Sources: D, T<sub>e</sub> [6-10]; ages [11]; N = Noachian, H = Hesperian, A = Amazonian, L = lower, M = middle, U = upper.

## **Research on Structure and Evolution of Planetary Interiors**

G. Schubert, Department of Earth and Space Sciences, University of California, Los Angeles, L. A., CA 90024

### Mercury's Thermal History

We wrote a review paper, "Mercury's Thermal History and the Generation of its Magnetic Field," by G. Schubert, M. N. Ross, D. J. Stevenson and T. Spohn, for the University of Arizona Press. We advocated a Mercury model with a hot start and early core formation. Mercury's large iron core cools and partially freezes, but complete solidification of the core is prevented by the depression of the core-freezing temperature by sulfur in the core. It is possible to maintain convection in Mercury's outer liquid core to the present, perhaps accounting for the dynamo generation of Mercury's magnetic field. Tidal heating in the inner solid core may have been a significant source of energy for the core.

### Martian Crater Morphology

We have used Goldstone 13-cm radar observations of Mars during the 1971-1982 oppositions to study the morphology of Martian craters as revealed in their topographic profiles. Degraded Martian craters are shallow and have very low rim heights. Structures without a discernable rim have retained a basin shape. Low exterior relief rather than overall low relief distinguishes the large degraded craters in the Goldstone sample. The paper describing these results, "Radar Altimetry of Large Martian Craters" by L. E. Roth, R. S. Saunders, G. S. Downs and G. Schubert, is in press in Icarus.

### Lunar Orbital Evolution

We modelled the coupled thermal-dynamical evolution of the Earth-Moon system including solid planet tidal dissipation and dissipation by the Earth's oceans. Solid Earth tidal friction has been the main energy sink in the Earth-Moon system; oceanic dissipation has a relatively small effect over geologic time, even though it is important at present. About 90% of the angular momentum transferred from the Earth to the Moon is a consequence of solid-body tidal friction. These results are discussed in more detail in "Evolution of the Lunar Orbit with Temperature and Frequency-Dependent Dissipation," by M. N. Ross and G. Schubert (J. Geophys. Res., in press).

### Atmosphere-Interior Evolution of Planets and Satellites

We have written a review paper for a forthcoming University of Arizona Press book ("Evolution of the Atmospheres-Interiors of Planets and Satellites" by G. Schubert, D. L. Turcotte, S. C. Solomon, and N. Sleep) that discusses how the atmospheres and interiors of terrestrial planets evolve in a coupled manner. The physical mechanisms that couple the atmospheres and interiors of planets are analyzed in detail.

## MERCURY: A KEY TO UNDERSTANDING THE FORMATION AND EVOLUTION OF THE TERRESTRIAL PLANETS

Robert G. Strom, Department of Planetary Sciences,  
University of Arizona, Tucson, Arizona 85721 U.S.A.

Mercury is an end-member planet because it formed nearest to the Sun in the hottest part of the solar nebula. Although it superficially resembles the Moon, there are significant differences in both the internal constitution and surface geology. Mercury has an uncompressed mean density of  $5.3 \text{ g/cm}^3$ ; larger than any other planet or satellite in the Solar System. This indicates that it has an enormous iron core about 75 percent of the planet radius. The presence of a dipole magnetic field further suggests that the outer portion of the core is currently in a molten state. This requires a light alloying element in the core to lower the melting point and retain a partially molten core to the present time. Although oxygen is such an element, it is not sufficiently soluble in iron at Mercury's low internal pressures and, therefore, sulfur is the most reasonable candidate. The present extent of the outer molten core and the onset of solid inner core formation are highly dependent on the abundance of sulfur in the core. For a sulfur abundance less than 0.2 percent the entire core should be solidified at the present time, while an abundance of 7 percent results in an entirely fluid core at present. Inner core formation begins about 3.9 GY ago for 0.2 percent sulfur and results in an outer fluid core about 100 km thick at present. For 5 percent sulfur the inner core begins to form about 2 GY ago, and results in an outer fluid core about 1150 km thick at present (Schubert et al., 1988).

How Mercury acquired such a large percentage of iron is a major unsolved problem. Initial chemical equilibrium condensation models for Mercury's position in the solar nebula predicted an uncompressed density of only  $4 \text{ g/cm}^3$  rather than the observed  $5.3 \text{ g/cm}^3$  and the complete absence of sulfur (Lewis, 1972). Modified models (Lewis, 1988) where 60-90 percent of the material accreted at Mercury's present distance and 10-40 percent accreted from planetesimals perturbed into Mercury's position from the feeding zones of other terrestrial planets, still fail to provide enough iron to account for Mercury's uncompressed density (4.2 vs.  $5.3 \text{ g/cm}^3$ ). They do, however, predict from 0.1 to 3 percent FeS (Lewis, 1988).

Three very different hypotheses have been proposed to account for the large discrepancy between the iron abundance indicated by Mercury's high density and that predicted by equilibrium condensation models. One hypothesis (selective accretion) proposes a mechanical accretion process for concentrating the required iron at Mercury's position in the solar nebula, while the other two (post-accretion vaporization and giant impact) account for Mercury's high density by removing a large fraction of Mercury's silicate mantle early in its history. In the selective accretion model, a differential response of iron and silicates to impact fragmentation and aerodynamic sorting leads to iron enrichment owing to higher gas densities and shorter dynamical time scales in the innermost part of the solar nebula (Weidenschilling, 1978). The post-accretion vaporization model proposes that intense bombardment by solar electromagnetic and corpuscular radiation in the earliest phases of the Sun's evolution (T-Tauri phase) vaporized and drove off much of the silicate mantle (Cameron et al., 1988). In the giant impact hypothesis, a collision of a planet-sized object with Mercury ejected much of the planet's silicate mantle, which is subsequently swept-up principally by Venus and Earth (Cameron et al., 1988; Wetherill, 1988). Each of these hypotheses has major consequences for the formation of the other terrestrial planets. Fortunately, each model predicates a significantly different chemical composition for Mercury's silicate mantle and, therefore, compositional information from a Mercury orbiter can help decide between these competing hypotheses. Until we understand how Mercury formed, we will not clearly understand the formational history of the other terrestrial planets.

Mariner 10 imaged only about 45 percent of Mercury's surface at resolutions comparable

to Earth-based telescopic resolution of the Moon. As a consequence, our understanding of its geologic history and the origin of some of its surface features is incomplete. The surface viewed by Mariner 10 shows an ancient heavily cratered terrain, and younger smooth plains which primarily fill and surround the 1300 km diameter Caloris impact basin and occupy a large area of the north polar region. These surfaces are similar to the lunar highlands and maria of the Moon. Unlike the Moon, Mercury contains large areas of old intercrater plains interspersed among the heavily cratered terrain and a system of presumably global thrust faults (lobate scarps) that resulted from a period of global compression caused by planetary contraction. A peculiar hilly and lineated terrain occurs antipodal to the Caloris Basin and probably resulted from large vertical surface movements caused by focused seismic waves from the Caloris impact.

Mercury's intercrater plains are the major terrain on Mercury and formed at various times during the period of late heavy bombardment. These plains are thought to be volcanic deposits erupted through fractures caused by planetary expansion during heating and core formation. The younger, smooth plains are also interpreted as volcanic deposits primarily erupted through fractures caused by the large basin-forming impacts with which they are associated. The global system of thrust faults post-dates intercrater plains formation suggesting that the onset of planetary contraction began relatively late in Mercurian history. The decrease of Mercury's radius estimated from the number and dimensions of thrust faults is about 2 km. Both the time of onset of global contraction and the amount of radius decrease based on the geologic relationships are at variance with current thermal history models which predict that contraction began immediately following accretion and resulted in a radius decrease of about 6 to 8 km (Schubert et al., 1988).

Almost nothing is known about Mercury's surface composition. The major terrain units (smooth plains, intercrater plains, and crater rays) have systematically higher albedos than comparable terrains on the Moon. The photometry and colorimetry suggest that Mercury's surface material may be depleted in iron and titanium relative to lunar rocks.

A Mercury orbiter with an imaging device and instruments for measuring the surface composition could provide the information required to decide between the various hypotheses for Mercury's origin and geologic and thermal evolution. Answers to these questions would, in turn, shed new light on the formation and evolution of the other terrestrial planets.

#### References

- Cameron, A.G.W., et al., The Strange Density of Mercury: Theoretical Considerations, in Mercury, Univ. of Arizona Press, 1988.
- Lewis, J.S., Metal/Silicate Fractionation in the Solar System, *Earth Planet. Sci. Lett.*, **15**, 286-290, 1972.
- Lewis, J.S., Origin and Composition of Mercury, in Mercury, Univ. of Arizona Press, 1988.
- Schubert, G., et al., Mercury's Thermal History and the Generation of its Magnetic Field, in Mercury, Univ. of Arizona Press, 1988.
- Weidenschilling, S.J., Iron/Silicate Fractionation and the Origin of Mercury, *Icarus*, **35**, 99-111, 1978.
- Wetherill, G.W., Accumulation of Mercury from Planetesimals, in Mercury, Univ. of Arizona Press, 1988.



## Implications of Convection in the Moon and the Terrestrial Planets

Donald L. Turcotte, Department of Geological Sciences, Cornell University, Ithaca, NY  
14853-1504

In the last year we have published a paper on the tectonic implications of radiogenic noble gases in planetary atmospheres (1).

Studies of the radiogenic isotopes  $^4\text{He}$  and  $^{40}\text{Ar}$  in planetary atmospheres provide important constraints on tectonic processes within planetary interiors. For mantle K/U and Th/U mass ratios  $R_{\text{K/U}} = 12,700$  and  $R_{\text{Th/U}} = 3.8$  and a Urey number  $U_r = 0.7$ , the  $^{40}\text{Ar}$  in the Earth's atmosphere can be obtained by complete outgassing of the crust and upper mantle and a 7% outgassing of the lower mantle or by a 23 to 33% outgassing of the whole mantle and crust. The flux of  $^4\text{He}$  from the mantle can be derived by complete, steady-state outgassing of the upper mantle or by partial outgassing (9%) of the entire mantle. The  $^{40}\text{Ar}$  in the Venus atmosphere can originate from the outgassing of only the upper 6 km of an enriched crust, 8.5% of the entire mantle, or 28% of the upper mantle. The low concentration of  $^{36}\text{Ar}$  in the Earth's atmosphere relative to Venus strongly supports the collision hypothesis for the origin of the Moon; such a major collision would have eroded a large fraction of the Earth's atmosphere.

We have also proposed (2) a heat pipe mechanism for the transport of heat through the lithosphere on Venus. This mechanism allows the crust and lithosphere on Venus to be greater than 150 km thick. A thick crust and thick lithosphere can explain the high observed topography and large associated gravity anomalies. For a 150-km-thick lithosphere the required volcanic flux on Venus is  $200 \text{ km}^3/\text{yr}$ ; this is compared with a flux of  $17 \text{ km}^3/\text{yr}$  associated with the formation of the oceanic crust on Earth. A thick basaltic crust on Venus is expected to transform to eclogite at a depth of 60 to 80 km; the dense eclogite would contribute to lithospheric delamination that returns the crust to the interior of the planet completing the heat pipe cycle. Topography and the associated gravity anomalies can be explained by Airy compensation of the thick crust.

We are currently carrying out a series of parameterized convection calculations to model the thermal evolution of the Moon, Mars, and Venus. These calculations yield the time dependence of the crustal thickness, the lithosphere thickness, the rate of volcanism, and whether the body contracts or expands. The preliminary results appear very promising in terms of explaining a variety of observed features on these bodies.

1. D.L. Turcotte and G. Schubert. Tectonic implications of radiogenic noble gases in planetary atmospheres. *Icarus* 74, 36-46 (1988).
2. D.L. Turcotte. A heat-pipe mechanism for volcanism and tectonics on Venus. Presented at the 19th Lunar and Planetary Science Conference, Houston, Texas, March 14-18, 1988. *Lunar Planet. Sci. XIX*, 1207-1208, (1988b).
3. D.L. Turcotte. Early evolution of the Martian interior. Presented at the 1988 Spring Meeting of the American Geophysical Union, Baltimore, Maryland, May 16-20, 1988. *Trans. Am. Geophys. Un.* 69, 389 (1988a).

# OLIVINE ALTERATION PHASES IN SHERGOTTITE ALHA 77005: INFORMATION FROM 4.2°K MOSSBAUER SPECTRA

Roger G. Burns, Department of Earth, Atmospheric and Planetary Sciences,  
Massachusetts Institute of Technology, Cambridge, Massachusetts 02139.

**Introduction.** Olivine phenocrysts in certain SNC meteorites (notably Nakhla, Chassigny, ALHA 77005) have characteristic brownish colorations which have been attributed to oxidized (ferric) iron {1,2}, either retained in the olivine structure, or present as low-temperature alteration products (e.g. "iddingsite"). The distinctive brown cumulus olivines in the shergottite ALHA 77005, which constitute more than 50% of this meteorite collected in Antarctica {3,4}, are of particular interest because Mossbauer spectral measurements {5,6} have identified ~4.5 wt.% of the total iron in the olivine to be in the ferric state. However, ambiguity exists {2,5} as to whether the oxidized iron is a product of pre-terrestrial alteration, or was produced during residence of the meteorite in the Antarctic ice-cap, or resulted after collection when it was exposed to melt water {7}. In an attempt to further characterize the ferric iron speciation of olivine-rich ALHA 77005, results of correlative Mossbauer spectral measurements with experimentally oxidized olivines {8,9} are reported here.

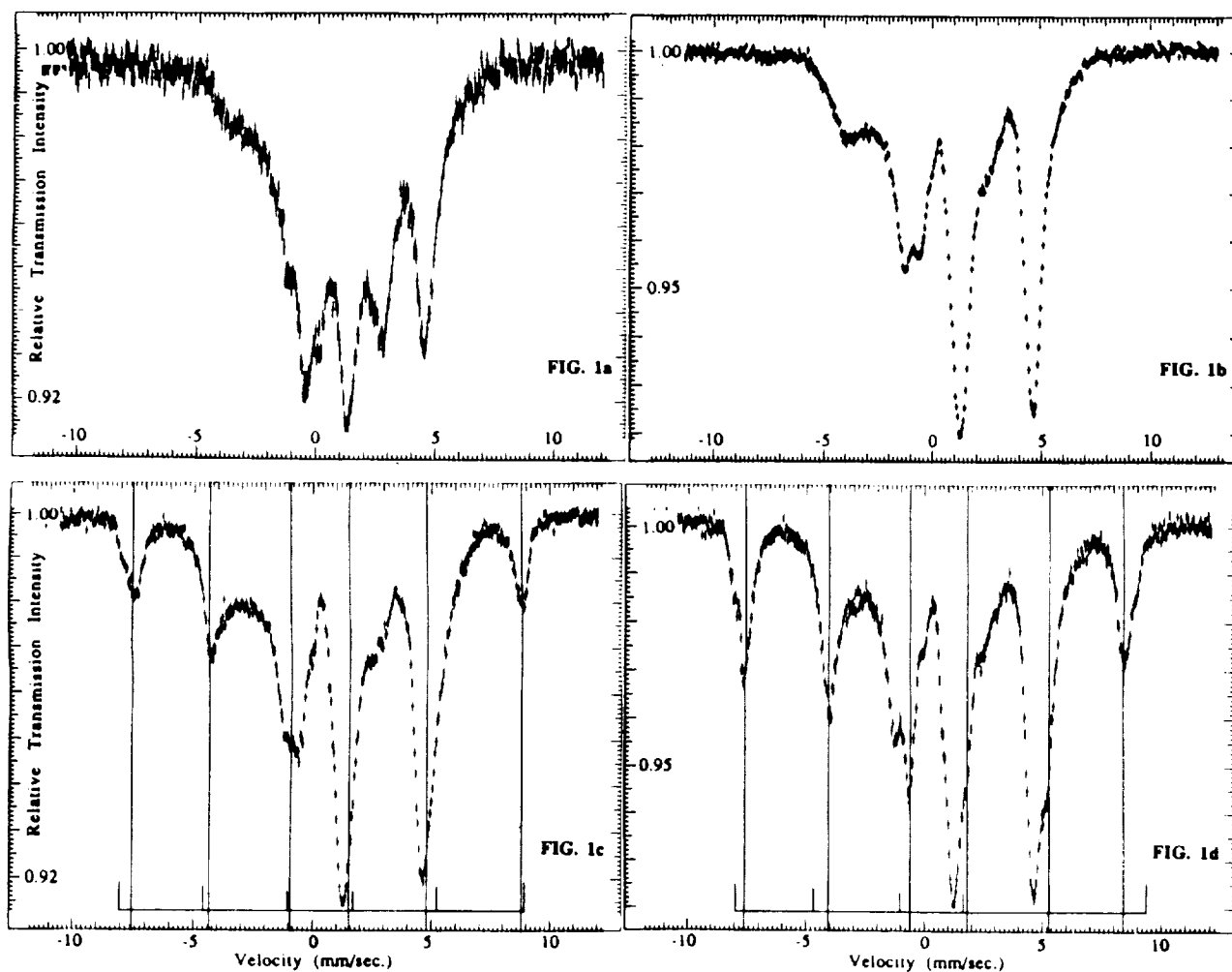
**Experimental Details.** Homogenized powders of ALHA 77005, the modal mineralogy of which consists of 52% olivine (Fa<sub>26</sub>), 26% pigeonite, 11% augite, 10% plagioclase and 1% chromite {4}, were acquired from the Antarctic Meteorite Collection. The two 50 mg powders supplied to us had been separated into "dark" (olivine-rich) and "light" (olivine-depleted) fractions, and each sample was used separately in the Mossbauer spectral measurements {6}. A reference hortonolite (Fa<sub>49</sub>) from the Bushveldt Complex that is being used in contemporaneous heat-oxidation {8} and sulfuric acid-alteration {9} experiments to simulate aerial oxidation and groundwater weathering reactions on Mars, served as a standard for the identification of any ferri-olivine component or nanocrystalline ferric oxide phase that might be detectable in the Mossbauer spectrum of the olivine-rich ALHA 77005 meteorite measured at 4.2°K.

**Results.** Assembled in Figure 1 are the 4.2°K Mossbauer spectra of olivine-rich ("dark" fraction) ALHA 77005 meteorite (Fig. 1a), unreacted hortonolite (Fig. 1b), hortonolite after heat-oxidation in air at 600°C for 10 hours (Fig. 1c), and hortonolite after reaction with H<sub>2</sub>SO<sub>4</sub> (pH 2) at 80°C for 14 days (Fig. 1d). The central portions of each spectrum (between -6 and +6 mm/sec.) are complicated by the onset of magnetic ordering of Fe<sup>2+</sup> ions in the olivine M1 sites and by contributions from pyroxenes in the meteorite sample. However, the regions of the spectra at higher and lower velocities are much more informative. The heat-oxidized hortonolite (Fig. 1c) shows the locations of peaks originating from ferri-olivine and, perhaps, maghemite. The H<sub>2</sub>SO<sub>4</sub>-degraded hortonolite (Fig. 1d) indicates where peaks due to goethite (and hematite) occur. It is immediately apparent from the spectra illustrated in Figure 1 that none of these Fe<sup>3+</sup>-bearing phases is detectable in the specimen of ALHA 77005; if present, they constitute <2% of the meteorite.

**Discussion.** Although a doublet attributable to ~4.5% ferric iron was previously resolved in the room-temperature Mossbauer spectrum of the olivine separate from ALHA 77005 {5}, its parameters (particularly the value for quadrupole splitting) are significantly different from those obtained from 295°K spectra of naturally-occurring ferri-olivines {10} and heat-oxidized olivines {8}, in which magnetic ordering of Fe<sup>3+</sup> ions was induced by 4.2°K. The absence of comparable ferric magnetic sextets in the 4.2°K spectrum of the olivine-rich ALHA 77005 specimen may be due to magnetic-dilution of the structural Fe<sup>3+</sup> ions, or to nanocrystallinity of any ferric oxide intergrowths.

**References.** {1} T.E.Bunch & A.M.Reid, *Meteoritics*, **10**, 303 (1975); {2} J.V.Smith & I.M.Steele, *Meteoritics*, **19**, 121 (1984); {3} H.Y.McSween Jr., *et al.*, *Science*, **204**, 1201 (1979); {4} M.R.Smith *et al.*, *Proc. 14th LPSC; JGR*, **89**, B612 (1984); {5} R.Ostertag *et al.*, *Earth Planet. Sci. Lett.*, **67**, 162 (1984); {6} R.G.Burns & T.C.Solberg, *Lunar Planet. Sci.*, **XIX**, 146 (1988); *Proc. 19th LPSC*, in press; {7} D.D.Bogard & J.O.Annexstad, *Smithsonian Contrib. Earth Sci.*, **23**, 8 (1980); {8} K.S.Bartels & R.G.Burns, this vol.; {9} D.S.Fisher & R.G.Burns, this vol.; {10} M.W.Schaefer, *Am. Mineral.*, **70**, 729 (1985); {11} Research supported by NASA grants NSG-7604 and NAGW-1078.

**Figure 1.** Mossbauer spectra measured at 4.2°K of (a) olivine-rich shergottite ALHA 77005; (b) unreacted olivine (Fa<sub>49</sub>); (c) olivine heated in air to 600°C for 10 hours; and (d) olivine reacted with H<sub>2</sub>SO<sub>4</sub> (pH 2) for 14 days at 80°C in the presence of ferric sulfate. Highlighted in Fig. 1c are locations of the major ferri-olivine sextet and minor maghemite peaks, and in Fig. 1d the major goethite sextet and minor hematite peaks.



# OXIDIZED OLIVINES ON MARS: SPECTROSCOPIC INVESTIGATIONS OF HEAT-INDUCED AERIAL OXIDATION PRODUCTS

Karen S. Bartels and Roger G. Burns, Dept. of Earth, Atmospheric and Planetary Sciences, Massachusetts Institute of Technology, Cambridge, Massachusetts 02139.

**Introduction.** Olivines in komatiitic lavas that erupted onto the surface of Mars were vulnerable to low-temperature aerial oxidation as the magma cooled, by analogy with the occurrence of ferrifayalite (intergrowths of fayalite,  $\text{Fe}_2\text{SiO}_4$ , and laihunite,  $\text{Fe}^{2+}_{0.8}\text{Fe}^{3+}_{0.8}\text{SiO}_4$ ) in terrestrial near-surface and extrusive igneous rocks {1,2}. Similar ferric-bearing Mg-Fe olivines on Mars, contributing to remote-sensed reflectance spectral profiles of the martian surface, could interfere with diagnostic  $\text{Fe}^{2+}$  crystal field bands used to identify ferromagnesian silicates occurring there, particularly in the visible-near infrared spectra of "dark" regions on Mars {3}. We report here measurements made on heated olivines that were aimed at characterising spectral features originating from products of aerial oxidation.

**Experimental Details.** Several olivines [synthetic ( $\text{Fa}_{100}$ ) and Rockport ( $\text{Fa}_{96}$ ) fayalites, hortonolite ( $\text{Fa}_{49}$ ), peridot ( $\text{Fa}_{15}$ ), and knebelite ( $\text{Fa}_{51}\text{Te}_{47}$ )] were heated in air in the temperature range 300-900°C. Mossbauer spectra measured at ambient (295°K) and liquid He (4.2°K) temperatures aided in the identification of structural (olivine) and superparamagnetic (hematite)  $\text{Fe}^{3+}$  ions. Reflectance spectra were obtained for selected specimens using the RELAB facility at Brown University {4}.

**Results: Mossbauer Spectra.** The presence of structural paramagnetic  $\text{Fe}^{3+}$  ions in fayalites heated in air between 300 and 600°C is suggested by Mossbauer spectra of reaction products measured at ambient temperatures. However, an additional sextet originating from magnetic hyperfine splitting of hematite appears in heat-treated fayalites, the intensity of which increases with prolonged heating. Analogous heat-oxidation experiments on hortonolite, peridot and knebelite also produced ferric-bearing assemblages, the 295°K Mossbauer spectra of which yielded  $\text{Fe}^{2+}$  and  $\text{Fe}^{3+}$  doublets but negligible magnetic sextet peaks. The ferric doublet could originate from structural  $\text{Fe}^{3+}$  ions in the ferri-olivines and/or interstitial nanocrystalline  $\text{Fe(III)}$  oxides {5} resulting from oxidation of  $\text{Fe}^{2+}$  in, and diffusion of  $\text{Fe}^{3+}$  from, the olivine structure {2}. The 4.2°K spectra, however, reveal a magnetic sextet originating from ferrifayalite alone, in fayalites heated to 300°C and 400°C. By 600°C, hematite sextets are also present and, after 10 days' heating at this temperature, a maghemite sextet joins that of hematite. These two  $\text{Fe}_2\text{O}_3$  phases persist in fayalites heated to higher temperatures, but the proportion of ferrifayalite decreases. In 4.2°K spectra of Mg-Fe and Mn-Fe olivines heated to 600°C, sextets comparable to that of ferrifayalite appear (c.f. Fig. 1c in the accompanying abstract {6}) but no hematite is present. Prolonged heating at 600°C and higher temperatures produced maghemite-like sextets (which could also be assigned to spinel  $\text{MgFe}_2\text{O}_4$  or  $\text{MnFe}_2\text{O}_4$  phases) in the 4.2°K spectra of each olivine.

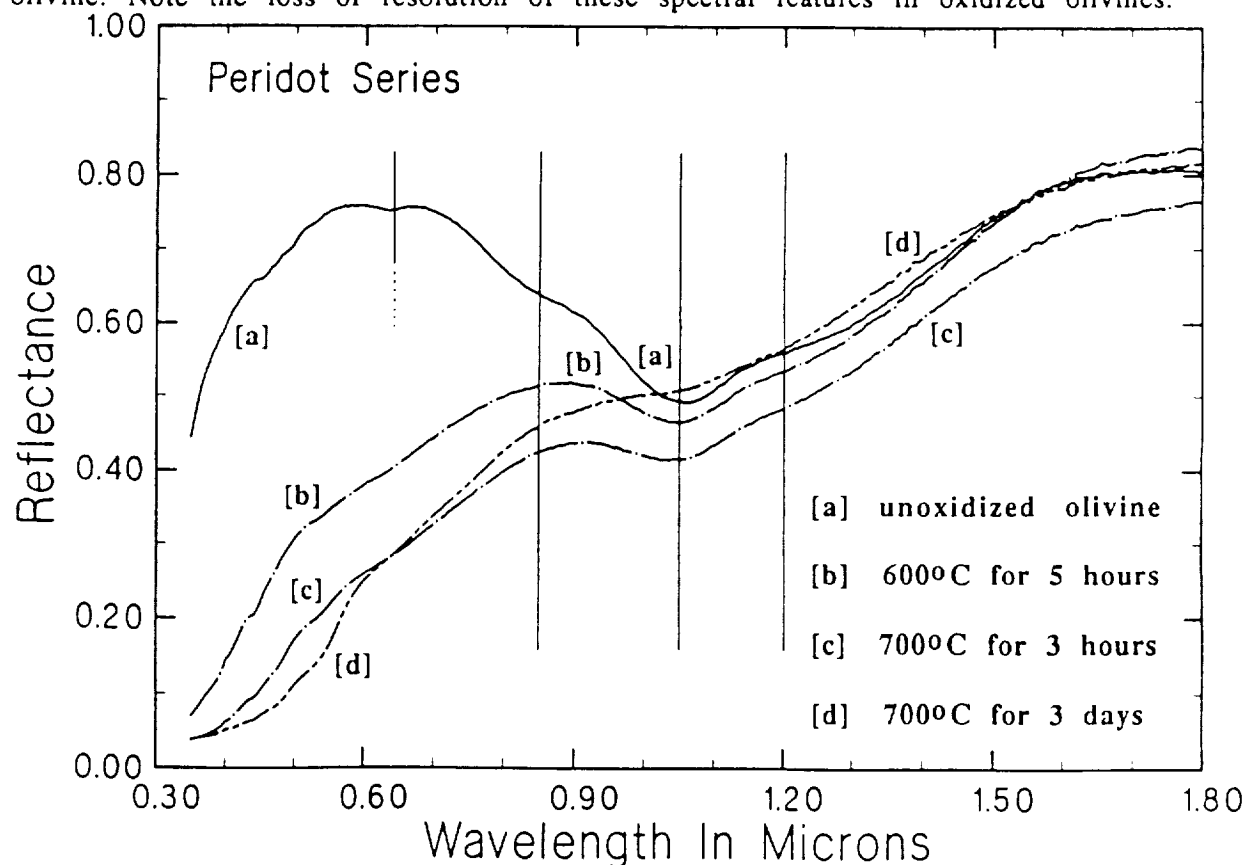
**Results: Reflectance Spectra.** Characteristic spectral features of olivine in the visible-near infrared region, which enable this Mg-Fe silicate to be identified in telescopic reflectance spectral measurements of terrestrial planets {7}, are highlighted in Figure 1 and include: the  $\text{Fe}^{2+}$  (M2 site) band centered at 1.05  $\mu\text{m}$ ; the  $\text{Fe}^{2+}$  (M1 site) bands occurring at ~0.85 and ~1.20  $\mu\text{m}$ ; and, sometimes, the  $\text{Fe}^{2+}$  (spin-forbidden) peak at 0.63  $\mu\text{m}$  (Fig. 1a). However, with increasing oxidation of structural  $\text{Fe}^{2+}$  ions in olivine to  $\text{Fe}^{3+}$ , a red-shift of the ultraviolet absorption edge into the visible region occurs which obliterates the 0.63  $\mu\text{m}$  peak and masks the 0.85  $\mu\text{m}$  band (Figs 1b & c). The appearance of  $\text{Fe}_2\text{O}_3$  phases further obscures the diagnostic olivine- $\text{Fe}^{2+}$  bands at 1.05 and 1.20  $\mu\text{m}$  (Fig. 1d). The reflectance spectra illustrated in

Figure 1 indicate that absorption due to  $\text{Fe}^{3+}$  ions in  $(\text{Mg},\text{Fe}^{2+})_x\text{Fe}^{3+}_y\text{SiO}_4$  ferri-olivines, as well as maghemite or hematite, contribute significantly to the 0.40-0.90 micron region, in which  $\text{Fe}^{3+}$  crystal field and  $\text{Fe}^{2+}$ - $\text{Fe}^{3+}$  intervalence transitions are located {8}.

**Applications to Mars.** Petrological studies {9,10} suggest that Fe-rich basaltic melts, formed by partial melting of the martian mantle, may have erupted as highly turbulent komatiitic lava flows {11} which, on account of their very low viscosities, covered vast areas of the planet and underwent rapid cooling as they thermally eroded the surface {12}. Hortonolite crystallizing from the lava flows was vulnerable to aerial oxidation and might have produced ferric-bearing olivine and nanocrystalline  $\text{Fe}_2\text{O}_3$  phases. These surface oxidation products on basaltic lava flows may contribute to the 0.8-1.2  $\mu\text{m}$  region of "dark" areas on Mars {3}. The olivines would also be susceptible to chemical weathering by acidic hydrosphere if sub-aqueous extrusion of the komatiitic lavas occurred {13}.

**References.** {1} M.W.Schaefer, *Am. Mineral.*, 70, 729 (1985); {2} S. Kondoh *et al.*, *Am. Mineral.*, 70, 737 (1985); {3} R.B.Singer, *Adv. Space Sci.*, 5, 59 (1985); {4} C.Pieters, *JGR*, 88, 9534 (1983); {5} R.W.Morris *et al.*, *Lunar Planet. Sci.*, XVIII, 668 (1987); *JGR*, in press.; {6} R.G.Burns, this vol.; {7} C. Pieters *et al.*, *JGR*, 90, 12393 (1985); {8} R.G.Burns, *Ann. Rev. Earth Planet. Sci.*, 9, 345 (1981); {9} G.Bussod & T.R.McGetchin, *Lunar Planet. Sci.*, X, 172 (1979); {10} C.M.Bertka & J.R.Holloway, *Proc. 18th LPSC*, 723 (1988); {11} H.E.Huppert *et al.*, *Nature*, 309, 19 (1984); {12} A.K.Baird & B.C.Clark, *Nature*, 311, 18 (1984); {13} D.S.Fisher & R.G.Burns, this vol.; {14} Research supported by NASA grants NSG-7604 and NAGW-1078. We thank Steve Pratt for the reflectance spectral measurements.

**Figure 1.** Reflectance spectra of olivine ( $\text{Fa}_{15}$ ) before and after aerial oxidation. Positions are highlighted of the characteristic  $\text{Fe}^{2+}$  crystal field transitions in olivine. Note the loss of resolution of these spectral features in oxidized olivines.



## SULFIDE MINERALIZATION RELATED TO EARLY CRUSTAL EVOLUTION OF MARS

Roger G. Burns and Duncan S. Fisher, Department of Earth, Atmospheric and Planetary Sciences, Massachusetts Institute of Technology, Cambridge, Massachusetts 02139.

**Summary.** Komatiitic magmatism, which occurred on Earth during stabilization of the crust in the Archean and was associated with ultramafic Fe-Ni sulfide ores and massive volcanogenic Fe-Cu-Zn sulfide deposits, lasted longer on Mars. As a result, ore deposits evolved little on Mars from these pyrrhotite-pentlandite and pyrite-chalcopyrite-sphalerite assemblages due to minimal interactions of martian mantle with the crust, hydrosphere and atmosphere.

**Background.** The age and formation of continental crust on Mars and the existence of highland terrains in the southern hemisphere remain fundamental problems in the evolution of that planet. On Earth, stabilization of the crust and the development of proto-continentals took place during the Archean, >3.8 to 2.5 billion years (b.y.) ago, and were associated with rock-types characteristic of that era, including komatiitic mafic and ultramafic igneous rocks in greenstone belts. Distinctive ore deposits are associated with these komatiites and other Archean rock-types [1], including banded iron formations, gold-uraninite conglomerates, and disseminated and massive sulfide mineralizations hosted by volcanic and plutonic rocks [2,3]. However, terrestrial ore-forming processes have evolved over geologic time as a result of plate tectonic activity along subduction zones, as well as by interactions of the crust with the hydrosphere, developing atmosphere and evolving biosphere [2-4]. The inference that sulfide ore deposits may exist on Mars [5] is based on compositional and petrographic similarities noted between komatiites (the host rock for terrestrial massive Fe-Ni sulfides), SNC meteorites and the silicate portion of Martian regolith fines [6-8]. Paragenetic relationships that might exist between these mafic and ultramafic igneous rocks on Mars raise questions about the localities of possible Archean-type sulfide and related ore deposits on Mars, and whether or not they have undergone tectonically-induced temporal variations on that planet, too. Did ore deposition take place on Mars during the formation of its crust, what were the emplacement mechanisms, and how have such ore deposits influenced the geochemical evolution of the surface of that planet? These problems are central to our investigations of the evolution of Fe-S minerals on Mars [5,9], clues to which may be deduced from associations of terrestrial ore deposits with Earth's earliest crustal rocks.

**Temporal Patterns of Ore Distribution on Earth.** The types and stratigraphic settings of ore deposits have changed through geologic time in response to the tectonic and chemical evolution of the Earth [1-4]. They encompass chromite deposits found in the oldest preserved crustal rocks (e.g. the pre-3.8 b.y. old Isua supracrustal belt in West Greenland) to present-day sulfide "chimneys" and ferromanganese oxide crusts forming at oceanic spreading centers (e.g. at 21°N along the East Pacific Rise). The ore deposits include mineralizations occurring in different types of igneous and sedimentary environments. Types of mineral deposit are unequally distributed in time due to the interplay of processes related to the composition, heat flow and convective motions of the Earth's mantle, and the evolution of Earth's oxygen budget, the atmosphere, and life. The temporal patterns demonstrate that the proportion of ore deposits associated with volcanic activity was greater in the Archean than in more recent geologic eras. Sediment-hosted and granitic crust-controlled mineralizations became increasingly important during the second half of Earth's history as crustal (tectonic), biological, and atmospheric (oxidation) interactions took effect. Thus, volcanic-hosted porphyry copper, Cyprus-type (ophiolites), and Kuroko-type massive sulfides, as well as sediment-hosted Pb-Zn sulfide ores, are comparatively recent deposits and probably did not evolve on Mars. Although sedimentary ore-types such as banded iron formations and placer gold-pyrite-uraninite conglomerates were prevalent during the Archean [2,3], it is the igneous-hosted sulfide ore deposits that are diagnostic of that era of early crustal development on Earth [1] and may be more relevant to Mars. Since the focus is on sulfide mineralization, cumulate chromite deposits which are found in mafic igneous rocks spanning the whole range of geologic time (and may also exist on Mars because they are observed in some SNC meteorites [10,11]) are not considered further.

**Sulfide Mineralization During the Archean.** Sulfide ores associated with mafic and ultramafic igneous rock-types [12] that were deposited in terrestrial rocks during the Archean include: (1) komatiitic (Kambalda-type) and tholeiitic (Noranda- or Abitibi-type) flows and intrusions in greenstone belts; (2) gabbroic intrusions either feeding flood basalt activity associated with intracontinental rift zones (e.g. Duluth) or occurring as layered complexes (e.g. Stillwater); and (3) norites intruding an astrobleme (Sudbury-type). The komatiitic suites, alone, are almost totally confined to the Archean era. Although they are associated in space and time with Noranda-type calc-alkaline suites, the latter volcanogenic massive sulfide deposits in a modified form are also found in younger igneous rocks [2,3]. So, too, are sulfides in layered intrusions (e.g. Bushveld), while the impact event producing sulfide ores at Sudbury 1.84 b.y. ago is also relatively young.

**Komatiitic Sulfide Deposits.** In Archean greenstone belts, older broad basal platforms of mafic and ultramafic komatiitic flows are overlaid by scattered subshields and stratovolcanic calc-alkaline volcanic rocks consisting of tholeiitic basalt and andesitic flows and pyroclastic deposits which are capped by dacitic to rhyolitic tuffs [13]. Repeated cycles built thick (~10 km) sequences of these volcanic deposits which were extruded in a continuously subsiding submarine environment. The komatiitic suites host sulfide mineralization consisting of pyrrhotite-pentlandite ( $\pm$  chalcopyrite, pyrite) deposits which occur as stratabound lenses or sheets a few meters thick at the base of magnesian ultramafic lava flows. These Fe-Ni sulfides appear to have formed by gravitational separation of an immiscible sulfide liquid from the mafic or ultramafic magma. Petrogenic models based on experimental studies [14] indicate that komatiitic magmas may represent large-percentage partial melts of the mantle, requiring very high extrusion temperatures (1425-1650 C, [12,14]) and suggesting diapiric emplacement from depths in excess of 200-400 km [14,15]. Such magma erupting to the Earth's surface could transport high concentrations of sulfur, either dissolved in the magma, or as immiscible FeS melts. Experimental measurements [16,17] have demonstrated that the solubility of sulfur increases with rising temperature, pressure, FeO content, and sulfur fugacity (but decreasing oxygen fugacity) of silicate melts. Temperature, in particular, magnifies the capacity of a melt to dissolve sulfur by a factor of 5 to 7 times per 100 degree increment [16]. Thus, an experimental komatiitic melt accommodating 0.1 wt % S at 1200 C indicates that several percent of dissolved sulfide could be transported to the surface at extrusion temperatures believed to be in the range 1400-1600 C, particularly during the Archean when geothermal gradients were significantly higher than they are now.

The Noranda-type massive sulfides occurring in overlying volcanogenic deposits associated with komatiites are stratabound lenticular bodies of pyrite mineralization containing variable amounts of chalcopyrite and sphalerite [1]. These Fe-Cu-Zn sulfides were deposited on and below the seafloor by hydrothermal solutions quenched by seawater. They differ from more recent Cyprus-type and present-day spreading-center ore bodies in their tectonic setting and by containing only minor Pb as galena.

**Archean Crustal Evolution.** Two mechanisms have been proposed for triggering the komatiitic peridotite-basaltic volcanism during the Archean [1,18]: first, sustained bombardment of the surface by meteorites which enabled the thinly crust-covered mantle to be tapped producing lunar maria-type vulcanism [18]; and second, magmatism resulted from the higher heat flow then, inferred from geochemical and radioactive decay data. Turbulent processes in the mantle probably resulted in smaller, more abundant convective cells than in later times. Initial volcanic activity characterized by ultramafic flows and Fe-Ni sulfide mineralization may have been initiated by breakage of the thin Archean crust, which established zones of high heat flow and set up partial melting of the upper mantle to provide basaltic magma. As foundering continued, the basaltic crust itself was recycled by partial melting, and andesite to rhyolite magmas were generated, along with Fe-Cu-Zn-S components for the ultimate massive sulfide ore-bodies. Thus, vertical tectonics involving the sinking of simatic lithospheric slabs accompanied by diapiric upwelling led to a succession of divergent magma types and ore deposits dominated by pyrrhotite-pentlandite and pyrite-chalcopyrite-sphalerite assemblages found in Archean greenstone belts.



## WEATHERING OF SULFIDES ON MARS

Roger G. Burns and Duncan S. Fisher, Department of Earth, Atmospheric and Planetary Sciences, Massachusetts Institute of Technology, Cambridge, MA 02139.

**Background.** The presence of massive volcanoes in the Tharsis and Elysium regions, the distinctive petrology of SNC meteorites, and a compendium of results from the Viking Lander experiments all point to extrusive and plutonic mafic and ultramafic igneous rocks on Mars having analogies to terrestrial komatiites [1]. On Earth, the latter are associated with massive and disseminated sulfides containing pyrrhotite, pentlandite, and accessory pyrite and chalcopyrite [2]. Near-surface oxidation of these sulfides have produced conspicuous rust-colored gossans, which often betray the occurrence of unexposed ore deposits (Figure 1). Studies of gossans and sub-surface minerals [3-5] suggest pathways of oxidative weathering reactions that may be applicable to Mars.

Pyrite is pivotal to chemical weathering reactions of sulfides. It may occur as a minor constituent of primary igneous sulfides, or be formed by supergene reactions involving deep weathering of pyrrhotite (see equation {1} in Table 1.). At or near the water table, oxidation of pyrite by aerated groundwater occurs {5},{6}. Ferric iron liberated in this reaction, not only promotes the initial alteration of pyrrhotite {1} and of pentlandite {2} to secondary sulfides in the absence of dissolved oxygen, but also aids the dissolution of pyrite {3} below the water table. Supergene enrichment reactions also occur there {4},{7}, leading to high concentrations of Ni, etc. in secondary sulfides. Strongly acidic and sulfate-rich groundwater is produced which stabilizes dissolved ferrous iron and a variety of complex ferric ions [6] including those listed in {11} and {12}). At elevated temperatures, these complexes produce a variety of hydroxo-ferric sulfate sols [7] (e.g. carphosiderite {11},{12}), which may be the precursors to a number of ferric sulfate minerals [8] often found in gossans in arid regions. In less acidic environments above the water table, dissolved ferric ions and monodispersed sols are hydrolysed to poorly crystalline FeOOH phases (e.g. ferrihydrite, goethite {8}-{10},{13},{14}), which coexist with silica (opal, jasper) and the hydrated ferric sulfate minerals in gossans. The fields of relative stabilities of gossaniferous phases are depicted in the oxidation-acidity diagram shown in Figure 2.

The reactions formulated in Table 1 demonstrate that groundwater in the vicinity of oxidizing sulfides is highly acidic. Such low pH solutions promote the chemical weathering of feldspars, pyroxenes and olivine in host igneous rocks [9], liberating dissolved silica, Al, Ca, Mg, Na and additional Fe ions, and producing secondary clay silicates (e.g. smectite) and iron oxyhydroxides. On Earth, seafloor basalts and gabbros erupting along submarine spreading centers have undergone extensive hydrothermal alteration by seawater circulating through underlying tectonically-fractured oceanic crust. As a result, the acidity of aqueous solutions is buffered by seawater-basalt interactions, leading to the slight alkalinity (pH 8.2) of present-day terrestrial oceans.

The oxidative power of atmospheric oxygen is the driving force in the weathering of sulfides (in the absence of bacterial activity). The dissolution of oxygen in groundwater and its migration to sulfide reaction centers involve diffusion processes and are probably rate-controlling. When the concentration of dissolved oxygen is very low and the supply of water is limited, oxidative reactions become sluggish and involve hydrogen peroxide. Furthermore, ferric-bearing solutions may liberate elemental sulfur. Thus, metastable sulfur is observed in pyrite-jarosite-sulfur assemblages associated with some ultramafic pyrrhotite-pentlandite deposits [10].

**Martian Weathering.** On Mars, where plate tectonic activity appears to have been insignificant, vast volumes of iron-rich basaltic magma has reached the surface of the planet via immense shield volcanoes. Fracturing associated with this volcanism, as well as impact cratering, facilitated deep-weathering reactions by permeating groundwater early in the history of Mars. However, the apparent absence of spreading centers and subduction zones, which cause recycling of the Earth's crust, has minimized acid-buffering of aqueous

Table 1. Chemical Weathering Reactions Involving Sulfides

<b>Oxidants:</b>	
-- at the surface:	$O_2 + 4H^+ + 4e^- = 2H_2O$ , or
	$O_2 + 2H_2O + 4e^- = 4OH^-$
--below the water table:	$Fe^{3+} + e^- = Fe^{2+}$
<b>Primary Sulfides:</b>	
--pyrrhotite $Fe_7S_8$ {+/- pentlandite $(Fe,Ni)_9S_8$ }	
<b>Deep-Weathering Reactions:</b>	
{1} $Fe_7S_8$ (pyrrhotite) + $6Fe^{3+} = 4FeS_2$ (pyrite) + $9Fe^{2+}$	
{2} $(Fe,Ni)_9S_8$ (pentlandite) + $2Fe^{3+} = 2(Fe,Ni)Ni_2S_4$ (violante) + $3Fe^{2+}$	
<b>Enrichment (Supergene) Reactions:</b>	
{3} $FeS_2 + 14Fe^{3+} + 8H_2O = 15Fe^{2+} + 2SO_4^{2-} + 4H^+$	
{4} $(Fe,Ni)Ni_2S_4 + 2Fe^{3+} = Ni_3S_4$ (polydymite) + $3Fe^{2+}$	
<b>Near the Water Table:</b>	
{5} $2FeS_2 + 2H_2O + 7O_2 = 2Fe^{2+} + 4SO_4^{2-} + 4H^+$	
{6} $4FeS_2 + 2H_2O + 15O_2 = 4Fe^{3+} + 8SO_4^{2-} + 4H^+$	
{7} $2Ni_3S_4 + 2H_2O + 15O_2 = 6Ni^{2+} + 8SO_4^{2-} + 4H^+$	
<b>Above the Water Table:</b>	
{8} $Fe^{3+} + 2OH^- = FeOOH$ (ferrihydrite, goethite, hematite) + $H^+$	
{9} $4Fe^{2+} + 6H_2O + O_2 = 4FeOOH$ (ferrihydrite, etc) + $8H^+$	
{10} $3Fe^{2+} + 3H_2O + 2SO_4^{2-} + 3/2 O_2 = [Fe_3(SO_4)_2(OH)_6]^-$ (jarosite)	
<b>Jarosite-Forming Reactions:</b>	
{11} $2FeSO_4^{1+} + FeOH^{2+} + 6H_2O = (H_3O)Fe_3(SO_4)_2(OH)_6 + 4H^+$	
{12} $Fe(SO_4)_2^{1-} + 2FeOH^{2+} + 5H_2O = (H_3O)Fe_3(SO_4)_2(OH)_6 + 3H^+$	
{13} $FeSO_4^{1+} + 2H_2O = FeOOH + SO_4^{2-} + 3H^+$	
{14} $(H_3O)Fe_3(SO_4)_2(OH)_6 = 3FeOOH + 2SO_4^{2-} + 4H^+ + H_2O$	

Figure 1 (top right). Zones of weathering associated with gossan formation above sulfide mineralization. The scale of the sulfide vein may be a few microns to several meters in diameter. Reactions {1} to {14} correspond to those in Table 1.

Figure 2 (bottom right). Caption is on the next page.

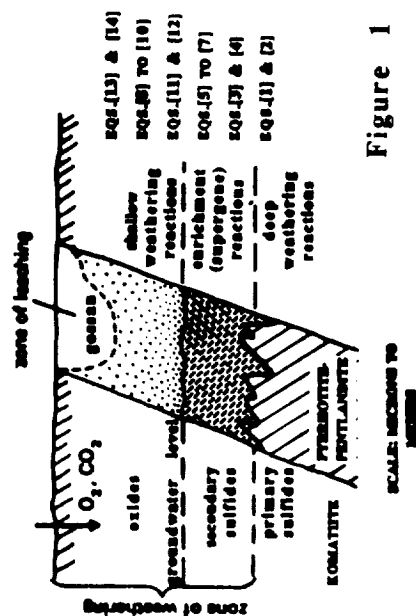


Figure 1

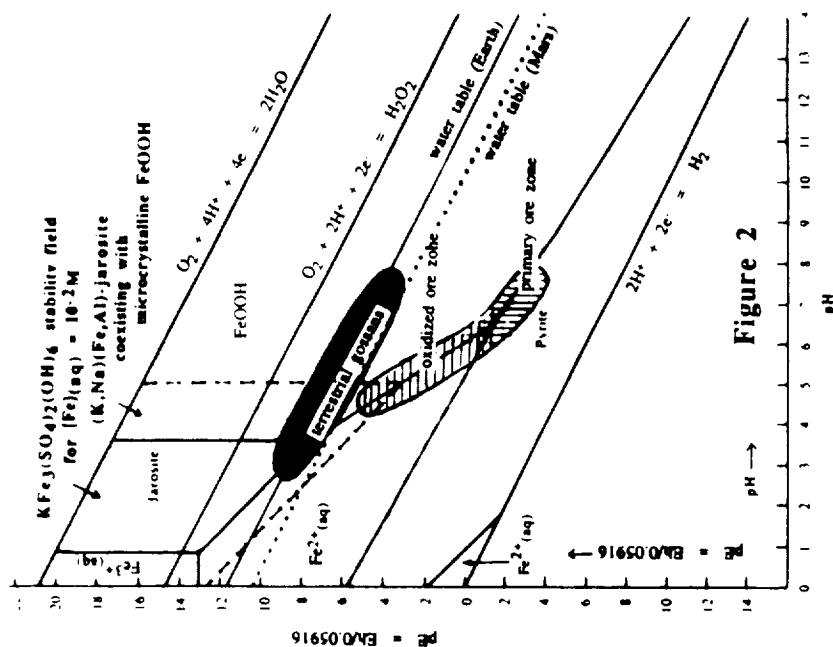


Figure 2

solutions by wall-rock alteration on Mars. Therefore, the acidity of groundwater, now permafrost, may have been maintained during the chemical evolution of the martian surface, thereby aiding the solubility and transport of Fe, Al, Mg, Ni, silica, etc. Geomorphological evidence attesting to the flow of water on Mars suggests that gossan-forming reactions may have occurred in the past. However, the present-day cold surface of Mars has impeded deep-weathering of sulfides in host basaltic rocks due to slow reaction rates and restricted access of dissolved oxygen or ferric iron to reaction centers. Nevertheless, some oxidative weathering may still be occurring in the frozen environment on Mars, as indicated by the oxidation of Fe and FeS phases observed in Antarctic meteorites [11]. When sublimation of martian permafrost occurs, species held in solution could be hydrolysed, precipitated as colloidal material and transported in dust storms.

**Discussion.** Evidence for gossan formation on Mars stems from several sources. First, remote-sensed reflectance spectral profiles are matched closely by ferrihydrite-silica gels and jarosite-bearing clay assemblages [12]. Second, jarosite which is so characteristically an oxidative weathering product of iron sulfides, may be present in SNC meteorites [13,14] believed to have originated from Mars. Third, the magnetic phase detected in the Viking magnetic experiment [15] may be remnant pyrrhotite which has been incompletely oxidized, particularly if the level of the water table has dropped on Mars. Finally, a limited supply of water and a low concentration of dissolved water, which favor the formation of hydrogen peroxide and promote the production of peroxide and superoxide phases, may account for results obtained in the Viking biology experiments [16].

**Summary.** Pyrrhotite-pentlandite assemblages in mafic and ultramafic igneous rocks may have contributed significantly to the chemical weathering reactions that produced degradation products in the martian regolith. By analogy with terrestrial processes, a model is proposed whereby supergene alteration of these primary Fe-Ni sulfides on Mars has generated secondary sulfides (e.g. pyrite) below the water table and produced acidic groundwater containing high concentrations of dissolved Fe, Ni and sulfate ions. The low pH solutions also initiated weathering reactions of igneous feldspars and ferromagnesian silicates to form clay silicate and ferric oxyhydroxide phases. Near-surface oxidation and hydrolysis of ferric sulfato- and hydroxo-complex ions and sols formed gossans above the water table consisting of poorly crystalline hydrated ferric sulfates (e.g. jarosite), oxides (ferrihydrite, goethite) and silica (opal). Underlying groundwater, now permafrost, contains hydroxo sulfato complexes of Fe, Al, Mg, Ni, etc., which may be stabilized in frozen acidic solutions beneath the surface of Mars. Sublimation of permafrost may replenish colloidal ferric oxides, sulfates and phyllosilicates during dust storms on Mars.

## References.

- [1] Baird, A.K. & Clark, B.C. (1981) *Icarus*, **45**, 113-123. [2] Guilbert, J.M. & Park, Jr, C.F. (1986) *The Geology of Ore Deposits* (W.H.Freeman). [3] Thornber, M.R. (1975) *Chem. Geol.*, **15**, 1-14 & 117-144. [4] Blain, C.F. & Andrew, R.L. (1977) *Minerals Sci. Engng*, **9**, 119-150. [5] Burns, R.G. (1987) *Lunar Planet. Sci.*, XVIII, 141-142; *Proc. 18th LPSC*, in press. [6] Sapienszko, R.S. *et al.* (1977) *J. Phys. Chem.*, **81**, 1061-1068. [7] Matijevic, E. *et al.* (1975) *J. Colloid. Interfac. Sci.*, **50**, 567-581. [8] Burns, R.G. (1987) *JGR*, **92** (B4) E570-574. [9] Siever, R. & Woodford, N. (1979) *Geochim. Cosmochim. Acta*, **43**, 717-724. [10] Nickel, E. (1984) *Mineral. Mag.*, **48**, 139-142. [11] Gooding, J.L. (1981) *Proc. 12th LPSC*, 1105-1122. [12] Sherman, D.A. *et al.* (1982) *JGR*, **87** (B12), 10169-10180. [13] Smith, J.V. & Steele, I.M. (1984) *Meteoritics*, **19**, 121-133. [14] Gooding, J.L. (1986) *Geochim. Cosmochim. Acta*, **50**, 2215-2223. [15] Hargraves, R.B. *et al.* (1979) *JGR*, **84**, 8379-8384. [16] Huguenin, R.L. (1982) *JGR*, **87** (B12), 10069-10082. [17] Supported by NASA Grants NSG-7604 and NAGW-1078.

**Figure 2** (previous page, bottom right). Eh-pH diagram at 25°C for pyrite and its oxidative products, including jarosite and FeOOH, occurring in gossans. Heavy lines correspond to 0.01M each of K, total Fe and total S dissolved species. The area bounded by dashed lines represents the approximate stability field of jarosite expanded by K-Na and Fe-Al atomic substitutions. Ranges of pE and pH measured in oxidized pyrrhotite-pentlandite assemblages are shown. Also shown are pE-pH curves for dissolved oxygen in equilibrium with the atmospheres of Earth and Mars.

# ACID WEATHERING ON MARS: SPECTROSCOPIC INVESTIGATIONS OF SULFURIC ACID-DEGRADED OLIVINES AND SULFIDES

Duncan S. Fisher and Roger G. Burns, Dept. of Earth, Atmospheric & Planetary Sciences, Massachusetts Institute of Technology, Cambridge, Massachusetts 02139.

**Introduction.** Komatiitic lavas derived from partial melting of the martian mantle may have transported significant concentrations of sulfur to the surface of Mars to be deposited there as massive and disseminated iron sulfides {1}. Oxidative weathering reactions have been proposed {2,3} in which supergene alteration of these primary pyrrhotite-pentlandite deposits by dissolved  $\text{Fe}^{3+}$  ions percolating from the regolith has generated secondary sulfides (pyrite, marcasite, violarite), producing acidic groundwater with high concentrations of iron and sulfate ions that initiated chemical weathering of igneous silicates and formed gossaniferous ferric oxide, sulfate and phyllosilicate phases {2,3}. To test this model of oxidative weathering of basalts on Mars, spectroscopic measurements described here were made on acid-degraded  $\text{Fe}^{2+}$ -bearing olivines and sulfides.

**Experimental Details.** Powdered samples of two olivines (hortonolite  $\text{Fa}_{49}$  and synthetic fayalite) and two sulfides (troilite and pyrrhotite) were reacted with sulfuric acid (pH 2 or 4) at  $60^\circ\text{C}$  or  $80^\circ\text{C}$  ( $\pm$  dissolved ferric sulfate added) for time periods ranging from 7 to 30 days. Reaction products were measured by Mossbauer spectroscopy at ambient ( $295^\circ\text{K}$ ) and liquid helium ( $4.2^\circ\text{K}$ ) temperatures to characterize x-ray amorphous  $\text{Fe}^{3+}$ -bearing phases. Reflectance spectral measurements in the  $0.4\text{--}1.8\ \mu\text{m}$  region were also made on the reaction products using the RELAB facility at Brown University {4}.

**Results: Mossbauer Spectra.** The  $295^\circ\text{C}$  spectrum of each olivine after its reaction with sulfuric acid contains a ferric doublet (in addition to the olivine  $\text{Fe}^{2+}$  doublet), the relative intensity of which is greater for fayalite and highest when catalytic  $\text{Fe}^{3+}$  ions are present. In  $4.2^\circ\text{K}$  spectra, sextets appear with magnetic hyperfine splitting parameters resembling those of goethite (see Fig. 1d in the accompanying abstract {5}). The goethite peaks are more intense in the presence of  $\text{Fe}^{3+}$  ions, hydrolysis of which is unlikely in these acidic solutions. Indeed, the appearance of goethite in solutions initially free of catalytic  $\text{Fe}^{3+}$  ions demonstrates that oxidation of structural  $\text{Fe}^{2+}$  ions in the olivines had occurred. Similar results were obtained for troilite and pyrrhotite. However, the  $4.2^\circ\text{K}$  spectra of each  $\text{H}_2\text{SO}_4$ -degraded sulfide reveal the presence of diamagnetic pyrite or marcasite in addition to goethite, the relative proportion of the  $\text{FeS}_2$  phase being highest in  $\text{Fe}^{3+}$ -catalysed reactions. This observation suggests that sulfuric acid (in the presence and absence of  $\text{Fe}^{3+}$ ) had induced pyrrhotite  $\rightarrow$  pyrite  $\rightarrow$   $\text{FeOOH}$  reactions, in support of our model for supergene reactions involving iron sulfides {2,3}.

**Results: Reflectance Spectra.** The degradation of olivine to goethite has drastic effects on  $\text{Fe}^{2+}$  crystal field spectra shown in Figure 1. Not only does the absorption edge extend further into the visible region with the appearance of goethite, but the diagnostic olivine- $\text{Fe}^{2+}$  crystal field bands at  $\sim 0.85\ \mu\text{m}$  (M1 site) and  $1.05\ \mu\text{m}$  (M2 site) become obscured, particularly in products of reactions catalysed by  $\text{Fe}^{3+}$  ions. These effects are caused by increased contributions to the reflectance spectra from goethite- $\text{Fe}^{3+}$  crystal field transitions at  $0.65\ \mu\text{m}$  and  $0.92\ \mu\text{m}$ , which appear also in the reflectance spectra of opaque troilite and pyrrhotite (Figure 2).

**Applications to Mars.** The presence of  $\sim 3\ \text{wt.}\%$  sulfur in the martian regolith, deduced to be present there as sulfate-bearing minerals (e.g. anhydrite, jarosite, scapolite), indicates that large quantities of sulfur was brought to the surface of Mars, either as sulfide mineralization associated with komatiite magmas {1}, or as

exhalates of  $\text{SO}_2$  or  $\text{H}_2\text{S}$  {6}. Sulfuric acid must have been produced, either by precipitation or condensation of volcanic gases {7}, or by oxidative weathering of the massive or accessory iron sulfide minerals {2,3}, resulting in acidic groundwater and permafrost on Mars. Chemical weathering of primary silicate and sulfide minerals in olivine-rich basalts by such acidic groundwater has produced Fe(III) oxide phases, which now may contribute to remote-sensed spectral profiles of the martian surface, particularly "dark-region" spectra {8}.

**References.** {1} R.G.Burns & D.S.Fisher, MEVTV/LPI Wkshp "Early Tectonic and Volcanic Evolution of Mars", in press; {2} R.G.Burns, *Proc. 18th LPSC*, p.713 (1988); {3} R.G.Burns & D.S.Fisher, *MEVTV/LPI Tech. Rept. 88-05*, 34 (1988); {4} C.Pieters, *JGR*, 88, 9534 (1983); {5} R.G.Burns, this vol.; {6} B.C.Clark & A.K.Baird, *JGR*, 84, 8395 (1979); {7} M. Settle, *JGR*, 84, 8343 (1979); {8} R.B.Singer, *Adv. Space Res.*, 5, 59 (1985); {9} Research supported by NASA grants NAGW-1078 & NSG-7604. We thank Steve Pratt for the reflectance spectral measurements.

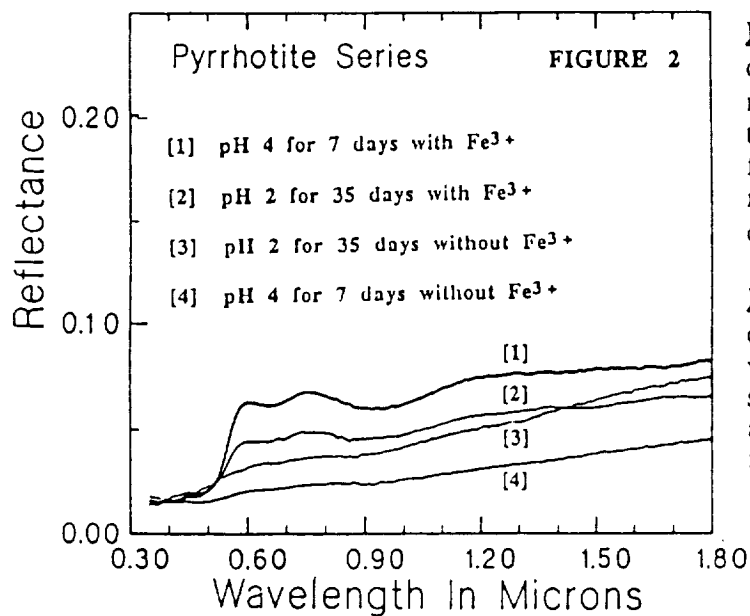
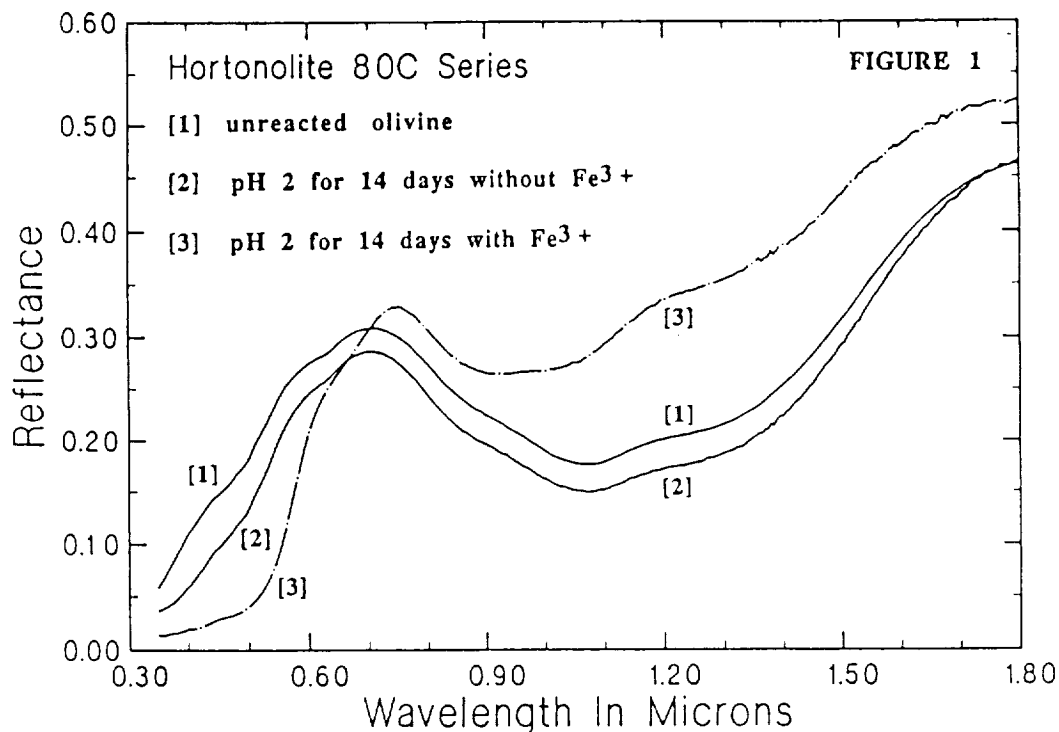


**Figure 1.** Reflectance spectra of olivine ( $\text{Fa}_{49}$ ) before and after reaction with sulfuric acid in the presence and absence of ferric sulfate. Note the loss of resolution of the characteristic olivine  $\text{Fe}^{2+}$  band at  $1.05 \mu\text{m}$ .

**Figure 2.** Reflectance spectra of pyrrhotite after reactions with sulfuric acid ( $\pm$  ferric sulfate added). Note the appearance of goethite spectral features at  $0.65$  and  $0.92 \mu\text{m}$

## CHEMICAL WEATHERING UNDER SUB-FREEZING CONDITIONS: SPECIAL EFFECTS OF ICE NUCLEATION.

James L. Gooding, SN21/Planetary Science Branch, NASA/Johnson Space Center, Houston, TX 77058.

**Introduction.** Chemical reactions between water and minerals on frozen planetary bodies should be seriously constrained by the very limited availability of water in its most reactive (liquid) form. For temperatures at or below the freezing temperature for pure bulk water, liquidity will be controlled by the physics of water in capillary pores and as films on mineral surfaces. Porosity and surface-area controls of unfrozen water have been elaborated by D. M. Anderson and co-workers since the early 1960s [1]. A separate effect, differential ice nucleation by various mineral substrates, has been recognized but not elaborated with regard to hydrocryogenic chemical processes. This paper emphasizes how the abilities of various minerals to nucleate ice from undercooled water can influence the course of low-temperature geochemical processes.

**Thermodynamic Impulse for Chemical Reaction.** At temperatures above the freezing point of water, where liquid water is freely available, the first-order measure of the likelihood of a water-based chemical reaction is the computed Gibbs free-energy change for the reaction,  $\Delta G$ . Because  $\Delta G = -RT \ln K$ , relative favorabilities are conveniently compared in terms of their respective values of the reaction constant,  $K$  (or  $\log K$ ). For all other factors being constant, and ignoring kinetics, favorability of reaction is expected to increase with increasing value of  $\log K$ .

**Ice Nucleation and Ice/Mineral Disregistry.** In geologic environments, including water-bearing atmospheres, condensation of liquid water or water vapor to water-ice occurs through heterogeneous nucleation on mineral particles. Minerals exhibit wide variations in efficiency in ice nucleation, leading to possible survival of undercooled liquid water to as much as 10-13° K below the equilibrium freezing point [2,3]. The relative favorabilities for ice nucleation on water-insoluble mineral surfaces can be estimated by computing the crystallographic mismatch between the mineral and ice structures. The minimum absolute value of the crystallographic mismatch or disregistry,  $\delta$ , for a given mineral can be compared with equivalent values for other minerals. All other factors being constant, minerals with lowest values of  $\delta$  are expected to nucleate water-ice most effectively and, hence, permit the least amount of undercooling below the freezing point [2].

**Aqueous Alteration At Sub-Freezing Temperatures.** Water-based chemical reactions should proceed if they have favorable thermodynamic impulse and if liquid water is available as a reactant or an enabling medium. At sub-freezing temperatures in a wet geologic medium, the prospects for undercooled liquid water should be inversely related to the effectiveness of the mineral grains in nucleating ice. Efficient immobilization of water by freezing into ice should largely arrest water-based processes and protect the mineral grains from aqueous reactions. Minerals with large values of  $\delta$  should be most susceptible to contact with undercooled liquid water. Accordingly, the relative susceptibilities of various minerals to hydrocryogenic alteration can be plotted in terms of thermodynamic impulse ( $\log K$ ) and vulnerability to contact with undercooled liquid water ( $\delta$ ).

Computations for common minerals in planetary rocks and meteorites (Fig. 1) suggest some important differences between alteration under sub-freezing conditions and alteration under non-freezing conditions. If ice nucleation can be ignored, olivine and pyroxene should have comparable propensities for reaction, as suggested by their similar ranges for  $\log K$ . If ice nucleation is important, however, olivine should be more susceptible to alteration than is pyroxene because olivine is less effective at nucleating ice (i.e., larger value of  $\delta$ ). In addition, plagioclase is expected to be less susceptible to alteration than is olivine (based on  $\log K$  values alone) unless sub-freezing conditions apply, in which case olivine and plagioclase should have very similar vulnerabilities to undercooled liquid water (i.e., similar values of  $\delta$ ). The computed thermodynamic impulse for reaction of basalt glass ( $\log K = 15-30$ ) is similar to that for augite. Although meaningful values of  $\delta$  cannot be computed for glasses, the value appropriate for basalt glass would probably be a very large number that would plot far to the right of augite in Fig. 1. Consequently, basalt glass might be the phase most

susceptible to chemical alteration under sub-freezing conditions on Mars. Similarly, glassy phases on other cold parent bodies should be highly susceptible to aqueous alteration.

The quantitative importance of the  $\delta$  parameter in predicting alteration susceptibility remains to be experimentally tested. To date, observational support has been limited mainly to studies of terrestrial weathering effects in stony meteorites recovered from Antarctica. The high susceptibility of basalt glass to Antarctic weathering seems abundantly clear for achondritic meteorites, as is evidence for enhanced vulnerability of plagioclase [4]. Further tests could focus on relative rustiness of metal and sulfide particles in Antarctic chondrites. By thermodynamic impulse alone, taenite should be much less vulnerable to rusting than is kamacite; the  $\delta$  index, however, predicts more closely comparable vulnerabilities to rusting. The  $\delta$  index also predicts greater rustiness for kamacite than for troilite (meteoritic FeS analog of pyrrhotite).

**References:** [1] Anderson D. M. and Morgenstern N. R. (1973) In *Permafrost: The North American Contribution to the Second International Conference*, National Academy of Sciences, Washington, DC, p. 257-288. [2] Gooding J. L. (1986) *Icarus*, 66, 56-74. [3] Gooding J. L. (1987) *Icarus*, 67, 519-527. [4] Gooding J. L. (1986) *Geochim. Cosmochim. Acta*, 50, 2215-2223.

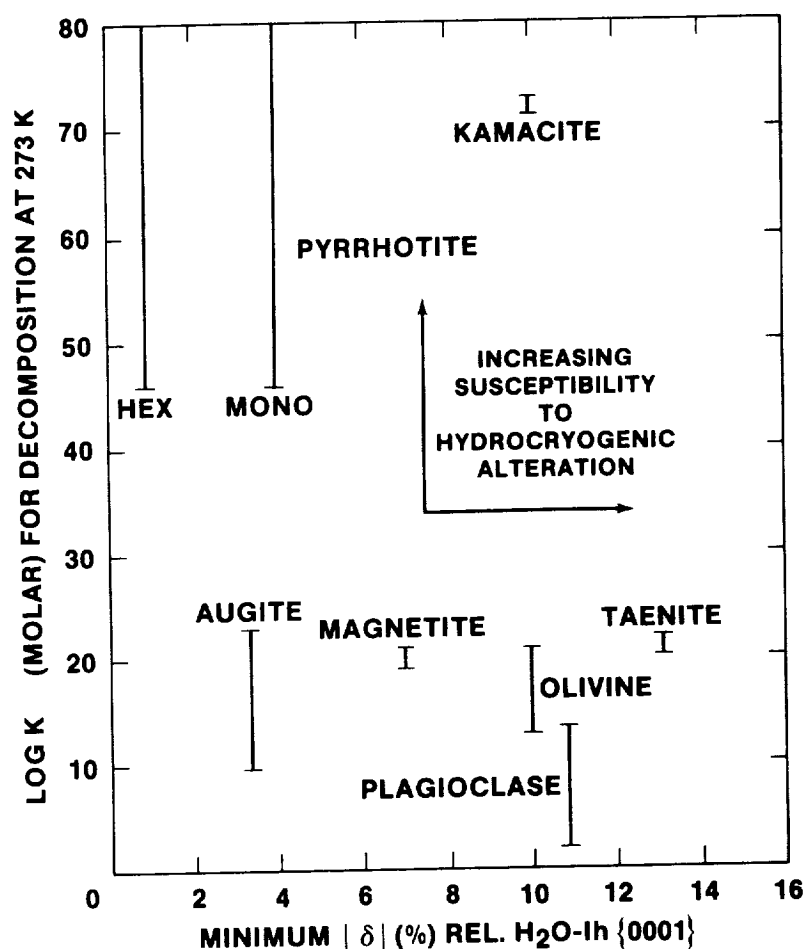


Figure 1. Prediction of relative susceptibilities of minerals to chemical weathering reactions under sub-freezing conditions. The y-axis coordinate represents thermodynamic impulse that should apply in the presence of liquid water. The x-axis coordinate represents the increasing likelihood (with increasing value of  $\delta$ ) that undercooled liquid water will survive freezing and persist as a reactant. (Kamacite and taenite are the two common Fe-Ni alloys in meteorites).

# DEPTH TO UNOXIDIZED MATERIAL IN THE MARTIAN REGOLITH

C.F. Chyba, S.W. Squyres, and C. Sagan

Laboratory for Planetary Studies, Cornell University, Ithaca, NY 14853 USA

The Viking landers found no organic molecules on Mars to the detection threshold ( $\sim 1$  ppm for simple compounds,  $\sim 1$  ppb for more complex organics) of the gas chromatograph mass spectrometer (GCMS) experiment (1). Yet extrapolations of the lunar meteoritic flux to Mars suggest a quantity of organics that should have been detectable by the Viking GCMS (1). In addition, photochemical reduction of carbon monoxide may provide an endogenous source of martian organics (2).

The Viking biology experiments strongly suggest the presence of powerful oxidants in at least the upper  $\sim 10$  cm of the martian regolith (3). In the gas-exchange (GEx) experiment, martian "soil" released  $70\text{--}790$  nmoles  $\text{O}_2 \text{ cm}^{-3}$  in the presence of water vapor; in the labelled-release (LR) experiment, martian soil plus organic nutrients released  $\sim 30$  nmoles  $\text{CO}_2 \text{ cm}^{-3}$ . Both these results are readily explained by the action of oxidants; for example, a possible mechanism for the LR result would be the oxidation of formate in the nutrient solution by hydrogen peroxide present in the martian soil:  $\text{H}_2\text{O}_2 + \text{HCOOH} \rightarrow 2\text{H}_2\text{O} + \text{CO}_2$  (3). Moreover, martian atmospheric modeling predicts the production of  $\text{H}_2\text{O}_2$  and other oxidants by UV photochemistry, leading to a flux  $F_o \approx 2 \times 10^9 \text{ cm}^{-2} \text{ sec}^{-1}$  of equivalent  $\text{O}_2$  molecules onto the martian surface (4). Such oxidants would destroy organic molecules rapidly and, if organics were ever present at GCMS-detectable levels on Mars, are the likely explanation for that instrument's negative results.

It has been argued that early Mars may have been more "earthlike" than at present (5). Such conditions could possibly have persisted until 3.5 Gyr ago (6); the current highly-oxidizing environment would then have set in since this time. To examine the original oxidation state of martian materials, as well as to investigate the nature of possible early martian organics, it will be necessary to drill or excavate below the current surface oxidizing layer. Key issues for future exploration of Mars therefore include the depth to which this oxidizing layer extends, and where a mission should go for the best chance of sampling beneath it. To this end, we have modeled oxidant diffusion into the martian regolith, following the diffusion formalism of Fanale *et al.* (7). We take the regolith temperature  $T=216$  K to be constant, and set background  $\text{CO}_2$  pressure  $P=6$  mbar. We take an average pore size in the regolith  $r_o=1\mu\text{m}$  (7). Core samples (8), penetration studies (9), and seismic data (10) all give a value  $\sim 40\%$  for the porosity of the lunar regolith. Lunar seismic data (10), as well as the porosities of nonindurated terrestrial material (11), are consistent with this value to a depth of hundreds of meters. We therefore set the porosity of the martian regolith  $f \sim 0.4$ . Finally, empirical values for tortuosities in bulk diffusion typically range from 2 to 6 (12); a value  $q=5$  is often used for the martian regolith (13,7). This definition of tortuosity assumes a bulk diffusion coefficient  $D_{eff}$  related to the diffusion coefficient for a cylinder  $D$  by the relation  $D_{eff}=(f/q)D$ ; the formalism employed here (7) instead puts  $D_{eff}=(f/3\tau)D$ , so that we set tortuosity  $\tau=q/3=5/3$ .

With these choices of parameters, we find that transport of oxidants into the martian regolith is dominated by Knudsen, rather than molecular, diffusion. In the absence of sinks, this diffusion is remarkably fast: oxidants produced at the martian surface would diffuse to a depth  $\sim 100$  m in  $\sim 100$  yr, and to  $\sim 1$  km in  $\sim 10^4$  yr. Therefore a consideration of potential oxidant sinks is critical. The most obvious "sink" for an oxidant produced at the martian surface is simple thermal decomposition. The thermal decomposition lifetime  $\tau_{th}$  and activation energy  $\Delta E$  of the active agent in the Viking LR experiment may be very crudely calculated on the basis of that experiment's thermal sensitivity (14); on finds  $\tau_{th} \approx 10^5 - 10^7$  yr, and  $\Delta E \approx 35\text{--}43 \text{ kcal mole}^{-1}$ , which may be compared to  $\Delta E$  for  $\text{H}_2\text{O}_2$  of  $48 \text{ kcal mole}^{-1}$ . Given the high diffusion rates previously found, a  $10^5 - 10$



yr lifetime provides no useful constraint for oxidant diffusion.

The most important sink for diffusing oxidants is the potential mineralogical sink of the martian regolith. In chondritic meteorites, only the element iron is typically not already in its highest oxidation state (15). Elemental analysis of martian fines (16) indicates that the regolith is ~13% Fe by weight. Thus an upper limit to the mineralogical sink of the regolith is given by assuming all Fe present was initially available as FeO to be oxidized to Fe<sub>2</sub>O<sub>3</sub>. One then finds a potential Fe sink  $[\text{Fe}] \approx 10^{21}$  equivalent O<sub>2</sub> molecules cm<sup>-3</sup>. With this sink, the oxidant flux  $F_o$  cited above would oxidize ~100 m of regolith in ~100 Myr. This is a lower limit to the depth of oxidation, as much of the Fe may be sequestered and unavailable to the diffusing oxidants. Other possible regolith sinks prove to be unimportant compared to the potential iron sink. Possible initial concentrations of organics, whether calculated via lunar extrapolation or *in situ* production in a hypothesized earth-analogous atmosphere, are  $< 10^{-2}$  [Fe]. Similarly, the Viking GEx experiment, interpreted as providing a measure of oxidants adsorbed in the regolith, yields  $\sim 10^{17}$  O<sub>2</sub> cm<sup>-3</sup>,  $\ll$  [Fe].

However, freezing of the diffusing oxidants may significantly curtail their penetration into the regolith. Quantifying the importance of this effect requires a vapor pressure/temperature relation, so that a definite choice of candidate oxidant must be made. Taking H<sub>2</sub>O<sub>2</sub> as a prototype, and given the above values for  $D_{eff}$  and  $F_o$ , we find that H<sub>2</sub>O<sub>2</sub> will reach its equilibrium vapor density over H<sub>2</sub>O<sub>2</sub> ice in the upper ~10 cm of the regolith, where it will begin to freeze out. Below this depth, diffusion is subject to the upper boundary condition that H<sub>2</sub>O<sub>2</sub> number density at the top of the regolith equals its vapor density  $n_o$ . It is then not difficult to show that the depth to the unoxidized layer in the regolith after diffusion for time  $t$  is given by  $l(t) \approx \sqrt{(2fn_oDt/[Fe])}$ , so that, in the ~3.5 Gyr since the onset of the current oxidizing regime on Mars, the regolith has been oxidized to a depth ~70 m. Freezing-out of the oxidant in the upper regolith may be the dominant process retarding its downward diffusion.

Thus the martian regolith is probably oxidized to depths ~10–100 m. It is unlikely that planned Mars landers will be able to drill well below ~1 m. However, subsurface ice models indicate that H<sub>2</sub>O ice on Mars is stable to within ~1 m of the surface poleward of ~60° over 3.5 Gyr (7), and ice in a martian permafrost may seal regolith pores and prevent oxidant diffusion. The situation is complicated, however, by cratering. 3.5 Gyr-old lunar maria are saturation cratered to ~5 m depth (17), and martian impactor fluxes are believed to be similar (18). Therefore, small-scale cratering has probably destroyed ice to a depth ~5 m at least once in the past 3.5 Gyr. To sample unoxidized martian material, future Mars landers should investigate high southern latitudes (where the terrain is ancient, and where there is stable shallow ground ice) and find a site where aeolian scouring or other processes appear to have eroded >5 m over the past 3.5 Gyr.

**References:** (1) Biemann, K. *et al.* (1977). *JGR* **82**, 4641-4658. (2) Sagan, C. *et al.* (1988). *Bull. Am. Astron. Soc.* **20**, 860-861. (3) Klein, H.P. (1978). *Icarus*, **34**, 666-674. (4) Hunten, D. (1979). *J. Mol. Evol.*, **14**, 71-78; *ibid.* (1987). *JPL D-4657*, 4-7-4-13. (5) Pollack, J. *et al.* (1987). *Icarus* **71**, 203-224. (6) McKay, C. (1986). *Adv. Space Res.* **6**, 269-285. (7) Fanale, F. *et al.* (1986). *Icarus* **67**, 1-18. (8) Langseth, M. *et al.* (1976). *Proc. Lunar Sci. Conf.* **7**, 3143-3171. (9) Mitchell, J. *et al.* (1973) *ibid.* **4**, 2437-2445. (10) Watkins, J. & Kovach, R. *ibid.*, 2561-2574. (11) Davis, S. (1969), in *Flow Through Porous Media* (ed. J. DeWiest), 54-90. (12) Satterfield, C. (1970). *Mass Transfer in Heterogeneous Catalysis*, secs. 1.6, 3.6. (13) Smoluchowski, R. (1967). *Science* **159**, 1348-1350. (14) Levin, G. & Straat, P. (1979). *J. Mol. Evol.* **14**, 167-183. (15) Mason, B. (1971). *Handbook of Elemental Abundances in Meteorites*, p. 8. (16) Clark, B. *et al.*, *Science* **194**, 1283-1288. (17) Shoemaker, E. *et al.* (1970). *Proc. Lunar Sci. Conf* **1**, 2399-2412. (18) Neukum, G. & Wise, D. (1976). *Science* **194**, 1381-1387.

Lunar and Planetary Science XX, 157-158, 1989.



CHAPTER 6

SPECTROSCOPY AND REMOTE SENSING

PRECEDING PAGE BLANK NOT FILMED

PAGE 226 INTENTIONALLY BLANK



## **GEOLOGY REMOTE SENSING FIELD EXPERIMENT (GRSFE)**

Raymond E. Arvidson and Edward A. Guinness, McDonnell Center for the Space Sciences, Department of Earth and Planetary Sciences, Washington University, St. Louis, Missouri 63130

GRSFE is a combined effort of NASA's Planetary Geology and Geophysics Program (Code EL) and the Geology Program (Code EE). The experiment, which will take place late in the summer of 1989, will consist of airborne observations by the Airborne Visible and Infrared Imaging Spectrometer (AVIRIS), Thermal Infrared Multispectral Scanner (TIMS), and C. L. P band multipolarization radar imaging system. The impetus for conducting the experiment came from recommendations made at a Planetary Geology and Geophysics Strategic Planning Workshop held in Tempe, Arizona. Field measurements will be acquired at the same time to be able to independently calibrate the airborne data and to better understand the extent to which surface properties can be extracted from the airborne data. GRSFE is being implemented using a Working Group with membership consisting of Principal Investigators from both Code EL and EE Programs. The targets to be covered by GRSFE were selected on the basis of relevance to planetary surfaces and to NASA Geology Program objectives, which are focused on paleoclimatic indicators. Targets are located in the Mojave Desert and include the Cima and Amboy lava flows, alluvial fans in Death Valley, salt-encrusted playas (Devil's Golf Course, Soda Lake), the Ubehebe Maar, and dune fields (Kelso, Dumont, Death Valley dunes). A primary objective of GRSFE is to make the airborne and field data, together with documentation, available to the science community for use in developing and testing models for reduction and analyses of Magellan, Mars Observer, Lunar Geoscience Orbiter, and Earth-based data. Thus, GRSFE data will be published under the auspices of the Planetary Data System as a set of about 10 compact disks during calendar year 1990.

PRECEDING PAGE BLANK NOT FILMED

PHOTOMETRY AND SURFACE PROPERTIES OF THE GALILEAN SATELLITES  
Bonnie J. Buratti, JPL/Caltech

Photometrically accurate observations of planetary surfaces can be fit to scattering models to derive the physical properties of the surface, such as the single scattering albedo, the compaction state of the optically active portion of the regolith, and macroscopic roughness (Hapke, 1986). A recent analysis of ultraviolet observations of the Galilean satellites obtained by the IUE satellite show that they have important differences in their surface compaction states (Buratti et al., 1988a). Io and Callisto are extremely fluffy, while Ganymede and, especially, Europa have much more compacted regoliths. We have also made successful comparisons of our data with laboratory measurements of the phase curves of surface analogues with the same compaction states as those derived from modeling (Buratti et al, 1988b).

In an effort to extend our modeling of these satellites' surfaces, we have compiled a data set of all photometric measurements of Ganymede and Callisto. Because the spacecraft and telescopic observations cover complementary ranges in solar phase angle, we have derived a data set which is ideally suited to our analysis. Examples of the data are shown in the Figure.

REFERENCES

1. Buratti, B. et al. (1988a) *Nature* 333, 148-151.
2. Buratti, B. et al. (1988b) *Applied Optics* 27, 161-165,
3. Hapke, B. (1986) *Icarus* 67, 264-280.
4. Squyres, S., J. Veverka (1981) *Icarus* 76 137-155.

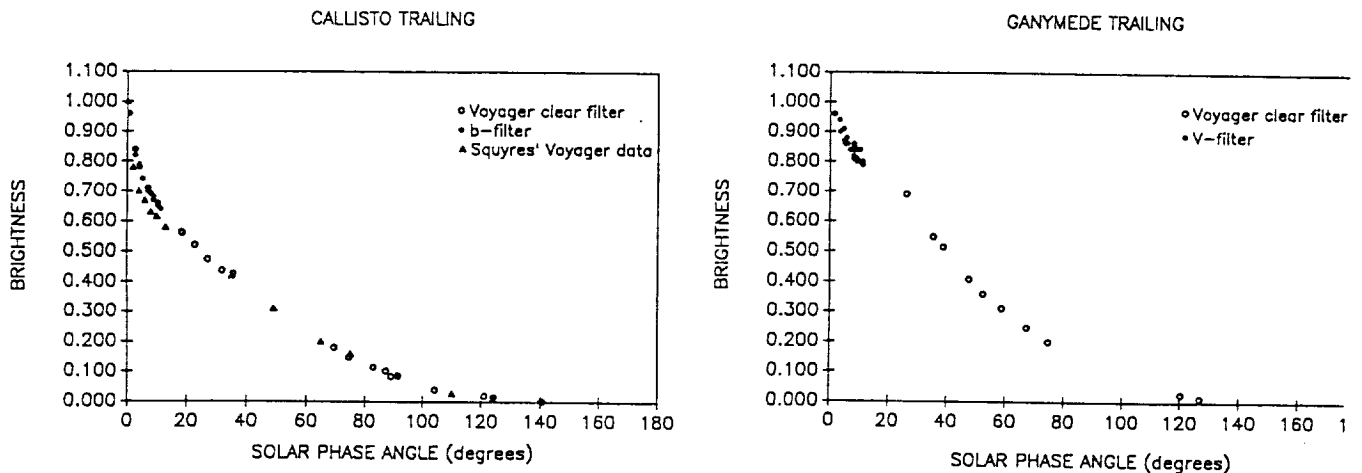


Figure. Examples of solar phase curves constructed from compilations of ground based and Voyager imaging observations (Squyres and Veverka, 1981, and our own). The data are normalized to unity at zero degrees.

ORIGINAL PAGE IS  
OF POOR QUALITY

ALBEDO AND COLOR MAPS OF MIMAS, ENCELADUS, TETHYS, RHEA AND DIONE  
B. J. Buratti, J. A. Mosher, T.V. Johnson (JPL/Caltech)

We have constructed maps of normal reflectance and color ratios of the five large inner Saturnian satellites from Voyager 1 and 2 multifilter images. Although all these satellites are high albedo objects, their albedo and color patterns differ significantly in magnitude and distribution (Buratti et al., 1989). Mimas (~0.8 normal reflectance) and Enceladus (~1.0 normal reflectance) are the most spectrophotometrically uniform and have slightly brighter (0.1 magnitude) leading sides (Buratti, 1988). Enceladus has a significantly brighter (15%), and possibly bluer southern polar region, which was not well-imaged by either Voyager cameras. The other three satellites are 10-20% brighter on the leading side. Tethys also appears to have a brighter southern polar region (see Figure). We confirm the finding by Verbiscer and Veverka (1989) of an albedo dichotomy for Rhea. A color ratio map of violet and orange images for Rhea shows no such anomaly; the trailing side is at most a few percent redder. We find a similar albedo dichotomy - and the lack of a significant hemispheric color difference - for Dione.

These satellites differ from those of Jupiter and Uranus in that their albedo and color markings bear little relationship to geologic units. The only examples we have found of such a correlation are the high albedo wispy streaks on the trailing sides of Rhea and Dione. More extensive comparisons of our maps with detailed geologic maps (J. Plescia, personal communication) are in progress.

We find that for specific areas on a satellite, there is no general correlation between color and albedo: some dark regions may be redder than the brighter ambient terrain while others may be bluer (see the Figure for an example). The only regions that exhibited the "expected" correlation between color and albedo (i.e., brighter areas are bluer areas) are the wispy streaks and possibly the bright southern polar region of Enceladus.

Our conclusion is that a complex interplay of exogenic processes is responsible for the optical properties of these satellites. Furthermore, the most commonly evoked mechanisms - magnetospheric interactions and micrometeoritic bombardment - cannot be solely, or even primarily, responsible. For both these mechanisms, the spectrophotometric properties of the underlying geologic structures are left intact and visible in imaging observations. For example, the trailing side of Europa, in which exogenically created color variations are caused by sputtering and implantation of sulfur ions, keeps the spectrophotometric properties of the preexisting geology (Buratti and Golombek, 1988).

# REFERENCES

1. Buratti, B. (1988) *Icarus* 75, 113-126.
2. Buratti, B., M. Golombek, (1988) *Icarus* 75, 437-449.
3. Buratti et al., (1989) *Icarus*, submitted.
4. Verbiscer, A., J. Veverka (1989) *Icarus*, in press.

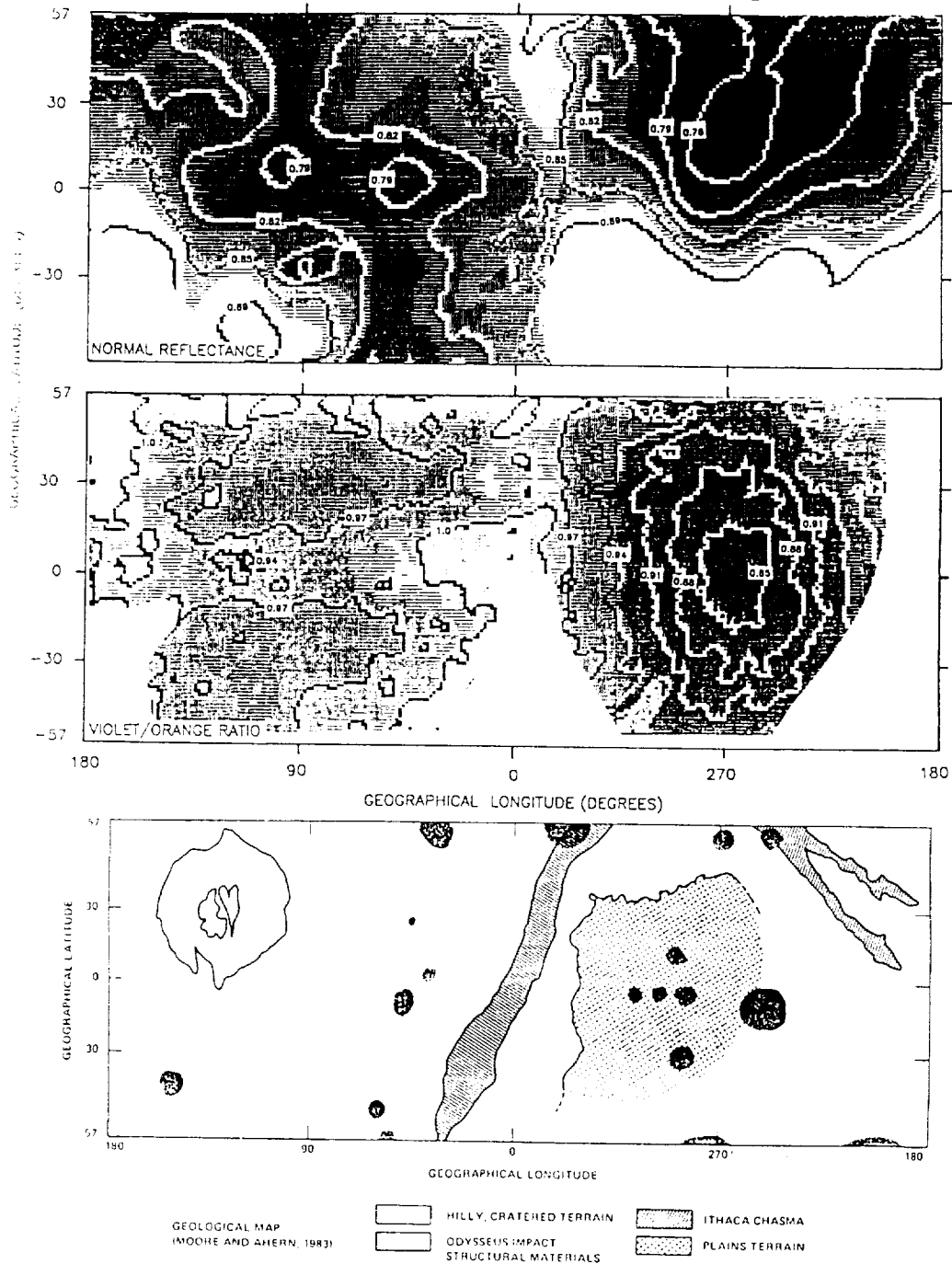


Figure. A map of normal reflectances in the clear filter and a violet/orange color ratio map for Tethys, compared with the geologic map of Moore and Ahern (1983), J.G.R. 88 Supplement A577-584.



# BACKSCATTERING FROST IN THE OUTER SOLAR SYSTEM

A. Verbiscer, P. Helfenstein, and J. Veverka, Cornell University

The backscattering nature of icy satellite surfaces in the outer solar system has been known for a long time [1-5]. Recently, we have applied a mixing model approach to demonstrate that the backscattering behavior of icy satellite surfaces must be due to the fact that the frost component itself is backscattering--unlike the situation for terrestrial snows/frosts, which tend to scatter light very strongly in the forward direction [7].

Our data on terrestrial snow/frost are derived from the work of Middleton and Mungall [8], who provide excellent *in situ* goniophotometric measurements extending to 154° in phase angle for a variety of terrestrial snow and frost surfaces. We fit Hapke's 1986 photometric equation [9] to determine the single scattering albedo  $\tilde{\omega}_o$  and the one-term Henyey-Greenstein [10] particle phase function  $g$  for each of the terrestrial samples and found very high single scattering albedos ( $\tilde{\omega}_o \sim 0.99$ ) and strongly forward scattering particle phase functions ( $g = +0.52$  to  $+0.79$ ), in good agreement with theoretical predictions based on Mie-type calculations. Surfaces of icy satellites behave quite differently: typically they have strongly backscattering (negative)  $g$ 's (Table 1). A simple two-component mixing model can be used to show that the negative  $g$ 's reflect the photometric properties of the frost/ice itself and cannot be explained entirely in terms of the dark non-icy component of the regoliths.

For a bimodal distribution of regolith particles, the single scattering albedo is given by

$$(\tilde{\omega}_o)_{\text{avg}} = \frac{\sigma_1 Q_{s1} N_1 + \sigma_2 Q_{s2} N_2}{\sigma_1 Q_{e1} N_1 + \sigma_2 Q_{e2} N_2} \quad (1)$$

where  $\sigma$  = geometric cross section of a particle;  $Q_e$  = particle extinction efficiency;  $Q_s$  = particle scattering efficiency; and  $N$  = number of particles per unit volume. The subscripts 1 and 2 refer to the two end-members. The corresponding equation for the average phase function (Henyey-Greenstein) asymmetry parameter is:

$$\bar{g} = \frac{\sigma_1 Q_{s1} N_1 g_1 + \sigma_2 Q_{s2} N_2 g_2}{\sigma_1 Q_{s1} N_1 + \sigma_2 Q_{s2} N_2} \quad (2)$$

Eqs. (1) and (2) can be combined and the dependence on  $\sigma$ ,  $Q_e$ ,  $Q_s$ , and  $N$  eliminated to derive an expression for the asymmetry parameter  $\bar{g}$  of the mixture as a function of  $g$  and  $\tilde{\omega}_o$  of the end members and of  $(\tilde{\omega}_o)_{\text{avg}}$ , the single scattering albedo of the mixture:

$$\bar{g} = \frac{\tilde{\omega}_{o1} g_1 ((\tilde{\omega}_o)_{\text{avg}} - \tilde{\omega}_{o2}) + \tilde{\omega}_{o2} g_2 (\tilde{\omega}_{o1} - (\tilde{\omega}_o)_{\text{avg}})}{(\tilde{\omega}_o)_{\text{avg}} (\tilde{\omega}_{o1} - \tilde{\omega}_{o2})} \quad (3)$$

Fig. 1 shows the graphs of Eq. (3) for two mixtures: one composed of terrestrial snow and Ceres-type material (solid line), and another made up of backscattering snow and Ceres-type material (dashed line). The "Ceres-type" material was chosen as a prototype of the dark, non-icy component of the regoliths: the values of  $\tilde{\omega}_o$  and  $g$  are those derived by Helfenstein and Veverka [11] for asteroid 1 Ceres.

Fig. 1 demonstrates that mixtures of terrestrial snow and Ceres-type material do not fit observed photometric parameters for Titania, Rhea, Enceladus, Mimas, and Europa, while a mixture of backscattering snow and Ceres-type material fits the observed parameters very well. The solid line in Fig. 1 also shows that normal frost can be made backscattering only if enough carbonaceous material is added to lower the  $\tilde{\omega}_0$  value to 0.2 or less. Since most icy satellites (cf. Table 1) have much higher values of  $\tilde{\omega}_0$ , their backscattering g's cannot be explained by the behavior of the dark, opaque component: rather, the frost component itself must be backscattering.

The cause of the backscattering remains uncertain. Johnson et al. [12] have proposed that "pitting" due to exposure to charged particles may be responsible. As an alternative, we suggest that on icy satellites frost grains are aggregated into particles of complex texture to produce the observed remarkable behavior. The extremely low temperatures prevalent in the outer solar system may be significant in preserving such highly textured aggregates.

This research was supported by NASA Grants NSG 7156 and 7606.

#### References:

1. Veverka, J., and J. Gradie (1983). Why don't icy satellites scatter light like model snow-covered planets? *Bull. Am. Astron. Soc.* 15, 853.
2. Buratti, B. J. (1985). Application of a radiative transfer model to bright icy satellites. *Icarus* 61, 208-217.
3. Helfenstein, P., J. Veverka, and P. Thomas (1988). Uranus satellites: Hapke parameters from Voyager disk-integrated photometry. *Icarus* 74, 231-239.
4. Verbiscer, A., and J. Veverka (1987). Rhea: Analysis of photometry using Hapke's Equation. *Bull. Amer. Astron. Soc.* 19, 822.
5. Verbiscer, A., and J. Veverka (1989). Albedo dichotomy of Rhea: Hapke analysis of Voyager photometry. *Icarus*, in press.
6. Veverka, J., P. Thomas, P. Helfenstein, R. H. Brown, and T. V. Johnson (1988). Satellites of Uranus: Disk-integrated photometry from Voyager imaging observations. *J. Geophys. Res.* 92, 14895-14904.
7. Verbiscer, A., and J. Veverka (1988). Icy satellites and terrestrial frosts: Comparison of Hapke's parameters. *Bull. Amer. Astron. Soc.* 20, 872.
8. Middleton, W. E. K., and A. G. Mungall (1952). The luminous directional reflectance of snow. *J. Opt. Soc. Am.* 42, 572-579.
9. Hapke, B. (1986). Bidirectional reflectance spectroscopy. 4. The extinction coefficient and the opposition effect. *Icarus* 67, 264-280.
10. Henyey, L. G., and T. L. Greenstein (1941). Diffuse radiation in the galaxy. *Ap. J.* 93, 70-83.
11. Helfenstein, P., and J. Veverka (1989). Physical characterization of asteroid surfaces from photometric studies. In *Asteroids II* (eds. R. P. Binzel, T. Gehrels, and M. S. Matthews), (U. Arizona, 1989).
12. Johnson, R. E., L. A. Batson, J. W. Boring, W. A. Jesser, W. L. Brown, and L. J. Lanzerotti (1985). Charged particle modification of ices in the Saturnian and Jovian systems. In *Ices in the Solar System* (Klinger et al., eds.), Reidel, pp. 302-315.

TABLE 1

Photometric Parameters for Model End Members and Icy Satellites

	Single Scattering Albedo $\tilde{\omega}_0$	Asymmetry Parameter $g$
A. Ceres-type material	0.06	-0.4
B. Terrestrial snow	0.999	+0.52
C. Backscattering snow	0.999	-0.3
Europa	$0.97 \pm 0.01$	$-0.15 \pm 0.04$
Mimas	$0.93 \pm 0.03$	$-0.30 \pm 0.05$
Enceladus	$0.99 \pm 0.02$	$-0.35 \pm 0.03$
Rhea	$0.89 \pm 0.01$	$-0.30 \pm 0.01$
Titania	$0.48 \pm 0.02$	$-0.28 \pm 0.01$

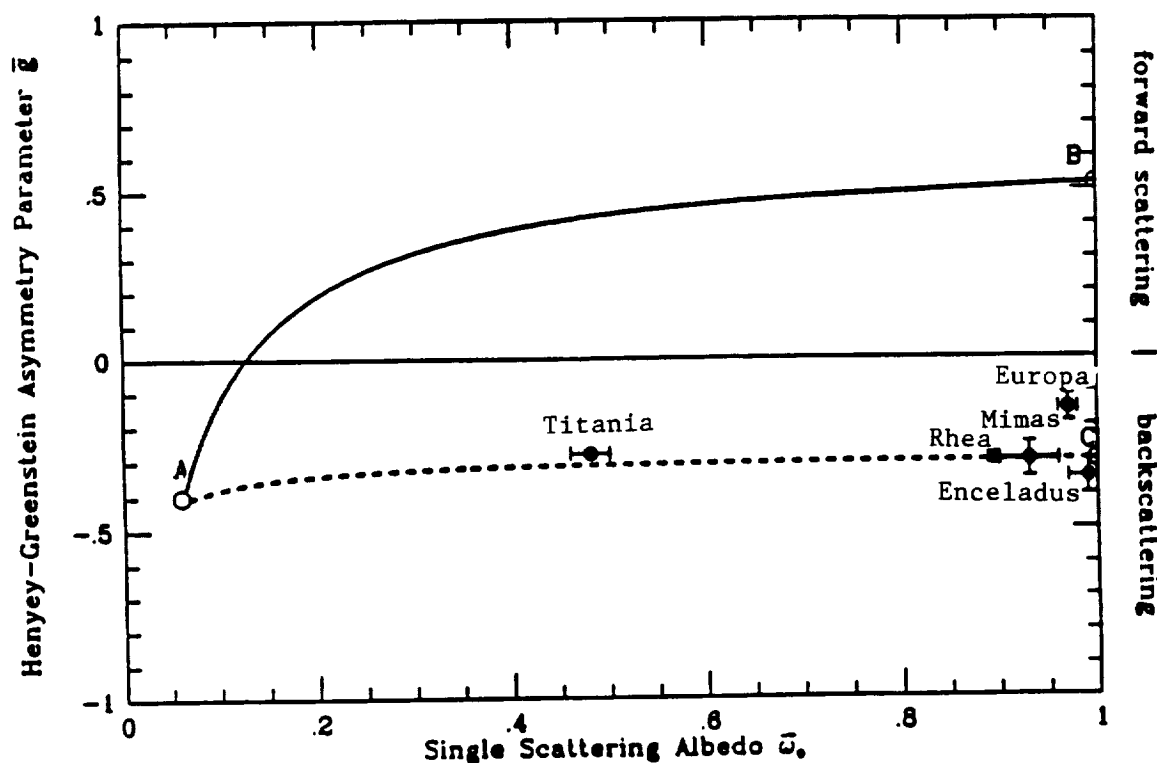


FIGURE 1. Single scattering albedos ( $\tilde{\omega}_0$ ) and Henyey-Greenstein asymmetry parameters ( $g$ ) for intimate mixtures of end members A and B (solid line) and A and C (dashed line). See Table 1 for photometric properties of the end members. Observed values of  $\tilde{\omega}_0$  and  $g$  for a number of icy satellites (solid circles) lie near the dashed line, indicating the icy component of their regoliths in strongly backscattering. We conclude from this that surface frost in the outer solar system is photometrically different from its terrestrial analog.

The absorption coefficient of liquid and frozen  $\text{CH}_4$  from 0.5 to 1.0 microns  
Uwe Fink and William Grundy  
Lunar and Planetary Laboratory, University of Arizona Tucson, AZ 85721

We have measured the absorption coefficient of liquid methane from 0.5 to 1.0 microns. For this purpose we have built a dewar which contains a 1 cm thick absorption cell. The dewar was cooled with liquid nitrogen causing liquid  $\text{CH}_4$  to condense in the cell. Further cooling of the dewar (by pumping on the nitrogen) resulted in solid methane which unfortunately was not perfectly clear but contained some bubbles. The resulting spectrum was quite close to that of the liquid but exhibited several sharper features. We plan to continue this work and obtain improved solid spectra which will be used to interpret the reflection spectrum of Pluto.

**ANALYSIS OF PLANETARY PHOTOMETRY WITH HAPKE'S MODEL: A WORKING ANALYTICAL STRATEGY.** Paul Helfenstein and J. Veverka, Center for Radiophysics and Space Research, Cornell University, Ithaca, NY 14853-6801.

**INTRODUCTION:** The photometric parameters of Hapke's bidirectional reflectance equation [1,2,3] are used with increasing frequency to interpret physical properties of planetary surfaces on the basis of their photometric behaviors. These parameters are:  $\omega_0$ , the average particle single-scattering albedo,  $h$ , which relates the angular width of the opposition surge to the state of regolith compaction and particle-size distribution,  $B_0$ , the amplitude of the opposition surge,  $g$ , the asymmetry factor of the particle phase function, and  $\bar{\theta}$ , the average slope angle of subresolution-scale macroscopic surface roughness. Values of Hapke's parameters for a given planetary surface are generally derived either from observations of disk-integrated phase curves, or from disk-resolved observations of surface brightness as a function of incidence angle ( $i$ ), emission angle ( $e$ ), and phase angle ( $\alpha$ ).

Critical concerns among users of Hapke's model involve the extent to which unique estimates of Hapke parameters can be derived from any given data set [4,5,6,7]. We have developed analytical methods and computer software which optimally fit Hapke parameters to disk-integrated phase curve observations and disk-resolved data. Our approach can be used on a case-by-case basis to demonstrate when unique solutions of Hapke parameters can and cannot be found. In the present study, we use Voyager photometry for Umbriel as a vehicle for demonstration.

**DATA SAMPLING STRATEGIES:** Disk-integrated phase curves, derived from Earthbased observations and/or spacecraft data, can be used to characterize only average global properties of planetary surfaces. In our approach, we require that the diameter of the object be known so that geometric albedo ( $p$ ) can be estimated and that the phase curve, on a stellar magnitude scale, be normalized so that the magnitude at  $\alpha = 0^\circ$  is  $-2.5 \log(p)$ .

Disk-resolved observations, derived largely from radiometrically calibrated spacecraft images, can be used to characterize surface properties of individual terrains in addition to average global properties. Spacecraft flyby missions often yield disk-resolved observations at radically different spatial resolutions for different phase angles. In order to insure that our sampled brightness measurements are obtained at similar resolutions at all phase angles and that fits of Hapke parameters are not too strongly dominated by a disproportionately large number of high-resolution data points, we collect average disk-resolved brightnesses binned in uniform increments of photometric latitude and longitude (usually  $5^\circ \times 5^\circ$ ) at each phase angle.

In order to sample brightnesses of individual geological features from a given series of spacecraft images, we first produce a digital geological unit map in standard cartographic coordinates (i.e., polar stereographic coordinates for Umbriel). These maps are then projected into the viewing perspectives of actual spacecraft images and registered with them. The projected maps then can be used as digital index templates which allow the extraction of photometric data for individual surface-resolved features.

**METHODS OF OBTAINING OPTIMAL PARAMETER FITS:** Our method of obtaining average global Hapke parameters from disk-integrated phase curves alone is described in detail elsewhere [7]. Briefly, we perform a grid-search of parameter space [8] for Hapke's  $\bar{\theta}$  parameter, and find the best non-linear least-squares fit combination of the remaining parameters for each assumed  $\bar{\theta}$  by using a gradient-search algorithm [9]. A scan of rms residuals as a function of  $\bar{\theta}$  (Fig. 1a) is often adequate to locate a unique solution, or at least the most physically reasonable of several possible solutions.

Average global Hapke parameters are actually found best by fitting simultaneously to disk-integrated and disk-resolved observations [10]. Our approach is to use the family of

plausible fits (as a function of  $\theta$ ) obtained from disk-integrated phase curves (Fig. 1a) to identify how the parameters are coupled (Fig. 1b). We then perform a grid-search over  $\theta$  space for the disk-resolved observations in which the remaining parameters are computed from the observed parameter coupling to  $\theta$ . Again, the optimal solution is found in the least-squares sense from the minimum of the residual vs.  $\theta$  curve (Fig. 1a).

Our primary method for finding Hapke parameters for individual geological features is similar to that for fitting to disk-integrated phase curves alone. A grid-search over  $\theta$  space is performed, and for each assumed  $\theta$ , the corresponding best combination of the remaining parameters are found by gradient-search methods. Table I lists values of Hapke parameters obtained for Umbriel by using the methods above.

**DISCUSSION:** Average global Hapke parameters are best obtained from simultaneous fits to disk-integrated and disk-resolved observations (1) because certain of Hapke's parameters like  $\theta$  are better constrained by limb-to-terminator brightness variations than by changes in brightness with phase angle, and (2) greater phase angle coverage sometimes provided by disk-integrated phase curves help to constrain the most strongly phase-angle dependent parameters ( $g$ ,  $h$ , and  $B_0$ ). Nevertheless, it is often useful to compare average global results obtained from separate fits to disk-integrated phase curves and disk-resolved data, respectively. Excellent agreement between such independently derived parameters has been obtained in studies of photometry of the Moon [11], Mercury [6,12], Rhea [13], and Titania [14], for example. On the other hand, sometimes considerable improvements are realized by fitting simultaneously to disk-integrated and disk-resolved data. In our Umbriel example, the best-fit values from disk-integrated analysis alone ( $\tilde{\omega}_0 = 0.31$ ,  $\theta = 18^\circ$ ,  $g = -0.32$ ) are slightly different from those obtained when disk-resolved observations are included ( $\tilde{\omega}_0 = 0.37$ ,  $\theta = 26^\circ$ ,  $g = -0.24$ ).

**REFERENCES:** [1] Hapke, B. (1981) *JGR* 86, 3039-3054, [2] Hapke, B. (1984) *Icarus* 59, 41-59, [3] Hapke, B. (1986) *Icarus* 67, 264-280. [4] Buratti, B. (1985) *Icarus* 61, 208-217. [5] McEwen, A. (1989) submitted to *Icarus*. [6] D. Domingue and B. Hapke (1989) *Icarus*, submitted. [7] Helfenstein, P. and J. Veverka (1989). *Asteroids II*, Univ. Ariz. Press, in press. [8] Bevington, P. (1969). *Data Reduction and Error Analysis in the Physical Sciences*, McGraw-Hill, NY 336 pp. [9] Marquardt, M. (1963) *J. Soc. Ind. Appl. Math.* 11, 431-441. [10] McEwen, A., et al. (1989) *Icarus* 75, 450-478. [11] Helfenstein, P. and J. Veverka (1987) *Icarus* 72, 342-347. [12] Veverka, J., et al. (1988). In *Mercury*, Univ. Az. Press. [13] Verbiscer, A. and J. Veverka (1989) *Icarus* (in press). [14] Thomas, P., et al. (1987). *JGR* 92, 14911-14917.

**ACKNOWLEDGMENTS:** This research is supported by NASA grant NSG 7606.

**TABLE I:** Hapke Parameters for Umbriel from Voyager Clear-filter Photometry

	$\tilde{\omega}_0$	$g$	$\theta$
Global Average	$0.372 \pm 0.001$	$-0.235 \pm 0.003$	$26 \pm 1$
Dark Cratered Terrain	$0.361 \pm 0.002$	$-0.246 \pm 0.003$	$25 \pm 1$
Bright Craters	$0.406 \pm 0.024$	$-0.225 \pm 0.028$	$30 \pm 7$
Annulus	$0.85 \pm 0.01$	$0.51 \pm 0.24$	$9 \pm 2$

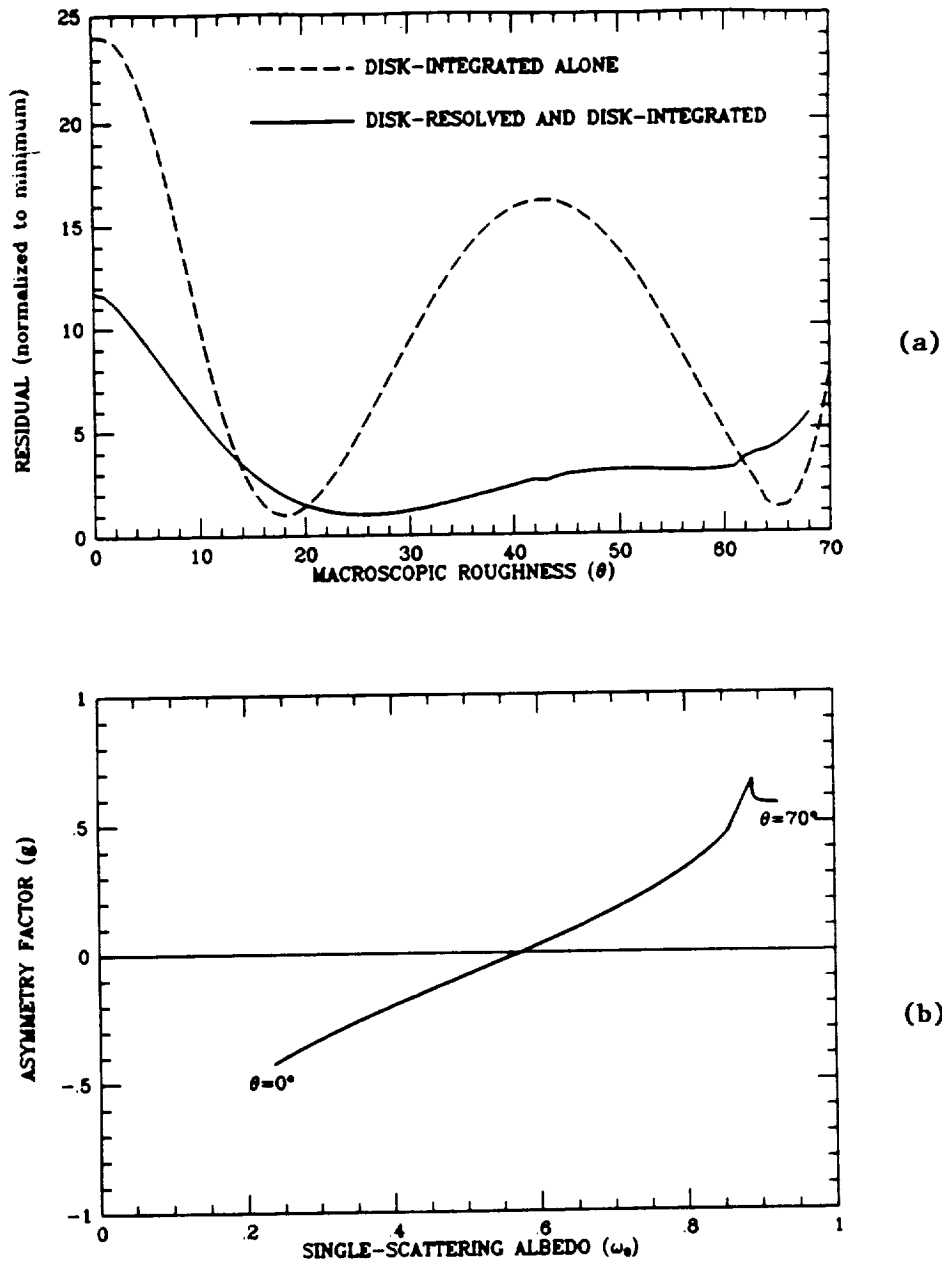


**FIGURE 1(a):** Least-squares residuals as a function of  $\theta$  for fits of  $\tilde{\omega}_0$ ,  $g$ , and  $\theta$  to Umbriel's disk-integrated phase curve (dashed line) and its phase curve plus disk-resolved photometric behavior (solid line). The two minima in the dashed line represent two possible solutions, of which only that for  $\theta = 18^\circ$ ,  $\tilde{\omega}_0 = 0.31$ ,  $g = -0.32$  is physically meaningful. By further constraining the solution with disk-resolved observations, an improved solution is found ( $\theta = 26^\circ$ ,  $\tilde{\omega}_0 = 0.37$ ,  $g = -0.24$ ). Because Umbriel's opposition surge was not well-observed by Voyager, we assumed parameters for a Titania-like opposition surge ( $h = 0.018$ ,  $B_0 = 0.65$ ).

(b) Coupling of  $\tilde{\omega}_0$ ,  $g$ , and  $\theta$  for all points along the dashed-line in (a). As  $\theta$  is increased,  $\tilde{\omega}_0$  and  $g$  must be increased systematically to optimally fit the disk-integrated phase curve.

Digital mosaics in two or more color filters have been produced from Viking images for a global study of the surface materials on Mars. We have completed four large mosaics in orthographic projections, each composed of more than 100 red- and violet-filter image frames, each with a scale of 1 km/pixel, and each covering a range of latitude from about  $-60^{\circ}$  to  $60^{\circ}$ . The data were acquired during early to middle northern summer at phase angles of  $35^{\circ}$  to  $55^{\circ}$ . The atmospheric "haze" (primarily from suspended dust) was low during this period, but a variety of condensate clouds were present. The "Valles Marineris Hemisphere" mosaic covers the region from  $\sim 30^{\circ}$  to  $130^{\circ}$  longitude, including Valles Marineris, Tharsis Montes, Lunae Planum, and Chryse and Acidalia Planitiae. The "Cerberus Hemisphere" mosaic covers the region from  $\sim 140^{\circ}$  to  $230^{\circ}$  longitude, including Elysium, Arcadia, and Amazonis Planitiae and ancient cratered highlands. The "Schiaparelli Hemisphere" mosaic covers the region from  $\sim 280^{\circ}$  to  $30^{\circ}$  longitude, including Arabia Terra, Syrtis Major Planum, Hellas Planitia, and the Oxia Palus area. The "Syrtis Major Hemisphere" mosaic covers the region from  $\sim 260^{\circ}$  to  $350^{\circ}$  longitude, including Arabia Terra, Syrtis Major Planum, and Isidis and Hellas Planitiae.

We have also completed mosaics of the north and south polar residual ice caps at a scale of 0.5 km/pixel. Together, these six mosaics cover about 75% of the surface of Mars; additional mosaics are in progress to cover the remaining surface. The Planetary Image Cartography System (PICS) has been used for all image processing. The latest procedures and software for radiometric calibration (E. M. Eliason and L. A. Soderblom, unpublished data) and for geometric control [1] were utilized. Large-scale filtering has been applied to the mosaics to normalize large-scale brightness variations, which are mostly due to variations in solar incidence angle. Scattering models for the atmosphere and surface of Mars are in progress. Following normalization of atmospheric and surface brightnesses, we will combine the individual unfiltered mosaics into a global color mosaic in sinusoidal equal-area projection for compatibility with other digital image and topographic datasets for Mars [2,3].

Parts of these mosaics have been geometrically registered to parts of the 1/64-degree digital elevation model [3] and to high-resolution monoscopic mosaics to produce oblique views and high-resolution color images and, thus, to show the relations among color units, surface morphology, and topography.

At least five major spectral units can be distinguished in the color mosaics: (1) a bright-red unit, which probably includes eolian dust; (2) a dark-red unit, which may consist of duricrust; (3) a very dark red unit, which occurs on the steep flanks of the Tharsis volcanoes and in portions of the southern highlands; (4) a dark-gray unit, which occurs in a variety of geologic settings; and (5) a bright white unit, consisting of  $\text{CO}_2$  and  $\text{H}_2\text{O}$  frost, ice, and clouds. Other more subtle or rare spectral units are also present, for example, some anomalous bright white layers in Gangis and Capri Chasmata [4].

The dark-red spectral unit dominates the surface in a broad swath from about latitude  $0^{\circ}$  to  $30^{\circ}$  and longitude  $350^{\circ}$  east to  $70^{\circ}$ . Elsewhere on the planet, this unit occurs in small patches or appears poorly developed. Previous workers [5,6,7] have suggested that this unit may consist of a duricrust, but the global distribution has not been explained.



The dark-gray materials are significant because their reflectance spectra suggest that they are relatively unaltered; they occur in a great variety of geologic settings, including dune fields, dark crater streaks, intercrater volcanic plains, local topographic lows such as crater floors, and large-scale topographic lows and regions of outflow channel deposition such as Acidalia Planitia. Furthermore, the dark-gray materials seem to occur in place at various locations in Valles Marineris: in the lower walls of the eastern canyons as a widespread stratigraphic layer, in recent volcanic domes and flows [8], and in finely stratified (possibly lacustrine) deposits. Because of this diversity of geologic occurrence, we suspect that the dark-gray spectral unit consists of several different materials that are spectrally similar in the broadband color filters of Viking. It is possible that a variety of spectral signatures will be detected in the dark-gray areas by mapping spectrometers such as VIMS (Visual-Infrared Mapping Spectrometer) or TES (Thermal Emission Spectrometer).

Images in the north polar mosaic were acquired at low phase angles ( $46^\circ$  to  $49^\circ$ ) and during clear atmospheric conditions (optical depth  $\sim 0.2$ ), thus providing high-quality data on the surface albedos and colors. Surface materials in the north polar region have a strongly trimodal distribution of spectral properties, consisting of a bright red unit (dust), a bright white unit (water ice mixed with dust), and a dark-gray unit (dune materials in the polar collar). The north polar residual ice cap has an albedo of  $\sim 0.5$ , whereas the south polar residual cap has an albedo closer to 1.0, consistent with previous suggestions [9,10] that the south polar residual ice may be sufficiently bright and cold for stability of  $\text{CO}_2$  frost.

#### REFERENCES

- [1] Edwards, K. (1987) Geometric processing of digital images of the planets. *Photogrammetric Engineering and Remote Sensing* 53, 1219-1222.
- [2] Batson, R. M. (1987) Digital cartography of the planets: New methods, its status, and its future. *Photogrammetric Engineering and Remote Sensing* 53, 1211-1218.
- [3] Wu, S. S. C., and Howington-Kraus, A. (1988) Digital elevation model of Mars. NASA TM 4041, 551.
- [4] McEwen, A. S., and Soderblom, L. A. (1989) Mars color/albedo and bedrock geology. Abstract for Fourth Int. Mars Conf., Tucson, Arizona, Jan. 9-13, 1989.
- [5] Kieffer, H. H., Davis, P. A., and Soderblom, L. A. (1981) Mars' global properties: Maps and applications. *Proc. Lunar Planet. Sci.* 12B, 1395-1417.
- [6] Presley, M. A., and Arvidson, R. E. (1988) Nature and origin of materials exposed in the Oxia Palus-Western Arabia-Sinus Meridiani region, Mars. *Icarus* 75, 499-517.
- [7] Arvidson, R. E., Guinness, E. A., Dale-Bannister, M. A., Adams, A., Smith, M., Christensen, P. R., and Singer, R. B. (in press) Nature and distribution of surficial deposits in Chryse Planitia and vicinity, Mars. *J. Geophys. Res.*
- [8] Lucchitta, B. K. (1987) Recent mafic volcanism on Mars. *Science* 235, 565-567.
- [9] James, P. B., Briggs, G., Barnes, J., and Spruck, A. (1979) Seasonal recession of Mars' south polar cap as seen by Viking. *J. Geophys. Res.* 84, 2889-2922.
- [10] Paige, D. A., and Ingersoll, A. P. (1985) Annual heat balance of Martian polar caps: Viking observations. *Science* 228, 1160-1168.

## REGIONAL ALBEDO AND PHOTOMETRIC STUDIES OF MARS: VIKING IRTM OBSERVATIONS

Steven W. Lee and R. Todd Clancy

Laboratory for Atmospheric and Space Physics, University of Colorado, Boulder, CO 80309

There is abundant evidence that, at present, aeolian processes are active over much of the surface of Mars [cf. 1; 2]. Previous studies have demonstrated that variations in regional albedo and wind streak patterns are indicative of sediment transport through a region [3; 4], while thermal inertia data [derived from the Viking Infrared Thermal Mapper (IRTM) data set] are indicative of the degree of surface mantling by dust deposits [5; 6; 7; 8; 9]. The visual and thermal data are therefore diagnostic of whether net erosion or deposition of dust-storm fallout is taking place currently and whether such processes have been active in a region over the long term. One of the consequences of variations in regional sedimentation patterns should be relative differences in surface texture and macroscopic roughness from region to region; photometric analysis of the visual brightness of a surface viewed under a variety of emission and phase angles may allow such differences to be quantitatively investigated [10; 11; 12]. In addition, determination of regional photometric properties will place constraints on the interpretation of the related albedo and thermal data sets.

Disk-resolved (as opposed to disk-integrated) photometric studies of planetary surfaces from spacecraft are not common, and photometric studies of Mars using spacecraft data are rare indeed. Voyager images of Io have been used to investigate porosity and macroscale roughness of the surface [cf. 13; 14]; these studies have indicated that it may be more appropriate to study relative regional differences in photometric properties, rather than to attempt physically rigorous modelling of the results. Images from the early Mariner missions were used to study a few selected regions [15]; indications were that significant variations in surface properties were detectable. Only the first few months of Viking Orbiter IRTM data were systematically analyzed [5]; again, significant variations in regional properties, as well as the effects of atmospheric aerosols, were detected.

During the course of the Viking missions, numerous IRTM observing sequences were designed with photometric analyses in mind. Several hundred emission-phase-function (EPF) sequences, in which the IRTM instrument observed the same area on the surface for an extended period as the spacecraft moved overhead, were obtained. Typical sequences consist of several thousand to several tens of thousand individual measurements of surface brightness gathered over a wide range of emission and phase angles and with spatial resolutions of better than ten to a few tens of kilometers. These observations were obtained randomly over much of the planet, but most lie within  $45^\circ$  of the equator. The IRTM data set, as a whole, is well calibrated, having been corrected for inter-spacecraft, inter-detector, and temporal calibration variations; a conservative estimate for the absolute uncertainty inherent in this data set is 1-2% [16]. Thus, differences in regional properties inferred from photometric studies should be attributable to variations in the surface and/or atmospheric characteristics and not to calibration errors.

We are investigating the relative photometric properties of several regions on Mars through analysis of the IRTM EPF observations. Individual sequences are sorted into  $0.5^\circ$  by  $0.5^\circ$  boxes (lat, lon); the individual observations falling in each box cover a wide range of emission and phase angles but a restricted range of incidence angles. A first-order correction for transmission loss through the atmosphere, direct scattering from atmospheric dust, and multiple scattering from the surface (Fig.1) is applied to determine phase-corrected albedos for the individual observations in each box. Finally, a nonlinear least squares fit of a simple Hapke photometric function [11] to the set of observations in each box is determined. In this fashion, the consistency of fits for numerous small areas covered by an entire sequence can be analyzed; regional differences can also be investigated by comparing results for broader areas.

EPF sequences for seven regions on Mars have been analyzed to date: Acidalia, Amazonis, Arabia, Cerberus, Isidis/Syrtis Major, Olympus Mons, and Syrtis Major/Arabia. Examples of fits for a small area within Arabia is shown in Fig.2; a scatter plot of the fits for this entire EPF sequence is shown in Fig.3. From our analysis to date, it is apparent that bright and dark regions are distinguishable on the basis of particle single scattering albedo. However, we feel that we will need to process more sequences before we can begin to interpret the apparent variations in compaction parameter. We will also continue to conduct tests of the sensitivity of the fits to the angular coverage of the sequences and the atmospheric correction. The results of these analyses, in conjunction with mapping of regional thermal properties and albedo variations (also derived from IRTM data), will be used to infer details of regional sediment transport and consequent properties of the martian surface. This study may also allow quantitative investigation of the properties of martian dust and aerosols.

This research has been supported by NASA grant NAGW-1378.

- REFERENCES:** [1] Veverka, J., P. Thomas, and R. Greeley (1977), *J. Geophys. Res.* 82, 4167-4187. [2] Thomas, P., J. Veverka, S. Lee, and A. Bloom (1981), *Icarus* 45, 124-153. [3] Lee, S.W., P.C. Thomas, and J. Veverka (1982), *J. Geophys. Res.* 87, 10025-10042. [4] Lee, S.W. (1986), In *Symposium on Mars: Evolution of its Climate and Atmosphere* (V. Baker et al., eds.), pp. 71-72, LPI Tech. Rpt. 87-01, Lunar and Planetary Institute, Houston. [5] Kieffer, H.H., T.Z. Martin, A.R. Peterfreund, B.M. Jakosky, E.D. Miner and F.D. Palluconi (1977), *J. Geophys. Res.* 82, 4249-4295. [6] Christensen, P.R. (1982), *J. Geophys. Res.* 87, 9985-9998. [7] Christensen, P.R. (1986), *J. Geophys. Res.* 91, 3533-3545. [8] Christensen, P.R. (1986), *Icarus* 68, 217-238. [9] Jakosky, B.M. (1986), *Icarus* 66, 117-124. [10] Goguen, J.D. (1981), Ph.D. dissertation, Cornell University, Ithaca, N.Y. [11] Hapke, B. (1981), *J. Geophys. Res.* 86, 3039-3054. [12] Hapke, B. (1984), *Icarus* 59, 41-59. [13] Clancy, R.T. and G.E. Danielson (1981), *J. Geophys. Res.* 86, 8627-8634. [14] Simonelli, D.P., and J. Veverka (1986), *Icarus* 68, 503-521. [15] Young, A.T., and S.A. Collins (1971), *J. Geophys. Res.* 76, 432-436. [16] Pleskot, L.K., and E.D. Miner (1981), *Icarus* 45, 179-201. [17] Martin, T.Z. (1986), *Icarus* 66, 2-21.

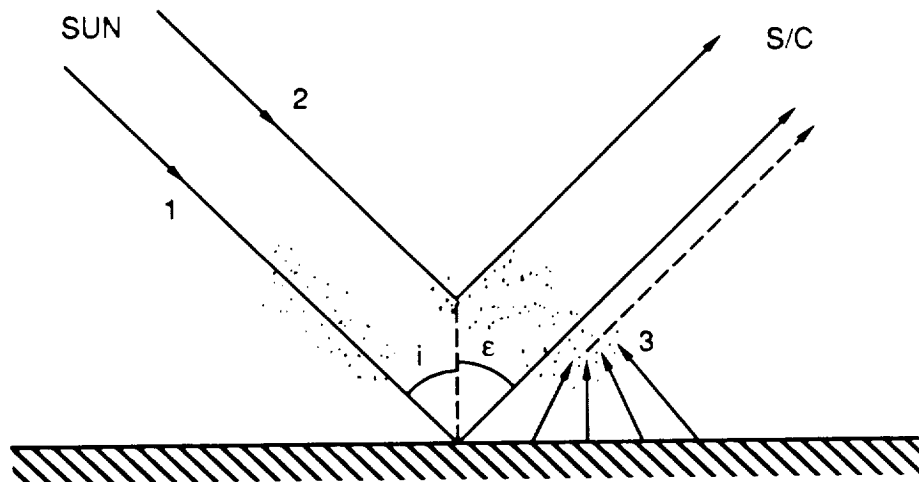


**Figure 1.** Diagram of the atmospheric correction model incorporated into the current analysis software. The three terms included are: Term 1: Transmission loss:  $(e^{-\tau/\mu_i}) (e^{-\tau/\mu_\epsilon})$  where:  $\tau$  = extinction opacity;  $\mu_i = \cos(i)$ ;  $\mu_\epsilon = \cos(\epsilon)$ ; Term 2: Direct scattered light:  $\tilde{\omega}_0 (\phi_{\epsilon+i}) (1 - e^{-\tau/\mu_\epsilon})$  where:  $\tilde{\omega}_0$  = dust single scattering albedo;  $\phi_{\epsilon+i}$  = dust phase function (backscatter); Term 3: Multiple scattering from surface:  $A \tilde{\omega}_0 \phi (1 - e^{-\tau/\mu_\epsilon})$  where:  $A$  = surface albedo;  $\phi$  = dust phase function (forward scattering). The latest estimates of the optical properties and phase function of atmospheric dust, as derived by Pollack et al. (personal communication, 1989), have been used in the initial modeling. The zonal mean opacity, appropriate for the location and  $L_s$  of each IRTM sequence analyzed [17], is also utilized.

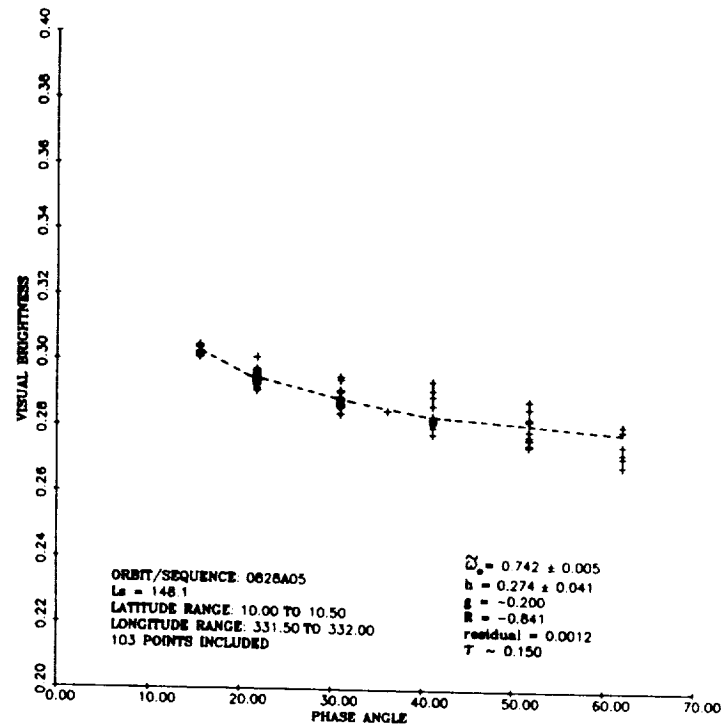


**Figure 2.** Fit of a photometric function to the visual brightness measurements in a  $0.5^\circ \times 0.5^\circ$  area in the bright region Arabia (centered at  $10.25^\circ$  latitude,  $331.75^\circ$  longitude). The crosses indicate the IRTM visual brightness measurements, and the dashed curve is the Hapke (1981) model dependence for the parameters shown above the plot. Phase angles for the data (and model) vary linearly with emission angle; incidence angles vary between  $7.5^\circ$  and  $10^\circ$ . The estimated atmospheric opacity is 0.15.

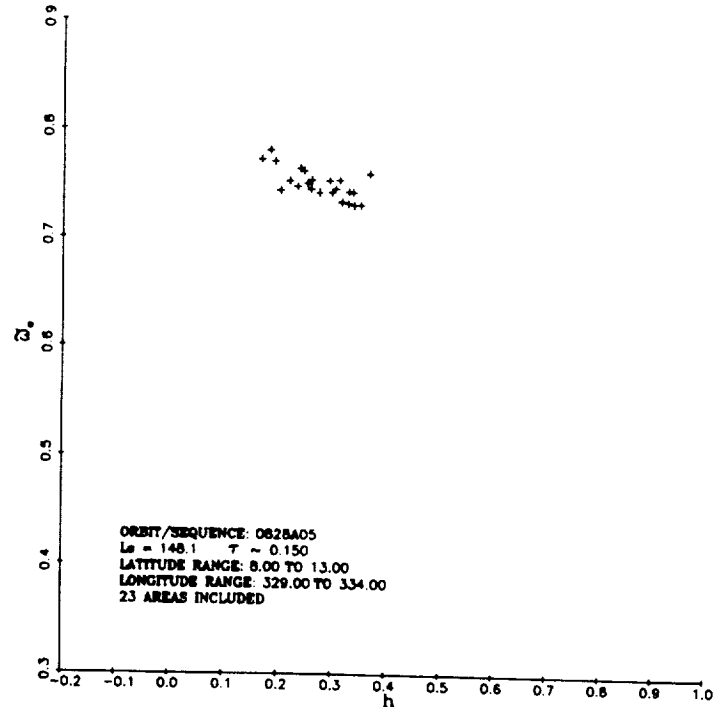


**Figure 3.** Scatter plot of the photometric parameters fit to a sequence of EPF observations of the bright region Arabia. Each of the crosses correspond to the fit for an individual  $0.5^\circ \times 0.5^\circ$  area.

# MULTISPECTRAL STUDY OF VALLES MARINERIS

P.E. Geissler, R. B. Singer , B. K. Lucchitta

Figure 1 illustrates the implications of the atmospheric correction for units representing extremes in color properties. As might be expected, removal of atmospheric radiance derived in part from light reflected first from the surface (and thus approximating the scene average in brightness and color) has resulted in an increase in contrast and color saturation: the relatively gray materials (low R/V) becoming grayer and the red regions becoming more red.

Preliminary results suggest that the dark materials in the Valles region are darker and grayer than previously reported, consistent with a composition of fresh mafic rock or glass. The darkest materials appear to have been recently excavated near the west margin of Juventae Chasma. This unit is spectrally similar to a dark layer in the Coprates Chasma south wall which occurs at a similar elevation. Continuing study will focus on whether the dark materials are laterally extensive units which are being exposed by erosion at specific locations, or local and discontinuous outcrops consistent with the interpretation of volcanic plugs and vents.

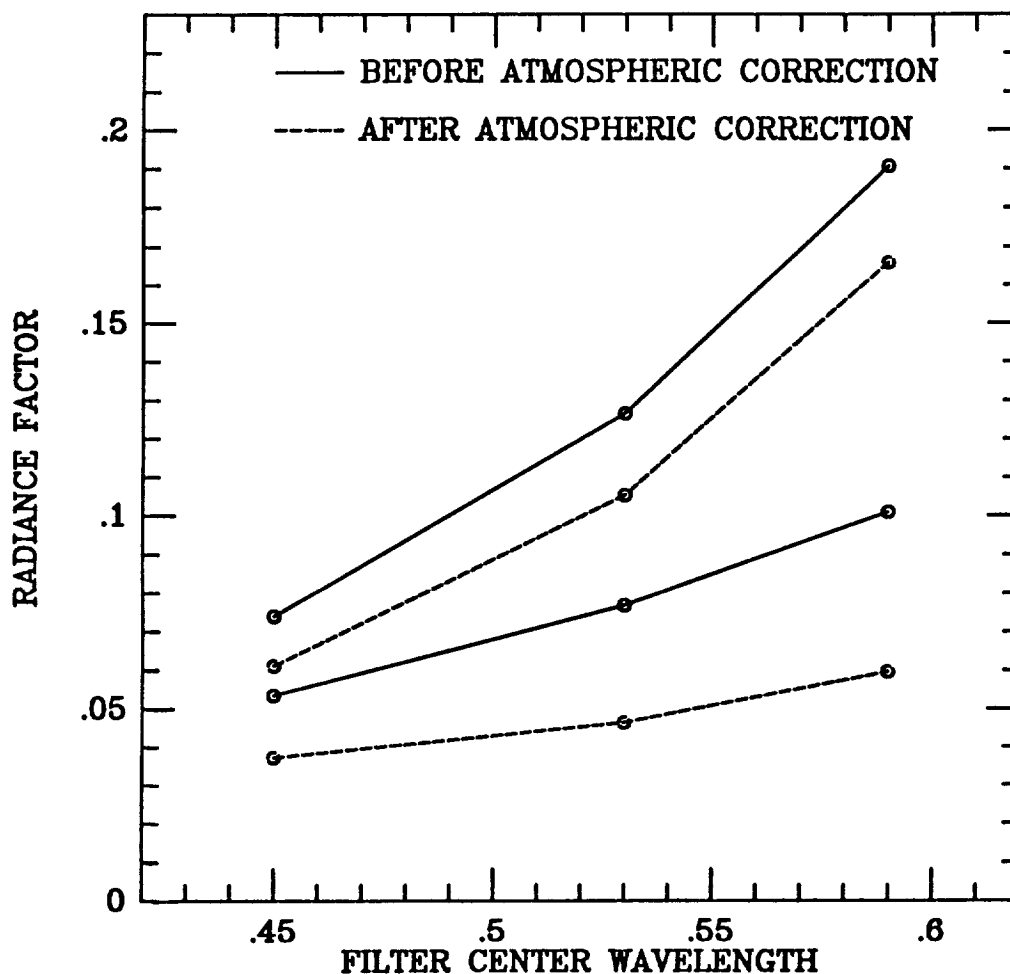


**Figure 1:** Solid lines represent Viking Orbiter 3-color data prior to atmospheric correction for bright and dark extreme units observed in Valles Marineris region. Dashed lines represent those same units after correction by a realistic multiple-scattering atmospheric model. While the radiance factor for both units has decreased, the contrast between them, both in color and albedo, has increased.

## VALLES MARINERIS: COMPOSITIONAL CONSTRAINTS FROM VIKING MULTISPECTRAL IMAGES

*P.E. Geissler, R.B. Singer (LPL, Univ. Arizona), B.K. Lucchitta (USGS, Flagstaff)*

The Valles Marineris offers a unique view of the interior of the martian crust to depths reaching 7 km. Using calibrated Viking color images along with earthbased telescopic observations and laboratory spectra, we are investigating the nature of the materials exposed on canyon floors and in layering observed in interior sedimentary deposits and in the canyon walls. The darkest materials are of particular interest, since they may represent recent excavation of spatially extensive geological horizons, and may include isolated outcrops of mafic extrusives, indicating relatively recent volcanism in Valles Marineris (Lucchitta, *Science* 237, 535, 1987).

Multispectral images obtained by the Viking orbiters are particularly valuable for defining compositional units within the canyon system and for constraining surface composition by comparison with terrestrial candidate materials measured in the laboratory. The data set under study includes 15 color composites of the central and eastern regions (0 to 20 degrees S., 45 to 85 degrees W.) taken at intermediate resolution (600-800 m/pixel) during clear conditions at mid morning in northern hemisphere Spring ( $L_s = 35$  to 90 degrees). The images span a range of phase angles from 20 to 110 degrees.

Because of the overlap of images recorded under various viewing conditions it is possible to separate the effects of single scattering albedo, particle scattering phase functions, and surface roughness which influence the radiance reflected from the planet surface. However, in order to obtain such geologic information it is necessary to first account for the influence of atmospheric aerosols in the measured signal. An atmospheric correction is required both for the absolute radiometry needed for comparison to lab standards, and for reducing images taken on different orbits and under different atmospheric conditions to a common basis.

In order to examine the effects of scattering by atmospheric aerosols we have employed the correlation between the brightness of shadows and the brightness of adjacent, directly illuminated regions to derive the airlight contribution to the scene radiance. The analysis shows that a large fraction of the scene brightness can be attributed to upwelling atmospheric radiance. The airlight is significant in the case of the dark materials in particular, because of their localized occurrence in a scene dominated by brighter materials.

A second quantity which can be obtained from the shadow brightness regression is the ratio of direct to diffuse illumination irradiance at the surface of Mars. Using a multiple scattering code made available by M. Tomasko (LPL) together with aerosol optical properties from Pollack et al. (*J. Geophys. Res.* 84, 2929), this quantity allows an estimate to be made of the atmosphere's optical depth which permits a multiplicative correction to be obtained for the attenuation due to atmospheric extinction. For our particular scenes, the diffuse illumination irradiance integrated over solid angle exceeds the total irradiance of the direct sunlight by a factor of three, resulting in an optical depth estimate of 0.6. The magnitude of the diffuse illumination is such that calculations of the directional reflectance distribution function for Mars should include consideration of this omnidirectional illumination.

## ISOLATION OF COMPOSITIONAL VARIANCE FROM VIKING LANDER MULTISPECTRAL IMAGES

Milton O. Smith and John B. Adams, Department of Geological Sciences,  
University of Washington, Seattle, WA 98185

Our objective is to compare Viking Lander and Viking Orbiter multispectral images with telescopic spectra and with laboratory reference spectra, and to understand the spectral variations in terms of surface composition and texture. Lander images show strong contrasts owing to shadows and shading. It is difficult to specify spectrally similar materials within a scene because of the variations in lighting geometry; this difficulty is compounded when comparing scenes taken by different cameras and by the two Landers over periods of several years because of uncertainties in instrument calibration and in atmospheric effects.

We have now analyzed three scenes from each of the Lander sites using a spectral mixing model (1), and have isolated the portion of the spectral variation due to composition, as opposed to effects arising from instrumental differences between cameras, temporal drift in camera electronics, instrumental noise, shade/shadow, spectral phase effects, atmosphere and illumination geometry. We examined one scene from each Lander site that was repeated two years later under identical lighting conditions, to test for temporal changes. Only areas of the surface of Mars were analyzed. Regions of sky and Lander apparatus were omitted.

At both Lander sites and at all time periods the multispectral data fit a linear mixture model consisting of the same three spectral endmembers, soil, rock and shade (1) in varying proportions. This analysis considers the fractions of each endmember in each pixel, the fit of the model to the data, and also yields the gains and offsets for each bandpass of each image (Fig. 1). The gains and offsets are the respective multiplicative and additive factors that convert image DN's to total hemispherical reflectance.

The gains and offsets include multiple factors: instrumental, atmospheric, and illumination intensity. The gains (Fig. 1a) show nominal differences of  $\pm 5\%$ . The offsets (Fig. 1b) were negligible ( $\leq .01$  reflectance). The pattern of offsets suggests that they arise from the instrumentation. Atmospherically caused offsets would be expected to change as a function of wavelength. A similar argument also applies to variations in gains. Gains for images taken by different cameras near the same time are equal in magnitude to the gain differences measured for images taken by the same camera over a period of two years.

The instrumental noise was computed as that component of the variance not explained by the spectral reference endmembers soil, rock and shade. While it is possible that the noise component also may include more than the three endmembers in the model, the spatial distribution of the noise in each image was either random or line oriented. In the Lander 1 image (12A168/028) the noise was especially high, but the spatial patterns were not related to contextual features of the Martian surface.

The spectral variance attributable to surface composition (Fig. 2b) was computed by determining that portion of the total variance arising from soil and

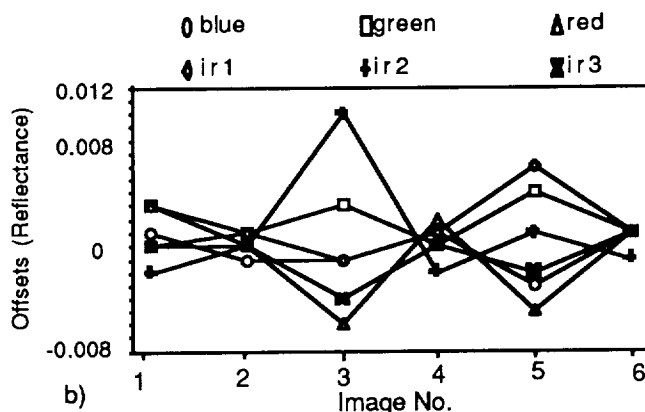
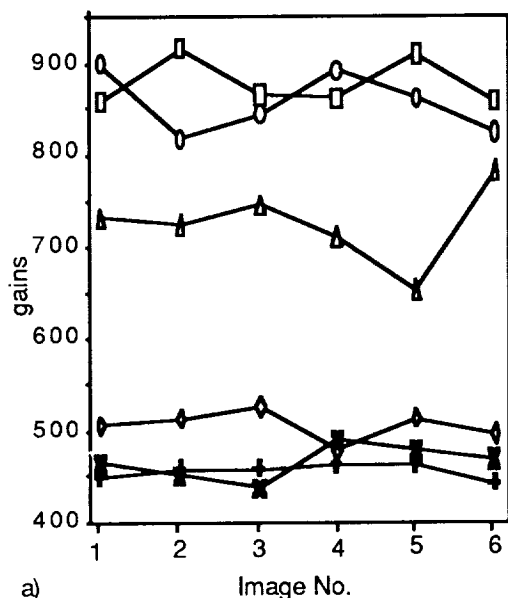
rock reference endmembers such that there was no shade or shadow component to the image. The fractions of soil, rock and shade were rescaled, omitting shade, and the reflectance from each pixel was computed from these rescaled fractions. The spectral variance due to shade/shadow/phase (Fig. 2a) was computed by subtracting the variance due to composition and instrumental noise from the total image variance. The spectral phase component of the image variance was spectrally flat so that it could not be separated from the shade and shadow variance.

Although the mean fraction of rock and soil for the Lander 1 and 2 sites is similar (Fig. 2c), compositional changes are evident over time in both the mean fraction (Fig. 2c) and the spectral variance due to composition (Fig. 2b). For the Lander 1 site we find a significant reduction in the spectral variance due to composition over a two year period with almost no change in the fraction of soil (Fig. 2c). In contrast, the Lander 2 site indicates an increase in compositional variance and in the mean fraction of soil.

#### Reference

1. Adams, J. B., M. O. Smith, and P. E. Johnson (1986), J. Geophys. Res., 8098-9112.





$$\text{Reflectance} = \text{Offset} + \text{Digital Number} / \text{gain}$$

Figure 1. The gains and offsets for the six Viking Lander 1 and 2 images are necessary to provide consistent fractions of spectral endmembers. The patterns are consistent with instrumental drift and differences between Lander cameras. The graphs are organized so that each line is the gain or offset for a single bandpass for each of the six Lander images.

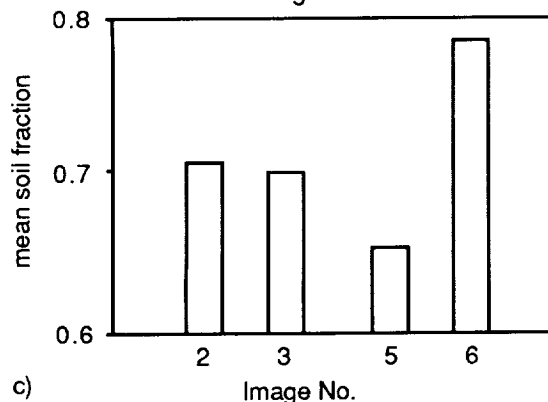
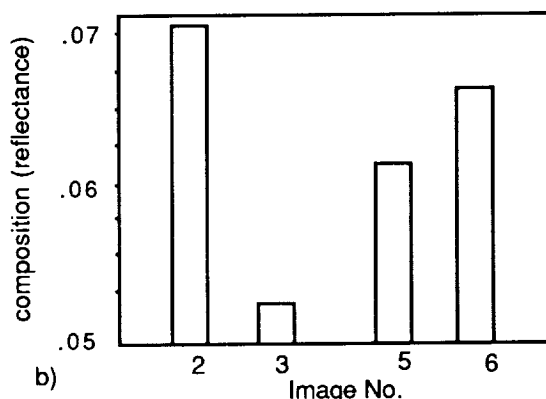
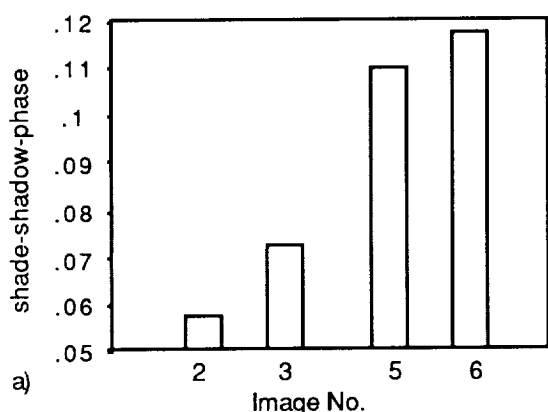


Figure 2. The spectral standard deviation of shade (a) and composition of soil-rock (b), and the mean soil fraction (c) in four Lander images indicate significant changes in the abundance and distribution of soil over time and at the two sites. The Lander 1 images (2 & 3) indicate a decrease in the soil-rock spectral variation with only almost no change in the mean soil fraction over a two year period. In contrast, Lander 2 images (5 & 6) indicate nearly a 10% increase in the fraction of soil and an increase in the rock-soil variance. The spectral variance attributable to shade/shadow/phase at the two sites increased over the two years.

Key to image nos. of Fig. 1 and Fig. 2: 1) 11A147/026; 2) 12A168/028; 3) 12H196/615 4) 21A190/023 5) 22A187/023; 6) 22G107/526. Images nos. 1 - 3 are from Lander 1 while nos. 4 - 6 are Lander 2. An elapsed time of nearly two years exist between image nos. 2 and 3 and nos. 5 and 6.

## **VIKING OPTICAL AND THERMAL EVIDENCE FOR WIDESPREAD DURICRUST SUBSTRATE ON MARS**

Edward A. Guinness and Raymond E. Arvidson, McDonnell Center for the Space Sciences, Department of Earth and Planetary Sciences, Washington University, St. Louis, Missouri, 63130.

Viking Orbiter visible and thermal observations provide information on the uppermost several centimeters of the martian surface. The atmosphere of Mars has clearly interacted with the surface and caused extensive modification of exposed rocks. An important question for the study of Mars is the extent to which local bedrock can be identified with visible and thermal data. Several recent workers [1-4] have used Viking Orbiter multispectral image data to study the martian surface in the equatorial region between Lunae Planum and Oxia Palus ( $0^{\circ}$  to  $80^{\circ}$  west longitude). In this abstract, we further characterize materials in this region by analyses of Viking Infrared Thermal Mapper (IRTM) data, along with Viking Orbiter multispectral images acquired at multiple phase angles. In addition, we use the results of these analyses to develop a model to explain the nature and distribution of surface materials and the relation, if any, to bedrock geology.

The equatorial region between Lunae Planum and Oxia Palus contains three dominant surficial units defined by their reflectance properties [1]. Bright red material has reflectance properties similar to palagonite-like dust. Dark gray material has reflectance properties similar to mafic fragments thinly coated with palagonite. In addition, there is a dark red unit that is a mixture of bright red and dark gray materials. The bright red unit is found as crater streaks and at the margin between dark gray and dark red units. The dark gray unit is found in Acidalia Planitia and as crater splotches and streaks in Xanthe Terra and Oxia Palus. The dark red unit is found in a continuous band from Lunae Planum through Xanthe Terra and into Oxia Palus. The dark red unit does not form aeolian features. Regional scale thermal inertia values for the three units were derived from pre-dawn temperature measurements with ground resolution of about 35 to 45 km. The bright red unit, where thicker than the diurnal skin depth, has low thermal inertias corresponding to dust-sized particles. Thermal inertias for the dark gray unit are relatively high and correspond to sand-sized particles (0.5-1.5 mm). The dark red unit has intermediate thermal inertias.

All three units are exposed in several crater streaks and the in surrounding plains of Oxia Palus. Color images of this region were obtained within a single orbit at six different phase angles between  $1^{\circ}$  and  $20^{\circ}$ . In addition, the same region was imaged with a phase angle of  $48^{\circ}$  on a subsequent orbit. At phase angles less than about  $2^{\circ}$  where the illumination and viewing angles were nearly normal to the surface, the dark red material falls along a color mixing line between bright red and dark gray materials. Typical mixtures are about 77% bright red dust and about 23% dark gray mafic fragments. When the phase angle increases above about  $5^{\circ}$  and the illumination and viewing becomes more oblique, the dark red material moves off the mixing line and towards a shaded surface. Comparison to the Hapke scattering function [5] suggests that the photometric behavior of the dark red unit can be explained as a mixture of the other two units, but having a rougher surface at a sub-pixel scale. This interpretation also explains the contrast reversal between the dark gray and dark red units reported by Thomas and Veverka [6].

The scale of roughness in the dark red unit was estimated from analysis of the color and thermal data. Several reflectance profiles were examined across the boundary between the dark red and bright red units in Oxia Palus. We find that the deviation of the dark red unit from the color mixing line decreases as the boundary of the bright red unit is approached. Close to the boundary the dark red unit can be explained by simple mixing of bright red and dark gray material without roughness. This implies that the roughness elements near the boundary become increasingly buried by bright red material. Several high resolution IRTM tracks (ground spot sizes of less than 20 km) suggest that the bright red dust has no distinct effect on the thermal inertia signature of the dark red unit. That is, the bright red dust cover on the dark red unit is optically thick, but is less than the diurnal skin depth. This constrains the thickness of the bright red dust to be less than a few centimeters since such low thermal inertia dust would dominate the thermal signature if its thickness were more than a few centimeters [7]. Thus, roughness elements in the dark red unit must have heights that are less than several centimeters.

The results of this study suggest the following model for the observed materials. The observed surface units can be explained by a mixture of two materials and variations in surface roughness. The bright red unit consists of deposits of an aeolian suspension load of ferric-rich, palagonite-like weathering products. The dark gray unit consists of immobile mafic materials and deposits of aeolian traction and saltation loads. Since the dark red unit does not form aeolian features, it is probably a cemented mixture of dust and mafic fragments, equivalent to disrupted duricrust at the Mutch Memorial Station. The duricrust at the Mutch Memorial Station contains clods of bright red dust and darker, less red rock fragments, based on the reflectance of soil clods in the Station's X-ray funnel [8]. There is little correlation of surficial units with bedrock geology throughout this equatorial region. The distribution of units is controlled by aeolian processes modulated by regional and local scale topography. The deposits are probably related to obliquity variations and are less than  $10^6$  years in age.

## REFERENCES

- [1] Arvidson, R. E., et al. (1989) *J. Geophys. Res.*, 94, 1573-1587.
- [2] McEwen, A. S., et al. (1988) *GSA Abstracts with Programs*, 20, n.7, A77.
- [3] Regner, P., et al. (1988) *Lunar and Planet. Sci.*, XIX, 968-969.
- [4] Presley, M. and R. Arvidson (1988) *Icarus*, 75, 499-517.
- [5] Hapke, B. (1986) *Icarus*, 67, 264-280.
- [6] Thomas, P. and J. Veverka (1986) *Icarus*, 66, 39-55.
- [7] Jakosky, B. M. (1979) *J. Geophys. Res.*, 84, 8252-8262.
- [8] Dale-Bannister, M. A., et al. (1988) *Lunar and Planet. Sci.*, XIX, 239-240.

An Independent Test of Reflection Theories for Intimate Mixtures through Monte Carlo Computer Simulations. J.W. Boardman (CSES/CIRES and Dept. of Geological Sci., U. of Colorado) and B.M. Jakosky (LASP and Dept. of Geological Sci., U. of Colorado).

Computer simulations that we have done of reflectance of intimate binary mixtures of particles re-create discrepancies between current analytical theories (Hapke, 1981, 1984, 1986; Hapke and Wells, 1981) and reported observations of actual physical mixtures (Mustard and Pieters, 1987). These computer simulations involve a Monte Carlo approach to modeling of directional-hemispherical reflectance from an isotropic half space of randomly packed grains. Twenty-eight different binary mixture models indicate that the abundance weighted average single-scatter albedo can be used as a single parameter to properly characterize the properties of the mixtures for modeling purposes. However, inversion of the resulting hemispherical albedo to obtain mixture component abundances, using the methods described by Johnson and others (1983), gives values differing in a systematic manner from the actual component abundances of the mixture models. These errors, for half spaces whose average single-scatter albedos are less than 0.7, cause an under-prediction of the abundance of the darker component, as is observed in the laboratory experiment. Various assumptions in the formulations of the first-order theories and the inversion scheme could account for this disagreement. The results of this study suggest that the errors observed in the physical mixture observations may be due to inaccurate theoretical assumptions rather than to any physical explanation such as incomplete or non-isotropic mixing geometry.

## SEEING THROUGH THE DUST AND ALTERATION PRODUCTS OF MARS

Carle M. Pieters, Geological Sciences, Brown University, Providence RI 02912

It has been known from all telescopic observations since the late 1960's that the surface of Mars is oxidized and contains iron in the ferric state (1). It is also well known that the surface frequently experiences dust storms (that may become global in nature). The elemental compositions of fine grained soil at the two Viking landing sites are almost identical (2) in spite of the great distance separating the sites. Except for minor scattering effects in the blue, spectral reflectance properties of a dust storm are apparently the same as those for areally extensive high albedo regions on Mars (3), which in turn also exhibit low thermal inertia (4). These characteristics taken together led to the concept of a fine grained "global dust" that has a high albedo and blankets the entire planet to varying degrees. Since remote spectral reflectance observations see only the uppermost millimeter or two of a surface, it has been suggested that visible to near-infrared measurements, intended to measure variations in surface mineralogy, will simply observe more and more dust. Such a suggestion is fundamentally flawed. The purpose of this discussion is to correct this misconception so that a scientifically sound exploration strategy can be developed that includes global assessment of martian surface composition and leads to the return of appropriate martian samples.

• **Mars Surface as a multicomponent mixture: Implications of albedo.** For almost a century, several large-scale (hundreds of km) albedo features (both high and low albedo) on Mars have remained roughly constant, while over the same extended period only approximately 25% of the equatorial region has exhibited significantly variable albedo (5). In spite of the frequent dust storms, most regions on the surface of Mars thus appears to have relatively constant long-term bulk properties indicative of an equilibrium balance between dust cover and surface exposure. As estimated both telescopically (6) and with the Viking IRTM instrument (4), the magnitude of the albedo difference between high and low albedo regions is about a factor of two. The IRTM results in fact show a distinct bi-modal distribution of surface albedo during the Viking.

Strictly speaking, all surfaces are mixtures of several materials and remotely acquired reflectance data are a combination of the reflectance characteristics of each component. If the mixing occurs on the macro-scale (eg. dust vs rock spatial mixtures) the resulting reflectance is a linear mix of the characteristics of each component according to their relative portion in a spatial context (eg. 7). Since the martian dust is relative homogeneous and exhibits a high albedo, in the dust-cover concept for the Martian surface, any variation in observed bulk reflectance properties of the surface would necessarily have to be due primarily to proportion of the surface not covered by dust. Since the general properties of high albedo areas have been shown to be representative of this dust (and are most likely largely dust covered) the extensive areas exhibiting lower albedo (by a factor of two) *must have significant exposure of low albedo materials (rocks, pebbles, or non-dusty soil) and must have less than 50% of their surface spatially covered by dust.* If the spectral reflectance properties of the high albedo dust are accurately obtained, a linear mixing model can easily extract the spectral reflectance properties of the exposed non-dust component from bulk reflectance data.

If mixing occurs at the microscopic scale (an intimate mixture such as occurs for most rock types where neighboring grains are of a different composition), the resulting reflectance is affected by the characteristics of each component in a very non-linear manner (absorbing materials have a larger effect). In this intimate mixture case, separation of individual components and estimating their abundance is achieved using theoretical modeling (8) which has been tested in the laboratory (9). Effects of particle size, microstructure, and viewing geometry are now relatively well understood for reflected radiation, and such modeling produces abundance estimates sufficiently accurate (~5%) for most geological problems. In either the macro- or the micro- scale of mixing, deconvolving the spectrum of a complex mixture into its individual components can be readily achieved when accurate reflectance data are acquired for the surface and possible/probable components of the mixture can be estimated.

• **Alteration of surface material and dust abundance.** Alteration of surface material has occurred on Mars, and various amounts of "global dust" exist almost everywhere on the surface. These are two separate issues and should not be confused. Neither of these complications, however, detract from the expected return from a carefully planned spectroscopic analysis of the martian surface at high spatial resolution.

The alteration processes that transformed martian rocks (presumed mafic) into the obviously ferric-bearing soil are not clearly known. Alteration may be ongoing today and/or occurred extensively early in the history of Mars. Experience with terrestrial materials involved in ongoing weathering effects that cause alteration (to ferric bearing phases and clays) indicates that alteration normally affects the outermost surface (which eventually flakes off and the process starts anew). As shown in the examples of Figures 2 and 3 the spectral character of such alteration is dominated by the ferric phases in the visible, but many/most of the diagnostic absorption bands of the host rock in the near-infrared nevertheless remain readily detectable. In some cases the diagnostic nearIR bands are easier to detect in the altered surface (Figure 3), apparently because the alteration affects the surface structure and allows a deeper penetration of radiation. On the other hand, a process that cause more extensive alteration (metamorphism) generally affects the whole rock and transform original minerals of the material (pyroxene, olivine, etc) into other species which have equally diagnostic absorption bands (amphibole, serpentine, etc.). If this latter form of alteration is more common, such mineral species should also be readily detectable in near-infrared reflectance spectra. Identification of their existence would in fact help identify the major alteration processes affecting the surface of Mars.

The dust storms observed on a global scale indicate that dust must exist in some proportion almost everywhere. The origin of the dust is linked to alteration processes, but because of its long-term mobility (and presumed homogenization), it is unlikely that a single rock type is the source. Even within the poor spatial resolution of earth-based measurements (Figure 1), lower albedo regions exhibit a range of variations beyond 0.8  $\mu\text{m}$  in the nearIR where mafic minerals begin to become

detectable (3,10). From the above albedo discussion concerning mixing, the lower albedo of these martian areas is totally inconsistent with dust dominating the spectrum in the near-infrared. Although dust exists, it is only a component, sometimes a minor one, of martian surface units. The remaining components are likely to be compositionally very heterogeneous and spatially variable and exhibit different degrees of alteration. [Note that we would infer the geology of the Earth and the Moon to be bland if we looked at spectra for these bodies with the terribly low spatial resolution of current earth-based spectra for Mars.]

• **Conclusions** Several direct results of this discussion are relevant to measurement strategy:

1. Alteration and dust deposition are two separate processes affecting the surface of Mars. Alteration is local. Ongoing alteration processes are surficial and often *only affect the visible*, allowing local lithology to be identified in the near-IR. Metamorphic alteration processes (impact, volcanic, etc) can transform, but not destroy, local lithology. Global dust, on the other hand, is likely to have resulted from several processes acting on a variety of lithologies over an extended period of time (ie. it has no singular origin). It is apparently homogeneous and forms a regular pattern of regional deposits resulting in different degrees of surface exposure.
  2. The visible part of the spectrum is strongly affected by both alteration and dust cover, and does not contain adequate information to characterize the composition of local material (other than ferric components). Any spectral variations in the visible can nevertheless be used to map the extent of surface units and help estimate dust cover.
  3. Only about 25% of the martian surface (high albedo) is expected to contain a sufficient thickness of dust cover to make compositional studies of local lithology difficult without data of the highest spatial resolution. Observations of these regions are scientifically very important nevertheless since they provide the best data on the nature (and homogeneity) of global dust.
  4. The remaining regions (intermediate and low albedo) contain varying amounts of dust cover. A typical low albedo area must have more than 50% of its surface exposed without dust cover. Given high quality near-infrared reflectance data (0.8 to  $\sim 4 \mu\text{m}$ ) of such areas and accurate reflectance data characterizing the dust component (# 3 above), mixing models can readily extract the spectral reflectance properties of local materials, the desired first step in deriving compositional information about surface units. Depending on the local geology, these local materials may be pristine or metamorphosed outcrops, lag deposits, non-mobile soil.
- **Summary.** Although Mars presents measurement and analysis challenges, all current information indicates advanced sensors will provide an excellent assessment of the compositional nature and diversity of materials.

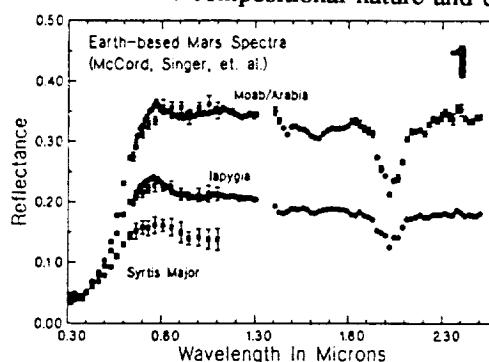
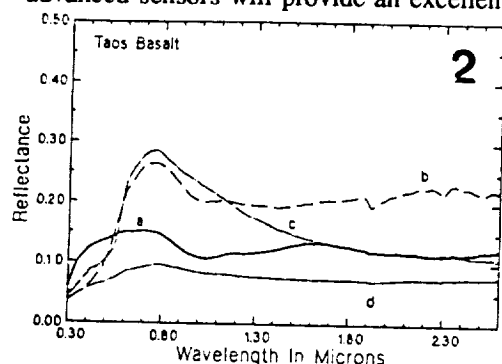


**Figure 1** Earth-based spectra for large Mars regions (3, 6, 10).

**Figure 2** Spectra of Taos Servilleta basalt (BVSP, Ch1). a--fresh surface, b-basalt with natural oxidized coating, c--heavily altered surface, d--massive interior of c.

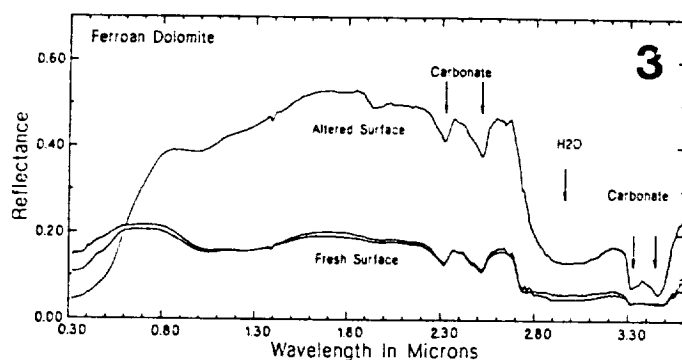


**Figure 3.** Spectra of a dolomite from Kings-Kaweah ophiolite melange (J.F. Mustard, unpublished). A freshly exposed surface exhibits the diagnostic features of carbonate as well as Fe+2 features. The exposed (natural) exterior exhibits ferric alteration in the visible, but the carbonate features of the host rock are readily apparent in the nearIR. The strong carbonate bands between 3.3 and 3.5  $\mu\text{m}$  are more easily detected in the altered surface.

This work results from research under NASA grants NAGW-28 and NAGW-1118. Spectra were obtained using RELAB, a multi-user facility under NAGW-748.

- References** 1. McCord and Adams (1969), *Science* 163, 1058; Adams and McCord (1969) *JGR* 74, 485. 2. Clark B.C. et al. (1982) *JGR* 87, 10059. 3. McCord et al. (1977) *Icarus* 31, 25. 4. Kieffer et al (1977) *JGR* 82, No28, 4249. 5. Pieters (1981) 3d Intern. Coll. on Mars, [abstracts]196. 6. McCord and Westphal (1971) *Astrophys J.* 168, 141. 7. Singer and McCord (1979) *PLPSC10th*, 1835. 8. Hapke (1981) *JGR* 86, 3039. 9. Mustard and Pieters (1987) *PLPSC17th*, *JGR*, 92, B4, E617. 10. Singer R et al. (1979) *JGR* 84, NoB14, 8415.

# DETERMINATION OF REGIONAL SURFICIAL GEOLOGY FOR AEOLIAN TERRAINS UTILIZING A LINEAR MIXING ALGORITHM FOR REMOTE SENSING DATA

G. Blount, R. Greeley, P.R. Christensen, N. Lancaster, J.B. Adams, and M.O. Smith, Dept. of Geology, Arizona State University, Tempe, Arizona, 85287

The objective of this study is to assess techniques for determining the source areas, transport paths and deposition sites of windblown sediments from remote sensing data. A linear mixing model was used to delineate sand populations on a regional basis by mapping minute spectral differences due to sand grain composition, surface coating, and grain size. Extensive field studies were performed to document granulometric variations within and to establish the dynamic state of a terrestrial sand sea, the Gran Desierto of Sonora, Mexico. Ground parameters were then correlated with observed spectral variations on Landsat thematic mapper (TM) data. Sediment source areas, transportation paths and deposition sites were established at >200 regional control points. The 5,700 km<sup>2</sup> study area is bounded by the Colorado River delta on the west; granitic mountain ranges to the north, the Cenozoic Pinacate volcanic shield to the east and the northern shore of the Gulf of California on the south (Lancaster et al., 1987).

Data from three sources (field studies, laboratory analysis of sediments and computer modeling of spectral reflectance) have been correlated to establish the relationships between variations in ground parameters and spectral variations delineated from orbital data. The linear mixing model of Adams et al. (1986) has been used to map the concentration of accessory grains mixed into aeolian sands and to delineate the spatial boundaries of spectrally distinct aeolian bodies. Synthetic fraction-images have been generated and utilized to delineate sand populations of differing ages. As a result of these investigations, a geologic history of sediment emplacement in the Gran Desierto has been proposed (Blount and Lancaster, in press). The study has shown that a majority of the sediments in the sand sea were delivered by fluvial processes and then subjected to aeolian reworking (Lancaster and Blount, 1988).

Thematic Mapper data, although of coarse spectral resolution, delineates distinct sand populations based on variations in grain composition, grain-size and grain surface coating. Spectral end-members such as vegetation, granite, carbonate, basalt lithics/dark minerals, active sand and inactive sand are also mapped on a regional scale as unique units. These modeled fractions have been correlated with point-count data from 188 field samples and found to have an accuracy level of ~93% for high-albedo materials and ~76% for low-albedo materials mixed with aeolian sand (Blount, 1988). Differences between the predicted and observed fractions of accessory grains were linear, and therefore, the fraction-images correctly map grain distribution trends on a regional scale. It was found that monochromatic near infrared data can be employed to discriminate active from inactive sand surfaces. The discrimination capability relates directly to the distribution of low-albedo grains as a function of grain-size in the two surface types. The problems associated with modeling low-albedo end-members, which have also been reported by other workers, can be substantially solved by including a thermal band, such as TM Band 6, in the mixing model, and generating second-order fractions based on differences between the shade end-member and thermal emission. The "shade" end-member, which maps spectrally flat low-albedo ground features, has proved useful as an image enhancement technique by effectively correlating small brightness variations on six of the seven bands simultaneously and leading to the recovery of superposed aeolian bedforms which were previously at the noise level of the TM instrument (Blount and Greeley, 1987). The existence and orientation of newly-resolved bedforms have been confirmed in the field.

Spatial variations in the concentration of an end-member can be used to successfully map the movement of sediments from source units into an aeolian environment without *a priori* knowledge of the geologic units present. End-members may be chosen strictly on the basis of the vertices of a *b*-dimensional mixing volume, where *b* = the number of spectral bands utilized. It was found that the linear mixing approach can be used to predict the fraction of each geologic end-member present in mixed pixels as well as to delineate spectrally distinct sand populations. The accuracy of

quantitative compositional mapping from remote sensing data is controlled by the normal variance of the geologic targets being investigated. Care must thus be exercised so that spectral variations arising from normal compositional, attitudinal and surficial parameters are not interpreted as discrete geologic units. Mapping of transportation pathways and mixing between spectrally different sand populations is possible precisely because of this variance. In general, the mixing approach may actually yield less interpretable results when used with high resolution spectral data. It is therefore imperative that the spectral mixing volume of each discrete unit be fully understood prior to the application of a mixing algorithm to spectral data. The fractional mapping capability demonstrated in this terrestrial study, which arises from small differences in grain mineralogy, grain-size and grain-coating, allowed the discrimination of three sand populations with ages inferred to range from >80,000 years b.p. to Recent. Modern aeolian deposition is inferred for active sand sheets originating from the Colorado River and from neritic sands derived from the adjacent Gulf of California. Local sand sources modify the surficial character of the Gran Desierto, but play a relatively minor role in the volumetric accumulation of sand. Tectonic and climatic processes in the Gran Desierto have combined to create a complex aeolian deposition site in which non-local fluvial and marine sediments overshadow the locally-generated sand supply.

These results have significant implications for determining the geologic history of decoupled surficial materials and establishing the dynamic state and recent geologic history of aeolian terrains on Mars. Data from the anticipated Mars Observer mission, including the Thermal Emission Spectrometer (TES) will allow linear mixing techniques to be applied with a much higher degree of spectral resolution than in the current TM-based terrestrial example. As noted above, however, such increased spectral resolution carries the potential for misinterpretation if the normal spectral variance of the surficial materials being investigated is not taken into account. The ability to determine sand source areas and transportation paths is important for addressing questions about desertification and establishing evidence for changes in climate. The geologic record makes it clear that the Earth has undergone many episodes in which aeolian processes were major factors in shaping the Earth's surface. The mixing approach demonstrated in this study was successful in establishing the relationship between local bedrock geology and pulses of aeolian sediments. The Gran Desierto test site also provided an example of the interplay between long-term tectonic and relatively shorter-term fluvial/aeolian processes in determining the geologic history of a study area. Recent attempts [Adams et al., 1987] to determine the distribution of surficial materials on Mars have generally been hampered by the paucity of spectral data available from the Viking lander and orbiter, respectively, as well as the relatively low spatial resolution of the orbiter cameras. Recent evidence [Arvidson et al., 1987] suggests that many Martian surface materials are uncorrelated with bedrock geology. It is important, therefore, that any attempts to map the spatial distribution of aeolian sediments on Mars take into account the spectral characteristics of both eroding bedrock outcrops, their resulting aeolian products and the mixing of these two with ubiquitous atmospheric dust layers.

#### References Cited:

- Adams, J.B., Smith, M.O. and Johnson, P.E., 1986, *J. Geophys. Res.*, v. 91, 8098-8400.
- Adams, J.B., Smith, M.O., Arvidson, R., Dale-Bannister, M., Guinness, E.A. and Singer, R., 1987, LPI/NASA/MEVTV Study Project, Napa, Ca., p. 1-3.
- Arvidson, R.E., Dale-Bannister, M.A., Guinness, E.A., Adams, J., Smith, M., Christensen, P.R. and Singer, R., 1987, Workshop Proc., LPI/NASA/MEVTV Study Project, Napa, Ca., p. 4.
- Blount, H.G., 1988, unpublished Ph.D. Dissertation, Ariz. State Univ., 227 p.
- Blount, G. and Greeley, R., 1987, *Bull. Amer. Astronomical Soc.*, v. 19, n. 3, 847.
- Blount, G. and Lancaster, N., in press, Development of the Gran Desierto sand sea, in press, *Geology*, 12 p.
- Lancaster, N., Greeley, R. and Christensen, P.R., 1987, *Earth Surf. Processes and Landforms*, v. 12, 277-288.
- Lancaster, N. and Blount, G., 1988, Abs., Symposium on Southwestern Geology and Paleontology - Flagstaff, Az., p. 9.



Thermal Conductivity and Near-Surface Temperature Gradients in Thermal-Infrared Spectroscopy of Planetary Surfaces. B.M. Jakosky (LASP and Dept. of Geological Sci., U. of Colorado, Boulder, CO 80309-0392)

Radiation to space can dramatically modify the temperature gradient within the uppermost tens to hundreds of microns of a regolith when the radiative component of subsurface thermal conductivity is important, as described by Logan and Hunt (1970). On Mars, all three components of conductivity -- radiation, solid, and gaseous conduction -- can play a role under different circumstances. The radiative contribution is generally small compared to the solid component for temperatures less than about 250 K. Both added together are small compared to the gaseous conductivity under most circumstances. Therefore, radiation-induced gradients are not usually important in martian spectroscopy. Near-surface gradients resulting from time variations of the surface and subsurface temperatures are also not generally important on Mars or on other planetary objects, although they can be important in laboratory situations. On outer-solar-system satellite surfaces, temperatures are low enough that the radiative contribution to conductivity will be small, and near-surface gradients are again not expected. On the Moon and Mercury, however, with midday temperatures above 350 K, the radiative component will dominate, and temperatures can vary by over 100 K within the depth range over which the observed infrared energy is generated. Additional laboratory experiments on the thermal conductivity of materials composed of very-fine-grained particles (down to 1  $\mu\text{m}$ ) at a variety of ambient pressures and temperatures are required both to understand the geologic implications of measured diurnal temperature variations of planetary objects and to determine the role of near-surface temperature gradients in mid-infrared spectroscopy.

Thermal models for the distribution of martian permafrost indicate that subsurface water ice could presently be stable throughout the year at depths ranging from 10 to 100 cm at latitudes poleward of  $\pm 40^\circ$  (1). Proof for the existence of such deposits would have important implications for our understanding of the initial volatile inventory, atmospheric evolution, geology, and climate of Mars. The goal of this study is to map the distribution of surface and subsurface permafrost at high latitudes by using Viking IRTM surface temperature observations in conjunction with diurnal and seasonal thermal model calculations.

Solid water ice or hard-frozen ground can be distinguished from fine, unconsolidated surface materials on the basis of thermal inertia. Solid water ice has a thermal inertia of  $I = 50 \times 10^{-3} \text{ cal cm}^{-2} \text{ sec}^{-1/2}$ , whereas mid-latitude martian surface materials have thermal inertias ranging from  $1 \times 10^{-3}$  to  $15 \times 10^{-3} \text{ cal cm}^{-2} \text{ sec}^{-1/2}$  (2). Thermal inertia can be inferred from remote sensing observations because it has a major influence on the amplitudes of diurnal and seasonal surface temperature variations. Since martian diurnal temperature waves penetrate a few centimeters into the surface, and seasonal temperature waves penetrate to at least a meter, surface temperature observations can be used to infer the presence of permafrost.

Very little work has been done to date on the degree to which subsurface thermal structure can influence surface temperature variations for inhomogeneous media. Of particular interest for this study is whether the results of thermal model calculations are unique. The comments we received from the Review Panel on our original proposal suggested that we explore the sensitivity of our results to our assumptions concerning the thermal properties of subsurface soil and ice layers.

We have addressed these concerns by performing thermal model calculations over a wide range of input parameters. Our conclusion is that the results of two layer thermal model calculations are unique, but for the purposes of this study, the primary limitations on our ability to infer subsurface thermal structure will come from the IRTM dataset itself. Figures 1, 2 and 3 illustrate key aspects of the sensitivity of surface temperature variations to subsurface thermal structure. The input parameters for the calculations shown in Fig. 2 were identical to those in Fig. 1, except that the thermal inertia of the lower layer was assumed to be  $20 \times 10^{-3} \text{ cal cm}^{-2} \text{ sec}^{-1/2}$ , which would be appropriate for "loose frozen ground" instead of solid water ice. Assuming a lower inertia for the frozen material decreases the magnitude of the seasonal temperature variations from their expected values. We have found that this same effect can also be produced by increasing the depth to the high inertia layer. The input parameters for the calculations shown in Fig. 3 were identical to those in Fig. 1, except the depth to the high inertia layer was assumed to be 15.5 cm instead of 10.6 cm. Comparing the three figures shows that the effects of decreasing the assumed thermal inertia of the lower layer are very similar to the effects of increasing its depth. Experience with the high latitude IRTM observations shows that they can typically be fit to an accuracy of  $\pm 3\text{K}$  with these types of models. Therefore, it seems unlikely that we will be able to simultaneously define the depths and thermal inertias of subsurface layers with the presently available observations in a unique manner.

As illustrated in the figures, the existence of high inertia subsurface material results in cooler than expected surface temperatures during early summer, and warmer than expected surface temperatures during late summer. It had come to our attention that this behavior could also be produced by the radiative effects of polar water ice or dust clouds. To assess the potential sensitivity of our results to these phenomena, we have added an atmospheric radiative module to our surface thermal model code. The present atmospheric model is a simple one-layer model that includes the effects of scattering, emission and absorption by aerosol particles at solar and infrared wavelengths. It does not include the radiative effects of gases, or vertical heat transfer due to convection. Despite its simplicity, this type model has proven adequate for addressing a wide variety of polar surface heating problems (3).

Examples of combined surface and atmospheric model calculations are shown in Figures 4, where we assume the presence of atmospheric dust with a solar spectrum vertical opacity of  $\tau = 1$ . The results show that the net effects of dust on polar surface temperatures are qualitatively similar to those at lower latitudes (4). Atmospheric dust suppresses the range of diurnal surface temperature variations, but has little effect on seasonal average temperatures. Dust will therefore cause us to overestimate near-surface thermal inertias, but will have no significant impact on our ability to detect subsurface high-inertia material.

The general conclusion that can be drawn from our sensitivity studies is that although dust and water ice clouds can substantially affect polar surface temperatures, their signatures differ substantially from those expected for subsurface ice. Our ability to calculate the effects of atmospheric aerosols will be especially valuable for analyzing the IRTM south polar observations, which are more seriously affected by atmospheric dust.

#### REFERENCES

1. Farmer, C. B. and P. E. Doms, *J. Geophys. Res.* **84**, 2881 (1979).
2. Palluconi, F. D. and H. H. Kieffer, *Icarus* **45**, 415 (1981).
3. Paige, D. A., *Ph.D. Thesis, California Institute of Technology*, (1985).
4. Pollack, J. B. *et al.*, *J. Geophys. Res.* **84**, 2929 (1979).

ORIGINAL SIGNATURE  
OF POOR QUALITY

VARIATIONS IN  $T_s$  AT  $75^\circ\text{N}$  DUE TO A CHANGE OF THERMAL INERTIA AT 10cm

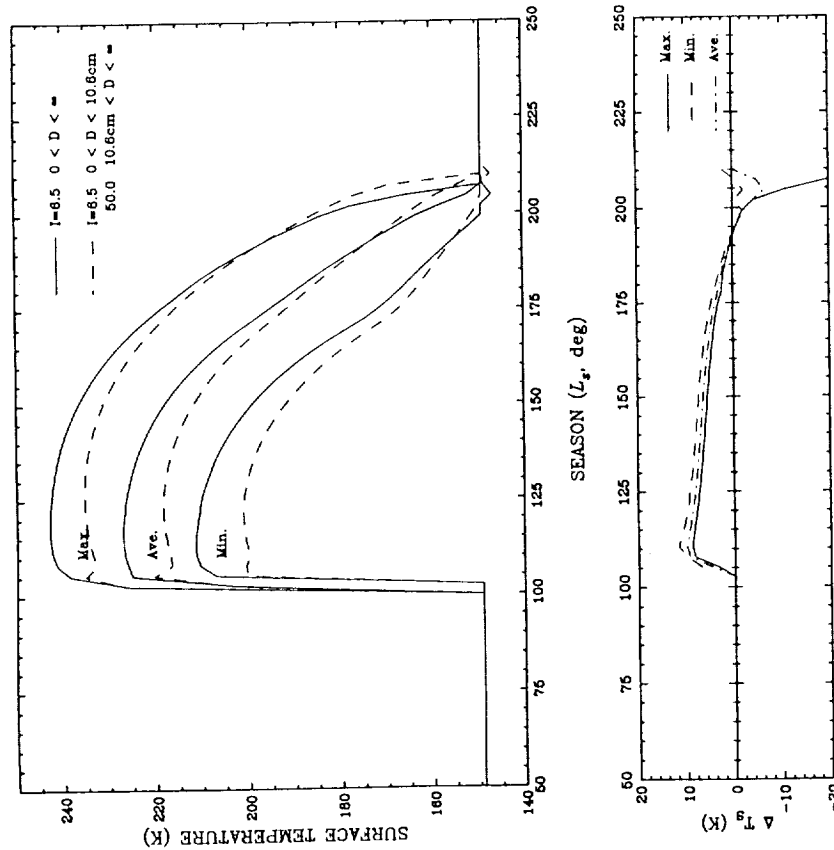


FIGURE 1: Calculated daily minimum, maximum, and average surface temperatures during Martian spring, summer and fall seasons at  $75^\circ\text{latitude}$ . Solid lines show results assuming no sub-surface ice. Dashed lines show results assuming sub-surface ice is present at a depth of 10.6cm below the surface. Lower panel shows the difference between the daily minimum, maximum, and average temperature as a function of season.

VARIATIONS IN  $T_s$  AT  $75^\circ\text{N}$  DUE TO A CHANGE OF THERMAL INERTIA AT 10cm

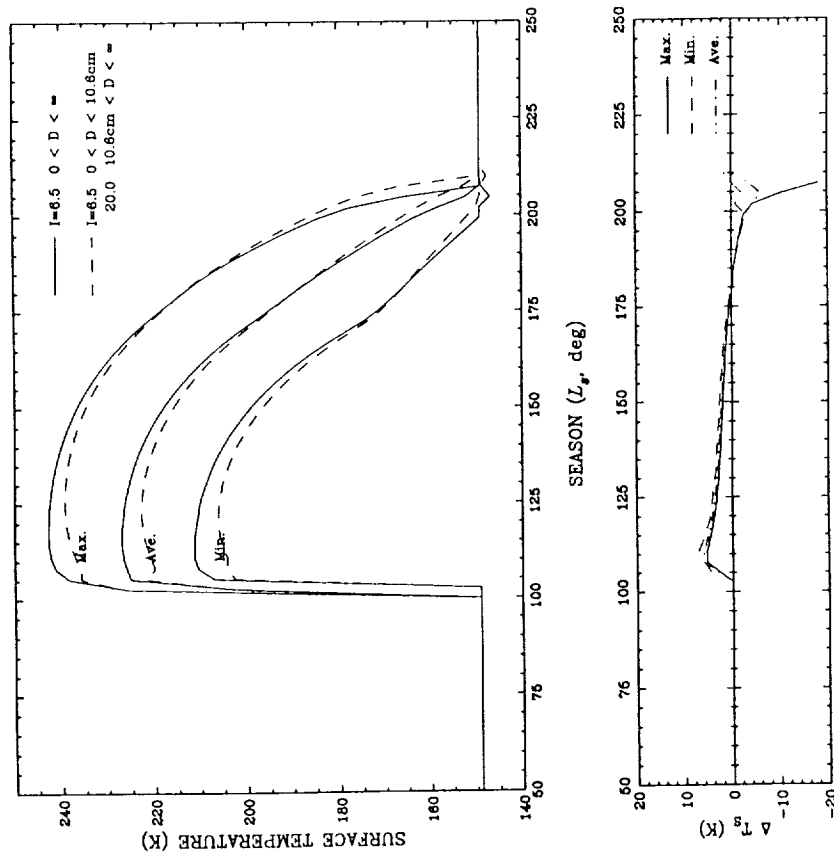


FIGURE 2: Calculated daily minimum, maximum, and average surface temperatures during Martian spring, summer and fall seasons at  $75^\circ\text{latitude}$ . Solid lines show results assuming no sub-surface ice. Dashed lines show results assuming sub-surface frozen soil is present at a depth of 10.6cm below the surface. Lower panel shows the difference between the daily minimum, maximum, and average temperature as a function of season.

VARIATIONS IN  $T_g$  AT  $75^\circ\text{N}$  DUE TO A CHANGE OF THERMAL INERTIA AT 15cm

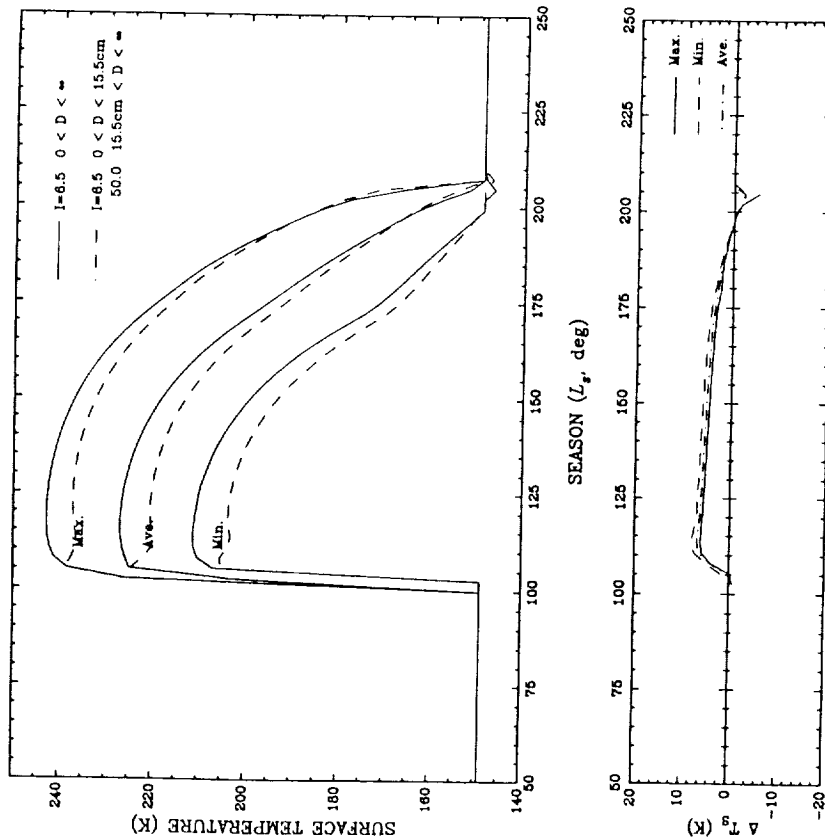


FIGURE 3: Calculated daily minimum, maximum, and average surface temperatures during Martian spring, summer and fall seasons at  $+75^\circ$  latitude. Solid lines show results assuming no sub-surface ice. Dashed lines show results assuming sub-surface ice is present at a depth of 15.5cm below the surface. Lower panel shows the difference between the daily minimum, maximum, and average temperature as a function of season.

VARIATIONS IN  $T_g$  AT  $75^\circ\text{N}$  DUE TO ATMOSPHERIC DUST AS A FUNCTION OF  $L_s$

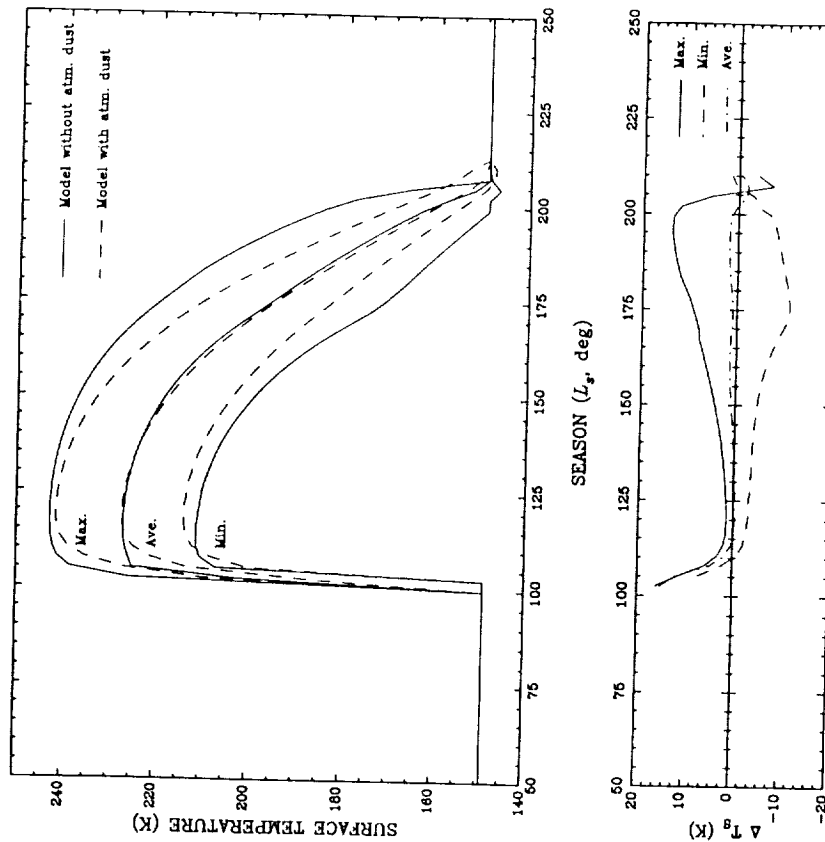


FIGURE 4: Calculated daily minimum, maximum, and average surface temperatures during Martian spring, summer and fall seasons at  $+75^\circ$  latitude. Solid lines show results assuming no sub-surface ice and clear atmospheric conditions. Dashed lines show how these results are altered if the polar atmosphere is assumed to contain substantial atmospheric dust.

## CO<sub>3</sub><sup>2-</sup>- AND SO<sub>4</sub><sup>2-</sup>-BEARING ANIONIC COMPLEXES DETECTED IN MARTIAN ATMOSPHERIC DUST

T. Roush, J. Pollack, C. Stoker, F. Witteborn, J. Bregman, D. Wooden, (Ames Research Center, M/S 245-3, Moffett Field, CA 94035) and D. Rank (Lick Observatory and Board of Studies, U. California Santa Cruz, Santa Cruz, CA 95064)

Seven spectra of Mars, in the 5.4- to 10.5  $\mu\text{m}$  wavelength region were obtained with the Faint Object Grating Spectrometer (FOGS) (1) during a flight of the Kuiper Airborne Observatory (KAO) on October 13, 1988(UT). A grating with a resolving power of 60 was used for these observations and wavelengths were calibrated by comparison with the absorption spectrum of polystyrene measured prior to each set of observations. Two sets of observations were obtained during the flight and each set consisted of 4 to 6 measurements of the individual Mars spots. The observations included some overlap of the regions, due to the relative size of the effective aperture ( $\approx 8.3''$ ) to the angular diameter of Mars ( $\approx 21.75''$ ). Spot locations include extensive coverage of the southern latitudes 35°N – 90°S, and longitudinal coverage of 75°W – 250°W. Mars flux levels were derived using  $\alpha$  Tau as a calibration star. The three representative curves shown in Figure 1 illustrate that the martian spectra exhibit several absorption and emission features. Peaks B and C, located near 7.8 and 9.8  $\mu\text{m}$ , correspond to surface emission by silicates. In order to enhance other features it is necessary to calculate flux ratios of the different spots on Mars. Mars center spot has low martian air mass and high surface temperature whereas, Mars northeast spot has low martian air mass and low surface temperature. Hence a ratio of center to northeast, as shown in Figure 2, will enhance subtle features due to both absorptions by materials suspended in the martian atmosphere and emissions by materials located on the surface. The wavelength positions of these features are listed in Table 1. Emission peak A, centered near 6.1  $\mu\text{m}$ , is due to H<sub>2</sub>O which we attribute to hydrated surface materials on Mars. Absorption bands 2, 3, 5, and 7 can all be explained by the presence of CO<sub>2</sub> gas in the martian atmosphere. This leaves absorption bands 1, 4, and 6 to be explained by other materials.

The central wavelength position of Band 1 is suggestive of the CO<sub>3</sub><sup>2-</sup> anionic complex located in a distorted crystallographic site. In a low symmetry environment a splitting of the  $\nu_3$  asymmetric stretch results in two absorptions located near 6.7- and 7.05  $\mu\text{m}$  (2). Since the 6.7  $\mu\text{m}$  band is obvious in Figure 2, one would expect a contribution due to CO<sub>3</sub><sup>2-</sup> near 7  $\mu\text{m}$ . Models of the martian atmospheric transmission indicate that the CO<sub>2</sub> gas absorption centered near 7.3  $\mu\text{m}$  provides no contribution at wavelengths shorter than 7  $\mu\text{m}$ . The additional absorption between 6.8- and 7  $\mu\text{m}$ , seen in Figure 2, and the wavelength position of Band 1 are both consistent with the suggestion that the CO<sub>3</sub><sup>2-</sup> complex is located in a crystal structure more complicated than calcite. This suggestion is consistent with the infrared spectra of both a variety of carbonates (2) and the recently suggested mineral scapolite (3,4).

The central position of Bands 4 and maybe 6 are suggestive of the SO<sub>4</sub><sup>2-</sup> or HSO<sub>4</sub><sup>-</sup> anionic complexes, which are commonly associated with the sulfates or bisulfates (5). The SO<sub>4</sub><sup>2-</sup>  $\nu_3$  asymmetric stretching fundamental occurs between 8.7- and 9.0  $\mu\text{m}$  depending upon the associated cation. In low symmetry sites the  $\nu_1$  symmetric stretch

becomes infrared active and in some sulfates occurs near  $9.8\mu\text{m}$ . We cautiously assign Band 6 to  $\nu_1$  but note that the central position of Band 6 lies near the strong silicate emission peak and hence is extremely sensitive to the relative contributions of both absorption and emission. Higher spectral resolution than currently used is required to derive specific details regarding both the associated cation or crystal site that the  $\text{SO}_4^{2-}$  complex is located in.

The data presented here indicate the presence of several anionic complexes associated with the solids suspended in the martian atmosphere. Bands associated with  $\text{CO}_3^{2-}$  occur at positions which indicate that complex is located in a distorted crystallographic site. One band, unambiguously associated with either  $\text{SO}_4^{2-}$  or  $\text{HSO}_4^-$ , is identified but conclusions regarding specific composition or mineralogy await higher spectral resolution. The presence of the  $6.1\mu\text{m}$  emission peak, due to  $\text{H}_2\text{O}$ , is indicative of the presence of hydrated materials on the surface of Mars. The identification of these anionic complexes illustrates the utility of obtaining spectral information in the wavelength region where vibrational fundamentals occur. The presence of these anionic complexes and hydrous nature of the surface material provide direct evidence for the occurrence of reservoirs on Mars which can accommodate many of the volatiles thought to have been outgassed during its evolutionary history (6).

**ACKNOWLEDGEMENTS:** These observations were made possible by the cooperation of the KAO technical support staff and flight crew.

**REFERENCES:** (1) Witteborn, F. and J. Bregman (1984) *Proc. SPIE*, **509**, 123. (2) White, W. (1974) in *The Infrared Spectra of Minerals*, V. Farmer, Ed., Mineralogical Soc. London, London, 539pp. (3) Weherenberg, J. (1971) *Am. Mineral.*, **56**, 1639. (4) Clark, R. et al. (1989) *4<sup>th</sup> Inter. Conf. on Mars*, 82. (5) Ross, S. (1974) in *The Infrared Spectra of Minerals*, V. Farmer, Ed., Mineralogical Soc. London, London, 539pp. (6) Pollack et al. (1987) *Icarus*, **71**, 203.

Table 1. Features in KAO Mars Data

Band	Position ( $\mu\text{m}$ )
<i>Absorptions</i>	
1	6.7
2	7.3
3	8.0
4	8.7
5	9.2
6	9.8
7	10.3
<i>Emission Peaks</i>	
A	6.1
B	7.9-8.0
C	9.6-9.8

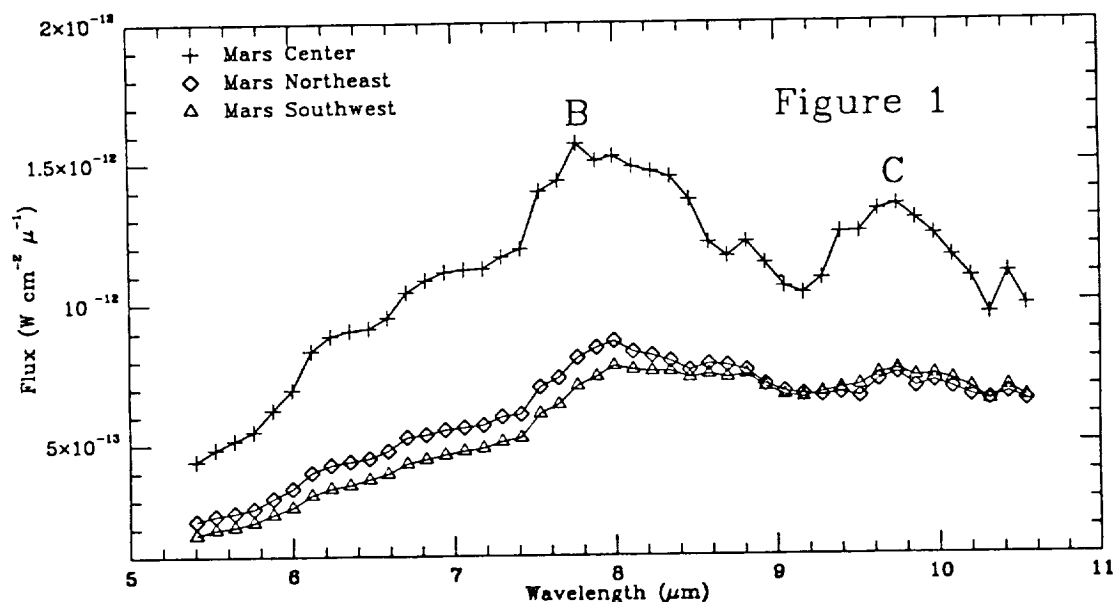


Figure 1. Flux ( $\text{W cm}^{-2} \mu^{-1}$ ) measured from three locations on Mars early in the evening of October 13, 1988(UT). Letters correspond to emission peaks listed in Table 1.

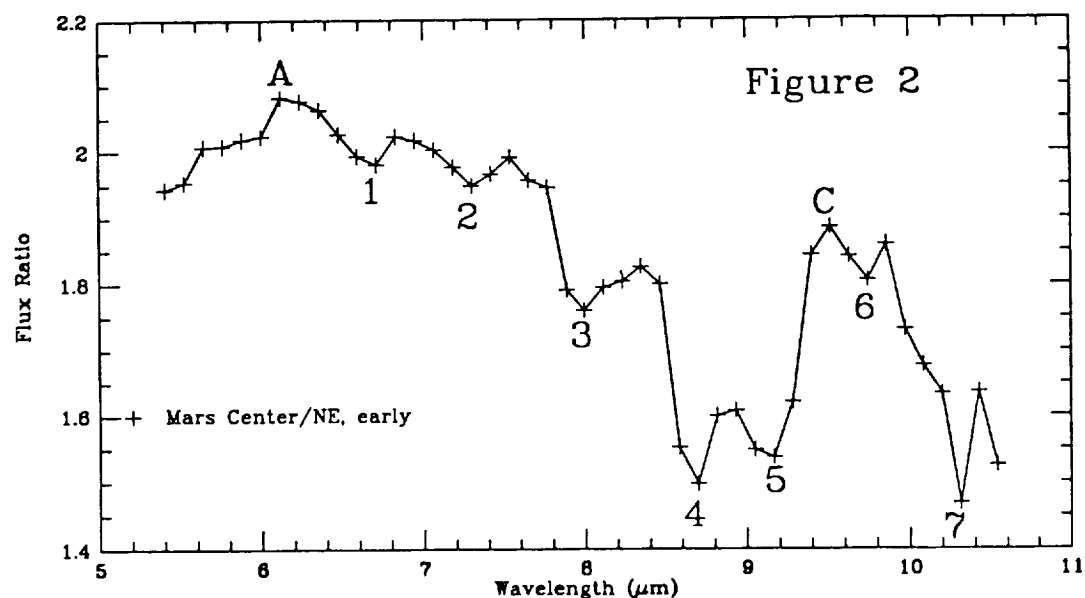


Figure 2. Mars center-to-northeast energy ratio is used to enhance both absorptions due to materials present in the martian atmosphere and emissions due to surface material. Numbers correspond to absorptions, and letters to emissions, listed in Table 1.

## SCAPOLITE ON MARS

Roger N. Clark, (U.S.G.S., Denver), Gregg A. Swayze (U.S.G.S., Denver), Robert B. Singer (U. Arizona, Tucson), and Jim Pollack (NASA Ames).

The mineral scapolite has been discovered in the near-infrared spectrum of Mars based on unique fine structure in an absorption band centered near 2.36- $\mu\text{m}$  that matches the spectrum of scapolite. The scapolite bands are apparent in many of the areas measured, so it appears to be nearly globally distributed, probably in the dust. The details of the newly observed 2.36- $\mu\text{m}$  complex also varies slightly with location on Mars, indicating compositional variation in different regions. These details uniquely identify scapolite, while eliminating many other minerals. The scapolite bands in the martian spectrum are weak, so it is but one component of the surface, with abundances ranging from near zero to as much as about 30 wt% based on calculations using a radiative transfer reflectance intimate mixture model.

The 2.1- to 2.5- $\mu\text{m}$  spectral region is particularly diagnostic for many minerals, including those bearing hydroxyl (e.g. clays), carbonates, and sulfates. The presence or absence of absorption bands in this spectral region is therefore very important for identifying possible martian mineralogy. So far, no absorption bands have been detected in the 2.2- $\mu\text{m}$  region of Mars ruling out the presence of well-crystallized minerals such as montmorillonite and muscovite. The only absorption band in the entire 2.1- to 2.5- $\mu\text{m}$  spectral region other than that caused by martian atmospheric CO and CO<sub>2</sub> is a weak absorption band near 2.36  $\mu\text{m}$ . This band has been known for some time (Singer *et al.*, LPSC XVI, 1985; Martin, BAAS 17, 723, 1985), but the specific mineral responsible could not be identified from the low resolution spectra. The absorption is unusual because it occurs at a longer wavelength than is typical for most minerals, yet the band appears similar at low spectral resolution to those in OH-bearing minerals. Typically, such minerals have bands that occur near 2.2  $\mu\text{m}$  if due to Al-OH (e.g. kaolinite, montmorillonite), near 2.3  $\mu\text{m}$  if due to Mg-OH (e.g. epidote, serpentine) or Fe-OH (e.g. nontronite).

In order to identify minerals with absorption bands that may match the martian band, spectra of hundreds of minerals were examined. The USGS digital spectral database was also queried and only certain members of one mineral group matches the position, width and asymmetry well: mizzonitic scapolite. Although mizzonitic scapolite is the best spectral match to the low resolution martian data, higher spectral resolution was required to unambiguously identify the mineral. The scapolite 2.36- $\mu\text{m}$  band can be resolved into at least 4 main absorptions, and an additional 5 weaker bands at 0.005- $\mu\text{m}$  resolution (Figure 1). The number and relative intensity of the absorptions depends on the scapolite composition.

During the period August 26 to 30, 1988 (UT), we obtained spatially resolved, high resolution spectra of Mars using the Cooled Grating Array Spectrometer (CGAS) instrument on the NASA Infrared Telescope Facility (IRTF). The CGAS spectrometer has 30 good detectors and a grating that gives a spectral resolution of about 0.004  $\mu\text{m}$  was purchased and integrated into the instrument. This grating has enough resolution to resolve the important fine structure in the spectra of all the minerals in the USGS



spectral library.

The observing run occurred during excellent weather and spectra were obtained with a 2.7-arc-second aperture (~850 km diameter spot) for over 30 selected martian areas. A spectral map of the disk was obtained as well, including Syrtis Major, Arabia and Meridiani Sinus. This map is a 16 by 16 pixel grid with 54 wavelengths measured from 2.07 to 2.46  $\mu\text{m}$  for every pixel.

The spectra of Mars from CGAS show the 2.36- $\mu\text{m}$  band and its position, width and depth agree with the earlier low spectral resolution data. However, the CGAS data show that the band has significant fine structure, being composed of 4 to 7 narrow bands as shown in Figure 1.

We conducted a study to determine whether there was any contribution by martian atmospheric bands. Carbon monoxide absorbs in the 2.33- $\mu\text{m}$  region, and synthetic models of the CO spectrum of Mars indicate absorption of about 1% in the 2.31 to 2.34- $\mu\text{m}$  region, only about 0.5% absorption in the 2.34 to 2.39- $\mu\text{m}$  region, and essentially no absorption at other wavelengths observed with the CGAS instrument. The weak CO absorption contrasts to observed absorption at 2.34  $\mu\text{m}$  as high as 3.7%. The weak CO was removed from the Mars data and sample spectra are compared to representative spectra of scapolites in Figure 1.

Terrestrial scapolites cover a complicated compositional range between two theoretical end-members:

marialite  $(\text{Na},\text{K})_4[\text{Al}_3\text{Si}_9\text{O}_{24}](\text{Cl},\text{F},\text{OH})$

and meionite  $\text{Ca}_4[\text{Al}_6\text{Si}_6\text{O}_{24}](\text{CO}_3,\text{SO}_4)$ .

This framework silicate has a structure that consists of four ring-like groups of (Si,Al)-O tetrahedra linked together to form chains parallel to the z-axis. The chains are in turn linked to other tetrahedra-ring chains to form an open framework of cavities, the larger of which are occupied by Na and Ca ions, and the smaller of which are occupied by Cl, F, OH,  $\text{CO}_3$  and  $\text{SO}_4$  ions (Deer, Howie, and Zussman, 1966).

The absorptions in the spectra of scapolite in the 2.3- $\mu\text{m}$  region are due to bicarbonate and bisulfate ions in the scapolite (Swayze *et al.*, 1989, JGR, submitted). The bands near 2.39 and 2.41  $\mu\text{m}$  are due to bisulfate and those near 2.33 and 2.36  $\mu\text{m}$  are due to bicarbonate. Thus, for the two areas shown in Figure 1, the scapolites in Hellas are more sulfate rich than are those in Eden.

Scapolites can store as much as 6 weight percent carbonate or 5 weight percent sulfate (though not as much simultaneously). Thus if there are a few hundred meter thick deposits of scapolite, globally averaged on Mars, it is possible to store bars of carbon dioxide, possibly explaining the residing place of an ancient thick martian atmosphere and the evidence of flowing water on the surface.

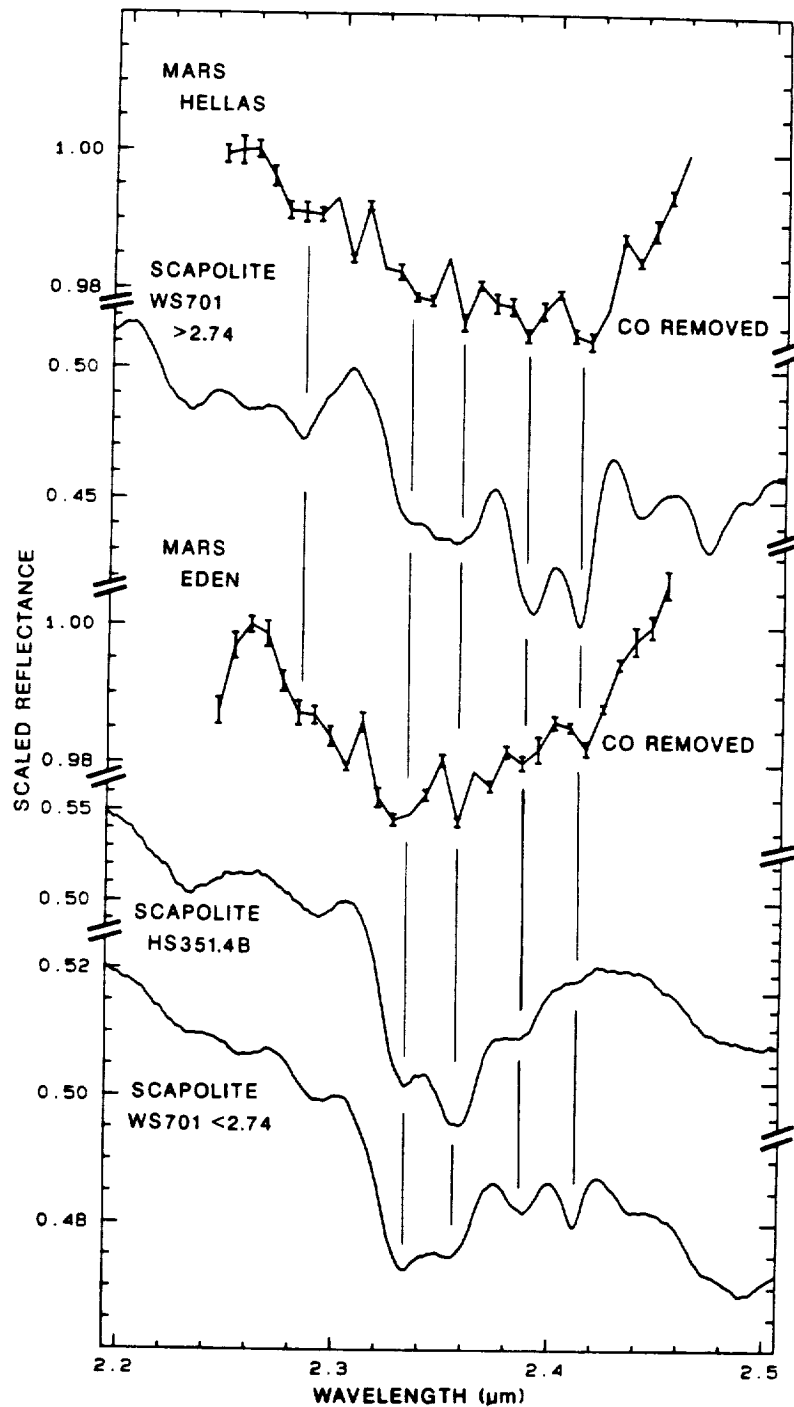


Figure 1. The complicated absorption bands of mizzonitic scapolites are compared to spectra of Mars. The relative band intensities and in some cases the apparent band position vary with scapolite composition. The contribution of atmospheric CO has been removed from the Mars data, but the removal produces small artifacts at 2.31 and 2.35  $\mu\text{m}$  because the wings of the CO band did not match Mars perfectly.

## Mid-Infrared (2.1-25.0 $\mu$ m) Spectroscopic Studies

John W. Salisbury, U.S. Geological Survey, Reston, VA 22092

Mineral Spectra: The first edition of a spectral library for minerals has been completed (Salisbury et al. 1987), and measurements for a second edition are underway. This digital spectral library is unique in that each mineral sample is carefully characterized and the nature and extent of characterization procedures is documented. Also, data are presented in transmittance, as well as in biconical reflectance for different particle size ranges, and are available in digital form from the Principal Investigator.

Of particular interest for remote sensing of planetary surfaces are the spectra of fine particulate materials. These data document the occurrence of two spectral features, transparency peaks and Christiansen frequency minima, that promise to be very important in interpretation of emittance spectra of fine particulate regoliths.

Transparency peaks occur in a region of relatively low absorption between the fundamental Si-O stretching and bending modes. In this wavelength region, fine particles are optically thin and photons undergo volume scattering that results in a reflectance maximum. This spectral feature often is more prominent than the fundamental vibration bands for fine particle size materials.

Another spectral feature that is prominent in spectra of fine particulates occurs at the principal Christiansen frequency. This is a reflectance minimum that occurs because the real part of the refractive index undergoes rapid changes (anomalous dispersion) at a slightly shorter wavelength than the most intense molecular vibration band. Consequently, the refractive index approaches 1, resulting in a minimum of scattering, at a wavelength where absorption is still relatively low. With little scattering and low absorption, infrared radiation can penetrate a sample relatively easily, resulting in a minimum in reflectance or a maximum in emittance.

Both of these spectral features shift wavelength positions in conjunction with the fundamental molecular vibration bands. Thus, they can be used as indirect indicators of mineral or rock composition (Salisbury and Walter, 1989).

Rock Library. A suite of 38 igneous rocks covering the full range of felsic to ultramafic rock types, and including coarse-grained, fine-grained and glassy varieties, has been carefully characterized both mineralogically and chemically. Directional hemispherical spectral reflectance measurements have been made of both solid and finely particulate samples of each rock (Salisbury et al, 1988).

Spectra of solid samples are most applicable to terrestrial remote sensing applications, in which rock outcrops are the principal targets. Although high resolution spectra are required to decipher mineralogy, planned terrestrial remote sensing systems use a broad-band multispectral approach to distinguish different rock types. Consequently, our first use of the

solid sample spectra was to assess the effect of variations in location, number and width of spectral bands in discriminating different rock types. Although the best results are always obtained with the highest resolution, we found that surprisingly accurate spectral identification of fresh igneous rocks can be accomplished with relatively few and relatively wide bands, because the overall envelope of aggregate mineral absorption bands yields diagnostic information on rock type (Walter and Salisbury, 1989). This permits design of multispectral scanners with broad bands and correspondingly higher signal-to-noise, which can be traded off against the important requirement for higher spatial resolution.

Meteorite Library. Bidirectional (actually biconical) spectral measurements of 34 chondrite and achondrite samples have been made. These measurements of powdered samples show systematic variations of Christiansen frequency and transparency peaks with meteorite class. However, as discussed in the next section on instrumentation, biconical measurements cannot be used to quantitatively predict emittance. Yet, most of our meteorite samples are too small to be used in the directional hemispherical reflectance attachment. During the past six months we have documented the spectral effects of viewing geometry and will now be able to publish these data. Early publication is important in view of the Russian intent to fly a thermal infrared spectrometer on the Vesta probe.

A second interesting result from initial studies of meteorite spectra concerns weathering and hydrocarbon contamination. Earlier work showed a correspondence between a "reddness index" and the depth of the water band near  $3\text{ }\mu\text{m}$  in chondrites (Salisbury and Hunt, 1974), which suggested that even fairly carefully preserved "falls" could be affected by limonitic weathering. In the case of the meteorites measured here, chemical analyses by Dr. Eugene Jarosewich of the Smithsonian National Museum of Natural History provided data on total water content of each meteorite. We have found excellent agreement between water content, band depth and reddness index, suggesting limonitic weathering as the source of the  $\text{H}_2\text{O}$  in these analyses. In addition, however, unexpected hydrocarbon bands have been found in spectra of the ordinary chondrites and achondrites, which shows that hydrocarbon contamination has also taken place.

Instrumentation Development. During the past two years we have developed both a directional hemispherical reflectance attachment for the laboratory spectrometer and a field portable spectrometer for measuring spectral emittance directly.

Development of a direction hemispherical reflectance attachment was necessary because all commercially available reflectance attachments are biconical. However, a quantitative prediction of band strength and position by Kirchhoffs' Law ( $E=1-R$ ), requires directional hemispherical reflectance (Nicodemus, 1965). In addition, there are environmental factors that may cause emittance spectra to depart from perfect Kirchhoffian behavior, but those factors can only be evaluated properly with good hemispherical data, as we have done with the effect of a vacuum environment

(Salisbury and Walter, 1989). Thus, the construction and calibration of a hemispherical reflectance attachment has been a significant step in this research program.

Another significant step has been the development under contract (with non-NASA funds) of a field spectrometer. This instrument, now fully tested and calibrated, will make possible direct measurements of spectral emittance to answer crucial questions about the effects of different environmental factors on spectral behavior.

Cooperation With Other Investigators. To date, the laboratory spectrometer has been used to measure the spectral reflectance of various asteroidal and planetary analogue materials in cooperation with Dale Cruikshank (then) of the University of Hawaii and Tom Jones of the Lunar and Planetary Laboratory at the University of Arizona. Early results of Christiansen frequency measurements on spectra of igneous rock powders have been sent to Ann Tyler of the University of Arizona for application to her ground-based measurements of Mercury, and to Paul Lucey of the University of Hawaii for application to his similar lunar measurements. Spectral measurements of shocked minerals and rocks have been made in cooperation with Jim Garvin of Goddard Space Flight Center. Mineral and rock samples have been measured by us in directional hemispherical reflectance and by Gordon Hoover of JPL in emittance to explore the effects of background radiance on apparent spectral emittance. Preliminary findings are that spectral contrast can be reduced by as much as 50% when warm objects are in the target's field of view, even under clear sky conditions.

#### References

- Nicodemus, F.E., 1965, Directional reflectance and emissivity of an opaque surface: *Applied Optics*, v. 4, p. 767-773.
- Salisbury, J.W., and Hunt, G.R., 1974, Meteorite spectra and weathering: *Journal of Geophysical Research*, v. 79, p. 4439-4441.
- Salisbury, J.W., and Walter, L.S., 1989, Thermal infrared (2.5 to 13.5  $\mu\text{m}$ ) spectroscopic remote sensing of igneous rock types on particulate planetary surfaces: *Journal of Geophysical Research* (in press).
- Salisbury, J.W., Walter, L.S., and Vergo, Norma, 1987, Mid-Infrared (2.1-25  $\mu\text{m}$ ) Spectra of Minerals: USGS Open-File Report 87-263, 357 pp.
- Salisbury, J.W., Walter, L.S., and D'Aria, Dena, 1988, Mid-Infrared (2.5-13.5  $\mu\text{m}$ ) Spectra of Igneous Rocks: U.S. Geological Survey Open-File Report 88-686, 136 pp.
- Walter, L.S., and Salisbury, J.W., 1989, Thermal-infrared (8-12  $\mu\text{m}$ ) spectral characterization of igneous rocks: *Journal of Geophysical Research* (in press).

**Introduction** Visible to near-infrared reflectance spectra are an important tool for remote analysis of surface composition in terrestrial and extraterrestrial geologic investigations. Compositional information is derived from the position, shape, and strength of absorption bands caused by electronic processes associated with transition metal ions (i.e.  $\text{Fe}^{2+}$ ) and overtones of fundamental stretching and bending modes in such ions as  $\text{OH}^-$ . Mineral groups displaying solid solution between Fe-rich and Mg-rich endmembers commonly exhibit systematic variations in the position and shape of  $\text{Fe}^{2+}$  absorptions related to the proportion of Fe to Mg in the minerals. Well studied examples include the important mineral groups olivine (1), and pyroxene (2,3). Another group of minerals which exhibit Fe-Mg solid solution, but have not been investigated in detail using reflectance spectra, are the amphiboles. Amphiboles are common terrestrial minerals, present in many different types of geologic terrain, and most commonly form in metamorphic environments where water or equivalent fluorine or chlorine are available. Given the evidence for possible abundant water during the early history of Mars (4) and the long history of volcanism (5), such minerals may also be expected in Martian geologic terrain. Reflectance spectra measured of the calcic amphibole actinolite, shown in Figure 1, exhibit distinct variations in the position of a  $\text{Fe}^{2+}$  absorption feature centered near 1.0  $\mu\text{m}$ . The purpose of this investigation is to examine the relationship of the position of this absorption to chemical composition.

**Sources of Absorptions in Calcic Amphibole Spectra** The spectra of the calcic amphiboles shown in Figure 1 are dominated by an intense band centered near 1  $\mu\text{m}$  and a broad band centered near 2.4  $\mu\text{m}$  which has several narrow sharp absorption bands superimposed on it. Detailed analysis of the 1.0 and 2.4  $\mu\text{m}$  bands by Goldman and Rossman (6,7) indicate that the broad bands arise from d-d orbital transitions of  $\text{Fe}^{2+}$  located in the highly distorted M(4) site. Although  $\text{Ca}^{2+}$  is the principle ion residing in the calcic amphibole M(4) site, it is rare to have a full complement of calcium ions in the structure and  $\text{Fe}^{2+}$  preferentially fills vacancies in the M(4) site over Mg (8). Absorptions associated with  $\text{Fe}^{2+}$  in the M(1), M(2), and M(3) sites occur between 0.8 and 1.2  $\mu\text{m}$ , but are much less distinct because these sites are more symmetric than the M(4) site. The broad band centered near 0.7  $\mu\text{m}$  is due to  $\text{Fe}^{2+}/\text{Fe}^{3+}$  intervalence charge transfer (9). The sharp bands at 1.4  $\mu\text{m}$  and between 2.3 and 2.5  $\mu\text{m}$  are due to vibrational overtones of  $\text{OH}^-$ .

The variations observed in the position of the 1  $\mu\text{m}$  band in the reflectance spectra of actinolite shown in Figure 1 indicates the crystal field stabilization energy (CFSE) of the M(4) site is varying. By analogy with studies of trends in the 1.0 and 2.0  $\mu\text{m}$  bands of pyroxenes (2), it is hypothesized that the position of the 1.0  $\mu\text{m}$  band in actinolite is associated with the proportion of Fe to Mg and Ca in the minerals. This hypothesis is supported by studies of Fe-Mg-Mn amphiboles using optical absorption and Mossbauer spectroscopies. Goldman (10) showed with Mossbauer spectroscopy that the quadrupole splitting (and hence M(4) distortion) was negatively correlated with  $\text{Fe}/(\text{Fe}+\text{Mg})$  ratios while optical absorption measurements by Burns (9) showed that all  $\text{Fe}^{2+}$  absorption bands move to longer wavelengths with increasing Fe, in agreement with the results of Goldman (10).

**Methods and Analyses** All reflectance measurements were made from 0.35 to 2.6  $\mu\text{m}$  with a wavelength sampling resolution of 0.005  $\mu\text{m}$ . Reflectance measurements were obtained using bulk powder for samples 1 and 2 which are relatively homogeneous. Since samples 3-6 are very heterogeneous, we have isolated the reflectance properties of the actinolite in the samples by measuring spectra from actinolite rich zones in thin section using a method which effectively sends the beam diffusely through the sample and corrects for the optical properties of the thin section glass and glue. Variations in thin section sample thickness contribute to the differences in the depths of the 1.0 and 2.4  $\mu\text{m}$  absorption bands for the spectra shown for samples 3-6. Chemical analyses shown in Table 1 were obtained with an electron microprobe.

**Discussion** Variations of the 1.0  $\mu\text{m}$  band minimum relative to the  $\text{Mg}/(\text{Mg}+\text{Fe}+\text{Ca})$  ratio ( $\text{Mg}^*$ ) are shown in Figure 2. If the hypothesis that the ratio of Fe to Mg and Ca controls the CFSE of the M(4) site, and therefore the position of the 1.0  $\mu\text{m}$  band minimum is true, then an inverse relationship between  $\text{Mg}^*$  and band minimum would be expected. Although the data shown in Figure 2 indicate that there might be a weak relationship, it is not a clear trend. This is not an unexpected result since chemical substitution in the tremolite-actinolite mineral series, and in amphiboles in general, occurs for a wide variety of cations. This complexity precludes a simple relationship between absorption band position and  $\text{Mg}^*$ , although more data may clarify the issue. There are, however several important aspects of the calcic amphibole spectra analyzed here relevant to the interpretation of remotely acquired data. The 1.0  $\mu\text{m}$  band in actinolite becomes much less distinct as the  $\text{Mg}^*$  decreases and absorptions due to Fe in the M(1,2,3) sites dominate. Also if there is sufficient Ca or equivalent ion to fill the M(4) site (i.e. 2.0 ions/unit structure), the 1.0 and 2.4  $\mu\text{m}$  bands would be absent from the spectra. Therefore the presence of these absorptions is indicative of a low Fe amphibole with less than 2.0 ions/unit structure. It should be noted that, the shape and position of the 1.0 and 2.4  $\mu\text{m}$  bands in these amphiboles is, to a first order, very similar to  $\text{Fe}^{2+}$  absorptions in high-Ca pyroxenes since the distortion of the amphibole M(4) site is similar to the M(2) site in pyroxenes. However, not only are the amphibole bands more widely separated, but the amphiboles also exhibit diagnostic hydroxyl bands at 1.4 and between 2.3 and 2.5  $\mu\text{m}$ . Given broad spectral coverage at high spectral resolution, high-ca pyroxene should be readily distinguished from calcic amphibole if  $\text{OH}^-$  bands due to other minerals or alteration do not interfere with the exact mineral assignment.

**Acknowledgments** Spectra were obtained with RELAB, a multi-user facility supported by NASA under grant NAGW-748. Thanks to J. Devine for obtaining the microprobe measurements. Research supported by NASA grant NAGW-1118.

**References** (1) Adams, J. B., in *Infrared and Raman Spectroscopy of Lunar and Terrestrial Minerals*, C. Karr ed., 91-116, 1975 (2) Adams, J. *Geophys. Res.* 79, 4829-4836, 1974 (3) Hazen, R. M., P. M. Bell, and H. K. Mao, *Proc. LPSC*, 9th, 2919-2934, 1978. (4) Carr, M. H., *Icarus* 68, 187-216, 1986. (5) Greely, R., and P. Spudis, *Rev. Geophys. Space Phys.* 19, 13-41. (6) Goldman, D. S., and G. R. Rossman, *Am Mineral.* 62, 205-216, 1977 (7) Goldman, D. S., and G. R. Rossman, *Am Mineral.* 67, 340-342, 1982 (8) Hawthorne, F. C., *Rev. Mineral.* 9A, 1-95, 1981. (9) Burns, R. G., *Mineralogic Applications of Crystal Field Theory*, 224 pp. 1970 (10) Goldman, D. S., *Am. Mineral.* 64, 1979

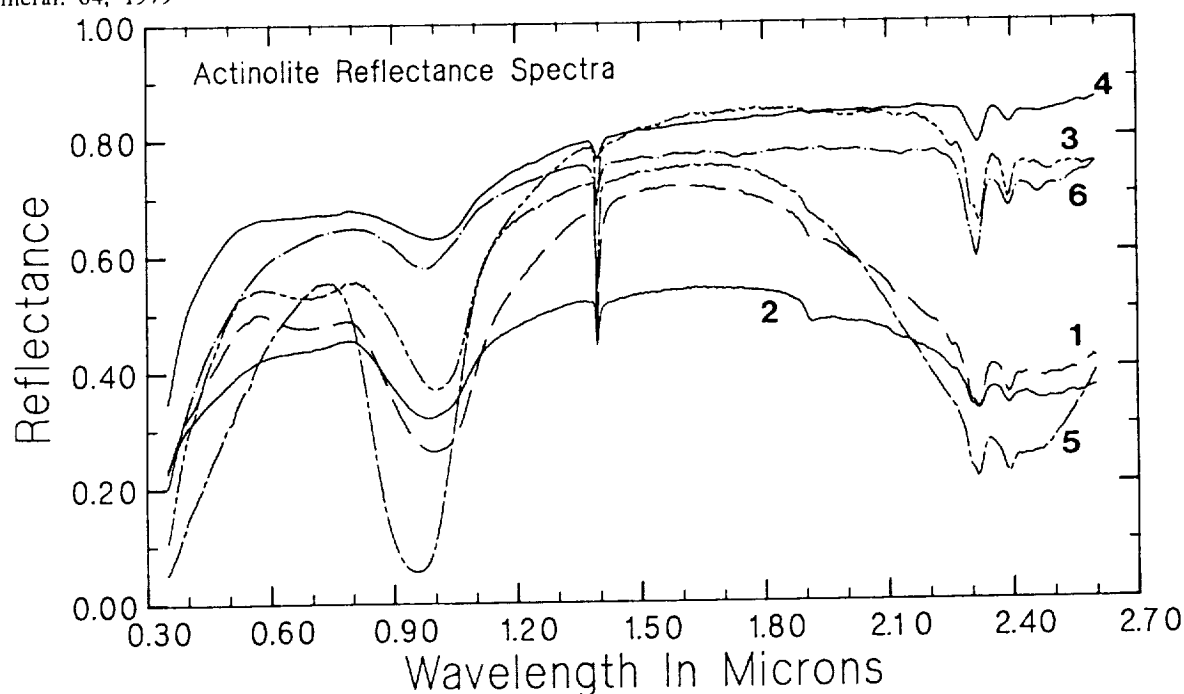


Figure 1. Bidirectional reflectance spectra of actinolite samples. Chemical compositions are given in Table 1 where the number of the spectrum corresponds to the chemical analysis number. Spectra 1 and 2 are from bulk powders while spectra 3-6 are from thin sections using a method described in text.

Table 1. Microprobe Composition of Actinolite

	1	2	3	4	5	6
SiO <sub>2</sub>	56.45	56.54	56.04	55.61	57.05	56.12
Al <sub>2</sub> O <sub>3</sub>	1.50	1.91	1.16	0.40	0.45	0.30
MgO	22.00	22.10	21.10	18.97	22.61	21.78
NaO	0.08	0.37	0.55	0.09	0.07	0.15
TiO	0.02	0.09	0.02	0.02	0.02	0.00
CaO	11.90	12.21	11.97	12.77	11.58	12.26
K <sub>2</sub> O	0.04	0.02	0.04	0.02	0.01	0.02
FeO <sup>†</sup>	5.38	4.83	6.28	8.93	5.55	5.93
MnO	0.29	0.15	0.32	0.14	0.22	0.24
Cr <sub>2</sub> O <sub>3</sub>	0.24	0.06	0.07	0.17	0.03	0.01
Cl	0.00	0.00	0.00	0.01	0.01	0.00
Total	97.91	98.27	97.56	97.11	97.60	96.78

† Total Fe given in FeO

Mg*	0.655	0.658	0.635	0.57	0.664	0.643
Mg* = Mg/(Mg+Fe+Ca)						
1.0 μm minimum	0.995	0.985	1.0	1.01	0.955	0.975

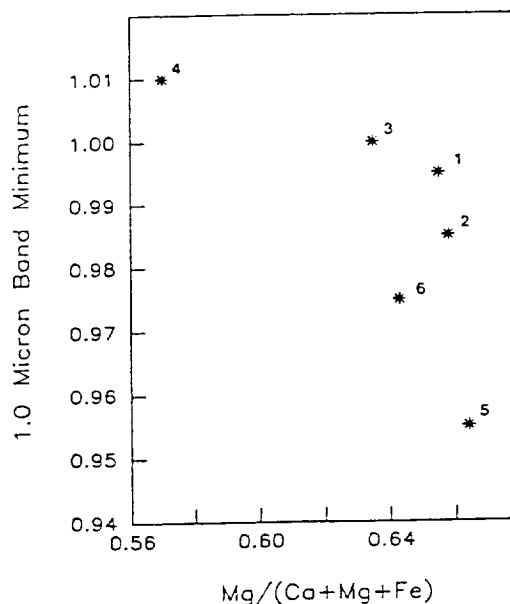


Figure 2. 1.0 μm absorption band minimum as a function of Mg/(Mg+Fe+Ca) ratio. Numbers correspond with numbered spectra shown in Figure 1 and chemical analyses in Table 1

At visible and near-infrared wavelengths, spectra of geologic surfaces contain absorption features that are composed of absorption bands. The strength and energy of these absorption bands are determined by the composition and structure of the absorbing species and thus represent mineralogical signatures. However, spectra from natural surfaces are rarely mono-mineralic and therefore contain combined signatures from the absorption bands of each mineral present. It is a non-trivial problem to deconvolve these composite signals to reveal the mineralogy of the target surface. Currently, most successful approaches require the acquisition of endmember spectra as well as an accurate mixing model [1]. However, the development of a consistent and objective approach to the classification of individual absorption features in spectra would allow for the independent identification and measurement of mineral species. The method pursued here is to represent the underlying absorption bands as discrete mathematical distributions and to then deconvolve the spectra using a least-squares fitting procedure.

**Gaussian Model.** Early work tested the practicality of using Gaussian distributions, as was done by many previous investigators [2-6]. Mathematically, a Gaussian distribution is described in terms of its center energy,  $\mu$ , its half-width,  $\sigma$ , and its strength,  $s$ , as  $g(x) = s \cdot \exp\{-(x-\mu)^2/2\sigma^2\}$ . Although an efficient non-linear least-squares fitting routine was developed [7], the Gaussian analysis proved to be inappropriate for deconvolving pyroxene spectra. It is possible to fit pyroxene spectra using Gaussians; however, the Gaussian distributions neither correlate to known absorption bands nor produce unique solutions. For example, the two well known pyroxene absorption features, at approximately 1.0 and 2.0  $\mu\text{m}$ , each require two Gaussian distributions to produce an acceptable fit (Figure 1a). Yet, each of these features is thought to be dominated by a single absorption band. The more complex olivine spectrum can easily be fit with Gaussian distributions (Figure 1b). However, because its 1.0  $\mu\text{m}$  feature results from three separate absorption bands [8], overlapping distributions are required, allowing for an over-abundance of free parameters. Fitting the olivine absorption feature becomes an over-constrained problem; olivine, therefore does not provide a good test of the model.

**Modified Distribution Model.** Since the Gaussian distribution does not provide an accurate description of the electron transition absorption bands found in pyroxene spectra, additional models have been explored to determine if a mathematical function that models such absorption bands exists. The symmetry of the Gaussian distribution can be modified by changing the exponent of  $(x^n - \mu^n)$ , to create modified distributions of the form  $g(x) = s \cdot \exp\{-(x^n - \mu^n)^2/2\sigma^2\}$ . In order to determine the best value of the exponent  $n$ , the 0.9  $\mu\text{m}$  orthopyroxene feature in both the  $\beta$ -transmission and reflectance spectra was fit. This absorption band was chosen because it is presumed to arise from a single absorption site. Experimenting with several different values of  $n$ , the RMS error of the fit to this pyroxene band was determined using a single modified distribution. As seen in Figures 2a,b, both the transmission and reflectance features appear to be best fit with modified distributions having  $n \approx -1.0$ . Furthermore, the difference between the RMS error of the true minimum value of  $n$  and  $n = -1.0$  is negligible. (It should be noted that the unmodified Gaussian model corresponds to  $n = 1.0$  and that  $n = 0.0$  is a discontinuity corresponding to a straight line.) As seen in Figure 3a, modeling the orthopyroxene spectrum with modified distributions of the form  $g(x) = s \cdot \exp\{-(x^{-1} - \mu^{-1})^2/2\sigma^2\}$  produces an excellent fit to the data and requires only one distribution per absorption band. Not surprisingly, the olivine spectrum is also easily fit with modified distributions (Figure 3b). Yet, as can be seen by comparing the Gaussian and modified deconvolutions of the olivine reflectance spectrum, the two methods are not consistent in their assignment of absorption bands to the 1.0  $\mu\text{m}$  feature. Based on analysis of the features in pyroxene spectra, one must conclude that the results from the modified model are more reasonable.

**Discussion.** The ability of this modified analytical procedure to precisely describe the electron transition absorption bands in pyroxene spectra with a single distribution represents a significant improvement over the Gaussian analysis technique. The extraction of mineralogical information from a spectrum of a mixture is considerably simplified with this approach. We have been able to readily identify pyroxene endmembers by using this technique on pyroxene mixture spectra. Furthermore, since the band center and strength of the absorption band are highly indicative of the nature of the absorption site, it is of the utmost importance that the correct deconvolution technique be used to determine the nature of absorption in crystals. We recommend that the modified distribution model described here be the analytical method of choice to characterize electron transition bands.

**Acknowledgements.** We wish to thank George Rossman for generously providing the pyroxene transmission spectra. All reflectance spectra were obtained using RELAB, a multi-user facility supported by NASA grant NAGW-748. The financial support for this research, NASA grant NAGW-28, is also greatly appreciated.

**References.** [1] Mustard, J.F. and Pieters C.M. (1987), *J.G.R.*, **92**, pp. E617-E626. [2] Farr, T.G. *et al.* (1980), *Proc. LPSC 11th*, pp. 719-729. [3] McCord, T.B. *et al.* (1981), *J.G.R.*, **86**, pp. 10833-10892. [4] Clark, R.N. (1981), *J.G.R.*, **86**, pp. 3087-3096. [5] Roush, T.L. and Singer, R.B. (1986), *J.G.R.*, **91**, pp. 10301-10308. [6] Gaffey, S.J. (1986), *Amer. Min.*, **71**, pp. 151-162. [7] Sunshine, J.M. *et al.* (1988), *LPSC 19th* (abstr.), pp. 1151-1152. [8] Burns, R.G. (1970), *Amer. Min.*, **55**, pp. 1608-1632.



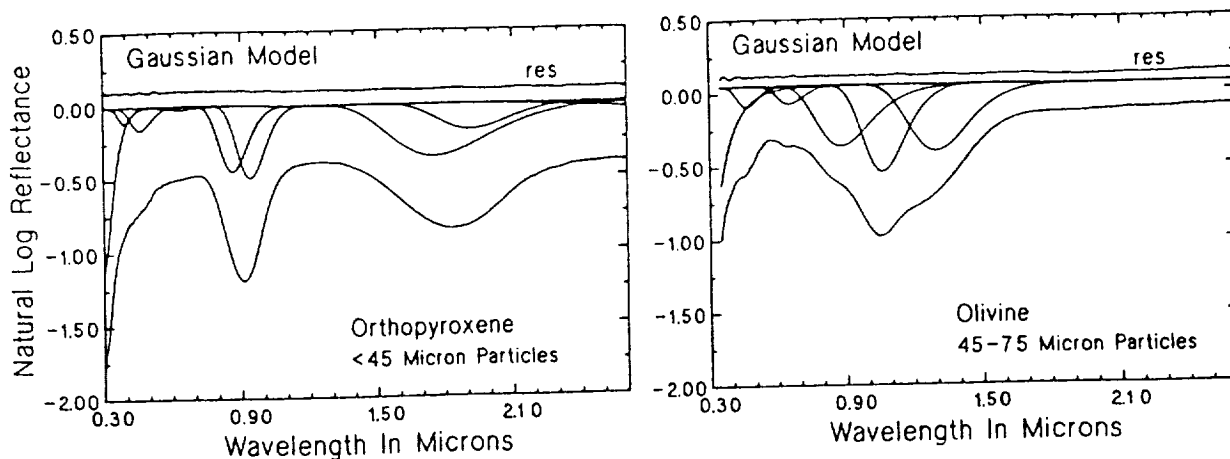


Figure 1. Bidirectional reflectance spectrum of (a) Websterite orthopyroxene and (b) olivine. (Bottom to top). The spectra, the individual Gaussian distributions that comprise the fits and the residual error of these fits (offset 10% for clarity).

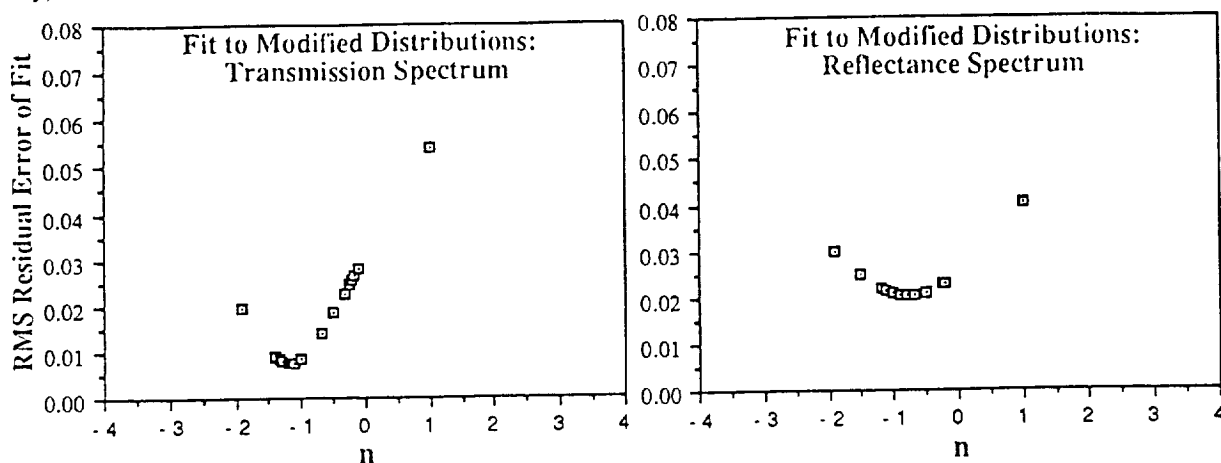


Figure 2. RMS residual error in the fit of modified distributions to the  $0.9\ \mu\text{m}$  absorption bands in orthopyroxene spectra. (a)  $\beta$ -transmission spectrum of Bamble enstatite and (b) reflectance spectrum of Websterite.  $n \approx -1.0$  appears to produce the best fit.

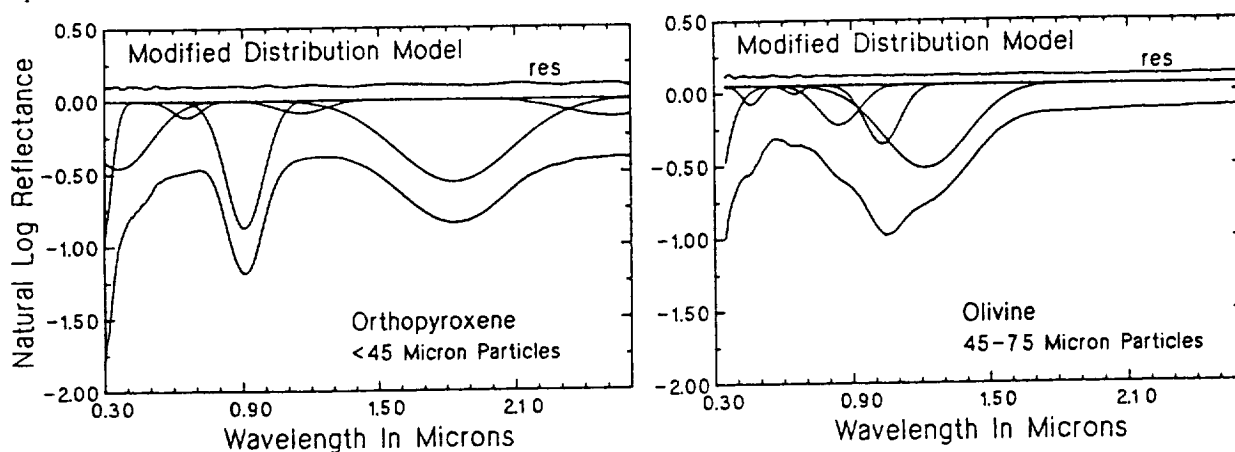


Figure 3. Bidirectional reflectance spectrum of (a) Websterite orthopyroxene and (b) olivine. (Bottom to top). The spectra, the individual modified distributions that comprise the fits and the residual error of these fits (offset 10% for clarity).

THE Fe-Al RELATION OF LUNAR SOILS AND ORBITAL CHEMICAL DATA:  
IMPLICATIONS FOR Al ABUNDANCES ESTIMATED FROM APOLLO ORBITAL GAMMA-RAY DATA.  
P.D. Spudis, P.A. Davis, and B. Pattanabornwornsak\*, U.S. Geological Survey,  
Flagstaff, AZ 86001. \*NASA PGGURP Summer Intern.

Several studies have noted that there is an almost perfect, linear inverse correlation between the Al and Fe concentrations in lunar samples [1,2]. This relation has been informally used by workers attempting to estimate regional Al concentrations from orbital gamma-ray Fe data for areas of the Moon where no X-ray Al coverage exists [e.g., 3]. In this study, we systematically examine both lunar samples and orbital data (where X-ray and gamma-ray coverage overlap) to quantitatively evaluate the Fe-Al relation and apply these results to the complete Apollo Fe gamma-ray dataset. Our aims are both to produce a "synthetic" Al concentration map of the lunar surface from the gamma-ray Fe data and to refine the estimate of global crustal Al abundance as a possible test of crustal origin mechanisms [e.g., 4].

The Fe-Al relation of lunar samples. Because the orbital sensors flown on the Apollo 15 and 16 spacecraft analyzed regolith, we have restricted our sample dataset to lunar soils (all published data, partly summarized in [5]) and two lunar meteorites ALHA 81005 and Y 791197 (both regolith breccias, included because they appear to represent portions of the Moon chemically different from the Apollo and Luna sites [6]). The Fe-Al relation for lunar soils is shown in Fig. 1; the near-perfect inverse relation is readily apparent. A linear least-squares fit to the data of Fig. 1 gives the following result:

$$\text{Al (wt.\%)} = -0.850 \text{ Fe (wt.\%)} + 17.4$$
$$r^2 = 0.960$$

Transformation of the data into semi-log space only slightly improves the correlation ( $r^2 = 0.979$ ) and for this effort, we prefer to use a simple linear fit. This result may be compared with the previous result of [2], where  $\text{Al} = -0.746 \text{ Fe} + 16.0$ ; that study not only was based primarily on rock data ( $n=69$  for regression analysis), but it also deliberately excluded Apollo 16 samples that fell well above the regression line [2]. Our analysis is restricted to materials representative of those analyzed from orbit, includes a larger database ( $n=148$ ), and the regression line is derived from all samples analyzed to date.

Fe-Al relation for orbital X-ray and gamma-ray data. We have analyzed the available Apollo orbital chemical data [7] to determine the Fe-Al relation. This analysis is based on the 9% of the lunar surface covered by both X-ray (Al/Si ratio) and gamma-ray (Fe) data. The Al/Si image was first filtered to an effective surface resolution of about 100 km, comparable to the Fe data. We converted the Al/Si data into Al concentrations by assuming a constant Si value of 21 wt.% [8] (the average Si content of lunar soils (mean  $\pm$  one sigma) in our database is  $21.052 \pm 1.008$  wt.%). Each pixel value in the resulting Al (from X-ray) and Fe (from gamma-ray) images are plotted in Fig. 2. The inverse correlation appears to be not as "clean" as that for the sample data; however, the broad trend mimics a linear inverse correlation. The best-fit line for these data is as follows:

$$\text{Al (wt.\%)} = -0.711 \text{ Fe (wt.\%)} + 15.7$$
$$r^2 = 0.555$$

Numerous subrends are evident in this plot (Fig. 2), similar to those found in our previous efforts to produce petrologic maps of the Moon [9,10]; we believe this reflects at least in part the presence of unsampled lunar compositions that contribute to mixing relations on the lunar surface. We applied the best-fit lines derived from both sample and orbital data analysis

to make synthetic maps of Al concentrations for areas of the Moon represented by the Apollo gamma-ray groundtracks. These results were then compared with the original Al X-ray map both to estimate the magnitude of errors and to determine where the best-fit relations do not hold up.

Al concentrations estimated from Apollo orbital Fe data. Using the best-fit line determined from sample data, the range of Al concentrations on the Moon is 4.7 to 17.3 wt.% with a global mean of  $12.1 \pm 2.6$  wt.%. Comparable results using the best-fit equation from the orbital data are a range of 5.1 to 15.6 wt.% and a global mean of  $11.3 \pm 2.2$  wt.%. Comparison of the two synthetic Al maps with the X-ray Al map of the eastern limb area shows that mare regions display the least difference between the two datasets (values agree within 2 wt.%); greatest differences occur in some highlands regions, particularly the areas around the Crisium and Smythii basin rims. We attribute this effect as largely reflecting the fact that errors associated with the orbital Fe data are lowest where Fe concentrations are highest; thus, in the synthetic Al map, values are most accurate in the maria and less so in highlands regions. We have used these synthetic Al maps to estimate the average Al concentration of only highlands areas; results indicate average Al values of  $12.3 \pm 1.6$  wt.% (determined from orbital data) to  $13.3 \pm 1.9$  wt.% (determined from the sample best-fit). Our previous estimate of Al in the highlands [4], based on petrologic mapping from orbital chemical data [9,10], is  $14.3 \pm 1.0$  wt.%. As previously discussed [4], we believe these values suggest that the lunar crust is too aluminous to have originated purely by a "serial magmatism" mechanism [e.g., 11] and they tend to support models calling for global plagioclase fractionation early in lunar history (recently summarized in [12]).

References. [1] Janghorbani, M., et al. (1973) PLSC 4, 1115. [2] Miller, M., et al. (1974) PLSC 5, 1079. [3] Spudis, P. et al. (1984) PLPSC 15, JGR 89, C197. [4] Spudis, P. and Davis, P. (1986) PLPSC 17, JGR 91, E84. [5] Morris, R. et al. (1983) NASA JSC 19069. [6] GRL Special issue (1983) 10, 773. [7] La Jolla Consortium (1977) PLSC 8, frontispiece. [8] Bielefeld, M. (1977) PLSC 8, 1131. [9] Davis, P. and Spudis P. (1985) PLPSC 15, JGR 90, D61. [10] Davis P. and Spudis, P. (1987) PLPSC 17, JGR 92, E387. [11] Walker, D. (1983) PLPSC 14, JGR 88, B17. [12] Warren P. (1985) Ann. Rev. Earth Planet. Sci. 13, 201.

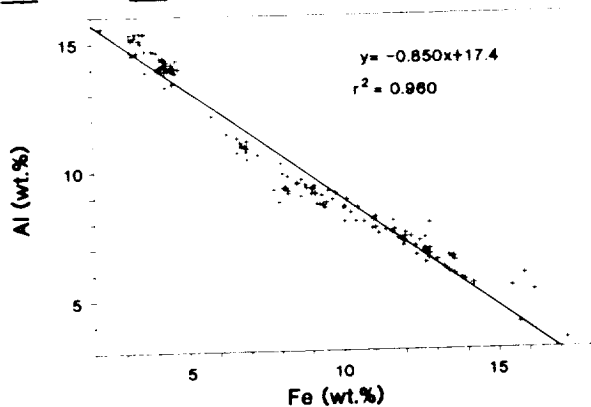


Figure 1. Fe-Al relation of lunar soils. Results of regression analysis shown. Source: all published chemical data.

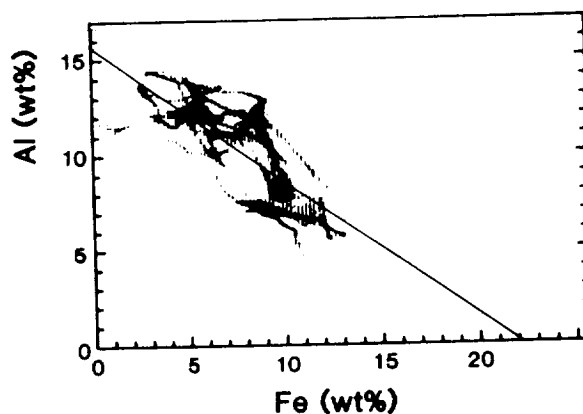


Figure 2. Pixel plot (1/4 degree) of orbital X-ray (Al) and gamma-ray (Fe) data on the lunar eastern limb. Results of regression analysis shown.

COMPOSITIONAL STRATIGRAPHY OF THE LUNAR HIGHLAND CRUST Carle  
M. Pieters, Dept. Geological Sciences, Brown University, Providence, RI 02912

The global properties of the Moon are still a mystery. This is particularly true concerning the composition of the crust - in both horizontal and vertical dimensions. Nevertheless, fundamental questions about the early evolution of the Moon depend of an accurate assessment of both the bulk composition as well as the abundance and spatial distribution of evolved materials. In order to propose answers to such first order questions, lunar scientists have had to extrapolate using the detailed compositional data on samples collected from only a few localized geologic terrains and on limited low resolution geochemical data (10-20% of the surface) obtained from orbit during Apollo 15 and 16. To discuss the origin and evolution of the Moon necessarily requires the assumption that the Apollo and Luna sample and orbital data provide sufficient and representative information to model the extensive unexplored regions. This is a potential fatal flaw in our understanding of the Moon.

Analyses of "pristine" lunar sample fragments have blossomed during the last decade and have presented the first serious challenge to the early concept of a singular global differentiation event responsible for highland crustal stratigraphy (1,2,3,4). Although spatial information about the source region of these valuable samples has been lost during the subsequent impact record (that also brought them to the sampling site), the growing geochemical statistics argue strongly for extensive plutonic activity (of varying compositions) throughout crustal formation. The Moon, of course, is no longer pristine. The highland surface, even if sampled extensively, consists of materials brecciated and mixed to some degree by more than 4 billion years of impact activity of all scales (5).

The spectral reflectance data summarized here are meant to remind lunar scientists that the Apollo and Luna data are very biased and should never be assumed to be representative. [In a more positive tone, we are now exceptionally well prepared to return to the job twenty years after Apollo.] The basic mineralogy of lunar material is relatively simple with most lunar rock types composed of different proportions of anhydrous plagioclase, low-Ca pyroxene, high-Ca pyroxene, olivine, and FeTi opaques. The radiogenic and the rare earth elements are additional important discriminants as well as unusual (?) species of other minerals concentrated and/or separated during differentiation events. In spite of the fact that most highland samples are breccias, the primary mineralogy can be determined using near-infrared spectral reflectance measurements (6,7,8). Reflectance spectra of lunar mineral, rock, and soil samples are shown in Figures 1 and 2. Diagnostic spectral features of mafic minerals near 1  $\mu$ m dominate the spectral character of lunar materials. Although significantly subdued, the weak absorption bands observed for mature lunar soils also exhibit features diagnostic of their bulk mineralogy.

Examples of near-infrared spectra of material exposed by large impact craters 50 -120 km in diameter are shown in Figures 3 and 4. The ejecta and central peaks of such craters probe the stratigraphy of the crust to depths near 15 km (eg. 7). The strength and nature of diagnostic features evident in these spectra demonstrate the compositional diversity of such deep-seated materials: the central peak of Petavius is a mountain of anorthosite (< 5% mafics); that of Arzachel is noritic anorthosite (plagioclase + minor lo-Ca pyroxene); of Copernicus is troctolite (ol + plag); of Tycho is gabbro (high-Ca pyroxene + plag); of Bullialdus is norite (plag + lo-Ca pyroxene). The spatial distribution of material excavated by such large craters provides information about the compositional diversity of the crust with depth. Several craters have been studied extensively: Aristarchus (9), Copernicus (10), Tycho (11), and more recently Bullialdus and Langrenus. The mafic mineral composition of crustal stratigraphy tapped by all near-side craters measured to date is summarized in Figure 5 and the accompanying table (band strength is related to mafic mineral abundance (eg. 8)). At Bullialdus an unusual three unit stratigraphy has been recognized for the first time from a concentric pattern of two distinct gabbroic components exposed throughout the rim and the wall (12).

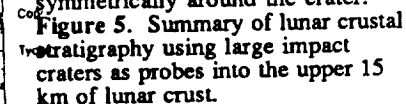
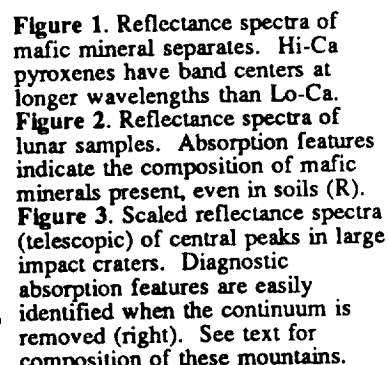
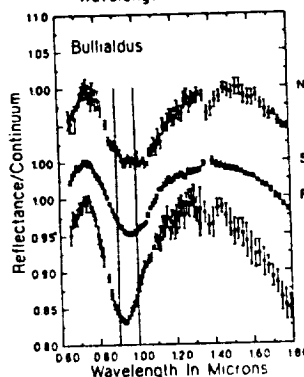
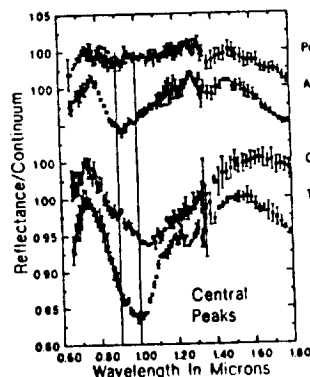
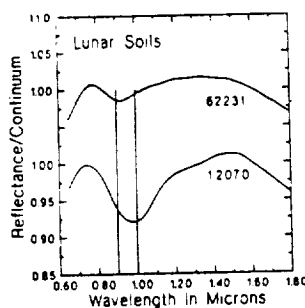
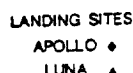
**Observations and Conclusions.** The range of geochemical data for the *eastern* highland crust (sample analyses as well as remote measurements of elemental and mineral composition) consistently describe the highland crust as very feldspathic with low-Ca pyroxene being the most common mafic mineral. These internally consistent data for the eastern crust are thus normally used as constraints for crustal evolution. The preponderance of gabbroic lithologies in the western hemisphere noted above (7,13), however, is in stark contrast to these traditional observations. Recognition first of the gabbro-norite subdivision of pristine samples (14) then of the additional range of pristine compositions sampled at Apollo 14, which clearly distinguish them from the eastern groups (15), add to the growing evidence indicating the evolution of the western nearside crust *must have been distinctly different* from that of the relatively well-studied east. Although we are all still perhaps like the blind men studying the elephant, it is reassuring that the remote observations and sample analyses seem to eventually converge, albeit with increasing complexity. A new era of detailed exploration of the Moon will inevitably provide the planetary science community a wealth of answers, questions, and important surprises about the Earth's nearest neighbor. We may learn that the largest (Procellarum) or the most recent (Orientale) basin forming event (5) dominates lunar evolution well beyond expectations. During the next decade it is anticipated advanced remote sensors will give us the first fully global assessment of this beloved ancient beast and should thus bring lunar science from uncertain adolescence to the first stages of mature activity.

Anorthosite 

Norite 

Gabbro 

Troctolite 



References: 1. P. H. Warren and Wasson (1977) *PLPSC* 8th, 2215. 2. O. B. James (1980) *PLPSC* 11th, 365. 3. ----- (1982) in *Pristine High. Rocks*, LPI-TR 83-02, 44. 4. Warren (1985) *Ann. Rev. Earth Planet Sci.*, 13, 201. 5. D. E. Wilhelms (1987) *USGS-PP* #1348. 6. McCord et al (1981) *JGR* 86 (B11) 10833. 7. Pieters (1986) *Rev. Geophys. Res.* 24 No3, 557. 8. Pieters and Taylor (1989) *PLPSC* 19th. 9. Lucey et al (1986) *PLPSC* 16, D344. 10. Pieters et al. (1985) *JGR* 90, 12393. 11. Hawke et al. (1986) *LPS XVII*, 999. 12. Pieters (1988) *BAAAS* V20, N3, 809. 13. Lucey and Hawke (1988) *PLPSC* 18th 355. 14. James and Floh (1983) *PLPSC* 13th, A603. 15 J.W. Shervais (1988) in *Moon in Transition*, LPI, 82.

## **RESULTS OF A REMOTE SENSING ANALYSIS OF THE ALPHONSUS CRATER REGION**

Cassandra R. Coombs, SN 15 Johnson Space Center, Houston, TX, 77058; Bernard Ray Hawke, Paul G. Lucey, Planetary Geosciences Division, Hawaii Institute of Geophysics, Honolulu, HI 96822; and James W. Head, Dept. Geological Sciences, Brown University, Providence, RI, 02912

### **INTRODUCTION**

Alphonsus crater, located on the central lunar nearside (13°S, 4°W), has long been a center of interest and controversy among lunar scientists. This pre-Imbrian crater is 118 km in diameter. The fractured floor of Alphonsus contains eleven dark-halo craters that are interpreted to be of endogenic origin.<sup>1,2,3,4,5,6,7,8,9,10,11</sup> To date, most studies associated with Alphonsus have centered around the nature of these dark halo deposits. There are however, several other unresolved problems associated with Alphonsus. These include: (1) the nature and origin of the light plains on the crater floor, (2) the composition of the localized dark mantle deposits associated with the endogenic craters on the crater floor, (3) the origin of the N-S trending ridge on the crater floor, (4) the processes responsible for the crater floor uplift, and (5) the effects of Imbrium ejecta on Alphonsus.

In an attempt to address the above questions, we have conducted a variety of remote sensing and geologic investigations of the region. This paper is a discussion of the preliminary results of this effort.

### **METHOD**

A variety of spacecraft and earth-based photography as well as topographic data was used to conduct the geologic studies of the region. Also, near-infrared reflectance spectra (0.6-2.5  $\mu\text{m}$ ) of a number of geologic units within Alphonsus crater were collected and examined. The geologic features from which spectra were collected include: (1) the central peak, (2) the light plains mantling the floor, (3) the very fresh small impact crater on the floor, and (4) three localized pyroclastic units surrounding the endogenic craters. Additional spectra in the 0.3 - 1.1  $\mu\text{m}$  region have recently been collected for many features in and around Alphonsus. These spectra are currently being reduced and analyzed. In addition, 3.8 cm radar data, collected by Zisk,<sup>12</sup> was also analyzed during the course of this study.

### **RESULTS AND DISCUSSION**

Alphonsus crater, located just east of Mare Nubium in the western portion of the central lunar highlands, has undergone a fairly complex history of formation. The slightly elongate main crater is pre-Imbrian in age, or greater than 3.85 b.y. old, and contains a central peak. The Imbrium basin impact appears to have had an effect on Alphonsus as

evidenced by the presence of Imbrium sculpture on the main crater rim. The Imbrium event may also have been responsible for the emplacement of the smooth plains deposits on the floor of Alphonsus.

After the Imbrium event, the 97-km-diameter crater Arzachel formed south of Alphonsus. Associated with the formation of this crater was the deposition of an ejecta blanket on the southern portion of the Alphonsus floor. Tectonic reshuffling then occurred to form the numerous linear rilles, or graben, that are located about the perimeter of the Alphonsus crater floor. Eleven previously identified endogenic dark-halo craters within the crater are associated with these linear rilles.<sup>2,9,10,13</sup> Studies by Head and Wilson<sup>9,10</sup> and Hawke et al.<sup>13</sup> have suggested that these deposits are basaltic in composition and most likely were emplaced as a result of individual vulcanian-type eruptions that occurred along the floor-fractures. In these types of eruptions gas is trapped beneath a cap-rock or plug-rock at the mouth of the magma conduit. Once sufficient pressure has built up, explosive decompression occurs and pyroclastic material is deposited about the mouth of the vent. Generally, these vulcanian-type eruptions produce small pyroclastic mantling deposits, that is, the material remains within a few kilometers of the vent, unlike the larger regional pyroclastic deposits. These larger deposits formed as a result of strombolian-type eruptions that deposited material over thousands of square kilometers. During the course of this research, a small dark-haloed impact crater was identified in the southern portion of Alphonsus crater floor, bringing the total number of Alphonsus dark-haloed craters now known to 12. Multispectral images (0.40/0.56  $\mu\text{m}$ , 0.56  $\mu\text{m}$ , 0.95/0.56  $\mu\text{m}$ ) exist for the Alphonsus region. The localized pyroclastic deposits (east and west DHC clusters) in the floor of the Alphonsus exhibit low 0.40/0.56  $\mu\text{m}$  (red) values and relatively high 0.95/0.56  $\mu\text{m}$  ratios. The "red" Alphonsus pyroclastics have 0.40/0.56  $\mu\text{m}$  values similar to the mare basalt deposits in nearby Mare Nubium.

Near-infrared reflectance spectra collected for these localized pyroclastic deposits have revealed that the Alphonsus pyroclastics are rich in olivine and pyroxene.<sup>13</sup> The spectra for these deposits have moderately deep (5 - 7 %) and relatively broad asymmetrical absorption bands in the 1.0  $\mu\text{m}$  region. The olivine was emplaced with the juvenile material. Lesser amounts of fragmented basaltic plug-rock and highlands-rich wall rock are thought to be present in these deposits. These deposits belong to the Group 3 spectral class as identified by Hawke et al.<sup>13</sup>, along with other similar deposits on the floor of J. Herschel and in the Cruger region.

Spectra collected of the Alphonsus central peak indicate that this feature is composed of anorthosite. This anorthosite is thought to have been derived from an anorthosite layer located at depth below the Alphonsus target site. Other highland features in the Alphonsus region exhibit a more orthopyroxene-rich composition. The spectra for these features suggests that they are noritic. The walls and central peak of

Arzachel crater, located directly south of Alphonsus, are composed of noritic anorthosite. Since the Arzachel central peak was derived from almost as great a depth (~10 km) as that of Alphonsus, the pure anorthosite layer may not be present beneath Arzachel crater. Alternatively, anorthosite may exist just below the layer sampled by the Arzachel peak.

#### **REFERENCES:**

- (1) Heacock R.L., Kuiper G.P., Shoemaker E.M., Urey H.C., and Whitaker E.A. (1966) *NASA Contract Rpt.*, CR-74894, 182 pp. (2) Salisbury J.W., Adler J.E., and Smalley V.G. (1968) *Mon. Not. R. Ast. Soc.*, 138, 245-249. (3) Carr M.H. (1968) *NASA Contract Rpt.*, CR-74894, 270-284. (4) Carr M.H. (1969) *U.S. Geol. Surv. Map*, I-599. (5) Hartmann W.K. (1967) *Commun.* 6, pp. 31-38, Lunar and Planet. Lab., Univ. of Ariz., Tucson. (6) Howard K.A. and Masursky H. (1968) *U.S. Geol. Surv. Misc. Geol. Invest. Map*, I-566. (7) McCauley J.F. (1969) *U.S. Geol. Surv. RLC Map* 15, I-586. (7) Head J.W. (1976) *Rev. Geophys. Space Phys.*, 14, 265-300. (8) Peterfreund A.R. (1976) *Eos Trans. AGU*, 57, 275. (9) Head J.W. and Wilson L. (1979) *Lunar and Planet. Sci. Conf. X*, 525-527. (10) Head J.W. and Wilson L. (1979) *Proc. Lunar Planet. Sci. Conf. 10th*, 2861-2897. (11) Zisk S.H., Pettengill G.H., and Catuna G.W. (1974) *The Moon*, 17, 17-50. (12) Bell J.F. and Hawke B.R. (1984) *J. Geophys. Res.*, 89, B8, 6899-6910. (13) Hawke B.R., Coombs C.R., Gaddis L.R., Lucey P.G., and Owensby P.D. (1988) *Proc. Lunar and Planet. Sci. Conf. 19th*, in press.



# A REMOTE SENSING ANALYSIS OF CRÜGER CRATER AND VICINITY ON THE MOON

B. Ray Hawke\*, Cassandra R. Coombs<sup>†</sup>, and Paul G. Lucey\*;

\*Planetary Geosciences Division, Hawaii Institute of Geophysics, University of Hawaii,  
Honolulu, HI, 96822;

<sup>†</sup>NASA/Johnson Space Center, SN 15, Houston, TX, 77058.

## INTRODUCTION

Crüger, a 46-km diameter crater, located at 17°S; 67°W, is a conspicuous geologic feature in the lunar highlands southwest of Oceanus Procellarum. Crüger is located south of the Grimaldi basin and near the contact between the inner and outer facies of the Hevelius Formation<sup>1</sup>, a deposit emplaced during the formation of Orientale basin. Considerable controversy has stemmed over the origin of Crüger crater as well as the other geologic units in the region.<sup>2,3</sup>

McCauley<sup>2</sup> and Wilshire noted that Crüger had some characteristics in common with a class of 30 smooth-rimmed craters identified on the lunar near side by Wilhelms and McCauley.<sup>4</sup> These workers<sup>2,3,4</sup> suggested that these craters, typified by Köpff on the floor of Orientale, might either be calderas or the products of unusual low-velocity and/or low-density impacts distinct from those that produced the rough high-rimmed craters of the main physiographic sequence.<sup>2</sup> Whatever the origin of Crüger crater, the geologic maps produced by several workers<sup>1,2,3,4</sup> indicate that Orientale deposits are superposed on Crüger crater exterior deposits. However, in a recent publication, Wilhelms<sup>5</sup> questioned the previously determined age relationships in the region.

The purposes of this study include the following: 1) to investigate the origin of Crüger crater, 2) to determine the composition, origin, and mode of emplacement of the dark mantle deposits on the south flank of Crüger, 3) to determine the composition of the various highlands units in the region, and 4) to investigate the relationship of the various highlands units to the Orientale impact event.

## METHOD

A variety of photographic and remote sensing data was utilized to address the unanswered questions in the Crüger region. Seven near-IR spectra (0.6-2.5  $\mu$ m) were obtained for the various geologic units in the region using the Planetary Geosciences Division CVF spectrometer at the UH 2.2-m telescope on Mauna Kea (Fig. 1). These spectra were reduced, processed, and analyzed using the procedures, techniques, and conventions presented by McCord *et al.*<sup>6</sup> and McCord and Clark.<sup>7</sup> In addition, the 3.8-cm and 70-cm radar data sets of Zisk<sup>8</sup> and Thompson<sup>9</sup> were used to study the various deposits in the Crüger region. Finally, the color-difference photograph of Whitaker as well as earth-based and spacecraft photographs with a wide variety of viewing geometries and sun angles were studied in order to help better define the geologic relationships in the Crüger crater region.

## RESULTS AND DISCUSSION

All of the highland terrain in the Crüger region appear relatively "red" (low UV/VIS

values) in the color-difference photograph produced by Whitaker.<sup>10</sup> In contrast, the mare materials in the region are relatively "blue" with the deposits within Crüger appearing slightly bluer than others. An intermediate  $\text{TiO}_2$  abundance for the basaltic fill is indicated.

Two near-IR spectra were obtained for the mare deposits within Crüger. Both exhibit characteristics typical of spectra collected for mature mare deposits elsewhere on the lunar near side. They have "1  $\mu\text{m}$ " absorption bands centered at about 0.98  $\mu\text{m}$  which indicates that the mafic mineral assemblage is dominated by high-Ca clinopyroxene.<sup>11</sup> Even though the deposit is relatively small, there is little evidence for contamination of the mare surface with highlands debris. This may be in part due to the relatively young Eratosthenian age of this mare deposit. Wilshire<sup>3</sup> noted that this unit exhibited far fewer superposed craters than mare material assigned to the Imbrium System in adjacent regions.

A dark mantle deposit which has a distinctly lower albedo than surrounding material occurs on the south flank of Crüger crater.<sup>3</sup> This unit is spectrally distinct in the color-difference photograph; it is much bluer than the adjacent highlands. Wilshire<sup>3</sup> interpreted this deposit to be volcanic material of probable pyroclastic origin. This interpretation is supported by an analysis of the 3.8-cm radar data for this region. There is a direct correlation between the dark mantle and an area of very low radar returns.

Two near-IR spectra were obtained for this dark mantle deposit. Both exhibit broad, composite "1  $\mu\text{m}$ " absorption features which we interpret to be due to the presence of an olivine-pyroxene mixture. These spectra are similar to the Group 3 spectra of localized pyroclastic deposits identified by Lucey *et al.*<sup>12</sup> Pyroclastic glass may or may not be present. Although no obvious volcanic source vents are visible in the dark mantled area, this does not rule out a pyroclastic origin. We suggest that this dark mantle deposit was emplaced by explosive eruptions during an early phase of the flooding of Crüger crater and that the source vent or vents were subsequently buried by mare lava. In addition, we have identified a previously unmapped dark mantle deposit NW of Crüger crater and SW of Mare Aestatis. This thin deposit appears to have been erupted from a vent in the southern-most portion of Aestatis.

Spectra were also obtained for a variety of highlands units in the region. The spectrum for the west rim of Crüger exhibits a very shallow "1  $\mu\text{m}$ " band centered at 0.93  $\mu\text{m}$ . The spectral parameters indicate that the area for which the spectra was obtained is composed of noritic anorthosite. It appears that this area is surfaced with material emplaced as a result of the Orientale impact event. The spectrum for Darwin C, a relatively fresh 16-km impact crater SW of Crüger (~20°30'S; 71°W), has a band centered at 0.92  $\mu\text{m}$ . Darwin C also exposes a deposit composed of noritic anorthosite. Both of these areas have a composition very similar to that determined for highlands deposits on the interior of Orientale basin by Spudis *et al.*<sup>13</sup> However, the spectrum for one feature in the Crüger region is very different. The Crüger G crater (diameter = 8 km) spectrum exhibits a "1  $\mu\text{m}$ " feature centered longward of 0.95  $\mu\text{m}$ . A gabbroic anorthosite composition is indicated. Crüger G is located SW of Crüger and exposes material from beneath the Orientale ejecta deposit.

## REFERENCES

- (1) Scott, D. *et al.* (1977) *USGS Map I-1034*. (2) McCauley, J.F. (1973) *USGS Map I-740*. (3) Wilshire H.G. (1973) *USGS Map I-755*. (4) Wilhelms D. and McCauley J. (1971) *USGS Map I-*

703. (5) Wilhelms D. (1987) *USGS Prof. Paper 1348*. (6) McCord, T. *et al.* (1981) *JGR*, 10883. (7) McCord T. and Clark R. (1979) *Pub. A.S.P.* 91, 571. (8) Zisk S.H. *et al.* (1974) *Moon* 10, 17. (9) Thompson, T.W. (1987) *Earth, Moon, and Planets* 37, 59. (10) Whitaker, E. (1976) Personal Comm. (11) Adams J.B. (1974) *JGR* 79, 4829. (12) Lucey P. *et al.* (1984) *LPS XV*, 495. (13) Spudis P. *et al.* (1984) *PLPSC* 15, C197.

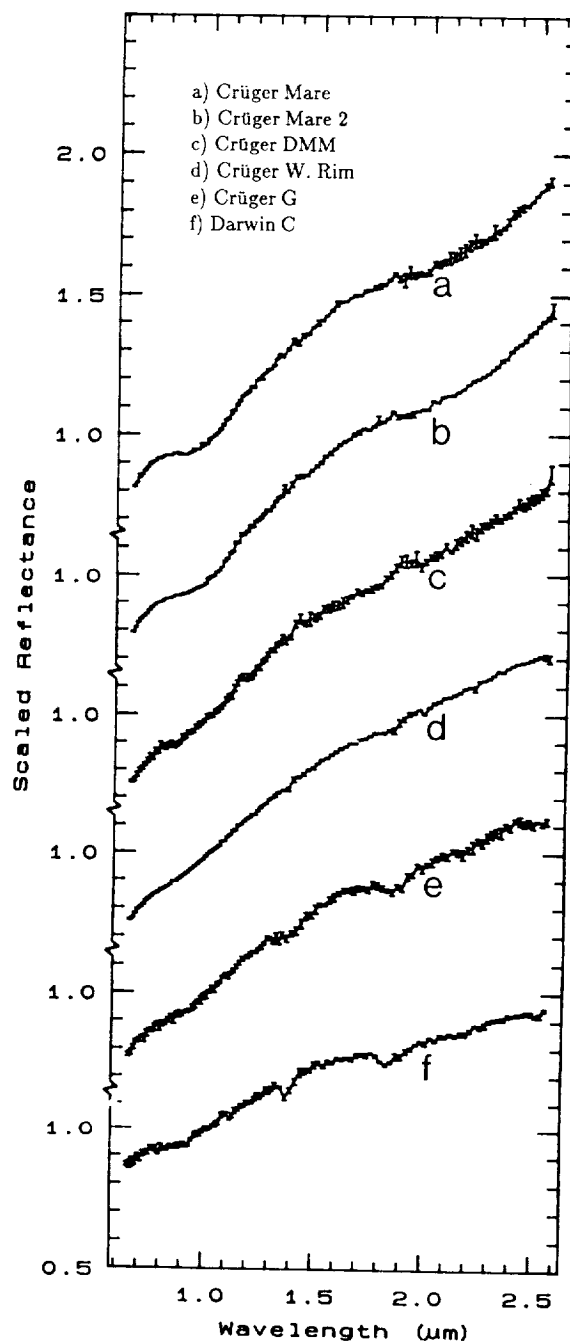


Figure 1. Near-infrared spectra obtained for units in the Crüger region.

C-4



CHAPTER 7

RADAR APPLICATIONS

PRECEDING PAGE BLANK NOT FILMED

PAGE 284 INTENTIONALLY BLANK



## New Arecibo High-Resolution Radar Images of Venus: Preliminary Interpretation

D.B. Campbell<sup>1</sup>, A.A. Hine<sup>2</sup>, J.K. Harmon<sup>2</sup>, D.A. Senske<sup>3</sup>, R.W. Vorder Bruegge<sup>3</sup>, P.C. Fisher<sup>3</sup>, S. Frank<sup>3</sup>, and J.W. Head<sup>3</sup> 1) National Astronomy and Ionosphere Center, Cornell University, Ithaca NY 14853. 2) National Astronomy and Ionosphere Center, Arecibo Observatory, Arecibo, PR 00612. 3) Department of Geological Sciences, Brown University, Providence, RI 02912.

Introduction: New observations of Venus with the Arecibo radar (wavelength 12.6 cm) in the summer of 1988 will provide images at 1.5-2.5 km resolution over the longitude range 260° to 20° in the latitude bands 12°N to 70°N and 12°S to 70°S<sup>1</sup>. We have made a preliminary analysis of images of low northern and southern latitudes including Alpha Regio, eastern Beta Regio, and dark-halo features in the lowland plains of Guinevere Planitia. Crater distributions and the locations of the Venera 9 and 10 landing sites are also examined.

Alpha Regio: (5°, 25°S) is a 1000 × 1600 km upland region located south of Pioneer-Venus and Venera 15/16 radar image coverage. It was the first area of anomalously high radar return discovered in the early 1960's by Earth-based radars (hence the name). Recent comparisons of Pioneer-Venus altimetry, reflectivity and r.m.s. slope data with different terrain types apparent in the Venera 15/16 images indicate that Alpha Regio has many similarities with tessera<sup>2-6</sup>. The new high resolution images (Fig. 1) show that Alpha itself is a region of high radar return with very sharp boundaries and a distinctive pattern of bright and dark linear bands with separation distances of 10-15 km and oriented approximately NNE. Two other less distinctive patterns of lineaments can be observed and are scattered throughout Alpha. On the basis of the linear segments and their orientations and spacings, the local plains deposits, and the distinctive structural relations of its boundaries, the Alpha region appears to be very similar to the tessera terrain (such as Tellus Regio) in the area imaged by Venera 15/16<sup>3</sup>.

Eastern Beta Regio: Located on the eastern flank of Beta Regio (293°, 25°N), is a region of elevated topography described as an upland plateau<sup>7</sup>. PV radar data shows this feature to possess properties similar to that of other areas mapped as tessera (high values of RMS slope, low values of reflectivity, high diffuse scattering) and on the basis of these properties, it was also predicted to be tessera terrain<sup>6</sup>. Examination of the high resolution Arecibo images shows this feature to be characterized by a distinctive pattern of parallel closely spaced ridges and troughs oriented generally N-S, spaced approximately 5-10 km apart, a second orthogonally-oriented fabric of less abundant but more through going lineaments, as well as a third set of northeast trending ridge and trough pairs. These characteristics are similar to those in Alpha and in other regions that have previously been interpreted to be tessera terrain<sup>3</sup>. Radar-dark material possessing characteristics similar to units mapped elsewhere as volcanic plains embays the tessera-like unit and we interpret this relationship to indicate the relatively old age of the tessera compared to the dark plains in the surrounding lowland.

Dark halo features: Extended, quasi-circular areas of low backscatter cross section (dark halos) with central bright spots of unknown origin and morphology have been observed in early earth-based radar images of Venus<sup>8</sup>

and Pioneer-Venus images<sup>7,9</sup>. The new images cover one group of these dark halos in the area between longitudes 320° and 340° and latitudes 15°N and 32°N. Whether the low backscatter cross section is due to a very smooth surface or low intrinsic reflectivity is still not known but most of the bright spots are resolved as craters with extended, very asymmetric bright surrounds. This is not a characteristic of the craters observed at higher latitudes and interpreted to be of impact origin<sup>10</sup>, and suggests, rather, a volcanic origin.

Impact Craters: The number of impact craters with diameters greater than 15 km in the latitude band 15°N to 30°N may be considerably lower than the approximately one per 10<sup>6</sup> km<sup>2</sup> observed at higher northern latitudes in the Venera 15/16 images<sup>10</sup>. A number of craters are apparent in the new images in the 15°N to 30°N latitude band but only three or four have characteristics similar to what one would expect based on the comparison of high incidence angle Arecibo observations of craters interpreted to be of impact origin in the Venera images. The remaining craters observed are primarily those in the dark halo features.

Venera lander sites: Two Venera landers, Veneras 9 and 10, are located within the region imaged. Venera 9, which landed in a region of steep slopes later known to be rough from Pioneer-Venus data<sup>11-13</sup> is located in the abundant blocks with no obvious bedrock exposures<sup>12,13</sup>. The blocky field within the lander image may be related to the linear bright scarp seen in the Arecibo image and an area of associated talus. Venera 10 is located near the edge of a radar-dark plains unit between two blocks of tessera-like material. The lander panorama shows the spacecraft to be located in a flat region with significant bedrock exposure, some thin soil cover, and a plains-like morphology<sup>12,13</sup>.

References: 1) D. Campbell et al (1989) LPSCXX, 142. 2) J. Head et al (1985) JGR, 90, 6873. 3) A. Basilevsky et al (1986) JGR, 91 D399. 4) D. Bindschadler and J. Head (1978) LPSC SVIII, 73. 5) D. Bindschadler and J. Head (1988) EMP, 42, 133. 6) D. Bindschadler et al (1988) LPSC XIX, 80. 7) G. Pettengill et al (1979) Science, 205, 90. 10) A. Basilevsky et al (1987) JGR, 92, 12869. 11) A. Basilevsky et al (1982) EMP, 27, 63. 12) C. Florensky et al (1977) GSA Bull., 88, 1537. 13) J. Garvin et al (1984) JGR, 89, 3381.





FIGURE 1

Alpha Regio and surroundings. Area covered is from longitude  $343^{\circ}$  to  $18^{\circ}$  and latitude  $45^{\circ}\text{S}$  to  $10^{\circ}\text{S}$ . The grid lines are at 10 deg. spacing. Pixel spacing is 4km in this image. The resolution of the basic data is 1.5km.

# MARTIAN QUASI-SPECULAR ECHOES: PRELIMINARY 1986 RESULTS

T.W. Thompson, Jet Propulsion Lab., C.I.T., Pasadena, CA 91109

H.J. Moore, U. S. Geological Survey, Menlo Park, CA 94025

Radar observations of Mars at Goldstone in 1986 were conducted by transmitting pure sinusoidal signals with 12.6-cm wavelengths and receiving the Doppler-spread signals at Earth. Radar transmissions were circularly polarized and the radar echoes were recorded in both senses. Thus, radar echoes from Mars were separated into the polarized (OC, opposite-sense circular) and the depolarized (SC, same-sense circular) components. Each polarized echo component consists of two parts: (1) a quasi-specular echo and (2) a diffuse echo. Two parameters can be estimated from a quasi-specular echo: (1) root-mean-square (rms) slope and (2) normal reflectivity. The rms slope is a statistical measure of surface undulations at slope-lengths larger than the radar wavelength and is roughly equivalent to the algebraic standard deviation of a slope probability distribution. Reflectivity can be interpreted as a relative dielectric constant. The bulk density of the surface materials can, in turn, be inferred from the dielectric constant.

For the latitude band of  $3.1^{\circ}$  to  $13.9^{\circ}\text{S}$ , we obtain an average rms slope of  $4.31^{\circ}$  with a standard deviation of  $2.16^{\circ}$ . The mode of the frequency distribution is near  $3.5^{\circ}$  (Fig.1). Our average rms slope is larger than an average rms slope along about  $22^{\circ}\text{N}$  ( $3.69 \pm 1.66^{\circ}$ ) [1,2] and the average rms slope farther south ( $2.0^{\circ}$ ) [3]. Above average rms slopes are typically found between  $110^{\circ}$  and  $230^{\circ}\text{W}$  (Fig.2). Below average rms slopes are typically found between  $230^{\circ}$  and  $110^{\circ}\text{W}$ . The roughest areas occur west and southwest of Arsia Mons; the smoothest areas occur near the central meridian.

We obtain an average reflectivity of 0.066 with a standard deviation of 0.027. This corresponds to an average dielectric constant of 2.87 and a standard deviation of 0.66. Our average reflectivity is slightly larger than an average reflectivity along about  $22^{\circ}\text{N}$  ( $0.061 \pm 0.033$ ) [1,2], but it is about the same as the average reflectivity obtained farther south (0.07) [3]. The frequency distribution of dielectric constants is bimodal with modes near 2.2 and 3.3 (Fig. 3). The variation of dielectric constants with longitude show that low dielectric constants are associated with the Syria-Sinai Planum and the southern Tharsis regions between  $75^{\circ}$  and  $190^{\circ}\text{W}$ ; elsewhere, dielectric constants are typically above average (Fig. 4).

An inspection of thermal inertia maps [4,5] along the  $3.1^{\circ}$  to  $13.9^{\circ}\text{S}$  latitude band suggests that there is a strong correlation between thermal inertias and our dielectric constants. A similar correlation has been noted previously [6,7]. Small dielectric constants and low thermal inertias are associated with each other in the Syria-Sinai Planum and Tharsis regions. Elsewhere, above average dielectric constants are associated with moderate to high thermal inertias, except in southern Arabia near  $330^{\circ}\text{W}$ .

The combination of small dielectric constants and low thermal inertias appears to be typical of the Tharsis region. Our average dielectric constant for southern Tharsis between  $115^{\circ}$  and  $145^{\circ}\text{W}$  is  $2.17 \pm 0.12$ . For northern Tharsis along about  $22^{\circ}\text{N}$  and between  $75^{\circ}$  and  $125^{\circ}\text{W}$  [2], the average dielectric constant is about  $2.3 \pm 0.4$ .

Tharsis is also characterized by strong polarized diffuse and depolarized echoes which suggest that there are significant concentrations of wavelength-size roughness elements at and near the surface [1,2,8].

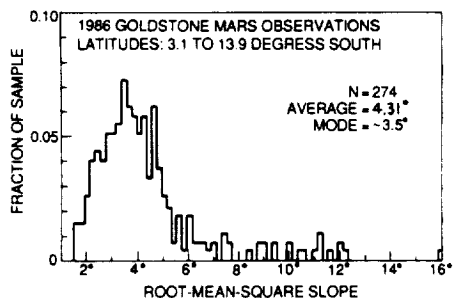


Figure 1. Frequency distribution of rms slopes.

Figure 2. Rms slope as a function of longitude.

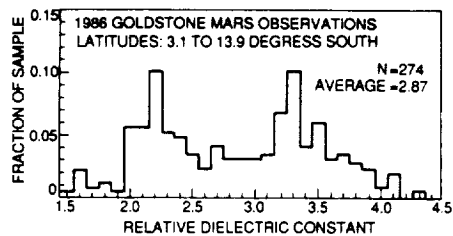
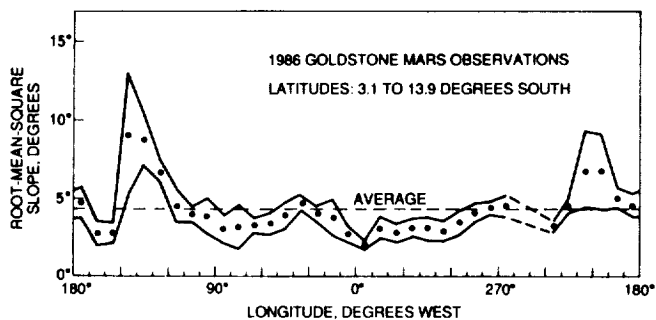
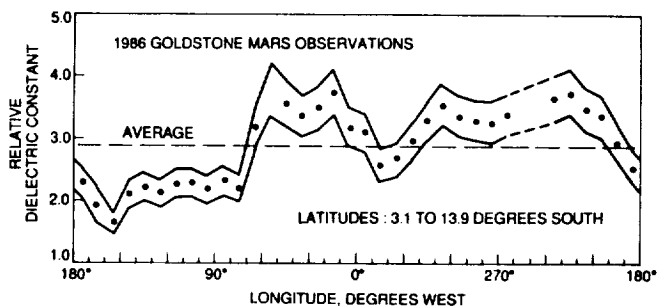


Figure 3. Frequency distribution of dielectric constants.

Figure 4. Dielectric constant as a function of longitude.



The association of small dielectric constants, low thermal inertias, and strong diffuse and depolarized echoes suggest that thick layers of loose dust, interspersed with rough surfaces, are present in some places such as southern Tharsis. Importantly, the radar and thermal data are consistent with geologic interpretation of Viking Orbiter high-resolution images of southern Tharsis where thick deposits of eolian mantle of dust are interspersed with rough aa and blocky lava flows [9].

#### REFERENCES

- [1] Harmon, J.K. and Ostro, S.J., 1985, Mars: Dual-polarization radar observations with extended coverage: *Icarus*, v. 62, p. 110-128.
- [2] Harmon, J.K., Campbell, D.B., and Ostro, S.J., 1982, Dual-polarization radar observations of Mars: Tharsis and environs: *Icarus*, v. 52, p. 171-187.
- [3] Downs, G.S., Reichley, P.E., and Green, R.R., 1975, Radar measurements of martian topography and surface properties: *Icarus*, v. 26, p. 273-312.
- [4] Palluconi, F.D. and Kieffer, H.H., 1981, Thermal inertia mapping of Mars from 60°S to 60°N: *Icarus*, v. 45, 415-426.
- [5] Christensen, P.R., 1986, Regional dust deposits on Mars: physical properties, age, and history: *J. Geophys. Res.*, v. 91, p. 3533-3545.
- [6] Jakosky, B.M. and Christensen, P.R., 1986, Are the Viking landing sites representative of the surface of Mars: *Icarus*, v. 66, p. 125-133.
- [7] Jakosky, B.M. and Muhleman, D.O., 1981, A comparison of thermal and radar characteristics of Mars: *Icarus*, v. 45, p. 25-38.
- [8] Thompson, T.W. and Moore, H.J., 1989, A model for depolarized radar echoes from Mars: *Proc. 19th Lunar and Planet. Sci. Conf.*, in press.
- [9] Schaber, G.G., 1980, Radar, visual, and thermal characteristics of Mars: rough planar surfaces: *Icarus*, v. 43, 159-184.

## ANALYSIS OF 1971 AND 1973 MARS GOLDSTONE DATA

A.P. Zent, F.P. Fanale, Planetary Geosciences Div., Univ. of Hawaii, Honolulu, HI 96822, and L.E. Roth, Jet Propulsion Lab, Cal. Inst. Tech., Pasadena, CA 91009.

The 1971 and 1973 Goldstone 12.6-cm radar observations of Mars are separate data sets which include measurements of inherent surface reflectivity as a function of latitude, longitude, and season. The data are discontinuous and incomplete. It has been argued that reflectivity variations might exist in these data (Zisk and Mouginis-Mark, 1980; Roth et al., 1985), which may be consistent with origin by subsurface melting (Roth et al., 1986; Zent and Fanale, 1986). We have examined both the 1971 and 1973 data sets to see if the subsurface melting model is compatible with the observations.

We have attempted to analyze the experimental error, i.e., the variation in the data sets not accounted for by differences between measured samples. We construct autocorrelograms of the reflectivity measurements in the 1971 and 1973 data sets. Collocated, simultaneous measurements should have a correlation of 1. The degree to which the extrapolated correlation coefficient at zero lag differs from 1 is a measure of the experimental error. Correlations of  $\sim 0.95$  at zero lag in both data sets indicate that the experimental errors are less than  $\sim 10\%$ . Given this estimate of experimental error we conclude that there is no *a priori* reason to discount reported reflectivity variations, provided the reported reflectivity change is greater than 10% of the absolute value.

Intra-annual radar reflectivity variations were mapped via two techniques. The first has high resolution, but suffers from the incomplete coverage of the data set. With this technique, overlapping scans that indicate appreciable reflectivity change are simply plotted on the planet's surface. While the second method offers more complete coverage, it is at the cost of diminished resolution. The imaged area is divided into 144 resolution cells, and the correlation of the reflectivity with time is plotted in each cell. Our examination has shown that there are broad areas which exhibit reflectivity increases of greater than 10% during the course of an observing run, particularly in the 1971 data. We have identified three areas in which strong reflectivity increases were present in both the 1971 and 1973 data. We conclude that these areas are unique in terms of their properties, which in some manner influences their 12.6 cm radar return.

We have attempted to reconcile the time and location of these identified areas with the hypothesis that radar variations are due to the seasonal melting of very salt-rich  $H_2O$  systems (brines) in the very shallow regolith of Mars. Examination of the energy budget of Mars during those periods in which reflectivity apparently increases reveals that during 1973 the surface was rapidly cooling at the time that melting is required by the brine hypothesis. A plot of the reflectivity histories of the test regions against season displays a step-like behavior that is difficult to reconcile with an origin by melt generation. It appears very unlikely that the apparent radar anomalies are due to subsurface melting of a brine. Any attempt to explain them as such must include a scenario for an active martian crust which is capable of emplacing  $H_2O$  in the very shallow martian regolith, probably within the last million years. Such a system would be greatly out of equilibrium with the thermal and chemical megaenvironment as revealed by the Viking Landers and Orbiters.

Further examination of the areas identified in this study is strongly recommended.

References

- Roth, L.E., R.S. Saunders, and G. Schubert (1985), *LPSC XVI*, 712-713.  
Roth, L.E., R.S. Saunders, G.S. Downs, and G. Schubert (1986), *LPSC XVII*, 730-731.  
Zent, A.P. and F.P. Fanale (1986), *J. Geophys. Res.*, **91**, D439-D445.  
Zisk, S. and P.J. Mouginis-Mark (1980), *Nature*, **288**, 735-738.

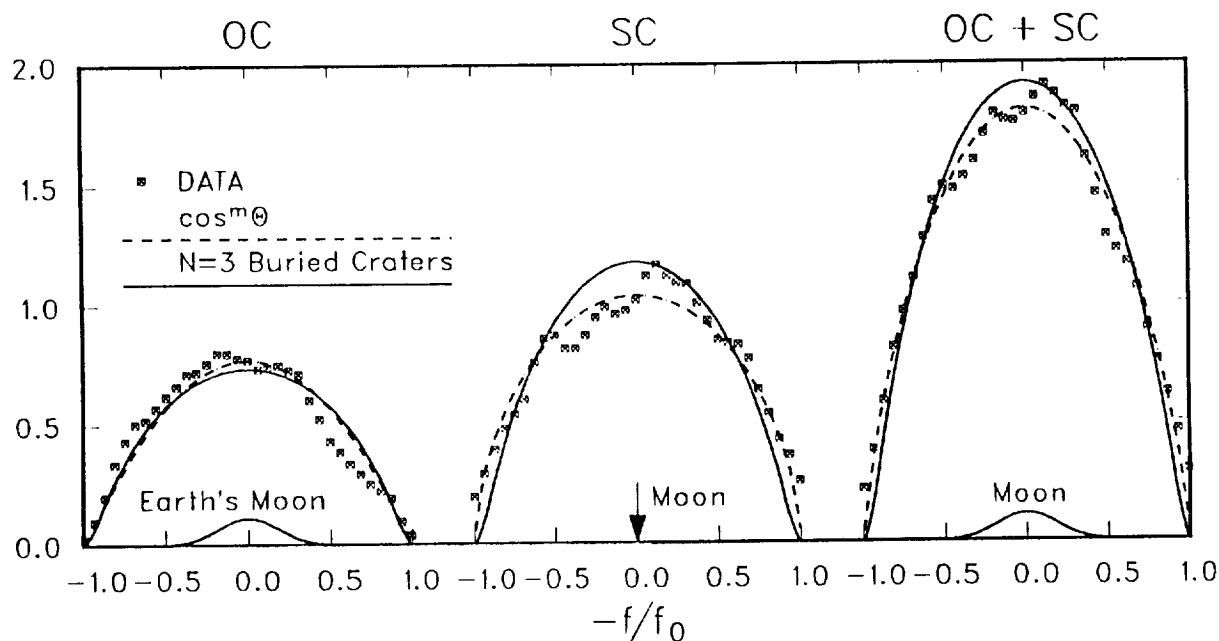
## Developments in the Buried-Crater Model for Radar Echoes from Icy Moons

E.M. Gurrola, V.R. Eshleman (Stanford University)

The buried-crater model introduced by Eshleman (*Science* 234 587, 1986) has been successful in accounting for anomalously large radar echoes with unexpected polarization ratios that have been observed from three icy moons of Jupiter: Europa, Ganymede, and Callisto. A simple model of a single buried crater with axially incident rays plus a single assumption regarding the ratio of refractive indices in the layers above and below the crater walls was found adequate to model the power in two orthogonal circular and linear polarizations for all three moons.

We find that, with further development of the model to include effects due to angular position of the craters, this model also provides a good fit to the only other type of well-established data: the doppler-frequency power spectra. The figure compares theoretical curves of radar cross-section for buried craters with typical Europa spectra (data from S. Ostro in *Satellites of Jupiter*, D. Morrison, Ed., U. Arizona Press 1982) and contrasts them with simulated spectra for Earth's moon which was the expected situation. The dashed curve is a least-squares fit of the data to a  $\cos^m \Theta$  law (where  $\Theta$  is the angle between the incident rays and the moon's surface normal). The buried-crater model gives circular and linear polarization ratios (ratio of power in the unexpected to the expected polarization) of 1.60 and 0.44; averages of the observations for Europa are 1.56 and 0.47 respectively.

We have compared this model with other models that have been proposed with regard to their correspondence to current data and find that the buried crater model predicts larger echoes than other models that can also account for the polarization ratios. Despite an uncertain geophysical hypothesis, the buried-crater model is distinguished by its ability to simultaneously account for the main features in all the types of data with a minimum of ad hoc assumptions. Also, by introducing a gradation in refractive index at the crater walls, this model can account for the sparse data indicating a frequency dependence in the polarization ratios.



## Numerical Modeling of Radiowave Scattering

R.A. Simpson and G.L. Tyler  
Center for Radar Astronomy  
Stanford University  
Stanford, CA 94305-4055

Radiowave scattering is an effective tool for remotely studying planetary surfaces. It is particularly sensitive to surface texture with dimensions comparable to the radio wavelength (a few centimeters to tens of meters, with present systems). Theoretical work, however, has lagged experimental discoveries with the result being that qualitative interpretations of relatively well characterized observations are the rule. Numerical techniques, in combination with rapidly improving computer technology, now provide an alternative to conventional theoretical development. Relatively simple and robust algorithms, but ones which demand considerable computation power, allow us to simulate some electromagnetic scattering problems. Although there are only a very limited number of analytical solutions which can be used for checking, the clarity with which the problems may be stated plus an understanding of the computer's numerical limitations provide assurance that the results are correct.

A large body of computer software has been developed nationally for calculating electric and magnetic fields near objects that can be described in relatively simple terms -- wires and plates (antennas, for example) and cylinders and cones (aircraft, missiles, ships, etc.). The calculations usually incorporate, either as initial conditions or as an intermediate result, information about the currents on the conducting surfaces involved. The radiated fields (including scattering as a special case) then represent the response to these currents. As in many electromagnetics problems, a particular solution may be derived more easily by concentrating on either the electric or the magnetic equations. Dielectric materials (as opposed to perfect conductors) and statistically rough surfaces (as opposed to those with well-defined curvature) increase the complexity of these problems considerably. Both variations, of course, must be accommodated in any application to real planetary surfaces.

We have identified the Numerical Electromagnetic Code (NEC) as being the best of several candidates for application to planetary problems. We have obtained a copy of this program from its "curators" at the Lawrence Livermore Laboratory and adapted it for operation on our Data General MV/10000. Although intended for study of scattering from "objects" rather than distributed targets such as "surfaces," NEC's relative generality has made it attractive. With some limitations our present version of NEC permits evaluation of the scattering from virtually any object that can be (approximately) described in terms of 300 or fewer wire segments or small plates.

We have both tested and used NEC in several scattering contexts. To test the program accuracy we have compared NEC results against analytical solutions for scattering from (a) a large, smooth plate and (b) a perfectly conducting sphere. In both cases we obtained good agreement. In fact, for the plate, we have concluded that the numerical solution is *superior* because of simplifications required in obtaining the analytic result (Simpson and Tyler, 1988). We have also constructed canonical geometrical objects (sphere, cylinder, and cube) -- models for "rocks" -- and calculated the scattering as a function of size and orientation.



The canonical geometrical objects were defined using the "plate" mode of NEC. Figure 1 illustrates how this is done and Figure 2 gives some of the results. When the objects have dimensions on the order of a wavelength, the three forms have distinct scattering patterns (Figure 2a). Note that scattering patterns in at least three planes are needed to characterize these objects; for present purposes we have limited illustration to a single plane, where the cylinder and cube are quite similar. As object size decreases, the scattering patterns (except for a scale factor) begin to look the same. For characteristic dimensions (*e.g.*, the diameter) on the order of  $\lambda/10$  the individual shapes cannot be distinguished from their scattering patterns nor can the orientation of any single object be determined.

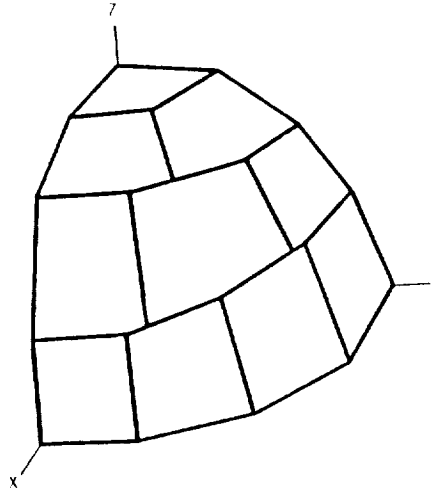


Figure 1. Octant of sphere defined in "plate" mode for NEC. 80 plates complete the sphere.

More recently we have begun to investigate the detailed interaction between two scattering objects -- rock to rock coupling. We anticipate that this study may produce the first useful *polarization* results from our work. We began by solving the scattering problem for a single sphere and then, again, for a displaced sphere. Coherent combination of those two solutions was expected to give the same answer as a single solution for two separated

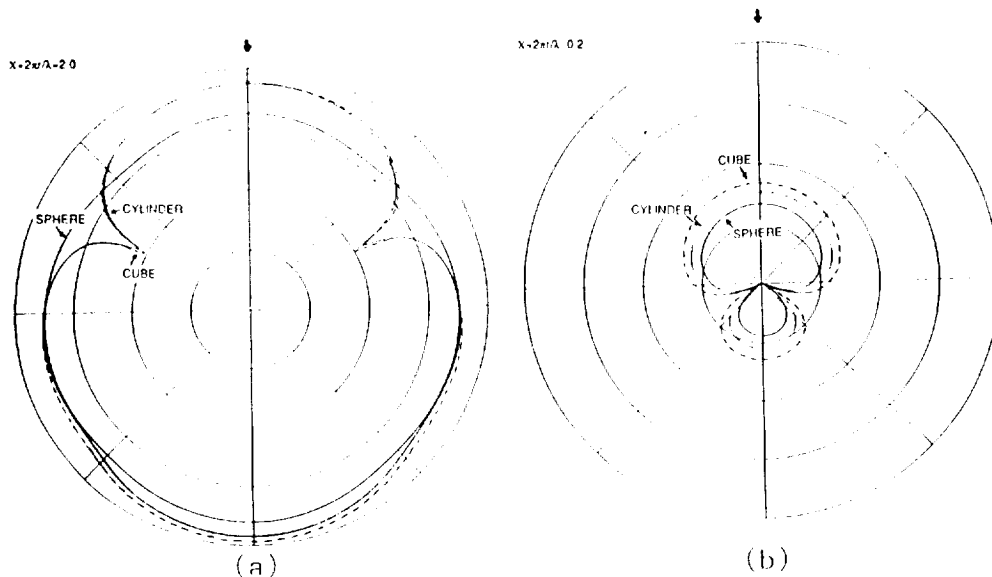


Figure 2. Scattering patterns for large (a) and small (b) canonical objects -- sphere, cylinder, and cube. Characteristic dimension (*e.g.*, diameter) of objects in (a) is  $2\lambda/3$ ; characteristic dimension in (b) is  $2\lambda/30$ . Illumination is from the *z* direction (top of figure; note arrow); incident electric field vector is parallel to *x* axis. Plot shows observed scattered field measured in the *x-z* plane with a probe polarized in the *x-z* plane.

spheres. We discovered at this point, however, that NEC will not solve the two sphere problem in the "plate" mode. We are now switching to spheres defined in the "wire" mode, but our present wire sphere is unacceptably sensitive to orientation. We are investigating modifications to the present design as well as alternatives such as approximation by an icosahedron; the latter is attractive on symmetry grounds, but it will not scale easily. We have used NEC in the meantime to study the interaction between two, separated wire elements and have confirmed that our general approach is valid.

The substitution of wire spheres for plate spheres represents a step we would have taken shortly anyway. NEC requires that scatterers constructed from plates be closed, so any attempt at modeling a "surface" would have required closure with a base plate, an unrealistic restriction. A wire mesh will be used for surface modeling; it can be solved directly by NEC. Further, the wire mesh model is more easily related to real topographic data (two-dimensional grids of regularly spaced points), and we can provide some degree of control on edge effects (scattering artifacts) through selective addition of resistance to wire segments near the perimeter. The present complication illustrates the care that must be taken in using codes such as NEC and the limitations in even this relatively general program.

-----  
Simpson, R.A., and G.L. Tyler, "Numerical modeling of radiowave scattering, Reports of Planetary Geology and Geophysics Program - 1987, NASA Technical Memorandum 4041, 245-247, 1988.

## **RADAR SCATTERING FROM DESERT TERRAINS, PISGAH/LAVIC REGION, CALIFORNIA**

J. J. Plaut (1), J. J. vanZyl (2), R. E. Arvidson (1).

(1) Department of Earth and Planetary Sciences, McDonnell Center for the Space Sciences, Washington University, St. Louis, Missouri 63130.

(2) Jet Propulsion Laboratory, 4800 Oak Grove Drive, Pasadena, California 91109.

A major component of the 1988 Mojave Field Experiment (Wall et al., 1988) involved the simultaneous acquisition of quad-polarization multi-frequency airborne SAR imaging radar data and ground measurements thought to be relevant to the radar scattering behavior of a variety of desert surfaces. The airborne SAR system acquired images at approximately 10 m resolution, at 3 incidence angles ( $30^\circ$ ,  $40^\circ$ ,  $50^\circ$ ) and at 3 wavelengths (P: 68 cm, L: 24 cm, C: 5.6 cm). The polarimetric capabilities of the instrument allow the simulation of any combination of transmit and receive polarizations during data reduction (Zebker et al., 1987; vanZyl et al., 1987). Calibrated trihedral corner reflectors were deployed within each scene to permit absolute radiometric calibration of the image data. We report here on initial analyses of this comprehensive radar data set, with emphasis on roughness, incidence angle, and polarimetric effects.

Detailed site characterization and sample collection were conducted at 5 compositionally and/or texturally distinct sites within the Pisgah Volcanic Field/Lavic Lake area. These included: a smooth undisturbed playa surface; a playa surface covered with basaltic cobbles; a moderately vegetated alluvial surface; and 2 basaltic lava flow surfaces of contrasting roughness.

Total (unpolarized) backscattered power values are well-correlated with ground determinations of wavelength-scale roughness for the various sites. For example, differences in measured backscattered power between the smooth and cobble-strewn playa surfaces are minor in P-band ( $<1$  dB) and L-band ( $<4$  dB), but are large ( $>5$  dB) in C-band. This is clearly due to the presence of scattering elements (cobbles) which occur primarily at the scale of the C-band wavelength (5-20 cm). A similar effect is seen at the two lava flow sites. Backscattered power differences between the rough (aa) and less rough (pahoehoe) surfaces are  $>4$  dB in P- and L-band but  $<2$  dB in C-band. In this case the longer wavelength bands are sensitive to the dominant roughness differences of the two sites, while the relatively uniform C-band response results from a common small-scale roughness.

Preliminary analysis of incidence angle effects indicates that all of the surface types exhibit the expected decrease in backscatter strength with increasing incidence angle. Future work will examine this effect in more detail, in the context of model scattering laws. Selection of an appropriate incidence angle to best distinguish two terrain types appears to depend on the nature of the surfaces. In unpolarized data, the two playa surfaces are better separated at large incidence angles, whereas the aa and pahoehoe lava flows show greater contrast at small incidence angles. This may be due to the relatively larger role of quasi-specular scattering at small incidence angles, an effect which is more likely to be important for rough surfaces.

Polarization signatures, which describe the behavior of radar backscattering cross-section as a function of send and receive polarization states (Zebker et al., 1987), were generated for each site at each frequency and incidence angle. The polarization signatures at all sites are generally consistent with theoretical signatures based on a Bragg scattering model for rough surfaces (vanZyl et al., 1987). The co-polarization signatures, for example, consistently display maxima at VV, and minima at or near the circular polarizations. Similarly, the cross-polarization minima correspond to linear send/receive pairs (e.g. HV), as expected. Preliminary examination of images synthesized in several standard polarization states shows that the HV polarization can be extremely useful in discriminating lava flow types. L-band images of the Pisgah lava flow in HV polarization show excellent discrimination of the three lava flows associated with the three eruptive phases of the Pisgah field.

The quad-polarization airborne SAR system is the most powerful and sophisticated radar imaging tool to be applied to geological studies. Future work will utilize the unique polarimetric data, along with absolute calibrations at multiple wavelengths, to develop and test models for inversion of image data for extracting geologically important properties of surfaces.

#### REFERENCES

- VanZyl, J. J., H. A. Zebker, and C. Elachi (1987) Imaging radar polarization signatures: Theory and observation: Radio Sci., 22, 529-543.
- Wall, S., J. J. vanZyl, R. E. Arvidson, E. Theilig, and R. S. Saunders (1988) The Mojave field experiment: Precursor to the planetary test site (abstract). Bull. Am. Astr. Soc., 20, 809.
- Zebker, H. A., J. J. vanZyl, and D. N. Held (1987) Imaging radar polarimetry from wave synthesis: J. Geophys. Res., 92, 683-701.

## COMPARISON OF TIMS AND AIRBORNE IMAGING RADAR DATA OVER THE PISGAH VOLCANIC FLOW AND ADJACENT LAVIC LAKE PLAYA

S. J. B. Petroy, R. E. Arvidson, McDonnell Center for the Space Sciences, Department of Earth and Planetary Sciences, Washington University, St. Louis, Missouri, 63130, and A. B. Kahle, Jet Propulsion Laboratory, Pasadena, California, 91103

The NASA airborne Thermal Infrared Multispectral Scanner (TIMS) and the JPL quad-polarization radar instrument were both flown over the Pisgah volcanic field and adjacent Lavic Lake playa within a two-day period in June, 1988. These flights were part of the Mojave Field Experiment (MFE) - a collaborative effort involving Washington University, Arizona State University, and JPL (Arvidson and Guinness, this volume; Wall et al., 1988). The concept of this experiment is based fundamentally on the acquisition of in-situ ground and subsequent laboratory data to provide information on surface properties that can be used to check results extracted from remote sensing data. What follows is the initial analyses of the thermal and radar data sets, with emphasis on determining physical properties of the surface materials, such as particle size and small-scale surface roughness.

The TIMS instrument has six wavelength channels in the thermal infrared between 8 and 12  $\mu\text{m}$ . Calibrated spectral radiance data from the TIMS day/night flights permit the calculation of day and night surface temperatures, surface spectral emittance, and apparent thermal inertia. Depths from which diurnal thermal observations are obtained range from a few centimeters to tens of centimeters, depending on the surface material (Kieffer et al., 1977). The radar instrument has three wavelength channels in the microwave region - the P band (68 cm), L band (24 cm), and C band (5.6 cm) - and can send and receive power in four polarizations modes (HH, VV, HV, and VH). Radar studies of planetary surfaces are sensitive to material properties to a depth which depends on the wavelength employed, but which could be as large as several meters (Evans, 1969; McCauley et al., 1982). Integration and comparison of measurements acquired in the thermal infrared and microwave regions of the spectrum can thus be used to constrain a range of surface properties, such as particle size, depth of loose regolith, moisture content, and degree of bonding.

Spectral and temperature information contained in the TIMS data were separated using a method developed by Kahle et al. (1980). An apparent thermal inertia (ATI) image was produced from the day and night temperature images coregistered with the Landsat TM data. Ideally, a reflectance image would be constructed from a combination of all six visible and near-infrared channels of the TM data convolved with the spectral response curve of the sun over the TM wavelength region. This would provide a measure of albedo or brightness of a surface (the ratio of total solar radiation reflected from the surface to that received by the surface) over the wavelength region sampled by the Landsat TM. However, for simplicity, Band 4 (0.76 to 0.90  $\mu\text{m}$ ) was used as the albedo image (this band contains the maximum amount of spectral variation within the scene). The apparent thermal inertia image was then constructed from the Price (1977) formula,  $\text{ATI} = K(1-A)/(T_D - T_N)$ , ignoring, for the present, topographic and atmospheric effects; A is the albedo image,  $T_D$  is the daytime temperature image,  $T_N$  is the nighttime temperature image, and K is a constant of proportionality. Thermal inertia, a bulk physical property of the surface materials, is equal to  $(Kpc)^{1/2}$  where  $K$ =thermal conductivity,  $p$ =density, and  $c$ =specific heat. Thus, determination of

thermal inertia provides constraints on specific physical properties described above and calculation of apparent thermal inertia for different surfaces allows for relative estimates of these physical properties.

Within the Pisgah/Lavic Lake study area, ATI values range from 0.01 to 0.04 in units proportional to those used for thermal inertia ( $\text{cal cm}^{-2} \text{K}^{-1} \text{sec}^{1/2}$ ; these units will be assumed throughout). The dominant thermal feature is the Pisgah volcanic flow which is characterized by ATI values between 0.024 and 0.04; Lavic Lake playa exhibits consistently lower ATI values of 0.01 to 0.018. Although the contact between the Pisgah flow and the playa is sharp in the ATI image, there is a gradational boundary between the playa and the adjacent alluvial fans. ATI values gradually increase away from the playa as the alluvial deposit appears to thicken and surface particle size and vegetation cover increases.

The radar data were processed by extracting the total power returned from each surface point sampled; a rough surface will scatter more power back to the detector than a smooth surface which tends to reflect power away from the detector. Thus, brightness variations within the radar images can be qualitatively related to the surface roughness in each of the three wavelength regions sampled (5.6, 24, and 68 cm; Plaut et al., this volume). The Pisgah volcanic flow is generally bright (i.e., rough) at all three wavelengths. Lavic Lake playa is fairly smooth and flat; it appears dark in all three bands. However, there is a small area on the playa adjacent to Pisgah flow that is covered with small basaltic cobbles (about 10-20 cm diameter). This area appears brightest in the C band image (5.6 cm wavelength) and can also be observed in the ATI image; it exhibits a slightly higher apparent thermal inertia ( $\text{ATI}=0.02$ ) than the surrounding playa.

Within the Pisgah/Lavic Lake site, comparisons between the ATI image and the radar images show a general correlation between smooth, low thermal inertia regions and rougher, higher thermal inertia regions. This does not imply that surface roughness is controlling the thermal inertia; rather, it suggests that the physical properties generally controlling the apparent roughness of a surface are related to those properties which control its thermal inertia. For example, the playa is composed of thick deposits ( $>68$  cm) of very fine-grained clay particles; thus, it is fairly smooth to the radar at all wavelengths. These same fine-grained clay particles result in the low thermal inertia observed over the playa. Where the playa is overlain by small basaltic cobbles, the surface is rough at small wavelengths; it is brighter than the playa in the C band (5.6 cm) but is not as easily distinguished from the playa in the L and P bands. This surface is composed of materials with different thermal inertia values - the playa deposits have low ATI values (0.01-0.018) while the denser, darker basaltic fragments are characterized by higher ATI values (0.024-0.04). The resulting ATI of this surface is intermediate between the ATI of the two materials (0.02). One future objective is to model this site as a two component surface (fine-grained sediment with some fraction of coarser blocks) using Christensen's (1986) block abundance model.

On the Pisgah volcanic flow, it is possible to distinguish between aa and pahoehoe flow textures within the radar images; primarily within the L band image. The pahoehoe surfaces appear darker (i.e., smoother) in the P and L bands while the aa flows appear bright. This distinction is not as clear in the ATI image, although where the two surface textures can be distinguished, the aa flows do appear to have slightly

higher apparent thermal inertia values (0.03-0.04). One possible explanation for this difference is that the highly vesicular and blocky nature of the aa flows not only makes the surface very rough, but results in air pockets which tend to moderate the diurnal temperature change over the aa surface. In contrast, the smoother, denser pahoehoe flows do not contain such a high density of air pockets and thus would not exhibit this moderating air temperature effect. We plan to test for this moderating air temperature effect during future field work.

Used in conjunction, thermal and radar measurements of surficial materials can provide constraints on the bulk physical properties of the surface. General correlations between small-scale surface roughness and thermal inertia are evident at relatively pristine sites, such as the Pisgah/Lavic Lake site where surfaces have not been highly weathered or altered. The estimated and model-dependent surface properties derived from these data will be compared to field and laboratory data to test the validity of procedures used to extract surface property information. In addition, these procedures will be explored to rigorously test their sensitivity to various input parameters such as estimated composition, thermal inertia, roughness, and albedo.

#### REFERENCES

- Arvidson, R. E., and E. A. Guinness (1989) Geology remote sensing field experiment (GRSFE); abstract, this volume.
- Christensen, P. R. (1986) The spatial distribution of rocks on Mars; Icarus, 68, 217-238.
- Evans, J. V. (1969) Radar studies of planetary surfaces; Ann. Rev. of Astron. Astrophys., 7, 201-249
- Kahle, A. B., D. P. Madura, and J. M. Soha (1980) Middle infrared multispectral aircraft scanner data: Analysis for geological applications; Appl. Optics, 19, 2279-2290.
- Kieffer, H. H., T. Z. Martin, A. R. Peterfreund, B. M. Jakosky, E. D. Miner, and F. D. Palluconi (1977) Thermal and albedo mapping of Mars during the Viking primary mission; JGR, 78, 4291-4312.
- McCauley, J. F., G. G. Schaber, C. S. Breed, M. J. Grolier, V. C. Haynes, B. Issawi, C. Elachi, and R. Blom (1982) Subsurface valleys and geoarchaeology of the eastern Sahara revealed by shuttle radar; Science, 218, 1004-1020.
- Plaut, J. J., J. vanZyl, and R. E. Arvidson (1989) Radar scattering from desert terrains, Pisgah/Lavic Lake region, California; abstract, this volume.
- Price, J. C. (1972) Thermal inertia mapping: A new view of the earth; JGR, 82, 2582-2590.
- Wall, S., J. VanZyl, R. E. Arvidson, E. Theilig, and R. S. Saunders (1988) The Mojave field experiment: precursor to the planetary test site (abstract). Bull. Am. Astr. Soc., 20, 809.





CHAPTER 8

FLUVIAL, PERIGLACIAL, AEOLIAN AND  
MASSWASTING PROCESSES

PRECEDING PAGE BLANK NOT FILMED

PAGE 304 INTENTIONALLY BLANK

305



## Distinguishing the Morphology of Sapping- and Runoff-Dominated Valleys on Earth and Mars

R. Craig Kochel and Suzanne M. Orbock Miller, Department of Geology,  
Southern Illinois University, Carbondale, Illinois 62901

The origin of small valleys widespread over the Martian surface has considerable significance in the interpretation of the paleoclimatic history of Mars. If these valleys can be ascribed to runoff processes, they imply an early and dense Martian atmosphere with precipitation and a normal hydrologic cycle. Alternatively, if the valleys were formed by groundwater sapping or ground-ice break-up, then no substantial climatic evolution need be invoked. This study compares the morphometry of valley networks formed dominantly by runoff processes with those strongly influenced by groundwater sapping processes at three terrestrial analog sites in Hawaii, Arizona, and Montana and then compares the results of the analog studies to similar data collected from Viking images of valley networks along Valles Marineris and in the Margaritifer Sinus region of the ancient cratered terrain of Mars. The goal was to determine if basin morphology reflects dominant channel formative processes and if basin types could be quantitatively distinguished using spatial parameters measured from aerial imagery.

Following a field reconnaissance of terrestrial sites in the Pryor Mountains, Montana; the islands of Hawaii and Molokai, Hawaii; and the southern Colorado Plateau, Arizona, valleys were classified as sapping- or runoff-dominated systems. Sapping dominance was assigned to valleys containing significant perennial streams with large springs and active seepage alcoves in their headward tributaries. Over 20 morphometric parameters were measured for a set of 61 basins from aerial imagery at approximately 1:100,000 scale. Most of the success in distinguishing sapping and runoff basins was achieved using the following morphometric variables: 1) ratio of canyon area/ basin area (can/bas); 2) junction angle (jct angle); bifurcation ratio (Rb); 4) lemniscate shape factor (k); 5) drainage density (dd); 6) ratio of length of first order streams/ length of second order streams (l1/l2); 7) length of second order streams/ length of third order streams (l2/l3); 8) ratio of number of first order streams/ number of second order streams (n1/n2); 9) number of second order streams/ number of third order streams (n2/n3); and 10) first order channel frequency (fs1).

The results of multivariate analyses show that sapping valleys can generally be distinguished on the basis of morphology from runoff valleys in aerial imagery of terrestrial sites. Established laws of network evolution and drainage development in terrestrial runoff basins show well-organized linear relationships between basin area and channel length and channel number parameters. Similar relationships plotted for sapping-dominated basins showed much less linearity. The scatter associated with the sapping basins may be indicative of the lack of integrated surface drainage compared to that expressed by basins where inconsequential sapping is occurring. Parametric plots of dd, k, fs1, and can/bas were successful in distinguishing sapping and runoff basins. Sapping basins tend to have lower drainage density and first order stream frequency because of their extensive development of subsurface drainage systems and subsurface piracy (Fig. 1). Sapping networks also generally have higher junction angles due to the enhanced influence of structural anisotropy upon channel evolution. High junction angles are attributed to channel location along joints and/or faults because they provide avenues of preferentially high permeability for groundwater movement.

A summary of the results of principal components analysis of the 61 terrestrial basins is shown in Table 1. Eigenvector 1 (E1) explains 39% of the total variance and represents runoff (due to its high positive loading on the class variable). E1 indicates that runoff valleys have low can/bas, high dd, low jct angle, and high fs1 compared to neighboring sapping

Table 1. PCA Summary Statistics Terrestrial Basins

Eigenvectors	Eigenvalue	% Variance
E1	4.25	38.7
E2	2.23	20.3
E3	1.27	11.6
E4	1.17	10.6

Table 2. PCA Summary Statistics for Mars Basins

Eigenvector	Eigenvalues	% Variance
E1	4.816	43.8
E2	1.841	16.7
E3	1.532	13.9
E4	1.233	11.2

VARIABLES	E1	E2	E3	E4
Class	0.415	-0.081	0.339	0.184
Canyon/Basin A	-0.356	0.113	-0.44	-0.306
Drainage Density	0.39	-0.3	-0.229	-0.193
k	0.263	-0.317	-0.398	-0.112
1 1st / 1 2nd	-0.235	-0.369	-0.087	0.084
1 2nd / 1 3rd	0.126	0.271	-0.215	0.407
no. 1st / no. 2nd	-0.249	-0.451	0.093	0.42
no. 2nd / no. 3rd	-0.066	-0.051	0.522	-0.63
Bifurcation Ratio	-0.243	-0.0494	0.234	0.109
Junction Angle	-0.424	-0.074	-0.209	-0.117
1st Order Freq.	0.322	-0.354	-0.218	-0.224

VARIABLES	E1	E2	E3	E4
Class	0.438	0.047	0.021	0.007
fs1	-0.44	-0.093	0.039	-0.012
jct angle	-0.385	0.062	-0.078	0.157
Rb	-0.063	0.692	0.216	0.11
no 2/no 3	0.011	0.217	0.694	-0.307
no 1/no 2	-0.086	0.594	-0.305	0.353
1 2nd/1 3rd	-0.124	0.062	-0.452	-0.508
1 1st/1 2nd	0.022	-0.298	0.177	0.688
k	0.261	0.083	-0.367	0.112
dl	-0.431	-0.076	-0.006	0.041
can/bas %	-0.43	-0.035	0.02	-0.007

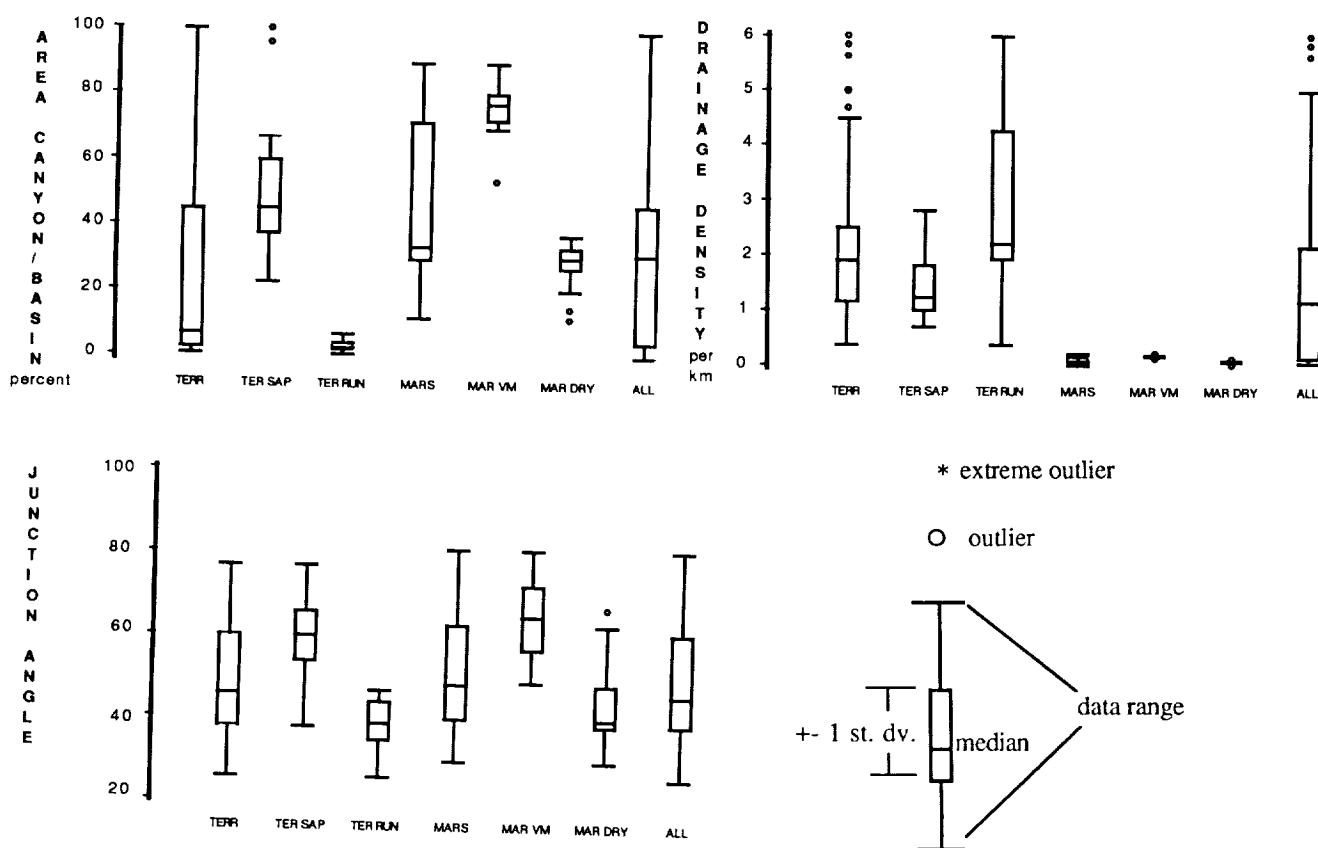


Figure 1. Examples of boxplots showing distinction in the raw morphometric data between sapping and runoff valleys and between networks on Mars.

basins. E2, which explains an additional 20% of the variance, indicates that basins with low fs1 (which tend to be sapping basins) have nearly equal numbers and lengths of first and second order channels. In addition, these basins tend to be more equidimensional in their shapes. Discriminant analysis performed on the terrestrial dataset was 100% successful in discriminating between sapping and runoff basins from their morphometry. All of the valleys interpreted in the field as sapping-dominated classified correctly, while all having little field evidence of sapping classified correctly as runoff basins. The canonical structure of the data indicates that the highest loadings occurred for the same variables which loaded heavily in the PCA analyses (can/bas, dd, fs1, and jct angle).

A wide variety of channel networks occur on Mars in addition to the enormous outflow channels (Baker, 1982). These include: 1) dry valleys with dendritic patterns occurring in the ancient cratered terrain; 2) longitudinal valleys such as Nirgal Vallis, which have long main trunk streams and infrequent, stubby tributaries; and 3) slope valleys found along the margins of Valles Marineris and on the slopes of some of the major volcanoes. Morphometric parameters were measured from Viking orbital imagery for a set of 11 slope valleys along western Valles Marineris and for 23 dry valleys located in the Margaritifer Sinus region of Mars for comparison to the terrestrial dataset. Martian slope valleys and dry valleys appeared to be quite different. The slope valleys have considerably larger can/bas, higher dd, and higher junction angles than the dry valleys.

Principal components analysis of the Mars basins showed that the parameters with high loadings were similar to those found to be useful in interpreting the terrestrial basins, namely: fs1, jct angle, dd, k, can/bas, n1/n2, l1/l2, and Rb (Table 2). Dry valleys, represented by the high positive loading in E1, are characterized by networks with low junction angles, low first order frequency, low drainage density, and low canyon/basin area. E2 shows that basins with high bifurcation ratios have large numbers of first order channels compared to higher order streams.

The discriminant function developed for terrestrial basins which successfully separated sapping and runoff basins was applied to the Martian networks. This function classified 100% of the Valles Marineris slope valleys as sapping networks, but was not successful in classifying dry valleys into either sapping or runoff categories. Dry valleys labelled runoff experienced 87% misclassification. A second discriminant analysis run on the Mars dataset alone resulted in 100% separation of the Valles Marineris valleys from the dry valleys, but it was intermediate between the terrestrial functions generated for sapping or runoff networks. Therefore, it appears that Mars dry valleys exhibit morphologies dissimilar to runoff or sapping end-members, but distinctly different than the slope valleys along Valles Marineris. These results are consistent with interpretations by Baker and Partridge (1986) which suggest that dry valleys may have formed initially by runoff processes and were later modified by sapping flows. Although these results indicate that valleys dominantly influenced by sapping or runoff processes can be distinguished on the basis of morphology, it must be emphasized that the linkages between process and morphology remain complex and uncertain. Further distinction of sapping and runoff basins on Earth using relief measures suggests that considerable refinement of the model and applicability to interpreting Mars valleys origins may be possible when detailed topographic data become available.

#### References:

- Baker, V.R., 1982, *The Channels of Mars*, Univ. Texas Press, Austin, 198p.
- Baker, V.R., and Partridge, J.B., 1986, Small Martian valleys: Pristine and degraded: *J. Geophys. Res.*, v. 91, p. 3561-3572.

## GEOTHERMAL HOT SPRINGS AS AN ALTERNATIVE HYPOTHESIS FOR SMALL VALLEY ORIGINS.

G. R. Brakenridge, Institute of Remote Sensing, Department of Geography, Dartmouth College, Hanover, NH 03755

The fluvial valley networks of Mars are commonly described as relict from an earlier warmer and denser atmosphere [*Mars Channel Working Group*, 1983; *Kahn*, 1985; *Pollack and others*, 1987]. If this inference is true, then these dry valleys constitute evidence for planetary-scale climatic change. The operation of an Earth-like hydrological cycle on Mars requires a much warmer atmosphere, and one very much denser than the 7 mbar atmosphere of today [*Pollack and others*, 1987]. Such a large amount of climatic change is most easily explained by slow or catastrophic depletion of an early dense atmosphere rich in CO<sub>2</sub> or some other greenhouse gas, and much modeling work has proceeded under the "mega-climatic change" assumption.

Calculations for ice-covered river flows on Mars [*Carr*, 1983], however, suggest that fluvial features could form at present if sustained water discharge at the surface were to somehow occur. Heat loss by conduction through modeled ice-covered rivers is slow, and latent heat is added to such systems by water freezing. Thus, the limiting factor for fluvial activity on Mars is water release, and not water persistence once discharged [*Carr*, 1983]. Such releases could be related to a formerly operating water cycle and a past denser atmosphere, but there are other alternatives: 1) solar heating and melting of dust-rich snow and ice deposited under high obliquity orbital conditions [*Jakosky and Carr*, 1987; *Clow*, 1987], and 2) geothermally heated waters reaching the surface through fractures and faults [*Brakenridge and others*, 1985; *Gulick and others*, 1988; *Wilhelms and Baldwin*, 1989]. Given these alternatives, the assumption of a dense paleoatmosphere may be in error. Cessation of valley genesis early in Mars history could be related instead to changed orbital parameters or to decreased geothermal activity.

The present research is directed at testing climatic versus geothermal causation for small valley networks by extracting the maximum possible geological and geomorphological information from Viking Orbiter imagery. Three research products are summarized here: A) a revised valley classification that explicitly includes the geological settings of the valleys; B) detailed geomorphological maps and related inferences concerning valley genesis and local volcanism and tectonism; and C) landform orientation data from specialized geomorphological maps prepared for Aeolis Quadrangle.

An earlier classification of martian valleys is based on planimetric and cross section morphology [*Brakenridge and others*, 1985]. Figure A is a modified version of that classification, and incorporates observed valley-local geology relations. The number of valley classes has been increased from five to six, and class numbers are revised to establish a size trend from smaller (classes I and II) to larger (classes III-VI) valleys.

Class I valleys (parallel slope valleys) and class II valleys (v-shaped branching valleys) occur on the flanks of large modified crater landforms or on other steep, relatively uniform slopes that are adjacent to low-albedo ridged plains. The v-shaped branching valleys are of similar dimensions and geologic setting, but branch upstream, and their upstream reaches exhibit narrow, v-shaped cross sections. Both valley morphologies commonly dissect the plateau sequence, and terminate at the margins of adjacent ridged plains.

Class III (flat-floored straight canyons) and class IV (flat-floored branching valleys) exhibit flat valley floors, and widths comparable to terrestrial river valleys of moderate to large size (5-10 km). The straight canyons are relatively short and commonly debouch at ridged plain/plateau sequence boundaries. Most exhibit dark floors that appear to be

continuous with the plains. The headward terminations of the canyons are steep, and the straight canyon walls suggest fault or fracture controls. The flat-floored branching valleys traverse hundreds of kilometers of complex plateau sequence landscapes. Large-scale circular patterns exhibited by some networks may relate to control by impact-related faults or fractures [Brakenridge and others, 1985; Gulick, 1986]; gaps between valley segments may result from post-valley faulting or from incremental valley network assembly through headward sapping. Two valley classes are not shown here, these are relatively young landforms not clearly indicative of changed conditions.

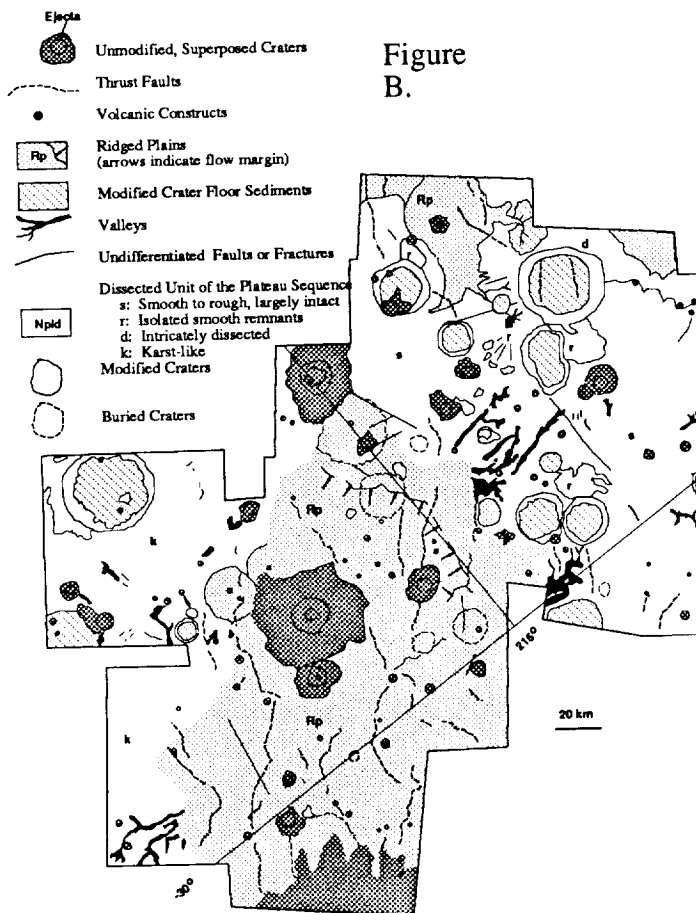
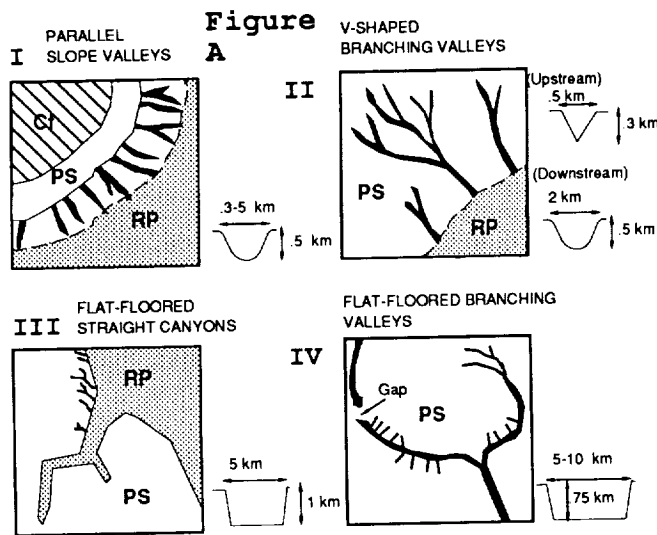


Figure B is a geomorphic map of a portion of southern Aeolis. A volcanic plain is illustrated, and also inferred thrust faults (wrinkle ridges), other faults or fractures, a prominent lava flow front within the ridged plain (arrows), flat-floored straight canyons, and small v-shaped branching valleys. The fluvial landforms are incised into plateau sequence deposits and terminate at the the ridged plain. The boundary between lava plain and the plateau sequence material is not sharp, as expected if simple overlap or embayment is involved. Instead, the boundary is irregular, and marked by collapse of the plateau sequence material (karst-like terrain).

The lava flow front is approximately parallel to the ridged plain/plateau sequence contact. However, no source areas for these lavas are visible, and the vents may be hidden beneath the modified plateau sequence materials to the west. Subsurface sill volcanism probably accompanied the extensive plains lava effusions, and may have been the direct local cause for plateau material modification and valley development through geothermal spring sapping.

In order to test for the presence of underlying structural controls on valley orientations, fluvial valleys, wrinkle

ridges (interpreted as thrust faults), and undifferentiated faults and fractures were mapped for Aeolis as a whole. The relevant descriptive statistics for the measured orientations are summarized in the table below. In computing the statistics, no weighting is used for feature lengths (short linear features are included on an equal basis with long ones), and, for gently curvilinear features, the two end points of the feature define the orientation.

Aeolis Landforms	n	Vector Mean <sup>1</sup>	Strength of Vector Mean <sup>2</sup>	Standard Error	Raleigh Test For Uniformity <sup>3</sup>
Small Valleys	264	N48W ± 12.0	0.39	6.1	0.00
Undifferentiated Faults and Fractures	83	N49E	0.19	23.1	0.05
Thrust Faults	56	N63W ± 11.2	0.75	5.7	0.00

<sup>1</sup> Vector mean is  $\arctan [X/Y]$ ;  $X = \sum \cos \Theta_i$ ;  $Y = \sum \sin \Theta_i$ ; shown with 95% confidence intervals

<sup>2</sup> Strength of vector mean is  $R/n$ , where  $R = [X^2 + Y^2]^{1/2}$

<sup>3</sup> Raleigh statistic is  $\exp [-R^2/n]$ ; for Raleigh values  $<0.05$ , the uniform vector distribution hypothesis is rejected at the 0.05 level of significance

Thus, valleys in Aeolis commonly occur in N to NW orientations; the vector mean is N48W ± 12 (95% confidence interval). The 56 inferred thrust faults exhibit quite similar orientations, with a vector mean of N63W ± 11 (95% confidence interval). The uniform distribution hypothesis for both valleys and thrust faults can be rejected at the 0.05 significance level, and the confidence intervals about both means overlap. These results are compatible with the inference that valley growth in Aeolis was affected by pre-existing or syngenetic, NW-oriented faults and/or fractures.

In summary, the Viking Orbiter-based mapping indicates that fluvial valleys in Aeolis exhibit strong preferred alignment. Such alignment is suggestive of regional structural controls over valley location. This supports the general conclusion that headward spring sapping is important in valley genesis [Pieri, 1980]. Also, evidence exists on many individual Viking frames for ancient volcanic activity near many Aeolis valleys. Probable fissure eruption ridges, exhumed lava sills, and collapsed, karst-like morphologies all occur within the fluvially dissected plateau sequence, and suggest the occurrence of extensive subsurface igneous activity. Much of this volcanism may have occurred coevally to the emplacement of the ridged volcanic plains, and, perhaps, to valley development. A possible model is that, in response to effusive volcanism in ice-rich terrains, intermittent hot spring discharges occurred at tributary valley headwalls within the plateau sequence. Such discharges then carved the valleys through a combination of down-valley fluid flows and headward erosion along the conduit faults and fractures.

#### References

- Brakenridge, G. R., Newsom, H.E., and Baker, V.R., 1985: *Geology*, v. 13, p.859-862
- Carr, M. H., 1983: *Icarus*, v. 56, p. 476-495; 1987: *Nature*, v. 326, p. 30-34
- Clow, G.D., 1987: *Icarus*, v. 72, p. 95-127
- Gulick, V., Marley, M.S., and Baker, V.R., 1988: *Abstracts, 19th Lunar and Planetary Science Conference*, Lunar and Planetary Science Institute, Houston, p. 441-442
- Jakosky, B.M., and Carr, M.H., 1987: *Nature*, v. 315, p. 559-561
- Kahn, R., 1985: *Icarus*, v. 62, p. 175-190
- Mars Channel Working Group, 1983: *Geological Society of America Bulletin*, v. 94, p. 1035-1054
- Pieri, D.C., 1980: *Science*, v. 210, p. 895-897;
- Pollack, J.B., Kasting, J.F., Richardson, S.M., and Poliakoff, K., 1987: *Icarus*, v. 71, p. 203-224;
- Wilhelms, D.E., and Baldwin, R.J., 1989: *Proceedings of the 19th Lunar and Planetary Science Conference*, Lunar and Planetary Science Institute, Houston, in press.



## MORPHOMETRY OF PLANIMETRIC LANDFORMS

Alan D. Howard, Department of Environmental Sciences, University of Virginia, Charlottesville, VA 22903

Many landforms are well characterized by their planimetric outlines. Examples include the outlines of escarpments and deep valleys, the shorelines of islands or lakes, the edges of basalt flows, drumlins, fluvial islands, some dune types, meteoric impact basins, tectonic basins and collapse depressions (sinkholes, periglacial alases, etc.). In some cases, such as remotely sensed images of planets and satellites, little other information is available. A suite of statistical measures of planform geometry are introduced below for landforms that exhibit systematic features but which display considerable superimposed irregularity. These techniques are applicable to both closed forms (e.g. islands or buttes) and open forms (many escarpments, valley systems, local shorelines, etc.).

Several types of spatial "time" series analysis are defined and are generally applicable to any "wiggly" line. They start from an outline of the landform digitized with a constant step length that is short enough to accurately portray the smallest features of the planform that are of interest (or are resolvable). Several statistical measures are made directly from the digitized trace. Each successive three points, or nodes, defines a local trace curvature at the central node. The first four statistical moments are calculated for the curvatures of the trace. The spectrum of the direction series is also calculated, and characterized by the wavelength of the spectral peak, the average period, and the standard error of the spectral variance. The curvature or direction series can also be examined for regularity by fitting of low-order ARMA models [1].

Another time series technique involves separation of the trace into "runs" of nearly constant curvature, similar to [2]. A run is terminated and a new run started when the absolute value of the difference between the next curvature in the series and the cumulative average curvature of the run exceeds a pre-assigned critical value. The runs can be statistically characterized by their length, their average curvature or cumulative direction change, and sense (left- or right-bending) as well as the magnitude and direction of change between runs. The analysis can also be conducted for different thresholds of curvature change.

An additional method models the scarp as a time series of curvature values characterized by stochastic disturbances of a small set of the individual curvature values by large deviations drawn from a normal population. The curvature values between these disturbances are modeled as decaying exponentially from the disturbed values. This gives a three-parameter model, where the parameters measure 1) the magnitude of the large disturbances, 2) the linear density of the disturbances, and 3) the rapidity of lateral decay of the disturbances. Statistical estimates of the model parameters are used to characterize the scarps.

The remaining procedures employ successive generalization of the original curve. The first method (termed here "path-cutting") employs a uniform "caliper" that walks along the curve, creating a new series of nodes (Figure 1) defined by the successive closest intersections of the original trace (including the straight-lines between the digitized points) with the caliper. The length of the generalized trace is also measured, and if the original curve is closed, the enclosed area and a shape factor (area divided by the square of the length) are also determined. The initial caliper length is twice the original digitizing interval, and successive generalizations of the original trace are made, with the caliper increasing in length by factors of two.

The second technique ("convex-stepping") also uses a caliper, but employed differently. The caliper is centered on a node and rotated counter-clockwise (assuming the inside of the landform lies to the left side when moving from the beginning to the end of the trace), starting from the direction pointing toward the node preceding the present node. When the rotating line defined by the caliper points first intersects a node on the original curve, that intersected node becomes the next node on the generalized curve, and the process is repeated from the new node. Where the generalized curve creates shortcuts between two non-successive nodes on the original curve (Figure 2), a valley is defined. Each valley can be characterized by its area, length (the length is defined as the longest perpendicular distance from a node on the original curve to the short-cutting line), and perimeter, which includes the short-cutting line segment. Shape factors can also be calculated. As with the previous technique, the caliper length is incremented by successive factors of two, with valley statistics being collected for each

generation of caliper length. Eventually, for a long-enough caliper, the generalized curve becomes completely convex relative to the landform inside (Figure 2).

A similar curve generalization can be made by rotating the caliper in the opposite sense, interior to the landform. This generalization defines headlands, or projections, which can also be measured by length, area, shape and perimeter.

The convex stepping approach has similarities to fractal modeling of form outlines [3-7], which assumes that a path develops by successive generations of elaboration of an original curve, either regularly or stochastically. The valleys or headlands defined by a path-cutting caliper can be considered to be a kind of elaboration of the generalized curve.

Several measures were devised to gauge orientation effects introduced by structural influences (joints, faults, etc). Each valley and each unit step along the landform profile is characterized as a vector and summarized into orientation categories. Several types of statistical parameters are defined based upon the orientation data, including landform asymmetry.

These above techniques yield a vast amount of raw information that must be summarized by statistical parameters. The first level of generalization employed here is to summarize the valley and headland lengths, areas, and perimeters (and derivative width and shape parameters) by size classes. The amount of information is still vast, since it is measured for a range of caliper lengths. To condense this data further, the values of the several parameters are examined as a function of the logarithm of the caliper length. Most parameters, or their logarithms, increase fairly regularly with caliper length, so that their behavior can be characterized by their rate of change, or slope, with respect to the caliper, and their intercept at a particular caliper length. Some parameters (particularly those related to valley shape) show a maximum or minimum at a particular caliper length. Such parameters can be characterized by their extreme value plus the caliper length of the minimum or maximum. Similarly, other parameters exhibit a maximum rate of change at a particular caliper value. Parameters showing a maximum, minimum, or maximum rate of change are also useful in defining a natural scale measure, or "metric", that is presumably independent of the digitizing length. This metric can be used to normalize parameters, such as curvature, that have a characteristic length dimension.

These parameters have been used to comparing terrestrial scarp and valley systems though to originate by scarp backwasting, sapping processes, and fluvial incision, as well as theoretical models of these processes. The suite of parameters has a high ability to discriminate between scarps formed by different processes. Figure 3 shows the use of the database to perform a discriminant analysis between various simulation models of scarp evolution [8] as well as a parallel classification of terrestrial scarps. The analysis is able to discriminate between the different types of scarps primarily using one function (Discriminant Function 2). A set of natural meandering streams [9] was included in the sample to test the ability of the morphometric approach to isolate these from the various types of escarpments. The other function (Discriminant Function 1) is primarily devoted to (convincingly) separating these streams from the scarps, thereby demonstrating the sensitivity of the measured variables to natural form variations. The same techniques are presently being applied to Martian scarps.

## REFERENCES

- [1] Box, G., and Jenkins, G.M., 1976, *Time Series Analysis: Forecasting and Control*, Holden-Day, Oakland, 575 p.
- [2] O'Neill, M.P., and Abrahams, A.D., 1986, Objective identification of meanders and Bends, *Journal of Hydrology*, 83, 337-353.
- [3] Mandelbrot, B.B., 1983, *The Fractal Geometry of Nature*, Freeman, New York, 468 p.
- [4] Pietgen, H., and D. Saupe, eds., 1988, *The Science of Fractal Images*, Springer-Verlag, New York, 312 p.
- [5] Anderle, R., and A.D. Abrahams, 1989, Fractal techniques and the surface roughness of talus slopes, *Earth Surface Processes and Landforms*, 14, 197-209.
- [6] Goodchild, M.F. and D.M. Mark, 1987, The fractal nature of geographic phenomena, *Annals Assoc. Amer. Geogr.*, 71, 265-278.
- [7] La Barbera, P. and R. Rosso, 1989, On the fractal dimension of stream networks, *Water Resources Res.*, 25, 735-741.

- [8] Howard, A.D., 1989, Simulation models of scarp and valley development, *[This Volume]*.  
 [9] Howard, A.D., *in press*, Multivariate characterization of meandering, *Geomorphology*.

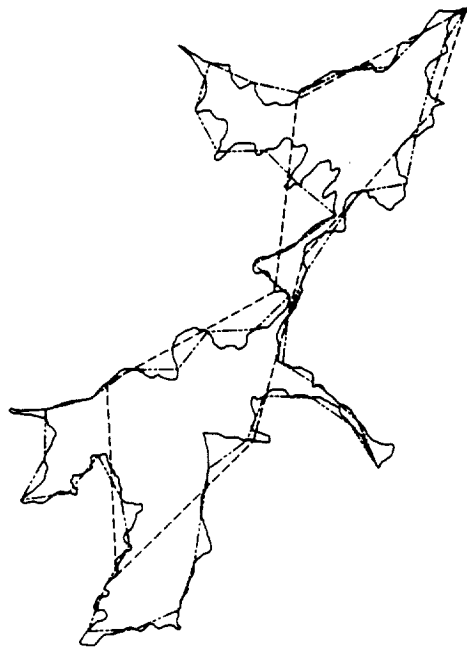


**Figure 1.** An escarpment outline is shown in solid line, and successive path-cutting generalizations in patterned lines.

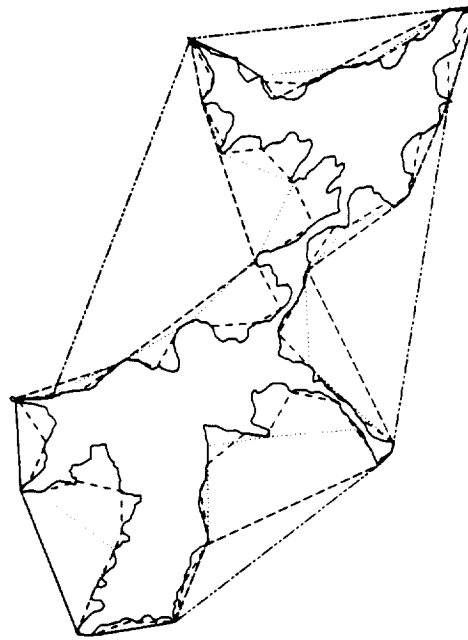


**Figure 2.** Successive convex-stepping generalizations of a scarp. Similar generalization can be done within the interior.

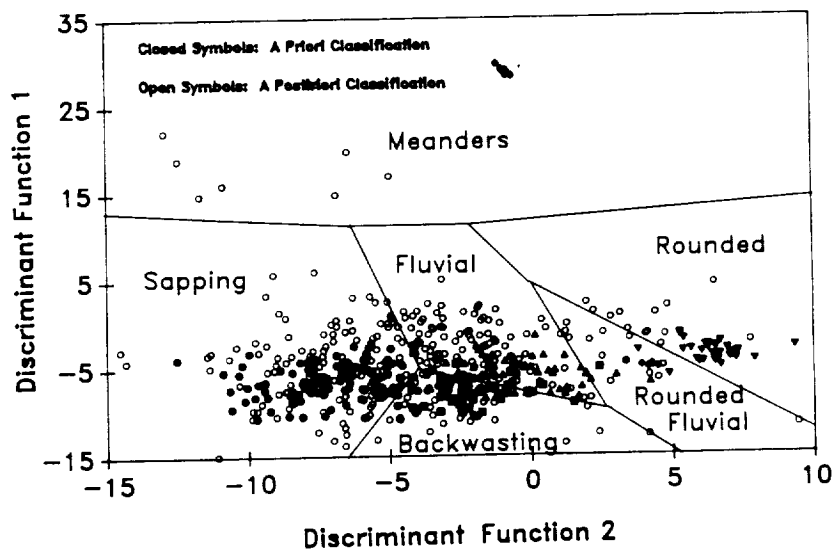


**Figure 3.** Discriminant classification of natural and simulated scarps and stream meanders.

## FLUVIAL PROCESSES: TOWARD A MARTIAN PARADIGM

Victor R. Baker, Department of Geosciences and Department of Planetary Sciences, University of Arizona, Tucson, Arizona 85721; and Virginia C. Gulick, Department of Geosciences, University of Arizona, Tucson, Arizona 85721.

The scientific study of channels and valleys on Mars was initiated with the acquisition of Mariner 9 images in 1971-72. Following this discovery, studies proceeded in three phases [1]: (a) early work relating morphological attributes to probable causes, (b) the development of explanatory models for causative systems identified in phase (a), and (c) revisionist work based on comparisons of model implications to details of planetary morphology. Much of the research has been guided by analogies with fluid systems on Earth, the only other planet besides Mars that seems to have exhibited a dynamic hydrological cycle.

As Martian fluvial geomorphology has moved into its revisionist phase, it has become apparent that Martian channels and valleys exhibit unusual attributes, at once strangely similar to Earth forms but also uniquely Martian. The Martian outflow channels, for example, display a complex of morphologies most consistent with cataclysmic flooding as a single explanation [2, 3, 4]. However, local sections of channel display depositional forms similar to those produced by debris flowage [5] and erosional forms similar to those produced by glaciation [6, 7].

As various models of channel-forming processes have been matched to available morphological data on Mars, we have identified some probable effects of the Martian environment of low atmospheric pressure, low temperatures, and low gravity in comparison to Earth. Water for outflow channel formation was probably released both as outburst floods and as slower seepage from subsurface reservoirs. Many channels seem to have grown headward by collapse of surface layers as fluid was removed. Present zones of chaotic terrain are probably the last vestige of such headward growth, in which the youngest flows eroded away downstream elements of collapse morphology.

The surface water encountered a low-pressure environment that favored cavitation in high-velocity flood flows [8]. Rock resistance to erosion was critical in determining sediment concentration. At low sediment concentrations flood flows would be macroturbulent, enhancing scabland erosion processes [8]. Erodible materials, however, would be readily entrained. The combination of low gravity and high stream power [9] could yield extremely high sediment concentrations in Martian floods [10]. The enhanced capacity might easily lead to transitional behavior to hyperconcentrated streamflow, inertial slurries, and inertial granular flows (terminology of Pierson and Costa [11]). Mobilized sediment was probably emplaced as widely distributed deposits in the northern plains [12, 13], and temporary water bodies of regional extent seem likely at times of outburst flooding.

Outflow flooding probably also engendered considerable ice-related activity. Transitions from water to frazil ice to surface ice sheets and ice drives are likely to have occurred in cataclysmic outbursts [8], while local freezing to ice masses may have occurred for slower seepage [7]. Although not strictly glaciers by definition, such transient, seepage-fed ice masses might, in theory, move by plastic flow and be intimately associated with ponded and released water floods.

The movement of sediment-laden water undergoing freezing would locally emplace ice-rich sedimentary deposits. Subsequent sublimation of interstitial ice might lead to exotic erosion of the fluvial sediments, as observed on the northern plains and in Mangalla Vallis.

Martian valley networks also have unusual attributes. The assumption that Martian valleys form by Earth-like rainfall-runoff processes has led to theoretical models of early atmospheric evolution, deducing a warm, wet paleoclimate from the primordial development of a dense CO<sub>2</sub> atmosphere [14, 15]. However, in conflict with this scenario is the remarkably low drainage density of Martian valleys [16] and abundant evidence for a sapping origin of the more ancient valley networks. Sapping may be facilitated by the endogenetic mechanism of hydrothermal circulation [17, 18] rather than the exogenetic mechanism of rainfall and recharge.

The most Earth-like valley networks on Mars occur locally on the northern flank of Alba Patera [19, 20], a volcano of Amazonian age. The Alba valleys have morphologies consistent with possible formation by surface rainfall-runoff processes, but the valleys are much too young for explanation by the model of a primordial planet-wide denser atmosphere.

The Alba valleys and those on other Martian volcanoes [21, 22] do show similarities to Earth analogs, including comparable drainage densities to the dry, leeward side of Hawaiian volcanoes [22]. The surface drainage development is facilitated by reducing infiltration into the bedrock through the emplacement of an ash mantle. Local water sources on Mars might include hydrothermal activity, both as hot spring discharge and as spot influxes of steam to the atmosphere. Water would be derived from and returned to subsurface reservoirs of ground ice that are inferred from many kinds of geomorphological evidence [23].

Because outflow channel activity occurred approximately coincident with the development of the Alba valleys, it is possible to hypothesize a connecting scenario. For present topographic constraints [24], the minimum amount of water estimated for outflow channel erosion [25] could have formed a temporary body of water on the northern Martian plains with an average depth of 660 m and a surface area of  $1.2 \times 10^7$  km<sup>2</sup>. The prevailing winds off this temporary "ocean" could have moved saturated air to Alba Patera, where precipitation on the rising volcano flanks would rapidly infiltrate the permeable rocks. Locally, however, ash mantling probably facilitated the development of rainfall-runoff valleys.

The widespread ancient valleys of the heavily cratered terrains can also be explained by local heating of ground ice, resulting in hydro-thermal systems driven either by impact [17, 26] or volcanic mechanisms [27, 18]. Unless this cause can be eliminated as a mechanism of Martian valley formation, models of denser primordial atmospheres will not be necessary to explain valley development on Mars.

- REFERENCES. [1] Baker, V.R. in Models in Geomorphology (ed. M. Woldenberg) 287-312 (Allen and Unwin, London, 1985). [2] Baker, V.R. & Milton, D.J. Icarus 22, 27-41 (1974). [3] Baker, V.R. The Channels of Mars (Univ. Texas Press, Austin, 1982). [4] Mars Channel Working Group Geol. Soc. America Bull. 94, 1035-1054 (1983). [5] Nummedal, D. & Prior, D.B. Icarus 45, 77-86 (1981). [6] Lucchitta, B.K., Anderson, D.M. & Shoji, H. Nature 290, 759-763 (1981). [7] Lucchitta, B.K. J. Geophys. Res. 87, 9951-9973 (1982). [8] Baker, V.R. J. Geophys. Res. 84, 7985-7993 (1979). [9] Baker, V.R. & Costa, J.E. in Catastrophic Flooding (eds. L. Mayer and D. Nash) 1-21 (Allen and Unwin, London, 1987). [10] Komar, P.D. Icarus 42, 317-329 (1980). [11] Pierson, T.C. & Costa, J.E. in Debris Flows/Avalanches: Process, Recognition, and Mitigation (eds. J.E. Costa and G.F. Wieczorek) 1-12 (Geol. Soc. America, Boulder, 1987). [12] McGill, G.E. Lunar and Planet. Sci. Conf. XVI, 534-535 (1985). [13] Lucchitta, B.K., Ferguson, H.M. & Summers, C. J. Geophys. Res. 91, E166-E174 (1986). [14] Pollack, J.B. & Toon, O.B. Icarus 50, 259-287 (1982). [15] Pollack, J.B., Kasting, J.F., Richardson, S.M. & Poliakov, K. Icarus 71, 203-224 (1987). [16] Baker, V.R. & Partridge, J.B. J. Geophys. Res. 91, 3561-3572 (1986). [17] Brakenridge, G.R., Newsom, H.E. & Baker, V.R. Geology 13, 859-862 (1985). [18] Gulick, V.C., Marley, M.S. & Baker, V.R. Lunar and Planet. Sci. XIX, 441-442 (1988). [19] Gulick, V.C. & Baker, V.R. Lunar and Planet. Sci. XVIII, 639-640 (1987). [20] Gulick, V.C. & Baker, V.R. in Fourth Int. Mars Conf. 121-122 (Tucson, Arizona, 1989). [21] Baker, V.R. N.A.S.A. Tech. Memo. 88383, 414-416 (1986). [22] Gulick, V.C. M.S. Thesis (Dept. Geosciences, Univ. Arizona, Tucson, 1987). [23] Carr, M.J. Nature 326, 30-34 (1987). [24] Wu, C.S. N.A.S.A. Tech. Memo. 88383, 614-617 (1986). [25] Carr, M.J. Icarus 68, 187-216 (1986). [26] Schultz, P.K., Schultz, R.A. & Rogers, J. J. Geophys. Res. 87, 9803-9820 (1982). [27] Wilhelms, D.E. Lunar and Planet. Sci. XVII, 946-947 (1986).

## SIMULATION MODELS OF SCARP AND VALLEY DEVELOPMENT

Alan D. Howard, Department of Environmental Sciences, University of Virginia, Charlottesville, VA 22903

The Mariner and Viking missions have revealed widespread occurrences of valley systems and scarps of diverse morphology on Mars. A variety of processes have been suggested to have created these features, including faulting, subsidence due to permafrost melting, fluvial erosion, landsliding, liquifaction, and sapping erosion. Many of these martian landforms have been shown to have morphometrically similar terrestrial analogs. However, the comparison of martian and terrestrial features is hampered by several difficulties: 1) Morphometric comparisons have generally been qualitative or have employed rudimentary morphometric parameters; 2) Two or more terrestrial processes may produce similar landforms; 3) The processes responsible for the terrestrial analogs may be uncertain or the evidence circumstantial, in large part due to the slowness or sporadic occurrence of the formative processes (for example, the evidence for the role of groundwater sapping in creating the valley systems on the Colorado Plateau [1,2] is largely circumstantial); and 4) Appreciable scale differences may be present between the martian landform and its presumed terrestrial analog.

**The Present Approach:** Laboratory experimentation and theoretical modeling offer more fundamental methods to inter-compare surface processes and their morphological products. Theoretical approaches offer the advantage of being able to numerically scale processes and material properties. In addition, temporal and spatial boundary conditions can be arbitrarily varied. However, theoretical modeling is limited to circumstances where the physical processes are understood and may be compromised by numerical errors or inadequacies of model structure. Theoretical models are reported below that simulate development of scarps and valley systems in layered rocks by scarp undermining, sapping erosion, and fluvial erosion. Three types of theoretical models have been developed to date: *scarp backwasting*, *fluvial downcutting*, and *groundwater sapping*.

**Scarp Backwasting:** Layered sedimentary or igneous rocks of diverse erosional resistance are nearly universally eroded into escarpments capped by resistant layers and bordered by cliffs created by lateral undermining of the resistant layer by erosion of an underlying weaker layer. Several processes may be involved in the undermining, including weathering and erosion of the weak layer, which trigger rockfalls or landslides in the superjacent resistant layer. The rate of backwasting depends upon several factors, including the weatherability of the weak layer, the steepness and height of the scarp, and the ease of weathering and erosion of caprock debris.

A simple first-order numerical model of scarp backwasting lumps these factors into a single "erodibility", which is assumed to vary randomly from location to location. The erodibility is assumed to be self-similar, or fractal, with variations at both large and small scales. The spatial variability of erodibility is characterized by three parameters, an average value, a variance, and a rate of change of variance with scale. The rate of lateral backwasting is assumed to be linearly dependent upon the erodibility. Figure 1 shows a plan view of successive scarp positions starting from a square "mesa". *Scarps produced by this type of backwasting are characterized by sharply terminating projections and broad reentrants, with reentrants produced by erosion through more erodible rocks.*

*In some cases the projections of natural scarps are rounded rather than sharply pointed. This suggests that the lateral erosion rates on the projections are enhanced relative to straight or concave portions of the scarp.* Several mechanisms may account for this. The rate of erosion of many scarps is limited by the rate that debris shed from the cliff face can be weathered and removed from the underlying rampart on the less resistant rocks. Debris from convex portions of scarps (projections) is spread over a larger area of rampart, so that weathering rates may be enhanced. Another mechanism leading to enhanced erosion rates of projections is that they commonly stand in higher relief than reentrants, leading to longer and/or steeper rampart. Finally, some scarp caprock may be eroded by undermining due to outward creep or weathering of the rocks beneath the caprock. Both processes are enhanced at convex scarp projections. Figure 2 shows a model scarp in which backwasting rates are enhanced by scarp convexity and restricted by concavity, and Figure 8 shows a similar natural scarp.

**Fluvial Downcutting:** Most natural escarpments exhibit more pronounced reentrants than are created by pure scarp backwasting. One process creating such reentrants is downcutting by streams originating on the top of the escarpment and which pass over the front of the escarpment. This is

numerically modeled by superimposing a stream system onto the simulated scarp and allowing it to downcut through time. If a resistant layer is present, the stream develops a profile characterized by a low gradient section developed upon the top of the resistant layer and a very steep section (rapids or falls in natural streams) which rapidly cuts headward. Erosion is assumed to be proportional to the product of the bed erodibility and the average channel bed shear stress. Figure 3 shows a simulated scarp eroded both by fluvial downcutting and scarp backwasting, and Figure 4 is similar but with convexity-enhanced scarp backwasting. Figures 9 and 10 are natural scarps similar to Figures 3 and 4, respectively. *Scarp morphology is similar to that produced by scarp backwasting, with the addition of several deep reentrants characterized by a gradually narrowing width and projections that are sharply-pointed in the linear case and rounded in the convexity-enhanced case.*

**Groundwater Sapping:** Strong evidence suggests that groundwater sapping is an important agent of backwasting of certain southwestern U.S. escarpments, with the suggestion that similar scarps and valley systems on Mars have been eroded by similar processes [1,2]. A simulation model of scarp backwasting by groundwater sapping assumes a planar caprock aquifer (that may be tilted) with uniform areal recharge and a self-similar areal variation in permeability. The rate of sapping backwasting,  $E$ , is assumed to depend upon the amount by which the linear discharge rate at the scarp face,  $q$ , exceeds a critical discharge,  $q_c$ :  $E = K (q - q_c)^a$ , where  $a$  is an exponent. Scarp erosion is simulated by solving for the groundwater flow, eroding the scarp by a small amount, with repeated iterations. Figure 5 shows a simulated scarp with  $q_c=0$  and  $a=1$ . Figure 6 shows a case with  $q_c=0$  and  $a=2$ . Figure 7 shows a case with  $q_c=0$ ,  $a=2$ , and superimposed scarp backwasting. Figure 11 is a natural scarp in Navajo Sandstone thought to be formed largely by sapping [2]. *Valleys developed by groundwater sapping tend to be linear or crudely dendritic, with nearly constant width, and rounded rather than sharp terminations.*

#### REFERENCES:

- [1] Laity, J.E. and Malin, M.C., 1985, *Bull. Geol. Soc. Am.*, **96**, 203-217
- [2] Howard, A.D. and Kochel, R.C., 1988, *Sapping Features of the Colorado Plateau*, NASA SP-491, Ch 2.

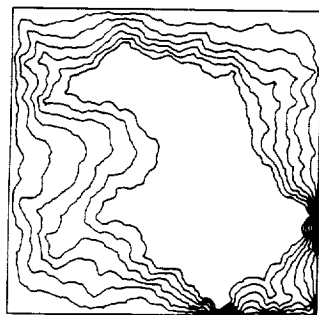


Figure 1.

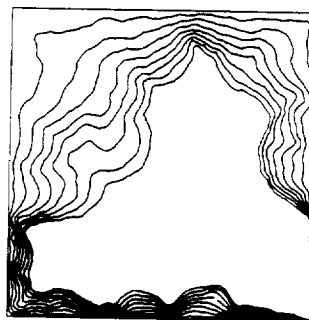


Figure 2.

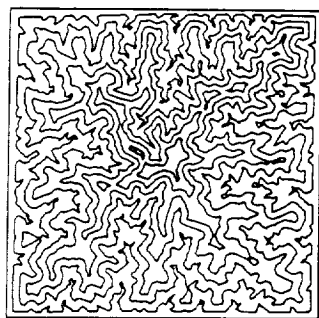


Figure 3.

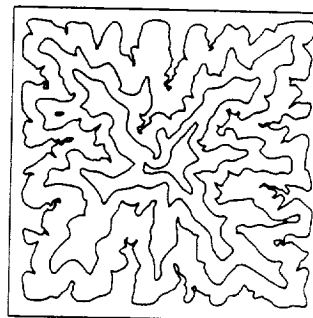


Figure 4.



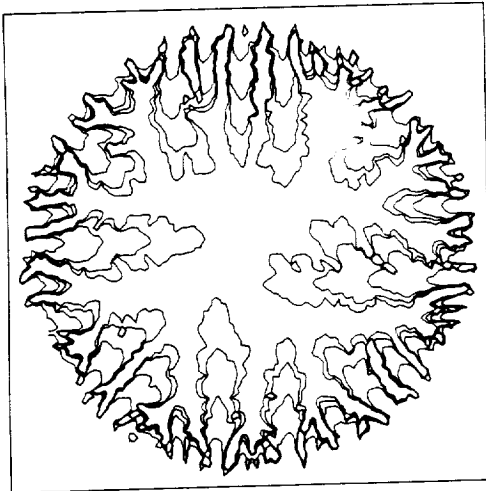


Figure 5.

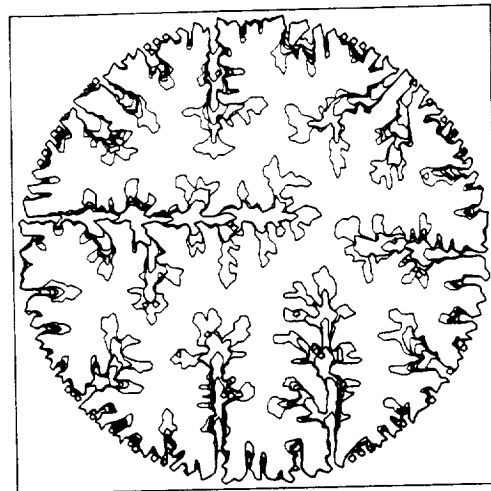


Figure 6.

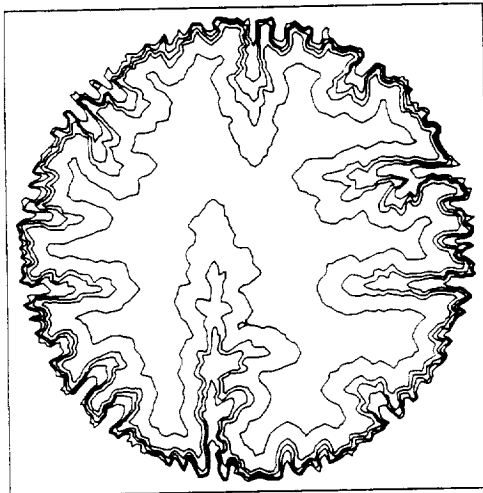


Figure 7.

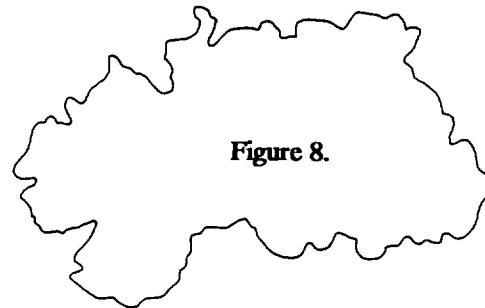


Figure 8.

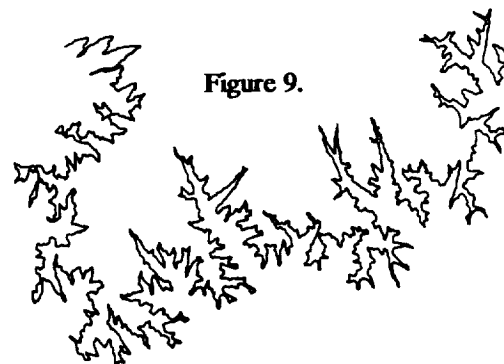


Figure 9.

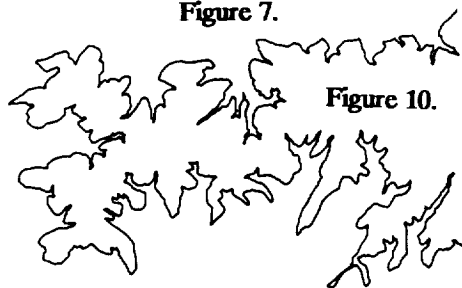


Figure 10.

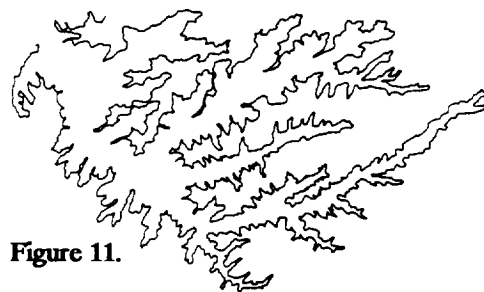


Figure 11.

## AN UNUSUAL MARTIAN CHANNEL

David H. Scott and Mary G. Chapman, U.S. Geological Survey, Flagstaff, Arizona 86001

Fluvial channels on Mars are commonly referred to as either "outflow" or "valley system" channels (1,2,3,4). Both types were initiated by different processes and at different times in Martian history. Their morphologic characteristics are distinctive. Outflow channels and their floodplains cover broad areas, extend for hundreds of kilometers, and contain streamlined bars and island remnants. The channels were carved by catastrophic floods (5,6) that probably originated from ground-ice melt waters within faulted, collapsed, or chaotic terrains in highland regions. Most outflow channels range from Hesperian to Amazonian in age (7,8,9). Valley system channels form narrow, sinuous networks that lace the ancient highlands around large crater rims and hilly, mountainous regions. Some investigators consider valley system channels to be very old (Noachian) because of their concentration in cratered highland regions (1,2,3,10). However, small channels are difficult to date by stratigraphic or crater count methods; they may have a very wide age range from Noachian to Amazonian (7,8,9). Valley system channels may have been produced by precipitation from a warmer and more dense Martian atmosphere (8,11).

Geologic studies of the Memnonia region of Mars using high-resolution Viking images has revealed a narrow, very young (Amazonian) channel that has the morphologic attributes of large outflow channels yet compares in size with many small valley system channels. Photoclinometric profiles show that the channel gorge is relatively deep (80 m) with respect to its width (1.0 km). At its terminus the channel fans out to form a broad discharge area with distributaries that enclose streamlined bars or islands. Unlike other Martian channels, its source area is in the lowlands where the upper reaches of the channel closely follow the contact between the Medusae Fossae Formation of Amazonian age and Hesperian ridged plains material (7). The Medusae Fossae Formation is postulated to consist of a series of ash-flow tuffs (7,12). Within the apparent source area of the channel, hummocky disintegrated material grades into the base of the lower member of the Medusae Fossae Formation. This hummocky terrain may have been produced by the melting of near-surface ground ice and release of water where the hot ash flow over-rode the ridged plains material. Other possible sources for the water that carved the channel are possible, but difficult to envisage. Similar type channels may exist, but their detection will depend upon the examination of high-resolution Viking images.

### References

- (1) Sharp, R.P., and Malin, M.C. (1975), *Geol. Soc. Am. Bull.*, 86, 593-609.
- (2) Pieri, D. (1980), *Science*, 210, 895-897. (3) Carr, M.H., and Clow, G.D. (1981), *Icarus*, 48, 91-117. (4) Squyres, S.W. (1987), *Mars Sample Return Science Workshop*, 129-130. (5) McCauley, J.F. et al. (1972), *Icarus*, 17, 289-327. (6) Baker, V.R., and Milton, D.J. (1974), *Icarus*, 27-41. (7) Scott, D.H., and Tanaka, K.L. (1986), *U.S. Geol. Sur. Misc. Inv. Ser. Map I-1082A*.
- (8) Masursky, H. et al. (1977), *JGR*, 82, 4016-4038. (9) Masursky H. et al. (1987), *LPSC*, 18, 600-601. (10) Baker, V.R., and Partridge, J.B. (1986), *JGR*, 91, 3561-3572. (11) Leighton, R.B., and Murray, B.C. (1966), *Science*, 153, 136-144. (12) Scott, D.H., and Tanaka, K.L. (1982), *JGR*, 87, 1179-1190.

**RELEASE OF MARTIAN CATASTROPHIC FLOODS BY FRACTURE DISCHARGE FROM VOLCANOTECTONIC REGIONS;** Kenneth L. Tanaka and David J. MacKinnon, U.S. Geological Survey, 2255 N. Gemini Dr., Flagstaff, Arizona 86001

Carr [1] proposed that catastrophic floods produced Martian outflow channels through discharges from highly permeable, confined aquifers made up of brecciated lava flows. On the basis of a study of impact fracturing, we think that fractured basement (probably mafic igneous) rocks have even greater permeabilities than brecciated lava flows [2]. Here we present topographic, structural, and other geologic evidence that indicate that a group of outflow channels were formed by catastrophic release of water from open fractures as a result of volcanotectonic activity.

Our model for Martian crustal hydraulic properties [2] is based on fracture and ejecta distributions generated during heavy bombardment. We suggest that Martian basement rocks broken by impacts may have fracture porosities as high as 10 to 20% and permeabilities of  $10^6$  to  $10^7$  darcies; these values greatly exceed those of porous sedimentary rocks. The discharge rate of water through fractures is a function of water viscosity, fracture density and width, hydraulic gradient, and flow turbulence. The fractured basement generally is covered by poorly sorted ejecta material having low inherent permeability that may be further reduced by freezing of interstitial water (as proposed by Carr [1]).

For outbreak to occur, pore-water pressure in the fractured basement rocks must exceed hydrostatic (i.e., artesian) conditions. Given this, we visualize two principal release mechanisms [2]. First, pore pressure buildup in the fractured zone until it exceeds the overburden pressure of confining deposits and outbreak occurs, similar to the model of Carr [1]. Because of the high permeability, fracture discharges would be sudden, widespread, and short-lived. Chaotic terrain, debris flows, and hyperconcentrated floods may initially be generated, as ejecta material is eroded away, followed by less sediment-charged floods as channels formed. Such outbreaks may explain most chaotic and channeled terrains south of Chryse Planitia and north and east areas of the Valles Marineris region [1].

The second release mechanism is to rupture the confining layer above the fractured basement rocks. Mechanical models for extensional fracturing in the Martian crust indicate that tension cracks may have formed in basement rock to relieve tectonic stresses, resulting in fracturing and collapse of the confining rocks [3]. Initial discharges would be accompanied by rapid erosional enlargement until catastrophic discharges were attained. The most propitious sites for such discharge would be where cracks are aligned with the dip direction of the permeable strata. On Mars, areas of tectonic uplift have produced raised, outward-dipping strata commonly cut by radial fractures.

We identify five areas of fracturing near volcanotectonic rises [4] that served as sources of Martian outflow channels. Surface gradients along the proposed source fractures and maximum lengths and rises of the fractures in terrain adjacent to the breakout (including sections that may be buried) are shown in Table 1. Each of the examples appears to be connected hydraulically by fracturing to large elevated areas of the Tharsis, Valles Marineris, and Elysium rises. (1) The fractures at Mangala Valles originate from a graben of Memnonia Fossae [5] that radiates from the vicinity of Arsia Mons; the point of discharge is in a regional trough. (2) Shallow channels emanate from some fractures of Sacra Fossae that cut a large mesa of ridged plains material in lower Kasei Valles. These fractures are eroded into V-shaped grooves of varying widths; they do not have the flat floors as do nearby grabens. The

fractures, which are oriented radial to Tharsis, have been interpreted to be joints [3]. The original plateau surface west of the fractures has been removed by Kasei Valles erosion, and so the gradient (Table 1) estimate was based on plateau surfaces to the north and south. (3) West of Gangis Chasma, two small outflow channels originate from large pits. These pits are at the end of a chain of widely separated pits that ends at Candor Chasma. The pits may have been formed by surface collapse in rocks above buried tension cracks [3]. Enlargement of fractures and pit formation at some channel sources may have occurred by piping (in which poorly consolidated material is eroded away by the discharging water). (4) Confined outflow channels in Utopia Planitia were discharged from Elysium Fossae along the periphery of flows from Elysium Mons. This periphery forms a distinct boundary between relatively flat plains and the sloping Elysium rise. (5) The youngest known outflow channel on Mars appears to originate from the west ends of two main fractures of Cerberus Rupes on the southeast flank of the Elysium rise [6]. These long, curvilinear fractures are radial to the southern part of the rise.

Although local stratigraphic controls vary in precision, it is possible that fracturing and discharge were coeval in each case. Most of the examples are late Hesperian to early Amazonian in age, when volcanotectonic activity at each of these areas was intense [7]. A late pulse of activity is associated with the Late Amazonian Cerberus Rupes channel, when Cerberus Rupes and possibly some volcanic rocks on Elysium Mons formed [8]. Most Martian valley networks, however, are Noachian in age and originate in ancient cratered terrain [7]. We speculate that the Noachian climate was warm enough to enable ground water to exist in near-surface materials, whereas by early Hesperian time the frozen ground proposed by Carr [1] developed. Uplift or hydrothermal circulation owing to igneous activity then produced local, artesian heads in rocks below the frozen ground at the periphery of volcanotectonic rises. The artesian conditions were probably short-lived; we have not found examples where impact fracturing has caused outbreak (although some relatively young outflow channels originate from ancient craters). Rather, outbreak ensued where the aquiclude was ruptured by tectonic fracturing.

## References

- [1] Carr M.H. (1979) JGR, v. 84, p. 2995-3007.
- [2] MacKinnon D.J. and Tanaka K.L. (unpublished data).
- [3] Tanaka K.L. and Golombek M.P. (unpublished data).
- [4] Wu S.S.C. and others (unpublished data) 1:15M topo map of Mars.
- [5] Carr M.H. (1981) The Surface of Mars, Yale Univ. Press, Fig. 10.15.
- [6] Tanaka K.L. and Scott D.H. (1986) LPSC 17 abstracts, p. 865-866.
- [7] Tanaka K.L. (1986) PLPSC 17, JGR, v. 91, p. E139-E158.
- [8] Tanaka K.L. and Scott D.H. (1987) LPSC 18 abstracts, p. 998-999.

**TABLE 1. The surface gradients of proposed source fractures and maximum lengths and rises of fractures in areas near volcanotectonic rises.**

Source	Gradient (rise/length)	Maximum length (km)	Maximum rise* (km)
Memnonia Fossae --east	1/250	1500+	5+
(Mangala Valles) --west	1/200	200	1
Sacra Fossae (Kasei)	1/400-500	500+	1+
Pits west of Gangis Chasma	1/250-300	600-800	3
Elysium Fossae	1/80	400-500	5+
Cerberus Rupes	1/350	700	2

\*Accuracy varies from a few hundred meters to about one kilometer.

The Eastern Lunae Planum Outflow Complex (1,2,3) extends from chaotic terrain of Juventae Chasma ( $-2^{\circ}$ ;  $62^{\circ}$ ) northward along the Lunae Planum--Xanthe Terra contact. Eleven hundred Kilometers to the north it turns eastward across Xanthe Terra and onto Chryse Planum. This outflow complex is divided into three distinct systems: the Upper Maja System (2), the incised channels of the Maja, Vedra, Maumee and Bahram Valles, and the unconfined flow of Lower Maja across Chryse Planitia. The erosional and depositional features of the Eastern Lunae Planum Outflow Complex suggest that it was formed over a short period of time by catastrophic flooding--analogous to the channeled scablands of Eastern Washington (4).

The southern reaches of the Upper Maja Vallis are composed of deeply incised anastomosing channels. Northward, the flow exhibits erosional scours, probable depositional bars, and streamlined residual uplands as it spreads laterally (2). Shallow, rimless depressions in this region ( $9^{\circ}$ ;  $58.5^{\circ}$ ) may be analogous to terrestrial thermokarst lakes (3). Small patches of chaotic terrain (Ister Chaos,  $12^{\circ}$ ;  $53.5^{\circ}$ ) along the eastern edge of the broad trough acted as secondary sources of water. Bedforms in the confined flow of the canyon section include longitudinal grooves, cataracts, erosional scours and possible pendant bars (2). In the Chryse section, numerous small anastomosing channels cut the surface of a broad, low cone of alluvial material at the mouth of Maja canyon. Further east, multiple channels dissect ridges in the plains-forming material of Chryse basin.

The initial outflow surged northward along the eastern edge of Lunae Planum and impounded on the plains surface (1) until the flood crested the Xanthe Terra highlands to the east and spilled eastward toward Chryse. At the eastern edge of Xanthe Terra ( $18^{\circ}$ ;  $54^{\circ}$ ), the flood waters ponded behind a high standing ridge of rugged terrain. This Xanthe catchment basin filled until a diversion channel directed the flow southward and eastward around the barrier. Continued influx into the Xanthe catchment was greater than the outflow in the diversion channel, and the water level eventually crested the barrier ridge to spill on to the Chryse surface. A gorge was rapidly cut through the ridge; the lake was drained; and the diversion channel was abandoned. An alluvial cone was built at the mouth of the gorge ( $18^{\circ}$ ;  $53.5^{\circ}$ ) as the confined flow spread laterally. Waning flow across the fan cut numerous small distributary channels. Flow from the canyon spread across the western edge of Chryse to be come ponded behind the wrinkle ridges (2). The Maja fan continued to develop as a fan-delta. Again, once the lake level crested the ridges, it continued to spread eastward across the plains surface.

Water on the Lunae Planum surface was not completely drained. This upper lake continued to exist after the canyon section was incised across Xanthe Terra. Smooth plains-forming materials on the floors of some craters represent lacustrine deposition within flooded craters. Benches along the Xanthe Terra contact ( $16^{\circ}$ ;  $55.8^{\circ}$ ) may represent wave cut terraces along the shoreline, and secondary channeling of the Maja fan may represent episodic flow through the canyon. Therefore, the upper lake was drained by episodic release to Maja Vallis and by encroachment of Bahram Vallis by headward erosion across northern Lunae Planum.

This scenario suggests that the outflow and catastrophic flooding, as with most consequent stream systems, was temporarily impounded at several localities along its course. The flow duration was extended by intermediate storage and release from catchment areas and by influx from secondary sources in chaotic terrains along the middle reaches of the outflow channel.

#### REFERENCES:

1. De Hon R.A. (1987) Lunar Planet Sci. XVIII, 227-228.
2. Baker V.R. and R.C. Kochel (1979) J. Geophys. Res. 84, 8183-8204.
3. Theilig E. and R. Greeley (1979) J. Geophys. Res. 84, 7994-8010.
4. Baker V.R. and D.J. Milton (1974) Icarus 23, 27-41.

**Hydrology of a Flow Event in Kasei Valles, Mars; Mark S. Robinson, *Hawaii Institute of Geophysics, University of Hawaii, Honolulu, Hawaii* 96822 and Kenneth L. Tanaka, *U.S. Geological Survey, Flagstaff, Arizona*, 86001.**

Kasei Valles is one of the largest outflow channels on Mars [1, 2] and is located ~2000 km north of Valles Marineris (25°N, 70°W). A fortuitous combination of stereo, low sun-angle ( $\text{INA} > 70^\circ$ ), and high-resolution (45 m/p, orbit 665A) Viking images has allowed us to investigate the topography of the channels in Kasei Valles. Integration of stereogrammetry, shadow measurements, and photogeology permit the production of a three-dimensional model of a late-stage, major flow event in Kasei Valles. We have calculated average velocity and peak discharge using hydraulic equations [3] modified for Martian gravity [4].

Stereogrammetric profiles were taken parallel and perpendicular to the center of the main northern channel. Profile A (Fig. 1) was taken to examine the bottom of the channel to determine if any anomalous high or low points were present. We found that as the channel makes a sweeping turn to the east, the channel bottom rises (C, Fig. 1) at least 350 m [5]. Five additional profiles were taken across this anomalous rise to confirm its existence and to determine its height.

Interpreting the origin of this rise is critical to measurement of the flow event. The change in floor relief could be the result of (1) post-flow infilling, (2) post-flow tectonic warping, (3) an increase in the physical strength of channel-floor material or (4) a local decrease in flow energy. A set of striations, etched on the floor of the channel, veer up and out of the main channel at the same place as the bottom rise (Fig. 2). We interpret these striations to be markers of the path of the flow event that we measured. If the rise was caused by deposition after the flow event, the striations would be covered; they are not. Secondly, if tectonic warping of the channel floor occurred, then the two main stratigraphic horizons [5] (pre-flow event in age) in Kasei should also be deformed, which they are not. If a change in the physical strength of rock units making up the floor of the channel at the rise actually exists, then the rise could have formed as a result of differing erosional rates. Lastly, locally increased turbulence and erosional plucking from roller vortices could have eroded potholes and created uphill gradients in a catastrophic flow; Baker has discussed similar features in the channeled scablands in eastern Washington State, caused by the catastrophic Lake Missoula flood [2, 6]. On the basis of these arguments, we interpret the rise to be an original feature of the channel flow event.

The high-resolution images show that the striations are continuous from the lower reaches of the channel up to the highest definable water mark, where they are deflected around streamlined bars. We interpret the continuity of these striations to indicate that the flow was a continuous event. If a subsequent flow eroded the channel, the striations would be cross-cut at the level of the later flow event.

Using the striations as a marker, we estimated a minimum flow depth. We used the striation that occurs at the highest point on the bar (A, Fig. 2), measured by a stereo profile, as a marker for the minimum vertical extent of the peak flow. From the channel-floor profile (B, Fig. 1) across the rise and the elevation of the highest striation on the streamlined bar, we estimated a minimum cross section of the flow event. From this cross sectional area, we then estimated velocity of the flow using standard hydraulic equations [3] adjusted for Martian gravity [4]. The maximum and average depths of the flow cross section were measured as 1280 and 374 m, respectively. The possible velocities for this peak flow event were calculated to be in the range of 40-50 m/sec. From the measured cross section and calculated velocity, we estimated a discharge by the following equation:  $Q = A \times V$ , where

Q=discharge, A=cross section, and V=velocity [3,4]. Due to insufficient coverage at high resolution, we could not determine whether striations occur at the southern edge of the channel rise; thus it is not possible to determine if erosion of the channel in this area occurred after the peak discharge event. Therefore, we calculate discharge for a number of depths to allow for erosion of this 'unseen' region (up to 400 m).

Water Level (m)	0	-100	-200	-300	-400
Discharge ( $\text{m}^3/\text{s} \times 10^9$ )	1.4	1.0	0.9	0.7	0.6

**Table 1.** Change in calculated discharge as a function of decreasing flow depth compared to peak discharge, within the main north channel of Kasei Valles.

Peak discharge in Kasei Valles could have ranged from 0.6 to  $1.4 \times 10^9 \text{ m}^3/\text{sec}$ , and could have been even greater, but the actual high-water mark is not known. In comparison, peak discharge of the Lake Missoula flood has been estimated at  $2 \times 10^7 \text{ m}^3/\text{sec}$  [2]. Our calculations show the peak discharge to be 1 to 2 orders of magnitude greater than that of the Missoula flood.

The next step in our analysis will be to apply the calculated discharge values to estimates of the carrying capacity and erosional rates for Kasei Valles, using techniques developed by Komar and Carr [7,8]. From these calculations, we will be able to make an order of magnitude estimation of the volume of the source area needed to support the flooding event. At this stage, however, it is clear that extracting elevation information from Viking images allows for a quantitative approach to the study of channeling and water on Mars.

#### References:

- [1] Carr, M. H. (1981) *The Surface of Mars*, Yale Univ. Press. [2] Baker, V. R. (1982) *The Channels of Mars*. [3] Sellin, R. H. J. (1969) *Flow in Channels*. [4] Komar, P. D. (1979) *Icarus* 37, 156-180. [5] Robinson, M. S., and Tanaka, K. L. (1988), LPI Tech Rpt. 88-05, 106-108. [6] Baker, V. R. (1974) *Icarus* 23, 27-41. [7] Komar, P. D. (1980) *Icarus* 42, 317-329. [8] Carr, M. H. (1979) *JGR* 84, B6, 2995-3007.

**Figure 1.** (below) Northern Kasei Valles, Viking image 519A10. Letters indicate locations referred to in text. North towards top ( $1'' = 70 \text{ km}$ ).

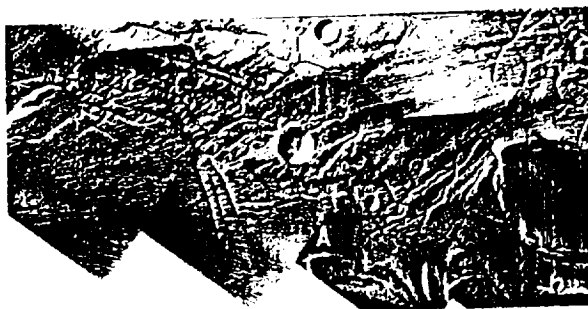


**Figure 2.** (above) High-resolution Viking mosaic (211-5882) showing striations and streamlined bars in northern Kasei Valles. Letters indicate locations referred to in text. North towards top ( $1'' = 14 \text{ km}$ ).

ORIGINAL TAGG IS  
OF POOR QUALITY

KASEI VALLES, MARS: FORMED BY FLOOD OR ICE?

B.K. Lucchitta, U.S. Geological Survey, 2255 N. Gemini Dr., Flagstaff, AZ 86001

The origin of outflow channels is not yet fully understood, even though many investigators prefer an origin by catastrophic flooding because morphologic features in the channels are similar to those formed by catastrophic flooding on Earth [1,2,3]. Yet, outflow-channel features on Mars are generally an order of magnitude larger than those caused by catastrophic floods on Earth, which implies that the volume of Martian floods was much larger than that of the largest known terrestrial floods. The difficulty with the catastrophic-flood model is determining the mechanism by which such large volumes were released from the ground in one sudden event. Even though models have been advanced to enable such a release [4,5], none of them are entirely satisfactory.

Lucchitta [6,7] noted that many of the channel features suggest sculpture by ice because of their similarity in morphology and scale to features of terrestrial glaciated terrains. In her model, water released from the ground froze and moved through the Martian channels in a manner similar to terrestrial wet-based glaciers. The advantage of this idea is that the volume of water emerging from the ground did not have to be excessively large; ordinary rivers or debris flows could have been sufficient to form glacier-like masses if the water froze near the source of their eruption or later during transport.

New information from Kasei Valles suggests that ice was the dominant erosional process forming this channel. The observations center on new topographic information and relations among longitudinal grooves and other features of the Kasei Valles floor.

A new topographic map at a scale of 1:500,000 [8] covering the region of north Kasei Valles [9] has contour intervals of 200 m. The map shows a conspicuous 90° bend in north Kasei Valles where the channel changes direction from north to east. At the bend, the channel funnels into a narrow trough whose floor lies 2 km below the adjacent plateau surface. In the northward leg before the trough, the channel floor gradually drops 1000 m over a distance of 85 km, at a gradient of 11 m/km. In the eastward leg beyond the trough, the channel floor rises more than 400 m over a distance of 45 km, at a gradient of at least 9 m/km. Beyond this point, the channel floor again gradually drops across two contours (more than 200 m) and then rises again. The deepest part of the channel is near its narrowest trough segment, the downstream rise is associated with channel widening, and the next downstream low corresponds again to a restriction. An important observation is that these gentle undulations of the channel floor are not present in the surrounding adjacent plateau. Therefore, the undulations cannot be attributed to postchannel structural warping but must be due to the erosional process carving the channel. The observation that confinements of the channel correlate with deepening also suggests that the erosional process is responsible for the undulations.

On Earth, rivers do not have undulatory floors with amplitudes of as much as 400 m and wavelengths on the order of 50 km; such undulations would imply that the water flowed uphill. However, the undulations in Kasei Valles could



have been formed by water, if one assumes that Kasei Valles, in this region, was filled to its brim, because the work done at the base of a fluid depends on its hydrostatic head. On the other hand, water of a 2-km-deep flood would be macroturbulent and would erode by transient eddies with near-vertical axes (kolks), gigantic transverse vortices, or large-scale cavitation [10]. Erosion by these processes is known to form potholes and other irregularities in the channel bed but is not known to produce smooth undulations such as those observed in this segment of Kasei Valles. Glacial erosion, however, typically yields smooth gradients that commonly go uphill, because the erosive power of ice depends on the basal shear stress, which is a function of the gradient of the ice's surface. Therefore, the newly discovered undulations on the Kasei Valles channel floor support the proposition that this section of the channel was carved by ice.

Kasei Valles, south of the bend, is 100 km wide and marked by parallel grooves across its entire width. The scoured channel in this area lies about 1 km below unscoured terrain at each side. Individual grooves are generally 100-500 m wide, but they locally reach widths of 1 km. Grooves are on the order of 100 m deep [12] but may be as deep as 250 m [13]. Some of the grooves cut across preexisting transverse crevices that are as much as 500 m wide and bowl-shaped craters as much as 7 km wide that have sharp, elevated rims. The grooves are not offset or markedly disturbed by these obstacles. In the Kasei Valles bend, grooves appear on the smoothly curving, gently sloping, outside channel wall.

Longitudinal grooves are interpreted to have been caused by longitudinal roller vortices in catastrophic floods, a feature of macroturbulent flow believed to have formed by transverse instabilities in straight channels [10,14]. Once established, the vortices may deepen and lengthen rapidly after the flow has become channelized. In Kasei Valles, some of these vortices would have been truly macroturbulent as they eroded 1-km-wide grooves. This size implies that the vortices must have been as much as 1 km in diameter and that they thus involved the entire depth of the flood waters. Problems with the vortex hypothesis are (1) that the vortices apparently persisted undisturbed across obstacles of considerable size and (2) that they are not confined to straight channel segments. Baker [10] states, "If defects occur in the bed, they may produce transverse flow separations that break up longitudinal patterns of vorticity". If he is correct, the formation of the longitudinal grooves in Kasei Valles by longitudinal roller vortices is unlikely, because vortices, even if as large as 1 km in diameter, would have been disrupted when crossing craters several kilometers in size. Because longitudinal roller vortices are supposed to be confined to straight channel segments, other mechanisms must have formed the grooves on the sloping channel walls in the curved segments.

Deep longitudinal scour marks are common in glacial terrain, however, and they extend across obstacles without deflection. Ice could have first filled the craters in the Kasei Valles floor and then could have overridden them without diverging its path. Furthermore, ice scour is common in sweeping curves on walls of glaciated valleys. No flood features on Earth are known to generate such forms.

Overall, the topographic information and morphologic features observed in north Kasei Valles near its bend are more consistent with sculpturing by ice than by flood waters, suggesting strongly that, in this area, the eroding fluid was predominantly ice.

#### References

- [1] Baker, V.R. and Milton, D.J. (1974) *Icarus* 23, 27-41.
- [2] Masursky, H., Boyce, J.M., Dial, A.L., Schaber, G.G. and Strobell, M.E. (1977) *JGR* 82, 4016-4038.
- [3] Baker, V.R. (1979) *JGR* 84, 7985-7993.
- [4] Carr, M.H. (1979) *JGR* 84, 2995-3007.
- [5] Milton, D.J. (1974) *Science* 183, 654-656.
- [6] Lucchitta, B.K., Anderson, D.M. and Shoji, H. (1981) *Nature* 290, 759-763.
- [7] Lucchitta, B.K. (1982) *JGR* 87, 9951-9973.
- [8] U.S. Geol. Survey, in prep.
- [9] U.S. Geol. Survey (1984) Misc. Inv. Map I-1588, scale 1:500,000.
- [10] Baker, V.R. (1982) Univ. Texas Press, 198 p.
- [11] Sugden, D.E. and John, B.S. (1976) Edward Arnold, London, 376 p.
- [12] Chapman, M.G. and Scott, D.H. (1988) this volume.
- [13] Wu, S.S.C. (1981) unpublished topographic map.
- [14] Einstein, H.A. and Li, H. (1958) *Trans. Am. Geophys. Union* 39, 1085-1088.

WATER OF THE ELYSIUM BASIN, MARS: VOLUMETRIC ANALYSIS AND SOURCES  
David H. Scott, Kenneth L. Tanaka, and Mary G. Chapman, U.S. Geological  
Survey, Flagstaff, Arizona 86001

The inventory of water once present near the surface of Mars has important climatic and biological implications. There is growing evidence that large standing bodies of water once existed on Mars (Haberle, 1986; Carr et al., 1987). It now seems plausible that ephemeral seas or large lakes occupied depressions along the foreland region of the highland plateau. A study of the Elysium basin is especially important for quantitative determinations of water volume, because it is the only known basin where direct geologic and topographic evidence of former water levels can be established around its perimeter. We have two objectives, to determine (1) the maximum extent of the Elysium basin and (2) the former volume of water in the basin.

To fulfill the first objective, we plan to map the Elysium basin at 1:2,000,000 scale and to determine its former (paleolake) shoreline from geologic indicators and new topographic maps (U.S. Geological Survey, in press). We will then compare the resulting calculation of volume with the estimates of water runoff from channels that drained into the basin (described below). The final map product, showing the entire basin, will be compiled at 1:5,000,000 scale.

To fulfill the second objective, we must determine the major sources of channel waters that once filled the Elysium basin. Examination of Viking photomosaics and images indicates that many channels within the Medusae Fossae Formation drained toward the basin. Geologic mapping of the channels and their drainage areas within the formation and other circumbasin materials will allow us to make semiquantitative estimates of their water contributions to the basin.

During the first months of the study, we have pursued tasks to complete both objectives. We have examined Viking images and mapped paleoshorelines and drainage channels between between lat 25° N. to 15° S., and long 175° to 220°. Four maps at 1:2,000,000 scale are near completion that show circumbasin materials and the basin proper. We had previously examined these maps during the compilation of the 1:5,000,000-scale geologic map of the Elysium region (Tanaka, Chapman and Scott, work in progress; see also abstract this volume). It is evident from this initial work that drainage into and out of the basin encompass a much larger area than that previously estimated. We have also observed several spillway areas, including some that appear to connect with Amazonis Planitia.

#### References

- Carr, M.H., Wu, S.S.C., Jordan, Raymond, and Schafer, F.J., 1987, Volumes of channels, canyons and chaos in the circum-Chryse region of Mars (abs): 18th Lunar & Planet. Sci. Conf., p. 155-156.  
Haberle, R.M., 1986, The climate of Mars: Sci. Amer., v. 254, p. 54-73.  
U.S. Geological Survey, Topographic map of Mars, eastern region: USGS Atlas of Mars Topo. Ser. 0/270T, scale 1:15,000,000 [in press].

VALLEY TERMINAL DEPOSITS: THE MARTIAN SEDIMENTARY RECORD;  
R. A. De Hon, Department of Geosciences, Northeast Louisiana University, Monroe  
LA 71209.

**INTRODUCTION.** Sedimentary deposits provide the most revealing materials for interpretation of a planet's history. The stratification of sedimentary deposits preserves a stepwise record of events in the source region and in the basin of accumulation. The constituents of the sediments provide samples of materials derived from outside the basin of deposition as well as evidence of the mode of transportation and the environment of deposition. Valley terminations provide obvious sites to be explored in the search for a martian sedimentary record.

Martian valley systems range from those which unquestionably were cut by flowing water, through those arguably cut by some fluid flow, to those of uncertain and possibly structural origin. Those which may reasonably be assumed to be cut by water constitute part of a flow system which transported sediments to lower topographic levels. This paper reports a preliminary search for recognizable sedimentary deposits near the termini of some valley systems.

Fluvial systems on Mars are recognized by distinctive patterns of erosional landforms. Broad outflow channels were cut by catastrophic flooding over short periods of time (1). Some sinuous valleys were cut by headward erosion as the result of sapping over longer durations (2). Dendritic and parallel drainage patterns on the flanks of some volcanoes and in the highlands may have been cut by rainfall (3) or groundwater release due to ground ice thaw during volcanic warming events (4). Axial lineations in some straight-walled valleys associated with transecting valley systems are suggestive of glacial action (5).

Observable depositional landforms include streamlined islands within the outflow channels which are probably, in part, depositional in origin (6), and inverted topography in Mangala which is evidence of deposition and erosion within the system. Many channels and valleys are unquestionably filled with sediments. Logically, the region of major sedimentation is the downstream terminus. A search for deposits at the mouths of outflow channels and other valley systems leads to mixed results.

**DEPOSITIONAL SITES.** Examples of probable alluvial fans include broad cones of low relief at the junction of valley and channel systems with lower plains. The mouth of Maja Vallis is marked by an alluvial fan where the outflow from the confines of the Maja canyon empties on to Chryse Planum (7). A small alluvial cone is located in Terra Sirenum where a short valley empties into a large crater. An alluvial fan is seen by its light albedo and channeled surface at the west end of Evros Vallis between Terrae Meridiani and Sabaea. In Schiaparelli basin, an extensive alluvial apron is formed by the coalescence of discharge of many short, parallel segments of the Brazos Valles. The relief is low, but the deposits are accentuated by a dark albedo rim and the contrast with the rougher topography of the basin floor. Another cone, at the mouth of Tader Valles in Terra Sirenum, is well defined by topography.

Deltas form where channels or valleys empty into standing water (lakes). Ephemeral lake basins are found along many of the outflow channels. A small delta formed on the Lunae Planum surface where the flow breached the highland contact and spilled into a small highland basin. The Maja alluvial cone on Chryse Planum underwent a period of fan-delta development as water was impounded behind the Chryse ridge system for a short period of time (8, 9). In a similar manner, a deltaic fan is seen in the Elysium Planitia region where volcano/ground ice interaction has resulted in release of water to the surface to form outflow channels, lakes, and deltaic sedimentation (4).

In the Deuteronilus Regio, a wedge-shaped deposit on the outside of a breach in a crater rim resulted from deposition of materials derived from inside the crater. This fan-shaped deposit is characterized by a strongly developed terminal ridge suggestive of a terminal moraine; hence, the possibility exists for glacially transported materials in this region. In the Hellas basin, Harmakhis Vallis terminates in an irregular pattern of hummocky materials which Moore (10) suggests may represent mudflow or glacial debris.

Areas of sedimentation without well-defined cones are associated with Amazonis (4, 10) and Ladon Valles (10, 11). In these systems the lower reaches of the valley terminate in a broad, smooth surface of level plains-forming materials which presumably represents a blanket of sediments derived from the channel. These materials bury existing topography without producing any relief. Often, the termini of these systems are marked by distinct albedo patterns that contrast with the surrounding plains materials. The lack of alluvial cones may be attributed to low gradients and the spreading of sediment to form a broad depositional surface of no relief. Alternately, the lack of an identifiable fan may represent delta progradation to the point of complete filling of the depositional basin.

The absence of deposits at the mouths of some channel and valley systems poses added problems. The abundant dendritic valleys in the central highlands as well as some of the outflow channels in eastern Chryse lack discernable fans or deposits at present imaging resolutions. In comparison with earth, alluvial fans are also notably lacking at the mouths of north African wadis. Here the junction between the channel and plains meets with little change in gradient. It is possible that sediments delivered to the termini of valley systems were redistributed by eolian processes as exemplified by Tinia and Taus Valles along the northern border of Terra Sirenum. They may also have been covered by later materials as at the mouths of the nearby Abus, Isara, and Munda Valles.

**SUMMARY.** The search for terminal deposits leads progressively from well-defined cones of alluvial fans or deltas to smooth plains. The distinction between deltas and fans on images of Mars is rather arbitrary and rests on the existence of a standing body of water for at least part of the time within the basin of deposition. Alluvial fans/deltas are present where some channels emerge from highland surfaces onto adjacent plains or terminate within craters. Most channels meet the surrounding plains with low gradients, and most alluvial fans/deltas are of low vertical relief. Other systems have no apparent cone of deposition, rather they are associated with fluvial or lacustrine basin-filling materials of no apparent relief.

#### REFERENCES:

1. Baker V.R. and D.J. Milton (1974) Icarus 23, 27-41.
2. Sharp R.P. (1973) J. Geophys. Res. 78, 4063-4072.
3. Masursky H. et al. (1977) J. Geophys. Res. 82, 4016-4038.
4. Mouginis-Mark P.J. (1985) Icarus 64, 265-284.
5. Lucchitta B.K. (1981) Nature 290, 759-763.
6. Baker V.R. and R.C. Kochel (1978) Proc. 9th Lunar Planet. Sci. Conf., 3193-3202.
7. De Hon R.A. (1987) Lunar Planet. Sci. XVIII, 227-228.
8. Baker V.R. and R.C. Kochel (1979) J. Geophys. Res. 84, 8183-8204.
9. Theilig E. and R. Greeley (1979) J. Geophys. Res. 84, 7994-8010.
10. Moore H.J. (1982) NASA Tech. Memo 85127, 213-215.
11. Boothroyd J.C. (1982) NASA Tech. Memo 85127, 209-212.

EPHEMERAL MARTIAN LAKES: TEMPORARY PONDING AND LOCAL  
SEDIMENTATION, R. A. De Hon, Department of Geosciences, Northeast Louisiana  
University, Monroe LA 71209.

INTRODUCTION. Outflow channels provide evidence for the existence of surface water on Mars. These channels carried diluvial floods from their source areas down slope to lower regions where flood waters debouch onto plains (1,2). Wherever there is an abundant flow of water and an irregular surface with closed basins to provide temporary catchment, transient lakes will form. Inspection along drainage courses allows identification of many sites of potential ponding of water as ephemeral lakes. Where water is impounded, velocity and turbulence decrease, and deposition of suspended sediments occurs. Hence, fine-grained, slack water or lake sediments should be found in such sites.

Lacustrine sedimentation produces landforms of scant relief. The primary geomorphic surface is a lacustrine plain which is a featureless, level plain within a depression. Related morphology in terrestrial lakes include deltas, wave cut terraces, bars, and other near shore features. Such features on Mars may be beyond Viking resolutions or scarce because of the short period of time that lakes existed and lack of sufficient wind strength to form waves and wave related features. Therefore, evidence of lacustrine sedimentation is primarily in the form of basin-filling, plains-forming materials along the outflow channels. Examples are plentiful. Some examples are cited here to demonstrate the variety of ephemeral lacustrine sites.

EXAMPLES. Lakes of varying dimensions formed along the Lunae Planum Outflow Complex. A large temporary lake was formed at the mouth of Maja Vallis canyon on the western edge of Chryse Planum where the outflow from Maja canyon was impounded behind wrinkle ridges on the Chryse surface (3,4). Near the mouth of Maja on the Xanthe terra surface the initial flow across Xanthe Terra was temporarily trapped behind a highland ridge at the eastern edge of Xanthe (5). The flow collected as a catchment basin and initially formed a diversion channel to the south before cutting the gorge across the barrier ridge. On the northern Lunae Planum surface, the initial outflow was confined to the upper plains before cresting the higher standing cratered terrain to the east (6), and numerous craters were flooded along the Lunae Planum--Xanthe Terra boundary and within Xanthe Terra.

Elsewhere on Mars, ephemeral lakes were formed in the Mangala Valles region of Terra Sirenum by flooding of large craters transected as the initial outflow cascaded across the landscape. This is especially evident in the Labou Vallis diversion where the flow first breached and flooded one crater, then spilled over into an adjacent crater. Ephemeral lakes in the Elysium Planitia region are associated with closed basins within chaotic and jokulhaup modified terrains and were feed by runoff initiated by volcanic warming of ground ice (7).

Possible lacustrine sediments are reported within Ophir and Candor Chasmas (8). The materials occupy the floors of the canyons and are composed of horizontal, thin-bedded, layered sediments. Layered materials within the crater Henry in Arabia Terra (MC-12SE) may be lacustrine in origin also. A system of broad valleys feed into Henry from the north. The norther crater wall is partially blanketed by a complex alluvial fan/delta with distributary channels. The floor of the crater is partially filled with flat-lying layered materials. These sediments are dissected by later erosion to leave a central flat-topped mesa as erosion carried materials westward through a breach in the crater wall.

DURATION AND SEDIMENTATION. Martian lakes existed for relatively short periods of time. Often the flow was temporarily impounded within a crater or other depression only until the surface level of the water rose above the down stream rim. Once waters spilled over the barrier, a crevasse was rapidly cut to release the water for continued flow. If the relief channel cut below the level of the lake floor, the basin would be entirely drained. If the relief channel did not cut below the level of the lake floor, some water would remain. The remaining ponded water may be lost by infiltration, by drainage following subsequent channeling, or by sublimation to the atmosphere (9).

The thickness of sediments at each site is a function of the total amount of sediment eroded from the source and channel and carried to the site of ponding. At present, the maximum volume of sediment within a flooded crater may be crudely estimated by comparing fresh crater morphology with that of the partially filled crater. Estimates of this type provide maxima and are upper limits at best. Lake sediments are composed of clastic material entrained in the flow along its course. If repeated ponding occurs, then each basin contains only that sediment entrained downstream from the preceding site of ponding.

The existence of lacustrine plains on Mars provides a challenge to interpretation of martian surface morphology and geology. Substantial areas of plains-forming materials within the highlands previously identified as volcanic may be sedimentary. Remote sensing of Mars, from earth or from martian orbit, should attempt to establish criteria for distinguishing between volcanic and sedimentary plains. Originally level, lacustrine plains provide excellent reference datum planes to establish subsequent surface deformation.

#### References:

1. Baker V.R. and D.J. Milton (1974) Icarus 23, 27-41.
2. Carr M.H. (1979) J. Geophys. Res. 84, 2995-3007.
3. Baker V.R. and R.C. Kochel (1979) J. Geophys. Res. 84, 7961-7984.
4. Theilig E. and R. Greeley (1979) J. Geophys. Res. 84, 7994-8010.
5. Rice J. et al. (1988) Lunar Planet. Sci. XIX, 976-977.
6. De Hon R.A. (1987) Lunar Planet. Sci. XVIII, 227-228.
7. Mouginis-Mark P.J. (1985) Icarus 64, 265-284.
8. McCauley J.F. (1978) U.S. Geol. Surv., Misc. Inv. Map I-897.
9. Wallace D. and C. Sagan, (1979) Icarus 39, 385-400.

## Water Wave Dynamics in Martian Gravity

Timothy J. Parker, Jet Propulsion Laboratory, California Institute of Technology, Pasadena, CA 91109

The presence of numerous valley networks and large outflow channels debouching into highland basins and into the northern lowlands on Mars suggests the possibility of ephemeral standing bodies of water (either liquid or frozen) associated with their formation. Parker et al., (in press) identified benches in the west Deuteronilus Mensae region that could have been cut into preexisting terrain by surface waves in a temporary standing body of water emplaced by catastrophic floods from the circum-Chryse and/or northwest Elysium channels. How would surface waves on Mars differ from those on Earth, and would they be capable of producing the observed morphologies?

Beginning with scaling for martian gravity, I have identified some interesting differences between water waves on Mars and Earth (figures 1-4). To keep the comparison between the two planets as simple and straightforward as possible, I restricted this exercise to linear or Airy waves in deep water (e.g., Komar, 1976) and assumed a 1 bar early martian atmosphere and a "warm" climate.

The phase velocity of an Airy wave in deep water is expressed by the equation

$$C_{\infty} = \frac{gT}{2\pi}$$

in which  $C_{\infty}$  is the phase velocity in deep water;  $g$  is the gravitational acceleration in  $\text{m/sec}^2$ ; and  $T$  is the period, in seconds, from one wave crest to the next. The ratio of martian to terrestrial wave phase velocity is about one third (figure 1). This is accommodated by a similar relationship between martian and terrestrial wavelengths, defined by the equation

$$L_{\infty} = \frac{gT^2}{2\pi}$$

such that martian waves must travel about one third as fast or have about one third the wavelength as terrestrial waves with the same period (figure 2).

An important factor to consider with regard to the erosive ability of martian waves is the diameter of particle orbits beneath the waves and the depth at which this motion essentially ceases ("wave base"). In deep water the particle orbits beneath waves are essentially circular, so the horizontal and vertical components of the orbit are equal. The orbit diameter is then determined by the equation

$$d = H \exp\left(4\pi^2 Z_0 / gT^2\right)$$

where  $d$  is the particle orbit diameter;  $H$  is the wave height; and  $Z_0$  is the depth below the still water level to the center of the particle orbit. The results of substituting martian and terrestrial gravity into the equation for the specific case of 1 meter high waves of 10 second period are shown in figure 3. On Mars,  $d$  decreases much more rapidly with depth than it does on Earth. This suggests that terrestrial waves are much more effective at moving sediment at depth than "equivalent" martian waves. On the other hand it also indicates that martian waves entering shallow water "feel bottom" later than terrestrial waves and that martian wave energy is focused within a narrower depth range than terrestrial wave energy. Martian shorezones should therefore be broader and have gentler slopes than "equivalent" terrestrial shorezones.

To determine how martian and terrestrial wave energies compare it is necessary to apply wave prediction models that include wind and fetch parameters. I used the fetch-limited wave spectrum method derived by Liu (1971) and described by Komar (1976):



$$E'(\sigma) = 0.4g^2 / \sqrt[4]{F_0} \cdot \sigma^5 \exp \left[ -5.5E3 \left( \frac{g}{U_* \sqrt[3]{F_0}} \sigma \right)^4 \right]$$

where  $E'(\sigma)$  is the "spectral energy density", expressed in  $m^2sec$ ;  $\sigma$  is the radian frequency  $2\pi/T$ ;  $F_0$  is the dimensionless fetch parameter; and  $U_*$  is the friction wind velocity.  $U_*$  is determined from a measure of the wind velocity 10 meters above the still water surface by the equation:

$$U_* = U_{10} \sqrt[3]{U_{10}^2 / g F}$$

in which  $F$  is the fetch.  $F_0$  is determined by the equation:

$$F_0 = gF / U_*^2$$

Graphed are the results of assuming a fetch of 1000 kilometers (well within reason for terrestrial oceans and plausible for an ephemeral sea within the northern plains on Mars) and a wind velocity 10 meters above still water level of 20 meters per second (figure 4). For this example,  $U_* = .689m/sec$  for the Earth,  $.952m/sec$  for Mars;  $F_0 = 2.064E7$  for the Earth,  $4.094E6$  for Mars. The terrestrial wave spectrum peaks at an energy density of about  $12m^2sec$  and a  $\sigma$  of  $.42$ , corresponding to a wave period of about 15 seconds. The martian spectrum peaks at an energy density of about  $114m^2sec$  and a  $\sigma$  of  $.2$ , corresponding to a wave period of about 31.4 seconds. The ratio between maximum spectral energy for Mars versus Earth, given these special conditions, is about 9.5.

This exercise suggests that martian wave energies, given the same atmospheric pressure, wind, and fetch conditions for each, might actually be much higher than terrestrial wave energies. Assuming a 1 bar atmospheric pressure early in Mars' history is an oversimplification, however. Pressure estimates, based on models of outgassing and volatile inventories (e.g., Rasool and Le Sergeant, 1977; Anders and Owen, 1977; Pollack and Black, 1979; Carr, 1986) range from a few hundred millibars to several bars.

## References:

- Anders, E., and Owen, T., 1977. Mars and Earth: Origin and abundance of volatiles: *Science* **198**, p. 453-465.
- Carr, M. H., 1986. Mars: A water-rich planet? *Icarus* **68**, p. 187-216.
- Komar, P. D., 1976, *Beach Processes and Sedimentation*: Prentice-Hall, Inc., New Jersey, 429p.
- Liu, P. C., 1971, Normalized and equilibrium spectra of wind waves in Lake Michigan: *Journ. Phys. Oceanog.* **1**, p. 249-257.
- Parker, T. J., Saunders, R. S., and Schneeberger, D. M., in press. Transitional morphology in the west Deuteronilus Mensae region of Mars: Implications for modification of the lowland/upland boundary: accepted for publication in *Icarus*, 41p., 15 figures.
- Pollack, J. B., and Black, D. C., 1979. Implications of the gas compositional measurements of Pioneer Venus for the origin of planetary atmospheres: *Science* **205**, p. 56-59.
- Rasool, S. I., and Le Sergeant, L., 1977. Implications of the Viking results for volatile outgassing from Earth and Mars: *Nature* **266**, p. 822-823.

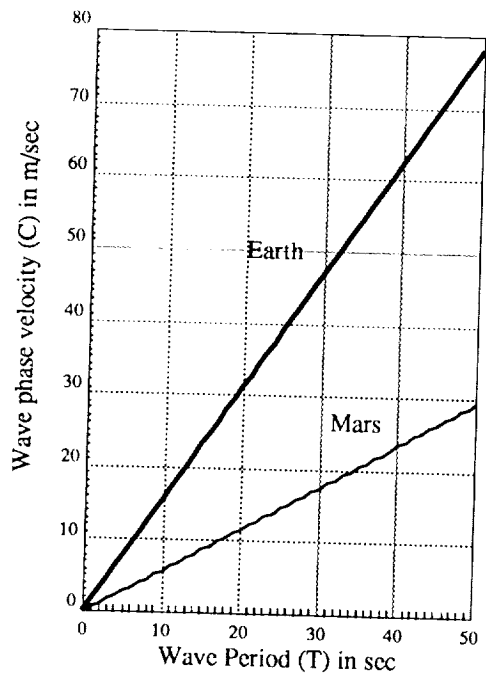


Figure 1

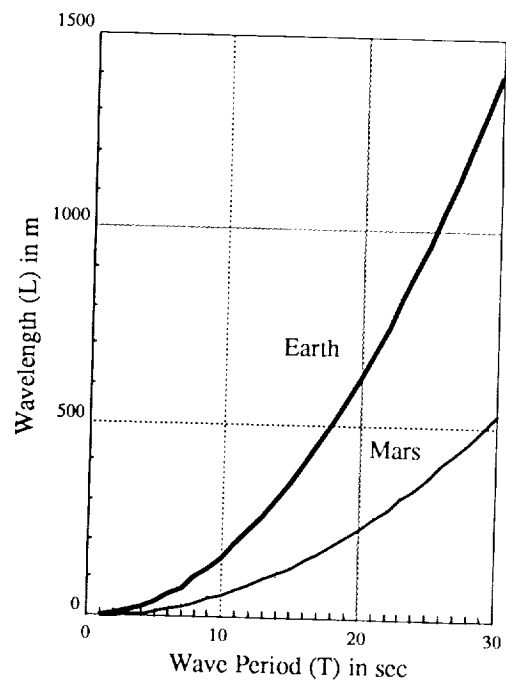


Figure 2

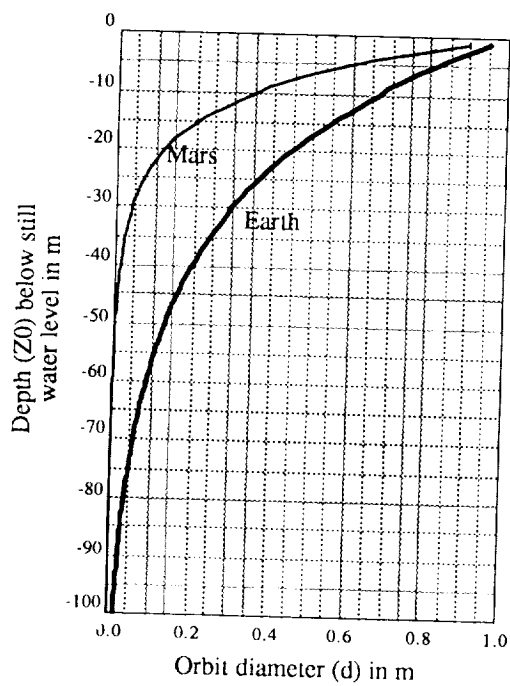


Figure 3

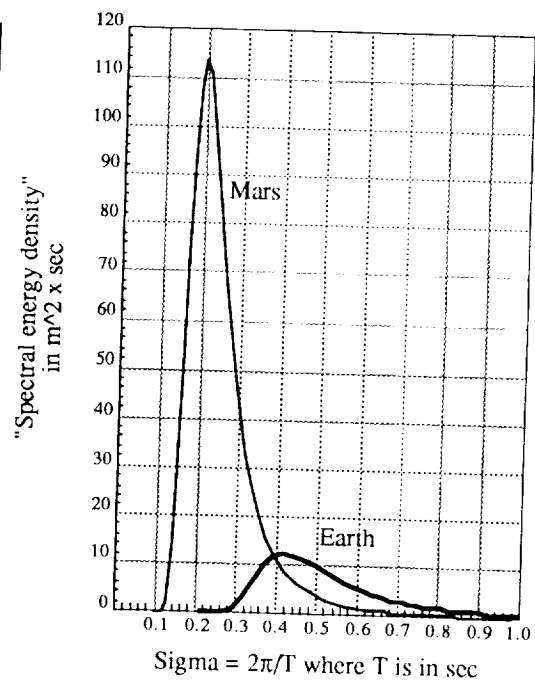


Figure 4

# A KINEMATIC WAVE MODEL FOR CATASTROPHIC FLOODING ON MARS

Stephen Baloga and Timothy Parker, Jet Propulsion Laboratory, California Institute of Technology, 4800 Oak Grove Drive, Pasadena, CA 91109

Steady state models of complex fluid and mass transport processes are often used for geologic applications. However, time-dependent effects are frequently important when free boundaries, such as the depth, width and extent of an unconfined flood, are involved. In this context, we have used a "kinematic wave" formulation to investigate the time-dependent behavior of a catastrophic flood on Mars and to compare the results with the corresponding steady-state case. The model is applied to a hypothetical channel on Mars to assess the implications of time dependent factors on the particle sizes that might be deposited along the channel and discharged into the associated outwash plains. A complete list of symbols and definitions is provided in Table 1.

A kinematic wave equation governing the depth of flow,  $h = h(x,t)$ , for a fluid flowrate  $Q = Q(x,t)$ , is given by

$$w \partial h / \partial t + \partial Q / \partial x = 0 \quad (1)$$

where a constant width,  $w$ , has been assumed. Eq. (1) is a local conservation law for fluid volume at each point along the path of the flood. To obtain a formulation that can be solved for flood profiles, eq. (1) must be supplemented with a prescription of the local flowrate as a function of  $h$  and a boundary or initial condition on either the flow depth or flowrate. The mean velocity of a laterally-confined turbulent flow is often modeled with a  $3/2$  depth dependence (e.g., Komar, 1980). With the assumption that this relationship remains valid under time-dependent conditions, the local flowrate is given by,

$$Q(x,t) = w h(x,t) \langle u(x,t) \rangle = w (g S / C_f)^{1/2} h(x,t)^{3/2} \quad (2)$$

Substituting eq. (2) into eq. (1) results in the kinematic wave equation

$$\partial h / \partial t + 3/2 (g S h / C_f)^{1/2} \partial h / \partial x = 0 \quad (3)$$

for the depth of flow during a turbulent stage of flooding.

The boundary condition appropriate for this type of governing equation may be specified as the flow depth at the source of the discharge, taken here as  $x = 0$ . For a steady-state discharge,  $h(0,t) = h_s$  (= constant), and eq. (3) shows that  $h(x,t) = h_s$ . Thus, the profile for the depth of flow remains constant in both space and time for the duration of the flood.

A more interesting case is the boundary condition

$$h(0,t) = h_0 (1 + t / \Gamma)^{-1} \quad (4)$$

where  $h_0$  represents the depth of the flow at the onset of discharge and  $\Gamma$  is a time constant. Figure 1 shows the qualitative behavior of the flow depth, flowrate and cumulative volumetric discharge derived from eqs. (3) and (4). Using standard methods of solution for eq. (3) with eq. (4) [e.g., Whitham, 1974; Zachmanoglou and Thoe, 1976], the kinematic wave for the evolution of the flow depth profile is

$$h(x,t) = h_0 \left[ x / L + \left\{ (x/L)^2 + 4 (1 + t / \Gamma)^{1/2} \right\}^2 / 4 (1 + t / \Gamma)^2 \right] \quad (5)$$

The location of the flood front,  $L_f = L_f(t)$ , is also an unknown free boundary that is determined from a more general fluid volume conservation requirement,

$$V(t) = \int_0^t Q(0, t) dt = w \int_0^{L_f(t)} h(x, t) dx \quad (6)$$

once the shape of the kinematic wave is known [Baloga, 1987]. Eq. (6) ensures that the cumulative volume discharged is always equal to the volume under the profile of the flood wave.

Figure 2 shows the evolution of the kinematic wave for the boundary condition model given by eq. (4) and parameters that might be appropriate for an episode of flooding at Mangala Vallis ( $h_0 = 100\text{m}$ ,  $w = 10\text{km}$ ,  $g = 3.7\text{m/sec}^2$ ,  $S = 0.003$ ,  $C_f = 0.005$ ,  $V(\infty) = 100\text{km}^3$ ). The flood is deepest at the front of the wave and progressively decreases in depth at each station after the front has passed. The depth of the flood at the front, and the advance of the front itself, steadily decrease with distance from the source. After approximately 4 days, the depth of the flow has dropped to 1m at the source and this value is taken as the completion of the episode.

Figure 2 also shows the comparable flow depth profile for a steady state discharge of  $100\text{km}^3$  over the same duration as the time-dependent case. For early times, the time-dependent wave is significantly deeper than the steady state case. Komar (1980) has suggested that the critical settling velocity for suspension of grains in a turbulent channelized flow is proportional to  $h^{1/2}$ . Because the time-dependent wave is much deeper than the steady state analog, significantly greater sediment transport capabilities are implied by the time-dependent case. Furthermore, because the kinematic wave progressively thins with distance from the source, one would expect a corresponding decrease in the maximum particle sizes with distance at the conclusion of the flood episode. In the Mangala-analog example shown in Figure 2, the sediment transport into the plains beyond the channel mouth is comparable in both cases. However, the particle deposition along the channel itself would be noticeably different for the steady-state and time-dependent cases.

The time-dependent catastrophic character of a flood or outflow could have a significant influence on the transport of particles through channels to outwash areas on Mars. Even though the volumetric discharge may be the comparable or equivalent, the time-dependent wave has more inherent kinetic energy, (and therefore more transport or erosion capability) than the comparable steady state solution. Future efforts will investigate energy transport in more detail and other processes such as infiltration and entrainment concurrent with flooding.

#### REFERENCES

Baloga, S. (1987) JGR 92, 9271-9279; Komar, P. (1980) ICARUS 42, 317-329; Whitham, G. (1974) Linear and Nonlinear Waves, Wiley; Zachmanoglou and Thoe (1976) An Introduction to Partial Differential Equations, Dover

TABLE 1

h	depth of flood	$C_f$	drag coefficient
x	distance from source	$\langle u \rangle$	mean flow velocity
t	time	V	cumulative volumetric discharge
w	width	$V(\infty)$	total volume discharge for boundary condition eq. (4)
$L_f$	location of flood front	S	slope
$\Gamma$	time constant	g	gravity
Q	flowrate		
L	length scale ( $= 1.5 \Gamma [g S h_0 / C_f]^{1/2}$ )		

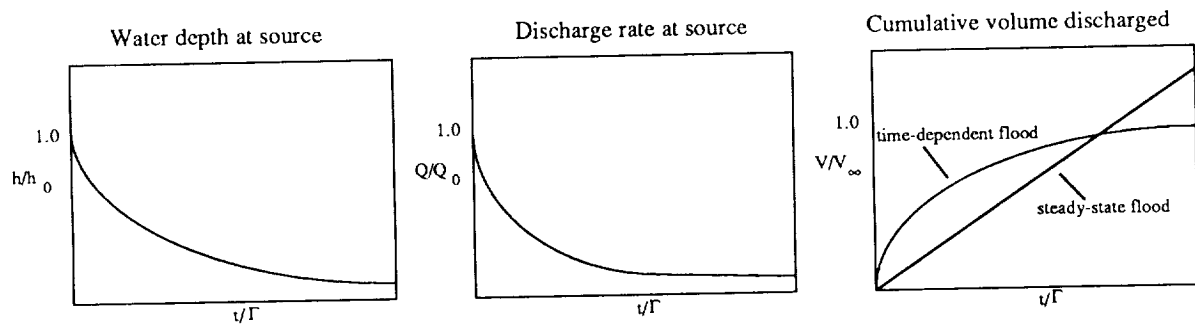


Figure 1

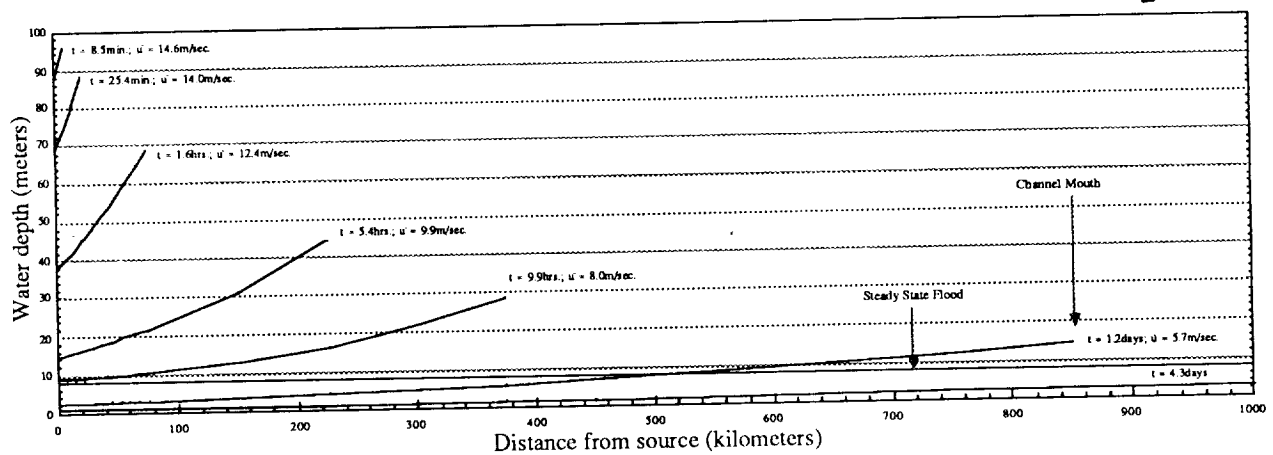


Figure 2

# MECHANISMS OF RESURFACING IN THE AMENTHES AND TYRRHENA CRATERED HIGHLANDS OF MARS.

Ted A. Maxwell and Robert A. Craddock, Center for Earth and Planetary Studies, National Air and Space Museum, Smithsonian Institution, Washington, D. C. 20560.

Using crater size frequency distributions as a means to determine relative surface ages is an established procedure (1-4) that presumes that craters were obliterated due to some event that occurred rapidly relative to the scale of the impact flux, thus "resetting" the surface upon which additional craters would accumulate. In the Amenthes and Tyrrhena region of Mars ( $-30^{\circ}$  to  $+10^{\circ}$  Lat.,  $225^{\circ}$  to  $270^{\circ}$  Long.), the surface of Noachian and younger materials is characterized by a unique set of rimless craters that may represent an incomplete episode of resurfacing, or may be a function of mechanical property variations in near-surface materials. Based on the size frequency distribution of this set of craters, the process that removed the rims was time transgressive, ceasing first at northerly latitudes ( $5^{\circ}$  to  $10^{\circ}$ ), and successively migrating southward (areas to  $-30^{\circ}$  Lat. have been studied) (5). These age relations are based on craters in the 8 to 50 km diameter range, so that the apparent ages are not simply a function of selective preservation of craters of different sizes. In order to more fully understand the method(s) of resurfacing, and to have confidence in the use of crater frequency surface dating techniques, we have analyzed the occurrence of these craters as a function of the geologic unit impacted, their morphology, and the diameter range over which they occur.

Two highland material units, cratered plateau and cratered highlands have a similar appearing population of rimless craters; craters in both units have flat floors of smooth plains material, and lack the distinctive raised rim of their younger counterparts. With the exception of the rugged nature of surrounding terrain, craters in the highlands are identical to those in cratered plateau and intercrater plains units, and occur on the rim crests of older, larger craters as well as in depressions between highland blocks. In the smoother, dissected portions of the cratered plateau material, such craters are randomly superposed on the gullied terrain of old drainage, indicating that the drainage occurred before early Hesperian time. Size frequency counts indicate little difference in age between rimless crater populations on both units, suggesting that mechanical properties of near-surface materials are not the cause of their distinctive morphology.

Simplistic models for resurfacing consist of two end-member hypotheses: deposition and erosion, both of which could account for the missing raised rims of these craters. However, within the rugged highland material, such craters are not preferentially located in low areas, as would be

expected if flooding of neighboring intercrater plains were the mechanism by which rims were removed. In addition, the morphology of individual rimless craters is not suggestive of deposition of material up to the rim crest, in which case we would expect to see large craters with distal portions of the raised rim subdued.

Further distinction between these two mechanisms of resurfacing can be made by considering what happens to a size frequency distribution as affected by both processes. For a depositional episode of resurfacing, craters would first have areas external to the rim crest smoothed, followed by breaching of the rim and deposition on the crater floor. As the crater became increasingly buried, the rim size would remain constant for medium- and large-size craters, but would be cut off at the small end of the frequency distribution due to burial of small craters. The rest of the curve would keep a slope equivalent to that of the original distribution (6). For a purely erosional mode of resurfacing, rim crest removal would be the first effect, followed by stripping of the surrounding terrain, and a gradual reduction in the apparent crater size as erosion proceeded downward. Smaller craters would initially be more affected by such a process, resulting in a decrease of the slope of the cumulative frequency curve.

Comparison of these predicted cumulative frequency distributions with those from the cratered plateau and cratered highlands, together with stratigraphic relations within the uplands indicate that both deposition and erosion have modified the original surfaces. Near the dichotomy boundary, differential weathering of ponded material suggests an early depositional phase that now buries cratered highland material. With increasing distance from the boundary, deposited material is confined to topographic lows, and erosional stripping of the terrain predominates as the mechanism for resurfacing. Because of the gullied nature of large (greater than 50 km) crater rims, it is likely that this episode of resurfacing occurred during a period of enhanced atmospheric conditions, when fluvial processes and surface weathering combined to erode weakly consolidated crater rims.

These results were presented at the 20th Lunar and Planetary Science Conference, Houston, Texas, March, 1989. Supported by NASA Grant NAGW-129.

References: (1) Neukum, G. and D.U. Wise, 1976, *Science*, 194, p. 1381-1387. (2) Neukum, G. and K. Hiller, 1981, *JGR*, 86, p. 3097-3121. (3) Basaltic Volcanism Study Proj. Volume, 1981, LPI, Houston, pp. 1050-1054. (4) Tanaka, K.L., 1986, 1981, *LPI*, Houston, pp. 1050-1054. (5) Tanaka, K.L., 1986, *Proc. Lunar Planet. Sci. Conf.*, 17th, in *JGR*, 91, p. E139-E158. (6) Craddock, R.A. and Maxwell, T.A., this volume. (6) Chapman, C.R. and Jones, K.L., 1977, *Ann. Rev. Earth Planet. Sci.*, 5, p. 515-540.

## Martian Sublimation Rates

Gary D. Clow, U.S. Geological Survey, Menlo Park, CA 94025

Robert M. Haberle, NASA/Ames Research Center, Moffett Field, CA 94035

Evaporation (sublimation) rates have very likely played a key role in the martian water cycle and have had a tremendous influence on ice-related surface features, many of which have been proposed to explain certain martian landforms. The theory of evaporation on Earth is fairly well developed (1,2), but has not been previously applied to Mars. Instead, nearly all studies of sublimation on Mars have utilized two parameterizations of uncertain validity. The first was designed to describe the water-vapor flux from the terrestrial oceans due to mechanically induced turbulence (3). This parameterization fails to account for environmental differences between the Earth and Mars. In addition, it substantially underestimates sublimation rates during the period (midday) when the bulk of sublimation occurs, because it ignores the effects of atmospheric stability within the atmospheric boundary layer (ABL). The use of this parameterization for rigid land or ice surfaces is also questionable. The second parameterization was designed to describe water-vapor diffusion due to molecular weight gradients in the near-surface boundary layer, under the assumption of no winds (4). It has been unclear to what extent this "self-buoyancy" process actually occurs on Mars, because wind-generated turbulent eddies would tend to disrupt the thick saturated boundary layer needed for this mechanism to work. In an attempt to reduce the uncertainty in predicted martian sublimation rates and to achieve a better understanding of the operating conditions for the self-buoyancy mechanism, we are extending the modern theory of evaporation developed for terrestrial conditions, to Mars. Atmospheric pressures between 6 and 3000 mb are being considered.

Two types of turbulence occur in the immediate vicinity of a planet's surface (i.e. the interfacial zone), depending on the ratio of the surface roughness  $z_0$  to the viscous length scale for gas within the ABL. The first type is associated with "aerodynamically" smooth surfaces while the second is associated with "aerodynamically" rough surfaces. Roughness Reynolds numbers indicate that, unlike the Earth, both types of turbulence should commonly occur for natural surfaces on Mars. Martian surfaces similar to terrestrial polar snowpacks ( $z_0 \sim 0.03$  cm), will switch between the two turbulent regimes, depending on atmospheric pressure and the friction velocity  $u_*$ . The Viking Lander sites ( $z_0 \sim 0.1 - 1$  cm) are expected to behave in an aerodynamically rough fashion for most martian  $P, T$  conditions. We have coupled the transport equations for nonsteady molecular diffusion into interfacial eddies with similarity-theory turbulent-flux profiles for the overlying surface sublayer. Thus, we now have a model describing water-vapor diffusion across the bulk of the atmospheric boundary layer via turbulent transport for both aerodynamically smooth and rough surfaces. The model fully accounts for environmental differences between the Earth and Mars, for atmospheric stability, and for surface roughness. Water vapor and heat are transferred across the ABL by very similar processes. For completeness, the analogous equations describing sensible heat transport across the ABL have also been developed.

We have determined the conditions under which turbulent eddies, generated by wind shear, will disrupt the thick saturated boundary layer needed for the self-buoyancy mechanism



to be effective. These conditions are found to be different for aerodynamically smooth and rough surfaces. For smooth surfaces, we find the friction velocity must be below a critical value (which is a function of pressure and temperature) for the self-buoyancy boundary layer (SBBL) to survive. Naturally occurring friction velocities are expected to exceed the critical values for the majority of anticipated  $P, T$  conditions on Mars, at least during daylight hours when the bulk of sublimation occurs. The exception to this occurs at high temperatures ( $T > 260$  K) and low pressures ( $P < 20$  mb). The criterion for whether the SBBL will be disrupted by turbulent eddies over an aerodynamically rough surface, is established by the surface roughness  $z_o$ . Self-buoyancy is found to be ineffective for polar snow-type surfaces whenever they behave in an aerodynamically rough fashion. The SBBL may survive at high temperatures and pressures ( $T > 240$  K,  $P > 100$  mb) for Viking Lander-type surfaces. However, the dynamic instability caused by self-buoyancy is rather weak at high pressures, so this may be of little consequence.

As a prelude to developing sublimation parameterizations specifically for Mars from the complete model, bulk ABL water-vapor transfer coefficients  $C_e$  have been determined for martian conditions on the assumption of neutral atmospheric stability. We find that  $C_e$  essentially reduces to a function of the viscous length scale in the ABL for smooth surfaces but that the situation remains more complicated for aerodynamically rough surfaces.  $C_e$  values are found to range 0.0007 – 0.003 for smooth surfaces and 0.0011 – 0.004 for rough surfaces. For comparison,  $C_e$  has historically been taken to be 0.0022 in previous martian sublimation studies.

## References:

- (1) Brutsaert, W. 1982. *Evaporation into the atmosphere*, D. Reidel Publishing Co., 299 pp.
- (2) Clow, G.D., C.P. McKay, G.M. Simmons, Jr., and W.A. Wharton, Jr. 1988. Climatological observations and predicted sublimation rates at Lake Hoare, Antarctica, *J. Climate*, **1**, 715–728.
- (3) Jacobs, W.C. 1942. On the energy exchange between sea and atmosphere, *J. Marine Res.*, **5**, 37–66.
- (4) Ingersoll, A.P. 1970. Mars: occurrence of liquid water, *Science*, **168**, 972–973.

## Laboratory Studies of Sublimation of Ice/Silicate Mixtures

Jeffrey Moore, Department of Geology, Arizona State University, Tempe, AZ 85287-1404

Fabrication of an experimental apparatus to investigate ice/silicate interactions during sublimation under martian conditions has been completed. The first set of experiments conducted was designed to investigate two end-member samples of pure ice: (1) non-porous massive or "block" ice, and (2) 0.25 to 1 mm granular ice. Calculations of ice grain growth rates and sintering have suggested that ice grains in martian polar deposits probably range between 0.1 mm and 1 cm (Clark *et al.*, 1983). Owing to these calculations, ice grains in this size range are planned to be utilized in all subsequent experiments involving the interaction of ice and non-volatile particulates. Thus, the initial runs were intended to understand the behavior of these end-members, to "debug" the test apparatus and procedures, and to determine the necessary duration of later experimental runs.

The first run investigated the properties of a sample of pure, 0.25-1.0 mm granular ice with a bulk density of  $0.41 \text{ gm cm}^{-3}$ . The sample was initially kept isothermal at  $-20^\circ \text{C}$ . At this temperature, the sublimation rate was determined to be  $2.6 \times 10^{-8} \text{ gm s}^{-1} \text{ cm}^{-2}$  in a 3 mb  $\text{CO}_2$  atmosphere. Following the method used in other martian ice sublimation studies (e.g. Clifford and Hillel, 1983), the calculation of the idealized sublimation rate can be made using an expression derived by Farmer (1976):

$$J_n = D (P/k) (T) (l)$$

where  $k$  (Boltzmann's constant) is  $1.38054 \times 10^{16} \text{ dyne-cm } ^\circ\text{K}^{-1}$ ,  $T$  is the temperature of the ice layer surface,  $l$  is the thickness of the actively subliming surface (assigned a value of 1 cm),  $D$  is the molecular diffusion coefficient of  $\text{H}_2\text{O}$  in an atmosphere composed of  $\text{CO}_2$  at 3 mb pressure, and  $P$  is the equilibrium vapor pressure of  $\text{H}_2\text{O}$  just above the ice layer at 3 mb and at a temperature equal to the surface temperature. The molecular diffusion coefficient can be calculated using the experimental results of Schwartz and Brow (1951), who show that the diffusion coefficient  $D$  (in  $\text{cm}^2 \text{ sec}^{-1}$ ) varies as temperature ( $T^{1.5}$ ) and ambient pressure ( $p^{-1}$ ), as given in the following expression:

$$D = 0.1654 (T/273.15)^{1.5} (1014 \text{ mb}/p)$$

The equilibrium vapor pressure  $P$  of  $\text{H}_2\text{O}$  ice can be calculated using the following equation presented by Labofsky (1975):

$$P = 1.333 \times 10^3 \times 10^{(-2445.5646/T + 8.23121 \log T - 0.0167706T + 1.20514 \times 10^{-5} T^2 - 6.75169)} \text{ dynes cm}^{-2}$$

Using these models, the calculated sublimation rate ( $1.4 \times 10^{-7} \text{ gm s}^{-1} \text{ cm}^{-2}$ ) is approximately 5 times larger than the observed value.

Following the "cold soak" exposure, the sample was heated from the top with the surface absorbing a total of  $3.4 \times 10^{-2} \text{ W cm}^{-2}$ . Sublimation reached an observed equilibrium value of  $7.1 \times 10^{-8} \text{ gm s}^{-1} \text{ cm}^{-2}$ , about 5 times less than the value calculated ( $3.5 \times 10^{-7} \text{ gm s}^{-1} \text{ cm}^{-2}$ ), i.e., similar to the earlier observed difference. The discrepancy between observed and calculated sublimation rates could be due to several factors. The most likely explanation involves the fact that advection and buoyancy can, in general, control the rate of sublimation (Ingersoll, 1970). These relatively minor phenomena may well become limiting factors for

small amounts of vapor diffusing into an atmosphere under conditions of extreme stability in the boundary layer. This initial run was conducted under just such conditions as the circulation pump was not in use at the time. Mukherjee (1971) has postulated that a "stagnant layer" above the ice could suppress the sublimation rate by well over the factor of five observed in the experiment.

A numerical model, derived from Clifford *et al.*'s (1987) martian thermal model, was used to generate a family of time-dependent temperature *verses* depth curves for the environmental conditions within the chamber. The actual temperature profile (Figure 1) was compared to these curves to extract the thermophysical properties of the test materials. A thermal conductivity of  $4.0 \times 10^{-2} \text{ W cm}^{-1} \text{ }^{\circ}\text{K}^{-1}$ , a thermal diffusivity of  $0.0463 \text{ cm}^2 \text{ s}^{-1}$ , and a thermal inertia of  $18.6 \times 10^{-3} \text{ cal s}^{-1/2} \text{ cm}^{-2} \text{ }^{\circ}\text{K}^{-1}$  provided the best back-fit to the observed temperature profile. These values imply that the granular ice behaved much like solid crystalline ice. The overall thermal characteristics of the sample were similar to those of martian materials with "intermediate" thermal inertia, thought to be composed of indurated fines (e.g., Jakosky and Christensen, 1986). The higher-than-expected inertia (at least considering the low density) arises primarily from the combination of relatively high conductivity and specific heat. The high conductivity may result from effective heat transfer by  $\text{CO}_2$ , as is under investigation by Christensen (personal communication, 1989).

## References

- Clark, R. N., F. P. Fanale, and A. P. Zent, Frost grain size metamorphism: Implications for remote sensing of planetary surfaces, *Icarus* **56**, 233-245, 1983.
- Clifford, S. M. and D. Hillel, The stability of ground ice in the equatorial region of Mars, *J. Geophys. Res.* **88**, 2456-2474, 1983.
- Clifford, S. M., C. J. Bartels, and E. P. Rubenstein, The Mars Thermal Model (MARSTHERM): A FORTRAN 77 Finite-Difference Program designed for general distribution, Lunar and Planetary Institute, 1987.
- Farmer, C. B., Liquid water on Mars, *Icarus* **28**, 279-289, 1976.
- Ingersoll, A. P., Mars: Occurrence of liquid water, *Science* **168**, 972-973, 1970.
- Jakosky, B. M. and P. R. Christensen, Global duricrust on Mars: Analysis of remote-sensing data, *J. Geophys. Res.* **91**, 3547-3559, 1986.
- Labofsky, L.A., Stability of frost in the solar system, *Icarus* **25**, 205-217, 1975.
- Mukherjee, N. R., Water on Mars, in *Geological Problems in Lunar and Planetary Research*, Vol. 25, *Science and Technology* (American Astronomical Society, Tarzana, CA), 1971.
- Schwartz, F. A. and J. E. Brow, Diffusivity of water vapors in some common gasses, *J. Chem. Phys.* **19**, 640-646, 1951.

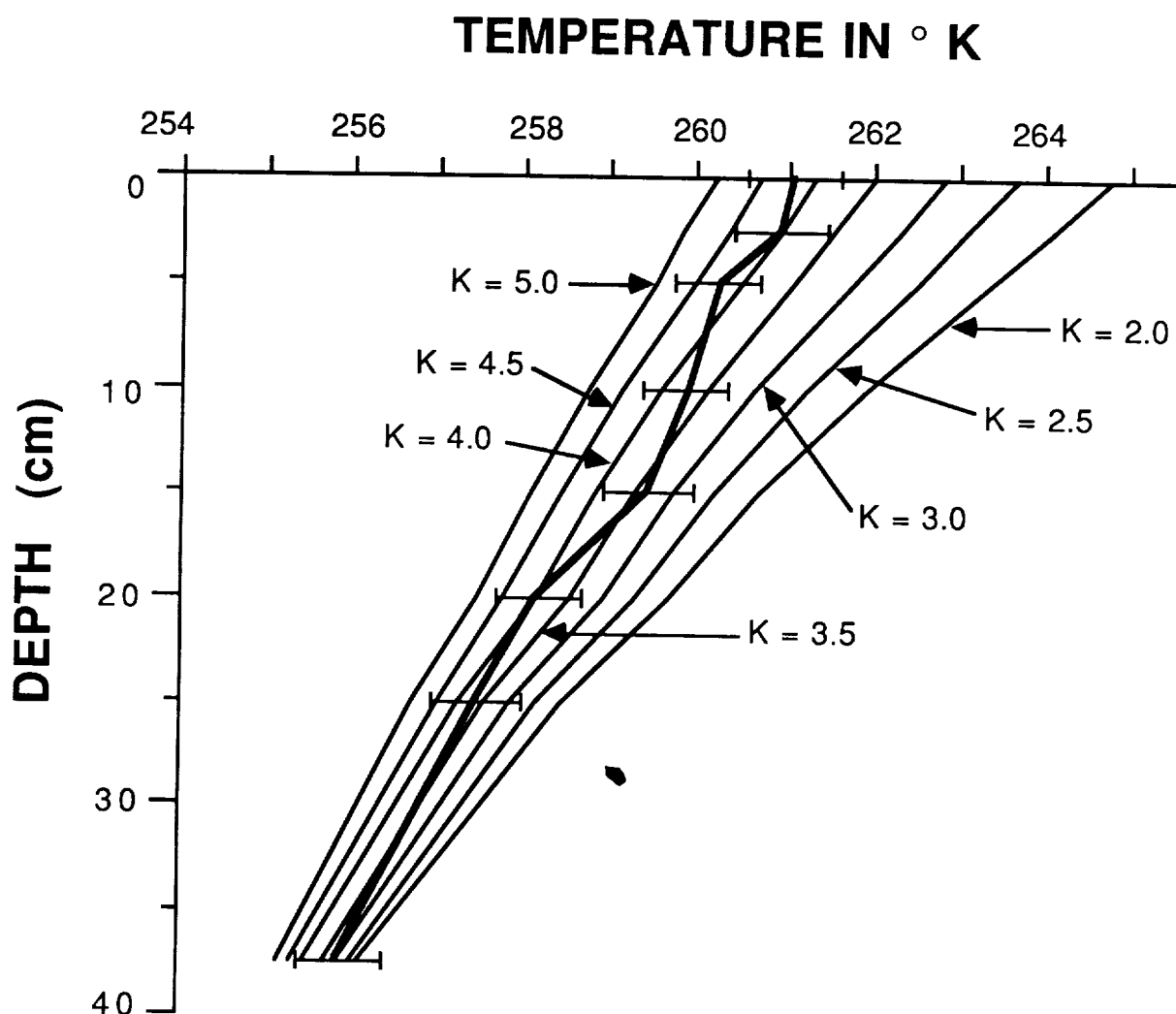


Figure 1: Graph of temperature versus depth for 0.25-1.00 mm granular ice with a basal temperature maintained at  $-20^{\circ}\text{C}$ , a surface temperature of  $-12^{\circ}\text{C}$ , subliming into a 3 mb  $\text{CO}_2$  atmosphere. Bulk density was  $0.41 \text{ gm cm}^{-3}$ . Also plotted are thermal conductivities calculated using the MARSTHERM model of Clifford *et al.* (1987).

GROUND ICE ALONG THE NORTHERN HIGHLAND SCARP, MARS  
B.K. Lucchitta and M.G. Chapman, U.S. Geological Survey, Flagstaff, Arizona  
86001.

The northern highland boundary on Mars is characterized in many places by a steep scarp that is locally dissected into mesas and buttes. These are particularly well developed in the region from about long  $280^{\circ}$  to  $350^{\circ}$  and lat  $30^{\circ}$  to  $50^{\circ}$  N, the "fretted terrain" of the Protonilus and Deuteronilus Mensae. In this latitude belt, mesas are typically surrounded by debris blankets that are generally thought to have formed by ice-lubricated flow [1]. This ice came either from frost deposition [1] or, as many researchers believe now, from ground ice [2,3,4]. The debris blankets are conspicuous features of this latitudinal belt and are young [2]. They are generally thought to indicate that ground ice may currently be present close to the surface [3]. Lucchitta [2] explained the occurrence of ice-charged debris blankets in this latitude belt by (1) the maintenance of ground ice near the surface, which, under current atmospheric conditions, is possible only poleward of about lat  $30^{\circ}$  to  $40^{\circ}$  N [5,6] and (2) the ambient temperature that is warm enough to permit ice to flow by dislocation creep, even though at very slow rates [2]. Farther north, where the atmosphere is colder, this type of ice deformation is less likely to occur [7].

We have observed a number of mesas in the Kasei Valles area that resemble fretted mesas in size and shape and that appear to have formed by similar processes. These mesas are located farther south (lat  $25^{\circ}$  N) than the Deuteronilus or Protonilus Mensae and are not presently surrounded by debris blankets. Instead, several of the mesas are surrounded by moats composed of flat-floored valleys (about 2 to 5 km wide) bordered on the outside by low, inward-facing scarps (Fig. 1, arrows). The moats have the same planimetric shape and dimensions as the debris blankets surrounding the fretted terrain farther north. The plains surrounding the moats are composed of probable Tharsis lava flows, whose relative crater density of 1300 craters  $>1$  m/ $10^6$  km<sup>2</sup> indicates that they are about 2.5 b.y. old (conversion of relative to absolute age from Neukum and Hiller, model 2 [8]). The similarity of the shape of the moat to the planimetric shape of debris blankets surrounding the fretted mesas farther north suggests that the mesas in Kasei Valles once were also surrounded by debris blankets and that these blankets must have been in place at the time of lava flooding; the lavas apparently embayed the debris blankets. Later, the debris blankets disappeared completely, leaving the moats.

The disappearance of the debris blankets suggests that they contained more ice than is commonly attributed to them (10% ice content according to Lucchitta [3] and Carr [5]). In order to disappear completely, only minor amounts of rock could have been incorporated, unless all the rock was of a grain size easily picked up and removed by the wind. However, no other wind erosion features are seen in the area. Also, such a uniform grain size is unlikely unless very unusual circumstances are invoked, such as debris blankets reworking largely fine-grained ash or sandy deposits. Considering, then, that the debris blankets were mostly composed of ice and that this ice was derived from ground ice underlying the mesas [2,3], the ground ice must have had a concentration so high that it may have resembled segregated ground ice in the Northwest Territories of Canada [10]. This observation suggests that the highland margin and associated mesas in fretted-terrain regions

locally were underlain by nearly pure ice masses. These ice masses could have been segregated from ice-rich highland-type breccia, or they could represent frozen water from ancient channel-mouth regions. Furthermore, if the debris blankets were composed largely of ice, sublimation of this ice on fresh exposures within the slowly churning debris would eventually deplete the ice, especially at the tip of the debris blankets where the ice is replenished only slowly. Sublimation of debris blankets in this manner would explain why most of the blankets on fretted mesas extend no farther than about 20 km from their source. Sublimation of debris blankets on gradually diminishing mesas would also explain the disappearance of material from the plains separating the mesas. Thus, the generation of the plains may have been caused by the fretting process [2] involving large-scale sublimation of ice and does not have to be ascribed to an unrelated earlier erosional episode [1].

The former existence of debris blankets in the Kasei Valles area also suggests that ground ice once occurred near the surface in a latitudinal belt that is now desiccated. This observation supports Fanale et al.'s [6] proposition that the southern limit of near-surface ground ice shifted gradually northward with time. Ground ice at lat 25° N 2.5 b.y. ago falls right on the equatorward limit permitted in Fanale et al.'s models of near-surface ice retention.

#### References

- [1] Squyres, S.W. (1978) Martian fretted terrain: Flow of erosional debris. *Icarus*, v. 34, p. 600-613.
- [2] Lucchitta, B.K. (1984) Ice and debris in the fretted terrain, Mars, in Proceedings of the 14th Lunar and Planetary Science Conference, Part 2. Journal of Geophysical Research, v. 89, Supplement, p. B409-B418.
- [3] Squyres, S.W., and Carr, M.H. (1986) Geomorphic evidence for the distribution of ground ice on Mars. *Science*, v. 231, p. 249-252.
- [4] Carr, M.H. (1986) Mars: A water-rich planet? *Icarus*, v. 68, p. 187-216.
- [5] Farmer, C.B., and Doms, P.E. (1979) Global seasonal variation of water vapor on Mars and the implications for permafrost. *Journal of Geophysical Research*, v. 84, no. B6, p. 2881-2888.
- [6] Fanale, F.P., Salvail, J.R., Zent, A.P., and Postawko, S.E. (1986) Global distribution and migration of subsurface ice on Mars. *Icarus*, v. 67, p. 1-18.
- [7] Shoji, H., and Higashi, A. (1978) A deformation mechanism map of ice. *J. Glaciology*, v. 21, p. 419-427.
- [8] Neukum, Gerhard, and Hiller, Konrad (1981) Martian ages. *Journal of Geophysical Research*, v. 86, p. 3097-3121.
- [9] Chapman, M.G., and Scott, D.H. (1988) Geology and hydrology of the North Kasei Valles area. Proceedings of the 19th Lunar and Planetary Science Conference.
- [10] MacKay, J.R. (1986) Fifty years (1935-1985) of coastal retreat west of Tuktoyaktuk, District of Mackenzie, in Current Research, Part A. Geological Survey of Canada, Paper 86-1A, p. 727-735.

SIZE-MOBILITY RELATIONS IN VALLES MARINERIS LANDSLIDES, MARS  
A. S. McEwen, U. S. Geological Survey, 2255 N. Gemini Drive,  
Flagstaff, AZ 86001.

The mechanism of transport of large rock avalanches has been the subject of considerable interest and controversy in recent decades. On Earth, the observed runout lengths ( $L$ ) for large rock avalanches, relative to the height of drop ( $H$ ), are much greater than can be explained by either sliding or dispersive grain-flow mechanisms. Most natural rock types have coefficients of friction (either sliding or internal friction) of 0.6 or higher [1,2], so movement is expected only over terrain with an average slope of at least  $30^\circ$  (or  $H/L$  at least 0.58); this expectation is confirmed for relatively small volume rock avalanches and other flows of dry granular material. However, as the volume increases in rock avalanches,  $H/L$  decreases to values as low as 0.1 or less, and a log-log plot of  $H/L$  versus volume shows a linear correlation [3, 4; see Figure 1].

Planetary comparisons under different conditions of gravity, atmospheric pressure, and volatile inventory may prove essential to resolving this question of mechanism. Mars is the only planetary body other than Earth known to have unequivocal long-runout landslides. Only two potential long-runout landslides have been identified on the Moon, and both of these were probably triggered by impact events [5-8], whose energy may have contributed to the runout lengths. Venus may reveal many such mass movements, but we do not yet have imaging data of sufficient resolution to identify such features. The virtual absence of long-runout avalanches on the Moon and Mercury seems to be evidence that volatiles in some form, in either the atmosphere or the ground, are necessary to initiate or sustain long-runout avalanches.

Were the Valles Marineris landslides "wet" or "dry"? ("Wet" is taken to mean that the mass was saturated with water, thus eliminating or greatly reducing grain-to-grain contacts.) Lucchitta [9] thought that they were probably wet. It has even been suggested that the landslides were subaqueous, collapsing into lakes [10]. However, the landslides are among the geologically youngest features on Mars [8], they clearly postdate the interior layered deposits in the troughs (which may be of lacustrine origin), and there is no evidence for liquid water on the surface of Mars during the time period of landslide formation. Near-surface primordial water or ice are unlikely to have persisted into recent geologic time near the equator of Mars due to losses by sublimation [11]. Furthermore, measurements of yield strength and  $H/L$  versus volume described below are not consistent with the mechanical behavior of saturated debris.

Landslide properties were measured in three regions of Valles Marineris, where 1:500,000-scale topographic maps with 200-m contour intervals are available: (1) the Tithonium and Ius Chasmata region from about lat  $-9^\circ$  to  $-4^\circ$ , long  $83^\circ$  to  $88^\circ$  [12]; (2) an additional part of Tithonium Chasma from lat  $-7.5^\circ$  to  $-4^\circ$ , long  $80^\circ$  to  $85^\circ$ ; and (3) a region including Ophir Chasma and part of Candor Chasma from lat  $-7.6^\circ$  to  $-3^\circ$ , long  $70^\circ$  to  $75.1^\circ$ . (Work is in progress by the U. S. Geological Survey on maps covering the last two regions.) Within these regions, 25 landslides with identifiable source locations and avalanche deposits were studied (Table 1). All of the relatively high resolution (200 m/pixel or better) Viking Orbiter images of these regions were utilized.

Landslide volumes were estimated by two methods. For the large landslides with well-defined slump scars, the missing volume was estimated from the geometry of the scars. For the smaller landslides the scars are too small relative to the topographic data for the missing volume to be estimated, but the deposits appear to have uniform thicknesses; thus the volumes were estimated from the landslide-deposit area times the estimated height of the flow front (see Table 1). The errors in the volume estimates are generally no greater than a factor of 2 but may be as high as a factor of 3 or 4 in some cases. Compared with the variations in landslide volume (more than 5 orders of magnitude, Table 1), these uncertainties are quite acceptable.

If we assume a Bingham rheology for the avalanche and uniform, steady flow conditions, then the yield strength,  $K$ , may be estimated by  $K = \rho g D \sin \theta$ , where  $\rho$  is the flow density,  $g$  is the gravitational acceleration (3.72 m/s for Mars),  $D$  is the height of flow front, and  $\theta$  is the ground slope at the flow front. For  $\rho$ , 2000 kg/m was assumed, which is characteristic of terrestrial rock avalanches [13-14]. Yield-strength estimates for 12 landslides are given in Table 1; the values range from  $10^4$  to  $10^5$  Pa. Terrestrial, dry-rock avalanches are characterized by yield strengths near  $10^4$  Pa [13-14], whereas water-saturated debris flows have yield strengths typically from  $10^2$  to  $10^3$  Pa [15]. Therefore, even with an uncertainty in the yield-strength estimates of an order of magnitude, the values are clearly consistent with the yield strengths typical of dry rock debris.

A plot of  $H/L$  versus volume for the Valles Marineris and terrestrial dry rock avalanches is shown in Figure 1. Trends of decreasing  $H/L$  with increasing volume are obvious from both datasets. Least-square fits to the datasets give linear correlation coefficients of 0.82 for the terrestrial points and 0.90 for the Valles Marineris points. The slopes of the two trends are nearly identical. These relations are very different from those seen in wet debris flows [16] or submarine debris flows [17], where  $H/L$  is almost always less than 0.1 irrespective of volume. If the Valles Marineris landslides were either wet debris flows or subaqueous flows, then the points would be expected to plot below the terrestrial values for dry rock avalanches. Instead, the Valles Marineris trend plots above the terrestrial trend.

Although the slopes of the terrestrial and Valles Marineris trends in Figure 1 are nearly identical, there is clearly an offset between the trends; the difference is actually quite astounding. For example, avalanches on Earth with  $H/L$  equal to 0.1 have a typical volume of  $2.2 \times 10^{10} \text{ m}^3$ , whereas those in Valles Marineris have a typical volume of  $1.4 \times 10^{12} \text{ m}^3$ . This difference, a factor of 65, is at least a factor of 10 larger than the uncertainties in the measurements. What can account for it? The difference in gravity (e.g., scaling by weight [8-9]) could account for a difference of only a factor of 2.6. Possible explanations will be considered in future work. Certainly the Valles Marineris size-mobility relation is significant and must be considered in future efforts to explain the mobility of large dry rock avalanches.

#### REFERENCES:

1. Jaeger, J. C., and Cook, N. G. W., 1969, *Fundamentals of Rock Mechanics*: London, Methuen, 513 pp.
2. Bagnold, R. A., 1954, *Roy. Soc. London Proc., Ser. A* 200, 49-63.



3. Scheidegger, A. E., 1973, *Rock Mechanics* 5, 231-236.
4. Hsu, K. J., 1975, *Geol. Soc. America Bull.* 86, 129-140.
5. Howard, K. A., 1973, *Science* 180, 1052-1055.
6. Guest, J. E., 1971, in Fielder, G., ed., *Geology and physics of the Moon*: Amsterdam, Elsevier, 93-103.
7. Lucchitta, B. K., 1977, *Icarus* 30, 80-96.
8. Lucchitta, B. K., 1979, *J. Geophys. Res.* 84, 8097-8113.
9. Lucchitta, B. K., 1987, *Icarus* 72, 411-429.
10. Shaller, P. J., Murray, B. C., and Albee, A. L., 1989, *Lunar and Planetary Science XX*, 990-991.
11. Clifford, S. M., and Hillel, D., 1983, *J. Geophys. Res.* 88, 2456-2474.
12. U. S. Geological Survey, 1980, *Misc. Inv. Ser. Map I-1294*.
13. Voight, B., Janda, R. J., Glicken, H., and Douglass, P. M., 1983, *Geotechnique* 33, 243-273.
14. Eppler, D. B., Fink, J., and Fletcher, R., 1987, *J. Geophys. Res.* v. 92, 3623-3633.
15. Johnson, A. M., and Rodine, J. R., 1984, in Brunsden, D., and Prior, D. B., eds., *Slope instability*: New York, Wiley, p. 257-361.
16. Siebert, L., 1984, *J. Volcanol. Geoth. Res.* 22, 163-197.
17. Lipman, P. W., Normark, W. R., Moore, J. G., Wilson, J. B., and Gutmacher, C. E., 1988, *J. Geophys. Res.* 93, 4279-4299.

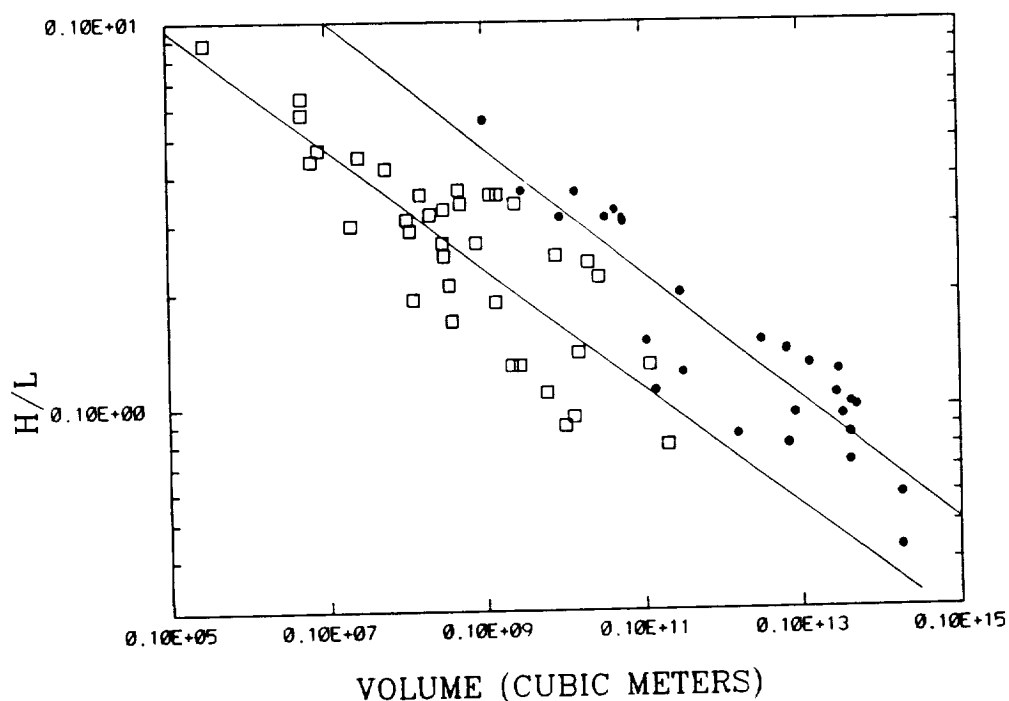


Figure 1. Plot of H/L versus landslide volume. Circles are datapoints from Valles Marineris (from Table 1); squares are terrestrial datapoints for dry rock avalanches of nonvolcanic origin [3, 4]. Lines are least-squared fits to each dataset.

Table 1. Dimensions and Yield Strengths of Some Landslides in Valles Marineris

1 Lat, Long (degrees)	H/L	2 Volume (km <sup>3</sup> )	Deposit Area (km <sup>2</sup> )	3 Height of Flow Front (m)	4 Slope at Flow Front (degrees)	Yield Strength (10 <sup>5</sup> Pa)
-6.4, 87.0	0.059, 0.043	17880	4716	--	--	--
-3.4, 70.7	0.100	4880	1175	291	--	--
-3.2, 71.2	0.102	4183	1244	--	--	--
-6.4, 85.2	0.072, 0.085	4047	2200	109	3.0	0.43
-3.1, 73.9	0.095	3267	1287	--	--	--
-3.1, 71.6	0.125	2960	1675	364	1.1	0.52
-5.2, 86.2	0.108	2761	1144	--	--	--
-3.1, 72.6	0.130	1282	1244	--	--	--
-3.9, 87.6	0.096	833	1075	--	--	--
-4.7, 79.7	0.080	688	888	--	--	--
-4.3, 86.8	0.142	668	656	--	--	--
-4.4, 70.0	0.141	655	470	146	3.4	0.64
-4.4, 86.6	0.150	321	312	--	--	--
-4.7, 82.7	0.085	157	325	33	2.9	0.12
-8.2, 85.1	0.124	32	125	--	--	--
-4.3, 74.4	0.200	29	350	36	--	--
-5.6, 87.6	0.111	14(*)	175	80	--	--
-4.9, 82.6	0.150	11	44	36	3.8	0.18
-4.4, 85.8	0.305	5.5(*)	84	66	3.5	0.30
-4.4, 85.4	0.310	5.3(*)	81	66	2.5	0.21
-4.4, 85.6	0.326	4.3(*)	66	66	3.5	0.30
-7.8, 84.4	0.313	3.3(*)	50	66	8.3	0.70
-4.4, 85.7	0.365	1.4(*)	22	66	3.5	0.30
-5.1, 81.2	0.314	0.9(*)	13	66	3.8	0.32
-5.1, 81.1	0.367	0.3(*)	4	66	7.6	0.64
-4.9, 84.8	0.560	0.1(*)	3	36	--	--

1. Location of center of slump scarp.

2. Estimated from geometry of slump scarp, except for landslide volumes followed by (\*), for which volume was estimated by flow-margin height x area.

3. Estimated by measuring width of flow front on best image and assuming a slope of 20°.

4. Ground slope near flow margin, measured from topographic maps.

## MINIATURE ANALOG OF SPUR-AND-GULLY LANDFORMS IN VALLES MARINERIS SCARPS

Alan D. Howard, Department of Environmental Sciences, University of Virginia, Charlottesville, VA 22903

The walls of Valles Marineris are generally dissected by intricate digitate scarps (spurs) extending downslope from the scarp crest (Figure 1), which are bordered by and give way downslope to concave gullies and talus which has accumulated at the angle-of-repose [1-5]. Small analogs of these *spur-and-gully* landforms develop in excavated slopes in slightly cohesive fine sands. Figures 2 and 3 show two examples of such crenelated erosional forms developed in pits excavated in slightly damp terrace sands along the Colorado River in the Grand Canyon. The photographs show scarps about 0.25 m high, although the slopes continue about 0.1 m below the base of the photographs. Figure 1 is an example of similar topography in Valles Marineris, where the overall relief is about 2-6 km. Features of similarity include the bifurcating spurs excavated in bedrock which are convex in longitudinal profile and intervening steep, spoon-shaped hollows and gullies in bedrock which give way downslope to gentler depositional slopes which have accumulated at the angle-of-repose. The longitudinal profile along the gullies is therefore concave. The overall gradient of the slope walls is only a few degrees steeper than the angle-of-repose. Slight layering in the sand is expressed as ledges and indentations on some of the spurs (Figure 3); similar layering is seen on some Valles Marineris spurs.

These probable small analogs are particularly intriguing because they give insight into the interplay of processes, relief, and materials that create spur-and-gully topography. Furthermore, these landforms develop rapidly at a convenient scale and are suitable for experimental manipulation. Such controlled experiments may permit quantification of processes and development of scaling relationships that will permit evaluation of rock properties and slope processes in Valles Marineris.

The terrace sands of the Colorado River are fine sand with as much as a few percent of silts and clays [6]. Unfortunately, no samples were obtained of the exact sands shown in Figures 2 and 3. The sands were noted to be very slightly damp when first excavated. The pits excavated in Figures 2 and 3 were initially about 0.5 m deep with side-slopes steeper than the angle-of-repose for loose sand, but partly filled with the backwasting sand. Spur-and-gully topography began to develop within a few seconds following excavation as a result of repeated small sand avalanches, and initially extended to nearly the base of the excavated slope as intricately branched spurs and long gullies. However, as loose sand accumulated at the base of the slope, the angle-of-repose slope extended progressively further upslope and the spurs became shorter and less branched, partly by wasting away and partly by burial. Because of the rapidity of initial mass wasting, no photographs of the early stages were obtained. The rate of mass wasting decreased with time but did not cease until all the spurs were finally consumed. This sequence of slope evolution parallels the historical evolution of Valles Marineris scarps inferred by Patton [5]. Note that this evolution of the spur-and-gully topography occurred subsequent to creation of the slope and required no net removal of material from the slope.

The similarity of form between the sand and Valles Marineris spur-and-gully topography suggests analogous processes may be occurring. The dominant mass-wasting process in the miniature forms is repeated small avalanches of sand. The triggering process, particularly in the later stages of scarp evolution, was drying of the sand, which reduced its cohesiveness. However, the rapid erosion early in the scarp evolution probably occurred largely by repeated progressive failures of inherently unstable slopes. An important question is whether the spur-and-gully topography develops primarily because the spurs lag in erosion relative to removal of material in the gullies or whether the avalanches have erosive potential. The smooth, branched profiles of the gullies suggest the avalanches have at least modest erosional capabilities.

It is clear from the nature of the erosional-depositional processes that all parts of the spur-and-gully landscape are marginally stable, being either angle-of-repose slopes of accumulation or steep, short bedrock slopes (damp sand in the miniature analog) on the verge of avalanche failure. The avalanching process is clearly the dominant mechanism on these slopes. At least three types of weathering processes may trigger the avalanching in natural spur-and-gully slopes:

- 1) *Decrease in shearing resistance due to alteration of bedrock on exposure to a dry atmosphere.* Drying of the sand occurs in the miniature landforms whereas loss of ground ice or some other

weathering process resulting from contact with air might occur in the Martian case.

2) *Weathering due to imported moisture.* Larger spur-and-gully topography in terrestrial alpine and polar landscapes may occur largely due to frost weathering or chemical alteration of exposed bedrock.

3) *Progressive failure of near-surface bedrock.* Marginally stable slopes may become weaker through time as fractures gradually extend and integrate under gravitational stresses.

In all these cases it is clear that the weathering process and failure surfaces are shallow as compared to more typical landslides, including those of Valles Marineris [7].

The characteristic scale of the spur-and-gully landforms, whether miniature or monstrous, is clearly controlled by the characteristic size and energetics of the avalanches. If the important factor is the characteristic size of the debris avalanche, then this in turn should be related to such factors as bedrock shearing resistance (including solid rock strength as well as density and orientation of primary and secondary fractures), overall slope steepness and height, the gravitational constant, and the characteristic depth of weathering. If the scale-controlling factor is the scouring potential of the debris avalanches, then this is in turn controlled by the characteristic size of avalanche, slope steepness, flow energetics (depth, velocity, grain dynamics), particle characteristics (size range, hardness, and durability), and bedrock erosion resistance. Only a few of these factors are likely to be important in any particular case, and it is unclear at present which control development of the miniature landforms.

Lucchitta [2] and Patton [3] have identified spur-and-gully analogs in terrestrial temperate and polar deserts. In addition, the fluted erosional pattern on many alpine peaks is probably also eroded by avalanches, but digitate spurs are less well developed due to the radial symmetry. Process studies on these large analogs is limited by their remoteness and the very sporadic occurrence of avalanching. The miniature analogs described here offer the potential for controlled experimentation over relatively short time scales. Spur-and-gully evolution can be photographically and photogrammetrically monitored to allow estimation of size, velocity, and depth of individual avalanches. Furthermore, material properties and "weathering" processes can be varied. Even smaller analogs occur in powders, and sediments with modest cohesion may provide somewhat larger analogs than those described here.

## REFERENCES

- [1] Sharp, R.P., 1973, Mars Fretted and chaotic terrains, *Jour. Geophys. Res.*, **78**, 4073-4083.
- [2] Lucchitta, B.K., 1978, Morphology of chasma walls, Mars, *Jour. Res. U.S. Geol. Survey*, **6**, 651-662.
- [3] Patton, P.C., 1981, Evolution of the spur and gully topography on the Valles Marineris wall scarps, *Rpts. of the Planetary Geol. Prog.* 1981, **NASA TM 84211**, 324-325.
- [4] Patton, P.C., 1982, Quantitative morphology of the Valles Marineris wall scarps, *Rpts. Planetary Geol. Prog.* 1982, **NASA TM 85127**, 242-243.
- [5] Patton, P.C., 1984, Scarp development in the Valles Marineris 1983, *Rpts. Planetary Geol. Prog.* 1983, **NASA TM 86246**, 234-236.
- [6] Howard, A. D. and R. Dolan, 1981, Geomorphology of the Colorado River in the Grand Canyon, *Jour. Geol.*, **89**, 269-298.
- [7] Lucchitta, B.K., 1979, Landslides in Valles Marineris, Mars: *Jour. Geophys. Res.*, **84**, 8097-8113.
- [8] Lucchitta, B.K., 1987, Valles Marineris, Mars: Wet debris flows and ground ice, *Icarus*, **72**, 411-429.



Figure 1.



Figure 2.



Figure 3.

# PRELIMINARY ESTIMATES OF SEDIMENT VOLUME IN THE NORTH POLAR SAND SEAS OF MARS.

*N. Lancaster and R. Greeley, Department of Geology, Arizona State University, Tempe, Arizona 85287-1404*

The North Polar region of Mars contains major accumulations of aeolian sediment in the form of extensive sand seas and dunefields (Breed et al., 1979; Tsoar et al., 1979). An estimate of the volume of sediment contained in the sand seas is necessary in order to assess their role in the martian sedimentary cycle. Spatial variations in sediment volume may provide information on the ways in which the sand seas have accumulated and suggest possible origins and sediment sources. In this abstract we provide a preliminary estimate of dune sediment volume based on studies of dune morphometry.

The approach used combines data from terrestrial analogs of martian dunes with detailed mapping of dune morphometry (dune spacing, cover) from Viking Orbiter images. Studies of dunes in terrestrial sand seas have shown that dune cross-sectional area increases exponentially with dune height, whereas dune height increases linearly with dune spacing (Lancaster, 1988). Therefore areas of large dunes, although widely spaced, represent a net accumulation of sediment. The sediment thickness represented by the dunes is given by their equivalent, or spread-out, sediment thickness (EST). The relation between EST and dune spacing for terrestrial dunes (Fig.1) provides the means to derive estimates of sediment thickness from a parameter (dune spacing) that is relatively easily measured on orbital images. In many areas, dunes do not completely cover the surface, so estimates of sediment thickness need to be reduced in proportion to the area covered by dunes. These estimates of sediment thickness should be considered as minimum values; they are estimates of the sediment contained in the dunes, and do not take into account sediment that has accumulated below the dunes.

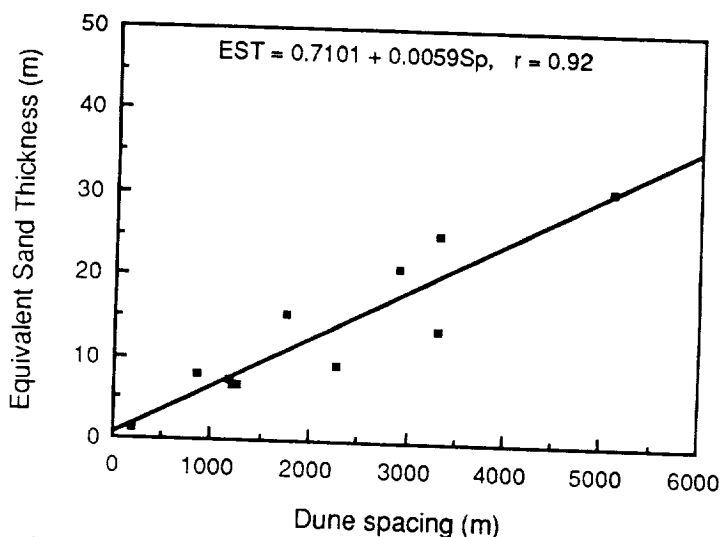


Fig.1. Relation between EST and dune spacing derived from terrestrial dunes.

Average dune spacing, and the percentage cover of dunes were measured on Viking Orbiter images of the North Polar region of Mars ( $> 70^\circ \text{N}$ ). Calculations of EST were derived from these measurements and the relation in Fig. 1, and mapped at a scale of 1:5 M (Fig. 3). Four major sand seas can be identified (Table 1), similar to those mapped by Tsoar et al. (1979) and Dial (1984). Within each sand sea, the area covered by dunes ranges from less than 5% to complete cover, with a mean cover of 50.7%. Dune spacing in the sand sea ranges between 150 and 2955 m, with a mean of 512 m (Fig. 2). Most North Polar dunes have a crest-to-crest

spacing of 300-650 m. Very widely spaced dunes (>900 m) are mostly scattered barchans in marginal areas of the sand seas. Assuming that martian dunes are a similar shape to terrestrial dunes, most are therefore 12 to 26 m high, based on relations between dune spacing and height for transverse dunes in a variety of sand seas (Lancaster, 1988).

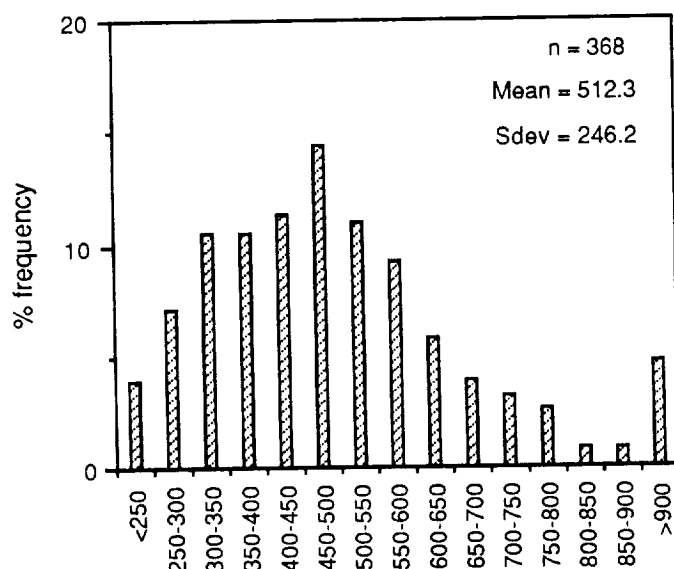


Fig. 2. Distribution of dune spacing (m) in the North Polar Sand Seas

Equivalent sediment thickness for the sand seas ranges from 0.10-0.50 m to a maximum of 5.0-6.0 m, with a mean of 1.81 m (Table 1; Fig. 3). EST is between 2 and 4 m over wide areas of the sand sea between 100 and 260° W. Average EST is greatest in this area and significantly lower in the other dune areas. Within each sand sea, EST follows a consistent pattern, with the greatest sediment thickness in the center, decreasing toward the margins.

Table 1. Percentage cover of dunes, mean EST, and sediment volume in major North Polar sand seas

Latitude (°)	Longitude (°)	Area (km <sup>2</sup> )	Dune cover (%)	Mean EST (m)	Sediment volume (km <sup>3</sup> )
74-80	40-70	1.06 x 10 <sup>5</sup>	37.5	1.28	155.6
76-81	85-105	5.00 x 10 <sup>4</sup>	42.8	1.33	62.3
76-83	110-260	4.70 x 10 <sup>5</sup>	57.0	2.13	935.7
76-80	260-280	3.25 x 10 <sup>4</sup>	33.0	0.89	3.3

Sediment volumes (Table 1) were computed from the isopachs of sediment thickness (Fig. 3). The total volume of sediment contained in the dunes of sand seas of the North Polar region is 1195 km<sup>3</sup>, of which 78% lies in the large sand sea between 110 and 260° W. This estimate is an order of magnitude less than that of Thomas (1982), but is based upon much more realistic views of the size of the majority of martian dunes, and the amount of sand they contain.

Our new estimate of dune sediment thickness tends to support hypotheses that the dune sands were derived from the polar layered deposits (e.g. Breed et al, 1979; Thomas, 1982, 1988). There are clear relationships between eroding scarps and areas of dunes. Major areas of dunes, such as those between 40 and 70° W, lie downwind of major dissected areas of the perennial polar cap. It is perhaps significant that the major area of dunes between 110 and 260°

W lies between the present limits and large outliers of the perennial ice. Dissected areas of the polar cap and layered deposits extend for some  $3.3 \times 10^5 \text{ km}^2$  (Thomas, 1982). If the layered deposits contained only 1% sand-sized material, some 275 m would have had to have been eroded to provide enough sediment to form the dunes. This is consistent with the local relief of 200-800 m noted by Blasius and Cutts (1982).

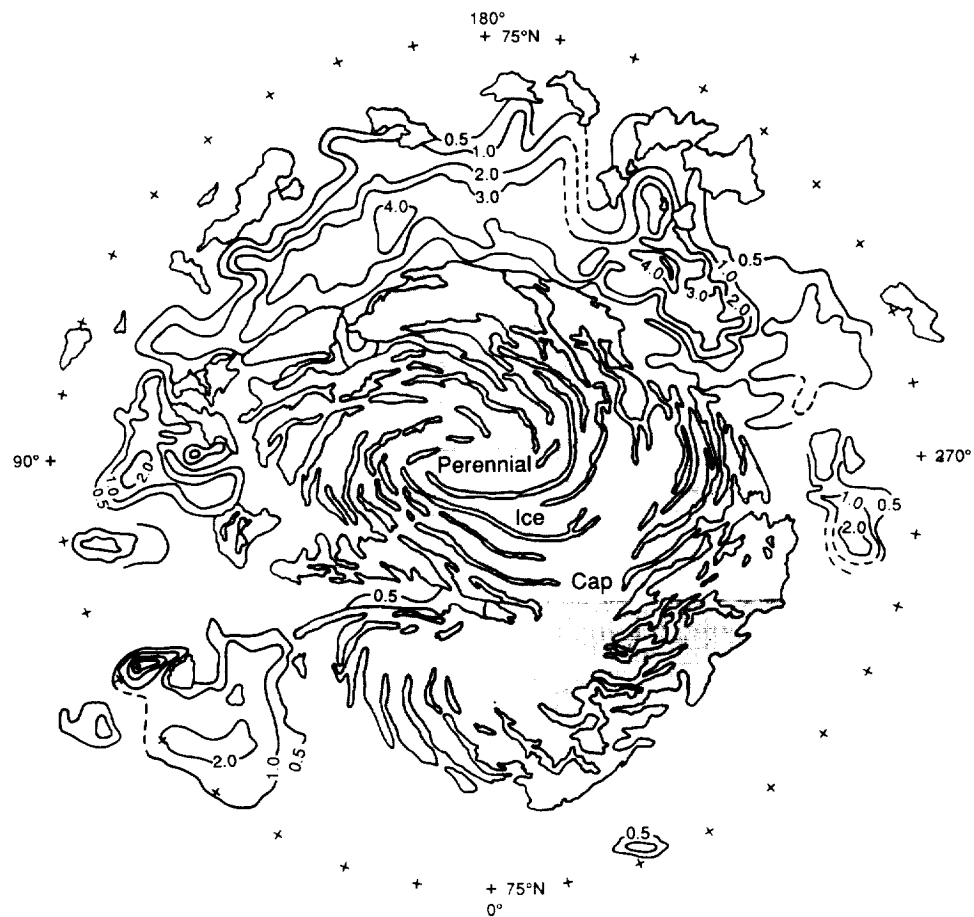


Fig. 3. Equivalent sediment thickness in the North Polar sand seas of Mars. Isopachs in meters.

## References

- Blasius, K.R., Cutts, J.A., and Howard, A.D., 1982. Topography and stratigraphy of Martian polar layered deposits. *Icarus*, 50: 140-160.
- Breed, C.S., Grolier, M.J., and McCauley, J.F., 1979. Morphology and Distribution of Common "Sand" Dunes on Mars: Comparison With the Earth. *Journal of Geophysical Research*, 84: 8183-8204.
- Dial, A.L., Jr., 1984. *Geologic map of the Mare Boreum area of Mars*. U.S. Geological Survey Miscellaneous Investigations Series. Map I-1640 (MC-1).
- Lancaster, N., 1988. The development of large aeolian bedforms. *Sedimentary Geology*, 55: 69-90.
- Thomas, P., 1982. *Present wind activity on Mars: relation to large latitudinally zoned sediment deposits*. *Journal of Geophysical Research*, 87: 9,999-10,008.
- Thomas, P., 1988. Mars: Dune sand sources in North Polar layered deposits. Reports of the Planetary Geology and Geophysics Program, NASA TM-4041: 286-287.
- Tsoar, H., Greeley, R., and Peterfreund, A.R., 1979. Mars: the North Polar Sand Sea and Related Wind Patterns. *Journal of Geophysical Research*, 84: 8167-8180.



## COMPARISON OF MARTIAN AEOLIAN FEATURES AND RESULTS FROM THE GLOBAL CIRCULATION MODEL

*R. Greeley, A. Skyeck, Dept. of Geology, Arizona State University, Tempe, AZ 85287-1404, and J.B. Pollack, NASA-Ames Research Center, Moffett Field, CA 94035.*

Aeolian (wind) processes link the atmosphere of a planet with its surface. Wind is apparently the dominant agent of surface modification on Mars today, as evidenced by frequent dust storms. Features attributed to aeolian processes include dunes, yardangs, grooves, deflation pits, and albedo patterns that are time-variable. In addition, vast regions appear to be mantled with sediments presumably deposited from the atmosphere. Because of the common occurrence of aeolian features on Mars and the frequent occurrence of dust storms, understanding the nature of the features and of the interaction between the atmosphere and lithosphere are critical for several aspects of martian science: (1) the presence or absence of active and inactive dust mantles may affect the interpretation of some remote sensing data for Mars, (2) the location and occurrence of aeolian deposits will strongly influence the selection of potential landing and sample return sites, and (3) interpretation of martian surface evolution must include the identification and separation of material units formed by a wide variety of processes (fluvial, periglacial, volcanic, etc.).

Some surface features can be used to infer wind directions and strengths. For example, Ward et al. (1985) described yardangs oriented with the prevailing winds at the time of formation. However, they noted several "sets" of yardang orientations and suggested that there had been shifts in wind patterns with time. Wind streaks probably constitute the best "wind vanes". As described by Thomas (1982) and others, many wind streaks change with time and may reflect seasonal shifts in wind patterns. Wind streaks and the interpretation of wind patterns have been relatively well documented by Sagan et al. (1973), Thomas et al. (1981), Veverka et al. (1977), Greeley et al. (1977), and others. Incorporation of Viking IRTM data have enabled assessment of sediment sources, transport paths, and deposition sites of windblown sediments (Christensen, 1986; Lee, 1986). Dunes occur in high to mid latitudes (Breed et al., 1979; Thomas, 1982) and in small fields in equatorial regions. Although most are crescentic and barchan types (Breed et al., 1979; Tsoar et al., 1979) indicating a unidirectional wind regime, reversing winds were also suggested by Tsoar et al. (1979). Cutts and Smith (1973) and Lancaster and Greeley (1987) identified reversing and star-like dunes in some areas, suggesting seasonal changes in wind direction. However, the relationship between dune patterns and formative winds remains uncertain and there is poor agreement between the alignment patterns of the dunes and some models of wind patterns (Ward and Doyle, 1983). This may suggest that the dunes formed when martian wind regimes were different. Breed et al. (1979) suggest that some North Polar dunes are eroding today, or being modified under long-term changes in wind regimes; Tsoar et al. (1979) and Ward and Doyle (1983) suggest that some dunes are currently active. Thomas (1981) suggests southern hemisphere dunefields are aligned with current winds.

Important questions remain about the nature of dunes and other aeolian features on Mars and their relationship to past and present winds. The Global Circulation Model (GCM) developed by Pollack et al. is a complex simulation of the martian atmosphere based on Toon et al. (1980). Among the parameter predictions of the martian atmosphere based on Toon et al. (1980). Among the parameter predictions made by this simulation are predictions of wind surface shear stress. A program running on the Cray 2 computer allows predictions to be made for the wind surface shear stress as a function of atmospheric temperature and pressure, location on Mars, and other parameters such as topography, atmospheric dust-loading, and local surface roughness. Output from the program includes maps with wind vectors and strengths for stated conditions of martian season and climate. The magnitude, position, and azimuth of the GCM stress vectors are read from tape and are projected to a mercator base map. Wind streak and other aeolian data are digitized from published maps. The position and azimuth of these data are then calculated and projected to match the base map. Map symbols representative of aeolian features (bright streak, dark streak, yardang, etc.) are then drawn.

To date, bright and dark streak patterns as well as an IRTM rock abundance distribution have been compared to GCM simulations between 65 and -65 degrees latitude for one martian year. We make several qualitative observations. Dark streak patterns show a poor correlation to the GCM predicted ground circulation patterns for all seasons. Bright streak patterns correspond very well to GCM to ground circulation during northern hemisphere winter (dust storm season) and at no other time. The northern hemisphere winter circulation shows a strong correlation to rock abundance. High surface stresses occur in regions of high rock abundance (Acidalia, Chryse, and Utopia). Low stresses occur in regions of low rock abundance (Amazonis, Tharsis, Sinus Sabaeus). In general, surface stress vectors are tangential to broad, regional rock abundance contours.

Several conclusions are drawn from these observations. Bright streak formation must occur during and after dust storm season as globally mobilized dust settles out of the atmosphere. This is consistent with the dust deposition theory of bright streak formation (Veverka et al., 1977). The lack of correlation of the dark streaks suggest that they are a reflection of local conditions, rough topography and surface material properties, invisible at the GCM resolution. The correlation between rock abundance and the dust storm season circulation further supports the conclusion rock abundance is strongly controlled by seasonal aeolian processes (Christensen, 1986).

In the near future evaluation of polar aeolian features will be made with respect to the GCM, as well as more quantitative usage of the GCM to examine sediment transport.

## References

- Breed, C.S., M.J. Grolier, and J.F. McCauley, 1979, Morphology and distribution of common "sand" dunes on Mars: Comparison with the Earth, *J. Geophys. Res.*, **84**, 8183-8204.
- Christensen, P.R., 1986, Spatial distribution of rocks on Mars, *Icarus*, **68**, 217-238.
- Cutts, J.A. and R.S.U. Smith, 1973, Eolian deposits and dunes on Mars, *J. Geophys. Res.*, **78** (20), 4139-4154.
- Greeley, R., R. Papson, and J. Veverka, 1977, Crater streaks in Chryse Planitia region of Mars: Early Viking results, *Icarus*, **34**, 556-567.
- Lee, S.W., 1986, Viking observations of regional sources and sinks of dust on Mars, *MECA Workshop on Dust on Mars II, LPI Tech. Rept. 86-09*, 44-45.
- Sagan, C., J. Veverka, P. Fox, R. Dubisch, R. French, P. Gierasch, L. Quam, J. Lederberg, E. Levinthal, R. Tucker, B. Eross, and J.B. Pollack, 1973, Variable features on Mars, 2, Mariner 9 global results, *J. Geophys. Res.*, **78**, 4163-4196.
- Thomas, P., 1981, North-south asymmetry of eolian features in martian polar regions: Analysis based on crater-related wind markers, *Icarus*, **48**, 76-90.
- Thomas, P., 1982, Present wind activity on Mars: Relation to large latitudinally zoned sediment deposits, *J. Geophys. Res.*, **87**, 9999-10008.
- Toon, O.B., J.B. Pollack, W. Ward, J.A. Burns, and K. Bilski, 1980, The astronomical theory of climate change on Mars, *Icarus*, **44**, 552-607.
- Tsoar, H., R. Greeley, and A.R. Peterfreund, 1979, Mars: The North Polar Sand Sea and related wind patterns, *J. Geophys. Res.*, **84**, 8167-8180.
- Veverka, J., P. Thomas, and R. Greeley, 1977, A study of variable features on Mars during the Viking primary mission, *J. Geophys. Res.*, **82**, 4167-4187.
- Ward, A.W. and K.B. Doyle, 1983, Speculation on martian north polar wind circulation and the resultant orientations of polar sand dunes, *Icarus*, **55**, 420-431.
- Ward, A.W., K.B. Doyle, P.J. Helm, M.K. Weisman, and N.E. Witbeck, 1985, Global map of eolian features on Mars, *J. Geophys. Res.*, **90**(B2), 2038-2056.

## Rock Populations as Indicators of Geologic Processes

Michael C. Malin, Department of Geology, Arizona State University, Tempe, AZ 85287-1404

The objectives of this work have been to 1) quantify the relationships between populations of large boulders and the processes and media that create and transport them, 2) correlate these relationships to remotely observable geomorphic factors and use a properly configured digital camera to then assess these factors, 3) use these relationships and factors to define observational goals for the Mars Observer Camera, and 4) use the relationships and factors to assess requirements for scientific and engineering observations in support of future Mars surface missions.

Boulders and finer materials from four field areas representing three different processes were examined: a) deposits of a catastrophic flood of the Jökulsá á Fjöllum in north central Iceland, b) surge-emplaced ejecta from Halemaumau in the summit caldera of Kilauea Volcano, Hawaii, and c) coarse rockfall accumulations below steep valley-wall escarpments in the central Wright Valley, Antarctica. For each area, the best available aerial photographs were used during the field work to focus study of specific relationships. Field measurements of all boulders  $\geq 0.5$  m in large areas (areas  $\geq 4 \times 10^4$  m<sup>2</sup>) were tabulated. Measurement of the complete surface cover were made in typically five, more limited areas (each one  $\sim 100$  m<sup>2</sup>). Unfortunately, digital data have not yet been acquired owing to the delay in the assembly and test of the Mars Observer Camera engineering model.

Figure 1 illustrates some of the initial results of these studies. The upper graph shows the cumulative number of boulders per square meter as a function of diameter. Basically, two different types of relationships are seen. Boulders that have been transported by, or that have experienced significant interaction with, a fluid (flood deposits, volcanic ejecta) display compoundly curved relationships when plotted on log-log axes, while those that reflect primary fragmentation and simple gravity motion (rockfall accumulations) follow more linear relationships. It should be noted that the "fall-off" with decreasing size is not a resolution effect as commonly encountered in crater counts--these are field measurements of the actual boulders present, and the decrease reflects a paucity of smaller boulders.

The lower graph in Figure 1 shows the areal percentage of surfaces covered by boulders and cobbles, calculated from the diameters measured in the field and *estimates* of the area of finer materials (based on collection and measurement of representative surface fines). A wide range of different relationships is seen. Again, the interaction of the sediment with the transporting media, in particular the continued exportation of only slightly finer fractions subsequent to the deposition of the boulders, appears chiefly responsible for the wide range in area covered by boulders. The volcanic ejecta also appears to have been separated from the finer components (which are found farther from the vent). The rockfall accumulations display an abnormally dense distribution as they were selected for study *specifically because* of their obvious high areal density.

For comparison, rock counts are included for the Viking Lander 1 and 2 sites, based on analyses made on the Viking Lander high resolution mosaics using techniques tested by performing comparable measurements on oblique photographs terrestrial areas studied in the field.

In general, it is not possible to predict on the basis of large boulders the presence or absence of smaller particles, nor is it possible to determine, using the cobble population, the number of large boulders, without first accounting for the nature of the mechanism(s) involved

in shaping the debris distribution function. Conversely, it is possible, using the shape of the debris curve, to distinguish processes, especially when the magnitudes of local slopes are also known. The surfaces studied represent extremes in the density of boulders, as they were biased by the need to acquire statistically significant numbers in order to characterize the size/frequency relationships. Indeed, at some locations, the areal coverage approached 100% (for example, where boulders are imbricately stacked on one another in bars). However, on the vast majority of surfaces, materials  $\geq 10$  cm diameter covered  $\ll 10\%$  of the surface. In fact, areas where boulders and cobbles covered more than a few percent ( $\sim 1-3\%$ ) of the surface accounted for less than 0.1% of the surfaces studied. Owing to sorting relationships, wherever cobbles or boulders *were* concentrated, only a relatively small range in debris size occurred. If, for example, a catastrophic flood bar had a mean boulder size of 3 m, there are few boulders less than a meter or greater than 5 m across.

Eolian processes, and surface creep and sheet flow phenomena, have significantly modified the fine components at each of the sites studied. Wind- or low discharge water-flow have exported sand and imported both gravel and silt, and water-aided infiltration has enriched the surface and near sub-surface in fines. The development of an equilibrium distribution of pebbles and cobbles by "wind shadowing" (the "Chepil Equilibrium") establishes an areal density maximum of about 30-35% of the surface area for most locations where sand comprises the dominant grain size. Materials with other dominant grain sizes do not show the same distribution, but rather reflect different and sometimes competing processes of deposition and erosion.

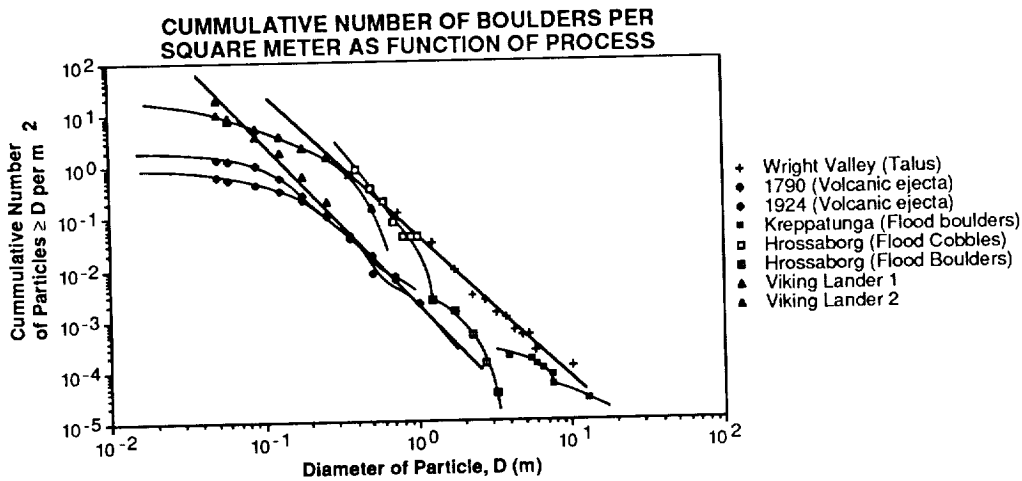


Figure 1 (top): Cumulative number of boulders per square meter as a function of boulder diameter. Note that boulders transported or interacting with a fluid display a compound curve while those reflecting fragmentation and gravity motion show a linear curve (in the log-log representation).

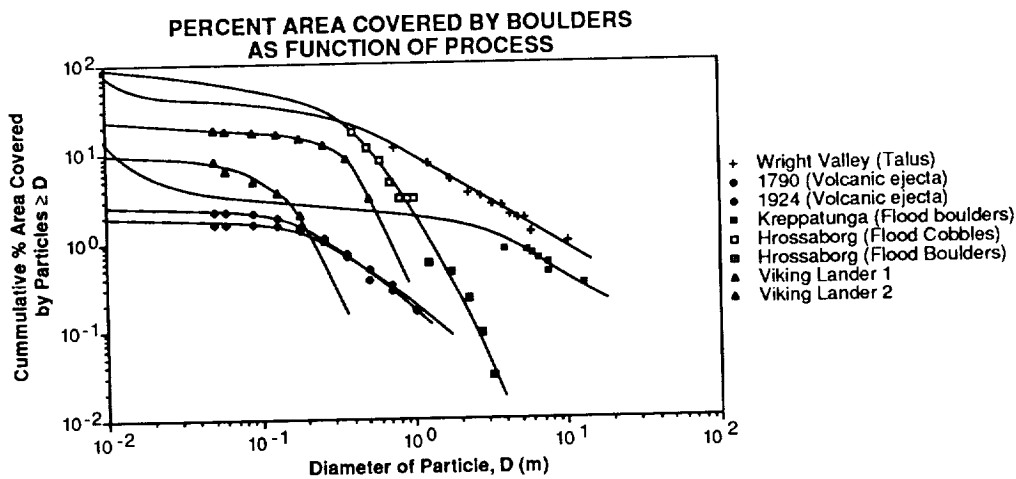


Figure 1 (bottom): Cumulative percent of area covered by rocks greater than or equal to diameter  $D$  as a function of diameter. Note the wide range of different types of curves, reflecting different processes. It is not possible to predict the density of 10 cm diameter cobbles from the abundance of 5 m boulders, nor is it possible to predict the number of 5 m boulders from the 10 cm cobble density.

## APPLICATIONS OF GRAIN-PIVOTING AND SLIDING ANALYSES TO SELECTIVE ENTRAINMENT OF GRAVEL AND TO FLOW-COMPETENCE EVALAUTIONS

Komar, Paul D., and Li, Zhenlin, College of Oceanography, Oregon State University, Corvallis, Oregon

Models of sediment threshold by grain pivoting or sliding over underlying particles are examined in order to explore their application to evalautions of selective entrainment of gravels by flowing water. Of special interest is whether such process-based models provide satisfactory evaluations of flow competence and the movement of large clasts by floods. A detailed derivation is undertaken, focusing first on the fluid flow and forces at the particle level. The resulting threshold equation for the particle-level velocity is then modified to yield the mean entrainment stress for the flow as a whole. This approach is appropriate for considerations of selective entrainment of grains of varying sizes within a deposit, the sorting being due to their relative projection distances above the bed and the dependence of their pivoting angles on grain size and shape. The resulting threshold equations contain a number of coefficients (e.g. drag and lift) whose values are poorly known, but can be constrained by requiring agreement with the Shields curve for the threshold of grains in uniform deposits. If pivoting coefficients based on laboratory measurements with tetrahedral arrangements of particles are used in the models, smaller degrees of selective sorting are predicted than found in the field measurements of gravel entrainment. However, if reasonable modifications of those coefficients are made for expected field conditions, then the models yield good agreement with the data. Sliding models, where sorting is due entirely to projection distances of the grains above the bed, yield somewhat poorer agreement with the field data; however, the sliding models may have support from laboratory experiments on gravel entrainment in that the data and theoretical curves have similar concave trends. The existing measurements lack documentation of the mechanisms of grain movement, so it is not possible to conclusively determine the relative importance of pivoting versus sliding. In spite of such uncertainties, the results are encouraging and it is concluded that pivoting and sliding models for grain entrainment do have potential for field computations of selective entrainment and flow competence.

## GRAIN-SIZE VARIATIONS DURING TRANSPORT AND THE EQUAL MOBILITY OF GRAVELS IN OAK CREEK, OREGON

Komar, Paul D., and Shyuer-Ming Shih, College of Oceanography, Oregon State University, Corvallis. Oregon

Size distributions of gravels transported in Oak Creek show systematic variations with flow discharges and bed stresses. At high discharges the transported gravels fit Rosin distributions, the distribution produced by crushed rock fragments. At low discharges the gravel distributions are Gaussian. Bimodal distributions are obtained at the early stages of floods, but none are found during waning stages, even though flow discharges are similar. Transformation from the Gaussian to a Rosin distribution with increasing discharge can be explained by processes of selective entrainment and transport. Samples of the armor and subarmor follow Rosin distributions, reflecting the source-rock nature of the gravels. At high discharges the transported materials reflect the Rosin distribution of the bed gravels, although there are distinct shifts in ranges of sizes. At lower discharges random-selection processes must be more important to gravel entrainment; the resulting Gaussian distributions of transported gravels then reflect similar distributions of bed stresses exerted by the stream flow.

The systematic changes in size distributions with discharge indicate a departure from a condition of equal-grain mobility which has been suggested for gravel transport in Oak Creek. Although all size fractions participate in the shifting distributions, the largest changes are found in the coarsest fractions. This permits flow-competence correlations which involve the measure of a current's sediment moving ability inferred from the sizes of the particles transported under a given set of hydraulic conditions. Flow competence equations have been developed for Oak Creek which yield evaluations of discharges, mean bed stresses and the Shields entrainment parameter as functions of the transported gravel sizes. The gravel sizes used in such correlations include the parameters of the Rosin distribution and the maximum clast diameters transported.

## FLOW-COMPETENCE EVALUATIONS AND THE NON-EQUAL MOBILITY OF GRAVELS IN OAK CREEK, OREGON

Komar, Paul D., College of Oceanography, Oregon State University, Corvallis, Oregon

Flow-competence assessments of floods have been based on the largest particle sizes transported, and yield either the mean flow stress, mean velocity, or discharge per unit flow width. However, questions have been raised concerning how meaningful those evaluations are in view of evidence for the equal mobility of all grain-size fractions in gravel-bed streams. In order to address this issue, the gravel bedload data of Milhous (1973) from Oak Creek have been analyzed to examine how percentiles ranging from the median to the 95th of the sieved distributions vary with flow stresses and discharges, and how these results compare with the variations of the maximum particle sizes transported. Of the several percentiles, the medians change most rapidly with increasing flow, the 60th percentile is next, and so on to the coarsest 95th percentile which shows the smallest response. The variations in the sizes of the maximum particles transported continue this trend, and are similar to those for the 95th percentile. These systematic variations are consistent with changes in the overall grain-size distributions which tend to be symmetrical and Gaussian at low discharges, but become skewed Rosin distributions at high flow stages. It is concluded that gravel transport in Oak Creek departs significantly from perfect equal mobility, and this permits flow competence evaluations from the changing bedload grain sizes. The simultaneous use of several percentiles from the bedload size distributions, together with the maximum particle sizes transported, yield the optimum competence evaluations of flood hydraulics.

Similar analyses are underway of the measurements by P.A. Carling of gravel transport in Great Eggleshope Beck, England. The bed material in that stream shows little if any development of an armor pavement, and therefore will provide an interesting contrast with the results from Oak Creek which is classically armored.



## CHAPTER 9

### VOLCANIC PROCESSES AND LANDFORMS



## RHEOLOGICAL EXTREMES OF CRYOGENIC LIQUIDS ON ICY SATELLITES

J.S. Kargel and S.K. Croft, Lunar and Planetary Lab, University of Arizona, Tucson, AZ 85721

Throughout the past decade of Voyager spacecraft explorations it has become increasingly apparent that the surfaces of many icy satellites have been constructed and shaped by extrusions and explosions of cryogenic liquids, and, in the cases of Titan and Triton, may also be washed by seas of cryogenic liquids.

The compositions of these cryovolcanic materials are not well known, but a well-educated guess holds that the cryovolcanic lavas were generally aqueous solutions, and in many cases probably also were ammonia-rich, and may have contained other substances as well. The hypothetical seas of Titan and Triton, if they exist, are probably rich in liquid nitrogen, containing also uncertain quantities of methane, ethane, and other non-polar hydrocarbons and heavy organics. Frozen lava flows of similar non-polar liquid solutions might also be expected in the coldest reaches of the Solar System.

The dimensions and morphology of cryovolcanic landforms, like their terrestrial silicate counterparts, depend sensitively on the exact compositions and rheological behaviors of the lavas. The response of cryovolcanic crusts to differential stresses (i.e. folding or faulting under compression) also depends on the lava flow layer thicknesses (therefore, lava rheology). Much of the variability in icy satellite surfaces can be attributed, directly or indirectly, to lava rheology.

Less is known about Titan and Triton. Do cryogenic seas, perhaps even cryogenic analogs of the terrestrial hydrologic cycle exist on Titan or Triton? The erosional potential and sediment-carrying capacity of waves and currents in these seas or streams, if they indeed exist, depend to a large extent on the viscosity of the liquid. Although this is still deep within the realm of speculation, the upcoming encounter with Triton may offer us an exciting glimpse of such activity. Whatever phenomena Triton exhibits, it almost certainly will be a world largely formed and shaped by liquids, past or present; the landforms, whatever they may be, will tell us something about the rheology of those liquids. The rheological properties of cryogenic liquids may allow us to infer the compositions of the surface materials. The remainder of this paper shows that plausible cryogenic liquids may span a dozen or more orders of magnitude in viscosity. Of all the satellites in the Solar System, Triton and Titan offer the greatest chance that landforms shaped by liquids spanning this full range of viscosities will be observed.

Figure 1 shows a plot of liquid viscosity vs. temperature. The silicates are shown only for reference, as these are certainly not expected to occur near an icy satellite's surface. The non-polar mixtures of nitrogen and methane, and weakly polar carbon monoxide (not shown), have very low viscosities, lower than that of water at ordinary temperatures. Figure 2 shows that liquid nitrogen is very "watery" in its consistency. These substances (and water as well) would form volcanic flows on the order of a few centimeters in thickness, perhaps like komatiite flows on Earth. Standing or flowing bodies of nitrogen-methane liquid, with unfrozen surfaces, would respond to wind and gravity much like water does on Earth.

The ammonia-water peritectic mixture, at the freezing point (176 K), has a viscosity comparable to basaltic liquids; this liquid pours readily (about like honey) (Figure 3). This material may form volcanic flows on the order of a meter thick. However, ammonia-water liquid/ice slurries are much more viscous; a few tens of percent ice crystals in a rapidly chilled ammonia-water liquid can yield viscosities orders of magnitude greater. Ammonia-water slurries that are largely solidified when erupted could form flows tens or even hundreds of meters thick, particularly on the smaller satellites where the gravity is low.

The viscosity of ammonia-water mixtures may also be increased dramatically by supercooling (Figure 4) or by the addition of freezing-

point lowering substances, such as methanol (Figure 5). The effect of methanol is very striking; the ternary ammonia-water-methanol eutectic liquid, at its freezing point (about 153 K) is so viscous (about  $10^5$  poise) that it is very difficult to manipulate by hand; Figure 5 was obtained at a temperature about 10K higher than the freezing point, so that the freezing point viscosity is actually about an order of magnitude greater than shown. Even small degrees of partial crystallization make this substance truly impossible to manipulate by hand; its viscosity becomes approximately like that of terrestrial rhyolite (or like candle wax at room temperature). Lavas so composed would probably generate flows on the order of a kilometer in thickness, and would irradiate to a dark gray color, perhaps offering an explanation for cryovolcanic flows on Ariel and Miranda.

Figure 1 (right).

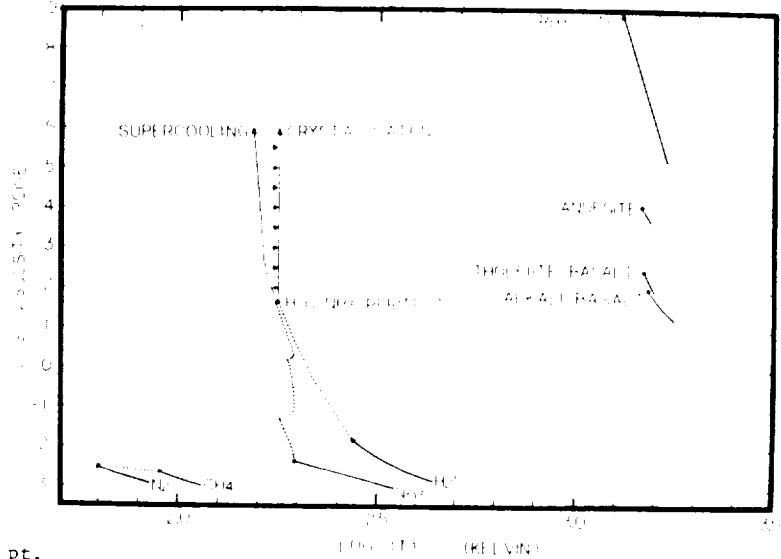
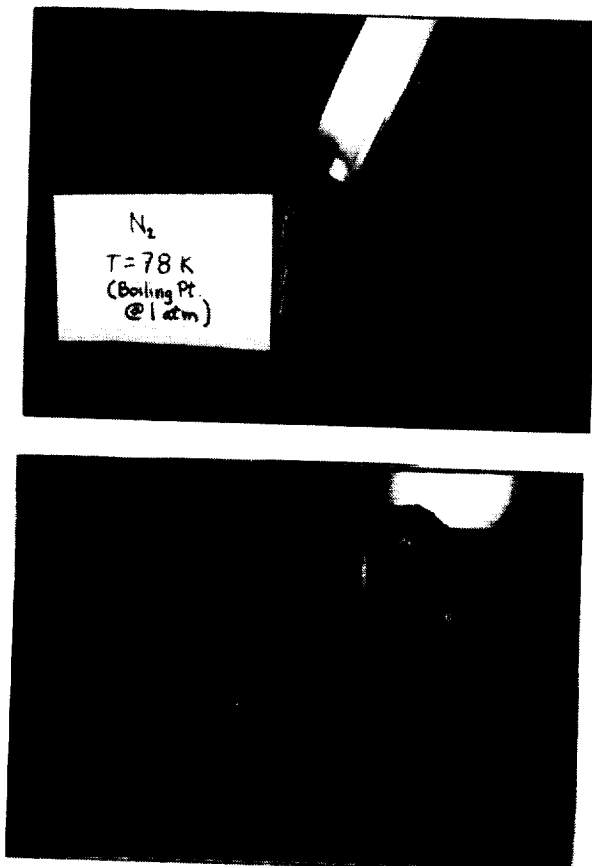


Figure 2, 3, 4, and 5, Below, Set of four, starting upper left, clockwise, 2) Liquid nitrogen 3) Ammonia-water peritectic liquid 4) Super-cooled ammonia-water,  $T = 165K$  5) Ammonia-water-methanol, above freezing pt.



# CAN WE RADIOMETRICALLY DATE CRYOVOLCANIC FLOWS ON ICY SATELLITES?

J.S. Kargel, Lunar and Planetary Lab, University of Arizona

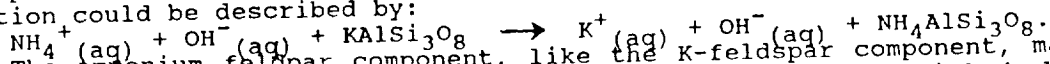
It is commonly assumed that radiometric dating of natural rocks and minerals is practical with silicate substances, but will not be possible with cryovolcanic ices on the icy satellites of the giant outer planets because of the presumed lack of high atomic weight radioactive and radiogenic elements in the ices. If true, this would seriously hinder our future efforts to understand the geological and cosmogonic histories of the icy satellites. This report is a preliminary assessment of the potential for obtaining absolute ages; the view from this lab is rather encouraging, if only we can obtain some samples!

We might be able to apply K-Ar methods of dating using degassed or partially degassed silicate xenoliths, such as certain phyllosilicates. A big problem frequently encountered in terrestrial K-Ar and Ar-Ar dating of clays and certain very fine-grained micas is that many of these (e.g. glauconite) readily lose their radiogenic Ar and even exchange Sr at Earth surface temperatures in the presence of fluids. This "problem" may be of great utility in dating icy satellite surfaces if some xenolithic phases tend to equilibrate with their surroundings at satellite interior temperatures, but then retain their radiogenic Ar at satellite surface temperatures. If so, the K-Ar isochron and  $^{40}\text{Ar}/^{39}\text{Ar}$  step heating methods applied to xenolithic silicates transported to the satellite surfaces may yield absolute cooling ages for the flows. However, beyond the many technical uncertainties at this point, these methods of dating will require the good fortune of sampling appropriate siliceous xenoliths, which may or may not be widely dispersed in cryovolcanic flows. Other dating techniques involving cosmogenic nuclide production (e.g.  $^{14}\text{C}$  and  $^{10}\text{Be}$ ) may turn out to be useful for dating very young cryovolcanic flows or pyroclastic deposits as may occur on Enceladus and Europa.

Other more conventional dating schemes rely on the presence of radioactive elements dissolved in the liquid at the time of eruption. Natural aqueous substances on Earth (river water, seawater, and hydrothermal fluids) contain plentiful dissolved salts, including the same elements used for radiometric dating of rocks. Clearly, water is a powerful leaching agent for temperatures near 300K. Additionally, the occurrence of water-soluble salts in carbonaceous chondrites indicate that processes of aqueous alteration, transport, and re-precipitation have occurred in some meteorite parent bodies. These considerations suggest that aqueous cryovolcanic liquids, believed to have been a chief geological re-surfacing agent on icy satellites, would also have contained dissolved salts leached from the silicate portions of these objects.

However, there are two important considerations which do not allow one to so quickly draw this conclusion: first, most common cryovolcanic lavas probably are ammonia-water-rich (but note that ammonia-water solutions are widely utilized in the mining industry as a leaching agent). Secondly, the ammoniacal aqueous cryo-lavas are probably generated by partial melting near the ammonia-water peritectic ( $-97^{\circ}\text{C}$ ), and the low temperatures generally should reduce salt solubilities, and may considerably affect the kinetics of the leaching reactions. The remainder of this report focusses on the solubility of potassium salts in ammonia-water liquids, determined in this lab experimentally.

If pure ammonia-water liquid was the reactive leaching agent, and if feldspar was the host phase for K in unaltered silicates, the chemical exchange reaction could be described by:



The ammonium feldspar component, like the K-feldspar component, may reside in solid solution in plagioclase, although several terrestrial hydrothermal deposits include a nearly pure ammonium end-member, buddingtonite, believed to have been formed by the low temperature (ca. 300K) reaction of plagioclase with ammonium-rich fluids (1). If this were the only important exchange reaction, then the leached K would exist in solution as dissolved KOH, which is highly soluble in the ammonia-water peritectic liquid. However, the likely presence of other ionic species in solution, including  $\text{Cl}^-$ ,  $\text{SO}_4^{2-}$ ,  $\text{HCO}_3^-$ ,  $\text{Mg}^{+2}$ ,  $\text{Ca}^{+2}$ ,  $\text{Na}^+$ , and  $\text{NH}_4^+$ , requires one to consider equilibria involving many different salts.

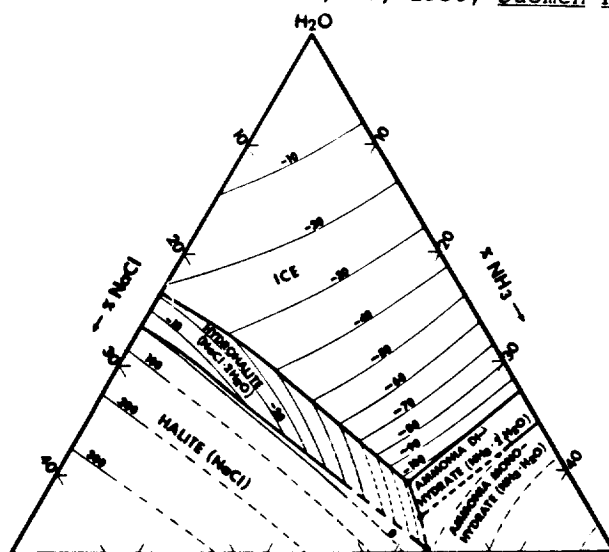
The approach used here is to simplify the chemistry to 3 and 4-component systems. Early experimental runs have indicated that several carbonate and sulfate salts have very low solubilities in the ammonia-water peritectic liquid (2); on the one hand, these low solubilities suggest that these salts will be early crystallizing phases in solidifying cryolavas; on the other hand, their

low abundances indicate that they may be insignificant with respect to K salt precipitation. Therefore, the first step toward chemical simplification is to ignore the sulfates and carbonates. And, the extremely high solubility of KOH indicates that KOH hydrate will never attain saturation. Some of the chlorides have intermediate solubilities, suggesting that these may be the most important salts in ammonia-water cryolavas.

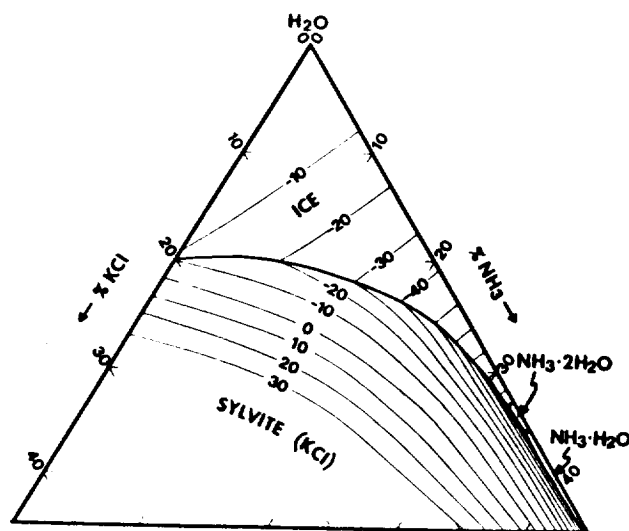
Figure 1 shows the liquidus surface for the ternary system  $\text{H}_2\text{O}-\text{NH}_3-\text{NaCl}$ . The rather high solubility of the halite component ( $\text{NaCl}$ ) in the peritectic liquid (13%) makes hydrohalite ( $\text{NaCl}\cdot 2\text{H}_2\text{O}$ ) unlikely to be near saturation in freshly erupted liquids. However, hydrohalite will probably be an important late-stage crystallization product along with other minor constituents and the dominant ammonia hydrates. The radioactive elements  $^{40}\text{K}$  and  $^{87}\text{Rb}$  do not substitute for Na significantly in halite structures at low temperatures; instead, K and Rb probably enter together into sylvite ( $\text{KCl}-\text{RbCl}$  solid solution) (3). Figure 2 shows the liquidus surface of the system  $\text{H}_2\text{O}-\text{NH}_3-\text{KCl}$ ; note that the KCl concentration in the ternary peritectic liquid is substantially lower than is the case with NaCl (0.65% vs. 13 weight %). The importance of NaCl with regards to KCl precipitation is the solubility moderation exerted by the common ion effect. A simple calculation shows that KCl solubility in the hydrohalite-saturated ammonia-water peritectic liquid will be reduced to about 0.03% (= 150 ppm of K). It seems likely that the progressive concentration of NaCl in the residual liquid of solidifying flows will force the precipitation of sylvite. The likely widely distributed occurrence of sylvite in at least minor quantities provides for the future possibility that sylvite can be separated from returned samples and can be dated by the K-Ar and Rb-Sr mineral isochron methods. On the other hand, KCl solubility is high enough that "whole-rock" samples may contain enough K to permit whole-rock K-Ar dating, which might be accomplished *in situ*. Alternatively, or additionally, K and Rb may precipitate in other salts not yet considered, such as carnallite ( $\text{KMgCl}_3\cdot 6\text{H}_2\text{O}$ ), schoenite ( $\text{K}_2\text{SO}_4\cdot \text{MgSO}_4\cdot 6\text{H}_2\text{O}$ ), or in ammonium salts by the replacement of  $\text{NH}_4^+$  (the ionic radii of  $\text{K}^+$ ,  $\text{Rb}^+$ , and  $\text{NH}_4^+$  are nearly identical).

It must be emphasized that these experimental studies and the comments pertaining to them ignore possible kinetic limitations on leaching at low temperatures. This deficit as well as the possibilities offered by additional salt components are being addressed by further work.

1. Erd, R.C. *et al.*, 1964, *J. Mineralog. Soc. America*, 49, 831.
2. Kargel, J.S., 1988, *Lun. Planet. Sci.*, XIX, 583.
3. Hovi, V., 1950, *Suomen Kemistilehti*, 232, 80.



SYSTEM  $\text{H}_2\text{O}-\text{NH}_3-\text{NaCl}$



SYSTEM  $\text{H}_2\text{O}-\text{NH}_3-\text{KCl}$

Figure 1. Liquidus surface in the ammonia-water-sodium chloride system. Isotherms give liquidus temperature in  $^{\circ}\text{C}$ , and are dashed where extrapolated.

Figure 2. Liquidus surface in the ammonia-water-potassium chloride system.

# **CHARACTERIZATION OF SMALL SCALE PROPERTIES OF BASALTIC LAVA PLAINS: APPLICATION TO MARS ROVER SAMPLE RETURN MISSIONS**

**J. C. Aubele and L.S. Crumpler,** *Department of Geological Sciences, Brown University, Providence, Rhode Island 02912*

Proposed Mars rover/sample return missions will traverse, or at least photograph and sample, small-scale surface blocks and outcrops within large flow units. Terrestrial field experience, Apollo mission analysis, and Viking Lander 1 site analysis show that, for thinly mantled volcanic plains areas, a reconnaissance traverse cannot readily distinguish (1) boundaries between petrologic/morphologic flow units; (2) gradational contacts; (3) albedo markings that may be visible in aerial or satellite images. Information can be acquired concerning (1) geomorphic/terrain units such as consolidated or unconsolidated outcrop, soil and boulder fields; (2) lava flow textural variations such as block/cobble population; (3) meter scale geomorphic features such as areas of aeolian transport or deposition; and (4) chemical and material properties. The scale of the feature to be observed is an important factor. Different scale features require different traverse lengths in order to accumulate adequate knowledge about that feature. Mineralogical/material properties can be characterized in short traverses while terrain or geologic unit recognition requires greater distances. In relatively homogeneous volcanic plains areas, basic knowledge necessary to characterize the general area can be acquired in relatively short traverse distances. Since scale is so important, it is necessary to define problems and anticipated information acquisition in accordance with rover distance capabilities. Volcanic plains units appear to be a dominant terrain type on Mars and may be favored landing sites due to engineering and sampling constraints. The small scale surface characteristics of a volcanic plains unit, (blocks, cobbles, outcrops, dunes, and other surficial materials) will be visible, and may even act as limiting parameters to rover trafficability or lander sampling strategies. These small scale surface characteristics can be interpreted in a geologic context if we understand the nature of degraded basaltic flow surfaces.

Recent field observation and numerical modeling of the pattern and origin of vesicle zones and joints in terrestrial basaltic flows has resulted in increased understanding of the processes which affect flow surface morphology. This work has documented the ubiquitous occurrence of three vertical zones in

basalt flows: (1) an upper vesicular zone; (2) a middle vesicle-free zone and (3) a lower vesicular zone. The upper vesicular zone is generally about one-half of the total flow thickness. Computer modeling of the development of these zones confirms that vesicle zonation is a result of the nucleation, growth and rise of bubbles in solidifying lava and can be expected to occur in all basaltic flows. Degradation of basaltic flows, therefore, will produce vesicular blocks until the erosional level reaches the central vesicle-free zone.

In addition, observation of terrestrial basaltic flows has shown that most thin (less than 10m thick) flows have a regular pattern of orthogonal joints in vertical section. The joint pattern characteristically occurs with individual joint planes oriented perpendicular and parallel to the flow surface. Parallel joints are generally laterally continuous in many flows, and increase in spacing downward. A few perpendicular joints penetrate the entire thickness of the flow, separated by a distance equivalent to the flow unit thickness. Between these joints, adjacent joints extend to shorter distances within the flow; and between these shorter joints, other joints extend to even shorter vertical distances. A modified model of contraction crack formation and interaction can explain the observed regular spacing of joints oriented perpendicular to the flow surface. The typical thin basaltic flow is jointed into slabs or blocks with dimensions which generally increase with depth beneath the flow surface. As a general approximation, the joint spacing at a specific level in the flow will be roughly equivalent to the depth from the primary flow surface to that level. Therefore, as a flow erodes vertically the degradational surface of that flow will be characterized by blocks of a size similar to the spacing of joints at that level in the flow. As a basaltic flow degrades, the erosional surface will be characterized by a bimodal distribution of fines and blocks. The mode of the block size population is an indication of the depth to which that flow has been eroded.

These studies, and the new understanding of basaltic flow surfaces that they provide, can be used to: 1) predict the surface properties of basaltic plains units which will act as limiting parameters to trafficability and sampling strategies for future Mars rover/ sample return missions; and 2) construct models of basaltic surfaces by which the images and samples from future missions can be evaluated and interpreted.



## Erosional and Depositional Processes in the Martian Heavily-Cratered Terrain

Jeffrey Moore, Department of Geology, Arizona State University, Tempe, AZ 85287-1404

Mosaics of high-resolution (20 to 80 m/pixel) contiguous images and other data (i.e. IRTM and radar) have been used to examine the erosional and depositional processes responsible for various surface features within large tracts of martian heavily-cratered terrain. Regional chronologies and stratigraphies have been developed in order to determine the succession of climatological and environmental factors that influenced surfaces of the heavily-cratered terrain.

A portion of the heavily-cratered terrain in northeastern Arabia (~20-30°N, ~285-325°W) was the first area of study. Within this area are two subdivisions of the Plateau Sequence as mapped in the recent USGS 1:15M geologic map of eastern Mars (Greeley and Guest, 1987). The upper unit is classified as *etched material*, interpreted to be a mixture of lava flows, pyroclastic material, and impact ejecta degraded by wind erosion, decay of ground ice, and minor fluvial processes. The lower unit is termed *ridged material*, interpreted as an uneroded deposit of materials similar to those composing etched material but subjected to normal faulting, volcanic construction, and/or compressional tectonics.

The findings of this study indicate that this region appears to be overlain by an extensive deposit of material with the following characteristics:

- 1) It forms the "cap-rock" of the fretted terrain mesas east of 300°W.
- 2) Channels (including the "fretted channels") cut through this deposit but do not significantly cut through underlying materials.
- 3) The deposit is  $\leq 0.4$  km thick where measured in channel cuts.
- 4) The deposit covers several 106 km<sup>2</sup> of heavily-cratered terrain north of ~10°N in Arabia.
- 5) The deposit is composed of at least four layers where it is differentially eroded in Auqakuh Vallis (30°N, 300°W).
- 6) Most of the uppermost layer is missing and assumed to be most easily eroded.
- 7) The middle layers form mesas of etched terrain where this deposit is undergoing widespread erosion.
- 8) Floors of some exhumed craters >10 km diameter are covered with an erosion-resistant, lower albedo layer presumably associated with this deposit. This lower-albedo material also forms free-standing, roughly circular mesas presumably at sites of craters now completely eroded away.
- 9) The deposit mantles pre-existing topography, rather than filling in all depressions as to destroy relief. It produces so-called "softened terrain" discussed in Squyres and Carr (1986).

- 10) The deposit was laid down over some period of time, probably on the order of millions of years. Evidence for this is:
- a) Inverted channel topography in Auqakuh Vallis indicates that following the erosion of a channel into a lower layer of this deposit, continued deposition filled the channel. Subsequent erosion formed the present Auqakuh Vallis system, including a channel immediately adjacent to the older, infilled channel. Widespread differential surface erosion of this deposit has exposed the material infilling the older channel, creating a ridge.
  - b) Of 120 craters >10 km in diameter counted in high-resolution images covering an area ~450,000 km<sup>2</sup>, 75% were completely mantled (no raised exterior rims) and 25% had raised rims and some interior crater morphology but no ejecta deposits. One-fourth of the craters >10 km in diameter formed after some of the deposit was in place but before the end of deposition.
- 11) The cumulative crater size-frequency curve for craters >10 km in diameter is indistinguishable from that of the intercrater plains seen elsewhere in the heavily-cratered terrain (Malin, 1976), implying that the deposit is quite old and did not form over much of martian history.
- 12) The IRTM models of Christensen (1986) indicate low block abundance (<5%) on the deposit surface, although the surface has an intermediate thermal inertia (~5 X 10<sup>-3</sup> cal cm<sup>-2</sup> sec<sup>-1/2</sup> °K<sup>-1</sup>). Most of the heavily-cratered terrain is blockier (~15%) and has a higher thermal inertia (~7 X 10<sup>-3</sup> cal cm<sup>-2</sup> sec<sup>-1/2</sup> °K<sup>-1</sup>). A low-rock, intermediate thermal inertia surface may be composed of a cemented, porous or low-density material.

If a deposit with the characteristics noted above were observed on the Earth (based on remotely sensed data), a reasonable conclusion would be that it is an extensive, undeformed, horizontal, massive, marine-laid sedimentary deposit presently undergoing erosion, such as is observed on the Colorado Plateau. The absence of significant evidence for ocean-sized bodies of water ever present on Mars forces the exclusion of this explanation. Two more plausible possibilities are that the unit is a differentially-welded pyroclastic tuff or a differentially-compacted, zonally indurated dust deposit.

A pyroclastic origin for the deposit is attractive for several reasons. Among the features the deposit shares with pyroclastic deposits on Earth are its ability to mantle rather than infill pre-existing topography, the apparent increase in deposit induration with depth, and the formation of large, flat-layered beds that erode to form mesas. However, the drawbacks to the pyroclastic hypothesis are significant. The martian deposit is very large in areal extent and there are no apparent source vents, and a pyroclastic origin would require a long episode of repeated eruptions from a number of sources that were later covered by subsequent deposits. The only candidate location for these now-covered putative source vents would be the younger lowlands beyond the highlands-lowlands boundary just north of the northern edge of the deposit under study. The absence of stoss-side banking of material against topographic obstacles would suggest that the deposit, if pyroclastic, was not emplaced by ground-hugging flows but as an air-fall that retained sufficient heat to partially weld.

The indurated dust hypothesis for this deposit's origin also explains several of its characteristics. An eolian dust deposit could be very large in areal extent and would mantle pre-existing topography. The deposition of airborne dust could take place episodically over long geologic periods. The greatest objection to this hypothesis is that terrestrial loess deposits do not erode to create steep-sided mesa. However, if the deposit were somehow wetted and subsequently dried, the materials in the deposit might become bonded. The stratigraphic relationships noted above would require such bonding to be a function of either depth (if it occurred after the deposit was formed), or time (lower, older layers were bonded while higher, younger layers were not). Additional information forthcoming from Mars Observer and/or Mars 94 may help resolve these issues.

## References

- Christensen, P. R., The spatial distribution of rocks on Mars, *Icarus* **68**, 217-238, 1986.
- Greeley, R. and J.E. Guest, Geologic map of the eastern equatorial region of Mars, *U.S. Geol. Surv. Misc. Inv. Map I-1802-B*, 1987.
- Malin, M.C., Age of the martian channels, *J. Geophys. Res.* **81**, 4825-4845, 1976.
- Squyres, S. W. and M. H. Carr, Geomorphic evidence for the distribution of ground ice on Mars, *Science* **231**, 249-252, 1986.

# MARS: VOLCANISM IN THE VALLES MARINERIS OVERLOOKED?

B.K. Lucchitta, U.S. Geological Survey, 2255 N. Gemini Dr., Flagstaff, AZ 86001

Do volcanic rocks exist in the Valles Marineris? This question is pertinent because the Valles Marineris are gigantic grabens, rivaling rift valleys on Earth in size and depth. They have been interpreted as extensional tectonic structures, perhaps incipient rifts (1, 2, 3, 4). On Earth, rift valleys commonly contain volcanic deposits. On Mars, deposits inside the Valles Marineris grabens do not have the unique morphologic signature of such easily identified volcanic features as shield volcanoes or lava flows. Therefore, many researchers have not recognized the deposits inside the Valles Marineris as volcanic. Is Mars, then, different from Earth in having formed riftlike grabens unaccompanied by volcanism?

An intensive study of high-resolution stereoscopic images found that deposits inside Valles Marineris reflect two episodes of deposition: in the older, a layered sequence was formed that now stands as high eroded mesas approaching the elevation of the bordering plateau (5); in the younger episode, material was deposited on a deeply eroded surface whose elevation is close to that of the present trough floors (6).

The older sequence consists of layers displaying a variety of morphologies and thicknesses. Thin-bedded layers alternate with thick-bedded ones. Some layers are single; others occur in repeated couplets. Dark and light layers are interbedded. Locally, dark layers are more resistant to erosion and form ledges that shed dark talus slopes; light layers tend to be more massive and are dissected by parallel flutes even on low slopes, attesting to susceptibility to wind erosion.

The origin of these deposits is controversial. Volumetric constraints and lack of source areas make it unlikely that the deposits are solely of fluvial or alluvial origin, deposited in water (5, 6). An eolian origin, for instance trapping of wind-blown material in ice-covered lakes (7), is questionable for volumetric reasons also. Therefore, a volcanic origin for the majority of these layered beds is plausible by default more than by incontrovertible evidence. Additionally, as shown below, younger interior deposits are probably volcanic, so that it stands to reason that the older layered deposits also had volcanic components. And, the observed morphologies are consistent with those of volcanic deposits on Earth: dark, resistant layers are similar to terrestrial basalt layers; massive, light layers resemble ash-flow tuffs.

The younger sequence of interior deposits consists of (a) very dark patches that are spectrally relatively blue and have short, stubby lobes in places; they occur characteristically along faults (8); (b) light-colored, thick, smooth deposits that are locally associated with apparent volcanic craters (9); and (c) deposits with lobate fronts, local layering, rough surface textures, and highly irregular albedos. The base of these younger deposits is an unconformity; they embay interior mesas, landslides, and tributary canyons. They are generally thin, but in western Candor Chasma they may reach a thickness of 3,000 meters. These materials are probably volcanic: the dark deposits have spectral signatures similar to mafic rocks on Earth (6); their association with structures suggests internal origin; the

locally varied, disordered, and rugged aspect of the thick deposits is not compatible with emplacement by wind; the layering in some sections and lack of a source area make debris-flow origin unlikely; and lobate fronts and embayments suggest flow material.

The very dark patches may be mafic. Because the albedo contrast between the dark and light deposits is not as large as the enhanced images would suggest, the light units could be palagonitic tuffs (10), a composition that also agrees with their reddish spectral signature. On the other hand, young light deposits in places form extensive flat sheets with lobate fronts, perhaps implying ash-flow emplacement; elsewhere, young light deposits are thick and have stubby lobes, implying viscous material. Both of these observations are consistent with volcanism more volatile rich, explosive, and perhaps more felsic than is generally assumed to have occurred elsewhere on Mars.

Overall, results from the study suggest that (a) volcanism was present in the Valles Marineris, (b) the volcanism was explosive in places, (c) some volcanism may have been more felsic than that generally assumed elsewhere, and (d) the younger sequence of interior beds was emplaced so late in Martian history that the planet may be considered to be still volcanically active.

#### References

- [1] Sharp, R.P. (1973) Mars troughed terrain. *Journal of Geophysical Research*, v. 78, p. 4063-4072.
- [2] Blasius, K.R., Cutts, J.A., Guest, J.E., and Masursky, H. (1977) Geology of the Valles Marineris: First analysis of imaging from the Viking 1 Orbiter primary mission. *Journal of Geophysical Research*, v. 82, no. 28, p. 4067-4091.
- [3] Masson, P. (1977) Structure pattern analysis of the Noctis Labyrinthus-Valles Marineris Region of Mars. *Icarus*, v. 30, p. 49-62.
- [4] Wise, D.U., Golombek, M.P., and McGill, G.E. (1979) Tharsis Province of Mars: Geologic sequence, geometry, and a deformation mechanism. *Icarus*, v. 38, p. 456-472.
- [5] McCauley, J.F. (1978) Geologic map of the Coprates quadrangle of Mars. U.S. Geological Survey Miscellaneous Investigations Series Map I-897, scale 1:5,000,000.
- [6] Lucchitta, B.K. (1982) Lakes or playas in Valles Marineris (abs.). Report of Planetary Geology Program-1982. National Aeronautics and Space Administration Technical Memorandum 85127, p. 233-234.
- [7] Nedell, S.S., Squyres, S.W., and Anderson, D.W. (1987) Origin and evolution of the layered deposits in the Valles Marineris. *Icarus*, v. 70, p. 409-441.
- [8] Lucchitta, B.K. (1987) Recent mafic volcanism on Mars. *Science*, v. 235, p. 565-567.
- [9] Lucchitta, B.K. (1985) Young volcanic deposits in the Valles Marineris, Mars (abs.). *Lunar Science* 16, The Lunar and Planetary Institute, Houston, Texas, p. 503-504.
- [10] Singer, R.B. (1982) Spectral evidence for the mineralogy of high-albedo soils and dust on Mars. *Journal of Geophysical Research*, v. 87, no. B12, p. 10159-10168.

**INTRODUCTION:** Crater statistics and surface morphology establish the late gradational histories of portions of the Tempe, Electris, and Casius regions of Mars. Significant erosion affecting a thick, unconformable deposit in the Tempe region ended at about the time of ridged plains formation in Hesperia Planum. Rapid emplacement and subsequent modification of a morphologically similar deposit occurred later in Electris coincident with: A) formation of unconformable deposits and increased geomorphic activity elsewhere on Mars (1, 2); B) development of fractured plains in Casius; and C) initial stages of Arsia Mons activity (3). Characteristics of both the Tempe and Electris deposits suggest that they were once volatile rich and resulted from air-fall deposition (4). The creation of these and other similar units implies that epochs of widespread gradation occurred until relatively late in martian history and that during these periods atmospherically transported volatiles and dust must have been in abundant supply.

**OBSERVATIONS:** The Tempe and Electris deposits are unconformable and occur over both intercrater plains and heavily cratered upland surfaces. Remnants of the Tempe deposit extend from near Tempe Fossae to Acidalia Planitia (50°W to 65°W and 37°N to 47°N). The Electris deposit is observed incompletely from 160°W to 200°W and 30°S to 47°S, but partially filled craters to the south imply initially broader coverage. The Electris deposits range from 300 to 700 m in thickness (based on shadow measurements) with an estimated volume of 900,000 km<sup>3</sup>. Although detailed estimates of the thickness of the Tempe deposit have not been made, it appears to average approximately 300 to 400 m. The deposits in both regions are partially dissected by enlarged, flat-floored, valley networks which are observed to head within the deposits, but rarely incise underlying units. Examples of inverted topography are common to both deposits including those at 55°W, 45°N in Tempe and 190.5°W, 40°S in Electris.

Four classes of the Tempe and Electris deposits can be delineated from thickness and morphology (1, 4). The first class of deposits grades from mantled to unmantled areas. A second, slightly thicker class resembles gullied cuestas that form partial rings at constant elevation within degraded impact craters; this second class is observed only in the Electris region. The third class forms irregular promontories and mesas that are 300 m to 400 m thick (thickness inferred in Tempe) and bounded by scarps without basal talus accumulations. The fourth class of the deposit is comprised of irregular blocks (resembling chaotic terrain) in Electris that are 400–700 m thick, typically grade into exhumed or only thinly mantled ridged plains, and isolated within large craters (5). In Tempe, the fourth class of the deposit may be superposed by plains units in Acidalia. In contrast to some other areas having thick unconformable deposits (3, 6), pedestal craters in the Electris region are uncommon.

The fractured plains of Adamas Labyrinthus in Casius extend from 245°W to 265°W and 28°N to 42°N (7, 8) where they grade to the north into the mottled plains of Utopia Planitia and where they are buried to the east (7). The erosional state of small craters and relict deposits to the east indicate that material has been removed from portions of the fractured plains.

**DISCUSSION:** Characteristics of all classes of the Electris and Tempe deposits demonstrate that they are the result of air-fall deposition and at least locally were once volatile rich. First, their occurrence over high-relief cratered uplands and low-relief ridged plains is inconsistent with formation by the extrusion of flood basalts, fluvial processes, or other processes. Second, the low density of valley networks/area exhumed, an absence of flow-related features, and a deficiency of talus at the base of most scarps, all demonstrate that eolian processes have dominated erosion of the deposits. Finally, these observations combined with the relative ease of erosion suggest that both deposits are comprised of fairly uniform fine-grained material resulting from air-fall. The locally volatile rich nature of the deposits is demonstrated by the presence of relatively young valley networks which head within the deposits in both regions and the occurrence of Electris clouds as well as observed high atmospheric water concentrations (9) over the Electris deposit. Prediction of the volatile-rich nature of the Tempe

deposit is consistent with previous conclusions by other workers (10-13). The absence of large pedestal craters (>2 km) in the Electris region and the similarity between crater densities on the deposit and the exhumed ridged plains indicates rapid deposition and subsequent erosion.

Cumulative crater statistics indicate that the log number of craters in production >5 km/10<sup>6</sup> km<sup>2</sup> (N5 age) superposed on the Tempe deposit is 2.5. Consequently, significant erosion of this deposit ceased at about the time of ridged plains formation in Hesperia Planum. Cumulative statistics from the Electris region indicate that emplacement of an unconformable deposit took place at an N5 age of 2.05. This age coincides with: A) time formation of Acidalia Planitia to the east of the Tempe deposit; B) emplacement and modification of similar debris mantles in Sinus Meridiani and Isidis Basin (14); C) a period of gradation affecting channeled and etched terrains to the west and northwest of Isidis Basin (1, 2); D) deposition of thicker accumulations over longer periods in Arabia and Mesogaea (3); and E) a period of increased geomorphic activity in Margaritifer Sinus (15). Formation of the major outflow channels occurred near this time (16, 17). Incremental statistics from the Electris region show a paucity of craters 1.5 km to about 3 km in diameter thereby indicating that a second period of erosion also affected the area. Cumulative statistics compiled for the Electris region from craters smaller than 3 km diameter indicate this second period had ended at an extrapolated N5 age of -1.1. Although cumulative statistics of larger craters in Casius indicate an emplacement N5 age of 1.95 for the fractured plains, high resolution images east of Adamas Labyrinthus indicate a later burial of the fractured plains in that area (extrapolated N5 age of -1.2). High resolution images of an area within Syria Planum suggest that a late period of gradation also affected this area until an N5 age of -1.4 to -1.1; however, a deficiency of pristine craters in this area and the stripped nature of the surface suggest that some degree of degradation continued to affect this surface even later.

**IMPLICATIONS:** The Tempe, Electris and Casius regions provide evidence that punctuated gradational epochs on Mars continued into the late history of the planet. These periods of gradational activity reflect the deposition and removal of widespread unconformable air-fall deposits and late stage valley network formation less than 3 billion years ago. Crater statistics and erosional style in Electris, Casius, and Syria Planum imply that less intense periods of at least regional gradation occurred even later. Possible mechanisms capable of producing these widespread gradational epochs include volatile release and redistribution caused by periods of localized and intense volcanic activity, polar wandering (3), and/or orbital forcing (18). Some pulses of volcanic activity may have been associated with the finite thermal history of large impact basins (19, 20).

- References:** (1) Grant, J.A. and Schultz, P.H., 1988, Gradation on Mars: Examples From West and Northwest of Isidis Basin and the Electris Region: In Prep. (2) Grant, J.A. and Schultz, P.H., 1988, p. 411-412, in *Lunar and Planet. Sci. XIX* (abstracts), Lunar and Planetary Institute, Houston, Texas. (3) Schultz, P.H. and Lutz, A.B., 1988, *Icarus*, v. 73, p. 91-141. (4) Grant, J.A. and Schultz, P.H., 1988, In MEVTV Workshop on Nature and Composition of Surface Units on Mars (J.R. Zimbelman, S.C. Solomon, and V.L. Sharpton, eds.), pp. 64-66, LPI Tech. Rpt. 88-05, Lunar and Planetary Institute, Houston. (5) Lucchitta, B.K. (1982), NASA Tech. Memo. 85127, 235-236. (6) Scott, D.H. and Tanaka, K.L. (1982), *J. Geophys. Res.*, 87, 1179-1190. (7) McGill, G.E., 1985, p. 534-535, in *Lunar and Planet. Sci. XVI* (abstracts), Lunar and Planetary Institute, Houston, Texas. (8) Greeley, R. and Guest, J.E., 1987, USGS Map I-1802-B (Eastern region of Mars). (9) Huguenin, R.L. and Clifford, S.M. (1982), *J. Geophys. Res.*, 87, 10227-10251. (10) Underwood, J.R., Jr. and Trask, N.J., 1978, USGS Map I-1048 (MC-4). (11) Wise, D.U., 1979, USGS Map I-1154 (MC-3). (12) Scott, D.H. and Tanaka, K.L., 1986, USGS Map I-1802-A (Western region of Mars). (13) DeHon, R.A., 1987, *Icarus*, 71, 287-297. (14) Grzaffi, P. and Schultz, P.H. (1987), *Lunar and Planet. Sci. XVIII* (abstracts), 370-371. (15) Grant, J.A. (1987), NASA Tech. Memo. 89971, 1-268. (16) Masursky, H.J. et al. (1977), *J. Geophys. Res.*, 82, 4016-4038. (17) Baker, V.R. (1982), *The Channels of Mars*, Univ. Texas Press, 198 p. (18) Jakosky, B.M. and Carr, M.H. (1985), *Nature*, 315, 559-561. (19) Wichman, R. and Schultz, P.H. (1987), *Lunar and Planet. Sci. XVIII*, 1078-1079. (20) Schultz, P.H. 1988, In MEVTV Workshop on Nature and Composition of Surface Units on Mars (J.R. Zimbelman, S.C. Solomon and V.L. Sharpton, eds.), pp. 117-119, LPI Tech. Rpt. 88-05, Lunar and Planetary Institute, Houston.

# ORIGIN OF THE MARTIAN HIGHLAND PATERAE: CONSIDERATION OF ERUPTIVE ACTIVITY AT HADRIACA PATERA AND TYRRHENA PATERA

*David A. Crown and Ronald Greeley, Department of Geology, Arizona State University, Tempe, Arizona 85287*

The martian highland paterae (Amphitrites Patera, Hadriaca Patera, and Tyrrhena Patera) are a morphologically distinct class of martian volcano which are located in the cratered highlands in the eastern hemisphere of Mars [1-2]. These volcanoes formed in Upper Noachian to Lower Hesperian time [1]. They are low relief (1-3 km in height) features with vast areal extents ( $\sim 10^5$  km<sup>2</sup>). The martian highland paterae are characterized by summit caldera complexes with associated effusive deposits and channels radiating from the calderas which dissect the flanks of the volcanoes producing plateau-like erosional remnants. The highland paterae are located in the Hellas region on proposed rings of the Hellas Basin [3]. Both Hadriaca Patera and Tyrrhena Patera display asymmetric plan forms which suggest that the topography created by the presence of the Hellas Basin may have influenced the deposition of the volcanic materials.

The channels on the flanks of the martian highland paterae are apparently erosional in nature. Some of the channels extend from the central calderas to the margins of the volcanoes, whereas others originate along the flanks, emanating from features such as small impact craters. The existence of the plateau-like outliers also suggests an erosional mode of origin for the observed channels. At Hadriaca Patera some of the channel floors are cut by smaller, deeply-incised, V-shaped channels. No pristine flow features, as are evident on the flanks of the martian shield volcanoes, are observed on the channeled flanks of the highland paterae. The smooth plains at the summit of Tyrrhena Patera and in the caldera at Hadriaca Patera display wrinkle ridges [4], and several sinuous rille-like structures are associated with the late-stage summit activity at Tyrrhena Patera [1].

Initially, due to their low, broad profiles, the highland paterae were thought to have been formed by eruptions of low viscosity, basaltic lavas [5]. However, currently they are believed to be composed predominantly of ash deposits on the basis of morphometric similarities to large terrestrial ash sheets [6] and their apparently easily erodible nature [1]. Greeley and Spudis [1], from an analysis of Tyrrhena Patera, proposed an evolutionary sequence for the paterae beginning with extensive pyroclastic eruptions due to the contact of rising magma with the water- or ice-saturated megaregolith followed by erosion of the ash deposits and late stage effusive eruptions with deposits concentrated near the summit. Although morphologic evidence suggests that the martian highland paterae are composed of pyroclastic deposits, analysis of Viking imagery has thus far not provided a definitive model for their formation.

Models for the origin of the lower flank materials of Hadriaca Patera and Tyrrhena Patera have been evaluated quantitatively [7-8]. If it is assumed that the eruptions producing Hadriaca Patera and Tyrrhena Patera occurred near the present summit regions (and there is no evidence to the contrary), the dimensions of the volcanoes can be used to constrain possible eruption mechanisms. As is the case for Alba Patera, an air-fall origin for most of the deposits can be dismissed because eruption clouds with heights comparable to the total widths of the volcanoes are required [9]. Models for the emplacement of a gravity-driven flow resisted by a frictional force are used to determine the lengths of terrestrial pyroclastic flows for a given pre-flow topography [10]. The relationship between the flow length and the initial velocity of pyroclastic flows potentially associated with Hadriaca Patera and Tyrrhena Patera for a slope of  $0.25^\circ$  (comparable to the present surfaces of the volcanoes) and for values of the apparent coefficient of sliding friction,  $\mu$ , equal to 0.05 and 0.10 are shown in Figure 1 [8]. Large volume terrestrial pyroclastic flows have values of  $\mu = 0.06 - 0.20$  [11]. On Mars, comparable coefficients of friction should be less due to the lower gravity and less dense atmosphere.

Figure 1 illustrates that for hydromagmatic eruptions (i.e. eruptions caused by the interaction of magma with near-surface groundwater) the entire range of paterae flank widths can be produced for both values of  $\mu$  if only slightly greater than 10% of the initial thermal energy of the magma is converted into the kinetic energy of the pyroclastic flows. This is in agreement with experimental



results for hydromagmatic activity which indicate a 1 - 10% energy conversion [12]. The initial thermal energies of the magmas associated with the paterae are calculated by assuming a density of  $1500 \text{ kg/m}^3$  in the deposits and estimating the volumes of Hadriaca Patera and Tyrrhena Patera from the mapped boundaries of the volcanoes and topographic data from the *1:15M Topographic Map of Mars Eastern Region* (Table 1).

Terrestrial magmatic eruptions feed pyroclastic flows either by ash fountaining or by eruption column collapse. To produce flows with lengths comparable to the entire range of flank widths of the paterae, a minimum initial velocity of  $\sim 350 \text{ m/sec}$  is necessary (for  $\mu = 0.05$ ) (Figure 1). For an eruption driven by magmatic water, this implies an exsolved magma volatile content of  $> 1\%$ , a mass eruption rate of  $> 10^7 \text{ kg/sec}$ , and eruption cloud height of nearly 70 km [Fig. 8 in 13]. The eruption rate and column height indicated are similar to those derived for the eruption at Hecates Tholus thought to have produced the mantling deposit seen near the summit.

From an energy perspective origins of Hadriaca Patera and Tyrrhena Patera can be explained by the emplacement of pyroclastic flows fed by eruptions driven by either magmatic or external water. Hydrovolcanic explosions would be favored in the near-surface environment on Mars as water in the megaregolith could come into contact with a rising magma body. Although the magmatic and hydromagmatic models are both viable, the formation of the paterae by hydromagmatic eruptions in only an early period of martian history is consistent with suggested global changes on Mars and could explain why this style of volcanism is not evident in later eras.

#### *The Frailes Formation, Bolivia: Analogue for the Martian Highland Paterae?*

The existence of large-scale explosive volcanic deposits on Mars is controversial. Various eruption mechanisms have been considered theoretically under martian conditions [13-14], and recently a number of investigations have focused on deposits possibly generated by explosive volcanic eruptions [7,13-16]. Many of these works cite as evidence for a pyroclastic origin the existence of an erosional morphology uncharacteristic of the effusive shield volcanoes on Mars. While this may allude to a pyroclastic origin, other hypotheses are also implied by the observed morphologies [17-18]. Interpretations of martian volcanic eruption styles are hindered by the relatively few observations of large, terrestrial explosive eruptions and the poor state of preservation of large, terrestrial ash deposits. For this reason, a remote sensing and field reconnaissance study of the Frailes Formation in the Central Andes of Bolivia has been initiated to develop morphologic and spectral criteria for the remote identification of ash deposits and the analysis of the eruption and emplacement processes leading to their formation.

The Frailes Formation is an extensive ( $> 100 \text{ km}$  diameter) ignimbrite plateau located on the western edge of the Cordillera Oriental in the Central Andes of southern Bolivia. The ash-flow sheets comprising the Frailes Formation cover  $\sim 8,500 \text{ km}^2$  and were erupted in late Miocene time [19]. These silicic tuffs display varying degrees of welding and are commonly  $\sim 100 \text{ m}$  thick; locally the thickness approaches  $1 \text{ km}$  [20]. The Frailes Formation overlies a folded sequence of Paleozoic and Cretaceous sediments and earlier Miocene volcanics. Local andesitic to rhyolitic domes and flows which post-date the ignimbrite occur throughout the plateau.

General objectives of this investigation include identifying the various eruptive centers and flow units and determining their nature and distribution. Using LANDSAT Thematic Mapper (TM) data the volcanic materials associated with the Frailes Formation can easily be distinguished from the surrounding sedimentary rocks present in the fold belts of the Andes and on the surface of the Altiplano. In addition, the extrusive volcanic materials exposed on the plateau can be distinguished from the ash deposits. Several extrusive centers which post-date the Frailes Formation have been suggested to be the possible locations of sources of the Frailes ash. Discrimination of probable ignimbrite source areas from other eruptive centers is based upon examination of the TM imagery and limited field observations. Within the ignimbrite, different regions have distinctive spectral characteristics. These spectral variations, which are predominantly the result of differences in post-depositional modification, allow four major eruptive centers and their associated flow materials to be identified within the Frailes Formation.

On a gross scale the western region of the Frailes Formation is morphologically similar to the martian highland paterae. The ignimbrite sheet in this area emanates from a topographically high region composed of late-stage lavas. The ash is dissected radially from its presumed source (by fluvial processes). Large channels with steep-sided walls are found with more deeply incised narrow channels in their interiors. At the margin of the plateau, small erosional outliers of the ignimbrite are evident. Continued analysis of the TM imagery in combination with laboratory reflectance measurements on collected representative samples is being utilized to further assess the suitability of the ignimbrites of the Central Andes as analogues for the martian highland paterae.

#### References

- [1] Greeley, R., and Spudis, P.D., 1981, *Rev. Geophys. Space Phys.*, 19, 13-41. [2] Plescia, J.B., and Saunders, R.S., 1979, *Proc. Lunar Planet. Sci. Conf.*, 10th, 2841-2859. [3] Schultz, P.H., 1984, *Lunar Planet. Sci. Conf.*, XV, 728-729. [4] Albin, E.F., 1986, Master's Thesis, Arizona State University. [5] Potter, D., 1976, *U.S. Geol. Survey Misc. Geol. Inv. Map I-941*. [6] Pike, R.J., 1978, *Proc. Lunar Planet. Sci. Conf.*, 9th, 3239-3273. [7] Crown, D.A., Greeley, R., and Sheridan, M.F., 1988, *Lunar Planet. Sci. Conf.*, XIX, 229-230. [8] Crown, D.A., and Greeley, R., 1988, *LPI Contribution 660*, 15-17. [9] Mouginis-Mark, P.J., Wilson, L., and Zimbelman, J.R., 1988, *Bull. Volcanol.*, in press. [10] Malin, M.C., and Sheridan, M.F., 1982, *Science*, 217, 637-640. [11] Sheridan, M.F., 1979, *Geol. Soc. Am. Sp. Paper 180*, 125-136. [12] Wohletz, K.H., 1986, *Bull. Volcanol.*, 48, 245-264. [13] Mouginis-Mark, P.J., Wilson, L., and Head, J.W., 1982, *J. Geophys. Res.*, 87, 9890-9904. [14] Wilson, L., and Head, J.W., 1983, *Nature*, 302, 663-669. [15] Wilson, L., and Mouginis-Mark, P.J., 1987, *Nature*, 330, 354-357. [16] Scott, D.H., and Tanaka, K., 1982, *J. Geophys. Res.*, 87, 1179-1190. [17] Schultz, P.H., and Lutz-Garihan, A.B., 1981, *Lunar Planet. Sci. Conf.*, XII, 946-948. [18] Tanaka, K.L., 1985, *Icarus*, 62, 191-206. [19] Schneider, A., and Halls, C., 1985, *Comunicaciones*, 35, 217-224. [20] Baker, M.C.W., 1981, *J. Volcanol. Geotherm. Res.*, 11, 293-315.

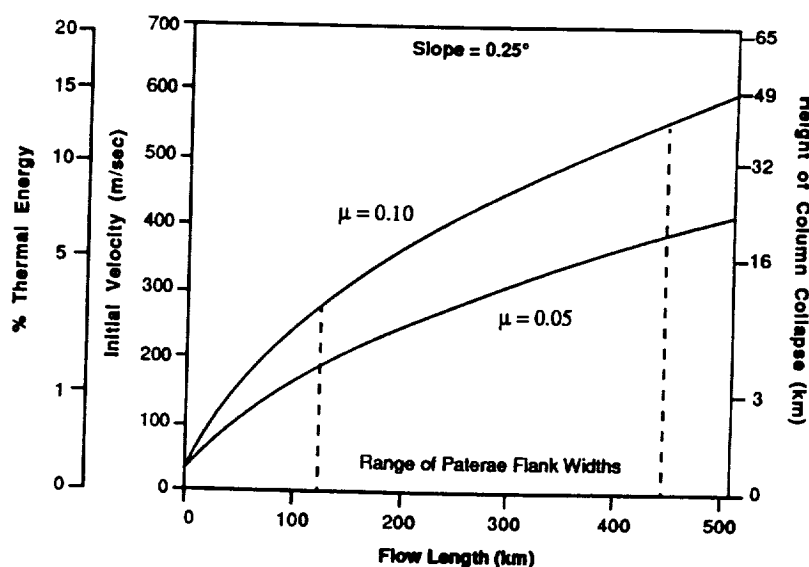
Table 1. Characteristics of Hadriaca Patera and Tyrrhena Patera

Volcano	Dimensions (km)	Edifice Height (km)	Flank Slopes	Caldera Diameter (km)	Volume (m <sup>3</sup> ) x 10 <sup>14</sup>	Mass <sup>#</sup> (kg) x 10 <sup>17</sup>	Thermal* Energy (kg m <sup>2</sup> /sec <sup>2</sup> ) x 10 <sup>23</sup>
Hadriaca	288 x 570	~3	0.05 - 0.60°	63 x 78	1.867	2.801	3.361
Tyrrhena	426 x 660	2+	0.16 - 0.28°	45	1.176	1.764	2.117

#assumes  $\rho = 1500 \text{ kg/m}^3$  in deposits

\*1 kg m<sup>2</sup>/sec<sup>2</sup> = 10<sup>7</sup> ergs

Figure 1. Relationship between flow length and initial velocity for martian pyroclastic flows over a 0.25° slope for coefficients of friction equal to 0.05 and 0.10 [7]. The initial velocity is correlated with the % of the available initial thermal energy of the magma and with a corresponding height of column collapse (by conversion of kinetic energy to potential energy). The observed range of flank widths for Hadriaca Patera and Tyrrhena Patera is indicated.



## MARTIAN AND TERRESTRIAL LAVA FLOWS

H. J. Moore, U. S. Geological Survey, Menlo Park, CA 94025  
J. A. Ackerman, North Dakota State Univ., Fargo, ND 58105

We assume that lava flows can be treated as Bingham fluids, and then, we calculate yield strengths and viscosities for mafic to felsic flows on Earth, near the summit of Ascræus Mons and Alba Patera on Mars. The calculations require estimates of: effusion rates, flow dimensions, and topographic gradients.

Three models for effusion rates are considered: (1) mixed cooling [1,2], (2) unmixed cooling [1,2], and Graetz number [3,4]. The unmixed cooling model parameters are calibrated with two terrestrial aa flows [5,6,7] and then applied to other flows on Earth and Mars. Effusion rates calculated with the mixed cooling model are about ten times larger than those of the unmixed cooling model; those of the Graetz number model are much lower than those of the unmixed model (Table 1) [see also 8].

To calculate yield strengths and Bingham viscosities, we use: (A) a wide flow model [9], (B) Hulme's model [3], and (C) model 1 of Baloga and Crisp [10]. Model C fulfills kinematic requirements by depositing moving lava from the channel to form stationary levees [10]. All calculations require estimates of effusion rate, topographic gradient, lava density, and acceleration of gravity. In addition, estimates of rest thickness and flow depth are used in Model A, channel and levee widths in Model B, and levee height and channel and flow widths in Model C.

For the Puu Kai flow in Hawaii [6], we find that both the yield strength and viscosity tend to increase with distance from the vent when the lava density is constant (Fig. 1). This trend is similar to previous results [11,12] for Hawaiian flows. No strong trend is found for the 1984 Mauna Loa, other terrestrial, or martian flows when the lava density is taken as constant.

Yield strengths from the three models are more or less the same. Bingham viscosities calculated with the mixed cooling model are about ten times larger than those of the unmixed cooling model; those calculated with the Graetz number model are lower than the unmixed cooling model. Comparison of yield strengths and viscosities suggest that there is a relation between the two (e.g., Fig. 2).

Estimates of compositions of martian flows are subject to many uncertainties [13]. One of these uncertainties is that yield strength and viscosity may vary along the length of the flow. If yield strengths and viscosities are compared using a given set of models, it is found that felsic flows tend to have larger yield strengths and viscosities than mafic flows (e.g., Fig. 2), but the magnitudes of the strengths and viscosities differ among the model sets. Our results suggest that the martian lavas are more akin to mafic and intermediate lavas, such as basalt and basaltic andesite, than felsic lavas, such as rhyolite and trachyte (Fig. 3) [see also 14].

## REFERENCES

- [1] Pieri, D.C. and Baloga, S.M., 1986, J. Volc. Geotherm. Res., v. 30, p. 29-45.

- [2] Harrison, C.G.A. and Rooth, C. 1976, in Aoki, H. and Iizuka, S., eds., Volcanoes and Tectosphere: Tokyo Tokai Univ. Press, p. 103-113.
- [3] Hulme, G., 1974, Geophys. J. Roy. Astron. Soc., v. 39, p. 361-383.
- [4] Hulme, G. and Fielder, G., 1977, Phil. Trans. Roy. Soc., Lond., ser. A, v. 285, p. 227-234.
- [5] Moore, R. B., et al., 1980, J. Volc. Geotherm. Res., v.7, p. 189-210.
- [6] Lipman, P. W. and Banks, N.G., 1987, U.S. Geol. Survey Prof. Paper 1350, p. 1527-1567.
- [7] Moore, H. J., 1987, U.S. Geol. Survey Prof. Paper 1350, p. 1569-1588.
- [8] Cattermole, P., 1987, J. Geophys. Res., v. 92, #B4, p. E553-E560.
- [9] Moore, H.J. and Schaber, G.G., 1975, Proc. 6th Lunar Sci. Conf., p. 101-118.
- [10] Baloga, S.M. and Crisp, J., 1988, unpublished report, 35p., 5 figs.
- [11] Moore, H.J., et al., 1988, Repts. Planet. Geol. Prog.- 1980-1981, NASA TM 82385, p. 269-271.
- [12] Fink, J.H. and Zimbelman, J.R., 1986, Bull. Volcan., v.48, p. 87-96.
- [13] Moore, et al., 1978, Proc. 9th Lunar Planet. Sci. Conf., p. 3351-3378
- [14] Zimbelman, J.R., 1985, J. Geophys. Res., v. 90, Suppl. D, p. D157-D162.

Tab. 1. Calculated effusion rates in  $\text{m}^3/\text{s}$  for terrestrial and martian flows using three models.

	Mixed Cooling	Unmixed Cooling	Graetz Number
Terrestrial Flows			
Mauna Loa 1	670	56	21
Mauna Loa <sub>2</sub> 1A <sup>1</sup>	770	64	7
Puu Kiai <sup>2</sup>	260	21	6
SP Flow	870	72	11
Mt. Shasta	480	40	4
Shastina	580	48	4
Mono Craters	220	18	1
Mammoth Lakes	280	23	2
Martian Flows			
Ascræus 12	1,200	96	30
Ascræus E14	1,400	120	44
Ascræus P14	730	61	21
Ascræus D16	950	79	25
Ascræus P16	890	74	12
Alba 6A	28,000	2,300	69
Alba 9	35,000	2,900	280
Alba 10	34,000	2,800	480

<sup>1</sup> Effusion rate, adjusted for volatile loss, is near  $55 \text{ m}^3/\text{s}$  [7].  
<sup>2</sup> Average effusion rate for eight days is about  $23 \text{ m}^3/\text{s}$  [5].

Fig. 1. Yield strength and Bingham viscosity versus fraction of length of flow for Puu Kiai flow (1977), HA.

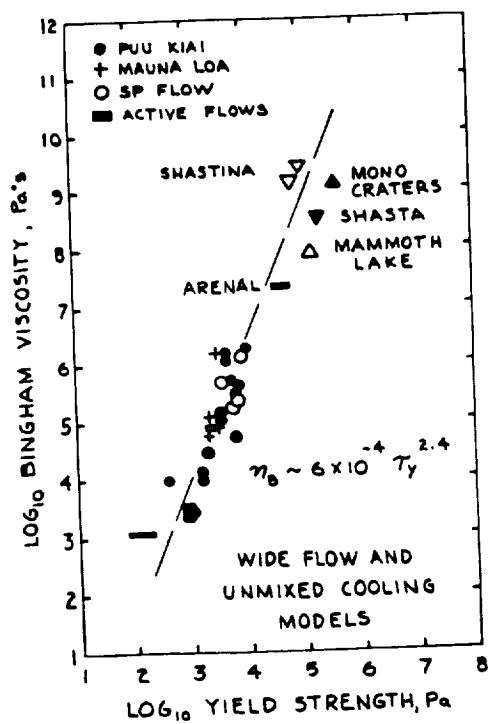


Fig. 3. Bingham viscosity versus yield strength showing martian flows and composition fields.

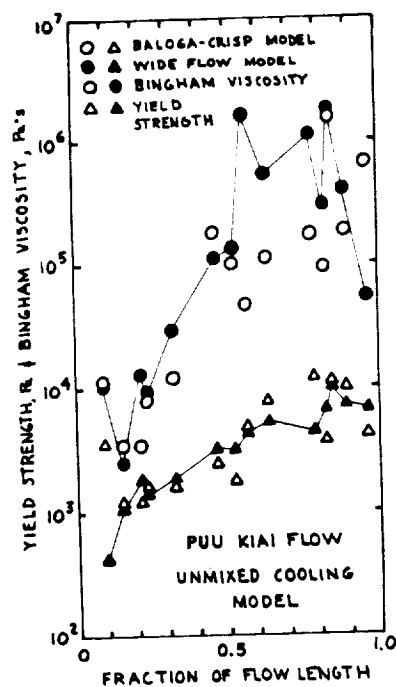
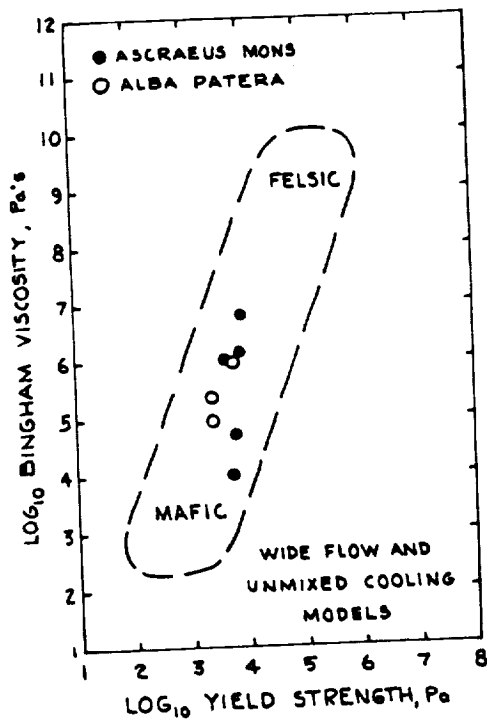


Fig. 2. Bingham viscosity versus yield strength for lava flows on Earth.



# METHODS FOR ESTIMATING ERUPTION RATES OF PLANETARY LAVA FLOWS

Joy Crisp and Stephen Baloga, Jet Propulsion Laboratory, California Institute of Technology, Pasadena, CA, 91109

Eruption rates provide a quantitative basis for comparing planetary and terrestrial eruptions. The rate of magma discharge is an important factor in effusive volcanism because it influences the eruption style and dimensions of lava flows. We will review three methods that have been used to estimate eruption rates of planetary lava flows and we will introduce a new method.

The first method [1] is based on the Bingham rheology of certain magmas. Lava flows are assumed to be isothermal during emplacement and advance until the hydrostatic pressure in the central channel cannot overcome the yield strength of the embanking levees. From the channel and levee dimensions, the yield strength of the lava can be computed. Then, if an independent estimate of the viscosity is available, eruption rate can be computed from an approximate balance of the shear stress and yield strength at the interface between the channel and the levee. One of the major problems with this method is that magmatic viscosity and eruption rate cannot be determined independently. Hulme used an empirical relationship between yield strength and viscosity, determined from observations of terrestrial flows, to estimate eruption rates of lava flows on the Moon. This method was also applied to leveed flows on Mars [2, 3, 4]. However, the assumption of an empirical relationship between yield strength and viscosity or silica content is highly suspect because of the strong dependence of magma rheology on temperature, crystallinity, magma composition, and water content.

The second method is based on an empirical study by Walker [5] of terrestrial eruption rates and flow lengths. He contended that eruption rate can be determined by measuring the length of a lava flow, once the proportionality factor has been determined empirically. For planetary applications, one can only speculate that an empirical relation for terrestrial flows is valid.

In an extension of Walker's method, Hulme and Fielder [6] conceded that cooling processes might limit the length of lava flows, although they assumed that all other dimensions are controlled by an isothermal Bingham flow model. They proposed a dimensionless critical Graetz number for lava flows

$$Gz_c = Q h / \kappa L W \quad (1)$$

They argued that heat transport in a lava flow is analogous to the Fourier conductive heat loss of a warm laminar fluid flowing through a cooler pipe, [where  $Q$  is eruption rate,  $h$  flow thickness,  $\kappa$  thermal diffusivity ( $\approx 7 \times 10^{-7}$  m/s<sup>2</sup> for basalt),  $L$  flow length, and  $W$  flow width]. Hulme and Fielder used Walker's [5] data to find  $Gz_c \approx 300$ .

If the critical Graetz number for terrestrial flows is valid for planetary flows, then eruption rates can be estimated from Eq.(1) (e.g., for flows on Mars [7,8]). Wilson and Head [9], Wilson [10], and Gaddis [11] used a Graetz number adjusted for Venusian gravity and ambient temperature ( $Gz_c \approx 270$ ) to estimate eruption rates of flows on Venus.

Recent terrestrial field studies suggest that a statistically meaningful  $Gz_c$  may not exist. Values ranging from 100 to 1500 have been computed for Etna flows [12, 13]. Figure 1 shows the spread of Graetz values for a set of 30 single-lobe flows from the 1983-1984 Puu Oo eruptions [14]. The Puu Oo data set yields  $Gz_c = 180 \pm 150$  ( $\pm 1\sigma$ ). The data for Etna and Puu Oo suggest that a detailed knowledge of the mode of flow emplacement is required before

determining the appropriate critical Graetz number.

The third method is based on the assumption that radiative cooling during emplacement is the key factor determining the dimensions of lava flows [15, 16, 17]. In the thermally "unmixed" model of Pieri and Baloga [17], a thermally homogeneous core is covered by an infinitely thin crust that radiates at an "effective radiation temperature" ( $T_e$ ) that remains constant during flow emplacement. The radiative cooling models can be recast in terms of  $Q/A$  ( $A$  = flow area), as a function of initial and cessation temperatures and the empirical parameter,  $T_e$ . This approach has been used for Hawaiian flows [17], martian flows [4, 8, 18] and flows at Io [19].

It is preferable, in a statistical sense, to test this model using an  $h$  versus  $\tau$  regression ( $\tau$  = eruption duration), because  $h$  and  $\tau$  are independently measured for lava flows, and  $h/\tau = Q/A$ . Analysis of the Puu Oo data set mentioned previously [14] shows that about 45% of the error due to regression of  $h$  on  $\tau$  is explained by the regression. This suggests that important factors have been omitted from the formulation of the thermal models that give rise to simple linear  $Q$  versus  $A$  or  $h$  versus  $\tau$  relationships.

A new method for estimating eruption rates is based on a two-component model of cooling by Stefan-Boltzmann radiation [20] and it supplants the method developed by Pieri and Baloga [17]. One component is a cooler crust and the other is a hotter inner core partially exposed at the surface along shear zones, cracks, and other areas. The average fraction ( $f$ ) of core exposure during emplacement is an important and previously unrecognized important parameter in the relationship between eruption rate and final flow dimensions. Applications to terrestrial basalt flows [20] indicate that  $f$  is typically between 0.001 and 0.1. Using these bounds on  $f$ , together with typical values for terrestrial basaltic flows for other parameters, the two-component model allows us to estimate eruption rates for planetary flows from

$$Q = 3 f \epsilon \sigma T_o^3 A / \rho C_p (1 - \delta/h) [ (T_o^3/T_f^3) - 1 ] \quad (2)$$

where  $\epsilon$  = emissivity,  $\sigma$  = Stefan-Boltzmann constant,  $T_o$  is the initial eruption temperature,  $\rho$  = density,  $C_p$  = heat capacity,  $\delta$  = average thermal boundary layer thickness ( $\approx$  crust), and  $T_{cf}$  is the temperature of the inner core when the flow stops advancing [20].

When applied to flows at Alba [4] and Ascraeus Mons [7], the new method yields eruption rates that are similar to estimates using the Hulme or Graetz methods, even though markedly different assumptions have been made about the dominant physical processes that govern flow dimensions [21]. Unlike the previous methods, however, the new method allows us to begin to assess the errors associated with the estimates.

It is currently possible to estimate the eruption rate of planetary lava flows with a precision of about two orders of magnitude. This uncertainty is associated with parameters such as  $f$  and  $T_f$ , which must be estimated from statistical studies of terrestrial flows. In contrast to the precision of the parameter estimates, the accuracy of the models depends on the validity of the assumptions that the planetary flows have compositions and eruption styles similar to terrestrial flows. Systematic errors in eruption rates due to an invalid choice of assumptions cannot be eliminated by modeling or statistical studies. However, one of the main virtues of a modeling approach is the ability to explore the sensitivity of eruption rate estimates to the individual assumptions. We need more statistical analyses of terrestrial flows, in combination with physical modeling, to determine the empirical parameters associated with the models and to assess the variability of the

parameters. With the goal of improving the confidence on estimates of eruption rates for planetary lava flows, it is hoped that correlations between the fraction of core exposure and different flow morphologies could be established from terrestrial data.

- [1] Hulme G. (1974) *Geophys. J. Roy. Astr. Soc.*, 39, 361-383. [2] Hulme G. (1976) *Icarus*, 27, 207-213. [3] Carr M.H., R. Greeley, K.R. Blasius, J.E. Guest, and J.B. Murray (1977) *J. Geophys. Res.*, 82, 3985-4015. [4] Cattermole P. (1987) *J. Geophys. Res.*, 92, E553-E560. [5] Walker G.P.L. (1973) *Phil. Trans. Roy. Soc. London A*, 274, 107-118. [6] Hulme G. and G. Fielder (1977) *Phil. Trans. Roy. Soc. Lond. A*, 285, 227-234. [7] Zimbelman J.R. (1985) *J. Geophys. Res.*, 90, D157-D162. [8] Moore H.J. and J.A. Ackerman (1989) *Lunar and Planetary Science XX*, pp.711-712. [9] Wilson L. and J.W. Head III (1983) *Nature*, 302, 663-669. [10] Wilson L. (1984) *Vistas in Astronomy*, 27, 333-360. [11] Gaddis, L.R. (1989) *Lunar and Planetary Science XX*, pp.317-318. [12] Pinkerton H. and R.S.J. Sparks (1976) *J. Volcanol. Geotherm. Res.*, 1, 167-182. [13] Guest J.E., C.R.J. Kilburn, H. Pinkerton, and A.M. Duncan (1987) *Bull. Volcanol.*, 49, 527-540. [14] Wolfe E.W., C.A. Neal, N.G. Banks, and T.J. Duggan (1989) *U.S. Geol. Surv. Prof. Paper* 1463, pp.1-98. [15] Shaw H.R. and D.A. Swanson (1970) *Proc. 2nd Columbia River Basalts Symposium*, Wash. State Coll. Press, Cheney, WA, pp.271-299. [16] Danes Z.F. (1972) Dynamics of lava flows. *J. Geophys. Res.*, 77, 1430-1432. [17] Pieri D.C. and S.M. Baloga (1986) *J. Volcanol. Geotherm. Res.*, 30, 29-45. [18] Baloga S. and D. Pieri (1985) *Repts. Planet. Geol. Geophys. Program - 1984*, NASA TM-87563, pp.245-247. [19] Pieri D.C., S.M. Baloga, R.M. Nelson, and C. Sagan (1984) *Icarus*, 60, 685-700. [20] Crisp J. and S. Baloga (1989a) A model for lava flows with two thermal components, to appear in *J. Geophys. Res.* [21] Crisp, J. and S. Baloga (1989b) Methods for estimating eruption rates of planetary lava flows submitted to *Lunar and Planetary 20th Proc.*

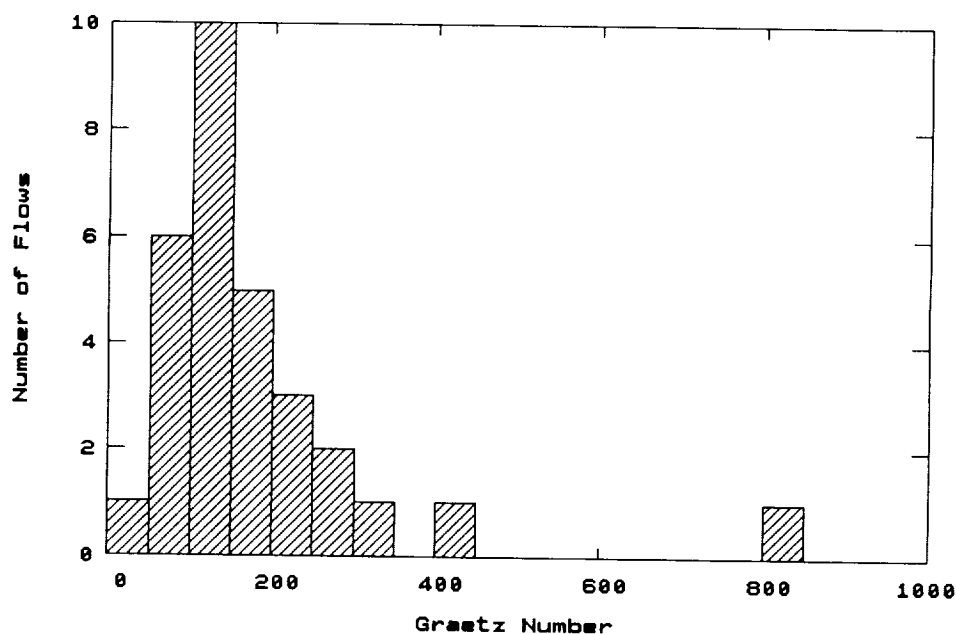


Figure 1. Frequency histogram of Graetz values calculated using Eq.(1) for 30 single-lobe basalt flows, using data from Wolfe et al. [14].



## ERUPTIVE CONDITIONS AND VOLCANO MORPHOLOGY

*Seth B. Posin and Ronald Greeley, Department of Geology, Arizona State University, Tempe, AZ 85287*

Terrestrial effusive volcanoes have been classified as either shields with convex slopes between  $1^\circ$  and  $10^\circ$ , stratovolcanoes with steep-sided concave slopes, or domes with gentle convex slopes near the vent that increase toward the construct perimeter. Possibly explaining these differences in morphology has been the observation that shield volcanoes tend to be basaltic, stratovolcanoes tend to be andesitic, and domes tend to be dacitic in composition. However, important exceptions include Fuji, Pico, Mayon, Izalco, and Fuego which have stratovolcano morphologies but are composed of basaltic lavas. Similarly, Ribikwo is a Kenyan shield volcano composed of trachyte (1) and Suswa and Kilombe are shields composed of phonolite (2). These exceptions indicate that eruptive conditions, rather than composition, may be the primary factors that determine volcano morphology (3). The objective of this study is to determine the relationships, if any, between eruptive conditions (viscosity, erupted volume, and effusion rate) and effusive volcano morphology. Moreover, it is the goal of this study to incorporate these relationships into a model to predict the eruptive conditions of extraterrestrial (martian) volcanoes based on their morphology.

Suggestions by Walker (4) and Malin (5) that eruption rate and/or volume of erupted lava control flow length raises the possibility that these factors may control volcano morphology. In order to evaluate this hypothesis lava volume data was collected for recent eruptions of 28 volcanic constructs of varying morphologies. Eruptions include both summit and flank eruptions and all lava volume estimates carry a possible 50% error due to degassing. Eruption rate data was calculated as the volume of lava divided by the eruption duration and does not include extended periods of quiescence. Results of this analysis show that flow length does not determine volcano morphology.

The initial viscosity of lava at the vent ("eruptive viscosity") and its role in determining volcano morphology was also assessed. Few measurements of eruptive viscosities have been made and those reported are usually derived through a variety of means ranging from Jeffrey's equations to various model dependent theoretical calculations. Although these reported eruptive viscosities constitute an important data base, the inconsistency in the method of data acquisition necessitated the addition of a second data base of uniformly derived viscosities. This was accomplished by means of a computer program (7) that estimates the effective viscosity of silicate melts as a function of composition, temperature, and crystal content. The temperatures used were eruptive temperatures measured at, or relatively near, the vent. Due to a lack of data regarding magmatic volatiles and crystal content it was assumed that all lavas were anhydrous and supraliquidous. Additionally, for both the reported viscosities (data base 1) and the calculated viscosities (data base 2), only the lowest eruptive viscosity was selected for each volcanic construct.

Results of the viscosity analysis (Fig. 1) show the lowest reported viscosities for 13 terrestrial volcanoes and calculated viscosities for 18 volcanoes plotted versus the average slopes of the constructs. For both data bases there is a general trend of increasing viscosity with increasing slope. For 11 volcanoes common to both data bases the calculated viscosities tend to be lower than the reported viscosities by factors of 10 to 100. The offset may result from the assumption made in data base 2, that all lavas are supraliquidous; this would explain why the offset increases towards viscous domes which are usually comprised of lavas erupted at lower (subliquidous) temperatures. Therefore, although the two data bases define an upper and lower viscosity bound for volcanoes of any given slope, the reported viscosities (data base 1) probably offer the best approximation.

In order to apply the results of Fig. 1 to extraterrestrial volcanoes, the slopes of martian volcanoes (6), lunar domes (6), and venusian volcanoes (8) were inserted into the equations for the best fit lines of data bases 1 and 2 (Table 1). If it is assumed that data base 1 offers the best approximation, then martian volcanoes have eruptive viscosities slightly greater than that of

Hawaiian basalt, whereas lunar and venusian eruptive viscosities are slightly less. Inherent in this analysis are the assumptions that all the volcanoes listed in Table 1 are effusive--which may not be the case for some martian paterae (9), that the exposed portions of semi-buried volcanoes such as Tharsis Tholus accurately represent the geometric shape of the entire volcanic construct, and that the extraterrestrial volcanoes have undergone little morphologic modification.

Efforts are currently being made to refine the morphologic data for both martian and terrestrial volcanoes as well as to develop new methods of expressing volcano morphology. Other possible influences on volcano morphology being investigated include effusion rate peaks, flow dimensions, pyroclastics, and the importance of summit versus flank eruptions.

## References

1. Webb, P.K. and Weaver, S.D., 1975, *Bull. Volc.*, v. 39, p. 294-312.
2. Wood, C.A., 1977, *Abst. Planet. Geol. Field Conf. Snake River Plain, Idaho*, p. 34-39.
3. Schuver, H.J., 1982, *Adv. Planet. Geo.*, p. 565-567.
4. Walker, G.P.L., 1973, *Phil. Trans. R. Soc. London*, v. 274A, p. 107-118.
5. Malin, M.C., 1980, *Geology*, v. 8, p. 306.
6. Pike, R.J. and Clow, G.D., 1981, Dept. of Interior, USGS, Open File Report 81-1038 (preliminary report), p. 1-40.
7. McBirney, A.R. and Murase, T., 1984, *Ann. Rev. Earth Planet. Sci.*, p. 337-357.
8. Stofan, E.R. et al., 1987, *Lunar Planet. Sci. Abst.*, p. 952-953.
9. Greeley, R. and Spudis, P.D., 1984, *Rev. Geophys. Space Phys.*, v. 19, n. 1, p. 13-41.

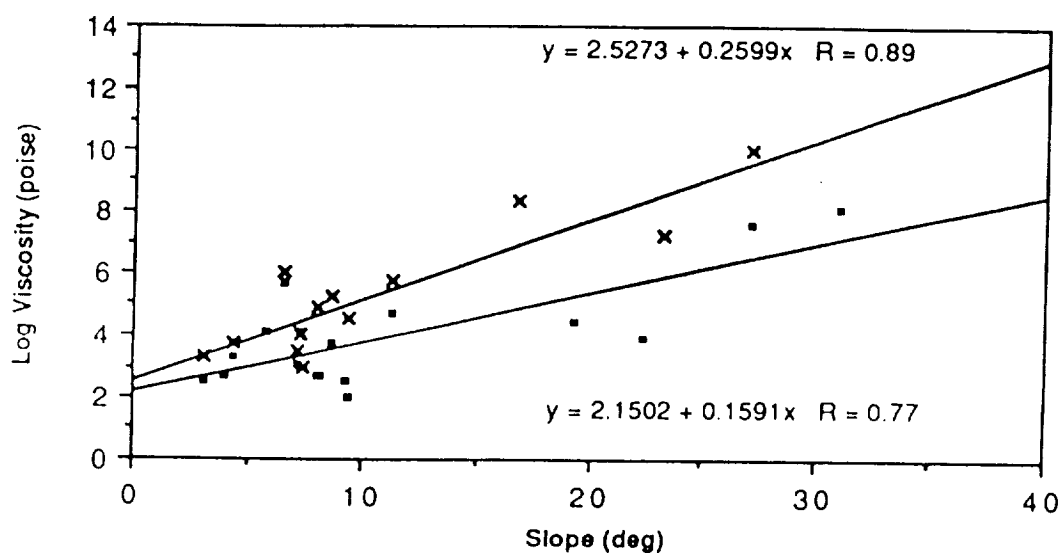


Fig. 1. Plot of log viscosity versus volcano slope for data base 1 (reported viscosities given by x) and data base 2 (calculated viscosities given by ■). Equations of best fit line for each data base are shown.

Table 1

Volcano	Viscosity (data base 1)	Viscosity (data base 2)
(Mars)		
Olympus Mons	$3.5 \times 10^3$ poise	$5.9 \times 10^2$ poise
Pavonis Mons	$5.8 \times 10^3$ poise	$7.9 \times 10^2$ poise
Ascreaus Mons	$1.0 \times 10^4$ poise	$1.1 \times 10^3$ poise
Arsia Mons	$1.5 \times 10^3$ poise	$3.6 \times 10^2$ poise
Elysium Mons	$2.9 \times 10^3$ poise	$5.2 \times 10^2$ poise
Hecates Tholus	$2.0 \times 10^3$ poise	$4.3 \times 10^2$ poise
Uranius Tholus	$2.2 \times 10^4$ poise	$1.9 \times 10^3$ poise
Ceraunius Tholus	$1.8 \times 10^4$ poise	$1.6 \times 10^3$ poise
Tharsis Tholus	$9.3 \times 10^3$ poise	$1.1 \times 10^3$ poise
Albor Tholus	$2.3 \times 10^3$ poise	$4.6 \times 10^2$ poise
Jovis Tholus	$1.5 \times 10^3$ poise	$3.5 \times 10^2$ poise
Biblis Patera	$2.9 \times 10^3$ poise	$5.2 \times 10^2$ poise
Ulysses Patera	$3.9 \times 10^3$ poise	$6.5 \times 10^2$ poise
Uranius Patera	$7.4 \times 10^2$ poise	$2.3 \times 10^2$ poise
Apollinaris Patera	$1.4 \times 10^3$ poise	$3.4 \times 10^2$ poise
(Moon)		
D crater (name prov)	$1.0 \times 10^3$ poise	$2.8 \times 10^2$ poise
Maraldi B 2NW	$8.1 \times 10^2$ poise	$2.5 \times 10^2$ poise
Cauchy Omega	$7.4 \times 10^2$ poise	$2.3 \times 10^2$ poise
Maraldi B 1SE	$1.2 \times 10^3$ poise	$3.1 \times 10^2$ poise
Rima Aristarchus 8	$9.8 \times 10^2$ poise	$2.7 \times 10^2$ poise
(Venus)		
Theia Mons	$8.9 \times 10^2$ poise	$2.6 \times 10^2$ poise
Rhea Mons	$1.0 \times 10^3$ poise	$2.8 \times 10^2$ poise

## **LUNAR PYROCLASTIC DEPOSITS: THEIR RESOURCE POTENTIAL**

B.Ray Hawke\*, Cassandra R. Coombs†, and Beth Clark\*

\*Planetary Geosciences Division, Hawaii Institute of Geophysics, University of Hawaii, Honolulu, HI, 96822; †NASA/Johnson Space Center, SN 15, Houston, TX, 77058

**INTRODUCTION:** It seems likely that a Permanent Lunar Base (PLB) will be established early in the 21st century. While the initial return to the Moon may be for the purpose of constructing a science outpost for geological, astronomical, and other basic research, a viable permanent settlement must return major benefits to the near-Earth space infrastructure. In recent years, attention has been focused on the production of oxygen propellant and helium-3. Ilmenite-rich lunar material is generally preferred for the production of these substances.<sup>1</sup> To date, efforts to locate ilmenite-rich deposits have concentrated on the various lunar maria. i.e. 1,2 In this paper we propose that ilmenite-rich pyroclastic deposits would be ideal locations for mining operations and the establishment of one or more PLB's.

**ILMENITE-RICH DEPOSITS AS LUNAR RESOURCES:** One lunar product with a potentially large market yet requiring minimal processing is liquid oxygen for spacecraft propellant.<sup>1</sup> In any future settlement of the Moon, oxygen is clearly one of the most important materials to be supplied.<sup>1,3</sup> It is required both for life support systems and propulsion. The production of oxygen propellant is particularly attractive because it immediately relieves some of the burden on the transportation system for lunar operations.<sup>1</sup> Lunar oxygen may prove to be a viable export to sustain operations in low Earth orbit and elsewhere in near-Earth space.<sup>4</sup>

A variety of methods for producing oxygen from lunar soil and rocks have been suggested.<sup>1,5</sup> However, reduction of ilmenite has been extensively studied and seems to be preferred by most workers.<sup>1,3,5,6</sup> Ilmenite is relatively abundant in many lunar soils, has been shown to be extractable from the soil, and can be stripped of its oxygen by relatively simple means.<sup>5,7</sup> Potentially useful by-products are produced by ilmenite reduction. Iron, almost 40% of the original mass of ilmenite, remains behind in a  $\text{TiO}_2$  matrix.<sup>5</sup> Ultimately, iron (and perhaps titanium) may be as useful as oxygen since it can be utilized for space construction.

The exploitation of lunar helium-3 as nuclear fusion fuel could dramatically improve our energy future.<sup>8,9</sup> He-3 could be used in D-He-3 fusion reactions and is not found in significant quantities on Earth. Preliminary estimates show that the available quantities of He-3 on the lunar surface could provide the equivalent of 40,00 years of the U.S. electrical power generation demand recorded in 1985.<sup>10</sup>

Lunar He-3 supplies originate from solar winds that are embedded in the near surface regions of fine grained regolith particles. Several factors were cited by

Cameron<sup>11,12</sup> as being important in controlling the helium abundance of the regolith. He noted that the helium content of a regolith is a function of its composition. In particular, mare regoliths rich in titanium are high in helium content. Helium is concentrated in the <50 $\mu$ m size fraction of regoliths.<sup>12</sup> An ilmenite-rich, mature regolith would be the best source of lunar helium.

During the course of operations to extract He-3 from the regolith, other valuable volatiles implanted by the solar wind could be collected with relatively small mass and power penalties.<sup>13</sup> These other constituents of the solar wind (H<sub>2</sub>, N<sub>2</sub>, CO<sub>2</sub>, CH<sub>4</sub>, etc.) can be used to meet the needs of such lunar base subsystems as transportation, life support, and agriculture.<sup>13</sup> Hydrogen and other materials might be exported to other space facilities.

**ILMENITE-RICH PYROCLASTIC DEPOSITS:** To date, efforts at selection and evaluation of sites for mining helium and oxygen on the Moon have focused on high-Ti maria.<sup>1,12,14</sup> However, we propose that ilmenite-rich pyroclastic mantling deposits of regional extent would be superior sites for mining operations.

An important objective of the Apollo 17 mission was to sample the "dark mantle" deposit at Taurus-Littrow; preliminary analysis indicated that this deposit might be of pyroclastic origin.<sup>15</sup> Orange glass droplets and partially crystallized black spheres from the Apollo 17 landing site were subsequently identified as pyroclastic components in the deposit.<sup>16</sup> The chemical composition of the orange and black spheres are indistinguishable, the only difference being that the black spheres are largely crystallized. The black spheres consist of very fine intergrowths of ilmenite and olivine, with olivine commonly occurring as euhedral crystals within the spheres. The Apollo 17 black spheres are rich in TiO<sub>2</sub> (9-10%) and ilmenite, and they are similar, though not identical, in composition to the Apollo 17 high-Ti mare basalts.

Although the orange and black pyroclastic spheres are not abundant at the Apollo 17 site, there is a major regional pyroclastic deposit (Taurus-Littrow) west of the site. A comparison of reflectance spectra obtained for the Taurus-Littrow deposit with laboratory reflectance measurements have demonstrated that Apollo 17 black spheres are the characteristic ingredients of the Taurus-Littrow pyroclastic mantling deposit.<sup>15,17,18,19</sup>

The Taurus-Littrow mantling deposit has an areal extent of >4000 km<sup>2</sup> and a thickness of many 10's of meters. The Taurus-Littrow deposit exhibits very weak to nonexistent echoes on the depolarized 3.8-cm radar maps of Zisk et al.<sup>20</sup> These low depolarized returns are thought to be due to the lack of scatterers (1-50 cm) on the smooth surface of the pyroclastic mantling deposit.<sup>15,17,20</sup> A very low degree of small-scale surface roughness and a relatively block-free surface are indicated.

Several other major occurrences of regional pyroclastic mantling deposits have been documented<sup>15,21</sup> including those at the following locations: Rima Bode, Aristarchus Plateau, Sulpicius Gallus, Mare Humorum, southern Sinus Aestuum, and southern Mare

Vaporum. These units have been characterized as extensive deposits of low albedo (0.79-0.96) material which appear to subdue or mantle underlying terrain. Low returns on Earth-based 3.8-cm radar backscatter maps confirm these observations of mantled areas indicating an absence of surface scatterers in the 1 to 50-cm size range.<sup>15,17,20</sup> Spectral studies have demonstrated that several (e.g. Rima Bode) of these regional dark mantling deposits are composed of high-titanium, ilmenite-rich black spheres of pyroclastic origin.<sup>15,17</sup>

**FACTORS FAVORING ILMENITE-RICH PYROCLASTIC DEPOSITS AS PLB SITES:** The recovery of significant amounts of He-3 may necessitate surface mining over areas of thousands or even tens of thousands of square kilometers. Hence, site selection must be directed toward the identification of large individual areas suitable for mining. Cameron<sup>2</sup> pointed out a variety of other factors that must be considered in site selection and evaluation. These include: 1) regolith uniformity, 2) ease of mining, and 3) absence of blocks of rock. Ilmenite-rich pyroclastic deposits of regional extent appear to meet these requirements. Individual deposits cover many thousands of square kilometers and exhibit uniform surface compositions. For example, the areal extent of the Rima Bode unit is 10,000 km<sup>2</sup> and the deposits in southern Aestuum cover 30,000 km<sup>2</sup>.

The relatively large thickness (at least 10's of meters) of the various regional deposits is also a positive factor. The deposits are deep enough that small impact craters 10's to 100's of meters in diameter have generally not penetrated the deposits and ejected subjacent blocky, low-Ti material. This has helped keep surface contamination by low-Ti debris to a minimum.<sup>15</sup> The regional pyroclastic deposits are apparently composed of loose, unwelded particles. Most small craters excavated only incoherent debris. Hence, the surface and near-surface areas are relatively free of blocks and rock fragments. These extensive, deep deposits of loose ilmenite-rich pyroclastic material that are relatively rock-free and uncontaminated by vertical mixing would be ideal for lunar mining.

**REFERENCES:** 1) W.Mendell (1985) *Lunar Bases and Space Act. in the 21st Cent.* 2) E.Cameron (1988) *Lunar Bases II*, p. 47. 3) M. Gibson and C. Knudson (1985) *Lunar Bases and Space Act. in the 21st Cent.*, p.543. 4) M.Simpson (1985) *Lunar Bases and Space Act. in the 21st Cent.*, p. 531. 5) R. Briggs (1988) *High Frontier Newsletter*, v. XIV, n. 6 6) A. Cutler and P.Krag (1985) *Lunar Bases and Space Act. in the 21st Cent.*, p. 453. 8) L. Wittenberg et al. (1986) *Fusion Technology*, v. 10, p.167. 9) Y. Li and L. Wittenberg (1988) *Lunar Bases II*, p. 158. 10) G. Kulcinski et al. (1986) *Lunar Development Symposium*. 11) E.Cameron (1987) *WCSAR-TR-AR3-8708*. 12) V.Busarev and V.Shevchenko (1988) *Lunar Bases II*, p.44. 13) T.Crabb and M. Jacobs (1988) *Lunar Bases II*, p. 62. 14) V. Shevchenko and V.Busarev (1988) *Lunar Bases II*, p. 219 15) L. Gaddis et al. (1985) *Icarus*, v. 61, p.461. 16) G.Heiken et al. (1974) *GCA* 38, 1703. 17) C.Pieters et al. (1973) *JGR* 78, p. 5867. 18) C. Pieters et al. (1974) *Science* 183, p. 1191. 19) J. Adams et al. (1974) *PLSC* 5, p. 171. 20) S.Zisk et al. (1974) *Moon* 10, p.17. 21) D. Wilhelms and J. McCauley (1971) *USGS Map I-703*.

# A SEARCH FOR INTACT LAVA TUBES ON THE MOON

Cassandra R. Coombs<sup>†</sup> and Bernard Ray Hawke<sup>\*</sup>

<sup>†</sup>SN 15, NASA/Johnson Space Center, Houston, TX, 77058; <sup>\*</sup>Planetary Geosciences  
Division, Hawaii Institute of Geophysics, Honolulu, HI, 96822

## INTRODUCTION

Early observations identified many meandering channels, or sinuous rilles, on the lunar surface.<sup>1</sup> Since then, numerous studies have shown that these features formed as a result of the extrusion of hot, fluid, low-viscosity basaltic magma (e.g., 2,3,4,5), some of which may have evolved into lava tubes when segments of the channels roofed over (e.g., 2,5,6,7,8). The prospect of using the natural cavity formed by a drained intact lunar lava tube for housing a manned lunar base has long been the subject of speculation (e.g., 9,10).

In his discussion of lava tubes as potential shelters for lunar habitats, Hörz noted that the lunar lava tubes would be ideal for locating the lunar base because they: (1) require little construction and enable a habitat to be placed inside with a minimal amount of building or burrowing; (2) provide natural environmental control; (3) provide protection from natural hazards (i.e., cosmic rays, meteorite and micrometeorite impacts, impact crater ejecta); and (4) provide an ideal natural storage facility for vehicles and machinery.

Depending on the rate of flow and the rheology of the lava, a lava tube may form by one of several methods (e.g., 8,12): (1) An open channel may form a crust that extends from the sides to meet in the middle and eventually thickens and forms a roof. (2) In more vigorous flows, the crustal slabs may break apart and be rafted down the channel. As the pieces are transported down the channel they may refit themselves together to form a cohesive roof. (3) Periods of spattering, sloshing, and overflow may form levees which may eventually build upward and inward and merge into a roof. (4) Continued lava flowage under a chilled crust may form a tube (see 13). Under the conditions of lunar basaltic eruptions (lower gravity field, no atmosphere), such processes would have produced lunar lava channels and associated tubes at least an order of magnitude greater in size than those found on Earth (e.g., 4). Such lunar lava tubes could be tens to hundreds of meters wide and deep and tens of kilometers long. These dimensions make lunar lava tubes ideal sites in which to house a lunar base habitat.

Terrestrial evidence indicates that a tube may or may not become plugged with lava depending on the viscosity, temperature, supply rate and velocity of the lava flowing through it. Other evidence, derived from the study of lunar volcanic features, suggests that not all lunar tubes are plugged with congealed lava and that void lava tubes do exist on the Moon.

This study proposed a set of criteria for the identification of intact lunar lava tubes. A study of all known sinuous rilles and channels as well as other selected volcanic features was conducted in an effort to locate lava tube-segments on the lunar surface. In addition, we have attempted to assess the potential of these tubes as candidates for lunar base sites.

## **METHOD**

A survey of all available lunar Orbiter and Apollo photographs was conducted in order to locate possible intact lava tubes. Criteria used to identify tube candidates were: (1) presence of an uncollapsed, or roofed, segment, or preferably a series of segments along a sinuous rille, (2) the presence of uncollapsed segments between two or more elongate depressions which lie along the trend of the rille, and (3) the presence of an uncollapsed section between an irregular-shaped depression, or source vent, and the rest of the channel.

## **RESULTS AND DISCUSSION**

More than ninety lava tube candidates were identified along twenty lunar rilles on the lunar nearside, sixty-seven of which were measured. These are located in four mare regions; Oceanus Procellarum, Northern Imbrium, Mare Serenitatis, and Mare Tranquilitatis. Each of these tubes has met our tube identification criteria and are considered candidates.

**Northern Procellarum:** Eleven rilles where probable intact lava tubes exist are found in the Oceanus Procellarum region; of these two may be considered prime localities at which to find an intact lava tube or series of tubes. The largest of these two is located just south of Gruithuisen K. It is 60 kilometers long and is broken into more than 15 segments, each of which may be a potential intact tube. The second candidate in this region is located in the Marius Hills area of Oceanus Procellarum. This rille is a combination of two rilles that meet at right angles at an irregularly-shaped depression that may have served as a common source vent.

**Southern Procellarum:** One good tube candidate was found in a complex of rilles just north of Mare Humorum. This tube segment is 1650 meters long and measures up to 440 meters wide.

**Northern Imbrium:** Three tube segments were found along one sinuous rille in the northern portion of Mare Imbrium. These three tube segments range in length from 840 to 1680 meters in length and in width from 210 to 290 meters.

**Serenitatis/Tranquilitatis:** Five rilles with probable intact lava tubes were identified in the Serenitatis/Tranquilitatis region. Two of these five rilles exhibit strong evidence for having intact tube segments. These vary between 320 and 880 meters long and 460 to 510 meters wide.

Many potential resources may be located in the vicinity of lava tubes. For example, lunar pyroclastic deposits are known to be associated with some source vents for the lunar sinuous rilles and lava tubes.<sup>4</sup> The black spheres which dominate some regional pyroclastic deposits are known to be rich in ilmenite.<sup>14,15,16,17</sup> These ilmenite-rich pyroclastics may in turn be a source of titanium, iron, and oxygen. Also, pyroclastics and regolith found in the vicinity of some of our "tube-candidates" may be a good source for sulfur as well as other volatile elements. Sulfur could be used as a propellant, as a fertilizer, as well as in industrial chemistry.<sup>18</sup>

## **CONCLUSIONS**

We conclude that lava tubes were formed on the Moon and that the probability of finding an intact, open tube segment would be suitable for housing a manned lunar base is quite high. Of the sixty-seven tube segments measured, nine tube segments associated with three



separate rilles were given the highest ranking. More analysis of the tubes identified in this study is needed before an adequate selection can be made of a specific lunar lava tube to house a manned lunar base. The construction of detailed geologic and topographic maps would greatly aid this effort. Also, further data are needed to confirm the presence of open channels/tubes. These data might include radar, gravity, active and/or passive seismic experiments, rover and "lunarnaut" reconnaissance and drilling.

## REFERENCES

- (1) Schröter J.H. (1788) In *Astron. jahrbuch für das jahr 1791*. Astronomisches Recheninstitut, 201.
- (2) Hulme G. (1973) *Mod. Geol.*, 4, 107-117.
- (3) Carr M.H. (1974) *Icarus*, 22, 1-23.
- (4) Wilson L. and Head J.W. (1981) *J. Geophys. Res.*, 86, n. B4, 2971-3001.
- (5) Coombs C.R., Hawke B.R., and Wilson L. (1987) *Proc. Lunar and Planet. Sci. Conf. 18th*, 339-354.
- (6) Oberbeck V.R., Quaide W.L., and Greeley R. (1969) *Modern Geology*, 1, 75-80.
- (7) Greeley R. (1971) *Science*, 172, 722-725.
- (8) Cruikshank D.P. and Wood C.A. (1972) *The Moon*, 3, 412-447.
- (9) Brown O.D.R. and Finn J.C. (1962) in: *Aerospace Medical Div., Aerospace Medical Research Labs./6570TH/*, Wright-Patterson AFB, OH., Biologistics for Space Systems Symposium, Final Rept, 233-241.
- (10) Henderson C.W. (1962) *Am. Rocket Soc. Ann. Mtg. 17th, and Space Flight Exposition*, LA, CA, Nov. 13-18, Paper 2688-62, ARS Paper 62-2688, 7p.
- (11) Hörz F. (1985) *Lunar Bases and Space Activities of the 21st Century*, W.W. Mendell, ed., 405-412.
- (12) Greeley R. (1987) *U.S.G.S. Prof. Paper 1350, Volcanism in Hawaii*, Ch. 59, 1589-1602.
- (13) Wentworth C.K. and MacDonald G.A. (1953) *Geol. Surv. Bull.* 994, pp. 98.
- (14) Heiken G.H., McKay D.S., and Brown P.W. (1974) *Geochem. Cosmochim. Acta*, 38, 1703-1718.
- (15) Pieters C.M., McCord T.B., Zisk S.H., and Adams J.B. (1973) *J. Geophys. Res.*, 78, 5867-5875.
- (16) Pieter C.M., McCord T.B., Charette M.P., and Adams J.B. (1974) *Science*, 183, 1191-1194.
- (17) Adams J.B., Pieters C.M., and McCord T.B. (1974) *Proc. Lunar Sci. Conf. 5th*, 171-186.

**Terrestrial Analogs to Lunar Sinuous Rilles:  
Kauhako Conduit System, Kalaupapa, Molokai,  
and Other Hawaiian Lava Channels**

Cassandra R. Coombs, Johnson Space Center, SN 15, Houston, TX, 77058, and  
Bernard Ray Hawke, Planetary Geosciences Division, Hawaii Institute of Geophysics,  
Honolulu, HI, 96822

Previous work done on lava tubes and channels associated with recent and historic lava flows in Hawaii has shown that the terrestrial features are similar in many ways to the sinuous rilles found on the lunar surface (e.g.: 1,2). As part of a larger study of the nature and origin of lunar sinuous rilles, and because of the current inaccessibility of the Moon for field work, we have studied the Kauhako Channel/Tube system on the Kalaupapa Peninsula of Molokai, Hawaii; a volcanic complex that has many of the characteristics of lunar sinuous rilles and appears to be a viable analog. In this study we investigated the basic processes responsible for the formation of the Kauhako conduit system and related it to the formation of lunar sinuous rilles and other Hawaiian lava channels. Here the geology, morphology, and volcanic history of Kauhako Crater and Channels are presented. Various data sets used during the course of the study include: field, topographic, photographic, and sample.

Recent photo and map reconnaissance of the crater and channel has shown that morphologically, Kauhako Crater/Channel is very similar to many lunar sinuous rilles.<sup>3</sup> Both the Kauhako and lunar channels studied formed as a result of basaltic volcanism, have deep source craters, exhibit some degree of tube formation, follow sinuous paths, and show evidence of some thermal erosion in their formational histories.

Kalaupapa is a 10 km<sup>2</sup> lava shield volcano that rises to 135 m above sea level at Pu'u 'Uao (Peacemaker Hill). The Kalaupapa shield is capped by Kauhako Crater, measuring 500 m wide by 650 m in diameter with a rim elevation of 135 m. The crater forms a funnel-like pit with one circum-crater terrace and a lake in the bottom. A second, smaller pit about 22 m wide by 10m deep is located on the northeastern part of the crater terrace, near the mouth of the lava channel. A sinuous lava channel/tube extends northward from the northeast side of Kauhako crater. This discontinuous channel is 1.0 km long, up to 30 m deep, and varies in width from 100 m to 150 m. Tumuli, formed by the squeeze-up of magma form an underlying tube system, and extend the line of the channel another 1.3 km to the N-NE.

The walls of the crater and main channel/tube system are composed of two stratigraphic units; one a composite of relatively thick and massive flow units, and the other a composite of very thin flow units. Many blocks of the thin layered "rim" material were found on the channel floor, suggesting that the lava once formed a shelf or crust that extended across the channel. A second prominent tube system extends N-NW from an elbow in Kauhako Channel to the eastern coast of the peninsula. The lava tube is discontinuous

along its trend but eight skylights were found in the field, six of which allowed entrance into the lava tube.

A second, previously unknown, source vent was identified during this field study. This second vent is located near the base of the pali bounding the S side of the peninsula, 1.4 km southwest of Kauhako Crater. That this cone is associated with the Kauhako eruption has not been firmly established. However, the two vents are aligned along the same trend as the Koko fissure and other alignments associated with the rejuvenation-stage volcanism on Oahu. <sup>4</sup>

Besides lunar sinuous rilles (e.g., Rima Mozart), an analogy may also be drawn between the Kauhako Crater/Channel/Tube system and other lava channel systems on the Big Island of Hawaii. These analogous systems include: the currently active Kupaianaha vent on Kilauea; the Mauna Ulu crater, tubes and channels; Thurston lava tube; Makapu'u lava tube, and the Whittington lava tube. Both the Whittington and Makapu'u lava tubes show evidence of thermal erosive activity in their formational histories. At least four stages of infilling and cross-cutting are evident in the Makapu'u tube, suggesting that thermal erosion was at least partly responsible for its formation. Evidence for thermal erosion in terrestrial lava tubes is difficult to establish; however, the Whittington lava tube provides excellent evidence that thermal erosion played an important role in its formation. Several tree molds were identified at the base of two older, successive lava flows adjacent to the tube, which are separated by a thin, weathered paleosol. The presence of these features indicates that some time interval occurred between the eruption and deposition of the two flows to allow the trees to grow and the soil layer to accumulate. The lava tube cuts through both of these lava flows. While it may be argued that the lava followed a pre-existing fault plane or stream channel, no evidence was found in the field for the pre-existence of either feature.

Several models have been developed for the formation of lunar sinuous rilles in conjunction with thermal erosion.<sup>5,6,7,8,9</sup> In this study we adapted Hulme's<sup>5</sup> model for thermal erosion of a lunar sinuous rille for use under terrestrial conditions to model the thermal erosion rate for the Kauhako system. Briefly, the Kauhako eruption was monogenetic, lasted for a period of just over 33 days and erupted a maximum volume of 2.2 km<sup>3</sup> at a rate of 7.8 m<sup>2</sup>s<sup>-1</sup>. Thermal erosion aided in the downcutting of this channel at a rate of 10.5  $\mu$ m s<sup>-1</sup>.

The morphology and eruptive history of this volcano make it a good analog to lunar sinuous rilles (i.e.: Rima Mozart). Morphologically, the Rima Mozart and Kauhako lava channels are very similar. Their channel floors are hummocky, their paths are sinuous and they begin at deep source craters. Volcanologically, the two are similar also. Both were carved out of basaltic material, were associated with a pyroclastic eruptive phase, and exhibit evidence that some degree of thermal erosion was involved in their formation.

References: (1) Greeley R. (1971) *Science*, 172, 722-725. (2) Cruikshank D.P. and Wood C.A. (1972) *The Moon*, 3, 412-447. (3) Coombs C.R. and Hawke B.R. (1988) In *LPSC XIX*, 207-208. (4) Walker G.P.L. and Coombs (1988) submitted to: *Bull. Geol. Soc. Am.*, 23 p. (5) Hulme G. (1973) *Modern Geol.*, 4, 107-117. (6) Carr M.H. (1974) *Icarus*, 22, 1-23. (7) Wilson L and Head J.W. (1980) *LPSC XI*, 1260-1262. (8) Wilson L and Head J.W. (1981) *J. Geophys. Res.*, 86, B4, 2971-3001. (9) Coombs C.R., Hawke B.R., and Wilson L. (1987) *PLPSC 18th*, 339-353. (10) Coombs C.R. (1988) PhD Dissertation, Univ. of Hawaii, 257 pp.

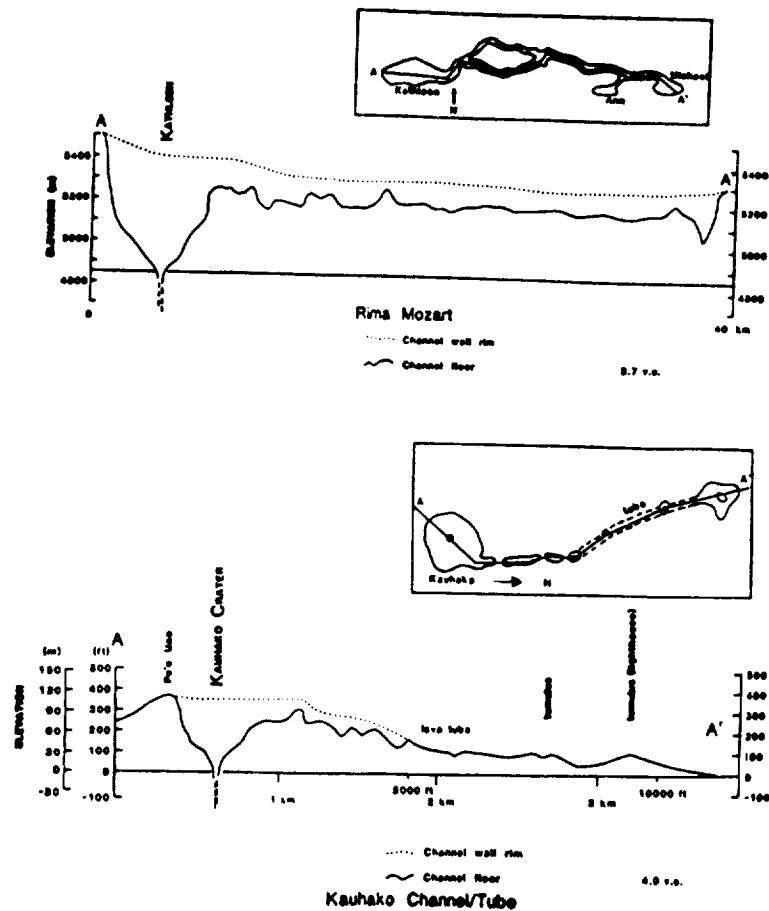


Figure 1: Comparative cross-sections of Rima Mozart and Kauhako Crater/Channel showing the morphologic similarity between the two volcanic complexes (after Coombs, 1988).<sup>10</sup>

## A Geologic Study of Picacho Butte and Vicinity, Arizona

Andrew P. Kisiel and John S. King, Department of Geology, University at Buffalo,  
4240 Ridge Lea Road, Amherst, N.Y. 14226

Picacho Butte is a volcanic construct located in north central Arizona, in the transition zone between the Colorado Plateau and Basin and Range physiographic provinces. It is a silicic dome located on the southern portion of the Mount Floyd volcanic field. An apparent alignment of silicic vents in the Mount Floyd field is presumably due to structural control. Picacho Butte, at  $9.8 \pm 0.7$  Ma (Goff and others, 1983), is the oldest silicic dome in a northward migrating silicic sequence. Detailed mapping revealed Picacho Butte to be an extensively eroded dome composed of hornblende rhyodacite. The rhyodacites are trachytic, containing variable amounts of plagioclase, hornblende, and biotite phenocrysts in a cryptocrystalline to glassy groundmass with plagioclase and opaques.

The dome is characterized by flow banding and flow folding. Attitudes of flow banding generally document flow outward from the center on all sides. Peripheral crumble breccias are found along the slopes, presumably formed during dome growth and expansion. With cooling, dome contraction resulted in the formation of large scale vertical joints along the western side of the dome. Massive gray hornblende rhyodacite can be found on the upper regions of the dome. Erosion has deeply incised the mountain exposing a vertical dike complex at the core.

Volcanic rocks of the field are dominated by basalts containing variable phenocryst proportions. Individual vents were short lived and apparently active for only short periods of time, commonly for a single eruption. Individual flows are restricted, apparently due to more viscous lava. Vesicular basalt is common, signifying a high gas content. Sections of flows indicate a vertical structure consisting of three zones. A thin ( $\approx 0.25$ m) lower vesicular zone is found beneath a thick nonvesicular zone. The top portion of the flows generally vesicular, but in varying degrees.

Picacho Butte is surrounded by basaltic cinder cones which exhibit a high degree of degradation. Many are eroded exposing radial dikes which once fed the cones. Volcanic activity was mixed. Initial activity is believed to have been moderately to weakly explosive producing fragmental, pyroclastic material and limited agglutinated lava deposits. A common early pyroclastic stage consists of a basal basaltic tuff, altered to a yellow to buff colored palagonitic tuff. Palagonitization may be a result of ordinary weathering processes, occurring after cone erosion (Macdonald, 1972, Haer and Illins, 1968). Most palagonitization occurs during low temperature weathering and diagenesis (Hay and Iijima 1968). The eruptive sequence is analogous to Strombolian type volcanism. Strombolian eruptions produce cones only a few feet in height to hundreds or thousands of feet in height (Macdonald, 1972). The basaltic cinder cones in the Picacho Butte area are small, less than 1 km in radius.

Often, the initial activity of the Picacho Butte basaltic vents was explosive. Interaction with ground water may have been a major factor in eruptive style of the basaltic volcanism, in the vicinity of Picacho Butte, early in the evolution of the vent. However, with the presence of some highly vesicular flows in the

study area, pyroclastic activity may have been a result of both volatile content of the magma and interaction with ground water.

The mafic rocks are olivine basalts with some quartz-bearing basaltic andesites. Chemically they are alkaline to subalkaline, with silica values ranging from 45.5–51.4% SiO<sub>2</sub> (normalized). The rocks are transitional in character between the alkali and subalkali fields. Their C.I.P.W. normative mineralogy supports this point, as the basalts range from hypersthene normative to mildly nepheline normative compositions. Quartz-bearing basaltic andesite (58.3–59.3% SiO<sub>2</sub>) underlies the basalts south of Picacho Butte. It contains phenocrysts of clinopyroxene, olivine, and embayed and sieved plagioclase in a hypocrystalline groundmass of the same minerals plus opaque oxide. The olivine basalts contain variable amounts of xenocrysts, some quartz grains which are fractured, embayed, and lined with clinopyroxene crystals.

The characteristic landforms produced by Strombolian style eruptions are cinder cones and surrounding lavas of moderate volume (Williams and McBirney, 1979). Intermittent explosive activity is caused by the disruption of magma due to bubble coalescence. In Strombolian eruptions ejecta are typically liquid on eruption but solid by the time they strike the ground (Macdonald, 1972).

Disruption of magma into pyroclasts is more likely to occur on Mars than on Earth due to the low atmospheric pressure on Mars (Wilson and Head, 1983). Assuming chemical environments are similar, and given sufficient magma volatile content, pyroclastic eruptions of basaltic compositions should be more common on Mars than on Earth (Wilson and Head, 1983).

Volcanic morphology on Mars implies formation by fluid lavas, inferred as basaltic in composition. Although large scale explosive volcanism is a subject of controversy, lesser volcanic structures may have been the result of explosive activity, possibly like the Strombolian activity in the Picacho Butte area.

Explosive pyroclastic volcanism was first proposed for Mars from the analysis of low resolution Mariner 9 images (West, 1974). Conical structures resembling terrestrial cinder cones have been identified on Mars (Carr and others, 1977). With the application of qualitative morphologic criteria such as relief, presence of a summit crater, circularity, and alignment along structural trends workers propose a volcanic origin for many of these structures.

Small conical summit crater cones are found in many regions of Mars including the Northern Plains from Arcadia through Utopia. In the Northern Plains Province numerous small cones with basal diameters up to 5 km are believed to be volcanic in origin (Scott, 1979; Wood, 1979). In the Cydonia region numerous kilometer to subkilometer small moundlike structures with summit pits were identified as possible cinder cones by Frey and Jarosewich (1982). Hundreds of subkilometer cratered volcanoes in Isidis, Utopia Planitia, and Elysium were proposed to be analogs of terrestrial cinder cones (Plescia, 1980; Frey and Jarosewich, 1982).

Frey and Jarosewich (1982) propose that a possible analog for the small cones are Icelandic pseudocraters, based on studies of crater/cone ratios, morphology, and distribution of the small cones. Icelandic pseudocraters form where lava flows over water or water saturated ground causing steam explosions

(Thorarinsson, 1953). If the small Martian cones are like Icelandic pseudocraters, they probably form as the result of the contact of lava with ice rather than water. The cones on Mars are however, 2-3 times the size of their terrestrial counterparts (Frey, 1982).

Terrestrial volcanoes exhibit a diverse range of morphologies due to a wide variety of styles of volcanic activity. The Picacho Butte vicinity Strombolian-like explosive eruptive activity is believed to have led to the formation of cinder cones. Identification of similar morphologic features on Mars implies explosive style eruptions on that planet have occurred in the past.

### References

- Carr, M.H., Greeley, R., Blasius K.R., Guest, J.E., and Murray, J.B., 1977, Some Martian volcanic features as viewed from the Viking orbiters: *J. Geophys. Res.* v.82, p.3985-4015.
- Frey, H., and Jarosewich, M., 1982, Subkilometer martian volcanoes: properties and possible terrestrial analogs: *Journal of Geophysical Res.*, v.87, no.B12, p.9867-9879.
- Goff, F.E., Eddy, A.C. and Arny, B., 1983, Reconnaissance geologic strip map from Kingman to south of Bill Williams Mountain, Arizona: LA 9202-MAP, Los Alamos, New Mexico.
- Hay, R.L., and Iijima, A., 1968, Nature and origin of palagonite tuffs of the Honolulu group on Oahu, Hawaii: *Geol. Soc. Amer. Mem.* v.116, p.331-376.
- Macdonald, G.A., 1972, *Volcanoes*: Prentice Hall, London, 510 p.
- Plescia, J.B., 1980, Cinder cones of Isidis and Elysium: *NASA Tech. Memo.* 82385, p.263-265.
- Scott, D.H., 1979, Geologic problems in the northern plains of Mars: *Proc. Lunar Planet. Sci. Conf.*, 10th, p.3039-3054.
- Scott, D.H., 1982, Volcanoes and volcanic provinces: Martian western hemisphere: *J. Geophys. Res.*, v.87, no. B12, p.9839-9851.
- Thorarinsson, S., 1953, The crater groups in Iceland: *Bull. Volcanol. Ser. 2*, 14, p. 3-44.
- West, M., 1974, Martian volcanism: Additional observations and evidence for pyroclastic activity: *Icarus*, v.21, p.1-11.
- Williams, H., and McBirney, A.R., 1979, *Volcanology*: Freeman, Cooper and Co., San Francisco, 397 p.
- Wilson, L., and Head, J.W., 1983, A comparison of volcanic eruption processes on Earth, Moon, Mars, Io, and Venus: *Nature*, v.302 21, p.663-669.
- Wood, C.A., 1979, Monogenetic volcanoes of the terrestrial planets: *Proc. Lunar Planet. Sci. Conf.*, 10th, 2815-2840.

## VOLCANISM AND TECTONISM OF THE COLORADO PLATEAU-BASIN AND RANGE TRANSITION ZONE OF WEST-CENTRAL ARIZONA: IMPLICATIONS FOR THE MARTIAN THARSIS UPLIFT

Ardyth M. Simmons and John S. King, Department of Geology, State University of New York at Buffalo, 4240 Ridge Lea, Amherst, NY 14226

One hypothesis for explaining differing styles of volcanism and compositions of eruptive products within a region is variation in crustal thickness. Another explanation is differing stress regimes. These hypotheses can be examined in the Mohon Mountains volcanic field of west-central Arizona, located in the Colorado Plateau-Basin and Range Transition Zone. A possible area for testing the applicability of such ideas on Mars is the Tharsis uplift.

The Mohon Mountains volcanic field was active from 20–6 m.y. ago with a hiatus from about 15–12 m.y. ago. The early, pre-15 Ma volcanics differ from the post-12 Ma volcanics not only in age, but also in chemistry, petrogenesis, eruptive style, and tectonic setting. Volcanism began with eruption of the Mohon alkaline stratovolcano beginning  $20.1 \pm 0.9$  m.y. ago and continued after deposition of the 18.3 Ma Peach Springs Tuff and flow of the Trout Creek olivine tholeiite. Most of the trachyandesites and dacites that make up the Mohon volcanic complex erupted from a central vent area, but dacitic domes peripheral to the volcano formed late in the field's history, along with minor intrusions of shonkinite and NW-trending alkalic basalt dikes. Following a hiatus of about 3 m.y., basalts and rhyodacites erupted south and east of the Mohon volcano in the Mount Hope area. These range in age from 12 to 6 Ma (1,2). The older volcanics erupted from a few central vents and were highly explosive, producing large volumes of airfall tuffs and breccias. The younger volcanics came from numerous widely scattered vents and were much more effusive.

In chemistry, the older lavas are enriched in K, Sr, Ba, P, and LREE. Initial  $^{87}\text{Sr}/^{86}\text{Sr}$  compositions exceed .7050 for the pre-15 Ma lavas and are less than .7050 for the post-12 Ma lavas, consistent with the temporal isotopic compositional pattern for Arizona rocks (3). The chondrite-normalized spider diagram, Ta-Th-Hf plot (4), and diagram of Ce/Y vs. Zr/Nb (5) for the pre-15 Ma lavas all demonstrate the signature of a lithospheric mantle source which may have been hydrated or metasomatized during earlier Cenozoic subduction and may have experienced crustal interaction. The older lavas can be related by open system fractionation and crustal interaction following partial melting of an enriched mantle source. Post-12 Ma basalts of the Mount Hope area were derived by polybaric fractionation or by varying degrees of partial melting of an asthenospheric source similar to the source for ocean island basalts (4,5).

The degree of crustal interaction with ascending magmas could relate to crustal thickness below the area of eruption and/or could relate to stress regimes at the time of eruption. The older lavas erupted through a thicker, more cohesive crust having a more ductile stress regime. They are contemporaneous with predominantly andesitic-rhyolitic volcanism elsewhere in the Transition Zone that erupted during an extensional period of detachment faulting, low-angle ductile shear zones, and regional tilting. The transition from ductile to brittle extension was complete by about 10 m.y. ago (6). The later volcanic period was characterized by thinner crust, high-angle normal faulting, and fundamentally basaltic volcanism.



The Tharsis province of Mars has frequently been compared to the Basin and Range-Colorado Plateau region of the western U.S. because both are uplifted and have experienced widespread volcanism. The Tharsis bulge formed early in martian history, possibly before the decline in impact cratering rates 4 b.y. ago (7). Most Tharsis volcanoes occur near its summit and toward its steeper, northwestern edge. The asymmetry of volcanic alignment occurs possibly because the Tharsis bulge straddles the plains-uplands boundary (7). Its three main shield volcanoes, Arsia Mons, Pavonis Mons, and Ascraeus Mons, are spaced 700 km apart on what appears to be a NE-SW trending fracture zone just northwest of the summit. Olympus Mons differs from the other Tharsis shields in being younger, larger, and higher, being located at the edge of the Tharsis bulge, being bordered by an outward-facing scarp, and having an enigmatic aureole that has been postulated as an ash flow tuff deposit.

Martian crustal dynamics are different from those on Earth. The martian lithosphere appears not to have been recycled through the underlying asthenosphere. The Tharsis region is underlain by a thinner lithosphere (normally 300 km thick) and a 0.2 gm/cc less dense mantle than elsewhere on Mars (8). The height and spacing of Tharsis volcanoes increase with decreasing inferred age (9). This may be the result of a lithosphere that thickens with time, as has been suggested for ocean islands (10).

It remains unclear whether the Tharsis topography and gravity anomalies are supported isostatically by density variations within the lithosphere, by strength of the lithosphere, or by dynamic processes in the deeper viscous interior. An isostatic model (11) and a model in which Tharsis is supported by the finite elastic strength of the lithosphere have been tested (8). Both models indicate that the tectonic features associated with Tharsis are related to incumbent loading of the lithosphere and are not the result of structural doming. Significant internal loading by mantle thinning or intrusives would not be ruled out, however. Tharsis topography would tend to sustain access of magma through the lithosphere because of the tensile stresses associated with its relief (8).

Nearly all structures recognized around Tharsis are extensional, including numerous radial fossae graben and the Valles Marinaris canyon. This is also true of active seismicity on the Colorado Plateau. The existence of seismically active normal faults is evidence that the Colorado Plateau interior is undergoing NE-SW tectonic extension (12).

The Colorado Plateau-Basin and Range region has a thinned crust, anomalously low mantle P-wave velocities, high heat flow and a conductive upper mantle (13). These suggest that the crust and upper mantle beneath this region is hot. Expansion caused by heating may support the elevation of the region. Whether the Tharsis bulge is being actively supported by convection or passively supported by a thick, rigid lithosphere is unknown, but volcanic activity in the Tharsis region suggests that the lithosphere may be too thin to support the bulge without active help (7). Crustal thickness decreases from 45 km at the center of the Colorado Plateau to 35-37 km in the Transition Zone and 30 km under the Basin and Range (14). In contrast the Tharsis province appears to have a thicker crust at its edge under Olympus Mons (100 km) than at its summit (50 km).

The simple shear model is one explanation for differing styles of Middle Tertiary and later volcanism in Arizona (15). According to this model, the lower

crust of the Transition Zone would have been as thick as that of the Colorado Plateau early in its development in Middle Tertiary time. During detachment faulting, approximately 10 km of lower crust beneath the Transition Zone would have been removed to the west. During removal it would have been available for mixing with mantle or crustal melts. Following thinning and removal of part of the lower crust and attendant greater extension, mantle derived melts rose more quickly to the surface or ponded in the upper crust where they produced rhyodacitic melts. Rocks of intermediate composition from the later period are absent either because the low-melt portion of the lower crust was unavailable for mixing with mantle melts or because the thinner and highly distended crust prevented large magma reservoirs that may be necessary for fractionation from forming. The older lavas evolved in a single magma chamber over a period of several million years. Magmatism was shorter-lived at a particular location in the younger lavas. This is because brittle deformation produced a more fragmented crust that provided many avenues for rapid ascent of magma but only allowed for development of small, short-lived magma chambers.

On Mars, thicker, more cohesive crust at the edge of the Tharsis bulge, as compared to thinner crust of the interior, may permit greater differentiation of magma. The thicker crust allows for development of larger magma chambers, longer crustal residence time, and greater depths of generation. The Tharsis Montes may be smaller because they erupted through thinner, more highly distended crust at the central portion of the uplift. Whereas the simple shear model (15) would not apply to Tharsis, the model of different stress regimes could be applied. Greater tensional stress in the summit area would create a highly fragmented crust with many avenues of ascent along fracture zones and numerous possible vents.

#### REFERENCES

- (1) Simmons, A.M., 1986, unpubl. M.A. thesis, SUNY/Buffalo, 156 p.
- (2) Nealey, L.D., and others, 1986, U.S.G.S. OF 86-423, 20 p.
- (3) Spencer, J.E., and Reynolds, S.J., in press, AZ Geol. Soc. Digest 17.
- (4) Wood, D.A., 1979, *Geology* 7, p. 499-503.
- (5) Fitton, J.G., and others, 1989, *J. Petrology* 91, p. 331-351.
- (6) Young, R.A., and others, 1985, LPI Contrib. No. 575, p. 152-155.
- (7) Carr, M.H., and others, 1984, NASA SP-469, 317 p.
- (8) Basaltic Volcanism Study Project, 1981, *Basaltic Volcanism on the Terrestrial Planets*, Pergamon Press, NY, 1286 p.
- (9) Plescia, J.B., and Saunders, R. S., 1979, *Proc. Lunar Planet. Sci. Conf.* 10th. p. 2841-2859.
- (10) Vogt, P.R., 1974, *Earth Planet. Sci. Lett.* 21, p. 235-251.
- (11) Sleep, N.H., and Phillips, R.J., 1979, *Geophys. Res. Lett.* 6, p. 803-806.
- (12) Wong, I.G., and others, 1987, *G.S.A. Abstr. Prog.* 19. p. 897.
- (13) McGetchin, T.R., and others, 1980, in Bally, A.W., and others, eds., *Dynamics of Plate Interiors*, AGU Geodynamics Series I, p. 99-110.
- (14) Hauser, E.C., and others, 1987, *Geology* 15, p. 1103-1106.
- (15) Wernicke, Brian, 1985, *Can. J. Earth Sci.* 22, p. 108-125.

## THE CHANGBAISHAN VOLCANOES OF EASTERN CHINA.

Feng Maoseng, Li Jiazhen, and J.L. Whitford-Stark. China University of Geosciences, Beijing, P.R. of China and Geology Department, Sul Ross State University, Alpine TX, 79832.

The Changbaishan volcanoes include two large volcanic domes, numerous parasitic cones, and vast surrounding lava fields covering an area of about 9,500 square kilometers in the Jilin Province of eastern China and roughly 5,000 square kilometers in adjacent Korea. The northern part of the Changbaishan range consists of the Baitoushan (P'aektu-san) volcanic dome enclosing a large crater lake called Tianchi with a depth of 312.7 meters. The geology of the area has been mapped up to a scale of 1:200,000 but the vast volcanic area has not yet been studied because of poor accessibility and forest cover. Early work on the volcano has been summarized by Whitford-Stark (1987). The height of Baitoushan is given as both 2741 and 2749 meters in Chen Shupeng (1984) - 2749 meters appears to be the more accurate. The dome to the southwest of Baitoushan is called Wangtianefeng and extends from 1400 to 2300 meters above sea-level.

Landsat images show that the two domes are surrounded by relatively smooth lava fields, numerous parasitic cones, and regional linear structures. Cones include the Maanshan-Longtoushan group to the northwest of Baitoushan and the Dongxiaoshan group to the southeast. A major linear structure trends WNW-ESE between Baitoushan and the more eroded Wangtianefeng. Airphotos reveal that the lineament marks the contact between lava flows from the two eruption centers. East to west trending faults disrupted and complicated the volcanic structures to the southeast of the Baitoushan dome. A second fault system trending north-south, roughly parallel to a section of the China-Korea border, separates areas with clearly contrasted volcanic features.

Arai and others (1986) have mapped an ash in the northern part of the Sea of Japan which they believe to be derived from Baitoushan. This ash was found to be up to 16 cm thick, being fine grained and vitric, with alkali feldspar, hornblende and clinopyroxene crystals. The eruption which produced the ash has been dated as about the eleventh or twelfth centuries on the basis of its association with archeological remains. The bulk volume of the ash is estimated at 40 to 50 cubic kilometers (Machida and Arai, 1983). Liu Jiaqi (1986) has identified six periods of volcanism in the Changbaishan area. 1) Basalts of the Naitoushan period with K-Ar ages of 13-16 Ma. 2) Basalts of the Laoyeling period with K-Ar ages of 7-11 Ma. 3) Basalts of the Junjianshan period with K-Ar ages of 2.0 to 4.2 Ma. 4) The Longgang colcano group with K-Ar ages of 0.8 to 1.5 Ma. 5) The Baitoushan volcanic rocks with K-Ar ages of 0.06 to 0.58 Ma. 6) A trachy pumice at the summit of Baitoushan with a Carbon fourteen age of 1050 B.P. The pumice is widely scattered around the volcano, extending up to 60 to 70 kilometers to the north and east. During caldera formation, a small amount of pantelleritic ignimbrite and trachytic agglutinate were erupted and preserved in downfaulted or depressed parts of the caldera, mostly on the northwest side. Historic documents provide short accounts of "ash rain" eruptions in the years of 1579, 1668, and 1702. These events possibly produced the scoria and lapilli beds on top of the northern slope of the caldera.

Recent isotopic analyses (Basu and others, 1986) indicate that although the Baitoushan rocks are subduction-related, they have similarities with a few oceanic areas and require three distinct sources for their petrogenesis: a depleted and a primitive mantle component, and a

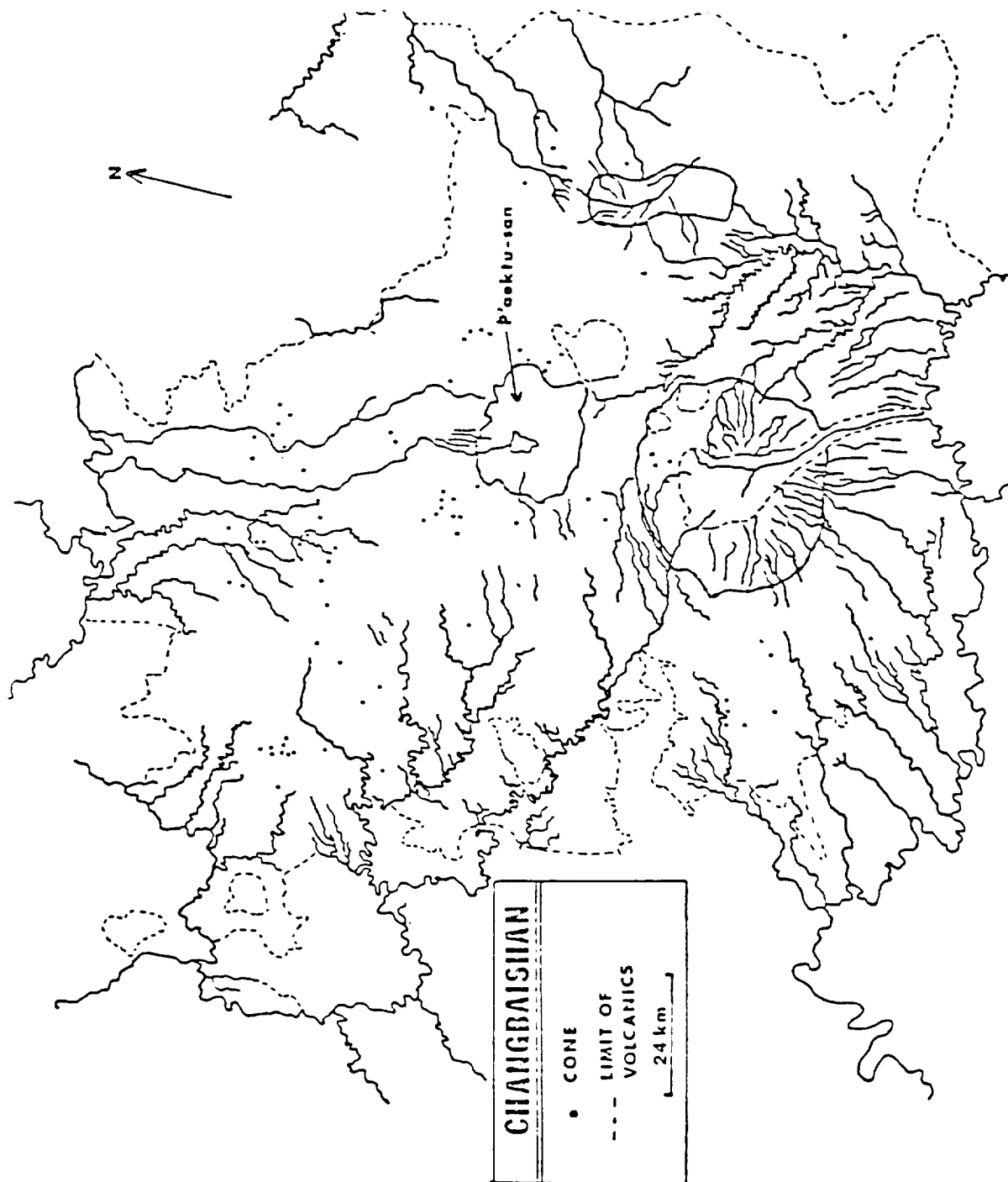
lower crustal reservoir. Rare Earth element patterns are similar to those of continental alkali basalts (Mei Houjun, 1986) and Sr and Pb data indicate that the younger trachytes and older basalts were not derived from the same magma source (Liu Beiling, 1986). Ultramafic inclusions are found in both the Baitoushan and nearby Longgang areas.

The Longgang volcano group includes 164 cinder cones and craters closely distributed over an area of 1,500 square kilometers. The older basalts are correlated with those in the Changbaishan area. Recent eruptions produced cinder cones, aa and pahoehoe lava flows, and small crater lakes.

### References

- Arai, F., Machida, H., Okumura, K., Miyauchi, T., Soda, T., and Yamagata, K. (1986), Catalog for Late Quaternary marker-tephras in Japan II - tephra occurring in northeast Honshu and Hokkaido. *Geographical Reports of Tokyo Metropolitan University*, 21, 223-250.
- Basu, A.R., Tatsumoto, M., Xie Guanghong, Wang Junwen, and Huang Wankang (1986), Isotopic study of alkalic rocks from Changbaishan, north eastern China. *EOS*, 67, 1278.
- Chen Shupeng (Editor), (1984) *Atlas of Geoscience Analyses of Landsat Imagery in China*. Science Press, Academia Sinica, 224 pp.
- Liu Beiling, (1986) *Petrogenesis of the Cenozoic volcanic rocks at Jingpohu, Wudalianchi and Changbaishan areas in northeastern China, the characteristics of regional evolution of mantle and their implications*. Thesis.
- Liu Jiaqi, (1986), Division of the Cenozoic volcanism in northeast China. Abstracts at the Third National Symposium on Isotope Geochemistry. p. 95.
- Machida, H., and Arai, F., (1983), Extensive ash falls in and around the Sea of Japan from large, late Quaternary eruptions. *J. Volcanol. Geothermal. Res.* 18, 151-164.
- Mei Houjun, (1986), Evolution of the Changbaishan volcanic rocks and China's continental rift system. *Annual Report, Institute of Geochemistry, Academia Sinica*. p. 251-252.
- Whitford-Stark, J.L., (1987), A survey of Cenozoic volcanism on mainland Asia. *Geol. Soc. Amer. Special Paper* 213, 74 pp.

Figure 1. Distribution of cinder cones in the Changbaishan. Baitoushan (P'aektu-san) and Wangtianefeng are outlined. Streams and Tianchi crater lake are also marked. Compiled from Landsat imagery and Shuttle hand-held orbital photography.



## LABORATORY SIMULATIONS OF LAVA FLOWS WITH SOLID CRUSTS.

Jonathan Fink<sup>1,2</sup> and Ross Griffiths<sup>2</sup>; <sup>1</sup> Geology Dept., Arizona State Univ., Tempe, AZ 85287,

<sup>2</sup> Research School of Earth Sciences, Australian National University, Canberra 2601, Australia

Planetary volcanology relies on the interpretation of flow morphology to constrain the compositions of remotely observed lavas. One of the tools available to assist in this task is laboratory simulation of flow processes. Properly scaled experiments can be used to replicate the overall geometry and structural details of features observed on natural flows. The appearance of a lava flow is controlled in large part by the presence of a cooled skin or crust at its surface, whereas overall dimensions are strongly influenced by rheology. Most previous laboratory simulations have not been able to generate surface crusts and, as a result, they have failed to produce realistic flow morphology. In addition, natural lavas have a temperature-dependent rheology that is only roughly approximated by the commonly used Newtonian and Bingham models. Here we report on a method of laboratory simulation which allows surface structures on lava flows and domes to be more accurately modeled using materials with temperature-dependent rheology.

We have performed a series of 25 experiments in which liquid carbowax, maintained at a temperature ( $T_i$ ) 1-3° above its freezing point ( $T_f$ ) of 18°C, was pumped at a constant flow rate ( $Q$ ) through a hole in the horizontal base of a 30 x 30 x 30 cm tank of sucrose solution held at a constant temperature ( $T_w$ ) between -3° and +16°C. When the fluid in the tank was sufficiently cold and the flow rate sufficiently low, a solid crust formed on the wax as it spread away from the central inlet. The extent of crust formation could be gauged using a dimensionless temperature,  $\theta = (T_i - T_w) / (T_f - T_w)$ , and a Peclet Number,  $Pe = (Q^{.75} g'^{.25}) / (\kappa v^{.25})$ , where  $g'$  is the reduced gravity,  $\kappa$  is the thermal diffusivity, and  $v$  is the kinematic viscosity of the wax. Crust growth was favored in those experiments having relatively high  $\theta$  and low  $Pe$ .

Digitization and analysis of sequential vertical photographs allowed radial growth rates to be determined, along with average radial velocities ( $v = \Delta r / \Delta t$ ) and radial strain rates ( $\epsilon_r = \Delta v / \Delta r$ ). For low  $\theta$ , crust did not form and radial growth rates were identical to those determined theoretically and in the laboratory for Newtonian viscous fluids [1]:

$$r = (g' Q^3 / 3v)^{0.125} t^{0.5}$$

( $t$  = time). At higher  $\theta$  values, crust appeared, imparting an effective yield strength ( $\tau$ ) to the flow. Growth was then better explained by a Bingham plastic model [2]:

$$r = (\rho g' Q^2 / \tau)^{0.2} t^{0.4}$$

A transition from viscous to Bingham behavior, marked by a change in slope of the radial growth curve (Fig. 1), was found to occur at the theoretically predicted time [2]:

$$T = [(g')^{0.75} (v)^{1.25} (\rho)^2 (Q)^{0.25}] / [(\tau)^{0.5}].$$

Strain rates were combined with laboratory-determined viscosities to compute stresses. In cases where the radial compression was high relative to gravity, regularly spaced transverse surface folds formed with wavelengths on the order of 1-3 mm and amplitudes of about 1 mm (Fig. 2). As predicted by theory and seen in lava flows [3], wavelengths increased as the crust thickened, in some cases resulting in more than one generation of super-imposed folds. Under circumferential tension, radial crust-free zones developed over the vent which evolved into multi-armed rift-like structures. As the crust thickened, the width and number of clear zones decreased, eventually leading to a single

elongate rift or a three-pronged structure. Spreading took place along circumferential strike-slip faults, analogous to transform structures seen on mid-ocean ridges and active lava lakes. For the coldest experiments (highest  $\theta$ ), pillow-like structures developed, rather than rifts or folds. In these runs, discrete narrow lobes of wax would advance a fixed distance and then stop, allowing the pressure to build up until a new break-out occurred, either along the same or a different lobe. The overall flow grew through this incremental process, producing a morphology analogous to submarine pillow basalt complexes and subaerial pahoehoe fields formed on shallow slopes.

By plotting  $Pe$  versus  $\theta$ , we were able to map out conditions under which folds, rifts, pillows, or no crust were favored. Transitions from one set of conditions to another correlated with the speed of crust growth. Crust growth rates were calculated analytically [4], so that transitions could be quantitatively related to eruptive conditions. We are currently calibrating the analytical model to our experiments and to natural flows in order to devise empirical expressions for effective viscosity and yield strength as functions of crust thickness. Such expressions will allow further quantitative interpretation of flow morphology.

REFERENCES: [1] Huppert HE (1982) The propagation of two-dimensional and axisymmetric viscous gravity currents over a rigid horizontal surface. *J. Fluid Mech.* 121:43-58. [2] Blake S (1989) Viscoplastic models of lava domes, in Fink JH (ed.) The mechanics of lava flow and dome growth. *IAVCEI Proc. in Volcanol.* 2 (in press). [3] Fink JH, Fletcher RC (1978) Ropy pahoehoe: surface folding of a viscous fluid. *Jour. Volcanol. Geotherm. Res.* 4: 151-170. [4] Turcotte D, Schubert G (1982) *Geodynamics*. New York: Wiley, 450 p.

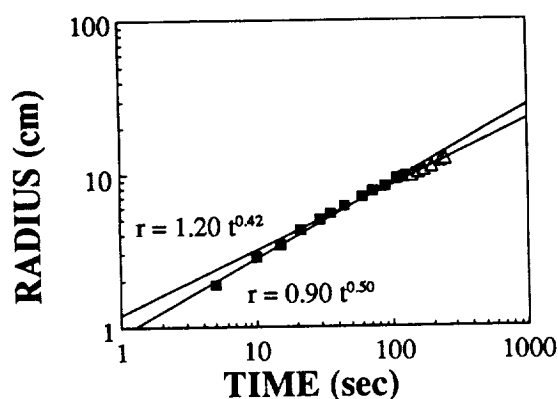


FIG. 1. Plot of average dome radius versus time for experiment with  $Pe=523$  and  $\theta=0.91$ . At times less than  $T=102$  sec, influence of the crust is negligible and spreading rate is Newtonian [1]. After  $T$ , yield strength effects slow the growth to the Bingham rate [2].  $r^2$  for both lines = 0.99.

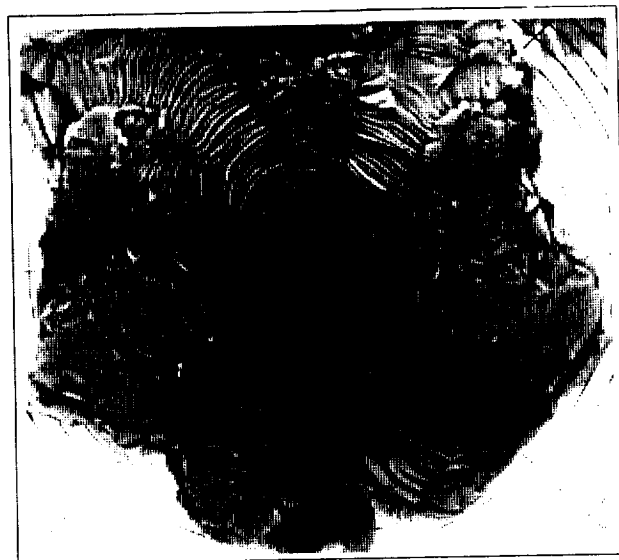


FIG. 2. Vertical view of carbowax dome formed with  $Pe=782$  and  $\theta=0.73$ , conditions which favor the production of surface folds. Field of view is approximately 30 cm across.

ORIGINAL PAGE

BLACK AND WHITE PHOTOGRAPH

COMPOSITION AND TEXTURAL VARIATIONS IN GLASS MOUNTAIN, CALIF.  
LAVA: EVIDENCE FROM THERMAL SPECTROSCOPY

ONDRUSEK, J., CHRISTENSEN, P., AND FINK, J., all at Dept. of Geology, Arizona State University, Tempe, AZ 85287 Bitnet: AGJXO@ASUACAD.

In order to better characterize the textures found in large silicic flows, we have begun spectroscopic studies of various vesicular, glassy, and crystalline textures in silicic lavas. Glass Mountain, in the Medicine Lake Highland of California, is a large silicic lava flow which appears to be the product of magma mixing. A map of the distribution of various compositions on the flow surface would be useful in the interpretation of the dynamics of this eruption. The Thermal Infrared Multispectral Scanner (TIMS) instrument generates images containing compositional information, and may have use in creating composition distribution maps. However, textural variations on lava flows also strongly influence TIMS imagery, and proper interpretation requires separation of textural and compositional components. Glass Mtn. is an excellent locality to test these effects on TIMS data. It is young (ca. 1100 yrs.), has little weathering, and virtually no vegetative cover.

Samples representing three textures in each of two compositions (rhyolite, ca. 73% SiO<sub>2</sub>); and dacite, ca. 62% SiO<sub>2</sub>) were collected. The textures are characterized as 1) coarsely vesicular pumice (CVP), with vesicles 1-5 mm in size; 2) finely vesicular pumice (FVP) with <1 mm size vesicles; and 3) glassy obsidian. High resolution thermal infrared emission spectra of these samples were obtained in the laboratory with a Mattson Cygnus FTIR spectrometer.

In the non-vesicular rhyolite samples, a broad spectral feature was observed centered at 1080 wavenumbers; non-vesicular dacite samples showed the same feature centered at 1120 wavenumbers. This shift in wavelength is consistent with compositional variations affecting the degree of polymerization and the bond strength of the Si-O tetrahedron. The depth of this absorption feature progressively decreases with increasing vesicularity, and is barely evident in samples with vesicles larger than a few millimeters. These changes due to texture are independent of composition and do not alter the absorption band location.

The implication for the interpretation of TIMS imagery is that glassy lavas of similar composition, such a dacite and rhyolite (about 10% difference in SiO<sub>2</sub>) may be distinguishable. Such separation is difficult to achieve over large areas by other methods. However, this discernibility diminishes with increasing vesicularity, due to the decrease in absorption band depth. Vesicles as small as a few millimeters have a profound effect on thermal IR spectra, and such vesicular lavas are quite common on silicic lava flows. Given sufficient spectral (and spatial) resolution, it may be possible to determine both compositional and textural variations. Based on these lab results, TIMS imagery from the non-vesicular portions of Glass Mtn. will be used to measure the areas of the various compositional zones; these data will then be inserted into various eruption models in order to test the models' applicability.



## CHAPTER 10

### CRATERING PROCESSES AND CHRONOLOGIES



## GIANT IMPACT THEORY OF THE MOON'S ORIGIN: FIRST 3-D HYDROCODE RESULTS

H. J. Melosh, Lunar and Planetary Laboratory, University of Arizona, Tucson, AZ 85721, and M. E. Kipp, Sandia National Laboratory, Albuquerque, NM 87185.

The giant impact theory of the moon's origin has rapidly gained a degree of acceptance among planetary scientists because of its apparent ability to explain the major features of lunar geochemistry and dynamics (1). More refined geochemical modeling, however, depends upon a greater understanding of the physics of planetary-scale impacts. This understanding can only come, at the present time, from detailed computer computation of the course of such an impact. Although the two-dimensional hydrocode models we have reported in the past are suggestive, full three-dimensional computations are needed to resolve many of the details of the putative collision between the protoearth and a Mars-size protoplanet.

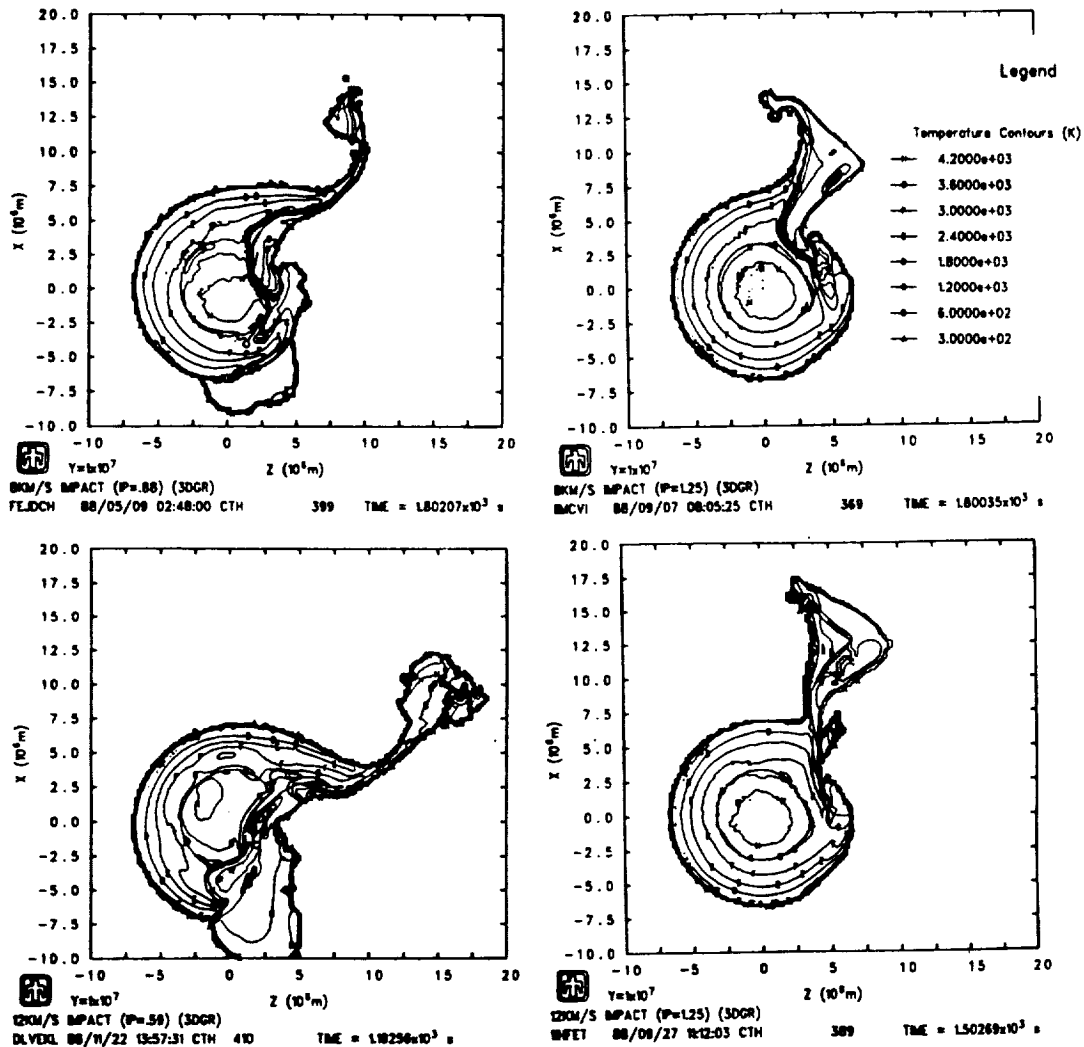
We report here on four successful computations of the collision between a Mars-size protoplanet and the protoearth. These computations were performed with a three-dimensional hydrocode called CTH, which was developed at Sandia National Laboratories over the past two years. CTH is an Eulerian continuum code that is capable of resolving the details of jetting and vaporization in the collision. It runs on the Sandia Cray I/XMP, and utilizes the new solid-state disk to handle the large number of variables in this problem. Zone sizes are cubes approximately 200 km on a side, so very fine resolution was obtained, although at the cost of employing several million zones in the overall computation. The numerical equation of state ANEOS was employed, and it was assumed that the planets' mantles are composed of dunite and their cores of liquid iron. The initial temperature and pressure distribution in the protoearth was modeled on the present distribution, although the 2-D runs previously performed (2) showed that the results depend only slightly upon these initial conditions.

The major simplification we had to make was to treat gravity as a purely central force: full self-gravity is beyond the reach of the present code. We do not believe this is a major source of error in the early part of the computation, as gas pressures and accelerations greatly exceed gravitational forces, but it may become important later on. During the course of our computations most of the initially vaporized material condenses, so ballistic extrapolations using self-gravitation may be performed on the code's output. This work is currently in progress. Although the smoothed-particle-hydrodynamic (SPH) code of Benz et al (3) can handle self-gravity more efficiently than conventional hydrocodes such as CTH, such SPH codes do not deal with pressure gradients well, so that we feel that the computations presented here provide a better picture of the early-time (about the first half-hour) events in a planetary collision than the current SPH computations can.

The four computations reported were performed for two approach velocities, 0 and 7.8 km/sec, and at impact parameters of  $0.88 R_e$ ,  $1.25 R_e$  (0 km/sec) and  $0.59 R_e$ ,  $1.25 R_e$  (7.8 km/sec). The impact parameters  $0.88 R_e$  and  $0.59 R_e$  were chosen because a Mars-mass impactor at these impact parameters impart the present angular momentum to the earth-moon system.  $R_e$  is the radius of the earth. The figures below illustrate temperature contours across the midplane (symmetry plane) of the collision at a time when the plume is fully developed. Compared with the older 2-D computations the 3-D models show, as expected, somewhat lower peak pressures and temperatures. Whereas the 7.8 km/sec impacts in 2-D developed a very high-speed plume, most of which escaped the earth, the present 3-D results produce a plume which travels at less than escape velocity and which may thus increase the amount of mass that eventually enters a closed orbit about the earth. We also find a surprising amount of material ejected to the sides, although this result is in at least qualitative agreement with an earlier analytic model of jetting (4). The major results of this simulation will be displayed at the

conference in the form of color computer graphic images of the plume at 100 second intervals out to times of about 2400 seconds from the impact.

REFERENCES: (1) eg, D. J. Stevenson, *Ann. Rev. Earth Planet. Sci.* **15**, 271-315 (1987). (2) Kipp, M. E. and Melosh, H.J. *Lunar and Planetary Science Conference XVIII*, 491-492 (1987). (3) W. Benz, W. L. Slattery, and A. G. W. Cameron, *Icarus* **66**, 515-535 (1986) and *Icarus* **71**, 30-45 (1987). (4) H. J. Melosh and C. P. Sonett in *Origin of the Moon*, LPI (1986) pp. 621-642.



ORIGINAL PAGE IS  
OF POOR QUALITY

# EARTH ROCKS ON MARS: MUST PLANETARY QUARANTINE BE RETHOUGHT?

H. J. Melosh, Lunar and Planetary Laboratory, University of Arizona, Tucson, AZ 85721.

Recent geochemical, isotopic and rare gas studies (1) have convinced a majority of planetary scientists that the eight SNC meteorites originated on the planet Mars. In addition, three meteorites found in Antarctica clearly originated on the moon (2). Detailed consideration of the mechanism by which these meteorites were lofted into space strongly suggest that the process of stress-wave spallation near a large impact (3) with, perhaps, an assist from vapor plume expansion (4), is the fundamental process by which lightly-shocked rock debris is ejected into interplanetary space. In the most plausible scenario, the SNC meteorites were ejected from Mars in the form of 10 m or greater diameter boulders 180 Myr ago by an impact that created a crater at least 100 km in diameter (5). These boulders were large enough to shield a substantial fraction of their interiors from cosmic rays until a breakup in space several million years ago exposed them to cosmic ray bombardment before they fell to the earth's surface.

The earth has also been struck by meteorites large enough to produce craters more than 100 km in diameter, such as Sudbury in Ontario, Canada (140 km diameter, 1850 Myr old), Veredfort in South Africa (140 km, 1970 Myr old), Poipgay in Siberia (100km, 39 Myr), Manicougan in Quebec, Canada (100 km, 210 Myr), and perhaps also the recently located Acraman structure in Australia (>90km, 600 Myr). In addition to the known large craters, the mounting evidence that the Cretaceous era was ended by the impact of a 10 km diameter asteroid or comet suggests that many other large impacts have occurred in Phanerozoic time whose craters either have not yet been found, or which have been modified beyond recognition. No craters have yet been located on the sea floor, which constitutes about 3/4 of the earth's present surface area.

These considerations lead naturally to the question, if Mars rocks are found on earth, why should not earth rocks be found on Mars? Furthermore, if earth rocks should find their way to Mars, might they contain spores or some sort of viable microorganisms that might then have the opportunity to colonize Mars?

To answer the first part of the question, I used the theory of spall ejection (6) to examine the mass and velocity of material ejected from the near vicinity of an impact. Since the spall mechanism only operates in the near vicinity of a free surface, the ejected rocks would all have originated from close to the surface, consistent with observations on both the Martian and lunar meteorites. The near surface is also the most biologically active region of the earth's crust, so the chance of ejecting spores and microorganisms with the spalled material is relatively high. The theory indicates that the volume of material ejected at a velocity greater or equal to greater than a predetermined velocity  $v_e$  is

$$\frac{V(\text{velocity} \geq v_e)}{V(\text{projectile})} = 4.8 \frac{P_M}{\rho \beta c_L U} \left[ 1 - \left( \frac{2v_e}{U} \right)^{1/3} \right]$$

where the volume is normalized by the projectile volume,  $\rho$  is the density of the target,  $\beta = 4$  for most applications,  $U$  is the impact velocity,  $c_L$  is the speed of the shock wave in the target, and  $P_M$  is the maximum pressure achieved in the material ejected.

If the ejection velocity  $v_e$  is taken to be the earth's escape velocity, this equation will yield the volume of material ejected from the earth for a given velocity and size of the initial

impactor. However, this equation neglects the effect of atmospheric interference, which could be of overriding importance on the earth. Numerical computations of the effect of a 10 km diameter asteroid on the earth's atmosphere (7) indicate that such a projectile clears the atmosphere away from its immediate vicinity, leaving behind a "hole" that takes minutes to close and through which early, fast spalled ejecta may escape. However, to be on the conservative side, I performed spall computations in which I assume that the atmosphere is present at its normal density. In a large impact the sheer mass of high velocity spalled material is so large that it exceeds the mass present in the atmospheric column, and so the spalled surface rocks may not be greatly hindered by the atmosphere. For the purposes of the computation I averaged the momentum of that spalled material which was ejected faster than the earth's escape velocity and the atmospheric gases along the escape trajectory. If the final velocity of both the spalled material and the atmosphere still exceeded escape velocity, then this material was counted as having escaped. If the average was less than escape velocity, then it was presumed that the material was stopped by the atmosphere and fell back to earth.

Much of the spalled material, while protected from the maximum pressure occurring in the shock wave by rarefactions from the free surface, nonetheless suffers significant shock damage. One of the SNC meteorites (EETA 79001) contains impact melt glass and may have experienced pressures as great as 50 GPa. Any organisms residing in the rock would certainly have been killed by the heat generated by the shock event. Only the rocks nearest the surface which receive the maximum protection from shock would escape heating to less than 100°C and thus retain viable microorganisms and spores. I take the corresponding shock pressure as equal to the stress necessary to crush the rock (when internal pores collapse the PdV work done during the collapse greatly enhances the energy deposition and at this point residual temperatures greatly exceed 100°C), or about 0.1 GPa (1 kilobar). The volume of ejected material thus escaping sterilization is thus considerably less than the total volume of spalled rock. However, this near-surface zone begins with a full complement of soil microorganisms, some of which appear likely to survive the ejection process. Behind the surface skin of spalled rock which has been raised to less than 100°C (which I will call the *fecund zone* in the following) is a larger mass of hot, sterilized rock that pushes the meter-plus-diameter boulders from the fecund zone through the atmosphere. Although some brief heating may occur at the surface of the fecund zone as the atmosphere is compressed in front of it, this heating is of short duration, since at 11 km/sec the ejecta clears the lower atmosphere in a matter of seconds. The thermal penetration depth of such a heat pulse is only a few millimeters, so that most of the ejected organisms will survive.

Figure 1 shows the volume of fecund material (which is only a few percent of the total spalled material) ejected from the earth as a function of impact velocity and transient crater diameter (the final crater will be about 65% larger than the transient crater size). Note that no ejecta escapes unless the impact velocity exceeds about 30 km/sec. This is a conservative limit: the spall model used to construct this plot assumes that no spall material is ejected faster than about 35% of the impact velocity. Direct observations on small scale impacts (8) indicate that some material may be spalled at speeds approaching 85% of the impact velocity. The contours in Figure 1 are labeled by the volume ejected in m<sup>3</sup>. It is clear that a 50-75 km diameter transient crater (which would produce a final crater comparable in diameter to the *observed* large craters on earth) could eject roughly a million cubic meters of meter-plus-diameter boulders from the fecund zone.

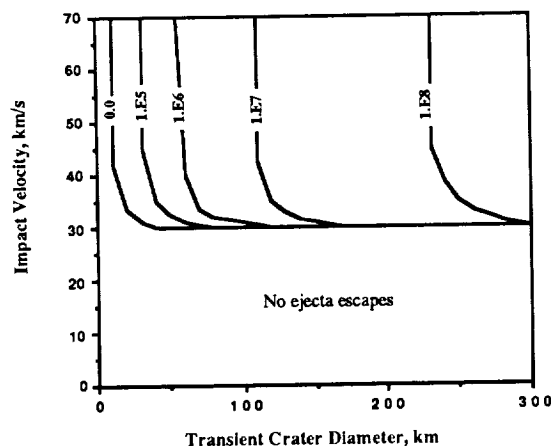
It thus seems likely that the half-dozen largest impact events on earth would have each ejected considerable masses (millions of tons) of near surface rocks carrying viable microorganisms into interplanetary space. Much of the ejected debris would have been in the form of boulders large enough to shield those organisms even from galactic cosmic rays, not to mention ultraviolet radiation and low energy solar cosmic rays. Under such circumstances

spores might remain viable for long periods of time. Even microorganisms active at the time of ejection might have been preserved for considerable periods by lopholization in hard vacuum. Viable organisms preserved by this process were recovered from the Surveyor 3 camera assembly after three years on the lunar surface (9).

No computations have yet been performed to indicate how long earth ejecta would take to reach Mars. Similar computations on the migration of Mars ejecta to earth (10) indicate mean transit times of millions of years. However, since earth's greater mass may result in larger perturbations to the orbits of nearby debris, the transit time from earth to Mars may be considerably shorter. Some debris, of course, could make the trip much more quickly than the mean time.

Once at Mars, boulders falling to the surface would be slowed even by Mars' thin atmosphere and might even be fragmented and their interiors exposed by aerodynamic stresses at low altitudes. This process is especially important for small objects, meter size and below (11). Terrestrial organisms in these rocks would thus have the *opportunity* to colonize the planet *if* they could find suitable conditions. I am not claiming that such conditions are present on Mars, only that it appears likely that viable terrestrial microorganisms have reached the surface of Mars by natural processes. It thus appears that the planets of the solar system are not completely isolated biologically: from time to time large impacts may inoculate planets the inner solar system with a sample of terrestrial life. The most recent such inoculation may have taken place 39 Myr ago with the event that created Popagi crater in Siberia.

In the light of these considerations the need for biological quarantine may not be as serious as was once supposed. Rocks from Mars have *already* fallen to earth without having undergone any sterilization other than that imposed by millions of years in space. Earth rocks may similarly have already reached Mars. In any event, the possibility that Mars has already been exposed to terrestrial microorganisms should be factored into any future discussions of planetary quarantine.

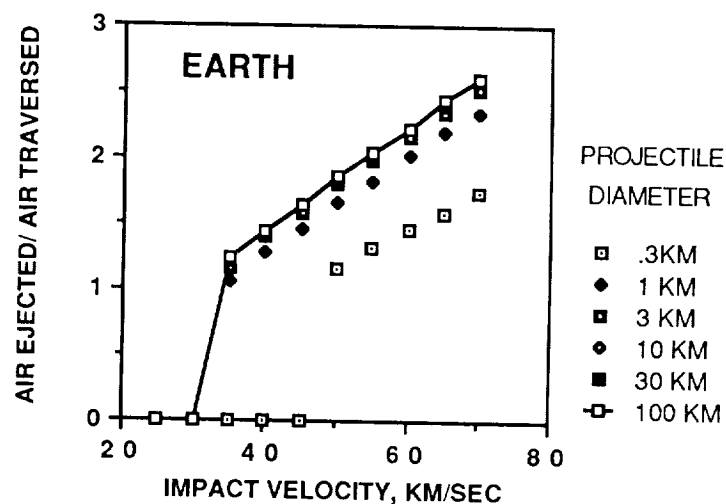


# Atmospheric Erosion by High Speed Impact Ejecta

H. J. Melosh and A. M. Vickery (Both at: Lunar and Planetary Laboratory, University of Arizona, Tucson, AZ 85721)

G. H. Watkins (1983) has proposed that impacts may have played a major role in the evolution of the atmospheres of the terrestrial planets by ejecting a significant fraction of the primordial atmosphere. J. C. G. Walker (1987), however, argued that the amount of ejected atmosphere is only slightly larger than that intercepted by the incoming projectile, and is thus far too small to affect the evolution of the atmosphere. Watkins' and Walkers methods differ greatly, however, and it is presently unclear how much of the atmosphere can be ejected by a large impact event.

Although this controversy can probably only be resolved by detailed numerical computations of an atmosphere's response to a large impact, it has been suggested that high speed ejecta might entrain and thus remove a large part of the atmosphere adjacent to an impact. This process is extremely difficult to model numerically, so we employed an analytical model of the very highest velocity (spalled) ejecta. The ejection velocity of this material near the surface of the earth was computed as a function of projectile diameter (0.1 to 100 km diameter), impact velocity (15 to 70 km/sec), and distance from the point of impact. Only material with ejection velocities greater than earth's escape velocity was considered. It was then determined whether the ejecta possessed sufficient momentum to entrain the atmospheric gases lying in its path and yet still escape the earth. If so, then these gases were considered ejected. The results (Fig. below) show that even the largest, highest velocity projectiles eject less than about 3 times the mass of the atmosphere intercepted, a result rather similar to Walker's (1987) conclusion. High speed ejecta thus do not seem to greatly facilitate the ejection of atmospheric gases in large impacts on earth.





# ATMOSPHERIC EROSION BY IMPACTS: AN ANALYTIC INVESTIGATION

A. M. Vickery and H.J. Melosh, Lunar and Planetary Laboratory, University of Arizona, Tucson, AZ 85721

Until recently, models for the origin and evolution of the atmospheres of terrestrial planets ignored the effects of accretionary impacts. In the 1970's, however, it was suggested that heating and/or vaporization of accreting carbonaceous-chondrite-type planetesimals could result in the release of their volatile components (1,2). Modeling of this process (e.g., 3,4) strongly suggests that substantial atmospheres/hydrospheres could develop this way. During most of the accretionary process, impact velocities generally differed little from the escape velocity of the growing proto-planet because most of the collisions were between bodies in nearly matching orbits. Toward the end of accretion, however, collisions were rarer but much more energetic, involving large planetesimals and higher impact velocities (5). It has been postulated that such impacts result in a net loss of atmosphere from a planet, and that the cumulative effect impacts during the period of heavy bombardment might have dramatically depleted the original atmospheres (6,7).

The transfer of momentum from an impactor to an atmosphere can occur in a number of ways. First there is the direct transfer of momentum as the impactor penetrates the atmosphere, compressing and accelerating the gas in front of it. O'Keefe and Ahrens (8) showed that the impactor delivers only a small fraction of its kinetic energy directly to the atmosphere, and Walker (9) showed that this energy is distributed in such a way that no significant amount of atmosphere escapes from a planet with an escape velocity  $\geq 10$  km/s. Second, solid ejecta thrown out of the growing crater can similarly transfer momentum to the atmosphere, but again this has been shown to result in negligible atmospheric loss (10). Third, for a sufficiently energetic impact, a great deal of very hot, dense vaporized impactor  $\pm$  target material will be produced that expands upward and outward at high velocities, driving the overlying atmosphere ahead of it.

The initial pressures in the impact-generated gas cloud will be so much higher than atmospheric pressure that one can, as a first approximation, consider the gas to be expanding in a vacuum. We used the analytic solutions of (11) to calculate the momentum of the impact gas, for which we needed to specify the mass and initial pressure and density of the gas. The pressure as a function of impact velocity for velocities of 10 to 50 km/s was estimated using impedance-matching (12), and the density was then estimated from the Rankine-Hugoniot relations. The mass of gas was arbitrarily chosen to range from  $10^{10}$  kg to  $10^{20}$  kg.

The maximum amount of atmosphere that can potentially be blown off in a single impact is that lying above a plane tangent to the planet's surface at the point of impact. We derived the following equation to calculate the mass of atmosphere as a function of zenith angle lying above the tangent plane :

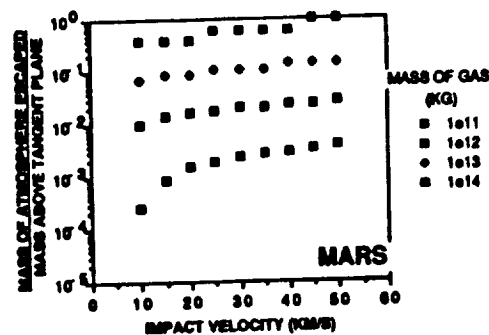
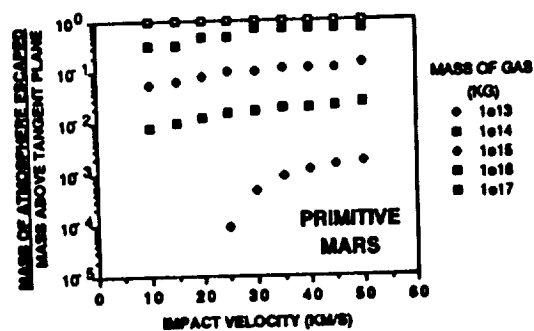
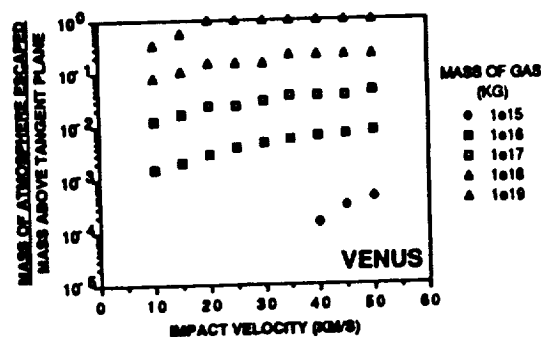
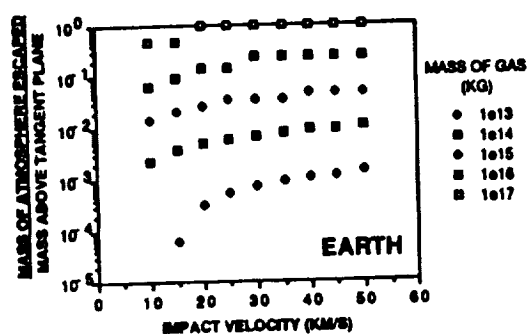
$$\frac{dM}{d\theta} = 2\pi \sin \theta \int \frac{\rho(z) \left[ \sqrt{z^2 + 2Rz + R^2 \cos^2 \theta} - R \cos \theta \right]^2}{\sqrt{z^2 + 2Rz + R^2 \cos^2 \theta}} (R + z) dz$$

where  $\theta$  is the angle from the zenith,  $z$  is altitude,  $\rho$  is density, and  $R$  is the radius of the planet. The atmospheric density profile for the earth was taken from (13), while those for Mars and Venus were calculated from temperature profiles, surface temperatures and pressures (13), the equation for hydrostatic equilibrium, and the perfect gas law. A series of calculations was also performed for a hypothetical primitive Martian atmosphere, arbitrarily chosen to be isothermal ( $T=300$  K) and to have a surface pressure of  $10^5$  Pa and surface density of  $1 \text{ kg/m}^3$ . The

results are shown in figures 1-4. As one would intuitively expect, the fraction of atmosphere blown off increases with both impact velocity and mass of impact-produced gas. The efficiency with which atmosphere is removed for a given impact velocity and impact gas mass increases in the order Venus, Earth, Mars, and the hypothetical primitive atmosphere of Mars is more efficiently removed than that of present day earth (which it resembles in surface pressure and density) because of Mars' lesser gravity.

The mass of impact gas is used as a parameter in these calculations rather than the mass of the impactor. This makes it impossible to cast these results in terms of impact energy or momentum, but was necessary because the use of the Zel'dovich-Razier equations (11) is only valid for the initial gas pressures  $\gg$  ambient atmospheric pressure, and there is no reliable way to estimate the mass of such gas as a function of impactor mass and impact velocity. Another complication is that oblique impacts apparently produce much more vapor than normal impacts with the same impactor mass and impact velocity (14).

REFERENCES: (1) Arrhenius et al. (1974) in: *The Sea*, vol 5 (E.D. Goldberg, Ed.), Wiley, p.839. (2) Benlow, A. and Meadows, A.J. (1977) *Astrophys. Space Sci.* **46**, 293. (3) Abe, Y. and Matsui, T. (1985) *Proc. Lunar Planet. Sci. Conf. 15th, Part 2, J. Geophys. Res.*, C545. (4) Lange, M. A. and Ahrens, T.J. (1982) *Icarus* **51**, 96. (5) Wetherill, G. W. (1985) *Science* **228**, 877. (6) Watkins, G. H. (1984) PhD Thesis, M.I.T. (7) Cameron, A. G. W. (1983) *Icarus* **56**, 195. (8) O'Keefe, J. D. and Ahrens, T. J. (1982) in: *Geol. Soc. Amer. Spec. Pap.* **190**, 103. (9) Walker, J.C.G. (1986) *Icarus* **68**, 87. (10) Melosh, H.J. (1988) *Nature*, **332**, 687. (11) Zel'dovich, Ya. B. and Razier, Yu. P. (1966) *Physics of Shock Waves and High-Temperature Hydrodynamic Phenomena*, vol I, Academic Press. (12) Gault, D. E. and Heitowit, E. D. (1963) *Proc. 6th Hypervelocity Impact Symp.*, vol. 2, 419. (13) Chamberlain, J.W. and Hunten, D. M. (1987) *Theory of Planetary Atmospheres*, 2nd ed., Academic Press. (14) Schultz, P.H. and Crawford, D. (1987) *Lunar Planet. Sci. XVIII*, 888.



## WAS THE EARLY ATMOSPHERE OF MARS SUSTAINED BY IMPACT-INDUCED RELEASE OF CO<sub>2</sub>?

Michael H. Carr, U. S. Geological Survey, Menlo Park, CA 94025

Valley networks have been widely interpreted as having formed by slow erosion of running water [1,2]. If this interpretation is correct, then warmer climatic conditions may have been required, irrespective of the origin of the water. Greenhouse calculations show that, for surface temperatures to approach 273°K, the atmospheric pressure at the surface must have been at least 1-2 bars [3,4]. Most of the valleys are very ancient. Most of those presently visible appear to have formed at the tail end of or shortly after the period of heavy meteorite bombardment, which is thought, by analogy with the Moon, to have terminated around 3.8 b.y. ago. While most of the very early evidence is destroyed by meteorite impact, it is reasonable to assume that high rates of valley formation prevailed throughout the early heavy bombardment. If water was stable at the surface, CO<sub>2</sub> would be scavenged from the atmosphere to form carbonates, at rates estimated at 1 bar every 10<sup>7</sup> years [5,6]. Thus, if water was stable at the surface at the end of heavy bombardment, some mechanism must have operated to recharge the atmosphere with CO<sub>2</sub>. The seeming coincidence between the decline in the rate of valley formation and the decline in the impact rate suggests that the two might be coupled. The high rates of impact may have contributed toward sustaining an early thick atmosphere so that, when the impact rate declined, the atmosphere thinned and the rate of valley formation declined.

Impacts could have helped sustain an early, relatively thick atmosphere in at least three ways: (1) carbonates that formed on the surface could have been folded so deeply into the megaregolith that they reached dissociation temperatures, (2) CO<sub>2</sub> could have been released from carbonates during impacts as a result of shock loading and heating, and (3) CO<sub>2</sub> could have been introduced onto the planet by the impacting meteorites. Order of magnitude estimates have been made of the efficacy of these three mechanisms on the assumption that impact rates on Mars at from the time of planet formation until the end of heavy bombardment were similar to the impact rates on the Moon during the Nectarian period, at the end of its heavy bombardment.

Burial rates were calculated by simply assuming that all the crater ejecta was distributed uniformly over the whole planet. Apart from the impact rate, the biggest uncertainties are first, how the depth and diameter of the transient cavity scale with the final crater diameter, and second, how much CO<sub>2</sub> had outgassed from the planet and so was available for formation of carbonates. Modelling of the thermal profiles within the crust suggests that the carbonates had to be buried to depths of 15-20 km for dissociation to occur. Burial rates as a result of impacts at the end of heavy bombardment are estimated to range from 20-45 m per 10<sup>6</sup> years. At these rates, and assuming that 10 bars of CO<sub>2</sub> had outgassed, 0.1 to 0.2 bars of CO<sub>2</sub> could have been released by burial of carbonates every 10<sup>7</sup> years. However, there is barely time between the formation of the planet and the end of heavy bombardment for burial to the required depths, unless volcanism contributed significantly to the burial.

Impacts could cause release of  $\text{CO}_2$  from carbonates directly by subjecting the carbonates to shock pressures over 200 kb [7], or by heating carbonates in the surface to temperatures above that required for dissociation. The Kieffer and Simonds model [8] was used to calculate the rate at which material would be shocked to 200 kb for the Nectarian impact rate. Dissociation as a result of the thermal anomaly left after the impact is significant only for large craters. For these craters the thermal anomaly extends to depths where the normal geothermal gradient approaches within a few hundred degrees of dissociation temperatures. At these depths a relatively small thermal anomaly can push the local temperatures over the dissociation temperatures. The results of the modeling suggest that the rates of release of  $\text{CO}_2$  as a direct result of the impacts are rather modest. Assuming 10 bars of outgassed  $\text{CO}_2$ , the rate of direct release is estimated to be only 0.01 to 0.02 bars every  $10^7$  years.

The third mechanism whereby meteorite impacts could have added  $\text{CO}_2$  to the atmosphere is by addition of carbon in the meteorites, followed by oxidation to  $\text{CO}_2$ . It is difficult to estimate how effective a mechanism this could be in sustaining the atmosphere, not knowing what types of meteorites dominated at the end of heavy bombardment. However, a reasonable upper limit on the amount of  $\text{CO}_2$  supplied to the atmosphere can be determined, on the assumption that the meteoritic material contained 3 percent carbon, the fraction present in the most carbon-rich meteorites, the CI carbonaceous chondrites. This upper limit is close to 0.3 bars every  $10^7$  years.

These calculations suggest that only under the most optimistic circumstances could impacts be effective in offsetting a loss of  $\text{CO}_2$  from Mars' early atmosphere at a rate of 1 bar every  $10^7$  years. Several possibilities suggest themselves: (1) warm surface conditions and a relatively thick atmosphere may not be required for valley formation, (2) estimates of the rate of fixation of  $\text{CO}_2$  in carbonates are too high, (3) other mechanisms, such as volcanism may have contributed significantly to sustaining an early thick atmosphere, and (4) the impact rates on Mars at the end of heavy bombardment were significantly larger than on the Moon. Of these, possibility (2) appears most likely. If liquid water was present at the surface only intermittently, then the fixation rates that have been estimated would be too high. Possibility (2) is plausible on other grounds, for the atmosphere would tend to buffer itself at temperatures just below that required to have liquid water at the surface and efficiently remove  $\text{CO}_2$ .

- REFERENCES. [1] Carr, M. H., 1981, *The Surface of Mars*. Yale Press. [2] Baker, V. R., 1982, *The Channels of Mars*. Univ. of Texas Press. [3] Pollack, J. B., 1979, *Icarus* **37**, 479-453. [4] Cess, W. G., Ramanathan, V., and Owen, T., 1980, *Icarus* **41**, 159-165. [5] Fanale, F. P., Salvail, J. R., Banerdt, W. B., and Saunders, R. S., 1982, *Icarus* **50**, 381-407. [6] Pollack, J. B., Kasting, J. F., Richardson, S. M., and Poliakoff, K., 1987, *Icarus* **71**, 203-224. [8] Kieffer, S. W., and Simonds, C. H., 1980, *Rev. Geophys. Space Phys.* **18**, 143-181.

## CLIMATIC EFFECTS OF EPISODIC RELEASE OF SO<sub>2</sub> ON MARS

S.E. Postawko and F.P. Fanale. Planetary Geosciences Div., Univ. of Hawaii, Honolulu, HI 96822.

We have investigated the possibility that intense episodic magma-generating events, such as fissure flows or large impacts, might have caused significant global warming on Mars. Our motivation for examining episodic climate change by SO<sub>2</sub> is that a given column abundance of SO<sub>2</sub> is vastly more effective than CO<sub>2</sub> at raising surface temperatures, and is supplied in comparable amounts to CO<sub>2</sub>. However, the mean residence time (M.R.T.) of SO<sub>2</sub> in the atmosphere is only on the order of a few years, as opposed to the CO<sub>2</sub> M.R.T. of  $\sim 10^7$  years. Therefore, for SO<sub>2</sub> only individual episodes of impact and extrusion, and only climatic effects of episodic (years) duration, are relevant; whereas for CO<sub>2</sub> only epochal effects are of importance.

We have taken estimates of magma production per martian epoch from Greeley (1987) and assumed the release of 1 % by weight of SO<sub>2</sub>. Note that this does not take into account any release of SO<sub>2</sub> by contact decrepitation from the country rock. We have considered two magma fluxes:  $5 \times 10^4$  m<sup>3</sup>/s, and  $10^6$  m<sup>3</sup>/s, which have been estimated as eruption rates for various flows on Alba Patera, Mars (Cattermole, 1986; Baloga et al., 1987)

In this extended study, we have also considered the release of SO<sub>2</sub> from impact melt, since impacts, like volcanism, are episodic in nature. In our calculations we have estimated the effects of SO<sub>2</sub> released by impact melt during the formation of an Argyre-size basin. According to calculations by M.H. Carr (pers. comm.), the formation of an Argyre-size basin by an impactor travelling 10 km/s would eject  $2.68 \times 10^6$  km<sup>3</sup> of melt, if the thermal gradient is ignored. When the thermal gradient is taken into account,  $5.24 \times 10^6$  km<sup>3</sup> of melt is ejected. We assume 1 wt.% of SO<sub>2</sub> is released from the melt.

Given a 1 year atmospheric lifetime of SO<sub>2</sub> (Settle, 1979), and using the above supply rates, we can calculate the steady-state column abundance of SO<sub>2</sub>. For a magma flux of  $5 \times 10^4$  m<sup>3</sup>/s, and a 1 year lifetime, the steady-state column abundance is about  $3.5 \times 10^{-2}$  g/cm<sup>2</sup>. If the magma flux is  $10^6$  m<sup>3</sup>/s, the column abundance of SO<sub>2</sub> is approximately  $6.9 \times 10^{-1}$  g/cm<sup>2</sup>. In the case of impact-released SO<sub>2</sub>, with the thermal gradient taken into account, and assuming the SO<sub>2</sub> is "instantaneously" globally distributed, the column abundance is on the order of  $10^2$  g/cm<sup>2</sup>.

The steady-state column abundance of SO<sub>2</sub> is put into a 1-dimensional radiative-convective model. Because of uncertainties in background conditions, we have run the program for various surface pressures of CO<sub>2</sub>, always assuming that CO<sub>2</sub> makes up 95% of the atmosphere. We assume that SO<sub>2</sub> is globally distributed and well mixed in the atmosphere. Although this may not be strictly correct, it sets a useful limit to the effect.

In the case of volcanically produced SO<sub>2</sub> surface warming of up to +20°K may take place, depending on the magma flux and background conditions, and in the absence of countervailing dust or aerosol effects. Since major basin-forming events could each have

generated up to 100 times the amount of SO<sub>2</sub> released by the largest suspected fissure flow, initial temperature increases would have been substantially greater, but would have dropped steadily as SO<sub>2</sub> continuously disappeared (by whatever mechanism).

Although epochal variations in climate, such as are due to atmospheric CO<sub>2</sub> or astronomical variations, can affect the deep regolith, the thermal skin depth directly affected by episodic SO<sub>2</sub> fluctuations is only 1 - 2 meters. Nonetheless, the effects related to episodic sublimation and melting of available surface ice could be significant. In addition, long term climate changes by CO<sub>2</sub> or astronomical variations provide a "baseline" climate which may be such as to barely allow melting at the equator. If so, repeated superimposed episodic excursions in climate may play an important role in martian weathering and the development of morphological features.

#### References

- Baloga, S.M., D.C. Pieri, J. Plescia, and P. Davis (1987), [Abstract] *Lunar Planet. Sci. Conf. 18th*, 42-43.
- Cattermole, P. (1986), [Abstract] *Lunar Planet. Sci. Conf. 17th*, 105-106.
- Greeley, R. (1987), *Science*, **236**, 1653-1654.
- Settle, M. (1979), *J. Geophysical Res.*, **84**, 8343-8354.

# IMPACT INDUCED DEVOLATILIZATION OF WATER IN SERPENTINE AND METEORITES AND D/H RATIO IN EVOLVING PLANETARY ATMOSPHERES

*James A. Tyburczy, R. V. Krishnamurthy, Samuel Epstein, and Thomas J. Ahrens, c/o Seismological Laboratory 252-21, California Institute of Technology, Pasadena, CA 91125.*

We have continued to carry out impact experiments on both natural serpentine and serpentine in which some of the hydrogen was replaced by deuterium because most of the water contained in carbonaceous chondrites (C1) meteorites is contained in serpentine-like minerals. We are also conducting impact experiments on Murchison meteorite, a primitive carbonaceous chondrite. This serpentine and meteorite material is widely believed to be similar in composition to the planetesimals which accreted to form the planets. Upon impact with the surface of a growing planet, volatiles are released and upon reaction with the metals and sulfides control the oxidation state of the accreting planet (Ringwood, 1979). The gas itself, contributes to the atmosphere of the planet (Earth, Venus, Mars, and Titan) during accretion (Benlow and Meadows, 1977; Arrhenius et al, 1974; Lange and Ahrens, 1982a).

Lange and Ahrens (1982b) pointed out that much of the impact-induced water production takes place in the porous regolith of the accreting planet. The results of such experiments (Lange and Ahrens, 1982b) have been used to calculate the evolution of an early water-rich atmosphere on the earth. Abe and Matsui (1986) and Matsui and Abe (1986a,b) have applied our experimental data to calculate the thermal history of an accreting planet taking into account the evolution of water upon impact devolatilization and its subsequent solution in a water-bearing magma ocean.

We have conducted a series of experiments in which 15 to 50 mg samples of serpentine D-enriched serpentine and Murchison meteorite initially held in  $10^{-3}$  Torr vacuum tight metal container were subjected to shock pressures in the 5.0 to 7.7 GPa range approximately corresponding to planetesimal infall velocity when a silicate planet has a radii in the range ~1000 to 1700 km.

We have been using the gas recovery method (Boslough et al. 1981). These techniques allow passage of impact-induced shock wave into a mineral or meteorite sample which is in turn inside a gas tight recovery chamber. The sample recovery container remains gas tight. After the impact experiment, the recovery chamber is transported to a gas source mass spectrometer laboratory for major element gas analysis.

We discovered that for shock pressures near the point of incipient devolatilization (17 GPa) there is little or no reduction of  $H_2O$  to  $H_2$  in the shock-evolved gases, and the hydrogen isotopic composition of the gas is very close to that of the starting material. For higher shock pressures, where more impact-induced devolatilization occurs (Fig. 1), the bulk evolved gas is significantly lower in deuterium than the starting material and there is a significant reduction of  $H_2O$  to  $H_2$ , caused by reaction of evolved  $H_2O$  with the steel container (Fig. 2). In meteorites, or planetesimals, more vigorous reactions should occur as the metal and sulfide phases are more intimately mixed with the hydrous phases. Upon reaction, we discovered that the evolved water and hydrogen is lighter (containing less deuterium) than the bulk initial material.

For both serpentine and Murchison meteorites the relative amount of D in the gas relative to the solid can be defined by the fractionation factor

$$\alpha \equiv (D/H)_{\text{gas}} / (D/H)_{\text{solid}}$$

This is shown as a function of shock pressure in Fig. 3. Two experiments conducted on a serpentine sample which we purposefully enriched in D to values of  $\delta D_{\text{SMOW}} = +667\text{‰}$ , as compared to  $\delta D_{\text{SMOW}} = -77\text{‰}$ , also shown on even greater decrease in  $\alpha$  than the ordinary serpentine in Fig. 3.

Mass balance consideration thus indicates that as  $\alpha$  decreases the remaining solid (serpentine) is enriched in D. As a planet grows, upon complete impact vaporization of the serpentine, the total gas

evolved should again have the bulk D/H ratio. Thus we conclude that during a portion of the accretion period of a planet, when partial devolatilization occurs, there is enhanced production of D depleted  $H_2$  and  $H_2O$ . We expect that the hydrogen depleted gas will escape by Jean's loss or hydrodynamic escape. Thus, the D/H ratio of the remaining non-volatilized (solid planet) material will increase in this regime and could, by this process, effect D/H ratios of the total planet inventory. In the case of Mars and Venus where the present D/H ratio in the atmosphere is a factor of 6 and 100 greater than earth, or average (bulk carbonaceous chondrite) meteorite values, the following scenario is suggested to occur. During the period of accretion, continued impact release of D-depleted  $H_2$  and  $H_2O$  to the atmosphere occurs. Preferential loss of H and D relative to water due to Jean's escape occurs. Thus, both impact and Jean's loss increase the relative solid planetary inventory of D. If giant impacts occurred late in the accretion history, these may have removed the primordial atmospheres of the terrestrial planets. We account for the present high ratios of D/H on Venus and Mars by initial impact accretion of the solid planets on the basis of post accretional volcanic outgassing of  $H_2O$  which is D rich.

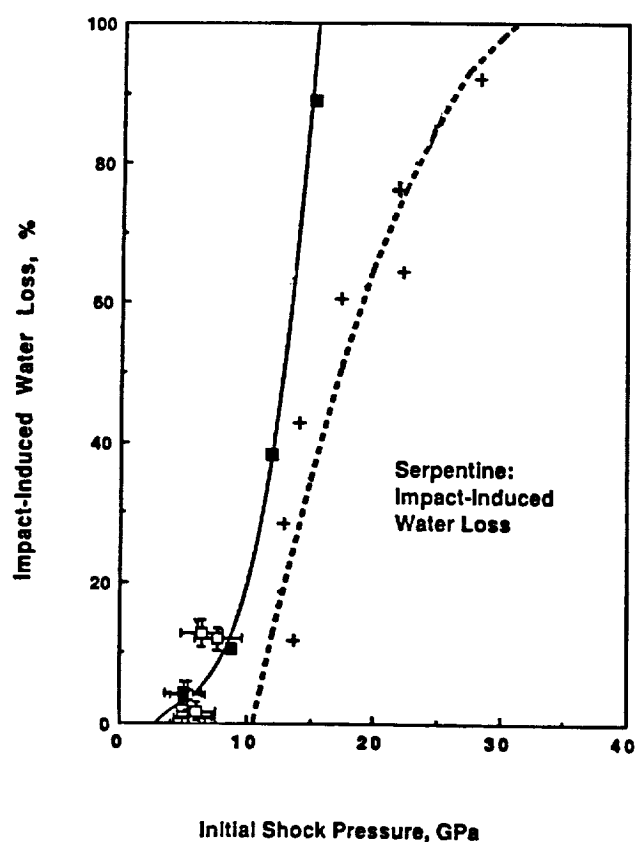


Fig. 1. Impact-induced water loss as a function of initial shock pressure for 20% porous serpentine (this study) and nonporous serpentine. Filled squares, solid recovery method, porous serpentine; open squares, gas recovery method, porous serpentine; crosses, solid recovery method, nonporous serpentine. Solid line empirical fit to data for porous serpentine; dashed line, empirical fit to data for nonporous serpentine.

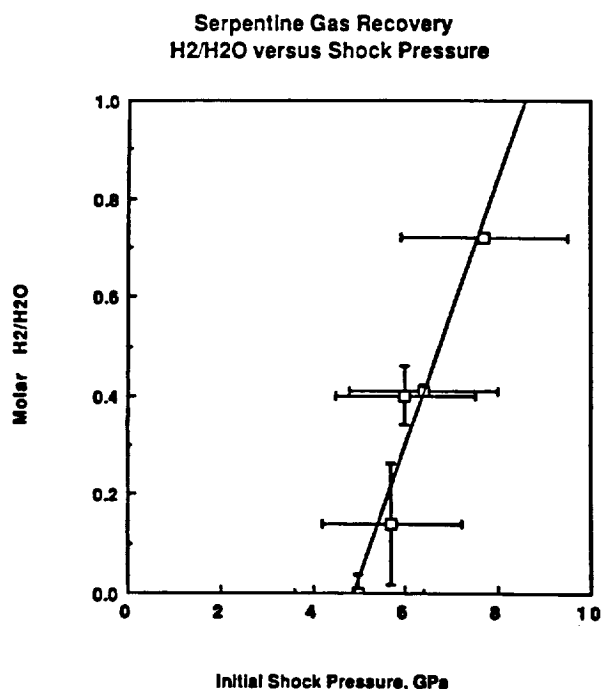


Fig. 2. Background corrected  $H_2/H_2O$  ratio versus initial shock pressure  $P_{initial}$ . Solid line is empirical linear fit to data.



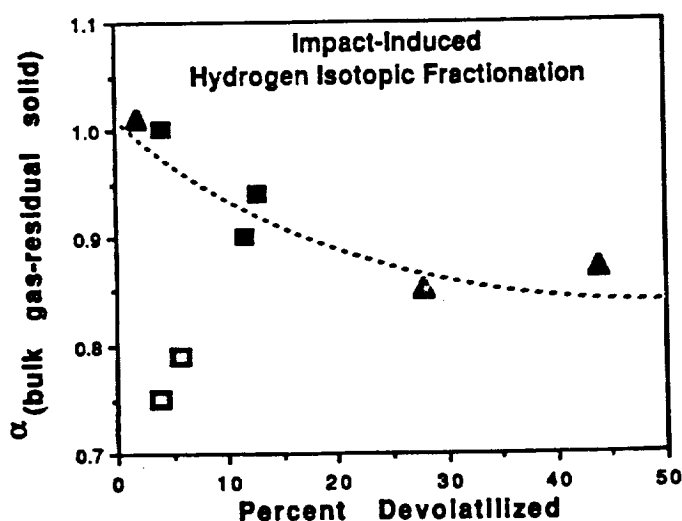


Fig. 3. Bulk gas-residual solid fractionation factor  $\alpha_{\text{bulk gas-residue}}$  versus percent devolatilized. Field triangles, Murchison; filled squares, serpentine; open squares, deuterium-enriched serpentine. Dashed line is polynomial fit to the data.

### References

- Abe, Y., and T. Matsui, Early evolution of the Earth: Accretion, atmosphere formation and thermal history, *Proc. XVII Lunar and Planet. Sci. Conf., I, J. Geophys. Res.*, **91**, E291-E302, 1986.
- Arrhenius, G., B. R. De, and H. Alfven, Origin of the ocean, in: *The Sea*, ed. by E. D. Goldberg, Wiley, New York, , 839-861, 1974.
- Benlow, A., and A. J. Meadows, The formation of the atmospheres of the terrestrial planets by impact, *Astrophys. Space Sci.*, **46**, 293-300, 1977.
- Boslough, M.B., T. J. Ahrens, J. Vizgirda, R. H. Becker, and S. Epstein, Shock-induced devolatilization of calcite, *Earth Planet. Sci. Lett.*, **61**, 166-170, 1982.
- Lange, M. A., and T. J. Ahrens, Impact-induced dehydration of serpentine and the evolution of planetary atmospheres, *Proc. Lunar and Planet. Sci. Conf. XIII, Part 1, J. Geophys. Res., Supplement*, **87**, A451-A456, 1982a.
- Lange, M. A., and T. J. Ahrens, The evolution of an impact-generated atmosphere, *Icarus*, **51**, 96-120, 1982b.
- Matsui, T., and Y. Abe, Evolution of an impact-induced atmosphere and magma ocean on the accreting Earth, *Nature*, **319**, 303, 1986a.
- Matsui, T., and Y. Abe, Impact induced atmospheres and oceans on Earth and Venus, *Nature*, **322**, 526-528, 1986b.

## IMPACT EROSION OF MARS' ATMOSPHERE: AN ANALYTIC MODEL

H. J. Melosh and A. M. Vickery, Lunar and Planetary Laboratory, University of Arizona, Tucson, AZ 85721.

Abundant geomorphic evidence for fluvial processes on the surface of Mars suggests that in the distant past Mars' atmospheric pressure was high enough that liquid water was stable on the surface. Many authors have proposed mechanisms by which Mars could have lost (or sequestered) an earlier, thicker atmosphere, but none of these proposals has gained general acceptance. We examine here the possibility that the vapor plume expanding away from the crater produced by a large, fast projectile may be able to eject a significant portion of the Martian atmosphere. This work follows in the wake of earlier work on atmospheric ejection by ourselves and others (1,2,3).

Although much of our work is based on detailed computer modeling, it is easy to construct a simple analytic model of atmospheric erosion due to impacts that seems to capture most of the essentials of the process. Only a few basic equations are needed if one is willing to overlook uncertainties and subtleties that could change the results by a factors of the order 2. The first essential feature for atmospheric erosion to occur is that the projectile must strike the planet with enough velocity for a vapor plume to form. Not only this, but the plume must expand at a speed faster than the planet's escape velocity,  $v_{esc}$ . A model of vapor plume expansion (4) gives the mean (mass averaged) velocity of expansion as  $[2(E-H_{vap})]^{1/2}$ , where  $E$  is the specific energy of the shocked projectile and target material and  $H_{vap}$  is the vaporization energy, taken here to be 13 MJ/kg for silicates and 3 MJ/kg for ice. The maximum expansion velocity of the gas cloud is approximately a factor 2.8 times faster than this, so use of the mean velocity is a conservative assumption. The specific energy  $E$  is, by the Hugoniot equations, equal to  $u^2/2$ , where  $u$  is the particle velocity behind the shock. The maximum particle velocity  $u$  is  $v/2$ , where  $v$  is the impact velocity, by the planar impact approximation when both target and projectile are nearly the same material, so  $E \approx v^2/8$ . The minimum impact velocity  $v_{min}$  for most of a vapor plume to exceed escape velocity is thus given by

$$v_{min} = \sqrt{8 \left( \frac{v_{esc}^2}{2} + H_{vap} \right)}$$

In the case of Mars  $v_{min}$  is 14.3 km/sec for silicate impactors and 11.1 km/sec for icy impactors. These minima are less than the estimated rms impact velocities (5) with either asteroids (19 km/sec), periodic comets (21 km/sec), or parabolic comets (42 km/sec), so most current Mars impactors are capable of producing vapor plumes that exceed escape velocity. During accretion impact velocities were undoubtedly lower so that at that time Mars could have accumulated its original atmosphere.

The second factor in estimating whether or not an impact can remove the atmosphere is that the mass of vapor from projectile and surrounding vaporized target (if any) must exceed the air mass  $m_{tp}$  above the plane tangent to the impact if the vapor plume is to carry away the atmosphere. This relation is supported by our more detailed numerical studies. Thus, we insist

$$m_* \geq \frac{4 \pi P_0}{g f} H R$$

Where  $m_*$  is the projectile mass just capable of removing the atmosphere above the tangent plane,  $P_0$  is the surface atmospheric pressure,  $g$  is the acceleration of gravity,  $R$  is the radius of the planet, and  $H$  is the atmospheric scale height.  $f$  is a factor that accounts for vapor produced from the target adjacent to the impact,  $f = [1 + (v/v_{min})^{1.6}]$ .  $f$  is always greater than 1. For

Mars, the smallest projectile that can remove the entire air mass above the tangent plane is thus about  $4 \times 10^{13}$  kg, or an object about 3 km in diameter. Note that this relation does not take account of possible enhanced vaporization in oblique impacts--such an angle-dependent phenomenon might reduce  $m_*$  by a factor of perhaps 5.

These results on the mass of the projectile necessary to remove the atmosphere above the tangent plane must be supplemented with information on the flux of projectiles to compute the evolution of atmospheric pressure with time. The cumulative flux (number/sec/m<sup>2</sup>) of projectiles with mass greater than or equal to  $m$  is parameterized by  $N_{cum}(m) = am^{-b}$ , where  $a$  and  $b$  are constants. Unfortunately, neither the over-all flux,  $a$ , nor the slope of the distribution,  $b$ , are well known. Shoemaker (1987 pers. comm.) suggests that for the moon in the post-late-heavy-bombardment era these constants are  $a = 1.26 \times 10^{-21}$  (MKS units) and  $b = -2/3$ . However, use of this distribution in conjunction with the revised Schmidt-Holsapple scaling relation predicts a distribution of lunar craters that falls too steeply with increasing diameter. A better pair of constants that predicts the correct *lunar* crater distribution is  $a = 1.23 \times 10^{-23}$  (MKS),  $b = 0.47$ . The slope of the crater distribution on the Martian plains is the same as the lunar distribution (6), while the overall cratering rate on Mars at present is estimated to be between 1 and 4 times the lunar rate, with a preferred mean of about 2 (5).

Using this cratering rate, the rate of mass loss from a planet's atmosphere  $dM_{atm}/dt$  is given by the flux  $N_{cum}(m_*)$  of projectiles large enough to remove the atmosphere above the tangent plane, times the planet's surface area  $4\pi R^2$ , times the mass above the tangent plane  $m_{tp} = M_{atm}(H/R)$  for  $R \gg H$ . Since  $m_*$  itself depends upon  $M_{atm}$ , a simple differential equation for  $M_{atm}$  (or, equivalently,  $P$ ) results whose solution, converted to a convenient and universal form, is:

$$\frac{M_{atm}(t)}{M_0} = \frac{P(t)}{P_0} = \left(1 - \frac{t}{t_*}\right)^{1/b}$$

Where the  $M_0$  is the present ( $t=0$ ) atmospheric mass,  $P_0$  is the present atmospheric pressure, and  $t_*$  is the length of time required for impacts to reduce the atmospheric pressure to zero. In terms of previously defined quantities,

$$t_* = \frac{1}{2\pi ab(RH)^{1-b}} \left( \frac{4\pi P_0}{fg} \right)^b$$

Note that the above equation for the time dependence of atmospheric mass or pressure can be used for times before the present ( $t < 0$ ), so that the atmospheric pressure at any previous era can also be computed. It is interesting to note that the atmospheric pressure declines rigorously to zero at time  $t_*$ --it does not simply fall exponentially towards zero. This interesting fact (first pointed out to us by K. Zahnle, 1988 pers. comm.) is a unique characteristic of the impact erosion mechanism. As the atmospheric pressure declines, smaller projectiles are capable of removing the atmosphere above the tangent plane. But by the distribution law, there are more smaller projectiles than larger ones, so a greater fraction of the atmosphere is removed in each unit time interval. The net result is the complete stripping of the atmosphere after time  $t_*$ .

The post-late-heavy-bombardment flux, along with other parameters, gives a value  $t_* \approx 10$  to 25 Gyr for Mars at the present time. These values predict an atmospheric pressure at the end of late heavy bombardment (3.8 Gyr) between 1.4 and 2 times the present low pressure. This would just marginally permit liquid water to exist over much of the surface of Mars, but the impact-driven evolution is evidently too slow to effect major changes. It is clear, however, that atmospheric loss would be rapid at the  $> 100$  times greater impact rates characteristic of late

heavy bombardment. We thus conclude that impact erosion of Mars' atmosphere could explain the apparent rapid decline in atmospheric pressure near the end of late heavy bombardment, but has probably not greatly affected the total atmospheric mass since then.

REFERENCES: (1) J. G. C. Walker, *Icarus* 68, 87 (1987). (2) H. J. Melosh and A. M. Vickery, *EOS* 69, 388 (1988). (3) H. G. Watkins, 1983 MIT PhD Thesis. (4) H. J. Melosh, *Impact Cratering*, Oxford (1989). (5) BVSP, *Basaltic Volcanism*, Pergamon (1981). (6) R. G. Strom, in NASA SP-429 (1984).

**THE MARTIAN IMPACT CRATERING RECORD.** R.G. Strom<sup>1</sup>, N.G. Barlow<sup>2</sup>, and S.K. Croft<sup>1</sup> <sup>1</sup>Lunar and Planetary Laboratory, University of Arizona, Tucson, AZ 85721; <sup>2</sup>Lunar and Planetary Institute, 3303 NASA Road One, Houston, TX 77586.

Impact craters occur on most solid objects within the Solar System and allow determination of terrain ages and near surface properties on the host object. Mars displays a distinct hemispheric asymmetry in crater density: 60% of the martian surface is heavily cratered, this percentage is predominately located in the southern hemisphere, the remaining 40% is lightly cratered and concentrated in the northern hemisphere.

Martian craters are different in many ways from their counterparts on Mercury and the Moon. The existence of an atmosphere and the accompanying erosional activity results in a range of degradational states among martian craters (1). The onset diameter of central peak craters is smaller, central peaks are larger, and central pits are more common in martian craters than in the lunar or mercurian counterparts (2,3). Martian crater ejecta is primarily lobate in form, distinctly different from the radial pattern around lunar and mercurian craters (4). Elliptical craters are widely distributed across the planet and have been interpreted as recording a lost swarm of satellites (5). Basin morphology also is different on Mars and effects of the basin on the structure of the surrounding terrain may account for observed variations in crater morphology (6), and the distribution of valley networks.

The transition from simple to complex craters on Mars occurs at diameters between 2.5 and 5.0 km, depending on terrain (7). Photoclinometry has been used to obtain relations between rim diameter and rim height, crater depth, floor diameter, etc., for fresh craters (8). Theoretical models and experimental work indicate that the lobate morphology results either from ejecta entrainment of volatiles during impact into ice-rich surface materials (4,9) or from ejecta curtain interaction with the atmosphere (10).

Crater size-frequency distribution analyses of martian terrain units indicate that heavily cratered regions show a multi-sloped distribution curve whereas lightly cratered regions exhibit curves following a -3 differential slope power law function. Observational evidence and computer simulations argue against saturation being the cause of the observed curve variation for crater diameters  $\geq 8$  km (11,12,13). Obliteration affects the size-frequency distribution curves (14), but the similarity of the martian, lunar, and mercurian highlands curves (15) and the multi-sloped nature of the martian intercrater plains fresh crater distribution curves (16) suggests that distinct production populations are the dominant cause of the different distribution curve slopes. If the cratered surfaces are in production, the origins of the impactors and the ages of the surfaces can be estimated.

The similarity of the crater size-frequency distribution curves on inner Solar System bodies suggests that all have been subjected to the same populations of impacting objects. The distribution curves for the satellites of outer Solar System planets are statistically different from the curves seen in the inner Solar System, indicating different origins of the impacting populations (17). In the inner Solar System, the crater population in the heavily cratered highlands of the Moon, Mercury, and Mars represents the period of late heavy bombardment that ended about 3.8 billion years ago on the Moon. The size/frequency distribution curves for these surfaces are laterally shifted with respect to each other in such a way that higher impact velocities are required at smaller semimajor axes. This is consistent with a population of objects in heliocentric orbits confined to the inner Solar System. The lunar mare and lightly cratered martian plains retain the impact record of asteroids and comets (15), but asteroid impacts were probably more frequent on Mars by a factor of about 7.

Differences in shape and density of the crater size-frequency distribution curves are used to determine relative chronologies for Mars. Martian surface units can be placed into three epochs: heavy bombardment (multi-sloped curve, high density), end of heavy bombardment (multi-sloped curve, intermediate density), and post heavy bombardment (single slope curve, low density). Fifty-two percent of the surface units (concentrated in the southern hemisphere) date from the heavy bombardment period, 8% (primarily ridged plains in the equatorial regions) formed during the end of heavy bombardment, and 40% (most of the northern hemisphere) date from post heavy bombardment (18).

Absolute chronologies can be extrapolated from the relative chronologies by using the lunar absolute age versus crater density relation and by making assumptions about the intensity and temporal dependence of the cratering flux at Mars compared to the Moon. Existing martian absolute chronologies assume a temporal distribution of the cratering flux identical to the smooth curve derived for the Moon---high cratering rates prior to 3.8 BY ago, decaying exponentially since that time (19). The chronologies vary in their estimates of the crater flux intensity, ranging from approximately lunar (19,20) to 20 times the lunar rate (21), with the most likely value being twice the lunar rate (22). Young surface features thus show considerable range in age, with estimates for the youngest feature (Olympus Mons) ranging from 3.3-0.1 BY ago. Estimates used in the computation of these absolute chronologies are still uncertain and arguments for fluctuations in impact flux with time cause even greater uncertainty in deriving the absolute ages of martian surface units using crater analyses.

Impact craters are dominant features across the martian surface and provide a means of obtaining chronologic information which can be used to constrain the geological history and thermal evolution of Mars. In addition, crater morphology provides information on near-surface properties not available through other remote sensing techniques. Finally, information derived from the crater size-frequency distribution curves can place constraints on the origins of the impacting objects.

#### REFERENCES:

- 1) Mutch T.A. et al. (1976) The Geology of Mars.
- 2) Wood C.A., Head J.W., and Cintala M.J. (1978) Proc. LPSC 9th, 3691.
- 3) Hale W.S. and Head J.W. (1981) LPS XII, 386.
- 4) Carr M.H. et al. (1977) JGR, 82, 4055.
- 5) Schultz P.H. and Lutz-Garihan A.B. (1982) Proc. LPSC 13th, A84.
- 6) Awwiller D. and Croft S.K. (1986) submitted to Rpts. of the Planet. Geol. and Geophys. Undergrad. Prog.
- 7) Pike R.J. (1980) Proc. LPSC 11th, 2159.
- 8) Pike R.J. and Davis P.A. (1984) LPS XV, 645.
- 9) Greeley R. et al. (1980) Proc. LPSC 11th, 2075.
- 10) Schultz P.H. and Gault D.E. (1970) JGR, 84, 7669.
- 11) Strom R.G. and Whitaker E.A. (1976) NASA TM X-3364, 194.
- 12) Neukum G. (1985) LPS XVI, 614.
- 13) Woronow A. (1978) Icarus, 34, 76.
- 14) Chapman C.R. and Jones K.L. (1977) Ann. Rev. Earth Planet. Sci., 5, 515.
- 15) Woronow A., Strom R.G., and Gurnis M. (1982) in Satellites of Jupiter, 237.
- 16) Barlow N.G. (1988) LPS XIX, 29.
- 17) Strom R.G. (1987) Icarus, 70, 517.
- 18) Barlow N.G. (1988) Icarus, 75, 285.
- 19) Soderblom L.A. et al. (1974) Icarus, 22, 239.
- 20) Neukum G. and Wise D.U. (1976) Science, 194, 1381.
- 21) Hartmann W.K. (1973) JGR, 74, 4096.
- 22) Neukum G. and Hiller K. (1981) JGR, 86, 3097.

CRATER SATURATION EQUILIBRIUM IN THE SOLAR SYSTEM: NEW  
EVIDENCE

W. K. Hartmann, Planetary Science Institute, Tucson AZ 85719

At the 15th LPSC in 1984, (and Icarus, 60:56-74, 1984) the writer suggested that many planet and satellite surfaces in the solar system have reached a state of crater saturation equilibrium. At this crater density, further impacts make new craters, but old craters are obliterated, especially by giant basins and their ejecta blankets. Ejecta may drop the total crater density below the mean saturation level in parts of the area, at diameters corresponding to depths shallower than the new ejecta. Thus, once saturation equilibrium occurs in the absence of endogenic resurfacing, the crater diameter distribution evolves its D-dependent structure, as well as oscillating around the mean saturation equilibrium value with time.

Attempts to model these effects by numerical simulation have led to controversies about the crater density level corresponding to saturation equilibrium curve in nature. The Voyager team, for example, in interpretations of outer solar system satellite surfaces, denies saturation equilibrium and assumes that all craters ever formed can be counted. Thus they translate structure in diameter distributions directly into structure in impactor populations. This conclusion appears internally inconsistent with their simultaneous conclusion that some of the same satellites have been hit so many times that they have been fragmented and reassembled. How can a satellite such as Mimas be fragmented and reassembled from impactors without attaining a crater-saturated surface, in the absence of any apparent endogenic resurfacing events?

The Icarus paper showed empirically that bodies such as Mimas, Rhea, Callisto, the moon, Phobos, and Deimos all have crater diameter distributions that reach maximum densities within a factor two or three of the curve

$$\log N_{HC} = -1.83 \log D_{km} - 1.33 \quad (1)$$

where  $N_{HC}$  = incremental no. craters/km<sup>2</sup> in log<sub>2</sub> diameter bins and D = crater diameter (km). It was noted that crater counts on lunar maria permit a test of these ideas. They show three well-known segments, illustrated with data from Mare Cognitum in Figure 1. Segment A at  $D \geq 4$  km is attributed to primary impact. Segment B,  $250 \text{ m} \leq D \leq 4 \text{ km}$ , is more steeply sloped and is generally attributed to dominance of secondary ejecta. The important segment in this discussion is segment C, at  $D \leq 250\text{m}$ , which rolls over to shallower slope. Segment D is the crater density in heavily cratered areas, i.e. equation (1). The important point is that segment C appears to flatten near the level of equation (1) consistent with the hypothesis that crater densities in nature do not exceed (1) because

saturation sets in at that point. At the time of the 1984 work, I had mare crater counts only down to  $D \sim 62$  m, not small enough to test whether the flattening really persisted to small  $D$  near equation (1). I proposed that a test of the saturation equilibrium hypothesis would be to see if the flattening (segment C) persists to small sizes, and in particular to see if it falls near equation (1), the putative empirical saturation equilibrium level.

Although some other counts of small lunar craters have been published, it is important in these tests to use a homogeneous data set by one author, since different authors and different techniques (such as stereo viewing by some authors) may lead to different detection limits in heavily cratered terrain where rolling depressions may be seen as craters by some authors but not others (see Lissauer, Squyres, and Hartmann, these abstracts). For these reasons I have begun some new counts of small craters on lunar high resolution photos; these are added to my older counts obtained by the same methods during the last 22 years.

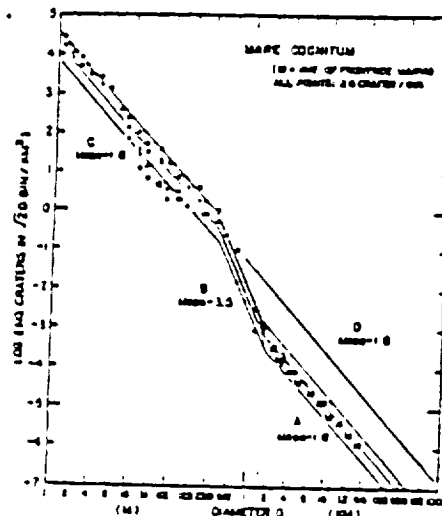


Fig. 1. Diameter distribution of craters in Mare Cognitum down to 1 m diameter.

The small craters relate to the question of saturation equilibrium through the pioneering work of Shoemaker (1966 Ranger VIII and IX reports, JPL Tech. Rep. 32-800; 1968 Surveyor Final Report, JPL Tech. Rep. 32-1265) and Gault (1970, Radio Science 5:273-291). They pointed out clearly that the formation of the mare regolith to depths of the order of tens of meters implied saturation cratering up to diameters sufficient to pulverize lavas to that depth. Indeed, Gault (Fig. 4) drew not only empirical but theoretical curves showing the rollover from segments B to C due to the saturation effect. In other words, they showed that segment C must fall along a saturation equilibrium line.

Figure 1 includes my new results on the position of segment C. Crater diameter distributions have been extended down to  $D = 1$  m by combining lunar Orbiter photos with older Ranger impactor photos. Two important conclusions are drawn. (1) The craters at small  $D$  do not continue upward along the steep segment B slope, but flatten to

ORIGINAL PAGE IS  
OF POOR QUALITY



a shallower slope along segment C. (2) Segment C falls roughly along the extension of segment D, i.e. near equation (1), which I previously identified as a hypothetical saturation equilibrium level. These results confirm Gault's. His results deserve further attention in the context of studies of heavily cratered surfaces, such as outer planet satellites.

I conclude that this supports the hypothesis that equation (1) lies close to an empirical saturation equilibrium level.

Further investigations of the behavior of curves in intensely cratered areas thus appear warranted, in view of their effect on Voyager and other interpretations, though present study has been retarded due to funding cutbacks. This work is supported through the NASA Planetary Geology and Geophysics Program.

The wide variety of styles of ejecta emplacement around impact craters on Mars may hold important clues for the subsurface. More likely—and equally important—this variety may reflect the relative roles of a wide range of impactor, target, and environmental factors. Most studies have emphasized the possible role of buried, unbound water owing to the fluid-like emplacement style (1, 2, 3). The present study reviews the broader set of variables in order to: explore the range of values expected on Mars; examine the processes controlled by each variable as revealed in the laboratory or by theoretical considerations; and constrain (if not test) the derived predictions in the cratering record. **Controlling Variables:** Three sets of variables encompass the factors affecting the style of ejecta emplacement: impactor, target, and environment. *Impactor* variables include velocity, size, angle, and composition. Impact velocity (and composition) controls the amount of vaporization and melting (4, 5). Equally important, however, the combination of impactor velocity and size controls the total kinetic energy within the vaporized fraction and contributes the over-all scale of the event. Impact vaporization affects early-time coupling with the atmosphere, but experiments indicate that impact angle also plays a pivotal role: not only in the amount of vaporization but also in the degree of coupling with the atmosphere due to containment within the early-time cavity (5). At high velocities ( $>30$  km/s), impactor composition becomes less important. If, however, impacts on Mars are dominated by low-velocity (6–12 km/s) objects derived from the asteroid belt, then not only is the amount of vaporization reduced but also the interior morphology of the crater may be different (6).

Principal *target* variables include composition, ejecta size distribution, and presence of water or water-ice. Composition refers to the distinction between crystalline and sedimentary targets (even without unbound water) that on the earth appears to affect the fate, if not production of impact melt (7). The distribution of ejecta sizes can be shown to be one of the primary controlling variables due to the effect of air drag (8, 9). Even under the presently low atmospheric densities on Mars, sand-size ejecta can be decelerated to terminal velocities provided that the crater is large enough (large ejection velocities). While there is ample and convincing evidence for water shaping many martian landforms in the past, this may be only one of many variables affecting ejecta emplacement.

Gravity and atmospheric pressure (density) are the primary pre-impact *environmental* variables. Gravity limits the growth of craters formed in particulate substrates and craters larger than a certain size (about 0.5 km on Mars) formed in competent substrates. In the absence of an atmosphere, gravity-limited growth necessarily implies that the distribution of ejecta follows a similar power-law decay with distance from the rim and increases in absolute thickness as  $(gR_p)^{1/2}$  (8, 10, 11). This geometric similarity further requires that undecelerated ballistic ejecta on Mars must have velocities 0.65 and 1.6 times those on the Earth and Moon, respectively, in order to arrive at the same scaled range (e.g., 2 crater radii). For the same size ejecta, the effect of secondary cratering should be in the same proportion. In the presence of an atmosphere, the outward-moving ejecta curtain creates a characteristic airflow (12) affecting ejecta decelerated by air drag to terminal velocities. Air drag directly scales with atmospheric density and crater diameter but inversely with gravity and ejecta size. This process controls not only the ballistic range but the fraction entrained in impact-generated airflow (i.e., wind), which scales directly with the square root of gravity and crater diameter. Laboratory experiments also reveal that increased entrainment results in a systematic increase in complexity of the ejecta deposits (13, 14): ballistic (no entrainment); to contiguous rampart; to rampart and flow lobe morphology; to multiple flow lobes; and finally to radially scoured ejecta.

The atmosphere also plays two additional important roles. First, aerodynamic forces atomize ballistic water if the ejection velocity (i.e., crater size) is sufficiently large. On Mars, these velocities become high enough at late stage for craters larger than about 2 km. Second, the finite scale height of the atmosphere limits the role of air drag affecting the continuous ejecta to crater diameters generally smaller than four crater diameters (i.e., about 50 km). While the atmosphere plays an increasing role for ejecta emplacement around craters larger than about 0.5 km (sufficiently large velocities but small ejecta), such effects decrease for craters larger than about 50 km under current atmospheric conditions due to the fine atmospheric scale height.

**Implications for Mars:** Not only does a wide variety of factors affect the style of ejecta emplacement but also different processes can affect different elements in the ejecta sequence. Crater ejecta facies can be divided into three zones: A near-rim zone within about one crater radius (Zone I); the more distant continuous ejecta deposits between 1R and 3R (Zone II); and distal ejecta region including the discontinuous ejecta and secondaries beyond about 3R (Zone III). The following summary progresses in reverse order.

The presence of easily released volatiles in the target (carbonates) has been observed in the laboratory to produce a broad, radially scoured Zone III. On Mars, the best preserved craters formed at high latitudes exhibit a scour zone extending up to 10 crater radii from the rim; some examples also have a faint distal lobe at the outer boundary (5). Older craters in the same unit at the same latitude erode in a common pattern producing an outward-facing ejecta scarp. This distinctive style of emplacement and erosion may indicate a volatile-rich (not necessarily unbound water) unconformable surface layer (5). While secondary impacts surround lunar craters larger than about 25 km in Zone III, secondaries are absent around many martian craters (15). Such examples may indicate either a fine-grained or a water-saturated target where ballistic trajectories have been changed to non-ballistic, ejecta flows expressed in Zone II.

The variety of ejecta emplacement styles in Zone II reflects a combination of target, impactor, and atmospheric conditions that can change with location and time. Zone II ejecta facies result from two styles of emplacement: direct emplacement controlled by airflow patterns modifying the ballistic ejecta curtain; and non-ballistic flow resembling a gravity-driven basal surge evolving from thermally and gas-lofted debris. In general, ejecta mobility in Zone II should increase with increasing atmospheric density and volatile content while decreasing with increasing *in-situ* grain size. Volatile content primarily affects mobility by the degree of entrainment and comminution, rather than directly lubricating the flow. Attempts to isolate the atmosphere from substrate effects by using elevation alone have not been totally successful since the possible range (less than a factor of 5) in atmospheric density at any given time can be far outweighed by other variables.

Ejecta facies in Zone I reflect modifying processes related to emplacement of ejecta in Zone II and post-emplacement flow. The extent of the inner ejecta lobe (15, 16) may provide the best indicator of post-emplacement mobility due to lubricating trapped water and may account for systematic, terrain-dependent differences.

With this perspective, different styles of emplacement and different degrees of inferred ejecta mobility need not indicate buried, unbound water. Contrasting erosional states of surfaces post-dating the period of heavy bombardment and the evidence for widespread debris mantles (17, 18) indicate that atmospherically transported material has played an important role on Mars to significant depths, particularly in regions poleward of 45° in recent time. Such surface/subsurface materials over broad regions already have been pre-sorted to sizes characterizing concurrent aeolian transport; hence, aerodynamic effects on ejecta emplacement will be important. Conversely, the style of post-impact erosion of ejecta facies provides a sensitive indicator of size distribution. This approach reveals that contiguous ejecta ramparts are relatively stable over time, whereas ejecta flow lobes are particularly vulnerable to erosion. Contiguous ramparts, therefore, are believed to indicate ejecta dominated by coarse debris mixed with fine ejecta, whereas ejecta flow lobes are dominated by fine debris vulnerable to present aeolian erosion. Hence, a dependence between latitude and mobility of Zone II ejecta may not be a unique indicator of subsurface water but simply reflect the importance of pole-controlled airfall deposits. The specific morphology of Zone I ejecta may be the more relevant diagnostic indicator of subsurface water. While most studies emphasize broad statistical similarities among craters, it is important to recognize that dramatically different ejecta morphologies exist on Mars within 100 km (the same lithology, latitude, and elevation). Changes in both volatile content or atmospheric pressure (factor of 5–10) must be invoked to account for such occurrences.

- References:** (1) Carr, M.H. *et al.* (1977) *J. Geophys. Res.* 82, 4055–4065. (2) Greeley, R., Fink, J., Gault, D.E., Snyder, D.B., Guest, J.E. and Schultz, P.H. (1980) *Proc. Lunar Planet. Sci. Conf.* 11th, 2075–2097, LPI, Houston. (3) Horner, V.M. and Barlow, N.G. (1988) *Lunar and Planet. Sci.* XIX, 505–506, LPI, Houston. (4) Ahrens, T.J. and O'Keefe, J.D. (1977) in *Impact and Explosion Cratering* (D. Roddy, R.O. Pepin, R.B. Merrill, eds.), 639–656, Pergamon, N.Y. (5) Schultz, P.H. (1988) *Lunar and Planet. Sci.* XIX, 1039–1040, LPI, Houston. (6) Schultz, P.H. (1988) *Mercury*, U. Arizona Press (in press). (7) Kieffer, S.W. and Simonds, C.H. (1980) *Rev. Geophys. Space Phys.* 18, 143–181. (8) Schultz, P.H. and Gault, D.E. (1979) *J. Geophys. Res.* 84, 7669–7687. (9) Tauber, M.E. and Kirk, D.B. (1976) *Icarus* 28, 351–357. (10) Post, R.L. (1974). Rep. AFWL-TR-74-51, Air Force Weapons Lab, Kirtland AFB, N.M. (11) Housen, K.R., Schmidt, R.M. and Holsapple, K.A. (1983) *J. Geophys. Res.* 88, 2485–2499. (12) Schultz, P.H. and Gault, D.E. (1982) in *Geol. Soc. Amer. Sp. Paper* 190 (L. Silver and P.H. Schultz, eds), 153–174. (13) Schultz, P.H. (1986) *MECA Symposium on Mars: Evolution of its Climate and Atmosphere* (abstract), 95–97, LPI, Houston. (14) Schultz, P.H. and Gault, D.E. (1984) *Lunar and Planet. Sci.* XV (abstract), 732–733, LPI, Houston. (15) Schultz, P.H. and Singer, J. (1980) *Proc. Lunar Planet. Sci.* XI, 2243–2259. (16) Horner, V.M. and Greeley, R. (1987) *Proc. Lunar Planet. Sci.* XVII, E561–E569. (17) Grizzaffi, P. and Schultz, P.H. (1987). Isidis Basin: Site of a volatile-rich debris layer. *Icarus* (in press). (18) Grant, J.A. and Schultz, P.H. (1988) *Lunar and Planet. Sci.* XIX, 411–412, LPI, Houston.

# CRATER SCALING, CALCULATIONS WITH VARIABLE GRAVITY, AND CRUSTAL STRENGTH

*John D. O'Keefe and Thomas J. Ahrens, Seismological Laboratory 252-21, California Institute of Technology, Pasadena, CA 91125.*

In order to examine the impact scaling relation for the maximum depths of projectile penetration of excavation and impact volatilization as well as the evolution of impact crater geometry we have been examining crater flows over a wide range of gravity,  $g_e$ , and crustal strength,  $Y$ . Here  $U$  is projectile velocity.

We show in Fig. 1 how consistently our present calculations scale over a gravity range of 1 to  $10^6 g_e$  from zero strength to very high values in the context of the three regimes (early, intermediate and late times) proposed by Holsapple and Schmidt (1987).

Fig. 1 is unique because it shows that the transition from simple to complex (e.g. multiring) crater occurs at the onset of the late time regime. This can occur immediately after the early time regime, e.g. no strength and  $10^6 g_e$ , or at later times (e.g.  $10^4 g_e$  and 0.3 kb strength). Because of gravity scaling, the curve for  $10^6 g_e$  and  $a=5$  m radius projectile, is equivalent to  $a=5000$  km radius, and impact at  $1 g_e$ . The coupling parameter,  $\mu$ , for a crater depth,  $D$ , is given as

$$D = k a \left( \frac{U t}{a} \right)^{\mu/(1+\mu)} \quad (1)$$

Here  $k$  is an empirical constant. If  $S = 0.38$ , the slope in the  $\log(D/a) - \log(Ut/a)$  plane in the intermediate regime, then

$$\mu = S / (1-S) = 0.58.$$

If we just examine the effect of size at fixed gravity and impact velocity, it appears that rebound occurs early ( $Ut/a = 4.0$ ) for impactors with a radius of 50 km (small diamond symbols) whereas for 500 m radius impactors rebound occurs much later ( $Ut/a = 50$ ). The effect of differing rebounds observed upon varying the crustal strength,  $Y$ , is demonstrated in the plot of normalized crater depth,  $D$ , versus normalized time of Fig. 2. In Fig. 3 we summarize the calculational results for varying strength, gravity, and velocity for impacts at speeds of 12 km/sec or less where impact vaporization does not affect penetration depth,  $D$ . In the left side of the figure the maximum depth of penetration is independent of  $g$  for a given strength and impact velocity. As gravity or radius of the impactor increases, or impact velocity decreases, the final crater will lie along the line specified by:

$$D/a = K_g (ga/U^2)^{-0.22} \quad (2)$$

Here  $-0.22 = -\alpha/3$  in the notation of Holsapple and Schmidt. Thus Fig. 3 demonstrates the transition between strength and gravity controlled cratering. Strength dependent scaling from our calculations gives

$$D/a = K_s (Y/\rho U^2)^{-0.185} \quad (3)$$

Taking the ratios of Eqs. 2 to 3 yield for the normalized transition diameter

$$D_T = (K_g/K_s)^{3/\alpha} Y/\rho g \quad (4)$$

using the relation,  $\alpha = 3\mu / (2+\mu)$  and  $\beta = 3\alpha/(3-\alpha)$ .

For viscosity,  $\eta$ , crater scaling

$$D/a = K_v (\eta/\rho U a)^{-\gamma/3} \quad (5)$$

where  $\gamma = 3\mu/(1-\mu)$  and  $K_V$  is a constant. Then the transition diameter between viscosity and strength scaling Eqs. (3 and 5) is

$$K_T = K_V (K_g/K_V)^{(\alpha+3/\alpha+\gamma)} g^{-\left(\frac{\alpha}{\alpha+\gamma}\right)\left(\frac{\gamma+3}{3}\right)}$$

$$= K'_V g^{-1/3} \quad (6)$$

Thus we find that the transition diameter for simple to complex craters for the terrestrial planets from Eq. (4), assuming a constant value of  $Y$  and  $\rho$ , goes as  $1/g$  (Fig. 4). In the case of the icy satellites, the transition diameter varies between  $g^{-1}$  and  $g^{-1/3}$  (Fig. 4), the latter is for the purely viscous case (Eq. 6).

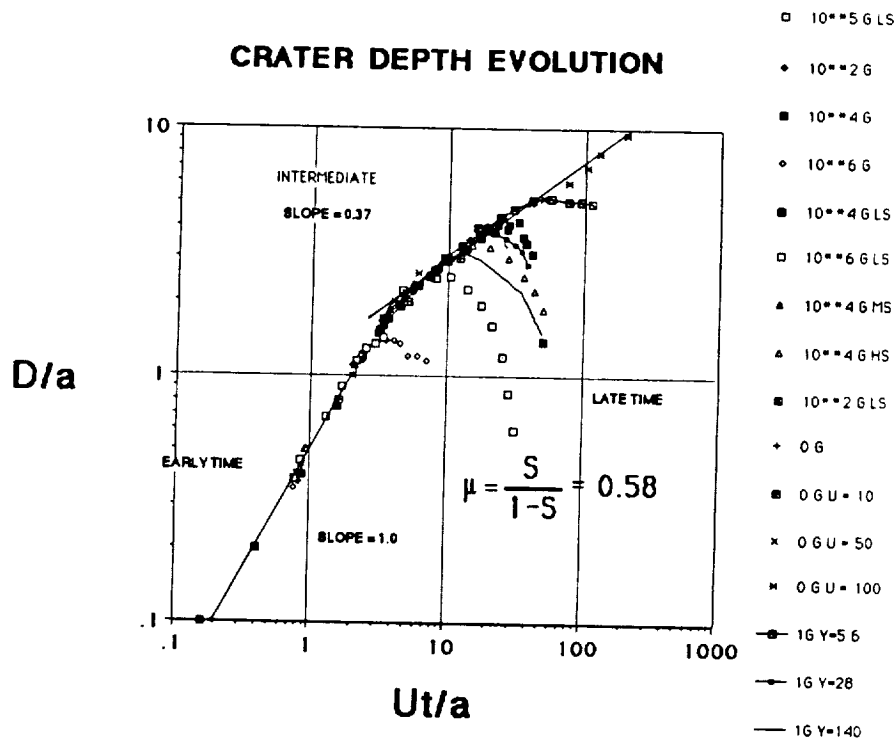


Fig. 1. Crater penetration depth,  $D$ , normalized by projectile radius,  $a$ , versus, normalized time for various gravities,  $g$ , relative to the earth and different crustal strengths,  $Y$ . Early (slope = 1), intermediate (slope,  $S = 0.37$ ), and late time regimes indicated. Trajectories for different gravities for 5 m radius, 12 km/sec silicate impactors are indicated. Three calculations at zero gravity for impacts at 10, 50, and 100 km/sec are from Holsapple and Schmidt (1987). HS and LS indicate crustal strengths of 0.3 and 3 kbar.

#### References:

- Holsapple, K. A., and R. M. Schmidt, Point-source solutions and coupling parameters in cratering mechanics, *J. Geophys. Res.*, **92**, 6350-6376, 1987.
- Schenk, P. M., Simple-to-complex crater transition diameters on the icy satellites of Uranus and Saturn, *Abstract, Lunar and Planetary Science XIX*, 1027-28, 1988.

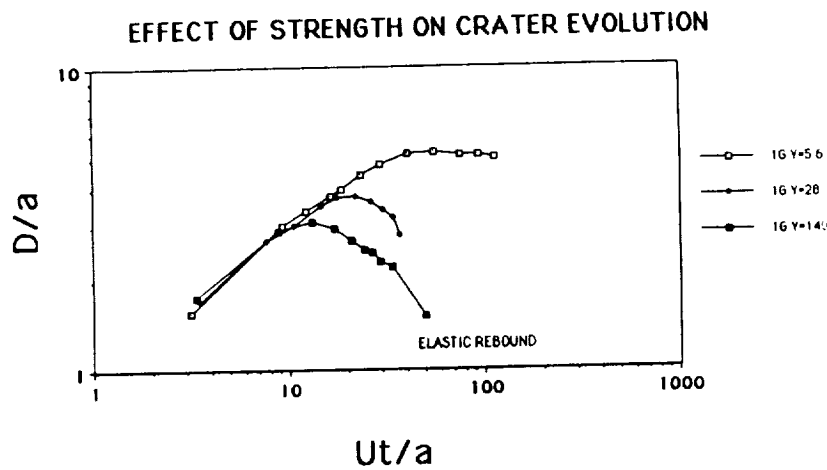


Fig. 2. Normalized crater penetration depth,  $D/a$ , versus normalized time for 12 km/sec impact of 5 m radius projectile, earth gravity and crustal strengths,  $Y$ , of 5.6, 28, and 140 kbar.

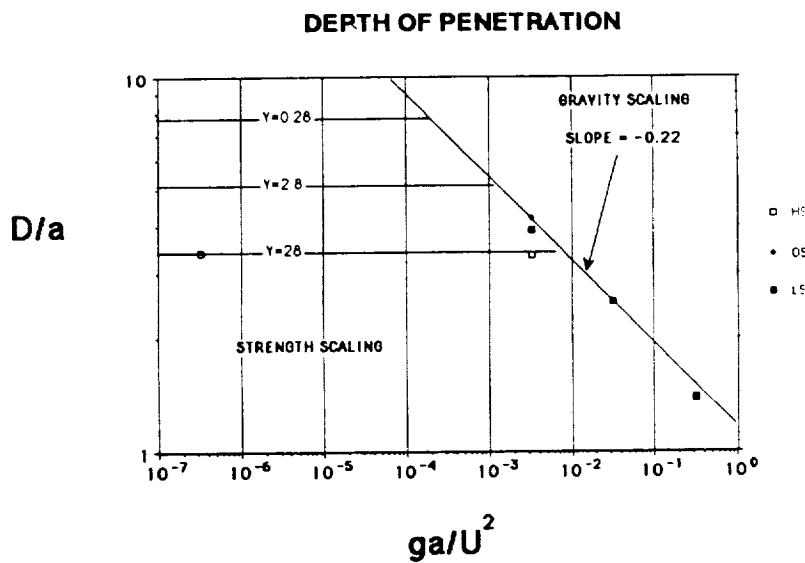


Fig. 3. Normalized crater penetration depth versus gravity scaling parameter showing regimes for strength and gravity scaling. Same abbreviations as in Fig. 1.

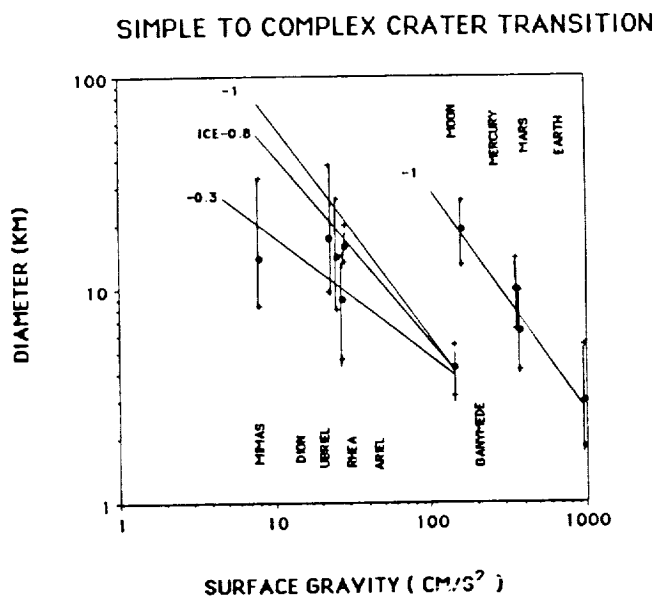


Fig. 4. Simple to complex crater transition diameter versus planetary gravity for terrestrial planets and icy satellites (modified from Schenk, 1988).

MULTI-RING BASINS ON MARS: GEOLOGY, STRUCTURE, AND STATISTICS. *Richard A. Schultz and Herbert V. Frey, NASA Goddard Space Flight Center, Greenbelt, MD 20771.*

Multi-ring basins define the fundamental tectonic framework upon which subsequent geologic and geophysical processes of many planets and satellites are superimposed. For example, most volcanic and tectonic activity on the Moon was localized by pre-existing impact basins [1]. Control of volcanism, tectonics, erosion, and perhaps even volatile dynamics on Mars by multi-ring basins can be discerned in many areas [2] even though endogenic processes were quite vigorous over the planet's history. On the other hand, the family of impacting objects that produced these impact basins probably is related to planetary accretion [3], and size-frequency characteristics of impactor populations can be estimated given an accurate inventory of impact craters and basins [4]. Thus the record of large impact structures on Mars provides a fundamental link between the planet's accretion and its later development.

We have compiled and evaluated available data on large martian impact basins [5] using the new 1:15 million scale geologic maps of Mars [6] and revised global topography [7] as base maps. Published center coordinates and ring diameters of martian basins were plotted by computer and superimposed onto the base maps. In many cases we had to adjust basin centers or ring diameters or both to achieve a better fit to the revised maps. We also found that additional basins can explain subcircular topographic lows as well as map patterns of old Noachian materials, volcanic plains units, and channels in the Tharsis region [8].

Smaller impact basins on Mars such as Ladon ( $D = 975$  km) are comparable dimensionally, morphologically, and structurally to Orientale ( $D = 930$  km) on the Moon. Additional concentric patterns of channels and structures can be developed around such basins in volcanically or tectonically active regions. In contrast, larger basins such as Isidis, Argyre, and Hellas typically show a rugged, blocky annulus with concentric grabens surrounding a central depression. Still larger structures show either multiple rings reminiscent of Valhalla on Callisto (Chryse) or persistent depressions surrounded by poorly expressed concentric structure (Elysium [9], Utopia [10]). Orientale-type morphology can be recognized only for martian basins smaller than Argyre ( $D = 1850$  km).

R-plots of basin diameters show that the martian multi-ring basin population dovetails into the smaller crater population [11] near 500 km diameter. Relative abundance of basins  $>1000$  km diameter is comparable on Mars and the Moon, perhaps suggesting an inner solar system source for the larger impactors [e.g., [4]]. R-plots normalized to a  $D^{-2}$  production function (instead of  $D^{-3}$ ) and least squares fit to cumulative frequency data both indicate that basins follow a shallow production function. Basins 500 to 1500 km show the characteristic Orientale morphology and a best-fit slope of  $D^{-0.8}$ . Basins larger than Argyre define a  $D^{-1.9}$  slope.

These results suggest a transition in basin morphology or structure and steepening of cumulative-frequency slope between 1500 and 1850 km diameter. Morphologic changes might reflect interactions of large impacts with relatively thin lithosphere [12] or spherical target geometry [13]. Thus, Orientale morphology may not scale linearly to the largest diameters on Mars. The cause of the slope change is not yet clear. Formation of large multi-ring basins on early Mars may be more analogous mechanically to impacts on icy satellites (e.g., [12]) than to late forming lunar basins.

REFERENCES: [1] Solomon & Head (1980) *Rev. Geophys.*, 18, 107-141. [2] Schultz, Schultz, & Rogers (1982) *JGR*, 87, 9803-9820. [3] Wetherill (1977) *Proc. Lunar Sci. Conf.*, 8th, 1-16; Wetherill (1981) in *Multi-ring Basins*, *Proc. Lunar Planet. Sci.* 12A, 1-18. [4] Strom (1987) *Icarus*, 70, 517-535. [5] R. Schultz & Frey (1989) *JGR*, in prep. [6] Scott & Tanaka (1986) USGS Map I-1802-A; Greeley & Guest (1987) USGS Map I-1802-B; Tanaka & Scott (1987) USGS Map I-1802-C. [7] Wu et al. (1986) *PGPI-1985*, NASA TM-88383, 614-617. [8] Frey & Schultz (1989) 4th Mars Conf., 106-107. [9] P. Schultz (1984) *Lunar Planet. Sci.*, XV, 728-729. [10] McGill (1989) *JGR*, 94, 2753-2759. [11] Barlow (1988) *Icarus*, 75, 285-305. [12] McKinnon & Melosh (1980) *Icarus*, 44, 454-471. [13] Thomas & Squyres (1988) *JGR*, 93, 14,919-14,932.



An important observation to be explained by any successful theory of the origin of the martian crustal dichotomy is the topographic dichotomy; i.e., much (but not all) of the northern hemisphere lies several km below the majority of the southern hemisphere. The actual topography of Mars is, however, not as simple as the above statement might appear to suggest. The northern hemisphere topography is complex, with several km of variability superimposed on the overall "lowness" of the north. Prominent in this variation is the highstanding region which includes the Elysium volcanic complex, and the relic cratered terrain immediately to the east. These characteristics alone make the origin of the northern lowlands by a single giant impact (1) unlikely. An alternative model, that the crustal dichotomy was the result of overlapping large impact basins (2,3,4) is more successful in explaining the observed topography and its variations.

We describe a model for the origin of the northern lowlands in eastern Mars and their relation to the overlap of two large impact basins. Schultz (5) and McGill (6) have suggested an Elysium Basin and a Utopia Basin, respectively, which together dominate the topography of the northern plains. Our own independent assessment of large impact basins on Mars (3,4) supports the existence of these two impact basins, but we disagree with McGill (6) on the choice of diameter for the Utopia Basin. Using the smaller lunar Orientale Basin as a model, we suggest that the diameter of the Utopia Basin is about 4750 km, with the rim lying along part of the highland/lowland boundary between 240 and 290° W. The rim of the Elysium Basin ( $D = 4970$  km) lies along this same boundary from 180 to 240° W; together these two better mark the highland/lowland boundary (3,4) than does the Borealis Basin (1).

Figure 1 shows these two basins in a rectangular, equal area projection centered on the Utopia Basin. Note the large amount of overlap between the two largest basins; it is in this region of overlap that the central volcanoes of Elysium and the youngest, Amazonian age Elysium volcanic flows (7) lie. This is one of the highest areas within the northern lowland plains (8); explaining this highstanding volcanic complex is important for any model of the origin of the northern lowlands. Due east and due west of the elevated region, the lowlands drop to -3 km where the Arcadia Basin and the Utopia Basin overlap the Elysium Basin (Figure 1). Our model provides at least a qualitative explanation for these highs and lows, and also explains why the rim portions of the Utopia and Elysium Basins lie several km below much of the southern hemisphere.

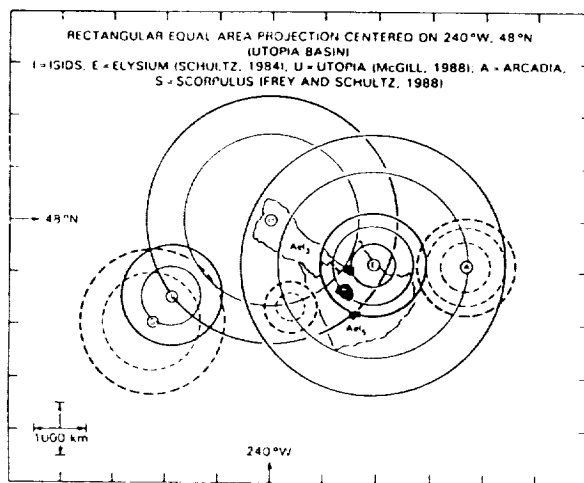
The model is illustrated in Figure 2 with one important geometrical aspect not shown: impact basins with  $D \approx 5000$  km stretch for nearly one quarter the circumference of Mars. In the interest of simplicity we have ignored the curvature of the martian surface (A); this may be important for quantitative models of long-term thermal and mechanical evolution of overlapping impact basins of this size.

The first major event in the region was the impact that produced the Elysium Basin (B). Because no viable scaling relations from an Orientale-size impact to the size of the Elysium Basin exist, we have not included a vertical scale. Perhaps the original basin was 10 km deep; whatever the true depth, Figure 2 has great vertical exaggeration in order to show the subsequent evolution. In addition to forming a large and deep basin, the impact also badly fractures the lithosphere to great depth and deposits a great deal of heat (horizontal bars) (9). Again the lack of scaling relations (especially for energy partition) prevents us from being more quantitative. Over time the basin topography will even out (C) due to viscous relaxation (10). In an earlier, hotter Mars, volcanism will probably accompany the uplift. The Utopia Basin impact (D) occurs sometime later, significantly altering the original Elysium Basin

structure on its western side (Figures 1, 2D), again fracturing the lithosphere and depositing heat (vertical bars). In the overlap region between the two basins these effects are multiplied and the lithosphere becomes weakest and hottest. This weakened region will later become the site of the prolonged Elysium volcanism.

Volcanic flooding of the combined basins will continue (E), but volcanism will likely become concentrated in the overlap region where the weakened lithosphere is most easily penetrated (F). Loading of the basin by volcanics, combined with thermal subsidence as the impact-deposited heat is lost (9), will reverse the relaxation of the basin, leading to subsidence and perhaps significant downwarping over even larger areas. In this way the basin rim areas may also be lowered such that they ultimately lie below the original pre-impact surface level (G). Over time the basin-volcanics decline, subsidence slows, but construction of Elysium continues (H) due to prolonged, enhanced volcanism in the overlap region between the basins, finally producing the central volcanic constructs which lie there.

FIGURE 1



REFERENCES (1)Wilhelms, D.C. and S.W. Squyres (1984) *Nature* 309, 138-140. (2)Frey, H. and R.A. Schultz (1988) *GRL* 15,229-232. (3)Frey, H. and R.A. Schultz (1988) *MEVTV Workshop: Early Tectonics: Volcanic Evolution of Mars*, 21-23. (4)Frey, H. and R.A. Schultz (1989) 4th International Conference on Mars, 106-107. (5)Schultz, P.H. (1984) *Lunar Planet. Sci.* XV, 728-729. (6)McGill, G.E. (1988) *Lunar Planet. Sci.* XIX, 752-753. (7)Greely, R. and J.E. Guest (1987) *Geol. Map of Eastern Equatorial Region of Mars*, MISM Atlas of Mars, Map I-1502B. (8)Wu, S.S.C., R. Jordan and F.J. Schafer (1986) *Reports Planetary Geol. Geophys. Prog.* 1985, NASA Tech. Memo TM 86383, 614-617. (9)Rat, S.R., S.C. Solomon and J.W. Head (1985) *JGR* 90, 12415-12433. (10)Solomon, S.C., R.P. Comer and J.W. Head (1982) *ET*, 3975-3992.

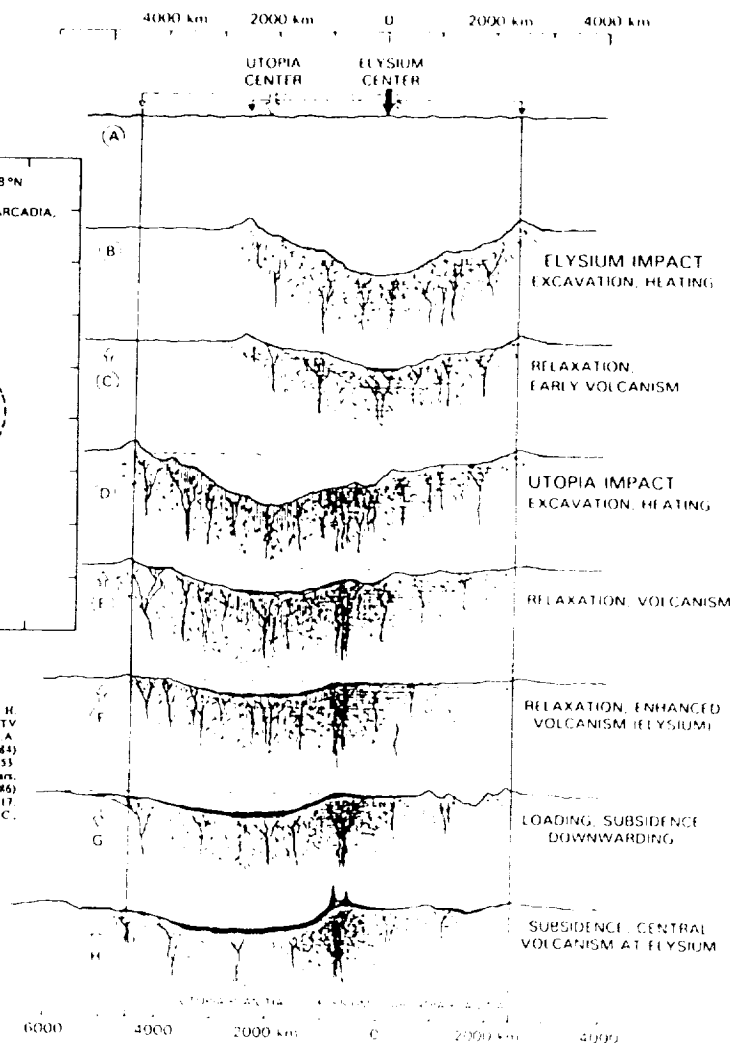


FIGURE 2. Model for origin of northern lowlands on Mars.

ORIGINAL PAGE IS  
OF POOR QUALITY

**THE CRATERING RECORD OF GANYMEDE AND CALLISTO: EVIDENCE FOR THE CHARACTER OF THE CRATER-FORMING IMPACTOR POPULATIONS** Scott L. Murchie and James W. Head, *Dept. of Geological Sciences, Brown University, Providence, RI*; Jeffrey B. Plescia, *National Aeronautics and Space Administration, Washington, D.C.*

**Introduction.** Impact craters observed on the surfaces of Ganymede and Callisto [1,2] were formed by bombardment of these satellites by some mixture of heliocentric impactors in solar orbit and planetocentric impactors in Jovian orbit. The relative importance of the two impactor populations is a controversial question [e.g. 3,4,5,6,7,8] with important implications for the use of crater densities as age measures of Ganymede and Callisto surfaces. For example, planetocentric impactors would bombard all longitudes approximately equally on either satellite; heliocentric impactors would bombard the leading hemispheres more heavily, producing a ratio of the cratering rate at the leading edge to that at the trailing edge ( $\delta$ ) in the range of 6-20 [3]. Thus, on either satellite, densities on different surfaces of craters formed by planetocentric impactors are directly related to the surfaces' relative ages. In contrast, densities of craters formed by heliocentric impactors require both assumption of a value for  $\delta$  and normalization to a standard distance from the leading edge (i.e.,  $90^\circ$ ) in order to be used as relative age indicators. In this abstract we summarize evidence for the character of the impactor populations that cratered Ganymede and Callisto. We begin by evaluating the evidence previously used to support models of planetocentric or heliocentric bombardment, and we then introduce new evidence that cratering of Ganymede was dominated by a single heliocentric population. Finally, we summarize implications of these results for the use of crater densities as age measures of Ganymede surfaces. Information in this abstract has also been presented in detail by Murchie *et al.* [9].

**Previous observations.** Leading edge/trailing edge density gradients found for several classes of craters have been interpreted as evidence of a heliocentric crater-forming bombardment [e.g. 8,10], whereas failure to observe such a gradient has been interpreted as evidence of a planetocentric bombardment [e.g. 8]. Both interpretations are based on the implicit assumption of spatially uniform crater retention times. In general, leading edge/trailing edge density gradients are exhibited by larger craters and younger crater deposits:  $\geq 60$ -km craters on Callisto [10];  $\geq 30$ -km craters on Ganymede in both light and dark terrains; and bright ejecta deposits on Ganymede [9] and Callisto [10]. Conflicting results are reported for smaller craters: Croft and Duxbury [8] report no significant gradient for 10- to 20-km craters in certain areas of light and dark terrains on Ganymede, whereas Bianchi *et al.* [11] report greater densities of small light terrain craters close to the leading edge, and Murchie *et al.* [9] report the same for small dark terrain craters. Croft and Duxbury also report no gradient for Callistoan craters  $\geq 10$ -km in diameter; given that a gradient does occur for  $\geq 60$ -km craters [10], the subset of Callistoan craters lacking a gradient is those 10-60 km in diameter.

For each of Ganymede and Callisto, there are two plausible explanations that reconcile the presence of a leading edge/trailing edge density gradient for large and young craters with the lack of a gradient for small older craters. First, heliocentric bombardment continuing to the present time has dominated formation of large and young craters, but an early period of planetocentric bombardment formed most of the smaller craters [cf. 8]. Second, both large and small craters were formed by heliocentric impactors, but the density gradient for small craters has been obscured in many localities by non-synchronous emplacement of resurfacing materials, such as those occurring on Ganymede in both light terrain [e.g. 1,2,9,11,12] and dark terrain [e.g. 4,9,13]. In this interpretation the gradient is expressed by larger old craters because these were less efficiently buried by resurfacing, and by younger craters because these postdate resurfacing. These alternate explanations are now tested.

**New observations.** Our crater-density measurements for Ganymede's dark terrain [9] were used to provide two types of evidence for the character of that satellite's crater-forming bombardment, neither of which assumes spatially uniform crater retention times.

First, we identified pairs of dark terrain surfaces whose stratigraphic age relations are apparent, but which are located at different distances from the leading edge. Measured and normalized crater densities (assumed  $\delta = 15$ ) were then compared with the stratigraphic relations to test the planetocentric and heliocentric bombardment models, respectively (Figure 1). Three pairs of surfaces have clear age relations: furrowed terrain in southeastern Nicholson Regio and superposed dark smooth material in northwestern Nicholson Regio; furrowed terrain of northwestern Marius Regio and superposed dark smooth material of east-central Marius Regio; and furrowed terrain of western Galileo Regio and superposed dark smooth material of southern Galileo Regio. The fourth pair consists of furrowed terrain of northwestern Marius Regio and the terrain of eastern Marius Regio; the latter strongly resembles the smooth material of east-central Marius Regio, and is also interpreted to have formed by resurfacing of terrain analogous to that of northwestern Marius Regio. The fifth pair consists of northwestern Nicholson Regio and western Galileo Regio. Northwestern Nicholson possesses furrows belonging to the concentrically arranged system which extends across the sub-Jovian hemisphere out to an angular distance of more than  $110^\circ$  of arc from its center of curvature at  $60^\circ\text{N}, 50^\circ\text{W}$  [14], and is the least cratered surface to exhibit these furrows. Galileo Regio is located only  $30^\circ\text{--}90^\circ$  of arc from the center of curvature, but it contains no furrows belonging to the sub-Jovian system; rather, it contains furrows belonging to a distinct crosscutting system [14]. We therefore interpret the surface of Galileo Regio to have a lesser age than the younger furrowed surfaces in the sub-Jovian hemisphere. Measured and normalized crater densities for the five pairs of surfaces are illustrated in Figure 1, where the older member of each pair is designated "1" and the younger member "2." Lower plots are densities of craters  $\geq 20$  km in diameter; upper plots show densities of  $\geq 10$ -km craters, which would not require such thick resurfacing to be "reset." Measured crater densities, which would indicate relative surface ages if the crater-forming bombardment had been planetocentric, are not always consistent with stratigraphic relations, but the normalized densities consistently are. We interpret this result as evidence that the impactor population which cratered Ganymede's dark terrain was dominantly heliocentric.

Second, we tested for bombardment of Ganymede and Callisto by a second, distinctive impactor population by assessing spatial and temporal variability of crater production functions. Four of ten dark terrain areas that we measured exhibit neither a depleted density of small craters nor morphologic evidence for significant resurfacing since crater formation, and are interpreted to be in production. Log (R) values for  $\leq 40$ -km craters in these areas are listed in Table 1. If bombardment by heliocentric and planetocentric populations with distinct size-frequency distributions had occurred, there would be a leading edge/trailing edge gradient in the shapes of the production functions. No such gradient is observed, suggesting the predominance of a single impactor population. Independent measurements of log (R) for undegraded craters in dark terrain and light terrain [4] reveal very similar size distributions of log (R) that resemble in shape the production functions we measured (Table 1), suggesting that both terrains were cratered by the same heliocentric population.

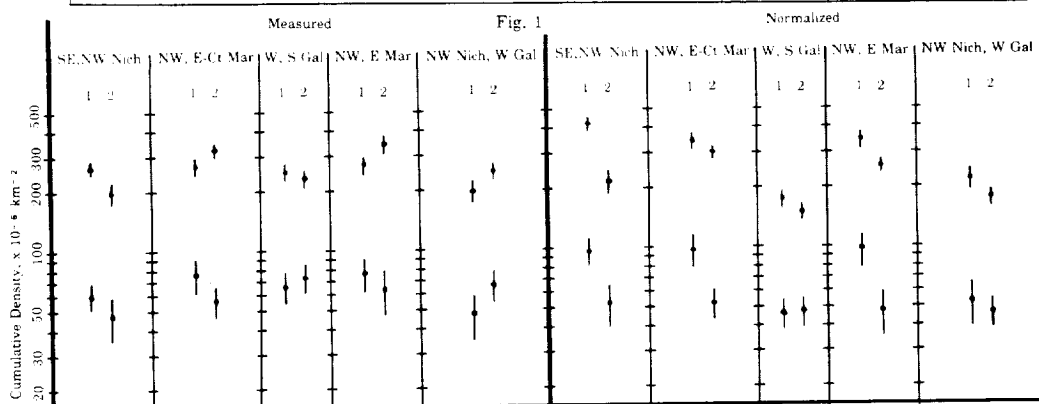
Callisto's surface is more heavily cratered than is Ganymede's, at least by craters  $< 40$ -60 km in diameter [4,5], and is therefore most probably older. Callisto's crater size-frequency distribution is similar in shape to Ganymede's for  $\geq 40$ - to 60-km craters, but smaller craters are more abundant than on Ganymede and the shape of their size-frequency distribution is much "flatter" (Table 1). This difference may result from "saturation" of small craters on Callisto, or from the presence on Callisto of craters formed by a planetocentric population rich in small bodies (as suggested by Croft and Duxbury [8]) that had become extinct before formation of Ganymede's presently observed surface.

**Conclusions and implications.** The observed surface of Ganymede has been cratered predominantly by a single, heliocentric impactor population; the surface of Callisto has been cratered by the same population and possibly by a planetocentric population that had become extinct before formation of Ganymede's observed surface. The leading edge/trailing edge density gradient of small craters on Ganymede has probably been obscured by non-synchronous emplacement of resurfacing materials within light and dark terrains.

These results imply that previously published normalized crater densities of different Ganymede surfaces [e.g. 15] are generally valid measures of *relative* ages. However, model *absolute* ages of the same surfaces [15], keyed to a lunar-like impactor flux history, are probably in error: The heliocentric impactor population should have penetrated the inner solar system, but it is difficult if not impossible to attribute crater populations on the terrestrial planets to the same impactor population that cratered Ganymede and Callisto [4,6,7]. Thus heavy cratering of Ganymede and Callisto (before formation of older light terrain areas on Ganymede) very probably *predated* heavy cratering of the inner solar system [12].

**References.** [1] Smith, B. *et al.*, *Science*, 204, 951-972, 1979a. [2] Smith, B. *et al.*, *Science*, 206, 927-950, 1979b. [3] Shoemaker, E. and R. Wolfe, in *The Satellites of Jupiter*, ed. by D. Morrison, pp. 277-339, Univ. of Ariz., Tucson, 1982. [4] Woronow, A. *et al.*, in *The Satellites of Jupiter*, ed. by D. Morrison, pp. 237-276, Univ. of Ariz., Tucson, 1982. [5] Neukum, G. and S. Pozio, *Lun. Plan. Sci.* XV, 601-602, 1984. [6] Chapman, C. and W. McKinnon, in *Satellites*, ed. by J. Burns and M. Matthews, pp. 492-580, Univ. of Ariz., Tucson, 1986. [7] Strom, R., *Icarus*, 70, 517-535, 1987. [8] Croft, S. and E. Duxbury, *Lun. Plan. Sci.* XIX, 227-228, 1988. [9] Murchie, S. *et al.*, submitted to *Icarus*. [10] Passey, Q. and E. Shoemaker, in *The Satellites of Jupiter*, ed. by D. Morrison, pp. 379-434, Univ. of Ariz., Tucson, 1982. [11] Bianchi, R. *et al.*, *Icarus*, 67, 237-250, 1986. [12] McKinnon, W. and E.M. Parmentier, in *Satellites*, ed. by J. Burns and M. Matthews, pp. 718-763, Univ. of Ariz., Tucson, 1986. [13] Casacchia, R. and R. Strom, *Proc. Lun. Plan. Sci. Conf. 14th*, B419-B428, 1984. [14] Murchie, S. and J. Head, *J. Geophys. Res.*, 93, 8795-8824, 1988. [15] Murchie, S. *et al.*, *Lun. Plan. Sci.* XIX, 821-822, 1988.

TABLE 1. Log (R) Size Distributions (Interpreted as Production Functions)						
Area	Angular dist. from apex, °	Diameter increment				
		7.1-10 km	10-14.1 km	14.1-20 km	20-28.3 km	28.3-40 km
Eastern Marius	*65	-1.64±0.04	-1.58±0.06	-1.24±0.07	-1.13±0.10	---
East-central Marius	*85	-1.70±0.06	-1.53±0.04	-1.37±0.06	-1.42±0.09	-1.06±0.10
SE Nicholson	114	-1.92±0.04	-1.65±0.05	-1.49±0.06	-1.30±0.07	-1.46±0.15
"Eastern Barnard"	131	-1.70±0.06	-1.60±0.08	-1.51±0.12	-1.39±0.15	---
From Woronow <i>et al.</i> (1982)						
Ganymede-light terrain, all craters	---	---	-1.83	-1.82	-1.72	-1.62
Ganymede-dark terrain, undegraded craters	-1.38	-1.38	-1.38	-1.36	-1.29	-1.24
Callisto-undegraded craters	---	---	-0.70	-0.69	-0.67	-0.72



GANYMEDE: "MOAT" CRATERS COMPARED WITH PALIMPSESTS AND BASINS  
B.K. Lucchitta and H.M. Ferguson, U.S. Geological Survey, Flagstaff, AZ  
86001.

Ganymede has varieties of impact structures not commonly found on terrestrial planets. These are (1) "moat" craters, having enlarged central pits with interior shallow domes, and (2) palimpsest craters [1], having flattened circular shapes and, if well preserved, indistinct, concentrically arranged hummocks or ridges surrounding a central plain. This abstract addresses the question of whether a study of moat craters can shed light on the interior structures of palimpsests and basins.

Moat craters have attracted attention previously: Passey and Shoemaker [2] called them penepalimpsests type II and considered them transitional between craters and palimpsests. They interpreted the inner smooth plains of palimpsests to reflect the former crater floor surrounded by the crater rim and the outer margin to reflect the edge of the continuous ejecta. Croft [3] called moat craters anomalous pit craters and also suggested a continuum between moat craters, craters, and palimpsests, even though morphometrically they appeared to be distinct. He placed the former crater rim of palimpsests somewhere within their concentric structures. Hartmann [4] mentioned that the former crater rim on palimpsests might lie near their outer margin and emphasized the importance of locating the crater rim accurately for studies of crater-density distributions. Bianchi and Pozio [5], in a thorough statistical study, referred to moat craters as craters with domed central pits. Their main conclusions, based on ratios of central-pit to crater-rim diameters, pertained to changes in lithospheric thickness with time. They did not address implications for palimpsests.

To better understand where the former crater rim is located in palimpsests, we assembled images of moat craters, palimpsests, and basins and analyzed them as members of a matrix having size on one axis and degradational state on the other. Thus, progressive morphologic as well as morphometric changes can be easily viewed (Fig. 1).

Figures 1a through c show a progression of similar-sized moat craters, from fresh to highly subdued. The fresh crater Osiris (Fig. 1a) has an interior, smooth dome surrounded by an inner pit margin and a shallow rise that is probably equivalent to the crater peak. The crater rim is distinct. In the more degraded crater of Figure 1b, the shallow rise has become a wreath with radial and concentric structures, and the outer crater rim is still distinct. In Figure 1c, the crater rim has become indistinct and is locally replaced by an outward-facing scarp.

Figures 1d through f display transitional forms from moat craters to palimpsests. Figure 1d shows the moat crater Ilus, which is similar to that of Figure 1c, clearly showing a central, smooth dome surrounded by a wreath of concentric structures. The outer crater-rim margin, in analogy with fresher moat craters, should lie a short distance beyond the outward-facing scarp surrounding the wreath. Figure 1e shows two palimpsests that have structures similar to crater Ilus (Fig. 1c), except they are more flattened and degraded. The similarity suggests that the central smooth area in these palimpsests is equivalent to the central, smooth dome of moat craters and the outer margin is equivalent to a position very near the outer crater-rim

margin. The best known palimpsest, Memphis Facula (Fig. 1f), is a larger and more subdued version of the palimpsests in Figure 1e. Therefore, the central plain here is also equivalent to the moat-crater dome, and the outer margin lies near the outer crater-rim margin. The circularity of palimpsests supports this interpretation.

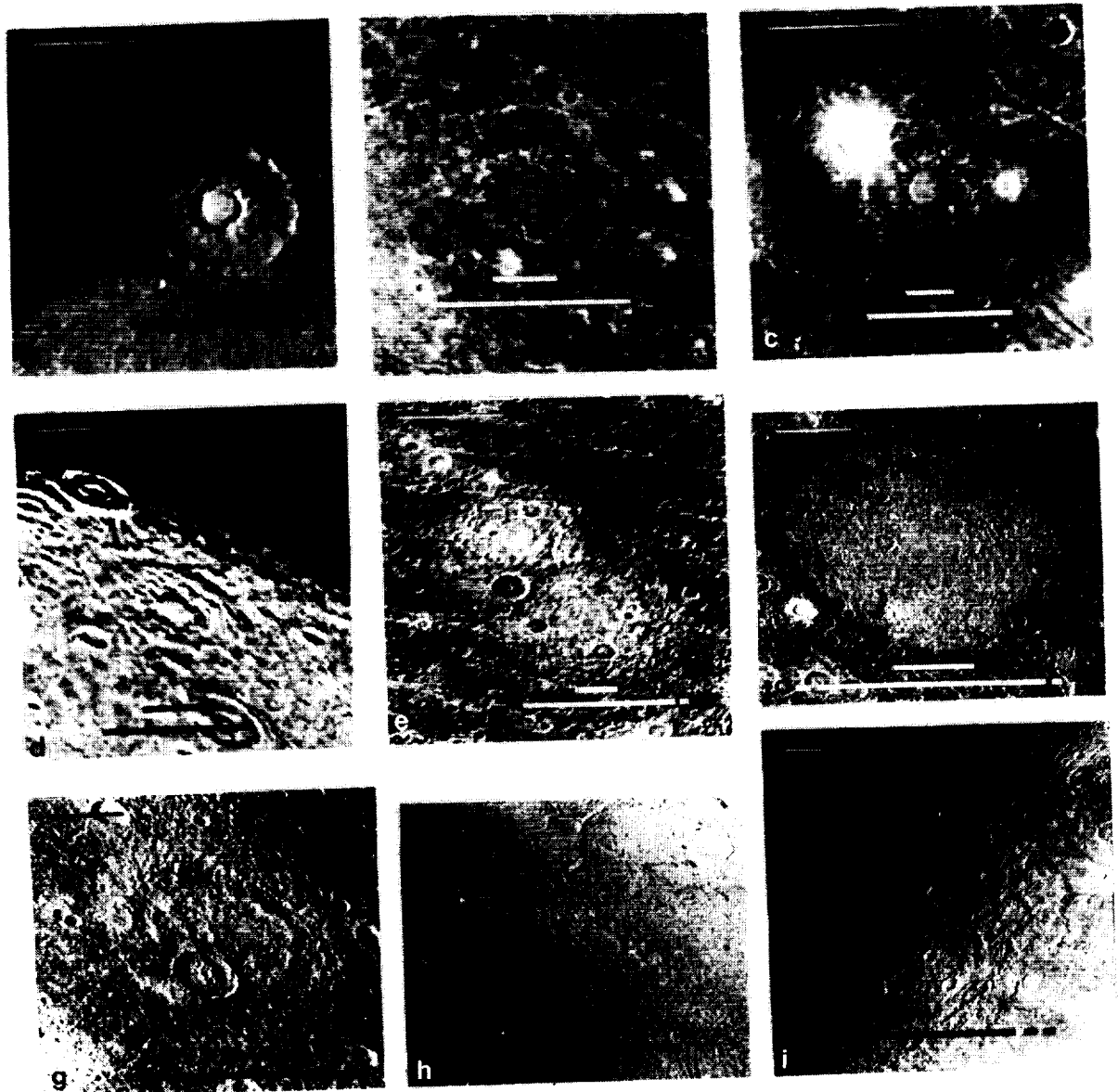
Figures 1g through i show a progression from palimpsests to basins. From the previous interpretations it follows that the inner plain of the basin Nidaba in Figure 1g represents the flat dome of moat craters, the inner ring scarp represents the inner pit margin, the outer ring scarp the inner crater-rim margin, and the outer edge is located only a short distance beyond the outer crater-rim margin. In the much younger crater Hathor (Fig. 1h), the central plain would still be equivalent to the inner dome of moat craters, but the shallow peak and crater rim are not easily separated out in the surrounding rugged concentric and radial structures. Secondary craters begin to occur only a short distance from an outward-facing scarp that probably marks the position of the outer crater rim; apparently the "continuous" ejecta are closely confined to the outer margin of the crater rim. According to the previous interpretations, the central plain of the Gilgamesh basin in Figure 1i also reflects the inner dome, the inner ring of rugged massifs the inner pit margin, and the crater rim crest is located most likely near the outer surrounding scarps. As Gilgamesh is an impact structure transitional in form to basins on the terrestrial planets, the observations of this paper also support the idea that the inner ring on small- and intermediate-sized terrestrial basins is equivalent to the pit margin of moat craters or a central-peak ring [6]; the crater-rim equivalent of terrestrial basins would be located farther out.

The number of degraded moat craters and palimpsests is small, so results remain open to question until better images are obtained from future missions. Nevertheless, a trend in the observations points toward two conclusions: (1) the inner smooth plain of palimpsests and basins is equivalent to the floor of the central pit and the dome of moat craters, and (2) the outer margin of palimpsests lies close to the former crater rim.

#### References

- [1] Smith, B.A. et al., 1979, *Science*, 206, 927-950.
- [2] Passey, Q., and Shoemaker, E., 1982, The Satellites of Jupiter, U. Ariz. Press, 379.
- [3] Croft, S.K., 1983, *PLPSC* 14, *JGR* 88, 1371.
- [4] Hartmann, W.K., 1984, *Icarus* 60, 56.
- [5] Bianchi, R., and Pozio, S., 1985, *Annales Geophysicae* 3, 129.
- [6] Hartmann, W.K., and Wood, C.A., 1971, *Moon* 3, 3.

Figure 1. Continuum from fresh-looking moat craters through degraded moat craters, palimpsests, and basins. Upper bar beneath crater gives diameter of pit-rim margin. Lower bar gives diameter of outer crater-rim margin. Bars dashed where margin location approximate. Scale bar in upper left is 100 km. a, north up, FDS 16405.02; b, north up, FDS 20637.44; c, north up, FDS 20635.49; d, north left, FDS 20631.33; e, north up, FDS 20636.56; f, north up, FDS 20638.29; g, north up, FDS 20638.31; h, north down, FDS 20640.51; i, north down, FDS 20638.14.





**STRATIGRAPHY AND CRATERING HISTORY OF THE MOON: OUR UNDER-  
STANDING 20 YEARS AFTER APOLLO 11.** Paul D. Spudis, U.S. Geological Survey, Flagstaff, AZ  
86001

Earth-based observations and robotic precursor missions led to the formulation of a generalized geological model of the Moon prior to Apollo 11 [1,2]. The geologic tasks left for Apollo were to: (1) confirm or negate this conceptual model; (2) provide samples for study, including radiometric dating to calibrate the relative time scale with absolute ages; and (3) make geologic discoveries on the Moon through human observation. The completion of these tasks gave us a more detailed knowledge of the evolution of the Moon than we have for any other planetary body. Despite our understanding, some important problems remain unresolved.

**Stratigraphy of the Moon: Then and Now.** A comprehensive geologic mapping program was developed to support Apollo lunar exploration [3]. The history of the Moon was subdivided into four periods: (1) the pre-Imbrian, encompassing all events prior to the formation of the Imbrium basin; (2) the Imbrian, from the time of the Imbrian impact until roughly the time of the impact that formed the crater Eratosthenes; (3) the Eratosthenian, from the Eratosthenes impact to the Copernicus impact; and (4) the Copernican, which extends to the present [1-3]. Material units of the Moon were classified in terms of relative age [2,3]. Units in the highlands are mostly crater deposits but several units of regional extent, mostly basin ejecta, were recognized [1-3]. It was assumed in the pre-Apollo era that basin deposits consist of primary ejecta; this assumption, in part, was the rationale for the selection the Fra Mauro Formation of the Imbrium basin for the Apollo 13 and 14 landing sites. Light plains and hilly-furrowed units were mapped and interpreted to have formed by highland volcanism [1-3]. Studies of Surveyor chemical analyses and photographs of flow lobes in Mare Imbrium from Lunar Orbiter led to the idea that the maria are basaltic lava flows [1-3]. In terms of absolute time, it was suspected that the Copernican and Eratosthenian Periods make up most of lunar history [2,4]; in terms of material units, however, it was clearly understood that most were emplaced in the Imbrian and pre-Imbrian Periods [2,3]. This model suggested an intensively active early Moon, followed by quiescence for most of geologic time [1,4].

Since Apollo, most of this view of lunar geologic evolution has appeared axiomatic [e.g., 5]. Samples collected by Apollo 11 confirmed the basaltic nature of the maria and documented the antiquity of lunar volcanism (at this site, about 3.7 Ga; [6]). Results from the successive Apollo missions (summarized in [5,7]) broadened our knowledge of the ages and types of rocks that make up the lunar crust. The early Moon underwent massive, probably global, differentiation to form a relatively feldspathic crust. An impact bombardment of this crust battered the highlands; using the deposits of the Nectaris basin as a regional stratigraphic datum, the pre-Imbrian was subdivided into the Nectarian and pre-Nectarian Periods [5,8]. Of a total of about 40 basins on the Moon, roughly 30 were formed in pre-Nectarian time, with the remainder formed mostly in Nectarian and early Imbrian time [5]. Results of the Apollo 16 mission stimulated a reevaluation of highland volcanism on the Moon [5,7], leading to basin-related hypotheses of origin [5]. The Fra Mauro Formation was sampled by Apollo 14, but its relation to the Imbrium impact remains contentious [5,12]. After the Imbrian impact at 3.85 Ga [5], mare basalt eruptions, which probably started much earlier, began to be preserved in large exposures. All mare surfaces sampled by Apollo and Luna were emplaced between 3.8 and 3.1 Ga ago [7]. At least seven post-mare cratering events on the Moon have been dated (or have had ages inferred) from Apollo samples, but these impacts are small and are difficult to date on a relative time scale in a manner comparable to the regional units emplaced early in lunar history. A possible exception is the age of Copernicus (estimated at about  $850 \pm 100$  Ma old [5]).

**The remaining problems: What do we really know?** Virtually all of the "facts" outlined in the above sketch of lunar evolution have been questioned. The resolution of these questions depends both on continued work to understand the Apollo legacy and new exploration of the Moon.

**Lunar bombardment history.** Probably the most controversial aspect of the cratering history of the Moon is the nature of its early bombardment. Based on isotopic data for highlands rocks, Tera et al. [9] proposed that the Moon underwent a sharp increase in bombardment rate (the "terminal cataclysm") at 3.9 Ga. Subsequent workers tried to refute this hypothesis [5,10,11], claiming that

the early Moon experienced a gradually declining cratering rate. In this view, the prevalence of 3.9 Ga ages in the lunar samples is attributed either solely to the Imbrium impact [11] or to a few basins [5]. Recently, Ryder [12] has advocated a cataclysm that produced virtually all basins and craters in the highlands at 3.9 Ga. This problem is crucial to lunar history and to the early histories of all the terrestrial planets.

"Highland" volcanism and the origin of KREEP. Despite the results of the Apollo 16 mission, the question of the existence, duration, and volumetric importance of highland (non-mare) volcanism is very much open. Spectrally distinct dome-like landforms may represent highlands volcanism [13]. The light plains of the Apennine Bench near the Apollo 15 landing site are composed of post-Imbrium volcanic KREEP basalts [14]; whether other light plains are deposits of volcanic KREEP is unknown. The origin and emplacement mechanism(s) of KREEP remain controversial; volcanism may [15] or may not [7] be one of a variety of processes involved in the history of KREEP.

Mare volcanism: When and how much? Sample studies have revealed that mare basalts were extruded onto the lunar surface prior to 3.9 Ga [e.g., 16], but the amounts are unknown. Highland light plains with dark-halo craters, indicating the presence of ancient buried basalts [17], constitute less than 12% of the lunar maria. Large amounts of an Fe-rich, chondritic Th/Ti component in the cratered highlands may be consistent with an extrusion rate of ancient mare basalts up to 30 times higher than the average rate since 3.9 Ga [18]. However, it is possible that this chemical signature is produced instead by (as yet unidentified) pristine ferroan rocks [19]. Determining which scenario is correct is important for understanding lunar volcanic and thermal history.

The question of when mare volcanism ceased is unresolved. The youngest mare basalts in the sample collections are from Apollo 12 (3.1 Ga). Several studies have documented maria younger than the Apollo 12 site [5,17], but how much younger is unknown; it is possible that the youngest basalts on the Moon may be less than 1 Ga old [17]. The only way to resolve this question is to return samples from young mare basalt flows.

Calibration of the relative age time-scale. One of the prime tasks of Apollo, providing absolute dates for stratigraphic events, remains controversial and largely unfinished. I believe that the formation of the Imbrium basin is well established at about 3.85 Ga [5], although some question this [20]. The Serenitatis basin, which is difficult to date relative to the Nectaris and Crisium basins, is about 3.87 Ga [5]. However, the age of the Nectaris basin, which defines the beginning of the Nectarian Period, is uncertain; the current best estimate is 3.92 Ga [5,21,22]. Dating the Nectaris basin is crucial; if it really is 3.92 Ga old, then the cratering flux definitely increased at 3.9 Ga, possibly as a "cataclysm" [9]. Similarly, the absolute age of the Copernican boundary is unknown; it could be as young as 800 Ma [5] or as old as 2 Ga [23]. We need additional lunar samples from a number of carefully selected sites.

**References.** [1] Mutch T. (1970) Geology of the Moon, Princeton Univ. Press, 324 pp. [2] Wilhelms D. and McCauley J. (1971) USGS Map I-703. [3] Wilhelms D. (1970) USGS Prof. Paper 599. [4] Hartmann W. (1966) Icarus 5, 406. [5] Wilhelms D. (1987) USGS Prof. Paper 1348, 302 pp. [6] Special issue, Science 167, no. 3918 (1970). [7] Taylor S.R. (1982) Planetary Science, LPI Press, 481 pp. [8] Stuart-Alexander D. and Wilhelms D. (1975) J. Res. USGS 3, 53. [9] Tera F. et al. (1974) EPSL 22, 1. [10] Hartmann W. (1975) Icarus 24, 181; (1980) Proc. Conf. Highlands Crust, 155. [11] Baldwin R. (1974) Icarus 23, 157. [12] Ryder G. (1988) Apollo 14 Workshop, 71; Science (submitted) [13] Head J. and McCord T. (1978) Science 199, 1433. [14] Spudis P. and Hawke B. (1986) Apollo 15 Workshop, 105. [15] Spudis P. and Davis P. (1986) PLPSC 17, JGR 91, E84. [16] Ryder G. and Spudis P. (1980) Proc. Conf. Highlands Crust, 353. [17] Schultz P. and Spudis P. (1983) Nature 302, 233. [18] Davis P. and Spudis P. (1985) PLPSC 16, JGR 90, D61. [19] Haskin L. and Korotev R. (1988) LPS XIX, 461. [20] Deutsch A. and Stöffler D. (1987) GCA 51, 1951. [21] James O. (1981) PLPSC 12B, 209. [22] Spudis P. (1984) PLPSC 15, JGR 89, C95. [23] Neukum G. et al. (1975) PLSC 6, 2597.

**THE LUNAR CRISIUM BASIN: GEOLOGY, RINGS, AND DEPOSITS.** Paul D. Spudis<sup>1</sup>, B. Ray Hawke<sup>2</sup>, and Paul G. Lucey<sup>2</sup>. 1. U.S. Geological Survey, Flagstaff AZ 86001 2. Planetary Geosciences-HIG, Univ. Hawaii, Honolulu HI 96822

The Crisium basin is on the eastern edge of the lunar near side north of Mare Fecunditatis and southeast of Mare Serenitatis. The basin impact appears to have occurred within typical highlands, although evidence exists that mare volcanism was active in this region prior to and immediately after the impact [1]. The basin interior is mare-flooded, obscuring relations for the basin floor and causing controversy regarding the true topographic rim of the basin [2,3].

**Geology of Crisium Deposits** The highlands bounding the basin consist of well-preserved massifs. The Crisium rim consists of platform topography in which mesa-like terra islands of polygonal outline contain undulatory to smooth interplatform deposits of light plains or hummocky deposits; the latter may also overlie the platforms. These platform massifs are much more prominent and abundant than those at the Nectaris [4] and Imbrium [5] basins and appear to make up most of the highlands that surround Mare Crisium for about a basin radius (250 km). Schultz [6] suggested that these platform massifs were produced by endogenic modification of basin topography.

The highlands on the southern border of the Crisium basin display several morphologies that render interpretation of basin geology difficult. Large exposures of hilly and furrowed material [7] occur in this region and appear morphologically similar to the Descartes materials exposed west of the Nectaris basin [4]. The rim of Cleomedes, a post-Crisium crater on the northern rim of the basin, is overlain by a deposit of this hilly material. Therefore, at least in this region, the hilly material cannot be a facies of Crisium basin ejecta because it overlies a crater that post-dates the basin.

Distal Crisium deposits are difficult to recognize in most regions [2]. Sparse patches of lineated terrain occur north of the basin, terminating near the crater Messala and probable basin secondaries are exposed near the crater Zeno. The elongate crater Rheita P, that is superposed on the Nectaris basin Janssen Formation, may be a Crisium basin secondary crater; this relation implies that Crisium post-dates the Nectaris basin [8].

**Rings and structural geology** A subtle ring structure 1080 km diameter has been interpreted as the main topographic rim of the basin [2,3]. Most other investigators interpret the main basin rim to be the scarp-like ring (740 km in diameter) just outside the massif ring bordering the mare (540 km diameter) [9,10]. Highland elevations of the 740 km ring equal or exceed those of the 540 km ring bordering the mare; thus, this ring probably represents the true topographic rim of the Crisium basin. Two large, exterior rings of 1080 and 1600 km diameter possess scarp-like morphology and resemble the outer rings of the Nectaris and Imbrium basins [4,5]. One additional inner ring (360 km diameter) is expressed by the wrinkle ridge system of Mare Crisium.

One of the most distinctive structural features of the Crisium basin is the presence of concentric troughs that occur between the platform massifs that make up the basin rings. These troughs are evident on both low-sun telescopic photographs and topographic data derived from orbiting spacecraft. The troughs appear to be structurally controlled and display polygonal outlines.

**Composition of Crisium basin deposits.** Orbital chemical and Earth-based spectral data. The regional composition of the southern Crisium terra is that of typical near side highlands. Mixing model calculations [11] performed on four regional units [12] show all to be more or less constant in petrologic composition. Three of the highlands units are nearly identical, being composed of anorthositic gabbro and low-K Fra Mauro basalt in the approximate proportions of 3:1. A fourth unit, correlated with interplatform light plains, displays a mare basalt component (almost 19 percent). Two near-infrared spectra exist for Crisium deposits [13]: that of the crater Proclus shows a composition of anorthositic norite while that for the small crater Eimmart A indicates a feldspathic rock with both orthopyroxene and olivine [13]. The compositions of Crisium basin ejecta are comparable with those observed in Nectaris [4], in which anorthositic components make up the majority of basin deposits and LKFM is less abundant. Both basins probably excavated comparable

stratigraphic levels (not necessarily comparable depths) of the lunar crust.

**Luna 20 Samples.** The Soviet unmanned spacecraft Luna 20 landed on the southern rim deposits of the Crisium basin near the crater Apollonius. Anorthositic particles are the most abundant component of the soil, making up about 75 percent of the sample, while Low-K Fra Mauro basalt contributes about 18 percent to the total Luna 20 soil [14]. Lithic fragments with LKFM composition are aphanitic impact melts. These rocks may represent ejected Crisium basin impact melt that is included within anorthositic clastic ejecta at the Luna 20 landing site. Such a relation is similar to that of VHA melt rocks found in the Apollo 16 samples that were probably derived from the Nectaris basin impact [4].

About 9 percent of the Luna 20 soils consist of mare basalt mineral fragments and agglutinates [14]; mixing model calculations of orbital data range from 2 to 18 percent mare basalt, in reasonable agreement. These mare basalt fragments may be derived from the post-basin Mare Crisium and Mare Fecunditatis flows, delivered to the site by impact craters but the evidence for ancient, basin-related mare deposits, both as ejecta and post-basin interplatform flows [1], suggests that at least some of these fragments may be part of the Crisium ejecta.

**Discussion.** Remote-sensing and Luna 20 data suggest that excavation at Crisium basin was limited to upper and middle crustal levels (40–45 km), as at the Nectaris basin [4]. The lowermost boundary for the transient cavity diameter is probably the inner mare ridge ring, about 380 km in diameter; if smaller than this, inner basin topography would probably be more prominent within Mare Crisium and terra islands would be evident within the mare fill of the basin. The maximum size of the transient cavity is probably less than or equal to about 540 km in diameter, corresponding with the prominent massif ring that contains the mare fill of the basin. If the impact cavity were much larger than this, lower crustal and mantle material would have been excavated. We suggest a transient cavity diameter of about 450 km for the Crisium basin [4,5].

Platform massifs result from the penetration of the lunar lithosphere by the basin-forming impact, followed by sub-lithospheric flow and foundering of crustal blocks. The impact induced radial and concentric fractures in the rigid lithosphere; such fracturing has been predicted theoretically [15] and documented by observations [16]. After the impact, the lunar asthenosphere flowed inward to compensate for the excavated mass. Because the viscosity of the asthenosphere was variable laterally on small scales, the regional inward flow produced platforms by selective removal of underlying support; the failure occurred along the zones of weakness induced earlier. Such a mechanism for the production of platform massifs would explain their absence around young lunar basins, such as Orientale; these basins formed after the lithosphere had grown so thick that the basin transient cavity occurred entirely within the rigid layer.

**References** [1] Schultz P. and Spudis P. (1979) PLPSC 10, 2899 [2] Wilhelms D. (1987) USGS Prof. Paper 1348, 302 pp. [3] Croft S. (1981) PLPSC 12A, 227 [4] Spudis P. et al. (1989) PLPSC 19, in press [5] Spudis P. et al. (1988) PLPSC 18, 155. [6] Schultz P. (1979) Conf. Highlands Crust, 141 [7] Wilhelms D. and McCauley J. (1971) USGS Map I-703 [8] Wilhelms D. (1976) PLSC 7, 2883 [9] Hartmann W. and Kuiper G. (1962) Commun. LPL 1, 55 [10] Howard K. et al. (1974) RGSP 12, 309 [11] Hawke B. and Spudis P. (1979) Conf. Highlands Crust, 53 [12] Bielefeld M. et al. (1978) Mare Crisium, 33 [13] Pieters C. (1986) Rev. Geophys. 24, 557 [14] Warner J. et al. (1972) EPSL 17, 7 [15] Melosh H. (1976) PLSC 7, 2967 [16] Mason R. et al. (1976) Proc. Geol. Assoc. London 87, 161.

**Introduction.** We have made a new estimate of the flux of seismically detected meteoroids impacting the lunar surface. Since earlier studies of the seismic impact flux (1,2) our database has significantly expanded and our knowledge on seismic energy transmission in the Moon has greatly improved. This new information allows us to take a new approach for such an estimate. Although earlier methods of flux estimate (1,2) relied on assumptions on how observed impacts were distributed, on average, with distance from the seismic stations, we are now able to eliminate these assumptions by using explicitly determined locations and energies of a large number of detected impacts. This enables us to estimate the flux in a more straightforward way than was possible earlier.

**Impact Location Estimates.** From the Passive Seismic Experiment Long-Period Event Catalog (3), we selected 91 impacts that showed peak-to-peak amplitude readings of 10 mm or more at two or more of the four seismic stations. Although earthquake hypocenters are usually located from the arrival times of seismic waves at different stations, only a limited number of lunar seismic sources provides accurate arrival-time readings for their locations because of strong scattering of signals. We located 18 impact sources by conventional arrival-time methods. For the rest of the impact sources we used seismic signal properties other than arrival times, such as amplitude decay with distance and the change in shape of the envelope of the seismic signal due to scattering. Once the impact locations are known, the impact energies can be determined using appropriate calibration data, such as those from impacts of the Saturn IV boosters (S-IVB) and the Lunar Module (LM), whose impact sites and energies are known.

Figure 1 shows the distribution of the impact locations of the selected events on the lunar surface. Events of smaller magnitude cluster near the seismic stations because they are detected only at short distances. More impacts are located on the western lunar hemisphere because events closer to the least sensitive (i.e., the westernmost Apollo 12) station are more likely to meet the criteria (large-amplitude readings at two or more seismic stations) under which the 91 impacts were selected.

**Results.** Figure 2 shows the cumulative distribution of impact energies. The occurrence rates on the ordinate are normalized to represent the observed impact rate on the Moon per year. Only events exceeding a certain impact energy ( $E > 3 \times 10^{11}$  J) can be detected over the entire lunar surface, while smaller ones are

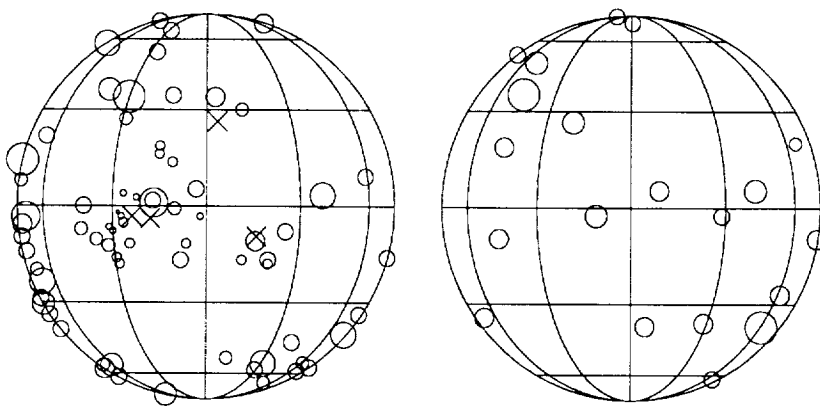


Fig.1: Distribution of 91 selected large meteoroid impacts on the lunar front (left) and far side (right). The sizes of the circles are proportional to the logarithm of the impact energy of the meteoroid. The seismic stations are marked with crosses.

incompletely sampled. We estimate the impact flux to be  $\log_{10} N(E) = -0.99 \log_{10} E + 11.38$ , where  $N$  is the number of impacts per year on the lunar surface having impact energies higher than  $E$  in the energy range  $3 \times 10^{11} \text{ J} < E < 10^{12} \text{ J}$ .

A comparison of our new result with the lunar cratering rate (4) using appropriate scaling laws relating crater size to impact energies (e.g., 5) shows a remarkably close agreement (Fig.2). However, the agreement may be deceiving because the flux determined from lunar crater statistics alone is rather uncertain. Various crater scaling laws exist with predicted crater sizes varying by as much as a factor of ten for given impact energy.

A comparison with the flux from terrestrially observed "airwave objects" (large meteoroids) (6,7) indicates that our lunar result is about a factor of four lower than the latter (Fig.2). The reduced focusing of meteoroid trajectories and reduced attraction in the Moon's gravity field have been taken into account. These corrections depend on the average velocities of the meteoroids, for which we adopted  $v=20\text{km/s}$  (encounter speed at the top of Earth's atmosphere).

**Discussion.** The new result significantly reduces previously reported discrepancies between lunar and terrestrial meteoroid flux estimates (1,2). That the seismic efficiency (i.e., the fraction of the pre-impact kinetic energy transformed into seismic energy) of the rocket boosters, which we used as calibration, could be significantly lower than that of meteoroids has been cited as a possible cause of the apparently low lunar flux estimates. However, this study shows that the difference in seismic efficiency need not be greater than a factor of four, provided that the terrestrially measured flux of meteoroids is correct.

Recent Monte Carlo studies of the seismic impact detection rate (8) suggest that the majority of observed impacts occur at closer ranges to the seismic stations than was assumed earlier. Although an explanation for this observation is yet to be found, it is most plausible that this effect, if not taken into account, also contributes to erroneous lunar impact flux estimates.

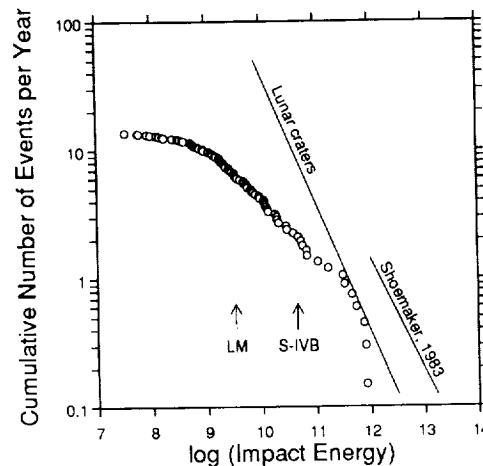


Fig. 2: Cumulative distribution of impact energies (in Joule) of the selected 91 events. Comparison with lunar crater statistics (4,5) and with Shoemaker's estimate of the energy distribution of large meteoroids (6) are shown. The mean impact energies of the S-IVBs and the LMs (which are used as calibration) are marked by arrows.

## References.

- (1) Latham G.V., M. Ewing, F. Press, G. Sutton, H.J. Dorman, Y. Nakamura, M.N. Toksöz, D. Lammlein and F.K. Duennebier, in Apollo 16 Preliminary Science Report, Sec 9, NASA SP-315, 1-29, 1972.
- (2) Duennebier F.K., H.J. Dorman, D. Lammlein, G.V. Latham and Y. Nakamura, Proc. Lunar Sci. Conf. 6th, 2417-2426, 1975.
- (3) Nakamura Y., G.V. Latham, H.J. Dorman and J.E. Harris, Galveston Geophysics Lab. Cont. No. 491, 1981.
- (4) Neukum, G. Habilitationsschrift, Universität München, 1983.
- (5) Dence, M.R., R.A.F. Grieve and P.B. Robertson, in: Impact and explosion cratering (D.J. Roddy, R.O. Pepin and R.B. Merrill, Eds.), Pergamon Press, New York, 247-275, 1977.
- (6) Shoemaker, E.M., Ann. Rev. Earth Planet. Sci 11, 461-494, 1983.
- (7) Shoemaker, E.M. and C.J. Lowery, (abstract), Meteoritics 3, 123-124, 1967.
- (8) Oberst, J. and Y. Nakamura, Proc. Lunar Planet. Sci. Conf. 19th, 1989 in press.

PHOBOS: COMPARISON OF SMALL CRATERS ON PHOBOS AND THE MOON  
William K. Hartmann, Planetary Science Institute, Tucson, AZ 85719

The Soviet PHOBOS mission may allow the first detailed comparisons of lunar crater diameter distributions with those of another airless planetary body at diameters down to meter scale. Several problems can be addressed.

Crater densities on Phobos have been measured at larger sizes by myself and by Thomas and Veverka from Mariner 9 and Viking data, respectively<sup>2 3</sup>. Thomas and Veverka's counts average slightly lower, but mostly have overlapping error bars. Here I compare both sets of Phobos counts to lunar crater counts from my own catalog, assembled from Ranger, Orbiter, and Apollo data since the 1960's. A particular value of my Phobos and lunar data set is uniformity of counting techniques applied to many data sets, mostly by the same observer.

In Figs. 1 and 2, the Phobos counts are plotted on the same format, but against different background data sets from two types of lunar surfaces. both plots are similar to the "R plots" introduced by Strom. Any horizontal represents a cumulative or log-incremental power law size distribution with an exponent of -1.83. The solid horizontal reference line is the best fit for a plot of many heavily cratered surfaces in the inner solar system, which I find to be remarkably similar in crater density, generally within a factor 2 or 3 of each other.

In reference 1 I hypothesize that this line represents an empirical determine of the cratering level corresponding to saturation equilibrium (henceforth "SE"). I also hypothesize that in nature, crater densities rise to this level, and then fluctuate around it, sometimes rising somewhat above, and sometimes dropping below, as surfaces are wiped clean by new craters or their ejecta sheets. Because an ejecta sheet in a specific region would have only a certain depth, shallower craters up to a limiting size would be obliterated and larger craters would show through, implying that different diameter ranges would evolve independently, and wavy structure would be seen around the horizontal reference line. These working hypotheses are controversial.

Phobos might be expected to have reached SE, not only because it has presumably been subjected to long bombardment without much internally-generated resurfacing, but also because most debris blown off it remain in Martian orbit and re-impact Phobos. The latter global "sandblasting effect" may explain the softened appearance of many Phobos craters.

Phobos thus gives a special opportunity to test ideas of crater saturation and evolution. Fig. 1 shows one test. If Phobos and the

most heavily cratered lunar highlands are both in SE, then the two surfaces should have similar crater densities. On the other hand, if SE occurs at densities some 5 x higher than the solid line, as suggested by some workers<sup>4</sup>, then there is no reason, other than coincidence, to expect Phobos to match the lunar highlands or the reference line. Fig. 1 shows that Phobos and the most heavily cratered lunar highlands both fall near the reference line, consistent with the hypothesis that they have been evolved toward a universal SE level.

Fig. 2 shows a second, more subtle test. The lunar regolith observed in mare regions is a layer of material pulverized by repeated impacts, and as such should be in SE by definition at diameters with depth comparable to the regolith,  $D < 200$  m or so. As noted by Gault and others years ago<sup>5</sup>, lunar mare crater counts rise sharply toward smaller diameters, but then roll over dramatically at this size range. Fig 2 shows that this rollover roughly follows the hypothetical SE line within a factor 2, and that the available Phobos counts fall in the same region. This strongly supports the idea that Phobos craters are near the SE condition defined by the lunar regolith.

Extensions of these tests to  $D \sim 1$  m with PHOBOS imagery is desirable. My program has been terminated by NASA in recent funding cuts, but I hope that similar work can be resumed either by myself or by others associated with future Phobos data.

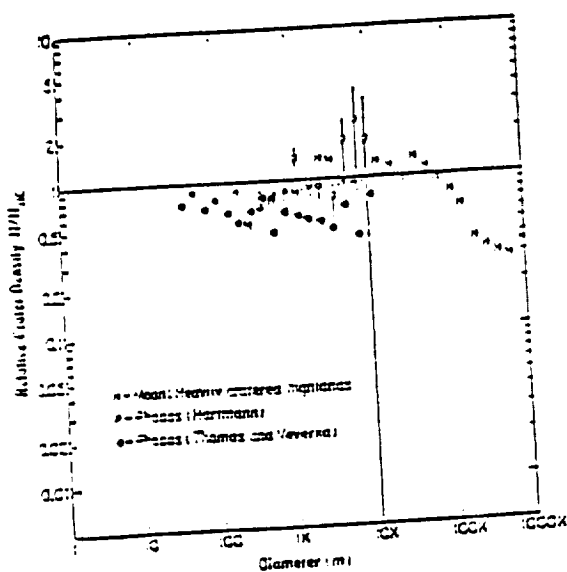


Fig. 1. Phobos log incremental crater densities roughly match those in the most heavily cratered lunar uplands. See text for further discussion.

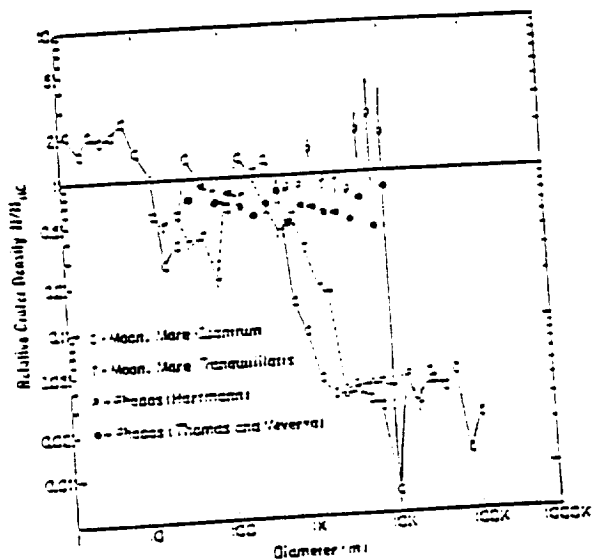


Fig. 2. Phobos log incremental crater densities roughly match those in the diameter range saturated during production of the regolith ( $D < 200$  m).

LOW QUALITY  
PHOTO COPY



- <sup>1</sup>Hartmann, W.K. (1984). Icarus 60, 56-70.  
<sup>2</sup>Pollack, J. and 8 others (1972). Icarus 17, 394-407.  
<sup>3</sup>Thomas, P. and J. Veverka (1980). Icarus 41, 365-380.  
<sup>4</sup>Woronow, A., R. Strom, and M. Gurnis (1982). In Satellites of Jupiter, ed. D. Morrison (Tucson: U. Ariz. Press).  
<sup>5</sup>Gault, D.E. (1970). Radio Science 5, 273-291.

**Background:** Proposed periodic cycles of mass mortality have been linked to periodic changes in the impact flux on Earth (1, 2, 3). Such changes in the impact flux, however, also should be recorded on the Moon. Without returned lunar samples, crater statistics provide one of the few available tools to test this hypothesis. Small "counter-craters" are used to establish the relative chronology of large "dated-craters." If sudden changes in the impact flux of 1–10 m bodies (producing 100 m-diameter counter craters) remain smaller than the subsequent net cratering record, then the areal density of these craters can establish the relative age of the larger dated craters. If changes in the counter-crater production rate approach the subsequent cumulative cratering record, however, then gaps and clusterings in the distribution of inferred ages of the larger dated craters instead could refer to changes in the production of smaller counter craters. Either interpretation is significant for recognizing changes in the impact flux.

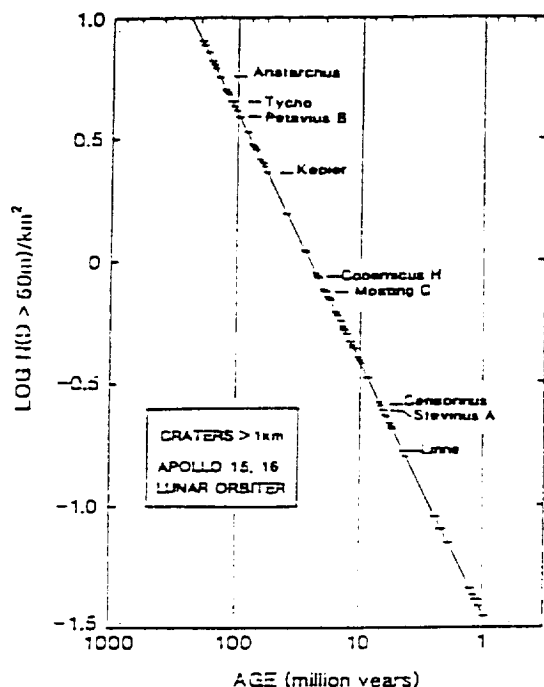
**Approach:** Previous studies have concluded that the impact flux on the Moon over the last 1–2 billion years has been reasonably constant (4), but sudden changes in the impact flux over time intervals as short as 30 my could not be detected in these studies unless the added crater population greatly exceeded the cumulative cratering record. Consequently this study focuses only on bright-rayed craters larger than 1 km thereby not only limiting the study to recent craters but also largely eliminating contamination by secondary craters. Preservation of ray patterns and other fine-scale surface textures in the ejecta provides first-order culling of craters younger than Tycho, i.e., about 100 my. Cumulative size-frequency distributions of small craters (20–60 m) superposing 10 selected craters including sample-dated craters (South Ray, North Ray, and Cone Crater) established very similar power-law distributions between  $-2.9$  and  $-3.1$  and the statistical significance of relative age differences. The distributions were then used to normalize the counter-craters to a common diameter ( $D = 50$  m) for 60 additional craters selected from Lunar Orbiter and Apollo photographs. The normalized counter-crater density for craters sampled and dated during the Apollo missions then provided calibration for estimating absolute ages of the dated craters.

The degradation of radar haloes around recent lunar craters may provide a separate assessment of the distribution of crater ages. The freshest lunar craters exhibit a broad 3.8 cm radar halo extending up to 30 crater radii from the impact (6, 7). The diameter of the radar halo decreases with crater age, an effect that is largely independent of terrain (mare vs. highlands). This data set encompasses most of the lunar nearside whereas craters dated by the statistics of small superposed craters are restricted to Apollo and Lunar Orbiter coverage. Overlap in the two data sets permits calibrating the change in the relative size of the radar halo with time. The derived calibration yielded a correlation coefficient better than 0.95 over inferred ages from 1 to 100 my. Restricting the selection of craters to diameters from 2 to 15 km limited possible scaling effects in the processes responsible for the radar halo and eliminated craters near the resolution limit.

**Results:** Figure 1 reveals that dated-craters exhibit distinct clusters and gaps in the density of the superposed counter craters. In absolute time, there is an inferred increase in the production of craters larger than 1 km at around  $60 \pm 10$ ,  $20 \pm 5$ ,  $15 \pm 5$ ,  $7 \pm 1$  my with an additional spike between 1 and 2 my. If only craters larger than 2 km are considered, then times of increased cratering occur at about  $65 \pm 3$ ,  $15 \pm 5$ , and  $6 \pm 2$  my. If normalized to a common time interval, however, only the enhancements at 2, 7, and 15 could be considered significant. These ages are only preliminary and depend on calibrations with sampled-crater ages, but they serve to illustrate that a non-random impact flux emerges from the data. If the significance alternatively should focus on the counter craters, then the paucity of dated craters between 7 and 12 my would reflect a sudden increase in the flux added to the background random flux at about 7 my. Such an increase would have to exceed 15 times the time-averaged rate if limited to a time interval of 1 my. The gap between 20 my and 60 my would require an increase exceeding 60 times the time-averaged flux if concentrated in a 1 my time interval. The derived time-averaged impact flux producing craters larger than 50 m is about  $4/\text{km}^2/100$  my whether referenced to Tycho, North Ray, Cone, or South Ray craters, thereby supporting previous conclusions that the cumulative flux of objects producing small craters has been reasonably constant over long time intervals (i.e., the last 0.1 to 1.0 by).

The age-calibrated radar-haloed craters provided 90 craters larger than 2 km on the lunar near-side of which 15 were also in the set of 38 craters dated by crater statistics. Well-defined clusterings in ages were found at  $6 \pm 2$  my and  $15 \pm 2$  my with inferred enhanced flux rates six times higher than average. Craters with inferred ages near 6 my tightly cluster in the eastern lunar hemisphere, whereas the 15 my group broadly cluster in the western hemisphere. In contrast, craters older than about 100 my are largely confined to the eastern nearside.

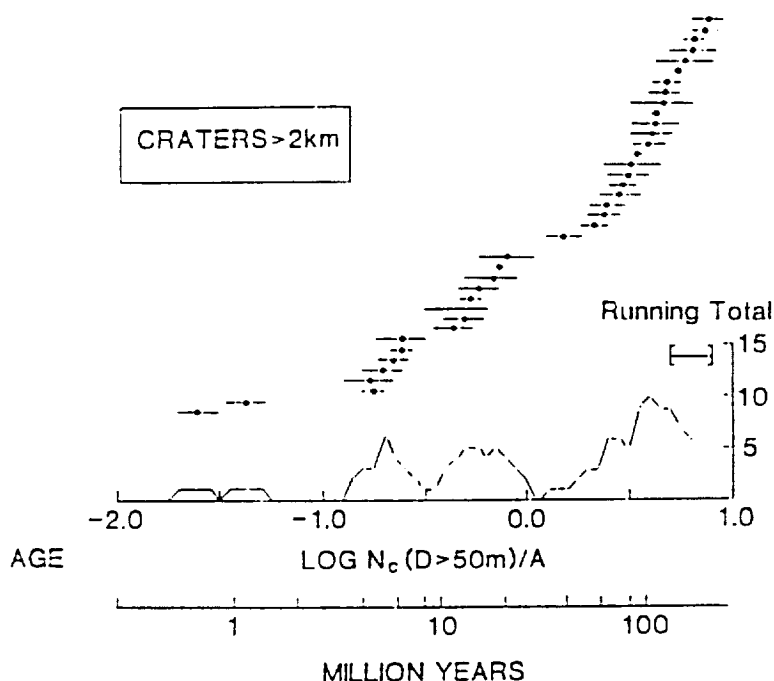
**Conclusions:** Although a periodic change in the impact flux in the Earth-Moon system cannot yet be confirmed from the data, a non-random component appears to exist with an increased flux around 7 and 15 my. The concentrations in different quadrants of the lunar hemisphere would be consistent with a shower of debris generally smaller than 0.5 km.



REFERENCES: (1) Alvarez, W. and Muller, R.A. (1984), *Nature* 308, 718-720. (2) Wilmers, D.P. and Jackson, A.A. (1984), *Nature* 313, 36. (3) Rampino, M.R. and Stothers, R.B. (1984), *Nature* 308, 709-711. (4) Guinness, E.A. and Arvidson, R.E. (1977), *Proc. Lunar Sci. Conf. 8th*, 3475-3494. (5) Drozd, R.J. et al. (1977), *Proc. Lunar Sci. Conf. 8th*, 3027-3043. (6) Thompson, T.W. et al. (1980), *Proc. Conf. Lunar Highlands Crust* (J.J. Papike and R.B. Merrill, eds.), 483-499. (7) Thompson, T.W. et al. (1981), *icarus* 4b, 201-225. (8) Burnett, D.S. and Woodrum, D.S. (1977), *Phys. Chem. of the Earth* 10, 63-101.

Figure 1. Distribution of dated craters larger than 1 km calibrated from the sampled dates of Tycho (5), North Ray (8), South Ray (8), and Cone (8) craters.

Figure 2. Histogram of dated craters larger than 2 km shown as a running total. Individual data with statistical error bars are shown above.



**SOURCES OF CLASTS IN IMPACT MELTS.** Kelli McCormick<sup>1</sup>, G. J. Taylor<sup>1</sup>, K. Keil<sup>1</sup>, P. D. Spudis<sup>2</sup>, R. A. F. Grieve<sup>3</sup>, and G. Ryder<sup>4</sup>. 1) Inst. of Meteoritics, Univ. of New Mexico, Albuquerque, NM 87131; 2) Branch of Astrogeology, U.S. G. S., Flagstaff, AZ; 3) Geophysics Division, GSC, Ottawa, Canada; 4) Lunar and Planetary Institute, Houston, TX.

Numerous studies of lunar and terrestrial impact melt rocks show that the melt matrices are chemically homogeneous (e.g., 1). The clast population within impact rocks, however, appear (at least in the lunar case) not to be representative of the chemical components in the melt matrices (2-4). To better understand clast/melt relationship, we are analyzing a suite of impact melt rocks from the Mistastin Lake Crater, Labrador, Canada. As opposed to the Moon where there is no geologic control, the target structure of this crater is well understood and there are only three types of country rocks (i.e., target material): granodiorite (a relatively minor component), quartz monzonite (also referred to as adamellite or mangerite) and anorthosite (5). Previous work on Mistastin Lake Crater indicates that the impact melt can be generated by mechanical mixing of the three rock types, calculated at about 65% anorthosite and 35% quartz monzonite plus granodiorite (5). Our preliminary data, however, indicate that the proportions of target rocks represented as clasts in the Mistastin Lake impact melts vary widely.

Polished thin sections of each type of target material and a suite of melt rock samples were analyzed with a JEOL 733 superprobe using a 10  $\mu$ m diameter beam. Feldspar grains in the three target materials were analyzed for general compositional variations within each grain as well as for compositional ranges among the separate feldspar grains of each rock type (Fig. 1). Clasts from anorthosites can be distinguished clearly from granodiorites and quartz monzonites. Feldspar clasts within each impact melt rock were also analyzed for comparison with feldspar compositions of the target material to determine the specific parent rock type for each clast. Only feldspars that clearly appeared to be clasts were analyzed. In addition, we tried analyzing only unaltered clasts. We found two general types of clast alteration: heat alteration, creating a checkerboard texture, and alteration resulting in a breakdown of the clast to what appears to be clay minerals.

We found that the percentage of each rock type as represented by the clasts varies considerably among the different melt rock samples (Table 1). Fractions of parent rock types within the impact melt rocks determined from clast populations vary from 100% anorthosite to about 66% granodiorite/quartz monzonite, 33% anorthosite. These variations are correlated with sampling location: anorthosite-rich rocks were collected on the north and west shores of Mistastin Lake, whereas those richer in granodiorite and quartz monzonite were collected on the south and southwest. There is, however, one exception: sample LM44-4B (91% anorthosite) was collected 1-2 meters above LM44-2A (34% anorthosite).

We accepted any analysis with a total oxide wt.% of between 98.5 and 101.5 and feldspar stoichiometry between 4.975 and 5.025 (5 cations based on 8 oxygens). Feldspars in a few of the rocks give low totals. In most cases, however, the stoichiometry of these points falls within our accepted 0.5% error. At present we are including the points with poor totals, but acceptable stoichiometry in our data set because (1) they plot within our country rock fields on the ternary An-Ab-Or diagram and (2) both the points with acceptable and those with low oxide wt.% sums give the same results in terms of representative lithologies (Figs. 1 and 2). These low sums may be due to the presence of water and/or glass lamellae smaller than 10  $\mu$ m within the feldspar clasts. These possibilities will be investigated.

From the data collected so far, we conclude that the clast population in the Mistastin Lake melt rocks do not quantitatively reflect the abundances of the components in the melt matrix. This may be caused by the heterogeneous distribution of the target material; that is, the preferential incorporation of clasts from one lithology over another as the melt flowed outward from the point of impact. Radial differences in the clast assemblage are clearly important, but the differences between LM44-2A and 44-4B suggest that the nature of clasts varies vertically

as well. In the lunar case an analogous situation may hold: clasts entrained in impact melts may be acquired from source areas far removed from those occurring where the melt formed. As a result, the clast population need not be representative of the components mixed into an impact melt. This work was supported by NASA Grant NAG 9-30.

References . 1) R. A. F. Grieve et al. (1977) *Impact and Explosion Cratering*, 791-814. 2) M. R. Dence et al. (1976) *PLSC 7th*, 1821-1832. 3) G. Ryder and J. F. Bower (1977) *PLSC 8th*, 1895-1923. 4) G. Ryder and J. A. Wood (1977) *PLSC 8th*, 655-668. 5) R. A. F. Grieve (1975) *GSA Bull.* 86, 1617-1629.

Table 1. Percentages of sources of clasts in melt rocks from Bistaatin Lake Crater, Labrador, Canada.

Rock	No. <sup>1</sup>	Gd-Qz <sup>2</sup>	Anor. <sup>3</sup>	Uncertain <sup>4</sup>
LM 52-A	54	0	100	0
LM 41A	34	8.8	91.2	0
LM 51BC	59	0	100	0
LM 38B	46	4.3	93.5	2.2
LM 43A	39	48.7	48.7	2.6
LM 44-2A	32	85.6	34.4	0
LM 44-4B	66	9.1	90.9	0
LM 4A	10	30	70	0
LM 55A	34	0	97	3
LM 59H	17	17.6	82.4	0

1. Number of analyses.
2. Percent of Granodiorite plus Quartz monzonite components.
3. Percent of Anorthosite components.
4. Undetermined source (either Gd-Qz or Anor.) in percent.

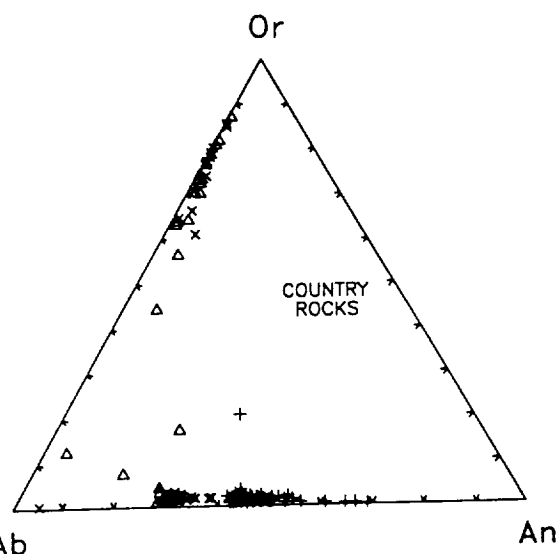


FIGURE 1. Feldspar compositions in country rocks (x = quartz monzonite, + = anorthosite, triangle = granodiorite).

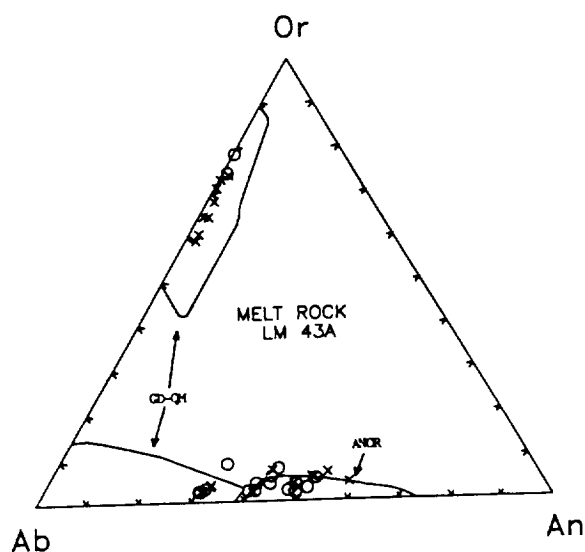


FIGURE 2. Feldspar compositions in melt rock LM 43A (o = good sums, x = bad sums).

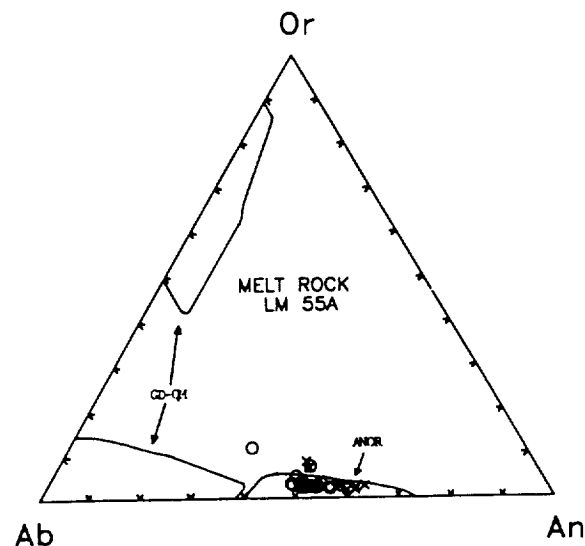


FIGURE 3. Feldspar compositions in melt rock LM 55A (o = good sums, x = bad sums).

## JETTING AND THE ORIGIN OF TEKTITES

A. M. Vickery, Lunar and Planetary Laboratory, University of Arizona, Tucson, AZ 85721

The origin of tektites was a hotly debated subject for many years. Tektite strewn fields extend hundreds to thousands of kilometers across the earth's surface, and the problem of propelling molten material through the earth's atmosphere without disrupting it into a fine mist (1) led a number of investigators to propose an extraterrestrial origin for tektites (2,3). A large amount of geochemical evidence, however, strongly suggests that tektites were produced by the (presumable impact-induced) melting of terrestrial sediments (4), and most people now believe that the terrestrial origin of tektites has been proved beyond a reasonable doubt (e.g.5). The most widely-cited mechanism for tektite production is jetting during the early stages of impact, although the only previous dynamic study of jetting with regard to this problem (1) concluded that the jet would break up into a fine mist. The problem is compounded by the evidence from the primary shapes and ablation characteristics of the australites, which strongly suggests that they solidified as spheres (implying extremely low differential pressures) and subsequently entered the earth's atmosphere from above (2).

In this study, the theory of jetting due to the collision of thin plates (6-10) was extended to the case of the impact of a sphere at arbitrary impact speed  $U$  and angle  $\alpha$  from the vertical onto a half-space (c.f. 11). The tangent to the sphere at the locus of intersection is assumed to correspond to the upper plate and the surface of the target, to the lower plate. There are two frames of reference that are typically used in jetting studies: In the standard frame, the two plates converge with equal and opposite velocities  $v_p$  perpendicular to the plates, the jet is directed along the bisector of the angle ( $2\theta$ ) between the plates, and the locus of intersection  $P$  moves forward as the plates converge. Jetting will only occur if  $\theta > \theta_{crit}$  (7-9), where  $\theta_{crit}$  is a function of  $v_p$ . The jet velocity is

$$v_j = |v_p| \left( \frac{1 + f \cos \theta}{\sin \theta} \right)$$

where  $f \sim 1$  from experiments. In the collision frame, the material in the plates moves with a velocity  $v_o = v_p \cot \theta$  along the plates into the now stationary intersection  $P$ . The jet velocity in this frame  $v_1 = f v_o \sim v_o$ , combined with information on the jet width (10) essentially gives the rate at which material is fed into the jet. In addition to these two frames of reference, the current problem requires the target frame, in which the target half-space is stationary, and the convergence velocity depends on both the impact velocity and the current geometry (the degree of penetration of the sphere into the half-space). The jet velocity in this frame is the ejection velocity relative to a stationary target and is initially unknown. A vector  $v_t$  is derived to translate from the target frame to the standard frame, which requires the assumption of differential slip within the jet (asymmetric jetting (7)). The translation vector is then applied in reverse to  $v_j$  to get the jet velocity in the target frame  $v_j'$ ;  $v_j'$  is not directed along the bisector of the angles between the converging surfaces nor is it directly radial from the center of impact. Similarly, the relation between the target and collision frames permits an estimate of the mass flux into the jet. Because jetting is asymmetric, the projectile and target contribute different amounts of mass to the jet.

The pressure at the stagnation point  $P$  was estimated using the method of (12) using a piece-wise linear shock velocity-particle velocity equation of state for olivine. It was assumed that release from pressures of  $7.3 \times 10^{10}$  Pa,  $1.0 \times 10^{11}$  Pa, and  $5.0 \times 10^{11}$  Pa would result in melting, incipient vaporization, and complete vaporization, respectively. A computer code was developed that calculates the mass ejected, its phase, the ejection speed, elevation and azimuthal ejection angles, and projectile fraction within the jet as functions of time. Mass averages of these quantities were calculated for each timestep and for the entire duration of jetting.

Because jetting is a hydrodynamic process, the mass jetted scales rigorously with the mass of the impactor; thus all the calculations involve an impactor with radius 100 m (density 3200 kg/m<sup>3</sup>). Impact velocities of 15, 20, and 25 km/s and impact angles ranging from 0° (vertical) to 75° in 15° increments were used.

RESULTS: (1) Overall Mass Averages: The total mass jetted increases with impact velocity ( $U_i$ ) and decreases (slightly) with increasing obliquity of impact for  $\alpha = 0 - 60^\circ$ , then increases for  $\alpha = 75^\circ$ . The increase is more pronounced at lower  $U_i$ . In all cases, vapor dominates the jet, most strongly at higher  $U_i$  and low  $\alpha$ . Overall jet velocity increases with  $U_i$  and decreases with increasing  $\alpha$ . Again, vapor strongly dominates except at  $\alpha = 75^\circ$ . The mean elevation angle of the jet increases with  $\alpha$  from  $\sim 7^\circ$  at  $\alpha = 0^\circ$  to  $20-25^\circ$  at  $\alpha = 75^\circ$ , with melt generally ejected at higher angles than the vapor. The projectile fraction in the jet ( $F_p$ ) varies between 0.40 and 0.50 and increases slightly with  $\alpha$ ;  $F_p$  in the melt ranges from  $\sim 0.2$  at high  $U_i$  and low  $\alpha$  to  $> 0.5$  at high  $\alpha$ . Jetting is azimuthally symmetric for  $\alpha = 0^\circ$ , and becomes increasingly focussed downrange with increasing  $\alpha$ . In general, the melt fraction is more concentrated downrange than the vapor fraction.

(2) Time Dependence: The mass flux is maximum at the onset of jetting and declines more rapidly for more nearly vertical impacts. Except for  $\alpha = 0^\circ$ , the mass flux either levels off, or goes to a local minimum and then increases slightly before a final decline; this effect is less pronounced at higher impact velocities and smaller  $\alpha$ . Similarly the jet velocity is greatest at the onset of jetting; the lower  $\alpha$ , the greater the initial velocity and the more rapid its decline. Vapor is ejected first and at the highest velocities. At  $U_i = 15$  km/s, the elevation angle is initially  $< 5^\circ$  for all  $\alpha$  and increases with time and  $\alpha$  to a maximum of  $\sim 35^\circ$  at  $\alpha = 75^\circ$ . The azimuthal extent of jetting decreases with increasing obliquity and with time at a given obliquity.

APPLICATION TO TEKTITE FORMATION: Although these results are preliminary, they suggest that for reasonable asteroidal impact velocities, a very high velocity vapor jet is produced that, as it expands adiabatically, can engulf and accelerate a significant volume of ambient atmosphere away from the impact site. The melt fraction of the jet is thus ejected into a much rarified ambient atmosphere, suppressing break-up of the molten jet. Whether and under what conditions this can explain the extraordinary extent of the Australasian and North American strewn fields and particular characteristics of the australites is beyond the scope of this study.

REFERENCES: (1) E. Adams (1965) *N. Jb. Miner. Mh.* **9**, 332. (2) D. R. Chapman and H. K. Larson (1963) *J. Geophys. Res.* **68**, 4305. (3) J. A. O'Keefe (1976) *Tektites and Their Origin*, Elsevier, N.Y. (4) S. R. Taylor (1973) *Earth Sci. Rev.* **9**, 101. (5) R. Brett and M. Sato (1984) *Geochim. Cosmochim. Acta* **48**, 111. (6) G. Birkhoff et al. (1948) *J. Appl. Phys.* **19**, 563. (7) J. M. Walsh et al. (1953) *J. Appl. Phys.* **24**, 349. (8) W. A. Allen et al. (1959) *Phys. Fluids* **2**, 329. (9) L. V. Alt'schuler et al. (1962) *Sov. Phys. JETP* **14**, 986. (10) F. H. Harlow and W. E. Pracht (1966) *Phys. Fluids* **9**, 1951. (11) H. J. Melosh and C. P. Sonnet (1986) in: *Origin of the Moon* (Hartmann, Philips, and Taylor, eds.) L.P.I., Houston. (12) S. W. Kieffer (1977) in: *Impact and Explosion Cratering* (Roddy, Merrill, and Pepin, eds.) Pergamon, N.Y.

### **Jetting: A Semi-Analytic Approach**

A. M. Vickery (Lunar and Planetary Lab, University of Arizona, Tucson, AZ 85721; 602-621-2703)

Jetting has not received much attention as a part of the impact process, presumably because it is of short duration and involves very little material relative to the main excavation flow. It is difficult to observe in detail experimentally or to resolve numerically with hydrocodes designed to model the main features of an impact. Furthermore, jetting seems to leave few traces after the impact event is over, with the possible exception of tektites (and maybe the moon). A semi-analytic model for jetting produced by the impact of a sphere on a half-space has been developed. Variables include impact angle and velocity, impactor radius, and material. A linear equation of state was employed. Vapor and melt fractions were estimated by assuming that material subjected to pressures of  $7.3 \times 10^{10}$  Pa,  $1.0 \times 10^{11}$  Pa, and  $5.0 \times 10^{11}$  Pa would melt, begin to vaporize, and completely vaporize, respectively, upon release from pressure. The code calculates the mass ejected as a function of time, along with ejection velocity, ejection angles (vertical and azimuthal), and the fraction of jetted material ( $F_p$ ) that is contributed by the projectile. Mass-averages for these quantities were calculated for each timestep and for the entire duration of jetting.

So far, calculations have been done for a vertical impact and for an impact  $15^\circ$  above the horizontal, both with impact velocities of 15 km/sec and a 200-m radius impactor. EOS parameters for dunite were used for both projectile and target. For the vertical impact,  $1.088 \times 10^9$  kg are ejected, 69.1% as vapor and the rest as melt. The maximum (=initial) jet velocity is 42.08 km/sec; the overall mass-averaged ejection velocity is 17.38 km/s. Jetting occurred over all azimuths symmetrically.  $F_p$  is initially  $\sim 0.45$  and decays with time; the overall average  $F_p$  is  $\sim 0.29$ . In contrast, jetting in the case of the very oblique impact started later, lasted longer, and ejected about 5 times as much material. The maximum jet velocity was 24.34 km/sec, with an overall average of  $\sim 15$  km/sec. As might be expected, the jet was concentrated in the down-range direction: when jetting begins, the mass-averaged ejection azimuth is  $\pm 30^\circ$  with respect to the down-range direction and it decays to  $\pm 5^\circ$ .  $F_p$  reaches a maximum of almost 0.70, with a mass-average of 0.58.

These preliminary results indicate a substantial increase in the amount of material jetting as impact angle decreases toward the horizontal, but not the spectacular increase inferred by Schultz and coworkers from their experiments. The model as currently developed, however, cannot treat an impactor and target of different materials such as were used in the experiments. Whether tektites can be demonstrated to result from jetting depends on an analysis of the interaction of the jet with the ambient atmosphere.



## INTENSE EARLY BOMBARDMENT AND ITS EFFECTS ON PRIMORDIAL EARTH

David H. Grinspoon, Lunar and Planetary Lab., Univ. of Arizona, Tucson, AZ and William K. Hartmann, Planetary Science Institute, Tucson, AZ

The integrated mass flux necessary to accumulate the Earth in the permitted formation interval of some 10-100 My yields an initial mass flux 4.55 Gy ago of the order  $10^9$  x the present flux (1). Studies of the lunar cratering record at dated Apollo and Lunar landing sites indicate that 4.0 Gy ago, the impact rate was roughly  $10^3$  x the present rate (2). These figures correspond to a half-life of some 24 My, averaged over the first few hundred My, in the planetesimal population, and slowly lengthening.

Coupling these results, we investigate the possibility that this dramatically declining flux represents a relatively smooth sweepup of planetesimals left over after Earth's formation. Wetherill (3) studied the dynamical properties of leftover planetesimals in an effort to explain a hypothetical terminal catastrophe, or short, sudden bombardment that was once hypothesized to have occurred 4 Gy ago. Although Wetherill's models were aimed at explaining the supposed cataclysm, one of the models showed the plausibility of a relatively smooth decline with an early half-life of 20-30 My, just as we observe. The analysis suggests that the half-life would slowly increase, as bodies are pumped up into more inclined and eccentric orbits due to close encounters with Earth. This matches the observations.

Based on these consistencies between the observed record and the dynamical analysis of planetesimal calculations, we attempt to reconstruct a plausible impact rate for primordial Earth as a function of time during its first few hundred My.

The extremely high impact rates have numerous possible consequences, some of which have already been discussed elsewhere. These include: a) a giant impact of the second largest body in Earth's zone, dislodging the material that formed the moon (4); b) disruption of any early homogeneous crust that was forming, with impact basins causing thin spots in some areas and piling up crustal debris in pseudo-continental masses in other areas (5); c) exposing the hot mantle and helping to initiate convection and plate tectonic motions (6); d) severe climatic consequences due to the constant dust pall of ejecta (7); e) impact frustration of the origin of life until the impact rate declined (8).

1. Hartmann, W.K. (1972). Astrophys. Space Sci. 12, 48-64.
2. Hartmann, W.K. (1980). Proc. Conf. Lunar Highlands Crust.
3. Wetherill, G.W. (1975). Proc. Lun. Sci. Conf. 6, 1539-61.
4. Hartmann, W.K. and D.R. Davis (1975). Icarus 24, 504-515.
5. Hartmann, W.K. (1987). Proc. Oxford Conf. Growth Early Crust.
6. Frey, H. (1977). Icarus 32, 235.
7. Grinspoon D.H. and C. Sagan (1987). Proc. Penn State Univ. Workshop on Long-Term Stability of the Earth System.
8. Maher, K.H. and D.J. Stevenson (1987). Nature 33, 512-614.

EFFECT OF EARLY IMPACT CRATERING ON GROWTH OF THE EARTH'S CRUST  
William K. Hartmann (Planetary Science Institute, Tucson, AZ 85719)

Some models of early evolution of Earth's crust have assumed that all evolutionary forces on the early crust arose from the inside of the planet, an example being tectonic activity. Such models might assume (for mathematical simplicity) a spherically symmetric primordial crust of uniform thickness, eventually broken by tectonic forces.

Such models are too simple. Current work reveals an early intense bombardment of Earth from outside the planet, by meteorite or asteroidal debris left over from Earth's formation. These included very large bodies, capable of making impact events that would affect continental-scale or hemispheric-scale regions. Some lines of evidence include (1) lunar crater counts; (2) 1000-km-scale impact basins on the moon, older than 3.9 Gy; (3) accretion of many asteroids up to 1000 km; (4) the hemispheric crustal asymmetry of Mars, possibly affected by early impacts; (5) the currently favored theory of lunar formation triggered by impact of a giant impact that blew out much of Earth's mantle -- the debris from which the moon apparently formed (Hartmann and Davis, 1975, Icarus).

The impact rate necessary to accumulate Earth and the moon within the permitted formation interval must have been some 10 x greater than the present flux, during the first few My of Earth's history (Hartmann 1980, Proc. Conf. Lunar Highlands Crust). Lunar crater counts show that even 500 My later, the flux was still some  $10^3$  x the present value. The implied rate of decline is consistent with the calculated sweep-up of the Earth-forming planetesimals during their collisions with Earth.

Earth's crustal development was affected in several ways. Large, basin-forming impacts, scattered through the first 500 My, excavated any crustal layers and piled up the debris in rim deposits. Therefore, primordial crust was not uniform, but patchy, and heterogeneous in thickness. Frey (1977, Icarus) proposed that exposure of hot mantle at impact sites triggered more rapid convection at these sites, initiating a sort of plate tectonics, perhaps with thick regions of crustal ejecta representing initial continental blocks.

Impacts of the scale of the hypothetical KT boundary event happened roughly annually during the first few million years. Thus, there were strong effects on climate and initial biochemical evolution (Grinspoon and Sagan, 1987, Proc. Penn. State Workshop on Long-Term Stability of the Earth System). David Grinspoon (Univ. Arizona) and the author are currently working on more detailed models of the intense impact rate.

The hypothesis that impacts caused major climate and biologic catastrophes at the end of the Cretaceous faces numerous paradoxes including: evidence for protracted extinctions (1), non-uniform but widespread dispersal of the meteoritic signature, conflicting evidence for oceanic (2) and continental (3) impact sites, indications of intense fires (4), massive nitrate production (5), and the absence of a putative crater of sufficient size. Not every known major impact can be associated with a biologic catastrophe as extreme as at the close of the Cretaceous. Either a rare set of geologic/environmental conditions is needed to enhance the effects of a particular impact, or a rare but probable impact condition must be invoked to increase the climate/biologic response. The latter alternative is addressed here by exploring further the suggestion (6, 7) that an oblique impact could significantly amplify normally cited vertical impact. Cited collision rates implicitly assume a 45° impact angle. If a 10-km diameter impactor represents a 40 my event, then a 15° and 10° strike represent a 300 my and 670 my event, respectively. The fate of the projectile (physical state, fragmentation, dispersal) and coupling with the atmosphere are key issues that are addressed here.

**Approach:** Laboratory experiments permit exploring the partitioning of energy and projectile fate as a function of impact angle. Although such laboratory experiments are at small scale, they nevertheless establish the first-order relative effects of impact angle and provide an important reference for testing computational experiments. Two series of experiments were performed at the NASA-Ames Vertical Gun Range for a given impact size (0.635 cm) and type (aluminum): the first varied impact velocity (2–6.3 km/s) with a constant impact angle (15°); the second varied impact angle (2.5–30°) with constant impact velocity (5.5 km/s). Aluminum witness plates placed downrange registered the degree and distribution of projectile fragmentation. Scaling laws for impacts into aluminum over the same range of velocities (and including projectile size effects, 8) permitted converting apparent pit diameter (referenced to the pre-impact surface) into fragment mass and mean fragment velocity by an iterative solution. First, individual fragment mass was derived from pit diameter with the assumption that the ricochet velocity was equal to the initial impact velocity. The assumed impact velocity was then reduced iteratively until the total calculated fragment mass was equal to the original impactor mass. This approach presumes that all of the high-velocity ricochet debris is comprised of projectile rather than target fragments. Previous studies indicated that at low impact angles (<30°), projectile fragments dominate the downrange debris (9, 10); hence, this approach establishes a lower limit to the ricochet energy fraction ( $KE_r/KE_i$ ). The derived ricochet energy added to the energy expended in excavating the crater in sand (ejecta plus compaction) as a function of impact angle demonstrated that total energy was conserved for the given impact conditions.

Fragmentation of a given projectile (type, size) was first examined as a function of specific energy ( $Q = KE_i/m_p$  = projectile kinetic energy divided by projectile mass), thereby paralleling analyses of bulk fragmentation of large bodies by small impactors (11). The percentage of fragments larger than a given mass fraction ( $m_L/m_p$ ) as a function of specific energy provides a measure of the degree of fragmentation. The onset of fragmentation should be reflected by either the largest fragment mass ( $m$ ) or the mass fraction fragmented more than once ( $1-m_L/m_p$ ). Derived cratering efficiencies into solid targets (9) suggest that the peak stress during impact varies as  $\sin^2\theta$  where  $\theta$  is the impact angle from the horizontal. Hence, the normal stress experienced by the projectile can be given by  $\sin^2\theta$  where  $n$  is derived either empirically or from physical considerations.

**Results:** Gault and Wedekind (9) previously demonstrated that projectile fragmentation depends on velocity and angle for a given projectile and target. The present analysis reveals two regimes of failure resembling disruption of larger suspended targets (12, 13): limited and complete. Limited disruption of the projectile is characterized by a single, large fragment ( $>0.3 m_p$ ), whereas complete disruption is characterized by the largest fragment mass less than about 0.1  $m$ . The simple expression  $Q\sin^2\theta = 1/2 v^2\sin^2\theta$  (i.e.,  $n = 1$ ) was found to accommodate the mass-frequency distribution of small fragments ( $m/m_p < 0.01 m$ ) for both limited and complete disruption. The same function accommodated data for the largest single fragment mass provided that complete projectile disruption occurred, i.e.,  $\theta \geq 15^\circ$  and  $v \geq 4$  km/s. Limited disruption characterizing lower impact angles and velocities required a larger exponent, i.e.,  $Q\sin^3\theta$  ( $n = 3$ ). This latter result can be shown to reflect the combined effects of three competing internal energy-loss processes in the projectile that cannot be neglected at very low impact angles. First, the maximum vertical compressive stress developed at impact reduces as  $\sin^2\theta$  as derived either from balancing observed energy expended in crater excavation and kinetic energy in the ricochet fraction or from the impact-angle dependence on

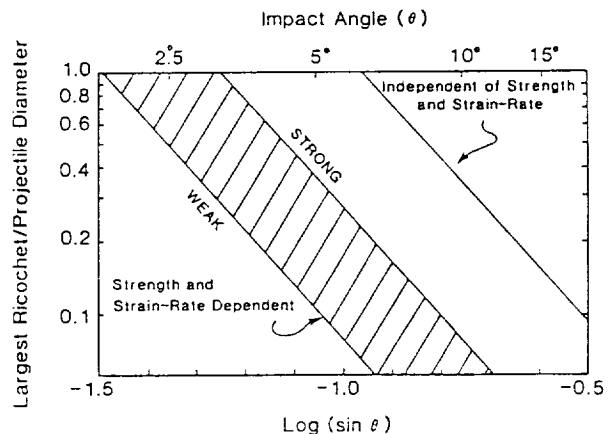
cratering efficiency in strength-limited targets. Second, a fraction of this transferred normal stress, however, will be lost due to shear heating along the projectile/target interface and will not be available for bulk projectile disruption. On the basis of an impact-angle dependence on vaporization of easily volatilized targets (14), this factor also depends on  $\sin^2\theta$ . Third, multiple fragmentation and localized spallation of the projectile further reduces the specific energy available for complete catastrophic disruption. The frequency distribution of the smallest fragments produced during limited disruption indicates a  $\sin^2\theta$  dependence as well. Hence, a  $\sin^6\theta$  dependence can be derived for limited projectile disruption.

The distinction between limited and complete projectile disruption also could be viewed as a distinction between shock and mechanical failure at high and low stress levels (and strain rates), respectively. Moreover, conditions leading to projectile failure should resemble conditions leading to target failure. With these two perspectives, the two disruption regimes can be compared with data from Davis and Ryan (13). When complete shock-controlled disruption is assumed and a correction factor for impedance matching is included, conditions for complete disruption (high  $v$  and  $\theta$ ) lead to a close match between projectile disruption and target disruption, even with a factor of 20 contrast in object size and up to a factor of 60 in object strength. Conditions leading to limited disruption (low  $v$  and  $\theta$ ), however, are not accommodated. For limited disruption largely controlled by mechanical failure, data for low  $v$  and  $\theta$  are now consistent for both data sets, whereas data for high  $v$  and  $\theta$  are not. A single expression can be derived that incorporates both failure conditions.

**Implications:** At much broader scales, strain-rate and strength effects may be important and need to be introduced. Figure 1 has incorporated a nominal case derived in (15) using dimensional analysis and provides a first-order range of estimates for the largest fragment surviving a 20 km/s impact from an initial 10 km-diameter object as a function of impact angle. At the very least, Figure 1 indicates that the projectile signature could be carried downrange ballistically, rather than entrained in the ejecta. Because the ricochet angle is typically lower than the impact angle (9), this fraction would induce increased coupling with the atmosphere and could create a broad, long, and potentially intense fire-line largely decoupled from the impact site. At sufficiently low impact angles, a single, large impactor could spawn numerous smaller but still substantial ricochet fragments impacting a wide range of geologic settings. From the laboratory analyses, the ricochet velocities asymptotically approach about  $0.5 v$  with increasing impact velocities at a given impact angle ( $15^\circ$ ). Consequently such fragments should produce a global deluge of hypervelocity debris re-entering the atmosphere. Because the consequences of low-angle impacts have not yet been fully explored, our interpretations could be considered in part speculative. Nevertheless, the mechanics and phenomena of low angle impacts are grossly different from the nominal high-angle impact scenarios and necessitate further serious study.

(1) Keller G. (1988) in *Global Catastrophes in Earth History*, pp. 88-89. LPI Contrib. 673. (2) Hildebrand A.R. and Boynton W.V. (1988) in *Global Catastrophes in Earth History*, pp. 76-77. LPI Contrib. 673. (3) Sharpton V.L. et al. (1988) in *Global Catastrophes in Earth History*, pp. 172-173. LPI Contrib. 673. (4) Wolbach W.S. et al. (1985) *Science* 230, pp. 167-170. (5) Prinn R. and Fegley B. (1987) *Earth Planet. Sci. Lett.* 83, pp. 1-15. (6) Schultz P.H. and Gault D.E. (1982) in *Geol. Soc. Am. Sp. Paper* 190, pp. 153-174. (7) Schultz P.H. and Gault D.E. (1988) in *Global Catastrophes in Earth History*, pp. 166-167. (8) Denardo P. et al. (1967) *NASA TN D-4067*. (9) Gault D.E. and Wedekind J.A. (1978) *Proc. Lunar Planet. Sci. Conf.* 9th, pp. 3843-3875. (10) Gault D.E. and Schultz P.H. (1986) *Meteoritics* 21, pp. 366-369. (11) Gault D.E. and Wedekind J.A. (1969) *J. Geophys. Res.* 74, pp. 6780-6794. (12) Fujiwara A. et al. (1977) *Icarus* 31, pp. 277-288. (13) Davis D.R. and Ryan E.V. (1988) On collisional disruption: Experimental results and scaling laws (preprint). (14) Schultz P.H. (1988) *Lunar and Planet. Sci.* XIX, pp. 1039-1040. Lunar and Planetary Institute, Houston. (15) Holsapple K.A. and Housen K.R. (1986) *Mem. S. A. It.* 57, pp. 65-85.

**Figure 1.** Size of the largest ricochet fragment surviving an oblique impact by a 10 km-diameter object at 20 km/s based on projectile and target fragmentation in the laboratory.



Abstract

A chief discovery from 25 years of planetary exploration by spacecraft is the pervasive role played by impacts. Recently it has been recognized that such major features of the solar system as the high bulk density of Mercury and the existence of Earth's moon were caused by "worlds in collision." Since that epoch of planetary formation, cratering bombardment by comets and asteroids continues to control the geology of some planets. Even on the tectonically active Earth, rare large impacts -- such as the hypothesized event responsible for the Cretaceous-Tertiary extinctions -- continue to have major, if sporadic, effects on climate and on biological evolution.

The cratering record from the beginning of the late heavy bombardment until now shows that the impact process has always been inherently "catastrophic" in the sense that the largest, rarest impacts surpass the cumulative effects of all the smaller, more frequent, intervening impacts. This unique feature of the impact process, stretching over dozens of orders of magnitude in energy, is due to the  $-3.5$  incremental power-law index that is characteristic of a population of collisional fragments. Observations of lunar and planetary crater populations, assessment of asteroid populations, and theoretical and experimental studies of cratering and fragmentation all confirm this trait of impactors, which guarantees that the energy and volumetric damage is dominated by the biggest events. The same principles apply to the threat to our civilization posed by Earth-approaching objects, such as 1989 FC, which "narrowly" missed the Earth on March 23rd.

**INTRODUCTION:** Although the Moon and Mars both preserve large impact structures over 200 km in diameter, no structure of this size has been recognized on Earth and only four impact structures larger than 100 km in diameter have been identified (1). Because most of the Earth's surface is significantly younger than surfaces on the Moon and Mars, it should be less heavily cratered. Nevertheless, 8 to 24 continental structures greater than 100 km in diameter are expected world-wide (Table 1), based on estimated terrestrial impact flux rates (2) and observed continental basement ages. If the average ocean floor age is 125 Ma, an additional 3 to 9 craters over 100 km in size would be expected in the ocean basins. Since the impact flux has decreased over time (3), the number of continental impact structures in the precambrian terrains may be much greater than the above estimates. These observations prompt the question of why more large impact structures (>100 km) have not been recognized on Earth. Erosion and sedimentation can obscure impact structures, and these effects have been addressed in detail by Grieve and Robertson (4). Large impacts also may be unrecognized, however, because of significant differences in the preserved appearance from impacts of smaller size. This alteration in appearance could reflect either later tectonic/volcanic modification or a change in the nature of cratering at larger sizes. The following discussion, therefore, first contrasts the modification of the largest observed terrestrial structures with observations from Mars and the Moon, and then considers possible changes in crater expression as the transient cavity size exceeds the lithospheric thickness, thereby complicating simple analogies with smaller structures.

**DISCUSSION:** Large terrestrial craters are best preserved in regions of stable continental crust and only one of the 8 largest terrestrial craters does not lie in a cratonic or shield unit (Table 2). The two largest, Sudbury and Vredefort, are both estimated to be ~140 km in diameter and are also the two oldest identified impact structures, although sufficient anomalous features relative to traditional impact models occur in both structures that endogenic as well as impact origins have been proposed (5,6,7). Of the two structures, Vredefort is the least altered by regional tectonism, but erosion has removed most of the surface structure to expose the underlying central uplift of the lower crust. In contrast, Sudbury has been heavily faulted, tilted and foreshortened, but preserves a significant section of the interior basin-filling deposits. Both craters should have excavated significant sections of the crust, but do not appear to have penetrated the local crustal section. At Vredefort the exposed central uplift represents a vertical crustal section some 12-15 km thick (8), while isotopic studies of the Sudbury Igneous Complex indicate a melt source above the mantle in the lowermost crust (9). The primary difference between the two impact sites appears to be the tectonic environment at the time of impact; Vredefort lies in a depositional basin in the craton interior (5,6), while Sudbury formed on an accreting craton edge during the Penokean orogeny (10). Two questions arise from these observations: why are structures excavating to mantle depths not recognized on Earth, and what is the role of cratonic regions in preserving large impact structures?

Several processes can localize deformation around large impact craters. On Mars, isostatic adjustment and lithospheric loading following the largest basin impacts lead to a characteristic sequence of radial and concentric fracture sets that control later volcanic conduits (11,12). On the Moon, large mare basins have features comparable to those in the martian basins, but a much smaller crater 40 km in diameter (Haldane) also exhibits similar radial and concentric fracture patterns and associated volcanic features (13). Application of analytical flexural models to these Haldane fractures requires a local mechanical lithosphere less than 10 km thick for crater-filling loads. Since Haldane formed during local mare volcanism and most lunar craters of the same size show no sign of similar modification, it appears that such extensive modification requires a locally high heat flux and thin lithosphere accompanying regional mare volcanism. Because isostatic adjustment, lithospheric loading and regional volcanism are also typical terrestrial processes, large impact structures (>100 km) on the Earth should be even more conducive to such modification than Haldane. The tectonically derived elliptical outline and concentric and radial volcanic dike patterns around Sudbury, in fact, may be a more typical pattern for large terrestrial impacts than Vredefort with its simple circular uplift and overturned collar. With this model, the preferential identification of craters in the cratonic regions reflects the reduced heat flows and geologic activity of these regions that would tend to limit such modification.

Recent studies of multi-ring basins on Mars and Callisto (11,12,14,15) also indicate that the nature of impact-induced fracturing may change at large crater sizes as the transient cavity size approaches the lithospheric thickness. Transient cavities penetrating an elastic layer to an underlying viscous region can induce concentric lithospheric fracture to great distances beyond the crater rim. Such a process has been proposed for both the formation of the extensive ring scarp system around Valhalla on Callisto (14,15) and the concentric canyons around the Hellas basin on Mars

over 600 km outside the outer, Cordillera-equivalent scarp (12). For extremely low underlying viscosities, this mechanism predicts complete disruption of the lithosphere (14), thereby providing a mechanism for effectively masking or even destroying the largest terrestrial impact structures. Impact structures smaller than some critical size defined by the elastic layer thickness, however, should be unaffected by such modification. If a 5:1 transient cavity diameter/depth ratio is assumed, typical flexural thicknesses for oceanic and continental lithospheres imply maximum preserved crater diameters of 150–250 km and ~300 km respectively, over twice the size of the largest observed structures. If the elastic layer instead reflects crustal thicknesses, then a maximum preserved diameter of 150–200 km (continental) and ~50 km (oceanic) would be expected. These values are consistent with the absence of identified mantle-excavating impacts and would place the Sudbury and Vredefort structures near the limit of expected crater sizes.

Reduction in elastic layer thickness to a value near that of the crustal thickness has several possible causes. First, reduced lithospheric thicknesses would be expected in the past due to increased radiogenic and convective heat fluxes (16). Second, the elastic layer in the impact environment, due to shock effects and impact heating, may not correspond directly to a flexurally or thermally defined lithosphere. In either case, preservation of large craters would be less likely in regions of high heat flow and thus the preferential identification of large craters in cratonic regions would reflect the reduced heat flows typical of these regions. More poorly preserved structures like Sudbury would be predicted for impacts into thermally active regions.

**CONCLUSIONS:** Only a fraction of the expected number of large (>100 km) terrestrial impact structures have been identified and those which are recognised are preferentially located in cratonic shield regions where they have not penetrated the local crustal sections. We propose that two processes, in addition to erosion and sedimentation, may help to account for the other unrecognized impact structures. First, large impacts should be preferred sites for tectonic and volcanic modification; the original impact origin of some tectonic/volcanic centers may thus have been obscured. Second, the absence of mantle-excavating structures in the identified impact record may reflect an increased disruption of the lithosphere associated with impacts whose transient cavities penetrated to viscous rheologies at depth. Ongoing theoretical models may help to characterize possible diagnostic clues for focussing further study of these modification processes.

**REFERENCES:** 1) Grieve, RAF and Robertson, PB (1987) Map 1658A, Geological Survey of Canada. (2) Grieve, RAF (1984) *J. Geoph. Res.* 89, B403–B408. (3) Hartmann, WK (1975) *Icarus* 24, 181–187. (4) Grieve, RAF and Robertson, PB (1978) *Icarus* 38, 212–219. (5) Schreyer, W (1982) *J. Petrology* 24, 26–47. (6) Simpson, C (1978) *Trans. Geol. Soc. S. Afr.* 81, 115–121. (7) Muir, TL (1984) in *The Geology and Ore Deposits of the Sudbury Structure*, Pye, EG, Naldrett, AJ and Giblin, PE eds, Ontario Geological Survey Special Volume 1, pp. 449–490. (8) Hart, RJ, Nicholaysen, LO and Gale, NH (1981) *J. Geoph. Res.* 86, 10639–10652. (9) Faggart, BE Jr, Basu, AR and Tatsumoto, M (1985) *Science* 230, 436–439. (10) Peredery, WV and Morrison, GG (1984) in *The Geology and Ore Deposits of the Sudbury Structure*, Pye, EG, Naldrett, AJ and Giblin, PE eds, Ontario Geological Survey Special Volume 1, pp. 491–512. (11) Wichman, RW and Schultz, PH (1987) *Lunar Planet. Sci. Conf.* 18, 1078–1079. (12) Wichman, RW and Schultz, PH (1988) *EOS* 69, 390. (13) Wolfe, RW and El-Baz, F (1976) *Proc. Lunar Sci. Conf.* 7, 2903–2912. (14) McKinnon, WB and Melosh, HJ (1980) *Icarus* 44, 454–471. (15) Melosh, HJ (1982) *J. Geoph. Res.* 87, 1880–1890. (16) Schubert, G, Cassen, P and Young, RE (1979) *Icarus* 38, 192–211. (17) Windley, BF (1984) *The Evolving Continents* (John Wiley and Sons, Ltd; New York, N.Y.).

TABLE 1: PREDICTED IMPACTS ON CONTINENTAL SURFACES

AVE AGE (Ma) <sup>1</sup>	AREA (10 <sup>6</sup> km <sup>2</sup> ) <sup>1</sup>	EXPECTED N(>100)	
		A <sup>2</sup>	B <sup>3</sup>
225	40.6	(7)	2
675	37.8	2	5
1125	14.6	1	3
1475	8.37	1	2
2025	20.6	3	9
2475	6.03	1	3
2925	1.03	(.2)	(7)

<sup>1</sup> derived from Windley (17) fig 22.16.

<sup>2</sup> derived from an impact flux of 2 N(>20)/10<sup>6</sup> km<sup>2</sup>/1000 Ma

<sup>3</sup> derived from an impact flux of 5.5 N(>20)/10<sup>6</sup> km<sup>2</sup>/1000 Ma

TABLE 2: THE 8 LARGEST TERRESTRIAL IMPACT STRUCTURES

NAME	SIZE (km)	AGE (Ma)	GEOLOGIC SETTING
Sudbury	~140	1850	Canadian Shield
Vredefort	140	1970	Kapvaai craton, S. Africa
Manicouagan	100	210	Canadian Shield
Popigai	100	39	Anabar Shield, Siberia
Puchez-Katunki	80	183	central Russian craton
Kara	60	57	coastal sediments, USSR
Siljan	52	368	Baltic Shield, Sweden
Charievoix	46	360	Canadian shield edge

AN IMPACT INTERPRETATION OF THE PROTEROZOIC BUSHVELD-VREDEFORT COMPLEXES,  
SOUTH AFRICA

Wolfgang E. Elston, Department of Geology, University of New Mexico,  
Albuquerque, New Mexico 87131, and David Twist, Institute for Geological  
Studies of the Bushveld Complex, University of Pretoria, Pretoria 0002,  
South Africa.

Bushveld Complex and Vredefort Dome (Fig. 1) are unique and penecontemporaneous (~ 2.0 - 2.1 Ga); both show evidence of catastrophic events in the shallow marine environment of the otherwise stable Kaapvaal Craton. Explanation by multiple impacts of an asteroid brecciated by an inter-asteroidal collision and disintegrating in Earth's gravity field (1, 2) is supported by pseudotachylite, shatter cones, coesite, and stishovite at Vredefort (3, 4, 5) but these shock phenomena have not been found in the Bushveld Complex (6). The Bushveld Complex was formerly interpreted as a lopolith (Fig. 2), a view incompatible with gravity, electrical resistivity, magnetic, and seismic-reflection data (7, 8, 9, 10, 11). It is outlined by at least three inward-dipping lobes of layered ultramafic-to-mafic plutonic rocks (Rustenburg Layered Suite, RLS, labelled Layered Mafic Sequence on Fig. 1) that partly coalesce to form a basin-like feature 400 km in diameter and 65,000 km<sup>2</sup> in area, equivalent to a small lunar mare (Figs. 1, 2). RLS and underlying sedimentary rocks (Transvaal Sequence) end abruptly below 11-13 km. The interior of the basin(s) consist(s) of one or more basement domes (Fig. 2), which lend credence to the interpretation of the Vredefort dome as a deeply eroded Bushveld outlier (2). By the impact interpretation, the central dome(s) correspond to uplifted floor(s) of one or more coalescing primary craters. Shock features could be expected there but the Bushveld domes are covered (unlike the Vredefort dome, where shock features do, in fact, occur). Between the inward-dipping Transvaal-RLS succession and the central dome(s) there is a collar of disturbed pre-Bushveld rocks (11). The collar is inferred to include two "fragments" of folded and cataclasized Transvaal sediments, Crocodile River (Assen on Fig. 1) to the west and Marble Hall-Stavoren to the east. Originally interpreted as roof pendants or floated xenoliths in a lopolith, the fragments were interpreted by Rhodes (2) as central peaks of separate impact craters. By the present impact interpretation, they are parts of the rim and flanks of a complexly modified and enlarged crater. This explains intense deformation below the level of shock metamorphism (13).

The Bushveld Complex is orders of magnitude larger than other proposed terrestrial impact structures and differs from them in important ways. Its principal members, in order of age, are Rooiberg Felsite, RLS, and Lebowa Granite. Rooiberg Felsite (initial volume 200,000 - > 300,000 km<sup>3</sup>; 12), the largest mass of related volcanic-like rocks on Earth, may hold the key to its origin. Its volume is ~20% of the Bushveld Complex, far more than impactite meltrock of known astroblemes (< 5%; 14). No calderas or other eruptive centers are known. It could be explained by excavation of the Earth's crust to isotherms above the ambient-pressure solidus of granite (~30 km); added kinetic energy of impact would explain textural and mineralogical evidence for quenching from unusually high temperatures



(skeletal clinopyroxene, swallow-tail plagioclase, quartz needles paramorph after primary tridymite, etc.) Repeated water influxes account for explosive volcanism (including ignimbrites and rheoignimbrites in the upper part) and complicated stratigraphy, including multiple flows, zones of accretionary lapilli, mudflows, and sedimentary interbeds (15). Principal deformation of the sedimentary floor occurred between times of the deposition of the Transvaal Sequence and emplacement of Rooiberg Felsite. Petrography and field relations show transitions from felsite to sedimentary rocks that were metamorphosed (sanidine facies, stability field of tridymite) or partly melted. Geochemical mixing models for major and trace elements show that the high-Mg group of felsites, confined to the lower part of the section (15), closely resemble a mixture of 64.5% average Archean basement and 35.5% sedimentary rocks of the Transvaal Sequence (shale, 22.0%; quartzite 6.5%, dolomite 1.8%; banded iron formation, 5.2%). Other chemical varieties (low-Mg and high-Fe) have more complex characteristics. RLS intruded along the unconformity between Transvaal Sequence and Rooiberg Felsite; by the impact hypothesis it represents partial mantle melts induced by deep fracturing near the crater wall. Remaining siliceous melts equilibrated with the crust to form anatectic granitic melts, mainly intruded as sheets of Lebowa Granite along RLS-Rooiberg contacts (16).

The Bushveld-Vredefort events occurred during the interval from neutral or reducing atmosphere to oxidizing atmosphere (uraninite- and pyrite-bearing pre-Bushveld sedimentary rocks; post-Bushveld redbeds of the Loskop Formation; (17). This transition is usually related to the evolution of photosynthesizing organisms (18). If the impact hypothesis for Bushveld-Vredefort can be confirmed, it may represent a global catastrophe sufficient to contribute to environmental changes favoring anaerobic photosynthesizing eukaryotes over aerobic prokaryotes.

References: (1) Shoemaker, E.M., 1985, in Holland, H.D. and Trendall, A.F., eds., *Patterns of Change in Earth Evolution*, Springer, 15-40. (2) Rhodes, R.C., 1975, *Geology* 3, 549-554. (3) Hargraves, R.B., 1961, *Geol. Soc. S. Africa Trans.* 64, 147-161. (4) Manton, W.I., 1965, *N.Y. Acad. Sci. Ann.* 123, 1017-1049. (5) Martini, J.E.J., 1978, *Nature* 272, 715-717. (6) French, B.M., in press, *Tectonophysics*. (7) Willemse, J., 1969, *Econ. Geol. Mon.* 4, 1-22. (8) Cousins, A.J., 1959, *Geol. Soc. S. Africa Trans.* 62, 179-189. (9) Meyer, R. & de Beer, J.H., 1987, *Nature* 325, 610-612. (10) Kleywegt, R.J. & du Plessis, A., 1986, *Geol. Soc. S. Africa Extended Abstr.*, *Geocongress '86*, 603-607. (11) du Plessis, A. & Levitt, J.G., unpublished, and de Plessis, A., personal communication, 1987. (12) Twist, D. and French, B.M., 1983, *Bull. Volcanologique* 46, 225-242. (13) Grieve, R.A.F., Dence, R.M., & Robertson, P.B., 1977 in Roddy, D.J., et al., *Impact and Explosion Cratering*, Pergamon, 791-814. (14) Phinney, W.D. & Simonds, C.H., 1977, *ibid*, 771-790. (15) Twist, D., 1985, *Econ. Geol.* 80, 1153-1165. (16) Twist D. & Harmer, R.E., 1987, *Jour. Volcanol. & Geothermal Research* 32, 83-98. (17) Twist, D. & Cheney, E.S., 1986, *Precambrian Research* 33, 225-264. (18) Walker, J.C.G., Klein, C., Schidlowski, M., Schopf, J.W., Stevenson, D.J., & Walter, M.R., In *Earth's Earliest Biosphere*, Schopf, J.W., ed., Princeton, 260-290.

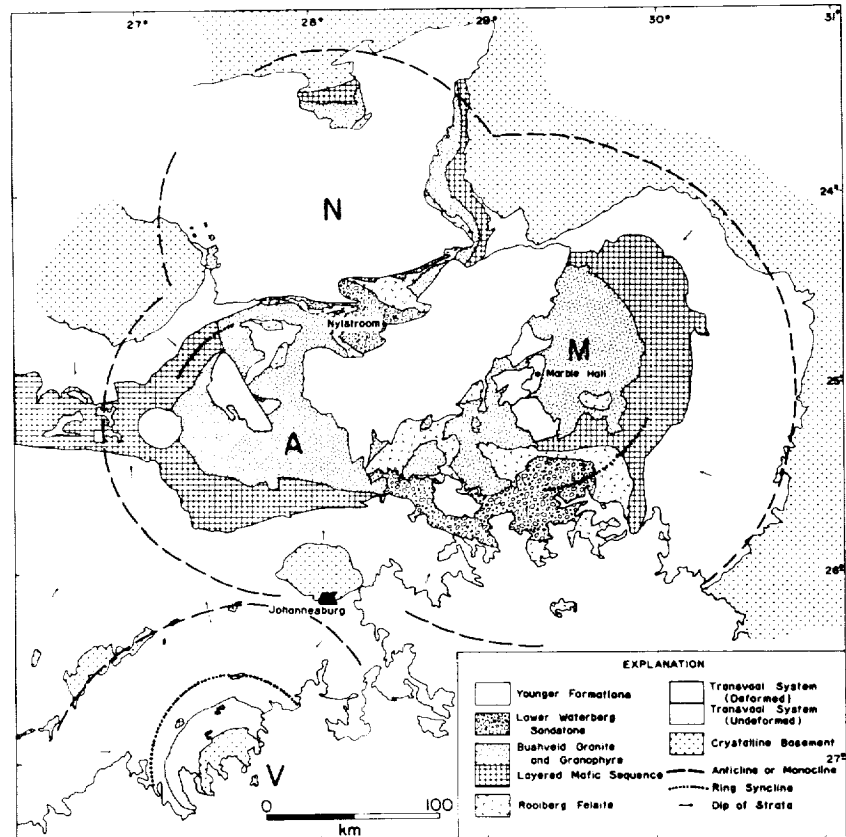
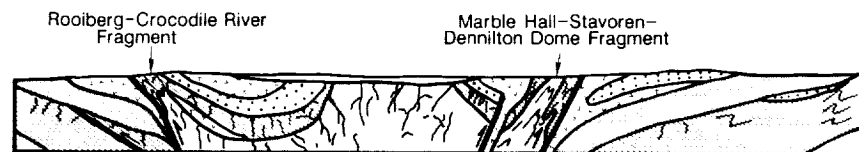


Figure 1. Generalized geologic map of the Bushveld Vredefort Complex, South Africa. From Rhodes (1975). A = Crocodile River - Rooiberg "fragment;" M = Marble Hall - Stavoren "fragment;" V: Vredefort dome.

## Figure 2 INTERPRETATIONS OF BUSHVELD COMPLEX

### (a) Impact Structure



Cartoon by W.E. Elston

Based on Meyer and de Beer (1987), Kleywegt and du Plessis (1986)  
du Plessis and Kleywegt (1987), du Plessis and Levitt (in press);  
Unpublished Data by F. Hartzler, J. Schweitzer, D. Twist;  
Sharpe and Chadwick (1982)

### (b) Lopolith



After Willemse (1969)

- |   |                               |   |                                 |
|---|-------------------------------|---|---------------------------------|
| 1 | Archean Crystalline Rocks     | 4 | Gabbro-Rustenburg Layered Suite |
| 2 | Proterozoic Sedimentary Rocks | 5 | Granite-Lebowa Granite          |
| 3 | Rooiberg Felsite              | 6 | Post-Bushveld Rocks             |

ORIGINAL FIGURE  
OF POOR QUALITY

**INTRODUCTION:** Preliminary results from study of the gradational history of the 20,000 to 30,000 year old (1,2) Meteor Crater in northern Arizona indicate that minimal erosion has affected both the present near-rim and more distal ejecta. Most of the observed erosion of the ejecta occurred during the early history of the crater. The various styles and estimated rates of gradation in the ejecta indicate that eolian and fluvial run-off processes have dominated and that erosion by sub-surface drainage and mass wasting has been insignificant. These results provide evidence that Meteor Crater ejecta retains an essentially pristine form. This interpretation contrasts (but may not conflict) with inferences drawn from previous studies that estimate considerable erosion of the slope-sensitive near rim region (1-3).

**EROSIONAL STATE:** Several independent observations provide information regarding the erosional state of the crater including: A) drainage systems/densities; B) the occurrence/morphology of ejecta blocks (>10 to 20 cm); C) the occurrence of ejecta remnants; D) surface/subsurface grain size comparisons; E) vegetation; and F) the occurrence/morphology of small secondary craters.

Dissection of the ejecta has occurred within ~75 small drainage basins located on the flanks of the crater that are drained by intermittent gullies which head along the rim-crest. Divides between adjacent basins are usually defined by topographic variations in the primary ejecta. Gullies are generally incised to depths of less than 1 to 2 m and in many cases have produced alluvial fans at the base of the outer rim. The drainage density around the crater out to 0.6 R from the rim is 8.6 km/km<sup>2</sup>. Although the volume of material contained in the alluvial fans and that which has been transported beyond is not yet well constrained, both the small size of the gullies and an absence of morphology indicating large amounts of erosion along their courses suggest little modification of the basins. Many of the alluvial fans are presently inactive as demonstrated by preliminary surface vs. subsurface grain size data, detailed study of soils developed on their surfaces (1), and the paucity of small-scale flow related features. Study of soil development (1) indicates that the inactive fans formed mainly during the Pleistocene. Holocene fluvial processes have been confined primarily to within the gullies and have resulted in incisement of the older Pleistocene fans and more distal deposition.

The concentration of large blocks/volume exposed in gullies appears to reflect *in situ* erosion of finer material and is not distinguishable from block concentrations observed in pits dug into pristine ejecta and on undissected surfaces. In addition, large blocks exposed at the surface do not display enhanced relief relative to their surroundings. These observations place limits on the total amount of ejecta removed and indicates minimal erosion. Although surface/subsurface block abundance is relatively constant at a given radius from the crater rim the total block abundance appears to decrease with increasing radius.

Field investigations also have revealed occurrences of ejecta in erosionally sensitive locations. A small lobe of ejecta superposes a pre-existing WSW-ENE oriented ridge of Moenkopi sand/siltstone located ~1 km (~2 R) from the crater rim. Preservation of such a subtle primary ejecta feature in an exposed site requires minimal erosion. Preliminary analysis of surface vs. subsurface grain size data from this ejecta lobe suggest that only 10 to 20 cm of erosion has occurred, thereby supporting this conclusion. The contrast between the uprange ejecta lobe and a downrange shadow from the Moenkopi ridge adds further support to a well preserved state. Similar grain size comparisons of near-rim materials suggests even less erosion there. Even these minor amounts of erosion have produced a coarse grained surface lag of relatively unweathered material in most locations.

Vegetation presently growing on the crater shows little evidence of windward scour of ejecta from roots areas and few examples of leeward deposition. Some trees growing on the ejecta are >700 years old (4), thereby limiting erosion over this time to at most ~10 cm. Exceptions to these observations occur in sandy areas along southeast portions of the outer rim where some grasses/bushes occur on ~10 cm to 20 cm topographic highs. It is not known if these small rises reflect sediment trapping or deflation of adjacent materials. Because this area has served as a major source of material to the windstreak (a veneer of well sorted sand extending northeast of the crater generally less than 50 cm

thick thinning distally), local deflation is more likely responsible for their origin. Trapping of alluvial material by vegetation higher along the rim in the same area has produced some minor terracing.

Several ejecta blocks ranging from 1 m to 3 m have been found in shallow, rimmed depressions 2 m to 5 m in diameter with rim-crest depths about 0.5 m. Blocks spalled off the Kaibab limestone ejecta during formation of these small craters can be easily traced to their original position and show little evidence for chemical dissolution. The degree of preservation is consistent with an interpretation that these are preserved secondary craters, formed by high-angle ejecta late in the cratering process (5).

**EROSIONAL STYLE:** Analysis of alluvium in the drainage gullies and in the alluvial fans demonstrates that grain sizes smaller than about 20 mm are efficiently transported; fragments up to 15 cm to 20 cm are infrequently carried. Surface flow rates outside of the gullies will be controlled by local topography/roughness and reduce the size of transportable material. Preliminary data indicate that fluvial transport of materials not associated with the gullies is limited to grain sizes ~3.0 to 4.0 mm. Grain size data from the windstreak demonstrate that eolian processes remove material predominantly less than 0.25 mm, but as large as 0.5 mm. Therefore, both fluvial and eolian processes are capable of transporting fine-grained material (<0.5 mm to 0.25 mm) from around the crater. Larger fragments are carried by fluvial processes. A paucity of evidence expected to be produced by long-term chemical/physical weathering of the ejecta indicates that there has been little *in situ* breakdown of material and that erosion is solely responsible for removal of the ejecta. There is little evidence of modification on the outside of the crater by mass wasting processes.

Three observations indicate that fluvial erosion of the ejecta has been dominated by processes related to surface run-off and that erosion by groundwater sapping processes is insignificant. First, drainage density calculations of 8.6 km/km<sup>2</sup> indicate that the ejecta beyond the crater rim is well drained by surface run-off of precipitation. Second, preliminary estimates of the subsurface hydraulic conductivity of the ejecta indicate moderate permeability; hence, flow properties are equivalent to an aquifer comprised of fine-grained sand (6). Finally, there is an absence of characteristic sapping features around the crater and there appears to be few aquicludes within the ejecta capable of producing the necessary lateral flow of groundwater.

Erosion of ejecta around Meteor Crater over at least the past 700 to 800 years (and probably under present climatic/vegetation conditions) has been minimal as demonstrated by: A) stability of the ejecta around the roots of vegetation in excess of 700 years old (4); B) the vegetated nature of the windstreak; and C) inactive alluvial fans. As further illustration, field work was conducted during a period when winds were measured in excess of 40 to 50 mph, yet insignificant amounts of eolian transport occurred. Numerous nearly transparent dust-devils were also observed over the ejecta which did not loft dust and sand. The conclusion that minimal erosion has occurred during the late history of the crater is consistent with evidence from the crater interior (1).

**CONCLUSIONS:** Both the near-rim and distal ejecta around Meteor Crater have remained remarkably unmodified by gradational processes. The coarse grained surface lag of unweathered material resulting from small amounts of erosion creates an armor that effectively protects underlying ejecta and is in disequilibrium with regional gradational rates and processes. Erosion appears to have been more active in the past than at present and has been dominated by eolian processes and fluvial processes related to surface run-off. Future work will provide more detailed and better constrained estimates of the rates and styles of erosion at specific locations around the crater. It is hoped that the results of this study can be applied to gradational studies of other terrestrial and possibly martian impact craters in an effort to understand their erosional histories.

**REFERENCES:** (1) Shoemaker, E.M. and Kieffer, S.E. (1974), Guidebook to the geology of Meteor Crater, Arizona: Arizona State University Center for Meteorite Studies Publication 17, Tempe, AZ., 66p. (2) Roddy, D.J., et al. (1975), Proc. Lunar and Planet. Sci. Conf., v. 6, p. 2621-2644. (3) Roddy, D.J. (1978), Proc. Lunar and Planet. Sci. Conf., v. 9, p. 3891-3930. (4) Barringer, D.M. (1905), Proc. Acad. Nat. Sci. Philadelphia, v.57, p. 861-886. (5) Schultz, P.H. and Grant, J.A. (1989), LPSC XX (abstract), This volume. (6) U.S. Dept. of the Interior (1977), Ground Water Manual: A Water Resources Technical Publication, U.S. Government Printing Office, Washington, D.C., 480p.

# EFFECTS ON AMBIENT MAGNETIC FIELDS AND PLASMA OF THE EXPANDING VAPOR CLOUD PRODUCED IN LUNAR BASIN-FORMING IMPACTS

L. L. Hood and Z. Huang, Lunar and Planetary Laboratory, University of Arizona, Tucson, Arizona 85721.

**Introduction:** Previous theoretical and experimental work has shown that vaporization of projectile and target material occurring in hypervelocity ( $> 10$  km/s) impacts results in the formation of a thermally expanding plasma cloud that may produce significant magnetic effects (1). More recent experimental studies of vapor-producing impacts (2) have established that transient magnetic fields are observed that fall into two major classes: (i) fields generated intrinsically within the plasma cloud as a result of non-aligned thermal and density gradients; and (ii) fields generated by currents induced near the surface of the cloud as it expands into the ambient geomagnetic field. Although the former class of fields may contribute substantially to the small-scale magnetization of lunar surface materials, scaling arguments indicate that their amplitudes will be reduced in large events because of decreased overall thermal gradients (1). This is consistent with the general absence of a direct correlation between lunar orbital magnetic anomalies and impact crater locations, including those of mare craters down to a few km in size (3). Interaction of the plasma cloud with ambient (e.g. solar wind) magnetic fields and plasma provides the major alternate mechanism for producing strong, large-scale fields that may have been responsible for a large component of lunar paleomagnetism.

According to a proposed model (4), external magnetic fields and plasmas may have been especially concentrated for a transient time interval in the zone *antipodal* to large impacts due to convergence of the impact plasma cloud. Shock effects (due to convergence of seismic waves and/or secondary impacts) in the presence of the enhanced magnetic fields may have produced relatively strong and coherent magnetization in basin antipode zones that could be responsible for the largest magnetization concentrations mapped from lunar orbit (5).

**Model Calculations:** In the work reported here, initial three-dimensional model calculations are reported of the expansion and interaction with the Moon of a basin-scale impact plasma cloud. Shown in the figure is a time sequence of plots of mass density resulting from a simplified numerical calculation of the expansion of a representative cloud using initial conditions (mass density, total mass, internal energy density) approximately appropriate for a 15 km/s normal impact of a 100 km radius gabbroic anorthosite impactor onto a gabbroic anorthosite lunar surface (6). A two-dimensional hydrodynamic code (made three-dimensional by the assumption of axial symmetry) was used in an Eulerian mode on a cylindrical grid (7). In each plot, the central circular disk represents the Moon and the outer shaded contour of the cloud corresponds to a mass density of  $10^{-11}$  g cm $^{-3}$ . The first plot is for a time of 64.4 seconds after impact. The second is for a time of 456 seconds. The initial vertical grid size was 21.7 km but was increased by a factor of two after expansion of the cloud to a size comparable to the lunar radius. Results are nearly insensitive to further reductions in grid size. Limitations of the calculation include the neglect of the interaction of the expanding gas with solid and liquid ejecta, neglect of radiative energy loss, and use of an ideal gas equation of state so that partial recondensation of the vapor is not accounted for. The most serious of these appears to be the latter and an effort is currently being made to account for recondensation using a more realistic equation of state. However, uncertainties regarding actual impact angle of incidence, size, velocity, and composition for a given lunar basin impactor are sufficiently large that no major qualitative revisions are expected of the current results.

As seen in Fig. 1b, the outer periphery of the cloud begins to approach the antipode after a time of 450-500 s for the chosen initial conditions. This time is of the same order as for propagation of compressive seismic waves through the Moon (400 - 500 s) and is significantly less than that for the arrival of basin secondaries (30 to 50 minutes). Thus shock effects of converging seismic waves in basin antipode zones may be a primary candidate for producing the observed magnetization, provided that a strong magnetic field enhancement occurs in the same zones. This would be consistent with a weak statistical correlation that is known to exist between electron reflection anomalies and seismically modified terrain in basin antipode zones (8).

**Interaction with Ambient Fields and Plasmas:** As the cloud expands, a shock wave will form between the periphery of the cloud and any ambient plasma with an embedded magnetic field. In the usual case when

the Moon is in the solar wind, the interaction will resemble that between a planetary ionosphere and the solar wind except for the expansion of the obstacle in the present case. As the impact cloud expands around the Moon, the region enclosed by the bow shock will include the antipodal zone so that the external plasma and its embedded magnetic field in this zone will be relatively stagnant. For this reason, the compression of the external medium in the antipodal zone can be modeled to a first approximation by assuming that the Moon is initially surrounded by a stagnant plasma with thermal and magnetic properties similar to that of the solar wind plasma. In the actual solar wind,  $\beta$ , the ratio of thermal to magnetic pressure is usually less than unity but varies to values above and below unity. As an initial calculation, we make the simplifying assumption that  $\beta$  is greater than unity so that a purely hydrodynamic numerical code can be used to model the external plasma dynamics in a first approximation. The change in the magnetic field is then calculated from  $\partial \mathbf{B} / \partial t = \nabla \times (\mathbf{v} \times \mathbf{B})$  using the hydrocode velocity field. Although these calculations are still in progress, initial results show significant magnetic field enhancements in the antipodal zone as expected from considerations based mainly on conservation of flux (4).

**Acknowledgment:** Supported under grant NSG-7020.

**References:** (1) Srnka, L. J., *PLSC 8th*, 795, 1977; Srnka, L. J., G. Martelli, G. Newton, S. Cisowski, M. Fuller, and R. Schaal, *Earth Planet. Sci. Lett.*, **42**, 127, 1979; Hood, L. L. and A. Vickery, *J. Geophys. Res.*, **89**, C211, 1984. (2) Crawford, D. A. and P. H. Schulz, *Nature*, **336**, 50, 1988. (3) Lin, R. P., *Phys. Earth Planet. Int.*, **20**, 271-280, 1979. (4) Hood, L. L., *Geophys. Res. Lett.*, **14**, 844, 1987. (5) Lin, R. P., K. A. Anderson, and L. L. Hood, *Icarus*, **74**, 529, 1988. (6) Ahrens, T. J. and J. D. O'Keefe, in *Impact and Explosion Cratering*, D. J. Roddy et al., eds., p. 639, Pergamon, N.Y., 1977. (7) Amsden, A. A., H. M. Ruppel, and C. W. Hirt, *Los Alamos Scientific Laboratory Report LA-8095*, 100 pp., 1980. (8) Hood, L. L. and C. R. Williams, *Proc. Lunar Planet. Sci. Conf. 19th*, in press, 1989.



(a)



(b)

ORIGINAL PAGE  
BLACK AND WHITE PHOTOGRAPH

**MAGNETIC PROBING OF EARLY-TIME IMPACT PHENOMENA.** D. A. Crawford and P. H. Schultz, Dept. of Geological Sciences, Brown University, Providence, RI 02912 and L. J. Srnka, Data Management and Interpretation Division, Exxon Production Research Co., Houston, TX 77001.

Laboratory hypervelocity impact experiments conducted at the NASA Ames Vertical Gun Range have demonstrated that macroscopic hypervelocity (4.5 – 6 km/s) impacts can generate up to 2500 nT intensity magnetic fields in low ambient field environments – typical of the ambient field found on the lunar surface[1]. Further experiments and analysis permit characterizing to first-order the impact-generated magnetic fields as a function of impact angle, velocity, and projectile and target materials.

Hide (1972) suggested that weak ambient fields could be amplified by electrically conductive, impact-generated ejecta[2]. Srnka (1977) proposed that magnetic fields could be generated with currents driven by non-aligned temperature and electron density gradients that must arise in the asymmetric, impact-generated plasma cloud[3]. In this simple approximation where we retain only the dominant source term[4], the time rate of change of magnetic induction can be written:

$$\dot{\mathbf{B}} = \nabla \times \mathbf{V} \times \mathbf{B} + \frac{c^2}{4\pi\sigma} \nabla^2 \mathbf{B} + \nabla \times \left( \frac{ck}{2en} \nabla (nT) \right) \quad (1)$$

where  $\mathbf{B}$  is the total magnetic field,  $\mathbf{V}$  is the plasma's fluid velocity,  $\sigma$  its electrical conductivity,  $k$  is Boltzmann's constant and  $n$ ,  $T$  and  $e$  are the electron number density, temperature and charge, respectively. The first term on the right of (1) represents convection of  $\mathbf{B}$  due to fluid motion; the second, represents diffusion of  $\mathbf{B}$  through the electrically conductive plasma; and the third, is a source term arising when the electron temperature and density gradients are not aligned.

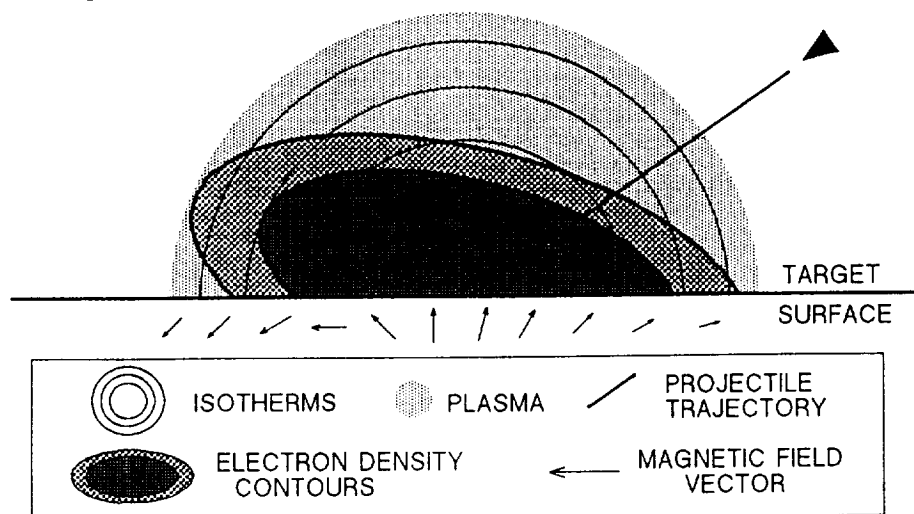


Fig. 1 Hypothetical asymmetric magnetic field produced by non-aligned electron temperature and density gradients during a non-vertical hypervelocity impact. This is a vertical slice of the impact-generated plasma with the projectile incident from the right.

The magnetic field shown in Fig. 1 depicts a hypothetical non-vertical impact as the electron density and temperature of the impact-generated plasma is increasing (highest at the impact point). Since the temperature is dominated by the presence of neutral gas (100 to 1,000 times more abundant than ionized gas), there is no *a priori* reason to believe that it will be aligned with the electron density distribution; consequently we have constrained the temperature ( $T$ ) to spherical symmetry, for clarity[5]. This simple model is based on two critical observations: 1) the field observed up-range of the impact point is lower than that down-range; and 2) the magnetic field far down-range typically has a polarity opposite to the field at the impact point.

Figures 2 and 3 show the vertical component of the magnetic intensity observed below the impact point during laboratory hypervelocity impacts into powdered dolomite and silica sand targets, respectively, under low (~1000 nT) ambient field conditions. The first signal to appear is a large amplitude, short duration pulse (unresolvable) arising from the rapid production of plasma at the projectile/target interface during first contact, perhaps related to the jetting process. The second signal is a negative pulse (shown prominently in Fig. 2) of relatively long duration (0.2 – 0.5 ms)

which may reflect continued plasma production/expansion. The third signal is a positive pulse (shown prominently in Fig. 3) of even longer duration (1 – 2 ms) that appears to be produced well after the projectile/target energy transfer. Contrasting figures 2 and 3, we see that the target composition has a pronounced effect on the signal character. During the impact into dolomite (Fig. 2), the bulk of the plasma, indicated by the large negative signal, is apparently produced during the interaction of the projectile with the target. The width of this negative pulse may, therefore, provide a measure of the projectile/target interaction time. The width of the late-time positive pulse shown in figures 2 and 3 indicates that plasma is retained/produced near the impact region well after the time of impact.

The simple theoretical model and the laboratory observations we have put forth suggest that magnetic anomalies produced by SRM or TRM in natural impact craters will most likely have a great deal of local asymmetric structure dependent on impact angle, the size of the impact crater and the timing of the remanence acquisition[1,6]. Characteristic differences in early-time impact-generated magnetic signals depending on impact angle, velocity and projectile/target composition provide a new approach for probing the impact process.

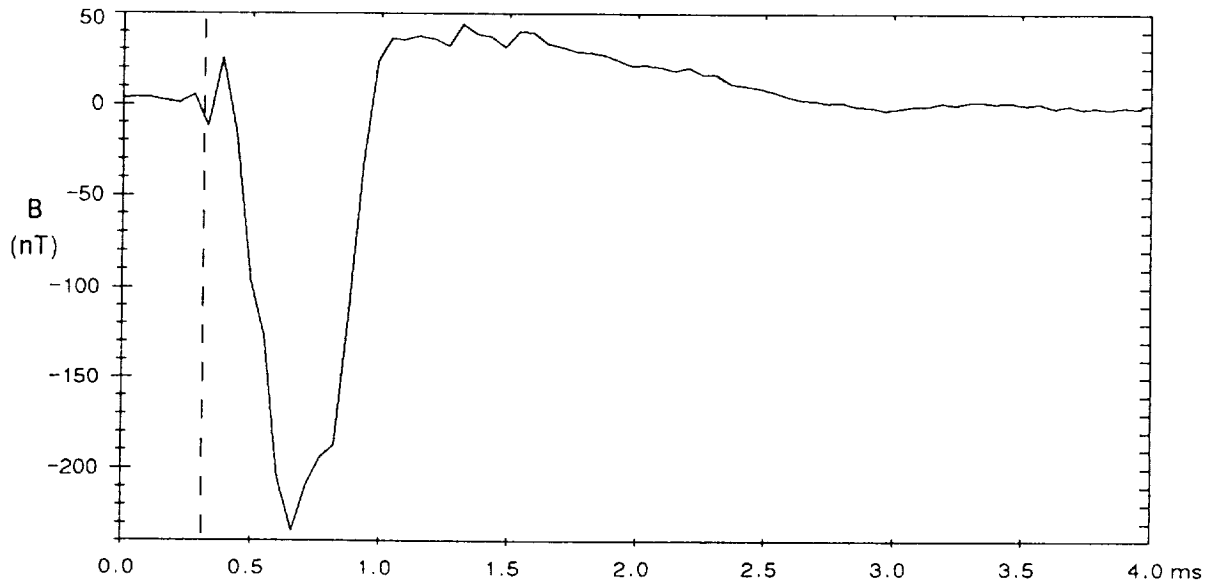


Fig. 2 Vertical component of the magnetic field intensity measured 9 cm below the impact point of a 0.64 cm Aluminum, 30°, 5.31 km/s impact into dolomite. (dashed line at time of impact).

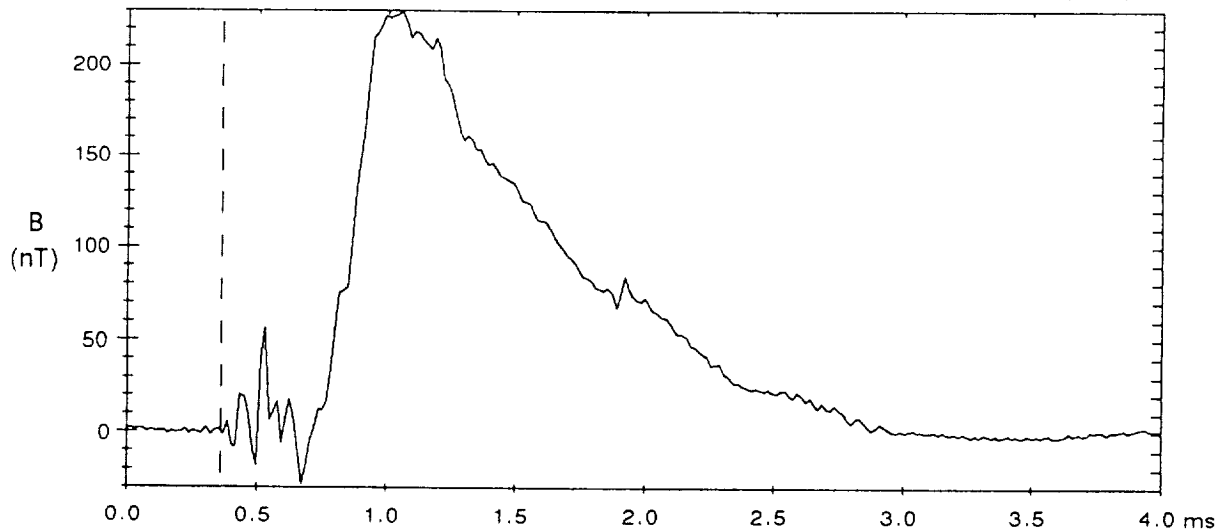


Fig. 3 Vertical component of the magnetic field intensity measured 11 cm below the impact point of a 0.64 cm Aluminum, 30°, 5.19 km/s impact into sand. (dashed line at time of impact).

[1] Crawford, D. A. and Schultz, P. H., *Nature* **336**, 50-52 (1988). [2] Hide, R., *The Moon* **4**, 39 (1972) [3] Srnka, L. J., *Proc. Lunar Science Conf.* **8th**, 893-895 (1977). [4] Pert, G. J., *J. Plasma Phys.* **18**, 227-241 (1977). [5] Schultz, P. H., *Lunar Planet. Science* **19th**, 1039-1040 (1988). [6] Fuller, M., *Nature* **336**, 12 (1988).



CHAPTER 11

STRUCTURE AND TECTONICS



## DISCONTINUITIES IN THE SHALLOW MARTIAN CRUST

P.A. Davis<sup>1</sup> and M. P. Golombek<sup>2</sup> (1) U.S. Geological Survey, Flagstaff, Arizona 86001; (2) Jet Propulsion Laboratory, California Institute of Technology, Pasadena, California 91109.

A number of discontinuities have been proposed to exist within the shallow Martian equatorial crust on the basis of (1) direct observation of Mariner and Viking data [1-3], (2) theoretical considerations of the stability of water within the Martian crust and atmosphere [4-6], and (3) considerations of the impact history of Mars primarily by analogy with the well documented case of the Moon [7,8]. On the whole, these hypotheses suggest the existence of at least three major mechanical discontinuities within the crust that are delineated by the following interfaces: (1) An upper sequence of interbedded igneous rock, impact ejecta, and sediments or sedimentary rock overlying a relatively thick and extremely weak zone of impact breccia; (2) either an ice-laden zone over a water-laden or dry zone of impact breccia or a chemically-cemented zone within uncemented, dry impact breccia; and (3) impact breccia over fractured basement rock. We examined the morphometry of a variety of erosional features and of grabens within the western equatorial region of Mars to determine if the depths of these observed erosional levels and the depth of the mechanical discontinuity related to graben formation correspond to previously proposed crustal discontinuities.

We obtained detailed photoclinometric profiles across 125 erosional features and 163 grabens within the study area using the methods of [9,10]. The erosional features included troughs, pits [1,11], and wall valleys [12-13] within and around Valles Marineris and Noctis Labyrinthus, and channel scarps within Sacra Fossae [1,14]. The grabens analyzed in this study belong to a special class of grabens that have a very simple surface morphology, which can be used to calculate the intersection depth of faults bounding simple grabens (i.e., thickness of the faulted layer). For this calculation, the dip of the faults must be known or approximated and corrections must be made for the effects of mass wasting on the fault scarps [15]. We calculated fault dips from the locations and depths of unambiguous fault traces on trough walls using Viking Orbiter image data and corrected fault trace locations for the effects of oblique viewing. The average fault dip resulting from this analysis was about 60 degrees.

Our data for the pits, troughs, and wall valleys within Noctis Labyrinthus and Valles Marineris and the escarpments within the fretted terrain show distinct erosional base levels at depths of 0.3-0.6 km, 1 km, and 2-3 km. Our graben calculations show that faults bounding grabens consistently initiate at the mechanical discontinuity at about 1-km depth. The shallowest discontinuity is indicated by the depths of a number of wall-valley heads and the upper reaches of Sacra Fossae. Its depth range (0.3-0.6 km) corresponds to thickness estimates for the ridged plains unit in this region [16,17], and, thus, the discontinuity probably represents the contact between the rock sequence making up this unit and the underlying megaregolith [18].

The 1 km discontinuity is indicated by base levels of erosion in all the features studied, as well as the depth at which faults bounding grabens initiate, and corresponds to the base of the proposed layer of ground ice on Mars [4,5]. This discontinuity may represent an interface between ice-laden and dry regolith, ice-laden and water-laden regolith [5,19], or pristine and cemented regolith [3]. A correlation between wall-valley head depth and local faulted-layer thickness suggests that this discontinuity is the same one that

controls both a base level of erosion in sapping valley development and the mechanical discontinuity at which faults that bound grabens initiated. There is no apparent relation between pit and trough depths and the local thickness of the faulted layer, which can be explained if pits and troughs developed by subsidence into underlying tension cracks that disrupted the 1 km discontinuity [20]. The data do suggest, however, that erosion of the shallow (less than 1.5-km depth) pits and troughs was influenced by the 1-km discontinuity.

The published photogeologic evidence for ground ice or ground water are not supported by the model studies of ground ice stability [6,21] that indicate  $H_2O$  has not been stable in the Martian equatorial crust since very early in Martian geologic history. These models do not, however, preclude some replenishment mechanism for the prolonged existence of  $H_2O$  in the crust. If  $H_2O$  was stable or periodically replenished in the crust, our evidence of a 1-km discontinuity may indicate the interface between ice-laden and dry regolith or the interface between ice-laden and water-laden regolith. Either scenario would provide the  $H_2O$  necessary for production of the observed sapping features. Regardless of the exact mode of formation of the discontinuity at the base of the ground-ice layer, faults that bound Martian grabens initiated at this depth, indicating that it was a mechanical discontinuity at the time of graben formation. This mechanical discontinuity separated cohesively frozen megaregolith above from weaker, less cohesive water-laden or dry ejecta below, if ground ice existed at the time of graben formation. Alternatively, if the layer beneath the mechanical discontinuity was cemented, the mechanical discontinuity would separate a stronger cemented megaregolith at depth from a weaker megaregolith above. This situation is in accord with models for failure of the shallow crust of Mars in the Valles Marineris region that suggest tension cracks form at depth in a cemented substrate beneath grabens [20]. The general correlation between the thickness of the faulted layer and the base of the layer of ground ice demonstrated in this paper supports the original suggestion that faults bounding grabens initiate at this subsurface mechanical discontinuity [22].

The third discontinuity at a depth of 2-3 km is indicated by the depths of some pits and troughs, the mouths of wall valleys, and the erosional base of Kasei Valles. This depth range corresponds to the proposed thickness of the Martian megaregolith and probably represents the interface between overlying ejected breccia and in situ fractured basement.

REFERENCES: [1] Sharp, R. (1973) JGR 78, 4073; [2] Carr, M., and Schaber, G. (1977) JGR 82, 4039; [3] Soderblom, L., and Wenner, D. (1978) Icarus 24, 622; [4] Fanale, F. (1976) Icarus 28, 179; [5] Rossbacher, L., and Judson, S. (1981) Icarus 45, 39; [6] Fanale, F., et al. (1986) Icarus 67, 1; [7] Short, N., and Foreman, M. (1972) Modern Geology 3, 69; [8] Woronow, A. (1987) LPI Tech. Rpt. 88-05, 135; [9] Davis, P., and Soderblom, L. (1984) JGR 89, 9449; [10] Tanaka, K., and Davis, P. (1988) JGR 93, 14893; [11] Lucchitta, B. (1987) Lunar Planet. Sci. XVIII, 572; [12] Lucchitta, B. (1978) J. Res. U.S.G.S. 6, 651; [13] Baker, V. (1982) The Channels of Mars, Univ. Texas Press, Austin, 198pp; [14] Kochel, R., and Burgess, C. (1983) NASA TM 85127, 288; [15] Golombek, M. (1979) JGR 84, 4657; [16] Plescia, J., and Saunders, R. (1980) PLPSC 11, 2423; [17] DeHon, R. (1985) Lunar Planet. Sci. XVI, 171; [18] Robinson, M., and Tanaka, K. (1988) LPI Tech. Rpt. 88-05, 106; [19] Smoluchowski, R. (1968) Science 159, 1348; [20] Tanaka, K., and Golombek, M. (1989) PLPSC 19, in press; [21] Clifford, S., and Hillel, D. (1983) JGR 88, 2456; [22] Runyon, C., and Golombek, M. (1983) Lunar Planet. Sci. XIV, 660.

**THE SHALLOW STRUCTURE OF THE MARTIAN LITHOSPHERE IN THE VICINITY OF THE RIDGED PLAINS; M.T. Zuber<sup>1</sup> and L.L. Aist<sup>2</sup>,<sup>1</sup>Geodynamics Branch, NASA/Goddard Space Flight Center, Greenbelt, MD 20771, <sup>2</sup>Department of Mathematics, University of Maryland-Baltimore County, Catonsville, MD 21228.**

One of the fundamental pieces of information required for determining the thermal and tectonic evolution of a planetary body is an understanding of the mechanical structure of the lithosphere. On a regional scale, direct constraints on the mechanical structure can be obtained from the geometries of tectonic features on the surface. Wrinkle ridges are tectonic features that commonly occur in martian smooth plains units [1,2]. Some of these features likely formed due to compressive stresses related to the response of the lithosphere to the Tharsis load [3-5]. In many areas the ridges exhibit either a linear, parallel trend or a nearly concentric pattern with an approximately regular spacing of 25-50 km [4,6-9]. In areas where the ridges exhibit such a pattern, their spacing can be used to infer the shallow structure of the lithosphere at the time the features formed.

A number of previous attempts have been made to ascertain the structure of the martian lithosphere on the basis of ridge spacing by applying models for simple rheological structures [7-10]. In the present study, we have developed a suite of compressional mechanical models of the lithosphere that incorporate a broader range of possible rheologies than did previous models, as well as more detailed vertical strength stratifications. Mathematically, we consider the regular spacing of the ridges to correspond to the dominant wavelength resulting from the growth of instabilities in a horizontally-compressing multi-layered medium. We invoke a continuum approach to the problem, on the assumption that deformation prior to ridge faulting controlled the development of the regular length scale. The baseline representation of the lithosphere includes: (1) a thin, competent surface layer that corresponds to the ridged plains; (2) a weaker underlying layer that has been inferred to correspond to an unconsolidated megaregolith [7]; and (3) a competent substrate that we interpret as basement. In all models the spacing of the ridges [7,9] and the known thickness of the plains units [ $\leq 2$  km; Refs. 7,11,12, R. Kuzmin, pers. comm.] constitute the primary constraints on the rheological structure.

The first model consists of a strong layer underlain successively by a weak layer and a strong halfspace, all of uniform strength. The entire lithosphere is free to deform in response to an imposed uniform horizontal compressive stress. This model represents a situation in which stresses of sufficient magnitude to induce deformation penetrate deeper than the base of the megaregolith. Figure 1 illustrates how the dominant wave number ( $k_d'$ ) and the dominant wavelength/surface layer thickness ratio ( $\lambda_d/h_1$ ) vary with the ratio of the thicknesses of the weak subsurface layer and surface layer ( $h_2/h_1$ ) for a range of values of the strength contrast between the surface and subsurface layers ( $R_1$ ). The strength contrast between the surface layer and substrate is assumed fixed at 0.5. Note that a parameter range that includes  $h_2/h_1 \geq 1$  and large  $R_1$  produces values of  $\lambda_d/h_1$  that are compatible with the observed ridge spacing. For example, a 1 km thick surface layer requires  $25 < \lambda_d/h_1 < 50$ . This can be achieved if the subsurface layer (megaregolith) is twice as thick and a factor of approximately 1000 less competent than the overlying ridged plains. A thicker megaregolith would permit a lesser strength contrast, while a megaregolith with a thickness less than that of the plains unit ( $h_2/h_1 < 1$ ) would require a much larger strength contrast to account for the ridge spacing. A thicker plains unit would be compatible with smaller  $R_1$  and/or  $h_2/h_1$ . These results are not particularly sensitive to other details of the subsurface density or strength stratifications. If the boundary at the base of the megaregolith layer is rigid rather than deformable, corresponding to the case of thin-skinned deformation, then values of  $R_1$  and  $h_2/h_1$  that are larger than those shown in Figure 1 would be required to explain the ridge spacings.

In the second model the lithosphere consists of a surface layer of uniform strength that overlies a substrate. The strength at the top of the substrate is less than that of the layer and increases exponentially with depth. This corresponds to a scenario in which the megaregolith and basement represent a continuum, in which the megaregolith becomes increasingly compacted with depth and grades into the crustal lithosphere. The length scale that describes the thickness of the megaregolith in this case is the e-folding length of the substrate strength ( $\zeta$ ). Figure 2 shows  $k_d'$  and  $\lambda_d/h_1$  vs. the parameter  $\alpha (= \zeta/h_1)$  for the limiting case of a "strong" surface layer in which buoyancy forces due to variations in topography do not play a significant role in influencing the pattern of deformation. In this case, a parameter range that includes  $\alpha \geq 1$  and large  $R_1$  yields values of  $\lambda_d/h_1$  that can explain

the ridge spacings. For example, a 1 km thick surface layer and an e-folding length of the megaregolith of 2 km ( $\alpha=2$ ) requires a strength contrast ( $R_1$ ) of on the order of 1000. A thicker plains unit would permit smaller  $\alpha$  or  $R_1$ . In the less likely case of a "weak" surface layer in which buoyancy forces significantly influence the deformation, somewhat smaller strength contrasts are allowable.

These results quantitatively illustrate that compression of a lithosphere consisting of a surface plains unit, underlying megaregolith, and basement can explain the regular spacings of the martian ridges. Results of a third model, which consists of a weak megaregolith layer that is underlain successively by a strong lithospheric layer and a weaker lithospheric substrate, demonstrate that the wavelengths of the ridges can also be explained if the surface plains unit is absent. This is interesting in light of the fact that the ridges most commonly occur in areas where plains units are present, and suggests the possibility that while the mechanical strength of the plains unit may have facilitated the nucleation of ridges, it may or may not have strongly influenced the spacings. However, for all models the mechanical properties of lithospheric basement significantly influence the predicted geometry of deformation.

**References:** [1]Chicarro, A.F., et al., *Icarus*, 63, 153-174, 1985. [2]Plescia, J.B., and M.P. Golombek, *GSAB*, 97, 1289-1299, 1986. [3]Banerdt, W.B., et al., *JGR*, 87, 9723-9733, 1982. [4]Maxwell, T.A., *JGR*, 87, A97-A108, 1982. [5]Sleep, N.H., and R.J. Phillips, *JGR*, 90, 4469-4489, 1985. [6]Wise, D.U., et al., *Icarus*, 38, 458-472, 1979. [7]Saunders, R.S., et al., *LPSC XIV*, 660-661, 1981. [8]Watters, T.R., *NASA TM 4041*, 473-475, 1988. [9]Watters, T.R., Conf. on *Early Tectonic and Volcanic Evolution of Mars*, 63-65, 1988. [10]Watters, T.R., *NASA TM 89810*, 481-483, 1986. [11]DeHon, R.A., *Third Int. Colloq. on Mars*, 59-61, 1981. [12]Frey, H., et al., Conf. on *Early Tectonic and Volcanic Evolution of Mars*, 24-26, 1988.

**Figure 1.** Plot of dominant wave number  $k_d'$  and wavelength  $\lambda_d/h_1$  as a function of  $h_2/h_1$  for a range of  $R_1$ . Parameters are defined in the text. The model assumes a Newtonian ( $n=1$ ) viscous lithosphere.

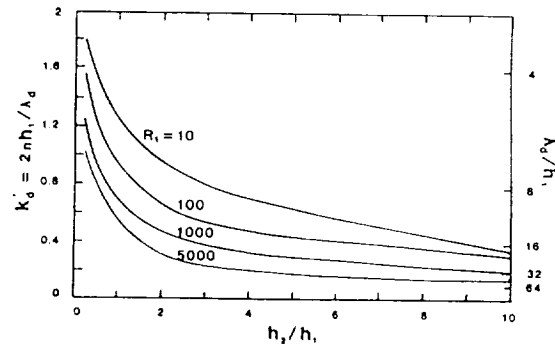
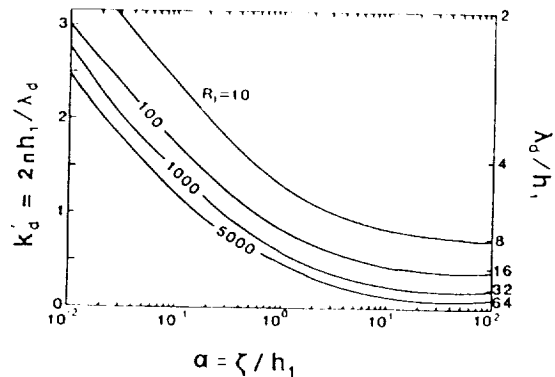


**Figure 2.** Plot of dominant wave number  $k_d'$  and wavelength  $\lambda_d/h_1$  as a function of the dimensionless e-folding thickness  $\alpha$  of the substrate for the limiting case of a lithosphere with a "strong" surface layer (i.e. buoyancy effects unimportant). The results are shown for a range of  $R_1$ . The model assumes a non-Newtonian ( $n=3$ ) viscous lithosphere.



## A REEVALUATION OF LONG-WAVELENGTH STRESS MODELS FOR MARS

W. B. Banerdt and M. P. Golombek, Jet Propulsion Laboratory, California Institute of Technology, Pasadena, CA 91109

Whereas gravity and topography observations at present provide the only direct data pertaining to the interior of Mars, the state of stress at the surface of the planet, as reflected in tectonic features, can provide an additional constraint on interior models [1]. Over the last several years a number of papers have been published using this concept to investigate the subsurface structure and tectonic history of Mars, with an emphasis on the Tharsis plateau [e.g. 1-7]. Two mathematical global stress models have been used to predict tectonic style for comparison with geological observations. The first, derived by Banerdt and others [1], consists of a thick spherical elastic shell over an inviscid mantle, whereas the second, by Sleep and Phillips [2], utilizes a thin spherical elastic shell approximation and retains only the membrane component of the stress, ignoring the bending component. These models predict very similar stress fields, and the first order investigations of Tharsis using these two models resulted in virtually the same conclusions: a simple uplift model for Tharsis is not generally supported by observed tectonic features, multiple stress regimes (operating at different times) are required to explain the orientations of these features, and Tharsis must have been nearly isostatic over a large portion of its history.

However there are some differences between the two published sets of stress fields which present ambiguities when attempting to make detailed comparisons between tectonic features and the theoretical stresses. Perhaps the clearest example is in the isostatic case. The Sleep and Phillips model gives a nearly circumferential (to Tharsis) orientation for the isostatic tensile stresses around Tharsis, whereas the Banerdt et al. model shows tensile stresses that have a pronounced east-west distortion to the circumferential pattern. This difference may be critical when attempting to identify sets of features that formed under either an isostatic or flexural regime (in order, for example, to establish their relative timing), as both models predict that flexural loading tensile stresses will be generally circumferential [e.g., 3].

In this study we investigate the differences between the model assumptions and their effects on stress directions in an attempt to reconcile the two theoretical stress models. We identify the primary differences between the models as: 1) thick shell vs. thin shell theory (and the exclusion of bending stresses from the thin shell formulation); 2) the value of Poisson's ratio used; 3) the depth in the lithosphere at which the stress tensor is evaluated; and 4) the treatment of the hydrostatic ellipticity. We then incorporate these results into a higher spatial resolution stress model suitable for detailed large-scale structural interpretation.

Thick shell vs. thin shell. Thin shell approximations are generally valid when the shell thickness is less than about 1/10 the radius of curvature [8], roughly 350 km for Mars. Thus for the 450 km lithosphere thickness used by Sleep and Phillips, the validity of the thin shell assumption is questionable. However this applies primarily to bending stresses, which are more strongly affected by shell thickness. The effect of shell thickness on membrane stress is considerably smaller. The bending stress contributions to the behavior of the shell are small compared to those of membrane stresses for harmonic degrees less than 5 for a lithospheric shell on Mars with a thickness of 450 km. Therefore the thin shell assumption is justified for these wavelengths; for thinner lithospheres, which are more likely on Mars, the approximation is even better. For shorter wavelengths, however, bending stresses must be included.

Poisson's ratio and depth of stress evaluation. For the Banerdt et al. model a value for Poisson's ratio of 0.25 (near that typical for rocks) was used and stress trajectories were evaluated at the deformed lithospheric surface. Sleep and Phillips incorporated a Poisson's ratio of 0.5 in order to remove bending stress contributions and displayed stress trajectories at the topographic surface. Both of these differences tend to change the magnitude of the predicted shear stress and the style of predicted faulting (suppressing extensional failure in favor of strike-slip), but principal stress orientations are unaffected by these parameters.

Rotational ellipticity. Sleep and Phillips derived an explicit treatment for the internal rotational ellipticity of Mars. From their results it is possible to derive the non-hydrostatic portion of  $J_2$  ( $-C_{20}^N$ ) as a function of the assumed moment of inertia factor ( $I/Ma^2$ ). Whereas the moment of inertia for Mars is not known, straightforward assumptions regarding the superposition of a symmetric Tharsis anomaly on an otherwise hydrostatic  $J_2$  yield an estimate for  $I/Ma^2$  of 0.365 [9]. Assuming this value, about 93% of the currently observed  $J_2$  should be due to the dynamic flattening by rotation, giving  $C_{20}^N = -6 \times 10^{-5}$ . For lack of such a dynamic ellipticity formulation and given the uncertainty in  $I/Ma^2$ , Banerdt et al. assumed simply that the entire observed  $J_2$  was due to rotation, or  $C_{20}^N = 0$ . This corresponds to  $I/Ma^2 = 0.376$ , near the upper bound of published estimates. For this value, the Tharsis high is elongated in the north-south direction, and Chryse and Amazonis correspond to major lows. In addition, an error was made in the computation of the rotational contribution to the topographic  $C_{20}$ , resulting in a similar appearance for the topography. When  $C_{20}^N = -6 \times 10^{-5}$  is used (and the proper topographic correction is used), Tharsis appears more circular (this follows directly from the assumptions involved in the estimate of  $I/Ma^2$  [9]), and the basin lows are subdued. When this latter  $C_{20}^N$  is used (as in the Sleep and Phillips model), virtually all of the discrepancy between the two stress models is eliminated. Thus the differences between the stress results in [1] and [2] are due primarily to the respective choices of  $C_{20}^N$ .

Higher resolution stress models. Lithospheric strength envelope calculations [e.g. 10] and volcanic loading studies [11] indicate that the martian lithosphere is unlikely to have been much thicker than about 200 km. Thus a thick shell treatment is unnecessary and we have used instead a full thin shell formulation including bending stresses [12], utilizing topography and gravity coefficients through degree and order 8 [13, 14]. The higher resolution stress trajectory plots thus generated (e.g., figure 1) can be used in conjunction with detailed mapping of tectonic features (e.g., [15]) in order to better understand the thermo-tectonic evolution of the martian lithosphere. For example, the choice of  $C_{20}^N$  (or, equivalently,  $I/Ma^2$ ) makes a small but significant difference in the predictions for the orientations of structural features in areas that appear to have been affected by multiple regional stress events. One of these areas is the Tempe Plateau region in northeastern Tharsis. For a value of  $C_{20}^N$  near zero (such as that used in [1]) flexural stresses predict the formation of northeast trending grabens, whereas the isostatic stresses predict north-northeast trending grabens. There are two appropriately aged graben systems in this area with these orientations [3]. Structural and superposition relationships indicate that the area was first affected by isostatic stresses, followed by flexural stresses. However if a larger  $C_{20}^N$  (such as that used in [2]) is assumed, there is no significant difference in the predicted orientations of grabens in this region for the two stress states and these fracture sets cannot be used to infer the relative timing of flexural and isostatic support for the Tharsis plateau. Conversely, it may be possible to use the differences in the orientations of fractures in areas such as these to constrain  $C_{20}^N$  and, by extension, the moment of inertia for Mars.



References: [1] Banerdt, et al., *J. Geophys. Res.* **87**, 9723, 1982; [2] Sleep and Phillips, *J. Geophys. Res.* **90**, 4469, 1985; [3] Golombek and Phillips (abs.), *Lunar Planet. Sci. Conf. XIV*, 253, 1983; [4] Phillips and Golombek (abs.), *Lunar Planet. Sci. Conf. XIV*, 604, 1983; [5] Hall et al., *J. Geophys. Res.* **91**, 11377, 1986; [6] Watters and Maxwell, *J. Geophys. Res.* **91**, 8113, 1986; [7] Francis (abs.), *Lunar Planet. Sci. Conf. XVII*, 235, 1986; [8] Kraus, *Theory of Thin Shells*, 1968; [9] Kaula, *Geophys. Res. Lett.* **6**, 194, 1979; [10] Banerdt and Golombek (abs.), *Lunar Planet. Sci. Conf. XVI*, 23, 1985; [11] Comer et al., *Rev. Geophys.* **23**, 61, 1985; [12] Banerdt, *J. Geophys. Res.* **91**, 403, 1986; [13] Bills and Ferrari, *J. Geophys. Res.* **83**, 3497, 1978; [14] Balmino et al., *J. Geophys. Res.* **87**, 1982; [15] Tanaka and Davis, *J. Geophys. Res.* **93**, 14893, 1988.

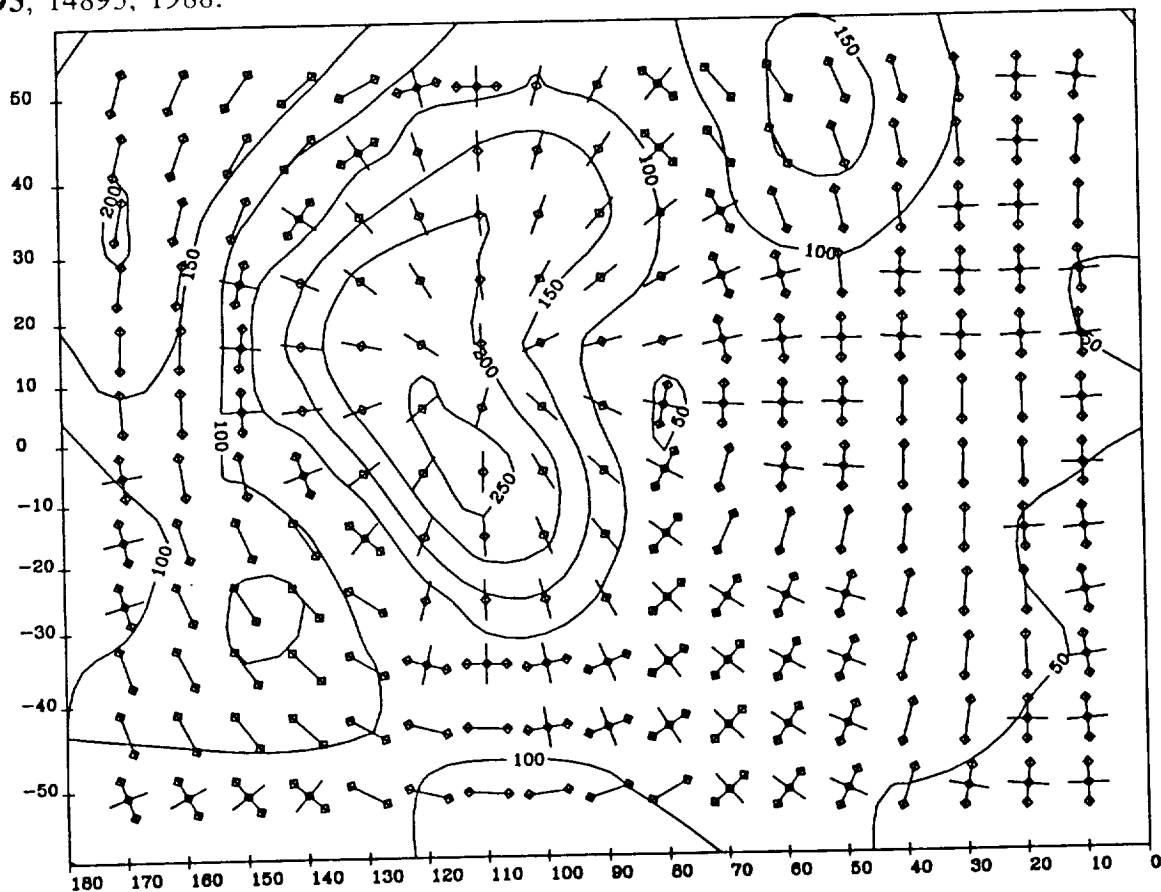


Figure 1. Flexural loading stresses for Tharsis, plotted on a mercator projection corresponding to the western equatorial 1:15M geologic map of Scott and Tanaka. Tharsis is centered at roughly 5° south, 105° west. Contours show the magnitude of the maximum stress difference at the surface in MPa. The stress orientation indicators with symbols at each end denote horizontal extension; those with symbols in the center denote compression. For this case Tharsis is formed by adding material to the surface, causing downward deflection of the lithosphere. The local thickness of the crust is simultaneously adjusted in order to satisfy the observed gravity. Stresses were calculated assuming lithosphere thickness = 200 km, crustal thickness = 50 km, Young's modulus =  $1.25 \times 10^{11}$  nt/m<sup>3</sup>, Poisson's ratio = 0.25, and the crust-mantle density contrast = 0.5 Mg/m<sup>3</sup>. Topography and gravity harmonics through degree and order 8 have been used as boundary conditions.

## INVOLVEMENT OF THE LITHOSPHERE IN THE FORMATION OF WRINKLE RIDGES ON MARS;

M. Golombek<sup>1</sup>, J. Suppe<sup>2,3</sup>, W. Narr<sup>3</sup>, J. Plescia<sup>1</sup>, and B. Banerdt<sup>1</sup>: <sup>1</sup>Jet Propulsion Laboratory, Caltech, Pasadena, CA 91109, <sup>2</sup>Seismological Laboratory, Caltech, Pasadena, CA 91125, <sup>3</sup>Dept. Geological and Geophysical Sciences, Princeton University, Princeton, NJ 08544.

Recent work on the origin of wrinkle ridges suggests that they are compressional structures, but the subsurface structure and the possible involvement of the lithosphere in their formation are not understood. In this abstract, we briefly review important characteristics of Martian wrinkle ridges, including their subsurface structure and amount of shortening, both of which suggest that they are the surface expression of thrust faults that extend through much of the lithosphere.

Photoclinometric topographic profiles across wrinkle ridges in Lunae Planum and Amazonis Planitia show an average regional elevation offset across the ridges (plains on one side of the ridge are at a distinctly different elevation than plains on the other) of about 100 m. The offset in regional elevation extends for many kilometers on either side of the ridge and requires a fault beneath the structure; simple fold structures or faults that flatten into a decollement cannot readily explain the elevation offset. Vertical faulting at depth does not provide an obvious mechanism for producing the broad low positive relief structure characteristic of wrinkle ridges. A combination of folding and low-angle faulting, however, can produce both the observed ridge morphology and the offset in regional elevation. The lateral extent of the regional elevation change requires a planar fault that does not shallow with depth, because the regional elevation change would decrease to zero above the point where the fault flattens to a decollement (Golombek et al., 1989).

We have calculated the amount of shortening due to folding for Martian wrinkle ridges (5-25 m) by simply unfolding the surface profile along the ridge. The shortening due to faulting was obtained by dividing the regional elevation change, which is produced by slip on the fault, by the tangent of the fault dip. Although the dip of the fault is not known, measurements of the dip of normal faults on Mars (Davis and Golombek, 1989) and lab experiments of prefractured rock suggest a dip of about 25° for thrust faults (Brace and Kohlstedt, 1980; Byerlee, 1978). Shortening due to faulting averages between 100 and 300 m. Total shortening across Martian wrinkle ridges is therefore on the order of hundreds of meters, similar to values for lunar wrinkle ridges (Golombek et al., 1988); strain is on the order of a few percent. The ratio of shortening due to faulting to that due to folding is in the range of 5 to 20, indicating that faulting is the dominant mechanism for accommodating shortening in Martian wrinkle ridges and that folding is subsidiary.

A number of attempts have been made to identify kinematic models capable of explaining the salient characteristics of wrinkle ridges. In particular, fault-bend and fault-propagation folding have been suggested as possible models for the development of wrinkle ridges (Plescia and Golombek, 1986; Watters, 1988). Fault-bend folding (Suppe, 1983) can produce an anticlinal fold when surficial rocks are translated over a surface-flattening bend in a thrust fault. Fault-propagation folding (Reidel, 1984; Suppe, 1985; Suppe and Medwedeff, 1984; Woodward et al., 1985; Jamison, 1987) occurs when displacement along a reverse fault at depth is accommodated by folding of overlying layers. Both types of structures are capable of producing surface folds with complex near surface faulting, similar to wrinkle ridges. More detailed considerations suggest, however, that the gross structure of wrinkle ridges is different from typical fault-bend and fault-propagation folds. In particular, faults responsible for both fault-bend and fault-propagation folds most commonly shallow out into horizontal decollements at bedding-plane contacts between rocks with distinct mechanical properties. In addition, where

observed on the earth, the step-up ramps associated with these types of structures are sharp, rather than gradual, so that a gradually changing fault dip (for example a thrust fault gradually shallowing with depth) beneath wrinkle ridges is not supported by observations on earth. If the fault dip shallowed or completely flattened with depth, the offset in regional elevation would also decrease or disappear and abrupt changes in fault dip would produce correspondingly abrupt changes in surface elevation away from wrinkle ridges. In addition, the slip across wrinkle ridges is small, much less than that likely by formation of these structures by fault-bend or fault-propagation folding. For these types of folds, the long rear limb of the fold is produced by translation of rocks above the thrust ramp. This in turn requires that the slip across the structure be roughly equal to the width of the rear limb. The rear limb of most wrinkle ridges is many kilometers wide, which is an order of magnitude greater than the shortening that can be reasonably accommodated across them. Thus, the lack of evidence for horizontal decollements beneath wrinkle ridges and the excessive strains suggested for fault-bend and fault-propagation folds indicate that a different deep subsurface structure might be more applicable for the overall geometry of planetary wrinkle ridges. Fault-bend and fault-propagation folding could still be responsible for the complex near-surface folding and faulting implied by wrinkle ridges.

In northwestern Lunae Planum wrinkle ridges are spaced about 50 km apart and consistently have an uplifted eastern side. Within the accuracy of the photoclinometric method the regional elevation change appears to persist laterally for many kilometers away from the ridges. There is no evidence for tilted blocks between the ridges (dips of  $1^\circ$  or greater would have been detected), and no evidence for any folding or warping of the surface between the ridges. To first approximation, the faults beneath these ridges must dip to the east, to produce the uplifted eastern side, and continue at least 50 km to the next ridge. If the fault dips at roughly  $25^\circ$ , then the fault is roughly 25 km beneath the surface at this distance. Steeper dips would result in greater depths of penetration; a  $45^\circ$  dipping fault would be at 50 km depth beneath the adjacent ridge. Note that even if the surface between adjacent wrinkle ridges was tilted at less than a degree, the underlying fault must still continue laterally to the next ridge, at which point it would probably be tens of kilometers below the surface (e.g., Erslev, 1986). This indicates that the faults responsible for wrinkle ridges clearly involve a significant thickness of the Martian lithosphere and are not simply surface folds affecting the upper few kilometers of the crust.

There is strong evidence that faults beneath foreland basement uplifts, such as the Rocky Mountains, are underlain by planar faults that root in the weak ductile lower crust near the Moho. Best known of these basement thrusts is the Wind River thrust (Smithson et al., 1979), which dips about  $40^\circ$ , has slipped about 5-7 km, and is clearly imaged on seismic profiles to about 20 km depth. Geometric considerations indicate the fault zone flattens near the Moho at about 35 km depth. Numerous other basement thrusts have been documented in the Rocky Mountain foreland and elsewhere worldwide in the course of petroleum exploration (for example Gries, 1983; Gries and Dyer, 1985). Many of these basement thrusts have small offsets on the order of hundreds of meters and have a change in elevation across the structure, similar to wrinkle ridges. Some of the best documented examples are in the Wind River basin (Gries and Dyer, 1985). The deformation is entirely by fault slip in the basement, but as the fault enters the 1-3 km thick sedimentary cover, fault-bend folding, wedging and fault-propagation folding produce structures that are quantitatively similar to the kilometer-scale aspects of wrinkle ridges.

On Mars, a number of supporting arguments and models also permit the rooting of faults responsible for wrinkle ridges in a weak ductile lower crust or lithosphere. The flexure of volcanic loads on the Martian surface (Comer et al., 1985) and the magma source region required beneath the giant Tharsis volcanoes (Carr, 1973; Blasius and Cutts, 1976) both suggest a lithosphere on the order of 50 km thick at the period in Tharsis history when wrinkle ridges formed. Assuming a 50 km thick lithosphere, with a basaltic crust 30 km (Bills and

Ferrari, 1978) to 100 km thick (Sjogren and Wimberly, 1981; Sjogren and Ritke, 1982; Janle and Ropers, 1983) and an olivine mantle (Wood and Ashwal, 1981; Francis and Wood, 1982), requires thermal gradients of 9°/km to 16°/km from ductile creep properties of basalt and olivine. Thermal evolution models of Mars (Toksoz et al., 1978) also predict a present average crustal thermal gradient of 9°/km, which is a likely minimum as thermal gradients were undoubtedly greater during Tharsis volcanic and tectonic activity. Given these constraints, we have assumed 9°/km, 15°/km, and 20°/km and various crustal thicknesses for the construction of lithospheric strength envelopes (brittle and ductile yield stress versus depth curves) to gain a better understanding of likely lithospheric strong and weak zones at depth.

Results show that even under the coolest conditions a lower crustal weak zone is present below 40 km, assuming a minimum 50 km thick crust. Under the warmer conditions more likely for Tharsis, lower crustal weak zones begin at about 20 km depth, with all strength in the upper mantle gone at 40-60 km depth. These calculations indicate that under conditions likely during Tharsis deformation, weak zones at fairly shallow depths existed within the crust and mantle in which thrust faults could root, analogous to faults beneath foreland basement uplifts on the earth.

In conclusion, the observation that some regularly spaced wrinkle ridges accommodate regional elevation changes with a consistent uplifted side suggests that planar thrust faults extend to depths of tens of kilometers. Consideration of earth analogs most compatible with this subsurface structure and the low strains measured across wrinkle ridges (a few percent) suggest foreland basement uplifts are more appropriate earth analogs for the overall structure of wrinkle ridges; fault-bend and fault-propagation folding are probably responsible for the near-surface folding and faulting associated with wrinkle ridges. Foreland basement uplifts on earth are typically underlain by moderately dipping thrust faults that root in a weak ductile zone at the base of the crust. Evaluation of likely conditions around Tharsis indicates that faults beneath wrinkle ridges also could have rooted in a ductile zone of the lower crust at depths of a few tens of kilometers. These results suggest that deformation associated with wrinkle ridges involves much of the lithosphere.

## REFERENCES

- Bills and Ferrari, 1978, *J. Geophys. Res.*, v. 83, p. 3497. Blasius, K., and J. Cutts, 1976, *Proc. Lunar Sci. Conf. 7th*, p. 3561. Brace, W. and D. Kohlstedt, 1980, *J. Geophys. Res.*, v. 85, p. 6248. Byerlee, J., 1978, *Pageoph.*, v. 116, p. 615. Carr, M., 1973, *J. Geophys. Res.*, v. 78, p. 4049. Comer, R., S. Solomon, J. Head, 1985, *Rev. Geophys.*, v. 23, p. 61. Davis, P., and M. Golombek, 1989, *Lunar Plan. Sci. Abs. XX*, p. 224. Erslev, E., 1986, *Geology*, v. 14, p. 259. Francis and Wood, 1982, *J. Geophys. Res.*, v. 87, p. 9881. Golombek, M., J. Plescia, and B. Franklin, 1988, *Lunar Plan. Sci. XIX*, 395. Gries, R., 1983, *Amer. Assoc. Petrol. Geol. Bull.*, v. 67, p. 1. Gries, R., and R. Dyer, 1985, *Seismic Exploration of the Rocky Mtn. Region*, Rocky Mtn. Assoc. Geol., 299p. Jamison, W., 1987, *J. Struct. Geol.*, v. 9, p. 207. Janle and Ropers, 1983, *Phys. Earth Planet. Int.*, v. 32, p. 132. Plescia, J., and M. Golombek, 1986, *Geol. Soc. Amer.*, v. 97, p. 1289. Reidel, S., 1984, *Amer. J. Sci.*, v. 284, p. 942. Sjogren and Ritke, 1982, *Geophys. Res. Lett.*, v. 9, p. 739. Sjogren and Wimberly, 1981, *Icarus*, v. 45, p. 331. Smithson, S., J. Brewer, S. Kaufman, J. Oliver, and C. Hurich, 1979, *J. Geophys. Res.*, v. 94, p. 5955. Suppe, J., 1983, *Amer. J. Sci.*, v. 283, p. 684. Suppe, J., 1985, *Principles of Structural Geology*, Prentice-Hall, 537p. Suppe, J., and D. Medwedeff, 1984, *Geol. Soc. Amer. Abst. Prog.*, v. 16, p. 670. Toksoz et al., 1978, *Moon and Planets*, v. 18, p. 281. Watters, T., 1989, *J. Geophys. Res.*, v. 93, p. 10,236. Wood and Ashwal, 1981, *Proc. Lunar Planet. Sci. Conf. 12B*, p. 1359. Woodward, N., S. Boyer, and J. Suppe, 1985, *An Outline of Balanced Cross Sections*, Univ. Tenn. Dept. Geol. Sci., *Studies Geol.* 11, 170p.

CHRONOLOGY AND GLOBAL DISTRIBUTION OF FAULT AND RIDGE SYSTEMS ON MARS  
David H. Scott and James M. Dohm, U.S. Geological Survey, 2255 N. Gemini Dr.,  
Flagstaff, AZ 86001.

A series of paleotectonic maps has been made showing fault and ridge systems on Mars as they existed during the geologic past. These structures have been classified chronologically by mapping their occurrence in rock units emplaced during successive geologic periods. The three Martian systems--Noachian, Hesperian, and Amazonian [1], and their eight subdivisions (series) [2] are the time-stratigraphic referents for assigning ages to the faults and ridges. System and series boundaries and the structures mapped within the chronostratigraphic units were extracted from geologic maps at 1:15,000,000 scale that cover the surface of Mars [3-5]. The paleotectonic maps are being compiled at the same scale for the western, eastern, and polar regions of Mars and at 1:2,000,000 scale for local, complexly faulted areas within these regions. Although similar procedures were used in the age classification of faults and ridges both regionally and locally, additional discriminations could be made at the larger scale by considering (1) crosscutting relations among structures, (2) morphologic appearance such as degree of degradation, and (3) the concurrence of structural trends that might be indicative of nearly contemporaneous periods of deformation. Crosscutting relations are the most definitive of these criteria, but because they are not clear in places, some structures cannot be relatively dated with assurance by this method.

Some of the more significant results obtained from this continuing study show that all major fault systems on Mars are associated (in order of decreasing abundance) with five large volcanic centers, three impact basins, and the highland-lowland boundary in the equatorial zone. Only normal faulting has been recognized, although the slip sense of some dislocations is unknown. Both faulting and volcanism have progressively decreased with time from the Noachian to the Amazonian. The most abundant and extensive faults bound grabens that either follow the Tharsis northeast-southwest axial trend or are radial to volcanic centers that lie along this trend. Concentric faults are relatively late stage dislocations that partly encircle all of the large volcanoes on Mars; in places they occur where no surface evidence of volcanic constructs is evident, suggesting the presence of magma chambers that did not develop to form extrusive vents and constructs.

Martian ridge systems consist of two types: (1) wrinkle ridges, similar to those on the lunar maria, characterized by sinuous to nearly linear axial traces, and (2) larger ridges having steep, bold flanks resembling fault scarps in places. Wrinkle-ridge development appears to have culminated during the Early Hesperian, whereas the larger ridge systems occur only in rock units of Noachian age. Both types of ridges broadly encircle the Tharsis rise and suggest, together with fault evidence, that this huge topographic high was the result of structural uplift that occurred largely during the Noachian and Hesperian Periods.

Paleotectonic maps of highly complex areas such as Tempe Terra reveal more than ten distinct episodes of faulting during the Noachian and Hesperian; minor faulting continued in the Amazonian along trends developed in the earlier periods.

## References

- [1] Scott, D.H. and Carr, M.H. (1978) U.S. Geol. Survey Misc. Inv. Series Map I-1083.
- [2] Tanaka, K.L. (1986) Proc. Lunar and Planet. Sci. Conf. 17, J. Geophys. Res., v. 91, no. B13, p. E139-158.
- [3] Scott, D.H. and Tanaka, K.L. (1986) U.S. Geol. Survey Misc. Inv. Series Map I-1082A.
- [4] Greeley, R. and Guest, J.E. (1987) U.S. Geol. Survey Misc. Inv. Series Map I-1082B.
- [5] Tanaka, K.L. and Scott, D.H. (1987) U.S. Geol. Survey Misc. Inv. Series Map I-1082C.

STRIKE-SLIP FAULTING IN THE RIDGED PLAINS OF MARS. *Richard A. Schultz, NASA Goddard Space Flight Center, Greenbelt, MD 20771.*

The surface of Mars shows abundant evidence of extensional and contractional deformation in the form of normal faults, grabens, and wrinkle ridges [1]. In contrast, strike-slip faults have been considered to be extremely rare or absent on Mars [2,3]. However, careful study of Viking Orbiter images is revealing that strike-slip faults were produced on Mars [4]. Here I document several well-preserved examples of martian strike-slip faults, examine their relationships to wrinkle ridges, and discuss their tectonic significance.

The strike-slip faults presented here deform moderately cratered plains of presumed volcanic origin southeast of Valles Marineris (Fig. 1)[5]. North-south striking wrinkle ridges also deform plains materials throughout the area. The strike-slip faults are defined by a series of echelon linear structures that bound polygonal or rhombohedral plateaus located within their stepovers. These arrays of echelon structures and plateaus are oriented obliquely (about  $60^\circ$ ) to the overall trend of the wrinkle ridges and differ morphologically from typical wrinkle ridges on the Moon and Mars [6]. The plateaus do not appear to result from disruption and lateral offset of pre-existing wrinkle ridge topography because the ridges do not match up across the echelon structures. Further, the location of plateaus within stepovers argues against simple offset because not all echelon arrays are associated with wrinkle ridges or other high topography outside the stepover. Thus, the presence of polygonal plateaus within the stepovers of echelon structures suggests that the plateaus formed as a result of mechanical interaction between those structures. Extensional basins can occur within stepovers along overlapping spreading centers [7] and extensional stepovers along strike-slip faults [8]; stepovers between dip-slip faults are not generally associated with basins or uplifts. [9]. The rhombohedral shape of many plateaus, is consistent with the geometry of rock fracture in a strike-slip stepover. Hence, the linear echelon structures in Coprates are probably strike-slip faults and the plateaus correspond to uplifts within contractional stepovers.

The echelon structures and plateaus on Mars are similar geometrically, and probably mechanically, to strike-slip faults and push-up ranges on the Earth (Fig. 2). The correlation between overlap and separation suggests that push-up length (overlap in Fig. 2) is related to propagation of faults in echelon arrays [10] rather than directly proportional to fault offset (see [8]). The minimum horizontal shortening associated with martian push-up ranges estimated by assuming that the plateaus are fault-bounded rigid blocks is 1.4 to 2.0 km. This kinematic estimate probably underestimates shortening because it assumes rigid materials with no internal deformation in the stepover region and neglects shortening within wrinkle ridges located near fault terminations. Horizontal offset (shortening) exceeds vertical offset (push-up height) by at least 2-3 times.

Determination of the sense of slip along echelon strike-slip faults is straightforward given the type of stepover and sense of step. For example, contractional stepovers occur for right steps along a left lateral fault or left steps along a right lateral fault. The northwest trending strike-slip faults (Fig. 3) step consistently to the right, implying left lateral slip along the echelon array. The northeast trending faults to the south step consistently to the left, implying right lateral slip along that array. Secondary structures such as end-cracks, joints, and normal faults or stylolites, folds, and reverse faults can grow near strike-slip fault terminations as a result of fault slip [11], and the locations of these structures depend on the sense of slip. For a right lateral fault, large horizontal compressive stresses build up in the north-east and south-west quadrants, promoting nucleation and growth of folds and reverse faults. The right lateral fault arrays are associated

with wrinkle ridges in the north-east and south-west quadrants, and left lateral faults join wrinkle ridges in north-west and south-east quadrants. Wrinkle ridges are notably absent in the opposing, extensional quadrants of these faults. These relationships suggest that these wrinkle ridges may have nucleated in response to slip along the strike-slip faults and propagated away from the fault termination regions. High-angle (but not orthogonal) intersections between wrinkle ridges and the strike-slip faults are consistent with this hypothesis. In some cases, small crenulations that extend away from some fault terminations are superimposed on larger ridges, perhaps implying multiple stages of contractional deformation and local uplift. The location and orientation of wrinkle ridges near terminations of strike-slip faults provide independent evidence that wrinkle ridges represent contractional deformation such as folding or reverse faulting. Relationships between several strike-slip faults and wrinkle ridges suggest that strike-slip faulting predated growth of at least some wrinkle ridges. In a few cases, however, apparent superposition of fault-termination wrinkle ridges on much larger ridges implies the reverse sequence. No examples were found that would suggest strike-slip faulting that clearly postdated wrinkle ridge formation. Thus, it appears that strike-slip faulting predated and overlapped the episodes of wrinkle ridge growth.

The remote stress state associated with the martian strike-slip faults is inferred from their orientations and sense of slip. Using typical values of fault friction [12] and a Coulomb slip condition, the direction of maximum horizontal compressive principal stress  $\sigma_3$  would be oriented  $30^\circ$  to the faults, or approximately east-west (Fig. 3). Orientations of maximum compressive stress associated with wrinkle ridge formation obtained by assuming that  $\sigma_3$  is oriented normal to the overall trend of the ridges [13] are very similar to those inferred from the strike-slip faults. However, the orientation of minimum compressive stress would be vertical for wrinkle ridges but horizontal for strike-slip faults. Thus, strike-slip faults and wrinkle ridges can grow under the same remote stress state only if one set of structures changes the local stress state in such a way that the other structures can form. The geometry and relative timing of structures in Coprates indicates that many wrinkle ridges nucleated and grew as a result of strike-slip faulting.

The orientations of both grabens and wrinkle ridges throughout western Mars are generally well predicted by Tharsis deformation models [13], and the strike-slip faults and associated wrinkle ridges may be related to isostatic adjustments in Tharsis. However, Tharsis principal stress trajectories [13] differ by  $10\text{--}30^\circ$  from those derived from structure orientations (Fig. 3). One possibility is that the differences between Tharsis geophysics and structure orientations arise from idealizations or assumptions in the geophysical models. On the other hand, the region south-east of Valles Marineris is tectonically complex, and Tharsis-related remote stress states may have been modified by more local deformation. More refined geophysical modeling of Tharsis deformation and analysis of local deformation will help resolve these alternatives.

Left lateral strike-slip faulting has been inferred along the northwest trending Gordii Dorsum escarpment located west of Tharsis [4]. Strike-slip and wrinkle ridge deformation in Coprates are of early Hesperian age (about 3-3.5 b.y. ago [14]) and either roughly comparable in age or younger than that inferred along Gordii Dorsum. However, principal stress trajectories from Tharsis deformation models [13] do not appear to be suitably oriented to drive left lateral slip along Gordii Dorsum faults, so strike-slip faulting along Gordii Dorsum may not be related to Tharsis tectonism. Thus, there were probably at least two episodes of strike-slip faulting in widely separated regions of Mars. Given the complexity of deformation observed in many ancient terrains, strike-slip faulting likely played an important role in crustal deformation on early Mars.



REFERENCES: [1] Plescia & Saunders, JGR, 87, 8775 (1982); Solomon & Head, JGR, 87, 9755 (1982); Chicarro et al., Icarus, 63, 153 (1985). [2] Wise et al., Icarus, 38, 456 (1979); Golombek, JGR, 90, 3065 (1985). [3] Mars is considered to be a "one-plate" planet [Solomon, GRL, 5, 461 (1978)] with predominantly vertical motions of its lithosphere. [4] Forsythe & Zimbelman, Nature, 336, 143 (1988); R. Schultz, in prep. [5] See Blasius et al. [J. Geophys. Res., 82, 4067 (1977)] for review. [6] Sharpton & Head, PLPSC 18th, (Cambridge Univ. Press), 307 (1988); Watters, JGR, 93, 10,236 (1988). [7] Pollard & Aydin [JGR, 89, 10,017 (1984)] and Sempere & Macdonald [Tectonics, 5, 151 (1986)]. [8] Aydin & Nur, Tectonics, 1, 11 (1982). [9] Aydin & Nur [in Strike-Slip Deformation, Basin Formation, and Sedimentation (ed., Biddle and Christie-Blick, SEPM SP-37), p. 35 (1985)] discuss important kinematic differences between along-strike and down-dip stepovers. [10] Aydin & R. Schultz, in Proc. U.S.G.S Workshop on Fault Segmentation and Controls of Rupture Initiation and Termination, USGS Open-File Report, in press (1989); and J. Struct. Geol., in press, (1989). [11] Rispoli, Tectonophysics, 75, 29 (1981); Segall & Pollard, JGR, 85, 4337 (1980); Aydin & Page, GSA Bull., 95, 1303 (1984). [12] Coefficients of static friction along well-slippped faults are commonly lower ( $f=0.6$ ) than those of unfaulted rock ( $f=0.85$ ). See Byerlee [Pure Appl. Geophys., 116, 615 (1978)], Rudnicki [Ann. Rev. Earth Planet. Sci., 8, 489 (1980)], Rice [Pure Appl. Geophys., 121, 443 (1983)], and Li [in Fracture Mechanics of Rock (Academic Press, London), 351 (1987)]. [13] Banerdt et al. [JGR, 87, 9723 (1982)]; Sleep & Phillips [JGR, 90, 4469 (1985)]. [14] Tanaka, PLPSC 17th, part 1, in JGR, 91, E139 (1986).

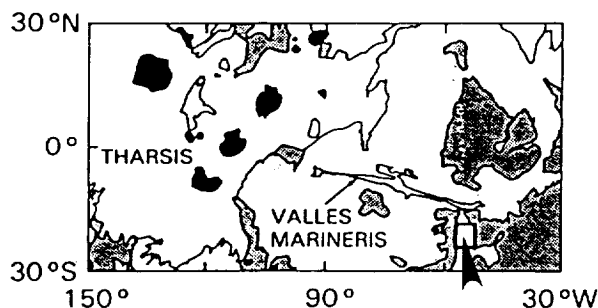


Fig. 1. Location of strike-slip faulting (inset).

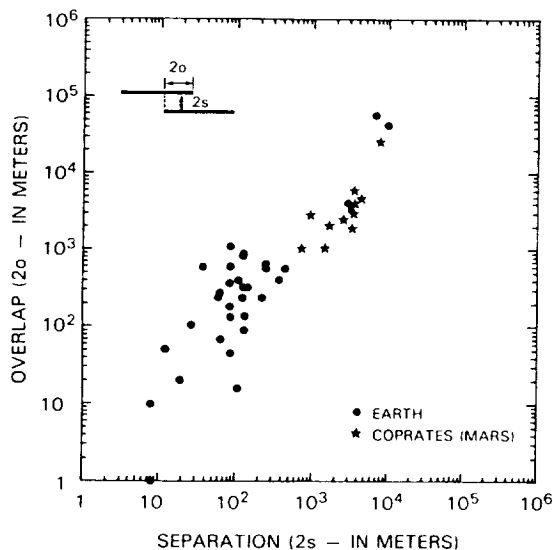


Fig. 2. Geometry of echelon strike-slip faults from Earth and Mars. Filled symbols, contractional stepovers.

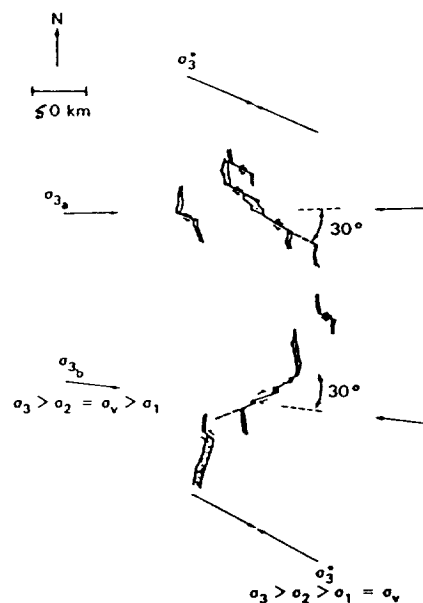


Fig. 3. Relationships between strike-slip faults and wrinkle ridges. Orientations of maximum compressive principal stress inferred from left lateral faults ( $\sigma_3a$ ), N90W; from right lateral faults ( $\sigma_3b$ ), N80-85W. These trajectories are consistent with orientations of wrinkle ridges. Principal stress trajectories calculated from Tharsis isostasy models ( $\sigma_3^*$ ) differ by 10-30° from those inferred from structure orientations and would predict reverse faulting or folding normal to  $\sigma_3^*$ .

STRIKE-SLIP FAULTING ASSOCIATED WITH THE FOLDED  
COLUMBIA RIVER BASALTS: IMPLICATIONS FOR THE DEFORMED RIDGED  
PLAINS OF MARS

Thomas R. Watters and Michael J. Tuttle, Center for Earth and  
Planetary Studies, National Air and Space Museum, Smithsonian  
Institution, Washington, D.C. 20560

The anticlinal ridges in the continental flood basalts of the Columbia Plateau (or Columbia Basin) are long, narrow, periodically spaced structures with broad relatively undeformed synclines. The orientation and spacing of the anticlines varies throughout the Yakima Fold Belt, but is consistent within certain domains (1). Associated with the steeply dipping vergent side of the asymmetric anticlines are reverse to thrust faults. Mechanisms suggested for the origin of the anticlines or Yakima folds include: 1) drape folding over high angle reverse faults (2); 2) buckling over shallow detachments in the basalt sequence followed by reverse to thrust faulting (3); 3) buckling of the basalt sequence simultaneously with the emplacement of the oldest flows followed by dominantly reverse to thrust faulting (4); and 4) initial buckling in response to a horizontal compressive load coupled with a layer instability between the basalts and sub-basalt sediments (1,5).

In addition to the anticlines, numerous strike-slip faults have been mapped in the fold belt. Anderson (6) reports 35 right-lateral strike-slip faults (mean strike N40°W) and 10 left-lateral (mean strike N13°E) in the southern portion of the fold belt. The lateral displacement along the most extensive faults is typically small (< 1 km). Tolan et al. (7) suggest that the strike-slip faults can be classified as either tear faults, faults of limited extent or regional faults. Based on paleomagnetic data, Reidel et al. (8) observe a clockwise rotation in the anticlines relative to the synclines that they attribute to rotation along a localized NW trending right-lateral shear system developed in the anticlines as they grew.

In an effort to find additional evidence of strike-slip faults within the fold belt, Landsat Thematic Mapper (TM) data (30 m/pixel), Seasat SAR (25 m/pixel) and topographic data are being examined for prominent lineaments. The TM data has been geometrically corrected and edge enhanced to optimize the discrimination of linear features. Mapped lineaments are then digitized to facilitate statistical analysis using double angle method. To date over 80 lineaments have been mapped, 73 of which are located in the southern domain of the fold belt. Many of these correspond to previously mapped right-lateral strike-slip faults. The mean direction of the known and suspected strike-slip faults in the southern domain is N37°W (circular variance = 0.15) (figure 1). No predominant secondary trend corresponding to conjugate left-lateral strike-slip faults is present in our data.

Tectonic domains where major fold trends are transected by conjugate strike-slip faults have been documented (9,10). Because of the limited extent and lateral displacements of the strike-slip faults in the fold belt, a pure shear rather than a simple shear mechanism should best explain the geometric relationships between the structures. Pure shear is consistent with the development of relatively short (< 100 km) conjugate sets of strike-slip faults (see 10). Given a N-S directed compressive stress, the system of structures possible includes E-W trending first-order folds and first-order right-lateral and conjugate left-lateral strike-slip faults with a angle  $\theta$  to the primary stress direction (figure 2). The angle  $\theta$  is constrained by the Coulomb-Navier criterion where  $\theta$  is related to the coefficient of internal friction  $\mu$ . For typical values of  $\mu$  between 0.58 and 1.0,  $\theta$  is in the range of 22.5°-30°. In the southern domain of the fold belt, the mean direction of the ridges is roughly N80°W. Taking the normal to this to be the approximate direction of the compressive stress, the mean direction of the known and suspected right-lateral strike-slip faults is within the range for  $\theta$ . Although the regional faults are thought to predate the Columbia River basalts (7), their orientation and extent are consistent with the expected system of tectonic features.

The anticlinal ridges in the Yakima Fold Belt have been shown to be good analogs to first-order ridges in wrinkle ridge assemblages that occur in the ridged plains material on Mars (5). If the ridged plains material has deformed in a similar style to the basalts of the Yakima Fold Belt, then strike-slip faults and their associated secondary structures may be common on Mars. In contrast to the Gordii Dorsum escarpment, interpreted by Forsythe and Zimbelman (11) to be a major transcurrent fault, the strike-slip faults associated with the first-order ridges, like their analogs in the Yakima Fold Belt, would be expected to be limited in extent, accommodating a portion of the relatively low bulk strain apparent in the ridged plains.

#### Reference Cited

- (1) Watters, T.R., in Geol. Soc. Am. Sp. Paper: Volcanism and Tectonism in the Columbia River Flood-Basalt Province, in press, 1989.
- (2) Bentley, R.D., in Geology excursions in the Pacific Northwest, Western Washington Univ., Bellingham, WA, 339-389, 1977.
- (3) Price, E.H., Ph.D. dissertation, Washington State Univ., Pullman, WA, 1982.
- (4) Reidel, S.P., Am. Jour. Sci., 284, 942-978, 1984.
- (5) Watters, T.R., JGR, 93, 10,236-10,254, 1988.
- (6) Anderson, J.L., Ph.D. dissertation, Univ. South. CA, 1987.
- (7) T.L. Tolan, J.L. Anderson and M.H. Beeson, in MEVTV Workshop: Tectonic Features on Mars, LPI, Houston, 37-38, 1988.
- (8) Reidel, S.P., G.R. Scott, D.R. Bazard, R.W. Cross, and B. Dick, Tectonics, 3, 251-273, 1984.
- (9) Tirrul, R., I.R. Bell, R.J. Griffis and V.E. Camp, Geol. Soc. Am. Bull., 94, 134-150, 1983.
- (10) Sylvester, A.G., Geol. Soc. Am. Bull., 100, 1666-1703, 1988.
- (11) Forsythe R.D. and J.R. Zimbelman, Nature, 336, 143-146, 1988.

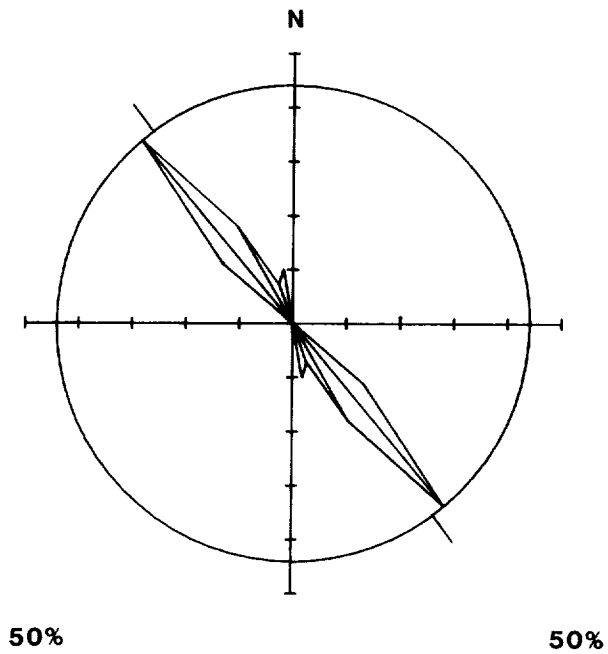


Figure 1. Rose diagram of known and suspected right-lateral strike-slip faults.

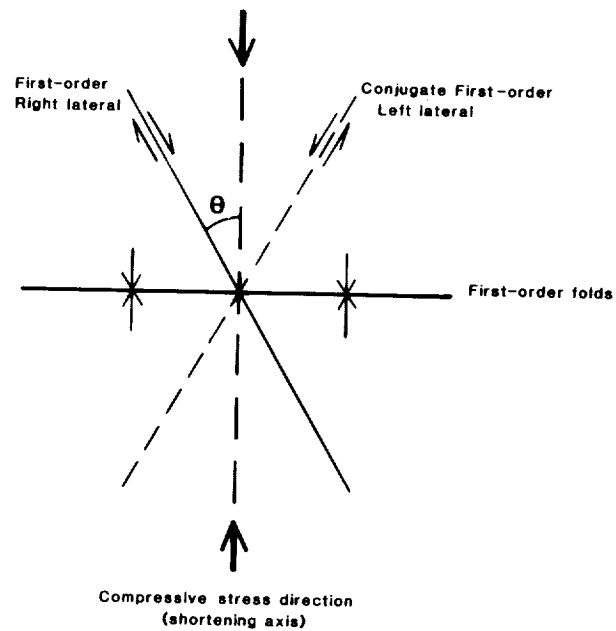


Figure 2. Geometric relationships between system of structures.  $\theta = \text{Arctan} (\mu^{-1}) / 2$

PERIODICALLY SPACED WRINKLE RIDGES ON THE THARSIS  
PLATEAU OF MARS. Thomas R. Watters, Center for Earth and  
Planetary Studies, National Air and Space Museum, Smithsonian  
Institution, Washington, D.C. 20560.

The ridged plains units of the Tharsis Plateau of Mars are characterized by smooth plains and the presence of landforms analogous to mare wrinkle ridges. The exact nature of the ridged plains material has yet to be determined. However, indirect evidence suggests that they are the result of flood volcanism. The origin of the wrinkle ridges has been the subject of a number of recent papers and some debate over the role of buckling and/or reverse or thrust faulting (1, 2, 3). The general consensus, however, is that wrinkle ridges are tectonic features resulting from horizontal compressive stresses. The periodic nature of the wrinkle ridges was first noted by Saunders and Gregory (4). In this study, statistics on the spacing were determined using a series of sampling traverses at roughly 12 km intervals oriented perpendicular to the mean orientation of the ridges. The greatest frequency in the observed spacing for the Tharsis ridge system occurs in the range of 25 to 35 km. The periodic spacing of the ridges suggests buckling at a critical wavelength. The model proposed here assumes that: 1) deformation has occurred at the free surface; 2) the ridged plains are a multilayered volcanic sequence resting on a mechanically weak regolith of finite thickness which is in turn resting on a rigid boundary (figure 1); 3) units of flows are separated by thin regolith interbeds that allow free slip between the individual units. Solutions for critical wavelength have been obtained for a linearly elastic material where the hydrostatic restoring force is considered and for a linearly viscous material where it is not. The wavelengths obtained from the two solutions are nearly identical. The critical wavelength as a function of thickness  $h$  of the ridged plains material for a strength contrast  $\xi/\xi_0 = 1,000$ ,  $t$  of 250 and 500 m, and a regolith substrate of 4000 m is given in figure 2. Here  $\xi$  and  $\xi_0$  are the elastic modulus or viscosity of the ridged plains material and substrate respectively. Many of the observed spacings in the Tharsis ridge system can be explained given a range in thickness of the ridged plains material of 1,900 to 4,000 m and  $\xi/\xi_0 \geq 1000$ . Thus, the ridged plains material would be expected to deform at least initially by buckling when subjected to a horizontal compressive load.

References Cited:

- (1) Watters, T.R., JGR, 93, 10,236-10,254, 1988.
- (2) Plescia, J.B. and M.P. Golombek, GSA Bull., 97, 1298-1299, 1986.
- (3) Sharpton, V.L. and J.W. Head, Proc. Lunar Planet. Sci. 9th, 307-317, 1987.
- (4) Saunders, R.S. and T.E. Gregory, NASA Tech. Memo. TM82385, 93-94, 1980.

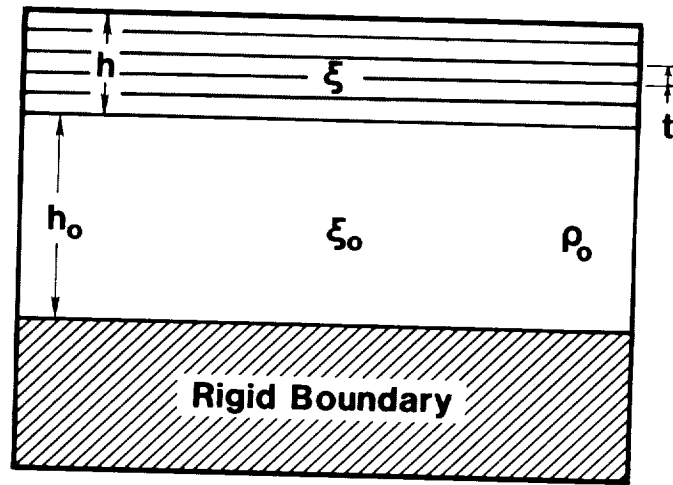


Figure 1. Diagram of the boundary conditions.

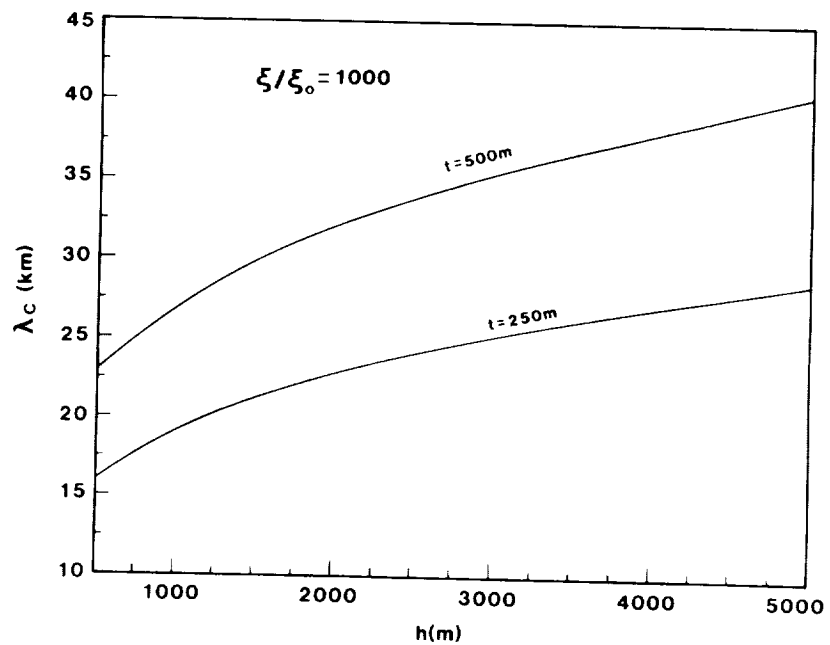


Figure 2. Critical wavelength of buckling as a function of thickness of the ridged plains material.

RESURFACING IN COPRATES AND THICKNESS OF THE RIDGED PLAINS; Herbert Frey, Goddard Space Flight Center, Greenbelt, MD 20771 and Tammie D. Grant, Astronomy Program, University of Maryland, College Park, MD 20742.

Major resurfacing events on Mars can be identified through analysis of the cumulative frequency curves using the Neukum and Hiller (1) technique. The curve is broken into branches (corresponding to different crater retention surfaces) where it departs from a standard production curve. The technique is highly dependent on the choice of production curve, and works best for resurfacing events that are efficient at removing craters and relatively discrete events (occurring over a time which is short by comparison with the repopulation time). We have shown the technique is useful for identifying major resurfacing events, determining their crater retention ages, and correlating these events over widely separated parts of Mars (2,3,4). It is also possible to determine the minimum extent of now buried surfaces (5,6) and the thickness of the materials associated with the different resurfacing events (6,7).

Such studies have shown a very important resurfacing event on Mars coincident with the emplacement of ridged plains in Lunae Planum and elsewhere (2-7). In this paper we discuss the resurfacing events which dominate the history of the ridged plains and other units in the Coprates region, and determine an average thickness of the ridged plains within the different terrain units in the area.

#### LUNAE PLANUM AGE (LPA) RESURFACING IN COPRATES

The Coprates region south of the Valles Marineris was subdivided based on terrain morphology into six regions. From west to east these are the relatively smooth plains of Solis Planum (SP), a transition region of subdued ridges (SR), a central region where ridges are prominent but which also contains small grabens (RG), an area of cratered terrain (CT) at 55 to 60 °W, a narrow trough of ridged plains (CR) and an extensive area of old cratered terrain east of 50°W (NPL3). For each of these areas we counted craters larger than 5 km diameter and broke the cumulative frequency curves into branches as described above. For all but the two most western units a strong branch was found with crater retention age  $N(1)=21,000$  to 24,000, associated with the LPA resurfacing (2-4,6,7). The LPA event is not restricted to the ridged plains units (RG,CR) but is seen in the heavily cratered terrains as well (CT,NPL3). In the region of ridges and grabens, a younger branch at  $N(1)=14,800$  appears to be a second episode of ridged plains volcanism, based on the superposition of the craters from this branch on the ridges. If true, then the oldest branch in the curve for SR with  $N(1)=13,700$  is probably a late-finishing resurfacing of the same kind. The lack of such a branch for the Solis Planum area where the oldest surface is  $N(1)=5000$  implies that ridged plains volcanics have been completely buried in this western-most unit.

#### THICKNESS OF RIDGED PLAINS IN COPRATES

We have shown elsewhere (6,7) that it is possible to derive thickness estimates for the resurfacing materials of any age from the smallest crater which survives from this age surface. Surviving craters actually give the total thickness of all overlying materials; differencing these total estimates for successive resurfacing events allow calculation of the thickness for any event. It is also possible to guess at the thickness or depth to surfaces not seen in the cumulative frequency curve branches. The production curve (1) provides an estimate of the largest (or fifth largest) crater that should be present on any size surface of a given age; the absence of such craters implies that the total overlying thickness is at least the amount of material needed to cover such craters (8). Using such estimates of the thickness of each unit and their ages, it is possible to develop a crude stratigraphy of resurfacing horizons, which we have done for Coprates in Figure 1.

In the eastern units of Coprates craters of moderate diameter show through the ridged plains (CR); these are survivors from before the LPA resurfacing. The lack of such craters in Lunae Planum implies that the thickness of ridged plains and later units is much greater. Our more quantitative estimates based on the smallest survivor bear agree. We estimate in CR that the thickness of ridged plains is about 100m, with an additional 245m of later resurfacing material above. By contrast the thickness of Lunae Planum ridged plains must be about 270m with an additional 315m above. This thickness is much more closely matched by the combined materials from the two episodes of LPA resurfacing in the RG unit, which total to 290m with an additional 225m above. The cratered terrains have very little LPA material; thickness of later materials are roughly the same. Younger resurfacing materials thicken dramatically toward the west through Solis Planum.

When combined with topographic data from ground-based radar, the stratigraphy of these units can be placed in a context which helps explain the variations in thickness. As shown in Figure 2, the great thicknesses of ridged plains materials occurs at the low portion of the downhill slope from Tharsis eastward into Coprates; in the central area the plains have contributed significantly to the height. Eastward the ridged plains thin in the higher-standing cratered terrain, and thicken somewhat in the trough region further east. Information of this sort is particularly useful when correlated with similar resurfacing events elsewhere on Mars (7).

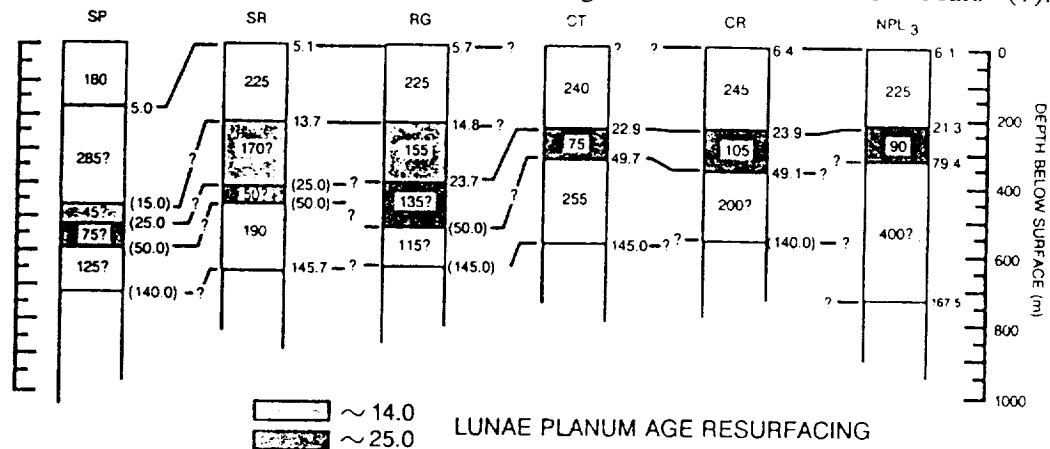


FIGURE 1. N(1) ages of resurfacing events (in thousands) are shown at the sides of each section. Thicknesses shown within each section.

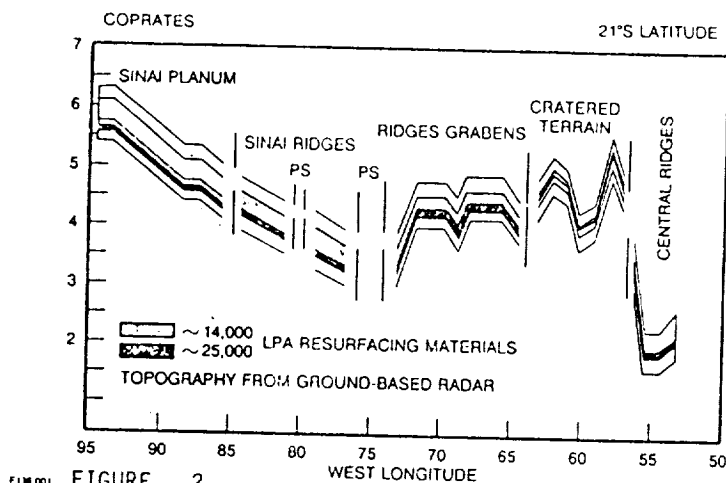


FIGURE 2



## References

- [1] Neukum, G. and K. Hiller, 1981. **JGR** 86,3097.
- [2] Frey, H. et al., 1983. **Proceed. LPSC** 18, 679.
- [3] Grant, T.D. and H. Frey, 1988. **Lunar Planet. Sci.** XIX, 413.
- [4] Grant, T.D. et al., 1988. **Lunar Planet. Sci.** XIX, 415.
- [5] Frey, H. and J.A. Semenick, 1988. **Lunar Planet. Sci.** XIX, 360.
- [6] Frey, H. et al., 1988. **MEVTV Workshop: Early Tectonic, Volcanic Evolution of Mars**, 24.
- [7] Frey, H. et al., 1989. **4th Intern. Conf. Mars**, 104.
- [8] Pike, R. and P. Davis, 1984. **Lunar Planet. Sci.** XV, 645.

CROSSCUTTING PERIODICALLY SPACED FIRST-ORDER RIDGES IN  
THE RIDGED PLAINS OF HESPERIA PLANUM: ANOTHER CASE FOR A  
BUCKLING MODEL

Thomas R. Watters and D. John Chadwick, Center for Earth and  
Planetary Studies, National Air and Space Museum, Smithsonian  
Institution, Washington, D.C. 20560

Hesperia Planum (20°S, 250°W) is one of the largest contiguous areas of ridged plains on Mars outside of the Tharsis Plateau. Ridged plains units on Mars are characterized by the presence of landforms analogous to those in mare wrinkle ridge assemblages (1). Like the ridged plains of Tharsis, those of Hesperia Planum are associated with a volcanic center. Tyrrhena Patera is a relatively small, heavily degraded shield volcano, surrounded and embayed by ridged plains material (2). The first-order ridges of Hesperia Planum are morphologically and dimensionally analogous to those on Tharsis. However, the spatial relationship of the ridges is much more complex. Many of the ridges crosscut one another at nearly orthogonal angles forming what have been termed as reticulate ridge patterns (3,4).

The ridged plains of Hesperia Planum with prominent reticulate ridge patterns lie to the east and southeast of Tyrrhena Patera. The reticulate pattern has been separated into two sets of first-order ridges, one with a predominant NW-SE trend and the other with a predominant NE-SW trend. Using the 1:2,000,000 Controlled Photomosaics as a base, ridge spacing was determined using a series of sampling traverses spaced at roughly 12 km intervals oriented perpendicular to the predominant trend of each set of ridges. Since the method used to determine ridge spacing includes all measurements between any two ridges along the sampling traverse including spacings between ridges that are not immediately adjacent, and the frequency distribution of ridge spacing is generally asymmetric, the mode is the most reliable measure of the average spacing. Based on the results of this study, both the NW-SE and the NE-SW trending ridge sets have an average spacing of 30 km.

The near consistent spacing of both sets of first-order ridges can be explained by two superimposed episodes of buckling of the ridged plains material at a critical wavelength where the maximum compressive stress direction has changed by roughly 90°. In this fold model (5), it is assumed that the ridged plains material: 1) deformed at the free surface under little or no confining pressure and, 2) behaves like a series of thin linearly elastic plates with essentially frictionless contacts. An elastic rheology was chosen over linearly viscous or power-law flow (see 6) because at low temperatures and pressures, ductility is rarely observed in rock (7). Free slip between layers is assumed based on the likely presence of regolith interbeds in the ridged plains volcanic sequence. The presence of such interbeds in a flood basalt sequence is consistent with subsurface data in Mare Serenitatis and Mare Crisium on the Moon and the Columbia Plateau.

The multilayer rests on a mechanically weak regolith substrate of finite thickness which is in turn resting on a rigid boundary. The rigid basement does not participate in the deformation, thus no assumption of whole lithosphere deformation is necessary to explain the periodically spaced ridges. In the model proposed here, the basement is assumed to have elastic properties equal to the ridged plains material. This is not unreasonable since it is assumed that the deformation involving the ridged plains is limited to the upper crust of Mars ( $< 10$  km). The observed wavelengths of many of the ridges can be explained by this model, at critical stresses below the maximum compressive strength envelope of a basalt-like material, given that: 1) the ratio in Young's modulus between the ridged plains material and the underlying regolith  $E/E_0 \geq 1000$ ; 2) the thickness of the ridged plains material is between roughly 2,000 and 4,100 m; and 3) the average thickness of a layer in the sequence is between 250 and 500 m (figure 2).

The origin of compressional stress that resulted in crosscutting ridges in Hesperia Planum is not clear. In the case of the ridged plains of the Tharsis Plateau, compressional stress may be the result of isostatic uplift (8,9,10). However, in the absence of a "Tharsis-like" uplift or load in Hesperia Planum and other ridged plains provinces on Mars (i.e., Syrtis Major Planum, Malea Planum), other mechanisms must be sought. Compressional stress may result from local subsidence due to loading from the ridged plains material (see 4). However, local subsidence will likely generate only a single dominant trend related to the geometry of the basin. A combination of local subsidence and a later superimposed regional tectonic event could account for the crosscutting ridge pattern.

#### References Cited

- (1) Watters, T.R., JGR, 93, 10236-10254, 1988. (2) Carr, M.H., R. Greeley, K.R. Blasius, J.E. Guest, and J.B. Murray, JGR, 82, 3985-4015, 1977. (3) Saunders, R.S. and Gregory, T.E., Reports of Planet. Geol. and Geophys. Program, 1980, NASA Tech. Mem. 82385, 93-94, 1980. (4) Raitala, J., Earth, Moon and Planets, 40, 71-99, 1988. (5) Watters, T.R., in Fourth International Conference on Mars, Program and Abstracts, 206-207, 1989. (6) Zuber, M.T. and L.L. Aist, in Fourth International Conference on Mars, Program and Abstracts, 215-216, 1989. (7) Jaeger, J.C., and N.G.W. Cook, Fundamentals of rock mechanics, 3rd ed., 593 pp., Chapman and Hall, London, 1979. (8) Banerdt, W.B., R.J. Phillips, N.H. Sleep, and R.S. Saunders, JGR, 87, 9723-9733, 1982. (9) Sleep, N.H. and R.J. Phillips, JGR, 90, 4469-4489, 1985. (10) Watters, T.R. and T.A. Maxwell, JGR, 91, 8113-8125, 1986.



Figure 1. Crosscutting first-order ridges in the ridged plains of Hesperia Planum.

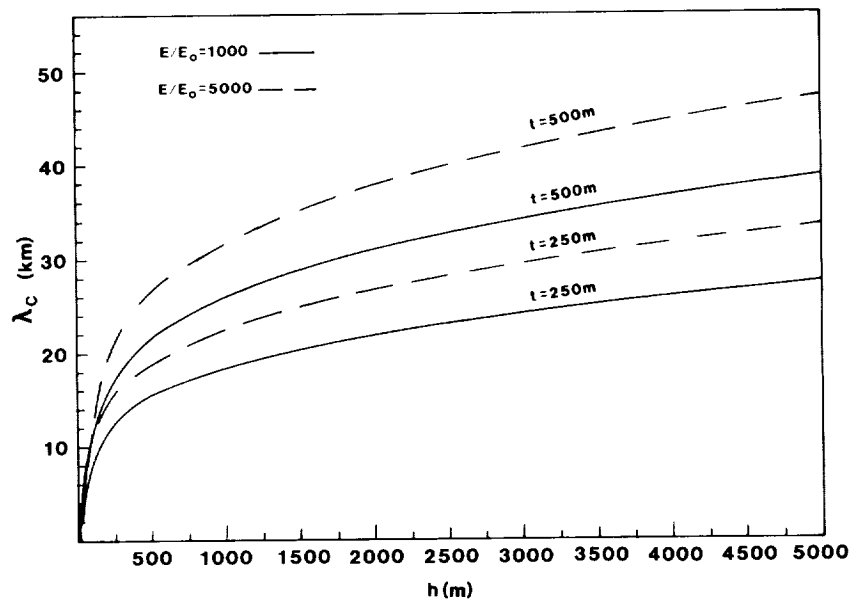


Figure 2. Critical wavelength of buckling as a function of thickness of the ridged plains material.

# THE OLYMPUS MONS SCARP AND AUREOLE: A STRUCTURAL AND RHEOLOGICAL MODEL FOR THEIR FORMATION

Andrea Borgia, Jet Propulsion Laboratory, California Institute of Technology, 4800 Oak Grove Drive, Pasadena, CA 91109.

The prominent scarp and aureole that surrounds Olympus Mons on Mars has been interpreted to be a result of: 1) differential erosion between outer more erodible tuff deposits and inner less erodible lava flows (Carr et al., 1973; King and Riehle, 1974; Williams, 1988); 2) land sliding of the outer flanks of the volcano (Head et al., 1976; Lopes et al., 1980; Francis and Wadge, 1983; Tanaka, 1985); 3) subglacial emplacement of lava flows (Hodges and Moore, 1979); and 4) thrust faults due to the gravity failure of the edifice (Morris, 1981a,b). These interpretations do not fully account for the ridges and the gentle counter slope uphill from the scarp, the secondary scarps downhill from the scarp, the mirror symmetry of the scarp around the volcano, source region of the aureole, major strike-slip faults in the aureole, and shape of the aureole. We suggest that the scarp is the surface expression of a fault-propagation fold that has formed by gravitational failure and spreading of the volcano; the fault propagation fold has created the necessary topographic relief for the formation of the extensive mass-flow deposits found in the aureole. Modeling of clay slurry flows shows that the rheology of the aureole during emplacement was similar to that of clay.

This thesis is based on a terrestrial analog found in the Central Costa Rica Volcanic Range. This west-northwest trending volcanic range is bordered by 10-20 km long and 100-200 m high scarps, which are symmetrically located 20 km to the north and to the south of the range, parallel to the range axis, and face away from it. A ridge and secondary scarps exist at the summit and at the base of the scarp respectively. The southern scarp (the Alajuela Scarp) was interpreted as: 1) a lake or alluvial terrace; 2) a normal fault of an intra-arc basin; or 3) lava flow fronts. The northern scarps (the San Miguel and the Guappiles Scarps) were interpreted as the normal faults delimiting a back-arc basin (the Nicaragua Graben).

Detailed geological and geophysical work was conducted on the Alajuela Scarp and preliminary work on the other two scarps (Borgia et al., 1987). The stratigraphic sequence consists of the Pliocene, clay-rich, volcano sedimentary Aguacate Formation overlain by Pleistocene, massive, >10 m thick, basaltic andesite lava flows and ignimbrites interbedded with weathered, partially consolidated ash beds. Recent fluvial and lake deposits crop out uphill and downhill from the scarp; lahars and talus slope deposits exist only downhill from the scarp. The structure shows that the scarps are the steeply dipping frontal limbs of asymmetric angular anticlines that verge away from the Volcanic Range (Fig. 1). The ridges correspond to the hinge zone of the anticlines whose back limbs gently dip towards the range. The geometry of these anticlines and associated faults suggest that they are fault-propagation folds (Suppe, 1983, 1985) formed in front of low-angle thrust faults at the base of the volcanic range. The thrust faults step up from depths of about 500 m over distances of approximately 2 km and terminate in the axial surfaces of the frontal synclines. Frequently, syncline breakthrough and high-angle breakthrough are observed. Tear faults separate blocks with different fault-propagation fold geometries. The hanging wall of each fault has been thrust about 200 m away from the volcanic edifice. The presence of secondary scarps in front of the main one suggests that thrusting might occur along secondary thrust faults also. Thrusting on the lower flanks of the range is compensated by extension on the range axis with the formation of summit grabens. Gravity and magnetic surveys of the Alajuela Scarp are consistent with this interpretation. Shallow seismicity in the volcanic range indicates that tear faulting and thrusting are still active. We suggest that the thrust faults are located at the Pliocene-Pleistocene boundary and formed by gravitational failure and consequent spreading of the Volcanic Range possibly triggered by the intrusion of magma over the last 50 ka.

The morphologies of the Olympus Mons scarp and related structures, such as tear faults and secondary scarps, are very similar to those of the Central Costa Rica Volcanic Range and to the geometry of fault-propagation folds. Thus, we envision a similar process for the formation of the scarps at Olympus Mons. In this scenario, the structure of Olympus Mons (and perhaps part of the

lithosphere) failed under the gravitational load of the volcano. The consequent spreading along low-angle thrust faults produced the scarps according to the fault-propagation fold mechanism. The presence of low-angle thrust faults on Olympus Mons and its aureole has also been suggested by Harris (1977) and Morris (1981a,b). Spreading of the lower flanks of the volcano was predominantly towards the northwest and the southeast, and induced rifting and volcanic activity along a northeast-southwest trend (Francis and Wadge, 1983). The increase in topographic gradient at the scarp during uplift of the anticline may have produced the large mass flow deposits common to the aureole. This model suggests that Olympus Mons has been fairly symmetric and that no ancestral Olympus Mons (Harris, 1977; Lopes et al., 1980) nor rotation in the stress field (Francis and Wadge, 1983) are necessary to account for the presence of the scarp and of the latest northeast-southwest volcanic activity.

Experiments using a clay slurry were conducted to simulate the growth of the lobes of the Olympus Mons aureole. The rheology of the clay slurry was tested in a wide-gap concentric cylinder viscometer and a novel general method for computing the constitutive equation of the non-linear rheology of the slurry was developed (see below). This slurry was found to be pseudoplastic and to have a shear rate dependent yield stress. The clay slurry was "erupted" down a variable slope both at constant and variable "eruption" rates, and the developing morphology of the flow was monitored in time. At small slope angles the morphology of the clay slurry flows was remarkably similar to the lobes of the aureole (Fig. 2). In particular, the shape and position of the strike-slip faults, and some of some features of the grooved surface of the aureole were reproduced, suggesting that the clay slurry had a rheology approximately similar to that of the mass flow deposits of the aureole. Analytical and numerical modeling of the clay slurry flows is currently underway. This modeling will allow the estimate of the rheological parameters of the aureole from its morphology and, as a consequence, a better definition of the of its probable composition.

The novel method for computing the constitutive equation of a non-linear fluid considers the propagation of errors for the recovery of the shear rate from wide-gap concentric cylinder viscometric measurements. A least square regression of stress on angular velocity data to a system of arbitrary functions is used to propagate the errors for the series solution to the viscometric flow developed by Krieger and Elrod (1953) and Pawlowski (1953), and for the first term of the series developed by Krieger (1968) ("power-law" approximation). A numerical experiment shows that, for measurements affected by significant errors, the first term of the Krieger-Elrod-Pawlowski series ("infinite radius" approximation) and the "power-law" approximation may recover the shear rate with equal accuracy as the full Krieger-Elrod-Pawlowski solution. An experiment on a clay slurry indicates that the clay has a larger yield stress at rest than during shearing, and that, for the range of shear rates investigated, a four-parameter constitutive equation approximates reasonably well its rheology. The error analysis presented is useful for studying the rheology of fluids such as particle suspensions, slurries, foams and magma. The viscometric measurements of these fluids are usually affected by significant errors that are introduced by "non-Couette" flow in the viscometer and by temperature, time and shear rate dependence of the rheological parameters.

## References

- Borgia A., Burr J., Montero W., Morales L.D., and Alvarado G.I., 1987. Transactions, American Geophysical Union, v. 68, n. 16, p. 406.
- Carr M.H., Masursky H., and Saunders R.S., 1973. Journal of Geophysical Research, v. 78, p. 4031-4036.
- Francis P.W. and Wadge G., 1983. Journal of Geophysical Research, v. 88, n. B10, p. 8333-8344.
- Harris S.A., 1977. Journal of Geophysical Research, v. 82, p. 3099-3107.
- Head J.W., Settle M., and Wood C., 1976. Nature, v. 263, n. 5579, p. 667-668.
- Hodges C.A. and Moore H.J., 1979. Journal of Geophysical Research, v. 84, p. 8061-8074.
- King J.S. and Riehle J.R., 1974. Icarus, v. 23, p.300-317.
- Krieger I.M. and Elrod H., 1953. J. Appl. Phys., v. 24, n. 2, p. 134-137.

- Krieger I.M., 1968. *Trans. Soc. of Rheol*, v. 12, n. 1, p. 5-11.  
 Lopes R. M.C., Guest J.I., and Wilson C.J., 1980. *The Moon and the Planets*, v. 22, p. 221-234.  
 Morris E.C., 1981a. *Proc. III Int. Coll. on Mars*, L. P. I., p. 161-162.  
 Morris E.C., 1981b. *Rep. Planet. Geology Program*, NASA Tech. Mem. 84211, p. 389-390.  
 Pawlowski Von J., 1953. *Kolloid Zeitschrift*, v. 130, p. 129-130.  
 Suppe J., 1983. *American Journal of Science*, v. 283, p. 684-721.  
 Suppe J., 1985. Prentice-Hall, Inc., pp. 537.  
 Tanaka K. 1985. *Icarus*, v. 62, p. 191-206.  
 Williams S.H., 1988. *Lunar and Planetary Science XIX*, p. 1279-1280.

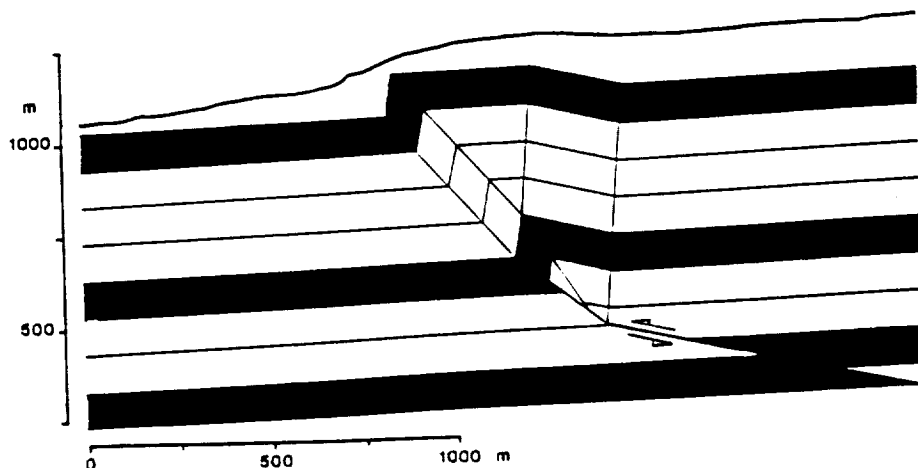


Fig. 1. Retrodeformable geologic cross-section of the Alajuela Scarp along Rio Itiquis. Geometry of surficial beds is measured, the dip structure is based on fault-propagation fold theory (Suppe, 1983, 1985). Upper continuous line is topography. North is to the right. A similar model may be applicable to Olympus Mons scarp.

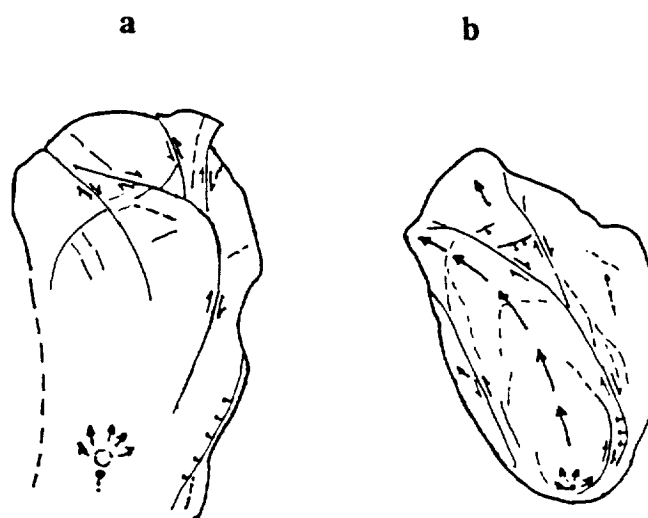


Fig. 2. Sketch of the northern lobe of Olympus Mons aureole (a) and of a clay slurry flow (b). Note similarity of overall shape and strikeslip faults.

## GEOMETRY OF STRESSES AROUND THARSIS ON MARS;

M. P. Golombek, Jet Propulsion Laboratory, Caltech, Pasadena, CA 91109

A variety of workers have attempted to use the location and orientation of tectonic features in and around the Tharsis province on Mars to constrain the geometry of the causative stress field. In particular, Tharsis is characterized by an enormous radiating system of grabens that extends over one half of the planet and a sweeping circumferential system of wrinkle ridges. Because the orientation of these structures is a result of the geometry of the stress field, traces of grabens and normals to wrinkle ridges can be used to test the true radial nature of the causative stress fields and to see if different tectonic features and episodes had geometrically similar stress fields.

Wise, Golombek and McGill (1979) first tried such a test by plotting the traces of the most strongly developed grabens and normals to representative wrinkle ridges on the upper hemisphere of an equal area net, centered on Tharsis. The lines were fit to great circles on the net, and the density of the great circle intersections was contoured. A similar analysis was done by Plescia and Saunders (1982) using a comprehensive data base of grabens and normal faults. Finally, Watters and Maxwell (1986) used a comprehensive data set of Martian wrinkle ridges to test their circularity. There are problems with each of these studies however. Wise et al. (1979) used a very small data set, Plescia and Saunders (1982) did not contour the great circle intersections, and Watters and Maxwell (1986) used a different plotting routine from that used by previous workers. As a result, a consistent quantitative test of the stress fields responsible for the radial grabens and concentric wrinkle ridges has not been done using the large data sets now available.

Part of the reason for the lack of quantitative analysis of the tectonic data sets is that the number of intersections of great circles on a net is  $n(n-1)/2$ , where  $n$  is the number of great circles. Contouring by hand therefore becomes impossible for any but small data sets. However, the analysis of the intersection points of traces of great circles on a net is identical to the beta analysis of lines produced from the intersection of planes on a net in structural geology, for which computer contouring programs exist. For this analysis a published FORTRAN program (Beasley, 1981) was modified for operation on a personal computer. The program takes the information defining the planes and iteratively counts their intersections on a net with the percentage density of intersections in finely divided 1.0% counting areas.

Note that this analysis implicitly assumes that the trace of a graben represents the trace of the intermediate principal stress,  $S_2$ , on the surface of the planet, and that the operative stress field had a vertical maximum principal stress,  $S_1$ , and a horizontal minimum principal stress,  $S_3$ , perpendicular to the fault trace. As a result, the great circle of a graben over an extended distance on a planet's surface is represented by the  $S_1 - S_2$  plane, which is everywhere vertical



at the planet's surface (along the grabens trace) and if extended would intersect the center of the planet. For a wrinkle ridge, the analysis assumes that its normal represents the  $S_1 - S_3$  plane, which is perpendicular to the surface of the planet along its entire trace and if extended would intersect the center of the planet. As a result, this analysis has a physical basis in terms of the inferred orientation of stresses within the lithosphere of the planet. The pattern of the contoured intersections can then be used to gauge how well the set of tectonic features is radial about a point. For example, a circular "bull's eye" pattern with one central concentration of high density is a good indication of a radial distribution, whereas an asymmetric pattern with a number of smaller density concentration maxima indicates a non-radial system.

For this analysis we have used the graben data compiled by Plescia and Saunders (1982), which includes only those faults that extend over several degrees of the planet's surface to represent truly regional events during the two main Tharsis faulting events: the earlier Syria faults ( $n=83$ ) and the slightly later (or possibly partially coeval) Pavonis faults ( $n=60$ ). We have used the wrinkle ridge data from Watters and Maxwell (1986), which represent  $10^\circ \times 10^\circ$  length-weighted means of 1850 ridge segments. The long faults and the length averaged wrinkle ridges most likely represent regional fault sets, indicative of regional stresses.

Contoured intersection plots for the data sets show significant concentrations with single maxima intersections of circular to slightly elongate bull's eye patterns. The 3403 Syria fault intersections define a slightly northeast-elongate single maximum pattern with a maximum concentration of just over 25% per 1% area, centered at  $-10^\circ, 101^\circ$ . This is very close to the Syria center ( $-8^\circ, 100^\circ$ ) defined by Plescia and Saunders (1982). The 1770 Pavonis fault intersections define a circular bull's eye pattern with a maximum concentration of about 40% per 1% area, centered at  $-5^\circ, 113^\circ$ , which is very close to the center ( $-4^\circ, 110^\circ$ ) defined by Plescia and Saunders (1982). It is remarkable that these results are so close to those of Plescia and Saunders, given that their centers were picked by hand. Furthermore, to a first approximation the quantitatively contoured plots support Plescia and Saunders' assertion that these centers of faulting are areally distinct, being separated by over  $10^\circ$  on the planet's surface. The 1225 intersections of normals to wrinkle ridges define a slightly west-elongate single maximum pattern with a maximum concentration of about 16% per 1% area, centered at  $-6^\circ, 101^\circ$ , which is virtually indistinguishable from the Syria center. This result is contrary to the results of Wise et al. (1979), based on a very limited sample, and slightly different from one of the centers of Watters and Maxwell (1986), based on a different data plotting routine. This suggests that the regional stress system responsible for the Syria grabens around Tharsis is very similar in orientation to that responsible for the wrinkle ridges. These results are intriguing, given that Watters and Maxwell (1986) place the formation of the ridges after the Syria-centered faulting and thus both have resulted from

similarly oriented stress fields, although the relative magnitude of the principal stresses must have changed.

Contoured intersection plots of combinations of the data sets also show single center intersection patterns. Intersections (10,153) of 143 faults from both the Syria and Pavonis fault sets define a northeast-elongate single maximum pattern with a maximum concentration of about 20% per 1% area, centered at  $-6^{\circ}$ ,  $105^{\circ}$ , roughly between the centers of the individual fault sets. Thus, although individually the two Tharsis fault sets appear to define different centers, taken together over the time during which both fault sets formed, which may be short, they also define a radial center of faulting, as has been suggested since the study of Tharsis began. This implies a broadly radial stress field and that the difference between the stress fields responsible for the Syria and Pavonis faults is small. The 18,528 intersections of both fault systems and the wrinkle ridge normals (all totaling 193) define a northeast-elongate single maximum pattern with a maximum concentration of about 14% per 1% area, centered at  $-5^{\circ}$ ,  $106^{\circ}$ . This center is close to that of both fault sets together as well as the centers defined by the Syria faults and the ridges individually.

In conclusion, careful consideration has been given to the gross geometry of the regional structural features around the Tharsis province on Mars using comprehensive data sets and a computer program for quantifying their great circle intersections. This data analysis technique has a direct link to the stress state that produced the structures over a hemisphere of the planet. Contrary to various analyses done previously, the normal faults and compressional wrinkle ridges around Tharsis define a radial system, with minor changes over time, and directly indicate that the causative stress field is radial to a region north of Syria Planum in the area of Noctis Labyrinthus near the maximum elevation of the Tharsis plateau. Although the relative magnitude of the vertical and horizontal principal stresses must have changed to form the grabens and the wrinkle ridges, the orientations of the horizontal principal stresses did not change substantially.

#### REFERENCES:

- Beasley, A. J. 1981, A computer program for printing geometrically accurate structural fabric diagrams: *Computers & Geosciences* 7, 215-227.
- Plescia, J. B., and R. S. Saunders 1982, Tectonic history of the Tharsis region, Mars: *J. Geophys. Res.* 87, 9775-9791.
- Watters, T. R., and T. A. Maxwell 1986, Orientation, relative age, and extent of the Tharsis plateau ridge system: *J. Geophys. Res.* 91, 8113-8125.
- Wise, D. U., M. P. Golombek, and G. E. McGill 1979, Tharsis province of Mars: Geologic sequence, geometry, and a deformation mechanism: *Icarus* 38, 456-472.

FAULTING AND ITS RELATION TO VOLCANISM: MARS WESTERN EQUATORIAL REGION David H. Scott and James Dohm, U.S. Geological Survey, 2255 N. Gemini Dr., Flagstaff, AZ 86001.

Recently completed geologic maps of Mars (1-3) show the global distribution of lava flows that were emplaced during each of the three Martian time-stratigraphic periods and the faults and ridges that originated during these periods. These data have been extracted from the geologic maps to make a series of volcano-tectonic maps for the Noachian, Hesperian, and Amazonian Periods. The map series is being compiled on Viking photomosaics at 1:15,000,000 scale. These maps will provide a basis for assessing the interactive roles of volcanism and tectonism in the crustal evolution of Mars.

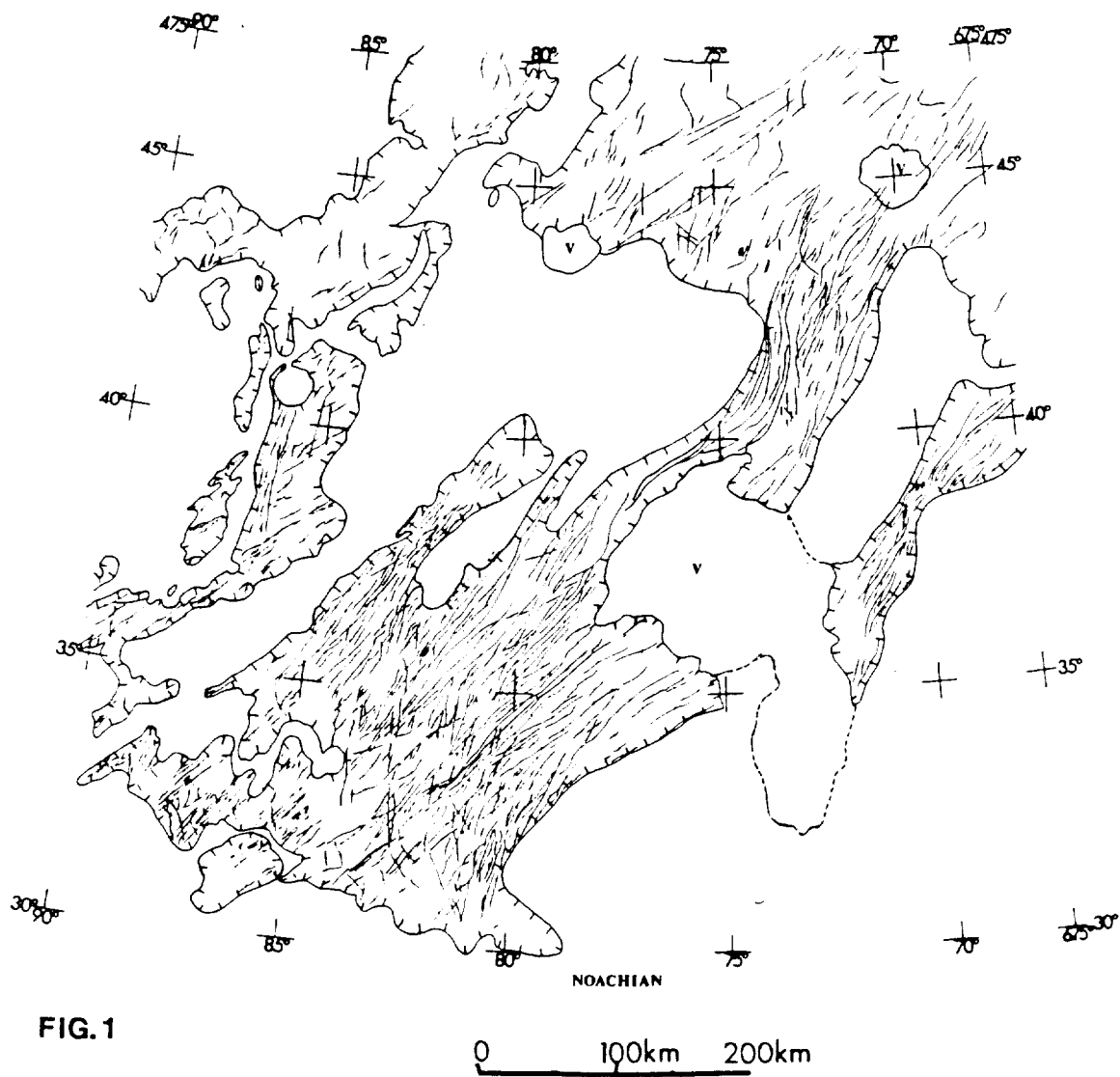
Volcano-tectonic maps of the western equatorial region of Mars have been completed. Some observations resulting from their study show that volcanic resurfacing in this region has progressively decreased with time from the Noachian Period to the Amazonian. A corresponding decrease in tectonic activity, evidenced by fault densities, occurred mostly during the Amazonian. Exceptions are seen around Alba Patera, where volcanism accompanied by faulting has continued from Hesperian into early Amazonian time and, to a lesser extent, around the Tharsis Montes. The major volcanic centers that include the Tharsis Montes, Alba Patera, Syria Planum and, to some degree, Olympus Mons are the loci of most fault systems. However, many mountains in the western part of the southern highlands that are interpreted to be volcanic (1, 4, 5) lie along arcs that conform to regional trends of fault and ridge systems older than those exemplified by the main tectonic axes of the Tharsis Montes.

Within the western equatorial region, the Tempe Terra volcanic and tectonic province is of particular interest. It consists of three distinct types of terrain (4): rugged hills and mountains, highly faulted ridge-and-valley structures, and relatively smooth uplands extending from the Lunae Planum plateau. Tempe Terra is embayed and partly covered by lava flows from the plains, from Alba Patera, and from the Tharsis Montes. The maps of Figures 1 and 2 (compiled on Viking photomosaics at 1:2,000,000 scale) show the location of faults that originated during the Noachian and Hesperian Periods in the tectonically complex Tempe Terra area. The relative ages of these faults can be deciphered from the stratigraphic position of rock units that either cover them or are transected by them; individual faults or sets of faults can be relatively dated by their degree of degradation and cross-cutting relations.

Results of the studies made at Tempe Terra show four distinct episodes of faulting during the Noachian and Hesperian Periods. Some faulting attributed to the Hesperian Period may have occurred during Amazonian time, but more accurate dating of the faults is prevented by the paucity of Amazonian-age rocks at Tempe Terra. A small volcano (lat 37° N., long 75°) in Tempe Terra, like Alba Patera on a larger scale, has controlled the divergence and concentricity of fault patterns around its center.

#### REFERENCES

- (1) Scott, D.H., and Tanaka, K.L. (1986) U.S. Geol. Survey Misc. Inv. Ser. Map I-1082A.
- (2) Greeley, Ronald, and Guest, J.H. (in press) U.S. Geol. Survey Misc. Inv. Ser. I-1082B.
- (3) Tanaka, K.L., and Scott, D.H. (in press) U.S. Geol. Survey Misc. Inv. Ser. Map I-1082C.
- (4) Scott, D.H. (1982) Jour. Geophys. Res., v. 87, no. B12, p. 9839-9851.
- (5) Scott, D.H., and Tanaka, K.L. (1981) Proc. Lunar Planet. Sci., no. 12B, p. 1449-1458.



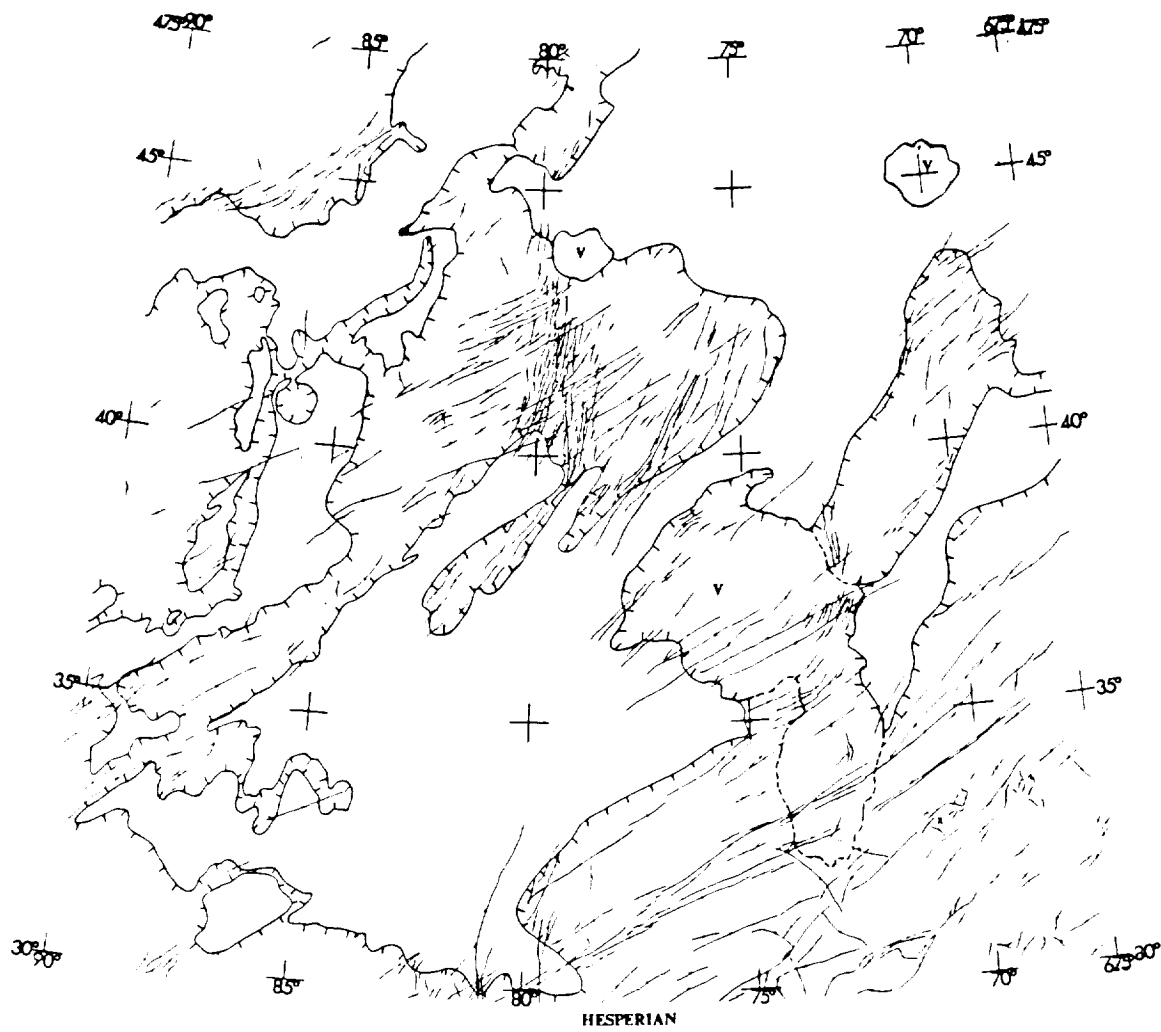


FIG. 2

0 100km 200km

FAULT AND RIDGE SYSTEMS: HISTORICAL DEVELOPMENT IN WESTERN REGION OF MARS  
David H. Scott and James Dohm, U.S. Geological Survey, 2255 N. Gemini Dr.,  
Flagstaff, AZ 86001.

The tectonic history of Mars can be traced, in part, by mapping faults and ridges that were formed during successive geologic periods. This has been accomplished in the western equatorial region by determining the relative ages of these structures based on their occurrence in rock units of known stratigraphic position. Three maps (Figs. 1-3) at reduced scale (1:50,000,000) show the areal extent of geologic units that were emplaced, and faults and ridges that originated during the Noachian, Hesperian, and Amazonian Periods. We extracted and compiled these data from the geologic map of the western equatorial region of Mars (Scott and Tanaka, 1986), considering that (1) faults and ridges of Amazonian age may extend across the boundaries of older rock units; (2) structures of Hesperian age may extend into Noachian but not Amazonian rocks; and (3) Noachian structures only occur within the Noachian units. We also recognized, however, that older rocks may contain younger faults and ridges whose ages cannot be determined unless they also transect younger rocks. To make these discriminations where the geologic base (1:15,000,000 scale) did not clearly reveal the age relations, Viking photomosaics (1:2,000,000 scale) were examined. In Figures 1-3, the rocks exposed within each Martian period are enclosed within hachured lines. Faults and ridges in each period are shown by lines marked by ball and diamond respectively. The locations of volcanic centers are shown for reference only, and do not necessarily reflect their time of origin.

Figure 1 and previous studies by Tanaka (1987) indicate that most faulting during the Noachian Period was associated with three centers: 1) the Tharsis Montes axial trend and its northeastern and southwestern extensions; 2) the Syria Planum rise ( $-15^{\circ}$  lat,  $105^{\circ}$  long); and 3) the Acheron Fossae structure north of Olympus Mons. Clusters of ridges also occur and are confined within Noachian rocks but may have originated during the Hesperian Period.

Figure 2 shows that extensive faulting continued during the Hesperian along the Tharsis Montes trend and in Syria Planum, and was initiated radial to Alba Patera. Fault activity ceased, however, at Acheron Fossae. This period marked the culmination in western Mars of formation of ridges where they occur in a broad oval pattern around the major volcanic centers; most ridges are older than the faults of this period, possibly suggesting that those that occur in Noachian rocks were formed during an earlier period.

Figure 3 shows the great general decline in tectonism during the Amazonian Period. Only Alba Patera remained as a major fault center where older radial systems were rejuvenated and concentric faulting was initiated around the crest of the volcano. Minor faults are associated with Olympus Mons and its aureole materials; some are very young as they cut Late Amazonian lava flows.

#### References

- Scott, D.H., and Tanaka, K.L., 1986, Geologic map of the western equatorial region of Mars: U.S. Geol. Survey Misc. Inv. Series Map I-1802A.  
Tanaka, K.L., and Davis, P.A., 1987, History and morphology of faulting in the Noctis Labyrinthus-Claritas Fossae region of Mars: Lunar and Planet. Sci. Conf. 18, p. 922-995.

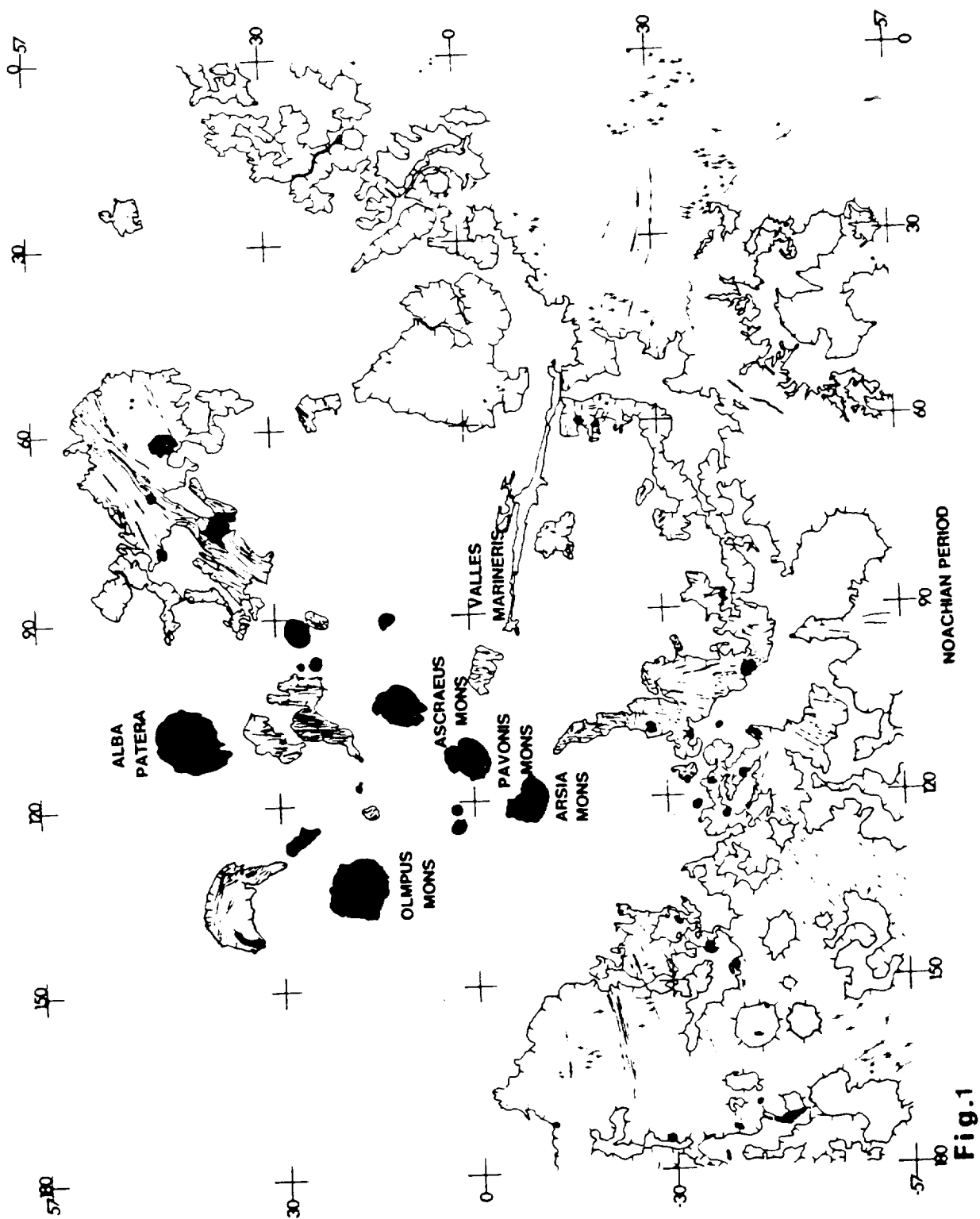
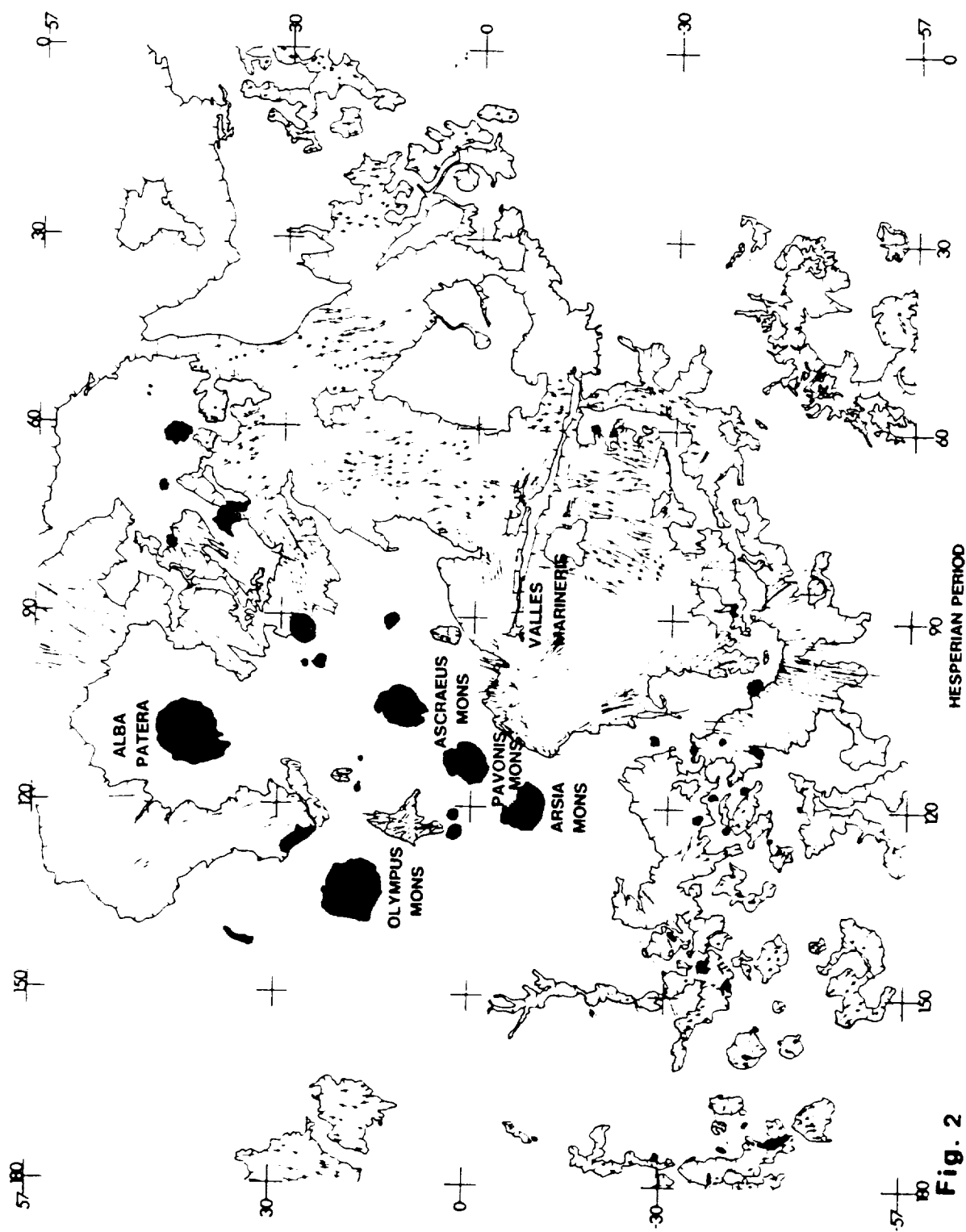


Fig.1



**Fig. 2**





Is Valles Marineris (VM) on Mars unique to processes associated with Tharsis relatively late in martian geologic history? Or is it only the last and best preserved major canyon system on the planet? A shallow trough system concentric to Hellas (1, 2, 3) may represent such an ancient canyon system comparable in width and extent to Valles Marineris. In this contribution we compare these two systems and consider the proposal (4) that Valles Marineris is an analogous Chryse-centered trough system rejuvenated by mobilization of trapped ground-ice during Tharsis tectonism/volcanism.

The shallow concentric Hellas canyons (HC) occur between 1900 and 2500 km from the basin center, outside both the extrapolated Hellas boundary scarp and the associated topographic expression of the Hellas basin (5). The individual troughs range from 30–100 km in width and from 300 to 800 km in length. The bounding scarps are generally slightly furrowed in appearance and rectilinear in plan with reliefs on the order of 0.5 km from earth-based radar data (6). To the south, the scarps lose relief and merge into the cratered plains, although ridge/scarp systems on Malea Planum (Chalcoporus and Pityusa Rupes in particular) may represent a continuation of the trend. To the northeast, the trend is lost near the crater Huygens, perhaps overprinted by Huygens-related fractures. The troughs have been floored by intercrater plains units, and a back-slope away from the troughs is suggestive of block rotation or relaxation after canyon formation.

The geometric similarity between the HC and VM relative to the Hellas and Chryse impact basins, respectively, are documented in Figure 1. The Hellas canyons are 1900–2500 km from the Hellas basin center, whereas the Valles Marineris canyons exhibit elements 1850–2500 km in distance from and concentric with the Chryse basin center (4). The characteristic lengths of the two systems are also similar: the Hellas canyons extending over 2600 km; Valles Marineris extending ~3300 km before disappearing among the chaotic terrains arching around Chryse to the east. Although Valles Marineris exhibit a broad spectrum of canyon widths in general (from 50 to 150 km), less modified elements mimic the size distribution of the narrower Hellas canyons (Figure 2). The histograms in Figure 3 further indicate a correlation in both continuous scarp length and linear segment length of the HC structures with observed lengths in the shorter, discontinuous VM canyons (Gangis, Juventae, Hebes). Deviations of boundary scarp strikes relative to the mean system strike between the two canyon systems are also similar.

The HC scarps are more subdued than the VM canyon walls, but possess similar spur and groove textures. Although the plains units cut by the VM canyons are regionally elevated along the VM trend (7), a raised lip along the VM walls is apparent in some topographic maps (8), thereby indicating local back slopes along the VM similar to those observed in the HC. Gravity analysis of the VM further indicates a mass excess at depth and poor compensation of the mass removed by canyon formation (9). Relative uplift due to compensation along the canyon would result in apparent rotation of the bounding scarps and produce a feature analogous to the HC troughs.

The most apparent difference between the two systems is the canyon depth: VM canyons typically 4 to 8 km (8) with HC canyons only ~0.5 km (6). This may partially reflect the much older age of the Hellas system. Crater counts and stratigraphic relations along the HC scarps yield crater ages of ~1000–2000  $N(D>5)/10^6 \text{ km}^2$ , whereas VM cuts volcanic plains units with  $N(>5)$  ages as young as 125–200 (9) with possible modern volcanic activity along the VM fault scarps (10). The oldest age for

VM has been largely consumed by backwasting although the associated outflow channels date from an N(>5) age of about 27 (11) and very ancient subparallel troughs extend to pre-Tharsis times (12, 13).

**Discussion:** We have modeled (3, 14) the Hellas canyons as impact-related fracturing of a lithosphere about 120 km thick. The geometric similarity of the Valles-Marineris/Margaritifer-Chaos system and the Hellas system with respect to basin centers (Figure 1) is consistent with a similar mechanism for the development of precursory weaknesses about Chryse. In profile, the two systems are similarly located relative to the topographically defined central impact basins. If scaled to the massif rings, however, the VM system is slightly farther from the basin center than the HC, perhaps due to thickening of the lithosphere with time or variations in global thickness.

The formation of Valles Marineris is thought to result primarily from an enlargement of graben and/or rift structures by mass-wasting, modified by subsequent deposition of interior fill deposits (15). The initial rifting episode is frequently cited as related to the evolution of the Tharsis rise to the west (7, 15) and to the Tharsis-radial trend of Valles Marineris (16, 17). Tanaka *et al.* (9) proposed more specifically that the VM developed from an initial elongate thermal anomaly beneath the VM region. Continued erosion and thinning of the lithosphere eventually mobilized ground ice by increased heat flow and magma. Thermal uplift led to doming and rifting near the surface and allowed volatile release, which further enhanced the surface expression of the rifting process.

Alternatively, the Chryse impact established a concentric zone of lithospheric failure analogous to Hellas. Subsequent erosion filled these canyons with a sequence of sedimentary and ejecta deposits capable of storing the water released by impact or volcanism into the early martian environment. After regional plains volcanism of Lunae Planum and Sinus Planum capped these units, the original impact canyon sequence would be preserved as volatile-rich reservoirs in specific zones about Chryse. Thermal reactivation associated with Tharsis would subsequently localize renewed fracturing and heating into an elongate region as in (9) and release the volatile reserves stored since the time of Chryse formation. Thus, thermal evolution during Tharsis construction could rejuvenate an older impact fracture system as the VM canyons through the mobilization of specific volatile traps.

**References:** (1) Peterson J.E. (1978), *Proc. Lunar Planet. Sci. Conf. IX*, 3411–3432. (2) Schultz P.H. (1984), *Lunar and Planet. Sci. XV*, 728–729. (3) Wichman R.W. and Schultz P.H. (1987), *Lunar and Planet. Sci. XVIII*, 1078–1079. (4) Schultz P.H. *et al.* (1982), *J. Geophys. Res.* 87, 9803–9820. (5) Wu, S.S.C. *et al.* (1985), *NASA TM 88383*, 614–617. (6) Roth, L.E. *et al.* (1987), personal communication. (7) Blasius, K.R. *et al.* (1977), *J. Geophys. Res.* 82, 4067–4091. (8) U.S. Geological Survey Maps I-1294 (1980) and I-1712 (1986). (9) Tanaka K.L. *et al.* (1985), *NASA TM 88383*, 603–604. (10) Lucchita B.K. (1987), *Science* 235, 565–567. (11) Masursky H.J. *et al.* (1977), *J. Geophys. Res.* 82, 4016–4038. (12) Schultz R.A. and Frey H.V. (1988), *EOS* 69, 389–390. (13) Wichman R.W. and Schultz P.H. (1986), *Lunar and Planet. Sci. XVIII*, 942–943. (14) Wichman R.W. (1988), Master's thesis, Brown University. (15) Lucchita B.K. (1987), *Lunar and Planet. Sci. XVIII*, 572–573. (16) Willemann R.J. and Turcotte D.L. (1982), *J. Geophys. Res.* 87, 9793–9802. (17) Banerdt W.B. *et al.* (1982), *J. Geophys. Res.* 87, 9723–9734.

STRUCTURAL MAPPING AND INTERPRETATION OF VALLES  
MARINERIS, MARS. *Richard A. Schultz, Geodynamics Branch, NASA Goddard Space  
Flight Center, Greenbelt, MD 20771.*

The Valles Marineris (VM) canyon system on Mars is a spectacular planetary rift. The erosional history of the canyons has been studied extensively [1-4]. In contrast, very little is known about original canyon structure beyond some early pioneering studies [1,2,5,6]. Detailed mapping of the VM canyons reported here clarifies their structure and evolution and provides needed constraints on geophysical models relating VM to Tharsis tectonic activity.

Topography of the canyons and vicinity is inferred from UV spectrometer data [7], stereophotogrammetry of central canyons [8], and scattered measurements from earth-based radar. Downs et al. [9] found that former USGS elevations were several km too high relative to radar measurements, with larger errors occurring over more rugged terrain. The latest USGS topographic map [7] agrees reasonably well with the radar data. However, the detailed Coprates topographic map [8] shows excessively high elevations of VM plateaus relative to both radar [9] and new USGS global topography [7]. Thus, canyon topography remains poorly constrained.

The plateau just north of VM slopes gently east between 80 and 65° W from 6.5-6 km (radar) or 10-8 km (USGS [8]). The southern plateau stands at 5-6 km (radar) and features a broad trough 0.5 km deep extending SSW from Melas Chasma. The topography south of the canyons is distinctly different from that to the north. Radar elevations of plateaus between 50-90° west longitude average 2-3 km north of 10° N (Lunae Planum) and 4-6 km south of 5° S. In contrast, western canyon plateaus locally reach 7.5 km (radar) and plateau elevations appear quite variable close to the canyons. The average gradient between 6° S and 10° N is only 2 m/km, or 0.2%. The regional elevations show that VM does not lie at the crest of a regional dome, as inferred originally from Mariner 9 topography, but instead deforms a moderately high plateau. Hence, the revised topographic data do not support an uplift-bending stress mechanism for localizing the canyons or producing near-canyon relief.

Intercanyon plateaus (e.g., Ophir Planum) vary nonsystematically in elevation, standing as high or higher than surrounding plateaus. Although canyon floors deepen from west to east, extra-canyon plateau elevations also decrease. Cross sections derived from [8] show that maximum canyon relief (not elevation) is a relatively constant 5-7 km along strike. This implies that, to first order, dip-slip displacements of canyon-bounding normal faults may have been insensitive to position in the central VM canyons. Short wavelength topography close to the canyons is probably related to dip-slip faulting instead of more regional processes.

Detailed structural mapping on enlarged 1:2 million scale photomosaics confirms that the original structural canyons are much narrower (factor of 3) than the present canyon width. Some canyons are controlled by 2 long, mutually parallel, inward dipping normal faults (Ius, Tithonium Chasmata). Other canyons are defined by one continuous fault scarp faced by several discontinuous, echelon scarps (Coprates). Structures forming one or both graben walls can be inferred in Ophir and Melas Chasmata only by extrapolating along isolated spurs and massifs on canyon floors or by examining canyon terminations. These wide canyons are probably composed of several parallel grabens.

Many structures found on plateaus surrounding VM now appear to have formed during early stages of canyon faulting [10]. For example, graben arrays on Ophir Planum may be related kinematically to faulting along the Planum's western margin, which produced 5-7 km of structural relief. This idea also supports the view that landslide headscarps were controlled by plateau graben locations and trends [3],

rather than the reverse. Abundance of grabens, pit crater chains (PCC), and wrinkle ridges varies considerably around the canyons. The distinct change in trend between Coprates and Capri/Eos Chasmata is actually reflected in the trends of plateau grabens and PCC more than 500 km to the west. Mapping shows a variety of PCC trends east of Melas Chasma. Some PCC are independent of (not parallel to) VM grabens, whereas others follow the canyon structure. This implies that the stress state associated with growth of PCC varied spatially along the canyon system and differed locally from that associated with VM grabens and canyons. Crosscutting relationships suggest that PCC south of Coprates formed before at least some canyon-related grabens. Thus, pit crater chains may record a set of early, pre-VM regional stress states.

Recent work [10] suggests that growth of wrinkle ridges and parallel graben sets near VM was not influenced by canyon proximity. Most grabens crosscut wrinkle ridges, so a sequence of ridges first, then grabens, then VM canyons was suggested. This sequence is consistent with mechanical models of fracture growth. Small grabens south of Coprates are separated by a few 10's of km, whereas longer graben sets and VM canyons show regular spacing of several hundred km [10]. How did parallel grabens grow, and what controlled their spacing? Two mechanisms can operate. Growth of shorter faults in echelon arrays can be stabilized by the influence of neighboring faults, which can impede fault growth. However, this effect becomes negligible for spacings  $>$  fault length [11], so parallel faults can grow. The longer wavelength spacing may be controlled by a mechanism analogous to joint elimination [12,13]. Thus, as VM canyons grew in length, they impeded further growth of smaller parallel grabens.

Several important questions remain to be addressed. The above sequence of faulting implies that VM canyons are younger than Lunae Planum-age ridged plains. Does canyon growth reflect new faulting or were canyon locations influenced by pre-Lunae Planum-age stratigraphy or structure? Why are the central canyons so deep? What controls the variations in width and structure of the canyons? What is the relationship between VM faulting and nearby volcanism in Lunae Planum? Answers to these questions are necessary before we can understand fully the relationship between Valles Marineris and Tharsis tectonism.

- REFERENCES: [1] Sharp, R.P. (1973) JGR 78, 4063-4073. [2] Blasius, K.R., Cutts, J.A., Guest, J.E. and Masursky, H. (1977) JGR 82, 4067-4091. [3] Lucchitta, B.K. (1979) JGR 84, 8097-9113. [4] Nedell, S.S., Squyres, S.W. and Anderson, D.W. (1987) Icarus 70, 409-441. [5] Frey, H. (1979) Icarus 37, 142-155. [6] Watters, T.R. and Maxwell, T.A. (1983) Icarus 56, 278-298. [7] Wu, S.S.C., Jordan, R. and Schafer, F.J. (1986) NASA TM-88383, 614-617. [8] USGS (1986) Topographic map, Coprates NW quad., Mars, Map I-1712. [9] Downs, G.S., Mouginis-Mark, P.J., Zisk, S.H. and Thompson, T.W. (1982) JGR 87, 9747-9754. [10] Schultz, R.A. and Frey, H. (1988) EOS 69, 389-390. [11] Aydin, A. and Schultz, R.A. (1989) Proc. USGS Workshop on Fault Segmentation and Controls of Rupture Initiation and Growth, USGS Open-File Report, in press. Also J. Struct. Geol., submitted, 1989. [12] DeGraff, J.M. (1987) Ph.D. diss., Purdue Univ., Chap. 5. [13] Pollard, D.D. and Aydin, A. (1988) GSA Bull. 100, 1181-1204.

QUANTITATIVE VOLUMETRIC ANALYSIS OF VALLES MARINERIS OF MARS  
 Sherman S. C. Wu, Patricia A. Garcia, and Annie Howington-Kraus,  
 U.S. Geological Survey, Flagstaff, AZ 86001.

Valles Marineris, the canyonlands of Mars, are among the most conspicuous features on the planet. They extend for about 5,000 km, from long 110° to 30°. The widest segment of the canyons is about 600 km wide and their deepest spot is about 9 km deep. By using a digital terrain model of seven 1:2,000,000-scale contour maps (MC17-NE, MC18-NW, -NE, -SE, MC19-NW, -SW, and MC11-SW; Wu et al., 1985), we calculated volumes of the canyon (Table 1) in two separate parts (Fig. 1a): the western segment, which includes Noctis Labyrinthus and the main body of Valles Marineris; and the eastern segment, which includes most of the troughs, chaotic terrain, and channels. By assigning an area of 1 km<sup>2</sup> with a thickness of 2 m to each pixel, according to the map scale, we calculated the volumes of the canyons and channels by filling cubic pixels from their bottoms to both backs within the boundary shown in Fig. 1b. Assuming a density of 3.0 g cm<sup>-3</sup> of missing material (Hiller et al., 1982), we estimate the missing mass of the canyons and the channels to be  $14.706 \times 10^{18}$  kg. The total volume and the mass of the western segment are  $2.891 \times 10^6$  km<sup>3</sup> and  $8.673 \times 10^{18}$  kg, respectively. This mass is about equal the mass of the Tharsis dome above 8-km elevation ( $9.88 \times 10^{18}$  kg), and one-sixth the mass of the Tharsis dome above 3-km elevation ( $53.28 \times 10^{18}$  kg) (Wu et al., 1988).

Table 1. Volumes of Valles Marineris Canyons and Channels. (All values are  $\times 10^6$  km<sup>3</sup>.)

Elevation (km)	Western Segment		Eastern Segment		Total Cumulative
	Increment	Cumulative	Increment	Cumulative	
-4			0	0	0
-3			0.009	0.009	0.009
-2	0	0	0.091	0.100	0.100
-1	0.006	0.006	0.382	0.482	0.488
0	0.039	0.045	0.586	1.068	1.113
1	0.100	0.145	0.398	1.466	1.611
2	0.187	0.332	0.312	1.778	2.110
3	0.264	0.596	0.207	1.985	2.581
4	0.348	0.944	0.025	2.010	2.954
5	0.409	1.353			3.363
6	0.489	1.842			3.852
7	0.512	2.354			4.364
8	0.428	2.782			4.792
9	0.104	2.886			4.896
10	0.005	2.891			4.901

## References

- Hiller, K. H., Janle, P., Neukum, G. P. O., Guest, J. E., and Lopes, R. M., 1982, Stratigraphy and gravimetry of Olympus and its aureole: Jour. Geophys. Research, v. 87, p. 9905-9915.
- U.S. Geological Survey, 1989, Topographic maps of the western, eastern, and polar regions of Mars: Misc. Inv. Ser. Map I-2030, 3 sheets, scale 1:15,000,000.
- Wu, S. S. C., Garcia, P. A., Howington-Kraus, A., and Kelly, C. T., 1988, Quantitative analysis of the Tharsis dome of Mars (abs.), XIX Lunar and Planetary Science Conference, p. 1300-1301.
- Wu, S. S. C., Jordan, Raymond, and Schafer, F. J., 1985, Compilation of the Mars 1:2,000,000-scale topographic map series, in Reports of Planetary Geology and Geophysics Program-1984, National Aeronautics and Space Administration Technical Memorandum 87563, p. 612-613.



Figure 1a. Part of topographic map of Mars (U.S. Geological Survey, 1989) showing western and eastern segments of Valles Marineris.



Figure 1b. Digital terrain model of western segment of Valles Marineris used in volumetric determinations.



A re-analysis of canyon structure and the mechanism(s) of canyon formation in and around Vallis Marineris is being carried out based on local high-resolution geologic mapping (primarily in Hebes and Juventae Chasmata), regional geologic analysis, topography and stability analyses, and regional spectral analysis. Several different types of canyon-related depressions exist in this area, including: closed, rough-floored canyons (Hebes), open, flat floored canyons (Echus, Gangis), closed sinkhole-like depressions (Ganges Catena), and rugged, closed depressions in and around pre-existing impact craters (Coprates Lx and Ku). Geometric relationships tie these multiple canyon types together into long (order 1000 km) "strings" related to the E-W regional tectonic structure (e.g., Echus-Hebes-Ganges Catena-Coprates Lx-Juventae). At least three major tectonic "strings" parallel each other through the entire Coprates quadrangle: Echus-Juventae, Candor-Gangis, and Ius-Coprates, with several smaller parallel branches. Each of the strings includes an obvious outflow channel, generally at the topographically low east end. These strings run along the crest of a topographic ridge extending eastward from the sub-circular Tharsis uplift. A few large N-S faults apparently cut through the area, e.g., the east wall of the box-like Ophir Chasma aligns with the west wall of Juventae. Three modes of slope failure have been identified(1) as having been active in widening individual canyons: 1) surficial debris slides (tens of km<sup>3</sup> off the steep walls of the rugged spur-and-gully type walls that comprise most of the canyon walls; 2) sapping channels that cut deeply into the surrounding plateau, frequently along small pre-existing grabens; 3) large debris slides (100's of km<sup>3</sup>) that form sheer arcuate segments of wall tens of km long that cut 5 - 10 km into the plateau. A fourth mode has been documented through the detailed mapping in Hebes: coherent subsidence blocks (100's of km<sup>3</sup>) with horizontal block dimensions up to several tens of km. (Gradational morphologies between the last two types exist.)

Several mechanisms have been proposed for formation of the overall canyon system, all of which have drawbacks(2,3). None of the simple observed modes of slope failure can account for the formation of the canyons, particularly the closed depressions like Hebes. Models invoking failure in ice-saturated soils and subsequent dispersal of the desiccated dust are untenable because such frozen soils cannot support the observed topography: the multi-kilometer high walls generate shear stresses of hundreds of bars that would drive plastic or shear failure on time scales of hours to days(4), incompatible with the great age of Vallis Marineris. Further, the observed failure surfaces of the large debris slides and block slumps cut several kilometers down and back into thawed zone of the pre-existing wall, which is extremely unlikely if wall cohesion and strength were provided by ice. Even assuming such slip surfaces could form, new scarp faces should show some form of flow or seepage, which are not evident, at the level in the wall (about one km down) where subsurface temperatures reached 273 K.

Spencer & Croft(5) proposed that the canyons formed at least in part as collapse structures in massive deposits of carbonate rock-"real" karst as opposed to "thermokarst". The competent rock could support the observed topography and produce the collapse structures. The original drawbacks of this model were the lack of any direct evidence for carbonate rocks and the extremely large volume of water that must be circulated to remove the observed volume of the canyons. However, the recent spectroscopic detection of a carbonate derived rock, scapolite (6), has now provided direct evidence for the existence of extensive carbonate deposits, and calculations using groundwater containing dilute sulfuric acid that probably exist on Mars reduces the required circulated water volume to reasonable levels (7). In addition to the karst-like collapse pits, there is evidence for tectonic subsidence as well. Blasius et.al.(1) noted post-wall faults in Melas-Coprates. Lucchitta (8) has argued for differential subsidence in eastern Ophir based on floor deposit patterns. Mapping in Hebes indicates chaotic terrain at two distinct topographic levels 4 and 5 km below the plateau level. All other occurrences of chaotic terrain are associated with surface layers that have been disrupted by near-surface subsidence. The implication is that the floor of Hebes has been tectonically dropped by several km. This is consistent with the more direct evidence of subsidence provided by the above noted block. Similarly, a 20 by 20 km block of plateau material sits at the bottom of Gangis Chasma,

indicating tectonic subsidence. Thus the preferred model here is a combination of the carbonate-tectonic models: tectonic fracture and graben formation along the axis of the topographic ridge during its formation formed the basic canyon structure and probably most of its apparent volume, including the subsidence blocks in Hebes; dissolving of carbonates due to caustic ground waters moving primarily along the major subsurface faults undermined the graben walls, causing wall slope failure, the chains of collapse pits, and the collapsed craters. This combined model can account for the "strings" of mixed depression types and is consistent with the regional setting.

REFERENCES. 1. Blasius K.R. et.al.(1977),JGR 82,4067. 2. Carr (1984) Mars, in NASA SP-469,p.207. 3. Croft S.K.(1989)4th Mars Conf.Prog. & Abstracts. 4. Phukan, A.(1985)Frozen Ground Engineering. 5. Spencer J.R.& S.K. Croft(1985)MECA Workshop on Evol. of Mars Atm.,p.40. 6. Clark, R.,G. Swayze, & R. Singer (1988)EOS Dec. 13,p.1634. 7. Spencer J.R. et.al(1989)4th Mars Conf. Prog & Abstracts. 8. Lucchitta B.K. (1989) Geologic Map of Vallis Marineris, in prep.

## DO PIT-CRATER CHAINS GROW UP TO BE VALLES MARINERIS CANYONS? *Richard A. Schultz, Geodynamics Branch, NASA Goddard Space Flight Center, Greenbelt, MD 20771.*

No.

The Valles Marineris (VM) canyon system on Mars is a spectacular planetary rift [1-3]. It has been proposed that the canyons nucleated and grew as collapse structures from a set of initially tiny pit-crater chains [4], but this scenario is not supported by structural relationships seen in Viking images.

A distinction should be made between canyons controlled by normal faulting and pit-crater chains that look superficially like canyons controlled by normal faulting. Structural mapping on enlarged 1:2 million scale photomosaics confirms that the original structural canyons are much narrower (factor of 3) than the present canyon width, and that normal faulting has controlled the lengths and depths of these canyons. Some canyons are controlled by 2 long, mutually parallel, inward dipping normal faults (Ius, western Tithonium Chasmata). Other canyons are defined by one continuous normal fault scarp faced by several discontinuous, echelon scarps (Coprates). Structures forming one or both graben walls can be inferred in Ophir and Melas Chasmata only by extrapolating along isolated spurs and massifs on canyon floors or by examining canyon terminations. These wide canyons are probably composed of several parallel grabens and are terminated in many cases by oblique trending normal faults.

In contrast, pit-crater chains (PCC) are restricted in extent and differ in morphology and structure from the canyons. Whereas grabens are found throughout VM plateaus, large PCC only occur north of Ius and South of Coprates Chasmata, respectively (Fig. 1). PCC distribution is neither random nor uniform but antisymmetric about the canyon system. Where PCC appear to merge into canyons, such as eastern Tithonium Chasma and Candor Chasma, the structure of each is distinct. Candor is defined by several parallel and oblique grabens, whereas eastern Tithonium is an echelon array of closed to partly closed depressions. Indeed, PCC are characterized by their segmented, echelon geometry [5], limited extent, and lack of clear fault control.

Mapping shows a variety of PCC trends along the canyon system. PCC north of Coprates Chasma are independent of (not parallel to) VM grabens and, somewhat surprisingly, are linked in orientation and location to wrinkle ridges (Fig. 1). In contrast, many large PCC nearest the major canyons parallel them, although the PCC south of Coprates are crosscut by oblique, northeast trending grabens. This implies that the stress state associated with the growth of PCC varied spatially along the canyon system, and certain PCC may record a set of early, pre-VM regional stress states. Valles Marineris and associated structures are said canonically to be oriented "radial to Tharsis" and this is taken to indicate some profound geometric, and presumably genetic mechanical, relationship [6]. Although a good correlation exists between principal stresses calculated from Tharsis loading models and the overall trend of VM canyons, the variety of structure locations, trends, and relative ages underscores the limited applicability of available geophysical models to canyon tectonics. Indeed, classification of structures as "radial or nonradial to Tharsis" probably is no longer a useful or precise exercise.

Structural relationships listed above suggest that pit-crater chains have a different origin than canyons. Echelon geometry indicates that the chains of pit craters behaved mechanically as interacting cracks. This suggests that pit-crater chains may be the surface expression of laterally propagating subsurface dikes or hydrofractures. The pits themselves may be surficial collapse depressions. Systematic locations of PCC in the canyon system and growth early in the rifting

process [7] perhaps suggest a magmatic (dike) origin as the more likely. Thus, the principal Valles Marineris canyons and pit-crater chains both have a structural origin, but canyons appear controlled by normal faulting (not dikes or cracks) and pit-crater chains by subsurface dikes or cracks (not normal faulting).

REFERENCES: [1] Sharp (1973) JGR 78, 4063-4073. [2] Blasius et al. (1977) JGR 82, 4067-4091. [3] Frey (1979) Icarus 37, 142-155. [4] See discussions by Croft (1989), 4th Intern.Mars Conf. (4IMC), 88-89; Spencer et al. (1989) 4IMC, 193-194; and Lucchitta et al. (1989) 4IMC, 36-37. [5] Pollard and Aydin (1988) GSA Bull. 100, 1181-1204. [6] For example, Wise et al. (1979) Icarus 38, 456-472; Plescia and Saunders (1982) JGR 87, 9775-9791; and Banerdt et al. (1982) JGR 87, 9723-9733. [7] Schultz and Frey (1988) EOS 69, 389-390; Schultz (1989) Lunar Planet. Sci. XX, 974-975.

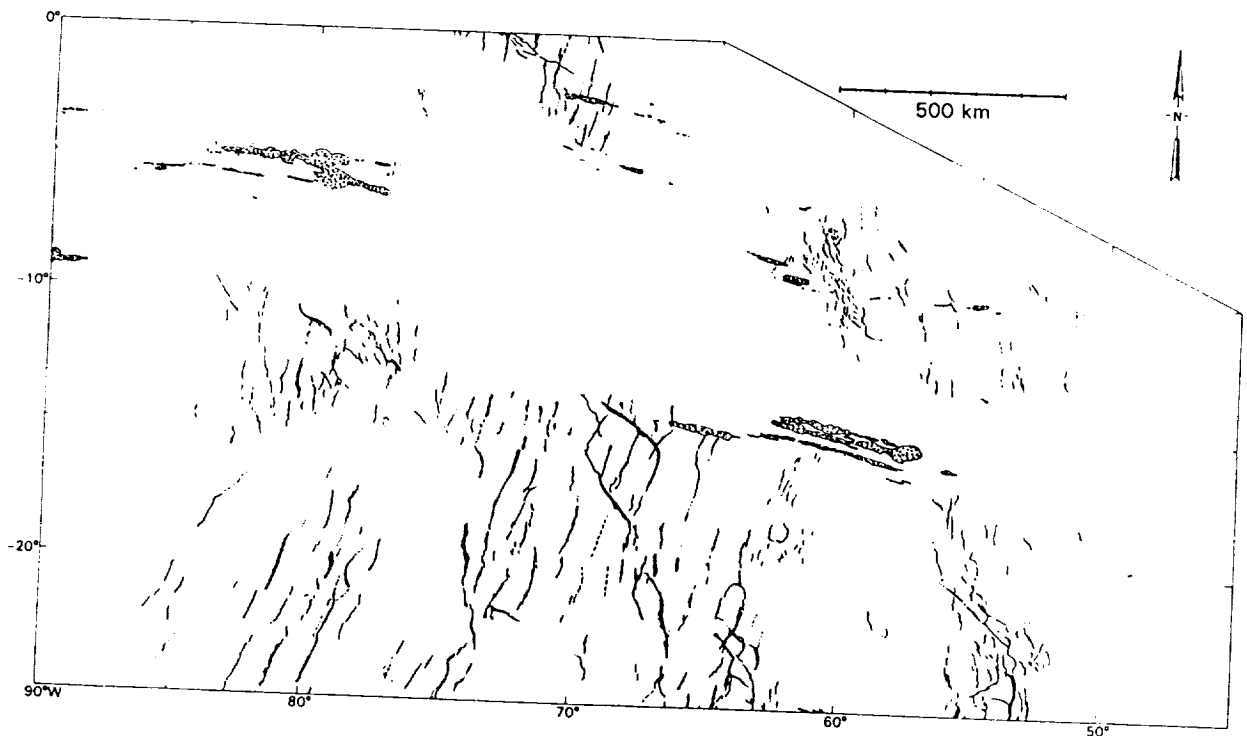


*Figure 1. Distribution of wrinkle ridges and pit-crater chains (stippled) in the Valles Marineris region. Canyon outlines omitted for clarity.*

ORIGIN OF THE MARTIAN CRUSTAL DICHOTOMY: A REVIEW; George E. McGill, Department of Geology and Geography, University of Massachusetts, Amherst, MA 01003.

The physiographic and stratigraphic contrasts between the northern lowland plains and the southern cratered uplands of Mars are generally interpreted to imply a first-order dichotomy in the martian crust. Two opposing types of hypotheses have dominated the debate over the origin of the dichotomy: 1) large-scale impact, and 2) endogenic processes. The published hypotheses (1-3) involve unusual events that occurred very early in martian history, and each implies physiographic, stratigraphic, and structural consequences that may be compared with observation. LOS gravity from Viking 2 (4) provides additional constraint.

The most recently proposed hypothesis for the origin of the crustal dichotomy involves focussing an excess of very large impact events onto what is now the lowland third of Mars (3). There is no reasonable mechanical explanation for the required focussing of large impacts. Even if an explanation could be devised, several closely spaced large impact basins must produce a topography that includes areas higher than the original surface as well as areas lower; there is no way they could form a single large hole, all of which is lower than the original surface. There are large basins in the lowland third of Mars (cf. 5-9), and locally the highland/lowland boundary is clearly controlled by these. But there is no evidence at all to suggest that the lowland third of Mars has more than its share of basins.

A single, giant Borealis basin (2) is a much more likely cause of the crustal dichotomy because no focussing is required, and a single large hole is the obvious result. If it exists at all, the Borealis basin must be older than the oldest defined time-stratigraphic units (10) because inliers of old upland terrain and remnants of pre-Noachian basins occur over much of the northern plains, indicating that ancient crust lies beneath most or all of the younger plains materials. Furthermore, the distribution of inliers implies a topographic high rather than a topographic low near the proposed center of the Borealis basin. LOS gravity data show clear mascons over large, post-Borealis basins under the northern plains but no mascon over the Borealis basin (4, 8-9). Either the Borealis basin does not really exist, or it formed so early that its gravity and topographic signatures relaxed completely, leaving only a lowland due to a thinned crust. Despite arguments to the contrary (3), the large size of the Borealis basin does not represent a statistical anomaly. However, its rim departs significantly from the highland/lowland boundary in places. This may be due to later erosional retreat of the boundary (e.g., 11). The oldest craters now buried beneath northern plains deposits have suffered extensive fracturing and erosion before burial, surviving as rings of knobs defining their rims. The maximum depth to which surface materials could have been removed since early to middle Noachian thus can be estimated by applying the crater dimensional equations of (12) to the smallest surviving "knob ghost" craters ( $D=10-15$  km). These calculations indicate a maximum of ~200 meters of lowlands-wide erosion of the ancient surface buried beneath the northern plains. This invalidates widespread southward migration of a dichotomy boundary with 2-3 km of relief since early Noachian. We cannot rule out erosional modification of the boundary before the Noachian, but there seems to be no independent evidence for this. There is evidence for late Noachian to early Hesperian erosion along the dichotomy boundary, but the knob ghosts are telling us that this erosion did not

cause significant migration of the boundary. These observations lead to the tentative conclusion that the dichotomy boundary is about where it has always been, and that it is a structural feature.

A number of recent studies suggest that the dichotomy boundary is not a stable ancient feature. There is clear evidence of relatively young faulting and major erosion in northern Mars, some of it demonstrably in early Hesperian (13), the rest less precisely dated as late Noachian through Hesperian (14). In fact, it is probable that the widespread fretted terrain and mesas were in large part formed at this time. It has been proposed (15) that most of the small drainage networks were developed at this time in response to pervasive volcanism and sill intrusion. Crater counts indicate that there was widespread resurfacing by lava flows at about the Noachian/Hesperian boundary (16). Finally, detailed analysis of Viking LOS gravity (17) indicates that there is a narrow negative anomaly associated with the dichotomy boundary, suggesting activity more recent than the presumed early origin of the dichotomy required by the mega-impact hypothesis.

Thus it appears as if the northern part of Mars experienced several possibly related events in late Noachian and/or Hesperian time: fracturing and faulting of the crust in the northern third of Mars, widespread erosion with formation of channels and valley networks, and extensive extrusive and intrusive igneous activity, most of it occurring near or on the dichotomy boundary. An internal process that thinned the crust from below is the most likely cause, but the specific mechanism envisaged by (1) is ruled out because if a "catastrophic" core-formation event occurred, it must have taken place very early in martian history. Nevertheless, the cause must be internal because the geological and geophysical observations discussed above require that a mega-impact occur much earlier in martian history.

#### References Cited

- (1) Wise, D.U., M.P. Golombek, and G.E. McGill, *J. Geophys. Res.*, **84**, 7934-7939, 1979.
- (2) Wilhelms, D.E., and S.W. Squyres, *Nature*, **309**, 138-140, 1984.
- (3) Frey, H., and R.A. Schultz, *Geophys. Res. Letts.*, **15**, 229-232, 1988.
- (4) Sjogren, W.L., *Science*, **203**, 1006-1009, 1979.
- (5) Schultz, P.H., *Lunar Planet. Sci.* **XV**, 728-729, 1984.
- (6) Schultz, P.H., and H. Glicken, *J. Geophys. Res.*, **84**, 8033-8047, 1979.
- (7) Schultz, P.H., R.A. Schultz, and J. Rogers, *J. Geophys. Res.*, **87**, 9803-9820, 1982.
- (8) McGill, G.E., *Lunar Planet. Sci.* **XIX**, 752-753, 1988.
- (9) McGill, G.E., *J. Geophys. Res.*, in press.
- (10) Tanaka, K.L., *J. Geophys. Res.*, **91**, E139-E158, 1986.
- (11) Hiller, K.H., *U.S. Geol. Surv. Misc. Invest. Ser.*, Map I-1110 (MC-14), 1979.
- (12) Pike, R.J., and P.A. Davis, *Lunar Planet. Sci.* **XV**, 645-646, 1984.
- (13) McGill, G.E., *Lunar Planet. Sci.* **XVIII**, 620-621, 1987.
- (14) Maxwell, T.A., and G.E. McGill, *Proc. Lunar Planet. Sci. Conf.* **18**, 701-711, 1988.
- (15) Wilhelms, D.E., and R.J. Baldwin, *Lunar Planet. Sci.* **XIX**, 1270-1271, 1988.
- (16) Frey, H., et al., *Proc. Lunar Planet. Sci. Conf.* **18**, 679-699, 1988.
- (17) Phillips, R.J., *Trans. American Geophys. Union*, **69**, 339, 1988.

STRUCTURAL MODIFICATION ALONG THE CRATERED TERRAIN BOUNDARY,  
EASTERN HEMISPHERE, MARS.  
Ted A. Maxwell, Center for Earth and Planetary Studies,  
National Air and Space Museum, Smithsonian Institution,  
Washington, D. C. 20560

Initial investigations of the Mars cratered terrain boundary (CTB) suggested that it formed progressively by erosional backwasting of the cratered terrain (1). Such conclusions were based on the presence of isolated knobs and mesas in the boundary zone adjacent to the southern cratered terrain, particularly in the Nilosyrtris Mensae region, and by the fact that the boundary is present now as an elevated scarp in the eastern hemisphere. Evidence for mass wastage of both the main bounding scarp and along the edges of isolated plateaus also supported such interpretations, further indicating that most of the erosion took place during a period(s) of wetter climate. Based on more recent investigations of the structure, topography and timing of the CTB, however, it is now apparent that the sequence of events that are responsible for the present appearance of the CTB, at least in the region between Nilosyrtris Mensae and Aeolis (Long.  $300^{\circ}$  to  $180^{\circ}$ ), occurred within a discrete time interval, indicating that the northern border scarp of the cratered plateau material is not the result of longterm migration of a previous structurally controlled topographic disruption. Based on structural mapping, detailed shadow measurements of plateaus and knobs, and age dating of the exposed surfaces in this region, the tectonic record of the eastern hemisphere is one of modification of the cratered terrain boundary, with little evidence that can be used to constrain theories for the original creation of the CTB.

Structural mapping of the CTB indicates little correlation between presumed compressional features (ridges and scarps) and the orientation of the boundary itself (2). Instead, compressional features are aligned in a primary NS direction, with local deflections where underlying topography reaches the near-surface in plains units (as judged by structural trends in nearby highland areas). The notable exception is in a wide trough that extends to the southwest between Isidis and the impact crater Herschel. Here, scarp orientations are predominantly axially symmetric, suggesting continued deformation by downdropping of this major trough past the times of plains emplacement (3). The 300 km wide block of cratered plateau material on the north side of the trough acted as a discrete structural unit during deformation, and may be analogous to the subsurface terrace that lies beneath the shallowly flooded region of plains to the north of the CTB.

Shadow-length elevation measurements of individual plateaus, knobs, and graben in and north of the cratered terrain boundary suggest that downdropping of the "terrace"

also occurred as a discrete crustal block rather than as individual faulted fragments of crust. If formed by erosional retreat, isolated remnants of the cratered plateau material would display a greater degree of erosion with distance from the present boundary. Such is not the case, due to either the presence of a significant resistant layer, or downdropping as a terrace. In the absence of confirmation of a widespread resistant unit from the limited Viking multispectral data (4), the latter interpretation is preferred here.

The timing of downdropping suggests structural modification as a discrete event, though for reasons listed above, not the event that created the dichotomy boundary itself. The faulting that produced the broad, 300 km wide terrace occurred in late Noachian or early Hesperian time (around N(5)=190), younger than the faults surrounding the Isidis basin (5). In other regions, however, faulting of plateau material occurred at different times, suggesting a protracted period of structural adjustment to the original boundary.

Current theories for creation of the Mars crustal dichotomy are 1) single mega-impact (7), 2) multiple large impacts (8), and 3) crustal overturn (9). Hypotheses 1 and 2 would be expected to show either concentric rims or radial fractures, neither of which occur in the highlands between Isidis and Aeolis. The large crustal block north of the graben-like trough east of Isidis suggests endogenic processes (regional extension) rather than impact for at least the modification of the presently observed boundary, which is consistent with hypothesis 3, though not conclusive. By looking at modification processes and prior geometry of the boundary region, more precise constraints can be placed on the geometric form of the original structure.

These results were presented at the Mars: Evolution of Volcanism, Tectonism and Volatiles Meeting in Easton, Maryland, October, 1988. Supported by NASA Grant NAGW-129.

References: (1) Sharp, R.P., 1973, JGR, v. 78, p. 4063-44083. (2) Maxwell, T.A. and Barnett, S.J., 1984, LPSC XV, p. 521-522. (3) Mason, D.B., 1988, Report to Planetary Geol. Intern Program. (4) Bougan, S.J. et al., 1988, ms in preparation. (5) Maxwell, T.A. and McGill, G.E., 1988, Proc. LPSC, 18th, p. 701-711. (6) Frey, H. et al., 1988, Proc. LPSC, 18th, p. 679-699. (7) Wilhelms, D.E. and Squyres, S.W., 1984, Nature, v. 309, p. 138-140. (8) Frey, H. and Schultz, R.A., 1988, GRL, v. 15, p. 229-232. (9) Wise, D.U. et al., 1979, JGR, v. 84, p. 7934-7939.



GEOLOGIC EVOLUTION OF THE HIGHLAND/LOWLAND TRANSITION ZONE IN THE ISMENIUS LACUS QUADRANGLE, MARS; Andrew M. Dimitriou, Department of Geology and Geography, University of Massachusetts, Amherst, MA 01003.

The topographic dichotomy on Mars has been a major subject of study for planetary geologists for over fifteen years. The northern 1/3 of the planet constitutes a region of 2-3 km average lower elevation than the southern 2/3 with the boundary between the 2 provinces approximating a small circle inclined at 28 degrees to the equator. This transition also separates 2 geologic areas of different age and genesis with the northern portion of the planet appearing in general as a more sparsely cratered younger surface and also being characterised by smoother surface materials. The prime cause for the dichotomy has been the topic of many studies which have placed the timing of this event in or before the Early Noachian, regardless of whether an endogenic [1,2] or exogenic [3,4] origin is considered.

This study is concentrating on a portion of the dichotomy boundary in the Ismenius Lacus (MC5) quadrangle where it is present both as a series of NW trending scarps and a complex set of eroded features forming a transition zone from the uplands into the lowlands; i.e. fretted terrain [5]. The purpose of the study is to constrain the number and timing of the identifiable resurfacing and fracturing events both on the upland and lowland sides of the boundary. This will enable the determination of relative age of the boundary zone itself in this area.

Geologic mapping at 1:15M scale [6] in this area has identified the upland surface material as ridged and etched plateau units of inferred volcanic origin which themselves exhibit various episodes of resurfacing. Preliminary investigation of this area using the 1:2M MC5-SE and MC5-SC control photomosaics as bases has revealed a systematic subduing of topography and a lessening of the crater density towards the transition zone in MC5-SE within the northern portion of the plateau sequence. However, cumulative crater counts also in MC5-SE on several geologic units have revealed a statistically significant older crater retention age for the ridged unit of the plateau sequence than for the etched unit. The etched unit is present here in the southern part of the subquad further away from the boundary zone than the ridged unit. At least one episode of resurfacing is therefore better evidenced away from the transition zone. The boundary itself shows evidence of mass wasting, slumped crater rims have been produced by erosion and valleys have been enlarged in an irregular manner back into the uplands. On the lowland side fretted terrain is present, representing eroded remnants of an upland surface up to 400 km north of the well defined boundary scarp. The fretted terrain is characterised by angular to subangular smooth and flat topped blocks standing proud of a lobate debris apron [7] presumably derived from the block and also of surrounding lowland plains material. In areas where fretted terrain is absent lowland plains embay the scarps at the margin of the upland, but evidence of an older surface underlying the lowland plains can be seen by the presence of "knobby terrain" [8]. This older surface is presumably the same as is present on the upland side but is at a 2km lower elevation.

Studies in the Amenthes area [9] have shown that fracturing and resurfacing experienced a peak in activity around the Late Noachian and Early Hesperian boundary. The dating results within even this restricted region indicate different resurfacing and fracturing chronologies for different areas. More recently, an attempt to combine all the disparate pieces of evidence for global Late Noachian/Early Hesperian tectonic and volcanic activity has been made [10], with an endogenic origin for the dichotomy being proposed.

Work underway in the Ismenius Lacus area includes detailed geologic mapping of critical areas using the 1:2M controlled photomosaics and crater counting of units based upon stratigraphic position, degradation state and cross-cutting fracture orientation relationships. This will enable harder constraints to be placed on the dichotomy forming events in this area.

#### References

- 1) Mutch, T.A. et al. (1976) The Geology of Mars, Princeton Univ. Press.
- 2) Wise, D.U., et al. (1979) J. Geophys. Res., 84, 7934-7939.
- 3) Wilhelms, D.E., and S.W. Squyres (1984) Nature, 309, 138-140.
- 4) Frey, H., and R.A. Schultz (1988) Geophys. Res. Letts., 15, 229-232.
- 5) Sharp, R.P. (1973) J. Geophys. Res., 78, 4073-4083.
- 6) Greeley, R., and J.E. Guest (1987) U.S. Geol. Survey, Misc. Invest. Series, Map I-1802-B.
- 7) Squyres, S.W. (1978) Icarus, 34, 600-613.
- 8) McGill, G.E. (1987) Lunar Planet. Sci. XVIII, 622-623.
- 9) Maxwell, T.A., and G.E. McGill (1987) Proc. 18th Lunar Planet. Sci. Conf., 701-711.
- 10) McGill, G.E., and A.M. Dimitriou (1989) J. Geophys. Res., in review.

ORIGINAL PAGE IS  
OF POOR QUALITY

# TIMING OF RESURFACING EVENTS IN THE AMENTHES AND TYRRHENA CRATERED HIGHLANDS OF MARS.

Robert A. Craddock and Ted A. Maxwell, Center for Earth and Planetary Studies, National Air and Space Museum, Smithsonian Institution, Washington, D.C. 20560

Determination of the ages and the nature of resurfacing events along the cratered terrain boundary on Mars is important for bracketing the age and origin of structural events along the boundary, for determining the types, extent, and evolution of geomorphic processes in this part of Mars, and eventually for understanding the origin of the dichotomy between the highly cratered southern hemisphere and the northern smooth plains. Previous work has concentrated on all geologic materials in the Amenthes region and has found a complex sequence of resurfacing and faulting events postdating the formation of the martian dichotomy (1). In this study, we concentrated on a class of rimless craters contained in the heavily cratered highland materials of the Amenthes and Tyrrhena regions in order to determine the timing of resurfacing events represented by their population distribution, and the geographical extent of these modified craters.

Two separate but similar highland units containing rimless craters were recognized: cratered plateau materials and cratered highland materials. These units correspond roughly to the cratered plateau and hilly and cratered materials of (2) and are a subdivision of the dissected plateau sequence of (3) based upon the etched and sculpted appearance of the intercrater plains (e.g., compare Viking Orbiter image 381S81 of the cratered plateau materials with image 365S61 of the cratered highland materials). Populations of both rimless and fresh (superposed) craters for both units were counted and normalized to measure the crater size-frequency distribution of the surfaces; a process that has been reviewed by (4,5,6). Because previous work (1) has shown that the determination of resurfacing ages is model dependent and that the production curve determined by (7) compares well with direct  $N(5)$  ages determined by (6), the resurfacing ages in this study were determined directly as in (6).

As opposed to previous work, a larger sampling area for the cratered plateau materials was used ( $494,000 \text{ km}^2$  versus  $173,000 \text{ km}^2$  in (1)), however, the crater size-frequency distribution remained basically the same. The  $N(5)$  age of this surface is equal to 790 (Early to Middle Noachian), with a resurfacing age of  $N(5)=250$  (Late Noachian). In contrast, the age of the cratered highlands materials is  $N(5)=540$ , apparently younger than the cratered highlands. However, the frequency distribution curves for these two units cross at 16 km, and only those craters greater than about 25 km indicate age relations consistent with stratigraphic observations,

with cratered highlands having a density greater than that of the cratered plateau. The age of resurfacing for the cratered plateau material is  $N(5)=200$  (Early Hesperian), slightly younger but essentially equivalent to that of the cratered highlands.

To determine whether the timing of resurfacing was related to the dichotomy boundary, counts on the cratered plateau surface were divided into  $5.0^\circ$  latitude bins. These frequency distributions suggest an increase in the age of resurfacing with increasing latitude, but only within craters in the 8- to 50-km diameter range. If resurfacing was a single process, these data imply a time transgression such that the surface nearest the dichotomy boundary became stable first, followed by cratered plateau surfaces at successive southerly latitudes, analogous to, but in another direction than (8), in which cessation of resurfacing within the younger smooth plains and fretted terrain was progressively younger west of Isidis, towards more northerly latitudes. Such an apparent age transgression could be caused by two (non-exclusive) processes: 1) Variations in the "efficiency" of the process occurring at a common time, or 2) An invariant process, which ceased affecting the surface at different times in different regions. If these results were a function of resurfacing with efficiency variations, we would expect to see the age relations to be defined by different crater diameter intervals (as found for units along the transition zone in ref. 8). However, the fact that the age relations found here are defined within the same diameter interval suggests that we are looking at a time transgressive event, as discussed in (9).

These results were presented at the 20th Lunar and Planetary Science Conference, Houston, Texas, March, 1989. Supported by NASA Grant NAGW-129.

REFERENCES: (1) Maxwell, T.A. and G.E. McGill, Proc. Lunar Planet. Sci. Conf., 18th, 701-711, 1988. (2) Scott, D.H. and M.H. Carr, Geologic Map of Mars, 1:25M scale, U.S.G.S. Map I-1083, 1978. (3) Greeley, R. and J.E. Guest, Geologic Map of the Eastern Equatorial Region of Mars, 1:15M scale, U.S.G.S. Map I-1802-B, 1987. (4) Neukum, G. and D.U. Wise, Science, 194, 1381-1387, 1976. (5) Neukum, G. and K. Hiller, J. Geophys. Res., 86, 3097-3121, 1981. (6) Tanaka, K.L., J. Geophys. Res., 91, E139-E158, 1986. (7) Neukum, G., Meteoritenbombardment und Daitierung Planetarer Oberflachen, Habilitationsschrift, Ludwig-Maximilians-Universitat, Munich, 186 pp., 1983. (8) Frey, H., Semeniuk, A.M., Semeniuk, J.A., and Tokarcik, S., Proc. Lunar Planet. Sci. Conf., 18th, 679-699, 1988. (9) Maxwell, T.A. and R.A. Craddock (this volume).

**GEOLOGIC EVIDENCE SUPPORTING AN ENDOGENIC ORIGIN FOR THE MARTIAN CRUSTAL DICHOTOMY;** George E. McGill, Department of Geology and Geography, University of Massachusetts, Amherst, MA 01003.

The division of Mars into two contrasting topographic regions -- a northern lowland third and a southern upland two-thirds -- is most likely related to a major difference in thickness of crust. Explanations for this thickness difference include: initial crustal inhomogeneity (1), subcrustal erosion by a global-scale convection current (2), and large impacts (3,4). All of these hypotheses except subcrustal erosion require a primordial origin for the dichotomy; obviously so for initial crustal inhomogeneity, but true also for large impacts because the buried surface of the northern lowlands carries a crater population comparable to that of the ancient surface of the southern uplands and thus could not have been destroyed by very large impacts at any time following the end of the primordial bombardment phase of solar-system history.

As pointed out by (2), the ~3 km average elevation difference between northern lowland and southern upland implies that a very large volume of crustal materials must be transported out of the northern lowland and distributed elsewhere (unless, of course, the dichotomy is an initial characteristic of the crust). Using simple buoyancy equations and densities of crust and mantle of 3.0 and 3.5 g/cm<sup>3</sup> (5), a 3 km elevation difference implies a 21 km difference in thickness of crust. The northern lowland is ~36% of the surface of Mars; thus  $\sim 1.1 \times 10^9$  km<sup>3</sup> of crustal materials must be displaced. This volume cannot be changed more than about 20% by adjusting crust and mantle densities or area of northern lowland within reasonable limits. The ejecta blanket of a single mega-impact basin must average ~19 km in thickness to account for the displaced volume; hence the added thickness immediately adjacent to the lowland would be much greater than 19 km. This represents significant local thickening that should be detectable. Substituting several large basins for one giant one (4) results in retention of displaced crust even closer to (and also within!) the lowland, yielding a global-scale topography distinctly unlike that observed (large basins clearly are present in the northern lowland, but they are responsible for second-order topography, not the global lowland/highland dichotomy).

Three types of geological evidence suggest that the martian crustal dichotomy is due to some endogenic cause acting after the end of primordial bombardment: 1) abundant fractures associated with the northern lowland and the dichotomy boundary, many demonstrably late Noachian or early Hesperian in age; 2) peak igneous activity in late Noachian or early Hesperian; and 3) the sequence of stratigraphic units partially filling the lowland includes nothing older than early Hesperian.

The ancient surface flooring the northern lowland has been severely fractured and eroded, with most crater rims surviving only as rings or arcs of knobs. Counts of all craters superposed on this knobby terrain provide good ages for the termination of the knob-forming process because unmodified craters would begin to accumulate as soon as knob formation ceased. Fracturing responsible for knobs terminated in late Noachian (6); when it began cannot be well constrained. Furthermore, the presence of knob rings as small as 10-20 km in diameter in many parts of the northern lowland eliminates any possibility of significant erosional stripping of northern lowland crust after late Noachian. Younger than the knob-forming fracturing event are the major fractures and faults forming local scarps and fretted terrain along the dichotomy boundary. These fractures and faults cross-cut depositional and erosional plateau surfaces of late Noachian to early Hesperian age (7,8), and thus cannot be older than late

Noachian. Because there can be no significant post-late Noachian erosional stripping of the northern lowland crust, scarps and fretted terrain represent the original position of the dichotomy boundary, hence it is difficult to escape the conclusion that the dichotomy itself must also be of late Noachian or younger age. Ages of northern plains materials embaying the boundary and surrounding fretted plateau remnants locally constrain the age of boundary faulting to no younger than early Hesperian (7).

Estimates of the surface area of volcanics as a function of age indicate that volcanic activity peaked in late Noachian and early Hesperian (9,10), indicating that heat loss reached a maximum 1-2 GA after Mars formed. A recent model relating a number of geological events and materials to massive sill intrusion in the early Hesperian provides additional support (11). The maximum in heat loss coincides in time with the fracturing and resurfacing events that characterize the tectonic history of the northern lowland.

The most likely time of formation of the lowland is thus late Noachian to early Hesperian. If true, an origin by impact is impossible. The associated heat-loss maximum suggests that the underlying cause is probably long-lived plumes or large-scale convection in the mantle, perhaps related to slow, non-catastrophic core formation (12). The lowland is envisaged as centered over a huge thermal plume or the rising limb of a large convection cell. Ductile thinning of the lower crust results from radial horizontal flow. The extensive fracturing responsible for knobby terrain and for boundary scarps and fretted terrain suggests a large-scale, pervasive extensional stress regime, such as might occur in surface rocks overlying a crust that is being ductilely extended at depth.

However, the problem of displaced volume is still with us. Ductile extension of the crust implies either an increase in surface area in the northern lowland, or transport of lowland crust laterally beneath adjacent upland crust. Increase in surface area cannot be a major contributor because the implied planetary expansion is totally unreasonable. Underthrusting of thinned lowland crust beneath adjacent upland crust produces an annulus of thickened crust around the lowland. The width of the annulus and the amount of thickening vary with assumed initial crustal thickness, but the numbers are roughly similar to those for the ejecta blanket of a single mega-impact basin. A near-global redistribution of displaced lowland crust will produce crustal thickening of less than 10 km. How this might occur is not clear, but it is at least possible with an endogenic process, whereas it is not possible with an exogenic process.

#### References

- 1) Mutch, T.A. et al., (1976) The Geology of Mars, Princeton Univ. Press.
- 2) Wise, D.U., et al. (1979) J. Geophys. Res., **84**, 7934-7939.
- 3) Wilhelms, D.E., and Squyres, S.W. (1984) Nature, **309**, 138-140.
- 4) Frey, H., and R.A. Schultz (1988) Geophys. Res. Letts., **15**, 229-232.
- 5) BVSP (1981) Basaltic volcanism on the terrestrial planets, pp. 687-689.
- 6) McGill, G.E., and A.M. Dimitriou (1989) J. Geophys. Res., in review.
- 7) Maxwell, T.A., and G.E. McGill (1987) Proc. 18th Lunar Planet. Sci. Conf., 701-711.
- 8) Frey, H. et al. (1987) Proc. 18th Lunar Planet. Sci. Conf., 679-699.
- 9) Greeley, R. (1987) Science, **236**, 1653-1654.
- 10) Tanaka, K.L. et al. (1987) Proc. 18th Lunar Planet. Sci. Conf., 665-678.
- 11) Wilhelms, D.E., and R.J. Baldwin (1989) Proc. 19th Lunar Planet. Sci. Conf., in press.
- 12) Davies, G.F., and R.E. Arvidson (1981) Icarus, **45**, 339-346.

## TERRESTRIAL ANALOGUES FOR PLANETARY EXTENSIONAL STRUCTURES

George E. McGill, Department of Geology and Geography, University of Massachusetts, Amherst, MA 01003.

Extensional structures have received much attention in recent years, and are among the "hottest" topics in structural geology. This is primarily a result of field studies indicating their importance in tectonic settings hitherto believed to be entirely characterized by compression. For several reasons, a thorough review of structures resulting from extensional stresses is not practical here; in fact, many of these structures have limited relevance as analogues for planetary features. What will be attempted is a rough classification of extensional structures, primarily based on scale, and an evaluation of their usefulness as analogues. Specific citations are intentionally sparse because of space constraints.

On the earth, extensional structures range in scale from features seen in thin section to features of global significance. Although beloved of many structural geologists, joints, boudinage, stretching lineations, dismembered bedding, and other indicators of extension seen in outcrop, hand specimen, and thin section are of little relevance to planetary studies because they range from one to four orders of magnitude below the resolution of the best orbital images. It is convenient to separate structures that are large enough to be resolved on orbital images into two categories: 1) those that are of crustal to global scale, and 2) those that are generally of less than crustal scale. The first group is intended to include structures associated with globally significant tectonic regimes, the second group incorporates a variety of more local structures generally not directly related to global tectonics. Structures from both categories are potentially useful as planetary analogues because they can provide clues to the kinematics and mechanics of their formation, and thus constrain hypotheses for the origin of similar structures on other planets. However, a major problem yet to be resolved is whether it is sound practice to transfer the specific crustal and tectonic environments associated with analogue structures from the earth to other planets. My bias is that this is, in general, a dangerous thing to do.

Structures of crustal to global scale: The importance of extensional structures within the earth's tectonic system has been greatly enhanced by some very exciting discoveries that have occurred in just the past few years. It is now apparent that extension is an important element in the structural evolution of all types of plate boundaries, not just divergent ones (1). The following paragraphs comment briefly on important terrestrial extensional structures, and on their probable value as analogues.

1. Mid-ocean ridges and rifts: The global system of oceanic divergent boundaries is the most prominent tectonic feature on the earth. In addition to the gross topography, there are several associated characteristics that derive from the specific processes occurring at mid-ocean ridges: positive Bouguer gravity anomalies, magnetic "stripes", elevation decrease with distance from the ridge that is correlated with age, high heat flow, ridge offsets across transforms, shallow seismic activity, and "anomalous" mantle. Furthermore, the great length of the mid-ocean ridge system clearly depends on the earth's dynamic plate tectonics; consequently, it seems risky to use mid-ocean ridges as analogues for short, discontinuous ridges with axial troughs on other planets. Even the presence of one of the associated characteristics does not help very much. For example, cross-structural offsets that, on another planet, might be interpreted as mid-ocean ridge transforms, also occur on the earth as synkinematic features in foreland thrust belts and belts of metamorphic core

complexes, and are common as later modifications of most of the earth's Archean tectonic belts.

2. Continental rifts: These are very promising analogues, because some on the earth appear to "fail", and thus are not required to be part of a dynamic global plate-tectonic system. The extension normal to the long axes of continental rifts is too great to be explained by bending and membrane strains generated by the associated uplift, but is generally less than a few 10's of km. (2). Gravity anomalies, high heat flow, and seismic data suggest that continental rifts overlie regions where the mantle lithosphere has been thinned, and some calculations suggest that this thinning is a necessary precursor to crustal-scale brittle failure (3). Brittle graben faults in the shallow crust thus pass downward into a more ductile regime. By making reasonable assumptions concerning fault attitude, the widths of continental rifts provide an upper bound on the effective elastic thickness of the crust or lithosphere (4), the best estimates coming from places where extension is least. Continental rifts have been used as analogues for inferring near-surface rheology and the existence of lateral tectonic movements on Venus.

There is a major controversy concerning the ultimate causes of continental rifts: either they are "passive", with extension and rifting caused by far-field stresses and with uplift following later as a result of lithospheric thinning; or they are "active", with uplift, lithospheric thinning, and rifting directly caused by a mantle thermal anomaly (5). Both types seem mechanically feasible, and the evidence needed to choose between them must come from geological and geophysical studies, as along the Red Sea rift where fission-track ages in rocks adjacent to the Red Sea demonstrate that uplift followed both rifting and the initiation of volcanism by 10-15 my. (6), requiring a passive formation mechanism. The distinction is of some importance, because the active mechanism implies vertical tectonics (at least locally), whereas the passive mechanism is more consistent with horizontal tectonics. At present, we cannot easily obtain diagnostic geological or geophysical data on other planets needed to distinguish between these, but such data are not totally out of reach when field work with landers begins.

3. Convergent plate boundaries: Extensional structures occur in a variety of tectonic environments associated with convergent boundaries. Normal-fault earthquakes occur oceanward of trenches as a result of tensional bending stresses in the upper part of the elastic lithosphere. Extension occurs behind many island arcs, commonly producing "back-arc basins", because the motion vector for the subducting slab is steeper than the slab itself (1), requiring that the hinge migrate away from the arc (this is sometimes inappropriately called "trench suction"). The value of either of these types of extensional structures for analogue studies is unclear. The Basin and Range and metamorphic core complex structures in the North American Cordillera may be continental equivalents of back-arc structures in the oceans, or they may be related in a more complex way to changes in relative plate motions (7). Recognition of either type of structure on another body would be strong evidence for horizontal tectonic movement. Despite the "blobby" distribution of exposed metamorphic core complexes, their origin requires large (>100%) horizontal extension, with proportionately less vertical movement. Consequently, we must avoid assuming automatically that planetary tectonic topography characterized by dome-like features is necessarily due to vertical movements.

Excessively elevated topography produced by collision commonly fails by extension simply due to gravity (8); in fact, there is a major young, low-angle normal fault cutting Mount Everest! Because gravitational failure of high topography does not depend on the mechanism for creating the topography, these



collapse structures could serve as potential analogues for studies of elevated terrain on other bodies.

4. Transform boundaries: Oblique movement vectors commonly produce transtensional basins on the earth, but their value as analogues is problematical because of the almost total absence of strike-slip faults on other bodies.

Structures of "local" scale: These include grabens and normal faults due to: 1) bending, 2) lateral slip or flow along a discontinuity, and 3) adjustments of surficial materials to topography or movements in underlying rocks.

1. From considerations of simple plate bending, shallow normal faults and grabens can form in the hinge regions of structural arches and domes, and along the anticlinal hinges peripheral to basins. Numerous examples are discussed in the literature. Because most of these structures are of less than crustal scale, and because most involve the bending of layered rocks, the total extensional strain developed is not very large.

2. If local conditions permit, surface materials can slide or flow laterally along a subsurface discontinuity, with the extension accommodated by the formation of normal faults and grabens. Even though the specific geologic conditions are unlikely to be duplicated on another body, these structures are useful analogues because they demonstrate that the spacing and width of geometrically simple grabens provide direct evidence for the thickness of the faulted layer (9).

3. Sediments deposited over a high-relief surface will develop drape structures when they compact. Drape anticlines ("supratenuous" anticlines) formed this way have been known for a long time. Normal faults are mechanically possible in the hinge regions of these drape anticlines, but I am not aware of any published studies describing them. In structurally active areas, poorly consolidated surface materials must adjust to bending and faulting in consolidated rocks buried beneath them. One common result is the development of collapse grabens in the surface materials such as the shallow grabens formed in gravels overlying bedrock gjáur that were opened in the winter of 1975-76 by rifting in northern Iceland.

Many of these "local" structures are geometrically and mechanically useful as analogues, and they have been used to infer the mechanisms of formation of faults and grabens on Mercury, Mars, Ganymede, and the Moon. The primary problem is one of scale -- most of the planetary features are larger than the earth analogues. There are good reasons why this might be so, but this scale difference requires that we use structural analogues with care. However, it is entirely possible that crustal-scale equivalents of smaller structures on the earth appear so important on other planets and moons simply because there are no dynamic tectonic and degradational systems to mask them.

#### References Cited

- 1) Hamilton, W.B., *Geol. Soc. America Bull.*, 100, 1503-1527, 1988.
- 2) Mohr, P., in Pálmason, G., ed., *Continental and Oceanic Rifts*, American Geophys. Union, 293-309, 1982.
- 3) Bott, M.H.P., in Illies, J.H. ed., *Mechanism of graben formation*, Elsevier, 1-8, 1981.
- 4) Illies, J.H., in Illies (Ibid), 249-266, 1981.
- 5) Morgan, P., & G.H. Baker, *Tectonophysics*, 94, 1-10, 1983.
- 6) Bohannon, R.G. et al., *J. Geophys. Res.*, 94, 1683-1701, 1989.
- 7) Rehrig, W.A., *Geol. Soc. America Sp. Pap.* 208, 97-122, 1986.
- 8) Dewey, J.F., *Tectonics*, 7, 1123-1139, 1988.
- 9) McGill, G.E., & A.W. Stromquist, *J. Geophys. Res.*, 84, 4547-4563, 1979.

Studies of the lithospheric tectonics of one-plate planets have used flat plate (1) and thin shell (2) approximations or inverted for stress states given additional topographic and gravitational data (3) to determine lithospheric thicknesses and stress histories in a number of applications. We have developed an exact analytical model to determine the stress state in a spherical lithosphere of finite thickness (4). For a superposed load, here modeled as a Gaussian distribution, the stress state is a function of four dimensionless parameters:  $LTH/R_p$ , the ratio of lithospheric thickness to planetary radius;  $q$ , the ratio of isostatic to flexural response;  $\sigma$ , the characteristic width of the load in radians; and  $\theta$ , the angular distance from the load center (Fig. 1). For a superposed load, the four required boundary conditions are: 1,2) shear stresses at the base and surface of the lithosphere are zero, 3) vertical stress at the lithosphere surface is that due to the overlying load and 4) the load and isostatic restoring forces are in equilibrium at the base of the lithosphere. The parameter,  $q$ , cannot be known exactly for most planetary bodies, but can be closely approximated. The tectonics of loading are relatively insensitive to  $q$ , being far more dependent on the width of the load ( $\sigma$ ).

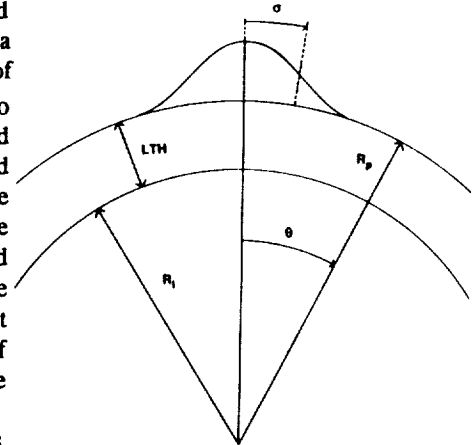
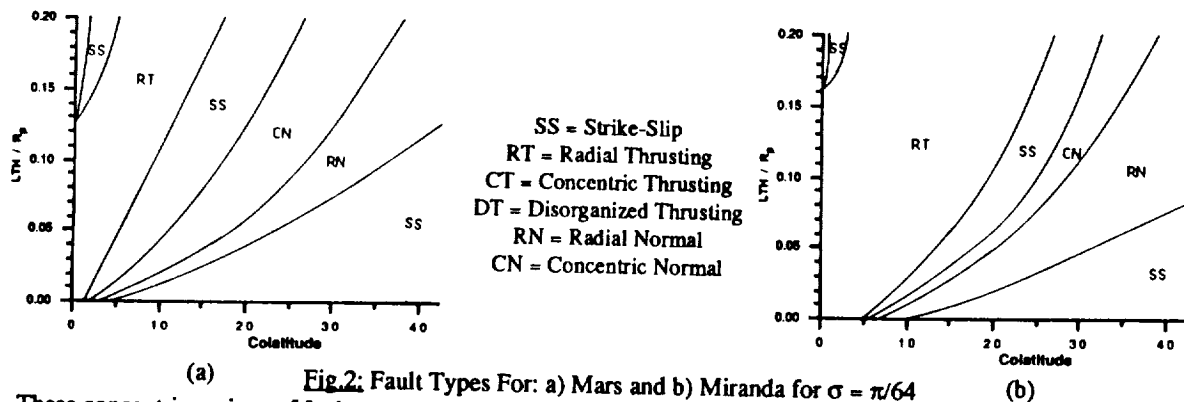


Fig. 1: Load Model Parameters

**NARROW LOADS.** The current study reproduces the stresses and tectonic patterns derived from flat-plate approximations when  $\sigma$  is small ( $\leq \pi/32$ ). Surface stresses derived from the model are converted into maps of predicted fault types as functions of angular distance from the load center and lithospheric thickness for a given  $\sigma$  and  $q$ . Fig. 2 shows the surface tectonics for a load of  $\sigma = \pi/64$ , and two values of  $q$ : a) 1.11 (Mars) and b)  $0.28 \times 10^{-2}$  (Miranda). These two planets represent the extremes of  $q$  among single-plate solar system bodies.



These concentric regions of fault types can be generalized as tectonic provinces surrounding the load center (Fig. 3). The major difference between the two cases is the magnitude of the stresses. For the smaller  $q$  (lower shell rigidity), greater deflection of the lithosphere is required to balance the load stress at the base, resulting in greater induced radial and hoop stresses.

**BROAD LOADS.** For broader loads that cover a significant degree of curvature on the planet, the results are sharply different from those obtained by a flat-plate approximation. Again using Mars and Miranda as the two type examples, the tectonics produced by a broad load with  $\sigma = \pi/8$  are given in Figs. 4a and b. These tectonic fields are shown graphically in Fig. 5 which differs considerably from the narrow load examples. In particular, the narrow load ('Flat-Plate') response produces radial thrusts and concentric graben while the broad load ('Shell') response produces neither of these features but instead results in radial thrusting. Again, the exact radial distances at which the transition

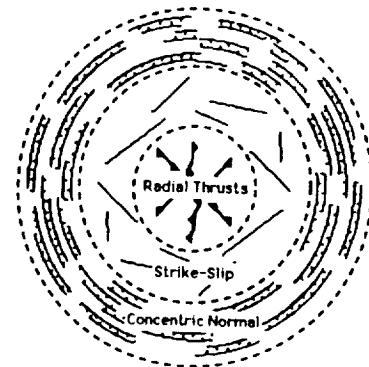
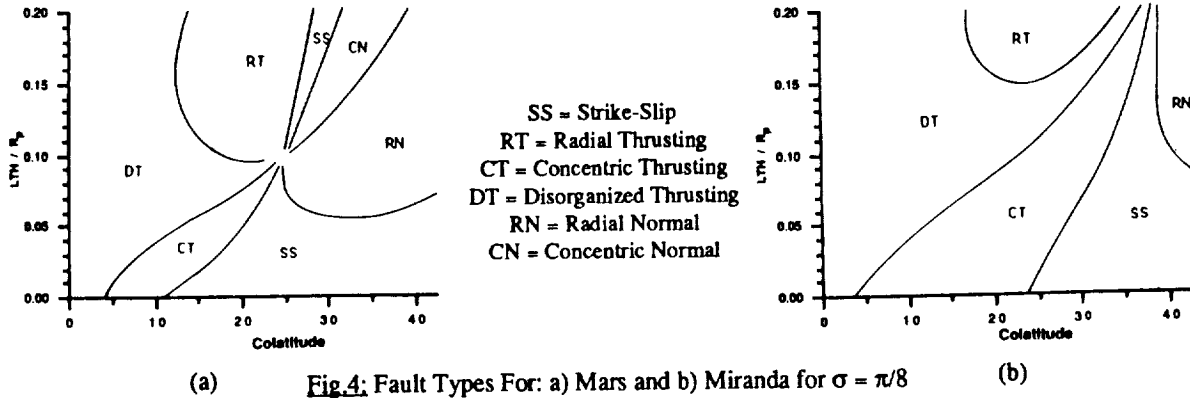


Fig. 3: Narrow Load Tectonic Pattern

**TRANSITION.** The transition between narrow and broad load responses can be seen in Fig. 4a. The singularity is a point of isotropic stress at the planetary surface. As the load width narrows, the isotropic singularity



and the changeover from wide to narrow load responses occurs in thinner lithospheres. The response type can be plotted as a function of width and lithospheric thickness (Fig. 6a and b).

**APPLICATIONS.** Generally,  $q$ ,  $\sigma$  and the tectonic response field are known for a given planet and load, while the lithospheric thickness at the time of loading is to be determined. A previous study (1), using a flat-plate approximation, demonstrated that lithospheric thicknesses can be determined from tectonic fields produced by lunar mascon loading. This study is in general agreement with those results. However, taking the finite width of the load into account results in a moderate lowering of the estimated lithospheric thickness. As Figures 4a and b show, two of the more intriguing features in the solar system straddle the transition between narrow load ('Flat-Plate') response and broad load ('Shell') response. If the Coronae of Miranda were initially surface loads, then the tectonics produced should be a very sensitive indicator of the lithospheric thickness at the time of their formation. The case of the Tharsis Rise on Mars is complicated by a long history of increasing load size in the Tharsis region and by having to determine the relative contributions to the stress field by mantle upwelling and the load. This study demonstrates that no model attempting to determine the history of this region solely on the basis of current Mars data can succeed, as Tharsis has passed through various response regimes during its construction.

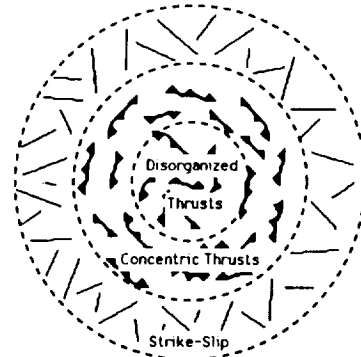


Fig. 5: Broad Load Tectonic Pattern

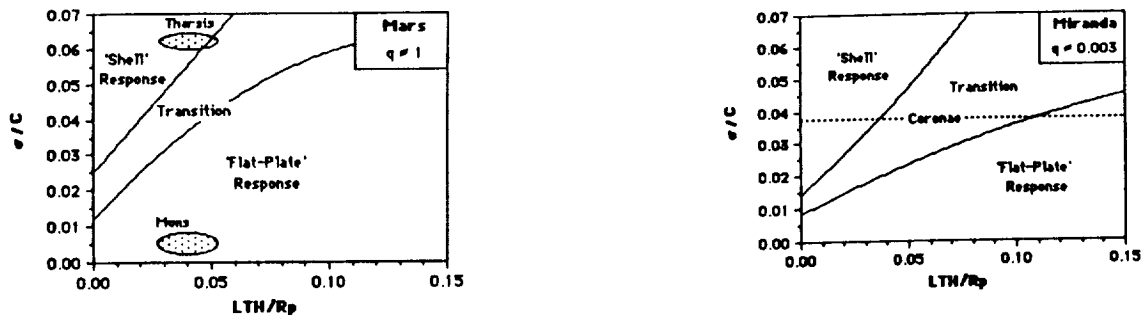


Fig. 6: Tectonic Response Fields For a) Mars and b) Miranda

**References:** (1) Melosh, H.J., The Tectonics of Mascon Loading, *Proc. Lunar Planet. Sci. Conf. 9th*, 3513-3525, (1978); (2) Comer, R.P., S.C. Solomon and J.W. Head, Mars: Thickness of the Lithosphere From the Tectonic Response to Volcanic Loads, *Rev. of Geophys.*, 23, No. 1, 61-92, (1985); (3) Banerdt, W.B., R.J. Phillips, N.H. Sleep, and R.S. Saunders, Thick Shell Tectonics on One-Plate Planets: Applications to Mars, *JGR*, 87, No. B12, 9723-9733, (1982); (4) Janes, D.M. and H.J. Melosh, Sinkers Tectonics: An Approach to the Surface of Miranda, *JGR*, 93, No. B4, 3127-3143, (1988)

Although the most recent tectonic activity on Mars is associated with the Tharsis volcanic province, much of the deformation preserved in the cratered uplands of Mars is independent of the predicted Tharsis stress fields (1,2). Many of these features can be associated with nearby impact basins (2,3), and tectonic patterns in the Hellas-Isidis region of Mars indicate that these multi-ring basins controlled early regional deformation by a variety of processes (4,5,6).

Early tectonic features around the Hellas and Isidis impact basins can be divided on the basis of distribution and age (see figure) into three stages of tectonic deformation that converge on the basin center over time (4,5). First, concentric canyons form outside the basin boundary scarp at or near the time of basin formation. Second, wide radial troughs form extending from the massif ring through the basin scarp. Finally, after a hiatus in observed activity, concentric graben develop around the central basin plains within the massif ring.

Three processes have been proposed to account for basin-centered tectonic deformation: elastic flexure due to basin loading (7,8); elastic flexure due to uplift (9); and extended impact-induced fracturing (10,11). Each of these processes can account for a different stage of deformation. Flexure under the load of the central basin plains can produce the graben in the massif ring. The required load thickness is comparable to the thickness of observed basin-filling units (6); and the inversion of observed load radius and fracture location for lithospheric thickness (6,12) agrees with the theoretical calculations of Schubert et al (13). Flexure due to isostatic uplift within the basin can form the radial troughs. The extent of observed deformation matches modeled stress fields for the predicted lithospheric thicknesses (6); and the age of the troughs is also consistent with a period of post-impact uplift and lithospheric stress concentration before surface fracture.

Elastic flexure under a basin-centered load also could account for the outer concentric canyons, but such a load requires lithospheric thicknesses significantly greater than those indicated by planetary thermal history calculations (6). Although flexure due to an additional load created by basin ejecta can reduce the required lithospheric thickness to acceptable values, the observed canyon widths (up to 100 km) exceed the size of graben attributed to flexure elsewhere on Mars and the Moon by an order of magnitude. Either some process (mass-wasting) widened the graben soon after basin formation or these features reflect an extended impact-induced fracture field. Rapid inward flow of the asthenosphere beneath the lithosphere during transient cavity collapse can extend lithospheric failure up to four crater radii beyond the basin scarp (11), thereby accommodating the observations. Further, fracturing the lithosphere as a whole produces failure on the scale of the lithospheric thickness, which is much greater than the scale of near-surface flexure.

This impact fracture mechanism is an extension of the process Melosh and McKinnon (14) proposed for the formation of scarps around multi-ring basins and requires that the transient cavity penetrate the lithosphere. Therefore, if the martian lithosphere is on the order of 100 km in thickness (13) and the transient cavity aspect ratio is 5:1, this mechanism should apply to basins with transient cavity (massif ring?) diameters over 500 km. Further, basins near this size should only develop a few concentric scarps (10). To develop the extended fractures of the Hellas region, a greater lateral flow of the asthenosphere is needed and a significantly larger transient cavity is required. Since distant concentric canyon systems have only been identified around Hellas (4,5) and perhaps Chryse (15,16), which is of similar size, the formation of distant concentric canyons appears to be limited to only the largest impacts in martian history.

In summary, the tectonic patterns around the Hellas and Isidis basins indicate a three stage deformation sequence reflecting three processes acting at different times. Distant concentric canyon systems form immediately after basin formation in response to either impact-induced failure extending beyond the basin or flexure under a basin ejecta load with immediate canyon enlargement. Radial trough formation soon follows after isostatic basin uplift and stress concentration have acted on the lithosphere. Finally, filling of the central basin cavity leads to lithospheric flexure inside the basin scarp, thereby producing concentric graben in the massif ring annulus outside the central basin plains.

**REFERENCES:** 1) Schultz, RA (1985) J. Geoph. Res. 90, 7849-7860. (2) Chicarro, AF, Schultz, PH and Masson, P (1985) Icarus 63, 153-174. (3) Schultz, PH (1984) Lunar Planet. Sci. Conf. XV, 728-729. (4) Wichman, RW and Schultz, PH (1987) Lunar Planet. Sci. Conf. XVIII, 1078-1079. (5) Wichman, RW and Schultz, PH (1988) Eos 69, 390. (6) Wichman, RW (1988) Master's Thesis, Brown University. (7) Solomon, SC and Head, JW (1979) J. Geoph. Res. 84, 1667-1682. (8) Solomon, SC and Head, JW (1980) Rev. Geoph. Space Phys. 18, 107-141. (9) Melosh, HJ (1976) Proc. Lunar Sci. Conf. 7, 2967-2982. (10) McKinnon, WB and Melosh, HJ (1980) Icarus 44, 454-471. (11) Melosh, HJ (1982) J. Geoph. Res. 87, 1880-1890. (12) Solomon, SC, Head, JW, and Comer, RP (1979) NASA TM 80339, 60-62. (13) Schubert, G, Cassen, P and Young, RE (1979) Icarus 38, 192-211. (14) Melosh, HJ and McKinnon, WB (1978) Geoph. Res. Ltr. 5, 985-988. (15) Schultz, PH, Schultz, RA and Rogers, J (1982) J. Geoph. Res. 87, 9803-9820. (16) Wichman, RW and Schultz, PH (1988) abstract presented at MEVTV Workshop "Early tectonic and volcanic evolution of Mars".

FIGURE 1. Hellas-centered Lambert projection showing tectonic features in the Hellas-Isidis region. H1, H2, H3 = Hellas concentric canyon systems; PR = Pityusa Rupes; AR = Amenthes Rupes; NF = Nili Fossae; AF = Amenthes Fossae; HMG = grabens in the Hellespontus Montes. Shaded regions show ridged plains units of the region: Syrtis Major Planum (SMP), Hesperia Planum (HP) and Malea Planum (MP); solid triangles denote volcanic calderae or highland paterae

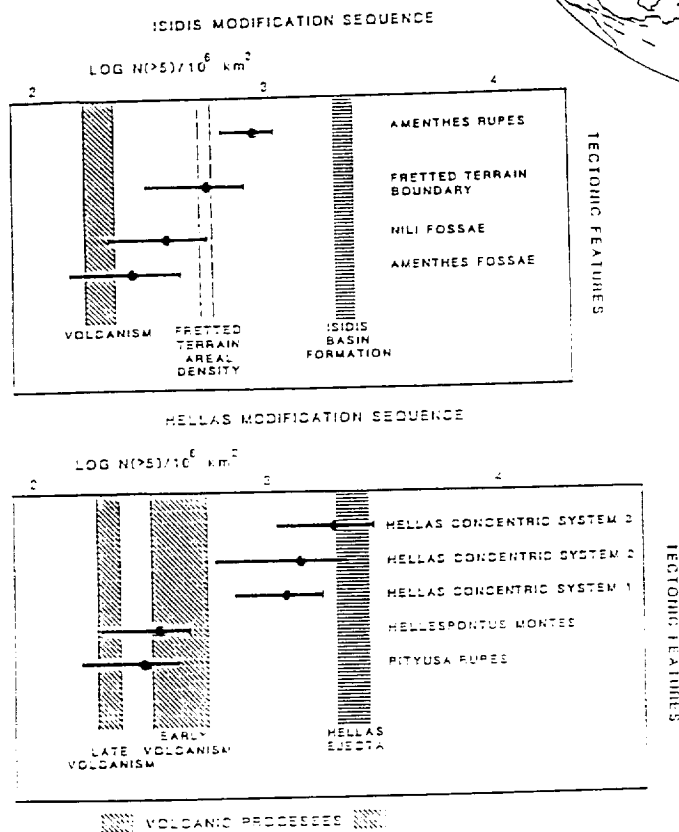
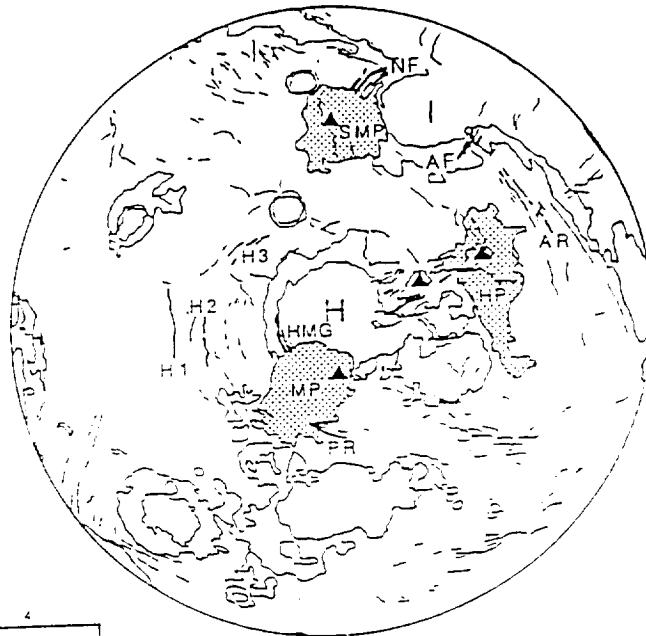


FIGURE 2. Age plots of dated tectonic systems around Hellas and Isidis. Early Hellas volcanism includes Malea Planum formation; late volcanism reflects Hesperia Planum formation; Isidis volcanism indicates age of Syrtis Major Planum.

ORIGINAL PAGE IS  
OF POOR QUALITY

## **Tectonic Response of One-Plate Planets to Loads: Variability due to Load Width, Lithospheric Thickness and Planetary Composition**

Daniel M. Janes (Lunar and Planetary Laboratory, University of Arizona, Tucson, AZ 85721) and H.J. Melosh (Lunar and Planetary Laboratory, University of Arizona, Tucson, AZ 85721)

We have developed an exact model for vertical loading of single plate, thick shelled planets. Loads are expressed as Gaussian distributions where  $4s$  is approximately the width of the load at its base. Factors controlling the tectonic response are:  $q = \rho m g r / m$ , a parameter that describes the physical dimensions of the planet;  $s$ , the size of the load; the ratio of lithospheric thickness to planetary radius; and angular distance from the load center.

The parameter  $q$  divides planetary bodies into two broad categories. For  $q < 1$ , stresses do not vary appreciably with depth in the lithosphere and tectonic response is only weakly dependent on  $q$  (small, icy satellites respond in nearly the same way as the Moon). For these bodies, the tectonics produced depend critically on the ratio between load breadth and planetary radius and on lithospheric thickness. Broad loads on thin lithospheres produce regions of randomly oriented thrusting, concentric thrusting and strike-slip faulting (in increasing distance from the load center); thicker lithospheres respond with random thrusts, radial thrusts, concentric thrusts, strike-slip and radial normal faults. Narrow loads produce regions of randomly oriented thrusts, radial thrusts, strike-slip, concentric normal faults, radial normal faults and strike-slip for all lithospheric thicknesses. The changeover in load response occurs at  $s \approx 11^\circ$ . For  $q > 1$ , (planetary size silicate bodies) load induced stresses vary markedly from the surface to the base of the lithosphere. Surface stresses produce radial thrusting in the region of the load while farther out from the load center regions of strike-slip faulting, concentric normal faulting and radial normal faulting occur.

In both categories, the radial distances from the load center at which the modes of faulting change are a sensitive function of lithospheric thickness, in agreement with previous models of mascon tectonics. The absence of the predicted tectonic responses by either the coronae of Venus (small-scale load,  $q > 1$ ) or those of Miranda (large-scale load,  $q < 1$ ) precludes their production solely by vertical loading.

## THE IMPORTANCE OF AN ELASTIC LITHOSPHERE FOR CRATER RETENTION ON ICY BODIES.

Valerie J. Hillgren and H. J. Melosh, Lunar and Planetary Laboratory, University of Arizona, Tucson, AZ 85721.

The images returned by the Voyager spacecraft of the Galilean satellites provoked speculation as to whether viscous relaxation was an important process in the modification of impact basins on these bodies [1,2]. This previous work involved extrapolations of the flow law for ice from terrestrial conditions to the lower temperatures of the outer solar system. However, recently Kirby *et. al.* [3] have actually measured the viscous properties of ice at temperatures appropriate to the Galilean satellites.

The flow law parameters determined by Kirby *et. al.* make ice, even at extremely low temperatures, very soft, and when Thomas and Schubert [4] used these values to numerically model the relaxation of a 300 km basin on Ganymede, they obtained an unrealistically short relaxation time on the order of  $10^7$  years. In their model Thomas and Schubert treated ice as a purely viscous substance and ignored its elastic properties.

We have also numerically modeled the relaxation of basins on Ganymede. However, we have used a fully maxwell viscoelastic finite element code, and thus, have accounted for the elastic properties of ice. We modeled basins ranging in diameter from 50 km to 300 km, and using the flow law parameters defined by Kirby *et. al.* for at temperatures less than 195 K.

We also used a variety of different temperature gradients in order to determine the importance of this factor compared to the presence of an elastic lithosphere in crater retention. The temperature profiles were conductive, with surface temperatures of 120, 130, and 140 K, and heat production rates of either 50% or 70% chondritic. In addition linear temperature gradients of 10 K per kilometer with surface temperatures of 120 and 130 K were also used. All temperature profiles were held constant once they attained a value of 163 K (.6 of the melting temperature of ice) under the assumption that convection would begin.

Finally, we used a Young's modulus of  $1 \times 10^{10}$  Pa which is appropriate to ice at very low temperatures. In order to investigate the role of the elastic lithosphere in viscous relaxation, we also performed calculations in which the Young's modulus was  $1 \times 10^9$  and  $1 \times 10^8$  Pa.

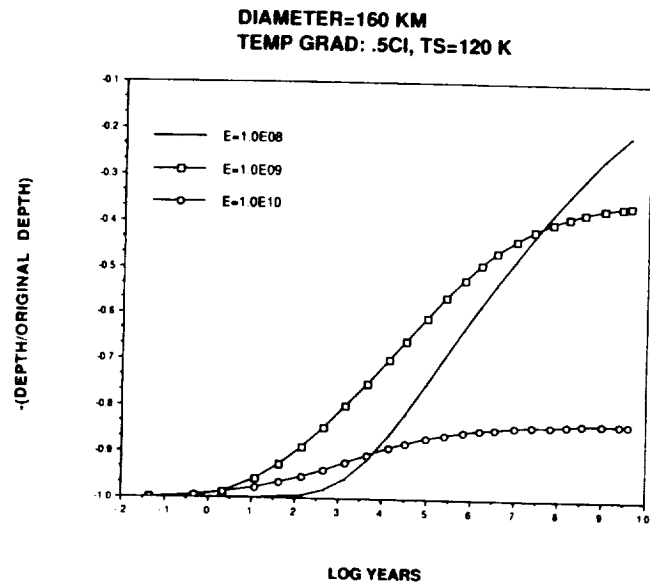
Figure 1 shows a plot of basin depth divided by original depth versus time for a 160 km diameter basin. In these calculations, the heat source for the temperature gradient was 50% chondritic, and the surface temperature was 120 K. Each curve represents the results of a calculation for a different Young's modulus. The crater with a Young's modulus of  $1 \times 10^{10}$  Pa has relaxed very little at the end of 4 Ga. While in sharp contrast, the crater with a Young's modulus of  $1 \times 10^8$  Pa has relaxed significantly after 4 Ga. This relationship holds true for basins of all sizes. Thus, the elastic properties of ice play a significant role in crater retention.

Figure 2 illustrates that the temperature gradient has little effect on the relaxation history. The plot shows basin depth divided by original basin depth versus time for a 300 km diameter basin with a Young's modulus of  $1 \times 10^{10}$  Pa subjected to a variety of temperature gradients. Very little difference exists between the curves. This holds true for all basin sizes, and demonstrates that the elastic properties of ice are more important than temperature gradient in crater retention.

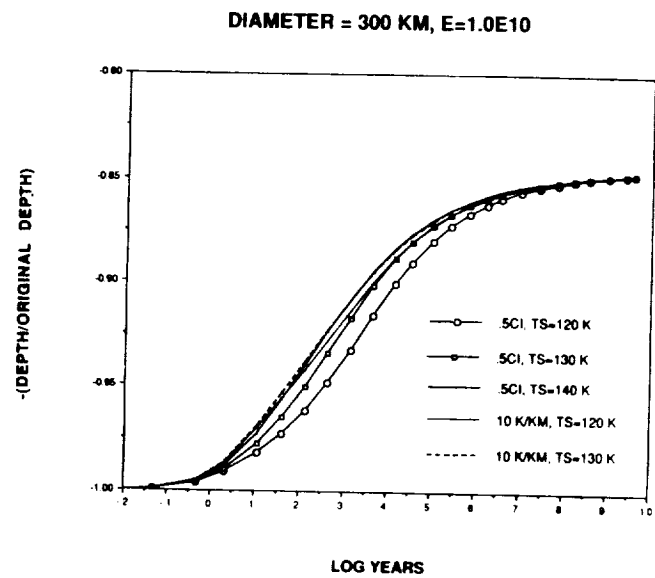
These results indicate that no appeal to special circumstances need be made to explain the observed crater populations on Ganymede and Callisto. Instead, an elastic lithosphere can easily account for the existence of large basins on these bodies.

**Refences:** [1] Passey, Q.R. and E.M. Shoemaker (1982) in Satellites of Jupiter, U of Az Press, Tucson, pp. 379-434. [2] Croft, S.K. (1983) *Abstracts of LPSC XIV*, pp. 136-137. [3] Kirby, S. H. et. al. (1987) *Journal De Physique*, 48, pp. 227-232. [4] Thomas, P. J. and G. Schubert (1988) *JGR*, 93, pp. 13,755-13,762.

**Figure 1:** See text for explanation



**Figure 2:** see text for explanation





## GEOLOGY AND DEPOSITS OF THE LUNAR NECTARIS BASIN

P.D. Spudis<sup>1</sup>, B. Ray Hawke<sup>2</sup>, and P.G. Lucey<sup>2</sup> 1. U. S. Geological Survey, Flagstaff AZ 86001. 2. Planetary Geosciences, HIG, Univ. Hawaii, Honolulu HI 96822.

The 860-km diameter Nectaris basin forms a conspicuous structural and stratigraphic marker on the lunar near side. This multiring basin was among the first recognized on the Moon [1] and its deposits were subsequently used to subdivide lunar geologic history [2]. We have undertaken studies of the geology of Nectaris basin deposits, morphology of its ring system, and the composition of its deposits as determined by remote-sensing techniques in order to better understand the regional geology of the Nectaris area, the provenance of possible Nectaris ejecta collected from Apollo landing sites (Apollo 16 in particular), and to provide additional constraints on the nature of the lunar basin-forming process. This study extends our ongoing investigation of lunar basins using the methodology we have previously applied to the Orientale [3] and Imbrium [4] basins.

**Nectaris basin deposits and ring system.** Although the Nectaris basin is heavily modified by age and the superposition of other basin deposits, we can still recognize several geologic units that by virtue of their position and stratigraphic relations, appear to represent Nectaris basin units. The most conspicuous unit is the Janssen Formation [2,5]; this unit is exposed primarily southeast of the basin rim and consists of coarsely lineated material whose lineations are radial to the center of the Nectaris basin (at 16° S, 34° E). The Janssen Fm. is analogous to the Imbrium basin Fra Mauro Fm. and the Orientale basin Hevelius Fm.; as such, it probably consists of both Nectaris basin primary ejecta and local material reworked by secondary cratering [6]. It has long been considered that Nectaris basin ejecta is absent elsewhere around the basin; however, several workers [e.g., 7, 8] have suggested that the hilly and furrowed Descartes material, which subtends a broad arc concentric to the Nectaris rim west of the basin, is Nectaris ejecta modified by superposed Imbrium basin secondary craters. If this interpretation is correct, the only sectors around the basin that do not have any exposed Nectaris ejecta are those which are covered by the later mare basalts (Maria Tranquillitatis and Fecunditatis). In addition to these basin exterior deposits, a knobby-textured unit crops out in the basin interior [7] that may be analogous to the knobby Montes Rook Fm. of the Orientale basin; moreover, numerous massifs delineate basin rings both within and outside the basin.

The Nectaris ring system is relatively well preserved. The main basin rim, well-defined in the west and south by the arcuate Altai scarp, is 860 km in diameter. A series of equant to rectilinear massifs, of which the Kant plateau is an example, define the main basin rim in the north and east sectors. Mare ridges and massif chains within the basin define three interior rings of 240, 400, and 620 km diameter. Additionally, several studies [e.g., 1, 9, 10] have recognized a large, subtle ring exterior to the Altai rim; this ring (1320 km diameter) passes through the Apollo 16 landing site. Thus, in terms of basin size, ejecta distribution and number of rings, the Nectaris basin may be considered analogous to the better-preserved Orientale basin.

**Composition of Nectaris basin deposits by remote-sensing.** The Apollo 16 orbital spacecraft overflew portions of the northern rim of the Nectaris basin measuring elemental concentrations of Al, Mg, Fe, Ti and Th; these geochemical data indicate that the regional composition of these deposits range from highly feldspathic (anorthosites) to anorthositic norite [11, 12]. Such a composition is in contrast to comparable deposits of the Imbrium and Serenitatis basins [4, 12], where low-K Fra Mauro basalt is a major component; however, Nectaris basin deposits are less anorthositic than comparable Orientale basin deposits [3]. Results of mixing model studies [12] indicate that LKFM basalt can constitute at most only about 25% to the deposit composition.

We have previously reported preliminary results from the analysis of forty near-infrared reflectance spectra in the Nectaris highlands region [13]. The Nectaris highlands display mineralogical compositions rich in Fe-bearing plagioclase and low-Ca pyroxene, comparable to the deposits observed around the Apollo 16 site (anorthositic norite to noritic anorthosite). We have found several localities around the Nectaris region that appear to consist of shocked plagioclase with virtually no mafic mineral phase present, e.g., within Kant crater on the Nectaris main rim, within the crater Cyrillus A inside the basin, and within the crater Bohnenberger F, located on top of a

highland massif that forms part of the inner (Montes Pyrenaeus) ring of the basin (620 km diameter). We interpret these spectra to indicate the presence of shocked anorthosites, comparable to those observed within the Orientale basin [3]. Spectra obtained for a portion of the hummocky basin unit north of the basin center suggest a relatively high concentration of low-Ca pyroxene in this unit [13]; together with an observed anomalously high Mg/Al value [14], we conclude that this area consists of a dominantly noritic composition, either pristine norites or a deposit rich in low-K Fra Mauro basalt. Remote-sensing studies of Nectaris basin deposits indicate that the regional compositions tend to be more anorthositic than those of the Imbrium or Serenitatis basins, but more mafic than typical Orientale basin materials.

**The Apollo 16 site and the Nectaris basin.** Several studies have emphasized the influence of the Nectaris basin on the geologic development of the Apollo 16 landing site (see summary in [15]). Of the two main geologic units at the site, the Descartes material is most likely to be Nectaris-related; as noted above, this unit probably makes up the continuous deposits on this side of the basin, modified by the superposition of subsequent Imbrium basin secondary craters. The Descartes material at the site appears to consist of a complex megabreccia of dominantly anorthositic to anorthositic norite composition. The overlying Cayley plains were probably emplaced by the Imbrium basin "debris surge" [6], and as such, would consist mostly of reworked local material (the Nectaris basin Descartes material).

Numerous impact melt rocks were collected at the Apollo 16 site; although the number of melt groups present is still debated [cf. 16, 17], the most abundant melt composition is that of "VHA basalt", an aluminous variety of LKFM. Because the regional composition around the Apollo 16 site is more aluminous and less KREEPy than these melt rocks, they are unlikely to be the products of local impact craters [e.g., 18]. They are either melt rocks from relatively large craters (> 100 km) that occur uprange to the Imbrium basin, transported to the site during the Imbrium debris surge [19], or they may represent fragments of the Nectaris basin melt sheet [8]. Our results are consistent with either of these two latter models.

**Discussion.** The Nectaris basin impact can be modelled by the proportional-growth cratering model [e.g., 20]. For a basin main rim diameter of 860 km, results indicate a transient cavity diameter of  $470 \pm 100$  km, a maximum depth of excavation of 40 to 55 km, and total excavated volumes between  $6.3$  and  $9.2 \times 10^6$  km<sup>3</sup>; greater than 90 percent of the excavated volume is derived from depths of less than 30-40 km. If the average crustal thickness is on the order of 70 km [21] and the crustal structure of [22] is approximately correct, then the bulk of Nectaris basin ejecta would be dominantly anorthositic in composition, as in fact is seen from the remote-sensing data. We suggest that the Nectaris basin formed by a proportional-growth mechanism, into a grossly layered lunar crust. The ejecta from this impact is dominantly of anorthositic composition; mafic components (i.e., noritic, LKFM) are present in the ejecta, probably in minor (10-20%) quantities. The bulk of the returned Apollo 16 samples are ultimately of Nectaris basin provenance; the relation of some Apollo 16 melt rocks to the Nectaris basin-forming event is possible, but has yet to be conclusively demonstrated.

**References.** [1] Hartmann W. and Kuiper G. (1962) *Commun. LPL* 1, 55. [2] Stuart-Alexander D. and Wilhelms D. (1975) *J. Res. USGS* 3, 53. [3] Spudis P. et al. (1984) *PLPSC* 15, JGR 89, C197. [4] Spudis P. et al. (1987) *PLPSC* 18, 155. [5] Stuart-Alexander D. (1971) *USGS Map I-694*. [6] Oberbeck V. (1975) *RGSP* 13, 337. [7] Wilhelms D. (1972) *NASA SP-315* [8] Spudis P. (1984) *PLPSC* 15, JGR 89, C95. [9] Wilhelms D. and McCauley J. (1971) *USGS Map I-703*. [10] Pike R. and Spudis P. (1987) *EMP* 39, 129. [11] Andre C. and El-Baz F. (1981) *PLPSC* 12B, 767. [12] Spudis P. and Hawke B.R. (1981) *PLPSC* 12B, 781. [13] Hawke B.R. et al. (1986) *NASA TM* 88383, 526. [14] Andre C. and Strain P. (1983) *PLPSC* 13, JGR 88, A544. [15] James O. and Horz F., eds. (1981) *LPI Tech Rpt.* 81-01. [16] Reimold W. and Borchardt R. (1984) *EPSL* 67, 9. [17] McKinley J. et al. (1984) *PLPSC* 14, JGR 89, B513. [18] Head J. (1974) *Moon* 11, 77. [19] Stoffler D. et al. (1985) *PLPSC* 15, JGR 90, C449. [20] Croft S. (1981) *PLPSC* 12A, 207. [21] *PLSC* 7, frontispiece, plate 3. [22] Spudis P. and Davis P. (1986) *PLPSC* 17, JGR 91, E84.

## SHALLOW MOONQUAKES — EXTRATERRESTRIAL ANALOG OF INTRAPLATE EARTHQUAKES

NAKAMURA, Y. and OBERST, J., Institute for Geophysics and Department of Geological Sciences, University of Texas at Austin, Austin, TX 78759-8345

Among numerous seismic events observed on the moon during the Apollo mission, most of which were not of tectonic origin, there were a small number of large moonquakes of distinct characteristics. Although fewer in number (28 identified in 6 years, 1971-1977) compared with, e.g., deep (>700 km) moonquakes of tidal origin (more than 3,000 identified), they included some of the largest seismic events observed on the moon, with an estimated body-wave magnitude of 5.8 or greater for the largest event in 6 years. These shallow (<100 km?) moonquakes are similar in many respects to earthquakes that occur in stable continental interiors. Since no structures associated with active plate motions are evident on the moon, these moonquakes cannot be related to plate tectonics exterior to the plate or along plate boundaries. Instead, large shallow moonquakes must be caused solely by the thermoelastic stress accumulated in the upper interior of the moon. Seismicity of single-plate planets such as the moon thus helps us to understand intraplate seismic activities on the earth.



CHAPTER 12

GEOLOGIC MAPPING, CARTOGRAPHY, AND GEODESY

PRECEDING PAGE BLANK NOT FILMED



New geologic maps of four of the uranian satellites have been prepared using the new USGS polar stereographic base maps. The major unit on Titania is the cratered terrain. It is subdivided into heavily cratered and less cratered subunits. The less cratered units are annular bands around the large craters Ursula and Gertrude, and are interpreted as their continuous ejecta blankets. A set of sinuous ridges similar to the ridges near the crater Anchises on Dione run E-W near Gertrude. The rift-like major canyons include both NW-SE and NE-SW trending components. All of the canyons are fresh in morphology and post-date nearly all other structures. A set of graben-like lineaments run NW-SE across much of the visible hemisphere in a pattern reminiscent of the lineament systems on Rhea. The global areal expansion calculated from the lengths and depths of the extensional features is about 0.7%. The major geologic unit on Oberon is also a heavily cratered unit. No subdivisions were detected, probably as a result of much lower resolution in the available images. A dark unit occurs in and around craters near Macbeth; the pattern is reminiscent of the volcanic deposits of Mare Australae on the Moon. No ridges comparable to Titania's were found. Oberon's canyon system includes both degraded and fresh components. The younger canyons (which post-date the large rayed craters) are narrower than the older, heavily cratered canyons. A NW-SE trending set of lineaments is also found. The areal expansion represented by Oberon's old canyons is about 0.5%, and about 0.4% for the young canyons. Both Titania and Oberon have been resurfaced(1), both have similar tectonic regimes and similar absolute expansions. Thus the new mapping indicates that these two satellites are geologically more similar than previously thought(2). The major geologic unit on Umbriel is a heavily cratered plain. Bright deposits occur on the floor of the crater Wunda and on the central peak of Vuver. Crater rays are much less prominent on Umbriel than on either Titania or Oberon. The orthographic projection shows that a set of light streaks near Wunda are sub-radial to that crater and may be its rays. Umbriel also has a set of extensional canyons, trending NW-SE. Definition is poor, but there seems to be both degraded(E of Wunda) and fresh(N of Alberich) canyons. The canyons near Alberich apparently extend through the limb profile of (3), accounting for one of the major limb features. A set of mesa-like features is mapped near Malingee. These features are shaped and truncated by both canyons and craters. They are very poorly defined, but seem to coincide with some of the "umbral polygons" of (4), and thus may be real. Nearly all of Umbriel's surface features are morphologically subdued. This impression becomes even stronger when the best images of Umbriel and Oberon (at nearly the same resolution) are compared: the features on Oberon are simply more crisp. It is speculated that this may be due to some type of physical blanketing by ejecta from a major impact in the unseen hemisphere, or some type of volcanic fallout. In any case, Umbriel is tectonically more active than previously thought, consistent with the crater statistics(1) and subtle albedo variations (4) suggesting extensive volcanic activity. The tectonic patterns on all three of these satellites are remarkably similar. The extent of endogenic resurfacing also appears to be global on all three. The new map of Miranda is also included, though aspects of its geology have been discussed elsewhere(5).

REFERENCES. 1.Strom, R.G.(1987) ICARUS 70,517. 2.Smith B. et. al. (1986)Science 233, 43. 3.Thomas P.C.(1988)ICARUS 73, 427. 4. Helfenstein P. & J. Veverka (1988)LPS XIX, p. 475. 5. Croft S.K. (1988)LPS XIX, p. 225 and references therein.

PRECEDING PAGE BLANK NOT FILMED

PAGE 566 INTENTIONALLY BLANK

**THE VOLCANIC AND TECTONIC EVOLUTION OF DARK TERRAIN ON GANYMEDE** Scott L. Murchie and James W. Head, *Department of Geological Sciences, Brown University, Providence, Rhode Island*; Jeffrey B. Plescia, *National Aeronautics and Space Administration, Washington, D.C.*

**Introduction.** The surface of Ganymede consists of two major terrains: heavily cratered dark terrain cut by tectonic troughs or "furrows," and stratigraphically younger, resurfaced "light terrain" possessing complexly crosscutting "grooves" [1,2]. Dark terrain has been widely interpreted to be the primordial upper layer of a differentiated ice mantle, darkened by intermixed meteoritic material, from which a dense, Callisto-like crater population has been removed by viscous relaxation [e.g. 3], although a few workers [e.g. 4] have proposed a volcanic origin of dark terrain. Furrows are commonly thought to be impact-generated fractures [e.g. 5], but a purely tectonic origin of furrows has also been proposed [4,6]. In this abstract we summarize three classes of observations which support a volcanic origin of dark terrain, and which are evidence for a combined impact-tectonic origin of furrows. To attempt to explain these observations, we propose a very different paradigm for the volcanic and tectonic evolution of dark terrain.

**1. Stratigraphy, albedo, and morphology.** Two major terrain types occur within dark terrain, dark smooth terrain and furrowed terrain [e.g. 4,5,6,7]. Within certain areas of furrowed terrain, such as Galileo Regio, discrete dark smooth deposits flanking individual furrows are distinct from surrounding terrain because of their slightly different albedo. The furrow-flank materials are in some cases observed to partially bury preexisting craters (Figure 1). Larger dark smooth deposits in northwestern Nicholson Regio and central Marius Regio are superposed on older furrowed terrain, and at their edges they embay older craters and only partially bury preexisting furrows. These deposits are themselves cut by younger furrows [7]. The variable stratigraphic relation of furrows with dark material and the association of dark smooth material with furrows suggest dark terrain experienced a complex sequence of volcanic dark-material resurfacing and furrow-forming tectonism [7]. Different regions of dark furrowed and dark smooth terrains also have very different albedos [8] and morphologies [4,9,10], suggesting that these regions may have had distinctive histories.

**2. Crater densities.** Determination of relative ages of widely separated surfaces using their crater densities requires some knowledge of whether crater-forming impactors were heliocentric or planetocentric: a planetocentric cratering flux would be nearly equal at all longitudes, whereas a heliocentric cratering flux would decrease systematically from the leading edge to the trailing edge. Thus crater densities should be directly related to the relative ages of widely separated surfaces if planetocentric impactor bombardment occurred; in contrast, if heliocentric impactor bombardment occurred, then crater densities must be normalized to a standard distance from the leading edge to be used as measures of relative age. Several investigations have tested for heliocentric or planetocentric bombardment by determining if there is or is not a leading edge/trailing edge density gradient for some class of craters [summarized in ref. 7], implicitly assuming spatially uniform crater retention times. These tests reveal that gradients do exist for young craters and for larger old craters, but are not always evident for small older craters. Murchie *et al.* [7,11] measured crater densities and size-frequency distributions in ten regions of dark terrain, and used these measurements to perform tests for heliocentric or planetocentric bombardment that do not assume spatially uniform crater retention times. The results of these tests support the hypothesis that dark terrain was cratered predominantly by a single, heliocentric impactor population, and suggest that the leading edge/trailing edge density gradient for small older craters has been obscured by non-synchronous resurfacing within dark and light terrains.



If heliocentric crater-forming bombardment of Ganymede's presently observed surface is assumed, then crater densities of different regions of dark smooth and furrowed terrain translate into significantly different relative crater ages [7]. Neither terrain has a globally younger crater age, although smooth deposits have a consistently younger crater age than do adjacent furrowed terrains. Three of four regions of dark smooth terrain and three of six regions of furrowed terrain have differing relative crater ages and depleted densities of small craters. In these same regions, some large craters have flat floors and lack ejecta deposits or are embayed by dark material. The remaining surfaces possess linear size-frequency distributions, but still have differing relative crater ages. These observations suggest a prolonged period of dark-material resurfacing, with some deposits being thick enough to bury all preexisting craters, and other deposits being thick enough to bury small craters but too thin to bury rim crests of large craters. Occurrence of furrows on surfaces of widely different crater age implies that furrow-forming tectonism occurred throughout the period of resurfacing [7].

**3. Furrow organization.** Furrows are organized into three hemispheric-scale systems. Two of these systems, one in the anti-Jovian hemisphere ("system I") (Figure 2) and one in the sub-Jovian hemisphere ("system III"), contain approximately concentric and less abundant subradial troughs [12]. System I and its associated dark materials appear to be superposed on the western portion of system III [2,7,12]. Within each system the concentric and subradial troughs have variable crosscutting relations and regionally different crater ages [7,12]. The center of symmetry of system III is obscured by younger light material, but the center of system I is located in dark terrain and contains a giant "palimpsest" (Figure 2 - a circular albedo feature interpreted to be of impact origin) [12 and references therein]. Thus the arrangements of systems I and III, but not their furrows' variable ages and associations with dark material, are consistent with an impact origin.

"System II" consists of troughs arranged radially to an area southeast of Galileo Regio (Figure 2), and these troughs crosscut all other furrows and all dark materials [12,13]. The central portion of the system contains a 3000-km radius circular patch of dark smooth material, and the dark materials with the globally youngest crater age [13]. This configuration is not suggestive of an impact origin, but rather has been interpreted to result from volcanism and fracturing on a circular thermal uplift [13].

**Paradigm of dark terrain evolution.** The observations and interpretations summarized herein are inconsistent with the "conventional" view of dark terrain geology. Rather, they are consistent with a very different paradigm proposed by Murchie *et al.* [13] (which is only slightly different from a similar paradigm developed by Croft [4 and references therein]): A Callisto-like, possibly primordial surface was fractured by two very large impacts, forming multiringed structures. These structures and preexisting craters were buried by dark ice-volcanic material, and the structures were reactivated by extensional tectonism to form systems I and III. Burial and reactivation each occurred one or more times in various locales. Resurfacing became concentrated with time in a thermally anomalous region, which was uplifted and fractured to form system II as dark-material volcanism gave way to emplacement of younger light terrain.

**References.** [1] Smith, B. and the Voyager Imaging Team, *Science* 204, 951-972, 1979. [2] Smith, B. and the Voyager Imaging Team, *Science* 206, 927-950, 1979. [3] McKinnon, W. and E.M. Parmentier, in *Satellites*, ed. by J. Burns and M. Matthews, pp. 718-763, Univ. of Arizona, Tucson, 1986. [4] Croft, S. and B. Goudreau, *Lunar Planet. Sci. XVIII*, 209-210, 1987. [5] Schenk, P. and W. McKinnon, *Icarus* 72, 209-234, 1987. [6] Casacchia, R. and R. Strom, *Proc. Lunar Planet. Sci. Conf. 14th*, in *J. Geophys. Res.* 89, B419-B428, 1984. [7] Murchie, S., J. Head, and J. Plescia, submitted to *Icarus*. [8] Helfenstein, P., Ph. D. thesis, Brown University, 1986. [9] Zuber, M. and E.M. Parmentier, *Icarus* 60, 200-210, 1984. [10] Murchie, S., Ph. D. thesis, Brown University, 1988. [11] Murchie, S., J. Head, and J.

Plescia, this volume. [12] Murchie, S. and J. Head, *J. Geophys. Res.* 93, 8795-8824, 1988.  
 [13] Murchie, S., J. Head, and J. Plescia, submitted to *J. Geophys. Res.*

Fig. 1. Southern Galileo Regio. Dark smooth deposits ("A") and partially buried craters ("B") occur in the topographic lows between higher-albedo furrow-flank materials. (Voyager 2 image 20636.59, centered near 23°N, 144°W.)

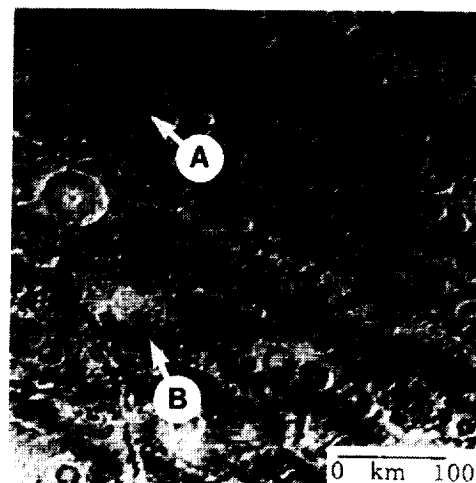
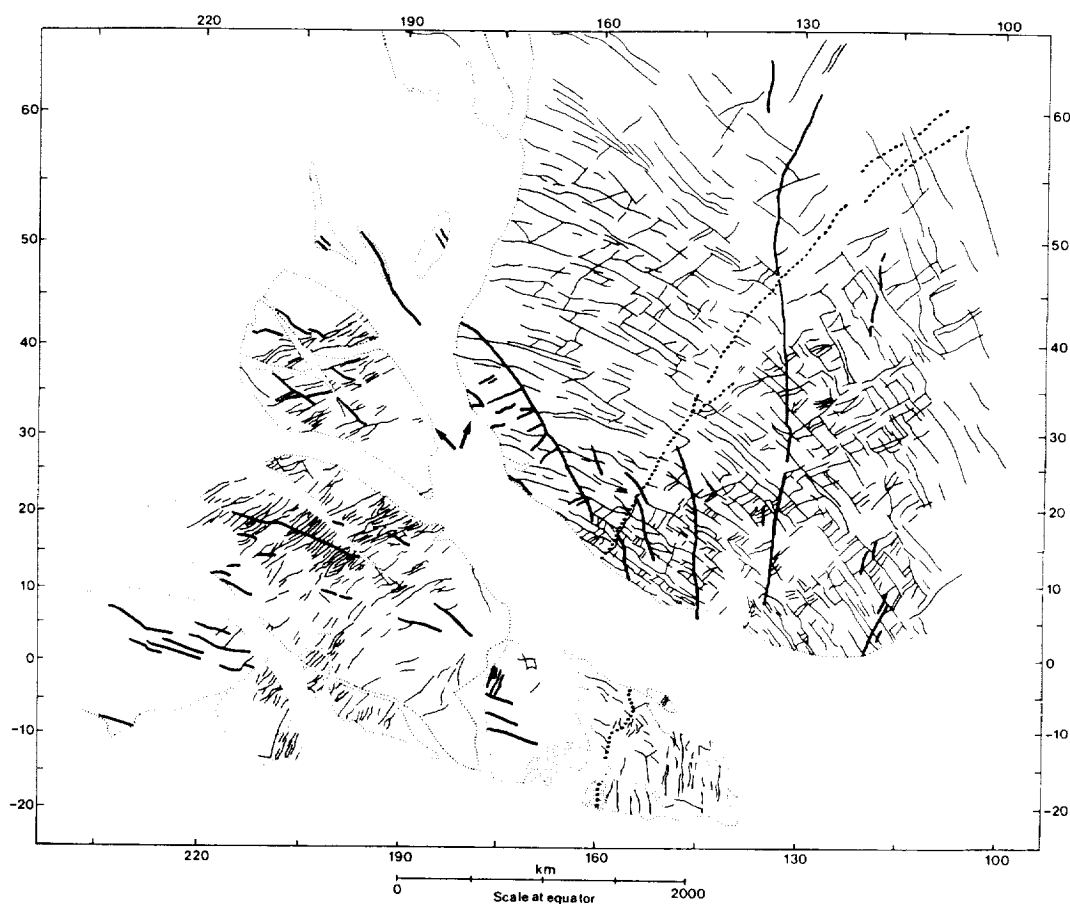


Fig. 2. Mercator map of dark terrain structures in the anti-Jovian hemisphere, including system I furrows (fine solid lines), system II furrows (heavy solid lines), and the giant palimpsest (stippling).



ORIGINAL SOURCE  
 OF FOUR QUALITY

## POLAR DEPOSITS OF MARS: NORTH-SOUTH COMPARISONS

P. C. Thomas, Cornell University, Ithaca NY 14853

Mapping of both polar deposits of Mars and measurement of colors and albedos of their surface materials allows a better comparison of some of the differences and similarities of the two polar sedimentary accumulations.

Layered deposits at both poles show a component that appears indistinguishable from typical bright Martian surficial dust or material raised in dust storms (Thomas and Weitz, 1989; Herkenhoff and Murray, 1989). The north polar deposits show admixtures of dark material at scales below resolution limits (50 m). The darkest polar materials are sand dunes, which have colors and albedos similar to dunes at other latitudes of Mars (Thomas and Weitz, 1989). The south polar deposits also appear to have a dark dune component (Thomas and Weitz, 1989; Herkenhoff and Murray, 1989).

The residual frost cap presents a problem in that some work suggests it should be much darker because of the included dust (Kieffer, 1988). The edges of the summer frost appear to mix with layered deposit materials at scales well below the resolution limit of about 50 m. Combinations of the clean and dirty frost at scales less than a few m may satisfy albedo and thermal balance requirements.

The morphologic mapping of layers, troughs, and dunes at both poles emphasizes the basic similarity of the polar geology even if the superficial appearances have some drastic differences. The deposits show considerable erosion from their maximum extent. Dune sand is a significant (few %?) component released by this erosion. Although summer winds move it away from the layered deposits, seasonally reversing winds (Thomas, 1982) confine most of the sand to latitudes above 65° (Fig 1a,b). The northern plains allow a widespread set of ergs (Lancaster and Greeley, 1989); the southern topography confines dunes to topographic traps such as craters.

Structural elements control locations of some troughs, but their nature and role in affecting trough migration (if any) are not known. Some southern deposit troughs align with linear troughs in the pitted terrain and suggest some factors in common in their origins.

Work on the frosting/defrosting of dunes and different layered deposits will give more insight into the similarities and differences between poles, which can then help in interpreting their overall sedimentary regime and long term history.

This work is supported by NASA Grant NAGW 111.

### References:

- Herkenhoff, K. E., and B. C. Murray, 1989. Color and albedo of the south polar layered deposits on Mars. *J. Geophys. Res.*, in press.
- Kieffer, H. H., 1988. How dirty is Mars's north polar cap and why isn't it black? Presented at MECA workshop: "Polar Processes on Mars," May, 1988.
- Lancaster, N. and R. Greeley, 1989. Sediment volume in the north polar sand seas of Mars. Submitted to *J. Geophys. Res.*
- Thomas, P. and C. Weitz, 1989. Dune sand materials and polar layered deposits on Mars. *Icarus*, in press.
- Thomas, P., 1982. Present wind activity on Mars: relation to latitudinally zoned sediment deposits. *J. Geophys. Res.* 87, 9999-10008.

### Figure 1:

Polar layered deposits, dunes, and troughs in polar materials. Maps cover the same latitude range and allow comparison of some of the major polar features. The widespread dunes in the north have some identifiable sources in the deposits; the dunes confined in craters in the south also appear to come from erosion of the layered deposits but have different source area morphologies. The southern deposits lacking significant troughs are the pitted terrain; they do not appear to be as good a source of dunes as are the layered deposits.

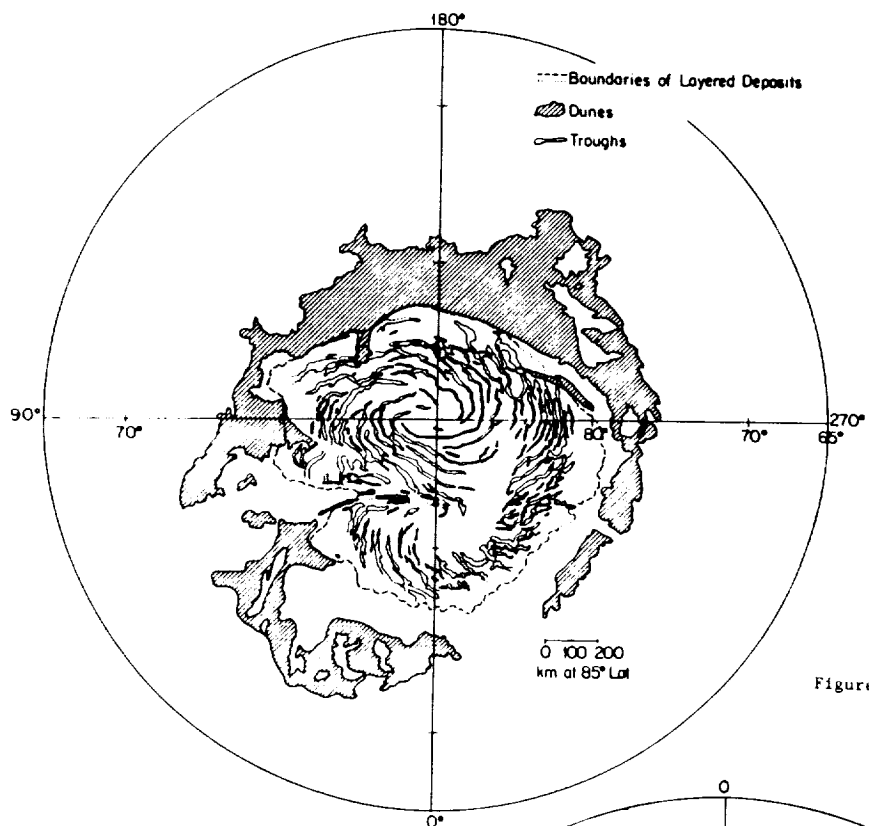


Figure 1a

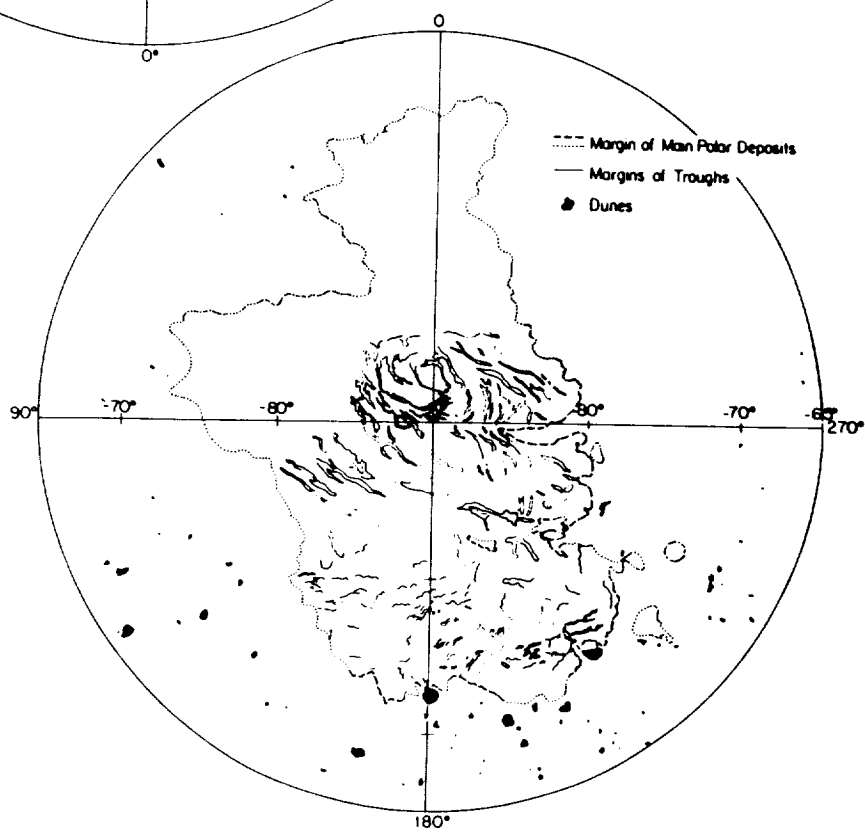


Figure 1b

## NORTH KASEI VALLES--GEOLOGY AND HYDROLOGY

M.G. Chapman and D.H. Scott, U.S. Geological Survey, Flagstaff, Arizona  
86001

Mapping of the north Kasei Valles area at 1:500,000 scale [1] provides new information regarding the geologic and hydrologic history of this large Martian outflow channel. Changes in water level or multiple erosional events occurred throughout the area, indicating both catastrophic flooding and glacial erosion. Relative ages of geologic units and various geomorphic features were established by stratigraphic relations and supported by crater counts; relief measurements were obtained in places by photoclinometric methods [2].

The oldest recognized geologic unit in the map area is Hesperian ridged plains material (Hr), interpreted to consist of basaltic lava flows. The material forms high plateaus (about 1.4 km above the Kasei Valles floor) and mesas that are erosional remnants of the broad Lunae Planum surface. Streamlined features, including islands and longitudinal grooves, occur locally on the ridged plains within and east of the map area. Degraded plateau material (Hpd), consisting of chaotic terrain, is transitional with the ridged plains unit on the plateau; the degraded material borders the Kasei channel and appears to have been formed where the surface material of the ridged plains was stripped, exposing less consolidated, fractured layers that may be richer in ice. Channeled plains material (Hchp) forms the Kasei Valles floor, and it has pronounced erosional features such as longitudinal grooves as deep as 170 m and streamlined islands exceeding 700 m in height. Channeled plains are overlain in the western part of the map area by basalt flows of member 4 of the Amazonian Tharsis Montes Formation (At<sub>4</sub>) [3]. Small sinuous channels that cut the basalt flows may be due to late-stage fluvial activity. Apron-forming material (AHa) consists of fans and slumps along the boundary between ridged plains and the narrow north channel of Kasei Valles. Theater-headed channels (AHcht), formed by sapping processes, cut channeled plains in the southern part of the map area. Basalt flows of member 5 of the Tharsis Montes Formation (At<sub>5</sub>) [3] overlie the narrow north channel of Kasei Valles in the southern part of the map area.

Kasei Valles lie on a plain that was topographically lower than Lunae Planum before erosion of the valley by water or ice. Some small buttes, remnants of plateau material within Kasei Valles, are polygonal in shape and appear to have been unaffected by erosion to the degree that they are not streamlined. Depressions on the northern extension of Lunae Planum (Sakra Fossae) predate channeling as indicated by erosional features on the plateau; these features can be traced back to the Sakra Fossae depression at lat 24° N., long 67° that connects to the south channel of Kasei Valles. Fretting along the open faces of grabens in Sakra Fossae may have initiated the mesa and butte morphology of the area. The east-west orientation of the narrow north and south channels of Kasei Valles is parallel to some major fracture patterns around Tharsis, an observation which suggests that the channels were not primarily formed by fluvial erosion but were structurally controlled and enlarged by scarp recession; during later flooding they became the narrow north and south channels [4].

Vastly different water levels during flooding are implied by streamlined islands on both the Kasei floor and the surrounding plateau. Streamlined features on Lunae Planum lie at an elevation 1 km above and are less pronounced than those on the Kasei Valles floor. The Lunae Planum features

probably were formed during an earlier erosional phase. Also, the relief between the plateau and channel floor may have been increased by scouring of the Kasei Valles floor during successive stages of erosion. Observations of features on the channel floor that support changes in water level, episodic flooding, or changes in stream alignment are (1) rectilinear crevices whose relations to longitudinal grooves indicate that they formed both before and after grooving; (2) longitudinal grooves heading in an easterly direction are transected perpendicularly by the south channel of Kasei Valles [5]; and (3) a topographic ridge bordering Kasei was first bisected and then streamlined. This ridge is unlike mare-type ridges, and it may be a depositional feature such as a levee because of its northeast trend, parallel to Kasei Valles.

Some streamlined islands have impact-crater rims on their upstream side. The floors of the craters are bowl-shaped and apparently unfilled, indicating that water had not overtopped the crater rims and deposited sediments inside. Those craters that have incised rims and whose floors are not filled appear to have been overtopped, but they may have been infilled by ice that has since sublimated.

Melted ground ice derived from the fractured and probably porous Lunae Planum lava flows could be responsible for Kasei flooding; water was apparently emitted by the faulting and collapse that produced Echus Chasma. The ridged plains materials of Lunae Planum appear to have been the major source for numerous fluvial features in the map area. Evidence suggesting that the ridged plains material was the primary source of water include the following: (1) theater-headed Sacra Fossae developed within ridged plains material were modified by sapping, (2) degraded plateau material may have been formed by removal of ground ice from ridged plains material, and (3) gullies cutting apron-forming material east of the map area appear to originate from within the ridged plains material. Large volumes of water may have come from the melting of interstitial ice in the subsurface by volcanic heating [6]; the release of large-scale floods could have been triggered by the development of Tharsis volcanism [7].

Evidence suggests that Kasei Valles was formed by catastrophic flooding, as indicated by large streamlined mounds, conspicuous flow lines, and possible cataract features [8,9]. Glacial erosion appears to have partly contributed to the formation of Kasei Valles [5]. The frigid temperatures of Mars (mean annual temperature of  $-40^{\circ}\text{C}$  at the equator [10]) and the ambiguity of processes forming geomorphic features suggests that the most likely explanation for Kasei Valles is a combination of catastrophic flooding and glacial action. The water levels either varied markedly during catastrophic flooding or flooding was episodic in nature. Flooding was succeeded by late-stage Tharsis volcanism that produced basaltic flows covering the channel floor.

#### References

- [1] Chapman, M.G., Masursky, Harold, and Scott, D.H., (MTM 25072, In Prep.).
- [2] Davis, P.A., and Soderblom, L.A., 1984, JGR, v. 89, p. 9449. [3] Scott, D.H., and Tanaka, K.L., 1986, USGS MI Map, I-1802A. [4] Carr, M.H., 1974, Icarus, v. 22, p. 1. [5] Lucchitta, B.K., 1982, JGR, v. 87, p. 9951. [6] Masursky, Harold, Boyce, J.M., Dial, A.L., Jr., Schaber, G.G., and Strobell, M.E., 1977, JGR, v. 82, p. 4016. [7] Greeley, Ronald, and Spudis, P.D., 1981, RGSP, v. 19, p. 13. [8] Baker, V.R., and Milton, D.J., 1974, Icarus, v. 23, p. 27. [9] Baker, V.R., and Kochel, R.C., 1978, Proc. 9th Lunar Sci. Conf., p. 3193. [10] Fanale, F.P., and Cannon, W.A., 1971, Nature, v. 230, p. 502.

## STRATIGRAPHY OF THE KASEI VALLES REGION, MARS; Mark S.

Robinson, *University of Alaska, Fairbanks, Alaska, 99775*, and Kenneth L. Tanaka, *U.S. Geological Survey, Flagstaff, Arizona, 86001*

### Introduction

We identify and describe thicknesses and geomorphology of the two principal stratigraphic units exposed in Kasei Valles to aid in interpreting (1) the nature of crustal materials and (2) the history of the channeling events in the area. Previous studies of Kasei Valles have related the channel landforms to glacial flow [Lucchitta, 1982], catastrophic flooding [Baker, 1982], and large-scale eolian erosion [Cutts, 1978].

The two units (an upper and a lower unit) form thick sheets, each having distinct geomorphologic features. Thicknesses of the units were determined through preliminary stereogrammetric profiles taken across many sections of western Kasei Valles and shadow measurements taken of scarp heights from calibrated Viking images having sun angles less than 25°; DN values were examined to confirm that true shadows were observed.

### Description and Interpretation of Upper and Lower Units

The upper unit is capped by ridged plains material. Along the margins of the unit (where it was partly removed by channeling), either steep-walled scarps (*A* in Fig. 1) or chaotic terrain (*B*) have formed. At the bases of the scarps are extensive talus slopes and debris aprons, and narrow moats (*C* in Fig. 1) border the chaotic terrain at the northwest edge of the Kasei Valles area. Carved into the upper unit are low-relief, streamlined forms (*D*, *E*) in high-standing, scoured interchannel areas. The upper unit is also incised by *Sacra Fossae* (*F*), large fretted valleys that mostly trend northwest and northeast. Shadow measurements and stereogrammetry show the upper unit to have an average thickness of 1000 m  $\pm$  200 m west of long 59° and to thin or dip down to the east.

The ridged plains material is apparently underlain by more friable material. Where exposed by channeling, the upper unit has been eroded by the sapping of ground water or ground ice to form the fretted valleys, debris aprons, and chaotic terrain (the streamlined forms at *D* and *E* (Fig. 1) did not reach this lower layer of the upper unit). At the east edge of Lunae Planum, the ridged plains material embays cratered plateau material. We therefore interpret that the more friable lower layer consists largely of impact breccias. Our thickness measurements correspond to De Hon's [1982] estimates of the thickness of ridged plains material and Battistini's [1984] estimate of the depth to a mechanical discontinuity.

The lower unit, where exhumed, has a smooth, flat surface. The unit is eroded mainly by channeling; no mass-wasting features formed from it. In lower channel reaches, low scarps formed in the unit, indicating that it consists of a series of thin, resistant layers. Etched into the unit's surface is an extensive series of subparallel striations (*G* and *H* in Fig. 1) that, on a regional scale, follow the course of the Kasei Valles channel. Teardrop-shaped forms (*I* and *J* in Fig. 1) occur in the unit throughout the channel system; some appear to be depositional while others may be erosional. Locally, the unit is extensively fractured by sets of cracks that trend northeast and northwest; the cracks have been widened by processes of uncertain nature. In places, small, widely dispersed channel networks (*H* and *I* in Fig. 1) that cut the lower unit do not follow the regional stream course but follow local gradients. Where the channel cuts through the top of the lower unit, its elevation drops abruptly (*K*, *L*). Wrinkle ridges on the lower unit are rare and somewhat degraded (e.g., at lat 26°, long 62° and lat 29.5°, long 58°).

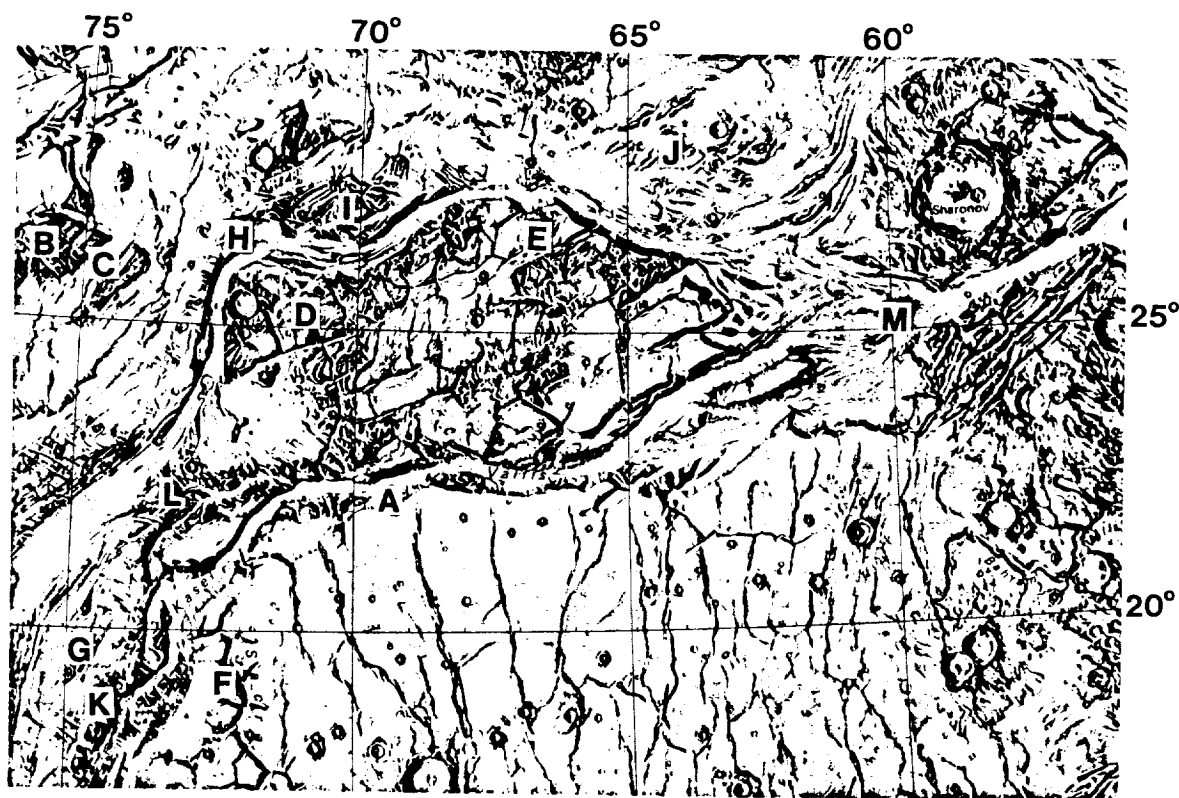


Figure 1. Shaded relief map of Kasei Valles; letters indicate locations referred to in text.

The lower unit occurs at depths ranging from about 1 km to at least 3.5 km. It therefore consists of material that is generally much lower in stratigraphic position than most exposed materials on Mars, including cratered plateau material. Its competence, layering, and low stratigraphic position indicate that it consists of a sequence of lava flows that correspond to basement material, which locally forms basin rims and massifs on Mars [Scott and King, 1984] of Early Noachian age [Tanaka, 1986].

#### Channeling

Streamlined channel forms in Kasei Valles occur predominantly within the lower unit and outside the deeply incised main channels. The streamlined forms of the lower unit commonly exhibit first-order length-to-width ratios (the form of a group of bars) of 3 to 4 and second-order length-to-width ratios (the form of an individual bar) of 2 to 3. The first-order ratios indicate high discharge rates, and the second-order values indicate waning discharge rates [Baker, 1978]. Within the upper unit no groups of bars are present, but the streamlined forms of individual bars on the upper unit (e.g., D in Fig. 1) have length-to-width ratios exceeding 3. The apparent sequence of events is as follows: (1) streamlined forms are carved into the ridged plains material that caps the upper unit; (2) the lower, friable material of the upper unit is removed by channeling, and streamlined forms and striations are cut into the surface of the lower unit; (3) the channel scarps continue to erode by mass wasting; and (4) the main channels are cut into the lower unit, which locally is fractured and channeled.



Preliminary stereogrammetric measurements show a rise of about 500 m in the floor of the main north channel where it turns to the northeast (at H in Fig. 1). Striations etched into the lower unit veer out from and leave the main channel in the area where the channel floor begins to rise. The major flow of the eroding substance apparently did not follow the course of the main channel, but rather it turned less sharply to the east and dispersed on the exhumed surface of the lower unit.

Heights of scarps in the lower unit in the south channel of Kasei Valles show a gradual decrease from west to east, and the lower unit is not incised between long 61° and 63°. Goldstone radar profiles indicate that the ridged plains material is nearly flat in northern Lunae Planum (lat 20°). These observations indicate that the contact between the upper and lower units rises eastward. Farther east, the channel floor steepens and again cuts through the lower unit. This steepening of the channel floor is reflected in the steeper channel walls (M in Fig. 1), similar to those seen in the area of headward erosion where the channel cuts through the lower unit 850 km upstream (K).

#### Future Work

We are continuing to analyze the stereogrammetry data to more accurately determine scarp heights, slope angles, and stratigraphic thicknesses in Kasei Valles. The 500-m rise in the north Kasei channel is currently under investigation. Detailed study of the channel walls, streamlined forms, and elevation relations will help to determine the nature of the exposed crustal materials, the history of Kasei Valles, and processes involved in the channeling that has shaped them.

#### References

- Baker, V. R. 1978. *Proc. Lunar and Plan. Science Conf.* 9<sup>th</sup>, pp. 3193-3203.
- Baker, V. R. 1982. *The Channels of Mars*: Austin, Texas, University of Texas Press, 132-139.
- Battistini, R. 1984. *Earth, Moon, and Planets.* 31:49-91.
- Cutts, J. A. 1978. *Abstracts Lunar Science Conference*, 9<sup>th</sup>, pp. 206-208.
- De Hon, R. A. 1982. *Journal of Geophysical Research.* 87:9821-9828.
- Lucchitta, B. K. 1982. *Journal of Geophysical Research.* 87:9951-9973.
- Scott, D. H., and King, J. S. 1984. *Abstracts Lunar and Planetary Science Conference*, 15<sup>th</sup>, pp. 736-737.
- Tanaka, K. L. 1986. *Journal of Geophysical Research.* 91:E139-E158.

GEOLOGIC MAPPING OF SOUTHERN MANGALA VALLES, MARS.  
James R. Zimbelman, Center for Earth and Planetary Studies,  
National Air and Space Museum, Smithsonian Institution,  
Washington, D.C. 20560.

Geologic mapping in the Memnonia region of Mars along the southern (headward) portion of Mangala Valles has been carried out as part of the Mars Geologic Mapping program. Three geologic maps at a scale of 1:500,000 (MTM sheets -10147, -15147, -20147) will result from this effort, two of which are under review and one that will be completed soon. Responsibility for the three maps is shared with other researchers at NASM and at Arizona State University.

Mangala Valles heads in terrain of complex and diverse geologic and tectonic history (Fig. 1). The oldest materials (Nplh and Nm) form ridges that run north-south through the region, separating some subsequent units. The orientation of the ridges is controlled by tremendous scarps, most likely faults, some with over 2 km of vertical relief (1). The faulting may be related to a basin-forming impact event (2) whose center is in Daedalia Planum, mostly buried by Tharsis volcanics (3). Superposed on the eastern margin of the ridges are old cratered plains (Npl). The Noachian materials are all embayed or truncated by the Mangala Valles materials which are Hesperian or younger in age. The most widespread material associated with the Valles system (Hchp) has a few streamlined features on its upper surface but it also has a pronounced lobate margin in places so that both fluvial and volcanic origins may be involved. This material is deeply scoured by the erosion associated with the formation of the Mangala Valles channels (Hch<sub>1,2</sub>). Topography derived from Earth-based radar measurements (4) show that east of the present main channel (Hch<sub>2</sub>) the oldest channel materials are 200 to 400 m higher than the channel, while the cratered plains west of the channel are tilted to the east (5; Fig. 2). The geometry of the deposits are interpreted to indicate that the main stream channel moved progressively westward during the course of outflow events at Mangala Valles. Radar-derived topography along the present main channel show that Mangala Valles follows an average gradient of .001 (Fig. 3), consistent with active rivers at a comparable distance from their source (6). This raises that possibility that some of the fluvial activity at Mangala Valles may have been sufficiently longlived to begin development of a graded profile. The youngest material in the map area are volcanic plains associated with Tharsis volcanism (Aht), kept from making contact with the Mangala materials by the topography of the Noachian materials.

This work was supported by NASA grant NAGW-1390.

REFERENCES: 1) J.R. Zimbelman, Trans. AGU 69(16), 390, 1988. 2) J.B. Plescia et al., LPS XI, 891-893, 1980. 3) R.A. Craddock et al., LPS XIX, 213-214, 1988 (submitted to JGR). 4) G.S. Downs et al., Icarus 18, 8-21, 1975. 5) J.R. Zimbelman, GSA Ab. Prog. 20(7), A147-A148, 1988. 6) Leopold et al., Fluvial Processes in Geomorphology, Freeman & Co., p. 190, 1964.

Figure 1 (right). Simplified geologic map of MTM sheets -10147, -15147, and -20147. See text for discussion of units.

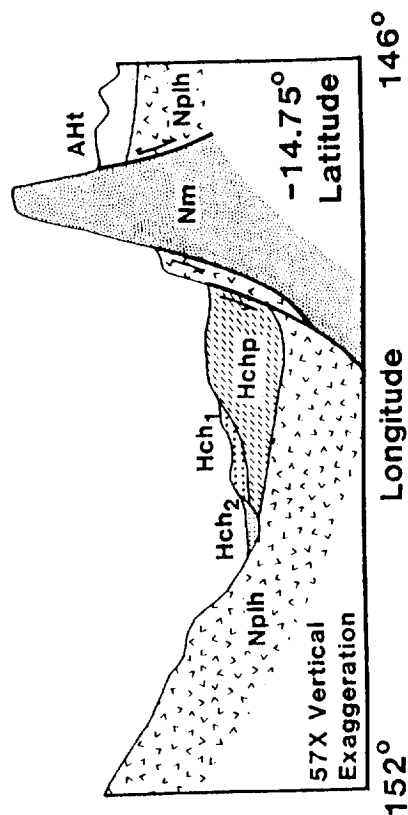
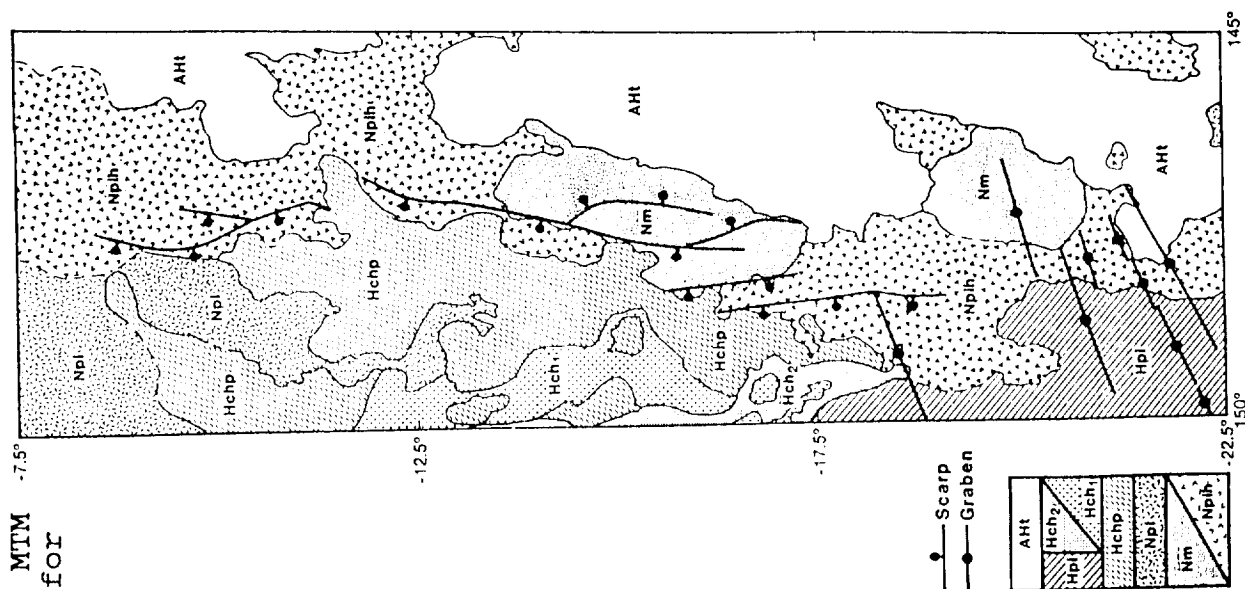


Figure 2. Geologic interpretation added to topographic profile obtained from Earth-based radar (data described in 4).

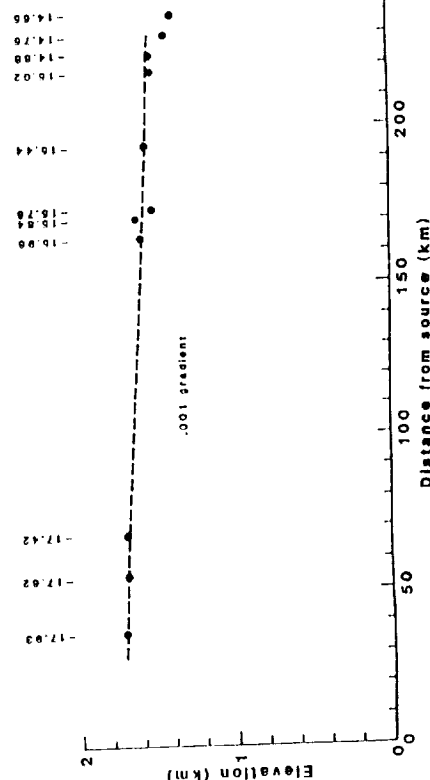


Figure 3. Relative elevations along the main channel of Mangala Valles (unit Hch<sub>2</sub>) obtained from Earth-based radar (data described in 4). Numbers give latitude of data point.

PRELIMINARY GEOLOGIC MAPPING IN THE WESTERN UTOPIA PLANITIA REGION OF MARS.

Steven H. Williams, Lunar and Planetary Institute, 3303 NASA Road 1, Houston, Texas 77058 and James R. Zimbelman, Center for Earth and Planetary Studies, National Air and Space Museum, Smithsonian Institution, Washington, DC 20560.

Introduction Geologic mapping in western Utopia Planitia (MC-6; 37.5-42.5°, 290-300°) is being conducted as part of the Mars Geologic Mapping project within the Planetary Geology and Geophysics Program. Final mapping will produce two 1:500,000 scale geologic maps, using MTM photomosaics 40292 and 40297 as bases. The mapping area is located in the knobby terrain on the lowland side of the highland/lowland boundary in MC-6SW, north of the Nilosyrtris Mensae. Geologic mapping of this region will allow the following questions to be addressed: 1) What is the sequence of geologic events that have formed and modified the lowland terrain near the highland/lowland boundary? Can the nature and age of the boundary be constrained? 2) Has burial and/or exhumation of the surface occurred, and, if so, how often have gradation cycles occurred and to what extent has terrain now exposed been protected from erosion in the past? 3) Can the origin and nature of mantling deposits be determined from their morphology? Preliminary investigation of the two study quads indicates a "yes" for all three questions; quantitative answers require more detailed work.

Background The largest-scale map containing the study area is the USGS MC-6 map (1), in which units are determined from Mariner 9 images based strictly on morphology. The units in the study area, youngest to oldest, were plains, volcanic plains, hilly terrain, knobby terrain and crater rim and fill. Three stratigraphic interpretations of the relationship between knobby and plateau material (which outcrops south of the study area): 1) The knobs are a unit beneath (older than) the plateau material that is being exhumed by erosion. 2) The knobs are erosional remnants of portions of the plateau material that are more resistant to erosion. 3) The knobs are the tops of igneous intrusions. Preliminary indications are that both 1 and 2 are correct. More recent maps incorporate the units into the developing martian stratigraphy (2,3), although at a much smaller scale. A global view is taken in (2), where the study area is mapped as having three units: Hesperian-age rolling plains, Hesperian-age knobby material, and Amazonian-age cratered plains. The older units are grouped together in (3) and the plains in the northern part of the study area are divided into Amazonian-age smooth and etched plains.

Results Preliminary examination of the study area in detail reveals a complex gradational history. Virtually the

entire area of both quads appears to be blanketed by an Amazonian-age unit of highly variable thickness composed of numerous subunits, each having limited lateral continuity. This unit corresponds to the smooth and etched plains of (3) and is thin enough in places to clearly show the much higher crater density and wrinkle ridges of the layer beneath, probably the Hesperian-age rolling plains unit of (2). There appears to be a morphologic distinction between knobs that are remnants of the stratigraphically higher plateau units (south of the study area) and the knobs found here that appear to be erosional remnants of Noachian-age material protruding from beneath the volcanic Hesperian-age plains. In many locations in the study area, the distribution of knobs is consistent with their being remnants of crater rims on heavily cratered terrain. The gradation history of the Amazonian plains is complex. Layering is present where wind erosion has truncated mantling layers over knobs. Many craters in the study contain concentric crater fill, which may be related to repeated episodes of deposition and erosion (4). Some channels are found in thicker portions of the Amazonian plains. The plains are erodable, and much more so than the older unit beneath them; hence, they are probably poorly-consolidated and fine-grained. Channels and some terrain softening features suggest that the Amazonian plains may be volatile-rich. Similarities in occurrence and morphology of the Amazonian plains to those in MC-5 (5) suggest that they are a series of airfall deposits of some sort. The upper few centimeters of the surface of many parts of the study area are currently subject to aeolian activity. Several erosional wind streaks and presumed sand patches occur in the study area. An example of the morphology of the Amazonian plains is shown in Figure 1.

Conclusion Preliminary geologic mapping of MTM quads 40292 and 40297 allows the questions raised in the introduction to be addressed. A complex series of erosion and deposition events have occurred throughout the Amazonian. Volatile-rich airfall material has undergone gravity flow and channelling in some locations. The crater dating in progress of the Amazonian plains and the Hesperian layer beneath (where sufficiently exposed) may help constrain the age of the highland/lowland boundary. The plains are probably airfall-type deposits that are fine-grained and poorly consolidated. Layering exposed by erosion around knobs and concentric crater fill are strong evidence, although working out details of burial/exposure cycles is not likely to be feasible. If the areas of thin Amazonian fill are erosional windows, then burial can protect older surfaces in a relatively pristine state until subsequent exhumation. The origin of the airfall deposits is not known.

This work was supported in part by NASA contract NASW-4066.

REFERENCES: (1) R. Greeley and J.E. Guest, U.S.G.S Map I-1038, 1978. (2) D.H. Scott and M.H. Carr, U.S.G.S. Map I-1083, 1978. (3) R. Greeley and J.E. Guest, U.S.G.S. Map I-1802-B, 1987. (4) J.R. Zimbelman, S.M. Clifford, and S.H. Williams, Proc. 19th Lunar and Planetary Science Conference, 397-407, 1989. (5) S.H. Williams and J.R. Zimbelman, (abs.), 19th Lunar and Planetary Science Conference, 1029-1030, 1989.

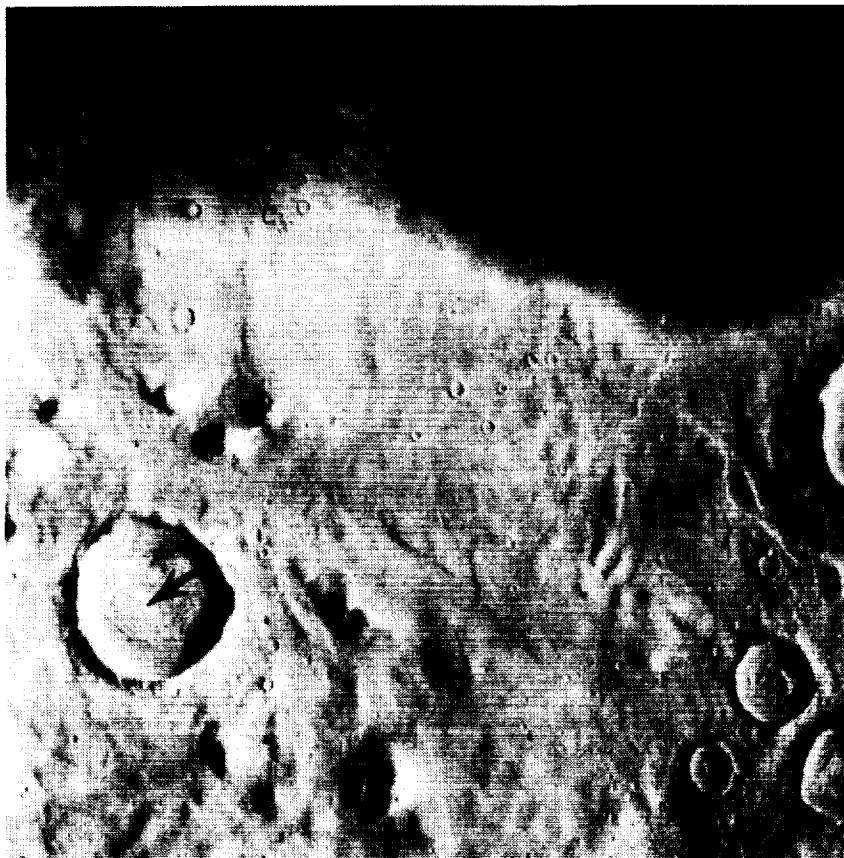


Figure 1. Some of the unusual features of the Amazonian-age plains are shown here. The unit is variable in thickness, thicker in the south and so thin in the north that wrinkle ridges and secondary crater clusters on the unit beneath show through. The exhumed surface is relatively uneroded. Many craters in the study area have concentric crater fill (arrow). Some channelling has occurred in the plains unit. This is a portion of Viking frame 235S03, centered at  $39.5^{\circ}$ ,  $291^{\circ}$ . The frame is about 70 kilometers wide; north is up.

**VOLCANOTECTONIC PATTERNS ON THE SOUTHEAST FLANK OF ALBA PATERA**  
C.D. Condit, U. Mass., Dept. Geology/Geography, Amherst, 01003

Alba Patera is the northernmost, and one of the oldest major volcanic centers associated with the Tharsis volcanic region [1-4], and is associated with a large array of grabens [5]. Understanding the volcanotectonic history of this feature offers the possibility to gain insights into both the early volcanic processes of Mars, and the complex tectonic history of the Tharsis region. This study focuses on these problems, examining the area within the 1:500,000 scale quadrangle MTM 35102 [6], located on the southwest flank of Alba Patera.

Found in the southeastern one-third of the quadrangle, the Ceraunius Fossae Formation [4] is the oldest unit mapped (crater densities  $\geq 2$  km dia.,  $666/10^6$  km<sup>2</sup>), and is composed of lava plains, as expressed by diffuse, usually indistinct flow scarps.

The middle member of the Alba Patera Formation [4] dominates the northwestern two-thirds of the quadrangle, overlies the Ceraunius Fossae Formation, and has crater densities of  $313/10^6$  km<sup>2</sup>. Three types of materials have been recognized within this unit. The oldest material is interpreted as pyroclastic flow deposits and dominates the central and northwestern part of MTM 35102. The material has a grainy, mottled appearance with gently undulating topography, broken by indistinct flow boundaries with frayed or feather edges, and numerous digitate to dendritic channels. Recognition of this unit confirms the findings of Mouginis-Mark et al. [7], strengthening their suggestion that Alba Patera should be reinterpreted as a transitional volcano between the older pyroclastic dominated highland paterae and the more recent flow dominated central vent volcanoes of the Tharsis Montes.

Interspersed with this pyroclastic flow material, and in some cases overlying it, the next younger unit occurs as smooth, broad oblate to slightly sinuous hills with moderate relief, a grainy texture and incipient linear patterns just at the limit of resolution. It is interpreted as pahoehoe flows. At some distal ends, these pahoehoe flows overlie the Ceraunius Fossae Formation, where they occur along the contact between the middle member of Alba Patera Formation the Ceraunius Fossae Formation in central and southwestern MTM 35102.

Lava flows overlie these pyroclastic and pahoehoe flows in many areas within the middle member of the Alba Patera Formation, and are most commonly found in the northeastern part of the quadrangle where, in some cases, they directly overlie the Ceraunius Fossae Formation. The 29 distinct flow lobes recognized occur as long ( $>170$  km), narrow (10-20 km wide) tongues; most display flow scarps along their edges and

distal ends; many display lava channels along narrow portions. At their distal ends, near the contact of the middle member of the Alba Patera Formation and the Ceraunius Fossae Formation many flows appear to have ponded, with widths increasing to as much as 30 km. Photoclinometric measurements suggest individual flow thicknesses of about 50 m along narrow tongues, and as much as 100 m where ponding has occurred, with edge (flow scarp) slopes generally  $<10^\circ$ , averaging about  $5^\circ$  (P. A. Davis, pers. commun., 1987). Where stratigraphic relations between individual flow lobes are most complete, 11 stratigraphic levels can be documented. The observation that lava channels and flow ponding has occurred in similar locations on both stratigraphically high and low flow lobes suggests little or no tectonic subsidence occurred during emplacement of these flow lobes.

Grabens are the dominate tectonic feature of MTM 35102; all units and channels have been cut by their faults. Three graben sets have been distinguished based on strike, maximum width, associated features and relative age, the latter derived from interpretations of intersection relations and offset patterns in a manner similar to that of [8]. Each set appears to have overlapping ranges of depth, to several hundreds of m, fault slopes of about  $65^\circ$  (P.A. Davis, pers. commun., 1987) and lengths exceeding quadrangle boundaries ( $>300$  km). The oldest set is dominated by three large grabens, spaced about 120 km apart and striking about N  $30^\circ$  E, with the middle of the three located in the center of the quadrangle. The floors share a unique feature to the graben sets: ubiquitous pit craters or pit-crater chains (catena). Six smaller grabens with the same trend, spaced from 10 to 50 km apart also share these pit crater features. The walls of these pit craters have slopes of about  $30^\circ$  (P. A. Davis, pers. commun., 1987), maximum widths of 10 km, and depths of about 2 km. This graben set has the maximum width (to 11 km) observed of the three sets. To the northeast, outside MTM 35012, these grabens display a continuing trend of about N  $30^\circ$  E which differs from the next two sets discussed. The last sets were separated based on differing trends (and age relations); the average trend of the intermediate age set is N  $28^\circ$  E; that of third (youngest) set, which are concentrated in the western part of the area, is N  $08^\circ$  E. Some intersection relations suggest the N  $08^\circ$  E set is a reactivated older trend of faulting. No clear distinction in length, depth or width could be found between the second and third graben sets. Because all flows in the area are cut by grabens, no crater density data to constrain relative timing of faulting could be obtained.

The relationship of grabens to a regional tectonic picture suggests that catena-bearing grabens may be related to the Pavonis I faulting of Plescia and Saunders [9], and, given the distinctive pit-bearing feature may have deeper seated



ORIGINAL PAGE IS  
OF POOR QUALITY

fractures. The relative youth of the N 08° E set argue they may be related to Pavonis II faulting, perhaps a reactivation of the Syria faulting [9] expressed in the Ceraunius Fossae directly south of Alba Patera. It appears likely the intermediate age (N 28° E) set, which curve to a more northerly (concentric) trend, cutting the catena-bearing grabens 200 km east of the summit calderas of Alba Patera, are of local origin, probably caused by stretching effects of a thin brittle skin as proposed by Wise [5].

The lack of any concentration of pit craters at the intersection of catena-bearing grabens and the two other graben sets leaves some doubt as the age of the catena-bearing grabens (proposed to be a young set by Roto and Tanaka [10]), if the formation of pits-craters is related to graben faulting: there is no question of their spatial relation to selected graben floors. If related to graben faulting of similar magnitude as other graben sets in MTM 35102, one would expect a higher concentration of pit-craters at graben intersections where cumulative throw would be amplified, as would be the case if catena-bearing grabens are younger than other graben sets. This argues that the pits and associated grabens were formed before younger graben faulting. If, as suggested to by Roto and Tanaka [10]], the catena-bearing grabens, or at least the last phase of movement on them (perhaps coincident with pit-crater formation) post-dates all other graben faulting, it leaves in question any mechanism associating pit-crater formation with graben faulting. Alternatively, this lack may suggest that faults of catena-bearing grabens are expressions of very deep fractures [as suggested by Tanaka and Golombek [11] in the Valles Marineris region] relative to any associated with other grabens in the map area (assuming all pit craters result from a similar mechanism), an intriguing problem yet to be addressed.

References

- [1] Wise D.U. (1979) USGS Misc. Inv. Series Map I-1154.
- [2] Scott D.H. and Tanaka K.L (1980) Proc. LPSC 11th, p. 2403.
- [3] Carr M.H. (1981) The Surface of Mars, 232p.
- [4] Scott D.H. and Tanaka K.L (1986) USGS Misc. Inv. Series Map I-1802A.
- [5] Wise D.U. (1976) Geologica Romana, v. 15, p. 430.
- [6] Condit C.D. (in review) USGS Misc. Inv. Series Map.
- [7] Mouginis-Mark P.J., Wilson, L., and Zimbelman, J.R., (1988) Bull. Volcanol., p. 19.
- [8] Tanaka K.L. and Davis P.A. (1988) JGR, v. 93, p. 14,893-14,917.
- [9] Plescia J.B. and Saunders R.S. (1982) JGR, v.87, p. 9775.
- [10] Roto, S. L., and Tanaka, K. L., (1989) Abstracts LPSC 20th, p. 926-927.
- [11] Tanaka, K.L., and Golombek, M.F., (in press) Proc. LPSC 19th.

## Geology of the Connolly Basin Impact Structure, Western Australia

E.M. Shoemaker and C.S. Shoemaker  
U.S. Geological Survey, Flagstaff, Arizona 86001

The Connolly Basin, recognized as a probable impact structure and formally named by E.M. Shoemaker and C.S. Shoemaker [1], lies in the Gibson Desert of Western Australia (lat. 23°33'S, long. 124°45'E). The rim of the basin, which is about 9 km in diameter, rises 25 to 30 m above the level of a small playa near the basin center. Drainage is chiefly exterior, as the rim is breached on the southwest side. Much of the bedrock is concealed beneath laterite of probable early Tertiary age [2] and Quaternary colluvium and alluvium. We mapped the geology and carried out a gravity survey of the basin in 1985 and 1986 in an effort to elucidate the geologic structure of the basin.

The oldest exposed rocks are found in the center of the basin in a subdued topographic rise with maximum relief of 5 m (Figure 1). Sheared, crushed, fine- to medium-grained sandstone crops out in a ring about 1 km in diameter. Dips in the sandstone ring, which can be determined from rare thin interbeds of coarse sandstone and conglomerate, are steep to overturned. The ring outlines a steep-sided structural uplift. Trends of sandstone ridges and local, well-defined attitudes in the sandstone show that the flanks of the uplift are puckered in small, tight, steeply plunging folds. The interior of the ring is occupied by steeply dipping siltstone and thin-bedded, fine grained sandstone, which form the core of the uplift. The structure of the core is locally discordant with the surrounding sandstone ring and is, in places, chaotic. We provisionally assign the beds of the central uplift to the Patterson Formation of early Permian age [3,4] which is exposed in the Woolnough Hills about 70 km to the south [5] or to the probably correlative Grant Group [6,7] of the Canning Basin to the north.

Bedrock exposed on the northeast rim of the basin (Figure 1) consists of gently dipping marine siltstone and sandstone of the Samuel Formation of Early Cretaceous age [8]. Crater ejecta deposits evidently have been entirely removed by erosion. As the Samuel Formation is the bedrock unit nearest the surface over a broad area in the vicinity of the basin, and is estimated to be only about 30 m thick [2], structural uplift of the basin rim cannot exceed about 30 m.

In the vicinity of the Connolly Basin the Samuel Formation is locally overlain by sandstone deposits provisionally assigned to the Lampe Beds of Cretaceous to early Tertiary age [8]. Similar deposits of sandstone are exposed in isolated outcrops in a circle surrounding the central uplift on the basin floor and also high on the northeast basin wall [Figure 1]. These latter deposits, which clearly represent a post-basin crater fill, are also provisionally assigned to the Lampe Beds but may well be of different age than the deposits found outside of the basin. Sandstone breccia is exposed in two places near outcrops of the Lampe Beds within the basin. It appears likely that this breccia is also part of the crater fill deposit. At several places in the basin floor, the Lampe Beds are in contact with laterite and are heavily ferruginized.

We interpret the circle of outcrops of Lampe Beds in the floor of the Connolly Basin as exposures of the eroded edges of sandstone strata that once occupied a larger part of the basin. The basin may once have been filled about to the level of the present rim and then partially exhumed during regional dissection of the landscape in early Tertiary time.

### References

- [1] Shoemaker, E.M. and Shoemaker, C.S. 1986, **Lunar Planetary Science Conf. XVII**, pp. 797-798.
- [2] Crowe, R.W.S. 1979, **Bur. Mineral Resources and West. Australian Geol. Survey 1:250,000 Ser. Explan. Notes**, Morris, W.A., 12 pp.
- [3] Talbot, H.W.B. 1970, **Geol. Survey West. Australia Bull.** 75.
- [4] Traves, D.M.; Cassey, J.N.; and Wells, A.T. 1956, **Bur. Mineral Resources, Australia, Rept.** 29.
- [5] Wells, A.T. 1980, **Bur. Mineral Resources Australia, Bull.** 198.
- [6] Guppy, D.J.; Lindner, A.W.; Rattigan, J.A.; and Casey, J.N. 1952, **XIX International Geol. Congress (Gondwana Symposium)**, Algiers.
- [7] Crowe, R.W.A. and Towner, R.R. 1976, **Geol. Survey West. Australia, Record** 1976/24.
- [8] Lowry, D.C.; Jackson, M.J.; Van de Graaff, W.J.E.; and Kennewell, P.J. 1972, **Geol. Survey West. Australia Ann. Rept.** 1971.

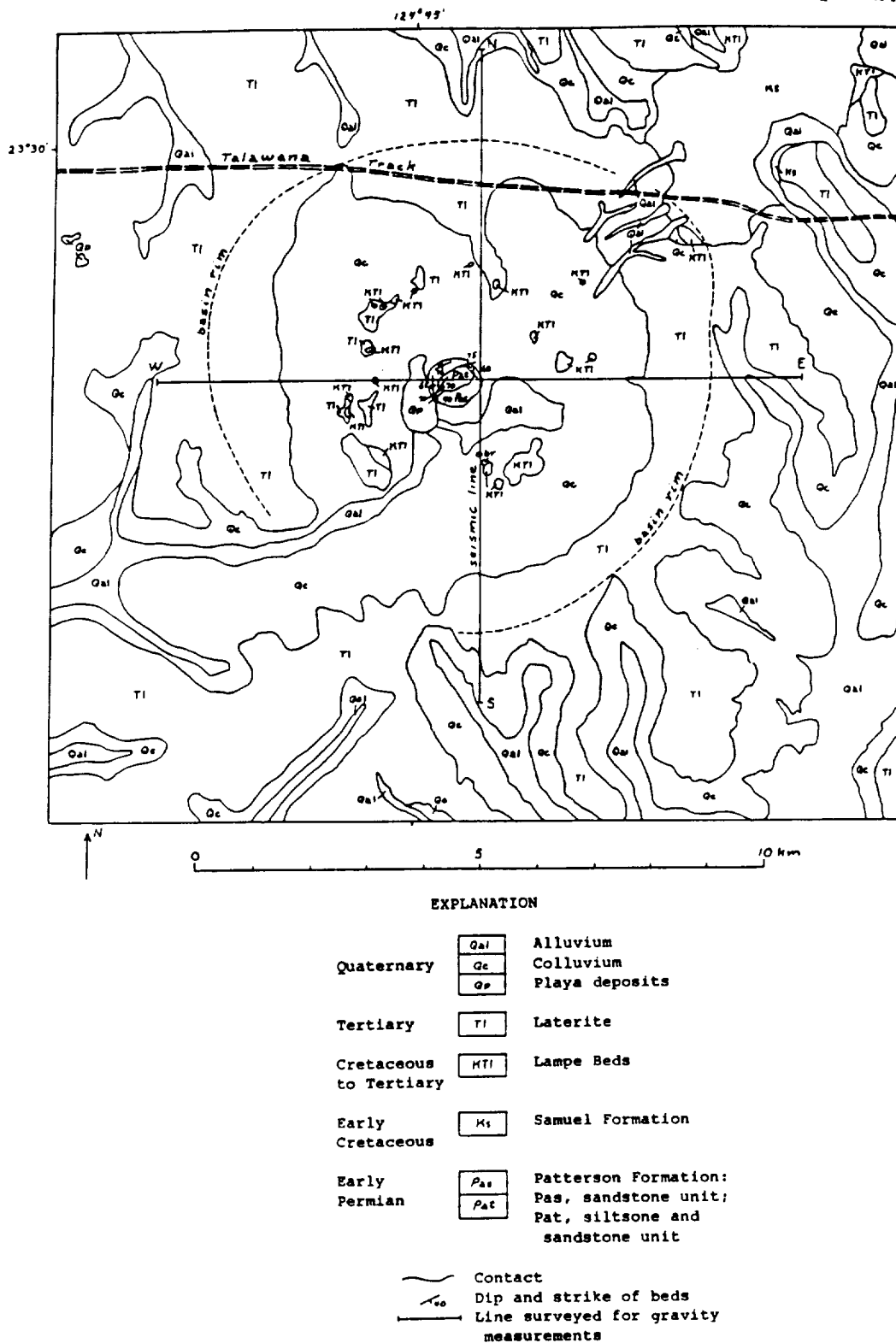


Figure 1. Geologic map of the Connolly Basin, Western Australia. Geology by E. M. Shoemaker and C. S. Shoemaker, 1985-1986.

## Gravity Investigation of the Connolly Basin Impact Structure, Western Australia

E.M. Shoemaker and C.S. Shoemaker, U.S. Geological Survey, Flagstaff, AZ 86001, and J.B. Plescia, Jet Propulsion Laboratory, Pasadena, CA 91109

The Connolly Basin is a 9-km-diameter impact structure [1] in Western Australia. Geologic mapping of the basin [2] indicates that the center of the basin is occupied by a steep-sided structural uplift a central peak. The mapping has been used to control the geophysical modeling reported here. Further control for the modeling is provided by a north-south seismic reflection line that completely crosses the structure. The line is slightly offset from the center of the basin, crossing along the eastern edge of the central uplift [2]. Strong, nearly horizontal reflectors are present at depths of about 0.7 to 0.8 sec beneath the basin rim and interior; these same reflectors are inclined and offset a few hundredths of a second beneath the central uplift. Reflectors at depths <0.7 sec are strongly disrupted and are offset by inward-dipping normal faults beneath the basin.

During the 1985 and 1986 field seasons, two gravity profiles, one oriented north-south and one east-west, were measured across the crater. The north-south profile corresponds to the location of the seismic section. Topographic control was obtained by alidade, theodolite, and tape survey. Stations were spaced 176.17 m apart and the profiles are 11.3 km long. Gravity measurements were made using a Worden Master Model meter. Both the gravity values and topographic control are relative, as these data are not yet tied to a preexisting network. The Bouguer gravity values included drift, free air, Bouguer (assumed density  $2.67 \text{ g cm}^{-3}$ ), and latitude corrections. No topographic correction was made as the correction is negligible ( $<0.01 \text{ mgal}$ ).

The regional gravity field in the Connolly Basin area is defined by a sparse gravity network (about 1 station/ $150 \text{ km}^2$ ) [3]. A broad northeast-oriented gravity high strongly influences the regional gravity gradient in the vicinity of the crater. The regional gradient is about  $0.4 \text{ mgal/km}$  along the north-south profile and  $0.8 \text{ mgal/km}$  along the east-west line. The residual (regional removed) gravity shows that the central uplift is marked by a pronounced gravity high (half-width about 1.6 km) having about 1.6 to  $2.0 \text{ mgal}$  of relief relative to the gravity values outside of the crater (Figure 1). Surrounding the uplift at a distance of 1.8 to 4.0 km is a gravity high exhibiting about 0.3 to  $0.5 \text{ mgal}$  of relief. This high is separated from the central uplift by an annular gravity low (a moat) about 0.5 km across having about  $0.3 \text{ mgal}$  of relief.

Figure 1 illustrates a possible relative density model for the Connolly Basin along the north-south and west-east gravity lines. The density model includes a high-density region corresponding to the central uplift and two shallow thin layers of material filling the basin. The central uplift is composed of material brought from depth (possibly the Patterson Formation), which has a positive density contrast of about  $0.06$  to  $0.07 \text{ g cm}^{-3}$  relative to the surrounding country rock. This contrast is derived from the observed gravity on the assumption that the structural amplitude of the uplift is 1 km, about that expected for a 9-km impact structure. The gravity data indicate that the margins of the uplift have variable dip.

We have postulated two shallow layers of diverse density contrast on the basis of geologic units mapped on the basin floor. The deeper layer is a ring of material with a density contrast of about  $-0.08 \text{ g cm}^{-3}$ , which we interpret as impact breccia. This low-density layer has a maximum thickness of the order of 100 m and is required to explain the low-gravity moat. The upper layer, which we correlate with an exposed unit of crater-fill sandstone, has a positive density contrast of about  $0.1$  to  $0.13 \text{ g cm}^{-3}$  and a maximum thickness of 100 m. We infer that this positive density contrast arises from the presence of low-density shales in the country rock in which the crater was formed. A tradeoff can be made between the thicknesses of the two layers and their density contrasts in modeling the gravity anomaly.

### References

- [1] Shoemaker, E.M. and Shoemaker, C.S. 1986, Connolly Basin, A Probable Eroded Impact Crater in Western Australia: L.P.S.C. XVII, pp. 797-798.
- [2] Shoemaker, E.M. and Shoemaker C.S. 1989, Geology of the Connolly Basin, Western Australia, this volume.
- [3] Crowe, R.W.A. 1979, Bureau Mineral Resources, Geology and Geophysics, Western Australia Geologic Survey, 1:250,000 Geological Series Explanatory Notes, Morris, Western Australia, 12 pp.

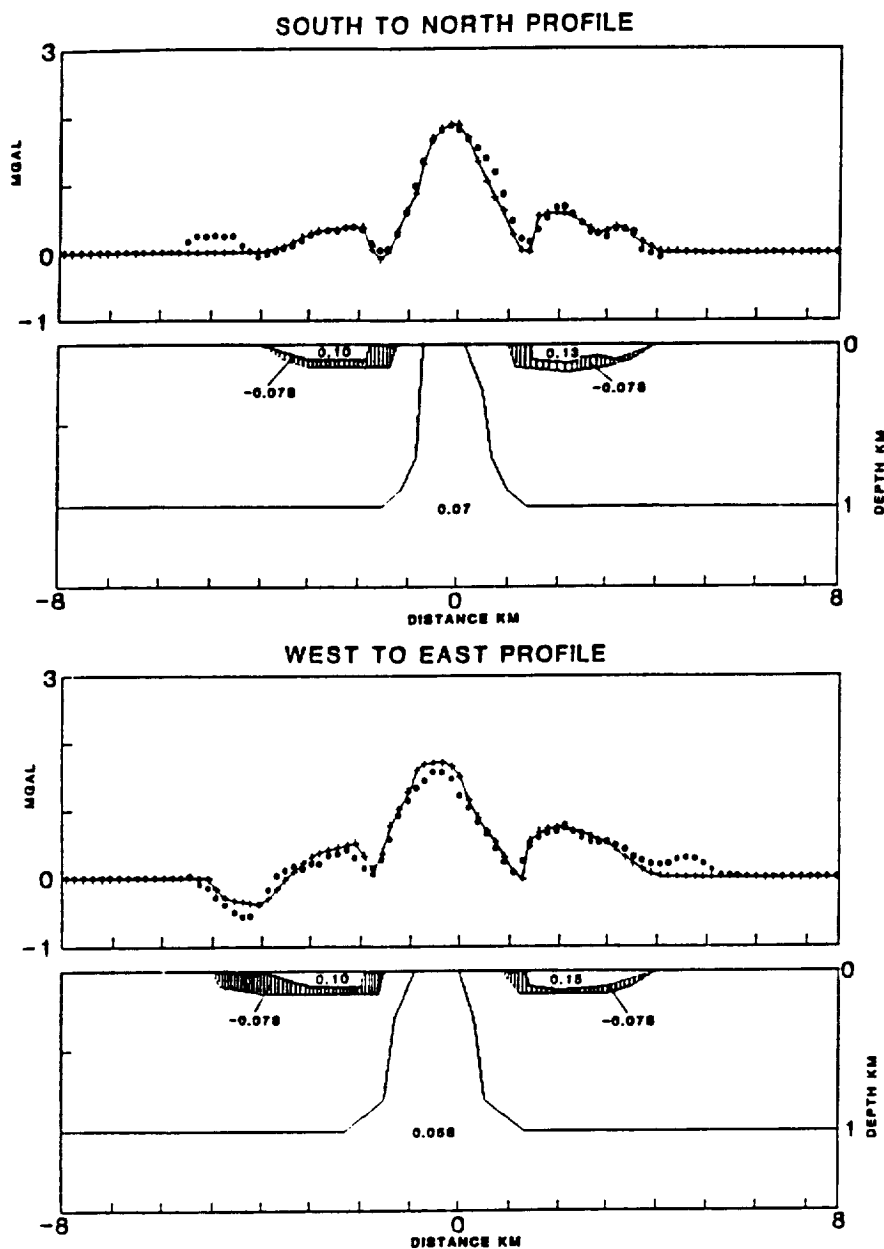


Figure 1. Gravity profiles and relative density models for the Connolly Basin. Dots show residual Bouguer anomaly; lines with + marks are modeled residual gravity corresponding to relative density models below profiles. Density is shown in  $\text{g cm}^{-3}$  relative to main unit above 1 km depth (which is unlabeled).

# TOPOGRAPHIC AND SHADED RELIEF MAPS OF PART OF THE NORTHERN HEMISPHERE OF VENUS

R.M. Batson, P.M. Bridges, Raymond Jordan, and Haig F. Morgan, U.S. Geological Survey, Flagstaff, Arizona 86001

The U.S. Geological Survey has recently prepared three maps at 1:15,000,000 scale of the hemisphere of Venus north of about lat 20° (U.S. Geological Survey, 1989). The maps are a result of a joint mapping project with the U.S.S.R., through the U.S./U.S.S.R. Joint Working Group on Solar System Exploration (Basilevsky et al., 1989). The map set consists of a topographic map (sheet 1); a shaded relief map made by correlation of data from Pioneer Venus altimetry, Venera 15 and 16 altimetry and synthetic aperture radar (SAR), and Earth-based radar images (sheet 2); and an SAR image mosaic based on data provided by the U.S.S.R. Academy of Sciences (sheet 3).

Venera images have resolutions of about 1 to 2 km, and, like all SAR images, display a narrow range of topographic frequencies, resulting in overemphasis of local-scale topographic structures. In the compilation of the shaded relief map, the regional and continental context of the local topography was restored by reference to information derived from a dataset containing reconciled altimetry measurements taken by Pioneer Venus and by both Veneras (Soderblom, written commun., 1989). Radar images provided by the Arecibo Observatory (Campbell and Burns, 1980) were also examined to insure consistency of portrayal with all data sources.

The altimetry dataset was also used to compile a contour overlay in register with the shaded relief image base and to derive a elevation color-coding scheme. The color scheme is experimental, and it may be modified for future Venus maps. The intent was to use warm colors, rather than the cool blues and greens used on previous Venus maps; on the current version, topographic highs are yellow and colors range to dark reds for the lowest areas. A continuous rather than a stepwise color gradation was used to avoid apparent ambiguity with the contour lines. The contour lines are expected to carry the metric elevation information, because relief shading necessarily distorts any elevation color code, especially on shaded or directly illuminated slopes.

## REFERENCES

- Basilevsky, A.T., Burba, G.A., and Batson, R.M., 1989, Maps of part of the Venus northern hemisphere: A joint U.S./U.S.S.R. mapping project, in Abstracts of Papers Submitted to the Twentieth Lunar and Planetary Science Conference, Houston, March 13-17, 1989, Lunar and Planetary Institute, p. 46-47.
- Campbell, D.B., and Burns, B.A., 1980, Earth-based radar imagery of Venus: *Journal of Geophysical Research*, v. 85, no. A13, p. 8271-8281.
- U.S. Geological Survey, 1989, Maps of part of the northern hemisphere of Venus: Miscellaneous Investigations Series Map I-2041.

# ATLAS OF THE SOLAR SYSTEM

R.M. Batson and Haig F. Morgan, US Geological Survey, Flagstaff, Arizona  
86001

An atlas of maps of all solid-surface planets and satellites explored to date is being prepared in conjunction with Ronald Greeley at Arizona State University. The atlas will be published by the University of Arizona Press, and it will provide a comprehensive geographical reference for professional planetary science investigators as well as interested amateurs.

All of the maps in the atlas have been compiled and published by the USGS (except the map of the lunar near side, now in compilation). The maps are digitized and are being reprojected to Lambert Azimuthal Equal Area projections for the atlas. The map scales of objects the size of Europa and larger will be 1:10,000,000. Scales of smaller bodies will be as large as 1:2,000,000. Simplified geologic maps of each object will be included, along with a brief discussion of its physical properties.

The reprojections are complete for the Galilean satellites. Geologic maps of Mercury, Mars, and the Moon have been digitized and reprojected to atlas format. The sinusoidal digital files from which the reprojections are being made will be made available to interested investigators through NSSDC.

MAPPING IRREGULAR SATELLITES: R.M. Batson, Kathleen Edwards, U.S. Geological Survey, Flagstaff, Arizona 86001, and T.C. Duxbury, Jet Propulsion Laboratory, Pasadena, California 91109

Mapping procedures for irregular satellites are being developed and tested by mapping Phobos and Deimos. Preliminary mapping of Phobos with Viking Orbiter data is complete. The mapping of Deimos is well under way. The maps are produced in digital form by projecting Viking Orbiter images onto a global topographic model made from collections of radii derived by photogrammetry. The format of a digital map differs in concept from that of a mathematical projection designed for visual use. As long as a computer can readily access a specified element of a digital map, it does not matter if the array has equal-area or conformal properties. Digital planetary maps are normally stored in the Sinusoidal Equal Area projection, which enables efficient computer access (Batson, 1987).

A body-fixed  $\overline{xyz}$  reference system (Figure 1), used to define the coordinates of the control points, was chosen to align with the three principal moments-of-inertia of each satellite (Duxbury and Callahan, 1989). In body-fixed  $\overline{xyz}$ ,  $\overline{z}$  lies along the spin axis,  $\overline{x}$  is normal to  $\overline{z}$  in the direction of the longest axis and defines the prime meridian, and  $\overline{y}$  completes the orthogonal, right-handed system. In stable dynamical configurations, the three radii of a triaxial ellipsoid approximating the mean surface have the longest radius  $a$  along  $\overline{x}$ , the intermediate radius  $b$  along  $\overline{y}$ , and the shortest radius  $c$  along  $\overline{z}$ .

The poles and prime meridian of Phobos are defined relative to the entire control network (unlike the procedure for the larger, more regularly shaped bodies, where prime meridians are defined by the longitude of one surface feature). Phobos' north pole lies on the spin axis vector above the invariable plane of the Solar System, in accordance with IAU convention (Davies et al., 1986). Planetocentric cartographic coordinates were used to define the body-fixed coordinates of the control points as well as the satellite mean surface.

The data analysis of image locations of landmarks involved estimating Phobos' rotational properties, the body-fixed coordinates of the landmarks, and camera pointing for each image. The photogrammetric geometry of narrow-angle imaging systems is too weak to derive camera-station positions; the spacecraft/Phobos positions previously derived by spacecraft tracking were therefore accepted without modification. The Phobos control network was derived by measuring the coordinates of about 450 landmarks in more than 100 images. Although the entire surface was visible to Viking Orbiter, only 70% of the coverage has sufficient overlap to yield mapping accuracies better than 500 m. Lesser accuracies, ranging from 500 to 1000 m, can be achieved in the north polar and northern leading-edge regions. The inherent accuracy of map coordinates produced from Viking images is about 50 m in the best observed regions.

Mosaics are made by projecting images onto a radius model, for which radii at control points provide the primary control. When the figure of a planetary object can be defined mathematically as a sphere or spheroid, topography is usually considered to be negligible and the projection can be done mathematically (Edwards, 1987). In the case of irregularly shaped



bodies, however, topography is dominant, and reasonably accurate models must exist before useful projections can be made. The preliminary Phobos radius model is based on interpolations from the control net. Eventual revision by stereophotogrammetry will allow compilation of continuous measurements and is capable of exceptionally high relative accuracies. However, absolute accuracy is a function of overall control accuracy (about 100 m: Duxbury and Callahan, 1989), and the absolute accuracy of the Phobos map is still an order of magnitude less than accuracies theoretically achievable by stereophotogrammetry (S. Wu, personal commun., 1989).

Projecting an image onto a radius model requires that the radius model first be projected to the plane of a spacecraft image so that the two digital arrays can be registered. Only after the image is registered can the latitude and longitude of each pixel in the image can be determined, allowing the image to be projected into the Sinusoidal Equal Area mapping array. This process is repeated for each frame to be used in the mapping, and each transformed frame is then added to the array. Each latitude/longitude bin in the completed sinusoidal array contains a brightness value from the best available spacecraft image and a radius from the geometric model.

Figure 2 shows a photomosaic of 30 Viking Orbiter images of Phobos, compiled in register with the geometric model. A three-dimensional reprojection of the entire mosaic to any desired perspective can now be performed by the model-to-image projection process mentioned above, using spacecraft vectors specified in terms of desired viewing geometry rather than those constrained by an actual spacecraft trajectory (figure 3).

Variations in resolution and surface illumination present in the Viking Orbiter dataset results in inconsistent portrayal of surface features in the mosaic. A shaded relief map was therefore made manually by methods described by Inge and Bridges (1976) and Batson (1978). The photomosaic was used for geometric control, and the entire Viking Orbiter image dataset for Phobos was examined in making the portrayal. The map was made in Sinusoidal Equal Area segments and digitized as a raster image, and the segments were merged into a single sinusoidal array for consistency with the rest of the Phobos database. Figure 4 shows one view of the airbrush map after digital reprojection.

## REFERENCES

- Batson, R.M., 1987, Digital cartography of the planets: New methods, its status, and future: *Photogrammetric Engineering and Remote Sensing*, vol. 53, no. 9., p. 1211-1218.
- Batson, R.M., 1978, Planetary mapping with the airbrush: *Sky and Telescope*, vol. 55, no. 2, p. 109-112.
- Davies, M.E., Abalakin, V.K., Bursa, M., Lederle, T., Lieske, J.H., Rapp, R.H., Seidelman, P.K., Sinclair, A.T., Teifel, V.G., and Tjuflin, Y.S., 1986, Report of the IAU/IAG/COSPAR Working Group on cartographic coordinates and rotational elements of the planets and satellites: 1985: *Celestial Mechanics*, vol. 39, p. 103-113.
- Duxbury, T.C., and Callahan, J.D., 1989, Phobos and Deimos control networks: *Icarus*, vol. 77, p 275-286.
- Edwards, Kathleen, 1987, Geometric processing of digital images of the planets: *Photogrammetric Engineering and Remote Sensing*, vol. 53, no. 9., p. 1219-1222.
- Inge, J. L., Bridges, P. M., 1976, Applied photo interpretation for airbrush cartography: *Photogrammetric Engineering and Remote Sensing*, vol. 42, no. 6, p. 749-760.

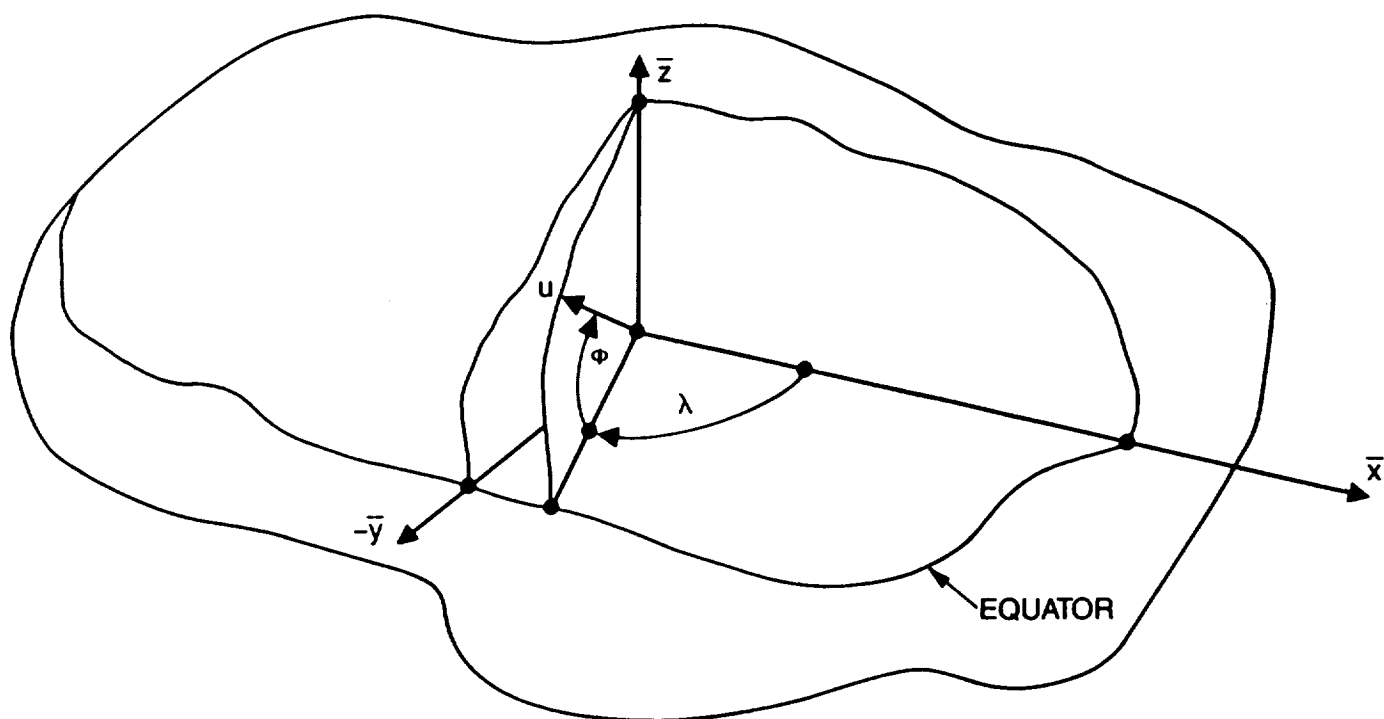


Figure 1. Cartographic coordinates  $(\phi, \lambda)$  of a control point ( $u$ ) on the surface of Phobos in a body-fixed  $\bar{x}\bar{y}\bar{z}$  system that aligns with the principal axes of Phobos. The  $\bar{x}$  axis is aligned with the direction to Mars the  $\bar{z}$  axis with the spin axis.

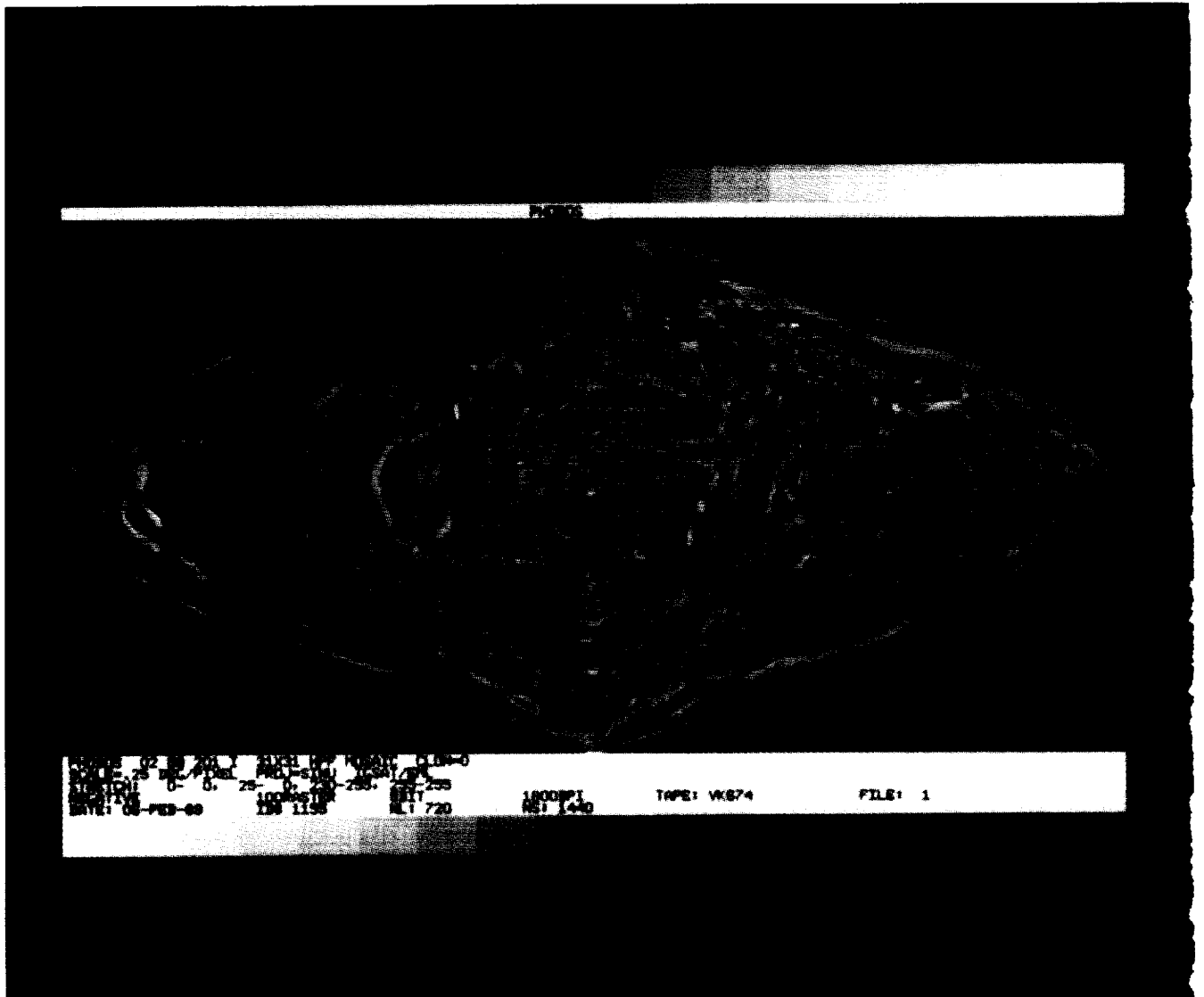


Figure 2. Photomosaic of Viking Orbiter images of Phobos in the Sinusoidal Equal Area projection.

ORIGINAL PAGE  
BLACK AND WHITE PHOTOGRAPH

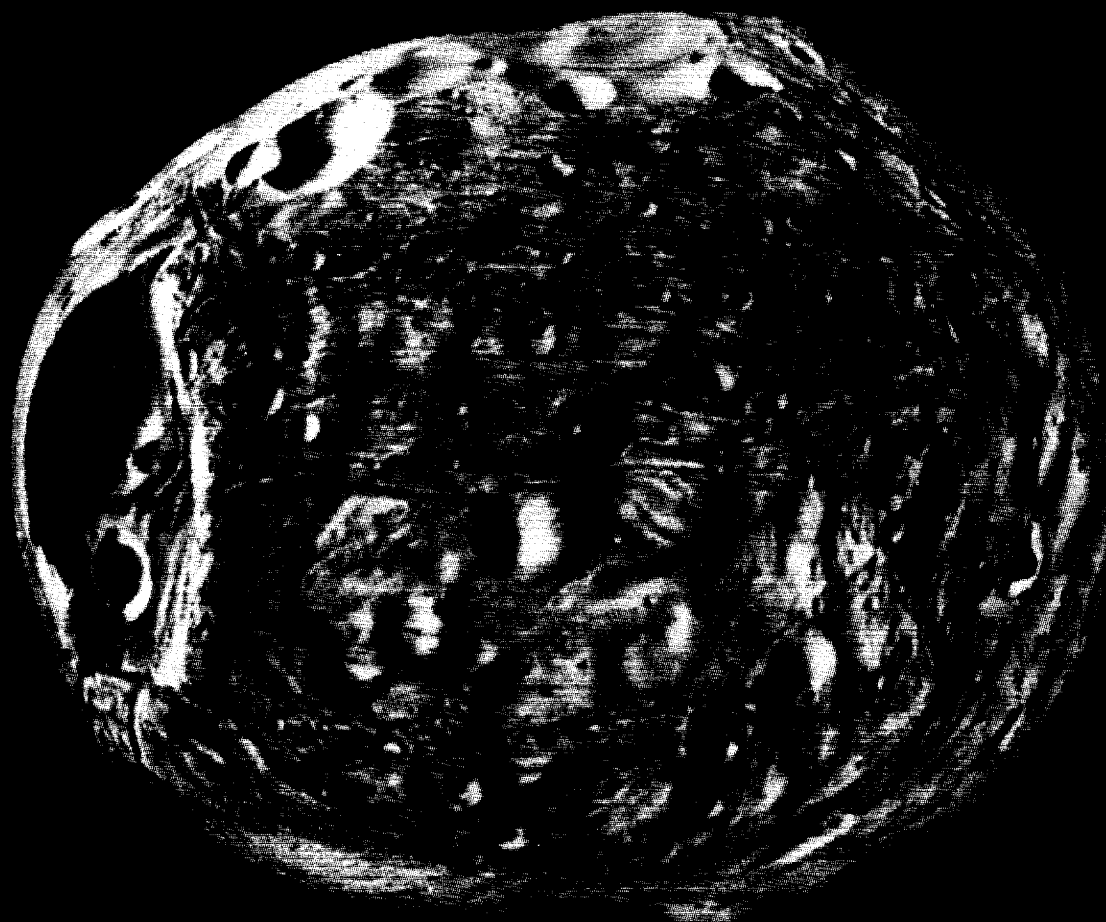
PHOBOS

PHOBOS 02 89 202 I POINT PERSPECTIVE CLON=C  
STRETCH: 0- 0, 25- 0, 230-255, 255-255  
NEGATIVE 100RASTER 8BIT 1600BPI  
DATE: 07-FEB-89 ID# 1171 NL: 500 NS: 500

Figure 3. Perspective view of preliminary mosaic of Phobos, centered on the Mars-facing side.

PHOBOS

0



PHOBOS POINT-PERSPECTIVE CLON=0 CLAT=0 IGSAT/EML  
STRETCH: 0- 0, 255-255  
NEGATIVE 100PASTER 8BIT 6250BPI TAPE: VK610 FILE: 1  
DATE: 14-JUN-89 ID# 3340 NL: 1000 NS: 1000

Figure 4. Perspective view of the digitized shaded relief map of Phobos, centered on the Mars-facing side. (Airbrush cartography by Patricia M. Bridges.)

#### PUBLICATION OF MARS CONTROL NETWORK

Sherman S. C. Wu, Francis J. Schafer, Annie Howington-Kraus, and Jennifer Billideau, U.S. Geological Survey, Flagstaff, Arizona 86001

A planetwide control network of Mars has been completed that consists of 4,502 control points produced from 1,157 high-altitude Viking Orbiter images (Wu and Schafer, 1984). The control network will be published as a book, which will be valuable for planetary studies and for planning future Mars missions such as the Mars Rover/Sample Return. We have begun the preparatory work toward this end, including the layout of the book and the marking of control points on the half-tone base of Mars 1:2,000,000-scale photomosaics. The book will be a NASA Special Publication that will include coordinates and elevations of control points; distribution of control points on a global chart and on individual quadrangles; photo-identifiable locations of control points; adjusted C- matrices of each image; description of the methods used and accuracy of the results; and guidelines for users. The preparatory work for publication will be completed during fiscal year 1990.

#### Reference

Wu, S. S. C., and Schafer, F. J., 1984, Mars control network: American Society of Photogrammetry and Remote Sensing, Technical Papers of 50th meeting, March 11-16, 1984, Wash., D.C., p. 456-463.

# DISTORTIONS IN LUNAR ORBITER PHOTOGRAPHS

Sherman S. C. Wu, Yeongji Kim, Patricia A. Garcia, and Annie Howington-Kraus  
U.S. Geological Survey, Flagstaff, Arizona 86001

Because of mechanical scanning and ground-reconstruction techniques, severe distortions exist on Lunar Orbiter photographs that preclude their direct use for topographic mapping. However, the broad coverage of the high-resolution Lunar Orbiter photographs is valuable in lunar topographic mapping for the support of geological studies as well as for the planning and operation of future lunar missions. During the summer of 1988, under the NASA Associate Program, we made a preliminary investigation of the problem of the Lunar Orbiter photographic distortions. The results indicate that photogrammetric quality can be improved with mathematical correction of the distortions. For example, elevation precision of control points of the Moon can be better than 20 m if distortion-corrected, high-resolution Lunar Orbiter photographs are used. This precision is similar to that of the Apollo metric photographs and much better than that of the control network of Mars derived from high-altitude Viking Orbiter images.

Our investigation involved the development of a mathematic model, the processing of Lunar Orbiter and Apollo photographs, and using Lunar Orbiter and Apollo photographs for the establishment of a small segment of a control network.

After testing several models, we adopted two fourth-degree, two-dimensional conformal polynomial equations:

$$DX = A_1 + A_2X + A_3Y + A_4(X^2 - Y^2) + A_5(2XY) + A_6(X^3 - 3XY^2) + A_7(3X^2Y - Y^3) + A_8(X^4 - 4XY^3)$$

and

$$DY = B_1 + A_3X + A_2Y - A_5(X^2 - Y^2) + A_4(2XY) - A_7(X^3 - 3XY^2) + A_6(3X^2Y - Y^3) - A_8(X^4 - 4XY^3)$$

These equations were applied for corrections of measured photo coordinates (on the Mann comparator) and of the processed digital data (VAX-750) of LOV-105 and -106 photographs. With distortion-corrected photo coordinates, an elevation precision of 15 m can be obtained. Distortions range from -0.162 to +0.121 mm. The average distortion correction with this adopted mathematical model is about 0.060 mm.

Although only 20% of the lunar surface is covered by the Apollo metric photographs, the entire surface is covered by photographs of the five Lunar Orbiter missions, particularly by the high-altitude photographs of the Lunar Orbiter IV mission. Such coverage will not be repeated in the near future. Therefore, it is worthwhile to continue the investigation of mapping the topography of the Moon using Lunar Orbiter photographs.



# PHOTOGRAMMETRIC MAPPING OF ARIEL USING VOYAGER 2 IMAGES

Sherman S. C. Wu and Francis J. Schafer, U.S. Geological Survey, Flagstaff, Arizona 86001

Using five Voyager 2 images, we have derived a control net consisting of 70 control points of Ariel, one of the major moons of Uranus. Images used for the control net were acquired using the narrow-angle camera of the Imaging Science System on the Voyager 2 spacecraft (Smith et al., 1986). The camera has a calibrated focal length of 1,503.49 mm (Davies et al., 1979). The images, 1546U2, 1548U2, 1661U2, 1663U2 and 1667U2, were obtained at altitudes ranging from 126,723 to 165,281 km. Each image consists of 800 x 800 image elements with a pixel size of 14  $\mu$ m and has a grid of 202 reseau marks. Calibration of reseau coordinates has an accuracy of better than 2  $\mu$ m (Benesh and Jepsen, 1978). Residuals of images produced from the Optronics Photowrite are about 3  $\mu$ m. Decalibration processing was performed at the U.S. Geological Survey image-processing facility in Flagstaff using reseau calibration data. For the control network, coordinate measurements were further corrected by a second-degree polynomial. Residuals of measured coordinates were then reduced to the 2- $\mu$ m level.

The control network was derived by using analytical photogrammetric methods and the block adjustment computer program (GIANT) that was employed for the planetwide control network of Mars.

We have also compiled a preliminary topographic map of part of Ariel's southern hemisphere (lat  $-30^{\circ}$  to  $-90^{\circ}$ , long  $270^{\circ}$  to  $20^{\circ}$ ). It was compiled from two stereomodels, 1663U2  $\alpha$  1646U2 and 1648U2  $\alpha$  1661U2, on the analytical stereoplotter. The map scale is 1:3,000,000, and the contour interval is 2 km.

## References

- Benesh, M., and Jepsen, P., 1978, Voyager Imaging Science System calibration report: Jet Propulsion Laboratory 618-802, 287 p.
- Davies, M. E., Hange, T. A., Katayama, F. Y., and Roth, J. A., 1979, Control network for the Galilean satellites, November 1979: R-2532 - JPL/NASA, The Rand Corporation.
- Smith, B. A., Soderblom, L. A., Beebe, R., Blish, D., Boyce, J. M., Brahic, A., Briggs, G. A., Brown, R. H., Collins, S. A., Cook, A. F., II, Croft, S. K., Cuzzi, J. N., Danielson, G. E., Davies, M. E., Dowling, T. E., Godfrey, D., Hansen, C. J., Harris, C., Hunt, G. E., Ingersoll, A. P., Johnson, T. V., Krauss, R. J., Masursky, H., Morrison, D., Owen, T., Plescia, J. B., Pollack, J. B., Porco, C. C., Rages, K., Sagan, C., Shoemaker, E. M., Sromovsky, L. A., Stoker, C., Strom, R. G., Suomi, V. E., Synnott, S. P., Terrile, R. J., Thomas, P., Thompson, W. R., and Ververka, J., 1986, Voyager 2 in the Uranian System: Imaging Science Results: Science, 233, p. 43-64.

#### **A UNIFIED LUNAR CONTROL NETWORK**

Merton E. Davies and Tim R. Colvin, The RAND Corporation, Santa Monica, CA 9040  
Donald L. Meyer, Defense Mapping Agency, Aerospace Center, St. Louis AFS, MO 63

This program has been designed to combine and transform many control networks of the Moon into a common center-of-mass coordinate system. The first phase, dealing with the near side, has been completed and published (Davies, et al., 1987). Coordinates of 1166 points on the near side of the Moon are given.

The most accurately defined points on the Moon are locations of the laser ranging retroreflectors (Ferrari et al., 1980) and the VLBI measurements of the locations of the Apollo 15, 16, and 17 ALSEP stations (King et al., 1976). Recent values for the coordinates of the retroreflectors have been received from Williams and Dickey, 1986. The accuracy of these locations is about 30 m and their locations are used to define the center-of-mass and, hence, the origin of the unified lunar coordinate system. The coordinates of the retroreflectors are given in both principal axis and mean Earth/Polar axis systems. Mean Earth/Polar axis coordinates have been recommended by the IAU (Davies et al., 1980) for the moon. The difference in the coordinates is important, more than 600 m in latitude and longitude.

The Apollo 15, 16, and 17 ALSEP stations have been identified on Apollo panoramic photography and their locations transferred to Apollo mapping frames. Thus, their coordinates are available in the control network computations.

Three control networks have been computed based on the Apollo mapping pictures. They are the DMA/A15 system (Schirmerman, 1976), the NOS/USGS system (Doyle et al., 1977), and the DMA/603 system (DMAAC Contract Report, 1981). Transformation parameters involving translation, rotation, and scale were derived to best fit the control network coordinates to the three ALSEP station coordinates. The DMA/603 transformed system was selected as the primary control for the unified network.

Many control networks have been computed based on pictures of the Moon taken through telescopes; these cover the Earth-facing region. Probably the most carefully prepared network is that published by Meyer, 1980. This is the one incorporated into the present program. 130 points common to Meyer's and the Apollo networks were selected and transformation parameters computed to shift Meyer's coordinates to the transformed Apollo network. The RMS of the residuals of this transformation is 808 m. The mean shift of the coordinates was 1352 m, with a maximum of 2336 m and a minimum of 803 m.

The Mariner 10 control network has been tied to this system through common points and the coordinates of ten points in the north polar region have been computed. Our report contains coordinates of 130 Apollo points, 1026 telescopic points, and ten Mariner 10 points.

At this time, the only control network of the far side of the Moon was published by the DMAAC in April 1975 (*Positional Reference System (PRS)*). It is based on Lunar Orbiter pictures.

The Apollo control network contains 1287 pictures and 12305 points. These points are either pug holes or very small craters identified on the single set of transparencies that were measured. There is no way to communicate the exact location of these points to another system. Selected points from the near side telescopic network were measured and coordinates computed. These are the ones used in the transformation of the telescopic network onto the center-of-mass Apollo network. Because the distribution of points in the PRS system is good and their locations are illustrated in the PRS report, we have decided to use the same set of points in our work.

The next task in this project was to identify the PRS points on the Apollo pictures and compute unified coordinates for them. This work is now almost completed. These new points are on the far side of the Moon. The next step will be to add a few Apollo 16 trans-Earth pictures to the data set.

## References

- Catalog of Lunar Positions Based on the Lunar Positional Reference System (1974), Defense Mapping Agency Aerospace Center, St. Louis AFS, MO 63118, April 1975.
- Davies, M. E., T. R. Colvin, and D. L. Meyer, "A Unified Lunar Control Network: The Near Side," *J. Geophys. Res.*, Vol. 92, No. B13, December 10, 1987, pp. 14177-14184.
- Davies, M. E. et al., "Report of the IAU Working Group on Cartographic Coordinates and Rotational Elements of the Planets and Satellites," *Celestial Mechanics*, Vol. 22, January 1980, pp. 205-230.
- Doyle, Frederick J., Atef A. Elassal, and James R. Lucas, "Selenocentric Geodetic Reference System," National Oceanic and Atmospheric Administration, Technical Report NOS70NGS5, February 1977.
- Ferrari, A. J., W. S. Sinclair, W. L. Sjogren, J. G. Williams, and C. F. Yoder, "Geophysical Parameters of the Earth-Moon System," *J. Geophys. Res.*, Vol. 85, No. B7, July 10, 1980, pp. 3939-3951.
- King, R. W., C. C. Counselman III, I. I. Shapiro, "Lunar Dynamics and Selenodesy: Results from Analysis of VLBI and Laser Data," *J. Geophys. Res.*, Vol. 81, No. 35, December 10, 1976, pp. 6251-6256.

Meyer, Donald L., "Selenocentric Control System (1979)," Defense Mapping Agency, DMA TR 80-001, April 1980.

Report on Lunar Control under Contract No. W-14, 453, Defense Mapping Agency Aerospace Center, St. Louis AFS, MO 63118, October 1981.

Schimerman, Lawrence A., "The Expanding Apollo Control System," Defense Mapping Agency Aerospace Center, August 1976.

Williams, J. G. and J. O. Dickey, "Coordinates of the Lunar Laser Retroreflectors," Letter to M. E. Davies, June 18, 1986.

# **THE CONTROL NETWORK OF MARS: FEBRUARY 1989**

Merton E. Davies, The RAND Corporation, Santa Monica, CA 90406-2138

The modern control network of Mars was begun in 1970, based on pictures taken by the Mariner 6 and 7 spacecraft. Pictures taken by Mariner 9 permitted the control network to be expanded to encompass almost the entire planet. The small crater Airy-0 was selected to define the prime meridian on Mars; thus the longitudes of all points are measured relative to Airy-0. Error associated with the coordinates of points was about 10 km.

The Viking pictures were a dramatic improvement over the Mariner 9 pictures and resulted in important changes to the control network. The Viking lander radio science team was able to accurately measure the direction of the spin axis and the coordinates of the two lander sites. (Michael, 1979). The Viking 1 lander site was identified on a high-resolution picture taken by the orbiting spacecraft (Morris and Jones, 1980). The Viking 2 lander site has never been located on orbiter pictures. Because the Viking 1 lander site coordinates could be transferred to orbiter pictures and because many high-resolution pictures were taken over the entire region, the coordinates of points in this area are known with considerable accuracy. High-resolution pictures of Airy-0 were added to the control network, and many strips of pictures were run between Airy-0 and the Viking 1 lander site to improve the measurements of longitude throughout the network.

The 1:2,000,000 map series consists of mosaics of pictures with a pixel size of about 250 m. Pictures identified on these maps have been used to form high-resolution strips. Strips were first run from Airy-0 to the Viking 1 lander and then from Airy-0 north along 0° longitude to 60° latitude. A strip was run from this point to the Viking 1 lander, forming a large triangle. A strip was run from the Viking 1 lander south to the equator and another around the planet at the equator and again at 60° north latitude. These latitude strips were tied by strips at longitudes 90°, 180°, and 270°. At 0° longitude, the strip continues south from Airy-0 to 60° south latitude, and a strip at 60° south latitude encircles the planet. Strips at 90°, 180°, and 270° longitude now tie the 60° south latitude strip to the equatorial strip.

High resolution pictures 452B05-15 (7-9 m pixels) cover the Viking 1 lander site. Stereographic pictures 27A27-41, 27A55-71 (38-45 m pixels) and 20A44-53, 20A66-75 (45-53 m pixels) also cover this region. Because these pictures are tied to the Viking 1 lander site, the coordinates of control points in this area should be accurate to 100 m. Along the strips, the coordinates of points should be from 2 to 5 km.

The status of the control network calculations is summarized as follows:

Number of points.....	9178
Number of pictures.....	2433 (1054 M9, 1379 Viking)
Observation equations.....	61,350
Normal equations.....	25,655
Overdetermination.....	2.39
Standard error ( $\mu\text{m}$ ).....	14.13

All computations are now performed in J2000 coordinates.

#### **References**

Michael, William H., Jr., "Viking Lander Tracking Contributions to Mars Mapping," *The Moon and Planets* 20, 149-152, 1979.

Morris, Elliot C. and Kenneth L. Jones, "Viking 1 Lander on the Surface of Mars: Revised Location," *Icarus*, 44, 217-222, 1980.

## THE CONTROL NETWORKS OF THE SATELLITES OF JUPITER AND SATURN

Merton E. Davies, The RAND Corporation, Santa Monica, CA 90406-2138

The control networks of the Galilean satellites continue to improve as measurement errors and misidentifications are corrected. The ellipsoidal shape of Io determined by Gaskell et al., 1988 has been adopted. A summary of the computations follows:

### STATUS OF THE CONTROL NETWORKS OF THE GALILEAN SATELLITES

	<u>Io</u>	<u>Europa</u>	<u>Ganymede</u>	<u>Callisto</u>
Points	712	179	1,884	818
Pictures	252	120	302	286
Measurements	12,356	3,848	25,780	15,782
Normal equations	2,184	718	4,674	2,494
Overdetermination	5.66	5.36	5.52	6.33
Standard error, $\mu\text{m}$	11.02	9.93	10.50	11.4

The three radii of Io are 1830.0 km, 1818.7 km, and 1815.3 km; computations using the mean radius of 1821.3 km have also been made to generate picture parameters convenient for making computer mosaics and map projections. The mean radius of Europa is 1565 km, of Ganymede is 2634 km, and of Callisto is 2403 km.

The control networks of the satellites of Saturn have also been improved. The ellipsoidal radii of Mimas (210.3 km, 197.4 km, and 192.6 km) were derived by Dermott and Thomas, 1988, and those of Enceladus (256.2 km, 247.3 km, and 244.0 km) were measured by Peter Thomas (personal communication). A summary of the computations follows:

### STATUS OF THE CONTROL NETWORKS OF THE SATELLITES OF SATURN

	<u>Mimas</u>	<u>Enceladus</u>	<u>Tethys</u>	<u>Dione</u>	<u>Rhea</u>	<u>Iapetus</u>
Points	109	111	110	126	331	62
Pictures	32	22	27	28	85	80
Measurements	1344	1340	924	1322	4902	1872
Normal Equations	318	292	301	336	917	364
Overdetermination	4.23	4.59	3.07	3.93	5.35	5.14
Standard Error, $\mu\text{m}$	12.67	12.62	10.67	10.05	11.21	11.32
Mean Radius, km	198.8	249.1	523	560	764	718

As with Io, computations for Mimas and Enceladus have been made assuming their mean radii to generate picture parameters.

A report on the control network of Phoebe has been written by T. R. Colvin, M. E. Davies and P. G. Rogers and submitted to *Nature* for publication. The north pole of Phoebe was calculated to be  $\alpha_0 = 355.0 \pm 9.6^\circ$ ,  $\delta_0 = 68.7^\circ \pm 7.9^\circ$  in J2000 coordinates.

#### References

1. Colvin, T.R., M.E. Davies, and P.G. Rogers, "The Control Network of Phoebe," submitted to *Nature*.
2. Dermott, S.F. and Thomas, P.C.: 1988, "The Shape and Internal Structure of Mimas," *Icarus* 73, 25-65.
3. Gaskell, R.W., Synnott, S.P., McEwen, A.S., and Schaber, G.G.: 1988, "Large-scale Topography of Io: Implications for Internal Structure and Heat Transfer," *Geophys. Res. Letters* 15, 6, 581-584.

ORIGINAL PAGE IS  
OF POOR QUALITY



## CHAPTER 13

### SPECIAL PROGRAMS



## IMAGE RETRIEVAL AND PROCESSING SYSTEM (IRPS) FOR THE REGIONAL PLANETARY IMAGE FACILITIES

S. Slavney, E. A. Guinness, B. Weiss, M. Dale-Bannister, R. E. Arvidson, McDonnell Center for the Space Sciences, Department of Earth and Planetary Sciences, Washington University, St. Louis, Missouri, 63130

This abstract is a progress report on the Image Retrieval and Processing System (IRPS) software being developed by Washington University. IRPS provides access to a database of information about the planetary images and image data products maintained by the Regional Planetary Image Facilities (RPIFs). IRPS allows the user to locate individual images stored on magnetic tape or compact disk, and provides access to software for reading, processing, and displaying the images. The image processing software used is the Planetary Image Cartography System (PICS) developed by the U. S. Geological Survey in Flagstaff.

IRPS is implemented on a MicroVAX II computer using a commercial data base management package, System 1032 from CompuServe Data Technologies. IRPS uses TAE, a menu-driven user interface developed and maintained by the Goddard Space Flight Center. TAE is also used by PICS. IRPS includes access to an image browse capability, currently implemented with an analog videodisk player, which allows the display of an image while accessing its record in the data base. Future plans include implementing the browse capability with compact disks instead of videodisks, as more image data become available in that format.

The IRPS database contains information on two levels, called the high-level and detailed-level catalogs. The high-level catalog includes descriptive information about planetary missions, spacecraft, instruments, and the image datasets produced by the missions. The information stored for each data product includes the product type, the producer's name, the product format, and the RPIFs that have each product. Over the past year the RPIFs have collaborated in an effort led by Washington University to compile data for the high-level catalog, including descriptive information about missions, spacecraft, and data products, along with inventories of each RPIF's holdings. Currently the high-level catalog contains data on the following missions: Viking, Voyager, the Mariner missions, the Apollo missions, and the Lunar Orbiter missions.

The detailed-level catalog contains data about individual planetary images, planetary maps, and mosaics. The information stored for each image includes data about the imaging instrument (filter, gain state, etc.), the time the image was taken, the center latitude and longitude, the lighting and viewing geometry, and other parameters, any of which can be used to specify a search of the data base. Also stored are the locations of an image on magnetic tape and compact disk. The user can locate all the images in a mosaic, or conversely all the mosaics in which a given image appears. Currently, the detailed-level catalog includes data for the Viking Orbiter and Voyager missions. For planetary maps, the catalog includes the latitude and longitude boundaries, the map scale, projection, and type, the cartographer's name, the publisher's name, and the publication date, among other items. The detailed-level catalog includes data for the Miscellaneous Investigations map series (the "I-series") published by the U. S. Geological Survey.

PRECEDING PAGE BLANK NOT FILMED

IRPS Version 1.0 incorporates several changes from the prototype version that has been in use at the Washington University RPIF. The user interface has been modified to reflect a more logical way of entering parameters, and the forms used to display data have been modified. New functions have been added: the user may now undo a search if the results were unsatisfactory, and may display (and store in a file) a list of the commands previously entered. An important change in IRPS Version 1.0 is the implementation of "user views" to guide the user's access to the data, thus relieving him of the need to understand exactly how the data are stored. With this modification IRPS is now more flexible and can provide more information with less work on the user's part.

At the design level, the IRPS data base schema has been reorganized for more efficient storage and ease of update. The code has been redesigned to make better use of the programming capabilities provided in System 1032. Functions have been provided to allow the data administrator to add and modify data and to maintain the data base schema and data dictionary.

## **VIKING ORBITER IMAGE CDROM PRODUCTION**

E. A. Guinness, S. Slavney, and R. E. Arvidson, McDonnell Center for the Space Sciences, Department of Earth and Planetary Sciences, Washington University, St. Louis, Missouri 63130

The planetary science community's need to access image data from the Viking Mission is becoming increasingly important with the upcoming Mars Observer Mission and with the availability of software for radiometric and geometric operations on these images. Currently, the set of over 50,000 Viking Orbiter images is available only on magnetic tapes from NSSDC or JPL. In May of 1988, an informal group of planetary scientists and people involved with the Galileo, Magellan, and Mars Observer projects met in Flagstaff, Arizona to discuss the use of CDROMs for planetary data sets. One of the recommendations of that meeting was to develop a plan for the transfer of all Viking Orbiter images to CDROMs. CDROMs are an ideal method of widely and inexpensively distributing these data. The disks are relatively inexpensive to master and reproduce. They hold much more data than magnetic tapes. They are more durable, less bulky, and faster to read than magnetic tapes.

We have developed a plan to transfer the Viking Orbiter images from magnetic tape to compressed-data format on compact disk. The plan provides for the production of more than 30 disks over a three-year period, involving personnel and equipment at Washington University, the Jet Propulsion Laboratory, and the U. S. Geological Survey in Flagstaff, Arizona. Copies of the Viking EDR images will be sent from JPL to Washington University. The images will undergo data compression using the same Huffman encoding algorithm as used for Voyager images. In addition, a PDS-standard image label with the best available SEDR information (including the reason for acquiring the image) will be attached to each image. The compressed data will be sent back to JPL for pre-mastering and delivery to a vendor for mastering and replication.

The roles and responsibilities for the three groups involved in this project are as follows. Washington University personnel will lead the data conversion activity. They will be responsible for transferring images from archive format to compressed format with PDS labels. This process will include data quality checking, data compression, and generation of a catalog of SEDR information. JPL personnel will supply the original EDR images, pre-master the data for CDROM, and handle the interaction with the vendor who produces the CDROMs. The USGS personnel will attempt to replace any bad or missing EDRs by reprocessing the Master Data Record tapes. They will provide advice and recommendations concerning the SEDR data. They will also provide most of the data compression and associated software. The funding for the Viking CDROM project is shared by the PDS and Code EL.

Work on the project began at the beginning of 1989. The image label has been designed and a subset of the image engineering data has been selected for inclusion with the image. Software development for the data compression and associated software has begun. A database of SEDR information from the USGS SPICE files, the archive image labels, and the MTIS photoproducts is being compiled. In addition, the Viking Orbiter imaging team's planning records that indicate the reason for acquiring sequences of images are currently being transcribed into machine-readable format. We plan to begin CDROM production with the Viking Orbiter 1 Survey Mission because

these data are presently available at Washington University. We expected that the software should be ready for operation by May, 1989. It is also expected that the production rate will be such that one CDROM worth of data will be processed each month.

MARS SAMPLE RETURN: A GENERAL PHILOSOPHY FOR SITE SELECTION  
David H. Scott, U.S. Geol. Survey, 2255 N. Gemini Dr., Flagstaff, AZ 86001

INTRODUCTION: The global distribution and relative ages of about 80 rock units are shown on the new geologic maps of Mars (1). Although the maps were compiled at 1:15,000,000 scale, the geologic units were identified and mapped by using Viking images and photomosaics at 1:2,000,000 scale (image resolution of 130 to 300 m per picture element). The stratigraphic positions of these units were established by superposition and crosscutting relations and supported by crater counts. The new geologic maps provide information on the relative times of occurrence of tectonic and volcanic episodes, formation of outflow channels and valley drainage systems, and impact-flux changes within and between the Martian time-stratigraphic systems. Of particular interest to exobiologists are the inferences that can be made from the maps about the locations of large standing bodies of water that once may have existed. Without ground truth, however, the ultimate value of planetary geologic maps is limited.

OPTIMUM SAMPLE OBJECTIVES--Ideally, a sample site would be free of surface obstacles and at an elevation low enough to permit atmospheric braking for the descent of the landing craft. A suite of rocks, insitu, and soil would be readily accessible to the sampling vehicle. The rocks would have a wide range in age, lithology, composition, and mode of origin; they would be correlative with major geologic units mapped in the Martian time-stratigraphic systems. Some of the sampled materials would be associated with important volcano-tectonic episodes and magmatic histories, others with fluvial, eolian, and polar processes that are indicators of climatic and atmospheric history. The ideal site would also be located where evidence of present or former biological activity would most likely be found.

FEASIBLE SAMPLE OBJECTIVES--With our present knowledge of Mars' geology, we have found no single locality where such optimum conditions exist. On the other hand, many areas are known where rock samples might resolve specific problem-oriented questions such as the following: the age and identification of possible ash flows (2); the times of occurrence of different fluvial periods (3,4,5); the nature and origin of valley layered deposits where evidence of early biological processes may exist (6,7); the processes that shaped the early history of Mars, determined in part from soil samples that also may contain residual organic matter (8,9); the composition of early volatiles preserved in the impact breccias of old craters (10); primary volatiles within glass inclusions of volcanic rocks (11); and the erosion and deposition rates within the polar layered deposits (12).

Most of these questions, though important, are narrow in focus and would leave untouched the broader aspects of Martian geology and evolutionary history. However, there are many locations on Mars where some of these questions would constitute secondary objectives, which would be resolved by study of samples from a primary objective site of impact breccias, eolian and weathering products, cosmogenic nuclides, inclusions within volcanic rock, and soil and atmospheric gases.

RATIONALE FOR PRIORITY OBJECTIVES--Primary objectives of the first sample-return mission to Mars must include certain elements of the ideal site, whether the location objectives be single or compound. At a single-objective location, only one rock/soil unit would be sampled and little or no mobility in the sampling operation would be required. At a compound-objective location, a variety of questions would be addressed by obtaining samples of

different rock types, origins, and ages (13). Compound sites require a roving vehicle whose range would depend on the location selected.

Single-Site Essential Elements--A volcanic flow with exposed rocks in place or clearly derived from nearby outcrops. The flow should be of regional extent, intermediate in geologic age (Hesperian), at a low elevation, and it should have a statistically valid crater-count record. Constraints on terrain roughness would be minimal, but the area within the target ellipse should be hazard free.

Geologic maps (1) show a good correspondence between Martian time-stratigraphy and crater-frequency distribution. However, without radiometric ages, absolute chronologic correlations are unknown. Thus, Hesperian-age samples are especially important because their absolute age would closely define the bend in the cratering chronology curve (14). This bend occurs where the high post-accretional impact flux changes to a nearly constant rate. Hesperian samples are also desirable because their time of emplacement closely corresponds with that of major geologic events--the onset of volcanism at Tharsis Montes, the development of huge outflow channels, the rifting that produced Valles Marineris, the rapid decline in tectonic activity, and the emplacement of extensive rock units within the northern plains.

Compound-Site Essential Elements--Similar to those of a single-objective site except that terrain roughness constraints would affect rover mobility. If the selected location affords rover access to two volcanic areas, one should be of Hesperian age for the reasons cited above; the second should contain very young lava flows, preferably of late Amazonian age such as an upper member of the Tharsis Montes Formation or the plains or shield members of the Olympus Mons Formation. Radiometric ages of these rocks would control the rate of descent of the cratering chronology curve during the period of low impact flux, show mineralogical differences between relatively old and young lavas, directly or indirectly provide upper limits on the age of outflow channels, and bracket the age of geologic units that cover parts of the lowland plains.

In some areas, a third stratigraphic unit could be sampled in conjunction with units of a two-sample site. Choices for additional sampling could be made among very old (Noachian) rocks and materials whose age and composition might solve perplexing geologic problems, i.e., the age and composition of vast sheets of material that may be ignimbrites (15), the age, composition, and origin of Olympus Mons aureoles (16), and the age and composition of material forming highly fractured terrains.

References \*denotes abstracts from Mars Sample Return Science Workshop, LPI 1987, Houston, Texas.

- (1) Scott, D.H. and Tanaka, K.L. (1986), Greeley, R. and Guest, J.E. (1987), Tanaka, K.L. and Scott, D.H. (1987), U.S. Geological Survey Misc. Inv. Series Maps I-1802 A,B,C. (2) Scott, D.H. and Tanaka, K.L. (1982) JGR, v. 87, 1179-1180. (3) Masursky, H. et al. (1987)\* 89-90. (4) Scott, D.H. (1987)\* 120-121. (5) Squyres, S.W. (1987)\* 129-130. (6) Lucchitta, B.K. (1987)\* 83-84. (7) Klein, H.P. (1987)\* 71-72. (8) Stoker, C.R. et al. (1987)\* 132. (9) Pang, K.D. and Fun-Dow Tsay (1987)\* 108-109. (10) Bogard, D. (1987)\* 17-18. (11) Anderson, A.T. (1987)\* 8. (12) Paige, D.A. and Krieger, D.B. (1987)\* 106-107. (13) Albee, A.L. (1987)\* 4-5. (14) Neukum, G. (1987)\* 98-99. (15) Scott, D.H. and Tanaka, K.L. (1982) JGR, v. 87, 1179-1180. (16) Morris, E.C. (work in progress).



THE GALILEAN SATELLITE GEOLOGICAL MAPPING PROGRAM, 1988  
B. K. Lucchitta, U.S. Geological Survey, Flagstaff, Arizona 86001

The Galilean Satellite Geological Mapping Program was established by the Planetary Geology Programs Office of NASA to illuminate detailed geologic relations on the four large satellites of Jupiter: Io, Ganymede, Europa, and Callisto. The program is administered by the U.S. Geological Survey, and it involves about 40 investigators from various universities, research institutes, and government offices in the United States, England, Germany, and Italy. A total of 24 researchers were assigned to map 15 quadrangles on Ganymede, 15 to map 6 quadrangles on Io, and 3 to map 2 quadrangles on Europa. The maps are at a scale of 1:5 million except for three on Io that cover selected areas where high-resolution pictures permit compilation at scales of 1:2 million and 1:1 million. A 1:15 million-scale map of Callisto has been assigned; it will be the basis for later geologic mapping at a scale of 1:5 million.

During 1988 all final base materials were distributed. Three geologic maps are now published (the Io maps Maasaw Patera, Ra Patera, and the Ganymede map Uruk Sulcus). One other Io map (Ruwa Patera) and one Ganymede map (Philus Sulcus) are in proof stage and publication is imminent. Eight maps are in various stages of review and editing: Ji4 has USGS Director's Approval; Ji3, Jg3, Jg7, and Jg9 are undergoing author's revision after technical reviews; and Je4, Jg10, and Jg15 are in technical review. Mapping is still in progress for Je2, Ji2b, Jg1, Jg5, Jg12, and Jg13. Summary maps for Io and Ganymede at 1:15 million scale, incorporating the data from the larger scale maps, are in progress.

PLANETARY GEOLOGY AND GEOPHYSICS PROGRAM: A SUMMARY, FY 88  
James R. Underwood, Jr., Code EL, NASA Headquarters,  
Washington, D. C. 20546

The Planetary Geology and Geophysics (PG&G) budget for FY 88 was \$10,500k, a further decline in a support level that has decreased 30 percent since FY 84, when the PG&G budget was approximately \$15,000k (Fig. 1). Intense pressure was felt throughout the program in FY 88, especially in graduate student support and in equipment maintenance and upgrade.

The distribution of PG&G funding by organization is shown in Figure 2 and the distribution of PG&G Principal Investigators by organization is shown in Figure 3. A histogram of FY 88 funding by project is shown in Figure 4, in which the median PG&G project funding level is shown to be \$30k-\$40k.

Nine new Principal Investigators, whose proposals were ranked highly by the Lunar and Planetary Geoscience Review Panel meeting at the Lunar and Planetary Institute in late September, were included in the FY 88 program; their start-up funding levels averaged \$23k.

The current Mars data analysis program - Mars, Evolution of Tectonism and Volcanism (MEVTV) - held a workshop on Nature and Composition of Surface Units on Mars at Napa, California, December 1987. A special symposium was held at the spring 1988 meeting of the American Geophysical Union on the origin of the crustal dichotomy of Mars, and a field workshop on basaltic volcanism was held in Hawaii in June.

A second workshop on planetary spectroscopy was convened at Bodega Bay, California in April, 1988, to identify the potential applications of the techniques of planetary spectroscopy in planetary science, to update the descriptive material in the report of a 1986 workshop, and to assess the state of the field.

The 1988 Lunar and Planetary Geoscience Review Panel (LPGRP) evaluated 366 proposals, and in so doing resolved to restructure the groups of the panel to distribute the workload more evenly. Six groups now constitute the panel: Group A: Mineralogy and petrology of meteorites/lunar samples/cosmic dust; Petrology of ancient terrestrial crust and mantle; Petrologically oriented field studies. Group B: Analytical geochemistry and cosmochemistry; Experimental petrology and geochemistry. Group C: Isotope (radiogenic/stable/cosmogenic) geochemistry; Geochronology of meteorites/lunar samples/terrestrial rocks. Group D: Planetary surface geology; Terrestrial structure/tectonics/cratering studies. Group E: Remote sensing of planets/

asteroids; Laboratory spectral studies of extraterrestrial materials/analogues; Non-dynamical studies of primitive bodies (comets/rings/asteroids); Group F: Planetary geophysics; dynamical studies; experiments at very high pressures.

The Mars Geologic Mapping (MGM) Program (1:500,000 scale) continued the support of mapping at that scale of areas of unusual scientific interest. One of the uses of those studies will be to provide information to the Mars Rover, Sample Return (MRSR) Program to assist in site selection of traverses and sample collections. In FY 88, eight people were active in the MGM program.

The PG&G Working Group met twice during FY 88, in the fall in conjunction with the Division of Planetary Science annual meeting in Pasadena and in the spring in conjunction with Lunar and Planetary Science Conference XIX. The working group provides broad oversight of PG&G programs and facilities, and especially it provides a perspective on future PG&G needs, opportunities and challenges.

Despite the hardships imposed by inadequate funding in FY 88, scientists in the PG&G program continued their vigorous attack on problems in planetary science and reported on the results of their research at numerous meetings in the United States and abroad. Furthermore, PG&G scientists continue to make major contributions through their service on a wide variety of advisory groups, working groups, and review panels.

## FUNDING HISTORY PLANETARY GEOSCIENCES PROGRAMS

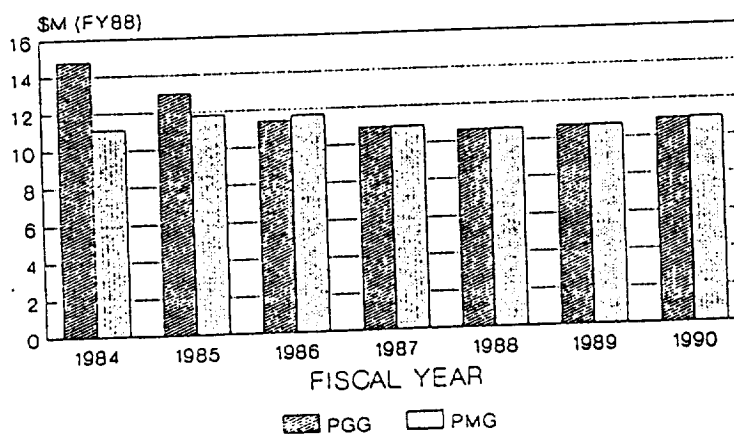
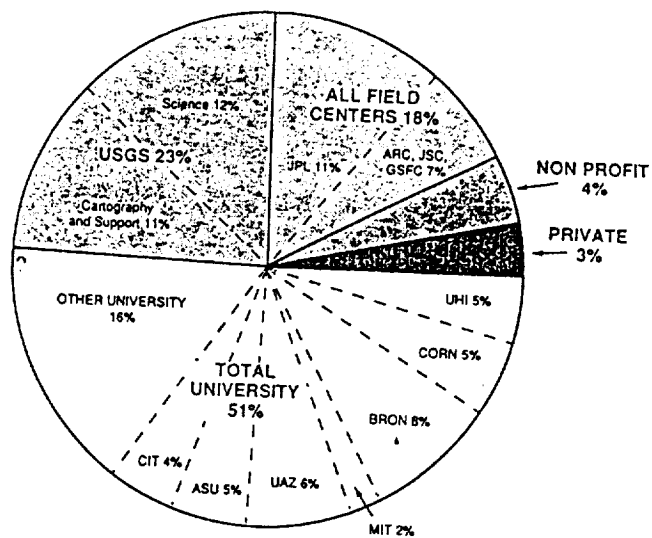


Figure 1

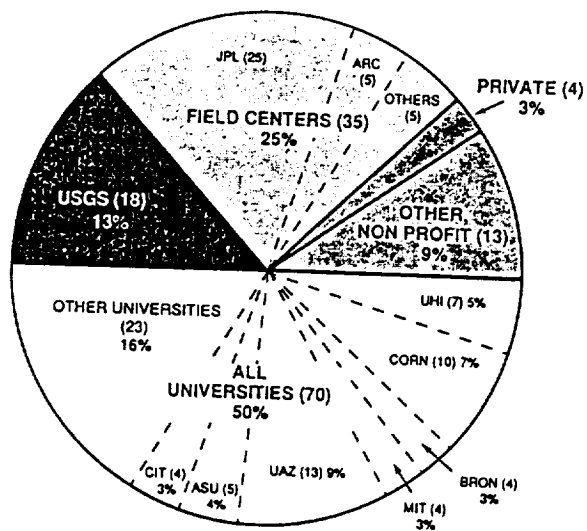
ORIGINAL PAGE IS  
OF POOR QUALITY



FY 88

PG & G FUNDING  
BY ORGANIZATION

Figure 2

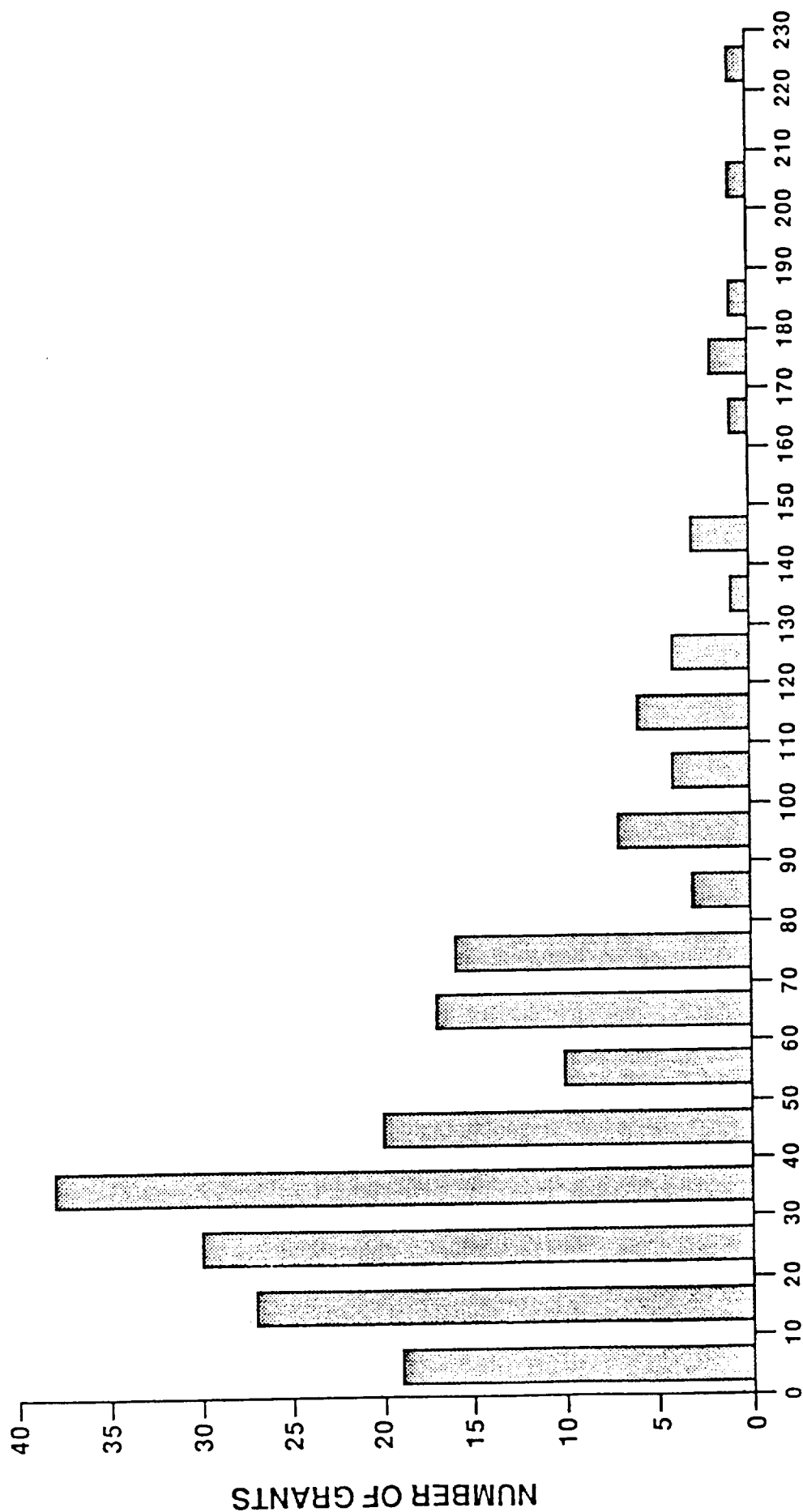


FY 88/89

PG & G PRINCIPAL INVESTIGATORS  
BY ORGANIZATION

Figure 3

# FY 88 FUNDING - LEVEL DISTRIBUTION PLANETARY GEOLOGY & GEOPHYSICS



FUNDING LEVEL X \$1,000

Figure 4



CHAPTER 14

LATE ABSTRACTS

PRECEDING PAGE BLANK NOT FILMED

~~PAGE~~ 622 INTENTIONALLY BLANK





# AN INFRARED REFLECTANCE STUDY OF LOW ALBEDO SURFACE CONSTITUENTS.

Larry A. Lebofsky and Thomas D. Jones, Lunar and Planetary Laboratory,  
University of Arizona.

Unaltered asteroids are thought to represent the raw materials available for terrestrial planet formation and so are important to our understanding of the origin and evolution of the Solar System. It has been shown [1] that the asteroid compositional types vary systematically with heliocentric distance and that the asteroids probably formed very close to their present locations in the asteroid belt. From their inferred composition Gradie and Tedesco [1] also concluded that the outer belt and Trojan asteroids were probably more "primitive" than the C-class asteroids which dominate the main belt. This interpretation was consistent with earlier studies of asteroid analogs that concluded that the low albedo D-class asteroids were probably "ultraprimitive" in composition, i.e., composed largely of hydrated silicates and organic material.

In order to understand the compositional distribution of asteroids, we rely upon theories of the origin and evolution of the solar system and on telescopic observations of the asteroids. In the latter case, we must depend heavily on the taxonomic classification of asteroids and their implied relationship to meteorites [1,2,3]. Unfortunately, the taxonomic classes are determined solely from observed parameters and do not in and of themselves involve any compositional determination. For example, can we assume that a D-class asteroid in the middle of the main belt at 2.9 AU is compositionally similar to a Trojan asteroid at 5.2 AU?

Our major emphasis over the last few years has been on the determination of the composition of low albedo asteroids. These asteroids have been assumed to be unaltered and are thought by some to represent the raw materials from which terrestrial planets formed and so are important to our understanding of the origin and evolution of the Solar System.

There now exists a body of data at much higher resolution and over a greater spectral range (out to 2.5 microns) [4]. Also, we now have 1- to 4-micron observations of over 40 low albedo asteroids [5,6]. These observations span all low-albedo taxonomic classes (C, D, F, G, P, and T). Several (e.g., the C asteroids) of these classes appear to be spectrally analogous to chemically primitive, volatile-rich carbonaceous meteorites (see Fig. 1). Others (e.g., the D asteroids) appear to be compositionally 'ultraprimitive' and thus are presumed to be more volatile-rich than the mainbelt C asteroids. Therefore, it had been presumed that these outer belt and Trojan asteroids should show a larger volatile content (i.e., hydrated silicates and organics) than the Cs. However, from our recent observations, we find that most of them do not show the spectral signature of hydrated silicates (see Fig. 2).

This is consistent with the scenario that in the outer part of the asteroid belt the kinetics of the nebula-solid reactions were too slow for chemical equilibrium to be attained. Under these conditions, all the asteroid belt started out as a mixture of ice and anhydrous rock. Asteroids

PRECEDING PAGE BLANK NOT FILMED

in the inner part of the belt may have undergone moderate heating, resulting in the melting of some of this ice and subsequent aqueous alteration; those in the outer belt were not so heated, and instead lost their water to gradual sublimation over the age of the solar system.

#### References:

- [1] Gradie and Tedesco (1982) Science 216, 1404--1407.
- [2] Tholen (1984) Ph.D. Dissertation, U. of AZ.
- [3] Tedesco et al. (1989) Astron. J. 87, 580--606.
- [4] Bell et al., in preparation.
- [5] Jones (1988) Ph.D. Dissertation, U. of AZ.
- [6] Lebofsky et al. (1989) Icarus, in press.

#### LOW ALBEDO ASTEROIDS

Lebofsky, L. A. and Jones, T. D.

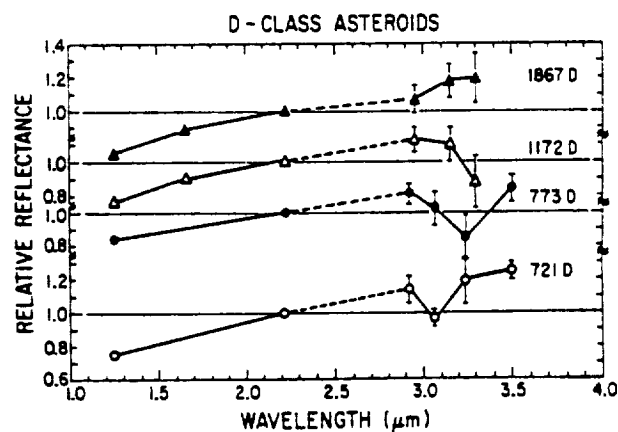
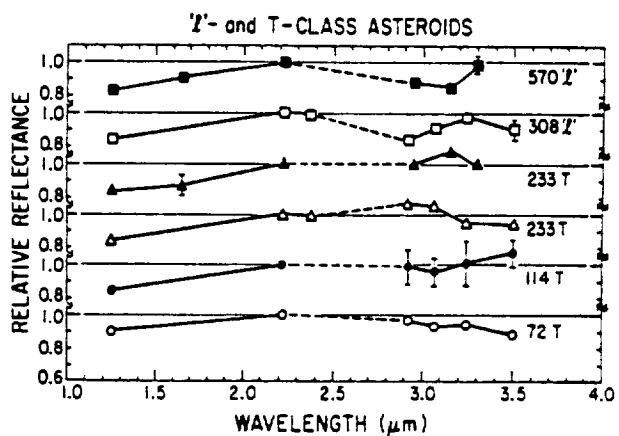
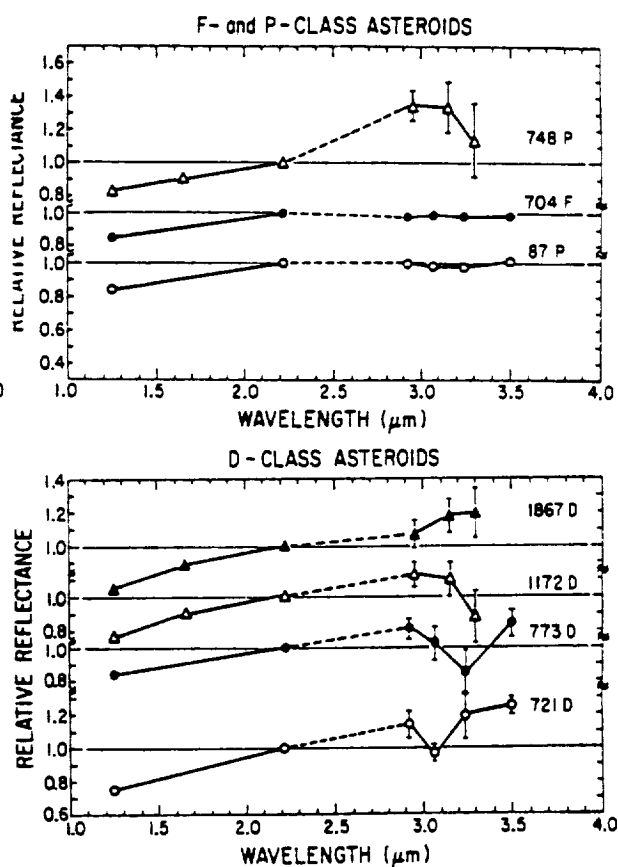
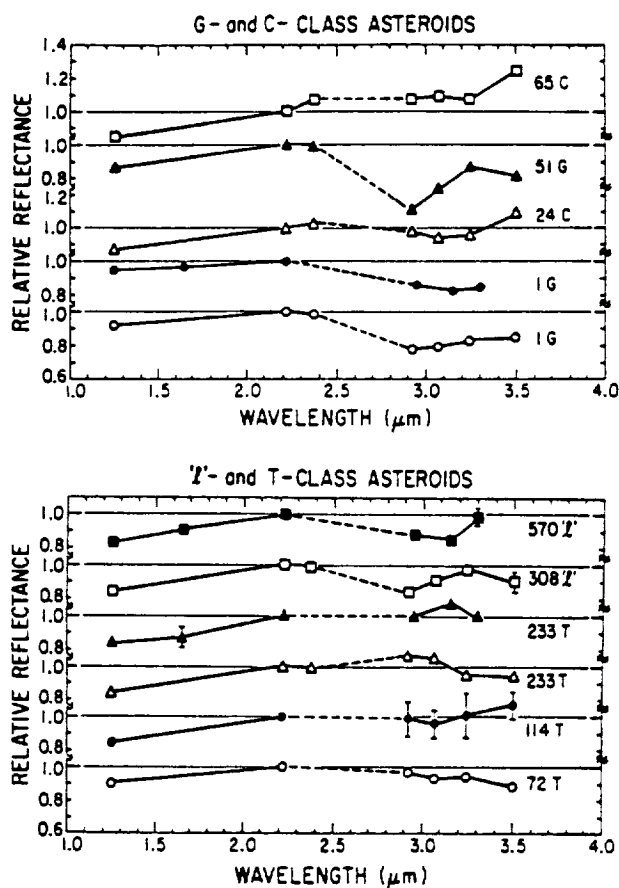


Fig. 1: Relative reflectance spectra (1.0 to 3.5  $\mu\text{m}$ ) of low albedo asteroids, most of which show the 3- $\mu\text{m}$  feature indicative of water of hydration.

Fig 2: Relative reflectance spectra of low albedo asteroids none of which show the 3- $\mu\text{m}$  feature indicative of water of hydration.

On The Origin and Aging of Comets  
Fred L. Whipple, Smithsonian Astrophysical Observatory

The enormous progress of recent years attained in measuring the composition and other physical properties of cometary nuclei now provides some hopes of solving problems of cometary genesis and geriatrics allowing for effects induced by varied environments and intrinsically by dimensions. Currently there are theoretical arguments that the Oort Cloud (consisting of very long-period comets) may not be the source from which short-period comets develop. It is vital in studies of cometary origins to determine whether there are intrinsic physical differences among short-period comets not induced by age, original size or environment. Among the long-period comets there may also be intrinsic differences dependent upon their place of origin. Thus a study of these possibilities is essential to improved understanding of cometary origins, their basic nature (or natures) and their role in the evolution of the solar system, particularly of the Earth.

The evidence from the Giotto space mission to P/Halley indicates strongly that the discrete nucleus is made of a large number of smaller "cometesimals" probably the order of a kilometer or so in size and smaller. Their densities are probably below  $1 \text{ g cm}^{-3}$  and their variable infall velocity was probably a few tens of meters per second. The result is a conglomerate of low-temperature cometesimal nuclei, essential unchanged from their origin, nestled within a "matrix" of crushed material, (ice grains of CHON, minerals and mixtures of the two) probably somewhat less volatile than the small nuclei.

During the passage of some  $4.5 \times 10^9$  years, the central region of the largest comets ( $> \sim 30 - 50 \text{ km}$  in dia.) probably were heated enough by radioactivity to move the most volatile ices to outer volumes of the nuclei and leave cores consisting largely of  $\text{H}_2\text{O}$  ice and mineral grains. For some comets the outer portions, before the comets were brought near the Sun, were subjected to cosmic-ray bombardment, increasing their volatility and activity at relatively great distances from the Sun (C/Kohoutek, 1973 XII, for example). Other received considerable heat from supernovae and young massive stars that left them with outer mantles of less active grains that may be blown off on approaching the Sun (C/Bowell, 1982 II, for example).

After the comets are captured into short-period orbits about the Sun, the normal aging processes of sublimation and heat transfer cover the nuclei with insulating mantles of mineral grains, so that activity is limited to small areas, even less than one percent of the total, and is variable erratically with time.

Hence among comets of a common origin and nature we may observe confusing variations in physical, chemical and activity characteristics, which may include:

- a) "New" comets, outer frosting of highly volatile materials.
- b) "New" comets blowing off thick grain mantles.
- c) Typical mix of cometesimals and matrix, activity being highly variable from area to area on the nucleus.
- d) Crushed matrix only.
- e) Cometesimals only.
- f)  $\text{H}_2\text{O}$  ice and grain only.
- g)  $\text{H}_2\text{O}$  ice almost alone.
- h) More volatile ices than  $\text{H}_2\text{O}$  along with variable grain compositions.

The author finds that observations of light curves, of discovery distances and of final distances from the Sun all indicate systematic aging of long-period comets with decreasing period. This result extends greatly the suggestions originally made by J. Oort and M. Schmidt nearly 40 years ago. But no evidence yet brings out or clarifies any basic generic differences among old comets, among new comets or between the two groups. For short-period comets the problem is exacerbated by the failure of orbital criteria to measure or even suggest the relative "ages" since the comets were captured into short-period low-inclination orbits. Thus suspected effects of aging are difficult to relate to time tables. Rendezvous space missions or more sophisticated missions to several comets may be needed to answer questions of origin.

The author is collating statistics of cometary properties in hopes of making progress in understanding origins. Of particular interest are the directions of aphelia among long-period comets related to galactic coordinates and physical properties. For example an elongated cluster of aphelia passing through the galactic pole noted by Delsemme contains relatively fewer comets with periods less than  $10^4$  years than does a cluster near the galactic plane and the elliptic studied by Biermann, Huebner and Lüst. The latter cluster contains some unusual comets including P/Halley (chance), the Kreutz sungrazers (chance?), Kohoutek (1973XII), C/1729 among 10 of the 20 comets listed by Marsden as "Great", and C/Morehouse 1908III. The other cluster seems to contain no comet of especial interest.

The dearth of new comets having aphelion directions within  $10^\circ$  of the galactic plane and around the polar regions was noted by R. Lüst and explained by several investigators as resulting from perturbations perpendicular to the galactic plane induced by the corresponding mass density gradient. Of the 17 such comets having aphelion within  $10^\circ$  of the galactic plane and not members of the cluster or sungrazers, only one has a period exceeding 16,000 yr. while 10 have periods in the range  $10^3$  to  $10^4$  yr. They show a systematic tendency to move normal to the galactic plane. Seven members are of special interest as they have aphelia at the intersection of the galactic and ecliptic planes within a range of only  $10^\circ$  in ecliptic longitude. All 7 are moving in direct orbits but with relatively high inclinations to the ecliptic ( $13 < i < 79^\circ$ ).

One asks whether the tendency for clustering near the two intersections of the galactic and ecliptic planes is coincidence or has a generic or dynamic basis. Are these comets and/or the other long-period comets different physically in any way from the short-period comets?

ORIGINAL PAGE IS  
OF POOR QUALITY

## STUDIES OF THE DYNAMICS OF PLANETARY RINGS

L. W. Esposito, T. G. Brophy, G. R. Steward and P.A. Yanamandra-Fisher (LASP, University of Colorado)

- 1) The Voyager RSS occultation data show that the optical depth in Janus 5:4 density wave decreases, whereas PPS and UVS data indicate an enhancement of optical depth. Two different scenarios have been proposed to explain this observation. At resonance locations, large particles break up into small particles which are transparent to RSS (Esposito, 1986). Although the A ring is relatively free of dust, there is a slight increase in the dust content of the outer A ring (inferred from Dones, 1987).

A bimodal size distribution for particles in Saturn's rings has been determined via an analysis of Voyager PPS, UVS and RSS occultation data. The size distribution is a power law down to about  $4\mu\text{m}$  and a gamma distribution for particles smaller than  $4\mu\text{m}$ . Our results for the Janus 5:4 density wave show the partial formation of a gap for both supra- and sub-centimeter sized particles, consistent with the predictions of Goldreich and Tremaine (1978). The number of sub-centimeter sized particles in the density wave is not significantly different from its value in uniform regions of the rings. Dust, however, is insensitive to the resonance; and the amount of dust present in the density wave is nearly twice that present in uniform regions of the rings.

These results show the response of the larger particles to the torque deposited by the density wave and the likely production of dust due to enhanced interparticle collisions.

- 2) A model kinetic equation is solved numerically for a flattened Keplerian disk using a phase-space fluid method which models the particle transport process as a Markov process. Ringlets composed of single sized particles and ringlets composed of two different sized particles are investigated. The accuracy of the new computational method is verified by close agreement with the analytical results of Shu and Stewart (1983), Goldreich and Tremaine (1978), Ward (1981), and Lin and Bodenheimer (1981), and the simulations of Spaute and Greenberg (1988) and Petit and Hénon (1988). The generally accepted theory of viscous spreading (e.g. Borderies, Goldreich and Tremaine, 1984) is verified for the special case of ringlets where all the particles are the same size. Ringlets composed of two components of particle size evolve in such a manner that the lighter particles are confined by the heavier particles. Some implications are that (1) a natural mechanism may sharpen the optical depth profile of edges even in the absence of an external forcing mechanism under some conditions. (2) In some cases intermediate optical depths are dynamically preferred. (3) Random velocities and spreading rates are dependent on the distribution of particle sizes. Simulation of the dominant features of observed planetary rings (sharp edges, microstructure) may have been excluded by some of the simplifying assumptions of analytic theories, such as single sized particles and the existence of a simple scalar viscosity.
- 3) The Krook kinetic equation formalism of Shu and Stewart (1985) has been extended to model the effects of non-uniform particle size is given a distinct mean velocity relative to the local circular orbit. This modification is required to model the azimuthal drift velocities that result from density gradients in non-uniform rings. Although the drift velocity has no effect on rings with only one particle size (where all particles have the same local mean velocity), the difference in drift velocities in multi-component systems cause rings particles to segregate by size. Second, the collision operator is modified to model the tendency of collisions to drive the system toward equipartition of random kinetic energy. The equipartition term has a strong effect on the velocity dispersion of the larger particles and can enhance the velocity dispersion gradient at ring edges. Numerical simulations of the Krook kinetic equation (Brophy and Esposito 1988) for two particle sizes show that the larger particles diffuse toward the center of a narrow ringlet whereas the smaller particles produce sharp density gradients at ring edges. These results have been confirmed by a numerical integration of two-component diffusion equations derived from the Krook equation. Since the diffusion equations are only valid for small density gradients, the direct simulation of the Krook equation is the preferred method for calculating sharp ring edges. Finally, we note that a similar tendency toward particle size segregation has also been reported by Petit and Hénon (1988), who used the entirely different approach of a Monte-Carlo n-body simulation.

## Papers Presented

Brophy, T.B., L.W. Esposito and G.R. Stewart, Simulation of asymmetric one and two component planetary rings, presented at the 20th annual meeting of the Division of Planetary Science of the American Astronomical Society in Austin, Texas, November 1988.

Esposito, L.W., Origin and Evolution of planetary rings, presented at the 20th COSPAR meeting in Helsinki, Finland, 20 July 1988.

Esposito, L.W., Origin and evolution of planetary rings, presented at the Lunar and Planetary Laboratory at the University of Arizona in Tucson, Arizona, 13 December 1988.

Esposito, L.W., Physics and microphysics of Uranus' rings, presented at the Uranus Conference in Pasadena, California, 18 June 1988.

Esposito, L.W., Recent advances in planetary ring studies, presented at the 20th annual meeting of the American Astronomical Society in Austin, Texas, November 1988.

Stewart, G.R., and T. G. Brophy, Particle size segregation in planetary rings, presented at the 20th annual meeting of the American Astronomical Society in Austin, Texas, November 1988.

Stewart, G.R., Planetesimal swarms perturbed by a distant protoplanet, presented at the Lunar and Planetary Science Conference at the Johnson Space Center, Texas, March 1989.

Yanamandra-Fisher, P.A. and L.W. Esposito, Variation of particle size distribution in Janus 5:4 density wave, presented at the 20th annual meeting of the Division of Planetary Science of the American Astronomical Society in Austin, Texas, November 1988

Yanamandra-Fisher, P.A., L.W. Esposito, and L.J. Horn, Comparison of density waves in the rings of Uranus and Saturn, presented at the Uranus Conference in Pasadena, California, June 1988.

## Publications

Brophy, T.G., and L.W. Esposito, Simulation of collisional transport processes and the stability of planetary rings, *Icarus*, 78, 181-205, 1989.

Brophy, T.G., G.R. Stewart, and L.W. Esposito, Simulation of two-component ring systems, *Icarus*, in press, 1989.

Colwell, J.E., L.J. Horn, A.L. Lane, L.W. Esposito, P.A. Yanamandra-Fisher, S.H. Pilorz, K.E. Simmons, M.D. Morrison, C.W. Hord, R.M. Nelson, B.D. Wallis, R.A. West, and B.J. Baratt, Voyager Photopolarimeter observations of Uranian Ring Occultations, *Icarus*, in press, 1989.

Esposito, L.W. and J.E. Colwell, Creation of the Uranus rings, *Nature*, in press, 1989.

Horn, L.J., Yanamandra-Fisher, P.A., Esposito, L.W., and Lane, A.L., Physical properties of Uranian Delta Rings, *Icarus* 76, 485-492, 1988.

## OUTER SOLAR SYSTEM NOMENCLATURE

Tobias Owen, Department of Earth and Space Sciences, State University of New York at Stony Brook, Stony Brook, NY 11794

During 1988, the principal activities supported by this grant consisted of meetings in conjunction with COSPAR (July 18-22 in Helsinki) and the IAU (August 10 in Baltimore) to discuss nomenclature in the outer solar system. The meetings were used primarily to develop and discuss banks of names to be used in the Neptune system after the Voyager encounter in August of 1989. A major issue at these meetings was the continuing effort to avoid duplication of names. In particular, names for new satellites of Neptune must not duplicate names of well-known asteroids. This eliminates the use of Amphitrite, even though she was Neptune's (Poseidon's) wife.

Categories that have been accepted are as follows:

New satellites: Names from Greek and Roman mythology associated with Neptune/Poseidon and the oceans in general.

Surface Features on Triton: Mythical names associated with water, but no names from Greece and Rome. E.g. primordial seas, water creatures, sacred lakes or rivers, frost deities (non-Norse).

The names in these categories from cultures around the world are being proposed and reviewed by committee members and will be applied during the Voyager encounters. They will then be subject to an additional review by the IAU Working Group on Planetary and Satellite Nomenclature before being passed on to the IAU Executive Committee for approval.



# LUNAR GEOLOGY FROM HIGH-RESOLUTION LUNAR RADAR IMAGES

S. H. Zisk, Planetary Geosciences, H.I.G., University of Hawaii,  
Honolulu, HI 96822

Accomplishments during the past year under this grant have been in three areas:

1. Initial analysis of new dual-polarization radar images of lunar craters;
2. Investigations into the relationship of radar backscattering to details of the planetary surface, using the full polarization-matrix terrestrial radar measurements made from the NASA DC-8 aircraft;
3. Analysis of the present surface and geologic history of the crater Alphonsus, with a view toward understanding a possible episode of late pyroclastic volcanism.

## I. CRATER STUDIES

New data has become available for a number of mid-size (30 to 120 km) craters. Stokes parameter images of all of them are being prepared and examined for the unusual polarization characteristics first observed on the floor of Copernicus last year. The new list includes the craters

Bullialdus	61 km	20.7S	22.2W
Eratosthenes	58 km	14.5N	11.3W
Kepler	32 km	8.1N	38.0W
Manilius	39 km	14.5N	9.1E
Menelaus	27 km	16.3N	16.0E
Plinius	43 km	15.4N	23.7E
Theophilus	100 km	11.4S	26.4E
Tycho	85 km	43.3S	11.2W

Earlier measurements also exist for the craters

Archimedes	83 km	29.7N	4.8W
Bessel	16 km	21.8N	17.9E
Copernicus	93 km	9.7N	20.0W

And finally, measurements also exist for various areas on the floor of the crater Alphonsus, but these are being analyzed as a separate project (see (III) below.)

## II. RADAR BACKSCATTERING THEORY

Several papers have been written during the past few years by H. Zebker and J. van Zyl of Jet Propulsion Laboratory on the methodology of analysis of the "quad-pol" data being obtained from the dual-polarization, quad-receiver terrestrial radar system being flown on the NASA DC8 flying laboratory. Work has been continuing here at U of H on the understanding and simplification of the mathematical techniques developed by Zebker and van Zyl, with a view toward using the improved understanding of the method, together with the new knowledge obtained from specific site studies of terrestrial volcanic and impact formations, to help in the analysis of the single-polarization, dual-receiver lunar data.

To this end, projects have been completed on the geological interpretation of the existing

radar and ground-truth data for areas around Snake River, Death Valley, and Meteor Crater. While most of the results are, unfortunately, site-specific, the one general result that has come out of this work is an apparent separation between short-wavelength (i.e. high spatial frequency) roughness, which mainly affects polarization ratio, and long-wavelength (i.e. low spatial frequency) roughness, which mainly affects cross-polarized signal strength. From a heuristic point of view, this result will not be a surprise to the planetary radar community; but the confirmation appears to be more quantitative than the usual arguments.

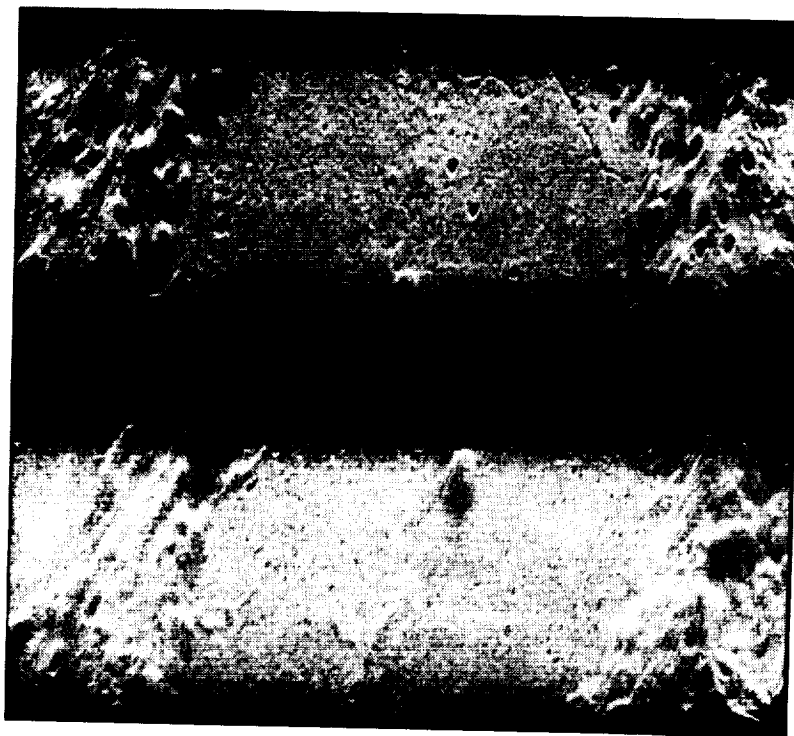
### III. ALPHONSUS STUDIES

It is now clear that, because of differences in the direction of illumination between the new high-resolution radar images and previous Lunar Orbiter and Ranger photographic images, the full complexity of the rille structure on the floor of Alphonsus has not been evident in past studies (cf Head, 197-). Several new major east-west-trending rilles are clearly delineated in the newest radar images (Fig. 1).

Fig. 1 shows polarized images of two neighboring areas on the floor of Alphonsus. The original data was obtained in April, 1989, as an output from some of the system testing of the Haystack Radar. The original radar resolution is 15 m in line-of-sight range. The processing sequence summed adjacent pixels in this image as an approximation to a multi-look image, in order to reduce the statistical effects of speckle. As a result, the surface resolution of the images as shown is approximately 80 m. Circular polarization was transmitted at 3.0-cm wavelength; these are images of the expected polarization (OC) echo. Each image covers about 40 km N-S (vertical direction) by 150 km E-W.

There may also be applications to the Lunar Bases study project, specifically the mapping of possible unbroken sections of lava tube, based on rille morphology.

Fig. 1. The crater Alphonsus: two radar images taken by the Haystack radar system during system tests.



## AUTHOR INDEX

- Ackerman, J.A. 387  
 Adams, J.B. 247, 255  
 Ahrens, T.J. 431, 444  
 Aist, L.L. 493  
 Archibald, S.M. 325  
 Arvidson, R.E. 12, 229, 250, 299, 301, 611, 613  
 Aubele, J.C. 9, 375
- Baker, V.R. 316  
 Baloga, S. 339, 390  
 Banerdt, W.B. 495, 498  
 Barlow, N.G. 437  
 Bartels, K.S. 213  
 Bassett, W.A. 197  
 Batson, R. 590, 591, 592  
 Becker, T.L. 240  
 Bell, J.F. 126  
 Benner, L.A.M. 54  
 Billideau, J. 599  
 Bindschadler, D.L. 15  
 Blount, G. 255  
 Boardman, J.W. 252  
 Boone, S. 198  
 Borgia, A. 517  
 Boring, J.W. 79  
 Boss, A.P. 156, 164, 168  
 Bowell, E. 129  
 Brakenridge, G.R. 310  
 Bregman, J. 261  
 Bridges, P. 590  
 Brophy, T.G. 629  
 Buratti, B.J. 230, 231  
 Burns, J.A. 95, 96, 97  
 Burns, R.G. 211, 213, 215, 217, 220
- Campbell, D.B. 287  
 Carr, M.H. 53, 427  
 Carroll, M.R. 193  
 Cellino, A. 112  
 Chadwick, D.J. 514  
 Champney, J.M. 158  
 Chapman, C.R. 477  
 Chapman, M.G. 322, 331, 349, 573  
 Christensen, P.R. 255, 416  
 Chyba, C.F. 224  
 Clancy, R.T. 242  
 Clark, B. 396  
 Clark, R.N. 264  
 Clow, G.D. 344  
 Coakley, T.J. 158
- Colvin, T.R. 602  
 Condit, C.D. 583  
 Coombs, C.R. 278, 281, 396, 399, 402  
 Craddock, R.A. 342, 547  
 Crawford, D.A. 487  
 Crisp, J. 390  
 Croft, S.K. 371, 437, 537, 567  
 Crown, D.A. 384  
 Crumpler, L.S. 21, 375  
 Cuzzi, J.N. 92, 97, 158  
 Cynn, H. 198
- Dale-Bannister, M. 611  
 Davies, M.E. 602, 603, 607  
 Davis, D. 112  
 Davis D.R. 115, 116, 146  
 Davis, P.A. 274, 491  
 De Hon, R.A. 325, 332, 334  
 Dimitriou, A.M. 545  
 Dobrovolskis, A.R. 158  
 Dohm, J.M. 501, 523, 526  
 Domingue, D. 129, 130  
 Durham, W.B. 69  
 Durisen, R.H. 92  
 Duxbury, T.C. 592
- Edwards, K. 592  
 Elston, W.E. 480  
 Epstein, S. 431  
 Eshleman, V.R. 295  
 Esposito, L.W. 629
- Fanale, F.P. 77, 119, 121, 293, 429  
 Farinella, P. 112, 115  
 Feng, M.S. 411  
 Ferguson, H.M. 454  
 Fink, J. 414, 416  
 Fink, U. 236  
 Fisher, P.C. 287  
 Fisher, D.S. 215, 217, 220  
 Frank, S. 287  
 Frank, S.L. 36  
 French, R.G. 91  
 Frey, H.V. 447, 449, 511
- Gaddis, L. 48, 123  
 Gaffey, M.J. 123  
 Garcia, P.A. 534, 600  
 Gault, D.E. 475  
 Geissler, P.E. 245, 246  
 Golombek, M.P. 491, 495, 498, 520

- Gooding, J.L. 222  
 Grant, J.A. 382, 483  
 Grant, T.D. 511  
 Greeley, R. 63, 66, 255, 358, 361, 384, 393  
 Greenberg, R. 72, 171  
 Grieve, R.A.F. 468  
 Griffiths, R. 414  
 Grinspoon, D.H. 149, 473  
 Grundy, W. 236  
 Guinness, E.A. 229, 250, 611, 613  
 Gulick, V.C. 316  
 Gurrola, E.M. 295
- Haberle, R.M. 344  
 Hager, B.H. 200  
 Hapke, B. 129, 130  
 Harmon, J.K. 287  
 Harris, A.W. 127, 129  
 Hartmann, W.K. 149, 439, 463, 473, 474  
 Hawke, B.R. 278, 281, 396, 399, 402, 459, 561  
 Head, J.W. 3, 15, 18, 21, 24, 26, 28, 30, 33, 36, 43, 203, 278, 287, 451  
 Helfenstein, P. 233, 237  
 Hillgren, V.J. 559  
 Hine, A.A. 287  
 Holloway, J.R. 196  
 Hood, L.L. 485  
 Howard, A.D. 313, 319, 355  
 Howington-Kraus, A. 534, 599, 600  
 Huang, Z. 485
- Jakosky, B.M. 252, 257  
 Janes, D.M. 554, 558  
 Jeanloz, R. 185, 186  
 Johnson, R.E. 85  
 Johnson, T.V. 231  
 Jones, T.D. 625  
 Jordan, R. 590  
 Jurgens, F. 12
- Kahle, A.B. 301  
 Kargel, J.S. 75, 371, 373  
 Kaula, W.M. 150, 162  
 Keil, K. 368  
 Kiefer, W.S. 200  
 Kim, Y. 600  
 King, J.S. 405, 408  
 Kipp, M.E. 187, 419  
 Kirby, S.H. 69  
 Kisiel, A.P. 405  
 KniTTLE, E. 186  
 Kochel, R.C. 307  
 Kolvoord, R.A. 95
- Komar, P.D. 366, 367, 368  
 Koumvakalis, A. 198  
 Kozak, R.C. 6, 13  
 Krishnamurthy, R.V. 431
- Lancaster, N. 255, 358  
 Leobofsky, L.A. 625  
 Lee, S.W. 242  
 Leith, A.C. 57  
 Li, J.Z. 411  
 Li, X. 186  
 Li, Z.L. 366  
 Lissauer, J. 101  
 Lucchitta, B.K. 245, 246, 328, 349, 380, 454, 617  
 Lucey, P.G. 278, 281, 459, 561  
 Lumme, K. 129  
 Lunine, J.I. 53, 60
- MacKinnon, D.J. 323  
 Magee, K.P. 30  
 Malin, M.C. 363  
 Matsui, T. 143  
 Maxwell, T.A. 342, 543, 547  
 McCormick, K. 468  
 McEwen, A.S. 53, 240, 351  
 McGill, G.E. 541, 549, 551  
 McGovern, P.J. 39  
 McKinnon, W.B. 54, 57  
 Melosh, H.J. 63, 187, 190, 419, 421, 424, 425, 434, 554, 558, 559  
 Meyer, D.L. 602  
 Moore, H.J. 290, 387  
 Moore, J. 346, 377  
 Morgan, H.F. 590, 591  
 Mosher, J.A. 231  
 Mueller, S. 57  
 Murchie, S.L. 451, 568  
 Mustard, J.F. 270  
 Myhill, E. 153
- Nakamura, Y. 108, 461, 563  
 Namiki, N. 143  
 Narr, W. 498  
 Nash, D.B. 82  
 Nelson, R.M. 88  
 Newman, W.I. 161, 162  
 Nicol, M. 198
- Oberst, J. 108, 461, 563  
 Ojakangas, G.W. 171  
 O'Keefe, J.D. 444  
 Ondrusek, J. 416  
 Orbock Miller, S.M. 307

- Ostro, S.J. 131  
Owen, T. 632
- Paige, D.A. 258  
Paolicchi, P. 112, 115  
Pappalardo, R. 66  
Parker, T.J. 336, 339  
Pattanaborwornsak, B. 274  
Patterson, C. 142  
Peale, S.J. 81, 101, 102, 167, 170  
Peltoniemi, J. 129  
Petroy, S.J.B. 301  
Phillips, R.J. 41, 46  
Pieters, C.M. 253, 270, 272, 276  
Plaut, J.J. 12, 299  
Plescia, J.B. 451, 498, 568, 588  
Pollack, J.B. 169, 261, 264, 361  
Posin, S. 393, 466  
Postawko, S.E. 429  
Pozio, S. 75  
Pratt, S.E. 270, 272
- Rank, D. 261  
Rice, J.W. 325  
Roberts, K.M. 24  
Robinson, M.S. 326, 575  
Roush, T. 261  
Roth, L.E. 293  
Ruden, S.P. 169  
Ryan, E.V. 116  
Ryder, G. 468
- Sagan, C. 224  
Salisbury, J.W. 267  
Salvail, J.R. 77, 119, 121  
Saunders, R.S. 12  
Schaber, G.G. 6, 13  
Schafer, F.J. 599, 601  
Schaffer, L.E. 96, 97  
Schubert, G. 177, 206  
Schenk, P.M. 54  
Schultz, P.H. 382, 442, 466, 475, 478, 483, 487, 530, 556  
Schultz, R.A. 447, 449, 503, 532, 539  
Scott, D.H. 322, 331, 501, 523, 526, 573, 615  
Senske, D.A. 26, 28, 287  
Shih, S.M. 367  
Shoemaker, C.S. 105, 586, 588  
Shoemaker, E.M. 105, 586, 588  
Showalter, M.R. 92  
Simmons, A.M. 408  
Simpson, R.A. 296  
Singer, R.B. 245, 246, 264  
Skypeck, A. 361
- Slade, M.A. 12  
Slavney, S. 611, 613  
Smith, M.O. 247, 255  
Smoluchowski, R. 103  
Smrekar, S. 46  
Smythe, W.D. 88  
Soderblom, L.A. 240  
Solomon, S.C. 39, 43, 203  
Spaute, D. 141, 142, 146  
Spudis, P.D. 274, 457, 459, 468, 561  
Squyres, S.W. 224  
Sraka, L.J. 487  
Stevenson, D.J. 137  
Steward, G.R. 629  
Stoker, C. 261  
Stolper, E. 193  
Strom, R.G. 110, 207, 437  
Sunshine, J.M. 272  
Suppe, J. 498  
Swann, J.D. 240  
Swayze, G.A. 264
- Tanaka, K.L. 323, 326, 331, 575  
Taylor, G.J. 468  
Thomas, P.C. 571  
Thompson, T.W. 290  
Tonks, W.B. 190  
Turcotte, D.L. 209  
Tuttle, M.J. 506  
Twist, D. 480  
Tyburczy, J.A. 431  
Tyler, G.L. 296
- Underwood, J.R., Jr. 618
- vanZyl, J.J. 299  
Verbiscer, A. 233  
Veverka, J. 233, 237  
Vickery, A.M. 424, 425, 434, 470, 472  
Vorder Bruegge, R.W. 33, 287
- Watters, T.R. 506, 509, 514  
Watts, A. 63  
Weathers, M.S. 197  
Weibel W.M. 162  
Weidenschilling, S.J. 146, 173, 174  
Weiss, B. 611  
Wetherill, G.W. 109, 139  
Whitford-Stark, J.L. 411  
Wichman, R.W. 478, 530, 556  
Williams, S.H. 580  
Williams, Q. 186  
Wisdom, J. 180  
Witteborn, F. 261

Wolfe, R.F. 105  
Wooden, D. 261  
Wu, S. 534, 599, 600, 601

Yanamandra-Fisher, P.A. 629

Zappalá, V. 112  
Zent, A.P. 293  
Zimbelman, J.R. 578, 580  
Zisk, S. H. 633  
Zuber, M.T. 493



## Report Documentation Page

1. Report No. NASA TM- 4130		2. Government Accession No.		3. Recipient's Catalog No.	
4. Title and Subtitle  Reports of Planetary Geology and Geophysics Program - 1988			5. Report Date  October 1989		
			6. Performing Organization Code		
7. Author(s)			8. Performing Organization Report No.		
			10. Work Unit No.		
9. Performing Organization Name and Address  Planetary Geosciences Program Solar System Exploration Division Office of Space Science and Applications			11. Contract or Grant No.		
			13. Type of Report and Period Covered Technical Memorandum		
12. Sponsoring Agency Name and Address  National Aeronautics and Space Administration Washington DC 20546			14. Sponsoring Agency Code		
			15. Supplementary Notes		
16. Abstract  This is a compilation of abstracts of reports from Principal Investigators of NASA's Planetary Geology and Geophysics Program, Office of Space Science and Applications. The purpose is to document in summary form research work conducted in this program during 1988. Each report reflects significant accomplishments within the area of the author's funded grant or contract.					
17. Key Words (Suggested by Author(s)) solar system evolution planetary geology and geophysics planetary geologic processes formation and evolution of planets comets and asteroids			18. Distribution Statement  Unclassified - Unlimited Subject Category 91		
19. Security Classif. (of this report) Unclassified		20. Security Classif. (of this page) Unclassified		21. No. of pages 660	22. Price A99





